

Advances in Sustainability Science and Technology

V. Bindhu

João Manuel R. S. Tavares

Ștefan Țălu *Editors*

Proceedings of Fourth International Conference on Inventive Material Science Applications

ICIMA 2021



 Springer

The Springer logo, which consists of a white chess knight piece on a pedestal, followed by the word 'Springer' in a white, serif font.

Advances in Sustainability Science and Technology

Series Editors

Robert J. Howlett, Bournemouth University & KES International,
Shoreham-by-sea, UK

John Littlewood, School of Art & Design, Cardiff Metropolitan University, Cardiff,
UK

Lakhmi C. Jain, University of Technology Sydney, Broadway, NSW, Australia

The book series aims at bringing together valuable and novel scientific contributions that address the critical issues of renewable energy, sustainable building, sustainable manufacturing, and other sustainability science and technology topics that have an impact in this diverse and fast-changing research community in academia and industry.

The areas to be covered are

- Climate change and mitigation, atmospheric carbon reduction, global warming
- Sustainability science, sustainability technologies
- Sustainable building technologies
- Intelligent buildings
- Sustainable energy generation
- Combined heat and power and district heating systems
- Control and optimization of renewable energy systems
- Smart grids and micro grids, local energy markets
- Smart cities, smart buildings, smart districts, smart countryside
- Energy and environmental assessment in buildings and cities
- Sustainable design, innovation and services
- Sustainable manufacturing processes and technology
- Sustainable manufacturing systems and enterprises
- Decision support for sustainability
- Micro/nanomachining, microelectromechanical machines (MEMS)
- Sustainable transport, smart vehicles and smart roads
- Information technology and artificial intelligence applied to sustainability
- Big data and data analytics applied to sustainability
- Sustainable food production, sustainable horticulture and agriculture
- Sustainability of air, water and other natural resources
- Sustainability policy, shaping the future, the triple bottom line, the circular economy

High quality content is an essential feature for all book proposals accepted for the series. It is expected that editors of all accepted volumes will ensure that contributions are subjected to an appropriate level of reviewing process and adhere to KES quality principles.

The series will include monographs, edited volumes, and selected proceedings.

More information about this series at <http://www.springer.com/series/16477>

V. Bindhu · João Manuel R. S. Tavares · Ștefan Țălu
Editors


Proceedings of Fourth International Conference on Inventive Material Science Applications

ICIMA 2021

 Springer

Editors

V. Bindhu
PPG Institute of Technology
Coimbatore, India

João Manuel R. S. Tavares 
Faculdade de Engenharia da Universidade
do Porto
Porto, Portugal

Ștefan Țălu
The Technical University of Cluj-Napoca
Cluj-Napoca, Romania

ISSN 2662-6829

ISSN 2662-6837 (electronic)

Advances in Sustainability Science and Technology

ISBN 978-981-16-4320-0

ISBN 978-981-16-4321-7 (eBook)

<https://doi.org/10.1007/978-981-16-4321-7>

© The Editor(s) (if applicable) and The Author(s), under exclusive license to Springer Nature Singapore Pte Ltd. 2022

This work is subject to copyright. All rights are solely and exclusively licensed by the Publisher, whether the whole or part of the material is concerned, specifically the rights of translation, reprinting, reuse of illustrations, recitation, broadcasting, reproduction on microfilms or in any other physical way, and transmission or information storage and retrieval, electronic adaptation, computer software, or by similar or dissimilar methodology now known or hereafter developed.

The use of general descriptive names, registered names, trademarks, service marks, etc. in this publication does not imply, even in the absence of a specific statement, that such names are exempt from the relevant protective laws and regulations and therefore free for general use.

The publisher, the authors and the editors are safe to assume that the advice and information in this book are believed to be true and accurate at the date of publication. Neither the publisher nor the authors or the editors give a warranty, expressed or implied, with respect to the material contained herein or for any errors or omissions that may have been made. The publisher remains neutral with regard to jurisdictional claims in published maps and institutional affiliations.

This Springer imprint is published by the registered company Springer Nature Singapore Pte Ltd. The registered company address is: 152 Beach Road, #21-01/04 Gateway East, Singapore 189721, Singapore

The conference is dedicated to the outstanding reviewers, authors, editors, and organizers of the conference to commemorate their inevitable contributions to advanced materials science and related fields. Without their participation, it would be impossible to hold 4th ICIMA 2021 successfully and ensure high quality of papers published in the conference proceedings.

Preface

We are very pleased to introduce the Proceedings of the 4th International Conference on Inventive Material Science Applications (ICIMA 2021). The 4th ICIMA event was held at PPG Institute of Technology, from May 14 to 15, 2021.

One of the significant and valuable aspects of this 4th conference edition is the way it brings together researchers, academicians, and engineers from various countries and initiates discussion on relevant issues, challenges, opportunities, and research findings. The primary focus of ICIMA 2021 is to provide an excellent platform for the conference participants to share and exchange novel and innovative ideas of original research and to build international association. The main intend of this conference is to create a smart and advanced research landscape for the areas of inventive material science.

As 282 number of submissions are received from different parts of the world, only 66 submissions were accepted as full papers for publication and presentation in ICIMA 2021. These papers provide brief illustration for current research on relevant topics, covering sustainable strategy, micro-/nano-materials, bio-materials, hybrid electronic materials, innovative electronic materials processing, computational material science, material characterization, fabrication, and synthesis technologies.

The success of the conference is due to the collective efforts of all the reviewers and advisory/review board members. We would like to express and record our gratitude and appreciation to the authors for their contributions. Many thanks to the reviewers, who helped us to maintain high-quality manuscripts included in the proceedings. We also express our sincere thanks to the members of the conference committees and organizing team for their hard work. We wish that all the authors and delegates find ICIMA 2021 proceedings interesting, exciting, and inspiring.

Coimbatore, India
Porto, Portugal
Cluj-Napoca, Romania

Dr. V. Bindhu
Dr. João Manuel R. S. Tavares
Dr. Ștefan Țălu

Acknowledgements

The Organizing Committee of the 4th ICIMA 2021 would like to acknowledge all supporters and editors of this conference. The organizers are pleased to acknowledge the keynote speakers for their presentation on ICIMA 2021. Also we wish to acknowledge all the valuable services provided by the reviewers.

On behalf of the organizers, editors, and readers of this conference, we wish to thank the reviewers and conference technical and non-technical committee members for their time, hard work, and dedication to this conference. Without their continual services, the editors could not be able to maintain the high-quality standards of material science research. The organizers wish to acknowledge the technical program chairs for their valuable and continuous suggestion, discussion, and cooperation in organizing the conference. The organizers also wish to acknowledge the speakers and participants, who attended this conference although there is a pandemic situation across the globe.

We are pleased to acknowledge the great efforts invested by the committee in reviewing the papers submitted to the conference and organizing the sessions to enable the participants to gain maximum benefit. We would also like to express our gratitude to the unbelievable number of authors for contributing their innovative and novel research results to the conference.

Special thanks to Springer publications. We also hope to meet again in the upcoming conferences.

Contents

1	Method of Heap Leaching of Copper from Off-Balance Ore Dumps	1
	Sokhibjon T. Matkarimov, Saodat B. Mirzajonova, Tursinoy P. Karimova, Malika S. Saidova, and Nigora K. Bakhodirova	
2	A Comparative Analysis of Step Channel TFET with the Impact of Work Function Engineering	9
	Manshi Kamal and Dharmendra Singh Yadav	
3	A Review on Biomaterials Based Biosensors for Bilirubin Detection	23
	Dheeraj Dhanvee Kairamkonda, Shreeja Bitla, and Harish Kuchulakanti	
4	Dimensional Optimization of Low-Frequency Piezoelectric Nanoenergy Harvesters	41
	Swathy S. Panicker and P. R. Sreenidhi	
5	A Review on Materials for Integrated Optical Waveguides	55
	Padmaja Jain and Rajini V. Honnungar	
6	Synthesis and Performance Evaluation of Supercapacitor Based on Manganese Loaded Biochar/Polyaniline Nanocomposite	67
	Diana Thomas, Noeline B. Fernandez, Manohar D. Mullassery, and R. Surya	
7	Assessment of Antibacterial Properties of Natural Extracts for Wound Healing Applications	81
	S. Patricia Nancy, S. Shanchana, S. Udhayanila, T. Divya, and Bharathi	

8	Current and Emerging Technologies for Resonance Frequency Analysis-Based Devices for Measuring Dental Implant Stability: A Review	87
	Srujana Joshi, Urvi Bora, Niharika Karnik, Karan Bhadri, and Pankaj Dhattrak	
9	Influence on Seismic Response Owing to the Variation in Size and Spacing of Building in a Building Cluster	103
	Shubham Srivastava and Rajesh Kumar	
10	Effect of Aluminium in Magnesium Alloy Fabricated Through the Squeeze Casting Process	113
	Navin Kumar and Shatrughan Soren	
11	Methods of Protection Against Destruction of Refractory Materials Used for Lining of Autogenous Smelting Furnaces	121
	Sokhibjon T. Matkarimov, Sardor K. Nosirkhujayev, Abdukahhar M. Saynazarov, Bakhriddin T. Berdiyarov, and Zaynobiddin T. Matkarimov	
12	Nano Biomaterials for Tissue Engineering Applications—Short Review	131
	Sasireka Rajendran, Vinoth Rathinam, Sugumari Vallinayagam, and Vipin Kumar Sharma	
13	Static Deformation of an Orthotropic Multilayered Elastic Half Space by Two-Dimensional Surface Loads	141
	Jatinder Kaur, Pankaj Thakur, and Namrata Singh	
14	Comparative Study and Analysis of HVAC Systems Using Solid and Liquid Desiccant Dehumidification Technology	151
	Abhijith Shah, Himank Santosh Sankhe, Yogesh Koushal Sharma, Sayli Sankhe, and R. V. Kale	
15	Optimization of Process Variables in Abrasive Water Jet Machining of Nimonic C-263 Super Alloy Using Taguchi Method	167
	S. Madhavarao, Ravi Varma Penmetsa, Ch. Rama Bhadri Raju, and Hema T. Raju Gottumukkala	
16	Material Composition and Development of Technology for Processing the Tailings of the Copper-Concentrating Plant of JSC “Almalyk MMC”	179
	J. M. Bekpulatov, M. M. Yakubov, Kh. Ahmedov, and Sh. A. Mukhametjanova	

17 Optimization of Vibration-Based Condition Monitoring of Motor Drive End Using Taguchi Technique: A Case Study on Milling Machine	187
B. K. Pavan Kumar, Yadavalli Basavaraj, N. Keerthi Kumar, and M. J. Sandeep	
18 Phase Change Materials and Techniques to Enhance Performance of Latent Heat Storage Based on Geometrical Considerations: A Review	195
Sangeeta S. Mundra and Sujit S. Pardeshi	
19 Performance Analysis of Different Types of Solar Photovoltaic Cell Techniques Using MATLAB/Simulink	203
M. Murali, CH Hussaian Basha, Shaik Rafi Kiran, P. Akram, and T. Naresh	
20 Investigation on Microstructural Characteristics of Zn Alloy MMC for Bearing Application	217
Santosh Janamatti, Umesh Daivagna, Madeva Nagaral, and Veerabhadrapa Algur	
21 Studies on Polymer Composites for Producing Hybrid Material Sheets Processed by Friction Stir Welding	227
Harish Kumar and S. V. Satish	
22 Optical and Electrical Properties of ZnO Dispersed Polymer Nanocomposites Films	237
Sushma Jha, Vaishali Bhavsar, K. P. Sooraj, Mukesh Ranjan, and Deepti Tripathi	
23 Experimental Study of Heap Leaching of Secondary Sulphides Using H₂SO₄ and NaCl: A Chilean Mining Company Case	253
Manuel Saldaña, Luis Ayala, Edelmira Gálvez, and Javier González	
24 A Posteriori Analysis of Analytical Models for Flotation Circuits Using Sensitivity Analyses	265
Edelmira Gálvez, Luis Ayala, Javier González, and Manuel Saldaña	
25 Modeling the Dynamic of a SAG Milling System Through Regression Models and Neural Networks	281
Manuel Saldaña, Luis Ayala, and Javier González	
26 Investigation of Structural and Optical Properties of PMMA/PVdF-HFP Polymer Blend System	295
Maheshwar Reddy Mettu, A. Mallikarjun, M. Vikranth Reddy, M. Jaipal Reddy, and J. Siva Kumar	

27	Theoretical Analysis of Functional Materials and Finishes for Anti-Ballistic Fabrics	307
	Gurumurthy B. Ramaiah, Asmamaw Tegegne, Bahiru Melese, Seblework Mekonnen, Eshetu Solomon, Kidist Tadesse, and Robel Legese Meko	
28	Rayleigh-Bénard Convection in the Presence of Synchronous and Asynchronous Thermal Rigid Boundary Conditions	323
	Palle Kiran	
29	Prediction of Aluminum Alloys Composition for Industrial Requirement Using Data Analysis Techniques	337
	M. Arunadevi, C. P. S. Prakash, Venugopal Prasanna Joshi, Rohit Shanakar Palada, Ravut Dixit, and Rahul Pandappa Chinnannavar	
30	Design of an Adaptive Fuzzy Logic Controller for Solar PV Application with High Step-Up DC-DC Converter	349
	CH Hussaian Basha, P. Akram, M. Murali, T. Mariprasath, and T. Naresh	
31	Nonlinear Thermal Instability of Couple-Stress Fluids in Porous Media Under Thermal Modulation	361
	S. H. Manjula and Palle Kiran	
32	Effect of Ceramic Particles on AMMC Through Stir Casting Method—A Review	373
	Ramesh Kurbet, Basavaraj, C. M. Amruth, and S. L. N. Jayasimha	
33	Preparation of Si-Graphite Composites as Anode Material in Li Ion Batteries	389
	Kevin Vattappara, Sushmit Bhattacharjee, Yashdeep Srivastava, Benson K. Money, and Parvati Ramaswamy	
34	Morphological, Spectroscopic, Structural and Electrical Properties of Mg⁺² Ion Conducting PMMA: PVDF-HFP Blend Polymer Electrolytes	401
	A. Mallikarjun, M. Sangeetha, Maheshwar Reddy Mettu, M. Vikranth Reddy, M. Jaipal Reddy, J. Siva Kumar, and T. Sreekanth	
35	Modelling of Acetaminophen Removal from Wastewater Using Response Surface Methodology	417
	P. Varshini, P. Chinnaiyan, K. Abinaya, R. Karthikeyan, and V. Manirajasekaran	
36	Speculative Testament of Corrosive Behaviour of Aluminium Composite Welded by FSW	429
	N. M. Siddesh Kumar, M. Sadashiva, and J. Monica	

37	Electrifying the Future with Green Vehicle: A Review on Prospects and Issues of Electric Vehicle in India	441
	Abhaysinha G. Shelake and Pravin R. Minde	
38	Multi-layered Epoxy Composites of Micro and Nano Bi₂O₃ and Ta₂O₅ for γ-ray Shielding	457
	Srilakshmi Prabhu, Ajith Geejo, Rohit Dagar, Divyasree Chakraborty, Andrews Jacob, Sriya Paul, S. G. Bubbly, and S. B. Gudennavar	
39	Carbon-Related Materials for Tribological Application	469
	Nitish Singh Jammoria, Mir Irfan Ul Haq, and Ankush Raina	
40	Cobalt Extraction Mechanisms	485
	Marcelo Rodríguez, Kevin Pérez, Luís Ayala, Rossana Sepúlveda, and Edelmira Gálvez	
41	Magnesium Extraction Mechanisms	495
	Yessica González, Edelmira Gálvez, Jonathan Castillo, and Norman Toro	
42	Machinability Study of IS2062 Steel During Milling Using Different Coated Tools: A Review	503
	Atul P. Kulkarni, Kedar Ramdasi, Omkar Kulkarni, Priya Murkewar, and Sampada Dravid	
43	Post-combustion Effect on Nickel and Cobalt Extractions from the Caron Process	515
	Hugo Javier Angulo Palma, Angel Legrá Legrá, Alisa Lamorú Urgellés, Edelmira Gálvez, and Jonathan Castillo	
44	Design and Analysis of Neural Network-Based MPPT Technique for Solar Power-Based Electric Vehicle Application	529
	M. Murali, CH Hussaian Basha, Shaik Rafi Kiran, and K. Amaresh	
45	Mechanical and Durability Properties of High Strength Concrete Incorporating Different Combinations of Supplementary Cementitious Materials: A Review	543
	B. Sankar and P. Ramadoss	
46	Fabrication of Rechargeable Lithium Ion Coin Cell Using a Biopolymer Electrolyte (Cellulose Acetate)	559
	R. Venkata Jyotsna, M. Vengadesh Krishna, Selvasekarapandian, P. Chandrasekar, and S. Monisha	
47	Building Knowledge Graph End to End: Data Integration with Semantic Web	569
	M. Lissa and V. Bhuvaneshwari	

48	Ordered Pt₃M (M = Early d-Block Metals) Intermetallic Nanocrystals: Synthesis and Electrocatalysis	585
	D. Saritha, N. Mahender Reddy, and Gubbala V. Ramesh	
49	Modern Progression in Anode Materials for Lithium-Ion Batteries: Review	595
	Gubbala V. Ramesh, N. Mahendar Reddy, and D. Saritha	
50	Experimental Investigation of Sliding Wear Characteristics on Aluminium-Based Metal Reinforced with SiC, Al₂O₃ and Cadmium Sulphide	605
	Sachin Pande, Ravindra G. Tikotkar, Asifqbal M. Doddamani, and Syed Sameer Hussain	
51	Investigation of the Influence of Impeller Type, Speed and Vertical Height on the Mixing Efficiency of a Biogas Plant Stirrer	617
	Temilola T. Olugasa, J. O. Omokayode, and N. Idusuyi	
52	Studies on Chemical Resistance, Swelling Behaviour and Biodegradability of Natural Fiber-Reinforced Biocomposite	635
	G. Sujaya and V. Anbazhagan	
53	Construction and Characterization of Graphene-Polyvinyl Alcohol Nanocomposite as Thermoelement With High ZT Factor	647
	K. R. V. Subramanian, B. V. Raghuvamsi Krishna, G. S. Rohith, Raji George, and T. Nageswara Rao	
54	Design of Nanoscale TIEO-Based Arithmetic Circuits Using QCA Implementation Paradigm	663
	M. Jagadeeswari, C. S. Manikandababu, M. Aiswarya, and S. Manju	
55	Experimental and Numerical Determination of Natural Frequency of Woven Basalt Fibre-Vinyl Ester-Reinforced Composite Plates	677
	J. Hemanth Kumar, Mahesh Dutt, and E. R. Babu	
56	Mechanical Characteristic of Al 6063 Pipe Joined by Underwater Friction Stir Welding	689
	Ibrahim Sabry, N. Gad Allah, Mohamed A. Nour, and M. Abdel Ghafaar	
57	Experimental Investigation on Mechanical Properties of Epoxy with Hybrid Filler Composites	701
	J. Balaji, M. M. Nataraja, K. L. Vinod, and K. Sadashiva	

58 Morphological and Thermal Behaviour of Monomer Dispersed Liquid Crystal	715
Santosh Mani, Sameer Hadkar, Krishnakant Mishra, Pushpendra Rai, and Pradip Sarawade	
59 Design and Analysis of Penta-Magnetic Tunnel Junction Circuit with Transmission Gate Logic	725
C. S. Manikandababu, M. Jagadeeswari, S. Manju, and M. Aiswarya	
60 Recent Progress in Energy Management System for Fuel Cell Hybrid Electric Vehicle	737
Md. Rawshan Habib, Koushik Ahmed, Ahmed Yousuf Suhan, Abhishek Vadher, Md. Rashedul Arefin, Md Shahnewaz Tanvir, Sayad Hasan Rizvee, and Md. Ashiqur Rahman Swapno	
61 Comparative Study of Application of Artificial Neural Networks for Predicting Engineering Properties of Soil: A Review	751
Arun W. Dhawale and Shailendra P. Banne	
62 Structural and Photocatalytic Studies of Ce and Dy Co-doped ZnO Nanoflowers	765
Syed Irtiqa and Atikur Rahman	
63 Investigate the Flexural Property of Polylactic Acid (PLA)-Based 3D Printed Part	779
Nitesh Kumar Dixit and Shweta Mishra	
64 Mathematical Modeling Influence Electromagnetic Wave Plane on Functional Materials	787
Olena Komisarenko, Nataliia Titova, Ievgev O. Zaitsev, and Ilona Chernytska	
65 Design and Analysis of Combinational Circuits Using Reversible and Irreversible Gates	801
S. Saiteja, Md. Munwar, Y. MadhukarReddy, and A. PramodKumar	
66 Strengthening a Pavement Layer by Using Fly Ash	811
Mudigonda Harish kumar and C. Freeda Christy	
Author Index	819

About the Editors

Dr. V. Bindhu received the B.E. degree in Electronics and Communication Engineering from Bharathair University, Coimbatore in 2002 and M.E. Degree in Applied Electronics from Anna University, Chennai in 2007 and Ph.D. Degree from Anna University, Chennai in 2014. She has 10 years of teaching experience and 5 years of research experience. Currently, she is a professor at PPG Institute of Technology, Coimbatore. Her area of interest includes Signal processing, and VLSI Design.

Dr. João Manuel R. S. Tavares graduated in Mechanical Engineering at the Universidade do Porto, Portugal in 1992. He also earned his M.Sc. degree and Ph.D. degree in Electrical and Computer Engineering from the Universidade do Porto in 1995 and 2001, and attained his Habilitation in Mechanical Engineering in 2015. He is a senior researcher at the Instituto de Ciência e Inovação em Engenharia Mecânica e Engenharia Industrial (INEGI) and Full Professor at the Department of Mechanical Engineering (DEMec) of the Faculdade de Engenharia da Universidade do Porto (FEUP).

João Tavares is co-editor of more than 60 books, co-author of more than 50 book chapters, 650 articles in international and national journals and conferences, and 3 international and 3 national patents. He has been a committee member of several international and national journals and conferences, is co-founder and co-editor of the book series “Lecture Notes in Computational Vision and Biomechanics” published by Springer, founder and Editor-in-Chief of the journal “Computer Methods in Biomechanics and Biomedical Engineering: Imaging & Visualization” published by Taylor & Francis, Editor-in-Chief of the journal “Computer Methods in Biomechanics and Biomedical Engineering” published by Taylor & Francis, and co-founder and co-chair of the international conference series: CompIMAGE, ECCOMAS VipIMAGE, ICCEBS and BioDental. Additionally, he has been (co-) supervisor of several M.Sc. and Ph.D. thesis and supervisor of several post-doc projects, and has participated in many scientific projects both as researcher and as scientific coordinator.

His main research areas include computational vision, medical imaging, computational mechanics, scientific visualization, human-computer interaction and new product development.

Dr. Ștefan Țălu works as a Professor in The Technical University of Cluj-Napoca, The Directorate of Research, Development and Innovation Management (DMCDI), Romania. His Research Interest includes Mechatronic systems, Optimization algorithms, Applied Mathematics, Mechanical Engineering, Material science, Computer graphics, Modeling and simulation, Fractal/multifractal geometry applied in technique.

Chapter 1

Method of Heap Leaching of Copper from Off-Balance Ore Dumps



Sokhibjon T. Matkarimov, Saodat B. Mirzajonova, Tursinoy P. Karimova, Malika S. Saidova, and Nigora K. Bakhodirova

Abstract The article deals with heap leaching of copper ores taken from the dump of the Kalmakyr mine. The depletion of the copper raw material base's reserves is focused on the Almalyk mining and metallurgical company's work. Despite the company also requires to find additional copper-containing geo-resources, the source of significant reserves of raw materials containing non-ferrous metals is the oxidized ores of Kalmakyr deposits dump. However, the processing of these ores with the traditional flotation method produces low-grade concentrates with low metal recovery (35–50%). Studies have found that the most promising direction of processing the ores is leaching. Simultaneously, as an object of physico-chemical technologies of great practical interest, it contains up to 0.04% mineralized copper water for performing natural leaching on overburden dumps.

Keywords Leaching in heaps · Copper · Sulfuric acid · Oxidized ore · Lean ore · Sample · Solution · Settling tank · Perforation · Percolation · Hydrometallurgy · Stack

1 Introduction

Following independence, the republic's mining and metallurgical industries confronted a slew of challenging issues. For starters, the complete depletion of rich and easily discovered ore deposits drives up environmental protection standards while simultaneously increasing the need for nonferrous metals such as copper and its associated elements. Increasing the complexity of raw material use, recycling all

S. T. Matkarimov (✉) · S. B. Mirzajonova · T. P. Karimova · M. S. Saidova · N. K. Bakhodirova
Tashkent State Technical University named after Islam Karimov, Tashkent, Uzbekistan

S. B. Mirzajonova
e-mail: mirzajonovasaodat@tdtu.uz

T. P. Karimova
e-mail: tursunoykarimova@tdtu.uz

N. K. Bakhodirova
e-mail: bakhodirovanigora@tdtu.uz

important components, and developing and implementing waste-free technologies are all pressing issues [1–10].

Nonferrous metal deposits concentrated in dumps and tailings at Almalyk MMC JSC are currently estimated to be in the hundreds of millions of tonnes. For instance, around 150 million tonnes of off-balance-sheet ores have accumulated in the Almalyk Mining and Metallurgical Company's landfills (AMMC). Substandard ores end up in dumps, and mountain losses remain in the subsoil of deposits. This raw material contains a high concentration of non-ferrous, rare, and noble metals [1, 11].

There is another component to the issue. Because of the spontaneous leaching of copper, zinc, lead, molybdenum, arsenic, and other metals, off-balance and off-balance ore dumps are a long-term source of environmental pollution.

2 Objects and Method of Research

However, the use of cumulus leaching is limited by particular requirements for the composition and preparation of ores: the ore should be as porous as possible, with microscopic channels that contribute to the penetration of solutions, the rock should crack, crumble under the action of the solution. Secondary sulfides (chalcosine and covelin) are successfully treated. Primary colchedans cannot be dissolved. The process requires favorable climatic conditions—climate dryness and high annual average temperature. The preparation of an impenetrable bed under the dump is essential. Experiments have found that with the wretched bed, copper extraction can decrease by 30–40%. Soil is prepared with a slope from 3.5° to 8°. The bed is usually designed from a layer of clay or sludge of concentration plants, wetted with oil and then dried (this operation is repeated several times). Only under such conditions is an impermeable layer obtained [1, 12].

For good results, the ore must be leached periodically and wholly dried. Suppose the surface of a piece of the ore having these beneficial properties is wetted with a solution. In that case, it will penetrate the pores of pieces and pass through the capillaries (if the veins are open at both ends) and have a dissolving effect on copper minerals. When the part dries, soluble salts (copper cuprous crystals) from the capillary under the influence of reverse capillarity will protrude to the surface.

In Arizona (USA), heap leaching is subjected to large dumps of rock with a copper content of 0.26–0.8%. Copper is leached with mine water. Water from the mine is first sent to the settling tanks, then to pyrite filters to produce divalent iron, and only then to cementation for the incomplete removal of copper. After passing the heaps, the solutions are sent again for cementation. Copper recovery is about 80%. In Uzbekistan, the heap leaching method is planned to be applied to the Kalmakyr deposit dump's poor ores.

Copper should be in ore in the form of easily leachable compounds (chalcosine or chalcantite—natural copper cuprous or oxides). Its reserves in the subsoil should be sufficient to justify the costs necessary to organize the process.

Sulfuric acid leaching of oxidized copper ores was carried out at two large plants in Chile, carried out at several plants in the USA, and one plant in the Congo. Each of these plants has its specific features related to ores' chemical composition and their physical properties. The characteristics of the technology of each of these enterprises are set out in the literature. Due to the sulfuric acid leaching in Chuquicamata in Chile, production of the zone of oxidized ores and the transition to the production of sulfide zones have now been replaced by flotation. It is no longer used at all [13].

Over the past decades, there has been a significant depletion of rich ores, especially in industrialized areas. In this regard, it became necessary to find and introduce new methods for producing metals from non-traditional raw materials sources. Such sources include oxidized, poor sulfide, and rich hard-to-rich non-ferrous metal ores. Off-balance and off-balance ore dumps and "treated" deposits are a long-term environmental pollution source due to the spontaneous leaching of copper, zinc, lead, arsenic, and other metals from them. The most rational way to avoid such objects' harmful impact on the environment is to intensify the natural leaching process by organizing heap and underground leaching (HL and UL) [1].

3 Results of the Proposed Research

The dump of the Kalmakyr mine with an ore mass of more than 4 million tons is filled on a slash with a slope of 5.7%, and lime forms an ellipse with a plan size of 380×240 m; the maximum dump height is up to 25 m. The top of the dump is divided into 12 ponds, where the amount of ore under the ponds ranges from 100 to 300 thousand tons, and the area of ponds is from 3 to 10 thousand m^2 .

Chemical composition of ore, %: Cu—0.25–0.27; Fe—5.00; S—1.23; Al_2O_3 —13.02; SiO_2 —60.46; CaO—1.81; MgO—2.38. Phase composition of copper in ore, %: oxides—29.6; secondary sulfides—18.6; primary sulfides—51.8. Granulometric composition of ore samples taken at the beginning, in the middle and at the end of the discharge of HL dump, %: (–400/200 mm)—7.3–18.2; (–200/100 of mm)—5.3–9.1; (–100/50 mm)—5.5–9.2; (50/10 mm)—24.3–36.6; (–10/0.0)—38.7–61.1.

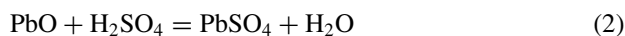
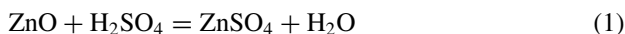
The soils at the dump base are composed of loess-shaped loams, with a particle size (–0.01 sound 0.005 mm), quartz, feldspar, kaolinite, and hydraulic slides. In terms of granulometry and composition, they belong to the dust of prominent rocks (–0.01–0.005 mm), containing approximately equal amounts of clay and dog particles. From a mixture of loam and bitumen, a base was built for a dump 150 mm thick, bitumen consumption—140 g per $1 m^3$ of soil [14].

The KB technology of copper from oxidized ores includes the following stages: crushing, laying ore on a hydro isolated base guide, leaching, extraction of copper from a productive solution (PR), retraction of copper, electrolysis of copper from a re-extract, and tailings disposal. The detailed flow chart of this process is shown in figure.

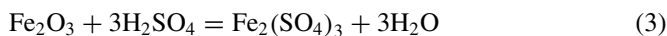
Ore crushing before FP is performed to increase technical and economic parameters of ore processing. In some cases, this operation's introduction leads to an increase in metal recovery by 1.5–2 times. Ore crushing before KB is carried out with sizes from 1000–300 to 50–7 mm (initial cereal content depends on ore extraction conditions and final—on the material composition of raw materials). The operation is most often carried out in standard cheek and cone crushers. Suppose a large amount of clay component is present in the crushed product, the eye hurts the filtration properties. In that case, the ore is pelleted with a sulfuric acid additive before being stacked. The addition of sulfuric acid at the clumping stage allows for shortening the duration of leaching.

Consider that the feedstock complex nature was essential to investigate the behavior of the valuable components associated with copper in sulfuric acid solutions to ensure the complete separation of copper into a separate product and the selectivity of copper recovery [2–9, 14, 15].

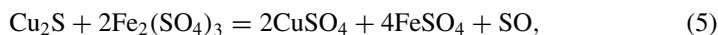
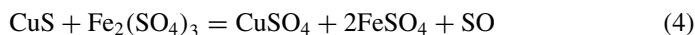
When leaching the product with sulfuric acid, in addition to the above reactions, reactions take place with the participation of primary minerals and impurities (FeO, ZnO, PbO, Fe₂O₃):



Impurities such as iron oxide also dissolve:



the resulting Fe₂(SO₄)₃ reacts with copper compounds:



It was found that the change in the concentration of ferric iron in the solution and the difference in the size of the mineral has practically no effect on the extraction of copper into the solution. A significant increase in the recovery of copper into the solution is observed with an increase in temperature. So in one day of leaching, at 35 °C 22% is recovered, and at 50 °C 32% of copper is already healed.

The experiments shown in Figs. 1, 2, and Table 1 show that when the product is leached with a sulfuric acid solution, the recovery of copper into the solution reaches 58.8%.

Fig. 1 Kinetics of copper leaching from ore with solution H_2SO_4 , g/l: 1–25, 2–50, 3–75, 4–100

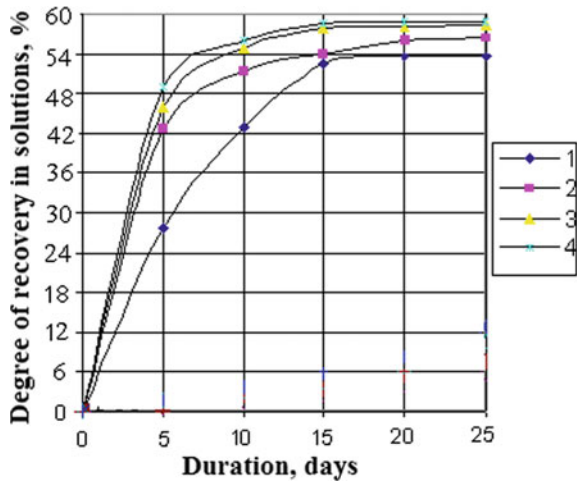
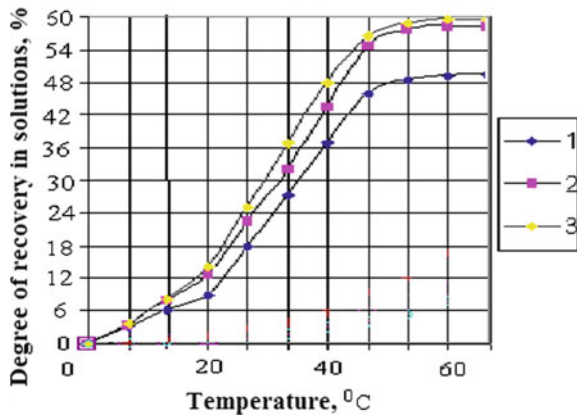


Fig. 2 The degree of copper extraction's dependence on the solution on the temperature at different durations of the experiment, days: 1–5; 2–10; 3–15—75 g/l



The degree of copper recovery from natural leaching is determined by the sulfuric acid concentration and the experiments' duration (Table 1). As can be seen from the experiments' results, the concentration of sulfuric acid 50–75 g/l is optimal.

4 Conclusion

The best conditions for leaching ore were determined as follows: sulfuric acid (49–76 g/l) for 16 days. Copper oxides are recovered in the solution at a rate of 99%.

Sulfide copper is present in 0.15% of the sulfuric acid leach cake. It is clear that the copper oxides have been completely transformed to sulfate solution. A minor number of sulfides remain in the solid phase.

Table 1 Results of experiments

Time, days	The volume of filled solution, l	The concentration of solution to be poured, g/l	The volume of solution to be drained, l	Drained solution concentration, g/l	Copper concentration in drain solution, g/l	Extraction, %
1	2	3	4	5	6	7
1	3.20	50	2.20	2.55	1.65	12.70
3	0.50	50	0.35	2.44	2.14	18.40
5	0.50	50	0.30	1.90	2.00	23.70
8	0.50	50	0.25	2.03	1.25	28.50
10	0.60	50	0.45	2.90	0.58	31.80
15	1.00	50	0.85	3.15	1.65	33.70
1	3.20	75	2.10	5.75	1.75	15.50
3	0.50	75	0.40	7.50	2.10	25.10
5	0.50	75	0.35	5.90	2.50	36.50
8	0.50	75	0.35	8.25	2.05	43.40
10	0.60	75	0.55	10.10	1.50	51.50
15	1.00	75	0.80	9.55	2.25	58.80

References

1. Mirzajonova S, Karimova T, Saidova M (2019) Research of sulfuric acid leaching of copper off-balance ores. *Int J Eng Adv Technol* 9(2):813–816. <https://doi.org/10.35940/ijeat.b3838.129219>. www.ijeat.org
2. Van Staden PJ, Kolesnikov AV, Petersen J (2017) Comparative assessment of heap leach production data—1. A procedure for deriving the batch leach curve. *Miner Eng* 101:47–57
3. Marsden JO, Botz MM (2017) Heap leach modeling—a review of approaches to metal production forecasting. *Miner Metall Process* 34:53–64
4. Bouffard SC, Dixon DG (2001) Investigative study into the hydrodynamics of heap leaching processes. *Metall Mater Trans B* 32:763–776
5. Matkarimov ST, Yusupkhodjayev AA, Berdiyarov BT, Qodirjon Ugli Nosirkhujayev S, Matkarimov ZT (2020) Technology of deep processing of copper slags by method of active thermal gravity. *Int J Adv Sci Technol* 29(03):5633–5639
6. Matkarimov ST, Berdiyarov BT, Yusupkhodjayev AA (2019) Technological parameters of producing metalized iron concentrates from poor raw material. *Int J Inno Technol Explor Eng* 8(11). <https://doi.org/10.35940/ijitee.K1586.0881119>
7. Matkarimov ST, Yavkochiva DO, Berdiyarov BT, Nosirov FD (2020) Hydrometallurgical processing of copper-smelting dust. *Int J Emerg Trends Eng Res* 8(7):3088–3094. <https://doi.org/10.30534/ijeter/2020/35872020>
8. Khojiev ST et al (2020) The technology for the reduction of metal oxides using waste polyethylene materials. Paper presented at the METAL 2020—29th international conference on metallurgy and materials, conference proceedings, pp 971–978. <https://doi.org/10.37904/metal.2020.3592>. Retrieved from www.scopus.com
9. Matkarimov ST, Yusupkhodjayev AA, Berdiyarov BB (2019, July 24). Development of technology of release of iron and its oxidic connections from dump steel-smelting slag. <https://doi.org/10.20944/preprints201907.0268.v1>

10. Umarova IK et al (2020) Development of a flotation technology for gold-bearing ores of the Amantaytau deposit. OBOGASHCHENIE RUD 2, 29–33. <https://doi.org/10.17580/or.2020.02.05>
11. Sanakulov KS (2009) The scientific and technical basis for processing waste from mining and metallurgical production.—T.: FAN AN RUZ, 405
12. Sanakulov KS et al. (2010) Heap leaching of gold from multi-tier stacks. -T.: “FAN,” 304
13. Kholikulov DB, Matkarimov ST (2021) Pilot tests of processing technologies of process solutions of copper production by ozonation. Mater Today: Proc. <https://doi.org/10.1016/j.matpr.2021.01.419>
14. Wu AX, Yin S, Qin W, Liu J, Qiu G (2009) The effect of preferential flow on extraction and surface morphology of copper sulphides during heap leaching. Hydrometallurgy 95:76–81
15. Zhan G, Haggarty S, Ludwick W (2012) Hydrological evaluation of gold leach pad rinsing. MineWater Environ 31:307–311

Chapter 2

A Comparative Analysis of Step Channel TFET with the Impact of Work Function Engineering



Manshi Kamal and Dharmendra Singh Yadav

Abstract In this research, we have introduced the step channel tunnel field-effect transistor (SCTFET) device used for the advancement in drain current and the diminishing of ambipolar conduction. The introduced device is based on hetero-dielectric engineering and work function engineering (WFE). Hetero-dielectric engineering (HDE) assists to improve electron tunneling which causes better drain current. Further, the work function engineering reduces the threshold voltage, SS , along with the I_{OFF} , and improves the I_{ON} of the device. A detailed study on the SCTFET has been performed with the analysis of different DC and analog characteristics. The device has been simulated in the TCAD tool to study its efficiency.

Keywords Step channel · BTBT · Hetero-gate oxide · Dual work function · Gate–drain capacitance

1 Introduction

According to Moore's law of semiconductors, MOSFET must be scaled to increase the number of transistors on the chip. Downsizing of the MOSFET technology shows several advantages in terms of cost, compactness of devices, capability to drive the current, speed of operation, and performance in high-frequency analysis. However, short channel effects (SCE), DIBL, large power consumption, and high leakage current are some severe issues, created by the continual reduction of device dimensions. Along with this, the sub-threshold slope brings a limitation ($SS > 60$ mv/decade) for MOSFET, and scaling of supply voltage becomes challenging to lessen the power dissipation [1–7]. To address these issues, researchers came up with a novel device called tunnel field-effect transistor (TFET) [8–12]. Low leakage current and low SS make TFET very prominent and more energy efficient than MOSFET [13,

M. Kamal (✉) · D. S. Yadav
Electronics and Communication Engineering Department, National Institute of Technology,
Hamirpur, Himachal Pradesh, India

D. S. Yadav
e-mail: dsyadav@nith.ac.in

14]. It operates on the band–band tunneling (BTBT) technique, where the motion of the electrons (e^-) takes place from the valence band (VB) to the conduction band (CB) of the source and channel, respectively, via source/channel (S/C) junction, also known as quantum tunneling. BTBT, an unlike approach from thermionic emission of MOSFET, helps to upgrade the sub-threshold slope (SS) ($\leq 60\text{mV/decade}$) for the low power devices [15, 16]. Low drain current and high ambipolar conduction are the severe concerns of TFET. Conventional TFET has been implemented with numerous methods such as bandgap engineering [17], hetero-dielectric material engineering [18], work function engineering [19, 20], high- k dielectric engineering [21, 22], gate underlapped engineering [23], gate overlapped engineering on the drain side [24], high concentration pocket layers [21], and doping profile engineering to resolve all the issues [25]. However, these methods come up with their disadvantages. A novel step channel TFET (SCTFET) device has been presented, where the step is presumed to be in the middle of the channel, to conquer the conventional TFET-related complications [26]. Asymmetry between the source and drain is necessary to resolve the ambipolar current. As a consequence of the asymmetry between source and drain introduced by the step channel thickness, ambipolar actions should be alleviated. The channel thickness (t_{si}) is also thought to have a major effect on the BTBT rate of DG TFETs. SCTFET proposed a lower sub-threshold slope (SS) and repressed ambipolar conduction in contrast with the conventional TFET, but the low on-current and large V_{th} degrade its performance [27]. To unravel these issues, we put forward a device called hetero-gate oxide SCTFET (HGO-SCTFET) comprised of the high- k dielectric material (hafnium dioxide) at the S/C side and the low- k material (silicon dioxide) at the D/C (drain/channel) side and hetero-gate oxide dual work function SCTFET (HGO-DW-SCTFET) consists of gate work function engineering (WFE) and hetero-gate oxide engineering (HGOE). HfO_2 has been used at the side of the source and the channel, having a high dielectric constant ($\epsilon = 22.0$) helps drain current to increase by reducing the width of the tunnel of the source–channel junction due to which more number of electrons move from the source through the junction to reach the channel. Work function engineering (tunneling gate (TG) = 3.9 eV, auxiliary gate (AG) = 4.5 eV) is implemented to lessen the ambipolar behavior and to escalate the current.

The paper is segmented further into three more sections: Section 2 includes the structures of different devices and their simulation setup. All the dc characteristics and RF parameters of devices are comparatively analyzed in Sect. 3, and finally, come to Sect. 4 which concludes the important points drawn from the study.

2 Device Structure

Schematics of the different SCTFETs are demonstrated in Fig. 1; these schematics are obtained using p^+ doped source ($10^{20}/\text{cm}^3$), intrinsic channel ($10^{17}/\text{cm}^3$), n^+ doped drain ($10^{18}/\text{cm}^3$), and the same structure with the addition of HGOE and dual WFE, called hetero-gate oxide SCTEFET (HGO-SCTFET) and hetero-gate oxide

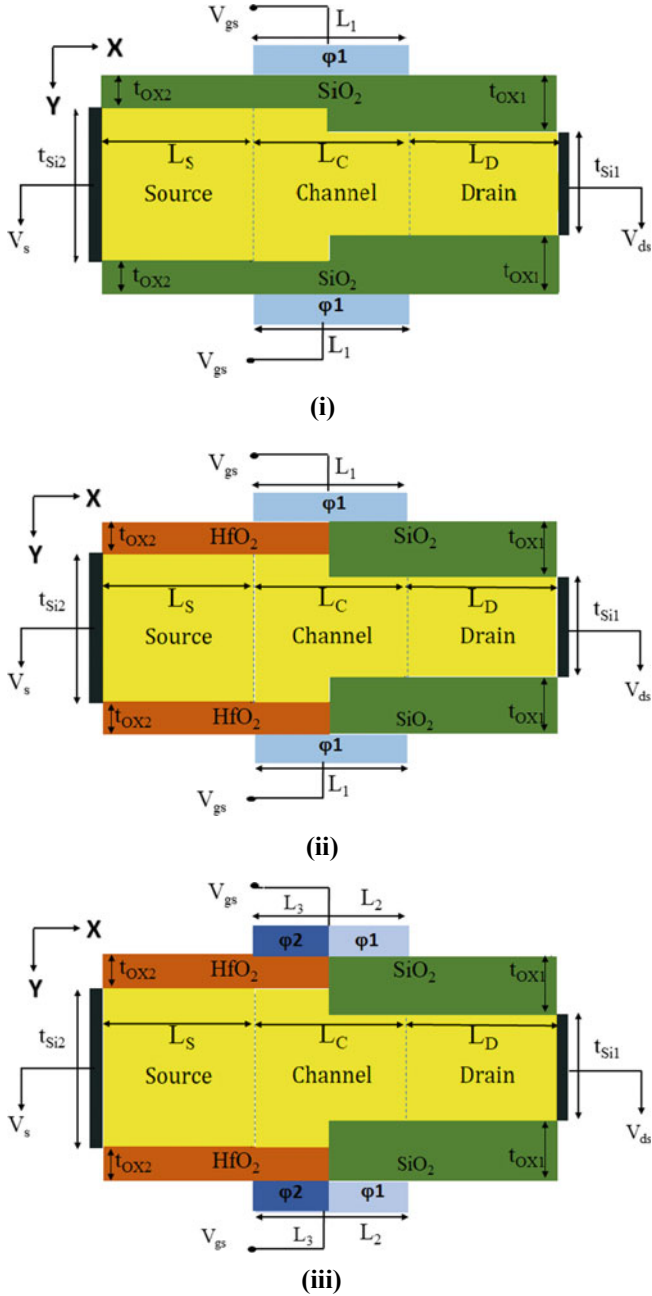


Fig. 1 Device schematics for **i** step channel (SCTFET), **ii** hetero-gate oxide (HGO-SCTFET), and **iii** HGO dual work function (HGO-DW-SCTFET)

Table 1 Structural dimensions of the devices

Parameters	SCTFET	HGO-SCTFET	HGO-DW-SCTFET
Source length (L_S) (nm)	20	20	20
Channel length (L_C) (nm)	10	10	10
Drain length (L_D) (nm)	20	20	20
Source doping (p type) (N_S) (/cm ³)	10 ²⁰	10 ²⁰	10 ²⁰
Channel doping (n type) (N_{CH}) (/cm ³)	10 ¹⁷	10 ¹⁷	10 ¹⁷
Drain doping (n type) (N_D) (/cm ³)	10 ¹⁸	10 ¹⁸	10 ¹⁸
Oxide thickness at D/C (t_{OX1}) (nm)	2	2	2
Oxide thickness at S/C (t_{OX2}) (nm)	1	1	1
Drain thickness (t_{Si1}) (nm)	6	6	6
Source thickness (t_{Si2}) (nm)	8	8	8
Gate length (L_1) (nm)	10	10	–
Gate length (L_2) (nm)	–	–	5
Gate length (L_3) (nm)	–	–	5
Gate work function ($AG = \varphi_1$) (eV)	4.5	4.5	4.5
Gate work function ($TG = \varphi_2$) (eV)	–	–	4.3

dual work function SCTFET (HGO-DW-SCTFET) [26, 27]. Device dimensional parameters, used in the tool, are shown in Table 1.

The structures of all devices and their simulations are constructed and performed by the TCAD simulator. The physical effects of the device are analyzed by using different models.

- a. bbt.nonlocal model
- b. bgn model
- c. consrh model
- d. conmob model

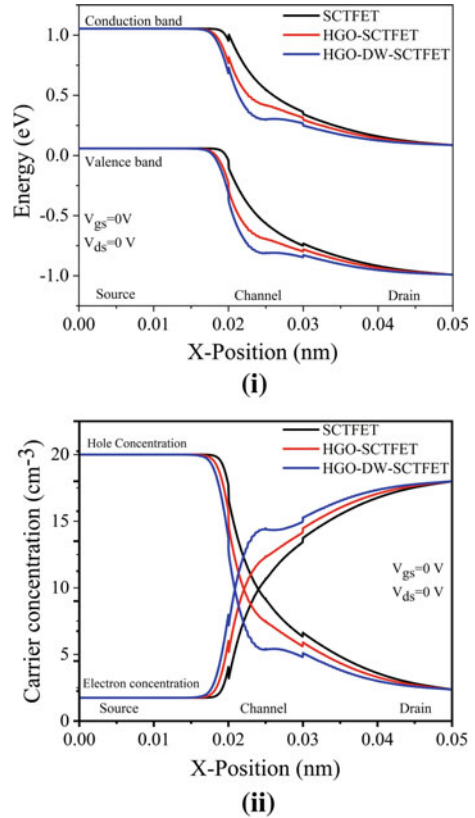
Electron and hole tunneling from band to the band is governed by the nonlocal band–band tunneling model (bbt. nonlocal), narrowing of the bandgap is reported by the bgn model, and consrh model is employed to determine the generation and recombination of holes and electrons in a semiconductor. To specify concentration-dependent mobility, the doping concentration-dependent model (conmob) is used.

3 Result and Parameter Analysis

This section of the paper involves a comparative inspection of DC and analog/radio frequency characteristics of all devices.

(a) DC Characteristics

Fig. 2 Thermal equilibrium state: **i** energy-band diagram and **ii** electron-hole concentration of SCTFET, HGO-SCTFET, and HGO-DW-SCTFET

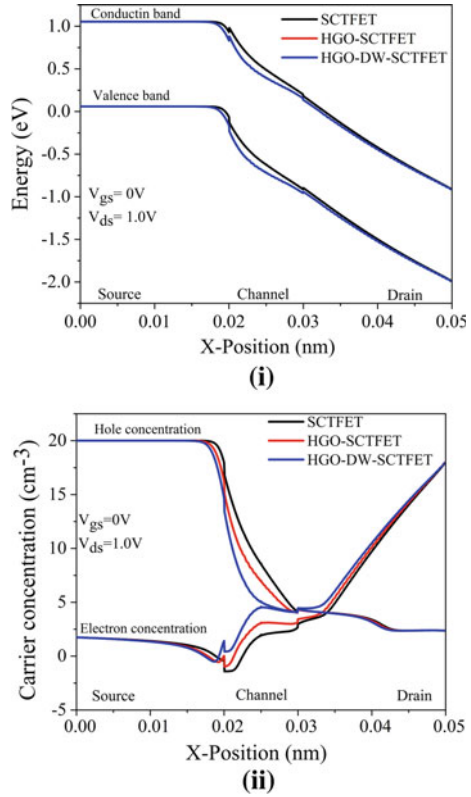


Thermal equilibrium: This is the state where no biasing ($V_{gs} = 0 \text{ V}$ and $V_{ds} = 0 \text{ V}$) is introduced. Figure 2i explains the reason behind no current as there is no alignment between the VB of the source and the CB of the channel so that electrons can move from source to channel. It is shown in Fig. 2ii that hole and electron concentrations are alike in the channel and high hole (h^+) accumulation in the channel widens the tunneling width of source/channel junction for all the devices.

OFF state: This is the state where $V_{ds} = 1.0 \text{ V}$ and $V_{gs} = 0.0 \text{ V}$. From Fig. 3i, on-current cannot be seen in the device because the valence energy band of the source lies separately from the conduction energy band of the channel that is why the movement of the charge carrier is restricted here and no tunneling occurs. Figure 3ii illustrates that higher V_{ds} causes a higher potential barrier between source and channel and it results in no current formation in all devices.

ON state: This is the state where $V_{ds} = 1.0 \text{ V}$ and $V_{gs} = 1.5 \text{ V}$; under this state in Fig. 4i, as the V_{gs} is applied and increased, the CB and the VB of the channel region start moving downward and the CB of the channel lies adjacent to the VB of the source; this helps to escalate the feasibility of tunneling through the junction. Lower work function and high- k dielectric material at the source/channel junction of

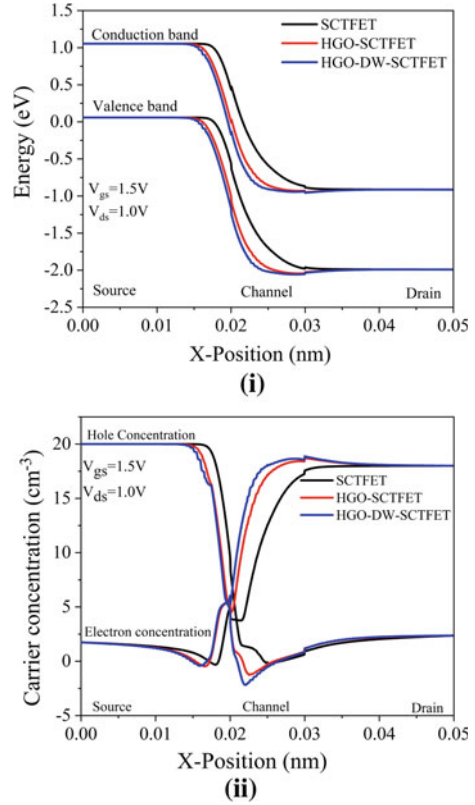
Fig. 3 OFF state:
i energy-band diagram and
ii electron-hole
 concentration diagram of all
 devices



HGO-DW-SCTFET help to increase the electron concentration and to narrow down the width of the tunnel. Figure 4ii represents that the application of V_{gs} increases the electron concentration in the channel; however, the hetero-gate oxide device is having a heavier electron concentration than SCTFET and HGO-SCTFET in the channel because of having HfO_2 ($\epsilon = 22.0$) at the source which develops a higher drain current for this device. As compared to materials with low dielectric constants, materials with high dielectric constants can store more energy. The gate capacitance increases as the dielectric constant grows, enhancing the current flow in the device. The energy band of semiconductor devices is modulated by the work function. The energy band is bent downward by a lower work function. Increased work function eliminates gate leakage at the d-c junction by raising the barrier height for tunneling through the oxide. As work function is increased at the s-c junction, the band alignment for tunneling is lowered, and the ion is reduced. So at the s-c junction, a lower work function was used to raise ion, while at the d-c junction, a higher work function was used to decrease the off-current. Figure 4i portrays the proposed device's narrow tunneling width in contrast to other devices, resulting in a higher drain current.

Ambipolar state: This is the state where $V_{ds} = 1.0 V$ and $V_{gs} = -0.5 V$, and in Fig. 5i, it is shown that the CB of drain and VB of the channel are not lined up and the

Fig. 4 ON state:
i energy-band diagram and
ii electron-hole
 concentration of all devices



possibility to move the hole concentration from the drain to channel decreases which is why ambipolar conduction in all devices is extremely low. Figure 5ii demonstrates that the accumulation of holes at the channel-drain junction of all devices is very low that results in increasing the width of tunneling junction between drain and channel which lessens ambipolar current to a very large extent.

Electric field: Fig. 6 shows that at the junction of the source and channel there is a formation of electric field owing to the high rate of electron tunneling through the junction of the source and the channel region. The high- k material and lower work function of the gate are used to provide the high kinetic energy to the electrons and the steepness to the band bending and that is why HGO-DW-SCTFET is showing the highest electric field in comparison with other devices.

Transfer characteristics: Fig. 7 shows that the drain current has been plotted against gate voltage to show the input characteristics of the devices. The better current is achieved by the HGO-DW-SCTFET because of HGOE and dual WFE. Electron tunneling probability is increased by introducing HfO_2 at the junction of the source/channel region and lower work function material also helps to boost it.

Fig. 5 Ambipolar state:
i energy-band diagram and
ii electron-hole
concentration of all devices

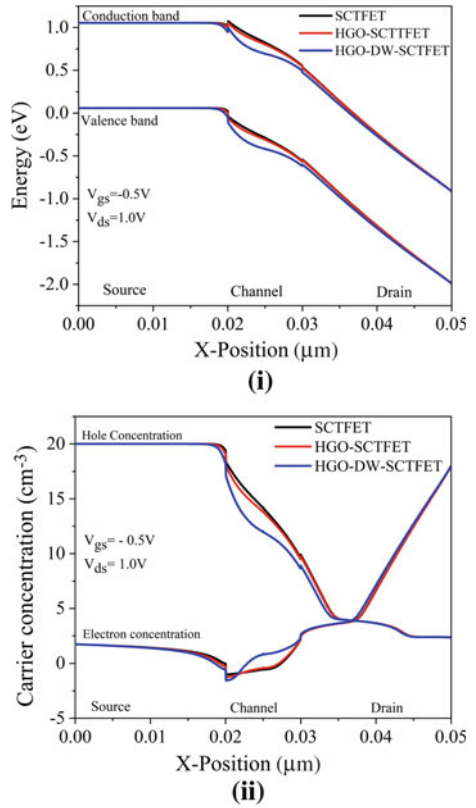


Fig. 6 The electric field
variations of all devices

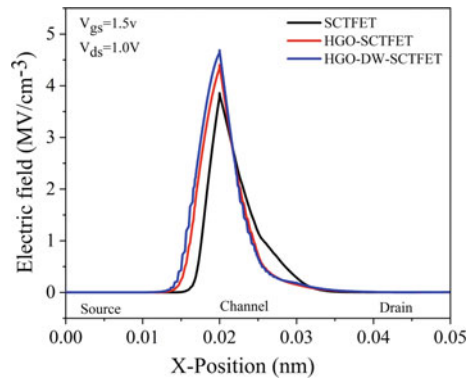


Fig. 7 Transfer characteristic of all devices

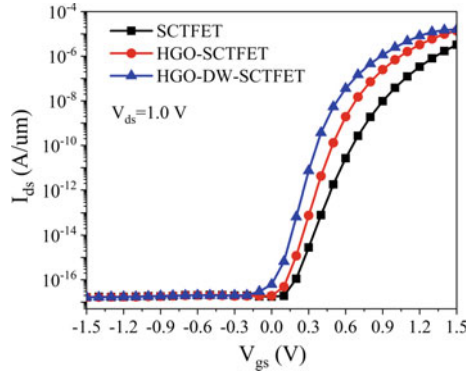


Table 2 Comparative analysis of drain current

Device	I_{ON} (A/ μ m)	I_{OFF} (A/ μ m)	I_{ON}/I_{OFF}
SCTFET	3.27×10^{-6}	1.76×10^{-17}	1.86×10^{11}
HGO-SCTFET	1.36×10^{-5}	1.91×10^{-17}	7.12×10^{11}
HGO-DW-SCTFET	1.58×10^{-5}	6.16×10^{-17}	2.56×10^{11}

After the analysis, extracted data are shown in Table 2. The introduced device also shows better V_{th} and SS in comparison with the other devices.

(b) **Analog/Radio Frequency Parameters**

In this segment, the behavior of the analog/radio frequency parameters is analyzed as they decide the performance of the device. Some of the important and basic parameters are parasitic capacitance, transconductance (g_m), and cutoff frequency (f_T).

Fig. 8 $C_{gate-drain}$ variation with V_{gs}

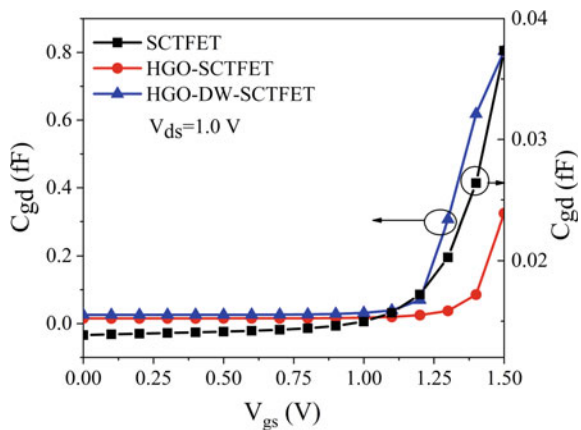
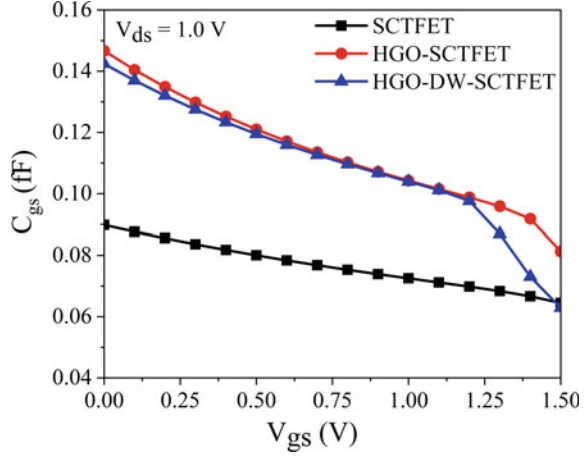


Fig. 9 $C_{\text{gate-source}}$ variation with V_{gs}



Gate-drain capacitance: Fig. 8 illustrates that the increment of V_{gs} increases the value of $C_{\text{gate-drain}}$. Parasitic capacitance is a combination of $C_{\text{gate-gate}}$, $C_{\text{gate-drain}}$, and $C_{\text{gate-source}}$, but the major problems are faced by the feedback capacitance ($C_{\text{gate-drain}}$). It is observed that HGO-DW-SCTFET attains maximum value of $C_{\text{gate-drain}}$, because when V_{gs} increases HfO_2 and lower work function material increases the number of electrons in the inversion layer of the devices.

Gate-source capacitance: Fig. 9 displays the graph between $C_{\text{gate-source}}$ and gate voltage (V_{gs}). The maximum $C_{\text{gate-source}}$ is shown by the HGO-DW-SCTFET and HGO-SCTFET in comparison with SCTFET due to the introduction of HGOE and dual WFE.

Transconductance: It is an analog characteristic that relates output current (I_{ds}) to the input voltage (V_{gs}) of the device. The formula for calculating the g_m is given by

$$g_m = \frac{\partial I_{\text{ds}}}{\partial V_{\text{gs}}}. \quad (1)$$

According to Eq. (1), g_m is directly proportional to drain current and indirectly proportional to V_{gs} . According to the I_{ds} and V_{gs} analysis, g_m has a high value for the devices having higher drain currents that is why HGO-SCTFET and HGO-DW-SCTFET achieve the high transconductance value. Initially, g_m starts increasing along with the increase in V_{gs} because of the drain current increment. As soon as current attains saturation its effect decreases on g_m , and after this, it starts decreasing because of the reciprocity between g_m and V_{gs} (Fig. 10).

Cutoff frequency: Fig. 11 shows the plots between f_T and V_{gs} of all devices. f_T is calculated with the help of g_m and with the combined effect of $C_{\text{drain-gate}}$ and $C_{\text{gate-source}}$. The proportional relationship of the cutoff frequency with transconductance and drain current explains the increment of the cutoff frequency. Cutoff frequency reaches a maximum value when charge carriers attain mobility saturation.

Fig. 10 Transconductance variation with the V_{gs}

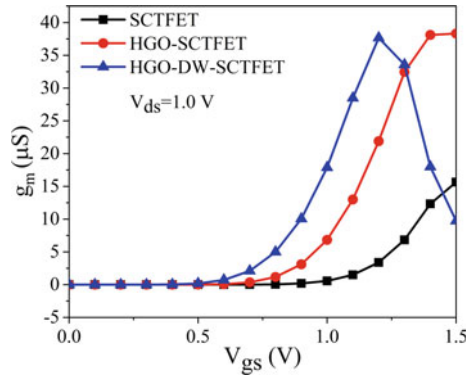
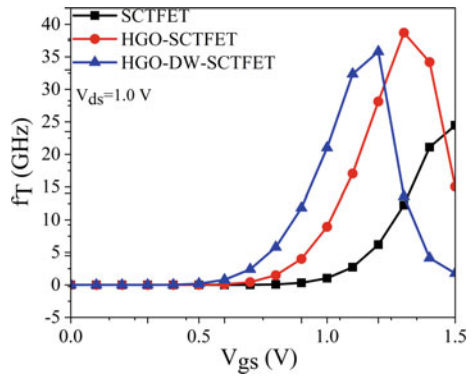


Fig. 11 Cutoff frequency variation with gate voltage



It starts decreasing because of the saturation of drain current and the reduction of g_m . The $C_{\text{drain-gate}}$ of the HGO-SCTFET has the lowest value, as seen in Fig. 8, resulting in the highest value for f_T .

$$f_T = \frac{g_m}{2\pi(C_{gd} + C_{gs})}. \quad (2)$$

Output characteristics: This plots the graph between output current (I_{ds}) at one axis and the output voltage (V_{ds}) at another axis. Figure 12 shows the comparative analysis of the drain current where HGO-DW-TFET is showing the highest current.

The drain current of the proposed device is high, indicating that the drain-source resistance will be low, resulting in lower power loss.

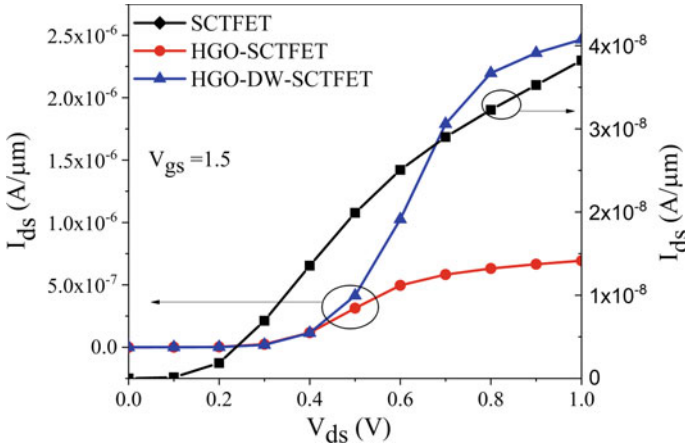


Fig. 12 Output characteristics of all devices

4 Conclusion

In this paper, different structures of SCTFET have been introduced by applying two different and efficient methods, hetero-dielectric engineering and dual WFE. The DC and the analog performance have been studied by using the TCAD tool. The introduced techniques help SCTFET to improve its ion and suppress ambipolar conduction, off-current, V_{th} , and SS. HGO-DW-SCTFET shows better V_{th} , SS, and I_{ON} in comparison with SCTFET and HGO-SCTFET. The presented device HGO-DW-SCTFET shows the drain current in the range of 10^{-5} (A/μm), off-current in the range of 10^{-17} (A/μm) and I_{ON}/I_{OFF} is in the range of 10^{11} along with the improved ambipolar conduction. Hence, the overall study shows that HGO-DW-SCTFET is better than SCTFET and HGO-SCTFET in the DC and analog analysis.

Acknowledgements The authors would like to thank Dr. Dip Prakash Samajdar from Department of Electronics and Communication Engineering, PDPM Indian Institute of Information Technology, Design and Manufacturing, Jabalpur, Madhya Pradesh, India, for providing valuable suggestions and support to carry out this research work.

References

1. Iwai H (2009) Technology roadmap for 22 nm and beyond. In: 2nd international workshop on electron devices and semiconductor technology, IEDST '09, pp 7–10. <https://doi.org/10.1109/EDST.2009.5166100>
2. Iwai H (1999) CMOS technology—year 2010 and beyond. IEEE J Solid-State Circuits 34(3):357–366. <https://doi.org/10.1109/4.748187>
3. Iwai H (2009) Si MOSFET roadmap for 22 nm and beyond. In: 4th International conference on computers and devices for communication, CODEC 2009, pp. 2007–2010

4. Liu H, Zhang G, Huang R, Zhang X (2004) Impact of leakage currents on MOSFET noise performance in deep sub-micron regime. In: International conference on solid-state and integrated circuit technology proceedings, vol 2, pp 1167–1170. <https://doi.org/10.1109/icsict.2004.1436730>.
5. Joseph S, James G, Mathew TV (2009) Reduction of off-state leakage current on fully depleted DG-MOSFETs. In: International conference on emerging trends in electronic and photonic devices and systems, ELECTRO'09, pp 148–151. <https://doi.org/10.1109/electro.2009.5441150>
6. Mutlu AA, Rahman M (2000) Two-dimensional analytical model for drain induced barrier lowering (DIBL) in short channel MOSFETs. In: Conference proceedings—IEEE SOUTH-EASTCON, pp 340–344. <https://doi.org/10.1109/secon.2000.845589>
7. Xie Q, Lee CJ, Xu J, Wann C, Sun JYC, Taur Y (2013) Comprehensive analysis of short-channel effects in ultrathin SOI MOSFETs. *IEEE Trans Electron Devices* 60(6):1814–1819. <https://doi.org/10.1109/TED.2013.2255878>
8. Nisha Justeena A, Nirmal D, Gracia D (2017) Design and analysis of tunnel fet using high K dielectric materials. In: Proceedings of IEEE international conference on innovations in electrical, electronics, instrumentation and media technology, ICIEEIMT 2017, vol 2017-Jan, no 978, pp 177–180. <https://doi.org/10.1109/ICIEEIMT.2017.8116830>
9. Boucart K, Ionescu AM (2007) Double-gate tunnel FET with high- κ gate dielectric. *IEEE Trans Electron Devices* 54(7):1725–1733. <https://doi.org/10.1109/TED.2007.899389>
10. Aswathy M, Biju NM, Komaragiri R (2012) Simulation studies of tunnel field effect transistor (TFET). In: International conference on advances in computing and communications, ICACC 2012, pp 138–141. <https://doi.org/10.1109/ICACC.2012.31>
11. Satheshkumar R. Performance of various tunnel transistors
12. Avci UE, Morris DH, Young IA (2015) Tunnel field-effect transistors: prospects and challenges. *IEEE J Electron Devices Soc* 3(3):88–95. <https://doi.org/10.1109/JEDS.2015.2390591>
13. Wu J, Min J, Taur Y (2015) Short-channel effects in tunnel FETs. *IEEE Trans Electron Devices* 62(9):3019–3024. <https://doi.org/10.1109/TED.2015.2458977>
14. Zhang Q, Zhao W, Seabaugh A (2006) Low-subthreshold-swing tunnel transistors. *IEEE Electron Device Lett* 27(4):297–300. <https://doi.org/10.1109/LED.2006.871855>
15. Jokinen TA, McNamara S (2017) Band-to-band tunneling diode for ultralow-voltage applications. *IEEE Trans Electron Devices* 64(6):2702–2706. <https://doi.org/10.1109/TED.2017.2692772>
16. Woo R, Serene Koh HY, Onal C, Griffin PB, Plummer JD (2008) BTBT transistor scaling: can they be competitive with MOSFETs?. *Dev Res Conf—Conf Dig DRC* 28(8):75–76. <https://doi.org/10.1109/DRC.2008.4800741>
17. R. E. Dqg, V. Hhh, J. Frp, D. Q. G. Pul, H. H. H. Nhxw, and D. F. Eg, “0R6 %DVHG 7)(7 6WXG RQ &KDOQHO 7KLFNQHVV Dependent Performance,” pp 2–7
18. Ghosh S, Pachal P, Kumar R, Kundu S, Ghosh J, Sarkar SK (2020) Double gate p-n-p-n TFET with hetero oxide dielectric and high-k spacer engineering. In: Proceedings of 2nd international conference on VLSI device, circuit and system VLSI DCS 2020, vol 1, pp 18–19. <https://doi.org/10.1109/VLSIDCS47293.2020.9179943>
19. Yadav DS, Sharma D, Raad BR, Bajaj V (2017) Dual workfunction hetero gate dielectric tunnel field-effect transistor performance analysis. In: Proceedings of 2016 international conference on advanced communication control and computing technologies, ICACCCT 2016, no 978, pp 26–29. <https://doi.org/10.1109/ICACCCT.2016.7831593>
20. Soni D, Sharma D, Yadav S, Aslam M, Yadav DS, Sharma N (2018) Gate metal work function engineering for the improvement of electrostatic behaviour of doped tunnel field effect transistor. In: Proceedings of IEEE international symposium on nanoelectronic and information systems, iNIS 2017, vol 2018-Feb, pp 190–194. <https://doi.org/10.1109/iNIS.2017.47>
21. Yadav DS, Sharma D, Raad BR, Bajaj V (2016) Impactful study of dual work function, underlap and hetero gate dielectric on TFET with different drain doping profile for high frequency performance estimation and optimization. *Superlattices Microstruct* 96:36–46. <https://doi.org/10.1016/j.spmi.2016.04.027>

22. Gupta S et al (2018) Examination of the impingement of interface trap charges on heterogeneous gate dielectric dual material control gate tunnel field effect transistor for the refinement of device reliability. *Micro Nano Lett* 13(8):1192–1196. <https://doi.org/10.1049/mnl.2017.0869>
23. Dutta R, Rahaman M, Guha A, Paitya N (2019) Study of gate source-drain overlap/gate-channel underlap in Heterojunction (50nm Ge channel) n-Double Gate TFET for different λ -spacer. In: *Proceedings of 2nd international conference on smart systems and inventive technology, ICSSIT 2019*, vol 10, no Iessit, pp 672–676. <https://doi.org/10.1109/ICSSIT46314.2019.8987903>
24. Abdi DB, Kumar MJ (2014) Controlling ambipolar current in tunneling FETs using overlapping gate-on-drain. *IEEE J Electron Devices Soc* 2(6):187–190. <https://doi.org/10.1109/JEDS.2014.2327626>
25. Vijayvargiya V, Vishvakarma SK (2014) Effect of drain doping profile on double-gate tunnel field-effect transistor and its influence on device RF performance. *IEEE Trans Nanotechnol* 13(5):974–981. <https://doi.org/10.1109/TNANO.2014.2336812>
26. Zhang M, Guo Y, Zhang J, Yao J, Chen J (2020) Simulation study of the double-gate tunnel field-effect transistor with step channel thickness. *Nanoscale Res Lett* 15(1). <https://doi.org/10.1186/s11671-020-03360-7>
27. Kumar S, Yadav DS, Saraswat S, Parmar N, Sharma R, Kumar A (2020) A novel step-channel TFET for better subthreshold swing and improved analog/RF characteristics. In: *2020 IEEE international students' conference on electrical, electronics and computer science, SCEECS 2020*. <https://doi.org/10.1109/SCEECS48394.2020.104>

Chapter 3

A Review on Biomaterials Based Biosensors for Bilirubin Detection



Dheeraj Dhanvee Kairamkonda, Shreeja Bitla, and Harish Kuchulakanti

Abstract Bilirubin is a yellowish product of heme degradation that is conjugated in liver and excreted in bile. It is imperative to administer bilirubin concentration in the human body as an increase in its concentration indicates abnormal functionality of liver or any underlying disease. Yellow discoloration of skin or jaundice is due to the build-up of bilirubin under the skin. Neonatal jaundice is very common, affecting nearly 60% of the newborn with implications affecting brain cells in severe cases; it can also lead to seizures and even death. While there are different methods like invasive and non-invasive for bilirubin detection, we focused on invasive methods as they are proven to give accurate results. Under them, we considered advanced biosensing methods over the conventional analytical methods as they incorporate both biosensors and biomaterials for the detection of an analyte. In today's world, biomaterials are highly focused on research purposes due to their outstanding properties and advantages. There are many reviews focused extensively on biosensors or biomaterials used for various applications. In comparison, this review revolves around different biomaterials used with biosensors specifically to detect bilirubin as they offer rapid, sensitive, and effective results.

Keywords Biomaterials · Biosensors · Bilirubin · Nanoparticles · Quartz crystal microbalance · Molecular-imprinted polymers · Quantum dots

1 Introduction

Bilirubin (BR) is a yellow analyte in the human body produced by the breakdown of heme or hemoglobin, i.e., the breakdown of red blood cells. The bilirubin in the body is called total serum bilirubin that is further classified as conjugated and unconjugated

D. D. Kairamkonda (✉) · H. Kuchulakanti
Osmania University, Hyderabad, India

H. Kuchulakanti
e-mail: harish.k@uceou.edu

S. Bitla
Hyderabad, India

bilirubin. The conjugated bilirubin is a water-soluble substance that is processed by the liver and eventually excreted in the feces [1]. On the other hand, the unconjugated bilirubin cannot be processed by the liver. It is a water-insoluble compound that cannot be removed from the body either through feces or through urine, leading to jaundice. A jaundiced person's skin, sclera of the eye, and body become yellowish because of bilirubin's yellow color. Jaundice can also be called icterus. The extreme accumulation of bilirubin in the body is known as hyperbilirubinemia, leading to brain damage called kernicterus. Reports say that jaundice is more in babies of 1–2 weeks of age than in adults. It is also alarming that neonatal jaundice is rampant worldwide, and up to 50% of the term newborn and 80% of preterm newborns have jaundice. This is due to the reduced capacity of the liver to process unconjugated bilirubin. Hence, it is essential to measure bilirubin's concentration as it indicates the liver's functioning and helps doctors provide effective treatment [2].

A number of methods are employed for detection of bilirubin like spectrophotometry (dialysis reaction) and colorimetric assays. Recently biosensors are used for detection of bilirubin as they are selective and effortless. Biosensors are instruments that measure the concentration of an analyte. These are made of biological materials like proteins and nucleic acids that interact with the analyte to produce a change (physical or chemical), converted into a measurable electrical signal. The three fundamental components of a biosensor are a detector that interacts with the target substance, a transducer, which converts the chemical or biological reaction resulting from the interaction with the detector into a measurable electrical signal and the signal processing unit [3].

Cross-sensitivity, low shelf life, and limited linear range are common complications of the biosensors that can be solved by the use of biomaterials. Biomaterials based biosensors are proven to be very efficient and found applications in various fields. Various kinds of biomaterials have been used with biosensors to measure the concentrations of different substances and can produce efficient diagnostic systems. The use of molded polymeric biomaterials can improve biocompatibility, superparamagnetic properties, lower toxicity, and find wide clinical diagnostic applications. Biomaterials provide stable conditions to achieve catalytic recognition at a high level for their specific binding or interaction with the biological or chemical species. Thus, combining biosensors and biomaterials is useful for producing sensors capable of detecting various human body analytes [4].

While there are papers that discuss both invasive and non-invasive methods for bilirubin detection, the results obtained by the invasive techniques have shown promising results compared to non-invasive techniques. Nevertheless, non-invasive techniques are nowadays used to detect bilirubin using the concepts of spectrophotometry. They were also proven to be an effective way of sensing, and in that, they avoid causing trauma to the babies and avoid transmission of infections [5]. In this review, we want to focus on the invasive biosensing techniques enhanced by using biomaterials in combination with the sensor. We focused on invasive methods because they have better results than non-invasive methods, and the use of a variety of biomaterials has increased their capabilities. It has led to further research in these areas. While there is an extensive review of the various techniques used to sense bilirubin

where the emphasis was on the biosensors [6], our review focuses on providing extensive information on biomaterials and their usage in the detection of BR.

2 Gold Nanoparticles

Gold nanoparticles are being used widely in various applications and specifically in nanobiotechnology for detection and therapeutic purposes. They can be found in various shapes and predominantly used in the form of spheres and rods. Their dimensions range between 1 nm to 8 μm , and these sizes may be changed depending upon the field of application. Their extensive use in biomedical applications is due to their high biocompatibility, high surface-to-volume ratio, and good conductivity. They are also ideal for designing biosensors owing to their magnetic, optical, and catalytic properties [7, 8].

Gold nanoclusters are a kind of gold nanomaterials of sizes ranging from 0.3 to 3 nm. They are also finding numerous applications in biomedical engineering for high sensitivity detection and target-specific treatment because of their properties such as compatibility, excellent photostability, and water stability. They are widely used as fluorescent probes due to their stability and adjustability in the presence of fluorescence. Their well-defined structure, high optical properties, biocompatibility, and easy surface functionalization are being investigated and researched extensively in biomedical applications [9].

2.1 *Multiwalled Carbon Nanotubes (COOH/Graphene/Gold Nanoparticles)*

The gold nanoparticles have incredible properties which makes their usage a huge value addition to the biosensor in sensing the analyte. It exhibits high biocompatibility and reduced toxicity, thus enabling favorable conditions for sensing, and increased affinity toward the target analyte like BR or any other biomolecule. When used in combination with substrates like MWCNTs-COOH/GNs, it provides an ideal environment for the immobilization of biomolecules and to retain them. They act as a catalyst and allow faster transfer of electrons, thus making it a biomaterial with high conductivity. To sum up, this biomaterial shows high biological activity, low toxicity, and catalytic capability resulting in lower limit of detection and very good sensitivity [10].

2.2 *Human Serum Albumin Gold Nanoclusters (HSA-AuNCs)*

The AuNCs provide favorable conditions for the detection of the specimen and act as an electron transfer bridge to promote the interaction between the sensor and the analyte at the interface. Though HSA is a BR's primary carrier, it failed to promote any reaction or induce electrical activity. The AuNC's ability to act as a catalyst and electron bridge has helped the sensor detect the target analyte and further enhanced sensor performance parameters like sensitivity, selectivity, level of detection, and linear range. The electrochemical results showed the potential of HSA-AuNCs for the redox conversion of the target analyte and revealed a way for sensitive detection of the free BR with a linear range of 0.24–7 μM [11].

2.3 *Polydopamine for Fluorescent Sensing (BSA-AuNCs)*

A composite film consisting of polydopamine/gold nanocluster was fabricated for fluorescent sensing. Polydopamine functions as an adhesion for immobilizing AuNCs. To overcome the limitations posed by dispersing fluorescent probes into the solution for BR sensing that restricts recycling of the probes, this method uses surface sensors implemented by incorporating AuNCs that provide a long lifetime, large Stoke's shift, biocompatibility, reduces the reagent consumption, experimental cost, and risk of environmental pollution. Bovine serum albumin-templated AuNCs are covalently bonded onto polydopamine film to prevent the leaching of AuNCs and also increase its sensitivity. Here, BSA functions as the biorecognition element and AuNCs act as fluorescence reporting unit. The use of BSA instead of HSA makes it cost-effective [12].

3 Graphene Oxide Nanoparticles

Nanomaterials are being used for nearly a decade now. Graphene is an atomically thin, honeycomb structured 2D sheet of sp^2 carbon atoms. Graphene oxide has hydrophilic groups, which allow it to be coated on a wide range of materials as a thin film [13]. Additional fascinating properties of graphene oxide like electrical conductivity, thermal conductivity, and low maintenance cost make them more preferable over other nanomaterials [14]. Graphene oxide nanoparticle's (GONPs) excellent properties like long shelf life, specific surface-to-volume ratio, and low detection limit make them an alternative to graphene, and it is emerging as a new carbon-based nanoscale particle. Graphene oxide is generally prepared using Hummer's method.

3.1 *GONP@Ppy*

Polypyrrole is an oxidative polymer of pyrrole. Its properties like biocompatibility, stability, and others have brought this polymer a wide range of applications like drug delivery systems, biosensors, and nerve tissue engineering. Graphene oxide (GO) is used with polypyrrole (Ppy) to avoid aggregation. Ppy with GO for biosensor provides better stability, sensitivity, and electrical conductivity than Go and Ppy alone. The biosensors used in conjunction with these graphene oxide nanoparticles have shown promising outcomes by enhancing the sensor's detection capabilities for bilirubin and produced reliable results, rapid response with limit of detection (LOD) 0.1 nm, a vast working concentration range of 0.01–500 μM , and high storage stability of 150 days [15].

3.2 *Graphene Oxide-Based Nanocomposites*

Thangamuthu et al. [16], developed a bilirubin sensor by using the screen-printed carbon electrode functionalized with electrochemically reduced graphene oxide (ErGO). They found that this electrode had better results than the MWCNT functionalized electrode because of their faster electron transfer rate and high electrical conductivity of ErGO. A miniaturized, low-cost, and reliable point of care electrochemical sensor has been offered.

3.3 *BO_x/GrONPs/NiNPs*

Graphene oxide nanoparticles combined with nickel nanoparticles biosensor utilizes the advantage of metal nanoparticles and their distinguishing characteristics like great chemical action, rapid mass transfer, and large surface area. Ni-based nanoparticles are durable, biocompatible, and electrochemically stable to detect bilirubin. The biosensor fabricated by BO_x/GrONPs/NiNPs/ITO/Glass bioelectrode has shown improved results in detecting bilirubin with a lower detection limit of 0.15 μM , linear range of 0.01–600 μM , the high storage stability of 180 days, and good selectivity [17].

4 Other Nanostructures

4.1 IAO Nanorods

IAO nanorods are highly potential biomaterials for the detection of BR. They are further enhanced by doping with Sb_2O_4 , as it plays an important role in transmission of electrons and as a catalyst. After doping with the metal oxide, the IAO nanorod film is coated onto the electrode for sensing of the analyte. This combination has improved the abilities of the system to detect bilirubin. This modified IAO/GCE has excellent electrical conductivity and chemical stability, thus making it capable of detecting ultra-low concentrations of bilirubin. The IAO NRs releases electrons in the conduction band and allow the reduction of BR on the electrode's surface. This reduction is the critical element in increasing the selectivity and sensitivity of the sensor [18].

4.2 MoS_2 Nanostructures (Nano Flowers)

Although graphene has been used widely as a compelling option because of its excellent properties, MoS_2 is prioritized. They are promising in the design and fabrication of novel and next-generation sensing devices. MoS_2 is advantageous due to its low-cost, abundance, tailorable morphologies, and tuneable band gap with good visible-light absorption properties. They also have a prominent role in the biosensor field because of their outstanding features such as large surface area, high biocompatibility, and structural adaptability. Further, nowadays, MoS_2 nanoflowers are gaining attention due to their enhanced properties and structural vantage. On account of their promising applications in chemical sensing and electronic devices, surface functionalization of MoS_2 nanostructures with the noble metal nanoparticles are being researched extensively [19, 20].

The number of active states, polarity, and optical properties of MoS_2 depends upon the abundance and vacancy of sulfur, and therefore, the sulfur ratio is always monitored or controlled in MoS_2 . Although the petal-like structure of MoS_2 NFs enhances the surface area, its selectivity is increased only by functionalizing AuNPs onto its surface. This has further improved the output signal compared to bare MoS_2 , to the extent that it could now detect up to picomolar concentration. The substrate exhibits high stability, reproducibility, selectivity, and sensitivity [21].

4.3 Zirconia Coated Silica Nanoparticles/Chitosan Films

Silica nanoparticles, also known as silicon dioxide nanoparticles, are widely used in biological applications because of their low toxicity, ease of functionalization,

thermal stability, large-scale synthetic availability, and large surface area. Their size, porosity, and shape can be easily manipulated, making them ideal for various applications [22]. Due to their excellent biocompatibility and film-forming ability, chitosan is a crucial biopolymer for immobilization, and due to the presence of $-\text{NH}_2$ group, it provides very good hydrophilic environment that elevates the detection efficiency of an analyte [23].

$\text{SiO}_2@ZrONPs$ enables rapid e^- transfer rate between the enzyme and the electrode. The biocompatible environment restricted the pH change in the immobilized enzyme's vicinity, thus providing a stable environment throughout the solution and better detection with broad linear range of $0.02\text{--}250\ \mu\text{M}$, rapid response of 2 s, and long stability for a period of 4 months at $4\ ^\circ\text{C}$, low detection limit of $0.1\ \text{nM}$, and good reproducibility. The material $\text{SiO}_2@ZrONPs$ and CHIT together exhibit an excellent electrocatalytic effect for the oxidation of H_2O_2 , thus leading to the biosensor's outstanding performance. It is also found that the detection limit and stability of enzyme electrode of this sensor [24] was better than that of hydroxyapatite [25].

5 Quantum Dots

Quantum dots are man-made nanoparticles of semiconductors or "droplets" of charge that can transport electrons [26]. Theorized in the 1980s [27], these nanoscale crystals, when illuminated by ultraviolet rays, excite to a higher energy state and emit light of various colors based on their size. Dimensional similarities of these particles with that of biological macromolecules like proteins and nucleic acids with a physical dimension smaller than Bohr exciton enable them to be used in various biological applications [28]. QDs stabilized by bovine serum albumin (BSA) offer rapid and precise detection of bilirubin in human fluids. BSA in these synthesized QDs help in better interaction of bilirubin and CdSe-BSA quantum dots [29]. L-cysteine capped manganese-doped zinc sulfide quantum dots (Mn: ZnS Quantum dots) are used for the detection of BR in human urine and serum samples. The probable principle of BR induced luminescence quenching is reductive photo-induced electron transfer (PET). Mn: ZnS QDs act as an electron acceptor and BR act as an e^- donor [30]. Carbon dots doped with sulfur and nitrogen (S, N-CDs) paper stripes based fluorescent probe can be used for visual detection of bilirubin [31].

5.1 CdSe-BSA Quantum Dots

BSA not only provides stability to QFDs in aqueous environment due to its high affinity [32] to bilirubin, it also gives an added advantage with its well resolved emission maximum, with that of QDs semiconductors which makes detection more precise, efficient, and selective with 90% of emission intensity quenched by addition on only $40\ \mu\text{M}$ BR [30]. CdSe-BSA quantum dots also have shown a high specificity

toward free bilirubin even in mixture compounds like in that of serum and urine where metal ions and other biomolecules are present.

5.2 *Mn: ZnS QDs*

Being one of the actively researched topics for years now, for their interesting features like wide band gap (3.6 eV) [33], photostability, high quantum yield, tunable narrow and symmetric emission spectra and low toxicity compared to other ODs like CdSe and CdTe QDs [34] zinc sulfide quantum dots (ZnS QDs) are finding their way in lasers, electroluminescent devices, biosensing, bioimaging, and may more. Doping of ZnS with Mn^{2+} ions help to make ZnS QDs a good biosensor probe by eliminating disturbances like random light scattering and autofluorescence background. L-cysteine with a thiol subchain helps in detection by tweaking its biocompatibility with linearity from 10.99 to 63.84 μM bilirubin [31].

6 Molecular Imprinted Polymers

Build on the basic concept of “lock and key” hypothesis of enzyme–substrate recognition, molecular imprinting is art for trapping the desired target onto a polymer matrix, customized to have high affinity to target molecules [35]. As these are target specific, molecular -imprinted polymers or molecularly imprinted films are used as chemical and biological sensors, drug delivery, controlled drug release systems, and biomolecule separators.

6.1 *Quartz Crystal Microbalance or QCM*

QCM is a sensitive instrument that can measure mass per unit area variations in nanolevel. QCM is used to set apart structurally complex thin films by measuring the molecular interactions and polymer interactions with the help of a sensor. It is an efficient and cost-effective sensing instrument.

Combining the high sensitivity power of quartz crystal microbalance and high selectivity of molecular-imprinted technology, MIP/QCM films are produced with multiple combined advantages like high selectivity, high sensitivity, low detection limit, short response time, wide linear range, and reproducible. Having comparatively a short response time than other detection procedures, these are rapid and reusable, making them cost-effective. The high selectivity of these films indicates their high efficiency in binding only to target molecule even in the presence of other competitive and interfering molecules.

MIP/QCM/FIA

Developed in mid-70s, flow injection analysis (FIA) is automated, a highly efficient and versatile technique for chemical analysis of sample. The principle is similar to that of segmented flow analysis (SFA), but a constant volume of samples is injected rather than continuous injection like in SFA [36]. A biosensor was fabricated by coating BIP (4-Vpy-co-DVB) on thiol-penetrated gold electrode surface of QCM with a detection cycle time of 41 min. MIP/QCM/FIA offers a rapid, efficient, and selective detection (compared to biliverdin, greenish-yellow pigment which is converted to bilirubin-by-bilirubin reductase enzyme) [37].

Hydroxyapatite

Hydroxyapatite is a natural calcium apatite found in human bones, tooth enamel, and some parts of the brain. Good biocompatibility, slow biodegradation rate, and resemblance to human bone's inorganic components make HAP a promising biomaterial used in biomedical applications in tissue repairs, as scaffolds in bone repair, as biomolecule carriers, including bioimaging and diagnosis [38].

Zhengpeng Yang et al., institute of material science and engineering, China, developed a bilirubin-imprinted HAP film on QCM for bilirubin detection. Surface sol-gel technique was employed and morphology of film. The biosensor showed a linear response from concentrations 0.05–80 μM . It also showed a very short response time of only one hour with good reproducibility and high sensitivity [25].

Titanium Film

Titania or titanium (IV) oxide is a chemically inert compound with a wide range of pharmaceutical industries and medical science applications. Titania nanostructures are used as drug delivery systems, drug release controllers, biosensors, and solar cells. Titania, in general, is said to increase the biocompatibility of imprinted devices [39]. Similarly, molecularly imprinted titania film also showed new absorption bands than that of pure titania film. The frequency change to bilirubin concentration showed a linear response between 0.1 to 50 μM concentration of bilirubin with a detection limit as low as 0.05 μM , hence demonstrating high absorption and selectivity of titania film [40].

Red Mud/MIPPy

As the name suggests, red mud or bauxite residue is a byproduct of Bayer's process, an industrial process for extracting alumina from its ore, i.e., bauxite. The red color is due to iron oxides and various other oxides of calcium, silicon, sodium, titanium, aluminum, etc. Its high absorption capacity is used for water treatment and gas cleaning [41]. Modified red mud microparticles with surface molecularly imprinted polypyrrole (MIPPy) on QCM electrode were employed to detect bilirubin. A linear response was shown in the concentration range of 0.1–120 μM with detection limit of only 0.003 μM [42].

6.2 *Diamond-Like Film Modified Electrodes*

Diamond-like films (DLF) are made by the plasma-enhanced chemical vapor deposition (PECVD) process where a chemical vapor is deposited onto a substrate from its vapor state to solid state. Diamond-like film on glassy carbon (GC) electrodes are studied for unconjugated bilirubin detection. DLFs are insulating materials unlike other carbon forms like graphene and graphite. It is due to this insulating property (high resistivity), DLF/GC electrode offers less background current, thus increasing signal-to-noise ratio compared to bare GC electrode. However, high concentration of bilirubin could not be detected using this method due to certain limitations like low solubility of BR in water [43].

7 Others

7.1 *Pyrene*

Pyrene, a polycyclic aromatic hydrocarbon (PAH) is produced by incomplete combustion of organic compounds. It is the smallest yellow-colored PAH solid. The highly symmetrical and aromatic pyrene system is due to its structure, which is made of four tightly fused benzene rings. These features make it a material that exhibits excellent electronic properties. It also has a highly sensitive fluorescence spectrum; thus, it is used as a probe to detect the solvent environment.

Owing to their excellent fluorescent properties, the pyrene schiff (PS) is used to detect bilirubin. The PS aggregates have shown excellent quantum yield and responded well to the BR when combined with BSA to which it has strong binding and interaction [44] (Table 1).

8 Conclusion

In this review, various biomaterials with biosensors have been explored with special emphasis on bilirubin detection like gold nanoparticle, graphene oxide nanoparticles, quantum dots, molecularly imprinted films, and other. We have also discussed how biomaterials have increased the functionality and effectiveness of the biosensors by improving its parameters. The biomaterials were found to enhance the interface between the sensor and the target analyte. The biomaterial has played different roles in different types of sensing, these act as electron bridge in some cases while as a catalyst in other, and they also improve the biological environment, thus supporting the overall performance of the biosensor. In future, the extensive use of engineered-biomaterials with biosensors may further upgrade their performance.

Table 1 Various biomaterials used in different biosensors, function of biomaterial, sensitivity, and detection limit in detection of bilirubin

Biomaterials	Type of biosensors	Functions of the biomaterials	Sensitivity	Detection limit	Limitations	References
<i>Gold nanoparticles</i>					Its optical signals are not stronger than quantum dots	
Multivalled carbon nanotubes (COOH/Graphene/AuNPs)	Electrochemical sensor	Provide ideal environment for immobilization and retaining biomolecules, favorable affinity, and high conductivity	$0.327 \mu\text{A} \mu\text{M}^{-1} \text{cm}^{-2}$	$0.34 \mu\text{M}$	Carbon nanotubes are hydrophobic and they have non-uniform morphology	[10]
<i>Gold nanoclusters</i>						
HSA-AuNCs	Amperometric detection	Electron bridge and catalyst	$0.34 \mu\text{A} \mu\text{M}^{-1}$	86.32 nM		[11]
BSA-AuNCs	Optical sensor (Fluorescence)	Provides long shelf life, makes it cost effective and ecological		$0.61 \pm 0.12 \mu\text{M}$		[12]
<i>Graphene oxide nanoparticles</i>					There is a main concern with its chemical structure	

(continued)

Table 1 (continued)

Biomaterials	Type of biosensors	Functions of the biomaterials	Sensitivity	Detection limit	Limitations	References
GONP@Ppy	Electrochemical sensor	Avoids aggregation, boosts electrical conductivity, sensitivity and, stability	$0.914 \mu\text{A } \mu\text{M}^{-1}$	0.1 nM	Instable in biological environment, very difficult to process	[15]
Graphene oxide-based nanocomposite	Electrochemical sensor	Increases electrocatalytic ability of the sensor by enabling larger surface area	$30 \text{ nA } \mu\text{M}^{-1} \text{ cm}^{-2}$	$0.1 \pm 0.018 \text{ nM}$		[16]
Box/GrONPs/NiNPs	Amperometric sensor	Modified glass electrode lowers detection limit		0.15 nM	NiNPs are expensive and complex to produce	[17]
IAO Nanorods	Electrochemical sensor	Enables the sensor to detect ultra-low concentration of BR by improving electrical conductivity and chemical stability	$2.347 \mu\text{A } \mu\text{M}^{-1} \text{ cm}^{-2}$	$16.5 \pm 0.05 \text{ pM}$	The number of active sites on IAO NRs may decrease after each run	[18]

(continued)

Table 1 (continued)

Biomaterials	Type of biosensors	Functions of the biomaterials	Sensitivity	Detection limit	Limitations	References
MoS ₂ NFs	Electrochemical sensor	MoS ₂ NFs petals increases the surface area and further AuNPs provide affinity toward BR		10 ⁻¹² M	Bare MoS ₂ cannot produce significant SERS signal, unless combined with Au	[21]
Zirconia-coated silica nanoparticles/Chitosan	Electrochemical sensor	Enhance biosensor response and sensitivity by acting as a mediator for electron transmission		0.1 nM	The techniques for producing ZrO ₂ are complicated	[24]
<i>Molecularly imprinted polymers</i>					Deposition of mass decreases the frequency of QCM	
Hydroxyapatite	QCM	Provides favorable environment for biosensing		0.01 μM	Cannot coat complex substrates. Some processes need controlled atmospheric processing	[25]

(continued)

Table 1 (continued)

Biomaterials	Type of biosensors	Functions of the biomaterials	Sensitivity	Detection limit	Limitations	References
Titania film	QCM	Increase biocompatibility		0.05 μM	TiO ₂ exhibit high energy bandgap and smaller wavelength	[40]
Red mud/MIPpy	QCM	Provides high absorption capacity		0.003 μM	Red mud has poor absorption selectivity	[42]
Diamond-film modified electrode	Electrochemical and electro-chemiluminescent	Reduces the background current due to its insulating property, thus increasing S/N ratio		3 nM	Unlike graphene and graphite diamond-based films are insulators and have high resistivity	[43]
Pyrene	Fluorescence	Increases sensor response to BR		0.3 $\mu\text{g/ml}$	Pyrene chromophore is extremely prone to aggregate at high concentrations	[44]

Acknowledgements We would like to thank Dr. Fabiola Munarin, Assistant Professor (Research), Brown University, for her valuable guidance throughout this work.

References

1. Stocker R, Yamamoto Y, McDonagh A, Glazer A, Ames B (1987) Bilirubin is an antioxidant of possible physiological importance. *Science* 235(4792):1043–1046
2. Ullah S, Rahman K, Hedayati M (2016) Hyperbilirubinemia in neonates: types, causes, clinical examinations, preventive measures and treatments: a narrative review article. *Iran J Public Health* 45:558–568
3. Mehrotra P (2016) Biosensors and their applications—a review. *J Oral Biol Craniofacial Res* 6:153–159
4. Prasad A, Mahato K, Maurya PK, Chandra P (2016) Biomaterials for biosensing applications. *J Anal Bioanal Tech* 7(2)
5. Burritt M (1998) Noninvasive and invasive sensors for patient monitoring. *Lab Med* 29:684–687. <https://doi.org/10.1093/labmed/29.11.684>
6. Rawal R, Kharangarh P, Dawra S, Tomar M, Gupta V, Pundir C (2020) A comprehensive review of bilirubin determination methods with special emphasis on biosensors. *Process Biochem* 89:165–174
7. Jiang P, Wang Y, Zhao L, Ji C, Chen D, Nie L (2018) Applications of gold nanoparticles in non-optical biosensors. *Nanomaterials* 8(12):977
8. Yu X, Jiao Y, Chai Q (2016) Applications of gold nanoparticles in biosensors. *Nano LIFE* 06(02):1642001
9. Kaur N, Aditya RN, Singh A, Kuo TR (2018) Biomedical applications for gold nanoclusters: recent developments and future perspectives. *Nanoscale Res Lett* 13 (1)
10. Feng Q et al (2013) Synthesis of the multi-walled carbon nanotubes-COOH/graphene/gold nanoparticles nanocomposite for simple determination of Bilirubin in human blood serum. *Sensors Actuators, B Chem* 185:337–344
11. Santhosh M, Chinnadayala SR, Singh NK, Goswami P (2016) Human serum albumin-stabilized gold nanoclusters act as an electron transfer bridge supporting specific electrocatalysis of bilirubin useful for biosensing applications. *Bioelectrochemistry* 111:7–14
12. Li Z et al (2019) A gold nanoclusters film supported on polydopamine for fluorescent sensing of free bilirubin. *Sensors (Switzerland)* 19(7):1726
13. Eda G, Fanchini G, Chhowalla M (2008) Large-area ultrathin films of reduced graphene oxide as a transparent and flexible electronic material. 3:1–5
14. Priyadarsini S, Mohanty S, Mukherjee S, Basu S, Mishra M (2018) Graphene and graphene oxide as nanomaterials for medicine and biology application. *J Nanostructure Chem* 8:123–137
15. Chauhan N, Rawal R, Hooda V, Jain U (2016) Electrochemical biosensor with graphene oxide nanoparticles and polypyrrole interface for the detection of bilirubin. *RSC Adv* 6:63624–63633
16. Thangamuthu M, Hsieh KY, Kumar PV, Chen GY (2019) Graphene- and graphene oxide-based nanocomposite platforms for electrochemical biosensing applications. *Int J Mol Sci* 20(12):2975
17. Rawal R, Chauhan N, Tomar M, Gupta V (2017) A contrivance based on electrochemical integration of graphene oxide nanoparticles/nickel nanoparticles for bilirubin biosensing. *Biochem Eng J* 125:238–245
18. Rahman MM, Ahmed J, Asiri AM (2019) Selective bilirubin sensor fabrication based on doped IAO nanorods for environmental remediation. *New J Chem* 43:19298–19307
19. Liu X et al (2019) Rosette-like MoS₂ nanoflowers as highly active and stable electrodes for hydrogen evolution reactions and supercapacitors. *RSC Adv* 9:13820–13828

20. Lu Y et al (2015) MoS₂ nanoflowers consisting of nanosheets with a controllable interlayer distance as high-performance lithium ion battery anodes. *RSC Adv* 5:7938–7943
21. Singha SS et al (2018) Au nanoparticles functionalized 3D-MoS₂ nanoflower: an efficient SERS matrix for biomolecule sensing. *Biosens Bioelectron* 119:10–17
22. Bitar A, Ahmad N, Fessi H, Elaissari A (2012) Silica-based nanoparticles for biomedical applications. *Drug Discovery Today* 17(19–20):1147–1154
23. Jiang T, James R, Kumbar S, Laurencin C (2014) Chitosan as a biomaterial. In: *Natural and synthetic biomedical polymers*, pp 91–113
24. Batra B, Lata S, Sunny, Rana JS, Pundir CS (2013) Construction of an amperometric bilirubin biosensor based on covalent immobilization of bilirubin oxidase onto zirconia coated silica nanoparticles/chitosan hybrid film. *Biosens Bioelectron* 44:64–69
25. Yang Z, Zhang C (2011) Molecularly imprinted hydroxyapatite thin film for bilirubin recognition. *Biosens Bioelectron* 29:167–171
26. Kouwenhoven L, Marcus C (1998) Quantum dots. *Phys World* 11(6):35–40
27. Klostranec BJM, Chan WCW (2006) Quantum dots in biological and biomedical research: recent progress and present challenges. *Adv Mater* 18(15):1953–1964. <https://doi.org/10.1002/adma.200500786>
28. Jamieson T et al (2007) Biological applications of quantum dots. 28:4717–4732
29. Karmakar S, Das TK, Kundu S, Maiti S, Saha A (2020) Physicochemical understanding of protein-bound quantum dot- based sensitive probing of bilirubin : validation with real samples and implications of protein conformation in sensing. *ACS Appl Bio.*<https://doi.org/10.1021/acsbm.0c01165>
30. Abha K et al (2019) Photoluminescence sensing of bilirubin in human serum using L-cysteine tailored manganese doped zinc sulphide quantum dots. *Sensors Actuators, B Chem* 282:300–308
31. Anjana RR et al (2017) S, N-doped carbon dots as a fluorescent probe for bilirubin. 2:1–11
32. Bloomfield V (1966) The structure of bovine serum albumin at low pH*. *Biochemistry* 5:684–689. <https://doi.org/10.1021/bi00866a039>
33. Wu P, Yan XP (2013) Doped quantum dots for chemo/biosensing and bioimaging. *Chem Soc Rev* 42(12):5489. <https://doi.org/10.1039/c3cs60017c>
34. RC H, Schiffrman J, Balakrishna R (2018) Quantum dots as fluorescent probes: Synthesis, surface chemistry, energy transfer mechanisms, and applications. *Sens Actuators B: Chem* 258:1191–1214. <https://doi.org/10.1016/j.snb.2017.11.189>
35. Mujahid A, Dickert FL (2016) Molecularly imprinted polymers: principle, design, and enzyme-like catalysis, pp 79–101. <https://doi.org/10.1016/B978-0-12-801301-4.00005-0>
36. Outline C (2014) Evolution and description of the principal flow techniques.<https://doi.org/10.1016/B978-0-444-59596-6.00001-2>
37. Wu AH, Syu MJ (2006) Synthesis of bilirubin imprinted polymer thin film for the continuous detection of bilirubin in an MIP/QCM/FIA system. *Biosens Bioelectron* 21:2345–2353
38. Lin K, Chang J (2015) Structure and properties of hydroxyapatite for biomedical applications. In: *Hydroxyapatite (HAP) for biomedical applications*, vol 4214. Elsevier Ltd
39. Three C (2017) *Industrial inorganic chemistry* 3.1. <https://doi.org/10.1016/B978-0-12-849891-0.00003-5>
40. Yang Z, Yan J, Zhang C (2012) Piezoelectric detection of bilirubin based on bilirubin-imprinted titania film electrode. *Anal Biochem* 421:37–42
41. Wang S, Ang HM, Tadé MO, Mud R (2008) Chemosphere Novel applications of red mud as coagulant , adsorbent and catalyst for environmentally benign processes. 72:1621–1635
42. Zhang C, Bai W, Qin T, Yang Z (2019) Fabrication of red mud/molecularly imprinted polypyrrole-modified electrode for the piezoelectric sensing of bilirubin. *IEEE Sens J* 19:1280–1284
43. Snizhko D, Zhulodov Y, Bilash O (2019) Sensor based on diamond-like film modified electrodes for bilirubin detection. In: *2019 IEEE 39th international conference on electronics and nanotechnology, ELNANO 2019—proceedings*. Institute of Electrical and Electronics Engineers Inc., pp 471–474. <https://doi.org/10.1109/ELNANO.2019.8783811>

44. Srinivasan V et al (2019) Pyrene-based prospective biomaterial: in vitro bioimaging, protein binding studies and detection of bilirubin and Fe^{3+} . *Spectrochim Acta—Part A Mol Biomol Spectrosc* 221:117150

Chapter 4

Dimensional Optimization of Low-Frequency Piezoelectric Nanoenergy Harvesters



Swathy S. Panicker and P. R. Sreenidhi

Abstract Energy harvesting is the technology which scavenges energy from the ambient sources of energy. Several researches are moving in the field of energy harvesting to get maximum output power from the ambient sources. This paper deals with the optimization on the dimensions of a piezoelectric energy harvester (PEH) which can work at low frequency using different piezoelectric materials. An analysis of a rectangular block-shaped geometry was done with its height and length varied to study the effect of length and height of the geometry with its natural frequency. Thus, the optimized geometry was used as a piezoelectric energy harvester by using a fixed constraint at one end. An electrical circuit with a resistor is connected to the PEH device, which measures the output voltage and current through the device. An optimized dimension of 100 mm × 1 mm for the nanogenerator with PVDF material yielded a good performance including maximum current and voltage at low frequencies of 0–30 Hz. The study of perturbations was implemented on the optimized geometry of the piezoelectric material, which reduced its resonant frequency to 11.96 from 1373.05 Hz.

Keywords Energy harvesters (PENG) · Piezoelectricity · Polarization · Nanogenerators · Resonant frequency · Voltage conversion efficiency

1 Introduction

Energy harvesting is the technology which scavenges energy from the ambient sources of energy like sun, wind, thermal energy, etc., and converts it into some usable energy like electrical energy which is either directly used or stored it for some of the devices like sensor networks, wearable devices, etc. With the recent

S. S. Panicker (✉) · P. R. Sreenidhi
Amrita Vishwa Vidyapeetham, Amritapuri, India
e-mail: swathysp@am.amrita.edu

P. R. Sreenidhi
e-mail: sreenidhipr@am.amrita.edu

© The Author(s), under exclusive license to Springer Nature Singapore Pte Ltd. 2022
V. Bindhu et al. (eds.), *Proceedings of Fourth International Conference on Inventive Material Science Applications*, Advances in Sustainability Science and Technology,
https://doi.org/10.1007/978-981-16-4321-7_4

research and emerging trend, this energy harvesting technique is a better alternative for conventional battery. There are different ways of energy harvesting like photo-voltaic energy harvesting, thermoelectric energy harvesting, electromagnetic energy harvesting, piezoelectric energy harvesting, pyroelectric energy harvesting, triboelectric energy harvesting, etc. [1]. Among them, piezoelectric energy harvesting attains a relevant importance because it works on the basis of vibrations, and these vibrations are abundantly available in nature. Piezoelectricity is the phenomenon when a stress is applied on the material, an electrical energy is generated. This is called direct piezoelectric effect. A material deformation is observed when an electric field is applied on piezoelectric material. This phenomenon is known as converse piezoelectric effect. This direct piezoelectric effect can be used to convert some forms of vibrational energy into an electric energy, and it can be stored and used in low-power electronic devices to make it self-powering [2].

The four main categories of piezoelectric materials that are used for the energy harvesting applications are as follows [3]:

- Single crystals (include Lithium niobite, Rochelle salt and quartz crystals)
- PiezoCeramics (barium titanate (BaTiO_3), potassium niobite (KNbO_3), lead zirconate titanate (PZT))
- PiezoPolymers (cellulose and derivatives , polylactic acid (PLA), polyvinylidene fluoride (PVDF))
- Polymer composites or nanocomposites (polyvinylidene fluoride—zinc oxide, cellulose BaTiO_3 , polyimides-PZT)

When these materials are manipulated into nanometer size range, they can be used in various implantable and wearable devices as nanogenerators, so that they can harvest energy from body motions like breathing, muscle movements, walking, joint motion, etc. Since the input energy to these nanogenerators is of low frequency, the authors aim to study the dimensional optimization of some piezoelectric materials which can operate at low frequencies to self-power some low-power devices.

2 Materials and Methods

2.1 Materials

The piezoelectric material used for the study includes aluminium nitride (AlN) [4], cadmium sulphide (CdS) [5] and polyvinylidene fluoride (PVDF). One of the newest material which is added in the ceramic family is AlN, which is a covalently bonded material with a hexagonal structure. They have good thermal conductivity, mechanical properties, electrical insulation and dielectric insulation. Cadmium sulphide is a yellow-coloured inorganic compound with two different crystal structures. CdS is a direct band gap semiconductor with a piezoelectric effect. PVDF is a fluoropolymer which is thermoplastic in nature and also non-reactive. Its piezoelectricity is very

Table 1 Properties of AlN, CdS, PVDF

Property	AlN	CdS	PVDF
Piezoelectric coefficient (pm/v)	d33 = 3.0	d33=10.32	d33 = 21
Density (kg/m ³)	3300	5678	1780
Young's modulus (GPa)	308	48.1	8.3
Relative permittivity	9	9.01,9.52	7.4,9.3,7.6
Poisson's ratio	0.28	0.3	0.37

large, when this PVDF film is poled, it produces piezoelectricity ten times larger than other polymers. The different properties like piezoelectric coefficient, density, Young's modulus, relative permittivity and Poisson's ratio are illustrated in Table 1.

2.2 Methods

To study piezoelectric effect, Comsol Multiphysics software was used by choosing "Physics" as piezoelectricity, so that solid mechanics and electrostatics physics will appear automatically into the model builder window as piezoelectric effect includes strain and electricity. Under the global parameters, different variables for dimension optimization can be given so that a parametric analysis of these variables can be studied to obtain an optimum result. To analyse a piezoelectric energy harvesting device [6–9], an electric circuit has to be enabled by connecting an external terminal to the device.

2.3 Geometry of the Nanogenerator

A rectangular block with three sides as a variable length, breadth and height is chosen. Length is varied from 10 to 100 mm, and height is varied from 1 to 10 mm. Figure 2a shows the image of the geometry chosen. A boundary load of 0.5 N is applied in the $-z$ direction of the piezoblock. In order to reduce the resonant frequency, perturbations with width of the perturbation (w_1) varying from 0.1 to 1 mm and space between the perturbation (s) varying from 0.1 to 0.3 mm were implemented into the piezoblock as depicted in Fig. 2b.

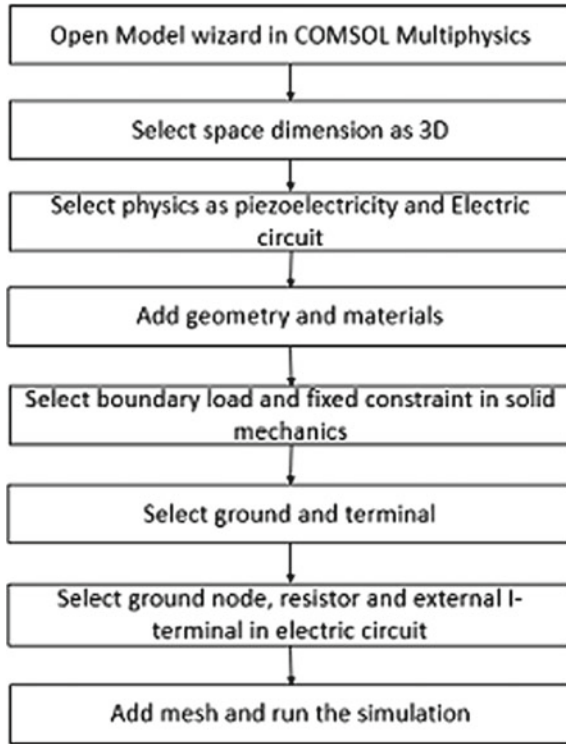


Fig. 1 Methodology for the simulation

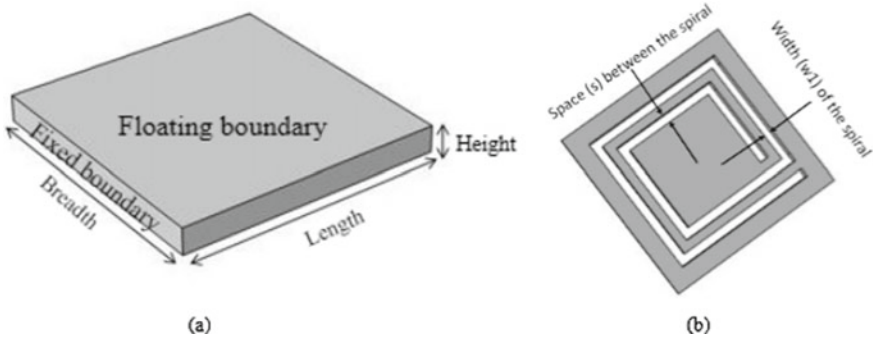


Fig. 2 a Geometry for dimension optimization. b Geometry when perturbations are implemented

3 Results and Discussions

3.1 Analysis of Piezoelectric Materials by Varying Length

The length of rectangular block of AlN, CdS and PVDF kept varying from 10 to 100 mm by keeping breadth as 10 mm and height as 1 mm. The Eigen frequency and floating potential are calculated, and the results are depicted in Tables 2 and 3, respectively.

As per the table, it is understood that as the length of the material increases, the resonant frequency of the material decreases, i.e. the resonant frequency is inversely proportional to the length squared as per the fundamental frequency of a singly clamped Euler–Bernoulli beam with a rectangular cross section of Eq. (1) [10–12]. The breadth variation by keeping length constant resembles same as that of the length variation. From the result, it is observed that only PVDF responds at low frequencies, and the floating potential for PVDF decreases when the length increases. CdS shows a better result compared to AlN at lower lengths.

$$f_1 = \frac{1}{2\pi} \frac{h}{L^2} \sqrt{\frac{E}{\rho}} \quad (1)$$

where E is the Young's modulus and L is the length.

Table 2 Eigen frequencies for the three materials when length is varied from 10 to 100 mm

Length (mm)	Eigen freq of AlN (Hz)	Eigen freq of CdS (Hz)	Eigen freq of PVDF (Hz)
10	17194.59	5191.61	13073.05
20	4287.71	1280.7	517.23
30	1892.26	558.08	227.3
40	1059.41	310.09	126.92
50	675.8	196.72	80.81
60	468.25	135.89	55.94
70	343.45	99.46	41
80	262.61	75.91	31.33
90	207.27	59.82	24.72
100	167.74	48.36	20

Table 3 Floating potential for the three materials when length varies from 10 to 100 mm

Length (mm)	FP of AlN (pV)	FP of CdS (pV)	FP of PVDF (pV)
10	0.759	1.22	1.31
20	1.11	9.58	0.898
30	-1.26	-0.494	-1.93
40	-4.12	-3.11	-6.76
50	-2.76	-3.58	-4.47
60	-3.24	-3.14	-5.32
70	-1.12	-1.70	-8.26
80	0.450	-0.5843	2.20
90	-0.633	-0.926	0.170
100	-0.937	-1.78	-0.621

Table 4 Eigen frequencies for the three materials when height is varied

Height (mm)	Eigen freq of AlN (Hz)	Eigen freq of CdS (Hz)	Eigen freq of PVDF (Hz)
1	17194.59	5191.61	2080.64
2	33375.21	9950.69	4031.96
3	48020.35	14162.78	5790.93
4	60896.65	17785.29	7329.2
5	71991.7	20833.26	8640.03
6	81475.83	23401.45	9752.23
7	89524.91	25533.83	10682.68
8	96368.66	27322.79	11463.31
9	102190.57	28818.63	12117.28

3.2 Analysis of Piezoelectric Materials by Varying Height

The height of all the three selected materials is varied from 1 to 10 mm by keeping the length as 100 mm and breadth as 10 mm. The results for Eigen frequency and floating potential are illustrated in Tables 4 and 5, respectively. Due to software limitation, the length is reduced from 10 to 9 mm. The results show that resonant frequency increases with increase in height and obeys Eq. (1). In this case, also PVDF shows good results at lower frequencies [11].

Table 5 Floating potential for the three materials when height is varied

Height (mm)	FP of AlN (pV)	FP of CdS (pV)	FP of PVDF (pV)
1	0.759	1.22	1.31
2	-2.87	-7.49	-9.09
3	-0.103	0.230	-0.138
4	1.47	-1.51	-0.254
5	7.84	14.1	10.4
6	-1.53	-5.87	-6.03
7	6.85	12.6	8.99
8	0.172	-4.88	0.902
9	-7.65	-12.1	-10.8

Table 6 Output voltage of three materials

Freq (Hz)	Output V of AlN (pV)	Output V of CdS (pV)	Output V of PVDF (pV)
10	-0.909	1.02	4.23
20	-3.67	4.63	127
30	-8.37	13.3	-22.2
40	-15.2	37.9	-11.6
50	-24.4	252	-5.43
60	-36.5	-125	0.885
70	-52.01	-66.6	8.50
80	-71.7	-51.5	18.4
90	-97.0	-44.8	32.2
100	-130	-41.0	53.7

3.3 Analysis by Inserting Electric Circuit

A resistor of 1000Ω is added to the piezoelectric block. The voltage across the resistor is obtained and depicted in Table 6. The graph for the voltage when frequency varied from 0 to 1000 Hz is shown Fig. 4a. From Fig. 3a, it is clear that only PVDF [13–16] has high output voltage. Figure 4b emphasizes the performance of PVDF at the lower frequency of 20 Hz. CdS also shows a better result but at higher frequency than that of PVDF.

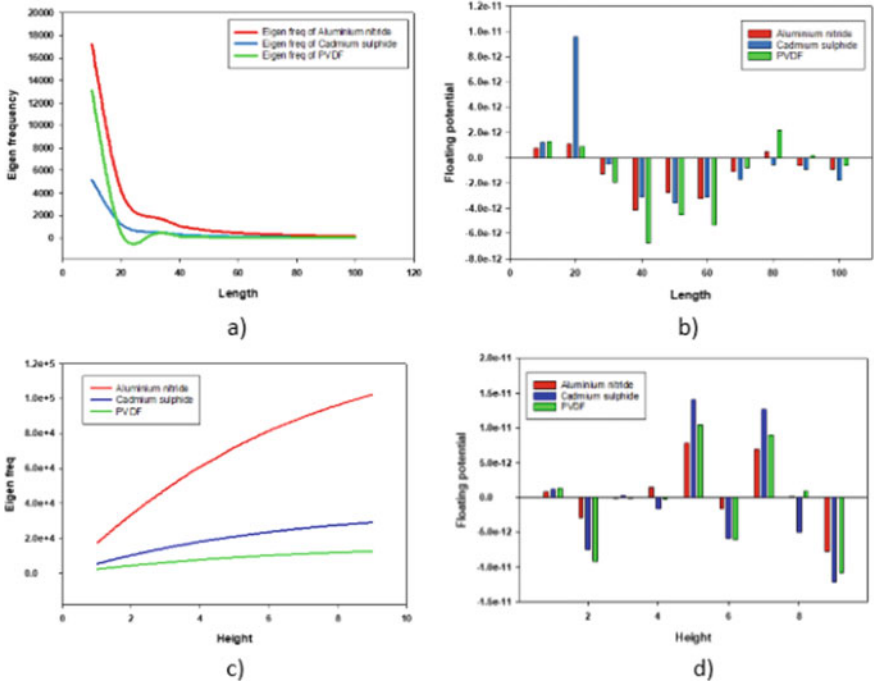


Fig. 3 **a** Length versus Eigen frequency for AlN, CdS and PVDF. (Length in mm and freq in Hz) **b** Length versus floating potential for AlN, CdS and PVDF. (Length in mm and floating potential in volts. **c** Height versus Eigen frequency (Height in mm and freq in Hz) **d** Height versus floating potential. (Height in mm and potential in volts)

3.4 Efficiency of the Optimized Piezoelectric Material

Efficiency of energy harvesting is defined as the ratio of output electrical power to the input mechanical power. The efficiency for all the three materials is analysed, and PVDF is having high efficiency at the low frequency of 20Hz, which is the resonant frequency of the analysed PEH device [17]. The efficiency graph for all the three materials is depicted in Fig.4c.

$$E\% = \frac{E_e}{E_m} \times 100 \tag{2}$$

3.5 Analysis by Varying Resistance

The resistance(in Ω) connected to the electric circuit is varied from 100 to 1000 ohm, and voltage (in V) across the resistor is studied. The results are shown in Table 7,

and corresponding figures are depicted in Fig. 5a. From the table, it is clear that as the resistance increases, the voltage increases (Fig. 5).

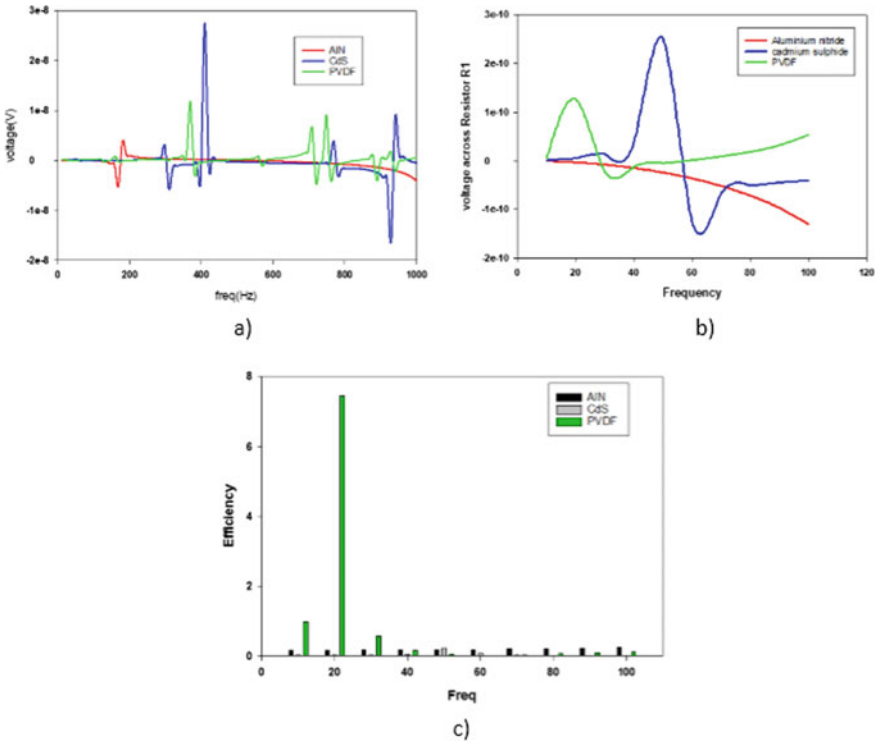


Fig. 4 **a** Output voltage when frequency varied from 10 to 1000Hz. **b** Output voltage when frequency varied from 10 to 100Hz. **c** Efficiency of the three materials

Table 7 Output voltage of three materials when resistance is varied

Resistance (ohm)	Voltage of PVDF (pV)	Voltage of CdS (pV)	Voltage of AlN (pV)
100	1.27	2.52	-51.5
200	5.07	10.1	-206
400	20.3	161	-824
600	45.6	161	-1850
800	81.1	161	-3300
1000	127	252	-5150

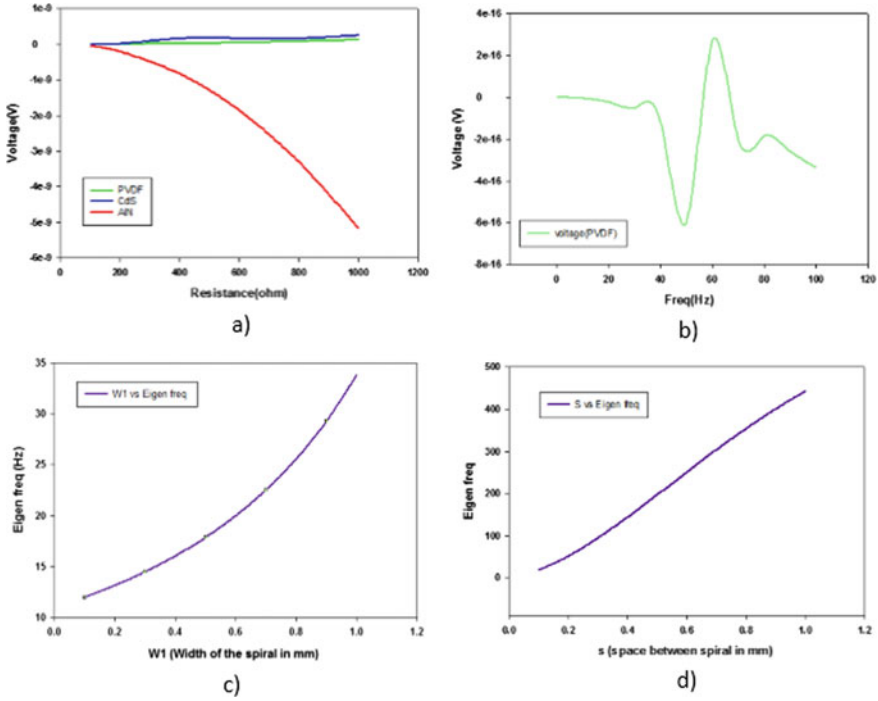


Fig. 5 **a** Voltage of three materials when resistance is varied. **b** Voltage through the PVDF material at low frequency, **c** relationship between Eigen frequency and width of the spiral, **d** relationship between Eigen frequency and space of the spiral

3.6 Analysis by Incorporating Perturbations in PVDF Material

From the optimization of AlN, CdS and PVDF discussed above, it is clear that PVDF can work at low frequencies, with high efficiencies. So the further step aims to reduce the resonant frequency at smaller lengths to use it in some personal equipments for self-powering.

When length and breadth equal 10 mm, PVDF produced a resonant frequency of 13073.05 Hz, which is very high. To reduce the Eigen frequency, the length of the material is increased, since they are having inverse relations. Increasing length cannot find applications in low-frequency devices [18–20] so some perturbations are introduced in the PVDF material by keeping the length and breadth as 10 mm and height 1 mm, respectively. The configuration is shown in Fig. 2b. A rectangular spiral was inserted into the rectangular PVDF block and studied the effect of width of the perturbations (w_1) on frequency and also the spacing between the perturbation (s) on the resonant frequencies [21, 22]. The possible combinations of w_1 and s with

Table 8 Eigen frequencies for varying width (w_1) and space (s) of the spiral

Space (s)	Width (w_1)	Freq (Hz)
0.1	0.1	11.96
0.1	0.2	13.10
0.1	0.3	14.47
0.1	0.4	16.03
0.1	0.5	17.84
0.1	0.6	19.97
0.1	0.7	22.51
0.1	0.8	25.56
0.1	0.9	29.24
0.1	1	33.81
0.2	0.1	34.10
0.2	0.2	37.57
0.2	0.3	41.44
0.2	0.4	45.92
0.2	0.5	51.12
0.2	0.6	57.25
0.2	0.7	64.57
0.2	0.8	73.29
0.2	0.9	83.73
0.2	1	96.51
0.3	0.1	62.63
0.3	0.2	69.26
0.3	0.3	76.76
0.3	0.4	84.95
0.3	0.5	94.74

resonant frequency less than 100 Hz are illustrated in Table 8. Also their relationships are plotted in Fig. 5c,d.

From Fig. 5c, d, it is understood that as the width of the spiral and spacing between the spiral increases, the Eigen frequency also increases. The reason behind this shift can be studied from Eq. (3), which shows that the resonant frequency is inversely proportional to the inductance and capacitance.

$$f_r = \frac{1}{2\pi\sqrt{LC}} \quad (3)$$

When spiral perturbations are introduced, the mutual capacitance produced due to the spacing(s) between the spirals and mutual inductance produced due to the interactions of field due to the current flow through the spiral increase, so as a result the resonant

Table 9 Output voltage when perturbation of $w_1 = 0.5$ mm and $s = 0.2$ mm are introduced

Freq (Hz)	Voltage (μ V)
10	-5.44E-6
20	-2.24E-5
30	-5.40E-5
40	-0.000114
50	-0.000601
60	-0.000274
70	-0.000203
80	-0.000183
90	-0.000259
100	-0.000337

frequency will be decreased or shifted to the lower side of the frequency graph. When spacing between the spirals is less, the mutual capacitance will be more resulting in lower resonant frequencies. To study the voltage, a resistance of $1k\Omega$ is connected and kept w_1 as 0.5 mm and s as 0.2 mm. The voltage for this specification is shown in Table 9 and Fig. 5b. When perturbations are introduced, the voltage is more at their resonant frequencies when compared to the one without perturbations.

4 Conclusion

An optimization of piezoelectric materials like AlN, CdS and PVDF is done to find the apt piezoelectric material which is suited to operate at low frequencies. In the length-varying analysis, it is obtained that as the length increases, resonant frequency decreases, and in the height variation it is obtained as the resonant frequency increases with the increase in the height. From the Eigen frequency study, it is observed that PVDF is the best material which can operate at low frequencies. In the frequency domain, study with an electrical circuit also shows that PVDF responds with high voltage at low frequencies. The voltage conversion efficiency for PVDF is high at its low resonant frequency of 20 Hz. But increasing length to adjust the resonant frequency is not practical, while using them in wearable electronics. To compensate the limitation of increase in length with decrease in frequency, perturbations are introduced into the geometry, which reduces the resonant frequency even at lower lengths. The PVDF material with length and breadth of 10 mm and height 1 mm produced a resonant frequency of 13073.05 Hz, but by incorporating the spiral perturbations ($w_1 = 0.1$ mm and $s = 0.1$ mm) the resonant frequency reduced to 11.96 Hz. Thus, in the implementation of perturbations in the PVDF material with the optimized geometry, it can be suited in several wearable devices. With the PVDF material, adjusting the design with perturbations can be a next stage of PEH design for the researchers.

References

1. Sarma AS, Sreekala CO, Menon SK (2020) Microstrip fed monopole antenna on Barium Titanate-PDMS substrate. *Mater Today Proc* 33:1308–1311. <https://doi.org/10.1016/j.matpr.2020.04.087>
2. Covaci C, Gontean A (2020) Piezoelectric energy harvesting solutions: a review. *Sensors* 20(12):3512. Multidisciplinary Digital Publishing Institute
3. Prakash Raju GKS, Ashok Kumar P, Srinivasa Rao KS, Aravapalli V (2017) Design and simulation of cantilever based MEMS bimorph piezoelectric energy harvester. *Mech Mater Sci Eng J* 9(1). doi:<https://doi.org/10.2412/mmse.16.9.490>
4. Gu L (2011) Low-frequency piezoelectric energy harvesting prototype suitable for the MEMS implementation. *Microelectron J* 42(2):277–282. Elsevier
5. Harb A (2011) Energy harvesting: state-of-the-art. *Renew Energy* 36(10):2641–2654. (Elsevier)
6. Hullavarad NV, Hullavarad SS, Karulkar PC (2008) Cadmium sulphide (CdS) nanotechnology: synthesis and applications. *J Nanosci Nanotech* 8(7):3272–3299. American Scientific Publishers
7. Li H, Tian C, Deng ZD (2014) Energy harvesting from low frequency applications using piezoelectric materials. *Appl Phys Rev* 4:041301. (AIP Publishing LLC)
8. Liu H, Lee C, Kobayashi T, Tay CJ, Quan C (2012) A new S-shaped MEMS PZT cantilever for energy harvesting from low frequency vibrations below 30 Hz. *Microsystem technologies* 18(4):497–506. (Springer)
9. Lu L, Ding W, Liu J, Yang B (2020) Flexible PVDF based piezoelectric nanogenerators. *Nano Energy* 105251. (Elsevier)
10. Massaro A, De Guido S, Ingrassio I, Cingolani R, De Vittorio M, Cori M, Bertacchini A, Larcher L, Passaseo A (2011) Freestanding piezoelectric rings for high efficiency energy harvesting at low frequency. *Appl Phys Lett* 98(5):053502. (American Institute of Physics)
11. Mercy A, Selvaraj RS, Boaz BM, Anandhi A, Kanagadurai R (2013) Synthesis, structural and optical characterisation of cadmium sulphide nanoparticles. NISCAIR-CSIR, India
12. Mhetre MR, Nagdeo NS, Abhyankar HK (2011) Micro energy harvesting for biomedical applications: a review. In: 2011 3rd international conference on electronics computer technology, vol 3. IEEE, pp 1–5
13. Mishra S, Unnikrishnan L, Nayak SK, Mohanty S (2019) Advances in piezoelectric polymer composites for energy harvesting applications: a systematic review. *Macromol Mater Eng* 304(1):1800463. (Wiley Online Library)
14. Chandran R, Sreekala CO, Menon SK (2020) BaTiO₃/V₂O₅ composite based cylindrical dielectric resonator antenna for X-band applications. *Mater Today Proc* 33:1367–1370
15. Selvarathinam J, Anpalagan A (2016) Energy harvesting from the human body for biomedical applications. *IEEE Potentials* 35(6):6–12. (IEEE)
16. Sreeja SDB, Gopalan S, Sreekala CO (2019) Piezoelectric energy harvesting system suitable for remotely placed sensors with inter-digitated design. *AIP Conf Proc* 2162(1):020052
17. Rajeev SP, John SK, Cherian R, Karumuthil SC, Varghese S (2020) Next-generation rooftop tribo-piezoelectric energy harvesting from rain power. *Appl Nanosci* 10(3):679–686
18. Rajeev SP, Sivapriya S, Cherumannil Karumuthil S, Varghese S (2020) Prototype of energy harvesting door handles using polymer nanocomposite. *Appl Nanosci* 10(1):1–13
19. Rajeev SP, John VN, Sabarinath S, Ashfaq A, Subash CK, Varghese S (2020) Nature-inspired PDMS cumulonimbus micro-energy-harvesting cloud. *Appl Nanosci*
20. Suhailrashid S, Sreekala CO, Menon SK (2019) Dielectric resonator antenna on Ba TiO₃ embedded with TiO₂ nano composite for Wi-Fi applications. *IOP Conf Ser Mater Sci Eng* 577:012190

21. Siang J, Lim MH, Salman Leong M (2018) Review of vibration-based energy harvesting technology: mechanism and architectural approach. *Int J Energy Res* 42(5):1866–1893. (Wiley Online Library)
22. Tiwari S, Gaur A, Kumar C, Maiti P (2019) Enhanced piezoelectric response in nanoclay-induced electrospun PVDF nanofibers for energy harvesting. *Energy* 171:485–492. (Elsevier); Zhao Y, Peng X, Fu T, Huang C, Xiang H, Hu N, Yan C (2018) Investigation of mechanical behaviour of amorphous aluminium nitride. *Materialia* 2:148–156. (Elsevier)

Chapter 5

A Review on Materials for Integrated Optical Waveguides



Padmaja Jain and Rajini V. Honnungar

Abstract To meet the expected future requirements, optical devices are required for ultrafast and ultrahigh bandwidth communication and computing. These optical devices are capable of overcoming the bottleneck imposed by the limited bandwidth of electronic circuits in the areas like data storage, computing, or telecommunication networks (Selvaraja and Sethi in Chapter 6: review on optical waveguides. IntechOpen, 2018). The optical waveguide is the basic element of any optical circuits. Waveguides permit the optical connection of different devices. Integrated optical waveguides with light confinement in size of the order of the wavelength are required to build integrated optical circuits that substitute micro-electronic circuits. There are several materials available for waveguide design. This paper is an overview of the various waveguide materials.

Keyword Electro-optic · Bandgap · Optoelectronic · Polarization · Optical waveguides

1 Introduction

Integrated optics is now a day becoming sophisticated. Optical waveguides are generally used as the basis of active and passive devices in the field of integrated optics. For computing and communication applications, waveguides are invaluable since these are resistant to electromagnetic interference (EMI)-induced cross-talk. Using copper-based interconnects, future-generation, high-end information processing is very difficult. Optical interconnects are required to transmit information through the optical waveguide, and these waveguides provide a possible solution for improving data transmission [1].

P. Jain (✉)
BNMIT, Bangalore, India

R. V. Honnungar
RNSIT, Bangalore, India

1.1 Lithium Niobate (LiNbO_3)

Lithium niobate (LiNbO_3) consists of niobium, lithium, and oxygen. Its single crystals are an important material for optical waveguides. Lithium niobate single crystal can be grown by the Czochralski process. Lithium niobate optical waveguide has got diffused index profile, and it can be used as guided-wave devices. The Z-cut X-propagating lithium niobate optical waveguide is shown in Fig. 1. In figure, X, Y, Z are the crystal orientations. Different techniques are used for the fabrication of lithium niobate-based optical waveguide substrates, like titanium in-diffusion, silver-lithium ion exchange, ion implantation, annealed proton exchange, silver-lithium ion exchange, and Li_2O out-diffusion. In this, the first available techniques are the Li_2O out-diffusion. The drawbacks of this technique are single-polarization and low optical confinement. The proton exchange process with high optical confinement is the next fabrication technique. This technique has got drawbacks like less electro-optic efficiency because of high proton concentration while proton exchange process and also large propagation loss. In [2], two important techniques, which are annealed proton exchange and titanium in-diffusion, were discussed in detail.

Since the 1970s, lithium niobate has gained a lot of attention because of its ability to alter light by using an electric control. From Ti-diffused waveguides to photonic crystals, we can see the advancement of electro-optical (EO) LiNbO_3 waveguides throughout the years. Numerous studies are going on in developing fewer EO components with smaller optical losses and lower power consumption. The challenge lies in strongly confining the light meanwhile maintaining fewer losses (Fig. 2).

Fig. 1 Crystal orientation (X, Y, Z) of LiNbO_3 optical waveguides [2]

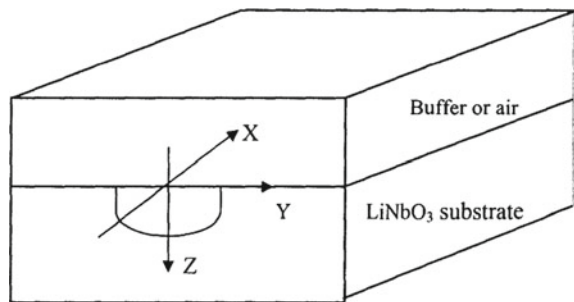
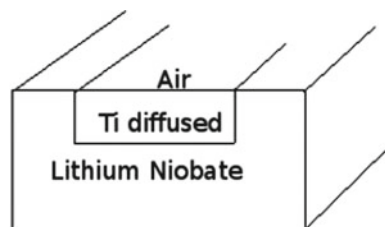


Fig. 2 Lithium niobate waveguide structure [3]



Since the invention of electricity, electrical regulation of light has become an interesting matter. Lithium niobate has become a material of interest because of its electro-optical (EO) properties and its refractive index, which regulates light speed and is sensitive to electrical signals. Lithium niobate is popularly used where modulation of light is needed, like in telecommunication systems. Modulators developed from lithium niobate can adjust the intensity of the light without any perturbation on the phase as compared to the semiconductors. Although semiconductors are successful for short-range telecommunication system, modulation offered by lithium niobate-based components are favorable when optical signals of high bit rate need to travel long distances which are in the range of thousand kilometers [4].

1.2 III–V Semiconductors

III–V compound semiconductor is an alloy. It contains elements from group III and V in the periodic table. Binary compounds are GaAs, GaN, InP, and InAs. A fraction of the lattice sites in a binary semiconductor is replaced by other elements to form quaternary (e.g., InGaAsP, InAlGaAs) compounds or ternary (e.g., InGaAs, AlGaIn) compounds (Table 1).

By changing the composition of different elements, it is possible to engineer the lattice constant and bandgap of III–V semiconductors. Figure 3 shows the relation between bandgap energy, crystal lattice constant, and emission wavelength of III–V compound semiconductors.

For many optical applications, there are significant advantages in using III–V semiconductors compared to glass or LiNbO₃. There is a lot of interest in III–V semiconductor guide wave devices. It is largely been accepted as single-mode optical waveguides for communications transmission applications [5].

The rapid speed of development for electronic circuits was largely due to scaling, which without integration could not have been feasible. Integration refers to the location of all device components on the same chip. The fabrication of the entire chip from a single wafer is represented by monolithic integration. Hybrid integration, on the other hand, specifies the creation of certain components of a chip from various wafers and then assembles the parts together in the form of a single chip. In addition to allowing complex systems to have a smaller footprint (and therefore lower costs), monolithic integration often significantly simplifies the assembly process that would be needed if all the components were discrete or if hybrid integration were used. The

Table 1 Group III and group V elements

Group III	Group V
B	N
Al	P
Ga	As
In	Sb

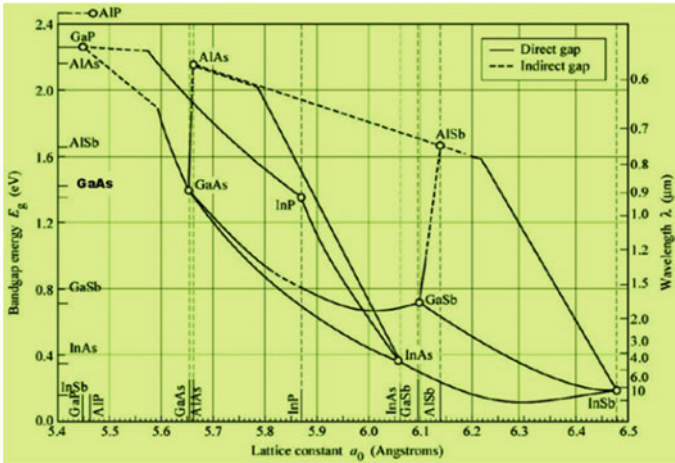


Fig. 3 Bandgap as a function of lattice constant for III–V binary and ternary compounds [5]

fact that III–V semiconductors are well-suited for monolithic integration makes it an exciting research area for III-V photonics [5].

1.3 Gallium Arsenide (GaAs)

GaAs is an III–V semiconductor. It is having a zinc blende crystal structure. GaAs has got direct bandgap. The meaning of direct bandgap is that here the minimum of the conduction band is directly over the maximum of the valence band. As compared to the indirect bandgap materials, here transition between the conduction and valence band only requires a change in energy, and there is no change in momentum. This direct bandgap property of GaAs is very useful, and it is used in the manufacture of semiconductor lasers and light-emitting diodes because here a photon is emitted whenever an electron changes its energy levels from conduction band to the valence band. Figure 4 shows the direct bandgap of GaAs as compared to silicon which is of the indirect bandgap.

Waveguides made from GaAs/AlGaAs produce very interesting optical properties for nonlinear optical signal processing. Compared to crystalline silicon, the optical Kerr coefficient of GaAs material is four times larger. Working with a low-loss, highly nonlinear material system which allows the construction of passive and active devices is the key feature in the realization of on-chip integrated optical devices. GaAs and their alloys are useful materials in the creation of low-loss waveguides.

GaAs/AlGaAs rib waveguides are recommended for optical and electro-optical devices like filters, modulators, and switches. Most of these devices are necessary for a single mode. It is difficult to achieve efficient coupling of single-mode GaAs/AlGaAs and optical fiber. In [7], a single-mode gallium arsenide/aluminum

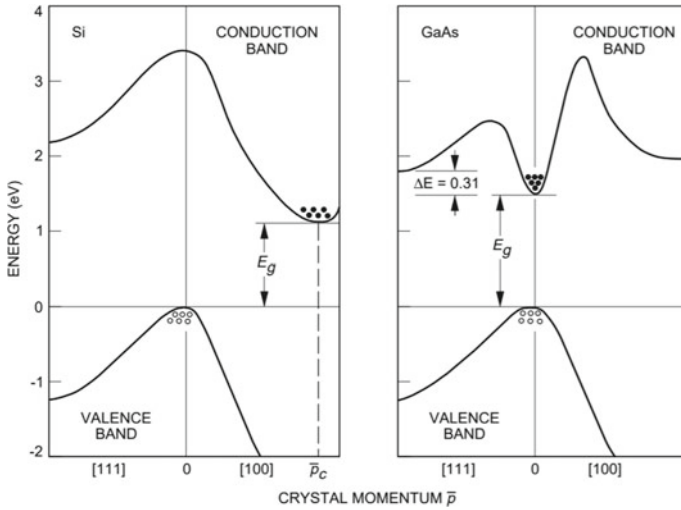
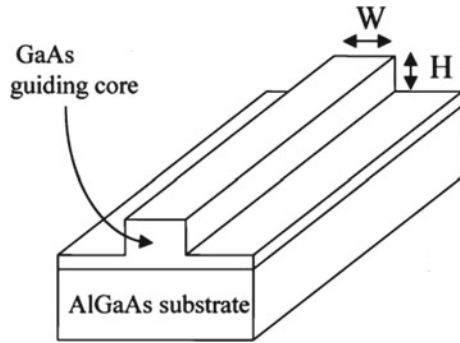


Fig. 4 Energy band structure of Si and GaAs [6]

Fig. 5 GaAs rib waveguide structure



gallium arsenide waveguide which is in fundamental mode with well-matched dimensions to optical fiber is explained. Here, gas/AlGaAs rib waveguides are designed with a core thickness $< 1 \mu\text{m}$ to achieve single-mode operation (Fig. 5).

1.4 Indium Phosphide (InP)

The material system of indium phosphide is an essential subset of III–V semiconductors. Indium phosphide is a semiconductor binary III–V that has a crystal structure with a lattice constant of 5.87 \AA and two overlapped face-centered cubic lattices. InP is available as large wafers at moderate rates, but not as cheap as Si, making it desirable for the study and, in some cases, the development of electrical and photonic

devices. InP can be used in communications devices where high speed is a requirement since its electron mobility is far higher than that of silicon. At room temperature, indium phosphide has a direct bandgap of 1.344 eV, which corresponds to a near-infrared wavelength of 923 nm.

Indium phosphide material can be used as a substrate for the epitaxial growth of other III–V materials, and this is an advantage of this material. Ternary (GaAs, InAlAs), quaternary (InGaAsP, InGaAlAs) compounds can be generated by combining one or more binary compounds (GaAs, InP, InAs). These materials are limited to emission wavelengths corresponding to their bandgap energies in three-dimensional bulk form. InP has the potential to cover the wavelength spectrum of 0.9–2 μm [1355] if stressed materials are also added. Fortunately, the bandgap energy has an inverse relationship with the refractive index, which makes it possible to use larger bandgap materials, such as InP itself, as a waveguide cladding, and smaller bandgap materials, such as InGaAs, as a waveguide core.

1.5 Silicon-on-Insulator (SOI)

Silicon is the second most abundant material in the earth's crust. Silicon has got a diamond cubic crystal structure. The optical, electrical, thermal properties of the silicon material are excellent, because of this it has become one of the attractive material for obtaining systems on-chip.

Silicon has got excellent properties that are very important in photonic devices, like high optical damage threshold and high thermal conductivity. Silicon is having a low-loss wavelength window which extends from 1.1 μm to nearly 7 μm and also high third-order optical nonlinearities [5]. The main advantage of silicon is that silicon-based optoelectronic systems can incorporate with silicon electronics, and they achieve high integration densities (Fig. 6).

Silicon-on-insulator materials shown better performance since nanometer-scale dimensions are obtained using advanced fabrication process. A silicon-on-insulator waveguide structure is shown in Fig. 7.

For many electronic and optical products, silicon's flexibility and low cost have made it the material of choice. There are other semiconductors, however, which in many respects have advantages over silicon. Gallium arsenide and indium phosphide materials have much greater electron mobility than silicon and have been used to manufacture high-power and high-frequency electronics. Also, III–V semiconductors have a direct bandgap, unlike silicon, enabling them to emit and absorb photons efficiently with energies slightly above their respective bandgaps. There are no silicon-based commercial optical emitters today. Although many of today's photovoltaics are silicon-based, III–V semiconductors are still the highest performance solar panels. III–V semiconductors also have the added capacity for monolithic integration that is not possible for many other optical materials.

Fig. 6 Mineral composition of earth's crust

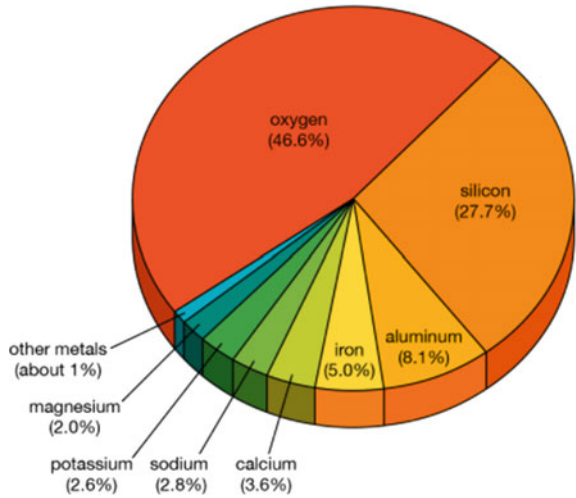
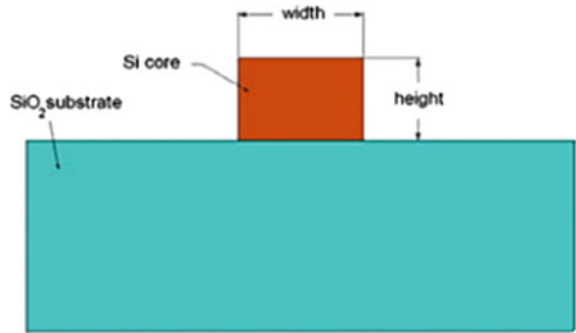


Fig. 7 SOI strip waveguide structure



1.6 Silicon-on-Silicon (SOS)

It has long been known that semiconductors in the photonic field provide substantial benefits compared to materials, like lithium niobate and silica. Due to this, interest in optoelectronic devices based on semiconductors, also in particular guided-wave structures, is continuously growing. In the applications whose requirement is of low performance and cost, we can predict that there will be increasing use of silicon-based components. In the VLSI industry, the known fact is that the low-cost processing of silicon circuits are well developed, these processing methods are used for the fabrication of optoelectronic devices.

In the earlier years, silicon-on-silicon [8], silicon-on-insulator [9], and silicon-germanium-on-silicon [10] waveguiding structures were demonstrated. Even if lower attenuation characterizes the last two kinds of waveguides, all-silicon structures have many advantages. Silicon-on-silicon waveguide structures can be constructed by the

epitaxial growth process, which is more attractive, whereas SiGe or SiGeC waveguide fabrication demands costly and complex techniques. Besides, silicon-on-silicon waveguide-based electrically driven devices are superior to them which are using the silicon-on-insulator structure.

In [8], a technique that will enhance the performance of silicon-on-silicon waveguide is presented. Here, there is a heavily doped buffer layer which is present between wafer substrate and waveguiding epilayer. A single-mode, rib waveguide structure with good characteristics at 1.3 and 1.55 μm is reported.

1.7 Silicon Nitride (Si_3N_4) in Silicon

Si_3N_4 material is of interest since the late 1970s. Today, a lot of applications have emerged in silicon nitride, complementing the capabilities of III–V and SOI waveguide. In today's world, signal data rates and bandwidth are continuously increasing, Si_3N_4 can provide the solution for optical signal processing functions which can decrease the cost, size, and energy consumption.

Si_3N_4 photonic-integrated technology provides low optical attenuation, in the visible to beyond the infrared, which is not possible with the other platforms. The waveguide consists of a core of Si_3N_4 , which is embedded in a silicon dioxide cladding layer. The refractive index of core and cladding at 1.55 μm allowed the design with propagation losses of 0.3 dB/m–1.0 dB/cm in the range, ~ 400 –2350 nm [11] (Fig. 8).

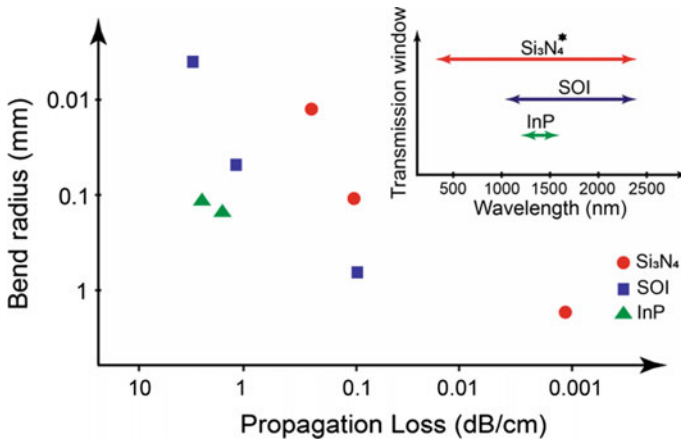


Fig. 8 Bend radii, propagation loss, and window of transparency for published Si_3N_4 , SOI, and InP waveguides [11]

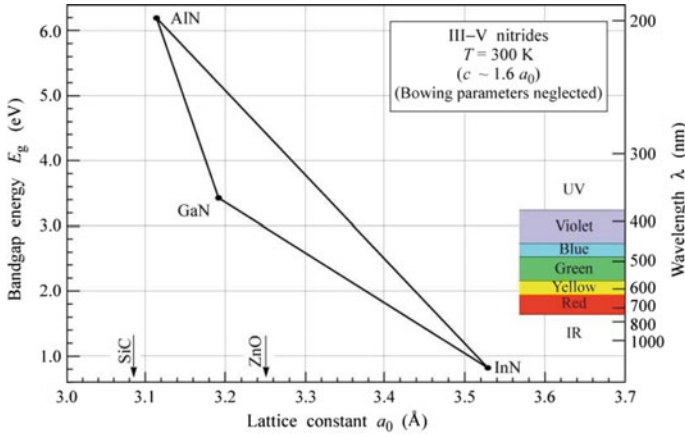


Fig. 9 Bandgap energy versus lattice constant for group III-nitride materials [13]

1.8 III-Nitride Semiconductors

There is a lot of developments happening in the field of group III-nitrides, during the last three decades. The breakthrough took place in the 1990s. For both optoelectronic and electronic applications, these materials are viewed as highly promising material. III-nitride materials are formed due to the bonding between one of the group III elements like indium, boron, aluminum, and gallium with the group V element, nitrogen. These III-nitrides and their alloys have got direct bandgap. The bandgap of these materials varies from 0.7 eV which is for indium nitride to 6.2 eV for aluminum nitride [12]. The main advantages of III-nitride materials are their high breakdown field, high thermal conductivity, high electron mobility, high saturation velocity for high speed, and high-power electronics. We can say that III-nitride-based materials are more environmentally friendly since these materials do not contain elements such as toxic arsenic (Fig. 9).

1.9 Indium Nitride (InN)

There is a great deal of effort being done to implement an all-optical solution to future telecommunication networks aimed at completely leveraging the incredibly high bandwidth of optical fibers. New optical devices are needed for this purpose to perform active all-optical functions at 1.55 μm through various nonlinear optical processes. One of the promising material for all-optical signal processing is III-nitride semiconductors at 1.55 μm due to asymmetry present in the crystalline structure. In [14], InN based waveguide's fabrication, design, and optical characterization for the application as all-optical limiters at the wavelength of 1.55 μm are reported. By

the method of radio-frequency sputtering, InN guiding layers are grown on sapphire substrates.

1.9.1 Gallium Nitride (GaN)

GaN is an III-nitride semiconductor material. There is a great success in the fabrication of active optical devices like laser diodes and light-emitting diodes using GaN-based III-nitride semiconductors, and here they showed high radiative efficiency at the visible wavelengths, in the spectral range which is unattainable with other materials. At the ultraviolet and visible wavelengths, III-nitride materials are expected to produce high-performance passive optical devices because of their wide bandgaps (Fig. 10).

In [15], GaN-on-sapphire waveguide structure is taken, here theoretical analysis on the optical losses in this waveguide is described. In this, the losses like free carrier loss, scattering loss, and two-photon absorption loss are studied, and also their contributions to the overall performance of the waveguide is also discussed. Figure 11 shows one of the losses, i.e., calculated sidewall scattering loss vs. wavelengths for GaN waveguides with dimensions of $1.6 \mu\text{m} \times 1.6 \mu\text{m}$ and $0.6 \mu\text{m} \times 0.6 \mu\text{m}$.

Fig. 10 GaN waveguide structure [15]

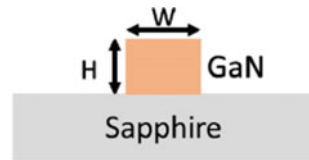
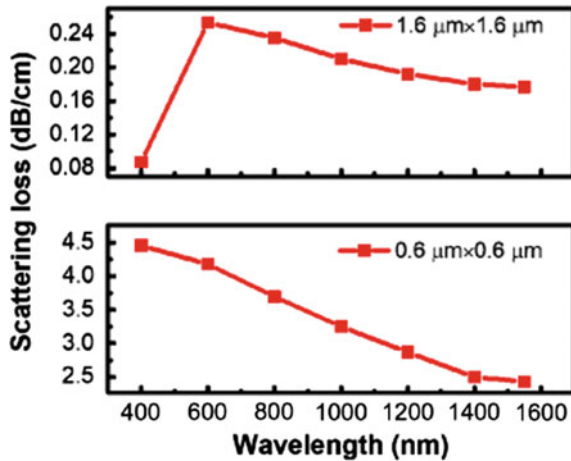


Fig. 11 Calculated sidewall scattering loss versus wavelengths for GaN waveguides with dimensions of $1.6 \mu\text{m} \times 1.6 \mu\text{m}$ and $0.6 \mu\text{m} \times 0.6 \mu\text{m}$ [15]



2 Conclusions

Waveguides built from semiconductors mainly belongs to the III–V group, like GaAs and InP. These materials have got properties like high electron mobility and velocities, compared to Si and Ge, which are very important characters for the construction of electronic devices which are of high speed. These are very important optoelectronic materials because of their direct bandgaps and high radiative efficiency. Nowadays, SOI material has become one of the main element for photonics and also for CMOS VLSI electronics. Silicon has got better native oxide, superior mechanical and thermal properties, and better crystal perfection compared with III–V materials.

Both in industry and research, lithium niobate is a material of interest because of its reproducible properties and robustness. Although the first modulators were invented in the 1970s, a lot of progress is visible.

It is observed from the survey that InN based devices can act like an all-optical limiter at 1.55 μm within the III-nitride-based photonic-integrated circuits [14], also it is possible to achieve a low loss of ~ 2 dB/cm by using GaN waveguide in the visible spectral range [15]. III-nitride integrated photonics in the visible and ultraviolet range can be used for quantum photonics and nonlinear optics applications.

Acknowledgements I would like to thank various researchers for working in the field of photonics because which lot of papers were published, and it is encouraging others to follow the research in the area of photonics.

References

1. Selvaraja SK, Sethi P (2018) Chapter 6 review on optical waveguides. IntechOpen
2. Wang H (2006) Design and simulation of lithium niobate waveguides and devices. McMaster University, June
3. Honnunar RV, Yadunath TR, Sujitha P, Srinivas T (2011) Design of S bend waveguides for delay line applications in integrated optics. IEEE Recent Adv Intell Comput Syst
4. Courjal N, Bernal MP, Caspar A, Ulliac G, Bassignot F, Gauthier-Manuel L, Suarez M (2018) Lithium niobate optical waveguides and microwaveguides. <https://doi.org/10.5772/intechopen.76798>
5. Tong XC (2014) Advanced materials for integrated optical waveguides. Springer Nature
6. Kayali S. GaAs material properties. <https://parts.jpl.nasa.gov/mmic/3-I.PDF>
7. Ferguson AD, Kuver A, Heaton JM, Zhou Y, Snowden CM, Iezekiel S (2006) Low-loss, single-mode GaAs/AlGaAs waveguides with large core thickness. IEEE Proc Optoelectron 153(2)
8. Cocorullo G, Della Corte FG, Iodice M, Rendina I, Sarro PM (1998) Silicon-on-silicon rib waveguides with a high-confining ion-implanted lower cladding. IEEE J Sel Topics Quantum Electron 4(6)
9. Dorin BA, Winnie NY (2013) Conditions for single-mode and birefringence-free ultrasmall SOI rib waveguides at 1310 nm. J Lightwave Technol
10. Splett A, Schmitthen J, Schuppert B, Kasper E, Kibbel H (1990) Low loss optical ridge waveguides in a strained SiGe epitaxial layer grown on siliconIn: Electron Lett 26(14):1035–1037

11. Blumenthal DJ, Heideman R, Geuzebroek D, Leinse A, Roeloffzen C (2018) Silicon nitride in silicon photonics. In: Proceedings of the IEEE
12. Acharya AR (2013) Group III-nitride semiconductors: preeminent materials for modern electronic and optoelectronic applications. *Himalayan Phys* 4(4)
13. Hussain S (2014) Structural and optical characterization of green-yellow light emitting devices with high indium concentrated (In, Ga) N quantum wells. In: *Physics*. Univeristé Nice Sophia Antipolis
14. Montegudo-Lerma L, Naranjo FB, Jimenez-Rodríguez M, Postigo PA, Barrios E, Corredera P, Gonzalez-Herraez M (2015) InN-based optical waveguides developed by RF sputtering for all-optical applications at 1.55 μm . In: *Funded project*
15. Chen H, Fu H, Huang X, Zhang X, Yang TH, Montes JA, Baranowski I, Zhao Y (2017) Low loss GaN waveguides at the visible spectral wavelengths for integrated photonics applications. *Optics Express* 25(25):31758

Chapter 6

Synthesis and Performance Evaluation of Supercapacitor Based on Manganese Loaded Biochar/Polyaniline Nanocomposite



Diana Thomas, Noeline B. Fernandez, Manohar D. Mullassery, and R. Surya

Abstract Carbon developed from biomass is employed in the electrochemical energy storage device. By the development of novel carbon-based substances, especially the cost-effective, abundantly available biomass and its nanocomposite electrodes have gathered significant interest in formulating energy storing devices. The electrochemical energy storage properties of biochar-based composites had been analyzed in the present work. Banana stem (BS), a naturally abundant agricultural waste material was used as raw material for the study. It was pyrolyzed at 500 °C for 12 h under nitrogen atmosphere. Biochar (BC) was then converted into a binary composite with manganese (BC-Mn) and then to a ternary composite with PANI (BC-Mn/PANI). The composite formation was confirmed by the electronic transitions at 296 and 396 nm. The prominent peaks in XRD at 2θ values 38.3°, 42.6°, 56.4°, and 65.6° and 20.8° confirmed the presence of γ -type MnO_2 and PANI in the composite. SEM images clearly displayed compact granular spherical morphology. The average particle size for BC-Mn and BC-Mn/PANI found to be 21.43 nm and 10.10 nm respectively from TEM images. The charge transfer resistance of BC-Mn (17.5 Ω) was found to be greater than BC-Mn/PANI (10.3 Ω), make the PANI composite a promising electrode material, though derived from a biomass. The specific capacitance values for BC-Mn (138 Fg^{-1}) and BC-Mn/PANI (241.5 Fg^{-1}) composites further proved the potential of the material. To satisfy the high demand for energy density a new concept hybrid supercapacitor came into an existence. By this approach energy density and the capacitance can be increased. In this current period, a composite electrode material-based biomass proved to be more promising one and highlighted as an alternative electrode material. We can combine relatively cheap materials to attain high electrochemical performance.

Keywords Supercapacitor · Biochar · Capacitance · Impedance · Equivalent circuit

D. Thomas · N. B. Fernandez (✉) · M. D. Mullassery · R. Surya
Department of Chemistry, Fatima Mata National College (Autonomous), Kollam 691001, India

1 Introduction

Existence of human beings depends on the natural resources, which is in turn dependent on its fuel resources [1]. The fuel resources on which humans largely depend upon is the non-renewable energy sources. On long run, it will be unwise to be only dependent on such resources as they are depreciating over the years. Moreover, the environmental scientist cautions about the pollution effects in the processing and application stages. Researchers are looking forward to adopt renewable resources and develop new energy storage systems. The irregular nature of renewable sources makes energy storage systems more inevitable. Among the storage systems like batteries, supercapacitors need special attention as they can impart excellent power transmission into the grid along with fast charge–discharge properties by offering appreciable cyclability [2]. Supercapacitors store energy in the form of electrical energy. Designing and development of excellent electrode materials thus become the prime focus in supercapacitor research.

There are a lot of reports of electrode materials showing double layer capacitance employing activated carbons, nanocarbon tubes, graphene, etc. [3]. The structural diversity and abundance of carbon materials make them an efficient candidate in EDLCs electrode material. The carbon materials particularly obtained from natural resources are gaining more attraction due to their novelty, availability and low cost. The electrochemical performance of these materials fully rely on pore shape, surface functional groups, and electrical conductivity. Reports suggested that carbon alone as electrode material displayed poor electrochemical performance (electrical double layer capacitance) [4]. Several reports are also on using pseudocapacitive materials as electrodes like metal oxides, conducting polymers, etc. Among transition metal oxides RuO_2 , Fe_3O_4 , MnO_2 , etc. are more explored electrode materials, in which lot of studies were carried out for RuO_2 due to its high electrochemical reversibility and ideal capacitive behavior. Polyaniline (PANI), polypyrrole (PPy) and polythiophene derivatives are well-known pseudocapacitive electrode materials. The most widely explored conducting polymer is PANI owing to its features like lightweight, highly conductive ($0.1\text{--}5.00\text{ S cm}^{-1}$), mechanically flexible, low cost, environment friendly and have high theoretical capacitance. Though conducting polymers exhibit better pseudocapacitance, it has got some limitations. To reinforce the stability of conducting polymers, compositing with carbon is proved to be effective. The moderate amount of carbon materials on conducting polymers enhances the structural and the cycling stability. Like conducting polymers, the low electronic conductivity, poor capacitance value and low chemical stability of transition metal oxides can be improved and enhanced by the application of carbon materials. The applicability of electrical double layer-pseudocapacitive composites is also explored to a considerable extent. Recently, there are reports on synthesis of ternary composites, where, metal oxides are sandwiched between the carbon-polymer composites which ensure better specific capacitance, stability and overall performance of the material.

Analysis of the comprehensive performance of the transition metal oxide sandwich composites showed that ternary composites highlight better electrochemical behavior

compared to binary carbon-polymer composites. There are also reports on the effect of preparation procedures on capacitance [5]. Graphene/MnO₂/Polymer systems are promising. Polyaniline has been widely used in such composites in the view of the better conducting network it offered. The present work is focused on developing biochar-based composite electrode materials. Biochar was derived from a cellulosic agricultural residue, banana stem. The BC-Mn and BC-Mn/PANI composites were prepared by mixing the aqueous solution of KMnO₄ under mild conditions and then mixed it with aniline monomer which is a simple yet effective strategy of preparation. Electrical and electrochemical analysis showed that the developed electrode material may be suggested for practical energy storage systems.

2 Materials and Methods

2.1 Synthesis of the Composite

The methodology of preparation of biochar taken for the present work has been reported [6]. The precursor used for the study was banana stem, was procured locally. About 10 g of the powdered biomass heated at 500 °C in an inert atmosphere of N₂. The above treated material was characterized by elemental analysis, FTIR, XRD, NMR, UV-Visible and SEM. Manganese loading of biochar was then done by immersing in the aqueous solution of KMnO₄ as reported by Wan et al. [7]. KMnO₄ and biochar mixture were taken in a beaker and heated at 60 °C for 12 h. Finally, the washed sample was kept at 60 °C for 24 h in a hot air oven. The aniline monomer was then added onto Mn-BC dispersed in HCl solution under ultrasonication at temperature 0–5 °C to prepare PANI coated Mn-BC (Mn-BC/PANI) [8]. The schematics of preparation and the modifications of biochar are given Fig. 1.

2.2 Characterization of Electrode Materials

The functional group analysis (400–4000 cm⁻¹) was performed by FTIR (Bruker-Germany). The SEM images (Philips model XL 30 CP) and TEM images (Joel/JEM2100) were taken to ascertain the surface morphological features. Surface area was determined by BET method (Quantasorb Surface Area Analyzer Qs/7).

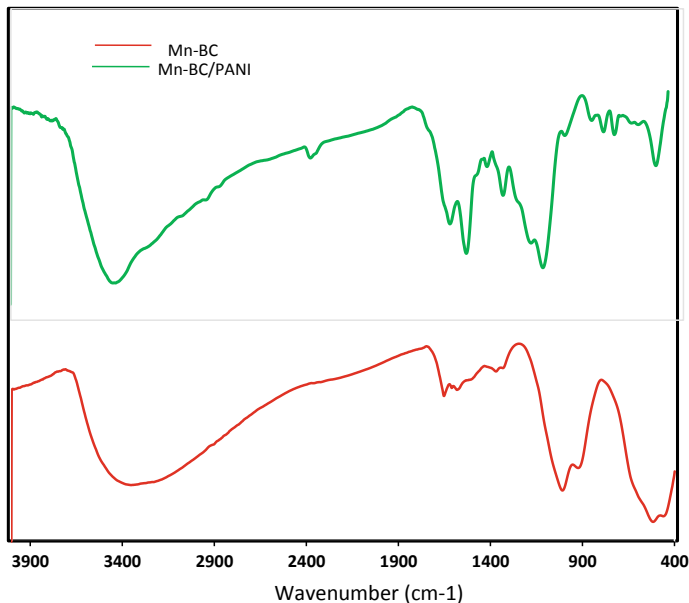


Fig. 1 FTIR spectra of Mn-BC and Mn-BC/PANI composite

2.3 *Electrical Conductivity and Electrochemical Measurements*

The electrical conductivity of Mn-BC and Mn-BC/PANI composites were found out by two probe method (Keithley 2400 model DC voltage-current detector). Conductivity determination was done by varying the weights of Mn-BC and aniline monomer. Capacitance measurements of fabricated supercapacitor electrodes were done with Cyclicvoltametry (Biologic Science Instrument, SP 200) using three-electrode electrochemical cell at room temperature. 1 M Na_2SO_4 solution was used as electrolyte. Silver–silver chloride (Ag–AgCl) and platinum rod were acted as reference and counter electrodes respectively. EIS analysis was carried out using EC–Lab software, version 10.40. Equation (1) represents the C_s (F/g) value of the electrodes, where I (A) is the response current, V (V) is the applied potential, ΔV (V) is the potential window, ν (mV/S) is the potential scan rate and m (g) represents the mass of active material in the electrode [8]. Equation (2) can be used to determine the energy density [9].

$$C_s = \left(\int I dV \right) / \nu m \Delta V \quad (1)$$

$$E = 0.5 \times C_s \times V^2 \quad (2)$$

3 Results and Discussion

3.1 FTIR

Figure 1 showed the FTIR spectra of BC-Mn and BC-Mn/PANI composite. The peaks at 1303, 1504 and 1594 cm^{-1} may be due to Ph-N, benzenoid and quinonoid structures respectively [10]. Peak at 1391 corresponds to C-N stretching of aromatic amine given in BC-Mn/PANI. The N-H stretching of aromatic amine is evident from a sharp peak at 3440 cm^{-1} . Moreover, the contribution of Mn-O vibrations is evident from a sharp peak at 562 cm^{-1} . The peak at 1149 and 1084 cm^{-1} can be assigned to -C-O-C- bond structure. The broad peak at 3351 cm^{-1} (OH- stretch) and a peak at 1652 cm^{-1} (OH- bend) in Mn-BC is due to vibration of water molecules adsorbed onto MnO_2 . Further the peak at 516 cm^{-1} suggests the presence of Mn-O vibration in MnO_2 -biochar. Two peaks around 1504 and 1594 cm^{-1} validate the existence PANI in the sample. Thus, FTIR clearly supports the attachment of PANI in the composite. FTIR spectrum of the Mn-BC and Mn-BC/PANI displays both the characteristic band of PANI and MnO_2 , which substantiate the presence of both the components in the composites [11].

3.2 Surface Morphology Observations

The SEM images of Mn-BC (Fig. 2) further validate the intergrowth of tunnel like structures of $\gamma\text{-MnO}_2$ on the biochar surface. The heterogeneous pore size distribution is evident from the scanning electron micrographs. This heterogeneous pore size distribution can be attributed to the breaking down of lignocellulosic structure at elevated temperatures which led to the formation down of meso- and micropores by the loss of volatile matters from the biomass. This further reflected in surface area of biochar, which is higher than that of precursor biomass. The surface morphology of

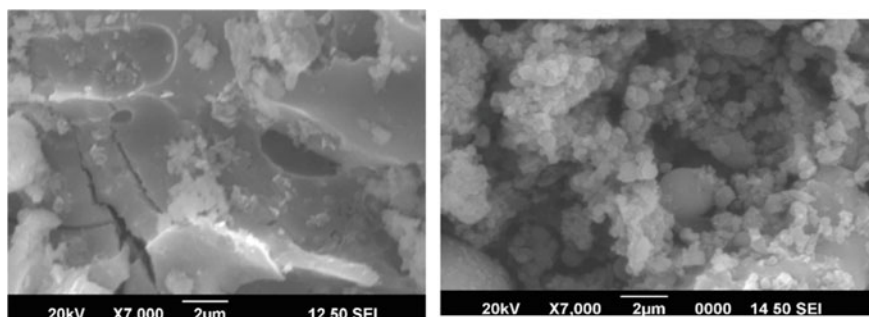
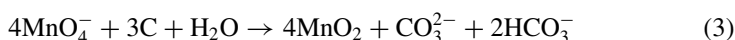


Fig. 2 SEM images of **a** Mn-BC and **b** Mn-BC/ PANI composite at different magnifications

Mn-BC/PANI composite confirmed the existence of PANI particles on Mn-BC. The images clearly displayed the attachment of PANI on the meso- and micropores of Mn-BC. Ultrasonication improved the dispersion of PANI particles onto the Mn-BC surface.

To prepare Mn loaded biochar, the biochar derived from the natural lignocellulosic residue banana stem was dipped in KMnO_4 solution for 12 h at 60 °C. Consequently, redox reaction occurred between KMnO_4 and biochar producing MnO_2 species. The specific surface area found to be increased from $7.97 \text{ m}^2\text{g}^{-1}$ to $90.18 \text{ m}^2\text{g}^{-1}$ after impregnation substantiated the presence of MnO_2 species on the surface of biochar [12].



The SEM images of Mn-BC clearly revealed several wrinkles and ripples. MnO_2 crosslinked carbon sheets of few nanometer thickness with high porosity evidently facilitate the diffusion of electrolytes, which is a requisite to serve as a supercapacitor electrode material.

The TEM images of BC-Mn revealed the fact that MnO_2 nanoparticles with particle size ranging from 13.57 to 34.60 nm are layered over the biochar support. That is biochar is the core part and MnO_2 layer is the shell part suggesting it as a core-shell composite [7]. The average particle size was found to be 21.43 nm. The SAED pattern with d spacing 0.2 nm could be indexed to plane (300).

The SEM images of the PANI composite of Mn-BC (Fig. 2) displayed very compact granular spherical morphology. Spherical particles with particle size 742 and 749 nm demonstrated the 3D nanostructures in the composites. These structures allow a shorter ion diffusion path which would improve the specific capacitances [13]. From the comparison of the particle size of BC-Mn and BC-Mn/PANI composite, it was observed that the PANI composite exhibited smaller particle size than BC-Mn. Thus, it is inferred that the aggregation of PANI over BC-Mn is prevented which in turn improved the specific surface area. A greater interaction between composite surface and the electrolyte becomes possible which would enhance the specific capacitance.

The particles with size ranging from 4.92 to 14.36 nm in TEM images of PANI composite suggested that significant reduction in particle size had occurred during compositing (Fig. 3). The average particle size was observed to be 10.10 nm.

3.3 Electrical Conductivity

Among the various composite materials for electrochemical applications MnO_2 derived composites are of considerable importance as MnO_2 is naturally abundant, environmentally benign and ensure safety during various operations [14]. But the poor electrical conductivity and densely packed structure of MnO_2 impedes its performance. In order to achieve high electrical and electrochemical performance, it is crucial to enhance the conductivity of MnO_2 [15]. Doping with carbon induces

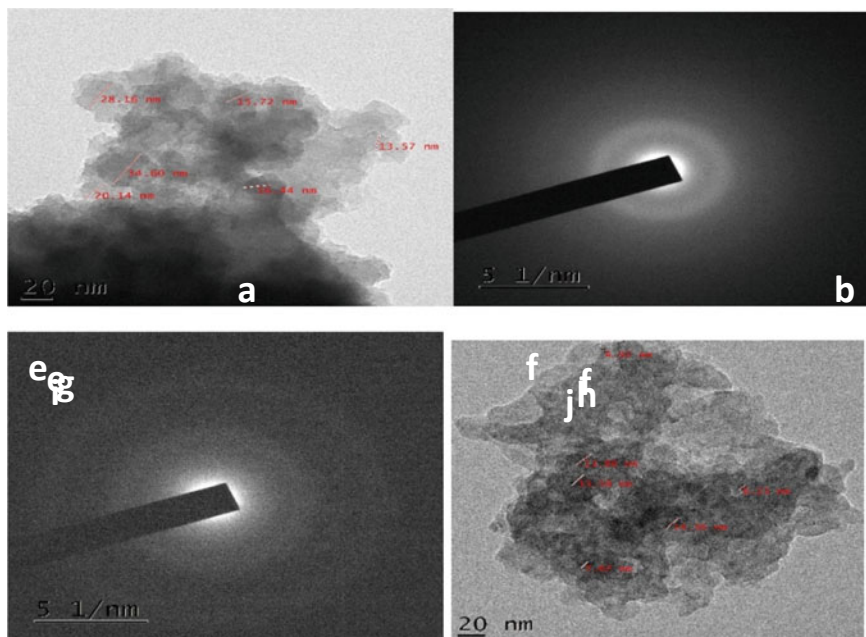


Fig. 3 TEM images and SAED pattern of **a** Mn-BC and **b** Mn-BC/PANI

a conductive network to increase the electrical conductivity. Biochar provides high surface area, mechanical support and serve as current collector for the MnO_2 phase.

To achieve superior electrical properties, conducting polymers are often coupled with MnO_2 [16]. PANI offers a promising supporting material in this regard. Biochar provides not only a strong conductive network but also it strongly holds the polymer matrix and prevents from the mechanical degradation of polymer chain. The electrical properties of polyconjugated systems are mainly due to delocalization and polarization processes. Apart from preventing the dissolution of MnO_2 phase in the electrolyte, PANI also forms a core-shell hybrid structure which would enhance the electrical conductivity of the hybrid electrode. The dopant which is firmly attached to the polymer undergo redox processes, thereby liberating electrons which are the charge carriers [17]. During oxidation/reduction process the dopant is extracting electrons from the conducting polymer and at the same time transfer electrons to the polymer backbone. This transport of charge carriers delocalized over polymer chain and contributes to conductivity.

Optimization was carried out by variable quantities of the amounts of the carbon doped MnO_2 and the polymer and analyze the conductivities of resulting composites. 3, 4, 5 and 6 mmol solutions of aniline monomers were prepared. For each concentration of the monomer, composites were prepared varying the mass of the BC-Mn (0.2, 0.4, 0.6, 0.8 and 1.0 gm) and conductivities were measured, shown in Table 1. For 3 mmol aniline monomer, as the mass of BC-Mn was increased from

Table 1 Electrical conductivity values of Mn-BC and Mn-BC/PANI composite

Aniline monomer	Weight of Mn-BC (g)	Electrical conductivity (S cm ⁻¹)
3 mmol	0.2	5.11
	0.4	5.53
	0.6	5.68
	0.8	6.01
	1.0	6.22
4 mmol	0.2	6.92
	0.4	8.72
	0.6	5.10
	0.8	4.83
	1.0	4.51
5 mmol	0.2	5.81
	0.4	6.01
	0.6	5.21
	0.8	5.02
	1.0	4.93
6 mmol	0.2	4.89
	0.4	4.99
	0.6	3.93
	0.8	3.20
	1.0	3.11
Mn-BC		2.00

0.2 to 1.0 g the electrical conductivities also increased. The increase in the electrical conductivities in the composites is because of the increase in the charge transfer in the dopant through the polysemiquinone radical cation network in polyaniline [18]. The maximum conductivity was observed for 0.4 g BC-Mn/4 mmol aniline composite. This may be because of the greater availability of charge carriers in the dopant, where current flow is enhanced through the conducting network of the polymer. For 5 and 6 mmols of aniline monomers, conductivities showed a slow increase as the weight of BC-Mn in the composite was increased from 0.2 to 0.4 g and thereafter a reduction was observed. A dip in the conductivity on raising the mass of BC-Mn may be because, though the PANI network favored the charge transport, increasing density of Mn-BC may block the available pores on its surface which in turn, affect the movement of electrons.

3.4 Electrochemical Performance

The electrochemical performance of BC-Mn and BC-Mn/PANI were assessed by cyclic voltammogram (CV) measurements at different potential scan rates. The capacitance of PANI arises from the redox transitions of PANI-the leucoemeraldine-emeraldine transition and emeraldine- pernigraniline transition. MnO_2/PANI offer pseudocapacitance, whereas, the carbon-based materials show electrical double layer capacitance. The energy storage mechanism in EDLCs arises from the reversible electrostatic charge accumulation on electrode/electrolyte interface. The commonly known nanoporous carbon materials with high specific surface area ($>1000 \text{ m}^2 \text{ g}^{-1}$) are acted as active electrode materials, which provide a huge capacitance as compared to electrostatic capacitors. While in pseudocapacitors the basic mechanism is the faradaic charge storage mechanism, which is a fast and highly reversible surface redox reaction with valence state change of electrode material during electron transfer.

Symmetrical rectangular curves were observed in CV suggesting high electrochemical reversibility of both binary and ternary composites. The capacitance value of BC-Mn/PANI was found to be higher (241.5 Fg^{-1}) than that of BC-Mn (138 Fg^{-1}). As the capacitance is because of the combination of EDLC of carbon material and the pseudocapacitance of the conducting material, the ternary composite is expected to show improved performance due to the pseudocapacitance of hybrid PANI- MnO_2 . This was again inferred from the lower peak potential difference of the ternary composite, which suggested effective redox reactions after hybrid formation. In MnO_2 -based electrode materials, the redox reaction between Mn(III) and Mn(IV) accounts for intercalation of alkali metal cations in the electrolyte [19].



Another advantage of MnO_2 compositing is that the larger surface area of MnO_2 nanoparticles prevent the congregation of the composite particles. Thus, the effective surface area increases and optimum charge storage occurs. PANI coating on MnO_2 favors diffusion of protons. Moreover, PANI can occupy the pores of the porous MnO_2 oxide, enhancing the surface area and resulting in a more active material.

The scan rates chosen for present study were 10, 20, 50 and 100 mV/s. As the scan rate increased from 10 to 100 mV/s, the specific capacitance decreased from 138 to 10 Fg^{-1} for the binary composite and from 241.5 to 11.73 Fg^{-1} for the ternary composite given in Table 2. At high scan rates, the electrolyte ion could access only the outer surface of the electrode which contribute less to the pseudocapacitance. The shift in the cathodic and anodic peaks with scan rates from 10 to 100 mV/s may be attributed to the electrode resistance. On optimizing the ratio proportion of the composites, it was observed that maximum specific capacitance was obtained, when 4 mmol aniline monomer was composited with 0.4 g of BC-Mn. On further increasing the concentration of PANI specific conductance decreased. This may be ascribed to the dense morphology which decreases the effective surface area [20]. Comparative study of the capacitance of carbon-based ternary composites revealed

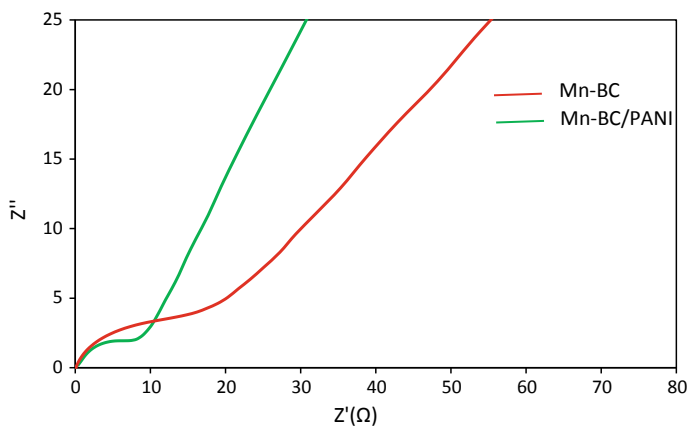
Table 2 Capacitive performance of Mn-BC and Mn-BC/PANI composite

Material	Scan rate (mVs ⁻¹)	Cs values (Fg ⁻¹)	Energy density (Wh kg ⁻¹)	
Mn-BC	10	138.00	17.25	
	20	84.52	10.56	
	50	21.80	2.72	
	100	10.00	1.25	
<i>Polymer composite</i>				
Composition of aniline monomer	Weight of the Mn-BC (g)			
4 mmol	0.4	10	241.50	30.18
		20	86.25	10.78
		50	30.36	3.79
		100	11.73	1.46

that BC-Mn/PANI composite could be used as an efficient electrode material for electrochemical applications.

3.5 Electrochemical Impedance Spectroscopy

The evaluation of the structure, charge transport properties and resistance offered by BC-Mn and BC-Mn/PANI composite were analyzed with the help of EIS technique shown in Fig. 4. Both BC-Mn and BC-Mn/PANI composites present straight lines in the low frequency region implying better capacitive behavior and lesser diffusion

**Fig. 4** Nyquist plots of Mn-BC and Mn-BC/ PANI composite

resistance of charge carriers. The Nyquist plots comprises three main regions: (1) a semicircle appears in the high to medium frequency region and the intersection point at real impedance axis gives the bulk solution resistance (R_s) and its diameter constitute the charge transfer resistance (R_{ct}); (2) a straight line at low frequency region with a slope 45° indicates Warburg impedance arises due to the frequency dependent ion diffusion in the electrolyte; (3) a vertical line at low frequency region purely represents the capacitive behavior electrode materials [21]. The Nyquist plots of both the binary and the ternary composites revealed semicircles in the high frequency region. The internal resistance offered by the electrode because of the ionic resistance of electrolyte, the intrinsic resistance at the electrode/current collector interface is evaluated from the x intercept in the high frequency region [22, 23]. The charge transfer resistance ($R_{ct} = 10.3 \Omega$) in BC-Mn/PANI composite is lower than that found in BC-Mn ($R_{ct} = 17.5 \Omega$). It may be inferred that when PANI is attached onto the Mn-BC surface, electron transfer is enhanced at the BC-Mn/PANI interface, thereby improving the electrical conductivity. The lower R_s value of BC-Mn/PANI composite may be because of the increased surface area of the material over Mn-BC.

4 Future Perspectives

Naturally abundant biomass materials are a new innovative solution for electrochemical energy storage and conversion techniques. The performance of these agricultural biowastes is yet moderate. The potential of this material can be robust through a good understanding of the interrelation between pore size, surface area, surface chemistry and its molecular interactions. In addition to this a feasible approach necessary to carry out large-scale and cost-effective production of biochar. Furthermore, an in-depth study needed to bring about an impressive improvement on the existing electric double layer capacitors and special attention given to minimize possible environmental contamination, thereby this area opens a new window of opportunities and diverse applications in many fields.

5 Conclusion

Banana stem after pyrolysis was modified into composites having attractive electrochemical properties. The biochar produced at 500°C was transformed to BC-Mn, by treating it with KMnO_4 solution. The increase surface area from 7.97 to $90.18 \text{ m}^2 \text{ g}^{-1}$ has contributed to its excellent capacitive behavior. Further modification to a ternary composite (BC-Mn/PANI) with PANI showed to enhance its electrochemical potential. Cyclic voltammetry and impedance analysis highlighted that the ternary composite BC-Mn/PANI (241.5 Fg^{-1}) is superior to the binary composite BC-Mn (138 Fg^{-1}). MnO_2 crosslinking facilitated the diffusion of electrolytes. PANI coating favored the diffusion of protons, resulting in a more active material. The advantage of

using biomass and organic waste as precursor for electrode material is that it enhances the economic viability of supercapacitor technology and the problem of solid waste management could be solved to a great extent. Though the biochar-based electrode materials exhibit capacitance, it displays slow capacitance value when compared to synthetic one.

References

1. Jafri N, Wong WY, Doshi V, Yoon LW, Cheah KH (2018) A review on production and characterization of biochars for application in direct carbon fuel cells. *Process Saf Environ Prot* 118:152–166
2. Lei R, Zhang H, Lei W, Li D, Fang Q, Ni H, Gu H (2019) MnO₂ nanowires electrode-positated on freestanding graphenated carbon nanotubes as binder-free electrodes with enhanced supercapacitor performance. *Mater Lett* 249:140–142
3. Teimuri-Mofrad R, Hadi R, Abbasi H, Payami E, Neshad S (2019) Green synthesis of carbon nanotubes @tetraferrocenylporphyrin/copper nanohybrid and evaluation of its ability as a supercapacitor. *J Organomet Chem* 899:120915
4. Yang G, Park S-J (2018) MnO₂ and biomass-derived 3D porous carbon composites electrode for high performance supercapacitor applications. *J Alloys Compd* 741:360–367
5. Thomas P, Lai CW, Bin Johan MR (2019) Recent developments in biomass-derived carbon as a potential sustainable material for super-capacitor-based energy storage and environmental applications. *J Anal Appl Pyrolysis* 140:54–85
6. Fernandez NB, Mullassery MD, Thomas D, Surya R, Das JY (2018) Characterization of biochars from a plant biomass and its effect on lead sorption capacity. *Desalin Water Treat* 108:189–197
7. Wan C, Jiao Y, Li J (2016) Core-shell composite of wood derived biochar supported MnO₂ nanosheets for supercapacitor applications. *RSC Adv* 6:64811–64817
8. Thines KR, Abdullah EC, Ruthiraan M, Mubarak NM, Tripathi M (2016) A new route of magnetic biochar based polyaniline composites for supercapacitor electrode materials. *J Anal Appl Pyrol* 121:240–257
9. Ullah S, Yu J, Liu H, Iqbal W, Yang B, Li C, Zhu C, Xu J (2019) Fabrication of MnO₂-carbonized cotton yarn derived hierarchical porous active carbon flexible supercapacitor electrodes for potential applications in cable-type device. *Appl Surf Sci* 487:180–188
10. Zhang J, Shu D, Zhang T, Chen H, Zhao H, Wang Y, Sun Z, Tang S, Fang X, Cao X (2012) Capacitive properties of PANI/MnO₂ synthesized via simultaneous-oxidation route. *J Alloys Compd* 532:1–9
11. Gabal MA, Hussein MA, Hermas AA (2016) Synthesis, characterization and electrical conductivity of polyaniline-Mn_{0.8}Zn_{0.2}Fe₂O₄ nano-composites. *Int J Electrochem Sci* 11:4526–4538
12. Zhao X, Zhang L, Murali S, Stoller MD, Zhang Q, Zhu Y, Ruoff RS (2012) Incorporation of manganese dioxide within ultraporous activated graphene for high performance electrochemical capacitors. *ACS Nano* 6:5404–5412
13. Teng F, Santhanagopalan S, Wang Y, Meng DD (2010) In-situ hydrothermal synthesis of three-dimensional MnO₂-CNT nanocomposites and their electrochemical properties. *J Alloys Compd* 499:259–264
14. Stafstrom S, Bredas JL, Epstein AJ, Woo HS, Tanner DB, Huang WS, MacDiarmind AG (1987) Polaron lattice in highly conducting polyaniline: theoretical and optical studies. *Phys Rev Lett* 59:1464–1467
15. Nayak PK, Devaraj S, Munichandraiah N (2010) An EQCM investigation of electrochemical precipitation of Mn(OH)₂ and its capacitance behavior. *Electrochem Solid State Lett* 13:29–32

16. Guo W, Yu C, Li S, Wang Z, Yu J, Huang H, Qiu J (2019) Strategies and insight towards the intrinsic capacitive properties of MnO₂ for supercapacitors: challenges and perspectives. *Nano Energy* 57:459–472
17. Huang Z-H, Song Y, Xu X-X, Liu X-X (2015) Ordered polypyrrole nanowire arrays grown on a carbon cloth substrate for a high performance pseudocapacitor electrode. *ACS Appl Mater Interfaces* 7:25506–25513
18. Molapo KM, Ndongili PM, Ajayi RF, Mbambisa G, Mailu SM, Njomo N, Masikini M, Baker P, Iwuoha EI (2012) Electronics of conjugated polymers (I): polyaniline. *Int J Electrochem Sci* 7:11859–11875
19. Naveen AN, Selladurai S (2015) Fabrication and performance evaluation of symmetrical supercapacitor based on manganese oxide nanorods-PANI composite. *Mater Sci Semicond Process* 40:468–478
20. Wu H, La M, Li J, Han Y, Feng Y, Peng Q, Hao C (2019) Preparation and electrochemical properties of MnO₂/PANI-CNTs composites materials. *Compos Interfaces* 26:659–677
21. Li K, Liu X, Zheng T, Jiang D, Zhou Z, Liu C, Zhang X, Zhang Y, Losic D (2019) Tuning MnO₂ to FeOOH replicas with bio-template 3D morphology as electrodes for high performance asymmetric supercapacitors. *Chem Eng J* 370:136–147
22. Han J, Li L, Fang P, Guo R (2012) Ultrathin MnO₂ nanorods on conducting polymer nanofibers as a new class of hierarchical nanostructures for high-performance supercapacitors. *J Phys Chem C* 116:15900–15907
23. Thomas D, Fernandez NB, Mullassery MD, Surya R (2020) Iron oxide loaded biochar/polyaniline nanocomposite: synthesis, characterization and electrochemical analysis. *Inorg Chem Commun* 119:108097

Chapter 7

Assessment of Antibacterial Properties of Natural Extracts for Wound Healing Applications



S. Patricia Nancy, S. Shanchana, S. Udhayanila, T. Divya, and Bharathi

Abstract Generally, the term wounds refer to the discontinuity in the skin. Wounds mainly occur due to minor accidents, surgery, skin infections, burns, and many other factors. Microbial pathogens such as *Staphylococcus Aureus* and *Streptococcus* sp. are commonly associated with infections. The main aim of proposed study is to provide an overview on wound healing using hydrogels made with natural plant extracts. Usage of natural plant extracts such as neem, tridax, and combination of neem and tridax for the synthesis of hydrogels. Hydrogels will create a moist environment in the wound site to remove exudates and clear infections by providing a smooth cooling effect. It is an ideal wound dressing method, which initiates the tissue regeneration process. The hydrogels are successful in the wound healing, when compared to other traditional methods.

Keywords Wound · Plant extracts · Hydrogels

1 Introduction

The occurrence of wound is very common in human lives. The traditional healing method for wounds is by sticking band aid over the wound, but this can cause irritation during its application and removal. On the other hand, the proposed hydrogels create a moist environment in the wound site to provide a smooth cooling effect, which can accelerate wound healing by initiating the process of tissue regeneration. Synthesizing hydrogels using natural plant extracts are found to be highly effective in the wound healing process. The natural extracts such as neem and tridax leverages a high rate of antimicrobial and antioxidant properties, and it greatly helps in clearing the skin infections.

S. P. Nancy (✉) · S. Shanchana · S. Udhayanila · T. Divya · Bharathi
Department of Biomedical Engineering, K.P.R. Institute of Engineering and Technology, Arasur,
Coimbatore 641407, India

2 Literature Review

Artem Ataide et al. [1] suggested that skin injuries are common, and the human body has the ability to promote the repair spontaneously. Some external and internal factors may interfere with the skin's natural activity, and later, it leads to non-healing lesions and chronic wounds. Despite the achievements in modern medicine, further high-quality studies are required to firmly establish the clinical efficacy of plants. This paper reviews the traditionally used natural actives for wound healing by highlighting their characteristics and mode of action. Bromelain inhibits platelet aggregation, exhibits fibrinolytic activity, has anti-inflammatory action, promotes skin debridement, and interferes with the growth of malignant cells.

Bardaa et al. [2] suggested that even though there is a drastic change in the medical field, there is no effective treatment of second degree burns till now. Second degree burns are partial thickness burns that affect the epidermis and dermis (lower layer of the skin) and cause pain, redness, swelling, and blistering. From this study, we conclude the types of extract for the wound healing process and also their efficiency rate. Here, they used three extracted oils from the *Opuntia*, which are commonly called as prickly pear, pumpkin, and linseed and observed their wound healing efficiency.

Ejaz et al. [3] reported that successful wound healing depends upon angiogenesis, and impaired angiogenesis is a hallmark of the chronic wounds encountered with diabetes and venous or arterial insufficiency. To intervene and improve wound closure, it is essential to investigate the effects of different natural remedies in wound healing. They used a different concentration of aged garlic solution (AGS) for wound healing.

Majewska et al. [4] suggested that the healing potential of phytomedicines is often associated with angiogenesis, which is a critical step of wound healing. It is the essential part of the repair process as it enables the nutrient supply to sustain cell metabolism, creates an intact delivery system, and facilitates the clearance of debris.

3 Materials and Methods

3.1 *Materials Used*

A total of 450 ml of ethanol was used as the solvent for the extraction of neem leaves, tridax, neem + tridax combinations (150 ml each). The Soxhlet apparatus containing the percolator, thimble, and the siphon mechanism were used for the extraction process. The ethanol is placed in the distillation flask, and it is allowed to pass through the thimble containing the leaves.

3.2 Collection of Plant Leaves

The neem [5] and tridax [6] leaves were collected and washed without any kind of impurities. The leaves are allowed to dry completely for about 10 min. The leaflets of neem and tridax are preferred as their extract shows great antimicrobial activity when compared to big leaves. A total of 10 g of neem leaves, 10 g of Tridax leaves, 5 g of neem, and 5 g of tridax were weighed by using the weighing balance.

3.3 Packing of Leaves

A total of 10 g of neem leaves were packed in a filter paper and placed in the first thimble. A total of 10 g of tridax leaves were packed and placed in the second thimble. A total of 5 g of neem and 5 g of tridax leaves together were packed in the filter paper and placed in the third thimble.

3.4 Extraction Process

Three distillation flasks containing 150 ml of ethanol each were placed on top of the heating element. The three thimbles containing their respective leaf packages were placed on top of their corresponding distillation flasks. The reflux condenser was placed on top of them. The water inlet was connected from the water pipe to the reflux condenser 1, and the water outlet of reflux condenser 1 was connected to the second and second to the third, and the third one was given to the sink for draining the water. The heating element is set a temperature of 75 °C as it is the boiling point of ethanol. The extraction process took place for about 1 and half hours as the solvent was allowed to pass through for four cycles until the complete essence of the leaves were extracted. The thimble containing the leaf packs were disposed, and the leaves were found to be in white color after the extraction process. This indicates the complete extraction of the essence of the leaves. The extracts were transferred into glass bottles and closed with their lids and stored in the refrigerator.

3.5 Synthesis of Hydrogels Using Natural Extracts

A sample concentration with nil amount of leaves extract was prepared to show the absence of antimicrobial activity. This sample was used as a control. The materials such as honey, gelatin, and chitosan [7] were weighed according to the proportions (mentioned in the Table 1) and put in the glass bottles. A total of 0.5 ml of acetic acid was added to each sample for the chitosan to dissolve completely. The samples

Table 1 Concentrations of the natural extract samples

Concentration no	Honey (g)	Gelatin (g)	Chitosan (g)	Acetic acid (g)	Neem (ml)	Tridax (ml)	Neem + tridax (ml)
Concentration 1	10	10	0.5	0.5	–	–	–
Concentration 2	10	10	0.5	0.5	10	–	–
Concentration 3	10	10	0.5	0.5	20	–	–
Concentration 4	10	10	0.5	0.5	–	10	–
Concentration 5	10	10	0.5	0.5	–	20	–
Concentration 6	10	10	0.5	0.5	–	–	10
Concentration 7	10	10	0.5	0.5	–	–	20

Here, the concentration 1 is used as the control

were made up to 50 ml using distilled water. The magnetic pellet was dropped into the glass bottles and kept in the magnetic stirrer. The samples were allowed to spin at around 650 rpm, and a little amount of heat was applied. The sample was allowed to spin until there were no chitosan fibers and solid particles. The pellets were taken out using the forceps and kept in the hot air oven at 60 °C in order to maintain the colloidal state of the hydrogels.

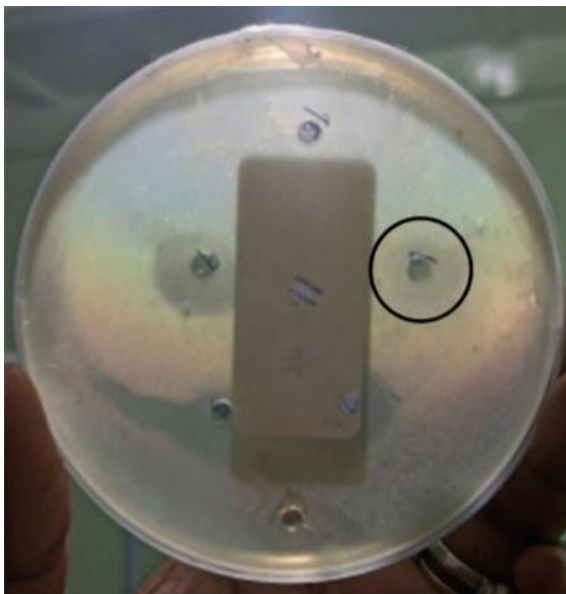
3.6 Preparation of Bacterial Medium

The preparation of bacterial medium for testing the antimicrobial activity of the hydrogels was done using blood agar. A total of 4 g of blood agar was dissolved in 100 ml of distilled water contained in a conical flask. The conical flask is closed tightly with the help of a cotton plug. The conical flask was packed with paper. The autoclave was thoroughly cleaned, and the trapped air was completely removed as trapped air is a bad medium for achieving sterility. The conical flask with the medium is placed inside the autoclave at 121 °C for one hour. The conical flask is taken from the autoclave after an hour, and the medium is allowed to cool for some time. The cooled agar medium is poured onto the petri plates and allowed to solidify.

3.7 Check for Antimicrobial Activity

The cotton buds are rubbed against the skin as human skin contains *S. aureus*, which is responsible for a wide range of skin infections. The bacterial medium is then streaked with the buds containing the bacteria from the skin. The petri plates containing the agar are placed in the incubator for 24 h at room temperature of 37 °C in order to prevent contamination of the bacteria. Wells of diameter 1 cm are put in the bacterial medium. The wells are then filled with the control and samples in each plate.

Fig. 1 Zone of inhibition formed around 20 ml of *Tridax Procumbens* is large than the 20 ml of *Azadirachta Indica* and *Azadirachta Indica* + tridax samples



4 Results

A clear ring was formed around the wells with 20ml of *Tridax Procumbens* sample than in 20 ml of *Azadirachta Indica* sample that indicates high antimicrobial activity. No ring was formed around the wells containing other sample extracts that indicate nil antimicrobial activity. The diameter of the clear ring was measured in order to formulate the efficiency of the synthesized hydrogels. The shelf life of the hydrogels were assessed at different time spans such as Day 1, Day 7, Day 10, and Day 15. The day at which the hydro gels showed nil antimicrobial activity is called the shelf life of the hydrogels. The hydrogels showed nil antimicrobial activity at day 15, and it is the shelf life of the synthesized hydrogels (Fig. 1).

5 Conclusion

Thus, the hydrogels synthesized using natural plant extracts showed a great amount of antimicrobial and antifungal activity against the infectious pathogens. Hydrogels act as an ideal wound healing aid, and it does not cause any irritation while application and removal on the wound site. Therefore, the hydrogels have a limited shelf life, but at the same time, it is effective in angiogenesis.

Acknowledgements We are grateful to Ms. T. DIVYA BHARATHI, MTech., Assistant Professor, Department of Biomedical Engineering, the Project Supervisor for his timely suggestions and constant encouragement and support that led to the accomplishment of the project.

References

1. Artem Ataide J, Caramori Cefali L, Machado Croisfelt F, Arruda Martins Shimojo A, Oliveira-Nascimento L, Gava Mazzola P (2018) Natural actives for wound healing: a review. *Phytotherapy Res* 32(9):1664–1674
2. Bardaa S, Chabchoub N, Jridi M, Moalla D, Mseddi M, Rebai T, Sahnoun Z (2016) The effect of natural extracts on laser burn wound healing. *J Surg Res* 201(2):464–472
3. Ejaz S, Chakarova I, Cho JW, Lee SY, Ashraf S, Lim CW (2009) Effect of aged garlic extract on wound healing: a new frontier in wound management. *Drug Chem Toxicol* 32(3):191–203
4. Majewska I, Gendaszewska-Darmach E (2011) Proangiogenic activity of plant extracts in accelerating wound healing—a new face of old phytomedicines. *Acta Biochimica Polonica* 58(4)
5. Chundran NK, Husen IR, Rubianti I (2015) Effect of Neem leaves extract (*Azadirachta Indica*) on wound healing. *Althea Med J* 2(2):199–203
6. Udupa AL, Kulkarni DR, Udupa SL (1995) Effect of Tridax procumbens extracts on wound healing. *Int J Pharmacogn* 33(1):37–40
7. Sarhan WA, Azzazy HM, El-Sherbiny IM (2016) Honey/chitosan nanofiber wound dressing enriched with *Allium sativum* and *Cleome droserifolia*: enhanced antimicrobial and wound healing activity. *ACS Appl Mater Interfaces* 8(10):6379–6390
8. Thakur R, Jain N, Pathak R, Sandhu SS (2011) Practices in wound healing studies of plants. *Evid Based Complementary Altern Med* 1:2011

Chapter 8

Current and Emerging Technologies for Resonance Frequency Analysis-Based Devices for Measuring Dental Implant Stability: A Review



Srujana Joshi, Urvi Bora, Niharika Karnik, Karan Bhadri, and Pankaj Dhatrak

Abstract In modern clinical dentistry, the success rate of implants depends on many biological and mechanical aspects, the main factor affecting it is osseointegration. The proper anchorage of the implant into the bone is extremely necessary to avoid implant failure. The stability of the implant is classified into two stages, the primary stability and the secondary stability. Measuring the primary stability before loading the implant is of the utmost importance. Owing to its non-invasiveness and reliability, resonance frequency analysis (RFA) has become one of the most commonly used techniques for implant stability measurement. The aim of the present study is to highlight or focus on current and emerging technologies for resonance frequency analysis-based devices to measure the implant stability. This paper provides a brief overview of the working principle, development, challenges and advantages of these different RFA technologies and existing commercial devices developed for stability measurement. The electromagnetic RFA is the most widely used. The vibro-acoustic method has showed potential to overcome the challenges faced by the electromagnetic technique, but it needs more clinical trials and in vitro experimentation.

Keywords Dental implant · Electromagnetic · ISQ · Primary stability · RFA · Vibro-acoustic

1 Introduction

Dental implants are used very popularly by dentists for the replacement of missing teeth. The success rate of dental implants, over the last ten years, has been about 90–95% [1]. Implant stability is a major contributor to ensuring longevity and success of dental implants [2]. The stability of the implant is assessed in two phases [3]. The

S. Joshi (✉) · U. Bora · N. Karnik · K. Bhadri · P. Dhatrak
School of Mechanical Engineering, Dr. Vishwanath Karad MIT-WPU, Pune, India

P. Dhatrak
e-mail: pankaj.dhatrak@mitwpu.edu.in

primary stability is measured immediately after surgical placement in the jawbone, while secondary stability is measured after osseointegration [4]. Primary stability of dental implants is an indicator of the firm mechanical engagement between the implant and surrounding bone [5, 6]. It also evaluates the micromotion occurring at the bone-implant interface till osseointegration has taken place [7, 8]. Excessive micromotion may induce the formation of fibrous tissue instead of promoting bone contact, leading to implant failure [9, 10]. Subsequently, primary stability plays a vital role in facilitating osseointegration. The design, geometry of the implant, surgical aspects like insertion torque and quality of the bone surrounding the implant are factors that affect the primary stability [11–13]. A quantitative measurement of the implant's initial stability also helps dentists decide the loading protocol and customize the post-operative treatment for patient [14–17]. Thus, there is a need to evaluate implant stability at different stages of its service life to ensure successful implantation [18]. Over the years, various methods like histomorphometric analysis, radiographic analysis, push- and pull-out tests, percussion tests, Periotest and resonance frequency analysis (RFA) have been employed to assess the stability of dental implants [19–21]. The technique of RFA has progressively outperformed the different methods to assess implant stability due to its soundness and high reproducibility [22]. This review article aims to give brief information regarding the development and drawbacks of various technologies used for resonance frequency analysis till date.

2 Resonance Frequency Analysis

RFA is a non-invasive intraoral method designed to assess bone-implant interface and therefore may provide clinical evidence of implant stability [23–25]. RFA has also shown great reliability to assess the implant stability after placement in the jawbone [26, 27]. The method of RFA for clinical evaluation of implant stability was first proposed by Meredith et al. [28] in 1996. RFA works on the principle that when a dental implant is repeatedly vibrated by a frequency in the audible range, resonance occurs at a higher frequency as the strength of the bone-implant interface increases [29, 30]. RFA uses a transducer to apply a small magnitude bending force to the implant-bone system. This bending force mimics the loading condition clinically by applying a constant force in the lateral direction of the implant and measuring the resulting displacement [31]. The resonance frequency is affected by the stiffness at the bone-implant interface and the effective length of the fixture due to bone loss [14]. Implant stability is evaluated as a function of the stiffness at the bone-implant interface [31]. As a result, any change in the stiffness value is assumed to represent a change in the level of osseointegration at the bone-implant interface. Thus, as the bonding level of the implant with the surrounding bone/tissue complex increases, the resonant frequency will also increase [32]. Eventually, the resonant frequency will attain a constant value, indicating the implant stability after osseointegration [33, 34]. The second factor affecting the resonance frequency is the effective length of fixture (exposed length above the alveolar crest due to bone loss) [31, 35]. Hence,

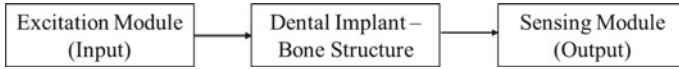


Fig. 1 Block diagram of resonance frequency analysis for implant stability measurement

there is an inverse relationship between the effective length of the fixture and the resonance frequency. Thus, the integrity of the implant system can be assessed using RFA [36].

In RFA, the implants are vibrated externally either by steady-state waves or transient impulse force [37]. The frequency resulting into maximum amplitude of vibrational displacement is recorded as the resonance frequency [38]. In order to conduct RFA for dental implants, there are mainly two modules required as shown in Fig. 1. The excitation module is responsible for giving the necessary external excitation to the dental implant, whereas the sensing module is required to record the resonance frequency. Different excitation/actuation and sensing techniques have been developed to evaluate the stability of the implant. The actuation can be either contact or non-contact type depending on whether the actuating medium touches the implant. Similarly, the sensing half can either detect the micromotion by establishing contact with the implant or by adopting a contactless technique. The various methods described in this section differ mainly according to their excitation technique.

2.1 Electronic RFA

The electronic method for resonance frequency analysis is considered to be the first generation of RFA [19]. This method was first proposed and developed by Meredith et al. [28] in 1996. For electronic RFA, a titanium or stainless-steel transducer comprised of a L-shaped beam having two piezoceramic elements [39] as shown in Fig. 2a was used. The vibrational input was given to one of the piezoe-

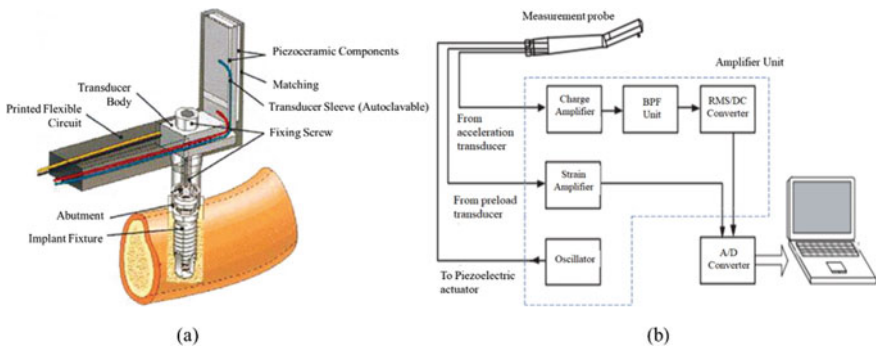


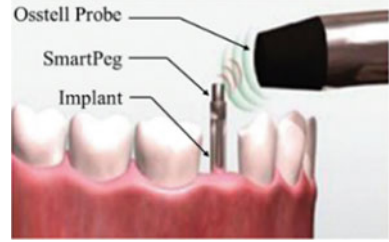
Fig. 2 a L-shaped transducer setup [19]. b Dental implant movement checker setup [43]

ramic elements in the form of a sinusoidal signal [40]. The frequency of this signal is ranged between 5 and 15 kHz. The signal was also incorporated with a frequency analyser and a personal computer. The vibrational response of the beam, recorded by the second piezoceramic component, was amplified by a charge amplifier. The first bending (flexural) frequency was identified by an increase in the magnitude of the output signal as well as a phase change. Thus, the frequency at which the peak occurred was termed as resonance frequency, measured in Hertz. In 1998, a modification in the transducer design was suggested by Cawley et al. [14]. By the year 2000, the device was commercialized by a Swedish company (Osstell). This device introduced the term “Implant Stability Quotient” (ISQ). Resonance frequency was converted to an ISQ value on the scale of 1–100 for easier interpretation by clinicians. An ISQ value of 1 denoted the lowest stability while that of 100 implied maximum stability [41]. Over the years, the electronic RFA method was tested with different setups. In a study by Delgado et al. [42], an accelerometer was used instead of piezoceramic elements to measure the transducer response. Wijaya et al. [43] came up with a modified experimental setup as shown in Fig. 2b. The setup constituted of piezoelectric actuators to excite the implant, strain gauges to measure the pre-load and an acceleration transducer to measure the vibration response. A band-pass filter (BPF) was introduced for filtering out noises. While the electronic RFA method proved useful in measuring the dental implant stability, there were certain shortcomings such as mounting difficulty on implants due to the presence of wires and also limited applicability for certain implant systems [44]. This led to the development of the next generation of RFA devices which were based on an electromagnetic principle.

2.2 *Electromagnetic RFA*

The electronic RFA setup proposed by Meredith et al. [28] had portability issues as a direct connection wired instrument was utilized between the transducer (L-shaped cantilever beam) and the RF analyser unit which made it expensive to develop and maintain. This led to the development of the electromagnetic method to assess the resonant frequency of the dental implant–bone structure [45]. The electromagnetic form of RFA is a second-generation method of measuring implant stability and is a major non-contact actuation technique as it does not require any direct interference with the implant system [46, 47]. The first electromagnetic-based commercial device, Osstell Mentor, consisted of a magnetic accessory called the SmartPeg made of aluminium [44] which was fitted on the implant. The device probe is held normal to the SmartPeg [48, 49]. The electromagnetic waves produced in the probe stimulate the magnetic core of the SmartPeg, causing it to vibrate as shown in Fig. 3. The latest development of electromagnetic device is the Osstell ISQ [50]. The Osstell ISQ is more resistant to the noise generated by electromagnetic waves and is user-friendly as compared to Osstell Mentor.

Fig. 3 Electromagnetic RFA (Osstell) working principle [15]



Another commercial device that uses the same electromagnetic technology for RFA is the Penguin RFA device. The only difference between this device and the Osstell devices is the magnetic accessory. For the Osstell devices, each SmartPeg could be used only once for measurement. As it was made of aluminium, any attempt at sterilization resulted into corrosion and damage [40]. Hence, for the Penguin RFA device, the magnetic accessory was made out of titanium (MultiPeg), a biocompatible material that could be sterilized and used for multiple measurements. A study was conducted by Bural et al. [44] to assess the reliability of the commercial devices Osstell ISQ and Penguin RFA along with the respective magnetic elements SmartPeg and MultiPeg, respectively. The study revealed a higher intra-observer reliability of Osstell-MultiPeg combination as compared to Penguin-SmartPeg. The Osstell device was also proven to be useful in measuring implant stability of mini-dental implants with the help of a universal adaptor arrangement [51].

While these commercial devices have been in use, there have been different studies to come up with experimental setups or devices to overcome the drawbacks with these existing devices. Yamane et al. developed an experimental setup for detecting the primary stability of an implant by using an enamel wire coil wrapped around a ferrite rod as the electromagnetic inductor [52]. The setup used an accelerometer to detect the vibrations of the implant which were transferred to a FFT setup to obtain the resonant frequency of the implant as shown in Fig. 4a. This was a semi-contact type device as the accelerometer had to be attached to the implant and would thus

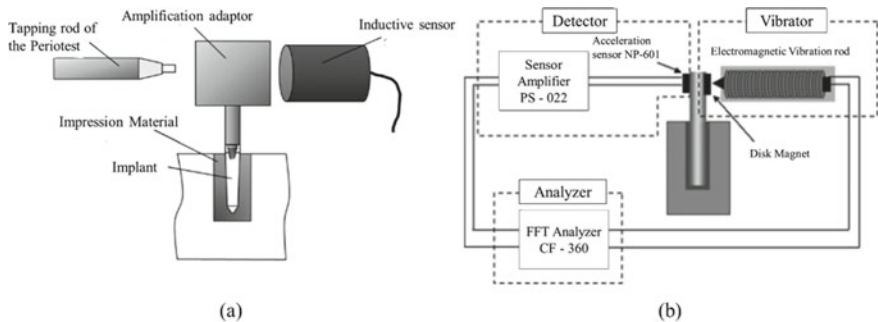


Fig. 4 a Schematic diagram of RFA using Periotest actuation and inductive sensor measurement [54]. b Electromagnetic RFA experimental device components [52]

apply a mass effect that could distort the actual resonance frequency. Kim et al. [53] developed a new system which used a Periotest device to provide an impulse to the implant system. The vibrations of the implant were detected by an inductive sensor as shown in Fig. 4b which were then amplified by an amplification adaptor and were finally fed to a spectrum analyser to obtain the resonant frequency [54]. Tang et al. [55] suggested a new technique called Torsional RFA where they designed a T-shaped cantilever bilateral beam transducer to detect the torsional vibrations of the implant when excited by an electromagnetic field. Mou et al. [56] made a non-contact sensing and actuating electromagnetic device that used two inductors in series to develop magnetic flux and hall sensors to detect the vibrations of the implant. Another setup was designed that employed an electromagnet for actuation and dual Hall-effect sensors for detection [57]. Further Pan et al. developed a handheld device for detecting primary stability of dental implants by using electromagnetic inductors which were driven by a Morlet wavelet signal [46]. The repeatability, accuracy and sensitivity of this device was found consistent with results obtained by comparing with the Osstell ISQ device.

The electromagnetic RFA method has been employed clinically for evaluating the dental implant stability for many years [23]. However, there are certain drawbacks and limitations to this method [58]. SmartPegs/MultiPegs increase the total cost of the procedure. In addition, different implant systems require respective SmartPegs/MultiPegs. This limits the usage of the technique for measuring implant stability.

2.3 Impulse Force Triggered RFA

When a transient force like an impact hammer is used as a source of excitement and the frequency response is analysed, the RFA technique is known as an impulse triggered resonance frequency analysis [59]. The Implomates device produces an impact force through a tiny electrically driven rod inside the device that causes the implant to vibrate [38]. The sound produced by the impact hammer or rod is consequently captured by a device like the microphone or an acoustic receiver and is processed through the fast Fourier transform (FFT) [39]. The Fourier transform converts the time response signal into a signal that can be analysed in the frequency domain and the peak value of the amplitude of vibration gives us the resonance frequency.

In 1991, Kaneko supplied a sinusoidal wave to a driving probe to produce a mechanical impulse and analysed an amplified electrical signal from the receiver probe on an oscilloscope screen [60, 61]. In another article, Kaneko et al. compared an acoustic impulse with a mechanical impulse for providing a transient force to the implants [62]. However, most of these studies concentrated on analysing the vibratory response waveform in the time domain instead of the frequency domain [63, 64]. For the impulse force technique to be classified under resonance frequency analysis, a fast Fourier transform was required to convert the time domain signal

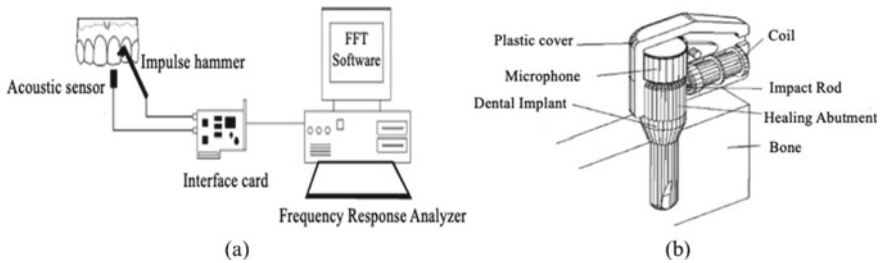


Fig. 5 **a** Impulse force experimental setup. **b** Device construction [59]

into the frequency domain signal [65]. Huang et al. [66, 67] developed a prototype for assessing the natural frequencies of dental implants. The setup consisted of an impulse force hammer to trigger the vibrations of the implant and a piezoelectric microphone to capture the vibration signals [68]. This setup was first tested in vitro by fixing the implants on a metal clamp stand and varying the clamping force and torque. The setup was also tested in vivo with six healthy rabbits which were divided into two groups with cavities of diameters 3.75 and 5 mm to simulate different fitting conditions [69]. Finally, Huang et al. [59] developed a device that consisted of a small electromagnetic rod for triggering the implant and an acoustic receiver for recording the vibrational signals. This device was miniaturised in such a way that it fit right into the healing abutment of the implant and the vibration signal captured was analysed by a spectrum analyser. In 2007, Chang et al. [70] tested the device in vivo to analyse the device's sensitivity and repeatability. The results were consistent with Osstell Mentor and other RFA devices. Figure 5 shows the experimental setup and the device constructed, respectively.

The impulse triggered resonance frequency analysis is quite suitable for estimating the primary stability of an implant which depends mainly on the initial osseointegration process. The repeatability and accuracy of this technique is quite high as shown in both the experimental setup and the device. However, the impulse triggered RFA technique becomes a contact type technique as the impulse hammer or the electromagnetic rod strikes the implant to produce vibrations which may hamper the implant–bone bonding. Nevertheless, the small size of the impact hammer proves to be superior ergonomically which provides a good measure of primary stability.

2.4 Electromechanical Impedance RFA

The electromechanical impedance (EMI) method is not predominantly used in the biomedical industry [71]. However, there have been some studies that use the EMI technique to measure dental implant stability. In EMI technique, piezoceramic transducers or PZTs are attached to the dental implant. When an electric field is subjected to the transducer, it induces a varying frequency range causing the excitation of the

implant–bone structure. The reaction forces are measured by the transducer in the form of its admittance (reciprocal of electrical impedance). This electrical admittance is influenced by changes in mechanical properties of the structure.

In 2011, Boemio et al. [71] designed an experimental setup that consisted of two dental implants fitted in polyurethane foams. In order to simulate inverse osseointegration conditions, the foams were immersed in nitric acid solution to cause its degradation. The PZTs were attached to the dental implants, and their output was the admittance. Graphs of conductance (real component of admittance) were plotted against the excitation frequency. The changes in the conductance values showed correlation to the resulting changes in the bone–implant interface’s stiffness values. Similar studies by Rizzo et al. [72] and Tabrizi et al. [73] showed that the EMI technique can also prove to calculate the loss of calcium from the surrounding bone. This research was furthered by Ribolla et al. [74, 75] who showed experimentally and numerical, using finite element method, that the electromechanical method can be used indirectly to evaluate the stiffness of the implant–bone structure and hence, consequently its stability too. From these studies, it is safe to say that these electromechanical impedance studies are an indirect RFA method as we can determine the frequencies and mode shapes from the admittance graphs.

In a study by Ghosal et al. [76], a single, two-terminal piezo transducer was attached to the dental implant–plaster mixture that simulated osseointegration. The magnitude and phase plots of the transducer’s impedance were measured to identify the resonance frequency. It was shown that the impedance phase plots were a better indicator in terms of reliability for RFA. Baruah et al. [33] furthered this study by designing an economical instrumentation setup which included a phase detector circuit in order to record the resonance frequencies. This method proved to be useful for implant stability measurement, but further improvements are to be made. The transducer’s resolution and performance in real-time have to be improved. There are many advantages to the EMI technique: the transducer’s low-cost, lightweight design and its sensitivity to changes in the mechanical properties around the transducer [71]. However, this method has to be tested clinically and also should be compared to the results from commercial devices like Osstell ISQ and Periotest [74].

2.5 *Vibro-Acoustic RFA*

The vibro-acoustic method for RFA comprises of an acoustic source to excite the dental implant–bone structure and a sensor to measure the resulting displacement and the resonance frequency. The first vibro-acoustic setup was designed by Zhuang et al. [77]. The setup consisted of a miniature loudspeaker as the acoustic excitation source and a capacitive displacement sensor was used on the measuring end to record the vibration response as shown in Fig. 6. The experimental results were compared to the in vivo results determined using numerical modal analysis. It was found that the resonance frequencies taken in the lateral direction had some variations in their values. This preliminary vibro-acoustic setup succeeded to measure

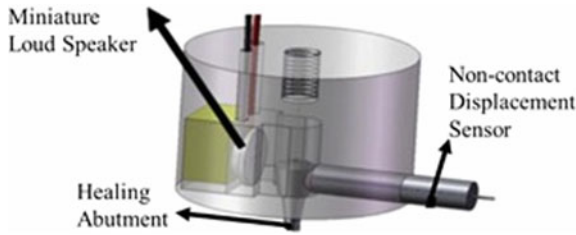


Fig. 6 Proposed vibro-acoustic setup for non-contact type RFA [78]

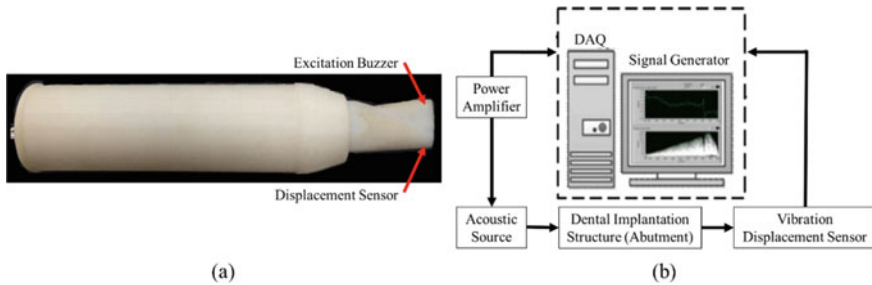


Fig. 7 a Handheld vibro-acoustic device. b Working principle of vibro-acoustic RFA [80]

the resonance frequencies of the implant. In another related study by Zhuang et al. [78], a linear relationship between the resonance frequencies and clamping heights was established. Pan et al. [79] furthered these studies by establishing a correlation between the vibro-acoustic resonance frequencies and their corresponding ISQ values by using linear regression analysis based on two parameters: clamping height and direction of measurement.

Recently in 2020, Pan et al. [80] developed a handheld non-contact type device which completely avoided the use of the SmartPegs used in the Osstell devices. Figure 7a shows the handheld device with its measurement probe and Fig. 7b shows the block diagram of the vibro-acoustic RFA method. The vibro-acoustic method is a recent development and a new emerging technology. Along with being a non-contact actuation method, the elimination of the smart peg is the biggest advantage of this method. Although it depends on various factors such as the acoustic pressure, clamping height, direction of measurement and the signal-to-noise ratio, this method is effective enough to be used by dentists.

3 Summary

In the present review article, the different non-invasive methods like electronic, electromagnetic and vibro-acoustic RFA and invasive methods like the impulse triggered

Table 1 Comparative summary of different RFA technologies used for implant stability measurement

Technique	Invasive/Non-invasive	Contact/Non-contact	Instrumentation	Commercially available
Electronic RFA	Non-invasive	Contact	Wired device	Yes (Osstell Mentor)
Electromagnetic RFA	Non-invasive	Non-contact	Handheld device	Yes (Osstell Beacon, Penguin RFA)
Impulse triggered RFA	Invasive	Contact	Experimental setup	Yes (Implomates device)
EMI RFA	Invasive	Contact	Handheld device	No
Vibro-acoustic RFA	Non-invasive	Non-contact	Handheld device	No (Only prototype)

and electromechanical impedance RFA have been studied extensively. These techniques have been compared on the basis of parameters like contact/non-contact, instrumentation setups and their commercial availability as shown in Table 1.

4 Conclusion and Future Scope

Primary stability assessment in the field of dental implants is crucial to investigate the level of osseointegration with the surrounding bone and to avoid its failure. This paper aimed at reviewing the various sensing and actuating techniques used in the resonance frequency analysis (RFA) for measuring primary stability of dental implants. The electronic RFA methodology is one of the first techniques to be commercially developed. However, due to the portability and mounting issues, alternative RFA techniques were developed by researchers. The impulse triggered RFA showed potential due to its accuracy and ergonomic suitability. The experimental setup of electromechanical impedance provides a light weight and low-cost solution, which needs to be developed further. Osstell ISQ and Penguin RFA are the commercially developed devices based on the electromagnetic RFA principle that provide a non-contact actuation to vibrate the implant. However, these devices require the use of a magnetic accessory like SmartPegs and MultiPegs which ultimately increase the total cost of manufacturing/procedure. To avoid the use of the magnetic accessory, the vibro-acoustic RFA method was developed. The vibro-acoustic RFA technique has appreciable accuracy and repeatability, but it might be susceptible to noise. The variation in the different methods based on RFA technique for measurement of primary stability of dental implants has been hypothetically proven on the basis of present review. A device that can identify both the bone–implant interface characteristics and the

primary stability will provide an all-round solution towards detecting the level of osseointegration of implants and will subsequently lead to a reduction in their failure rates.

References

1. Raikar S, Talukdar P, Kumari S, Panda SK, Oommen VM, Prasad A (2017) Factors affecting the survival rate of dental implants: a retrospective study. *J Int Soc Prev Community Dent* 8(5):71–81
2. Gupta RK, Padmanabhan TV (2011) Resonance frequency analysis. *Indian J Dent Res* 22(4):567–573. <https://doi.org/10.4103/0970-9290.90300>
3. Badalia I, Kumar M, Bansal A, Pradesh H, Pradesh H (2017) Measuring implants stability—a review. *Dent J Adv Stud* 5(2321):105–111
4. Brunski J (1992) Biomechanical factors affecting the bone-dental implant interface. *Clin Mater* 10(1):153–201
5. Kittur N, Oak R, Dekate D, Jadhav S, Dhatrik P (2020) Dental implant stability and its measurements to improve osseointegration at the bone-implant interface: a review. *Mater Today Proc* 43:1064–1070. <https://doi.org/10.1016/j.matpr.2020.08.243>
6. Chen M, Lyons K, Tawse-Smith A, Ma S (2019) Resonance frequency analysis in assessing implant stability: a retrospective analysis. *Int J Prosthodont* 32(4):317–326. <https://doi.org/10.11607/ijp.6057>
7. Javed F, Ahmed H, Crespi R, Romanos G (2013) Role of primary stability for successful osseointegration of dental implants: factors of influence and evaluation. *Interv Med Appl Sci* 5(4):162–167. <https://doi.org/10.1556/IMAS.5.2013.4.3>
8. Joshi S, Dhatrik P, Nimbalkar S, Gherde C (2020) An effect of various parameters on insertion torque to improve the success rate of dental implantation: a review. *Mater Today Proc* 43:928–934. <https://doi.org/10.1016/j.matpr.2020.07.222>
9. Noyes D, Solt C (1973) Measurement of mechanical mobility of human incisors with sinusoidal forces. *J Biomech* 6:439–442
10. Lioubavina-Hack N, Lang NP, Karring T (2006) Significance of primary stability for osseointegration of dental implants. *Clin Oral Implants Res* 17(3):244–250. <https://doi.org/10.1111/j.1600-0501.2005.01201.x>
11. Eliasa CN, Rocha FA, Nascimento AL, Coelho PG (2012) Influence of implant shape, surface morphology, surgical technique and bone quality on the primary stability of dental implants. *J Mech Behav Biomed Mater* 16(1):169–180. <https://doi.org/10.1016/j.jmbbm.2012.10.010>
12. Hiranmayi KV (2018) Factors influencing implant stability. *J Dent Implant* 8(2):69. https://doi.org/10.4103/jdi.jdi_14_18
13. Rittel D, Dorogoy A, Haiat G, Shemtov-Yona K (2019) Resonant frequency analysis of dental implants. *arXiv*, pp 1–27. <https://doi.org/10.1016/j.medengphy.2019.02.008>
14. Cawley P, Pavlakovic B, Allicyn DN, George R, Back T, Meredith N (1998) The design of a vibration transducer to monitor the integrity of dental implants. *Proc Inst Mech Eng Part H J Eng Med* 212(4):265–272. <https://doi.org/10.1243/0954411981534042>
15. Swami V, Vijayaraghavan V, Swami V (2016) Current trends to measure implant stability. *J Indian Prosthodont Soc* 16(2):124–130. <https://doi.org/10.4103/0972-4052.176539>
16. Shokri M, Daraeighadikolaei A (2013) Measurement of primary and secondary stability of dental implants by resonance frequency analysis method in mandible. *Int J Dent* 2013:1–5. <https://doi.org/10.1155/2013/506968>
17. Glauser R et al (2004) Resonance frequency analysis of implants subjected to immediate or early functional occlusal loading. Successful vs. failing implants. *Clin Oral Implants Res* 15(4):428–434. <https://doi.org/10.1111/j.1600-0501.2004.01036.x>

18. Bischof M, Nedir R, Szmukler-Moncler S, Bernard JP, Samson J (2004) Implant stability measurement of delayed and immediately loaded implants during healing. A clinical resonance-frequency analysis study with sandblasted-and-etched ITI implants. *Clin Oral Implants Res* 15(5):529–539. <https://doi.org/10.1111/j.1600-0501.2004.01042.x>
19. Kastala V (2018) Methods to measure implant stability. *J Dent Implant* 8(1):3. https://doi.org/10.4103/jdi.jdi_7_18
20. Atsumi et al (2007) Methods used to assess implant stability: current status. *Int J Oral Maxillofac Implants* 22(5):743–754. DOI <http://www.ncbi.nlm.nih.gov/pubmed/17974108>
21. Mistry G, Shetty O, Shetty S, Singh R (2014) Measuring implant stability: a review of different methods. *J Dent Implant* 4(2):165. <https://doi.org/10.4103/0974-6781.140891>
22. Lachmann S, Jäger B, Axmann D, Gomez-Roman G, Groten M, Weber H (2006) Resonance frequency analysis and damping capacity assessment—Part I: an in vitro study on measurement reliability and a method of comparison in the determination of primary dental implant stability. *Clin Oral Implants Res* 17(1):75–79. <https://doi.org/10.1111/j.1600-0501.2005.01173.x>
23. Herrero-Climent M et al (2013) Assessment of Osstell ISQ's reliability for implant stability measurement: a cross-sectional clinical study. *Med Oral Patol Oral Cir Bucal* 18(6). <https://doi.org/10.4317/medoral.19120>
24. Mall N, Dhanasekar B, Aparna IN (2011) Validation of implant stability: a measure of implant permanence. *Indian J Dent Res* 22(3):462–467. <https://doi.org/10.4103/0970-9290.87071>
25. Kanth KL, Swamy DN, Mohan TK, Swarna C, Sanivarapu S, Pasupuleti M (2014) Determination of implant stability by resonance frequency analysis device during early healing period. *J Dr NTR Univ Heal Sci* 3(3):169. <https://doi.org/10.4103/2277-8632.140936>
26. Kunnekel AT, Nair KC, Naidu EM, Sivagami G (2011) Validation of resonance frequency analysis by comparing implant stability quotient values with histomorphometric data. *J Oral Implantol* 37(3):301–308. <https://doi.org/10.1563/AAID-JOI-D-09-00137>
27. Ito Y, Sato D, Yoneda S, Ito D, Kondo H, Kasugai S (2008) Relevance of resonance frequency analysis to evaluate dental implant stability: simulation and histomorphometrical animal experiments. *Clin Oral Implants Res* 19(1):9–14. <https://doi.org/10.1111/j.1600-0501.2007.01419.x>
28. Meredith N, Alleyne D, Cawley P (1996) Quantitative determination of the stability of the implant-t interface using resonance frequency analysis. *Clin Oral Implants Res*:103–111. <https://doi.org/10.1115/IMECE2002-33490>
29. Satwalekar P, Nalla S, Reddy R, Chowdary SG (2015) Clinical evaluation of osseointegration using resonance frequency analysis. *J Indian Prosthodont Soc* 15(3):192–199. <https://doi.org/10.4103/0972-4052.165171>
30. Park J-C, Lee J-W, Kim S-M, Lee J-H (2011) Implant stability—measuring devices and randomized clinical trial for ISQ value change pattern measured from two different directions by magnetic RFA. In: *Implant dentistry—a rapidly evolving practice*, no Meredith 1998, 2011. <https://doi.org/10.5772/18309>
31. Sennerby L, Meredith N (2008) Implant stability measurements using resonance frequency analysis: biological and biomechanical aspects and clinical implications. *Periodontol* 47(1):51–66. <https://doi.org/10.1111/j.1600-0757.2008.00267.x>
32. Argatov I, Iantchenko A (2019) A simple mathematical model for the resonance frequency analysis of dental implant stability: implant clamping quotient. *Mech Res Commun* 95:67–70. <https://doi.org/10.1016/j.mechrescom.2018.12.004>
33. Baruah M, Banerjee P, Nandy A, Goswami B, Ghosh R (2012) A low cost instrumentation system for determining stability of dental implants. In: *Proceedings—2012 3rd international conference on emerging applications of information technology EAIT 2012*, pp 81–84. <https://doi.org/10.1109/EAIT.2012.6407867>
34. Charatchaiwanna A, Rojsiraphisa T, Aunmeungtong W, Reichart PA, Khongkhunthian P (2019) Mathematical equations for dental implant stability patterns during the osseointegration period, based on previous resonance frequency analysis studies. *Clin Implant Dent Relat Res* 21(5):1028–1040. <https://doi.org/10.1111/cid.12828>

35. Soni G, Bhutada G, Borkar S, Baisane V, Maheshwari S (2017) Implant stability measurement using resonance frequency analysis: a review update. 3(5):85–91
36. Su YH, Yue Peng B, Wang PD, Feng SW (2020) Evaluation of the implant stability and the marginal bone level changes during the first three months of dental implant healing process: a prospective clinical study. *J Mech Behav Biomed Mater* 110(May):103899. <https://doi.org/10.1016/j.jmbbm.2020.103899>
37. Nokes LDM (1999) The use of low-frequency vibration measurement in orthopaedics. *Proc Inst Mech Eng Part H J Eng Med* 213(3):271–290. <https://doi.org/10.1243/0954411991534979>
38. Harirfroush R (2012) Dental implant stability analysis by using resonance frequency analysis. Simon Fraser University
39. Zanetti EM, Pascoletti G, Cali M, Bignardi C, Franceschini G (2018) Clinical assessment of dental implant stability during follow-up: what is actually measured, and perspectives. *Biosensors* 8(3). <https://doi.org/10.3390/bios8030068>
40. Sennerby L (2015) Resonance frequency analysis for implant stability measurements. a review. In: *Integration Diagnostics update*, vol 1, pp 1–11. Available <http://www.penguinrfa.com/wp-content/uploads/2016/09/RFA-Review.pdf>
41. Huang H, Wu G, Eb H (2020) The clinical significance of implant stability quotient (ISQ) measurements: a literature review. *J Oral Biol Craniofacial Res* 10(4):629–638. <https://doi.org/10.1016/j.jobcr.2020.07.004>
42. Delgado D, Fuentes AA, Jones R, Lumsdaine A (2002) Quantitative determination of the stability of implant-bone interface using resonance frequency analysis. In: *ASME international mechanical engineering congress and exposition proceedings*, pp 103–111. <https://doi.org/10.1115/IMECE2002-33490>
43. Wijaya SK, Oka H, Saratani K, Sumikawa T, Kawazoe T (2004) Development of implant movement checker for determining dental implant stability. *Med Eng Phys* 26(6):513–522. <https://doi.org/10.1016/j.medengphy.2004.02.007>
44. Bural C, Dayan C, Geçkili O (2020) Initial stability measurements of implants using a new magnetic resonance frequency analyzer with titanium transducers: an ex vivo study. *J Oral Implantol* 46(1):35–40. <https://doi.org/10.1563/aaid-joi-D-19-00126>
45. Valderrama P, Oates TW, Jones AA, Simpson J, Schoolfield JD, Cochran DL (2007) Evaluation of two different resonance frequency devices to detect implant stability: a clinical trial. *J Periodontol* 78(2):262–272. <https://doi.org/10.1902/jop.2007.060143>
46. Pan MC, Lin HP, Chen CS (2021) Design/exploration and verification of an electromagnetic probe for assessing dental implant osseointegration. *Meas J Int Meas Confed* 174(Jan):109054. <https://doi.org/10.1016/j.measurement.2021.109054>
47. Ohta K et al (2010) Influence of factors related to implant stability detected by wireless resonance frequency analysis device. *J Oral Rehabil* 37(2):131–137. <https://doi.org/10.1111/j.1365-2842.2009.02032.x>
48. Andreotti AM et al (2017) Relationship between implant stability measurements obtained by two different devices: a systematic review. *J Periodontol* 88(3):281–288. <https://doi.org/10.1902/jop.2016.160436>
49. Hurst SJ (2002) Investigation of periosteal and osstell instruments measuring craniofacial implant integrity. University of Alberta, <https://doi.org/10.7939/R33J39C3J>
50. Zix J, Hug S, Kessler-Liechti G, Mericske-Stern R (2008) Measurement of dental implant stability by resonance frequency analysis and damping capacity assessment: comparison of both techniques in a clinical trial. *Int J Oral Maxillofac Implants* 23(3):525–530. DOI <http://www.ncbi.nlm.nih.gov/pubmed/18700378>
51. Hosein YK, Jeffrey Dixon S, Rizkalla AS, Tassi A (2019) A novel technique for measurement of orthodontic mini-implant stability using the Osstell ISQ device. *The Angle Orthodontist* 89(2):284–291. <https://doi.org/10.2319/011518-46.1>
52. Yamane M, Yamaoka M, Hayashi M, Furutoyo I, Komori N, Ogiso B (2008) Measuring tooth mobility with a no-contact vibration device. *J Periodontal Res* 43(1):84–89. <https://doi.org/10.1111/j.1600-0765.2007.00997.x>

53. Kim DS et al (2011) Development of a dental implant mobility measurement system using an inductive sensor. In: Proceedings of the annual international conference of the IEEE engineering in medicine and biology society EMBS, pp 361–364. <https://doi.org/10.1109/IEMBS.2011.6090118>
54. Kim DS et al (2012) A new method for the evaluation of dental implant stability using an inductive sensor. *Med Eng Phys* 34(9):1247–1252. <https://doi.org/10.1016/j.medengphys.2011.12.012>
55. Tang YL, Li B, Jin W, Li DH (2015) Torsional resonance frequency analysis: a novel method for assessment of dental implant stability. *Clin Oral Implants Res* 26(6):615–622. <https://doi.org/10.1111/clr.12350>
56. Mou RZ, Lin SB, Chen CS, Pan MC (2015) Detection device for dental implant osseointegration using inductors and hall sensors. *J Med Devices Trans ASME* 9(2):2015–2017. <https://doi.org/10.1115/1.4030193>
57. Chia TS, Chen CS, Pan MC (2014) Assessment of dental implantation osseointegration through electromagnetic actuation and detection. *J Med Devices Trans ASME* 8(3):2014–2016. <https://doi.org/10.1115/1.4027108>
58. Khuntia P, Nayak R, Das AC, Mohanty R, Satpathy A, Das S (2020) Resonance frequency analysis and oral implant stability: a long term relationship. *Indian J Forensic Med Toxicol* 14(4):8577–8580. <https://doi.org/10.37506/ijfmt.v14i4.13047>
59. Huang HM et al (2006) Damping effects on the response of maxillary incisor subjected to a traumatic impact force: a nonlinear finite element analysis. *J Dent* 34(4):261–268. <https://doi.org/10.1016/j.jdent.2005.06.007>
60. Kaneko T (1991) Assessment of the dental implant–bone interface from a pulsed microvibration. *J Mater Sci Lett* 10(4):185–187. <https://doi.org/10.1007/BF00723800>
61. Kaneko T (1991) Pulsed oscillation technique for assessing the mechanical state of the dental implant–bone interface. *Biomaterials* 12(6):555–560. [https://doi.org/10.1016/0142-9612\(91\)90050-K](https://doi.org/10.1016/0142-9612(91)90050-K)
62. Kaneko T (1989) Comparison between acoustic and mechanical tapping methods for assessing the interfacial states of bone implants. *J Mater Sci* 24:2820–2824
63. Kaneko T (1987) Assessment of the interfacial rigidity of bone implants from vibrational signals. *J Mater Sci* 22(10):3495–3502. <https://doi.org/10.1007/BF01161448>
64. Kaneko T, Nagai Y, Ogino M, Futami T, Ichimura T (1986) Acoustoelectric technique for assessing the mechanical state of the dental implant–bone interface. *J Biomed Mater Res* 20(2):169–176. <https://doi.org/10.1002/jbm.820200206>
65. Dario LJ, Cucchiari PJ, Deluzio AJ (2002) Electronic monitoring of dental implant osseointegration. *J Am Dent Assoc* 133(4):483–490. <https://doi.org/10.14219/jada.archive.2002.0208>
66. Huang HM, Pan LC, Lee SY, Chiu CL, Fan KH, Ho KN (2000) Assessing the implant/bone interface by using natural frequency analysis. *Oral Surg Oral Med Oral Pathol Oral Radiol Endod* 90(3):285–291. <https://doi.org/10.1067/moe.2000.108918>
67. Huang HM, Lee SY, Yeh CY, Wang MS, Chang WJ, Lin CT (2001) Natural frequency analysis of periodontal conditions in human anterior teeth. *Ann Biomed Eng* 29(10):915–920. <https://doi.org/10.1114/1.1408925>
68. Huang HM, Lee SY, Yeh CY, Lin CT (2002) Resonance frequency assessment of dental implant stability with various bone qualities: a numerical approach. *Clin Oral Implants Res* 13(1):65–74. <https://doi.org/10.1034/j.1600-0501.2002.130108.x>
69. Huang H-M, Chiu CL, Yeh CY, Lin CT, Lin LH, Lee S-Y (2003) Early detection of implant healing process using resonance frequency analysis. *Clin Oral Implants Res* 14:437–443
70. Chang WJ et al (2007) A newly designed resonance frequency analysis device for dental implant stability detection. *Dent Mater J* 26(5):665–671. <https://doi.org/10.4012/dmj.26.665>
71. Boemio G, Rizzo P, De Nardo L (2011) Assessment of dental implant stability by means of the electromechanical impedance method. *Smart Mater Struct* 20(4). <https://doi.org/10.1088/0964-1726/20/4/045008>

72. Rizzo P, Tabrizi A, Berhanu B, Ochs MW (2012) Nondestructive methods to assess dental implant stability. In: *Nanosensors, biosensors, info-tech sensors systems*, vol 8344, p 83441E. <https://doi.org/10.1117/12.914793>
73. Tabrizi A, Rizzo P, Ochs MW (2012) Electromechanical impedance method to assess dental implant stability. *Smart Mater Struct* 21(11). <https://doi.org/10.1088/0964-1726/21/11/115022>
74. Ribolla ELM, Rizzo P, Gulizzi V (2015) On the use of the electromechanical impedance technique for the assessment of dental implant stability: modeling and experimentation. *J Intell Mater Syst Struct* 26(16):2266–2280. <https://doi.org/10.1177/1045389X14554129>
75. LaMalfa Ribolla E, Rizzo P (2015) Modeling the electromechanical impedance technique for the assessment of dental implant stability. *J Biomech* 48(10):1713–1720. <https://doi.org/10.1016/j.jbiomech.2015.05.020>
76. Ghosal S, Goswami B, Ghosh R, Banerjee P (2011) Determination of stability of dental implant from impedance studies using resonance frequency analysis. In: *Proceedings—2nd international conference on emerging applications of information technology EAIT*, pp 71–74. <https://doi.org/10.1109/EAIT.2011.58>
77. Zhuang HB et al (2013) Non-contact vibro-acoustic detection technique for dental osseointegration examination. *J Med Biol Eng* 33(1):35–44. <https://doi.org/10.5405/jmbe.993>
78. Zhuang HB, Pan MCH, Chen JZ, Wu JW, Chen CS (2014) A noncontact detection technique for interfacial bone defects and osseointegration assessment surrounding dental implants. *Meas J Int Meas Confed* 55:335–342. <https://doi.org/10.1016/j.measurement.2014.05.039>
79. Pan MC, Zhuang HB, Chen CS, Wu JW, Lee SY (2013) A noncontact resonance frequency detection technique for the assessment of the interfacial bone defect around a dental implant. *Med Eng Phys* 35(12):1825–1830. <https://doi.org/10.1016/j.medengphy.2013.05.006>
80. Pan MC, Wang SY, Chen CS (2021) Handheld device for assessing dental implant osseointegration through the vibro-acoustic technique. *Meas J Int Meas Confed* 169:108419. <https://doi.org/10.1016/j.measurement.2020.108419>

Chapter 9

Influence on Seismic Response Owing to the Variation in Size and Spacing of Building in a Building Cluster



Shubham Srivastava and Rajesh Kumar

Abstract Soil–structure interaction (SSI) effects on both the strong motions transmitted to structures and the structural response to these motions. In cities, buildings are arranged in clusters or groups. However, while designing a building it is assumed to be an isolated structure with fixed base for simpler calculations. The complexities of SSI effect increase many folds by considering neighbouring buildings. The seismic response of a building depends upon the soil–foundation–structure interaction and is effected significantly by the response of adjacent building. The building height, depth and size of foundation, soil properties, etc., affect the seismic response of a building group. Response of a single building is higher as compared to building cluster. However, not all buildings in the cluster are equally affected by the earthquake owing to the difference in position of building within the cluster and also due to the spacing between two adjacent buildings. This study investigated the impact of variation in placement of building in cluster and variation in spacing of buildings on the seismic response of structure by modelling the building and soil bed using finite element approach. It also analyses the time taken for damping of variation in building group in comparison to isolated single buildings.

Keywords Soil-structure interaction · Building clusters · Peak response · Frequencies · Displacement contour

1 Introduction

The concepts for design of structures have changed rapidly over the last few decades. The latest concept is the performance-based design. The performance of any structure depends upon several factors which affect its response under static as well as dynamic

S. Srivastava (✉) · R. Kumar
Department of Civil Engineering, Indian Institute of Technology, Banaras Hindu University (BHU), Varanasi, Uttar Pradesh, India
e-mail: shubhamsrivastava.rs.civ19@itbhu.ac.in

R. Kumar
e-mail: rkumar.civ@iitbhu.ac.in

loading conditions. Likewise, for dynamic conditions, the seismic performance of any structure is majorly dependent upon the soil–foundation–structure interaction (SFSI). Until recently, buildings were conventionally designed as isolated structure with fixed based for seismic loads owing to the incomplete understanding of SFSI and to make calculations simpler. The interaction between two adjacent buildings, soil–structure interaction, was not considered as it would lead to complex design calculations. However, the effect of adjacent buildings or group of building and that of soil properties are significant enough to be ignored. More recent works have been carried out on seismic design of building clusters because in most of the cities today the buildings are constructed in clusters or groups.

The earliest works on soil–structure interaction (SSI) were related to application of boundary element method to homogeneous isotropic unbounded domains. Later on, dynamic responses on various foundations were studied like rigid circular footing [1], arbitrary-shaped rigid massless foundation [2] and on heterogeneous isotropic and anisotropic soils [3]. Exact solution in terms of dual integration equations was also presented for response of body resting on transverse isotropic half plane surface [4]. Finite element method was also used for predicting responses of building [5, 6]. The seismic response of structures is affected by the flexibility of the foundation support and variations foundation and free field ground motion [7]. In further studies, boundary element method was applied for the first time to dynamic soil–structure interaction problem [8]. From early 1970s, the boundary integral methods have been used for dynamic analysis of SSI in anisotropic soils. More studies on SSI were based on frequency domain than time domain [9]. Seismic behaviour of reinforced concrete building with underground storeys was analysed to estimate safe number underground storeys with fixed ground conditions by incrementally increasing the number and investigating the changes and performance [10].

Most of the studies were carried out for single isolated buildings, and study of building clusters hasn't been the area of interest until recently. Very few number of studies have been carried out on the response of building cluster. Earlier works dealt with analysis of effect of various building types and densities on seismic wave fields in both 1D and 2D [11]. Seismic response of idealised small city composed of five equally spaced buildings on soft soil layer was carried out which resulted in response amplification of building in near field [12]. Also, realistic scaled centrifuge experiments were carried out where induced motion, ground conditions, ground motions and structural response were observed and back analysis was done to enhance the understanding of SSI effects of buildings in dense urban environment. Comparison between various provisions of SSI in ASCE 7-16 and 7-10 was done [13].

Lately, studies on analysing the effect on seismic response of building cluster due to variation in the building size and spacing have also been carried out. The building height, depth and size of foundation, soil properties, etc., affect the seismic response of a building group. Response of a single building is higher as compared to building cluster. It has been found that the seismic response of buildings in a cluster varies significantly due to adjacent buildings in the groups. The displacement response decreases with the increase in number of buildings in cluster. Also, the acceleration response was witnessed to increase. Although the change in response ceased for

building cluster with more than 8 storeys, it could not be ascertained that all the building in a cluster experienced equal response irrespective of their position in the cluster. This study covers the behaviour of individual building within the cluster, in respect of its position and with each other. In this study, the effect on response with respect of the building position in cluster has been analysed with help of modelling using PLAXIS 8.2 software.

2 Methodology and Modelling of Cluster Effect

Analysis of SFSI is carried out using various methods broadly classified as direct method and multistep methods. In finite element method (FEM), a continuum consists of elements and elements of nodes. Each node has various degree of freedom which correspond to discrete value of unknowns. Within an element, the displacement field u is obtained from the discrete nodal values in a vector v using interpolation functions assembled in matrix N :

$$U = Nv \quad (1)$$

The interpolation function in matrix N is often denoted as shape functions. Substituting the above in kinematic relation gives:

$$\varepsilon = LNv \quad (2)$$

Finite element has been earlier used to compare seismic response of structure under various load combinations using fictional contact to imitate SSI effect [14]. Also, a review of the developed methods of SSI study was carried out to emphasise on deficiency and merits of each method [15]. However, for seismic analysis, dynamic modelling is required. Time integration becomes an essential factor for stability in numerical implementation of dynamics. Boundary displacements were introduced for static deformation in FEM.

The basic equation for time-dependent movement of a volume under the influence of a dynamic load is:

$$F = M\ddot{u} + C\dot{u} + Ku \quad (3)$$

However, for dynamic calculations, the boundaries need to be farther away than those in static calculations, to avoid distortions due to stress wave reflections. In order to counteract reflections, special measures are taken like absorbent and silent boundaries. Various models of boundary conditions which allowed energy transmission have been presented [16], although the most common in FEM is of viscous types. It was further understood from various studies that the location of transmitting boundary must be farther than at least 8–10 times of foundation width [17].

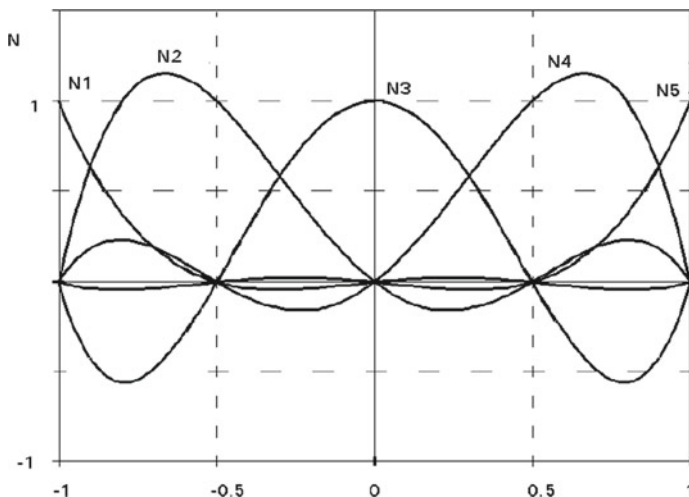


Fig. 1 Shape function for five-node element

A model of 1250 m span with maximum span of 140 and 25 m depth of soil was prepared. A five-node line element was used as plate element (Fig. 1).

A triangular soil element having 15 nodes was chosen for 2D analysis. The stresses were evaluated within the element. Mohr–Coulomb model was used, as first approximation, to model soil behaviour involving five parameters: Young’s Modulus E , Poisson’s ratio ν , Cohesion c , friction angle φ and dilatancy angle ψ . For soil damping, Rayleigh’s coefficients were defined for soil media. The SSI was modelled using interfaces at junctions between foundation and soil. The interface modelling was carried out by selecting suitable value for strength reduction factor, which relates to interface strength to soil strength. The interface strength is dependent upon foundation friction, and adhesion while soil strength is dependent upon cohesion and friction angle.

The Coulomb’s criterion was used to model elasto-plastic behaviour at interfaces considering both small and large displacements. Standard boundary conditions with fixed base at bottom and $u_x = 0$ at sides were used. In order to absorb energy at sides of the model to mimic the unbounded nature of soil, viscous-type absorbent boundaries are used.

Soil–structure interaction in urban environment was studied based on numerical simulation for hypothetical tall building [18]. Similarly, in this study, a building cluster of 9 buildings was adopted for number of storeys in each building ranging from 2 to 10 storey for numerical simulation. The proposed model was applied to study dynamic response of RCC building cluster to harmonic excitation. Mesh densities were increased near boundary and around building cluster to account for higher strain gradients and for improvement in accuracy of the results (Fig. 2). The time taken for damping of vibration with respect to different building positions within the

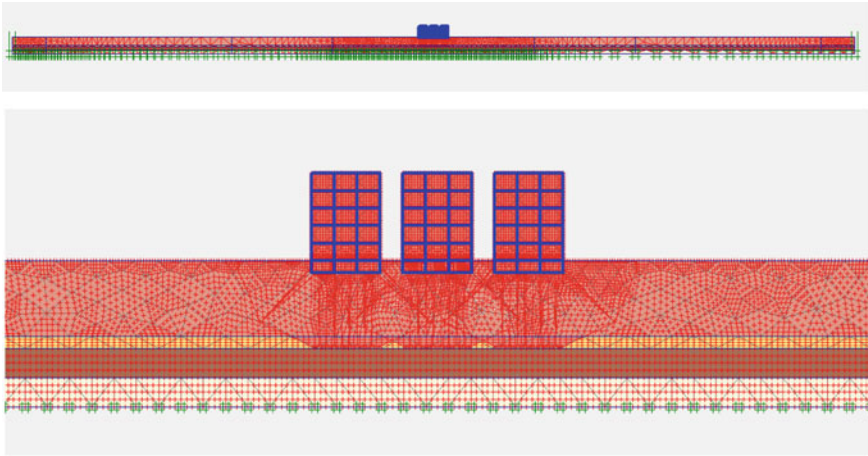


Fig. 2 Meshing in computational model of building cluster in Plaxis software

cluster was also determined to understand the effect of seismic vibration and the time interval for which the building shall be subjected to deformation and displacement.

3 Numerical Analysis and Results

See Fig. 3.

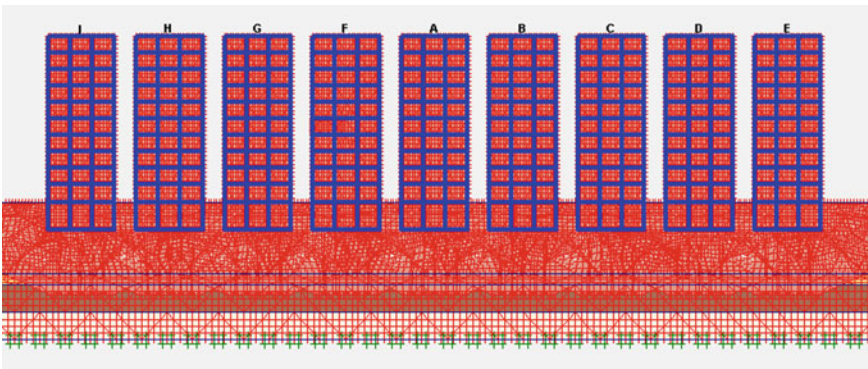


Fig. 3 The building position in the cluster can vary from -64 to $+64$, and a total of 9 simulations were carried out for 2 to 10 storeys

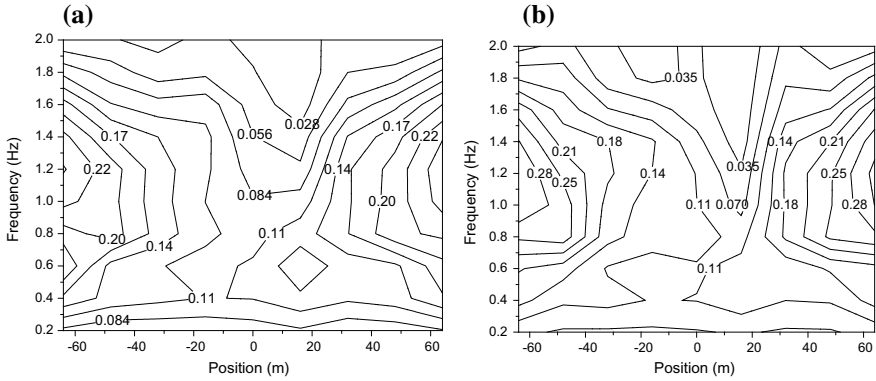


Fig. 6 Contour of displacement response for **a** six- and **b** seven-storey building

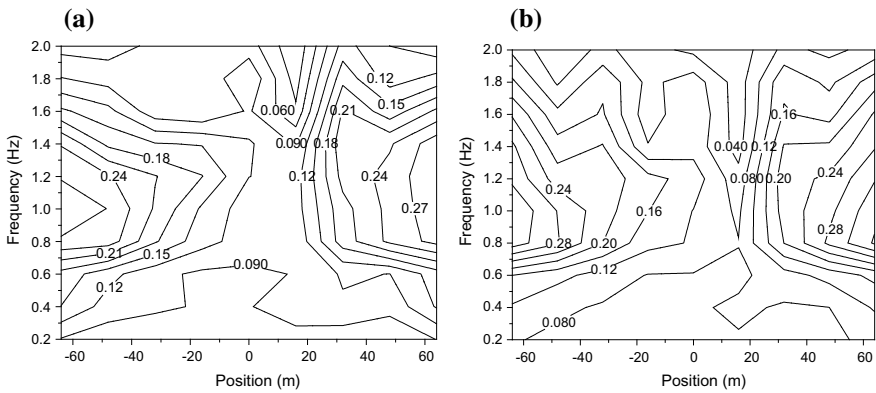


Fig. 7 Contour of displacement response for **a** eight **b** nine storey building

taken for damping both at the center and at the edges of the cluster are summarized in Table 1 below:

4 Conclusion

For the proposed building cluster, the peak responses were always observed at the both the edges as compared to the centre of the building cluster. The displacement response increased at the edges with the increase in frequency. However, for lower frequencies, i.e. up to 0.4 Hz, position of the building inside the cluster did not affect the displacement response of the structure. The acceleration response was not affected by the change in building position. With the increase in number of storeys, the displacement contour became finer towards the edges, unlike the response at

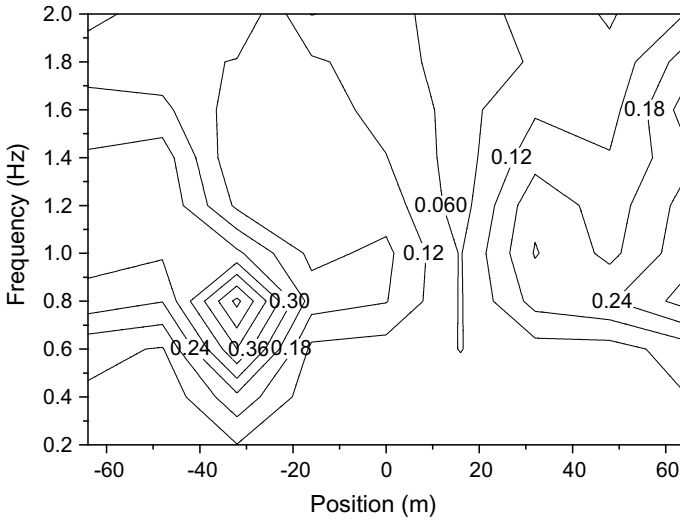


Fig. 8 Contour of displacement response for ten-storey building

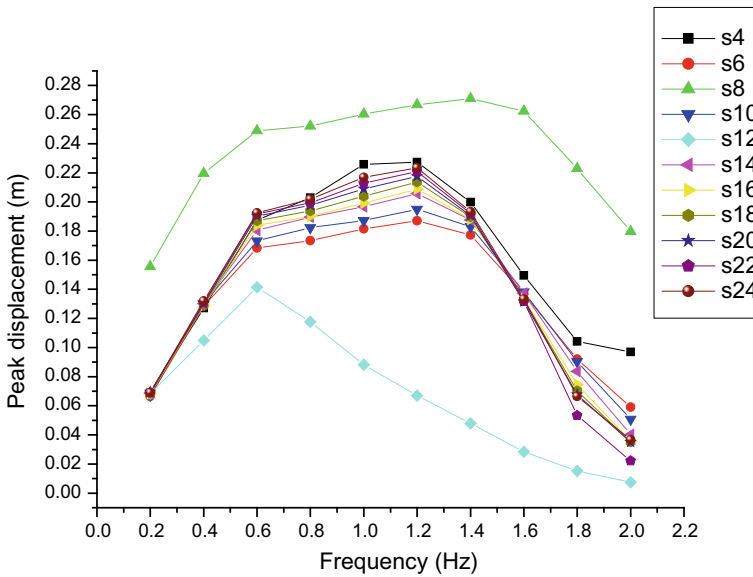


Fig. 9 Variation of displacement response spectra with spacing of buildings in cluster

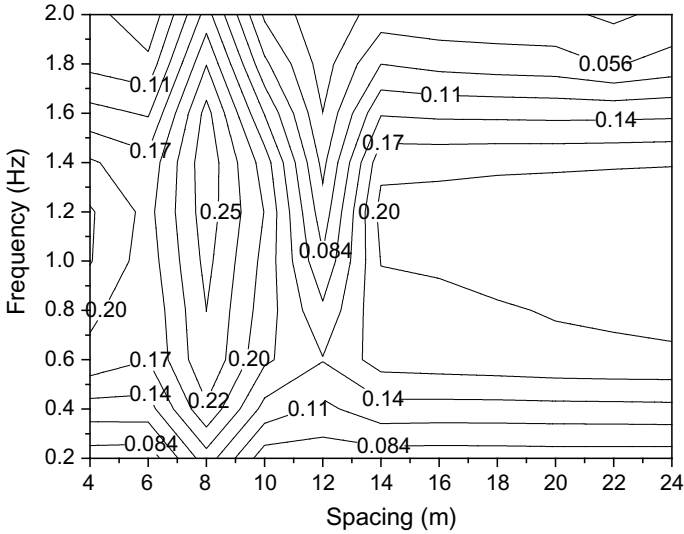


Fig. 10 Variation of displacement contour with spacing in cluster

Table 1 The time taken for damping of response in building at the edges and at the centre in building cluster

No. of storeys	Time taken for acceleration response to become <0.01 g in free vibration mode	
	Centre (9 buildings)	Edge (9 buildings)
2	10.55	11.7
3	10.85	11.3
4	10.55	11.5
5	10.6	11.05
6	10.65	10.7
7	10.75	11.65
8	11.15	11.15
9	11.6	11.55
10	10.85	11.45

the centre where the effect was negligible. Also, in concurrence to the results of displacement response, it was also observed that the buildings placed at the edges of the cluster took more time to dampen the vibrations than the building at the centre. It can thus be concluded that the buildings towards the edges in any cluster must be designed to bear more displacement for the same seismic load. The displacement response is highest for isolated building and decreases with the cluster size. The building position is a factor affecting the response for higher values of frequencies, although it is not as much significant for lower frequencies.

References

1. Luco JE, Westmann RA (1971) Dynamic response of circular foundations. *J Eng Mech ASCE* 97:1381–1395
2. Wong HL, Luco JE (1976) Dynamic response of rigid foundations of arbitrary shape. *Earthquake Eng Struct Dyn* 4(6):579–587. <https://doi.org/10.1002/eqe.4290040606>
3. Ahmed S, Leyte F, Rajapakse RKND (2001) BEM analysis of two-dimensional elastodynamics problems of anisotropic solids. *J Eng Mech ASCE* 127:149–156
4. Freedman JM, Keer LM (1972) Vibratory motion of a body on an orthotropic half plane. *J Appl Mech Trans ASME* 39(4):1033–1040
5. Bathe KJ (1996) *Finite element procedures*. Prentice Hall
6. Vermeer PA, Van Langen H (1989) Soil collapse computations with finite elements. *Ingenieur-Archiv* 59:221–236
7. Das B.M (1995) *Fundamentals of soil dynamics*. Elsevier
8. Dominguez J (1978) Dynamic stiffness of rectangular foundations. Research report R78-20. Department of Civil Engineering, Massachusetts Institute of search Technology, Cambridge, Massachusetts
9. Wang CY, Achenbach JD (1995) 3-dimensional time-harmonic elasto-dynamics Green's functions for anisotropic solids. *Proc R Soc London Ser A-Math Phys Sci* 449:441–458
10. Saad G, Saddik F, Najjar S (2012) Impact of soil structure interaction on the seismic design of reinforced concrete buildings with underground stories. In: 15th World conference on earthquake engineering. <https://doi.org/10.13140/2.1.1662.4008>
11. Semblat JF, Kham M, Bard PY, Gueguen P (2004) Could site-city interaction modify site effects in urban areas?. In: 13th World conference on earthquake engineering, Vancouver, B.C., Canada, 1–6 Aug, Paper No. 1978
12. Gouasmia A, Djeghaba K (2010) Direct approach to seismic soil-structure-interaction analysis for building group case. *Statybinės Konstruktijos ir Technologijos* 2(1):22–30
13. Khosravikia F, Mahsuli M, Ghannad MA (2018) Comparative assessment of soil-structure interaction regulations of ASCE 7-16 and ASCE 7-10. In: Conference: ASCE structures congress, At Fort Worth, Texas, USA. <https://doi.org/10.1061/9780784481325.040>
14. Jha AK, Utkarsh K, Kumar R (2015) Effects of soil-structure interaction on multi storey buildings on mat foundation. In: *Advances in structural engineering*. Springer India, pp 703–715. Online ISBN: 978-81-322-2190-6. https://doi.org/10.1007/978-81-322-2190-6_56
15. Dalili MS, Huat BBK, Jaafar MS, Alkarni A (2013) Review of static soil-framed structure interaction. *Interact Multisc Mech* 6(1):51–81. <https://doi.org/10.12989/imm.2013.6.1.051>
16. Lysmer J, Kulilmeyer RL (1969) Finite dynamic model for infinite media. *ASCE J Eng*:859–877
17. Kausel E, Rosset JM (1976) Dynamic stiffness of piles. In: *Proceedings of 2nd International Conference on Numerical Methods in Geomechanics*, Blacksburg, Virginia, vol 2, pp 1001–1012
18. Mercado JA, Monsalve LGA, Terzic V (2019) Seismic soil structure interaction response of tall buildings. In: Eighth international conference on case histories in geotechnical engineering, geo-congress

Chapter 10

Effect of Aluminium in Magnesium Alloy Fabricated Through the Squeeze Casting Process



Navin Kumar and Shatrughan Soren

Abstract Magnesium alloy containing aluminium is specifically utilized in aerospace and automobile industries to supply lightweight, excessive-strength materials. Aluminium, the essential strengthening element in Mg alloys, is normally added below its stable solubility limit of 12.5 wt%. By using addition of aluminium above this limit, alloy strengthening properties deteriorated, and the material starts to become brittle and relatively porous. Within the current study, binary systems of Mg–Al with Al-content above the solubility limit had been developed via the squeeze casting technique and tested for their microstructural, physical, and mechanical properties. Microstructural studies showed the distribution and amount of intermetallic phase β -Mg₁₇Al₁₂. The material analysis shows an growth in porosity and density of 6.15% and 1.98 in magnesium alloy containing 50 wt% Al.

Keywords Magnesium alloy · Aluminium · Squeeze casting · Density · Porosity · XRD · Mg₁₇Al₁₂ phase

1 Introduction

In the case of lightweight structural material design, magnesium is mostly used by engineers. Its properties allow to weld, forge, machine or cast like aluminium and other metals [1]. It has good heat dissipation and damping properties. Instead of all these properties, magnesium applications are infrequent due to its volatility at high temperatures, and it is highly corrosive in a wet environment. Therefore magnesium is used in its alloy or metal matrix composites form in aerospace and automotive industries to produce lightweight machine parts [2–4]. As an example, in an average general motors (GM) car, aluminium consumption is 123 kg in place of 4 kg magnesium. In some of the cars, the magnesium amount was higher, e.g. 12 kg magnesium used for the seat frame, device panel, gear box cover, steering wheel, and side mirror cover of a GMT800 pickup truck. Nevertheless, in general,

N. Kumar · S. Soren (✉)
Department of Fuel, Mineral and Metallurgical Engineering, Indian Institute of Technology (ISM), Dhanbad, India
e-mail: ssoren@iitism.ac.in

it is far less than 1% of the whole vehicle's weight [5, 6]. The common weight of magnesium in European automobiles is about 2.5 kg. It is expected that the three hundred distinct magnesium parts utilized in European vehicles these days and will be doubled within the next ten years. Magnesium and its alloy show limited research and development due to a lack of large-scale application in the past. The primary region behind the restricted use of magnesium is its low elastic modulus, limited high strength and creep resistance at improved temperature, excessive degree of shrinkage on solidification, limited cold workability and toughness [7–9]. It is not feasible to apply a conventional alloying method to enhance some properties because the solubility of alloying element in magnesium is limited, restricting the opportunity to enhance a few mechanical properties. Therefore, limited casting alloy and wrought alloy of magnesium are available commercially.

Magnesium forms alloy with aluminium, zinc, manganese, silicon, copper, rare earth and zirconium [10, 11]. In all these, aluminium is mainly used as an alloying element with magnesium to improve its strength and creep resistance at high temperatures. Zinc will increase room-temperature strength, fluidity in casting and corrosion resistance. AZ31, AZ61, AZ91, AM60, AE44, etc., are a common alloy of magnesium with aluminium [12]. An alloy of any materials shows low solidus temperature as compared to its pure metals. Due to this, the melting point lowers when pure metals are alloyed with different metals or non-metals, making the metals easily fusible. This property is applied to make beneficial alloys at low temperatures. This research's main objective is to squeeze cast magnesium alloy with a different percentage of aluminium to analyse its density and porosity behaviour and different phases present in alloy through XRD.

2 Experimental Work

2.1 Material and Methods

Commercially available magnesium and aluminium billet of 99% of purity were used to fabricate magnesium alloy. The melts have been prepared from high natural magnesium and aluminium billet, melted in a graphite crucible positioned in an electrical resistance furnace at 750 °C. 50 wt% of aluminium was added to the base material. The melt was held at this temperature for 15 min to melt billets completely and, after that, stirred mechanically for 5 min. Both materials were mixed uniformly by using a mechanical stirrer. Then the melt was poured into a preheated (400 °C) cylindrical steel casting mould of 50 mm diameter and 220 mm length as shown in Fig. 1. Squeeze the molten metal alloy by applying 20 matric tones of pressure. Solidification of the alloy was carried under applied pressure and then taken out from the die. The entire fabricating system was conducted under the protecting surroundings of natural argon or SF₂ to avoid oxidation.

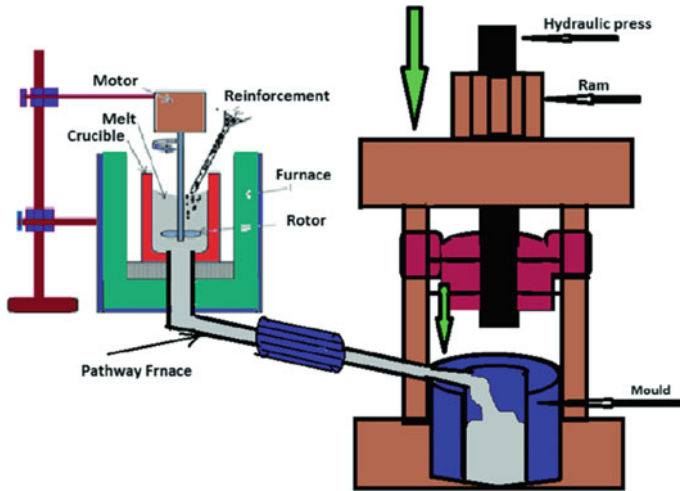


Fig. 1 Stir and squeeze casting machine [13]

The produced composites with a high percentage of aluminium were sectioned to determine their microstructural stress and different phase present with the X-ray diffraction process (Fig. 2).

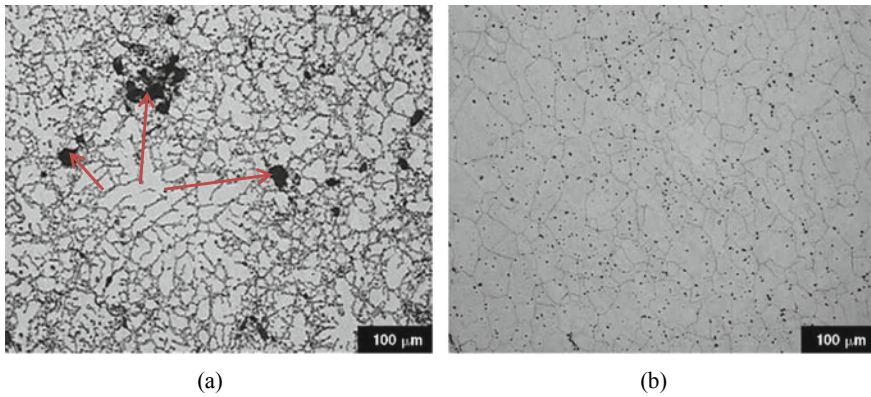


Fig. 2 Optical micrograph showing microstructure in a die cast and b squeeze cast AM50 with a section thickness of 10 mm [14]

2.2 Density and Porosity Evaluation

The sample's theoretical density was measured by dividing the total mass by its volume. The average of four samples was taken as the final theoretical density of the given alloy. The actual density was obtained using the Archimedes principle. The cylindrical shape samples were weighed in the air (W_a) and distilled water (W_w) using a digital weighing machine with 0.01 mg accuracy. The actual density of the sample was measured using Eq. 1 given below.

$$\rho_a = \frac{W_a}{W_a - W_w} \times \rho_w \quad (1)$$

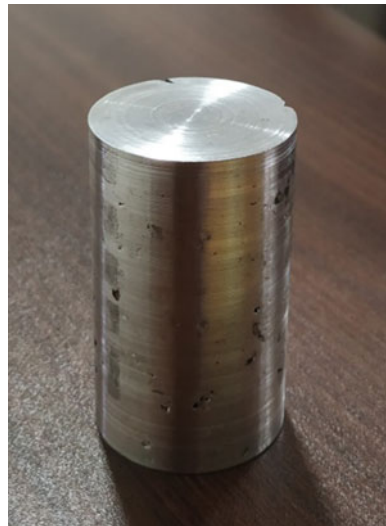
where ρ_a and ρ_w are the actual density of samples and the density of water, respectively.

The porosity was calculated using the sample's theoretical and actual density value in Eq. 2 given below.

$$\text{Porosity \%} = \left[\frac{\rho_t - \rho_a}{\rho_t} \right] \times 100 \quad (2)$$

where ρ_t is the theoretical density of magnesium alloy (Fig. 3).

Fig. 3 Squeeze cast magnesium alloy with high contain of aluminium



2.3 X-Ray Diffraction (XRD)

XRD analysis helps us to recognize microscopic problems together with simple phase identifications, crystallite size measurements and resolution of crystal lattice parameters. To carry out XRD, polished samples with heights five to eight mm had been exposed to copper- $k\alpha$ X-rays ($\lambda = 1.54056 \text{ \AA}$) with scan speed: 2 degree/min and experiment range: 5–90 degrees. From the diffraction patterns, crystalline peaks were identified for the respective stages by way of matching them with standard Mg peaks, Al peaks and associated peaks of intermetallic compounds [15].

3 Results and Discussion

3.1 Phase Composition Analysis

XRD analysis indicates patterns wherein the crystalline peak has different intensities. It was observed that in addition to natural Mg peaks, the β - $\text{Mg}_{17}\text{Al}_{12}$ secondary phase was formed in alloys. The obtained peaks show that the number of peaks of the $\text{Mg}_{17}\text{Al}_{12}$ section improved, corresponding to the Al-content material growth. $\text{Mg}_{17}\text{Al}_{12}$ phase was mostly obtained along the grain boundary and a little bit within the grain. In previous research, it was found that $\text{Mg}_{17}\text{Al}_{12}$ phase is responsible for reducing the ductility of alloy. So, it may be possible due to the high content of the $\text{Mg}_{17}\text{Al}_{12}$ phase, the material becomes more porous and brittle. We will fabricate alloy of the same composition by powder metallurgy process and compare their properties in our further studies.

3.2 Density and Porosity in Magnesium Alloy

The density of alloy with specific percentages of Al shows that squeeze casting's porosity elimination should be attributed in well known to the excessive-applied pressure in the course of solidification and low filling speed for the duration of the mould filling procedure. Figure 2 shows big-sized pores on the alloy's surface, which may be possible due to the entrapment of gases into the die while pouring molten metal into the die. The low filling velocity is to avoid air entrapment, which commonly takes place inside the die casting process because of the turbulent flow of molten metal at a high rate. In Table 1, we can see that the alloy's porosity increases with increasing Al percentage into the alloy. The excessive carried out pressure suppresses gas porosity and reduces the shrinkage porosity by squeezing the semiliquid molten metallic alloy through a robust skeleton network inside the fine porous region of the casting to solidify. So we are able to say 20 matric tone applied pressure is not sufficient to suppress the pores present within the alloy.

Table 1 Density and porosity of different magnesium alloy

S. No.	Alloy	Density		Porosity (%)
		Actual (ρ_a) (gm/cm ³)	Theoretical (ρ_t) (gm/cm ³)	
1	Mg	1.705	1.738	1.89
2	Mg–Al 50 wt%	1.984	2.114	6.15

4 Conclusion

- The alloy's actual density is significantly less than the theoretical density due to the highly porous nature of the alloy. The surface porosity can be controlled by reducing molten metal's turbulence flow into die during the casting process.
- The addition of aluminium above the fusibility level is not suitable for casting. High contains Al increase intermetallic phase Mg₁₇Al₁₂, responsible for increasing brittleness nature in magnesium alloy and reduce mechanical properties.
- In squeeze casting of magnesium alloy, an applied pressure of 20 matric tone is insufficient to surpass gas porosity and reduce shrinkage porosity in semiliquid metallic. So more high pressure is required to minimize casting porosity and refinement of microstructural grains.

References

1. Luo AA (2013) Magnesium casting technology for structural applications. *J Magnes Alloy* 1(1):2–22
2. Kumar D, Phanden RK, Thakur L (2020) A review on environment friendly and lightweight magnesium-based metal matrix composites and alloys. *Mater Today Proc*
3. Kulekci MK (2008) Magnesium and its alloys applications in automotive industry. *Int J Adv Manuf Technol* 39(9–10):851–865
4. Monteiro WA (2014) The influence of alloy element on magnesium for electronic devices applications—a review. *Light Met Alloy Appl* 229–241
5. Kaneko T, Suzuki M (2003) Automotive applications of magnesium alloys. *Mater Sci Forum* 419–422(I):67–72
6. Luo AA (2002) Magnesium: current and potential automotive applications. *Jom* 54(2):42–48
7. Pathak SS, Mendon SK, Blanton MD, Rawlins JW (2012) Magnesium-based sacrificial anode cathodic protection coatings (Mg-Rich primers) for aluminum alloys. *Metals (Basel)* 2(3):353–376
8. Maiti RK, Bidinger FR (1981) Aerospace materials characteristics. *J Chem Inf Model* 53(9):1689–1699
9. Mordike BL, Ebert T (2001) Magnesium properties—applications—potential. *Mater Sci Eng A* 302(1)37–45
10. Bahmani A, Arthanari S, Shin KS (2021) Achieving a high corrosion resistant and high strength magnesium alloy using multi directional forging. *J Alloy Compd* 856:158077
11. Monteiro WA (2014) The influence of alloy element on magnesium for electronic devices applications—a review. *Light Met Alloy Appl*

12. Moosbrugger C (2017) Engineering properties of magnesium alloys. ASM Int M:1–12
13. Verma P, Kumari P, Ghose J, Pandey V (2019) Innovation in materials science and engineering. Springer, Singapore
14. Zhou M, Hu H, Li N, Lo J (2005) Microstructure and tensile properties of squeeze cast magnesium alloy AM50. *J Mater Eng Perform* 14(4):539–545
15. Jayalakshmi S, Singh RA, Mohan S, Sankaranarayanan S, Macheмба V (2021) Microstructure and mechanical properties of magnesium-aluminium (Mg-Al) alloys with high aluminium content (Al = 10, 15, 20 wt. %), vol 59, pp 184–189

Chapter 11

Methods of Protection Against Destruction of Refractory Materials Used for Lining of Autogenous Smelting Furnaces



Sokhibjon T. Matkarimov, Sardor K. Nosirkhujayev,
Abdukahhar M. Saynazarov, Bakhriddin T. Berdiyarov,
and Zaynobiddin T. Matkarimov

Abstract In the article, the technology to protect fire-resistant materials of metallurgical melting furnaces against any destruction is considered. In work, it has offered previously targeting skull, or on a fire-resistant laying in the period of its bookmark to apply a copper grid and a tax on it as a positive charge obtained from an external direct-current power source. Simultaneously, positively charged ions of metals will make a start infusion, and further the complicated silicon-oxygen anion complexes will densely adjoin to a positively charged skull. They will not allow them to collapse due to the abrasive influence of burdening materials.

Keywords Slag · Refractory material · Processing · Pyrite concentrate · Dissociation · Sulphuric iron · Atomic sulfur · Garnish · Coalescence · Conversion to bottom phase · Low-waste technology

1 Introduction

The main problem of modern copper production in the world is the complex processing of slags, recycling of valuable components, and the increase in multiple uses of raw materials. Over time, this problem will increase, as there is a complete depletion of fatty and easily opened ore deposits, which constitutes to an increase

S. T. Matkarimov (✉) · S. K. Nosirkhujayev · B. T. Berdiyarov
Tashkent State Technical University named after Islam Karimov, Tashkent, Uzbekistan

S. K. Nosirkhujayev
e-mail: sardor.nosirxujayev@tdtu.uz

A. M. Saynazarov
JSC “Almalyk MMC”, Amir Temur St., 53, Tashkent Region, Almalyk, Uzbekistan
e-mail: a.saynazarov@agmk.uz

Z. T. Matkarimov
Tashkent Chemical-Technological Institute, Navoiy Street, 32, Tashkent, Uzbekistan

in environmental protection requirements along with an increase in the demand for non-ferrous metals by including copper and related elements [1].

The problem of technological processing solutions of on-site copper production has been one of the most critical issues in heavy metals pyrometallurgy [2].

The construction of a modern metallurgical furnace requires various materials, wherein the most important materials are refractory materials, metals, alloys, and construction materials. A working chamber of furnaces is constructed from refractory materials, in which all high-temperature processes are carried out. In furnaces, refractory materials are under the most severe conditions, i.e., exposed to high temperatures of molten slags, mats, metals, dust, gasses, and various mechanical loads. The refractory's quality and stability depend on the furnace's intensity and productivity and the duration of their continuous operation.

Refractory materials play an essential role in the metallurgical industry in processing raw materials using high temperatures. Without stubbornness, there is no other practical way to limit the spread of heat into the environment and maintain long-term high temperatures in large volumes of different furnaces. The refractory, in this case, is used as high-temperature heat insulators. In some others, on the contrary, the refractory must have a high thermal conductivity. Refractory can be used at high temperatures both as conductors of electric current and as electric insulators.

According to the structural characteristic, the furnaces are divided into lined and commissioned. Autogenously furnaces are generally made in a lined embodiment; Vanyukov furnaces in a questioned version.

However, in the design of I.R. furnaces, there are elements made of refractories (tuyere zone, siphons, etc.). Partial cooling of the fence with embedded caissons (FSF, KIVCET, etc.) is increasingly introduced inlined units.

Evaluation of the quality of metallurgical units according to their reliability is of great importance since it is possible to determine specific types of structures' economic feasibility. To select the optimal kind of production materials systems, predict the unit's elements' life, reasonably plan capital and current repairs, etc.

The ability of refractories to resist the aggressive effects of slags is called slag resistance. The most common "aggression" of slag in autogenous processes is the result of corrosion (chemical interaction of refractory and slag) and erosion (mechanical wear process of lining with flowing slag). Decline facilitates the flushing of the upper slag film from the refractory surface. This refractory-saturated film reacts relatively poorly with it and plays the role of a protective layer. Therefore, without erosion, the slag decomposition process would stop rather quickly. On the other hand, corrosion considerably loosens the refractory, due to which decline is accelerated. Slag resistance of refractory materials is one of the critical indicators determining the metallurgical unit lining's service life.

At present, significant progress has been made in studying the processes and causes of wear and tear in increasing aggregate campaigns' duration, especially in matte conversion. The results of these works are primarily applicable to autogenously smelting units. The technology for the manufacture of chromitoperic-laser heat-resistant refractories has been developed, and their production has been organized.

The service of refractory lining of the reaction shaft of suspended smelting furnaces at the NMMC was relatively well studied. It has been found that the most practical operation of the mine is on a side layer, which forms a layer at a critical lining thickness of 50–60 mm. Another technical solution is to exclude lining and switch to a commissioned version of suspended smelting furnaces' reaction shaft.

Particular attention should be paid to the issues of shotcreting during the repair of units to keep the refractory lining in working condition and, therefore, extend the working campaigns. This activity is widely used in steelmaking but is relatively slow in the practice of non-ferrous metal plants, although some experience is already available.

Embedded cooled elements (caissons) are widely used to increase campaigns' duration and increase the reliability of V.F., FSF, KIVCET furnaces. Without this, it is impossible to further increase the duration of campaigns and increase the units' reliability.

The campaign of pyrometallurgical units, as already noted, is limited by the resistance of structures enclosing working simplicity. Harsh working conditions of walls are created in companies with the bubbled bath of melt. As already noted, the bath's bubbling intensifies heat and mass exchange processes, accompanied by the intensive circulation of the melt and splashing. These phenomena lead to an increase in heat flows to the walls of the chambers and an acceleration of the processes of thermal, hydrodynamic (mechanical), and physicochemical wear [3]. For continuous bubbling processes, it is advisable to use a captioned version of the unit. This design of the team is based on the process of melting in a liquid bath.

The most promising autogenously smelting units are cooled elements obtained from a high-heat pipeline of a high-heat material, with an increased wall thickness on the melt side. Sufficient wall thickness and high thermal conductivity (for example, copper rolled stock) prevent or significantly reduce the possible consequences of short-term deviations from stationary thermal conditions—local heat shocks, ensuring a rapid spread of heat throughout the caisson mass. Some design versions of such caissons developed for the evaporative cooling system are given below.

Particularly noteworthy are structural units in canonized units that include parts without direct, exceptional cooling. Their regular operation (resistance) is ensured due to contact with intensively cooled elements [4]. Such units (copper pressure bars for lining, partition bars, replaceable nozzles of blow tuyeres, etc.) were tested on semi-industrial and industrial P.V. units. As a result of the test, thermal calculation methods of contacting metal bodies have been developed, making it possible to improve the team's similar companies with the bubbled bath of melt [5].

Embedded caissons in the lining of smelting units in the gas phase are mainly made of copper casting, round or square copper pipes. The design of these caissons and corresponding units is given in.

2 Objects and Method of Research

The object of this project's study is refractory materials in which smelting furnaces are built-in metallurgy.

Refractory materials can divide time at temperatures above 1000 °C to maintain mechanical strength and shape. Fire-resistant materials have to meet the following the basic requirements: (1) the high fire resistance—isn't lower than 1580 wasps; (2) sufficient mechanical strength at a temperature above 1000 °C; (3) the ability to tolerate temperature fluctuations; (4) chemical resistance to components of metallurgical processes; (5) constant shape and volume during heating; (6) necessary physical properties—thermal conductivity, porosity, bulk mass, etc.

According to the current GOST, refractory products are divided depending on the degree of stubborn strength into refractory ones that withstand a temperature of 1580–1770 °C, high refractory (above 1770–2000 °C), high persistent strength (above 2000 °C).

In most cases, chemical destruction (corrosion) can be considered as the dissolution of a solid in a liquid. The rate of steady-state dissolution is determined by the difference in the concentration of the solids in the liquid in the saturation state and in the volume of the melt with the thickness of the layer through which molecular diffusion occurs:

$$v = \left(\frac{D}{x} \right) (C_n - C_v), \quad (1)$$

D —diffusion coefficient.

D 's values depend on the viscosity; with a decrease in thickness, D a reductions. Therefore, thickness has the most significant effect on dissolution. It is important to note that according to experimental data, slag interacts with a refractory when the melt viscosity is less than 3.5 Pa s (the maximum, minimum temperature of the slag interaction with the refractory can be determined by this value).

In general, the layer's thickness depends on the nature of the melt and its mixing conditions. For the case of a melt-rotating disk (sample), states are created under which the entire surface of the model is equally accessible in diffusion ratio. For this case, in the course of chemical hydrodynamics, the following equation is given:

$$x = 1.61(D/v)^{-1/3} \sqrt{j/\omega}, \quad (2)$$

where v -kinematic viscosity; w -angular velocity of the sample rotation.

From Eqs. (2) and (3), the Levich equation is obtained

$$v = 0.62 D^{2/3} v^{-1/3} (C_n - C_v) \sqrt{\omega} \quad (3)$$

Or for diffusion dissolution mode

$$v \approx K\omega^{0.5} \tag{4}$$

With the dissolution of cylindrical samples, the conditions of the melt movement are slightly different from the previous case, and the kinetic equation (according to Kinteri) takes the form

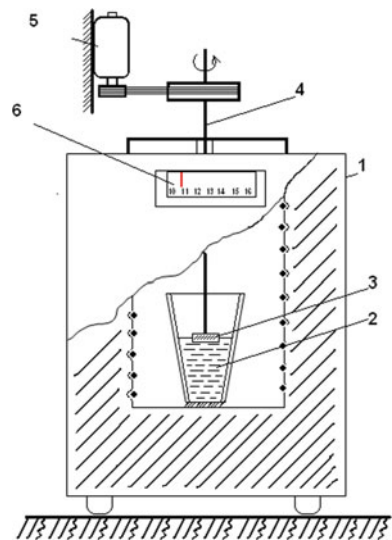
$$v = 0.79 \left(\frac{D}{d} \right) \text{Re}^{0.7} \left(\frac{v}{D} \right)^{-0.64} (C_n - C_v) \tag{5}$$

where is the Reynolds criterion for sample diameter? The dissolution rate, in this case, depends on the degree of 0.7, i.e.,

$$v = K/\omega^{0.7} \tag{6}$$

The determination of the dissolution of the refractory in the slag using the results of Eqs. (4) or (6) in the treatment is as follows. Sample in the form of disk or cylinder is rotated in molten slag at a constant temperature with specified frequency within 64–650 min⁻¹. Optics were carried out at the laboratory installation, which is shown in Fig. 1. From the decrease in sample weight, area, and dissolution time (1–10 min), the dissolution rate, mg/(sm² s), was calculated. Then, a graph is plotted and in coordinates, (mg/(sm² s)) (rad/s) 0.5 for the sample in the form of a disk and the example in the form of a cylinder [6–17]. The graph can result in two types: linear, which is indicative of a diffusion dissolution regime, and nonlinear, which indicates that dissolution is limited by the kinetics of the chemical act itself—such a process is called kinetic.

Fig. 1 Installation for investigating diffusion rate of liquid smelting products into refractory materials and dissolution of refractory materials in metallurgical melts. 1—shaft electric furnace SHSHOL; 2—alund melt crucible; 3—spin sample disk; 4—steel disk shaft; 5—electric motor; 6—automatic adjustment of process temperature in the furnace



3 Results of the Research

The data obtained by the described method are shown in Fig. 1 and are given in Table 1. According to the diffusion nature of the process, the dissolution rate correlates with the melt viscosity. The temperature dependence of the dissolution rate is shown in Fig. 1.

The apparent activation energy for the Al_2O_3 , MgO , and chromium-magnesia spinel is approximately the same and is 180.6 kJ/mol, for SiO_2 64.3 kJ/mol. The diffusion coefficients D approximately according to Eq. (5) at 1400 °C are 2.9×10^{-6} – 3.2×10^{-5} sm^2/s and increase with the transition from Al_2O_3 (2.9×10^{-6}) to MgO (9.3×10^{-6} sm^2/s) and further to SiO_2 (3.2×10^{-5} sm^2/s) (Figs. 2 and 3).

Below are comparative data of solubility of pure substances (less than 0.5% impurities) in open-hearth slag of the following composition, %; CaO —50.7, MgO —7.0,

Table 1 Rate of dissolution of refractory materials in oxide melts $\text{mg}/(\text{sm}^2 \text{ s})$

Molten	Quartz	Corundum	Melted magnesium oxide	Chromomagisial spinel
Iron oxide (Fe^{2+})	40.0	8.5	9.4	4.4
Fayalite	3.8	0.66	1.3	0.32
Tefroit	2.0	0.33	0.7	0.13
Iron-manganese-silicate (50% $2\text{FeO} * \text{SiO}_2$ + 50% $2\text{MnO} * \text{SiO}_2$)	4.3	0.95	2.5	–

Samples are tested at 1400 °C and frequency of rotation 120 min^{-1}

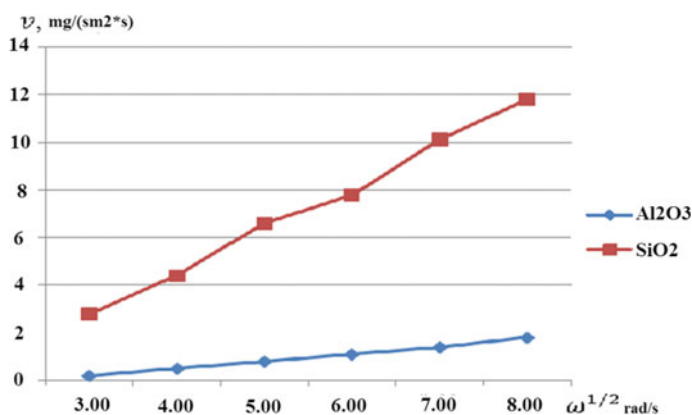


Fig. 2 Influence of frequency of rotation of samples from SiO_2 (1) and Al_2O_3 (2) on the speed of dissolution of oxides fayalite at 1300 °C

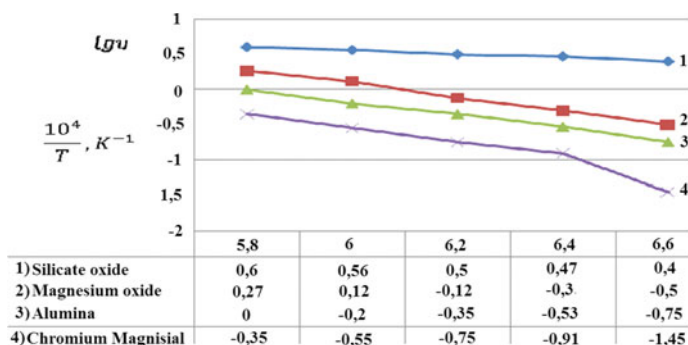


Fig. 3 Effect of temperature T on the dissolution rate of samples from SiO_2 (1), MgO (2), Al_2O_3 (3), and chromium-magnesia (4) in fayalite; sample speed 120 min^{-1}

Table 2 The content of the material dissolved by saturation in 1 g of the starting slag at $1550 \text{ }^\circ\text{C}$

Material	MgO	Al_2O_3	$\text{MgO} \cdot \text{Al}_2\text{O}_3$
Contents (g)	0.006	0.43	0.45
Material	ZrO_2	$3\text{Al}_2\text{O}_3 \cdot 2\text{SiO}_2$	Y_2O_3
Contents (g)	0.27	2.2	1.08

Al_2O_3 —6.0, MnO —6.4, SiO_2 —17.9, $(\text{Fe}_2\text{O}_3 \cdot \text{FeO})$ —12.0. The content of the material dissolved by saturation in 1 g of the starting slag at $1550 \text{ }^\circ\text{C}$ (the slag was melted in a platinum crucible, the sample was immersed in slag and rotated to full saturation) is given in Table 2.

Thus, dissolution rate and the nature of the process at different temperatures are established depending on the hydrodynamic model.

4 Conclusion

It has been found that refractory materials used for the lining of metallurgical furnaces are destroyed by exposure to high temperatures, a sharp change in temperature in the furnace, and direct exposure to slag melt. It was revealed that refractory materials used for lining the sidewalls of melting furnaces in the zone of interaction with melts are destroyed from the influence of slag melt.

To prevent damage to the lining, the walls of the furnaces on the inside are covered with a protective coating (garnish), which can be applied both after major repairs and at the start of the furnace after significant maintenance and is also installed between the walls of water-cooled caissons.

It is determined that refractory materials used for lining metallurgical furnaces are divided into the following types by chemical composition: siliceous, aluminosilicate,

magnesia, chromium. For the lining of metallurgical furnaces from silica bricks, fire-clay bricks from aluminosilicate, dolomite ones from magnesia, chromium magnesite are more often used magnesite-chromite refractory products from chromium.

It has been found that refractory properties such as refractory properties, gas permeability, porosity, mechanical strength, electrical conductivity, heat resistance, which in turn depend on the feedstock for the production of refractory materials and their production technology, affect the resistance of refractory materials against destruction.

The most common mechanism of refractory destruction in interaction with metallurgical melts is installed, which consists of a blowing layer. The slag in contact with the refractory lining enters into chemical business (corrosion), due to which the slag and refractory melt are formed. This melt penetrates the coating foot or includes a thin contact layer on the refractory's working surface. The contact layer washes or drains.

It was found that the interaction of liquid smelting products with refractories is based on the laws of diffusion of liquid material to solid. The rate and depth of impregnation of the liquid into the refractory depend on its porosity.

References

1. Matkarimov ST, Yusupkhodjayev AA, Berdiyarov BT, Qodirjon Ugli Nosirkhujayev S, Matkarimov ZT (2020) Technology of deep processing of copper slags by method of active thermal gravity. *Int J Adv Sci Technol* 29(03):5633–5639
2. The Japan Refractories Association (2019) *J Jpn Refract Assoc* 829:12
3. Kholikulov DB, Matkarimov ST (2021) Materials today: proceedings pilot tests of processing technologies of process solutions of copper production by ozonation. *Mater Today Proc.* <https://doi.org/10.1016/j.matpr.2021.01.419>
4. Guzman IYa (2003) Chemical technology of ceramics. *Build Mater* 496
5. Slovikovsky VV et al (2006) *Non-ferrous metals* 6:34–37
6. Slovikovsky VV, Rozhin YuI (2004) *Non-ferrous metals* 2:14–16
7. Yusupkhodjaev AA, Khojiev ST, Berdiyarov BT, Yavkochiva DO, Ismailov JB (2019) Technology of processing slags of copper production using local secondary technogenic formations. *Int J Innovative Technol Exploring Eng* 9(1):5461–5472. <https://doi.org/10.35940/ijitee.a4851.119119>
8. Khojiev ST, Matkarimov ST, Narkulova ETK, Matkarimov ZT, Yuldasheva NS (2020) The technology for the reduction of metal oxides using waste polyethylene materials. In: *Metal 2020—29th international conference on metallurgy and materials, conference proceedings*, pp 971–978. <https://doi.org/10.37904/metal.2020.3592>
9. The Japan Iron and Steel Federation: *Steel Production by Steelmakers*
10. Rigaud M et al (2006) *Silic Indus* 71(5/6):79
11. Matkarimov ST (2020) Heat treatment processes of steel-smelting slags in the recovery environment. In: Paper presented at the METAL 2020—29th international conference on metallurgy and materials, conference proceedings, pp 105–112. <https://doi.org/10.37904/metal.2020.3439>. Retrieved from www.scopus.com
12. Matkarimov ST, Yavkochiva DO, Berdiyarov BT, Nosirov FD (2020) Hydrometallurgical processing of copper-smelting dust. *Int J Emerg Trends Eng Res* 8(7):3088–3094. <https://doi.org/10.30534/ijeter/2020/35872020>
13. The Japan Refractories Association (2019) *J Jpn Refractories Assoc* 829:26

14. Matkarimov ST, Berdiyarov BT (2020) Development of the wasteless technology of processing of steel-smelting slags. https://doi.org/10.1007/978-3-030-46817-0_35. Retrieved from www.scopus.com
15. Kholikulov DB, Abdurahmonov S, Boltaev ON, Matkarimov ST (2020) Separation of metals from technological solutions copper production. *Int J Emerg Trends Eng Res* 8(7):3557–3561. <https://doi.org/10.30534/ijeter/2020/110872020>
16. Matkarimov ST, Berdiyarov BT, Yusupkhodjayev AA (2019) Technological parameters of the process of producing metallized iron concentrates from poor raw material. *Int J Innovative Technol Exploring Eng* 8(11):600–603. <https://doi.org/10.35940/ijitee.K1586.0881119>
17. Uebo K et al (2019) *Nippon Seitetsu Giho* 413:185

Chapter 12

Nano Biomaterials for Tissue Engineering Applications—Short Review



Sasireka Rajendran, Vinoth Rathinam, Sugumari Vallinayagam,
and Vipin Kumar Sharma

Abstract The nanostructured biomaterials find its importance in the field of tissue engineering especially tissue regeneration and repair. The materials are developed in concordance to work with tissues so that it can promote rejuvenation of affected or damaged tissues. Recently, available nano materials are found to possess several drawbacks which make it incompatible for practical applications. Nanotechnology provides a better platform to create a lot of important novel materials for tissue engineering applications. Predominantly, organic nanomaterials and inorganic nanomaterials are mostly preferred for tissue engineering, since it overcomes limitations that occur in other approaches. This article highlights synthesis and applications of nano biomaterials in hard and soft tissue engineering.

Keywords Nano biomaterials · Tissue engineering · Bone structure

1 Introduction

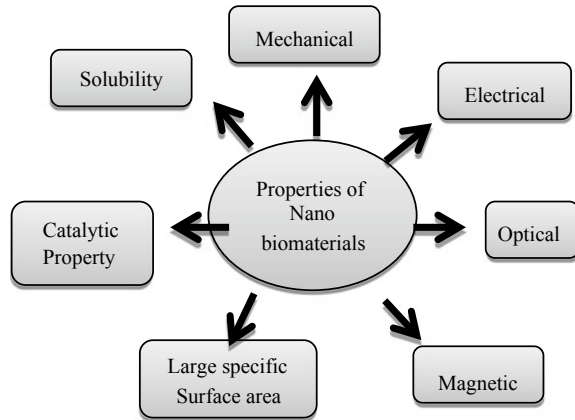
Materials that occur in nanometer size range are classified as nano biomaterials. Nano biomaterials can be of natural or synthetic materials, usually made of different compounds that interact with biological systems. Nano biomaterials possess significant novel features that made them compatible for biomedical applications. The combination of nanotechnology and biomaterials are called as Nano biomaterials and it provides better opportunity to improve diagnosis, preclusion, and the treatment of

S. Rajendran (✉) · S. Vallinayagam
Department of Biotechnology, Mepco Schlenk Engineering College, Sivakasi, Tamilnadu 626005,
India

V. Rathinam
Department of Electronics and Communication Engineering, P.S.R. Engineering College,
Sivakasi, Tamilnadu 626140, India

V. K. Sharma
Department of Biochemistry, Central University of Haryana, Jant Pali, Mahendergarh 123031,
India

Fig. 1 Properties of nanomaterials



diseases. Traditionally, nano biomaterials are considered a special category of biomaterials since their size falls less than 100 nm. They are classified as extraordinary materials since these materials possess unique structures and properties like optical, electrical, and mechanical when compared to bulk traditional materials which have microscopic and macroscopic structures [1]. Nano biomaterials include nanofibers, nanoparticles, nanotubes, nanocomposites, nanocoatings and so on which find its suitable applications in the biological and biomedical field such as Delivery of Drug molecules and genes, Biosensors, Imaging, Medical Implant, Wound healing, Cancer therapy, and in the diagnosis. Polymers, metals, ceramics, and composites are used for the preparation of nanosized or nanostructured biomaterials. Since biomaterials are designed for use in living tissues, biocompatibility and safety clinical considerations are of major concern [2, 3]. Different approaches involved in the construction of nano biomaterials are illustrated in Fig. 1. The core part of nano biomaterial is composed of nano particles and looks spherical in shape. In addition cylindrical and plate like structures are also available. The core region is found to have several layers and is multifunctional.

2 Properties of Nano Biomaterials

The physico-chemical properties of nanomaterials are fully correlated with nanomaterials structure. Atoms retain higher level of percentage which makes the nanomaterial more bulk because of various properties [4]. Depends on the shape nanomaterials exhibit different useful applications in diverse areas. The major challenge in tissue engineering applications is often the mechanical stability and compatibility. In order to overcome these drawbacks often it should be combined with other kinds of materials [5, 6].

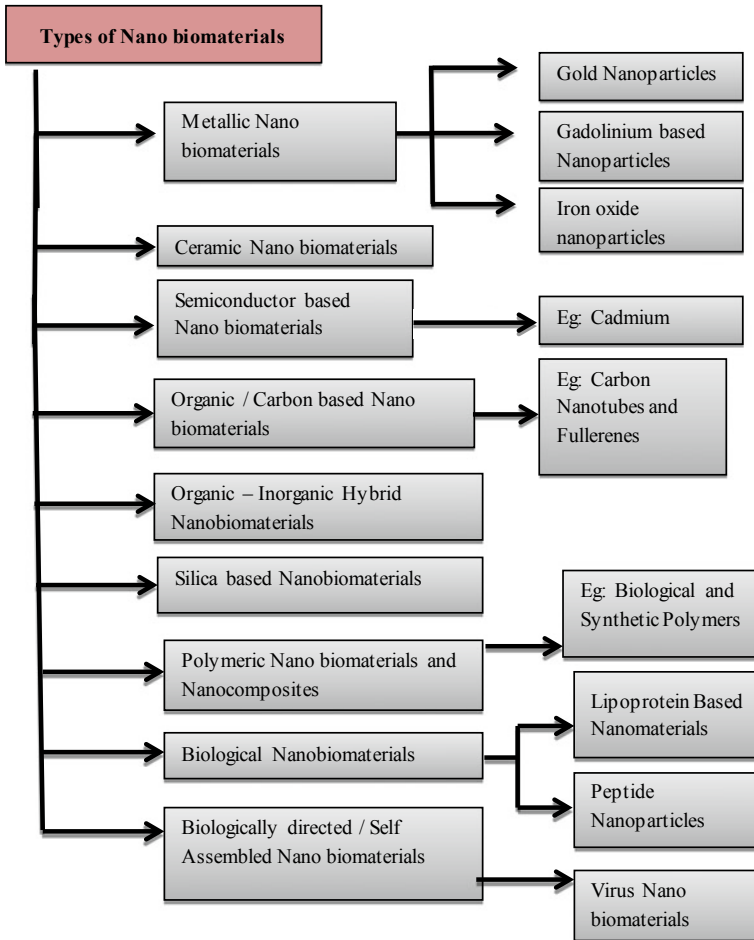


Fig. 2 Types of nanomaterials [7-9]

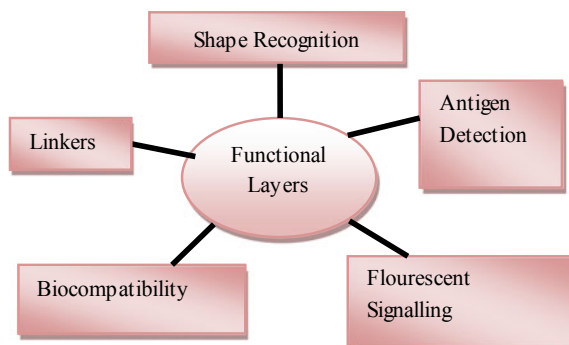
3 Types of Nano Biomaterials

See Fig. 2.

4 Synthesis of Nanomaterials

Nanotechnology is one of the emerging areas in the research field. Mostly it deals with nanotechnology and nano science for the efficient production of nano biomaterials

Fig. 3 Illustration of nano biomaterials construction



of varying compositions structure, different dimensions, and synthesis of nanoparticles of different chemical compositions, dimensions, and regulated mono-dispersity. Presently studies related to the utilization of phytochemicals extracted from the plant parts as capping agents, reducing agents, and stabilizing agents since it finds importance in the development of different types of metal based nanoparticles in conjugation with phytopharmaceuticals. Green synthesis is another approach which involves the use of plants, fungi, bacteria, and algae for nanoparticles synthesis and provides numerous benefits of better environment and in the field of biomedical, it provides biocompatibility since it does not involve toxic chemicals while synthesizing the nanomaterials. The method is economically important and is eco-friendly. In addition parameters like high energy, temperature, high pressure is not followed in the green synthesis of nano materials [10, 11] (Fig. 3).

Physical and Chemical methods of nanoparticle synthesis are followed from the ancient periods, however, green synthesis of nanomaterials is attractive since the process is easier and non-toxic. The technique involves includes utilization of reducing agents for, e.g., Microbes and plant extracts. Highlighting features include ease of availability, stability, cost effectiveness, and preparation methodology when compared to other nanoparticles production with the implication of chemicals and microbes. Few plant extracts like gallnut extract, *Kalopanax pictus* extract, etc. have been evolved for the following nanoparticle synthesis like gold, silver, indium oxide, copper, iron oxide, selenium nanoparticles, palladium, manganese dioxide, etc.

4.1 Silica Nanoparticles

The production of silica nanomaterials with controlled size, morphology, porosity, and its chemical stability enhances silica for different types of nano-technological applications. Efforts made in this field helps in the development of new mesoporous and nanosized particles with varying surface functionalities directed for designing a new material for mimic the organ systems and tissues for alternative organs designing

like 3D printing and model applications. Silica was prepared with polymeric materials to improve the stability of the scaffolds [12, 13].

4.2 Graphene Nanomaterials

Graphene oxide-based Nanoparticles for Tissue Engineering is emerging research in 3D printing. A carbon nanotube composed of rolled graphene sheets and is having wide applications especially targeting sports gear to biomedicine. Graphene oxide-chitosan nanocomposite scaffolds is the most established combinations which have improved mechanical characteristics. High numbers of graphene oxide (GO) can be employed by preferring the oxidative-exfoliation methods. Graphene oxide (GO) is a graphene-like nanosheet normally considered a defective type and for its activation additional treatments are required to bring down to reduced graphene oxide (RGO). Green chemistry emphasizes controlled, less temperature mediated and biocompatibility pathway for synthesis of nanostructured materials of metal oxide, metal, and carbon including graphene. An innovative ternary nanocomposite reduced graphene oxide/hydroxyapatite/silver (rGO/HAP/Ag) was organized by hydrothermal method involving $(\text{NH}_4)_2\text{HPO}_4$, graphene oxide nanosheets, AgNO_3 and $\text{Ca}(\text{NO}_3)_2$, as initiating materials. Electrochemical (EC) approaches have been devised and appropriately used for the synthesis of graphene sheets since it focuses on eco-friendly, cost effectiveness and high efficiency [14–16].

4.3 Silver Nanoparticles

Silver is found to have inhibition against different species which finds its importance in industrial and medical processes. The most important property is that they exhibit larger surface area to volume ratio. So it is widely used as scaffold materials in tissue engineering. When compared to other methods, biological method of nanoparticles synthesis using enzyme, microorganisms and plant extract provide numerous benefits; that can be easily scaled up for large synthesis. El-Rafie et al. 2013 reported that the synthesis methods of silver nanoparticles with the help of water soluble polysaccharides obtained from four marine macroalgae and it was characterized by techniques such as TEM, FTIR analysis, and UV–Vis spectroscopy [17]. Antimicrobial activity efficacy was further analyzed.

4.4 Zinc Nanoparticles

Susan Azizi et al. 2013 analyzed a methodology called one pot technique for the development of Zinc oxide nanoparticles via green process with the help of aqueous

extract of *Sargassum muticum* (Brown marine macroalgae). Data obtained from the FTIR spectra showed that sulfate and hydroxyl of polysaccharide in the macroalgae are involved in the establishment of ZnO nanoparticles. The degree of purity is achieved after calcinations of *S. Muticum* made ZnO at 450 °C.

Analysis using FESEM suggests that ZnO nanoparticles in pre form ranged in size from 30 to 57 nm [18]. Diallo et al., 2015 reported development of ZnO NPs using green approach by means of *Aspalathus linearis*'s natural extract which is considered an effective oxido-reductive agent. Optical property and structural analysis by X-rays photoemission spectroscopy, X-ray diffraction, electron microscopy, Raman, and room temperature photoluminescence are described [19].

4.5 Applications of Nano Biomaterials for Tissue Engineering

Materials like ceramics, metals, and polymers could be employed for 3D printing technology. Advantages include production of 3D tissues complex form, low wastes, mass production, and scaffolds with the capability to be utilized by the cells. So, 3D printing is a promising technique in field of tissue engineering. 3D scaffolds can be efficiently generated with the help of promising method so called 3D printing. The produced scaffolds display good mechanical properties, good cellular behavior, and porosity. The 3D printing process involves pre-processing, processing, and post-processing. In the initial stage of pre-processing, the structure, images, and details acquired from the site specific tissue are transported to the CAD system and analyzed before being printed for the construction of target tissue. At processing level, new tissues are developed by considering factors by a 3D printer. In post-processing stage, tissue was optimized and prepared for use in the human body. 3D printing uses various approaches for fabricating scaffolds [20]. Nano biomaterials are currently used in both hard and soft tissue engineering. Implementation of various materials and cells in diverse layers mimics 3D structures. Scaffolds enhance the renewal of skin and stimulate dermal vascularization. Scaffold made of Gelatin-sulfonated silk composite with fibroblast growth factor 2 is a favorable approach for skin tissue engineering. 3D printing is preferred for fabrication of scaffolds for bone tissue engineering. Materials made of ceramic play a crucial role in bone tissue engineering. Different types of applications are illustrated in Fig. 4. Table 1 explains some methods and materials, which were used in the previous research for the synthesis the artificial organs.

Nano biomaterials in field of soft category of tissue engineering are classified as shown in Fig. 5.

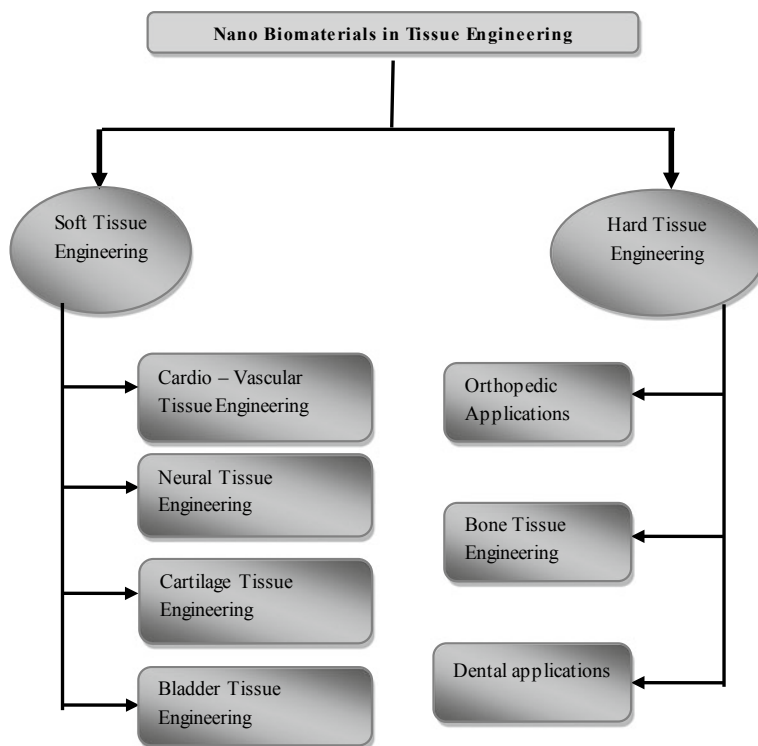


Fig. 4 Different types of applications

Table 1 Methods and materials to design the tissues

Method	Tissue	Scaffolds materials
UV-integrated 3D bioprinting method	Endothelial cells (coronary artery)	Carbon nanotubes, collagen (methacrylated), and alginates
3D printing methodology using novel cryogenic	Mesenchymal stem cells	PLA (poly-lactic acid)/calcium phosphate nanoparticles
3D printing technique	Neuroblastoma cells derived from humans	Carbon nanotubes/nanocellulose
3D printing methods	Human bone tissue	Nano-hydroxyapatite and collagen

4.6 Nano Biomaterials for Hard Tissue Engineering

Implications of nano biomaterials in the field of hard tissue engineering are shown in Fig. 6.

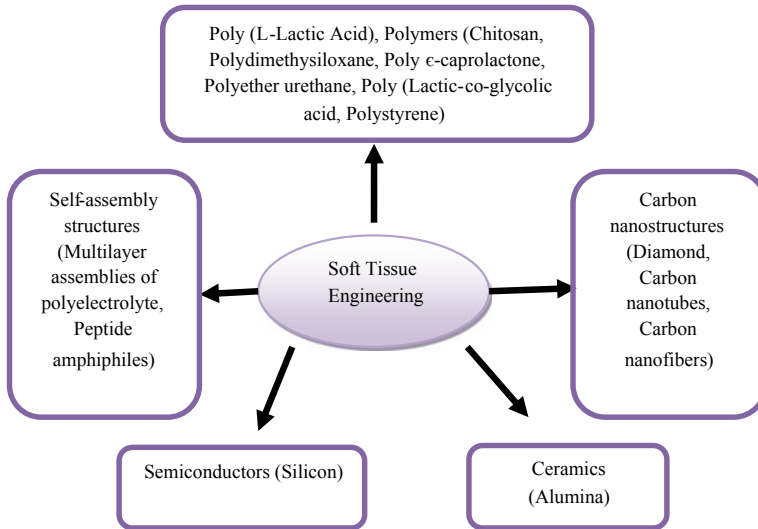


Fig. 5 Various types of materials for soft tissue engineering

5 Conclusion

Overview of different types of organic and inorganic nano biomaterials and their synthesis are outlined in this review article. Specifically, the importance of nano biomaterials in the field of tissue engineering is focused since it is an emerging field. It makes the researchers develop new concepts to improve the existing strategies. Because of its biocompatibility, non-toxic nature nano biomaterials are preferred widely to bring new innovations. Nano biomaterials in different forms make the researchers develop innovative ideas in the field of tissue engineering.

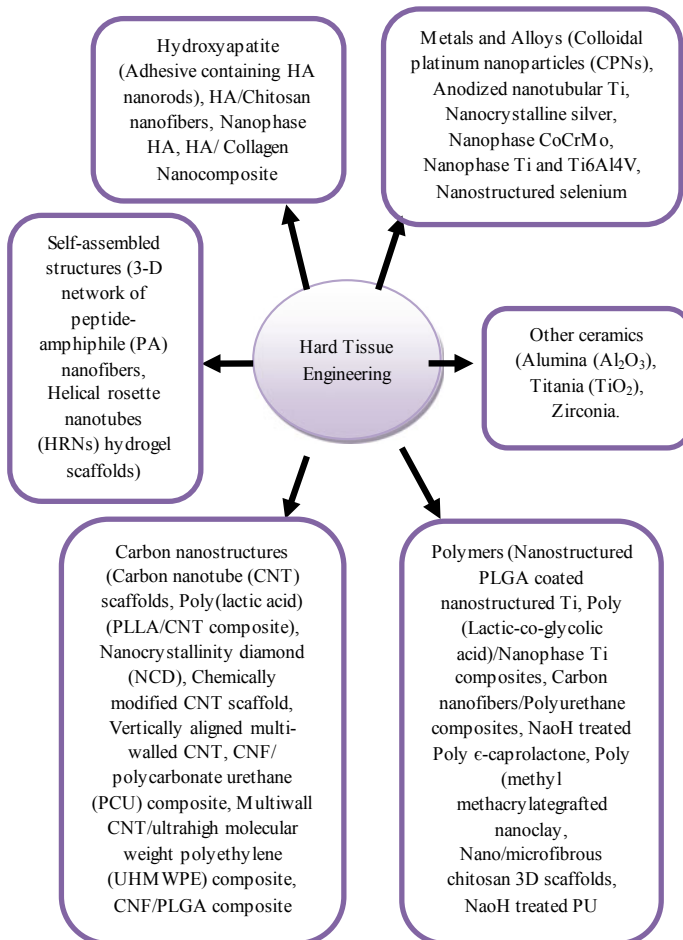


Fig. 6 Various types of materials for hard tissue engineering

References

1. Jandt KD, Watts DC (2020) Nanotechnology in dentistry: present and future perspectives on dental nanomaterials. *Dental Materials*
2. Eivazzadeh-Keihan R et al (2020) Recent advances in the application of mesoporous silica-based nanomaterials for bone tissue engineering. *Mater Sci Eng C* 107:110267
3. Cui L et al (2020) Nanomaterials for angiogenesis in skin tissue engineering. *Tissue Eng Part B Rev* 26(3):203–216
4. Saleem H, Zaidi SJ (2020) Sustainable use of nanomaterials in textiles and their environmental impact. *Materials* 13(22):5134
5. Zhou S et al (2020) Molecule editable 3D printed polymer-derived ceramics. *Coord Chem Rev* 422:213486
6. Alksne M et al (2020) In vitro comparison of 3D printed polylactic acid/hydroxyapatite and polylactic acid/bioglass composite scaffolds: insights into materials for bone regeneration. *J*

- Mech Behav Biomed Mater 104:103641
7. Goenka S, Sant V, Sant S (2014) Graphene-based nanomaterials for drug delivery and tissue engineering. *J Control Release* 173:75–88
 8. Nalwa HS (2014) A special issue on reviews in biomedical applications of nanomaterials, tissue engineering, stem cells, bioimaging, and toxicity. *J Biomed Nanotechnol* 10(10):2421–2423
 9. Eivazzadeh-Keihan R et al (2019) Carbon based nanomaterials for tissue engineering of bone: building new bone on small black scaffolds: a review. *J Adv Res* 18:185–201
 10. Gaharwar A et al (2013) *Nanomaterials in tissue engineering: fabrication and applications*. Elsevier
 11. Saracino GA et al (2013) Nanomaterials design and tests for neural tissue engineering. *Chem Soc Rev* 42(1):225–262
 12. Li K et al (2015) Composite mesoporous silica nanoparticle/chitosan nanofibers for bone tissue engineering. *RSC Adv* 5(23):17541–17549
 13. Rosenholm JM et al (2016) Mesoporous silica nanoparticles in tissue engineering—a perspective. *Nanomedicine* 11(4):391–402
 14. Bei HP et al (2019) Graphene-based nanocomposites for neural tissue engineering. *Molecules* 24(4):658
 15. Xie X et al (2015) Graphene and hydroxyapatite self-assemble into homogeneous, free standing nanocomposite hydrogels for bone tissue engineering. *Nanoscale* 7(17):7992–8002
 16. Shamekhi MA et al (2019) Graphene oxide containing chitosan scaffolds for cartilage tissue engineering. *Int J Biol Macromol* 127:396–405
 17. El-Rafie H, El-Rafie M, Zahran M (2013) Green synthesis of silver nanoparticles using polysaccharides extracted from marine macro algae. *Carbohydr Polym* 96(2):403–410
 18. Azizi S et al (2013) Preparation, characterization, and antimicrobial activities of ZnO nanoparticles/cellulose nanocrystal nanocomposites. *BioResources* 8(2):1841–1851
 19. Diallo A et al (2015) Green synthesis of Co₃O₄ nanoparticles via *Aspalathus linearis*: physical properties. *Green Chem Lett Rev* 8(3–4):30–36
 20. Di Marzio N et al (2020) Bio-fabrication: convergence of 3D bioprinting and nano-biomaterials in tissue engineering and regenerative medicine. *Front Bioeng Biotechnol*

Chapter 13

Static Deformation of an Orthotropic Multilayered Elastic Half Space by Two-Dimensional Surface Loads



Jatinder Kaur, Pankaj Thakur, and Namrata Singh

Abstract In the present study, the investigation of the effect of surface loads on the static deformation of multilayered orthotropic horizontal elastic slab has been done. The layers are assumed to be in welded contact. The plain strain problem of normal strip loading has been discussed. The objective of this paper is to study effect of surface loads on static deformation of an orthotropic multilayered horizontal slab by using matrices method. Process of layered matrices is used at any point of medium to obtain the displacements and stresses. Effect of uniform half space deformation and isotropic half space has been discussed numerically.

Keywords Static deformation · Orthotropic · Surface load · Elastic · Stresses · Displacement

1 Introduction

In 1985, the analysis of static deformation by 2D surface loads of an isotropic multilayered half space was done by Garg and his co-workers [1]. However, later in the year 1987, surface load behaviour of a transversely isotropic multi-layered half space was performed [2].

In 2011, Ben-Dor et al. [3] analyzed the problem of optimization of multilayered metallic shield, where the determination of the sequencing of the material was the motive behind study along with the thickness of the layers that provide maximum ballistic limit velocity of the shield. Bache and Harkrider, 1976 [4] assumed Earth as layered structure and system of body waves has been framed as a result of seismic source. Under vertical loading, Ai et al. [5] have analysed the transient-response of transversely isotropic multilayered elastic half space, in 2017. The author also extended this work under the effect of moving loads in three-dimensional dynamic

J. Kaur (✉) · N. Singh
Department of Mathematics, Chandigarh University, Mohali, India

P. Thakur
Department of Mathematics, Faculty of Science and Technology, ICFAI University Baddi, Solan, India

responses of transversely isotropic materials. Zhang et al. [6] analysed the behaviour of multilayered transversely isotropic medium due to axisymmetric loads in 2015. Recently, Vashishth et al., in 2020, investigate the two-dimensional quasi-static deformation of multilayered thermo elastic medium under surface load and temperature source [7]. In the present study, the analysis of the effect of surface loads on the static deformation of multilayered orthotropic horizontal elastic slab has been done. The layers are assumed to be in welded contact. To obtain the relations for stresses and displacements at any point of the medium, layered matrices method is used.

2 Formulation of the Problem

An elastic slab consisting of $(n - 1)$ parallel orthotropic homogeneous half space is selected for study. The origin of the coordinate system is considered at the upper boundary of the elastic slab, and x -axis is taken vertically downward into the medium. We assume that the layers are in welded contact [7]. We presume the thickness of m th layer as d_m and is bounded by the interface $z = z_{m-1}, z_m$ $d_m = z_m - z_{m-1}$, $z_0 = 0$, $z_{n-1} = H$, the thickness of the slab. We further assumed the welded contact of the slab with the elastic half space. Due to loads acting on the bounding surface ($z = 0$), the static deformation of the medium will be determined.

2.1 Solution of the Problem

The basic governing equations of equilibrium for zero body force are [1]:

$$\frac{\partial T_{11}}{\partial x_1} + \frac{\partial T_{21}}{\partial x_2} + \frac{\partial T_{31}}{\partial x_3} = 0 \quad (1)$$

$$\frac{\partial T_{12}}{\partial x_1} + \frac{\partial T_{22}}{\partial x_2} + \frac{\partial T_{32}}{\partial x_3} = 0 \quad (2)$$

$$\frac{\partial T_{13}}{\partial x_1} + \frac{\partial T_{23}}{\partial x_2} + \frac{\partial T_{33}}{\partial x_3} = 0 \quad (3)$$

where T_{ij} is the symmetric stress tensor. Let (u_1, u_2, u_3) be the displacement vector. The strain–displacement relation [8] are

$$e_{ij} = \frac{1}{2}(u_{i,j} + u_{j,i}) \quad (4)$$

The stress–strain relations for the orthotropic elastic medium are

$$\begin{bmatrix} T_{11} \\ T_{22} \\ T_{33} \\ T_{23} \\ T_{13} \\ T_{12} \end{bmatrix} = \begin{bmatrix} \alpha_{11} & \alpha_{12} & \alpha_{13} & 0 & 0 & 0 \\ \alpha_{21} & \alpha_{22} & \alpha_{23} & 0 & 0 & 0 \\ \alpha_{31} & \alpha_{32} & \alpha_{33} & 0 & 0 & 0 \\ 0 & 0 & 0 & \alpha_{44} & 0 & 0 \\ 0 & 0 & 0 & 0 & \alpha_{55} & 0 \\ 0 & 0 & 0 & 0 & 0 & \alpha_{66} \end{bmatrix} \begin{bmatrix} e_{11} \\ e_{22} \\ e_{33} \\ 2e_{23} \\ 2e_{13} \\ 2e_{12} \end{bmatrix} \quad (5)$$

in which there are nine independent elastic constants.

When the medium is isotropic [8]

$$\begin{aligned} \alpha_{11} &= \alpha_{22} = \alpha_{33} = \lambda + 2\mu \\ \alpha_{12} &= \alpha_{13} = \alpha_{23} = \lambda, \alpha_{44} + \alpha_{55} + \alpha_{66} = \mu \end{aligned} \quad (6)$$

2.2 Plane Strain Problem

We consider 2D problem in which the deformation is independent of one coordinate x_1 , so that [2]

$$\begin{aligned} \frac{\partial}{\partial x_1} &= 0 \quad \text{and} \\ u_1 &= 0, \quad u_2 = u_2(x_2, x_3), \quad u_3 = u_3(x_2, x_3) \end{aligned} \quad (7)$$

are the displacement components.

In case of plane strain problem, the non-zero values of strain [2] are:

$$e_{22} = \frac{\partial v}{\partial y}, \quad e_{33} = \frac{\partial w}{\partial z}, \quad 2e_{23} = \left(\frac{\partial v}{\partial z} + \frac{\partial w}{\partial y} \right) \quad (8)$$

and non-zero relation of stresses are

$$\begin{aligned} T_{11} &= \alpha_{11}e_{22} + \alpha_{13}e_{33} \\ T_{22} &= \alpha_{22}e_{22} + \alpha_{23}e_{33} \\ T_{33} &= \alpha_{23}e_{22} + \alpha_{33}e_{33} \\ T_{23} &= 2\alpha_{44}e_{23} \end{aligned} \quad (9)$$

The equilibrium equations for the plane strain problem reduce to

$$\frac{\partial T_{22}}{\partial y} + \frac{\partial T_{23}}{\partial z} = 0, \quad \frac{\partial T_{23}}{\partial y} + \frac{\partial T_{33}}{\partial z} = 0 \quad (10)$$

and the first equilibrium equation is identically zero. Let $U(y, z)$ be the Airy stress function satisfying the relations

$$T_{22} = \frac{\partial^2 U}{\partial z^2}, \quad T_{33} = \frac{\partial^2 U}{\partial y^2}, \quad T_{23} = -\frac{\partial^2 U}{\partial z \partial y} \quad (11)$$

Using these relations, we find that equilibrium equations in (10) are identically satisfied.

In plane strain problem, the equation

$$2 \frac{\partial^2 e_{23}}{\partial y \partial z} = \frac{\partial^2 e_{22}}{\partial z^2} + \frac{\partial^2 e_{33}}{\partial y^2} \quad (12)$$

as the only non-zero compatibility condition [9], other remaining five conditions are identically satisfied. Putting the values of e_{22} , e_{33} , e_{23} of in term of stresses T_{22} , T_{33} , T_{23} and for Airy's stress function, [2], i.e. U

$$\left(\alpha^2 \frac{\partial^2}{\partial y^2} + \frac{\partial^2}{\partial z^2} \right) \left(\beta^2 \frac{\partial^2}{\partial y^2} + \frac{\partial^2}{\partial z^2} \right) U = 0 \quad (13)$$

where constants α , β are given by

$$\alpha^2 + \beta^2 = \frac{\alpha_{22}\alpha_{33} - \alpha_{23}^2 - 2\alpha_{32}\alpha_{44}}{\alpha_{33}\alpha_{44}} \quad (14)$$

$$\alpha^2 \beta^2 = \frac{\alpha_{22}}{\alpha_{33}}$$

As a special case, when the medium is isotropic, $\alpha = \beta = 1$ and the Airy stress function satisfies the biharmonic equation

$$\left(\frac{\partial^2}{\partial y^2} + \frac{\partial^2}{\partial z^2} \right)^2 U = 0 \quad (15)$$

We can make use of the Fourier transformation to solve the partial differential equation.

The Fourier transforms [1] $\bar{U}(k, z)$ of $U(y, z)$ defined as

$$\bar{U}(k, z) = \int_{-\infty}^{\infty} U(y, z) e^{iky} dy \quad (15a)$$

So that

$$U(y, z) = \frac{1}{2\pi} \int_{-\infty}^{\infty} \bar{U}(k, z) e^{iky} dy \quad (15b)$$

Fourier transform of partial differential equation (1) gives

$$\left(\frac{\partial^2}{\partial z^2} k^2 \alpha^2 \right) \left(\frac{\partial^2}{\partial z^2} k^2 \beta^2 \right) U = 0 \quad (15c)$$

We assume that $\alpha > 0$, $\beta > 0$ and $\alpha \neq \beta$. A solution of ordinary differential equation (15c) is

$$\bar{U} = [C e^{-\alpha|k|z} + D e^{\alpha|k|z} + E e^{-\beta|k|z} + F e^{\beta|k|z}] \quad (16)$$

And, therefore, the Airy stress function in the integral form is as given below:

$$U(y, z) = \frac{1}{2\pi} \int_{-\infty}^{\infty} [C e^{-\alpha|k|z} + D e^{\alpha|k|z} + E e^{-\beta|k|z} + F e^{\beta|k|z}] e^{-iky} dk \quad (17)$$

where the coefficients C, D, E, F can only depend on k .

From Eqs. (9) and (17), we find the values of the stresses in terms of integral as:

$$T_{23} = \frac{-i}{2\pi} \int_{-\infty}^{\infty} S(z) e^{-iky} (k|k|) dk \quad (18a)$$

$$T_{33} = \frac{-i}{2\pi} \int_{-\infty}^{\infty} N(z) e^{-iky} (k^2) dk \quad (18b)$$

where

$$S(z) = C \alpha e^{-\theta} - D \alpha e^{\theta} + E \beta e^{-\phi} - F \beta e^{\phi} \quad (19a)$$

$$N(z) = C \alpha e^{-\theta} + D \alpha e^{\theta} + E \beta e^{-\phi} + F \beta e^{\phi} \quad (19b)$$

And

$$\theta = \alpha|k|z, \quad \phi = \beta|k|z \quad (20)$$

Also, we find

$$T_{22} = \frac{1}{2\pi} \int_{-\infty}^{\infty} [C\alpha^2 e^{-\theta} + D\alpha^2 e^{\theta} + E\beta^2 e^{-\phi} + F\beta^2 e^{-\phi}] e^{-iky} k^2 dk \quad (20a)$$

To express displacements v and w in terms of integrals, we follow as given below: From Eqs. (6) and (7)

$$T_{22} = \alpha_{22} \left(\frac{\partial v}{\partial y} \right) + \alpha_{23} \left(\frac{\partial w}{\partial z} \right) \quad (21a)$$

$$T_{33} = \alpha_{23} \left(\frac{\partial v}{\partial y} \right) + \alpha_{33} \left(\frac{\partial w}{\partial z} \right) \quad (21b)$$

$$T_{23} = \alpha_{44} \left(\frac{\partial v}{\partial z} + \frac{\partial w}{\partial y} \right) \quad (22)$$

Solving these equations, we get

$$\frac{\partial v}{\partial y} = \Delta^{-1} [\alpha_{33} T_{22} - \alpha_{23} T_{33}] \quad (23a)$$

$$\frac{\partial w}{\partial z} = \Delta^{-1} [\alpha_{22} T_{33} - \alpha_{23} T_{22}] \quad (23b)$$

where

$$\Delta = \alpha_{22}\alpha_{33} - \alpha_{23}^2 \quad (24)$$

Integrating (23a), (23b) we find

$$v = \Delta^{-1} \int (\alpha_{33} T_{22} - \alpha_{23} T_{33}) dy + F(z) \quad (25a)$$

$$w = \Delta^{-1} \int (\alpha_{22} T_{33} - \alpha_{23} T_{22}) dz + G(y) \quad (25b)$$

F and G are arbitrary functions.

Equations (18a), (18b), (20a), (22), and (25a), (25b) show that

$$F'(z) + G'(y) = 0$$

And therefore, functions F and G represent a rigid body displacement and can thus be neglected in the analysis of deformation. Taking $F = G = 0$ in Eqs. (25a), (25b) and using (18a), (18b) and (20a); we find that

$$v = \frac{i}{2\pi} \int_{-\infty}^{\infty} V(z) e^{-iky} (k) dk \quad (26a)$$

$$w = \frac{i}{2\pi} \int_{-\infty}^{\infty} W(z) e^{-iky} (|k|) dk \quad (26b)$$

where

$$V(z) = [Cq_1 e^{-\theta} + Dq_1 e^{\theta} + Eq_2 e^{-\phi} + Fq_2 e^{-\phi}] \quad (27a)$$

$$W(z) = [Cr_1 e^{-\theta} - Dr_1 e^{\theta} + Er_2 e^{-\phi} - Fr_2 e^{-\phi}] \quad (27b)$$

where

$$q_1 = \frac{\alpha_{33}\alpha^2 + \alpha_{23}}{\alpha_{33}\alpha_{22} - \alpha_{23}^2}, \quad q_2 = \frac{\alpha_{33}\beta^2 + \alpha_{23}}{\alpha_{33}\alpha_{22} - \alpha_{23}^2} \quad (28a)$$

$$r_1 = \frac{\alpha_{23}\alpha^2 + \alpha_{22}}{\alpha(\alpha_{33}\alpha_{22} - \alpha_{23}^2)}, \quad r_2 = \frac{\alpha_{23}\beta^2 + \alpha_{22}}{\beta(\alpha_{33}\alpha_{22} - \alpha_{23}^2)} \quad (28b)$$

Four equations in (19a), (19b) and (27a), (27b) can be put together in the following matrix equation

$$[Y(z)] = [Z(z)][K] \quad (29)$$

This matrix notation gives a systematic computational procedure which avoids mathematical expressions and facilitates the computational test. We use the transfer matrix approach to solve the problem of multilayered media. This approach is also called Thompson-Haskell matrix method. With this matrix technique, the deformation inside a multilayered elastic medium becomes known when the surface deformation is given. The subscript m is specified for terms related to the m th layer of the elastic medium. Then, Eq. (29) becomes

$$[Y_m(z)] = [Z_m(z)][K_m] \quad (30)$$

Then at the boundaries of this layer, we have $[Y_{m-1}(Z_{m-1})] = [Z_m(Z_{m-1})][K_m]$, using the continuity condition at the interface $z = z_{m-1}$, $[Y_m(z_m)] = [Z_m(z_m)][K_m]$.

Eliminating the matrix $[K_m]$; we get

$$[Y_{m-1}(z_{m-1})] = [a_m][Y(m)(z_m)] \quad (31)$$

$$[a_m] = [Z_m(z_{m-1})][Z_m(z_m)]^{-1} \quad (32)$$

is called layer matrix.

Thus

$$[Y(0)] = [M][K_n] \quad (33)$$

For the half space i.e. layer n , we must have $D_n = F_n = 0$.

So that

$$[K_n] = [C_n, 0, E_n, 0]^T \quad (34)$$

From Eqs. (33) and (34), we write

$$V(0) = M_{11}C_n + M_{13}E_n \quad (35a)$$

$$W(0) = M_{21}C_n + M_{23}E_n \quad (35b)$$

$$S(0) = M_{31}C_n + M_{33}E_n \quad (36a)$$

$$N(0) = M_{41}C_n + M_{43}E_n \quad (36b)$$

When the surface load is given, then $S(0), N(0)$ are known quantities and consequently, the coefficient C_n, E_n be obtained from Eqs. (36a), (36b).

3 Uniform Half Space Deformation

Considering if the semi-infinite medium is a half space without any layer lying over it.

Here, $n = 1$ and

$$[M] = [Z(0)], [N] = [Z(z)] \quad (37)$$

The integrals giving the stresses T_{23}, T_{33} evaluated analytically using the standard integrals given by Grandshteyn and Ryzhik [9]. The other stresses can be obtained by using the stress-displacement relationships and then using the regular integrals to obtain closed-form expressions.

3.1 *Isotropic Half Space*

We know that for an isotropic medium $\alpha = \beta = 1$, the results for the stresses in an isotropic half space as a result of normal strip loading can be obtained as a particular case by taking the limit $\beta \rightarrow \alpha$ and then putting $\alpha = 1$.

4 Conclusion

The layers are assumed to be in welded contact. The plain strain problem of normal strip loading is discussed. Processes of layered matrices are used at any point of the medium to obtain the displacements and stresses. The procedure established is appropriate for numerical computations.

References

1. Garg NR, Singh SJ (1985) Residual response of a multilayered half-space to two-dimensional surface loads. *Bull Indian Soc Earthq Tech* 22:39–52
2. Garg NR, Singh SJ (1987) 2-D static response of a transversely isotropic multilayered half-space to surface loads. *Indian J Pure Appl Math* 18:763–777
3. Ben-Dor G, Dubinsky A, Elperin T (2011) Optimization of multi-layered metallic shield. *Nucl Eng Des* 241(6):2020–2025
4. Bache TC, Harkrider DG (1976) The body waves due to a general seismic source in a layered earth model, I formulation of the theory. *Bull Seismol Soc Am* 66(6):1805–1819
5. Ai ZY, Liu CL, Wang LH (2017) Transient response of a transversely isotropic multi-layered half-space due to vertical loading. *J Appl Math Model* 50:414–431
6. Zhang P, Lin G, Liu J, Wang W (2016) Response of multilayered transversely isotropic medium due to axisymmetric loads. *Int J Numer Anal Meth Geomech* 40:827–864
7. Vashishth AK, Rani K, Singh K (2020) Two dimensional deformation of a multilayered thermoelastic half-space due to surface loads and heat source. *Int J Appl Mech Eng* 25(1):177–197
8. Biot MA (1954) Theory of stress-strain relations in anisotropic viscoelasticity and relaxation phenomena. *J Appl Phys* 25(11):1385–1391
9. Gradshteyn IS, Ryzhik IM (1980) *Tables of integrals, series and products*. Academic press, New York

Chapter 14

Comparative Study and Analysis of HVAC Systems Using Solid and Liquid Desiccant Dehumidification Technology



Abhijith Shah, Himank Santosh Sankhe, Yogesh Koushal Sharma,
Sayli Sankhe, and R. V. Kale

Abstract This paper reviews and surveys desiccant technology, which can be used in the optimization of the HVAC system for high indoor air quality. Also, it compares the electricity consumption of both the technologies. Additionally, it aims to demonstrate the capabilities of modern high-performance desiccants and to enhance the cooling efficiency of the system and to provide comfortable airspace for occupants in humid climates, and simultaneously reducing the electricity requirement. Liquid desiccant system and solid desiccant wheels are used for dehumidification and optimization of the HVAC system. Using dehumidification techniques, latent cooling offers significant energy savings, as well as good indoor air quality as the number of pollutants, are removed directly by co-adsorption. In humid climates, the desiccant system can prevent microbial growth which is essential nowadays. Thus, desiccant dehumidification is a suitable technology for advanced humidity control and can provide benefits over conventional cooling-based dehumidification.

Keywords HVAC optimization · Solid desiccant · Adsorption · Dehumidification · LDAC · Desiccant wheel

1 Introduction

Heating, ventilation, and air conditioning (HVAC) systems control the indoor environment throughout the year to ensure human comfort. In the twenty-first century, air conditioning is no more a luxury; however, it has become a need in numerous nations. HVAC is to improve the quality of life for billions of people in a rapidly developing world, and we face many potential problems. The source of the majority of these problems is the air conditioner's heavy reliance on electricity. Indoor air quality is another challenge to the HVAC industry, especially in humid climates like

A. Shah (✉)

B/705, Suprabhat Housing Society, Bhandup West, Mumbai 400078, India

H. S. Sankhe · Y. K. Sharma · S. Sankhe · R. V. Kale

Rajiv Gandhi Institute of Technology, Andheri (W), Mumbai 400053, India

Mumbai. In humid climates, the increased ventilation can raise indoor humidity to levels that are uncomfortable as well as unhealthy.

HVAC is used in various industries. Businesses consume the largest proportion of energy in a commercial building, and electricity consumption can typically account for 40% of total building consumption and approximately 70% of base building electricity consumption [1]. Hence, energy efficiency plays a very important role in the HVAC industry. An energy-efficient system reduces energy consumption which results in improved reliability of the system, reduced maintenance costs, and enhanced occupant comfort. Optimization of the system in a cost-effective way to improve the efficiency and overall performance of the HVAC system is the main objective of the research paper. Conventional AC has fundamental limitations in humidity control. Mechanical AC allows coincidental drying when it lowers air below its dew-point temperature, condensing water vapor on its cooling coils. To give separate control over temperature and humidity, it must cool the air. But this is excessively energy-intensive. A large amount of electrical energy is consumed by conventional air conditioning systems, especially in climatic conditions having high humidity, hot weather, and high latent load. Desiccant dehumidifier-based air-conditioning system is one of the promising alternatives to overcome the high latent load efficiently as in this system sensible and latent heats of air are removed separately [2]. For optimization, two methods are proposed which use liquid and solid desiccant, respectively. Desiccant wheels are promising alternatives to handle high latent heat load and also among the current technologies for improving indoor thermal comfort and air quality. Liquid desiccant air conditioning (LDAC) has emerged as an attractive option in terms of humidity control and energy consumption [3, 4]. Furthermore, the liquid desiccant system can provide high indoor quality air as liquid desiccants can filter the bacteria, microbial contaminations, and viruses [5].

Significant energy is consumed for apartment/building cooling, heating, and dehumidification. Thus, increasing energy efficiency is essential to reduce greenhouse emissions and global energy usage. Several efforts are made on the development of HVAC and the application of various sustainable and low energy technologies for promoting building energy efficiency [6].

1.1 Need for Dehumidification

We live in surrounding where humidity is present in air in different proportion, and it varies with different geographical location. This humidity when crosses a limit can cause various problems. In many cases, moisture is undesirable and can hamper the functioning of electrical and mechanical devices. Many electrical relays are threatened by pitting and corrosion due to high content of moisture. It results in failure of internal electrical circuits, and in utmost cases, there may be permanent damage to electrical equipment. There is loss in efficiency and a high maintenance cost when the electronic equipment is exposed to humid condition. Equipment life and proper function depends upon factor like work environment and humidity control.

Also, excessive humidity can cause bacterial growth which may lead to infectious diseases and cause various health problems. It is always essential that HVAC system has low energy consumption and high efficiency. Hence, humidity control has become necessity.

1.2 Methodology

Basics of Desiccant Technology:

A desiccant is a substance having a strong affinity toward water vapor. They are classified as solid and liquid as per their physical state. Both types of desiccant are widely used in industrial applications in which the air with a low dew point is needed. The strength of a desiccant is measured by its equilibrium vapor pressure. This equilibrium vapor pressure increases exponentially with the increase in temperature of the desiccant also it increases as the desiccant adsorbs more and more water. Desiccants are hygroscopic substances which are used as dry agents [7].

Humidity control is necessary for comfort as well as maintaining the temperature and air quality. Hence, using desiccants, the dehumidification process can be achieved easily and reduces the latent heat load on the system, resulting in less consumption of electricity. Generally centralized and decentralized HVAC systems are effective at handling the space's sensible cooling and heating loads. However, they are unable at handling ventilation air or latent heat loads as mentioned in the ASHRAE handbook [8, 9].

2 Use of Liquid Desiccant Air Conditioners

Despite the fact that LDAC is less experienced than vapor-compression technology, air conditioners based on liquid desiccants are more promising alternatives. As the LDAC runs generally on heat, electric demand is typically one-fourth of that of a vapor-compression air conditioner. The LDAC is exceptionally efficient at dehumidifying air; therefore, almost all of the cooling it provides can be latent cooling. LDAC offers enhanced humidity control with significant energy savings in applications where latent loads (moisture) are very high relative to sensible loads [4, 6].

Figure 1 represents the basic operation of liquid desiccant in which the conditioner and the regenerator are porous, working like adiabatic beds deluged by desiccant. When process air is passed through bed, it is cooled and dried by desiccant. A stream of desiccant is continuously recirculated between conditioner and regenerator. For re-concentration of liquid desiccant, thermal energy is used.

LDAC simultaneously regulates the humidity and temperature of air by removing moisture using a liquid desiccant. The total latent load of the processed air is controlled by the absorption rate of moisture into the liquid desiccant. The liquid

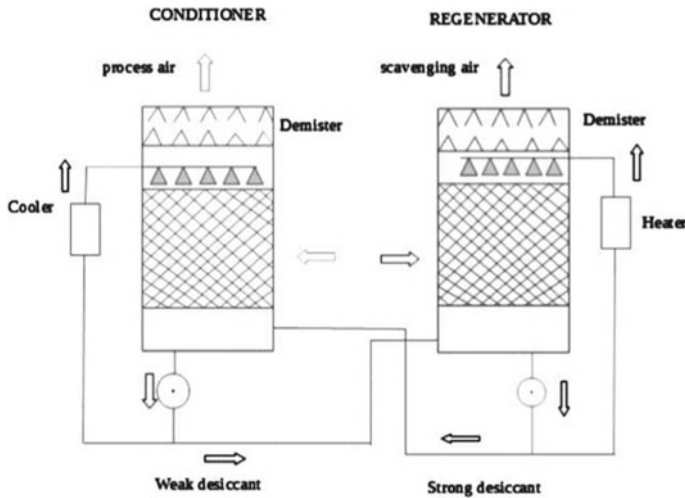


Fig. 1 Operation of liquid desiccant system [10]

desiccant solution can then be regenerated by removing excess water. Thermal evaporation is used as desalination process. In thermal evaporation, heat is the primary energy input in the LDAC. Waste heat (i.e., heat recovered from engines) is readily available. Therefore, electricity consumption by LDAC is only one-fourth of that of a vapor-compression air conditioning system for the same cooling output [11]. Hence, LDAC can be more energy-efficient compared to conventional air conditioning methods which are based on vapor-compression technology [11, 12].

A liquid desiccant enhances heat transfer by a mechanism that is the inverse of evaporative cooling. At the point when wind flows over a surface wetted by water, evaporation from the film of water will bring down the temperature of the water–air interface and wet-bulb temperature of the air. This wet-bulb temperature is a function of the air’s initial temperature as well as humidity. A line of constant enthalpy that passes through the state point of air intersects the saturation line on a psychrometric chart approximately at the wet-bulb temperature [13]. When air flows over a surface that is wetted with a desiccant, the desiccant either absorbs or desorbs water, depending on whether the desiccant’s equilibrium relative humidity is above or below the air’s relative humidity [14].

There is an increase in demand for proper dehumidification in HVAC. The widespread use of liquid desiccant systems in buildings, either as stand-alone dehumidification or integrated into AC systems, has been mitigated by the perceived high complexity of maintenance and operational challenges. The potential significant energy savings which liquid desiccant systems offer have generally not been perceived because of higher operational complexities in HVAC systems. A wider application would include specialized industrial buildings such as hospitals, where precise humidity control is important, also more generalized use of dehumidification systems in commercial or residential buildings.

The separation of humidity and temperature control in buildings under the premise of changing thermal loads can be achieved using a liquid desiccant. Historically, AC systems were installed to provide desired thermal conditions; humidity control was of a lower priority and occurring through passing humid air over cold coils. This infers that latent load removal becomes more important regarding control and efficient dehumidification [15, 16].

2.1 Performance Metrics of Dehumidifiers

The performance of dehumidifiers is described by parameters stated below.

2.1.1 Moisture Removal Rate (MRR)

Moisture removal rate is the metric accounted for the removal of the latent heat load of the process air, where da_{in} and da_{out} are the air humidity ratio if the inflowing and outflowing process air.

$$\Delta da = da_{in} - da_{out}$$

2.1.2 Dehumidification Efficiency (ϵ_{de})

Dehumidification efficiency describes the efficiency of dehumidifier which we are using. ϵ_{de} as the dimensionless humidity ratio that describes how the dehumidification process approaches the assumed optimum one, where da_{equ} is the humidity of air that is in vapor pressure equilibrium along with the vapor surface pressure of the inlet desiccant solution.

$$\epsilon_{de} = (da_{in} - da_{out}) / (da_{in} - da_{equ})$$

2.1.3 Air to Solution Mass Ratio (MR)

Air to solution mass ratio is a dimensionless parameter for optimization of dehumidification, where m_a and m_s are mass flow rates (kg/s) of the process air flow and desiccant solution, respectively.

$$MR = m_a / m_s$$

Extreme mass flow ratios can affect the dehumidification process as follows.

- (1) Too small flow rate of the desiccant solution can lead to an uneven spread of desiccant solution over the packing layer.
- (2) Too high mass flow rate will cause small concentration difference between inlet and outlet desiccant solution. This renders regeneration of the weak solution more difficult and requires more energy for pumping larger quantities of desiccant solution. Hence, by using liquid desiccant, we can save significant electricity used for latent cooling. Some experiments carried out using liquid desiccant technology, and the results of those experiments are listed below.

3 Desiccant Wheel

A desiccant wheel is analogous to a thermal wheel, except the layer applied for purpose of dehumidifying or drying the air stream. “The desiccant normally coated is silica gel” [17]. As the name implies “Gel,” it is not a “Gel,” but a porous granular form of silica made from sodium silicate. Two types of silica gel are available in the market, “Indicating” type and “Non-Indicating” type. Standard silica gel is generally of Non-Indicating type, since it absorbs moisture and remains physically unchanged. Non-Indicating type silica gel is both cost-effective and efficient [18, 19].

The desiccant wheel can be defined as a dehumidification wheel or rotary dehumidifier. As supporting material, the matrix material is used to create the channel walls. The matrix materials used are paper, synthetic fiber, aluminum, or plastic. The matrix material is then layered with desiccant materials which are known as adsorbents. Several adsorbents are utilized for fabricating desiccant wheels including silica gel, activated alumina, lithium chloride, synthetic polymers, and natural and synthetic zeolites [20, 21].

3.1 Operating Principle of a Desiccant Wheel

Figure 2 shows the desiccant wheel dehumidifier consisting of two primary air streams, process stream, and reactivation stream. The incoming humid process air passes through a dehumidifier (desiccant wheel) area. It is made up of silica gel that is capable of adsorbing water molecules which results in the dehumidification of the moisture present in the air after it traverses the rotor.

Then along a “regenerating” zone, the moist air is dried using desiccant and dry air is ejected. The desiccant wheel rotates continuously, and the adsorbent process is recurrent. Around 75% of the desiccant wheel is exposed to incoming process air. At the time of regeneration, the desiccant is heated by a direct-fired gas burner or indirect-fired water [17, 23] resulting in the dehumidification of the moisture present in the air after it traverses the rotor.

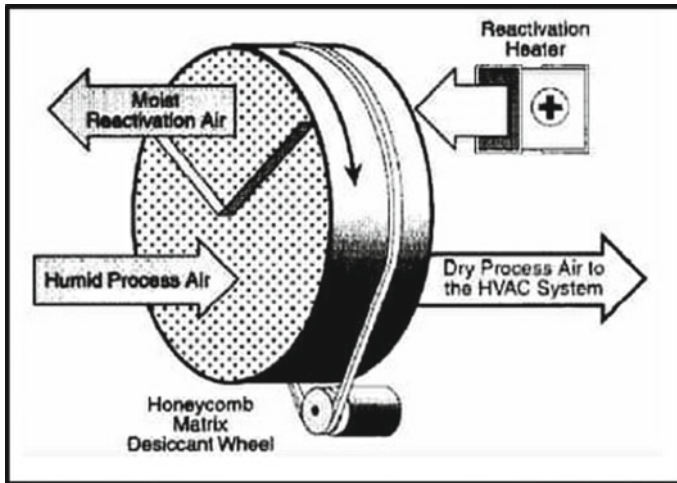


Fig. 2 Schematic diagram of a solid desiccant dehumidifier [22]

There are different types of solid desiccants such as silica gel, lithium chloride [LiCl], and molecular solid desiccant [13]. Solid desiccants are usually inside a wheel or other means, which allows the desiccant material to be in contact with two different air streams. The humid process air crosses the rotary wheel, and the moist content in the air is engrossed by the desiccant, which leaves the air in drier state, but comparatively hotter. The sensible temperatures can be maintained by use of another heat exchange, evaporative cooler, or cooling coils. The wheel rotates so as to use the desiccant repeatedly. The hot air absorbs the moist content from the desiccant material present inside the wheel. The cycle is repeated by the desiccant material absorbing and releasing the moisture content with process air and regenerated air.

Pennington introduced process commercially although it was invented in 1933 by miller and Fonda. But it was introduced in 1935 by Hausen and was developed by other such as shipman in 1936, Fliesher in 1939, larriver in 1941 and 1944, but none of them were close to come up with a commercial product to reduce the energy for AC Pennington patented what was called “the ventilation cycle” by utilizing a solid silica inside the rotating wheel [19].

The solid desiccant system can be used in open cycle or closed cycle configuration. The position of the rotating wheel determines the performance of the cycle with respect to the cooling coil. During dehumidification process which takes places in the upstream of air, a high-capacity cooling coil is needed than compared to lower or downstream of cooling coil.

3.2 *Desiccants Materials*

A desiccant material that can absorb significant amount of water vapor and can also absorb easily at low regeneration temperature is required for the desiccant air conditioning [DAC] system [24].

There are many ways in which desiccant can be classified, e.g., solid or liquid desiccant, physisorption or chemisorption desiccants, natural or artificial desiccant, bio or rock-based desiccant, composite and polymer-based desiccant, etc. The bond strength is reflected between adsorbate and adsorbent by the term physisorption or chemisorption.

Physisorption is a process of removal of water vapor from the air because of low coalition strength between adsorbent and adsorbate. The bond strength in DAC system is kept optimal for efficient regeneration process. Now desiccant including composite material is also developed which gives better result as compared to conventional desiccant silica gel [25, 26].

3.3 *Methodology*

3.3.1 **Moisture Removal**

Moisture removal by desiccant dehumidification is dependent on several parameters; one of those parameters is “surface area” of the desiccant that is revealed to the incoming process air stream. More the surface area per cubic foot of rotor volume, the more the adsorption enhances. “The surface area multiplied by the internal pore surface area results in thousands of square feet of area of desiccant obtained for the adsorption process” [27]. The high proportion of surface area to volume is one of the crucial grounds for the better accomplishment of the desiccant dehumidifier. The rotor speed is also enhanced such that the overheating is precluded in the desiccant. Thus, the adsorption cycle is cautiously well-adjusted against the desorption cycle.

3.3.2 **Adsorption**

The process of adsorption occurs when the attractive forces of a desiccant capture the water vapor. It adheres to the surface of desiccant. The water vapor is then drawn into macropores and then to micropores by capillary action. In this process, the moisture converts adiabatically from water vapor to a quasi-liquid and is stored within desiccant. The desiccant which does not undertake a phase change during the adsorption process, i.e., silica gel is used for dehumidification [17].

3.3.3 Process Inlet

Air that has to be dehydrated/dehumidified, i.e., outdoor air, indoor air, or combination of air with high humidity present.

3.3.4 Process Outlet

“Air is dried by the desiccant wheel, and the relative humidity is substantially low and temperature slightly raised” [28].

3.3.5 Reactivation Inlet

Air supply, usually outdoor air that removes dampness off the wheel. Reactivation air is warmed up by the direct-fired gas burner or indirect-fired water or steam.

3.3.6 Reactivation Outlet

Through the heat exchanger the warm, wet air from the wheel is drained outside. Using the heat exchanger to preheat incoming process, air is beneficial as it offers considerable saving in the northern climate.

3.3.7 Dehumidification

Dehumidification of air can be achieved by two methods: (1) Cooling the air below its dew point and removing the moisture by condensation. (2) Sorption by the desiccant material [29, 30]. In this case, it is the process of removing the moisture from the process air through a desiccant wheel unit when the air passes through a desiccant wheel. The micro-granules of the silica gel adsorb moisture and give dry air. The dry air is then fed to the heat exchanger which cools this dry air [17] (Fig. 3).

3.4 Working

The complete solid dehumidifier wheel unit consists of two zones, i.e., cooling zone and regeneration zone. By using blower, the outside process air is drawn and is fed to the desiccant wheel where all the moisture present in that process air is absorbed by the silica gel desiccant wheel. Now, the dry air is fed into the evaporative cooler where there is a drop in temperature due to change in the sensible heat, and then this cooled air is fed into the room [18, 31].

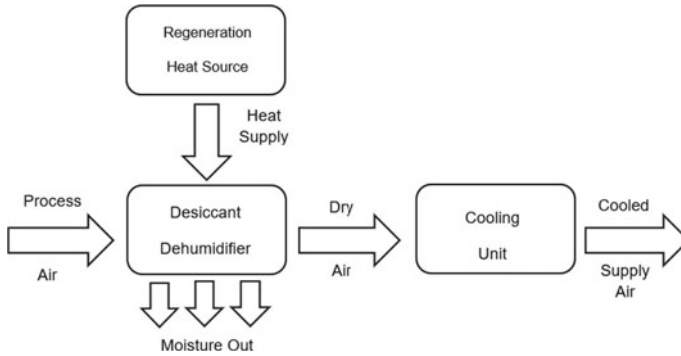
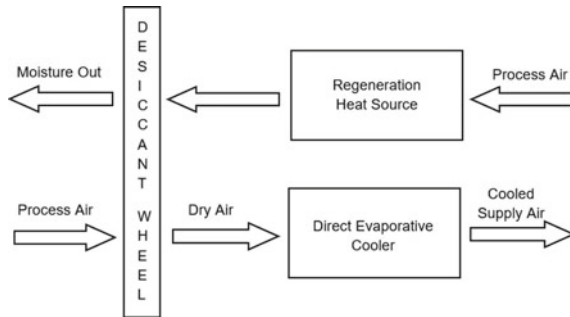


Fig. 3 Block diagram of energy transfer process [17]

Fig. 4 Block diagram of the complete dehumidifier system [18]



The desiccant dehumidifier wheel continuously rotates at a speed of 10–20 RPH [18], and the moisture locked in the desiccant material is passed into the regeneration zone when the temperature is maintained at 55–75 °C with the help of the heating source viz and direct-fired gas burner or indirect-fired water or steam. That part of the desiccant wheel gets regenerated due to the removal of moisture present. This moisture is expelled out of the room by the duct, and the cycle is repeated [32] (Fig. 4).

3.5 Analytical Method/Performance Assessment of Desiccant Wheel and the Estimated Drying Process

For evaluating performance assessment of desiccant wheel system, two phases are taken into consideration, i.e.,

3.5.1 Process of Regeneration

The regeneration process is the process in which drying of silica gel desiccant that has been used during the dehumidification process takes place [33].

3.5.2 Dehumidification

Dehumidification process involves adsorption of moisture from the incoming process air so that the air will become drier, and thus, the temperature is increased [34].

4 Nomenclature

T_1 —Dry bulb temperature of air into dehumidification process/process air inlet temperature ($^{\circ}\text{C}$).

T_2 —Dry bulb temperature of air out from dehumidification process/process air outlet temperature ($^{\circ}\text{C}$).

T_3 —Dry bulb temperature of air into regeneration process/Reactivation Inlet Temp ($^{\circ}\text{C}$).

T_4 —Dry bulb temperature of air out from regeneration process/Reactivation Outlet Temp ($^{\circ}\text{C}$).

$E_{\text{reg.se}}$ —Regeneration sensible effectiveness.

$E_{\text{reg.lt}}$ —Regeneration latent effectiveness.

$E_{\text{dh.se}}$ —Dehumidification sensible effectiveness.

$E_{\text{dh.lt}}$ —Dehumidification latent effectiveness.

m_{reg} —Mass air flow rate for dehumidification process (kg dryair/h).

m_{min} —Minimum value of either mass flow rate (kg dryair/h).

h_1 —Absolute humidity of air into dehumidification process (g/m^3).

h_2 —Absolute humidity of air out from dehumidification process (g/m^3).

h_3 —Absolute humidity of air into regeneration process (g/m^3).

h_4 —Absolute humidity of air out from regeneration process (g/m^3).

h_{in} —Absolute humidity of air entering the drying chamber (%) (g/m^3).

h_{out} —Absolute humidity of air leaving the drying chamber (%) (g/m^3).

h_{as} —Absolute humidity of air entering the dryer at the point of adiabatic saturation (%) (g/m^3).

S —Dry matter content (%).

t —Drying time (s).

V —Volumetric airflow rate (m^3/s).

W —Weight of the water evaporated from the product (kg).

W_{AC} —Water absorption capacity.

ρ —Density of air (kg/m^3).

η_{hc} —Heat collection efficiency.

η_p —Pick up efficiency.

η_s —Drying system efficiency.

G_a —Dry air mass flow rate (kg dryair/h).

5 Dehumidification Process

Equations for dehumidification process are as follows

$$E_{dh,se} = m_{dh}/m_{min} = (T_1 - T_2)/(T_1 - T_3) \quad (1)$$

$$E_{dh,lt} = m_{dh}/m_{min} = (h_1 - h_2)/(h_1 - h_2) \quad (2)$$

From Eqs. (1) and (2), the temperatures and absolute humidity of air, which has passed the humidification process, can be calculated as:

$$T_2 = \{(m_{min}/m_{dh}) \times E_{dh,se} \times (T_3 - T_1)\} + T_1 \quad (3)$$

and

$$h_2 = \{(m_{min}/m_{dh}) \times E_{dh,lt} \times (h_3 - h_1)\} + h_1 \quad (4)$$

6 Regeneration Process

Equations for regeneration process are as follows.

Sensible/Thermal Effectiveness

$$E_{\text{reg.se}} = (m_{\text{reg}}/m_{\text{min}}) \times (T_4 - T_3)/(T_1 - T_3) \quad (5)$$

Latent Effectiveness

$$E_{\text{reg.lt}} = (m_{\text{dh}}/m_{\text{min}}) \times (h_4 - h_3)/(h_1 - h_3) \quad (6)$$

From Eqs. (5) and (6), the temperature and absolute humidity of air that has passed through the process of regeneration are as follows:

$$T_4 = \{(m_{\text{min}}/m_{\text{dh}}) \times E_{\text{reg.se}} \times (T_1 - T_3)\} + T_3 \quad (7)$$

$$h_4 = \{(m_{\text{min}}/m_{\text{dh}}) \times E_{\text{reg.lt}} \times (h_1 - h_3)\} + h_3 \quad (8)$$

Adiabatic efficiency can be calculated by the following equation,

$$E_{\text{adiabatic}} = 1 - (h_2 - h_1)/h_1 = (2h_1 - h_2)/h_1 \quad (9)$$

7 Drying Analysis

In this analysis, drying time will be calculated theoretically with the assumption of ideal drying process. Basically, this analysis will show reduction in water content in the dried material using pickup efficiency [11].

$$\eta_p = \frac{h_{\text{out}} - h_{\text{in}}}{h_{\text{as}} - h_{\text{in}}} = \frac{W}{\rho V t (h_{\text{as}} - h_{\text{in}})} \quad (10)$$

If $W = m_o - m_t$ then,

$$\eta_p = \frac{m_o - m_t}{\rho V t (h_{\text{as}} - h_{\text{in}})} \quad (11)$$

$$m_t = m_o - \rho V t (h_{\text{as}} - h_{\text{in}}) \eta_p \quad (12)$$

$$G_a = \frac{m \cdot C_p}{h_{\text{in}} + 1} = \frac{V}{h_{\text{in}} + 1} \quad (13)$$

Moisture removal rate (g/s)

$$m_w = m_a \times (h_1 - h_2) = \rho V A (h_1 - h_2)$$

where

ρ = density of air (kg/m^3)

V = Processed air velocity (m/s)

A = Cross sectional area of pipe

8 Conclusion

We have done comparative analysis of HVAC with the help of liquid as well as solid desiccants from various research. The analysis shows that using desiccant technology provides desiccant dehumidification, cooling and advanced humidity control has more benefits over the conventional cooling-based dehumidification. In less amount of work, the dehumidification can be carried out which is necessary for good indoor air quality. Thus, from the above, it can be concluded that humidity control should be given priority in modern HVAC systems. Also, liquid desiccant saves more energy than solid desiccant wheels, and LDAC has less electricity usage than the solid desiccant wheels. However, all the liquid desiccants we use today are of corrosive nature, and overall, it is more expensive and non-convenient as compared to that of solid desiccant wheels. The optimization of the HVAC system can be done by using desiccant technology. Compared to conventional air conditioning, cooling efficiencies can be improved. The indoor air quality, recipient comfort, and moisture removing capacity can be improved substantially, and the electricity demand can be reduced significantly.

The reviews on solid and liquid desiccant in drying application and its regeneration methods were carried out, and it can be concluded that:

1. Desiccant system in drying application has several advantages including continuous drying even during off-sunshine hours, due to hot and dry air, increased drying rate, more uniform drying, and increased product quality especially for heat-sensitive products.
2. The use of renewable energy like solar energy or waste heat from industrial processes for regeneration of desiccant material will make the system run at low operating cost.
3. The development of non-corrosive and low surface tension desiccant: Advance research and discovery of non-corrosive desiccant to improve the efficiency of the system. Currently, desiccants used in LDAC are nontoxic but corrosive, the development of non-corrosive desiccants is required for the larger acceptance of LDAC. The uniform wetting is required for high working efficiency. The current desiccants have a high surface tension which complicates the uniform wetting; hence, the desiccants should be developed which is non-corrosive and have low surface tension.
4. Development of hybrid energy: Use of a hybrid energy system which can be a combination of desiccant air conditioning as well as other renewable sources

such as solar energy, wind energy which curtails the pollution as well as mitigates the electricity consumption.

5. Development of desiccants to prevent spreading of airborne viruses: Desiccant technology can be used in automobiles as well as various closed spaces to prevent microbial growth. By developing desiccants that can cleanse the contaminated air, the spreading of many airborne viruses can be reduced.

References

1. Lecamwasam L, Wilson J, Chokolich D (2012) Guide to best practice maintenance & operation of HVAC systems for energy efficiency. Dept Clim Change Energy Effi 36
2. Subramanyam N, Maiya MP, Srinivasa S, Murthy (2004) Application of desiccant wheel to control humidity in air-conditioning systems. *Appl Thermal Eng* 24:2777–2788 (Elsevier)
3. Mei L, Dai YJ (2008) A technical review on use of liquid-desiccant dehumidification for air-conditioning application. *Renew Sustain Energy Rev* 12:662–689 (Elsevier)
4. Rafique MM, Gandhidasan P, Bahaidarah HMS (2016) Liquid desiccant materials and dehumidifiers: a review. *Renew Sustain Energy Rev* 56:179–185 (Elsevier)
5. Rafique MM, Gandhidasan P, Bahaidarah HMS (2016) Liquid desiccant materials and dehumidifiers: a review. *Renew Sustain Energy Rev* 56:186–195 (Elsevier)
6. Guo Y, Ma Z, Al-Jubainawi A, Cooper P, Nghiem LD (2016) Using electro dialysis for the regeneration of aqueous lithium chloride solution in liquid desiccant air conditioning systems. *Energy Build* 116:285–295 (Elsevier)
7. Collier RK (1989) Desiccant properties and their effect on cooling system performance. *ASHRAE Trans* 95(1)
8. ASHRAE (1992) Desiccant cooling and dehumidification special publication. American Society of Heating, Refrigerating, and Air Conditioning Engineers
9. ASHRAE (2009) ASHRAE handbook—fundamentals. American Society of Heating, Refrigerating and Air-Conditioning Engineers
10. Lowenstein A, Slayzak S, Kozubal E (2006) A zero-carryover liquid desiccant air conditioner for solar applications. National Renewable Energy Sources, ASME International Solar Energy Conference
11. Cheng Q, Zhang X (2013) Review of solar regeneration methods for liquid desiccant air-conditioning system. *Energy Build* 67:426–433 (Elsevier)
12. Lowenstein A (2009) Review of liquid desiccant technology for HVAC applications. *HVAC&R Res* 14(6):819–839
13. Davanagere BS, Sherif SA, Goswami DY (1991) A feasibility study of a solar desiccant air conditioning system—part I: psychometrics and analysis of the conditioned zone. *Int J Energy Res* 23:7–21
14. Duong HC, Hai FI, Al-Jubainawi AH, Ma Z, He T, Nghiem LD (2017) Liquid desiccant lithium chloride regeneration by membrane distillation for air conditioning. *Sep Purif Technol J* 177:121–128 (Elsevier)
15. Oberg V, Goswami DY (1998) Experimental study of the heat and mass transfer in a packed bed liquid desiccant dehumidifier. *J Sol Energy Eng* 120(4):289–297
16. Harriman III LG, Plager D, Kosar D (1997) Dehumidification and cooling loads from ventilation air. *ASHRAE J* 37–45
17. Tiwari EA (2005) Design and fabrication of desiccant wheel dehumidifier. *Int J Adv Res Mech Eng Technol* 1(1)
18. Patel R, Patel S, Patel P, Kandoliya P (2017) Dehumidification process by the desiccant wheel in air-conditioning, vol 4, no 3

19. Munters C (2015) Desiccant wheels. Report accessed via <https://www.munters.com/globalassets/pdf-files/muntersdesiccantwheels.pdf>
20. De Antonellis S, Joppolo CM, Molinaroli L (2010) Simulation, performance analysis and optimization of desiccant wheels. *Energy Build* 42:1386–1393 (Elsevier)
21. Nia FE, Van Paassen D, Saidi MH (2006) Modeling and simulation of the desiccant wheel for air conditioning. *Energy Build* 38:1230–1239 (Elsevier)
22. Hasan Ali M, Mizanur Rahman ANM, Hossain NUI, Islam KS (2010) Conference: international conference on mechanical, industrial and energy engineering, pp 23–24
23. Slayzak S, Pesaran J, Hancock AA (1996) Experimental evaluation of commercial desiccant dehumidifier wheels. In: Conference: international absorption heat pump conference
24. La D, Dai YJ, Li Y, Wang RZ, Ge TS (2010) Technical development of rotary desiccant dehumidification and air conditioning: a review. *Renew Sustain Energy Rev* 14:130–147 (Elsevier)
25. Jia CX, Dai YJ, Wu JY, Wang RZ (2006) Experimental comparison of two honeycombed desiccant wheels fabricated with silica gel and composite desiccant material. *Energy Convers Manage* 47:2523–2534 (Elsevier)
26. Shimooka S, Yamazaki M, Takewaki T, Akashige E, Ikehata F, Kakiuchi H (2006) Development of hydrophilic active carbon for high performance adsorption heat pump, vol 32, pp 528–534
27. Giordano MC, Tzschoppe M, Barelli M, Vogt J, Huck C, Canepa F, Pucci A, Buatier de Mongeot F (2020) Self-organized nanorod arrays for large-area surface-enhanced infrared absorption. *ACS Appl Mater Interfaces* 12(9):11155–11162
28. Masoud WAB, Bucklin RA, Porter WA, Zhao X, Lane PW, Correll MJ (2017) Controlling temperature and relative humidity in greenhouses using a liquid desiccant dehumidification system. In: Conference: 2017 meeting of Florida section of American society of agricultural and biological engineers (ASABE)
29. Pesaram AA (1993) A review of desiccant dehumidification technology. National Renewable Energy Laboratory, U.S. Department of Energy
30. Rambhad KS, Kalbande VP, Walke PV (2015) Solid desiccant dehumidification and regeneration techniques. *Int J Anal Exp Finite Elem Anal (IJAEFEA)* 2(1):1–5
31. Mei VC, Chen FC, Lavan Z, Collier RK (1992) An assessment of desiccant cooling and dehumidification technology. US Department of Energy
32. Ge TS, Qi D, Dai YJ, Wang RZ (2018) Experimental testing on contaminant and moisture removal performance of silica gel desiccant wheel. *Energy Build* 176:71–77 (Elsevier)
33. Kamsah N, Kamar HM, Khairuzzaman MIW, Idrus Alhamid M, Zawawi FM (2016) Performance assessment of a solid desiccant air dehumidifier. *J Technol (Sci Eng)* 78:57–64
34. Suyono T, Mat S, Yahya M, Ruslan MH, Zaharim A, Sopian K (2011) Theoretical and experimental analysis of desiccant wheel performance for low humidity drying system. In: Conference: proceedings of the 10th WSEAS international conference on system science and simulation in engineering

Chapter 15

Optimization of Process Variables in Abrasive Water Jet Machining of Nimonic C-263 Super Alloy Using Taguchi Method



**S. Madhavarao, Ravi Varma Penmetsa, Ch. Rama Bhadri Raju,
and Hema T. Raju Gottumukkala**

Abstract The current research work focuses on the optimization of the process variables of abrasive water jet machining (AWJM) process on Nimonic C-263 alloy by using the Taguchi method. The design and experiments are conducted by Taguchi L-27 orthogonal array technique. The three process variables: water jet pressure (WJP), transverse speed (TS) and standoff distance (SOD) are considered at three different levels. The considered output responses are: Kerf Taper (KT), material removal rate (MRR) and surface roughness (SR). The surface morphology of machined surface is analyzed by using the scanning electron microscope (SEM) images. Analysis of variance (ANOVA) was conducted to analyze the significant impact of each variable. From the analysis of all the responses, it is evident that all the responses are greatly influenced by transverse speed. The SEM images have revealed the micro-cuts and plastic deformation at various locations of the machined surface.

Keywords Nimonic C-263 · AWJM process · MRR · SR · Kerf Taper · Taguchi · ANOVA · SEM images

S. Madhavarao (✉) · R. V. Penmetsa · Ch. Rama Bhadri Raju · H. T. R. Gottumukkala
Sagi Ramakrishnam Raju Engineering College (A), Bhimavaram, Andhra Pradesh W.G-534204,
India
e-mail: madhava690@srkrec.ac.in

R. V. Penmetsa
e-mail: ravivarma.mechengg@srkrec.ac.in

Ch. Rama Bhadri Raju
e-mail: bhadri.mech@srkrec.ac.in

H. T. R. Gottumukkala
e-mail: tammiraju@srkrec.ac.in

1 Introduction

Non-traditional machining was a process in which machining a piece of hard materials like super alloys, hybrid metal matrix composites, hybrid glass fiber reinforced plastic composites and complex shapes are performed. The abrasive water jet (AWJM) process was one of non-traditional processes. AWJM process was performed on nickel-based super alloy. The nickel-based super alloys are largely used in aerospace industry to design the aircraft turbine blades and engine components. Among nickel-based super alloys, nickel–chromium–cobalt–molybdenum, namely Nimonic C-263, has good mechanical properties like high corrosion resistance to withstand the high temperatures, good creep, oxidation resistance and better surface finish. AWJ machining of nickel-based alloys was carried out with three different process variables at three different levels [1]. The optimization of machinability process variables is assessed by using gray relational analysis technique. The silicon carbide abrasive particles grain size has influenced the surface morphology and Kerf Taper [2–4]. The AWJ machining characteristics of various hybrid composites like green and GFRP were studied [5–7]. The characterization of nano-composites was studied at different process parameters of AWJ. Surface roughness was affected with an increase in reinforcement of particles. Nano-indentation testing was performed across thickness of samples in order to measure the micro-hardness and elasticity module [8, 9]. The surface integrity was affected with angular position of jet, and it has also identified the better position of jet. ANOVA analysis was applied to individual process variables in order to study the characteristics of machining parameters [10, 11]. The surface parameters obtained by cutting the specimens with unconventional machining process were found to be superior, when contrasted to the conventional machining process [12].

The AWJ machining process is performed on hybrid composite or super alloy materials along with the flow of water mixed with abrasive particles, which was entered and leaving the nozzle water with a pressure called water jet pressure. In this process, nozzle moves with certain speed that the speed of nozzle, transverse speed and the distance are maintained between nozzle and workpiece that distance refers to the standoff distance. These three process variables were most effected on the machining of workpiece. The machining characterization is mostly MRR, SR and KT.

2 Experimentation

2.1 Material and Equipment

The workflow of the process is shown in Fig. 1.

The chemical composition of workpiece Nimonic C-263 super alloy is shown in Table 1. The dimensions of flat plate $300 \times 150 \times 3$ mm were considered. The

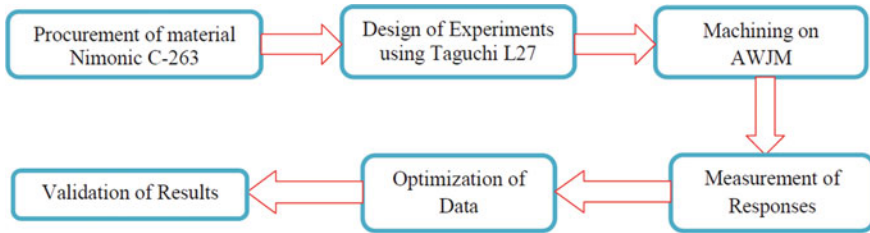


Fig. 1 Workflow of the process

Table 1 Chemical composition (weight %) of Nimonic C-263

Constituents	Ni	Cr	Co	Mo	Ti	Al	Fe	Cu	C
Weight %	49.0	19.0–21.0	19.0–21.0	5.6–6.1	1.9–2.4	<0.6	0.7 max	0.2 max	0.04–0.08

material used for present work is shown in Fig. 2. The chemical composition of Nimonic C-263 [1] is shown in Table 1. AWJM is largely used for cutting of glass fiber reinforced, hybrid metal matrix composites, nickel-based super alloys, steels and super alloys. It is used to cut the material that has a Kerf narrow slots, very smooth cutting edges, lack of heat, less MRR, good surface finish and very less waste of material. The machining process occupies less floor space, very low noise, safe and ecofriendly AWJM process. Sand particles were used as abrasive materials.



Fig. 2 Nimonic C-263 workpiece and abrasive water jet machine

Table 2 Machining variables used in experimentation

S. No.	Process variables	Level 1	Level 2	Level 3
1	WJP in Mpa	200	220	240
2	TS in mm/min	10	20	30
3	SOD in mm	1	2	3

2.2 Selection of Machining Parameters

The process variables are selected based on the literature survey. The input variable has selected water jet pressure in Mpa (WJP), transverse speed in mm/min (TS) and standoff distance in mm (SOD). Different levels of each process variables are also recorded. The observed output responses are metal removal rate (MRR), surface roughness (SR) and Kerf Taper (KT). The machining parameters used in the experimentation are shown in Table 2. The design of experiments is performed in MINITAB software by using Taguchi L-27 orthogonal array technique, which helps in reducing the total number of experimentations. The abrasive water jet machining was used to perform the cutting operation on Nimonic C-263 material. The mixture of water with sand abrasive particles contacts the surface of workpiece; the slots are formed due to removal of material from workpiece.

The pressurised steam of water along with abrasive particles which is used for machining through AWJM can generate a pressure upto 45,000 Psi. The AWJM setup is shown in Fig. 2.

3 Performance Evaluation

3.1 Material Removal Rate

The MRR depends upon the size of abrasive particles, type of abrasive particles, transverse speed and diameter of nozzle. The MRR is measured to cut the material at 20 mm length and thickness of workpiece constant for all the experimental processes. MRR is measured to consider weight of workpiece before and after cutting and count the time taken for each machining process with use of stopwatch. The MRR calculated ratio of weight difference and time taken for machining.

From analysing the results for MRR obtained through main effects plots indicates that by increasing the WJP and TS the MRR increases, while MRR increases with increase in SOD value upto 2 and then decreases as shown in Fig. 3.

The MRR is analyzed along with the observation of ANOVA analysis. In Table 3, the measured input process parameter contributions are transverse speed 73.34%, WJP 19.16% and SOD 1.15%. The transverse speed is considered as the most influenced parameter of MRR.

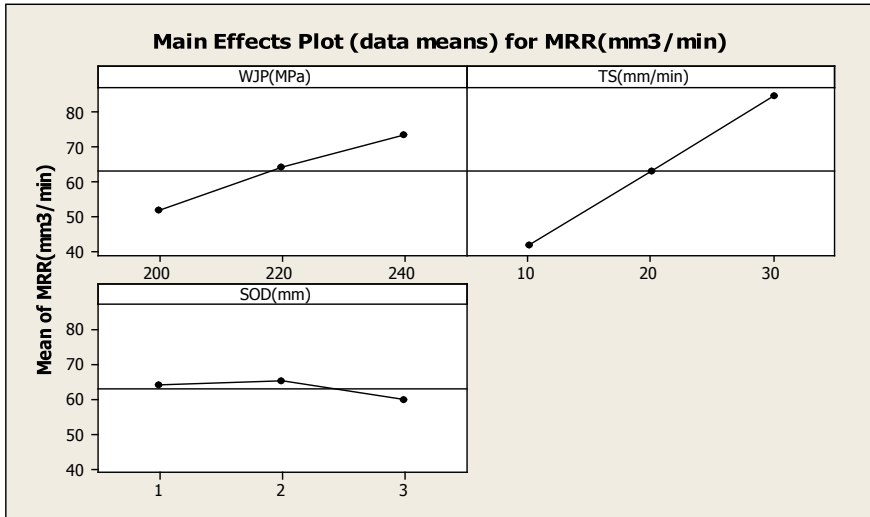


Fig. 3 Main effects plot for MRR

Table 3 ANOVA analysis for metal removal rate

Source	DOF	SOS	MOS	F	P	% Contr.
WJP (MPa)	2	2140.6	1070.3	30.27	0.000	19.16
TS (mm/min)	2	8192.0	4096.0	115.86	0.000	73.34
SOD (mm)	2	129.5	64.8	1.83	0.186	1.15
Error	8	707.1	35.4			6.33
Total	14	11,169.2				100

From the observation of signal-to-noise ratio Fig. 4, “larger is better” for metal removal rate. The optimum conditions of input process parameter are WJP 240 MPa, TS 30 mm/min and SOD 1 mm for optimum MRR.

3.2 Surface Roughness

The surface roughness is measured on the cutting surface of material. It is one of the most influenced parameters; the low value of surface roughness indicates high surface finish. The surface roughness is measured with contact-type surface roughness tester used on the shop floor. A diamond stylus is traversed across the workpiece specimen, and a piezoelectric take-up records all vertical movements. The surface roughness is denoted as “Ra.”

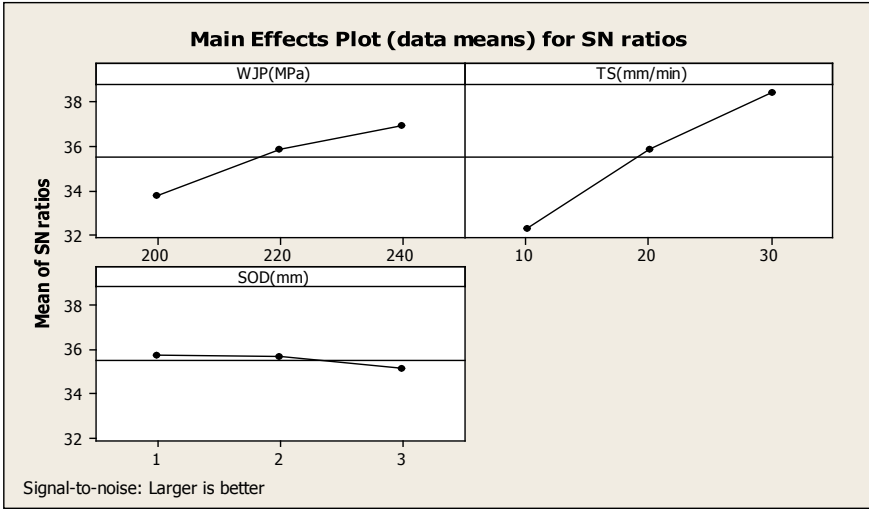


Fig. 4 SN ratios plot for MRR

The main effects plots for SR indicates that with increase of WJP the SR decreases, with increase in TS value upto 20 mm/min SR increases and then decreases and also the SR increases with increase of SOD upto 2 mm and then decreases as shown in the Fig. 5.

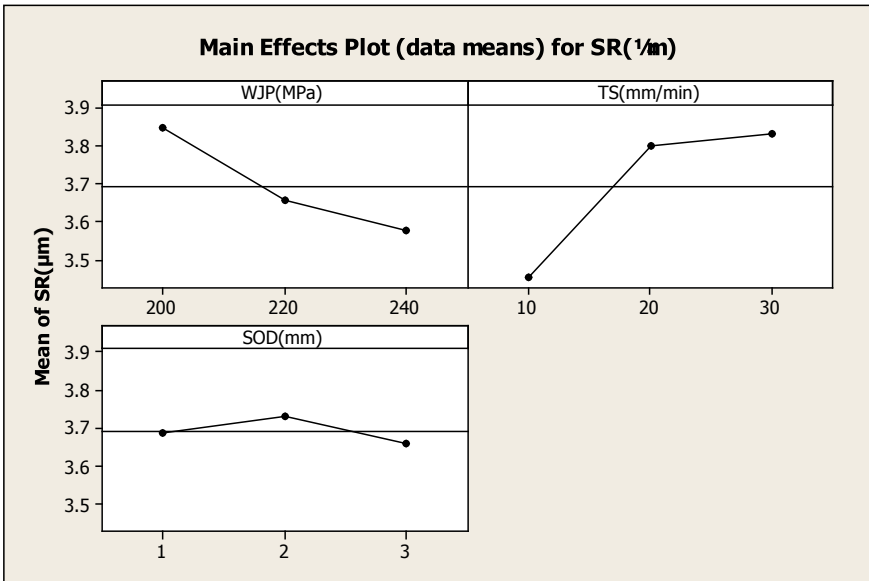


Fig. 5 Main effects plot for SR

Table 4 ANOVA analysis for SR

Source	DOF	SOS	MOS	F	P	% Contr.
WJP (MPa)	2	0.35021	0.17511	10.98	0.001	23.70
TS (mm/min)	2	0.78323	0.39161	24.56	0.000	53.01
SOD (mm)	2	0.02503	0.01252	0.78	0.470	1.69
Error	8	0.31889	0.01594			21.58
Total	14	1.47736				100

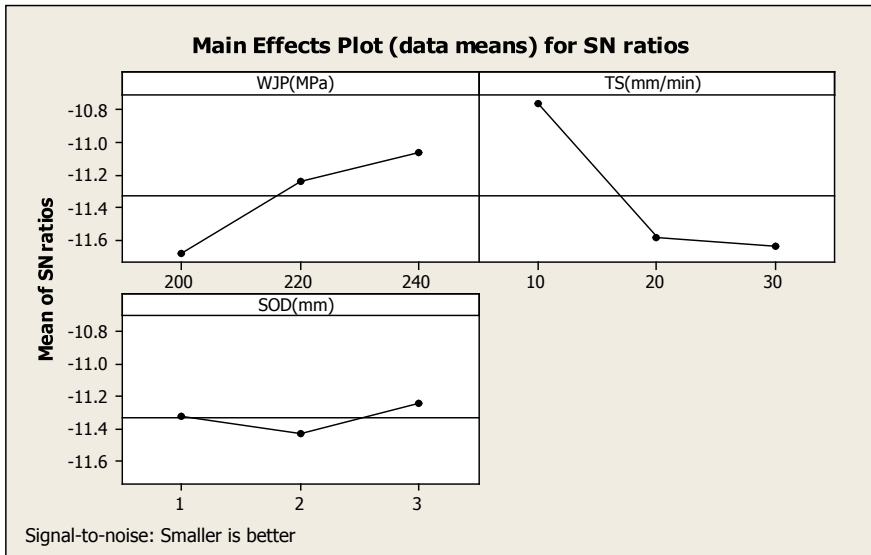


Fig. 6 SN ratios plot for SR

The SR is analyzed with the observation of ANOVA analysis of Table 4. The input process parameter contributions are transverse speed 53.01%, WJP 23.70% and SOD 1.69%. The transverse speed is more influenced parameter of SR.

From the observation of signal-to-noise ratio Fig. 6, “smaller is better” for SR. The optimum conditions of input process parameter are WJP 200 MPa, TS 30 mm/min and SOD 2 mm for optimum SR.

3.3 Kerf Parameters

The width of material that is removed by a machining process is known as Kerf. Kerf Taper means half of Kerf width variation per millimeter of depth of cut. The

optimization of the process variables for cutting Nimonic C-263 using water jet cutting is observed.

The main effects plots for KT indicates that KT decreases with increase in WJP value upto 220 Mpa and then increases while the KT increases with increase in TS value and the KT increases with increase in SOD value upto 2 mm and then decreases. The main effects plots for KT are shown in Fig. 7.

The KT is analyzed with the observation of ANOVA analysis of Table 5. The input process parameter contributions are transverse speed 15.03%, WJP 3.98% and SOD 70.44%. The SOD is more influenced parameter of KT.

From the observation of signal-to-noise ratio Fig. 8, “smaller is better” for Kerf Taper. The optimum conditions of input process parameter are WJPN 240 MPa, TS 30 mm/min and SOD 2 mm for optimum KT.

The multiple regression equations are

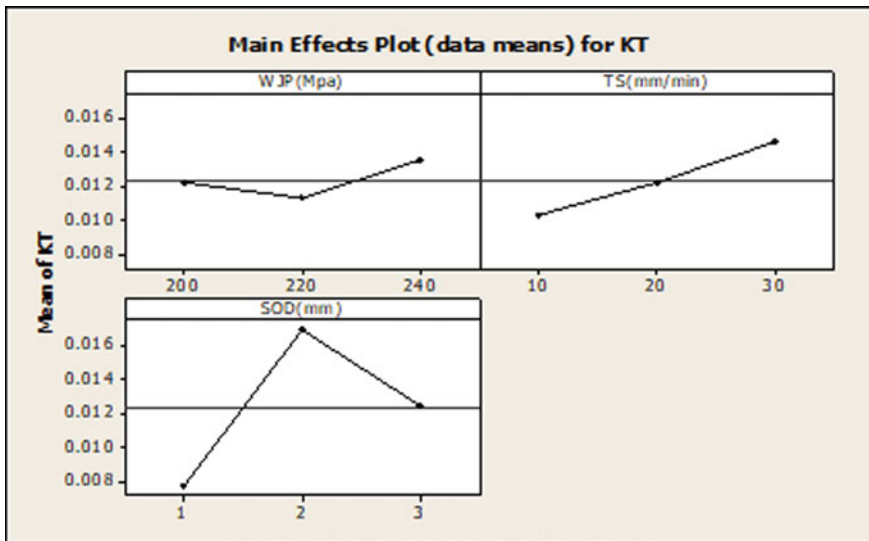


Fig. 7 Main effects plot for Kerf Taper

Table 5 ANOVA analysis for KT

Source	DOF	SOS	MOS	F	P	% Contr.
WJP (MPa)	2	0.0000214	0.0000107	3.77	0.041	3.98
TS (mm/min)	2	0.0000807	0.0000403	14.25	0.000	15.03
SOD (mm)	2	0.0003782	0.0001891	66.79	0.000	70.44
Error	8	0.0000566	0.0000028			10.54
Total	14	0.0005369				100

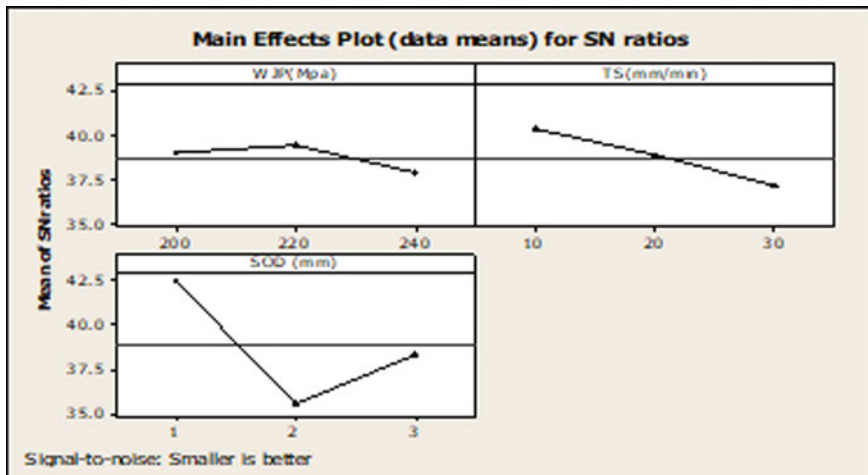


Fig. 8 SN ratios plot for Kerf Taper

$$\begin{aligned}
 \text{MRR} \left(\frac{\text{mm}^3}{\text{min}} \right) = & -281 + 2.29 \text{ WJP (MPa)} - 1.44 \text{ TS} \left(\frac{\text{mm}}{\text{min}} \right) + 30.5 \text{ SOD (mm)} \\
 & + 0.0155 \text{ WJP} * \text{TS} + 0.067 \text{ TS} * \text{SOD} - 0.0979 \text{ SOD} * \text{WJP} \\
 & - 0.00424 \text{ WJP} * \text{WJP} + 0.0006 \text{ TS} * \text{TS} - 3.07 \text{ SOD} * \text{SOD}
 \end{aligned} \tag{1}$$

$$\begin{aligned}
 \text{SR}(\mu\text{m}) = & 7.90 - 0.0559 \text{ WJP (MPa)} + 0.211 \text{ TS} \left(\frac{\text{mm}}{\text{min}} \right) + 0.504 \text{ SOD (mm)} \\
 & - 0.000591 \text{ WJP} * \text{TS} + 0.00002 \text{ TS} * \text{SOD} - 0.00129 \text{ SOD} * \text{WJP} \\
 & + 0.000144 \text{ WJP} * \text{WJP} - 0.00157 \text{ TS} * \text{TS} - 0.0589 \text{ SOD} * \text{SOD}
 \end{aligned} \tag{2}$$

$$\begin{aligned}
 \text{KERF TAPER} = & 0.169 - 0.00169 \text{ WJP (MPa)} - 0.000392 \text{ TS} \left(\frac{\text{mm}}{\text{min}} \right) + 0.0288 \text{ SOD (mm)} \\
 & + 0.000002 \text{ WJP} * \text{TS} + 0.000017 \text{ TS} * \text{SOD} + 0.000002 \text{ SOD} * \text{WJP} \\
 & + 0.000004 \text{ WJP} * \text{WJP} + 0.000003 \text{ TS} * \text{TS} - 0.00681 \text{ SOD} * \text{SOD}
 \end{aligned} \tag{3}$$

The optimum conditions for various responses are observed to lie outside the L-27 orthogonal array which necessitates the need for validation experiments. The validation run performed for the optimal conditions is listed in Table 6. For comparison with predicted optimum response values, the predicted values for optimum conditions from Eqs. 1–3 (MRR, SR and KT, respectively) are obtained from the multiple regression analysis conducted for experiment values [13]. The average error obtained between the predicted and experimental runs is 7.02%, i.e., the accuracy of the development models is as high as 92.97%.

Table 6 Validation of performance result

Output parameter	Optimum conditions	Predicted optimum value	Experimental value
MRR (mm ³ /min)	WJP-240 TS-30 SOD-1	99.26	102.75
SR (μm)	WJP-200 TS-30 SOD-2	3.30	3.513
KT	WJP-240 TS-30 SOD-2	0.0189	0.021

3.4 SEM Analysis

A SEM is a kind of electron microscope that generates images of a sample workpiece by scanning the surface with a focused beam of electrons.

Specimens are noticed in high vacuum in conventional SEM. Figure 9 shows the SEM micrograph of sample machined with WJP of 240 Mpa. The material removal or scars are noticed in the form of plastic deformation due to Max stress at perpendicular angle of impingement.

Under certain magnifications, the machined surface is noticed with large number of micro-cuts at the water jet pressure of 240 Mpa.

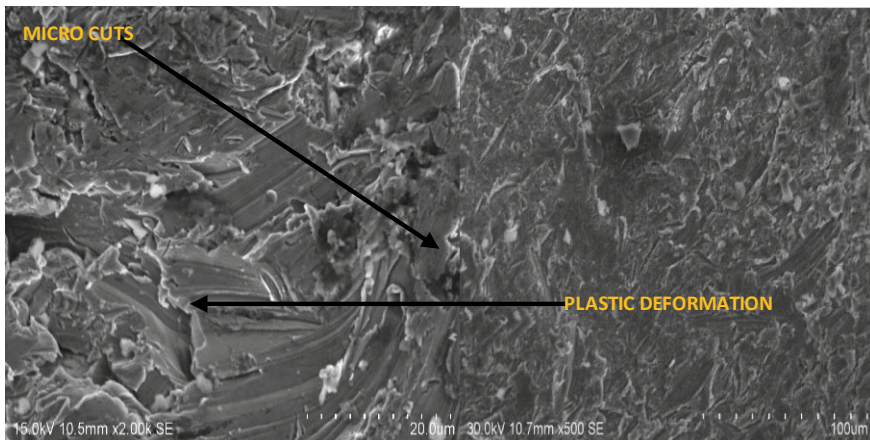


Fig. 9 Material removal morphology of the machined workpiece at 240 Mpa

4 Conclusion

The machinability of Nimonic C-263 super alloy using AWJM was studied and found that all the responses are greatly influenced by transverse speed. At the optimal conditions, MRR increases with increase in transverse speed and water jet pressure. The SR increases with the increase in transverse speed up to 20 mm/min and later it decreases, while Kerf Taper decreases due to the increase in WJP up to 220 MPa and later it increases. Validation experiments performed for optimal conditions showed improvement in different output responses compared to initial experimentation. SEM images revealed that plastic deformation and micro-cuts have been observed at various locations on the machined area.

References

1. Uthayakumar M, Khan MA, Kumaran ST, Slota A, Zajac J (2016) Machinability of nickel-based superalloy by abrasive water jet machining. *Mater Manuf Processes* 31(13):1733–1739
2. Joel C, Jeyapoovan T (2021) Optimization of machinability parameters in abrasive water jet machining of AA7075 using Grey-Taguchi method. *Mater Today Proc* 1(37):737–741
3. Senthilkumar TS, Muralikannan R, Kumar SS (2020) Surface morphology and parametric optimization of AWJM parameters using GRA on aluminum HMMC. *Mater Today Proc* 1(22):410–415
4. Saravanan K, Sudeshkumar MP, Maridurai T, Suyamburajan V, Jayaseelan V (2021) Optimization of SiC abrasive parameters on machining of Ti-6Al-4V alloy in AJM using Taguchi-Grey relational method. *Silicon* 1–8.6
5. Patel GM, Kumar RS, Naidu NS (2020) Optimization of abrasive water jet machining for green composites using multi-variant hybrid techniques. In: *Optimization of manufacturing processes*. Springer, Cham, pp 129–162
6. Tripathi DR, Vachhani KH, Bandhu D, Kumari S, Kumar VR, Abhishek K (2021) Experimental investigation and optimization of abrasive waterjet machining parameters for GFRP composites using metaphor-less algorithms. *Mater Manuf Processes* 13:1–1
7. Gnanavelbabu A, Rajkumar K, Saravanan P (2018) Investigation on the cutting quality characteristics of abrasive water jet machining of AA6061-B4C-hBN hybrid metal matrix composites. *Mater Manuf Processes* 33(12):1313–1323
8. Mardi KB, Dixit AR, Mallick A, Pramanik A, Balloková B, Hvizdos P, Foldyna J, Scucka J, Hlavacek P, Zelenak M (2017) Surface integrity of Mg-based nanocomposite produced by abrasive water jet machining (AWJM). *Mater Manuf Processes* 32(15):1707–1714
9. Mardi KB, Dixit AR, Srivastava AK, Mallick A, Scucka J, Hlaváček P, Hloch S, Zelenák M (2018) Effect of water pressure during abrasive waterjet machining of Mg-based nanocomposite. *Applications of fluid dynamics*. Springer, Singapore, pp 605–612
10. Yuvaraj N, Kumar MP (2017) Surface integrity studies on abrasive water jet cutting of AISI D2 steel. *Mater Manuf Processes* 32(2):162–170
11. Nair A, Kumanan S (2018) Optimization of size and form characteristics using multi-objective grey analysis in abrasive water jet drilling of Inconel 617. *J Braz Soc Mech Sci Eng* 40(3):121
12. Suárez A, Veiga F, Polvorosa R, Artaza T, Holmberg J, de Lacalle LL, Wretland A (2019) Surface integrity and fatigue of non-conventional machined Alloy 718. *J Manuf Processes* 48:44–50
13. Chekuri RBR, Ramakotaiah K, Jemaleswara P, Rajesh S (2019) Modeling and optimization of machining high performance nickel based super alloy nimonic c-263 using die sinking EDM. *Int J Mech Eng Rob Res* 8(2):196–201

Chapter 16

Material Composition and Development of Technology for Processing the Tailings of the Copper-Concentrating Plant of JSC “Almalyk MMC”



J. M. Bekpulatov, M. M. Yakubov, Kh. Ahmedov,
and Sh. A. Mukhametjanova

Abstract It is shown that the grinding of pyrite middlings from the beneficiation of porphyry copper ores, its flotation for the extraction of chalcopyrite and associated gold and silver, to obtain copper and iron concentrate, is economically acceptable in the conditions of JSC “Almalyk MMC.”

Keywords Copper · Chalcopyrite · Gold · Grinding · Pyrite · Intermediate product · Flotation · Valuable · Component · Silver

1 Introduction

Copper production is associated with releasing a large amount of industrial waste, much higher than the volume of produced copper. In connection with the increased requirements for environmental protection, special attention should be paid to increasing the complexity of raw materials, resource, and energy-saving technologies, the involvement, and processing of human-made non-ferrous metallurgy waste containing noble, non-ferrous metals and valuable components.

At present, the AMMC tailings have accumulated over 1 billion tonnes of concentrator tailings with a copper content of 0.07–0.112%. They contain over 1 million tons of copper, 11 thousand tons of molybdenum, 182 tons of rhenium, 500 thousand tons of zinc. More than 14 million tons of slags have already been accumulated in waste pyrometallurgical copper production. The dumps have accumulated about 500 thousand tons of zinc production clinker, which contains 50% of reducing elements, such as iron and carbon, and gold in 1–10 g/t and silver 100–750 g/t [1, 2].

J. M. Bekpulatov (✉) · Sh. A. Mukhametjanova
Tashkent State Technical University Named After Islam Karimov, Tashkent, Uzbekistan

M. M. Yakubov
Tashkent State Technical University Named After Islam Karimov Almalyk Branch, Tashkent, Uzbekistan

Kh. Ahmedov
Mineral Resources Institute, Dodoma, Tanzania

In this regard, the goal of this work was to improve the technology of copper production with an increase in its efficiency by creating energy and resource-saving technology that allows the maximum extraction of copper, gold, silver, and other valuable components by involving and processing human-made waste in the form of tailings of the concentrating factories of JSC “Almalyk MMC.”

2 Objects and Method of Research

At present, due to the unique specific physical and chemical properties, gold and silver are more and more in demand in science, technology, medicine: about 25% of consumed gold and more than 70% of silver are spent for technical purposes [3]. The strong demand for precious metals (gold, silver) since the 70th of the twentieth century has led not only to the processing of refractory and very poor ores but also to the search for new sources of gold and silver, such as human-made resources in the form of tailings from processing plants. In terms of gold content 0.2–2.7 g/t and silver 10–30 g/t in the tailings of concentration plants, they are comparable to ore deposits of mineral raw materials. Stale waste is an environmentally hazardous object, causing environmental pollution. For example, up to 100 billion tons of various industrial waste have been accumulated in Russia at present, with an annual increase of more than 2 billion tons, the resource potential of the gold contained in the waste is estimated at 5000 tons, which corresponds to 55–60% of the gold mined in the country [4, 5].

In this connection, the scientific and technological sphere’s innovative development includes the complex processing of technogenic raw materials, tailings from concentrating plants, and copper production. The solution to this issue is based on the study of the material composition, physicochemical and technological properties of waste in developing cost-effective technologies to extract non-ferrous metals [6, 7].

In recent years, complex traditional technologies, such as gravity, flotation, biochemical, cyanide, chloride, and sulfuric acid, have been tested and used for cost-effective processing of stale tailings from concentrators. So also non-traditional electrochemical, energy methods, several flotation reagents, and reactors for deep opening and leaching of precious metals gold and silver have been proposed [8–11].

However, efficient processing of the factory’s stale tailings has not been entirely resolved due to the persistence of mineral raw materials caused by stable associations of minerals containing finely dispersed gold, which leads to low productivity of the applied classical methods and reagents. There is a need for theoretical substantiation and development of innovative strategies for extracting gold, silver, and related valuable components from the old tailings of the factory—iron, copper, zinc into metal products for sale to ensure the comprehensive disposal of mining waste and reduce the environmental burden on the industrial region.

3 Results of the Research

At the Almalyk MMC, in the process of obtaining copper–molybdenum concentrates from non-ferrous metal ores [12], intermediate pyrite product is isolated, which is a valuable complex raw material for the additional production of noble (gold, silver, osmium), rare (selenium tellurium, rhenium, molybdenum), non-ferrous metals (copper, nickel, cobalt), and ferrous (iron) metals, as well as sulfuric acid. Pyrite concentrate can be obtained from this mediocre product in 120–180 thousand tons per year. Currently, pyrite middlings are combined with tailings and stored in tailings.

In the course of the research, the material composition of porphyry copper ores, pyrite middlings, as well as pyrite concentrates isolated from pyrite products and their technological properties, were studied, based on the mineral and technical characteristics of the studied products for the isolation of valuable components (Au, Ag, Cu, etc.) [13, 14].

The research object is pyrite mediocre, released during the dressing of porphyry copper ores at the CEP AMMC. It is released as a chamber product in the process of selective flotation of copper–molybdenum concentrate.

The starting product's material composition was studied using spectral and chemical analyses (see Tables 1 and 2).

Sulfide sulfur, iron, copper, gold, and silver should be considered valuable components.

Pyrite concentrate was obtained from middlings by flotation according to the scheme shown in Fig. 1.

The reagent mode of pyrite flotation was carried out under the following conditions: collector BCC—10 g/t, foaming agent T-92—15 g/t; flotation time: main operation 10, cleaning—5 min.

Table 1 Results of spectral analysis of the starting product

Object of study Pyrite middling product	Content (%)										
	Si	Fe	Al	Ti	Mn	Ni	Co	V	Cr	Mo	
	>1	>1	>1	0.3	0.1	0.002	0.003	0.004	0.003	0.001	
	Ba	Ca	Mg	K	Na	Zr	Pb	Cu	Be	Sr	Ag
	0.06	>1	>1	>1	0.4	0.003	0.01	0.06	0.001	0.01	0.001

Table 2 The results of the chemical analysis of the starting product

Object of study Pyrite middling product	Content (%)									
	SiO ₂	Al ₂ O ₃	TiO ₂	MnO	MgO	CaO	K ₂ O	Na ₂ O	P ₂ O ₅	CO ₂
	45.3	11.0	1.0	0.04	2.5	2.1	4.5	0.7	0.1	1.1
	Fe _{tot}	S _{total}	SO ₃	Mo	Se	Te	Co	Cu	Au g/t	Ag g/t
	7.5	10.0	0.1	0.003	0.001	0.0001	0.01	0.14	0.4	2.8

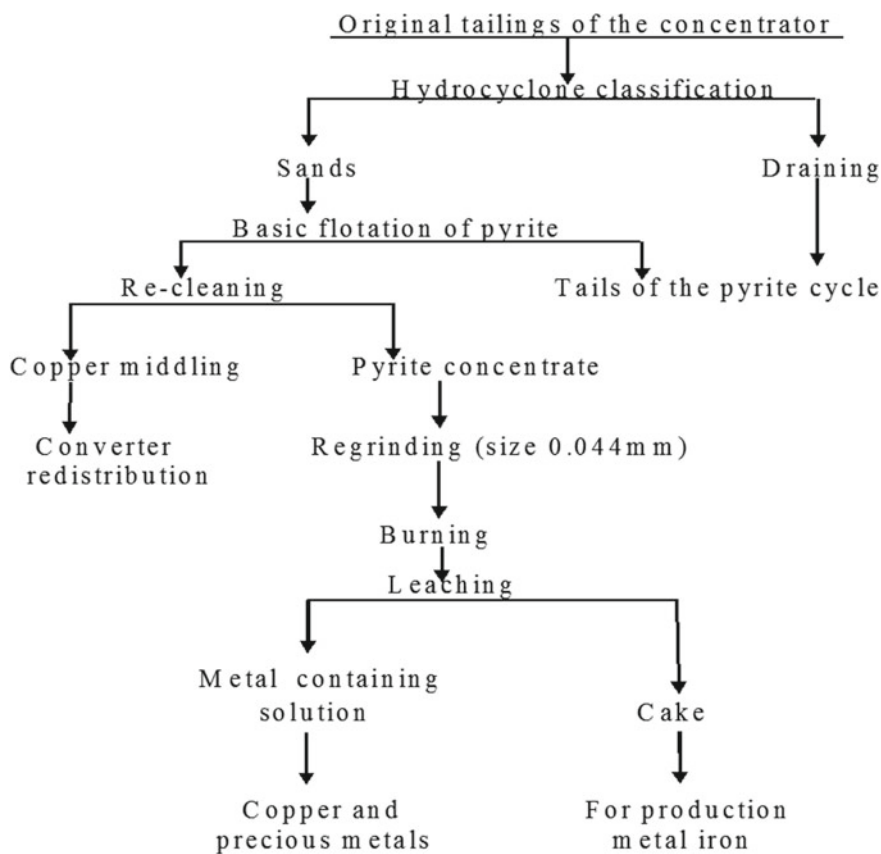


Fig. 1 Technological scheme for processing the tailings of a copper concentrator

Pyrite concentrate was directly obtained from pyrite industrial product under laboratory conditions.

It follows from the results (Tables 3 and 4) of the analysis that the pyrite concentrate meets the requirements of GOST 444-75 (grade KOF-2) for all the limiting components.

Table 3 Results of spectral analysis

Object of study Pyrite middling product	Content (%)								
	Si	Al	Mg	Ca	Fe	Mn	Ni	Co	Ti
	>1	>1	0.5	0.6	>1	0.04	0.001	0.02	0.06
	Mo	Zr	Cu	Pb	Sb	Bi	Zn	Ag	Ba
	0.03	0.006	0.3	0.08	0.1	0.001	0.02	0.001	0.01

Table 4 The results of the chemical analysis

Object of study Pyrite middling product	Content (%)							
	SiO ₂	FeO	Al ₂ O ₃	TiO ₂	CaO	MgO	P ₂ O ₅	CO ₂
	7.2	1.5	2.2	Undefined	0.7	0.4	0.05	0.3
	S _{total}	Co g/t	Cu	Mo	Se g/t	Te g/t	Au g/t	Ag g/t
	45.6	100	1.45	0.07	65	7	4.5	30

In pyrite concentration, gold, silver, copper, selenium, tellurium, cobalt, sulfide sulfur, and iron are of the most significant value.

Table 5 shows the results of rational analysis for gold and silver. As follows from the pyrite's logical analysis, direct cyanidation of the concentrate recovers 30% gold, 35% silver. It should be noted that more than 60% of gold is in a bound form with pyrite and chalcopyrite.

The peculiarity of pyrite middlings' material composition is that copper is in the form of chalcopyrite, and gold is in close association with it. Due to this, the cheapest

Table 5 Rational analysis of gold and silver in pyrite concentrate

1	2		3	
The form of precious metals and the nature of their connection with ore minerals	Distribution of gold		Distribution silver	
	g/t	%	g/t	%
Au, Ag in the form of intergrowths with ore components of Ag chloride and sulfide	1.2	26.9	1.9	21.7
Au, Ag associated in mineral and chemical compounds of copper (except for chalcopyrite), simple sulfides Ag	0.26	5.8	3.6	13.6
Au, Ag, associated with mineral and chemical compounds transition of metals, sulfosalts Ag	0.26	5.8	3.9	14.4
Au, Ag associated with Fe oxide and hydroxide	0.27	6.0	1.5	5.5
Au, Ag, finely associated in sulfides: pyrite, galena, and chalcopyrite	2	15.0	8.9	33.1
Au, Ag finely disseminated in quartz, aluminosilicates and other acid-insoluble	0.5	10.5	3.2	11.7
Total (concentrate)	4.5	100.0	27.0	100.0

and good technological process under the conditions of AMMC is regrinding of pyrite middlings and flotation recovery of valuable components, primarily chalcopyrite and associated gold and silver. The resulting copper middlings can be sent for pyrometallurgical processing together with copper concentrate.

The pyrite concentrate can be subjected to oxidative firing at a 450–550 °C temperature to obtain a cinder and after cleaning the dust. Sulfuric acid can be obtained from the gas mixture. According to the chemical analysis data, the content of components in the cinder was in %: SiO₂—11.9; Fe—55.7; Al₂O₃—3.72; CaO—1.16; MgO—0.66; CO₂—0.5; Cu—2.4; Au—7.45 g/t; Ag—49.6 g/t; Mo—0.09.

To extract copper, the cinder after regrinding was subjected to sulfuric acid treatment with a 3% solution of sulfuric acid at a liquid ratio: solid = 4:1, process temperature 85–90 °C for 1 h. After processing, the pulp was filtered off, and the cake was washed with water. Copper is recovered from the filtrate by traditional methods.

Extract noble metals; the cake was subjected to cyanidation. Cyanidation conditions liquid: solid = 2:1; the concentration of protective alkali in terms of CaO was 0.02%, the concentration of sodium cyanide was 0.06%, and cyanidation duration was 24 h with filtering the pulp and washing the cake. Gold and silver are extracted from the solution. It is possible to carry out the extraction of noble metals using a sorption process, followed by the resin's desorption and its reuse. After drying, the cake can be coarse and transferred to a metallurgical plant to obtain metallic iron.

4 Conclusion

Based on the material composition of pyrite middlings, it has been established that copper is in the form of chalcopyrite, and gold is in close association with it. It is shown that under the conditions of the AMMC, the flotation recovery of valuable components, primarily chalcopyrite and associated gold and silver, is economically acceptable. The resulting copper middlings can be sent to copper production by the pyrometallurgical method to convert copper pipes of the first period when producing blister copper as cold additives.

References

1. Sanakulov KS (2009) The scientific and technical basis for the processing of mining and metallurgical waste. Tashkent "Fan" 404
2. Mukhametdzhanova ShA, Yakubov MM, Akhmedov Kh, Yokubov OM (2020) Development of effective technology to concentrate from converter slags of copper production. *J Uzbek Chem J* 4:S.58–S.65
3. Matkarimov ST, Yusupkhodjayev AA, Berdiyarov BT, Qodirjon Ugli Nosirkhujayev S, Matkarimov ZT (2020) Technology of deep processing of copper slags by method of active thermal gravity. *Int J Adv Sci Technol* 29(03):5633–5639

4. Kholikulov DB, Matkarimov ST (2021) Materials today: proceedings pilot tests of processing technologies of process solutions of copper production by ozonation. *Mater Today Proc.* <https://doi.org/10.1016/j.matpr.2021.01.419>
5. Benevolsky BI (2011) Two aspects of the problem of utilization of mining and industrial waste (Benevolsky BI, Krivtsov AI, Romanchuk AI, Mikhailov BK (eds) *Mineral resources of Russia*). *Econ Manage* 1:37–42
6. Yusupkhodjaev AA, Khojiev ST, Berdiyarov BT, Yavkochiva DO, Ismailov JB (2019) Technology of processing slags of copper production using local secondary technogenic formations. *Int J Innovative Technol Exploring Eng* 9(1):5461–5472. <https://doi.org/10.35940/ijitee.a4851.119119>
7. Khojiev ST, Matkarimov ST, Narkulova ETK, Matkarimov ZT, Yuldasheva NS (2020) The technology for the reduction of metal oxides using waste polyethylene materials. In: *METAL 2020—29th international conference on metallurgy and materials, conference proceedings*, pp 971–978. <https://doi.org/10.37904/metal.2020.3592>
8. Matkarimov ST (2020) Heat treatment processes of steel-smelting slags in the recovery environment. In: Paper presented at the *METAL 2020—29th international conference on metallurgy and materials, conference proceedings*, pp 105–112. <https://doi.org/10.37904/metal.2020.3439>. Retrieved from www.scopus.com
9. Matkarimov ST, Yavkochiva DO, Berdiyarov BT, Nosirov FD (2020) Hydrometallurgical processing of copper-smelting dust. *Int J Emerg Trends Eng Res* 8(7):3088–3094. <https://doi.org/10.30534/ijeter/2020/35872020>
10. Matkarimov ST, Berdiyarov BT (2020) Development of the wasteless technology of processing of steel-smelting slags. https://doi.org/10.1007/978-3-030-46817-0_35. Retrieved from www.scopus.com
11. Kholikulov DB, Abdurahmonov S, Boltaev ON, Matkarimov ST (2020) Separation of metals from technological solutions copper production. *Int J Emerg Trends Eng Res* 8(7):3557–3561. <https://doi.org/10.30534/ijeter/2020/110872020>
12. Matkarimov ST, Berdiyarov BT, Yusupkhodjayev AA (2019) Technological parameters of the process of producing metallized iron concentrates from poor raw material. *Int J Innovative Technol Exploring Eng* 8(11):600–603. <https://doi.org/10.35940/ijitee.K1586.0881119>
13. Umarova IK, Matkarimov ST, Makhmarezhabov DB (2019) Study of the material composition and gravitational concentration of gold-bearing ores of the Amantaytau deposit/modern technologies: topical issues, achievements and innovations collection of articles. In: *XXXII international scientific and practical conference in Penza, November 25, 2019*, pp 65–69
14. Akhmedov H, Bekpulatov ZhM, Khaitov OG (2018) Study of the material composition and development of technology for processing gold-bearing sulfide ore from one of the deposits of the Republic of Uzbekistan. *Bulletin TSTU Tashkent* 2:S.183–S.189

Chapter 17

Optimization of Vibration-Based Condition Monitoring of Motor Drive End Using Taguchi Technique: A Case Study on Milling Machine



B. K. Pavan Kumar, Yadavalli Basavaraj, N. Keerthi Kumar, and M. J. Sandeep

Abstract Maintenance plays a vital role in recent trending technologies used in industries. This paper focuses on the novel aspect of predictive maintenance using signal processing techniques. Mainly, data are collected from the rotating machines using vibrometer and obtained spectrums are analysed for the purpose of process control using Taguchi for optimization and signal processing techniques for defining clearly the severity level of vibration in a component. Maintenance means prevention of expected problem by monitoring in time for the machine run which includes keeping the machine running, logistics, improvement. Results show the improvement of condition monitoring activity indicates high frequency level which reflects positivity on profit and safety.

Keywords Condition monitoring · Taguchi · Signal processing techniques · Vibration · Predictive maintenance

1 Introduction

Technology in predictive maintenance [1] is growing fast and so is condition monitoring [2] which is one of the most important activities. Nowadays, fault detection and diagnosis of contemporary commercial structures represents a major challenge

B. K. Pavan Kumar (✉)
Department of Mechanical Engineering, BITM, Ballari, Karnataka 583104, India

Y. Basavaraj
Mechanical Engineering Department, BITM, Ballari, Karnataka 583101, India

N. Keerthi Kumar
Department of Mechanical Engineering, BMS Institute of Technology and Management,
Bangalore, Karnataka 560064, India
e-mail: keerthikumarn@bmsit.in

M. J. Sandeep
Department of Mechanical Engineering, Dayanand Sagar University, Bangalore, Karnataka
560078, India

and an energetic subject of studies. There are four types of preventive maintenance [3] process in milling machines mainly are custom schedule, providing root for reporting failures, spare parts availability and records maintenance. Fault means the partial or total failure of a device, and the detection is the capability to apprehend the purposeful potential of a device. Fault detection is crucial in lots of industries to offer secure operation of technique. Fault detection [4] is used to taking pictures of the fault and estimating the time of fault prevalence. It causes like design errors, implementation mistakes, human mistakes, use, wears, deterioration, damages, getting old. Consequences of the fault are worse performances, power waste, waste of raw materials, economic losses lower exceptional, decrease manufacturing, environmental damages, human damages [5].

Milling machine is a machine tool that uses a multi-point cutter tool to remove the layer of material or metal in the form of grooves from the surface of workpiece [1, 6].

- It consumes more electricity.
- Ordinary lay man can't operate this milling machine.
- Cost effective for small projects.

2 Literature Survey

Zheng [7, 8] paper describes the different monitoring applications of recent developments in fault diagnosis which in turn forwards an approach to machine online maintenance. The approach focus on fault diagnosis of mechanical faults like gears, looseness and coupling using artificial neural network, wavelet and Fuzzy logics which is a hybrid system. ANN Results show in the increase of accuracy by comparing with other techniques. Mazurkiewicz [9] paper compares between support vector machines and neural network techniques for fault diagnosis in roller bearings which plays an important role in rotating machines. Preheated 369 tests were experimented, stored and analysed to predict the faults for variation of speed and load with the parameters like RMS, kurtosis, crest factor etc., and results found that support vector machine approach is more accurate and precise than neural network generalisation for the reduction of noise and vibration. Petruschke [10] paper describes clearly about the machine health monitoring and proves to be very efficient in diagnosis by data mining algorithm from the collected vibration data. To enhance the service life of bearings proper maintenance is essential to explore the frequency from FFT analyser. Later, SAFF tree algorithm is proposed which has many spectrum patterns and uses them in failure detection. Shankar [11] paper reviews the online condition monitoring of wind turbines for the failure detection and diagnosis using signal analysis. The overall investigation for maintenance of wind turbines is analysed by applying the current signature spectrum analysis. This work limits to the maintenance and further investigations on gearbox components and induction motor can be focussed for the diagnosis and of faults using modern tools like signal treatment and artificial intelligence [12].

4 Graphical Analysis of Motor Driver Spectrums

Figure 3 represents the peak value of 0.58 and 0.31 m/s velocity at 100 Hz frequency before and after replacement of components which are analysed by spectrums and proper diagnosis is suggested for the machine to increase the production rate and accuracy.

Figure 3 represents the peak value of 0.31 and 0.29 m/s velocity at 100 Hz frequency before and after replacement of components that are analysed by spectrums.

Figure 4 represents the peak value of 0.58 and 0.33 m/s velocity at 100 Hz

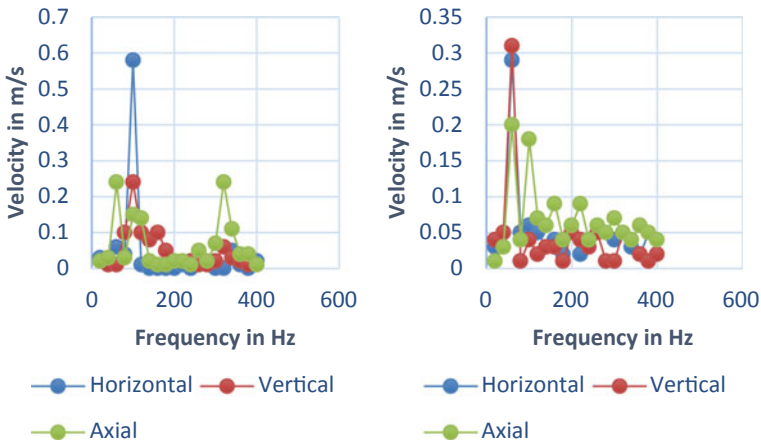


Fig. 3 a Motor Drive readings on Jan 2019; b Motor Drive readings on June 2019

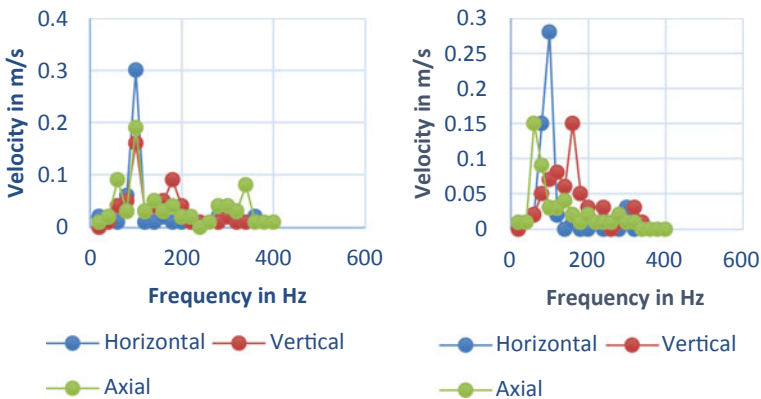


Fig. 4 a Motor drive readings on Jan 2020; b motor drive readings on June 2020

frequency before and after replacement of components which are analysed by spectrums and proper diagnosis is suggested for the machine to increase the production rate and accuracy. The graphical spectrums results shows three different positions data collected from the instrument and optimum level of data are analysed by using Taguchi technique to find major contribution parameter.

5 Taguchi Technique

The taguchi technique shows the optimum parameters for the experimental results which is an efficient approach for the response factors. Optimal parameters can be identified with less number of experimental resources than traditional DOE approach. Table 1 shows the Input variables such as spindle speed (A), feed rate (B), depth of cut (C) like 1400, 1450 and 1500 rpm for speed, 2000, 2600 and 3200 mm/min for feed rate, 0.6, 0.75 and 0.9 mm, respectively, for the responses such as velocity and frequency are obtained from the vibrometer device (Table 2).

Table 1 Process parameters and level

Control factors	Level 1	Level 2	Level 3
Spindle speed (A)	1400	1450	1500
Feed rate (B)	200	260	320
Depth of cut (C)	0.6	0.75	0.9

Table 2 Taguchi L9 orthogonal array experimental results

Control factors			Response parameters	
Spindle speed	Feed rate	Depth of cut	Velocity	Frequency
1400	200	0.6	1.8	20
1400	260	0.75	2.9	40
1400	320	0.9	9.1	60
1450	200	0.75	1.5	80
1450	260	0.9	1.8	100
1450	320	0.6	4.2	120
1500	200	0.9	6.3	140
1500	260	0.6	2.3	160
1500	320	0.75	1.9	180

Table 3 Response table for signal to noise ratios: smaller is better

Outputs		Rank responses			
Control factors	Levels	A	B	C	S _T
SFL	1	140	140	184	570
	2	131	158	154	
	3	299	272	232	
SSD		53,586	30,744	9288	93,618
PCR		57.24	32.84	9.92	100
Optimum levels		A1	B1	C3	
Optimum values		1400	200	0.9	

Bold indicates Signal noise

6 Results and Discussions

From the L9 orthogonal array of input and output parameters upon considering smaller is better, analysis was carried to find the major effect of parameter for the machine for the optimum level of contribution towards machine life (Table 3).

The above table of rank in frequency decides the major contribution towards the parameter that influencing the machine life.

7 Conclusion

The machines are integral part of the production chain during the unexpected failure and hence production will not be affected. Companies allow, having to replace the parts placed along with another, to maintain the production on time. Henceforth, condition monitoring is the technique used to frequently monitor the machines. Data were collected using Vibrometer and readings are analysed using signal processing techniques to check the severity level of the rotating machines. This paper presents the findings of an experimental study on the impact of process parameters on surface roughness and Dimensional deviation accuracy in the end milling process of a cam indexing drive casing. Using a Taguchi orthogonal array, the effect of control variables on frequency and velocity deviation was investigated. The best end milling conditions for minimising production characteristics were identified.

References

1. Luo W, Hu T, Ye Y, Zhang C, Wei Y (2020) A hybrid predictive maintenance approach for CNC machine tool driven by digital twin. *Robot Comput Integr Manuf* 65(September 2019):101974. <https://doi.org/10.1016/j.rcim.2020.101974>

2. Stief P, Dantan J, Etienne A, Siadat A (2019) ScienceDirect ScienceDirect ScienceDirect Condition monitoring system machine tool auxiliaries Condition monitoring system for machine tool auxiliaries A new methodology to analyze the functional and physical architecture of existing products for an oriented product identification. *Procedia CIRP* 88:358–363. <https://doi.org/10.1016/j.procir.2020.05.062>
3. Xu K et al (2020) Advanced data collection and analysis in data—driven manufacturing process. <https://doi.org/10.1186/s10033-020-00459-x>
4. Linnéusson G, Ng AHC, Aslam T (2020) A hybrid simulation-based optimization framework supporting strategic maintenance development to improve production performance. *Eur J Oper Res* 281:402–414. <https://doi.org/10.1016/j.ejor.2019.08.036>
5. Gustafsson M et al (2020) ScienceDirect A unified approach towards performance monitoring and condition-based 28th maintenance A unified approach towards performance monitoring and condition-based in grinding machines maintenance in grinding machines A new methodology to analyze the functional and physical architecture of for an, assembly oriented product family identification. *Procedia CIRP* 93:1388–1393. <https://doi.org/10.1016/j.procir.2020.04.094>
6. Mohanraj T, Shankar S, Rajasekar R, Sakthivel NR, Pramanik A (2020) Tool condition monitoring techniques in milling process—a review. *Integr Med Res* 9(1):1032–1042. <https://doi.org/10.1016/j.jmrt.2019.10.031>
7. Zheng M, Ye H, Wang D, Pan E (2021) Joint optimization of condition-based maintenance and spare parts orders for multi-unit systems with dual sourcing. *Reliab Eng Syst Saf* 210(August 2020):107512. <https://doi.org/10.1016/j.ress.2021.107512>
8. González-Muñiz A, Díaz I, Cuadrado AA (2020) DCNN for condition monitoring and fault detection in rotating machines and its contribution to the understanding of machine nature. *Heliyon* 6(2):e03395. <https://doi.org/10.1016/j.heliyon.2020.e03395>
9. Mazurkiewicz D, Zabin T (2020) Expert systems with applications machining sensor data management for operation-level predictive model, p 159. <https://doi.org/10.1016/j.eswa.2020.113600>
10. Petruschke L, Burkhardt M, Kohne T, Schraml P, Helfert M, Abele E (2020) Method to identify energy efficiency potentials of metal cutting machine tools in industry, vol 90, pp 522–527. <https://doi.org/10.1016/j.procir.2020.01.066>
11. Shankar NVS, Shankar HR, Kumar NP, Saichandu K (2020) ScienceDirect process parameter optimization for minimizing vibrations and surface roughness during turning EN19 steel using coated carbide tool. *Mater Today Proc* 24:788–797. <https://doi.org/10.1016/j.matpr.2020.04.387>
12. Mickiewicz AA, Mickiewicz AA (2020) On Integrated maintenance platform for critical platform cranes Integrated maintenance maintenance cranes under operation: operation: Database for maintenance purposes Integrated maintenance under operation: Integrated maintenance platform under operation: Database for purposes Database for maintenance purposes Integrated maintenance platform under for. *IFAC Pap* 53(3):167–172

Chapter 18

Phase Change Materials and Techniques to Enhance Performance of Latent Heat Storage Based on Geometrical Considerations: A Review



Sangeeta S. Mundra and Sujit S. Pardeshi

Abstract In recent years, phase change materials (PCMs) are widely employed to store energy in the way of latent heat and for subsequent use. It is suitable for applications like exhaust heat recovery, solar heating and temperature control of building spaces. The latent heat storage process is characterized by excellent energy storage density and constant storage temperature. But there exist certain issues with Latent energy storage devices which make the systems less efficient. Thus, there is need to improve thermal performance of such systems by various means. Addition of high thermally conductive materials to PCM, use of multiple PCMs and geometrical modifications are some of the available techniques for performance enhancement of such systems. The current review paper summarizes PCMs, performance improvement techniques for latent heat storage (LHS) system with special attention to extended surfaces and geometrical alterations. The insight presented here will form a guideline for appropriate choice of PCM and thermal transfer enhancement technique to cater particular application.

Keywords Energy storage · PCM · Geometry · Extended surface · Encapsulation · Fined pipe

1 Introduction

The ever-widening gap between energy demand and supply across the globe can be lessened by means of efficient ways of energy storage and reuse. One of the ways to store energy is in the form of thermal energy. Thermal energy can be stored in two ways, namely sensible and latent depending on range of operating temperatures of which latent heat storage is most sought-after technique. PCMs are utilized in LHS systems as medium of energy storage. PCM changes phase upon receiving

S. S. Mundra (✉) · S. S. Pardeshi
Mechanical Engineering, College of Engineering Pune, Pune, Maharashtra, India
e-mail: ssm.mech@coep.ac.in

S. S. Pardeshi
e-mail: ssp.mech@coep.ac.in

and losing heat. During this process, it gains, stores heat energy and subsequently releases it to other medium.

Efficient energy storage via LHS is a function of many factors such as geometrical configurations of storage units and thermophysical properties of PCMs. In other words, synchronized efforts are needed to overcome energy storage-related issues to achieve higher standards of system efficiency. A detailed overview of existing PCMs for energy storage and related applications has been presented by Sharma et al. [1].

Any LHS system in general possesses important constituents such as a suitable PCM having melting temperature in the operating temperature zone, heat exchanger and container for PCM. Therefore, building LHS system involves thorough understanding of PCMs, life span and repeatability of PCM, choice of material for container unit, design and geometrical considerations for heat exchangers, simulation and experimental investigations.

2 PCM as Energy Storage Media

Phase change materials are broadly categorized as inorganic, organic and eutectics. However, many of the available PCMs do not satisfy from perspective of storage media. Therefore, need arises to adopt techniques to overcome these shortcomings. PCMs must have certain necessary thermal, chemical and kinetic properties to be categorized as PCM [2]. Commonly used organic PCMs are fatty acids and Paraffins. Paraffins are cheap, predictable, reliable and stable below 5000 °C. Salt hydrates and metallics fall in the category of inorganic. Thermal cycling does not diminish their latent heat of fusion. Eutectic is blend of two or more materials. They do not separate from each other during phase change and crystallization [3].

Exhaustive review based on heat of fusion of organic and inorganic PCMs for operating temperature range of 0–1200 °C was presented by Abhat [4]. Review about paraffins and hydrates salts as PCMs, their stability and drawback were done by Farid et al. [5]. PCM database was developed for cooling and heating of spaces using a software application by Barreneche et al. [6]. They classified around 300 PCMs on the basis of their properties and having phase change temperature range – 500 to 1500 °C. The classification of PCMs is shown in Fig. 1.

Usually, PCMs possess low thermal conductivity that leads to low heat flow rates during charging and discharging. Recent years have seen increased research in order to build efficient energy storage systems. Stearic acid, paraffin wax and acetamide as PCMs were subjected to thermal testing for 1500 runs to investigate thermal stability by Sharma et al. [7]. It was noticed that stearic acid serves between wide range of temperature and heat of fusion. Thermal stability of organic and inorganic PCMs was investigated by Shukla et al. [8].

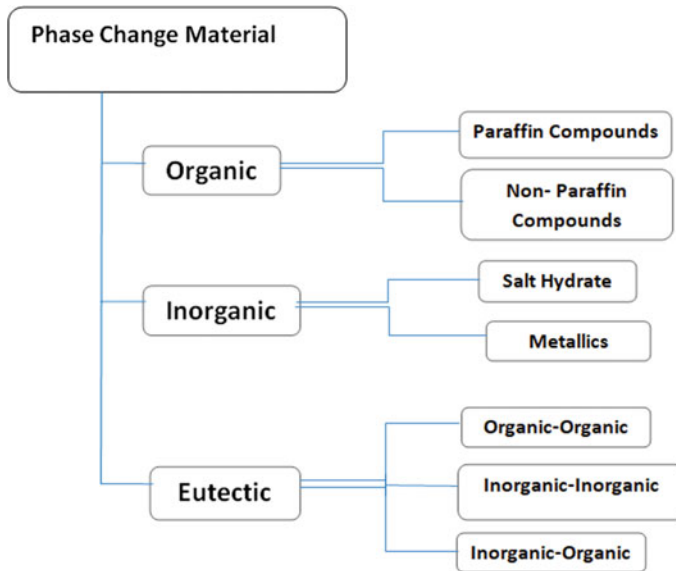


Fig. 1 Types of PCMs for energy storage

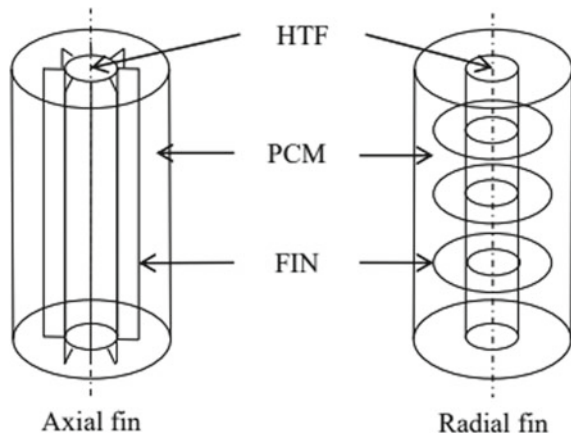
3 Performance Enhancement by Geometric Considerations for LHS Systems

PCMs typically possess low thermal conductivity and so the heat transfer is slow during charging and discharging. LHS systems can be made more efficient by implementing techniques like modifications in geometry and design, enhance thermal conductivity of PCM and optimize process parameters. A comprehensive review about performance improvement techniques has been presented by Jegadheeswaran and Pohekar [9]. Heat transfer rate in PCM-based systems depends upon parameters such as PCM thermal conductivity and available area for heat transfer. Therefore, extended surfaces augment the heat transfer rate through PCM. Surfaces can be extended in different ways such as attaching circular, axial fins and encapsulation of PCM. Incorporating fins for shell and tube type LHS container is commonly practiced for improve efficiency.

3.1 Extending Surfaces by Fins

Sebastian et al. [10] analyzed circular fin arrangement for shell and tube type LHS device with evolution of simulation model. It was concluded that number and arrangement of fins had significant effect on discharge performance. Rathod et al. [11] used longitudinal fins to enhance heat flow rate. It was seen that using three fins

Fig. 2 Fins as extended surfaces



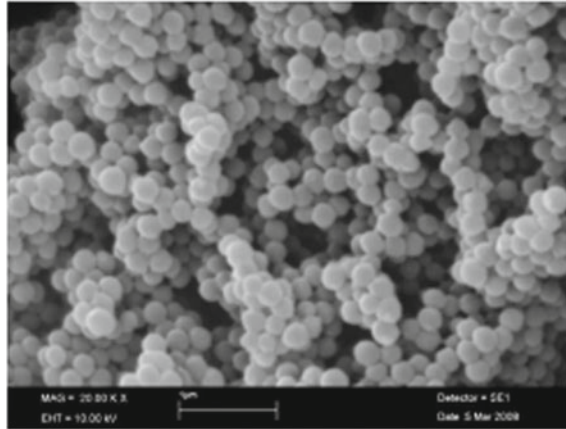
reduced discharge time up to 43%. Kabbra et al. [12] worked with finned tube heat exchange device. It was observed that inlet temperature of hot fluid has dominant effect compared to flow rate. Significance of characteristic length of device was also emphasized.

Tiarri et al. [13] have analyzed discharging process of system with square container having finned pipes and potassium nitrate as PCM. The effect of arrangement of heat pipes and geometry of fins on discharging rate was also investigated by them. Dhaidan et al. [14] in their paper have summarized various numerical and experimental work aimed at performance enhancement using high thermal conducting fins. Figure 2 presents schematic of finned extended surfaces.

Various methods for improvement in heat transfer rates have been compared by Velraj et al. [15]. Their work concluded that Lessing rings and use of fins can be adopted for improvement in discharging rate while bubble agitation is suggested to improve charging. Inclusion of metal screens/spheres within PCM enhanced heat transfer performance pipe in pipe heat storage device. This study was carried out by Ettouney et al. [16]. Diameter and count of spherical inserts were considered as experimental parameters. Nusselt number and Fourier number analysis were performed. Ismail et al. [17] studied the role of radial fins and turbulence enhancers on heat transfer rate. Stainless steel wire as a helical structure was used to increase flow turbulence in tube. The solid–liquid interface was tracked and investigated.

Liu et al. [18] done experimental worked with cylindrical LHS with a finned copper pipe placed at center of cylindrical container. The results obtained using straight fins and fins at angle were compared. Axial fins investigated by Hosseini et al. [19]. Width of fin and Stephen number were selected as experimental variables. Thermal behavior, liquid fraction, temperature contours were analyzed. It was established that fins lead to lesser melting time and better heat penetration. Zayed et al. [20] have presented exhaustive review on recent advances on design and geometry of heat storage containers. It is highlighted that rectangular containers apt for bulk storage because of superior melting and efficiency.

Fig. 3 Microscopic image of PMMA/octacosane microcapsules [21]



3.2 PCM with Encapsulation

Another way of extending heat transfer area is to enclose PCM into thin shells. Depending on size of the shell, it can be either micro- or macroencapsulation. Microencapsulation is usually applied to organic PCMs operating at low temperature. It leads to confinement of PCM material into tiny thin natural/manmade polymer layer. Sari et al. have studied microencapsules of polymethylmethacrylate (PMMA) and PMMA/octacosane. The surface characterization was done by scanning electron microscopy (SEM) technique. Thermal behavior of PMMA/octacosane was studied using differential scanning calorimetry (DSC) and thermal gravimetric analysis (TGA). The results indicated that microencapsulated octacosane possesses fair energy storage ability (Fig. 3).

Double-shell alginate microshells wrapping paraffin as PCM were used and analyzed for energy storage by Nemeth et al. [22]. TGA analysis and exposure to thermal cycling showed superior thermal stability and enough mechanical strength for leak proof microcapsules. Cylindrical encapsulations were analyzed for charging and discharging by Kalaiselvam et al. [23]. Prediction of time for phase change was done using various models. The results were validated by rigorous experimentation. Stefan number and heat generation parameter influence solidification time while average thermal conductivity is the deciding factor for melting time. As internal heat generation is considered in this research work, the findings are useful in application fields like nuclear fuel freezing.

Tao et al. [24] proposed a novel combined method incorporating internal tube enhancement and use of multiple PCMs. The result comparison revealed that enhanced tube reduces the melting time. PCM nanocapsules were successfully developed using in situ polymerization method by Fang et al. [25] for heat transfer enhancement. Guangjian Peng et al. have reviewed various aspects of microencapsulation of PCMs such as capsule material, characteristics of encapsulation and applications [26].

Fins undoubtedly enhance heat transfer rates but the PCM volume is reduced as a part of storage volume is occupied by fins causing reduced storage capacity. Also fins inhibit the free convection flow of molten PCM. Therefore, holistic approach towards finned surfaces is needed to ascertain the optimum fin geometry, count and orientation.

4 Conclusion

Available studies in past have shown considerable amount of success in accomplishing performance improvement in LHS systems by different means yet lot of scope exists in this particular field. The present review paper highlights on heat transfer enhancement of energy storage systems by use of extended surfaces. Attaching fins is a decent and effective way to enhance heat transfer rates. But there are certain drawbacks of using fins such as reduced space available for PCM and slow down of heat transfer by natural convection of molten PCM. Hence, there exists a need for extensive study on fin profile, fin location and fin material. Fins can be incorporated on either PCM side or Fluid side. For low temperature organic PCMs, it is provided on PCM side. Encapsulation for high temperature applications still remain a challenge. Another way is encapsulation of PCM that greatly augments the performance. Most of the encapsulating shells are spherical or cylindrical. Manufacturing of encapsulation poses big problem, and therefore, innovative methods must be explored to incorporate encapsulation of PCM. A careful selection of type of extended surface should be deployed based upon critical performance affecting parameters. Also, more research is required for using multiple techniques in combination with achieve better results. Profound research is available for limited use of PCM but large-scale practical application of PCM still remain a challenge that can be addressed in future.

References

1. Sharma A, Tyagi VV, Chen CR, Buddhi D (2009) Review on thermal energy storage with phase change materials and applications. *Renew Sustain Energy Rev* 13:318–345
2. Buddhi D, Sawhney RL, Seghal PN, Bansal NK (1987) A simplification of the differential thermal analysis method to determine the latent heat of fusion of phase change materials. *J Phys Appl Phys* 20:1601–1605
3. George A (1989) Hand book of thermal design. In: Guyer C (ed) Phase change thermal storage materials (chapter 1). McGraw Hill Book Co.
4. Abhat A (1983) Low temperature latent heat storage: heat storage materials. *Sol Energy* 30(4):313–332
5. Farid MM, Khudhair AM, Razack S, Al Hallaj S (2004) A review on phase change energy storage: materials and applications. *Energy Convers Manage* 45:1597–1615
6. Barreneche C, Navarro ME et al (2015) New database to select phase change materials: chemical nature, properties, and applications. *J Energy Storage* 3:18–24

7. Sharma A, Sharma SD, Buddhi D (2002) Accelerated thermal cycle test of acetamide, stearic acid and paraffin wax for solar thermal latent heat storage applications. *Energy Convers Manage* 43:1923–1930
8. Shukla A, Buddhi D, Sawhney RL (2008) Thermal cycling test of few selected inorganic and organic phase change materials. *Renew Energy* 33:2606–2614
9. Jegadheeswaran S, Pohekar SD (2009) Performance enhancement in latent heat thermal storage system: a review. *Renew Sustain Energy Rev* 13:2225–2244
10. Sebastian K, Andreas K, Dieter B (2017) Numerical analysis of shell-and-tube type latent thermal energy storage performance with different arrangements of circular fins energies, vol 10, p 274
11. Rathod MK, Banerjee J (2015) Thermal performance enhancement of shell and tube latent heat storage unit using longitudinal fins. *Appl Therm Eng* 75:1084–1092
12. Kabbra M, Groulx D (2016) Experimental investigations of a latent heat energy storage unit using finned tubes. *Appl Therm Eng* 101:601–611
13. Tiari S, Qiu S, Mahdave M (2016) Discharging process of a finned heat pipe-assisted thermal energy storage system with high temperature phase change material. *Energy Convers Manage* 118:426–437
14. Dhaidan NS, Khodadadi JM (2017) Improved performance of latent heat energy storage systems utilizing high thermal conductivity fins: a review. *J Renew Sustain Energy* 9(3)
15. Velraj R, Seeniraj RV, Hafner B, Faber C, Schwarzer K (1999) Heat transfer enhancement in a latent heat storage system. *Sol Energy* 65(3):171–180
16. Ettouney HM, Alatiqi I, Al Sahali M, Al Ali SA (2004) Heat transfer enhancement by metal screens and metal spheres in phase change energy storage systems. *Renew Energy* 29:841–860
17. Ismail KAR, Lino FAM (2011) Fins and turbulence promoters for heat transfer enhancement in latent heat storage systems. *Exp Therm Fluid Sci* 35:1010–1018
18. Liu C, Groulx D (2014) Experimental study of the phase change heat transfer inside a horizontal cylindrical latent heat energy storage system. *Int J Therm Sci* 82:100–110
19. Hosseini MJ, Ranjbar AA, Rahimi M, Bahrampoury R (2015) Experimental and numerical evaluation of longitudinally finned latent heat thermal storage systems. *Energy Build* 99:263–272
20. Zayed ME, Zhao J et al (2020) Recent progress in phase change materials storage containers: geometries, design considerations and heat transfer improvement methods. *J Energy Storage* 30
21. Sari A, Alkan C, Karaipekli A, Uzun O (2009) Microencapsulated n-octacosane as phase change material for thermal energy storage. *Sol Energy* 83:1757–1763
22. Nemeth B, Nemeth AS, Toth J, Dodor-kardos A, Gyenis J, Feczko T (2015) Consolidated microcapsules with double alginate shell containing paraffin for latent heat storage. *Sol Energy Mater Sol Cells* 143:397–405
23. Kalaiselvam S, Veerappan M, Aaron AA, Iniyar S (2008) Experimental and analytical investigation of solidification and melting characteristics of PCMs inside cylindrical encapsulation. *Int J Therm Sci* 47:858–874
24. Tao YB, He YL (2015) Numerical study on performance enhancement of shell-and-tube latent heat storage unit. *Int Commun Heat Mass Transf* 67:147–152
25. Fang G, Li H, Yang F, Liu X, Wu S (2009) Preparation and characterization of nano-encapsulated n-tetradecane as phase change material for thermal energy storage. *Chem Eng J* 153:217–221
26. Peng G, Dou G, Hu Y, Sun Y, Chen Z (2020) Phase change material (PCM) microcapsules for thermal energy storage. *Adv Polym Technol* (article id 9490873)

Chapter 19

Performance Analysis of Different Types of Solar Photovoltaic Cell Techniques Using MATLAB/Simulink



M. Murali, CH Hussaian Basha , Shaik Rafi Kiran, P. Akram, and T. Naresh

Abstract At present, solar photovoltaic (PV) technology is playing a major role in all hybrid and distribution power generation systems because of its advantages are less sustainability, and excess availability in nature. In this work, different types of solar PV cell topologies are designed and which are analyzed by using the MATLAB/Simulink window. The types of PV cell topologies are single-diode circuit PV cell, two-diode model PV cell, and three-diode model PV cell and its comparative study have been done in terms of peak power extraction, efficiency, and fill factor. In addition, the PV cell characteristics are analyzed at different atmospheric conditions.

Keywords Efficiency · Fill factor · Irradiations · Power versus current characteristics · Solar cells · Temperature conditions

1 Introduction

Nowadays, the consumption of electrical power is increasing excessively because of the well-established industries, increased population, and an improvement in electrical technologies. The utilization of conventional power generation is reducing gradually because of its less availability in nature, high power generation cost, and less flexibility [1]. The drawbacks of conventional power generation systems are overcome by using the renewable energy source. The renewable energy sources are wind, tidal, biomass, solar, and hydro energy [2–4]. The advantages of wind power generation are cost-effective, create more jobs, high sustainable, and domestic source of energy [5]. The wind power plants are built on existing farms. The major disadvantages of the wind power plants are inconsistent, visual impact, required high capital cost, and it takes significant portion of the land.

M. Murali · CH Hussaian Basha (✉) · P. Akram · T. Naresh
Department of EEE, K.S.R.M. College of Engineering, Kadapa, Andhra Pradesh, India

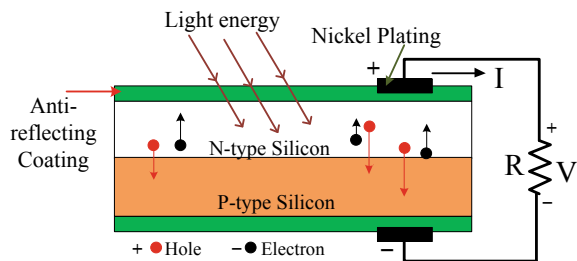
S. R. Kiran
Department of EEE, S.V. College of Engineering, Tirupati, Andhra Pradesh, India

The drawbacks of wind power generation are overcome by using the tidal power plant. The advantages of the tidal power generation are high energy density, low operational cost, and inexhaustible energy [6]. The demerits of the tidal power generation are building is too expensive, and output power generation is not constant. In addition, it is not good for the atmosphere around them. The disadvantages of tidal power generation are overcome by using a biomass renewable energy. The merits of biomass energy are widely available source, carbon neutral, and less expensive when compared to the fossil fuels [7]. Also, it limits the overreliance of fuels. The major drawback of the biomass is it requires high installation area. Hydro is the one of the renewable sources to generate the electricity. But it is having the drawback of high initial cost. However, the drawbacks of the above renewable sources are overcome by using the solar.

At present, solar is the most popular renewable energy source and it is converted to electrical source by using the photovoltaic effect. The attractive features of the PV systems are high robust, more sustainability, free of cost, high abundance and ubiquity [8]. In addition, it is an environmental pollution free source and there are no rotational parts included in it. As a result, no noise pollution takes place. The working behavior of the PV cell topologies is similar to the P–N diode. The solar irradiations are incident to the P–N silicon diode material, the electrons are getting energized and it runs away from one layer to another layer as shown in Fig. 1. From Fig. 1, when the P–N circuit closed the current flows from P-type material to N-type material [9].

From the literature survey, the PV module is designed and implemented by interconnecting the number of PV cells. In similar, the PV array is designed by the parallel and series combination of PV modules. For industrial high voltage applications, the PV modules are interfaced in a parallel manner and for high current rating applications which are interfaced in series manner [10]. Due to the interconnection of cells, the sun irradiations incident area on PV is increased. As a result, the power generation capability is improved. Based on the operating efficiency, the PV cell design technologies are illustrated as mono, poly, and thin film methodologies [11]. The monocrystalline and polycrystalline semiconductor cells are designed by applying a microelectronic methodology and their corresponding giving efficiencies are 12.8% and 9.8% respectively. Similarly, thin film semiconductor cells are designed by combining the Cdte, a-Si, and CuInSe₂ materials. The thin film operated

Fig. 1 Detailed operation of solar PV cell



technique efficiency is 9.5%. So, most of the PV array design manufactures prefers monocrystalline technology.

The PV system works based on atmospheric irradiation intensity and temperature conditions. The solar irradiations are not constant in an entire day and are maximum at mid-day only. As a result, the PV array generates nonlinear behavior current versus voltage characteristics. Based on that, the operating point of the solar PV vary continuously. Hence, the output power of the PV system is not constant [12]. In order to obtain the high efficiency and constant output power of PV cell, an MPPT technique is used. The maximum power point tracing methodology is in PV fed boost converter system in order to extract the peak power of the solar PV [13]. Here, in this work, the single-, two-, and three-diode model-based PV cells are designed, and compared in terms of peak power output, performance effectiveness, and fill factor.

Based on application, some of the research scholars focusing on single and ideal diode circuit-based PV cell technologies and some other are using two- and three-diode circuit model PV cell technologies for analyzing the performance of I–V and P–I characteristics. The design of single-, two-, and three-diode model-based PV cell technologies and their corresponding performance analysis at different atmospheric irradiation and temperature conditions are given in Sects. 2 and 3. Section 4 gives the conclusion of the article.

2 Mathematical Design of PV Cells

The accurate I–V and P–V characteristics of solar PV generation is the challenging task in solar PV technology. For that, here, different PV cell technologies are discussed in order to obtain the high accurate power versus voltage characteristics.

(a) Design of Ideal Diode PV Cell

From the literature survey [14], the design of ideal PV cell circuit topology is easy, and it gives approximated I–V and P–V curves. In this topology, a current source is connected in parallel with the diode. The output current of ideal diode PV cell is given in (1).

$$I_{\text{out}} = I_{\text{PV_cell}} - i_{\text{orev}} \left(e^{\left(\frac{q * V_{\text{out_cell}}}{\eta K T} \right)} - 1 \right) \quad (1)$$

$$I_{\text{PV_cell}} = (I_{\text{PV_STC}} + K_i \Delta T) * \frac{G}{G_{\text{STC}}} \quad (2)$$

For the total number of cells (n_s), the PV cell output current is derived as,

$$I_{\text{out}} = I_{\text{PV_cell}} - i_{\text{orev}} \left(e^{\left(\frac{q * V_{\text{out_cell}}}{\eta K T * n_s} \right)} - 1 \right) \quad (3)$$

From (1), and (2), the short circuit current and open circuit voltages are derived as,

$$I_{sc_cell} = I_{out} = I_{PV_cell} \tag{4}$$

$$I_{sc_cell} = I_{PV_cell} = i_{orev} \left(e^{\left(\frac{q * V_{out_cell}}{\eta K T * n_s} \right)} - 1 \right) \tag{5}$$

$$V_{oc_cell} = \frac{n_s * \eta K T}{q} * \log \left(\frac{I_{PV_cell}}{i_{orev}} + 1 \right) \tag{6}$$

The output power generation of ideal diode-based solar PV cell is derived as,

$$P_{out_cell} = I_{out} * V_{out_cell} = \left(I_{PV_cell} - i_{orev} \left(e^{\left(\frac{q * V_{out_cell}}{\eta K T * n_s} \right)} - 1 \right) * V_{out_cell} \right) \tag{7}$$

(b) Design of Single-Diode Model-Based Solar PV Cells

The design of single-diode model PV cell circuit topology have been done by including an additional series resistance (R_s), and parallel resistance (R_{sh}) as shown in Fig. 2a, b. The suitable design parameters of solar PV cell are obtained by using diverse advanced soft computing optimization techniques. From Fig. 2, it is clearly observed that for designing of single-diode circuit PV cell requires five major parameters which are classified as photovoltaic current (I_{PV_cell}), peak current of PV (I_{MPP}), peak voltage (V_{MPP}), shunt resistance (R_{sh}), and finally series resistance (R_s). The detailed design parameters of solar PV cells are given in Table 1. From Fig. 2a, the output current (I_{PV_cell}), open circuit voltage (V_{oc_cell}), short circuit current (I_{sc_cell}), and the converted PV cell output power are derived as,

$$I_{out} = I_{PV_cell} - i_{orev} \left(e^{\frac{q(V_{out_cell} + I_{out} n_s R_s)}{\eta K T * n_s}} - 1 \right) \tag{8}$$

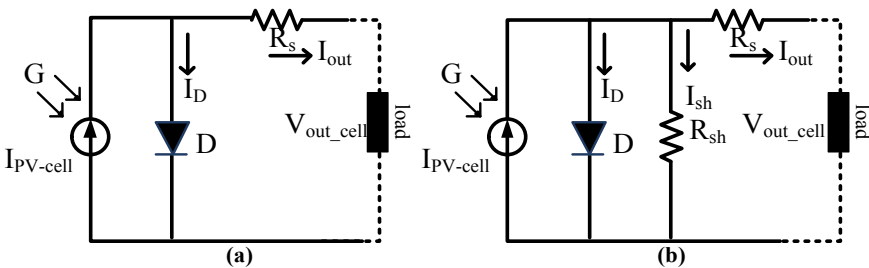


Fig. 2 Single-diode cell, a with series resistance b with series and parallel resistances

Table 1 One- and two-diode model-based PV cells with different resistances

Single-, two- and three-diode model-based PV cell parameters		
S. No.	Parameters	Values
1.	Maximum generated voltage (V_{MPP})	30.0 V
2.	Maximum generated current (I_{MPP})	7.51 A
3.	Peak to peak generated power (P_{MPP})	225 W
4.	Open circuit PV voltage (V_{oc})	37 V
5.	Short circuit PV current (I_{sc})	8.17 A
6.	voltage temperature coefficient	-0.33641 %/°C
7.	Current temperature coefficient	0.03847 %/°C
8.	Solar irradiations (G)	1000 W/m ²
9.	Diode ideality factors (a_1 , and a_2)	0.91, 0.9, and 0.96
10.	PV cell series resistive value (R_s)	0.340 Ω
11.	PV cell design shunt resistance (R_{sh})	106.78 Ω
12.	Nominal operating temperature (T_N)	25 + 273 K
13.	PV electrical charge (q)	1.601 × 10 ⁻¹⁹ C
14.	Boltzmann constant (K)	1.38 × 10 ⁻²³ J/C
15.	Total series connected cells (n_s)	60 numbers

$$V_{oc_cell} = \frac{n_s * \eta K T}{q} * \log\left(\frac{I_{PV_cell}}{i_{orev}} + 1\right) \quad (9)$$

$$I_{sc_cell} = I_{PV_cell} - i_{orev} \left(e^{\frac{q I_{sc_cell} R_s}{\eta K T n_s}} - 1 \right) \quad (10)$$

$$P_{out_cell} = I_{out} V_{out_cell} = \left(I_{PV_cell} - i_{orev} \left(e^{\frac{q(V_{out_cell} + I_{out} R_s)}{\eta K T n_s}} - 1 \right) \right) V_{out_cell} \quad (11)$$

From Fig. 2b, the single-diode circuit extracted output current with series and parallel resistance is derived as,

$$I_{out} = I_{PV_cell} - i_{orev} \left(e^{\frac{q(V_{out_cell} + I_{out} R_s)}{\eta K T}} - 1 \right) - \frac{V_{out_cell} + I_{out} R_s}{R_{sh}} \quad (12)$$

For n_s number of series connected cells, the PV cell current is derived as,

$$I_{out} = I_{PV_cell} - i_{orev} \left(e^{\frac{q(V_{out_cell} + I_{out} n_s R_s)}{\eta K T n_s}} - 1 \right) - \frac{V_{out_cell} + I_{out} R_s}{R_{sh}} \quad (13)$$

(c) Design of Two-Diode Model-Based Solar PV Cell

The design of two-diode model-based solar PV cell is similar to the single-diode model. But it requires two more additional parameters for its design purpose which

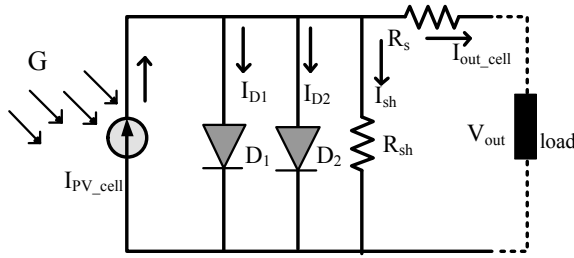


Fig. 3 Two-diode circuit model-based solar PV cell

are illustrated as diode ideality parameter (a), and reverse saturation current (i_{orev}) [15]. The design of double-diode-based PV cell has been done by adding an additional diode to the single-diode circuit. From Fig. 3, the output current of the cell is derived as,

$$I_{out} = I_{PV_cell} - i_{orev_1} \left(e^{\frac{q(V_{out_cell} + I_{out}R_s)}{\eta_1 kT}} - 1 \right) - I_x \tag{14}$$

$$I_x = i_{orev_1} \left(e^{\frac{q(V_{out_cell} + I_{out}R_s)}{\eta_1 kT}} - 1 \right) + \frac{V_{out_cell} + I_{out}R_s}{R_{sh}} \tag{15}$$

(d) Design of Three-Diode Model-Based PV Cells

From the literature review, the single- and two-diode PV cell models are designed, and which are analyzed by considering the different variable parameters such as irradiancies, and temperatures [16]. The voltage drops, and internal losses occur due to the current flowing through the PV cell which is indicated as a series resistor. In most of the practical conditions, the PV cell current flows through the ground which is represented as a shunt resistance. The three-diode model circuit topology with series resistance is shown in Fig. 4a, and the combination of both the resistances is given in Fig. 4b.

From Fig. 4a, the three-diode model-based PV cell current is derived as,

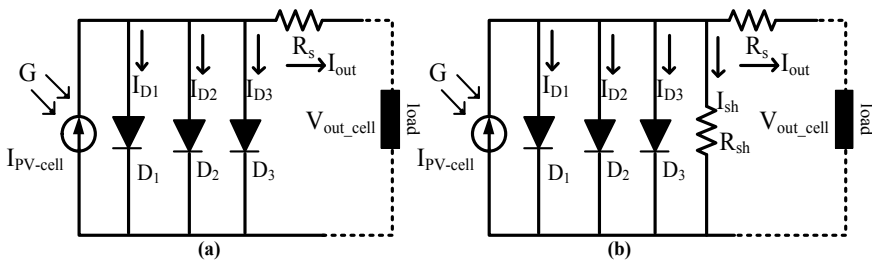


Fig. 4 Three-diode model PV cell, **a** with series resistance, and **b** parallel resistance

$$I_{\text{out}} = I_{\text{PV_cell}} - I_{\text{D1}} - I_{\text{D2}} - I_{\text{D3}} \quad (16)$$

$$I_{\text{out}} = I_{\text{PV_cell}} - i_{\text{orev_1}} \left(e^{\frac{q(V_{\text{out_cell}} + I_{\text{out}}R_s)}{\eta_1 kT}} - 1 \right) - I_y \quad (17)$$

$$I_y = i_{\text{orev_2}} \left(e^{\frac{q(V_{\text{out_cell}} + I_{\text{out}}R_s)}{\eta_2 kT}} - 1 \right) + i_{\text{orev_3}} \left(e^{\frac{q(V_{\text{out_cell}} + I_{\text{out}}R_s)}{\eta_3 kT}} - 1 \right) \quad (18)$$

From Fig. 4b, it is clearly observed that the PV cell current is the summation of diode currents and shunt resistance current, and it is derived as,

$$I_{\text{out}} = I_{\text{PV_cell}} - I_{\text{D1}} - I_{\text{D2}} - I_{\text{D3}} - I_{\text{sh}} \quad (19)$$

$$I_{\text{out}} = I_{\text{PV_cell}} - i_{\text{orev_1}} \left(e^{\frac{q(V_{\text{out_cell}} + I_{\text{out}}R_s)}{\eta_1 kT}} - 1 \right) - i_{\text{orev_2}} \left(e^{\frac{q(V_{\text{out_cell}} + I_{\text{out}}R_s)}{\eta_2 kT}} - 1 \right) - I_z \quad (20)$$

$$I_z = i_{\text{orev_3}} \left(e^{\frac{q(V_{\text{out_cell}} + I_{\text{out}}R_s)}{\eta_3 kT}} - 1 \right) + \frac{V_{\text{out_cell}} + I_{\text{out}}R_s}{R_{\text{sh}}} \quad (21)$$

$$I_{\text{orev_1}} = I_{\text{orev_2}} = I_{\text{orev_3}} = I_{\text{on}} \left(\frac{T}{T_N} \right)^3 e^{\frac{qE_g}{nk} \left(\frac{1}{T_N} - \frac{1}{T} \right)} \quad (22)$$

$$I_{\text{on}} = I_{\text{on_1}} = I_{\text{on_2}} = I_{\text{on_3}} = \frac{I_{\text{SC_n}}}{e^{\left(\frac{V_{\text{oc_n}}}{\eta V_{Tn}} \right)}} \quad (23)$$

3 Analysis of Different Types of Solar PV Cell-Based Modules

From the above equitations, the mathematical design of different PV cells has been done and which are analyzed at different irradiation conditions to obtain the accurate I-V and P-V characteristics. Here, the PV cells are implemented successfully by considering their corresponding parallel resistances, and series resistances. The single-diode model is designed by considering five general parameters which are explained in Sect. 2. From the previous literature survey [17], the single-diode model PV cell understanding, and implementation is easy when compared to the two-diode model. But the major disadvantage is less maximum power extraction and less accuracy.

The drawbacks of one- and two-diode models are overcome by using the three-diode circuit-based PV cell. The performance of PV cells is analyzed in terms of fill factor and efficiency. The fill factor is the ratio of the maximum extracted power with respect to the product of open circuit voltage, and short circuit current. The

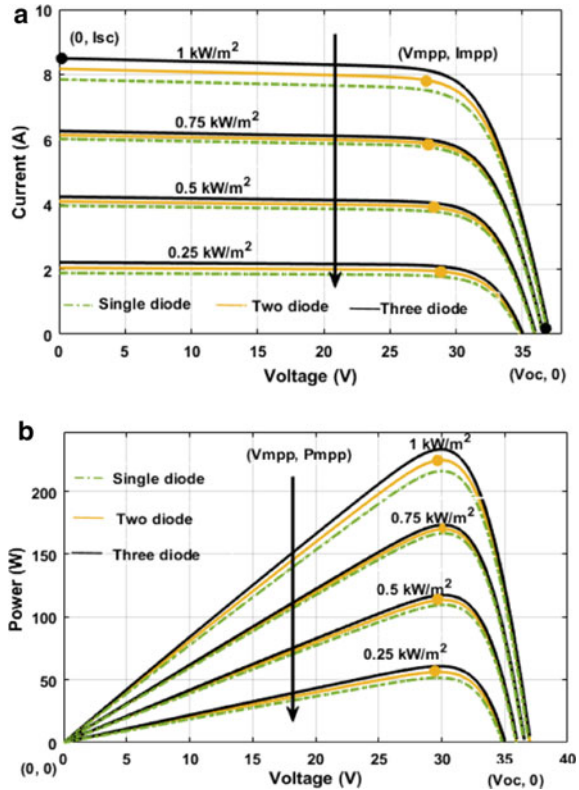
efficiency of the cell is determined from the output power of the cell with respect to the product of irradiations and cross-sectional area.

(a) At Different Irradiation Conditions (G)

From (2), (15) and (20), the maximum output power extraction of three-diode, two-diode, one-diode circuit-based PV cells is increased when the incident irradiations on solar PV module is increased. The incident irradiations on solar PV is improved by interconnecting the plenty of cells. As a result, the PV system output power is improved excessively. The single-, double-, and three-diode circuit-based PV modules output current versus voltage curve, and power versus voltage curves are shown in Fig. 5a, b at different irradiation conditions.

From Fig. 5a, at constant temperature condition ($25\text{ }^{\circ}\text{C}$), the maximum peak to peak output power, voltage, fill factor and efficiency of triple-diode model PV cell at 1000 W/m^2 are 225 W , 30.03 V , 0.744 , and 17.57% respectively. Similarly, at 1000 W/m^2 , the double-diode model and single-diode model PV cells peak to peak power, voltage, fill factor and efficiency are 221.44 W , 29.8 V , 0.732 , and 17.3% , 221.18 W , 29.15 V , 0.73 , and 17.28% respectively.

Fig. 5 a Different PV cells-based solar module I–V curves at different irradiation conditions, b different PV cells-based solar module P–V curves at different irradiation conditions



At 750 W/m^2 , the double-diode circuit-based PV cell peak to peak voltage, extracted output power, fill factor, and efficiencies are 28.1 V, 165.696 W, 0.54, and 17.26% respectively. From Fig. 5b, at 500 W/m^2 , the single-diode PV cell fill factor, maximum power extraction, efficiency, and output voltages are 0.362, 109.696 W, 17.14%, and 26.3 V respectively. Finally, at 250 W/m^2 , the triple-diode model-based PV cell output voltage, maximum power, efficiency, and fill factors are 26.28 V, 56.68 W, 17.09%, and 0.185 respectively. Hence, from the above observation, it is clearly indicated that the output power of double-diode circuit-based PV cell is high when compared to single-diode PV cell. The performance of PV cells is analyzed at different irradiation conditions and it is given in Table 2.

(b) At Different Atmospheric Temperature Conditions (T)

From (8), (11), (14), (18), and (22), the temperature of the PV cell increases then the corresponding PV cell reverse saturation current increasing excessively. As a result, the efficiency of the PV cell is reduced. In addition, the open circuit voltages of the PV cells are increased, and its corresponding temperatures are reduced. From Fig. 6a, at $45 \text{ }^\circ\text{C}$, the single, two, and triple-diode model-based PV cells maximum output voltage, efficiency, output power, and fill factors are 27.63 V, 16.72%, 208.4 W, and 0.680, 28.5 V, 16.74%, 206.7 W, and 0.683, 28.5 V, 17.01%, 218 W, and 0.72 respectively.

Similarly, from Fig. 6b, at $65 \text{ }^\circ\text{C}$, the two-diode, triple-diode, and single-diode model-based PV cells fill factor, efficiency, output voltage, and maximum extracted powers are 0.623, 16.18%, 26.31 V, and 188.5 W, 0.638, 16.45%, 26.2 V, and 193 W, 0.619, 16.16%, 26.85 V, 189.81 W respectively. Finally, at $105 \text{ }^\circ\text{C}$, the two-diode circuit-based PV cell output voltage, efficiency, maximum power extraction, and fill factors are 20.9 V, 15.06%, 152.61 W, and 0.5 respectively. Hence, it is observed that the efficiency of triple-diode model-based PV cell is high when compared to two and single-diode models.

(c) At Different Series Connected PV Cells (n_s)

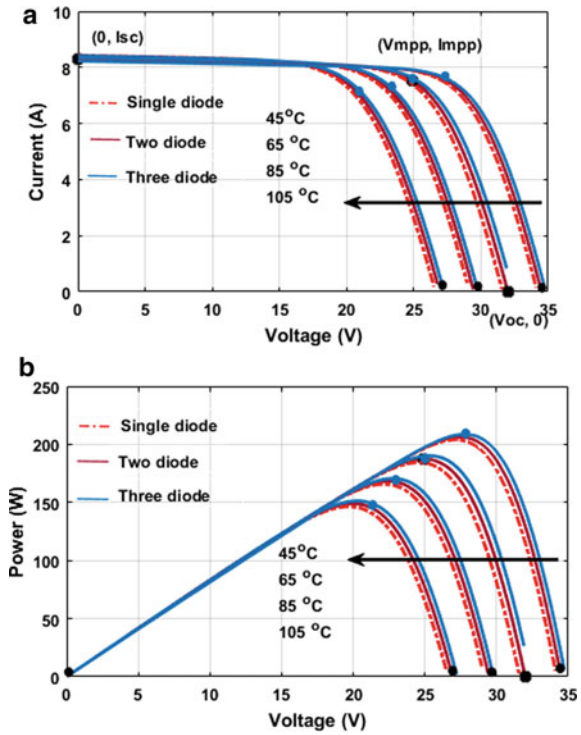
From (3), (10), and (13), it is showed that the series connected cell increases the open circuit voltage. Similarly, the entire solar PV module output power is increased by increasing its series connected cells. Due to the mismatch connection of series cells, the short circuit current and open circuit voltages are improved. As a result, the overall PV system condition and heating losses are improved. So that the efficiency of the PV cell is reduced gradually.

From Fig. 7a, at 55 cells, the two-diode, single-diode, and three-diode model-based PV cells output efficiency, maximum extracted power, fill factor, and output voltages are 16.01%, 179 W, 0.592, and 24.5 V, 15.98%, 175.2 W, 0.579, and 22.5 V, 16.27%, 186 W, 0.615, and 25.1 V. Similarly, from Fig. 7b, at 35 series connected cells, the single-diode, triple-diode, and two-diode model-based PV cells fill factor, output voltage, maximum output power, and efficiencies are 0.477, 14.01 V, 144.2 W, and 13.35%, 0.489, 14.8 V, 148 W, and 13.67%, 0.484, 14.32 V, 146.31 W, and 13.42% respectively. The detailed analysis of all PV cells model is given in Table 2.

Table 2 Analysis of different types of solar PV cells modules at different parameter variation conditions

	Three-diode model			Two-diode model			Single-diode model					
	P_{MPP} (W)	V_{MPP} (V)	FF	η %	P_{MPP} (W)	V_{MPP} (V)	FF	η %	P_{MPP} (W)	V_{MPP} (V)	FF	η %
Diverse irradiation conditions (W/m^2)												
1000	225.01	30.03	0.744	17.57	221.44	29.80	0.732	17.3	221.18	29.15	0.73	17.28
750	178.05	28.7	0.588	17.41	165.69	28.1	0.54	17.26	164.26	27.3	0.539	17.21
500	110.4	27.36	0.365	17.25	110.2	27.14	0.364	17.22	109.69	26.3	0.362	17.14
250	56.68	26.28	0.1875	17.09	54.912	27	0.1816	17.16	54.61	26.03	0.179	17.07
Diverse temperature conditions ($^{\circ}C$)												
105	159.2	21.8	0.526	15.31	152.61	20.9	0.5	15.06	149.62	20.7	0.4	15.04
85	178	24.03	0.588	15.89	176.2	22.8	0.582	15.62	172.01	22.98	0.56	15.6
65	193	26.2	0.638	16.45	188.5	26.31	0.623	16.18	189.81	26.85	0.619	16.16
45	218	28.5	0.72	17.01	206.7	28.5	0.683	16.74	208.4	27.63	0.68	16.72
25	225	30	0.744	17.57	221.4	29.8	0.732	17.3	221.8	29.15	0.73	17.28
Diverse series connected cells (n_s)												
35	148	14.8	0.489	13.67	146.31	14.32	0.484	13.42	144.2	14.01	0.477	13.35
45	160.3	19.5	0.55	14.97	160.5	19.2	0.531	14.72	158.01	16.98	0.522	14.65
55	186	25.1	0.615	16.27	179	24.5	0.592	16.01	175.2	22.5	0.579	15.98
60	225	30	0.744	17.57	221.4	29.8	0.732	17.3	221.18	29.15	0.73	17.28

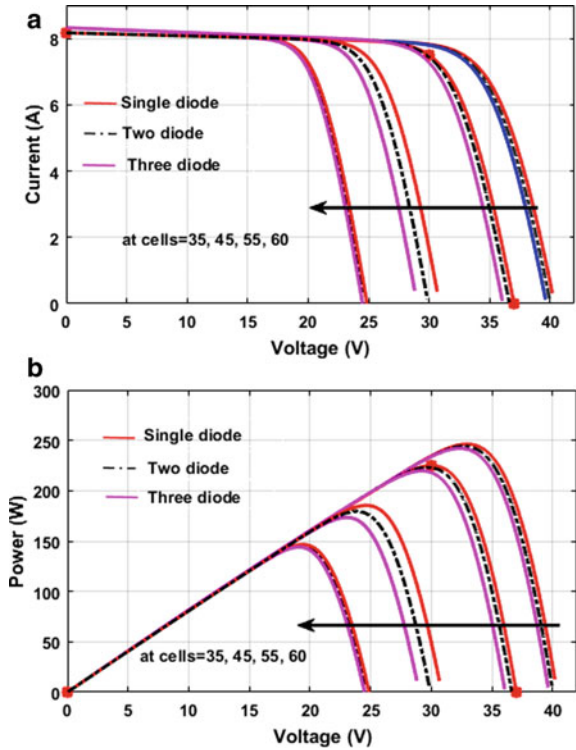
Fig. 6 a Different PV cells-based solar module I–V curves at different temperature conditions, **b** different PV cells-based solar module P–V curves at different temperature conditions



4 Conclusion

The single-diode circuit-based PV cell, two-diode circuit model-based PV cell, and three-diode-based solar PV cells are analyzed successfully at diverse atmospheric temperature conditions. In addition, those are analyzed at different irradiation, and series connected cells conditions. From the performance analysis results, it is clearly observed that the triple-diode model-based solar PV module gives high output power when compared to two- and single-diode model-based solar PV cells. In addition, the efficiency, and fill factor of the triple-diode model PV cell are very high. As a result, the triple-diode PV cell gives high accurate I–V and P–V characteristics.

Fig. 7 **a** Different PV cells-based solar module I–V curves at different series connected cells, **b** Different PV cells-based solar module P–V curves at different series connected cells



Acknowledgements We would like to thank the management of K.S.R.M. College of Engineering (Autonomous) for providing all the facilities to carry out our research work.

References

1. Meegahapola L et al (2020) Power system stability with power-electronic converter interfaced renewable power generation: present issues and future trends. *Energies* 13(13):3441
2. Hussaian Basha CH, Rani C (2020) Different conventional and soft computing MPPT techniques for solar PV systems with high step-up boost converters: a comprehensive analysis. *Energies* 13.2:371
3. Chowdary VG et al (2020) Hybrid fuzzy logic-based MPPT for wind energy conversion system. *Soft computing for problem solving*. Springer, Singapore, pp 951–968
4. Hussaian Basha CH, Rani C (2020) Design and analysis of transformerless, high step-up, boost DC-DC converter with an improved VSS-RBFA based MPPT controller. *Int Trans Electr Energy Syst* 30.12:e12633
5. Sankar VU et al (2020) Application of wind-driven optimization for decision-making in economic dispatch problem. *Soft computing for problem solving*. Springer, Singapore, pp 925–940
6. Hussaian Basha CH, Rani C (2020) Performance analysis of MPPT techniques for dynamic irradiation condition of solar PV. *Int J Fuzzy Syst* 22.8:2577–2598

7. Hussaian Basha CH et al (2020) Simulation of metaheuristic intelligence MPPT techniques for solar PV under partial shading condition. *Soft computing for problem solving*. Springer, Singapore, pp 773–785
8. Hussaian Basha CH et al (2020) Development of cuckoo search MPPT algorithm for partially shaded solar PV SEPIC converter. *Soft computing for problem solving*. Springer, Singapore, pp 727–736
9. Hussaian Basha CH et al (2020) Mathematical design and analysis of photovoltaic cell using MATLAB/Simulink. *Soft computing for problem solving*. Springer, Singapore, pp 711–726
10. Raj JS (2012) Energy efficient sensed data conveyance for sensor network utilizing hybrid algorithms. *IRO J Sustain Wirel Systems* 04(2019):235–246 (December 2012)
11. Shakya S, Lalitpur NP (2020) Intelligent and adaptive multi-objective optimization in WANET using bio inspired algorithms. *J Soft Comput Paradigm (JSCP)* 2(01):13–23
12. Suma V (2020) Automatic spotting of sceptical activity with visualization using elastic cluster for network traffic in educational campus. *J Ubiquit Comput Commun Technol* 2(2020):88–97
13. Sungeetha A, Rajesh S (2020) Novel shared key transfer protocol for secure data transmission in distributed wireless networks. *J Trends Comput Sci Smart Technol (TCSST)* 2(02):98–108
14. Hussaian Basha CH et al (2019) Design of an LPF based slider controller for THD reduction in solar PV B-4 inverter. In: 2019 IEEE international conference on electrical, computer and communication technologies (ICECCT). IEEE
15. Hussaian Basha CH, Rani C, Odofin S (2018) Design and switching loss calculation of single leg 3-level 3-phase VSI. In: 2018 international conference on computation of power, energy, information and communication (ICCPEIC). IEEE
16. Chandramouli A, Sivachidambaranathan V (2019) Extract maximum power from PV system employing MPPT with FLC controller. *Power* 1(4)
17. Hussaian Basha CH, Rani C, Odofin S (2018) Analysis and comparison of SEPIC, Landsman and Zeta converters for PV fed induction motor drive applications. In: 2018 international conference on computation of power, energy, information and communication (ICCPEIC). IEEE

Chapter 20

Investigation on Microstructural Characteristics of Zn Alloy MMC for Bearing Application



Santosh Janamatti, Umesh Daivagna, Madeva Nagaral,
and Veerabhadrapa Algur

Abstract In the recent trends, Zinc based composite materials are popular in most applications like automotive, aircraft, military and others. The main concern of the study is to prepare metal matrix composites [MMCs] wherein zinc and tin are used as matrix and B_4C is added as reinforcement. Varying the quantities of like B_4C 0, 2, 4, 6 and 8% by weight are added and the specimens are prepared by two step stir casting method and machined as per ASTM standards. The samples are then subjected to microstructural tests like SEM, EDS and XRD examinations. The obtained results are compared with those of as-cast conditions. SEM micrograph reveals the uniform distribution of B_4C particulates in the Zn–Tin matrix and is confirmed by EDS analysis. Further, XRD analysis confirmed the B_4C phases on Zn–Tin matrix

Keywords Zinc · Tin · B_4C particulates · Stirs casting · SEM · EDS · K_2TiF_6

1 Introduction

A MMC materials are materials made from two or more constituent materials with significantly different physical properties (Fig. 1).

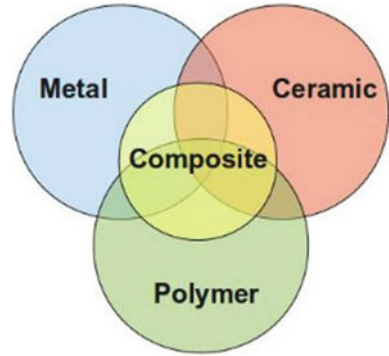
Most commonly used matrixes are aluminium, magnesium, copper, titanium and zinc. The most commonly used reinforcement is silicon carbide, alumina, boron, graphite and fly ash. Development of these materials is a subject of great interest as they offer attractive combination of physical and mechanical properties, which cannot be obtained in monolithic alloys. The zinc alloy is used as a replacement material for bronze alloys which is used for bearing applications [1]. Metal matrix composite

S. Janamatti (✉) · U. Daivagna
Department of Mechanical Engineering, BITM, Ballari, Karnataka 583101, India

M. Nagaral
Aircraft Research and Design Centre, HAL, Bangalore 560037, India

V. Algur
Department of Mechanical Engineering, RYMEC, Ballari, India
e-mail: veereshalgur@rymec.in

Fig. 1 Types of composites



(MMC) is widely used composite material in aerospace, automotive, electronics and medical industries (Fig. 2).

Zinc metal matrix composites (ZMMC) can be processed by methods as liquid metallurgy because of simplicity in processing and better properties. K_2TiF_6 halide salt is mixed uniformly with B_4C during casting and has resulted in better bonding between Zn alloy and B_4C and also use of mechanical stirrer and rigorous stirring helps in the homogeneous distribution of particulates in the metal matrix. Two-step addition of reinforcing particulates is adopted in liquid metallurgy which helps in the homogenous distribution and to overcome the agglomeration of particulates [2]. Metal matrix composite containing Zinc85%–Tin15% wt% with B_4C 0, 2, 4 and 6, 8 wt% reinforced samples were fabricates using two stage stir casting method.



Fig. 2 Types of composites components

2 Literature Survey

Nagaral et al. [2] studies the Influence of Two Stage Stir Casting Process on Mechanical Characterization and Wear properties of Al matrix Nanocomposites Manikandan et al. [3] describes the mechanical and tribological behaviour of Al7075 matrix by using boron carbide and cow dung as reinforcement. Park et al. [4] studied the dispersion in B_4C over Al matrix for automated quantification application. Mistrya et al. [5] finding the frictional properties of Si_3N_4 preinforced Al matrix by adopting the electromagnetic stir casting. Describes [6] the mechanical and tribological properties of silicon carbide based Al metal matrix composites. Balokhonov et al. [7] discussed the Microstructural analysis of deformation and fractural behaviour of MMC. Kumara et al. [8] describes the structural and tribological behaviour of Al–SiC–Cr hybrid MMC for high wear resistance applications. Aherwara et al. [9] studies the effect of B_4C on AA7075 based hybrid composite for tribological applications. Samuel [10] the paper finding that Al6061/sea sand composite has higher density and lower porosity compared with Al6061/ Al_2O_3 and Al16061/Sic. Akbar et al. [11] this review article contains substantial aspects of stir casting and effect of various reinforcement various challenges for future research. Kumar et al. [12] this paper finding with increasing % MWNCTs the wear rate and coefficient of friction decreases which is attributed the micro hardening. Abbas et al. [13] studied the Tribological effects of carbon nanotubes on magnesium alloy composites by stir casting process. Sharma et al. [14] worked on the study of fabrication methods of aluminium based composites focused on stir casting process. Bhowmik et al. [15] studied Tribological behaviour of Al7075– TiB_2 Metal Matrix Composites prepared by stir casting process.

3 Methods and Materials

The Zinc85%–Tin15% wt% with B_4C 0, 2, 4 and 6, 8 wt% reinforced samples were fabricates using two stage stir casting method. The electric resistance furnace and materials were used for casting is shown in Fig. 1. Required wt% of Zn–Sn alloy as matrix material as in billet shapes were placed in a carbide crucible, which was placed inside the furnace maintain at a temperature of around 750 °C. At this temperature entire Zn–Sn alloy was melt after melting of base alloy collect reinforcement and calculate required wt% of B_4C powder. Calculated amount of reinforcement was added into crucible which contains melted Zn alloy. Which involve two stage additions of calculated amount of reinforcement during stirring Potassium Titanium Fluoride (K_2TiF_6) degassing powder was also added into molten metal, which helps to remove the gases from the melt [2]. This two stage casting method helps to increase bonding strength of the matrix and ceramic reinforcement (Fig. 3).

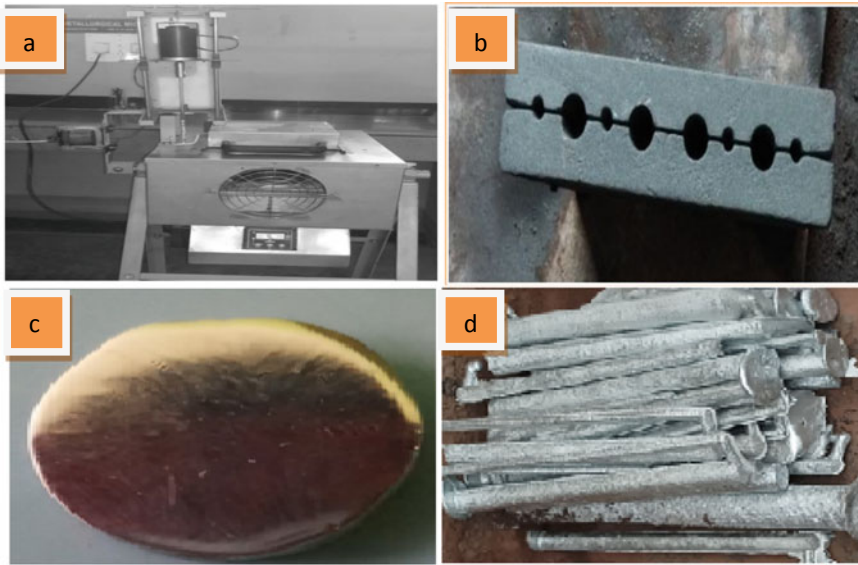


Fig. 3 a Electric arc furnace, b casting die, c fabricated specimen for SEM and d fabricated composite samples

4 Results and Discussion

The micrographic studies are useful in finding the uniform dispersion of reinforcement particulates over the base matrix, which have a tremendous effect on the mechanical and tribological properties. Microstructural features have been studied using SEM, EDS and X-Ray diffraction Analysis.

SEM Analysis.

Figure 4 shows that the Scanning Electron Microscope micrographs of (a) cast Zn85%–Sn15% alloy (b) Zn–Sn matrix with 2 wt% B₄C (c) Zn–Sn matrix 4 wt% B₄C composites (d) Zn–Sn matrix 6 wt% B₄C composites (e) Zn–Sn matrix 8 wt% B₄C composites. From Fig. 2(b–e) is the evidence of distribution of B₄C reinforcement particulates in different wt% of B₄C and it can be observed that there was a fine and uniform distribution of particles without any cluster formation. Further, from the photographs, that cast metal matrix composites shows very low segregation; due to its involved two stage reinforcement mixing method.

EDS Analysis.

From the Fig. 5a–d shows Energy Dispersive X-Ray Spectrographs of Zn85–Sn15 alloy with 2, 4 and 6 wt% of boron reinforcement respectively. The Energy Dispersive Spectroscopy analysis is the evidence to confirm the existence of boron particles in the Zn–Sn alloy matrix. And also this graph confirmed boron and carbide elements are present in Zn alloy matrix by indicating B (Boron) and C content (Carbide) in EDS analysis.

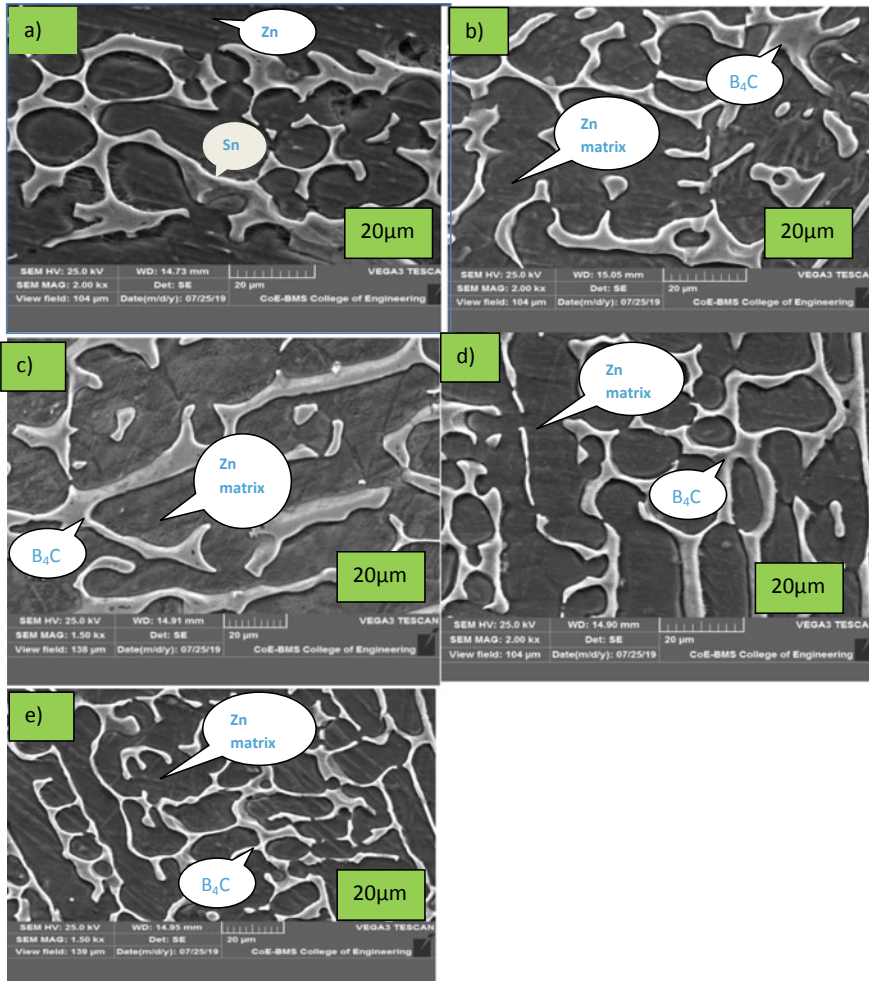


Fig. 4 The SEM micrographs of **a** casted Zn–Sn matrix and **b** Zn–Sn with 2 wt% of B₄C, **c** cast Zn–Sn with 4 wt% of B₄C reinforcement and **d** Zn–Sn with 6 wt% of B₄C reinforcement, **e** Zn–Sn with 8 wt% of B₄C reinforcement

XRD Analysis.

Figure 6a–e shows XRD Analysis of Zn–Sn alloy with 2, 4 and 6 wt% of B₄C reinforcement respectively. XRD Analysis is the evidence to confirm the presence of Sn phase over Zn matrix and boron carbide phase in the Zn–Sn alloy matrix.

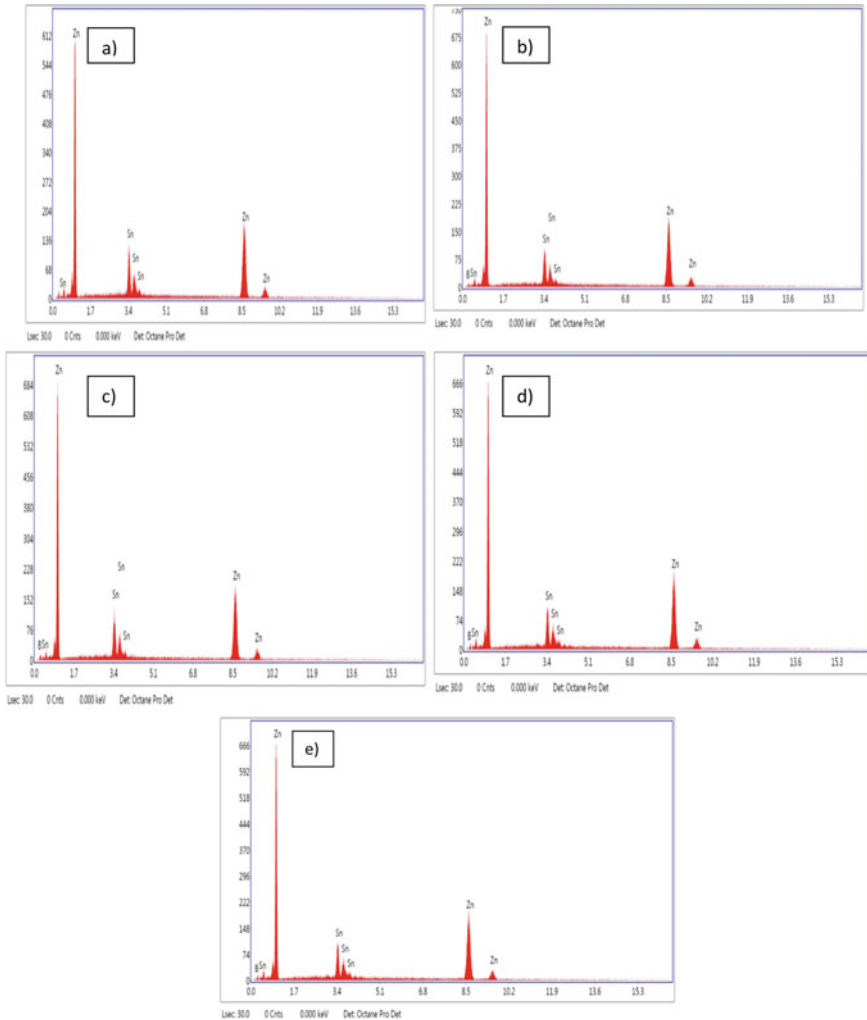


Fig. 5 a Energy dispersive spectroscopy of casted Zn85–Sn15 Alloy with b 2 wt% of c 4 wt%, d 6 wt% and e 8 wt% B₄C particulates

4.1 Future Work and Limitations of Proposed Work

Evaluation of mechanical properties like Tensile and compression behaviour Zn–85% Tin–15 and 2, 4 and 6, 8 wt% of B₄C nano composites.

Studies on wear behaviour of zinc–85% tin 15 and 2, 4 and 6, 8 wt% of B₄C nano composites by taking various parameters sliding velocity and varying load. Mechanical stirring is the vital importance of this process. Composites with up to

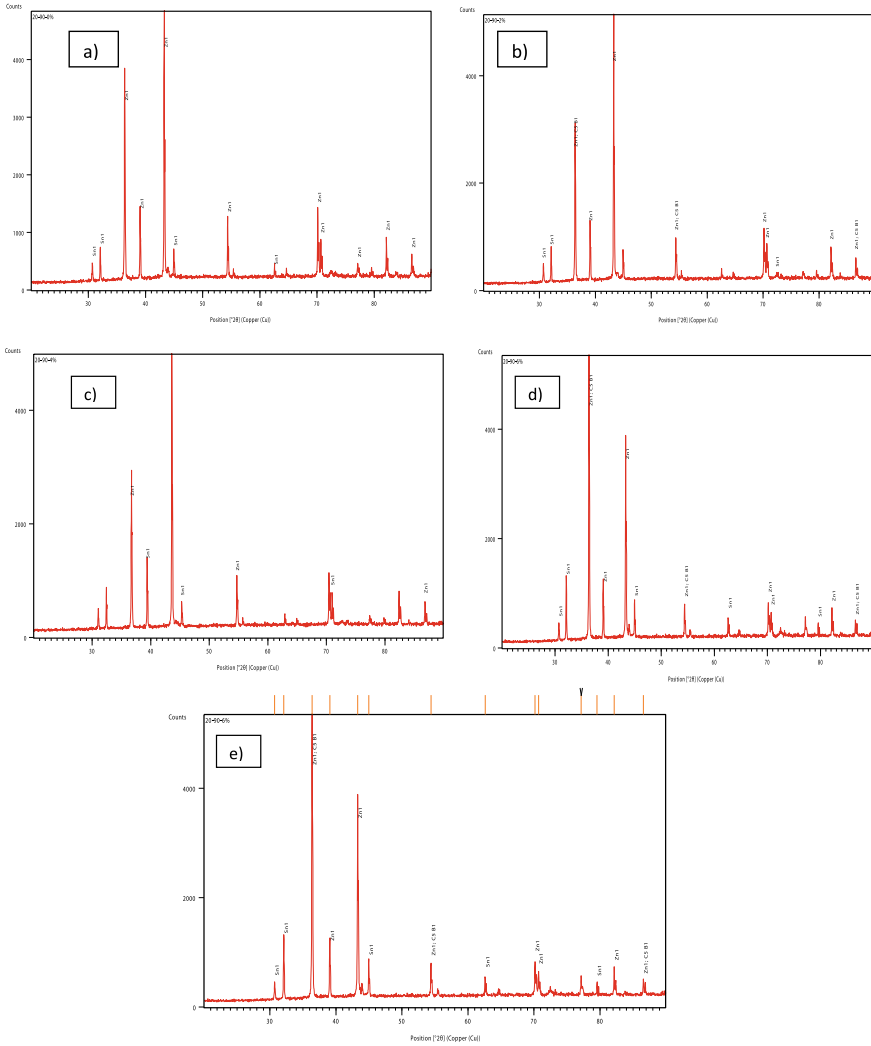


Fig. 6 a X-Ray diffraction analysis of casted Zn85–Sn15 Alloy with b 2 wt%, c 4 wt%, d 6 wt% and e 8 wt% of B₄C Reinforcement

30% volume fractions can be produced by using normal stir route. segregation of reinforcing particles is the problem of this stirring process during solidification.

5 Conclusion

The paper is focused on the development and characterization of the microstructure of Zinc alloy and its composites containing wt% of B₄C nano particles. From the above results and discussion, the following conclusions are made:

1. The nano composites containing 2, 4, 6 and 8 wt% of B₄C particulates were prepared from Two stage stir casting process technique which helps to increases bonding strength of the matrix and ceramic reinforcement by avoid segregation problems.
2. Zn–Sn alloy with 0, 2, 4, 6 and 8 wt% B₄C nano composites samples were prepared successfully by using two step stir casting route.
3. The SEM confirmed uniform distribution of nano B₄C particulates in Zn–Sn base alloy and presence of boron and carbide elements in Zn–Sn alloy Matrix.
4. The Energy Dispersive Spectroscopy analysis is the evidence to confirm the existence of boron particles in the Zn–Sn alloy matrix. And also boron and carbide elements are present in Zn alloy matrix by indicating B (Boron) and C content (Carbide) in EDS analysis.
5. XRD Analysis is the evidence to confirm the presence of Sn phase over Zn matrix and boron carbide phase in the Zn–Sn alloy matrix.

References

1. Algur V, Kabadi VR, Ganachari SM, Rao Chavan V (2017) Influence of mn content on tribological wear behaviour of ZA-27 alloy. *Mater Today Proc* 4(10):10927–10934. <https://doi.org/10.1016/j.matpr.2017.08.048>
2. Nagaral M, Hiremath V, Auradi V, Kori SA (2018) Influence of two-stage stir casting process on mechanical characterization and wear behavior of AA2014–ZrO₂ nano-composites. *Trans Indian Inst Met* 71(11):2845–2850. <https://doi.org/10.1007/s12666-018-1441-6>
3. Manikandan R, Arjunan TV, Akhil AR (2020) Studies on micro structural characteristics, mechanical and tribological behaviours of boron carbide and cow dung ash reinforced aluminium (Al 7075) hybrid metal matrix composite. *Compos Part B Eng* 183(October 2019). <https://doi.org/10.1016/j.compositesb.2019.107668>
4. Park B, Lee D, Jo I, Lee SB, Lee SK, Cho S (2020) Automated quantification of reinforcement dispersion in B₄C/Al metal matrix composites. *Compos Part B Eng* 181(May 2019):107584. <https://doi.org/10.1016/j.compositesb.2019.107584>
5. Mistry JM, Gohil PP (2019) Experimental investigations on wear and friction behaviour of Si₃N₄p reinforced heat-treated aluminium matrix composites produced using electromagnetic stir casting process. *Compos Part B Eng* 161(August 2018):190–204. <https://doi.org/10.1016/j.compositesb.2018.10.074>
6. Gowrishankar MC, Hiremath P, Shettar M, Sharma S, Satish Rao U (2020) Experimental validity on the casting characteristics of stir cast aluminium composites. *J Mater Res Technol* 9(3):3340–3347. <https://doi.org/10.1016/j.jmrt.2020.01.028>
7. Balokhonov R, Romanova V, Kulkov A (2020) Microstructure-based analysis of deformation and fracture in metal-matrix composite materials. *Eng Fail Anal* 110(January):104412. <https://doi.org/10.1016/j.engfailanal.2020.104412>

8. Kumar J et al (2020) Comparative study on the mechanical, tribological, morphological and structural properties of vortex casting processed, Al–SiC–Cr hybrid metal matrix composites for high strength wear-resistant applications: fabrication and characterizations. *J Mater Res Technol* 9(6):13607–13615. <https://doi.org/10.1016/j.jmrt.2020.10.001>
9. Aherwar A, Patnaik A, Pruncu CI (2020) Effect of B₄C and waste porcelain ceramic particulate reinforcements on mechanical and tribological characteristics of high strength AA7075 based hybrid composite. *J Mater Res Technol* 9(5):9882–9894. <https://doi.org/10.1016/j.jmrt.2020.07.003>
10. Akinwamide SO, Akinwamide SO, Lesufi M, Akinribide OJ, Mpolo P, Olubambi PA (2020) Evaluation of microstructural and nanomechanical performance of spark plasma sintered TiFe–SiC reinforced aluminium matrix composites. *J Mater Res Technol* 9(6):12137–12148. <https://doi.org/10.1016/j.jmrt.2020.08.068>
11. Akbar HI, Surojo E, Ariawan D, Putra GA, Wibowo RT (2020) Effect of reinforcement material on properties of manufactured aluminum matrix composite using stir casting route. *Procedia Struct Integr* 27(2019):62–68. <https://doi.org/10.1016/j.prostr.2020.07.009>
12. Kumar A, Singh RC, Chaudhary R (2020) Recent progress in production of metal matrix composites by stir casting process: an overview. *Mater Today Proc* 21(November):1453–1457. <https://doi.org/10.1016/j.matpr.2019.10.079>
13. Abbas A, Huang SJ, Ballóková B, Sülleiová K (2019) Tribological effects of carbon nanotubes on magnesium alloy AZ31 and analyzing aging effects on CNTs/AZ31 composites fabricated by stir casting process. *Tribol Int* 142(July):2020. <https://doi.org/10.1016/j.triboint.2019.105982>
14. Sharma AK, Bhandari R, Aherwar A, Pinca-Bretotean C (2020) A study of fabrication methods of aluminum based composites focused on stir casting process. *Mater Today Proc* 27:1608–1612. <https://doi.org/10.1016/j.matpr.2020.03.316>
15. Bhowmik A, Dey D, Biswas A (2019) Tribological behaviour of aluminium-titanium diboride (Al7075–TiB₂) metal matrix composites prepared by stir casting process. *Mater Today Proc* 26(March):2000–2004. <https://doi.org/10.1016/j.matpr.2020.02.436>

Chapter 21

Studies on Polymer Composites for Producing Hybrid Material Sheets Processed by Friction Stir Welding



Harish Kumar and S. V. Satish

Abstract Friction stir welding is a completely new technology for joining similar and different material combinations such as aluminum alloys, cast iron, copper, etc. and nonmetals such as thermoplastic polymers. The FSW (friction stir welding) process is mainly used in aerospace and automotive industries as it joins many thermoplastics without defects. In this paper, dissimilar thermoplastic materials (High density polyethylene and polypropylene) were friction stir butt welded, and some organic materials in the form of fibers (natural fibers or aramid) were added into the joint line during the welding process to make it a hybrid. By doing hybrid material we have more chances of improving the strength and toughness properties of the hybrid joint. As in the previous studies, only base or parent materials were friction stir welded without making hybrid material.

Keywords Friction stir welding machine · Organic materials · Thermoplastics · Thermoplastics joining · Process parameters · Material properties

1 Introduction

Friction stir welding (FSW) process was introduced in the industry in the year 1991 [1, 2]. The FSW process is a solid state joining technique which means that the joining of two materials will take place without melting the base materials. FSW process uses a rotating tool and is made of high speed steel (HSS) or high carbon steel material (HCS) to join two materials and the process is completed in five different stages (rotate, plunge, weld, pull off, and finish). In friction stir welding process the weld is created by both frictional heating and mechanical deformation.

The working principle of the process is shown in Fig. 1. The friction stir welding equipment uses a non-consumable spinning tool which has two major parts; a probe

H. Kumar (✉)

Department of Mechanical Engineering, Brindavan College of Engineering, Bangalore, India

S. V. Satish

Department of Mechanical Engineering, PESIT, Bangalore, India

e-mail: svsatish@pes.edu

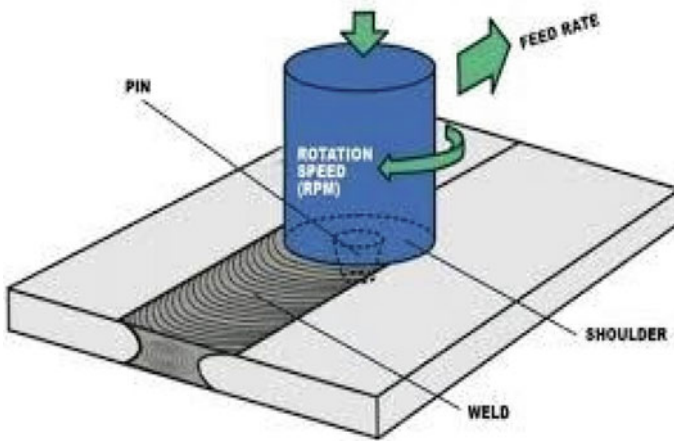


Fig. 1 The working principle of friction stir welding process

(pin) and a shoulder. The pin diameter is usually less than the shoulder diameter. The work pieces which are to be joined are properly clamped on the table of the machine using fixtures or using some other work holding devices. The non-consumable rotating tool which consists of a probe is slowly placed into the small gap between the two work pieces that are to be joined. Friction is generated between the spinning tool and work piece. The friction generated is mainly due to the tool rotation into the work material which moves across the joint line and causes the joining of the two sheets. The process is suitable for joining similar and dissimilar thick materials, thin metals, pipes, and hollow sections with less distortion and less wastage of material [3]. The FSW process was also suitable for joining both metals (steel, cast iron, copper, etc.) and non-metals (thermoplastics) with flat surfaces is produced. The FSW process can easily join many thermoplastic materials as it has good properties and is available at low cost. FSW has been successfully utilized for polymers. In joining any ferrous, nonferrous, and nonmetals especially polymers by friction stir welding process, rotational speed parameter plays a very important role. Whenever joining polymer materials by friction stir welding technology, a higher pin rotational speed causes damage to the base materials and lower pin rotational speed causes pores in the joint line which in turn causes weak joint strength. Therefore, before joining any material especially polymeric materials it becomes necessary to examine the different parameters in friction stir welding process especially pin rotational speed which contributes highest percentage in the joint strength in friction stir welding process.

Thermoplastic materials are mainly used in the automotive and aerospace industries as it has low density and can be easily manufactured.

The FSW process doesn't require additional materials such as filler rod, no shielding gas, requires less energy, less material waste is observed during the welding process and it also avoids harmful radiations associated with the fusion welding

processes [4, 5]. The FSW process is mainly used in transportation industries such as Ship building, automotive, aerospace, and railway industries.

2 Polymers

Polymer is a Greek word and is made of two parts. 'Poly' and 'mer' where poly means many and mer means part. Polymer is a large molecule made of many smaller units. Most polymers are based on carbon and are therefore considered organics. Most polymers are having adequate strength. Further, the strength of the polymeric materials can be increased by reinforcing the fibrous materials.

Types of organic polymers.

Organic Polymers are mainly of 2 types.

- a. Thermoplastic polymers
- b. Thermosetting polymers

3 Thermoplastic Polymers

Thermoplastics are meltable in nature which means that they soften upon heating and harden when cooled. Such types of materials can be recycled or remolded easily. Generally, most thermoplastics are soft and flexible. The main examples of thermoplastic materials are polyethylene, polypropylene, PVC (polyvinyl chloride), polystyrene, etc. Thermoplastics possess linear structure and due to this, they are soft as compared to thermoset materials. On the other hand, most thermoset materials are hard and are not flexible (Fig. 2).

Thermoplastics are alternative materials for steel and cast iron due to its low density, low cost, and ease of processing in many industries such as in aerospace and automotive industry.

Thermoplastics are mainly used for making many products such as pipes, bottles, and tanks, etc.

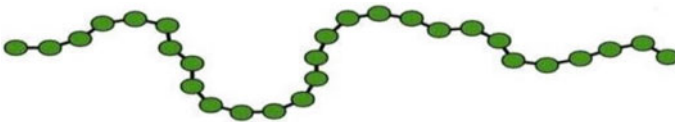


Fig. 2 Structure of thermoplastics

3.1 *High Density Polyethylene (HDPE) Appearance and Its Properties*

See Fig. 3 and Table 1.

3.1.1 Polypropylene (PP) Appearance and Its Properties

See Fig. 4 and Table 2.

3.1.2 Applications of Thermoplastics in Automotive Industry

See Figs. 5 and 6.

4 Hybrid Materials

Hybrid materials are formed by mixing organic and inorganic compounds. It is mainly used for improving the properties. The mixing of organic and inorganic compounds

Fig. 3 HDPE plastic

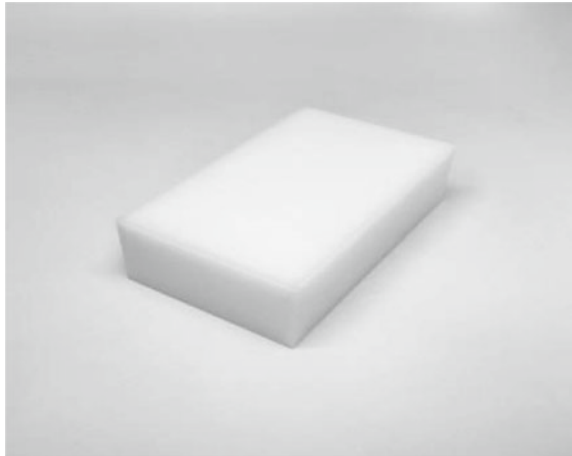


Table 1 Properties of high density polyethylene

Density °C	Melting point g/cm ³	Shrink rate %	Specific gravity	Chemical formula
0.93–0.97	132	1.7–2.9	0.95	(C ₂ H ₄) _n

Fig. 4 PP plastic**Table 2** Properties of polypropylene

Density g/cm ³	Melting point °C	Shrink rate %	Specific gravity	Chemical formula
0.895–0.92	160–166	1.5–2.0	0.91	(C ₃ H ₆) _n

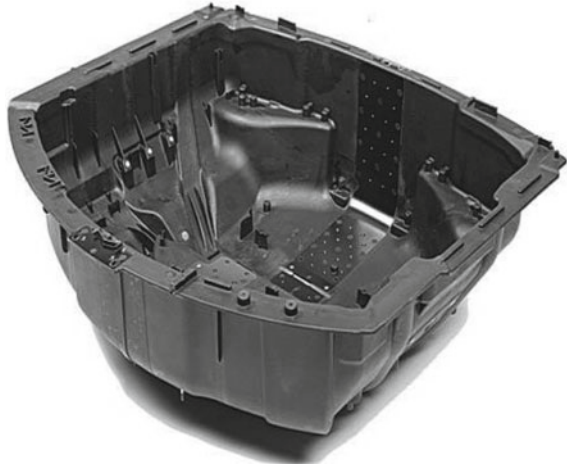
**Fig. 5** Car bumper

will be done at the nanometers scale. Hybrid materials are extremely new. They are strong, smart, and self-repairing.

Hybrid can be either same or they can be different with dimension of Angstrom to nanometer. The properties of the hybrid materials are different from that of the individual material properties. Therefore hybridization helps in improving the properties such as torsional rigidity, strength, toughness, etc.

Types of Hybrid Materials.

- a. Class I hybrids: In this type of hybrid, organic and inorganic compounds don't have chemical bonding between them.

Fig. 6 Car body

- b. Class II hybrids: In this type of hybrid materials organic and inorganic compounds have sufficient chemical bonding between them.

5 Thermoplastics Joining

Friction Stir Welding (FSW) process, in the beginning, was used only to join Al alloys [6, 7]. The process also has the capacity to join different types of ferrous, nonferrous, and nonmetals [8–10] such as thermoplastics materials. The main reason for using thermoplastics in various industries is its low density, cost, and good properties. Thermoplastic materials can be easily friction welded as it is meltable in nature. The different thermoplastics which are friction welded include polyethylene [11], polypropylene [12], polycarbonate, polyamide, and PMMA (Poly methyl methacrylate).

Dissimilar thermoplastic materials such as polyethylene and polypropylene were friction welded at higher rotational speed of 2500 RPM and 100 mm/min travel speed [13]. PMMA-ABS polymers were friction stir welded [14]. In FSW, tool geometry like pin diameter, pin length, and pin cross section affects the quality of weld [15].

5.1 Friction Stir Welding Machine

See Fig. 7.



Fig. 7 Friction stir welding machine

5.2 *Friction Stir Welding Machine Specification*

See Table 3.

6 **Conclusion**

This review paper presents the friction stir processing of Polymer composites (thermoplastic polymers). Thermoplastics which operates at higher temperatures require various process parameters like higher rotational speed, low travel speed, and a small amount of plunge depth is required during the welding process to achieve a high weld strength. Besides, to enhance the weld strength, efforts will be towards producing hybrid material sheets via friction stir welding process. Producing a hybrid will provide good mechanical properties especially the tensile strength at the joint. As the process also provides a stronger joint (strength equals or greater than the base material strength) without making hybrid but an attempt is made if including some kind of organic materials like aramid or natural fibers at joint line during the welding

Table 3 Equipment specification

Spindle motor	12 Kw/440 V
Spindle speed	300–3000 rpm
Spindle nose	ISO50
Vertical stroke (hydraulic)	00 mm
Manual stroke	25 mm
T slot table	250 × 600
Stroke	600 mm
Rapid rate	3000 mm/min
Feed rate (manual Feed)	0–1500 mm/min
Vertical cylinder	Ø300
Feed force	3–5 ton
Horizontal cylinder	Ø63
Feed force	0.5–2.5 ton

process will provide a higher weld strength or the weld strength remains same as the base material strength when it was not made as hybrid.

References

1. Thomas WM, Nicholas ED, Needham JC (1991) Friction stir welding international patent PCT/GB92102203 and Great Britain patent 9125978.8
2. Mishra RS, Ma ZY (2005) Friction stir welding and processing. *Mater Sci Eng* 50(1–2):1–78
3. Ghosh M, Kumar K, Kailas SV, Ray AK (2010) Optimization of friction stir welding parameters for dissimilar aluminum alloys. *Master Des* 31:3033–3037
4. Rodrigues DM, Loureiro A, Leitao C, Leal RM, Chaparron BM, Vilaca P (2009) Influence of friction stir welding parameters on the microstructural and mechanical properties of friction AA 6016–T4 thin welds. *Master Des* 30:1913–1921
5. Feng AH, Xiao BL, Ma ZY (2008) Grain boundary misorientation and texture development in friction stir welded SiC/Al–Cu–Mg composite. *Master Sci Eng A* 497:515–518
6. Colligan K (1999) Materials flow behaviour during friction stir welding of aluminum. *Weld Res Suppl* 78(7):229–237
7. Murr LE, Liu G, McClure JC (1997) Dynamic recrystallization in friction stir welding of aluminum alloy 1100. *J Mater Sci Lett* 16:1801–1803
8. Barlas Z, Uzun H (2010) Microstructure and mechanical properties of friction stir butt welded dissimilar pure copper/brass alloy plates. *Int J Mat R (Zeitschrift fur METALLKUNDE)* 101(6):801–807
9. Ramirez AJ, Juhas MC (2003) Microstructural evolution in Ti–6Al–4V friction stir welds. *Mater Sci Forum* 426432:2999–3004
10. Sato YS, Nelson TW, Sterling CJ, Steel RJ, Petterson CO (2005) Microstructure and mechanical properties of friction stir welded SAF 2507 super duplex stainless steel. *Mater Sci Eng A* 397(1–2):376–384
11. Bozkurt Y (2012) The optimization of friction stir welding process parameters to achieve maximum tensile strength in polyethylene sheets. *Mater Des* 35:440–445
12. Bilici MK (2012) Application of Taguchi approach to optimize friction stir spot welding parameters of polypropylene. *Mater Des* 35:113–119

13. Eslami S (2015) Effects of friction stir welding parameters with newly developed tool for lap joint of dissimilar polymers. *Procedia Eng* 114:199–207
14. Dashatan SH (2013) Friction stir spot welding of dissimilar polymethyl methacrylate and acrylonitrile butadiene styrene sheets. *Mater Des* 45:135–141
15. Threadgill P (2009) Friction stir welding of aluminium alloys. *Int Mater Rev* 54(2):49–93

Chapter 22

Optical and Electrical Properties of ZnO Dispersed Polymer Nanocomposites Films



Sushma Jha, Vaishali Bhavsar, K. P. Sooraj, Mukesh Ranjan, and Deepti Tripathi

Abstract A comparative study is carried out to observe the effect of dispersing Zinc Oxide (ZnO) nanoparticles in two different host matrices of Polyvinylalcohol (PVA)—Polyvinylpyrrolidone (PVP)—Polyvinylalcohol (PVA)—Carbomethyl Cellulose (CMC) on their structural, optical and electrical properties. The concentration of ZnO in the blend films was kept low. The XRD diffractogram of both the polymer nanocomposite films (PNCs) exhibited characteristic peaks of ZnO confirming the dispersion of nanoparticles in blended films. The SEM micrographs of these PNC films had shown uniform dispersion of ZnO nanoparticles in both matrices. The analysis of optical and electrical properties indicates appreciable modification in these properties on inclusion of small amount of ZnO in both the matrices. ZnO dispersed PVA—CMC film shows enhanced absorption in UV region with decreased band gap and higher σ_{dc} values as compared to ZnO dispersed PVA—PVP film suggesting PVA—CMC—ZnO film to be a promising material in the area of green electronics and optoelectronics.

Keywords Nanocomposite films · Polymer blends · Optical properties · Electrical conductivity

1 Introduction

Polymer nanocomposites (PNCs) based on bio-compatible polymers are the emerging class of material having less adverse impact on eco-system. Eco-friendly PNCs have attracted considerable interest of the scientific community as it elegantly carries the promising features of inorganic polymers and influential properties of

S. Jha (✉) · V. Bhavsar · D. Tripathi

Department of Physics, School of Science, Gujarat University, Ahmedabad, Gujarat, India

V. Bhavsar

Applied Sciences and Humanities Department, SAL College of Engineering, Ahmedabad, Gujarat, India

K. P. Sooraj · M. Ranjan

Institute for Plasma Research, Gandhinagar, Gujarat, India

nanofillers [1–5]. Thus, these are potential materials for various applications such as flexible optoelectronics, microelectronics, bio-sensors, UV absorbers, EMI shields, etc. [1–20]. The inclusion of a small amount of nanofillers in the matrix of polymers/polymer blends appreciably enhances their structural, optical, electrical, dielectric and mechanical properties [1, 4]. Modifications in these properties strongly depend upon the size, concentration, dispersion of nanofillers in the base matrix and their compatibility/miscibility with constituent polymers [1–6]. Therefore, the selection of polymers and suitable nanofiller is crucial in designing PNC material for a specific application. Among the wide range of polymers, Polyvinyl alcohol (PVA), Polyvinyl pyrrolidone (PVP), Polyvinyl chloride (PVC), Sodium carboxymethyl cellulose (CMC), Polyethylene oxide (PEO), and Polymethyl methacrylate (PMMA) are some of the important bio-compatible polymers extensively studied in the form of blends/nanocomposites for various applications [1–24].

The bio-compatible polymer blend of PVA and PVP is well studied base matrix possessing good film forming ability with good thermal and mechanical stability. These blend films are used to develop novel multifunctional PNCs due to the presence of –OH and –C–O functional group in the polymer main chain [3, 6, 7, 10–12] which makes it compatible with varied classes of nanofillers such as metal oxides, ceramics, ferrites, semiconducting oxides, etc. As observed for PVA–PVP, blending PVA with CMC, which is synthetically modified natural polymer with good biodegradation property and studying their various properties can also be of interest in terms of investigating their suitability for application in green electronics and biomedical fields.

Literature review shows that the polymer blend of PVA–CMC results in a bio-compatible, water soluble and low-cost material which possesses good mechanical strength [13–18]. Further, to develop various types of multifunctional PNC material with these polymer matrices researchers have used different types of inorganic bio-compatible nanofillers (Al_2O_3 , SiO_2 , TiO_2 , SnO_2 , and ZnO) as additives and carried out detailed studies on these PNCs [1, 3–5, 9–14]. Moreover from the mentioned nanofillers, ZnO is one of the important nanofillers possessing high UV-absorbance, low dielectric constant with appreciable chemical, thermal and environmental stability [1, 4, 10, 14, 20–24]. It belongs to the class of wide band gap semiconductors and has been in much focus recently. Being highly crystalline in nature and its ability to interact with variety of polymers and their blends [1, 10, 20], ZnO is vastly used nano-additive for the development of potential multifunctional PNC material applied in the area of optoelectronics, gas sensors, UV-shields and UV-emitters [1, 10].

Since PVA–PVP and PVA–CMC are promising host matrices, here an attempt has been made to carry out a comparative study to investigate the effect of ZnO on these matrices. Free-standing and flexible polymer nanocomposite films of PVA–PVP– ZnO and PVA–CMC– ZnO were prepared. Further, the effect of dispersing ZnO on the structural, optical and electrical properties of PVA–PVP and PVA–CMC matrices were studied and comparative results are reported.

2 Experimental Details

2.1 Materials

PVA of average molecular weight (M_w) 85,000–124,000 gm/mol and PVP of $M_w = 40,000$ gm/mol was supplied by Sigma Aldrich. CMC of high viscosity and ZnO nanopowder of particle size 10 nm–30 nm, purchased from HPLC. Distilled water was used as common solvent for the preparation of all films.

2.2 Preparation of Polymer Nanocomposites Films

For preparing films, solution cast technique was used. The films were prepared at 28 °C. For this PVA–PVP in ratio of 3:2 and PVA–CMC in ratio of 2:1 were dissolved separately in preheated double distilled water (DDW). Solutions were heated while simultaneously stirring them for 1 h. The heater was then turned off and the solution was further stirred at room temperature till a homogenous solution was obtained. Zinc oxide (ZnO) nanoparticles with 2, 5, 7 and 10% weight concentration were dissolved in DDW and two times it was sonicated. ZnO was then mixed with solutions of PVA–PVP and PVA–CMC and further stirred for 1 h. Entire mixture was further kept in sonication bath for 10 min to assure the homogeneous dispersion of ZnO. At last, the solution was poured into a glass petri dish and left to dry at room temperature. Further, the prepared samples were taken off from the petri dish and preserved for their characterizations.

2.3 Characterization Techniques

Structural characterization of the films was done using Bruker's X-ray Diffractometer (Model: D8 Discover) supplied by GMBH (Germany) with Cu–K α radiation ($\lambda = 1.540 \text{ \AA}$) in the scattering range of (2θ) 10°–60° with a scanning rate of 1° s⁻¹. Morphology of the samples was recorded on Scanning Electron Microscope (SEM) (Model: Merlin VP Compact) supplied by Carl Zeiss The UV–Visible absorption and transmission profiles of PNC films were recorded at room temperature in the range of 200–900 nm using Shimadzu-2600 Spectrophotometer. Absorption coefficient (α), optical energy band gap (E_{opt}), extinction coefficient (k) and Urbach energy (E_u) [2, 10, 19, 24] were estimated using absorption data. The DC electrical conductivity measurements were carried out by two probe methods using Agilent source metre (B2901A) attached with indigenous designed two probes of silver. The samples were placed between the silver plates and placed in a furnace at different temperatures. The current was measured at three different temperatures (298 K, 323 K and 353 K)

by applying voltage in the range of -20 V to $+20$ V DC. The activation energy was calculated using the slope of the curve according to the Arrhenius relation.

3 Results and Discussion

3.1 Structural Characterization

3.1.1 XRD Analysis

The XRD spectra of ZnO dispersed PNC films, PVA–PVP blend film and pure ZnO nanopowder are shown in Fig. 1a. The peaks observed at angle 31.77° , 34.44° , 34.44° , 36.27° , 45.47° , 47.54° , 56.59° , 62.87° , 66.36° , 67.93° , 69.05° , 72.57° , and 77.01° in XRD diffractogram of pure ZnO nanopowder correspond to hexagonal wurtzite structure of ZnO (JCPDS No: 36–1451) [21, 25, 26] and these peaks are in well accordance as reported in literature [10, 20, 21, 25]. The diffraction peaks seen at 19.09° , 31.20° , 32.71° , 33.88° , 35.82° , 43.85° , 46.95° , 56.17° , 62.28° ,

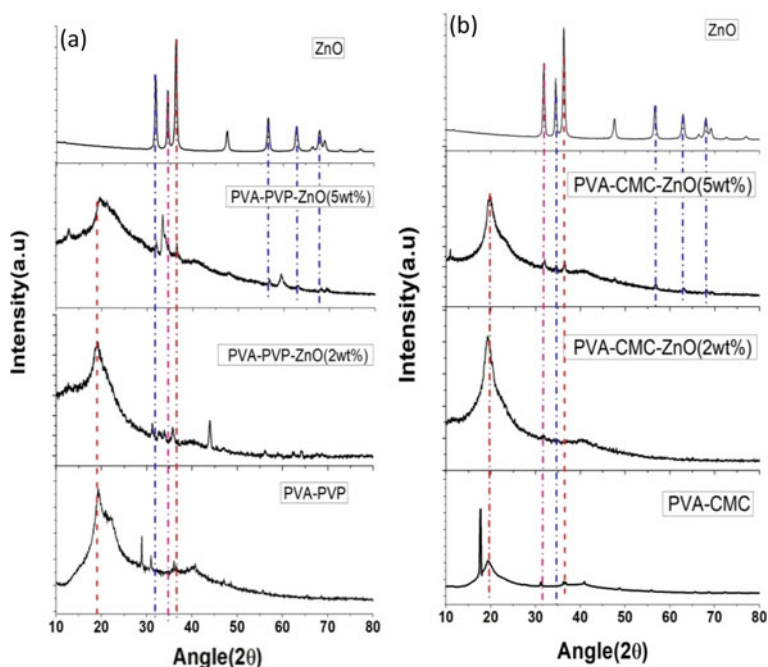


Fig. 1 XRD spectra of **a** PVA–PVP and ZnO (2 wt% and 5 wt%) dispersed nanocomposite films of PVA–PVP; **b** PVA–CMC and ZnO (2 wt% and 5 wt%) dispersed nanocomposite films of PVA–CMC

64.10°, 67.53°, and 68.70° in XRD pattern of PVA–PVP with 2 wt% concentration of ZnO correspond to the characteristic peaks of both (PVA–PVP) [6, 10–12] and ZnO. However, it was observed that the intensities of the peaks corresponding to ZnO in PVA–PVP–ZnO (2%) are low. On increasing the weight concentration of ZnO (5 wt%) in PVA–PVP matrix, the diffraction peaks associated with ZnO became prominent with more intensity whereas the peaks corresponding to PVA–PVP were turned broader. These observed modifications in the peak broadening indicate complexation of the functional group of ZnO with molecules of PVA–PVP and the presence of characteristic peaks of ZnO with marginal shifts in XRD pattern of PVA–PVP–ZnO suggests uniform dispersion of nanofiller in host matrix of PVA–PVP [4, 12].

The XRD pattern of PVA–CMC nanocomposite film with 2 wt% concentration of ZnO did not exhibit any distinct peaks of ZnO which may be due to lower concentration of filler content. For higher weight concentration of ZnO (5 wt%) in PVA–CMC blend, diffraction peak ($2\theta = 20^\circ$) associated with PVA–CMC broadens slightly which indicates the semi-crystalline nature of PVA–CMC film and complexation with ZnO [13–15, 17]. The peaks observed at 31.90°, 34.51°, 36.31°, 40.57°, 47.61°, 56.97°, 63.02°, 67.99° and 69.23° suggest the dispersion of ZnO in PVA–CMC matrix which undergo structural modification due to molecular interaction of constituent polymers with nanofiller [20, 21, 24]. A comparative analysis of XRD diffractograms of both the PNCs indicates that at lower weight concentration of nanofiller, the diffraction peaks associated with host polymer are more dominant with low intensities of the peaks associated with ZnO. Whereas, the intensities of the peaks associated with ZnO, were observed more pronounced for higher concentrations of nanofiller in both the PNC films. Peak broadening observed in the diffractogram of these PNC films suggest reduction in crystallinity on inclusion of ZnO in both the matrices which will expectedly result in enhanced optical and electrical properties of these films [26].

3.1.2 Morphological Analysis

The SEM micrographs of (PVA–PVP and PVA–CMC) blend films and nanocomposite films (PVA–PVP–ZnO and PVA–CMC–ZnO) were analyzed to observe the effect of ZnO nanofiller on the morphology of blend film and dispersion of nanofiller in the host. The SEM images of blend films and ZnO (5 wt%) dispersed nanocomposite films of (PVA–PVP and PVA–CMC) are shown respectively in Figs. 2a, b and 3a, b. It is observed that PVA–PVP blend film exhibits very smooth morphology indicating miscibility of PVA and PVP in the blend due to the formation of strong hydrogen bonding between (–O–H) hydroxyl and (–C=O) carbonyl groups present in PVA and PVP respectively [3, 10, 11]. For PVA–CMC blend film, uniform microstructure (floral pattern) can be seen throughout the surface which suggests marginal roughness in the morphology of blend film [13, 21]. The homogeneous surface of PVA–CMC blend film ascribed to the formation of strong hydrogen bond between carboxylic and hydroxyl group present in CMC and PVA respectively which ensure the miscibility of PVA with CMC [13–17, 21].

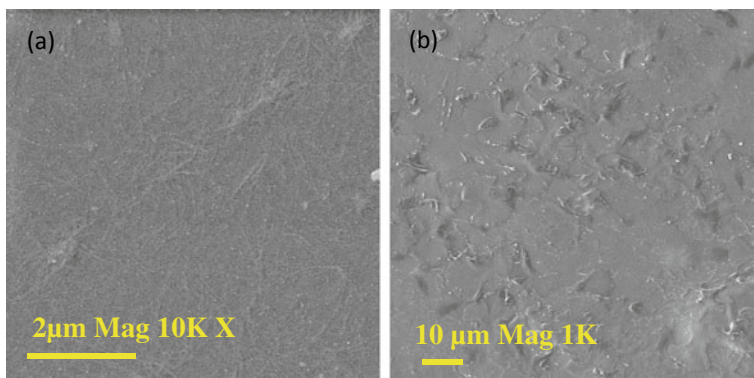


Fig. 2 SEM micrograph of pure **a** PVA–PVP blend and **b** PVA–CMC blend film respectively

The reported micrograph of ZnO nanoparticle in its pure form exhibit flowery, shuttle, flakey type, smashed flower like, scroll shaped, lung lobe type and spherical micro/nanostructures [10, 20, 21, 26]. The SEM micrograph of PVA–PVP–ZnO (Fig. 3a), exhibited smashed flower like structure throughout the surface which increases the overall roughness of the surface as compared to host matrix (PVA–PVP). For, PVA–CMC–ZnO (Fig. 3b) nanocomposite film, spherical structure of different sizes can be seen on the entire surface. Some traces of aggregation in the nanocomposite film can also be observed which attributes to the interfacial interaction between nano particles themselves [21]. Nano rod like or flaky structure was found in the enlarged view. The presence of these structures on the surface in both the matrices (Fig. 3a, b) indicate uniform dispersion of ZnO nanoparticle in host matrix and the interaction between the nanofiller and constituent polymers as also evident from XRD spectra of these nanocomposite films. On comparing the micrograph of ZnO dispersed nanocomposites of PVA–PVP and PVA–CMC, it was found that the growth of ZnO nanostructure and its dispersion in the matrix is different in both types of PNCs.

3.2 Optical Characterization

3.2.1 Absorption Spectra

Absorption spectra of ZnO (2 wt% and 5 wt%) dispersed nanocomposites films of (PVA–PVP) and (PVA–CMC) in UV–Vis range is shown in Fig. 4. All the films exhibited high absorption in UV region whereas the absorption decreases sharply with increasing wavelength (>500 nm) and become almost zero for host matrix. A sharp absorption peak centred at 232 nm was found in absorption spectra of PVA–PVP which corresponds to π – π^* and n – π^* electronic transition [3, 10, 19]. The

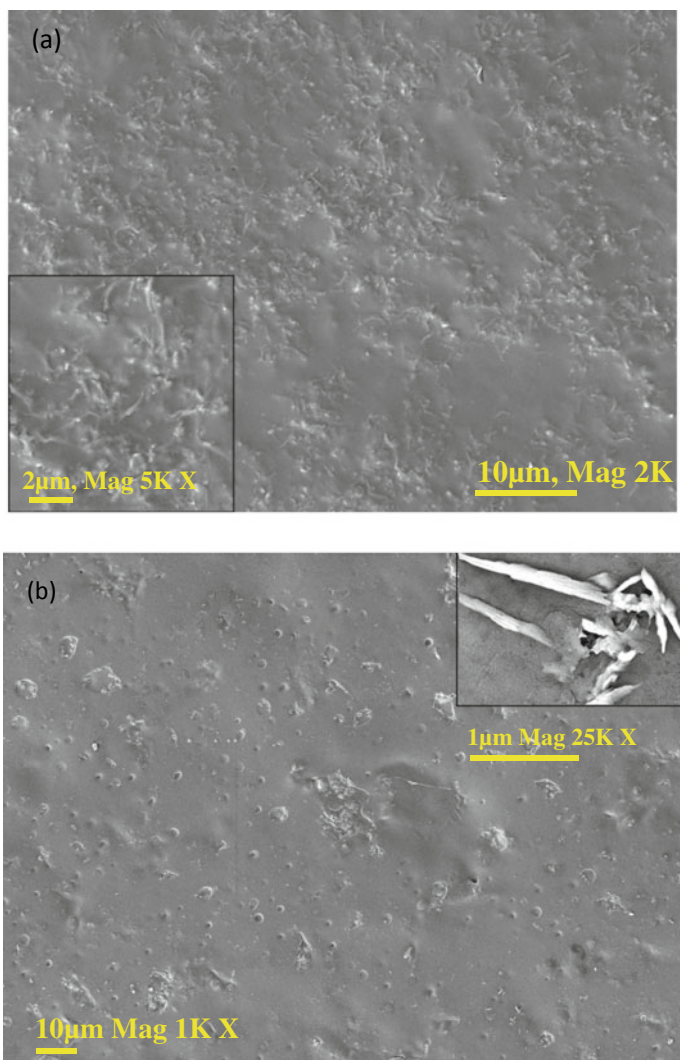


Fig. 3 **a** SEM micrograph of PVA-PVP-ZnO (5 wt%) nanocomposite film. Inset shows micrograph at higher resolution. **b** SEM micrograph of PVA-CMC-ZnO (5 wt%) nanocomposite film. Inset shows micrographs at higher resolution

nanocomposites films exhibited higher absorption as compared to host matrix in the entire range. A sharp absorption peak was found at 365 nm in the absorption spectra of ZnO (2 wt% and 5 wt%) dispersed PVA-PVP nanocomposites films which is a characteristic peak of ZnO nanoparticle and have been noted by many researchers [10, 21, 22].

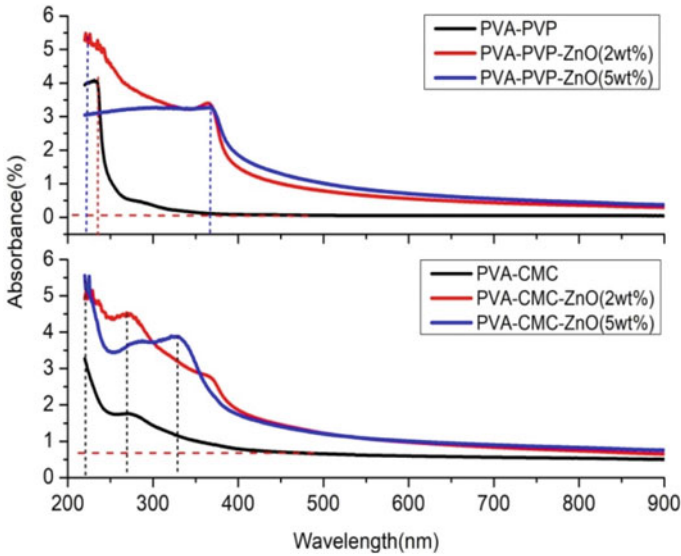


Fig.4 UV-Vis absorption spectra of PVA–PVP blend film, PVA–CMC blend film and ZnO (2 wt% and 5 wt%) dispersed nanocomposites films of (PVA–PVP) and (PVA–CMC)

Absorption spectra of PVA–CMC revealed absorption edge at 220 nm and a broad absorption peak centred at 275 nm which corresponds to the electronic transition of the functional group associated with PVA–CMC polymers [18]. The absorption spectra of ZnO dispersed nanocomposites films of PVA–CMC exhibit two absorption peaks at (272 nm and 367 nm) and (278 nm and 327 nm) respectively. The peaks at 367 nm and 327 nm indicate the presence of ZnO nanoparticles whereas the absorption band corresponding to host polymer undergoes minor shift [20, 22–26]. Comparative analyzes of these plots reveal that both types of PNCs show significant absorption in UV region. However PNC film of PVA–CMC–ZnO exhibited a notable feature of strong absorption of UVA and UVB rays whereas PNC film of PVA–PVP–ZnO strongly absorb UVA rays. Thus, these PNCs can be used as UV absorbing films in optical coatings.

3.2.2 Optical Energy Band Gap

The optical energy band gaps of these films were calculated using the following equation which relates the absorption coefficient as a function of band gap energy (E_g) and photon energy $h\nu$:

$$(\alpha h\nu)^n = A(h\nu - E_g) \quad (1)$$

where, α is absorption coefficient of the material, $h\nu$ is the photon energy, A is a constant, E_g is the optical band gap of the material and the exponent n depends on the type of transition. n can take values $1/2$, 2 , $3/2$ and 3 corresponding to the allowed direct, allowed indirect, forbidden direct and forbidden indirect transitions respectively [2, 10, 19].

The absorption coefficient (α) was evaluated using the relation [2]:

$$\alpha = \frac{2.303 \times \text{Abs}}{d} \tag{2}$$

where, Abs is the absorbance and d is the thickness of the film.

The absorption coefficient was used to determine the energy band gap using Tauc's relation [2, 23]. It was reported that near the fundamental band edge, both direct and indirect transitions occur which can be determined by plotting $(\alpha h\nu)^2$ and $(\alpha h\nu)^{1/2}$ as a function of photon energy [8, 10, 11]. The values of $(\alpha h\nu)^2$ and $(\alpha h\nu)^{1/2}$ were plotted as a function of $h\nu$ to determine the direct band gap and indirect band gap of the PNCs under study [2, 3, 10]. The extrapolation of the linear portion to $\alpha = 0$ gives the value of optical band gap energy [27]. The plot of $(\alpha hf)^2$ and $(\alpha hf)^{1/2}$ against hf for PVA–PVP blend, PVA–CMC blend and ZnO (2 wt% and 5 wt%) dispersed nanocomposites films are depicted in Figs. 5 and 6 respectively. The estimated values of direct energy band gap (E_{gd}) and indirect energy band gap (E_{gi}) are given in Table 1. For PVA–PVP blend film, the calculated value of E_{gd} is 5.09 eV whereas, ZnO dispersed PVA–PVP nanocomposites films exhibit significant decrease in E_{gd} values [10, 23].

Similarly, for PVA–CMC blend film, the calculated value of E_{gd} is 4.89 eV whereas, ZnO dispersed PVA–CMC nanocomposites films exhibit slight decrease

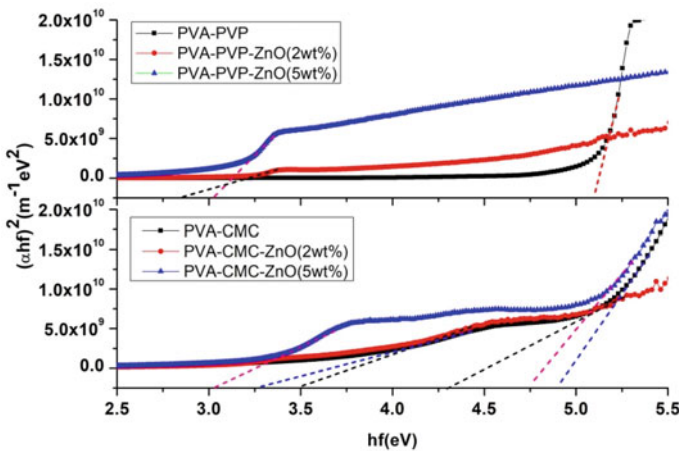


Fig. 5 Variation of $(\alpha hf)^2$ versus hf for PVA–PVP blend film, PVA–CMC blend film and ZnO (2 wt% and 5 wt%) dispersed nanocomposites films of (PVA–PVP) and (PVA–CMC)

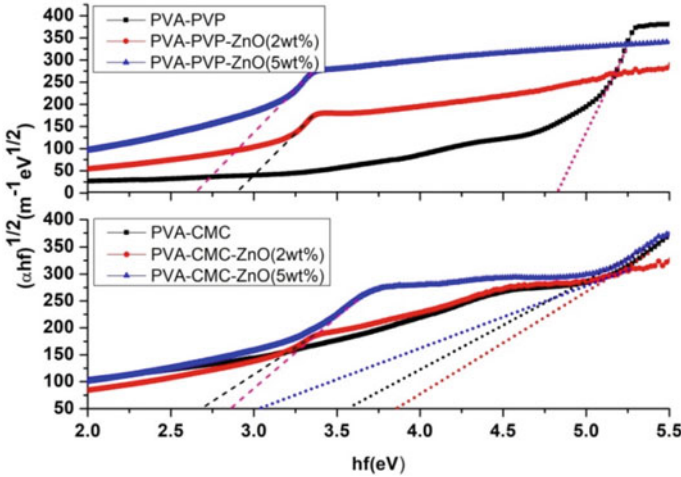


Fig. 6 Variation of $(\alpha hf)^{1/2}$ versus hf for PVA–PVP blend film, PVA–CMC blend film and ZnO (2 wt% and 5 wt%) dispersed nanocomposites films of (PVA–PVP) and (PVA–CMC)

Table 1 The calculated values of direct band gap energy (E_{gd}), indirect band gap energy (E_{gi}), Urbach energy (E_u) and refractive index (n) for all films

Sample	E_{gd} (eV) (Direct band gap energy)	E_{gi} (eV) (Indirect band gap energy)	E_u (Urbach energy)	n (Refractive index) at $\lambda = 500$ nm
PVA–PVP	5.09	4.82	7.29	0.12
PVA–PVP–ZnO (2 wt%)	2.85	2.89	1.19	0.32
PVA–PVP–ZnO (5 wt%)	3.03	2.65	1.17	0.44
PVA–CMC	4.89	3.86	5	0.26
PVA–CMC–ZnO (2 wt%)	4.30	3.05	1.86	0.62
PVA–CMC–ZnO (5 wt%)	4.74	3.56	2.65	0.60

in E_{gd} values, i.e. 4.30 eV and 4.74 eV for (2 wt% and 5 wt%) doping of ZnO respectively. A striking feature that can be seen from Fig. 5 is that out of two PNCs, PVA–CMC–ZnO PNC exhibited two different band gaps. The higher value corresponds to the electronic transition associated with host polymer (PVA–CMC) and the lower value is nearly equal to that of nanofiller (ZnO) [5, 10, 23, 24]. E_{gi} values for PVA–CMC blend and nanocomposites film of PVA–CMC were found to be lower than E_{gd} values which were observed by many researchers for various PNC materials [13, 15–19]. The reduction in energy band gap values of nanocomposites films is due to (i) the defects created by nanofillers in the host polymer blend which results in disordered arrangement in PNC films, (ii) these defects create some localized states in the forbidden energy band gap of the material [5, 13, 15, 16, 24].

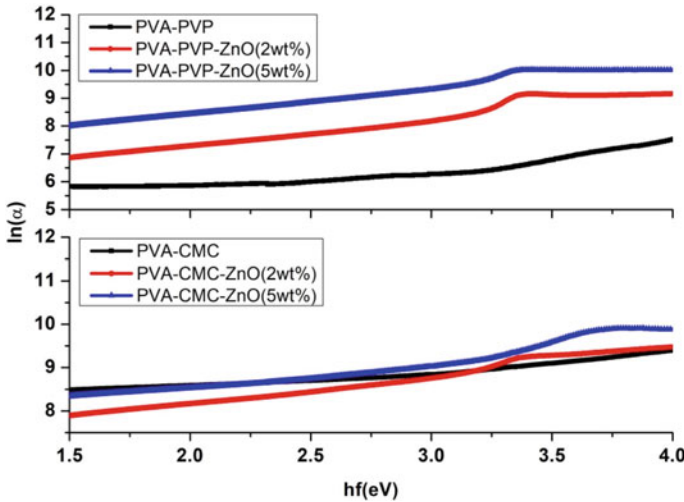


Fig.7 Variation of $\ln(\alpha)$ versus hf for PVA–PVP blend film, PVA–CMC blend film and ZnO (2 wt% and 5 wt%) dispersed nanocomposites films of (PVA–PVP) and (PVA–CMC)

3.2.3 Urbach Energy (E_u)

Along the absorption coefficient curve and near the optical band edge there is an exponential part called Urbach tail. This exponential tail is observed in the low crystalline, poor crystalline, disordered and amorphous materials because these materials have localized states which extend in the band gap [8, 15]. The absorption coefficient near the fundamental absorption edge exponentially depends on the incident photon energy and obeys the Urbach relation [8, 10, 15]

$$\alpha = \alpha_o \exp(h\nu/E_u) \tag{3}$$

where, α_o is a constant and E_u is the width of band tail which represents the degree of disorder [3, 8, 9]. The value of E_u is determined from the reciprocal of the slope of $\ln(\alpha)$ versus $h\nu$ plot as given in Fig. 7 and the estimated values of E_u are given in Table 1. The E_u values of ZnO (2 wt% and 5 wt%) loaded nanocomposites films of (PVA–PVP) and (PVA–CMC) dropped significantly as compared to host matrix.

3.2.4 Refractive Index and Extinction Coefficient

The refractive indices (n) and extinction coefficient (k) for the films were determined by the following equation [2, 19]:

$$R = \frac{(n - 1)^2 + k^2}{(n + 1)^2 + k^2} \tag{4}$$

where, R is reflectance and k is the extinction coefficient ($k = \alpha\lambda/4\pi$).

The variation of refractive index (n) and extinction coefficient (k) with wavelength (λ) for all the films are shown in Figs. 8 and 9 respectively. The values of n decreases with increase in wavelength and obtained values of n for nanocomposites films are higher than the host matrix. The enhanced value of n for nanocomposite films indicates the increased packing density owing to reduction in inter-atomic spacing on

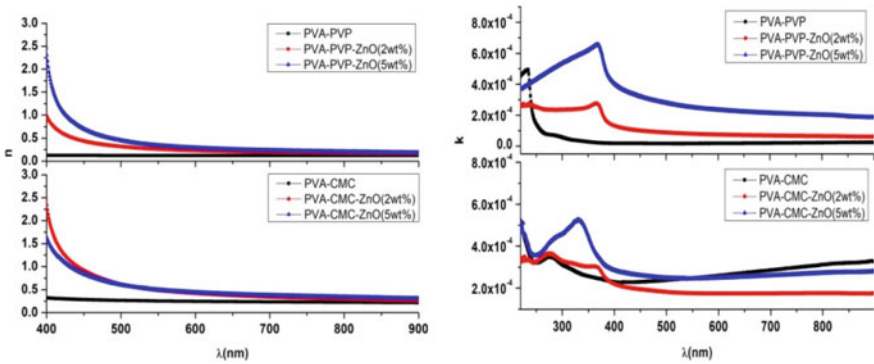


Fig. 8 Variation of refractive index (n) and extinction coefficient (k) with wavelength (λ) for all the films

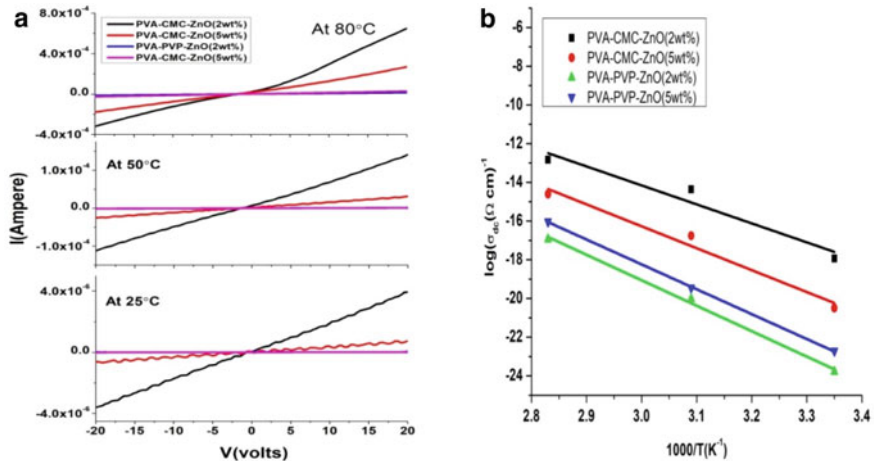


Fig. 9 **a** I - V response recorded at room temperature, 50 °C and 80 °C temperature for all the films. **b** Temperature dependent variation of $\log(\sigma_{dc})$ of all the films calculated at fixed voltage of 20 V for all the films respectively

inclusion of nanofillers [2, 9, 10, 19]. The values of n for ZnO dispersed PVA–CMC nanocomposites films was observed higher than the ZnO dispersed PVA–PVP nanocomposites films.

The extinction coefficient (k) is a measure of the fraction of light lost due to scattering and absorption [2, 3]. The values of k for ZnO dispersed nanocomposite films of (PVA–PVP) and PVA–CMC) are observed higher than host matrix. The k values decreases gradually with increasing wavelength whereas it shows anomalous behaviour in the UV region may be due to the scattering of photons due to the presence of ZnO [3, 16, 18].

Overall comparative analysis of optical properties of both types of PNCs show that depending upon technological requirement, PVA–PVP–ZnO or PVA–CMC–ZnO films with tunable optical bandgap and UV absorbing property can be used for optoelectronic devices.

3.3 Electrical Characterization

The current versus voltage (I – V) response of all the nanocomposites films recorded at different temperatures is shown in Fig. 9a. Reasonable rise in the value of current for all nanocomposites film was observed on increasing temperature up to 50 °C. However, the PNC films exhibited almost linear I – V response at temperature of 80 °C [28, 29]. The increasing value of I with increase in temperature suggest that these nanocomposites films are thermally activated [11, 13]. ZnO dispersed nanocomposites films of PVA–CMC show significant rise in current (I) value with changing voltage as compared to ZnO dispersed nanocomposites films of PVA–PVP.

The electrical conductivity is calculated by the formula [22, 28]:

$$\sigma = dI / AV \quad (5)$$

where, V is the applied voltage, I is the measured current, d is thickness and A is the cross sectional area of the sample.

Temperature dependent variation of electrical conductivity (at 20 V) of all the films is shown in Fig. 11. The relation between electrical conductivity (σ_{dc}) and the temperature is given by Arrhenius equation:

$$\sigma = \sigma_o \exp\left(\frac{E_a}{K_b T}\right) \quad (6)$$

where, E_a is the activation energy, K_b is the Boltzmann constant and T is the temperature in Kelvin (K) [28]. The values of (σ_{dc}) for all the nanocomposite films gradually increase with rise in temperature. The rise in temperature causes dissociation of ions/molecules and their aggregates which lead to increased number of free charge carriers and results in high value of σ_{dc} at higher temperature [8, 11, 28–30].

Table 2 The calculated values of dc conductivity (σ_{dc}) at different temperatures (298, 323 and 353 K) and activation energy (E_a) for all films

Sample	σ_{dc} (ohm cm) ⁻¹ at 298 K	σ_{dc} (ohm cm) ⁻¹ at 323 K	σ_{dc} (ohm cm) ⁻¹ at 353 K	E_a (eV)
PVA–CMC–ZnO (2 wt%)	1.63E–08	5.82E–07	2.67E–06	0.85
PVA–CMC–ZnO (5 wt%)	1.25E–09	5.25E–08	4.52E–07	0.98
PVA–PVP–ZnO (2 wt%)	4.73E–11	2.02E–09	4.41E–08	1.13
PVA–PVP–ZnO (5 wt%)	1.37E–10	3.57E–09	1.09E–07	1.11

PVA–CMC–ZnO nanocomposite films exhibited higher values of σ_{dc} as compared to PVA–PVP–ZnO nanocomposite films. The activation energy (E_a) values for the films under study were calculated from the slope of the line fitted in Arrhenius equation and these values are recorded in Table 2. On comparing the activation energy (E_a) values of PVA–CMC–ZnO films with those of PVA–PVP–ZnO films it is seen that the former has less value. This observation is supported by higher value of σ_{dc} exhibited by PVA–CMC–ZnO nanocomposite films as compared to nanocomposites of PVA–PVP–ZnO.

4 Conclusion

A comparative study of optical and electrical properties of ZnO dispersed nanocomposites films of (PVA–PVP) and (PVA–CMC) is carried out in the present work. Moreover, the effect of dispersing ZnO nano particles on structural and morphological properties of nanocomposite films is also studied. The presence of characteristic peaks of nanofiller along with the characteristic peaks of polymer blends in the XRD spectra of composite films with minor shifts in their position confirms the dispersion of ZnO in the host matrix. The interaction between the nanofiller and constituent polymers was ascertained from broadening of characteristic peaks of host polymer and variation in intensities of characteristic peaks of ZnO in XRD spectra of nanocomposite films. SEM micrographs show that the morphological structure of ZnO nanoparticles is different in both types of matrices and are in good agreement with findings of other researchers. Both types of nanocomposite films under study show significant enhancement in UV absorption and the band gaps of these nanocomposite films are found to be less than those of host matrix. Temperature dependent variation in dc electrical conductivity of the nanocomposites film shows substantial rise in σ_{dc} values. Comparative analysis of ZnO dispersed nanocomposites of PVA–PVP and PVA–CMC suggests better enhancement in electrical conductivity values for nanocomposites of PVA–CMC than PVA–PVP. Overall analysis indicates that ZnO dispersed PVA–CMC film with tunable optical bandgap and UV absorbing property can be used for optoelectronic devices. The enhancement in σ_{dc} value as compared to PVA–PVP–ZnO film, suggesting that PVA–CMC–ZnO

polymer nanocomposite film can be the material of technological importance in the area of green electronics and optoelectronics.

Acknowledgements Authors are thankful to KIRAN Division, Department of Science and Technology (DST), New Delhi for the financial assistance provided through WOS-A project SR/WOS-A/PM-44/2017. Experimental facilities developed using financial assistance provided through DST-FIST (Level- I) and DRS (SAP) program have been utilized to carry out this work and it is gratefully acknowledged. Authors are thankful to Prof. P. N. Gajjar, Head, Department of Physics, School of Science, Gujarat University, Ahmedabad for his constant encouragement. The experimental facility for I-V measurements extended by Prof. Dhaka and Prof. M. Roy, Department of Physics, MLSU, Udaipur are highly acknowledged.

References

1. Ponnamma D et al (2019) Synthesis, optimization and applications of ZnO/polymer nanocomposites. *Mater Sci Eng C* 98:1210–1240
2. Nangia R, Shukla NK, Sharma A (2019) Optical and structural properties of Se₈₀Te₁₅Bi₅/PVA nanocomposite films. *J Mol Struct* 1177:323–330
3. Dhatarwal P, Sengwa RJ (2021) Investigation on the optical properties of (PVP/PVA)/Al₂O₃ nanocomposite films for green disposable optoelectronics. *Phys B* 412989
4. Rithin Kumar NB et al (2015) Studies on structural, optical and mechanical properties of MWCNTs and ZnO nanoparticles doped PVA nanocomposites. *Nanotechnol Rev* 4.5:457–467
5. Dhatarwal P, Sengwa RJ, Choudhary S (2020) Multifunctional (PVP/PEO)/SnO₂ nanocomposites of tunable optical and dielectric properties. *Optik* 221:165368
6. Ali FM, Kersh RM (2020) Synthesis and characterization of La³⁺ ions incorporated (PVA/PVP) polymer composite films for optoelectronics devices. *J Mater Sci Mater Electron* 31(3):2557–2566
7. Yassin AY (2020) Dielectric spectroscopy characterization of relaxation in composite based on (PVA–PVP) blend for nickel–cadmium batteries. *J Mater Sci Mater Electron* 31(21):19447–19463
8. Chapi S, Raghu S, Devendrappa H (2016) Enhanced electrochemical, structural, optical, thermal stability and ionic conductivity of (PEO/PVP) polymer blend electrolyte for electrochemical applications. *Ionics* 22(6):803–814
9. Sengwa RJ, Choudhary S, Dhatarwal P (2019) Nonlinear optical and dielectric properties of TiO₂ nanoparticles incorporated PEO/PVP blend matrix based multifunctional polymer nanocomposites. *J Mater Sci Mater Electron* 30(13):12275–12294
10. Choudhary S, Sengwa RJ (2018) ZnO nanoparticles dispersed PVA–PVP blend matrix based high performance flexible nanodielectrics for multifunctional microelectronic devices. *Curr Appl Phys* 18(9):1041–1058
11. Mohammed G, El Sayed AM, Morsi WM (2018) Spectroscopic, thermal, and electrical properties of MgO/polyvinyl pyrrolidone/polyvinyl alcohol nanocomposites. *J Phys Chem Solids* 115:238–247
12. Rajesh K, Crasta V, Kumar NR, Shetty G, Rekha PD (2019) Structural, optical, mechanical and dielectric properties of titanium dioxide doped PVA/PVP nanocomposite. *J Polym Res* 26(4):1
13. El Sayed AM, El-Gamal S, Morsi WM, Mohammed G (2015) Effect of PVA and copper oxide nanoparticles on the structural, optical, and electrical properties of carboxymethyl cellulose films. *J Mater Sci* 50(13):4717–4728
14. Abutalib MM (2019) Effect of zinc oxide nanorods on the structural, thermal, dielectric and electrical properties of polyvinyl alcohol/carboxymethyl cellulose composites. *Phys B* 57:108–116

15. El-Gamal S, El Sayed AM, Abdel-Hady EE (2018) Effect of cobalt oxide nanoparticles on the nano-scale free volume and optical properties of biodegradable CMC/PVA films. *J Polym Environ* 26(6):2536–2545
16. Hashim A, Hadi Q (2018) Synthesis of novel (polymer blend-ceramics) nanocomposites: structural, optical and electrical properties for humidity sensors. *J Inorg Organomet Polym Mater* 28(4):1394–1401
17. Zhu J, Li Q, Che Y, Liu X, Dong C, Chen X, Wang C (2020) Effect of Na_2CO_3 on the microstructure and macroscopic properties and mechanism analysis of PVA/CMC composite film. *Polymers* 12(2):453
18. Hashim A, Hadi Q (2018) Structural, electrical and optical properties of (biopolymer blend/titanium carbide) nanocomposites for low cost humidity sensors. *J Mater Sci Mater Electron* 29(13):11598–604
19. Banerjee M, Jain A, Mukherjee GS (2019) Microstructural and optical properties of polyvinyl alcohol/manganese chloride composite film. *Polym Compos* 40(S1):E765–E775
20. Soliman TS, Rashad AM, Ali IA, Khater SI, Elkalashy SI (2020) Investigation of linear optical parameters and dielectric properties of polyvinyl alcohol/ZnO nanocomposite films. *Phys Status Solidi A* 217(19):2000321
21. Ji T, Zhang R, Dong X, Sameen DE, Ahmed S, Li S, Liu Y (2020) Effects of ultrasonication time on the properties of polyvinyl alcohol/sodium carboxymethyl cellulose/nano-ZnO/multilayer graphene nanoplatelet composite films. *Nanomaterials* 10(9):1797
22. Krishnaswamy S, Panigrahi P, Nagarajan GS (2020) Tailoring the optical properties of ZnO thin film by citrus limon doped polypyrrole. *J Mater Sci Mater Electron* 31(11):8502–8513
23. Dhatarwal P, Sengwa RJ (2020) Structural, dielectric dispersion and relaxation, and optical properties of multiphase semicrystalline PEO/PMMA/ZnO nanocomposites. *Compos Interfaces* 3:1–6
24. Sengwa RJ, Dhatarwal P (2021) Polymer nanocomposites comprising PMMA Matrix and ZnO, SnO_2 , and TiO_2 nanofillers: a comparative study of structural, optical, and dielectric properties for multifunctional technological applications. *Opt Mater* 113:110837
25. Albaris H, Karuppasamy G (2019) CuO–ZnO p–n junction enhanced oxygen sensing property of polypyrrole nanocomposite at room temperature. *J Mater Sci Mater Electron* 30(10):9989–9998
26. Ramesan MT, Greeshma KP, Parvathi K, Anilkumar T (2020) Structural, electrical, thermal, and gas sensing properties of new conductive blend nanocomposites based on polypyrrole/phenothiazine/silver-doped zinc oxide. *J Vinyl Addit Technol* 26(2):187–195
27. Sengwa RJ, Dhatarwal P (2021) Nanofiller concentration-dependent appreciably tailorable and multifunctional properties of (PVP/PVA)/ SnO_2 nanocomposites for advanced flexible device technologies. *J Mater Sci Mater Electron* 1–14
28. Naveen CS, Jayanna HS, Lamani AR, Rajeeva MP (2014) Temperature dependent DC electrical conductivity studies of ZnO nanoparticle thick films prepared by simple solution combustion method. In: AIP conference proceedings, vol 1591, No 1, pp 402–404. American Institute of Physics
29. Hemalatha KS, Sriprakash G, Ambika Prasad MV, Damle R, Rukmani K (2015) Temperature dependent dielectric and conductivity studies of polyvinyl alcohol-zno nanocomposite films by impedance spectroscopy. *J Appl Phys* 118(15):154103
30. Shanthala VS, Shobha Devi SN, Murugendrappa MV (2017) Synthesis, characterization and DC conductivity studies of polypyrrole/copper zinc iron oxide nanocomposites. *J Asian Ceram Soc* 5(3):227–234

Chapter 23

Experimental Study of Heap Leaching of Secondary Sulphides Using H₂SO₄ and NaCl: A Chilean Mining Company Case



Manuel Saldaña, Luis Ayala, Edelmira Gálvez, and Javier González

Abstract The volatility of the price of commodities generates the need for copper mining to control costs and make production processes more efficient. In this context, it is not possible to have real control over the productive indicators if it does not know the logistics of the processes, or you do not have a clear idea of the impacts of the variables or operational parameters on the dependent variables or responses. The present work aims to describe the production process for the leaching of secondary copper sulphides by means of heap leaching. This study focused on the search for theoretical relationships that define the behavior of copper recovery and the derivation of an analytical model that explains the response, developing a model capable of assertively representing the reality of the extractive process.

Keywords Mineral processing · Leaching · Secondary sulphides · Modeling · Analytical models

1 Introduction

Worldwide, approximately 20 million tons of copper were produced in the mine and 25 million tons of refinery production in 2020 [1], a commodity that is very

M. Saldaña (✉)

Department of Computing and Engineering Systems, Universidad Católica del Norte, Avenida Angamos 0610, 1270709 Antofagasta, Chile

e-mail: manuel.saldana@ucn.cl

L. Ayala

Faculty of Engineering and Architecture, Universidad Arturo Prat, Almirante, Juan José Latorre 2901, 1244260 Antofagasta, Chile

e-mail: luisayala01@unap.cl

E. Gálvez · J. González

Department of Metallurgical and Mining Engineering, Universidad Católica del Norte, Avenida Angamos 0610, 1270709 Antofagasta, Chile

e-mail: egalvez@ucn.cl

J. González

e-mail: javier.gonzalez@ucn.cl

important for the economy of various countries, like Chile, where mining copper contributes around 10% of the gross domestic product (GDP) [2, 3]. Large copper mining currently faces several challenges, such as decreases in ore grades [4–7], excessive increases in production to compensate for low grades [4], increases in environmental liabilities such as high generation of tailings [8–10], emission of polluting gases [11, 12] and water scarcity in arid zones [13–17]. Considering the above, there is a constant search of generation of models and/or algorithms for optimization of production processes, to improve the development of mineral processing in a sustainable way, increasing the recoveries of valuable minerals, reducing water consumption, limiting the impact on the environment, and adding the greatest possible value to stakeholders.

The oxidized copper ores processed through the hydrometallurgical way are increasingly scarce in Chile, while copper sulphides are more abundant [18]. 39.2% of Chilean fine copper production is produced by hydrometallurgy, while most of the production (60.8%) is developed through flotation processes. On the planet, most of the copper minerals are sulphides and a small part of oxides [19]. The mining industry has traditionally worked by pyrometallurgy for sulphur minerals, and hydrometallurgy, for oxidized minerals [20]. Both working mechanisms have proven profitable in the industry, however, pyrometallurgy has the main drawback of generating SO₂ emissions into the atmosphere, generating serious environmental problems [21].

Copper oxides and chalcocite leach readily, whereas chalcopyrite does not leach significantly under standard heap leach conditions. The mineral is crushed in the comminution phase to a uniform particle size, the size of which depends on the mineralogy and the operating conditions, to then agglomerate and pile up in heaps. The heap is generated on an impermeable pad, where a series of pipes distribute the solution with leaching agents (H₂SO₄ for oxidized minerals and H₂SO₄ + Chlorides for secondary sulphides) at the top of the pile, and the drainage lines collect the solutions they contain. copper at the base (see Fig. 1). Copper-rich PLS that is collected on a sloping impermeable surface below the heap is directed to a PLS pond [22], for further processing.

In Chile, the mining industries are implementing new processing methodologies, to use the assets used for hydrometallurgy in the processing of sulphide copper ores. Among the methodologies most used in the literature review, there is chalcopyrite leaching using MnO₂ and chloride as leaching agents [19, 20, 23], chalcopyrite leaching using H₂SO₄ and Cl [11, 24, 25] and the leaching of chalcopyrite with ionic liquid [26, 27]. Then, the generation of analytical models or adjustment of machine learning algorithms that represent the leaching dynamics has the potential to contribute to obtaining a better understanding of the interactions of the variables that explain mineral recovery considering variations in the operational conditions.

The development of this work considers the materials and methods section, where the operational data set and the sample to be used for modeling are explained, in addition to explaining the generation of mathematical models retrieved from the literature. In the results and discussions section, a correlation analysis between the independent variables and the response is developed, in addition to regression model fitted. Finally, the conclusions section presents the main findings.

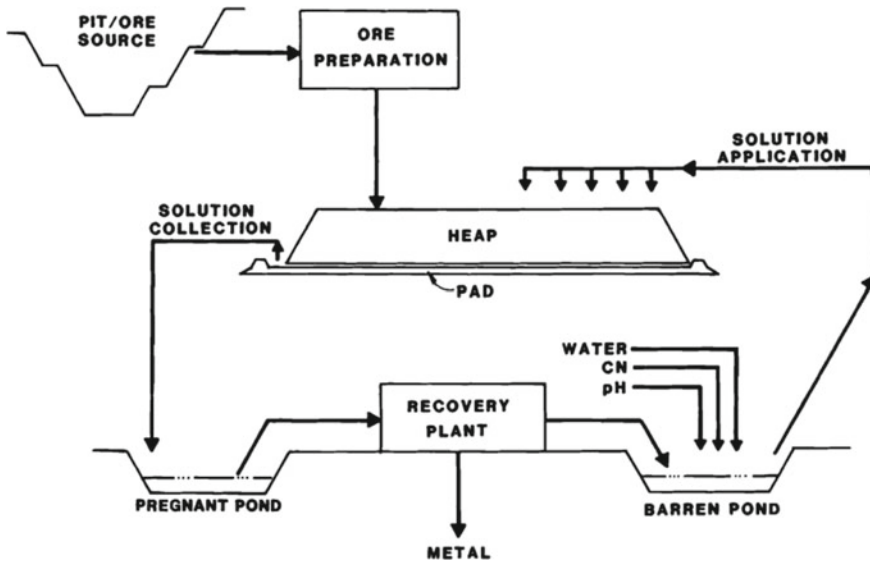


Fig. 1 Schematic heap leaching process

2 Materials and Methods

2.1 Design of Experiments

The experimental design is a statistical technique that allows to identify and quantify the causes of an effect (or more effects produced by independent variables or by manipulable parameters) within an experimental study [28]. 19 samples were taken under operational conditions, studying the effects of irrigation time (days), resting time (days), addition of agglomerated NaCl (kg/ton), refined acid (g/L), and Cu/Fe³⁺ solubility ratio on copper recovery (%). The design of experiments consists of a series of tests in which changes or disturbances are made intentionally in the input variables, collecting the output data for later analysis, however, considering the intervention costs of the variables to be used on industrial scale, for the purposes of this study, the operational parameters considered in the study were sampled, which are presented in Table 1.

While the copper recoveries under operational conditions for the total of samples are presented in Table 2.

Table 1 Sampled variables from an industrial heap leach process

Parameter	Unit	Codification	Minimum level	Maximum level
Resting time	(days)	x_1	11	51
Irrigation time	(days)	x_2	13	259
Agglomerated NaCl addition	(kg/t)	x_3	0	10
Acid in refining	(g/L)	x_4	11.90	14.12
Cu/Fe ³⁺ solubility ratio	–	x_5	0.19	0.77
Copper recovery	(%)	y	–	–

Table 2 Sampling values of the experimental design

Sample	x_1	x_2	x_3	x_4	x_5	y
1	16	234	0.00	14.06	0.73	71.04
2	15	249	0.00	14.12	0.77	70.15
3	15	216	0.00	14.03	0.64	68.96
4	12	259	0.00	14.10	0.57	67.34
5	14	245	0.00	14.01	0.72	64.03
6	19	13	0.00	11.90	0.19	0.58
7	17	250	10.00	14.07	0.40	74.52
8	11	232	10.00	13.42	0.31	81.06
9	29	224	10.00	13.57	0.39	71.16
10	36	180	10.00	13.42	0.37	72.82
11	36	158	10.00	13.17	0.34	72.61
12	31	149	10.00	13.15	0.35	64.64
13	32	95	10.00	12.87	0.35	54.06
14	51	84	10.00	12.43	0.30	59.31
15	33	84	10.00	12.53	0.19	45.95
16	34	50	10.00	12.38	0.34	30.96
17	31	42	10.00	12.25	0.30	30.66
18	34	32	10.00	12.10	0.31	22.92
19	32	24	10.00	12.00	0.30	11.84

2.2 Analytical Model Fit

The analytical model used to represent the heap leaching process is presented below [29–31], which considers that the behavior of the process could be modeled through a system of first order equations, as shown in Eq. 1.

$$\frac{\partial y}{\partial \tau} = -k_{\tau} y^{n_{\tau}} \quad (1)$$

where y is the as recovery (R_t), k_τ is the kinetic constant and n_τ is the order of the reaction. To solve Eq. 1, a delay is introduced since an initial condition is required. Then, the general solution for $n_\tau = 1$ is known and is shown in Eq. 2 (see Mellado et al. [29]).

$$R_\tau = R_\tau^\infty (1 - e^{-k_\tau(\tau-\omega)}) \quad (2)$$

where, R_τ^∞ is the maximum expected recovery and ω is a reaction delay factor. Then, modifying the equations to fit a model to the experimental design, the recovery of copper from secondary copper sulphides is proposed according to Eq. 3, where $g(X)$ is a polynomial equation, explained by the predictors indicated in Table 1.

$$R(X) = R^\infty (1 - e^{-g(X)}) \quad (3)$$

The development of the analytical model presented in Eq. 3 and the transformation of the function $g(X)$ (see Eq. 4), is proposed with the objective of modeling the exponent of the copper recovery model presented in Eq. 3 by means of the Eq. 5, where y and is assumed as a multiple regression whose independent variables are given by the factors presented in Table 1.

$$g(X) = \ln \left| \frac{R^\infty}{R^\infty - R(X)} \right| \quad (4)$$

$$y = g(X) = \alpha + \sum_{i=1}^n \beta_i x_i + \sum_{i=1}^n \sum_{j=1}^n \beta_{ij} x_{ij} / \forall i, j \quad (5)$$

Finally, incorporating the model in Eq. 5 in Eq. 3, the copper recovery is given by Eq. 6.

$$R_\tau = R_\tau^\infty \left(1 - e^{-\sum_{i=1}^n \beta_i x_i + \sum_{i=1}^n \sum_{j=1}^n \beta_{ij} x_{ij}} \right) \quad (6)$$

Additionally, the mean square error (MSE, see Eq. 7), mean absolute deviation (MAD, see Eq. 8), and the coefficient of determination (R^2 , see Eq. 9) are used to evaluate the goodness of fit [28].

$$\text{MAD} = \frac{\sum_{i=1}^n |y_i - \hat{y}_i|}{n} \quad (7)$$

$$\text{MSE} = \frac{\sum_{i=1}^n (y_i - \hat{y}_i)^2}{n} \quad (8)$$

$$R^2 = 1 - \frac{SS_{\text{Regression}}}{SS_{\text{Total}}} = \frac{\sum_{i=1}^n (\hat{y}_i - \bar{y})^2}{\sum_{i=1}^n (y_i - \bar{y})^2} \tag{9}$$

where $SS_{\text{Regression}}$ is defined how sum squared regression error, SS_{Total} is the sum squared total error, \hat{y}_i is the estimated response, y_i is the real response and \bar{y} is the average of the response.

3 Results and Discussions

Analyzing operational data sampled by means of the correlation matrix shown in Fig. 2 (Pearson’s correlation), there is a strong relationship between the independent variables, irrigation time ($r = 0.88$), acid in refining ($r = 0.85$) and Cu/Fe^{3+} solubility ratio in the recovery of copper from sulphide minerals.

Additionally, analyzing the distribution of copper recovery as a function of irrigation time (see Fig. 3), it is found that it agrees with the inverse exponential model (theoretical model, considering an ideal recovery in infinite time equal to 100%) cited in the literature [29–31], whose mathematical modeling was indicated in Eq. 2.

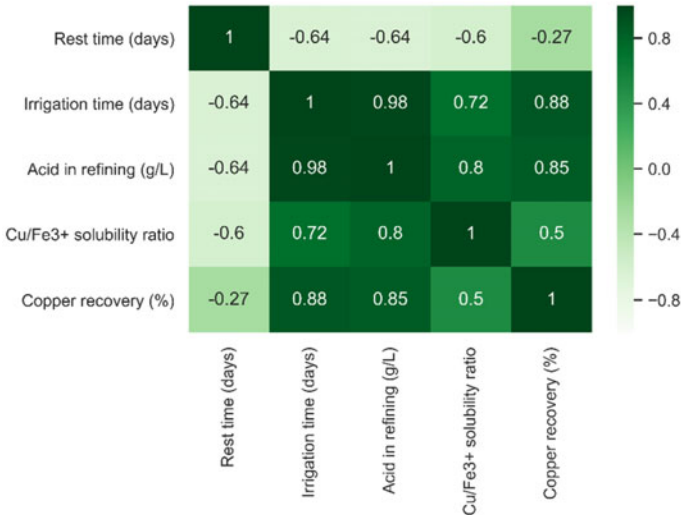


Fig. 2 Correlation plot for copper extraction from secondary sulphides

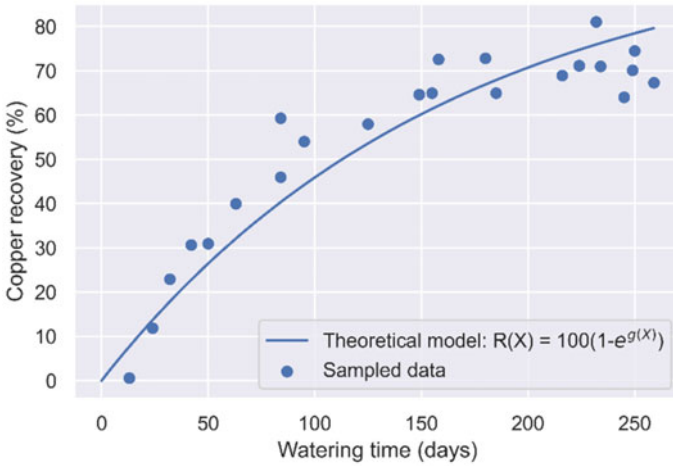


Fig. 3 Copper recovery versus irrigation time

Developing the fit of the model presented in Eq. 3, it proceeds to estimate the recovery in infinite time under operational conditions, considering for this the minimization of the errors. A contrast between the sample data with the curve of a theoretical model is developed, as shown in Fig. 3, and then, by incorporating expert knowledge, defining the recovery in infinite time at 80% in operational conditions approximately. The curves and the contrast with the model considering a copper recovery of 100% in infinite time (theoretical recovery in conditions ideal) are presented in Fig. 4.

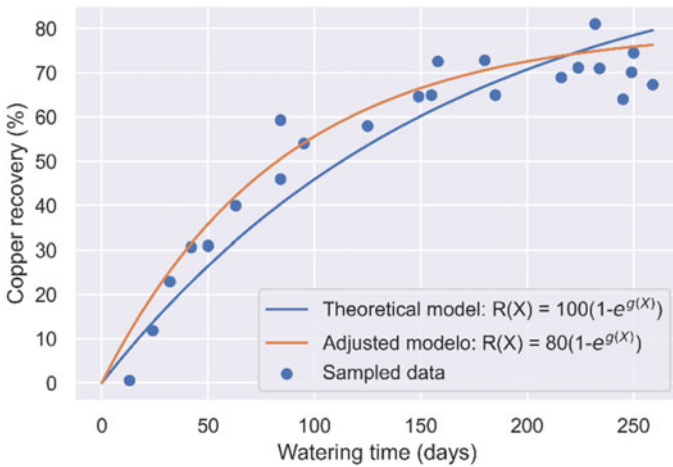


Fig. 4 Sample data and curves of the analytical models

Table 3 Goodness-of-fit indicators of the adjusted analytical model

Model/Indicator	MSE	MAD	R ²	R ² Adjusted
<i>g</i> (<i>X</i>)	0.0764	0.2108	0.924	0.896

Table 4 ANOVA multiple regression model

	Coef. <i>g</i> (<i>X</i>)	Std. Err	<i>t</i>	<i>p</i>
Intercept	1015.8512	297.2382	3.4176	0.0046
<i>x</i> ₃	1.5322	0.3972	3.8576	0.002
<i>x</i> ₈	−170.4148	49.6065	−3.4353	0.0044
<i>x</i> ₃ ²	0.0005	0.0001	3.487	0.004
<i>x</i> ₈ ²	7.1441	2.0722	3.4477	0.0043
<i>x</i> ₃ × <i>x</i> ₈	−0.1268	0.0335	−3.7805	0.0023

Additionally, the adjusted model presented in Fig. 3 has low indicators of goodness of fit (see Table 3), which validates the capability of the model to adjust to the sample data.

Adjusting the regression model using the ordinary least squares method, from the “statsmodels” library in Python [32], it has that the function *g*(*X*) (see Eq. 10) depends on the operational variables time and acid in refining, as shown in Table 4.

$$g(X) = 1015.85 + 1.53x_3 - 170.41x_8 - 0.13x_3x_8 + 5 \times 10^{-4}x_3^2 + 7.14x_8^2 \quad (10)$$

The ANOVA test indicates that the model is adequate to represent the copper concentration under the range sampled. There is no lack of model fit, and R² (0.924) and *p* statistic (<0.05, see Table 4), both, general model and of each variable, validates it. ANOVA test shows that the indicated factors impact the copper extraction, due to *F*_{Regression} (31.66) > *F* Table, 95% confidence level *F*_{5,13} (1,9512).

Then, once the multiple regression model has been validated, Eq. 11 represents the copper concentration from the secondary copper sulphide heap leaching process under operational conditions.

$$R(\%) = 78.66 \times \left(1 - e^{-(1015.85+1.53x_3-170.41x_8-0.13x_3x_8+5 \times 10^{-4}x_3^2+7.14x_8^2)} \right) \quad (11)$$

The contrast between the real results with those predicted by the model presented in Eq. 11 (see Fig. 5) and the normality test to the residuals (see Fig. 6), these again demonstrate the capability of the adjusted model to represent the studied system, while the normal probability plot showed that the residuals are normally distributed (*α* > 0.05), as shown in Fig. 6.

Although multiple regression models are quite efficient in the modeling of non-linear systems, as was demonstrated in the development of this research work, as the complexity or quantity of variables studied increases, the incorporation of factors

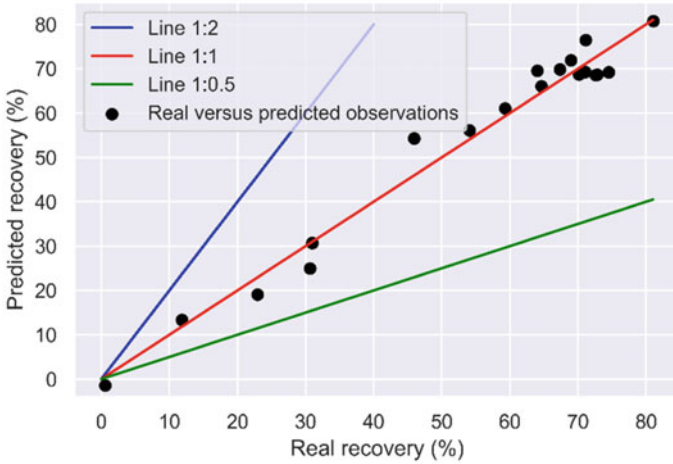


Fig. 5 Real versus predicted copper recovery from sulphurated minerals

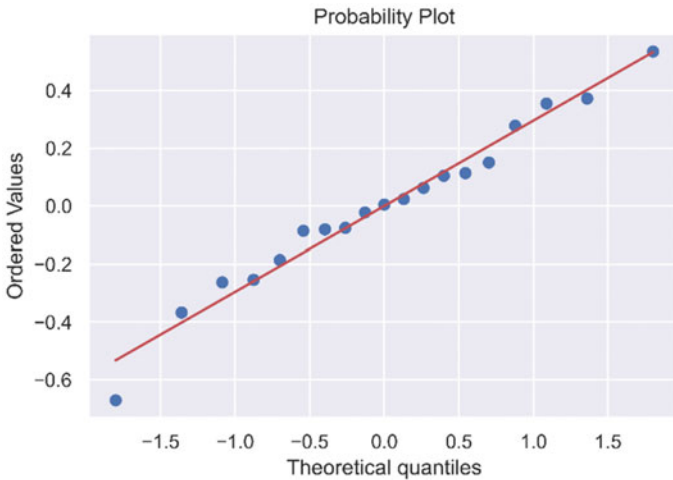


Fig. 6 Normal probability plot of the residuals

in exponential form (product of the inclusion of powers and interactions) makes the modeling difficult to handle. Considering the above, the application of artificial intelligence techniques to the modeling and study of mining production processes could bring important benefits, both to the generation of knowledge or discovery of knowledge, as well as economic ones.

4 Conclusions

In this research, an analytical model for the extraction of copper from sulphide minerals is generated by fitting an inverse exponential function, which considers the operating variables time of irrigation and acid in refinement in the response, however, the adjustment methodology can be extended to other time scales or other operational variables, such as pile height, granulometry, surface velocity of the leaching flow, etc. The generation of analytical or phenomenological models to represent multivariate processes such as leaching has the potential to support analysis, scaling, and optimization tasks, and can be used to predict the response variables on an industrial scale.

Finally, future works contemplate the modeling and simulation of the mineral flotation process on an industrial scale using tools such as techniques based on machine learning [33], ANNs [34] or Bayesian networks [3], among others.

References

1. Flanagan DM (2021) Copper. In: Mineral commodity summaries 2021, pp 52–53. U.S. Geological Survey, Reston, Virginia, USA
2. Kevin Pérez K, Toro N, Campos E (2019) Extraction of Mn from black copper using iron acid medium. *Metals (Basel)* 9(10):1–10. <https://doi.org/10.3390/met9101112>
3. Saldaña M, González J, Jeldres R, Villegas Á, Castillo J, Quezada G, Toro N (2019) A stochastic model approach for copper heap leaching through bayesian networks. *Metals (Basel)* 9(11):1198. <https://doi.org/10.3390/met9111198>
4. Toro N, Jeldres RI, Órdenes JA, Robles P, Navarra A (2020) Manganese nodules in Chile, an alternative for the production of Co and Mn in the future—a review. *Minerals* 10(8):674. <https://doi.org/10.3390/min10080674>
5. Toro N, Robles P, Jeldres RI (2020) Seabed mineral resources, an alternative for the future of renewable energy: a critical review. *Ore Geol Rev* 126(July):103699. <https://doi.org/10.1016/j.oregeorev.2020.103699>
6. Robles P, Picerós E, Leiva WH, Valenzuela J, Toro N, Jeldres RI (2019) Analysis of sodium polyacrylate as a rheological modifier for kaolin suspensions in seawater. *Appl Clay Sci* 183
7. Torres D, Pérez K, Trigueros E, Jeldres RI, Salinas-Rodríguez E, Robles P, Toro N (2020) Reducing-effect of chloride for the dissolution of black copper. *Metals (Basel)* 10(1):123. <https://doi.org/10.3390/met10010123>
8. Toro N, Saldaña M, Castillo J, Higuera F, Acosta R (2019) Leaching of manganese from marine nodules at room temperature with the use of sulfuric acid and the addition of tailings. *Minerals* 9(5):289. <https://doi.org/10.3390/min9050289>
9. Toro N, Saldaña M, Gálvez E, Cánovas M, Trigueros E, Castillo J, Hernández PC (2019) Optimization of parameters for the dissolution of Mn from manganese nodules with the use of tailings in an acid medium. *Minerals* 9(7):387. <https://doi.org/10.3390/min9070387>
10. Torres D, Ayala L, Saldaña M, Cánovas M, Jeldres RI, Nieto S, Castillo J, Robles P, Toro N (2019) Leaching manganese nodules in an acid medium and room temperature comparing the use of different Fe reducing agents. *Metals (Basel)* 9(12):1316. <https://doi.org/10.3390/met9121316>
11. Velásquez-Yévenes L, Torres D, Toro N (2018) Leaching of chalcopyrite ore agglomerated with high chloride concentration and high curing periods. *Hydrometallurgy* 181(September):215–220. <https://doi.org/10.1016/j.hydromet.2018.10.004>

12. Pérez K, Toro N, Saldaña M, Salinas-Rodríguez E, Robles P, Torres D, Jeldres RI (2020) Statistical study for leaching of Covellite in a chloride media. *Metals (Basel)* 10(4):477. <https://doi.org/10.3390/met10040477>
13. Jeldres M, Piceros EC, Toro N, Torres D, Robles P, Leiva WH, Jeldres RI (2019) Copper tailing flocculation in seawater: relating the yield stress with fractal aggregates at varied mixing conditions. *Metals (Basel)* 9(12):1–13. <https://doi.org/10.3390/met9121295>
14. Jeldres M, Piceros E, Robles PA, Toro N, Jeldres RI (2019) Viscoelasticity of quartz and kaolin slurries in seawater: importance of magnesium precipitates. *Metals (Basel)* 9(10). <https://doi.org/10.3390/met9101120>
15. Quezada GR, Jeldres M, Toro N, Robles P, Jeldres RI (2020) Reducing the magnesium content from seawater to improve tailing flocculation: description by population balance models. *Metals (Basel)* 10(3). <https://doi.org/10.3390/met10030329>
16. Quezada GR, Ayala L, Leiva WH, Toro N, Toledo PG, Robles P, Jeldres RI (2020) Describing mining tailing flocculation in seawater by population balance models: effect of mixing intensity. *Metals (Basel)* 10(2):1–15. <https://doi.org/10.3390/met10020240>
17. Castellón CI, Piceros EC, Toro N, Robles P, López-Valdivieso A, Jeldres RI (2020) Depression of pyrite in seawater flotation by guar gum. *Metals (Basel)* 10(2). <https://doi.org/10.3390/met10020239>
18. Comisión Chilena del Cobre (2017) Sulfuros primarios: desafíos y oportunidades. Santiago, Chile. Available at: http://www.cochilco.cl/ListadoTematico/sulfurosprimarios_desafiosyoportunidades.pdf.
19. Toro N, Briceño W, Pérez K, Cánovas M, Trigueros E, Sepúlveda R, Hernández P (2019) Leaching of pure chalcocite in a chloride media using sea water and waste water. *Metals (Basel)* 9(7):780. <https://doi.org/10.3390/met9070780>
20. Toro N, Pérez K, Saldaña M, Jeldres RI, Jeldres M, Cánovas M (2020) Dissolution of pure chalcocite with manganese nodules and waste water. *J Mater Res Technol* 9(1):798–805. <https://doi.org/10.1016/j.jmrt.2019.11.020>
21. Sosa BS, Banda-Noriega RB, Guerrero EM (2013) Industrias de fundición: aspectos ambientales e indicadores de condición ambiental. *Rev Metal* 49(1):5–19. <https://doi.org/10.3989/revmetalm.1171>
22. Schlesinger M, King M, Sole K, Davenport W (2011) Extractive metallurgy of copper. Fifth Edit
23. Torres D, Ayala L, Jeldres RI, Cerecedo-Sáenz E, Salinas-Rodríguez E, Robles P, Toro N (2020) Leaching chalcocite with high MnO₂ and chloride concentrations. *Metals (Basel)* 10(1):107. <https://doi.org/10.3390/met10010107>
24. Miki H, Nicol M, Velásquez-Yévenes L (2011) The kinetics of dissolution of synthetic covellite, chalcocite and digenite in dilute chloride solutions at ambient temperatures. *Hydrometallurgy* 105(3–4):321–327. <https://doi.org/10.1016/J.HYDROMET.2010.11.004>
25. Velásquez Yévenes L, Miki H, Nicol M (2010) The dissolution of chalcocite in chloride solutions: Part 2: effect of various parameters on the rate. *Hydrometallurgy* 103(1–4):80–85. <https://doi.org/10.1016/j.hydromet.2010.03.004>
26. Rodríguez M, Ayala L, Robles P, Sepúlveda R, Torres D, Carrillo-Pedroza FR, Jeldres RI, Toro N (2020) Leaching chalcocite with an imidazolium-based ionic liquid and bromide. *Metals (Basel)* 10(2):1–13. <https://doi.org/10.3390/met10020183>
27. Aguirre CL, Toro N, Carvajal N, Watling H, Aguirre C (2016) Leaching of chalcocite (CuFeS₂) with an imidazolium-based ionic liquid in the presence of chloride. *Miner Eng* 99:60–66. <https://doi.org/10.1016/j.mineng.2016.09.016>
28. Devore J (2010) Probability and statistics for engineering and the sciences, 8th edn. Cengage Learning, Boston, MA, USA
29. Mellado ME, Cisternas LA, Gálvez ED (2009) An analytical model approach to heap leaching. *Hydrometallurgy* 95(1–2):33–38. <https://doi.org/10.1016/J.HYDROMET.2008.04.009>
30. Mellado ME, Casanova MP, Cisternas LA, Gálvez ED (2011) On scalable analytical models for heap leaching. *Comput Chem Eng* 35(2):220–225. <https://doi.org/10.1016/j.compchemeng.2010.09.009>

31. Mellado M, Cisternas L, Lucay F, Gálvez E, Sepúlveda F (2018) A posteriori analysis of analytical models for heap leaching using uncertainty and global sensitivity analyses. *Minerals* 8(2):44. <https://doi.org/10.3390/min8020044>
32. Python Software Foundation (2019) Requests: HTTP for humans™. Available: <https://pypi.org/project/requests/>. Accessed on 11 Jul 2019
33. McCoy JT, Auret L (2019) Machine learning applications in minerals processing: a review. *Miner Eng* 132(November 2018):95–109. <https://doi.org/10.1016/j.mineng.2018.12.004>
34. Saldaña M, González J, Pérez-Rey I, Jeldres M, Toro N (2020) Applying statistical analysis and machine learning for modeling the UCS from P-wave velocity, density and porosity on dry travertine. *Appl Sci* 10(13):4565. <https://doi.org/10.3390/app10134565>

Chapter 24

A Posteriori Analysis of Analytical Models for Flotation Circuits Using Sensitivity Analyses



Edelmira Gálvez, Luis Ayala, Javier González, and Manuel Saldaña

Abstract The flotation of minerals is a multivariate physicochemical process that consists of applying the affinity of some mineral particles to the air, and also the affinity of other mineral particles for water, with the aim of obtaining a commercial product called concentrate, in addition to nonvaluable minerals called gangues. The flotation circuits, in charge of enriching the concentrate, generally consist of 3 stages, rougher, cleaner, and scavenger, which are made up of one or more cells, either in series or in parallel, depending on the architecture of the operational circuit. In this research, a local sensitivity analysis is developed for studying the behaviour of the stages that compose different flotation circuits. It is evaluated the concentrate grade quantifying the effect that circumstantial alteration has in the transfer rate of the concentration stages. The sensitivity analysis allows identify operation conditions that optimizing the concentrations offered by the flotation circuits. The results indicate that in simple circuits, the greatest impact on the concentration corresponds to rougher and cleaner cells, while in complex circuits (with additional cell banks), the sensitization of the rougher and cleaner cells, along with the early stages of the cleaner–scavenger cells have a greater impact on concentrate grade.

Keywords Mineral processing · Mineral flotation · Local sensibility · RCS circuit

E. Gálvez · J. González

Department of Metallurgical and Mining Engineering, Universidad Católica del Norte, Avenida Angamos 0610, 1270709 Antofagasta, Chile
e-mail: egalvez@ucn.cl

J. González

e-mail: javier.gonzalez@ucn.cl

L. Ayala

Faculty of Engineering and Architecture, Universidad Arturo Prat, Almirante Juan José Latorre 2901, 1244260 Antofagasta, Chile
e-mail: luisayala01@unap.cl

M. Saldaña (✉)

Department of Computing and Engineering Systems, Universidad Católica del Norte, Avenida Angamos 0610, 1270709 Antofagasta, Chile
e-mail: manuel.saldana@ucn.cl

1 Introduction

Worldwide, approximately 19.7 million tonnes of copper are produced [1, 2]. This commodity is very important for the economy of various countries, for example, in Chile, copper mining contributes 10% of the gross domestic product (GDP) [3, 4]. However, large-scale copper mining currently faces a number of challenges, such as decreases in mineral grades at the land surface [5–8], excessive increases in production to compensate for low ore grades [5], increase in environmental liabilities due to increased production [9–11], emission of polluting gases [12, 13] and water scarcity in arid areas where copper mining is carried out [14–18]. Then, despite that hydrometallurgical processes are less polluting in general than pyrometallurgical processes, they have not been able to be profitable for the treatment of primary copper sulphides, therefore, there is a constant search for optimization of copper recoveries through flotation processes, in addition to reducing the consumption of groundwater in them. The Froth Flotation Process involves taking advantage of the natural hydrophobicity of liberated (well ground) minerals/metals and making/playing with making them hydrophobic (water-repellent) individually in order to carefully isolate them from one another and the slurry they are in [19]. It employs the following chemicals/reagents for this purpose:

- Frothers are responsible for the creation of air bubbles.
- Collectors are used as a base to make metals hydrophobic (repellent to water) and to allow them to bind to air bubbles.
- pH Modifiers are used to increase or decrease the water-repellent effect of collectors on mineral surfaces. This enables Flotation Collectors to work selectively on specific minerals.

Froth flotation is a vital mineral concentration method used to extract a wide range of minerals containing essential resources. In the flotation process, ore is ground to a size sufficient to liberate desired minerals from waste rock (gangue); it is conditioned as a slurry using specific chemicals, collectively referred to as “collectors”, that adsorb to the waste rock (gangue). As a result, these mineral surfaces are hydrophobic and have a proclivity to bind to air bubbles. The conditioned mineral slurry is then processed in flotation cells (see Fig. 1), which are basically agitated tanks filled with finely dispersed air bubbles. The desired hydrophobic mineral would then cling to the air bubbles and float to the top of the flotation cell, where it will be separated [20].

The flotation process is the most widely used extractive process for copper recovery [21, 22], since the selective separation of materials is achieved, allowing the use of the hydrophobic and hydrophilic properties they possess the species involved [23, 24]. Since flotation is a widely used process, the study of the size and quantity of bubbles, the size of the particles and the hydrophobic conditions, and many other factors are of great importance [25, 26]. Flotation processes are predisposed in the mining industry by means of a structure in which series-ordered flotation banks are pre-established, in such a way that together they form flotation stages that are

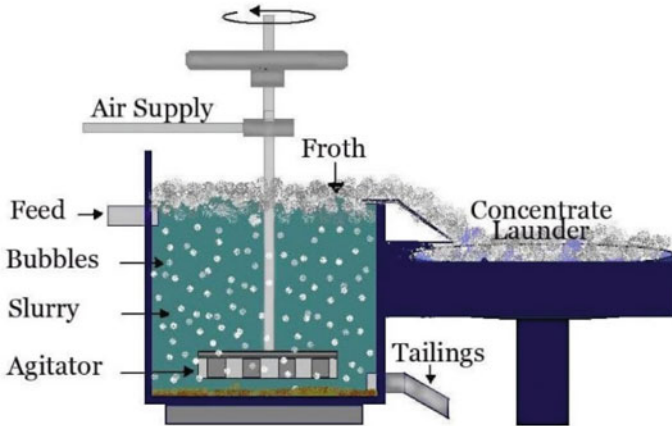


Fig. 1 Flotation process

interconnected with each other so that by means of the Joint processing achieves a sequential concentration of minerals that triggers the subsequent obtaining of a final concentrate [27, 28]. These concentration processes include the treatment of a large volume of material, that in turn produces an associated cost, for which studies are constantly being developed to make improvements in regard to the behaviour associated with flotation circuits [27, 29]. Regarding studies related to the search for improvements, Cisternas et al. [30] affirm that the literature focussed on this objective uses optimization techniques to a greater extent that allow the consideration of various operational structures in which it is analysed how the global behaviour of a circuit varies with respect to its own constitution, as well as the influence exerted by the stages that compose it [31–34]. Likewise, Cisternas et al. [35] refer to the use of tools such as sensitivity analysis [36], to identify the stages or variables that most affect the degree of recovery offered by flotation circuits [37], considering that a sensitivity analysis can be used to address the uncertainty links in the model and application scenarios, a fact that facilitates the evaluation of structures in flotation processes, as well as operational behaviours [38, 39].

The flotation process has been studied by several authors, highlighting works such as the adjustment of phenomenological models through mathematical programming [40], conceptual and analytical designs of concentration circuits [28, 29, 41], design and evaluation of flotation circuits using machine learning techniques [33, 34, 42, 43], studies of the dynamic behaviour of particles and bubbles on the recovery efficiency [44–50], the impact of gas dispersion measurements [51] and the effect of clay minerals on copper mineral flotation processes [52]. Then, within the simulation and optimization, there is the use of mixed linear and nonlinear integer programming algorithms [53], automated mineralogy data [54], and analysis of optimization methodologies that consider the effect of epistemic uncertainties and stochastics in the performance of the aggregate process or of some sub-processes [31, 55, 56].

Saltelli et al. [57] define sensitivity analysis as the study of how the uncertainty in the product of a model (numerical or otherwise) can be assigned to different sources of uncertainty in the input of the model, offering a wide spectrum of applications and identifying the most significant variables in a model, confirmed additionally by Cisternas et al. [30, 35]. Likewise, the sensitivity analysis can be separated into two large classifications, the global sensitivity analyses and the local sensitivity analyses [35, 57]. The first of these methods of sensitivity analysis is defined as the sensitivity analysis that allows the evaluation of an output model when all the factors of the model are evaluated simultaneously, being solved by means of numerical methods [28, 35, 57] such as regression methods, selection methods and variance-based methods [28, 35]. While the local sensitivity analysis methodology turns out to be defined as the local measure of the effect that an input value has on a given product [30, 35, 57], a measure that is represented by the first derivative partial of a model under evaluation [27, 30, 35, 57]. Due to the relevance of the search for new alternatives to improve the performance of flotation processes, such as optimizations of minerals concentration circuits, it proceeds to validate a local sensitivity analysis applied to an RCS circuit. In summary, the present work seeks to identify the stages of different floating circuits that have a greater impact on the responses. The findings of this type of study allow for a complete knowledge of which could be the bottlenecks or which stages are the most critical.

2 Materials and Methods

2.1 Flotation Circuit

In mineral processing, flotation can be defined as a technique used for the concentration and/or purification of mineral value, which is governed by the inter-phase properties of the solid–liquid–gas system and the changes in these properties through the addition of various reagents to the system [58]. The flotation process is defined as the concentration of minerals by separating the valuable minerals from the sterile ores or gangues [59]. This process is also called froth flotation and has how advantages the sufficient flexibility to selectively concentrate, producing clean and high-grade concentrates, through suitable combinations of additives, such as flocculants and/or frothing agents [31, 59]. The flotation mechanism comprises the attachment of mineral particles to air bubbles. The first circuit considered in the present study consist of three operational stages, these being the rougher (R), scavenger (S), and cleaner (C) stages [27, 56] (see Fig. 2). Likewise, these circuits present species and elements that are recovered from the sequential concentration, where useful species called species 1 or valuable mineral is recovered while a species 2 is scrapped, corresponding to a gangue [27]. Additionally, circuit models exposed by Calisaya et al. [56] (see Fig. 3) are studied, where additional cells are considered and the elements involved in the study are lead, copper, iron, and zinc.

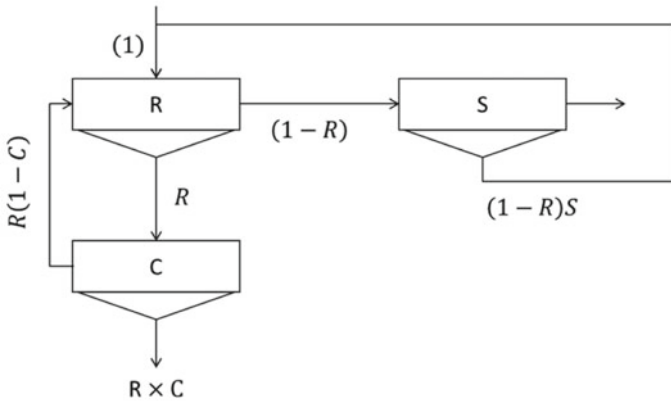


Fig. 2 Simple RCS circuit architecture

$$RCS_{\text{Concentration}} = \frac{R \times C}{1 - R \times (1 - C) - S \times (1 - R)} \quad (1)$$

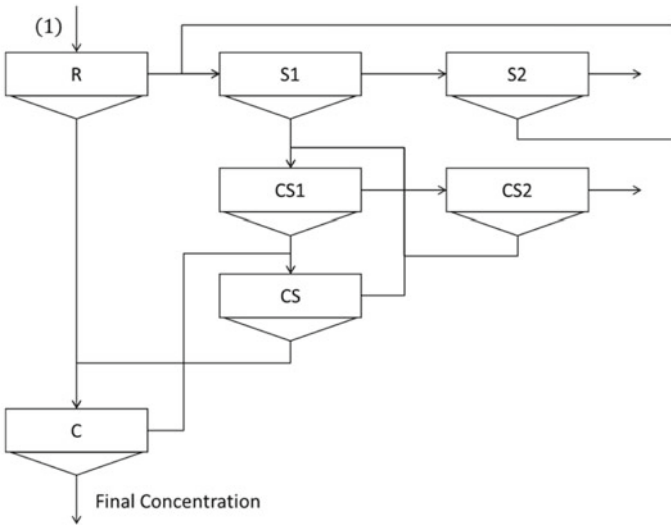


Fig. 3 RCS circuit operational architecture (Calisaya et al. [56])

Then, the transfer function of the concentration circuit presented in Fig. 2 is presented in Eq. 1. Where R , C , and S are concentrations obtained of rougher, cleaner, and scavenger cells, respectively.

$$\text{RCS}_{\text{Concentration}} = \frac{R \times C}{1 - R \times (1 - C) - S \times (1 - R)} \quad (1)$$

Where X (see Eq. 2) represents the feeding rate of cell scavenger 1 ($S1$), Y (see Eqs. 3.1, 3.2) represents the feeding rate of cell cleaner–scavenger-1 ($CS1$), Eq. 4 presents the balance of the feeding/outputs rates of the cleaner–scavenger-1 ($CS1$) cell, W (see Eq. 5) represents the feeding rate to the cleaner–scavenger (CS) cell and Z (see Eq. 6) represents the feeding rate of the cell cleaner of the circuit of Fig. 3 (C).

$$X = \frac{1 - R}{1 - (1 - S1)S2} \quad (2)$$

$$Y = \frac{X \times S1 + Z \times (1 - C) \times (1 - CS)}{(1 - CS2 \times (1 - CS1) - CS1 \times (1 - CS))} \quad (3.1)$$

$$Y = \frac{X \times S1 + R \times (1 - C) \times (1 - CS)}{(1 - CS2 \times (1 - CS1) - CS1 \times (1 - CS))(1 - (1 - C)CS) - CS1 \times (1 - C) \times (1 - CS)} \quad (3.2)$$

$$Y(1 - CS2(1 - CS1) - CS1(1 - CS)) = X \times S1 + \left(\frac{R + Y \times CS1}{1 - (1 - C) \times CS} \right) (1 - C)(1 - CS) \quad (4)$$

$$W = Y \times CS1 + Z \times (1 - C) \quad (5)$$

$$Z = \frac{R + Y \times CS1}{1 - (1 - C) \times CS} \quad (6)$$

Then, the recovery of the RCS circuit of Fig. 3 is presented in Eq. 7.

$$\text{Final Concentration} = Z \times C = \left(\frac{R + Y \times CS1}{1 - (1 - C) \times CS} \right) \times C \quad (7)$$

The CuFeS and CuS minerals in a rock mass can be physically isolated in a high-grade Cu concentrate, then profitably melted. The most effective method of isolating Cu minerals is froth flotation, a process that causes Cu minerals to selectively adhere to air bubbles that rise through a suspension of mineral. Flotation selectivity is generated using reagents, which make the Cu minerals water repellent and leave the waste minerals wet. In turn, this water repellency causes the Cu minerals to float in the rising bubbles, while the other minerals remain non-floating. The floating Cu -mineral particles overflow the flotation cell in a froth to become a concentrate containing ~30% Cu [29, 59, 60]. Flotation is preceded by crushing and grinding the extracted Cu ore into small particles (~50 mm).

The cleaner cells receive the froths from the rougher cells, their function is to eliminate the greatest amounts of impurities, depressing the non- Cu minerals in the concentrate from the rougher cell with CaO to produce a higher-grade Cu concentrate. Typical recoveries of Cu sulphide in flotation circuits are 85–90%, while typical grades of concentrate are 30% Cu (highest with chalcocite, bornite, and native copper

mineralization). Cleaner cells are particularly effective in giving a high degree of Cu in the concentrate [59].

Finally, the scavenger cells receive the tailings from the rougher cells and their function is to float the minerals of interest that did not float either due to lack of time, the addition of reagents, or some mechanical effect, however, the froth obtained from these cells does not. It can be sent to the concentrate thickener since it still contains many impurities, and neither can they be discarded since they also contain values, so they are returned to the circuit, in the flotation head part or are treated in intermediate cleaner–scavenger cells [61].

2.2 Sensitivity Analysis

Although there are many methods to carry out the sensitivity analysis [62, 63], two methods based on the calculation of variances were used: the extended Fourier method (FAST) and the Sobol method [64, 65] to obtain the first order sensitivity indices and the global sensitivity indices. The first order sensitivity index (S_i) represents the contribution of each input factor (X_i) to the total variance of the output ($V(Y)$) and is denoted by Eq. 8.

$$S_i = \frac{V[E(Y|X_i)]}{V(Y)} \quad (8)$$

where $V[E(Y|X_i)]$ is the amount of expected variance due to the main effect that would be removed from the total variance $V(Y)$ if the true value of the factor X_i could be determined [66].

3 Results and Discussions

3.1 Preliminary Quantification of Uncertainty in a Simple RCS Circuit

In this section, a quantification of the effect produced by each stage is carried out when performing the local sensitivity analysis, to identify the individual effect produced by each sub-process in the final concentrate, evaluating the effect of most critical stages in a global evaluation parameter, such as mineral recovery or the final concentration of the circuit. Considering the cases presented for the recovery of “species 2” shown in Fig. 4, both the operation of the rougher cell and that of the cleaner cell turns out to be crucial for the subsequent evaluation of the circuit presented in Fig. 2. Additionally, the scavenger cell has less impact on mineral recovery of “species 1”.

Figure 5 shows the differential variation of the impact on the global recovery of

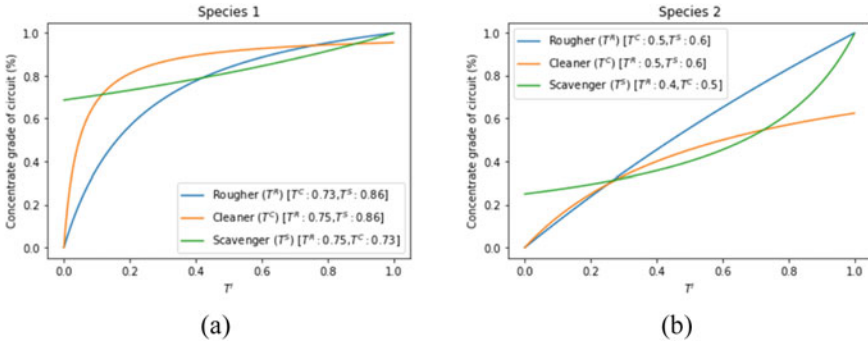


Fig. 4 Sensitivity analysis of the impact of the stages in the recovery of species 1 (a) and species 2 (b) in the RCS circuit of Fig. 2

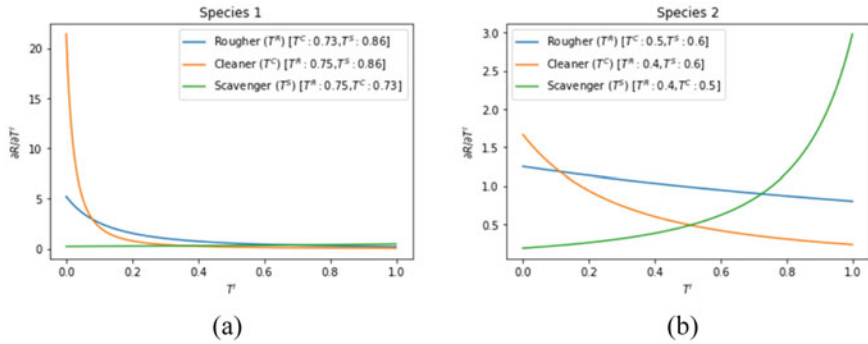
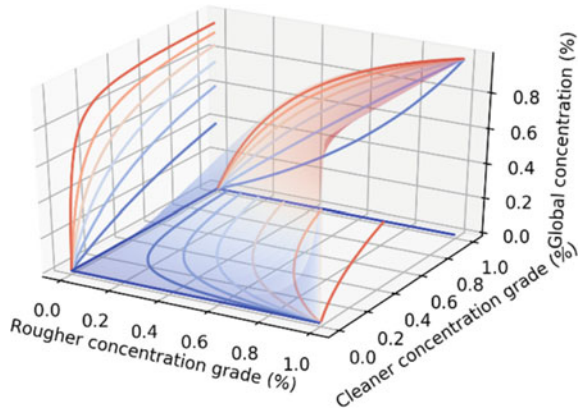


Fig. 5 Differential of the global recovery of an RCS circuit as a function of variations in the recovery of each unit of the aggregate circuit (Fig. 2)

the transfer rate of a given stage (for species 1), showing that at low levels of transfer functions of the cleaner and rougher cells, the greater the differential (decreasing). The incremental impact of the scavenger cell is negligible. Additionally, in the case of species 2, the differential of the scavenger cell is increasing, that of the cleaner cell is decreasing, and that of the rougher cell, slightly decreasing.

Finally, the response surface of the final concentration of the RCS circuit of Fig. 2 is presented in Fig. 6, shows the dynamics of the response to the degree of concentration of the rougher and cleaner cells.

Fig. 6 Response surface of the overall concentration as a function of the concentration



3.2 Results of Sensitivity Analysis

The local sensitivity analysis applied to flotation circuits provides valuable information regarding the effect of the stages involved [24, 30, 35], an effect that can be measured by evaluating one or several output parameters such as the grade of the final concentrate or the overall recovery percentage of a mineral species [27]. The measurement of the behaviour adopted by the global recovery of the different exposed circuits with respect to each one of the stages is carried out by means of the difference in percentage of global recovery obtained from a circumstantial increase or decrease in the recovery of species in a specific stage. Tables 1 and 2 show the results obtained from the local sensitivity analysis (where T^i represents the transfer ratio of stage i , and S_i the local sensitivity indicator), in addition to the effect that the stages generate by seeking an improvement in the overall recovery of a species (ΔR_g), being species 1 the valuable mineral (E1) (see Table 1) or on the contrary, reducing the gangue or species 2 recovered (E2) (see Table 2). It should be noted that in the case associated with the circuit in Fig. 2, the effect that the generate a specific

Table 1 Sensitivity analysis (circuit Fig. 2), Initial recovery E1: 93.99%

	R	S	C
T^i	75.00	86.00	73.00
S_i	50.00	43.00	13.50
ΔR_g	1.44	2.06	0.37

Table 2 Sensitivity analysis (circuit Fig. 2), Initial recovery E2: 45.46%

	R	S	C
T^i	40.00	60.00	50.00
S_i	50.00	30.00	25.00
ΔR_g	5.23	2.91	2.60

stage is measured by increasing the recovery focussed on species 1 by 5%, while the measurement associated with species 2 involves a reduction in recovery of 5%. By means of this measurement, it is identified which stages turn out to be the most critical when optimizing the global evaluation parameter present in flotation circuits such as the global recovery of species.

As in Fig. 2, the simplified results from local sensitivity analysis applied to the circuit of Fig. 3 (see Tables 3, 4, 5 and 6) are shown, indicating the effect associated with each of the stages (cells) by focussing their operation on improving the overall recovery of the valuable element, such as lead (see Table 3) or zinc (see Table 4), while the remaining elements are considered as gangues. It should be noted that the individual effect measured by the stages is carried out when they see their initial recovery of the zinc element increased by 10% while the initial recovery referred to the elements lead, iron and copper suffer an individual decrease of 10%.

On the other hand, Table 5 reflects the results by local sensitivity analysis when the process is sensitized by studying copper recovery, showing that the cells that have

Table 3 Local sensitivity analysis (circuit Fig. 3). Initial lead recovery: 33.20%

Pb	<i>R</i>	<i>S1</i>	<i>C</i>	<i>S2</i>	<i>CS1</i>	<i>CS2</i>	<i>SC</i>
T^i	40.00	38.00	35.00	30.00	35.00	37.00	60.00
S_i	16.74	3.44	16.13	16.31	16.13	16.05	13.33
ΔR_g	5.65	1.50	5.60	0.46	3.31	1.12	3.88

Table 4 Local sensitivity analysis (circuit Fig. 3). Initial zinc recovery: 89.39%

Zn	<i>R</i>	<i>S1</i>	<i>C</i>	<i>S2</i>	<i>CS1</i>	<i>CS2</i>	<i>SC</i>
T^i	80.00	67.00	60.00	60.00	56.00	62.00	82.00
S_i	42.00	13.41	13.33	13.33	14.10	12.88	6.53
ΔR_g	3.75	0.82	1.00	0.51	1.99	1.48	2.03

Table 5 Local sensitivity analysis (circuit Fig. 3). Initial copper recovery: 66.36%

Cu	<i>R</i>	<i>S1</i>	<i>C</i>	<i>S2</i>	<i>CS1</i>	<i>CS2</i>	<i>SC</i>
T^i	60.00	63.00	48.00	33.00	41.00	56.00	73.00
<i>I</i>	23.42	11.31	15.22	16.21	15.81	14.10	9.74
ΔR_g	5.42	1.71	3.79	0.55	4.47	2.14	4.48

Table 6 Local sensitivity analysis applied to circuit 2 considering only the iron element

Fe	<i>R</i>	<i>S1</i>	<i>C</i>	<i>S2</i>	<i>CS1</i>	<i>CS2</i>	<i>SC</i>
T^i	28.00	30.00	30.00	44.00	22.00	38.00	54.00
<i>I</i>	16.30	2.11	16.31	15.59	16.50	15.99	14.43
ΔR_g	-4.91	-0.96	-4.56	-0.32	-2.37	-0.61	-2.45

a greater impact on mineral recovery are the rougher cell (*R*), the scavenger–cleaner (*SC*), and the cleaner–scavenger 1 cells (*CS1*).

Then, Table 6 shows the results obtained by the local sensitivity analysis when a gangue element, such as iron, is taken into consideration. A quantification and measurement of the effect associated with the present stages are carried out, said associated effect is quantitatively reflected by means of the difference in the percentage of global iron recovery that is obtained by circumstantially reducing the initial recovery percentage of this element in a specific stage, identifying that the rougher (*R*) and cleaner (*C*) stages generate the highest degree of impact in reducing the overall recovery of iron.

Finally, sensitivity analysis describes the behaviour of the stages present in a flotation circuit, stages that have a similar or equal degree of initial recovery, showing what system component to generate a different impact on the response, which is attributed to individual behaviour of each stage when considering different recovery margins. Likewise, it is important to consider that this quantification of the individual effect of the stages (cells) ignores the recovery segments where the joint interaction of the stages turns out to be influential, a fact that does not occur in the global sensitivity analysis.

4 Conclusions

In the development of this study, local sensitivity analysis is developed to understand the importance of individual and group performance of the stages involved in a RCS circuit, reflected by means of a set of sensitivity indicators that allow inferring the degree of impact that the stages produce against a global evaluation parameter such as concentrate grade. Through of the results obtained, it is possible to corroborate the cases where the local sensitivity analysis allows to aspire to operational improvements in which the recovery of species and elements of economic interest is privileged, as well as achieve a decrease in the recovery of gangue. However, it is also possible to appreciate cases where the sensitivity of the stages turns out to be the same, which is not reflected in certain results referring to the measurement of the difference in percentage of global recovery, a situation that can be related because in the local sensitivity analysis, the degree of significance that the behaviour of the stages has together is not considered when considering a certain concentration percentage, but on the contrary, only the value that it has the significance of the stage.

Through the sensitivity analysis applied to flotation circuits studied, each operating parameter and factors involved in the operation are evaluated, as well as the behaviour of the stages in a specific and group way in the response, to understand which stages, turn out to be keys to meeting operational objectives. The results of the study indicate that in simple circuits (single cells for each stage of the RCS circuit), the greatest impact on the concentration of cells through sensitization corresponds to rougher, cleaner, and scavenger cells, respectively, while in complex circuits, which include additional cleaner–scavenger cell banks, the sensitization of the rougher and

cleaner cells, along with the early stages of the cleaner–scavenger cells have a greater impact on mineral concentration.

In future work is considering the local and global sensitization of models of the mineral flotation process on an industrial scale using machine learning techniques [67], such as neural networks [68] and Bayesian networks [4].

5 Conflicts of Interest

The authors declare no conflict of interest.

References

1. Toro N, Briceño W, Pérez K, Cánovas M, Trigueros E, Sepúlveda R, Hernández P (2019) Leaching of pure chalcocite in a chloride media using sea water and waste water. *Metals (Basel)* 9(7):780
2. Torres D, Ayala L, Jeldres RI, Cerecedo-Sáenz E, Salinas-Rodríguez E, Robles P, Toro N (2020) Leaching chalcopyrite with high MnO₂ and chloride concentrations. *Metals (Basel)* 10(1):107
3. Pérez K, Toro N, Campos E, Nazer A, Rodríguez MH (2019) Extraction of Mn from black copper using iron acid medium. *Metals (Basel)* 9(10):1–10
4. Saldaña M, González J, Jeldres R, Villegas Á, Castillo J, Quezada G, Toro N (2019) A stochastic model approach for copper heap leaching through bayesian networks. *Metals (Basel)* 9(11):1198
5. Toro N, Jeldres RI, Órdenes JA, Robles P, Navarra A (2020) Manganese nodules in Chile, an alternative for the production of Co and Mn in the future—a review. *Minerals* 10(8):674
6. Toro N, Robles P, Jeldres RI (2020) Seabed mineral resources, an alternative for the future of renewable energy: a critical review. *Ore Geol Rev* 126(July):103699
7. Robles P, Piceros E, Leiva WH, Valenzuela J, Toro N, Jeldres RI (2019) Analysis of sodium polyacrylate as a rheological modifier for kaolin suspensions in seawater. *Appl Clay Sci* 183
8. Torres D, Pérez K, Trigueros E, Jeldres RI, Salinas-Rodríguez E, Robles P, Toro N (2020) Reducing-effect of chloride for the dissolution of black copper. *Metals (Basel)* 10(1):123
9. Toro N, Saldaña M, Castillo J, Higuera F, Acosta R (2019) Leaching of manganese from marine nodules at room temperature with the use of sulfuric acid and the addition of tailings. *Minerals* 9(5):289
10. Toro N, Saldaña M, Gálvez E, Cánovas M, Trigueros E, Castillo J, Hernández PC (2019) Optimization of parameters for the dissolution of Mn from manganese nodules with the use of tailings in an acid medium. *Minerals* 9(7):387
11. Torres D, Ayala L, Saldaña M, Cánovas M, Jeldres RI, Nieto S, Castillo J, Robles P, Toro N (2019) Leaching manganese nodules in an acid medium and room temperature comparing the use of different Fe reducing agents. *Metals (Basel)* 9(12):1316
12. Velásquez-Yévenes L, Torres D, Toro N (2018) Leaching of chalcopyrite ore agglomerated with high chloride concentration and high curing periods. *Hydrometallurgy* 181(September):215–220
13. Pérez K, Toro N, Saldaña M, Salinas-Rodríguez E, Robles P, Torres D, Jeldres RI (2020) Statistical study for leaching of covellite in a chloride media. *Metals (Basel)* 10(4):477
14. Jeldres M, Piceros EC, Toro N, Torres D, Robles P, Leiva WH, Jeldres RI (2019) Copper tailing flocculation in seawater: relating the yield stress with fractal aggregates at varied mixing conditions. *Metals (Basel)* 9(12):1–13

15. Jeldres M, Piceros E, Robles PA, Toro N, Jeldres RI (2019) Viscoelasticity of quartz and kaolin slurries in seawater: importance of magnesium precipitates. *Metals (Basel)* 9(10)
16. Quezada GR, Jeldres M, Toro N, Robles P, Jeldres RI (2020) Reducing the magnesium content from seawater to improve tailing flocculation: description by population balance models. *Metals (Basel)* 10(3)
17. Quezada GR, Ayala L, Leiva WH, Toro N, Toledo PG, Robles P, Jeldres RI (2020) Describing mining tailing flocculation in seawater by population balance models: effect of mixing intensity. *Metals (Basel)* 10(2):1–15
18. Castellón CI, Piceros EC, Toro N, Robles P, López-Valdivieso A, Jeldres RI (2020) Depression of pyrite in seawater flotation by guar gum. *Metals (Basel)* 10(2)
19. Michaud D (2021) Froth flotation process. 911 *Metallurgist*. Available: <https://www.911metallurgist.com/blog/froth-flotation-process>. Accessed on 07 Apr 2021
20. Olin E (2021) Froth flotation circuit design and basic testwork requirements | SRK consulting. SRK Consulting. Available: <https://www.srk.com/en/publications/froth-flotation-circuit-design-and-basic-testwork-requirements>. Accessed on 07 Apr 2021
21. Araya G, Toro N, Castillo J, Guzmán D, Guzmán A, Hernández P, Jeldres RI, Sepúlveda R (2020) Leaching of oxide copper ores by addition of weak acid from copper smelters. *Metals (Basel)* 10(5):16–20
22. Toro N, Pérez K, Saldaña M, Jeldres RI, Jeldres M, Cánovas M (2020) Dissolution of pure chalcopyrite with manganese nodules and waste water. *J Mater Res Technol* 9(1):798–805
23. Agorhom EA, Lem JP, Skinner W, Zanin M (2015) Challenges and opportunities in the recovery/rejection of trace elements in copper flotation—a review. *Miner Eng* 78:45–57
24. Lucay F, Cisternas LA, Gálvez ED (2015) Global sensitivity analysis for identifying critical process design decisions. *Chem Eng Res Des* 103:74–83
25. Conejeros V, Pérez K, Jeldres RI, Castillo J, Hernández P, Toro N (2020) Novel treatment for mixed copper ores: leaching ammonia—precipitation—flotation (L.A.P.F.). *Miner Eng* 149(December 2019):106242
26. Salinas-Rodríguez E, Flores-Badillo J, Hernandez-Avila J, Cerecedo-Saenz E, del M, Gutierrez-Amador P, Jeldres RI, Toro N (2020) Assessment of silica recovery from metallurgical mining waste, by means of column flotation. *Metals (Basel)* 10(1):1–12
27. Lucay F, Mellado ME, Cisternas LA, Gálvez ED (2012) Sensitivity analysis of separation circuits. *Int J Miner Process* 110–111:30–45
28. Sepúlveda FD, Lucay F, González JF, Cisternas LA, Gálvez ED (2017) A methodology for the conceptual design of flotation circuits by combining group contribution, local/global sensitivity analysis, and reverse simulation. *Int J Miner Process* 164:56–66
29. Mendez DA, Gálvez ED, Cisternas LA (2009) State of the art in the conceptual design of flotation circuits. *Int J Miner Process* 90(1–4):1–15
30. Sepúlveda FD, Cisternas LA, Elorza MA, Gálvez ED (2014) A methodology for the conceptual design of concentration circuits: group contribution method. *Comput Chem Eng* 63:173–183
31. Cisternas LA, Lucay FA, Acosta-Flores R, Gálvez ED (2018) A quasi-review of conceptual flotation design methods based on computational optimization. *Miner Eng* 117:24–33
32. Xie Y, Cao B, He Y, Yang C, Gui W (2016) Reagent dosages control based on bubble size characteristics for flotation process. *IET Control Theory Appl* 10(12):1404–1411
33. Lucay F, Gálvez E, Cisternas L (2019) Design of flotation circuits using Tabu-search algorithms: multispecies, equipment design, and profitability parameters. *Minerals* 9(3):181
34. Massinaei M, Falaghi H, Izadi H (2013) Optimisation of metallurgical performance of industrial flotation column using neural network and gravitational search algorithm. *Can Metall Q* 52(2):115–122
35. Sepúlveda FD, Cisternas LA, Gálvez ED (2014) The use of global sensitivity analysis for improving processes: applications to mineral processing. *Comput Chem Eng* 66:221–232
36. Liu S (2008) *Global sensitivity analysis: the primer*, by Andrea Saltelli, Marco Ratto, Terry Andres, Francesca Campolongo, Jessica Cariboni, Debora Gatelli, Michaela Saisana, Stefano Tarantola 76(3)

37. Raghavan S, Hsu LL (1984) Factors affecting the flotation recovery of molybdenite from porphyry copper ores. *Int J Miner Process* 12(1–3):145–162
38. Mellado M, Cisternas L, Lucay F, Gálvez E, Sepúlveda F (2018) A posteriori analysis of analytical models for heap leaching using uncertainty and global sensitivity analyses. *Minerals* 8(2):44
39. Saldaña M, Ayala L, Torres D, Toro N (2020) Global sensitivity analyses of a neural networks model for a flotation circuit. *Hem Ind* 74(4):247–256
40. Bergh L, Yianatos J, Acuña C, Inostroza K (2018) Adapting a phenomenological model of a rougher flotation circuit to industrial historical operating data base. *IFAC-PapersOnLine* 51(21):111–116
41. Yianatos J, Carrasco C, Bergh L, Vinnett L, Torres C (2012) Modelling and simulation of rougher flotation circuits. *Int J Miner Process* 112–113:63–70
42. Jahedsaravani A, Marhaban MH, Massinaei M (2014) Prediction of the metallurgical performances of a batch flotation system by image analysis and neural networks. *Miner Eng* 69:137–145
43. Bascur OA, Soudek A (2019) Grinding and flotation optimization using operational intelligence. *Mining Metall Explor* 36(1):139–149
44. Dai Z, Fornasiero D, Ralston J (1999) Particle-bubble attachment in mineral flotation. *J Colloid Interface Sci* 217(1):70–76
45. Xu C, Gui W, Yang C, Zhu H, Lin Y, Shi C (2012) Flotation process fault detection using output PDF of bubble size distribution. *Miner Eng* 26(1):5–12
46. Guven O, Celik MS, Drelich JW (2015) Flotation of methylated roughened glass particles and analysis of particle-bubble energy barrier. *Miner Eng* 79:125–132
47. Kouachi S, Vaziri Hassas B, Hassanzadeh A, Çelik MS, Bouhenguel M (2017) Effect of negative inertial forces on bubble-particle collision via implementation of Schulze collision efficiency in general flotation rate constant equation. *Colloids Surf A Physicochem Eng Asp* 517:72–83
48. Ozdemir O, Karaguzel C, Nguyen AV, Celik MS, Miller JD (2009) Contact angle and bubble attachment studies in the flotation of trona and other soluble carbonate salts. *Miner Eng* 22(2):168–175
49. Yianatos J, Contreras F (2010) Particle entrainment model for industrial flotation cells. *Powder Technol* 197(3):260–267
50. Vallejos P, Yianatos J (2019) Analysis of industrial flotation circuits using top-of-froth and concentrate mineralogy. *Miner Process Extr Metall Rev* 00(00):1–10
51. Grau RA, Heiskanen K (2003) Gas dispersion measurements in a flotation cell. *Miner Eng* 16(11):1081–1089
52. Jeldres RI, Uribe L, Cisternas LA, Gutierrez L, Leiva WH, Valenzuela J (2019) The effect of clay minerals on the process of flotation of copper ores—a critical review. *Appl Clay Sci* 170(July 2018):57–69
53. Acosta-Flores R, Lucay FA, Cisternas LA, Gálvez ED (2018) Two-phase optimization methodology for the design of mineral flotation plants, including multispecies and bank or cell models. *Miner Metall Process* 35(1):24–34
54. Gu Y, Schouwstra RP, Rule C (2014) The value of automated mineralogy. *Miner Eng* 58:100–103
55. Cisternas LA, Lucay FA, Acosta-Flores R, Gálvez ED (2018) A quasi-review of conceptual flotation design methods based on computational optimization. *Miner Eng* 117(November 2017):24–33
56. Calisaya DA, López-Valdivieso A, de la Cruz MH, Gálvez EE, Cisternas LA (2016) A strategy for the identification of optimal flotation circuits. *Miner Eng* 96–97:157–167
57. Saltelli A, Tarantola S, Campolongo F, Ratto M (2004) Sensitivity analysis in practice: a guide to assessing scientific models (Google eBook)
58. The R Foundation (2020) R: the R project for statistical computing. The R project for statistical computing. Available: <https://www.r-project.org/>. Accessed on 05 Apr 2020
59. Schlesinger M, King M, Sole K, Davenport W (2011) Extractive metallurgy of copper, Fifth Edn

60. Bergh L, Yianatos J (2013) Control of rougher flotation circuits aided by industrial simulator. *J Process Control* 23(2):140–147
61. Bulatovic SM (2007) *Handbook of flotation reagents: chemistry, theory and practice* volumel, first edn, 2
62. Saltelli A, Annoni P, Azzini I, Campolongo F, Ratto M, Tarantola S (2010) Variance based sensitivity analysis of model output. design and estimator for the total sensitivity index. *Comput Phys Commun* 181(2):259–270
63. Makowski D, Naud C, Jeuffroy MH, Barbottin A, Monod H (2006) Global sensitivity analysis for calculating the contribution of genetic parameters to the variance of crop model prediction. *Reliab Eng Syst Saf* 91(10–11):1142–1147
64. Saltelli A, Ratto M, Andres T, Campolongo F, Cariboni J, Gatelli D, Saisana M, Tarantola S (2008) *Global sensitivity analysis. the primer*
65. Cariboni J, Gatelli D, Liska R, Saltelli A (2007) The role of sensitivity analysis in ecological modelling. *Ecol Modell* 203(1–2):167–182
66. Toro N, Pérez K, Saldaña M, Salinas-Rodríguez E, Hernández P (2020) Treatment of black copper with the use of iron scrap—part I. *Hem Ind* 74(4):237–245
67. McCoy JT, Auret L (2019) Machine learning applications in minerals processing: a review. *Miner Eng* 132(November 2018):95–109
68. Saldaña M, González J, Pérez-Rey I, Jeldres M, Toro N (2020) Applying statistical analysis and machine learning for modeling the UCS from P-wave velocity, density and porosity on dry travertine. *Appl Sci* 10(13):4565

Chapter 25

Modeling the Dynamic of a SAG Milling System Through Regression Models and Neural Networks



Manuel Saldaña, Luis Ayala, and Javier González

Abstract Due to the growth of the worldwide copper industry and the increase complexity of this process in front of feeding mineralogy and the cost structures, the generation of alternatives that improve efficiency of mining processes by studying his dynamics represents significant savings in capital costs, considering the situation facing the industry. Generate of models that represent the dynamic behavior of productive processes has the potential to contribute to understand the parameters that impact on the responses, identifying operating restrictions, distributions of the independent variables or the optimal levels of operation. This work proposes the development of regression models and ANNs models of the SAG milling process, studying the production in tons per hour, in function to 17 operational variables analyzed. The multiple regression model presents a good fit (77.45%), and the inclusion of the interactions and quadratic effects increases the coefficient of determination (89.2%), but, the neural network-based model is the one with the best fit (96.27%).

Keywords Comminution · Dynamic systems · Analytical models · SAG milling · Regression models

M. Saldaña (✉)

Department of Computing and Engineering Systems, Universidad Católica del Norte, Avenida Angamos 0610, 1270709 Antofagasta, Chile
e-mail: manuel.saldana@ucn.cl

L. Ayala

Faculty of Engineering and Architecture, Universidad Arturo Prat, Almirante Juan José Latorre 2901, 1244260 Antofagasta, Chile
e-mail: luisayala01@unap.cl

J. González

Department of Metallurgical and Mining Engineering, Universidad Católica del Norte, Avenida Angamos 0610, 1270709 Antofagasta, Chile
e-mail: javier.gonzalez@ucn.cl

1 Introduction

There is constant growth in the copper industry, and Flanagan [1] indicates that copper production has been increasing in recent years, increasing from 20 tons in 2017 to 21 (rounded) in 2018, while a more recent report generated by the International Copper Study Group [2] indicates that since 1900, the copper production worldwide has grown on average 3.2% per year, reaching 20.6 million tons in 2018, with an increase in the production of concentrates of 31.5% and solvent-electrodeposition extraction in 19.5% [3]. Chile is the main producer of copper worldwide with a 29% participation and with 23% of the reserves of this commodity [4], with 3817 copper mineral deposits within of the national territory [5], where their exploitation represents 91.1% of the composition of exports by the mining market in 2019 [4].

Copper oxides are increasingly scarce in Chile (and will decreasing of 30.8% in 2015 to 12% in 2027), while copper sulfides are in greater quantity [6]. On the other hand, 39.2% of the production of fine copper is processed through hydrometallurgical way, while most of the production (60.8%) is by flotation processes that generate environmental liabilities, such as tailings dams [1]. It is estimated that, in Chile, for each ton of copper obtained by flotation processes, 151 tons of tailings are generated [6]. Worldwide most of the copper minerals correspond to sulfides and a minor part to oxides [7]. The mining industry has traditionally worked in two ways, pyrometallurgy if it is sulfide minerals, which includes the flotation, smelting, and electro-refining processes. While in the hydrometallurgical route, it has mainly worked with oxidized minerals, breaking down in the leaching, solvent extraction, and electro-extraction stages [8]. Both working mechanisms have proven to be profitable in industry; however, pyrometallurgy has the main disadvantage of generate SO_2 emissions into the atmosphere, generating serious environmental problems [9]. As part of the mineral processing, the comminution process turns out to be a key stage, since it is where most of the energy invested in the operation is concentrated to reduce the size of the material [10]. For its part, the SAG grinding process means a greater reduction in particles through the use of large rotating equipment, where water is added to the mineralized material in sufficient quantities to form a milky fluid and the reagents necessary to carry out the following process [11].

Then, the analysis of models of productive processes like SAG milling (through statistic models [11, 12] or based on machine learning [13, 14]) could supposed important improves in production indicators, obtained from the simulation and/or optimization of these [15]. The development of this work considers the materials and methods section, where the operational data set to be used for modeling is explained, the generation of analytical models through regression analysis is explained, and the adjustment evaluation statistics are presented. In the section results and discussions, a correlation analysis between the independent variables and the response is developed, together with the distributions of the explanatory variables, the fit of statistical models for multiple linear regression model and quadratic regression is presented, in addition to the optimization of the quadratic model. Finally, the conclusions section presents the main findings of the research work.

2 Materials and Methods

2.1 Data

The database that is the object of analysis for the present research work comes from a plant that processes copper sulfide minerals. The circuit has a large SAG mill and two ball mills that carry out secondary grinding work (not considered in the modeling of this work). The operational data were collected in the circuit with hourly frequency. The period considered comprises the period March–August 2019, counting with the operational data of the SAG milling for a period of 6 months. The number of measured variables is 17, while the studied response is given by production in tons per hour (TpH).

2.2 Regression Models

Regression analyzes are part of statistics that investigate the relationship between two or more variables related in a non-deterministic form [16]. Simple linear regression analyzes relate an independent variable with an response variable, while multiples linear regressions relate the dependent variable or response (Y) with a set of independent variables called regressors (X1, X2, X3...). In other words, multiple regression models are an extension of simple linear regression. Then, regression models are useful to predict the dependent variable, to evaluate the impact that predictors have on it [17] or to optimize the response bounded to the sampling domain [15–20].

Multiple linear model can be expressed as presented in Eq. (1).

$$\begin{aligned}
 Y &= \left(\beta_0 + \sum_{i=1}^n \beta_i X_i + \sum_{i=1}^n \sum_{j=1}^n \beta_{ij} X_i X_j \right) \\
 + e_i Y &= \left(\beta_0 + \sum_{i=1}^n \beta_i X_i + \sum_{i=1}^n \sum_{j=1}^n \beta_{ij} X_i X_j \right) + e_i \quad (1)
 \end{aligned}$$

where $\beta_0\beta_0$ is the ordinate at the origin, YY , the dependent variable, XX , the independent variables and $e_i e_i$ is the error (difference between estimated and observed values).

2.3 Neural Networks

Artificial neural networks (ANNs) are machine learning (ML) techniques that determine associations between a known observations and to classify new and unknown data. ANNs have the capability to approximate nonlinear relationships and generalize complex systems from imprecise information, as well as being robust to handle noise, overfitting, and outliers [21]. One of the most used structures is the multilayer perceptron [22] (see Fig. 1), where x_i represents the independent variables (inputs), O_i the dependent variables (outputs), and σ are the activation function.

The output of each neuron is given by the function σ (The most used activation functions are the sigmoid, logistic, or hyperbolic tangent), where w_i is the synaptic weights, ω_0 is the threshold, and n is the total of synaptic weights connected to the neuron. Hyperbolic tangent was used as the activation function, while that backpropagation was the learning method used. The training process involves the following three stages [21]: feedforward of the input training patterns; calculation and backpropagation of the associated error; and finally, the adjustment of the weights.

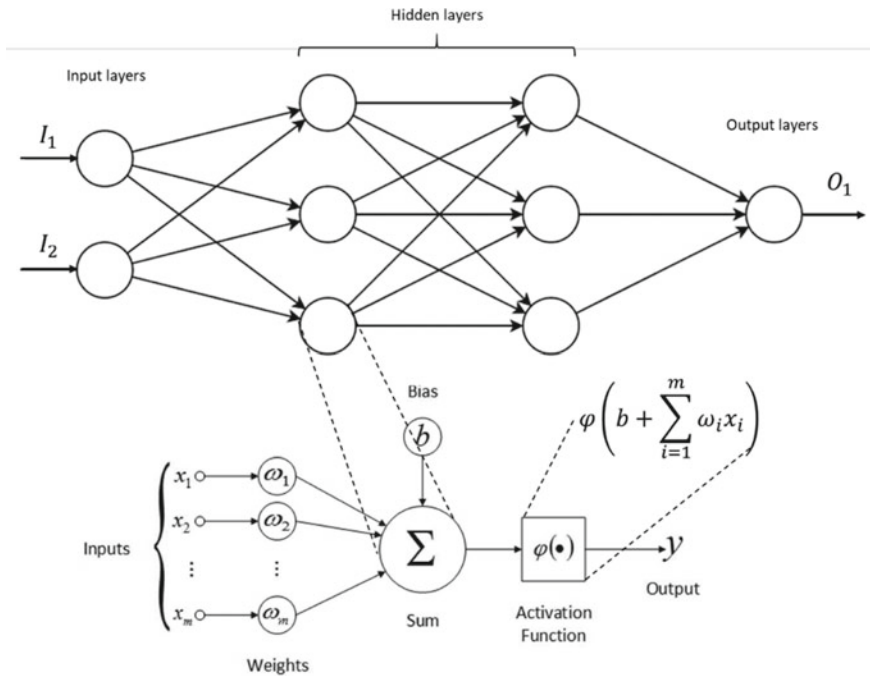


Fig. 1 Structure of a generic multilayer perceptron

2.4 *Fit Assessment*

Once the best model generated with the available data, its capacity should be checked by predicting new observations that have not been used to train it, thus verifying whether the models can be generalized. To do this, the data is randomly divided into two groups (70–30%), fitting the model with the first group and estimating the precision of the predictions with the second. The goodness-of-fit statistics mean absolute deviation (MAD), mean square error (MSE), accuracy (ACC), and determination coefficient (R^2) were used to evaluate the fitted models [23]. The fit of the statistical model was developed using version 3.7.0 of Python [24].

3 Results and Discussion

3.1 *Graphical Analysis and Data Distributions*

The use of mathematical models and machine learning techniques as instruments for evaluating alternatives is becoming increasingly important in the field of economic evaluation of services and products, with an increasingly relevant role as an aid in decision-making in the management of mining processes [21–31]. A total of 17 operating variables were evaluated, filtering the most significant variables, while that correlation matrix and distribution of recovery versus operative variables considered for modeling are presented in Figs. 2 and 3, respectively.

The variables considered for modeling are the production of the SAG mill in Tph (response), speed in RPM, mill pressure in PSI, mill power in MW, P80, water supply in m^3/h , sump level, hardness, and percentage of solids in the feed and pebbles.

From the analysis of the distributions of the independent variables, it is having that the water supply and P80 present a normal distribution with means 3500 [m^3/h] and 4 [inch] approximately. The sump level, the percentage of solids in feeding, and the SAG speed show a distribution with negative bias, with averages of 90 [m^3], 73%, and 9 [RPM], respectively. Finally, the minerals hardness in feeding and the pebbles have a positive bias distribution, with averages of approximately 35 and 350 [Tph].

3.2 *Fitting Statistical Models*

After the analysis of correlations shown in Fig. 2, models that represent the dynamics of the SAG milling process are generated by adjusting multiple linear regression models and quadratic regression models. The fitting of multiple regression model for representing the SAG milling process presents good indicators of goodness-of-fit (see Table 1). The determination coefficient R^2 is of 77.45%, and all the variables considered (and showed in Table 1) are significant ($p < 0.05$).

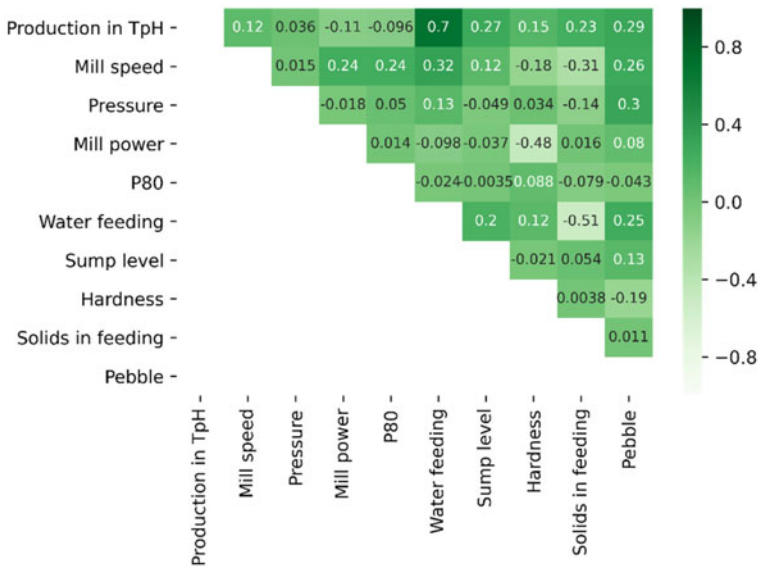


Fig. 2 Correlation graph of the operating variables of the SAG grinding process

The normality test of the residuals indicates that tend to distribute normally, despite the existence of multiple values that do not fit the normal probability line (see Fig. 4).

In addition to the adjustment of the multiple linear regression model, a quadratic regression model is generated (see Table 2). The quadratic model presents a better fit than the model linear ($R^2 = 89.20\%$), and the statistic p value (<0.05), for each individual parameter and the aggregate model, validates it. As in the simple linear regression model, the normal probability plot of the residuals validates their normality (see Fig. 5).

Then, the response surface designs for the quadratic model based on the independent variables indicate that production increases at high levels of solids and water in the feed (see Fig. 6a), at high levels of mineral hardness in the feed (see Fig. 6b), at high feeding of pebbles in TpH (see Fig. 6c), and low maximum size of ore that represent 80% of the feed (see Fig. 6c). On the other hand, the linear effect of SAG speed does not have a significant effect on production in TpH.

3.3 Fitting Neural Networks

For studying the fitting of production in TpH through ANNs, four architectures were modeled for training and testing, with network architectures of 2:3, 2:5, 3:3, and 3:5 hidden layer and neurons per hidden layer, respectively. The sample data was divided into a 70:30 rate for the training and testing phases. The activation functions

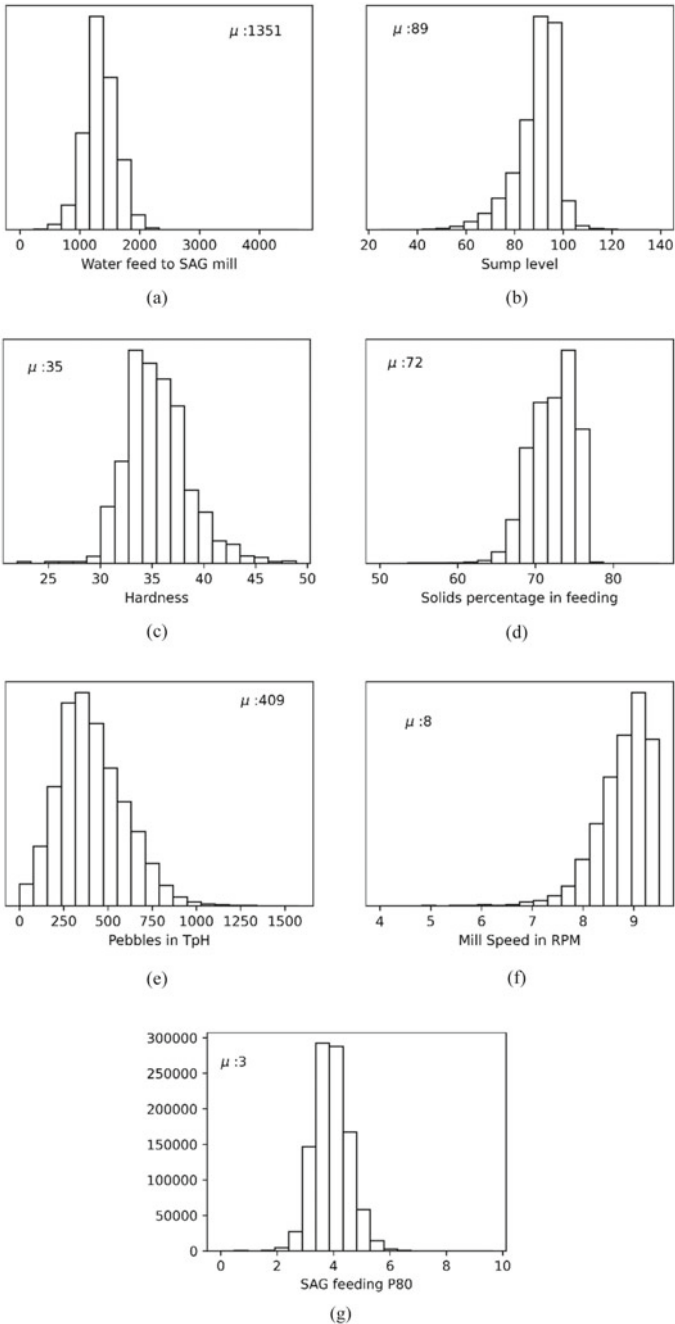
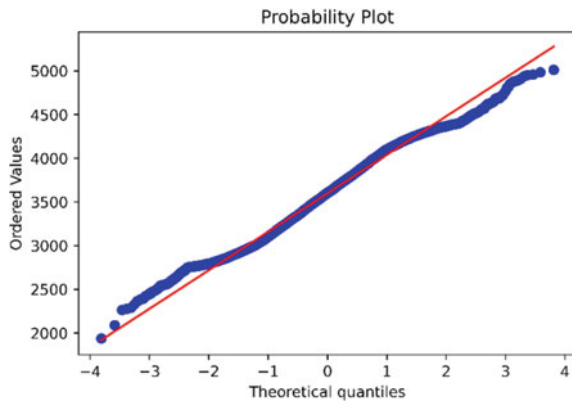


Fig. 3 Distributions of the operational parameters water supply (a), sump level (b), hardness of the mineral in the supply (c), percentage of solids in the supply (d), pebbles in TpH (e), mill speed in TpH (f), and SAG feeding p80 (g)

Table 1 ANOVA table of multiple linear regression model

	Coefficient	std err	<i>t</i>	<i>p</i> value
Intercept	-11,320.00	5.152	-2196.48	0.000
SAG speed	18.71	0.276	67.729	0.000
P80	-11.62	0.206	-56.508	0.000
Water feeding	2.40	0.001	3946.677	0.000
Sump level	0.23	0.014	16.524	0.000
Hardness	3.74	0.042	89.575	0.000
Solid in feeding (%)	156.48	0.051	3041.97	0.000
Pebbles	0.05	0.001	65.312	0.000

Fig. 4 Normal probability graph of multiple linear regression



are rectified linear activation functions or ReLU for hidden layers, and sigmoid functions in output layer. “Adam” was the optimizer used to update the attributes of the network, while what the epochs and batch size were 1000 and 100 respectively. The error measures (MAD, MSE), accuracy, and R^2 statistics have been summarized in Table 3.

The goodness-of-fit statistics showed in Table 3 indicate that the best configuration is three hidden layers with three neurons per layer, which is validated by the adjustment statistics: R^2 (0.963), accuracy (94.06%), MAD (0.153), and MSE (0.082).

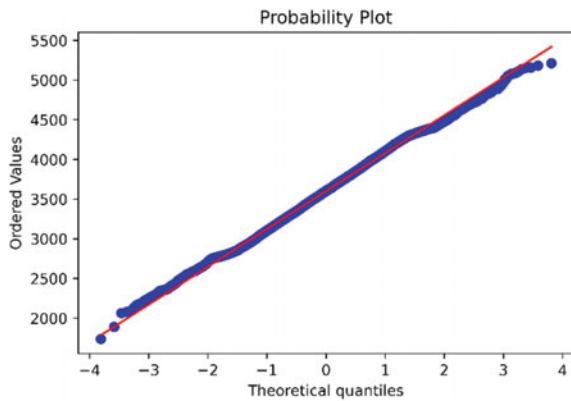
3.4 Discussion

Table 4 presents the results of all fitted models, relating production in TpH (explained variable) with the independent variables: SAG speed, P80 in feeding, water feeding, sump level, hardness, solid in feeding (%), and pebbles. Linear regression analyses

Table 2 Quadratic regression model results

	Coefficient	std err	t	p value
Intercept	2.09E + 04	44.924	464.801	0.000
SAG speed	243.1425	3.863	62.941	0.000
P80 in feeding	-92.974	4.31	-21.569	0.000
Water feeding	-4.7155	0.012	-386.87	0.000
Sump level	0.0558	0.009	6.105	0.000
Hardness	1.548	0.027	57.156	0.000
Solid in feeding (%)	-639.1473	0.972	-657.58	0.000
Pebbles	-0.0124	0	-27.017	0.000
SAG speed × P80	-5.071	0.238	-21.293	0.000
SAG speed × Water feeding	-0.0135	0.001	-23.557	0.000
SAG speed × Solid percentage in feeding	-2.7617	0.049	-56.263	0.000
P80 × Water in feeding	-0.0018	0.001	-3.531	0.000
P80 × Solid percentage in feeding	1.8517	0.046	40.212	0.000
Water feeding × Solid in feeding	0.1066	0	792.985	0.000
Water in feeding	-9.84E-05	1.04E-06	-94.659	0.000
Solid percentage in feeding ²	4.7348	0.006	753.663	0.000

Fig. 5 Normal probability graph of quadratic regression



present a R^2 statistics higher 77%, while that the quadratic model present a better fit of linear model ($R^2 = 0.8920$). On the other hand, the ANN presents the best fit for multivariate modeling ($R^2 = 0.9627$).

In addition, the validation of the fitted models is presented in Fig. 7, contrasting the predicted production generated by the model and the real production of the milling system using an X–Y graph. The scatter graphs that contrast the productions of the multiple linear regression models (see Fig. 7a), quadratic regression (see Fig. 7b), and the neural network (see Fig. 7c) confirm again that this last model is who best

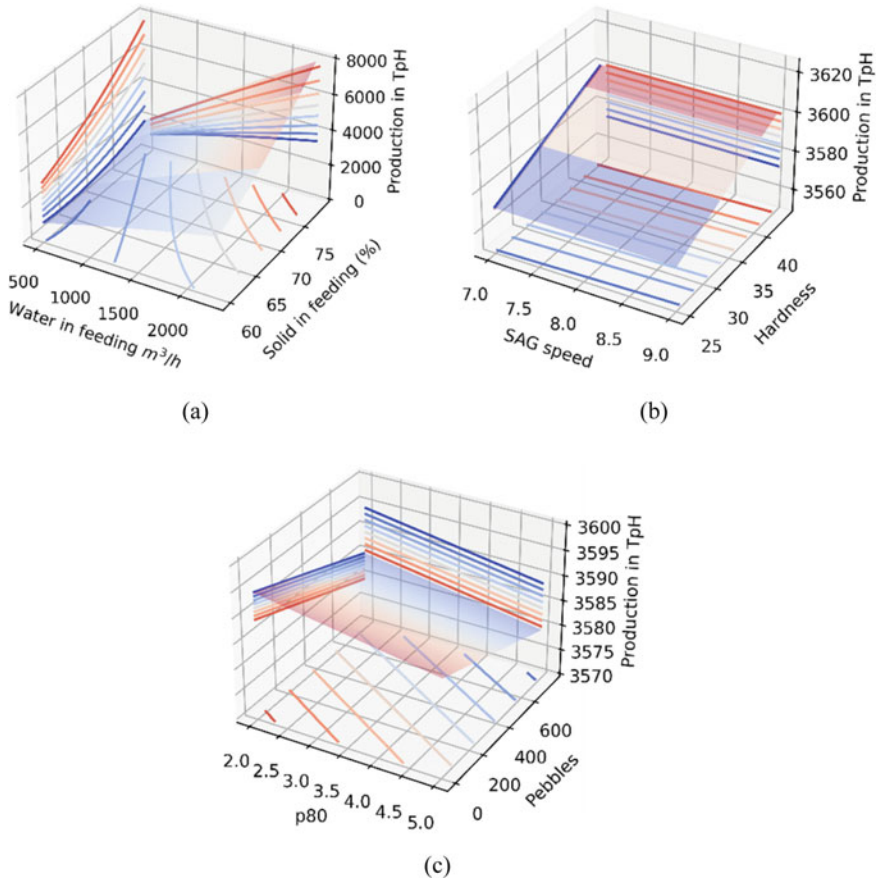


Fig. 6 Response surface plots for production in tons per hour versus water and solids in feeding (a), SAG speed and hardness (b) and p80 and pebbles (c) of quadratic model

Table 3 Adjustment statistics for ANN architectures

Architecture/Statistic	Training				Testing			
	MAD	MSE	ACC	R ²	MAD	MSE	ACC	R ²
2 layer, 3 neurons	0.192	0.099	83.41	0.791	0.215	0.100	81.92	0.774
2 layer, 5 neurons	0.172	0.097	88.73	0.917	0.191	0.098	87.72	0.892
3 layer, 3 neurons	0.142	0.081	95.53	0.984	0.153	0.082	94.06	0.963
3 layer, 5 neurons	0.146	0.081	95.65	0.985	0.149	0.081	94.05	0.963

Table 4 Summary of coefficients of determination of the generated models

Model	R ²
Multiple simple	0.7745
Multiple quadratic	0.8920
ANN (3 layers, 2 neurons)	0.9627

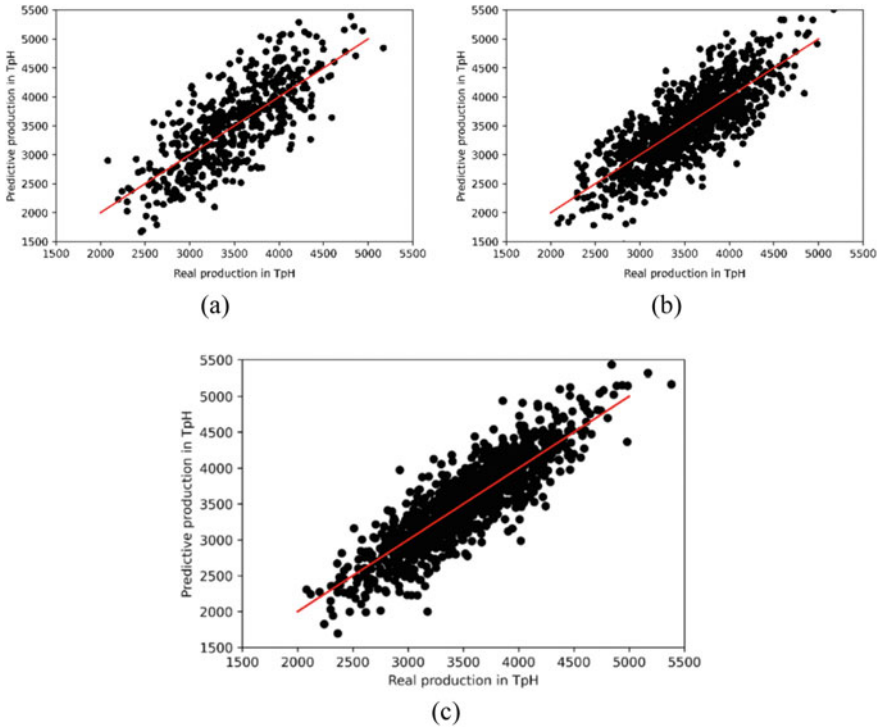


Fig. 7 Real production versus predictive production for simple (a), quadratic (b) regression model, and artificial neural network (c)

adjusts to the real production of milling production process. The scenarios presented on the red line are those with the highest theoretical production, while the scenarios that are under the red line are those with a lower theoretical production.

4 Conclusions

In this work, the modeling of the dynamics of the SAG grinding system was developed through regression models and artificial neural networks, for which the impact

of 17 operative variables on production in tons per hour was evaluated. The correlation between the independent variables and the response was studied, filtering the variables that impact on the explained variable, which are pressure, mill speed, percentage of solids in the feed, minerals hardness, water feeding, P80, and sump level. Multiple linear regression models and a quadratic model were generated, which represented significant adjustments to the sampled domain, with R^2 values of 77% and 89%, respectively. Regression models prove to be a powerful tool in modeling the studied system, in addition to presenting the potential of using optimization algorithms to calculate the values that maximize the response. However, artificial neural networks present greater efficiency in the modeling of the dynamics of the process, with an R^2 statistic of 96%. Finally, future works, what considered the dynamics of the SAG milling process, could be modeled, simulated, and optimized using additional machine learning techniques [14], such as Bayesian networks [32], or discrete event simulation [33].

References

1. Flanagan DM (2019) Copper. In: Mineral commodity summaries 2019, pp 52–53. U.S. Geological Survey, Virginia, USA
2. ICSG (2019) The world copper factbook 2019. Lisbon, Portugal. Available at: <https://www.icsg.org/index.php/component/jdownloads/finish/170/2965>
3. ICSG (2019) Release of ICSG 2018 statistical yearbook. Lisbon, Portugal. Available at: <http://www.icsg.org/index.php/press-releases/finish/170-publications-press-releases/2983-2019-12-09-press-release-yearbook-2019>
4. Minero C (2019) Cifras actualizadas de la minería. Santiago, Chile. Available at: <file:///Users/Manuel/Desktop/Cifras-actualizadas-de-la-mineria-Marzo-actualizado-2020.pdf>
5. Servicio Nacional de Geología y Minería (2017) Anuario de la minería de Chile 2017. Santiago, Chile. Available at: http://www.sernageomin.cl/wp-content/uploads/2018/06/Anuario_2017.pdf
6. Comisión Chilena del Cobre (2017) Sulfuros primarios: desafíos y oportunidades. Santiago, Chile. Available at: http://www.cochilco.cl/Listado-Temtico/sulfuros-primarios_desafios-y-oportunidades.pdf
7. Toro N, Briceño W, Pérez K, Cánovas M, Trigueros E, Sepúlveda R, Hernández P (2019) Leaching of pure chalcocite in a chloride media using sea water and waste water. *Metals (Basel)* 9(7):780. <https://doi.org/10.3390/met9070780>
8. Toro N, Pérez K, Saldaña M, Jeldres RI, Jeldres M, Cánovas M (2020) Dissolution of pure chalcopyrite with manganese nodules and waste water. *J Mater Res Technol* 9(1):798–805. <https://doi.org/10.1016/j.jmrt.2019.11.020>
9. Sosa BS, Banda-Noriega RB, Guerrero EM (2013) Industrias de fundición: aspectos ambientales e indicadores de condición ambiental. *Rev Metal* 49(1):5–19. <https://doi.org/10.3989/revmetalm.1171>
10. COCHILCO (2015) Caracterización de los costos de la gran minería del cobre. Santiago, Chile. Available at: https://www.cochilco.cl/Listado-Temtico/Informe_caracterizacion_de_los_costos.pdf
11. Villanueva M, Calderón C, Saldaña M, Toro N (2020) Modelling a sag grinding system through multiples regressions. *Met 2020—29th Int Conf Metall Mater Conf Proc* 1243–1248. <https://doi.org/10.37904/metal.2020.3665>

12. Pérez K, Toro N, Saldaña M, Salinas-Rodríguez E, Robles P, Torres D, Jeldres RI (2020) Statistical study for leaching of covellite in a chloride media. *Metals (Basel)* 10(4):477. <https://doi.org/10.3390/met10040477>
13. Saldaña M, Ayala L, Torres D, Toro N (2020) Global sensitivity analyses of a neural networks model for a flotation circuit. *Hem Ind* 74(4):247–256. <https://doi.org/10.2298/HEMIND20060523S>
14. McCoy JT, Auret L (2019) Machine learning applications in minerals processing: a review. *Miner Eng* 132(November 2018):95–109. <https://doi.org/10.1016/j.mineng.2018.12.004>
15. ICSG (2020) Copper: preliminary data for January 2020. Lisbon, Portugal. Available at: <https://www.icsg.org/index.php/component/jdownloads/finish/114/3011?Itemid>
16. Devore J (2010) *Probability & statistics for engineering and the sciences*, 8th edn. Cengage Learning, Boston, MA, USA
17. Steinhilber RK, Myers RH (1988) Classical and modern regression with applications. *J Am Stat Assoc* 83(401):271. <https://doi.org/10.2307/2288958>
18. Sabbagh HAK, Abudayah Z, Abudoleh SM, Alkhrad JA, Hussein MZ, Hussein-Al-Ali SH (2019) Application of multiple regression analysis in optimization of metronidazole-chitosan nanoparticles. *J Polym Res* 26(8). <https://doi.org/10.1007/s10965-019-1854-x>
19. Yang C, Zheng LH, Qiao HT (2014) Optimisation model of fuzzy ball fracture diverting fluid based on multiple quadratic regression method. *Mater Res Innov* 18:S2478–S2481. <https://doi.org/10.1179/1432891714Z.000000000457>
20. Al Mesfer MK, Danish M, Alam MM (2018) Optimization of performance model of ethyl acetate saponification using multiple regression analysis. *Russ J Appl Chem* 91(11):1895–1904. <https://doi.org/10.1134/S1070427218110228>
21. Hawkin S (2008) *Neural networks and learning machines*, 3rd edn
22. Wu YC, Feng JW (2018) Development and application of artificial neural network. *Wirel Pers Commun* 102(2):1645–1656. <https://doi.org/10.1007/s11277-017-5224-x>
23. Montgomery DC, Runger GC (2014) *Applied Statistics and probability for engineers*, 6th edn. John Wiley & Sons Inc., Hoboken, New Jersey, USA
24. Python Software Foundation (2019) Python 3.7.0. www.python.org/psf-landing/. Available at: <http://www.python.org/>. Accessed on 27 Oct 2019
25. Iqbal A (2013) Modeling milling process using artificial neural network. *Adv Mater Res* 628:128–134. <https://doi.org/10.4028/www.scientific.net/AMR.628.128>
26. Bafghi MS, Emami AH, Vahdati Khaki J, Zakeri A (2009) Development of a mathematical expression for the variation of amorphization phenomenon during intensive milling of minerals. *Int J Miner Process* 93(2):149–154. <https://doi.org/10.1016/j.minpro.2009.07.008>
27. Radziszewski P, Tarasiewicz S (1993) Modelling and simulation of ball mill wear. *Wear* 160(2):309–316. [https://doi.org/10.1016/0043-1648\(93\)90435-O](https://doi.org/10.1016/0043-1648(93)90435-O)
28. Radziszewski P (1997) Predictive model for ball mill wear. *Can Metall Q* 36(2):87–93. <https://doi.org/10.1179/cmqr.1997.36.2.87>
29. Tian Y, Liu Y, Wang F, Jing X, Zhang D, Liu X (2017) Modeling and analyses of helical milling process. *Int J Adv Manuf Technol* 90(1–4):1003–1022. <https://doi.org/10.1007/s00170-016-9418-2>
30. Moys M, Bwalya M, Van Drunick W (2005) Mathematical modelling for optimization of mineral processing operations. *J South African Inst Min Metall* 105(10):663–674
31. Tebassi H, Yaltese MA, Meddour I, Girardin F, Mabrouki T (2017) On the modeling of surface roughness and cutting force when turning of inconel 718 using artificial neural network and response surface methodology: accuracy and benefit. *Period Polytech Mech Eng* 61(1):1–11. <https://doi.org/10.3311/PPme.8742>
32. Saldaña M, González J, Jeldres R, Villegas Á, Castillo J, Quezada G, Toro N (2019) A stochastic model approach for copper heap leaching through bayesian networks. *Metals (Basel)* 9(11):1198. <https://doi.org/10.3390/met9111198>
33. Saldaña M, Toro N, Castillo J, Hernández P, Navarra A (2019) Optimization of the heap leaching process through changes in modes of operation and discrete event simulation. *Minerals* 9(7):421. <https://doi.org/10.3390/min9070421>

Chapter 26

Investigation of Structural and Optical Properties of PMMA/PVdF-HFP Polymer Blend System



Maheshwar Reddy Mettu, A. Mallikarjun, M. Vikranth Reddy, M. Jaipal Reddy, and J. Siva Kumar

Abstract The polymer PMMA and PVdF-HFP blend polymer films have been prepared by solution casting technique. These blending polymer films were investigated by X-ray diffraction (XRD), scanning electron microscopy (SEM), FTIR and UV optical absorption techniques. The peaks of PMMA are disappeared gradually with blending of PVdF-HFP which is revealed by XRD where structure modified semicrystalline to amorphous phase. PMMA surface morphology reveals a rough surface. SEM micrographs of pure PVdF-HFP polymer film have a rough, granular, irregular surface with dark micro pores with lamellar distribution, confirming the semi-crystalline existence of the film. As PVdF-HFP is added to the PMMA polymer, the surface morphology changes severely, showing the development of surface morphology from rough to smooth which indicating modification of structure to amorphous nature. From FT-IR, it is observed that the bands in all blend films of PMMA and PVdF-HFP were broadened and shifted to higher wave number side and also observed that intensity of crystalline phase peaks reduces with increasing concentration of PVdF-HFP to PMMA polymer. It indicating the fair formation of complex between the matrixes of PMMA and PVdF-HFP. The direct and indirect bandgap values were estimated using Tauc plots, and these values found to be

M. R. Mettu · J. S. Kumar (✉)

Department of Physics, Osmania University, Hyderabad, Telangana, India

M. R. Mettu

Department of Science and Humanities, Sreenidhi Institute of Science and Technology, Hyderabad, Telangana, India

A. Mallikarjun

Department of Physics, JNTUH, Kukatpally, Hyderabad, Telangana, India

Department of Physics, Vignan's Institute Of Management And Technology For Women, Hyderabad, Telangana, India

A. Mallikarjun

e-mail: mallikarjun.a@saimail.com

M. V. Reddy

Nilima Organics Private Ltd., IDA Uppal, Plot No. 105 & 106, Hyderabad, India

M. J. Reddy (✉)

Department of Physics, Palamuru University, Mahabubnagar, Telangana, India

changed when PMMA and PVdF-HFP blended when compared to pure PMMA and PVdF-HFP polymers.

Keywords PMMA · PVdF-HFP · XRD · SEM · FT-IR · UV-Visible spectroscopy · Bandgap

1 Introduction

There is a high demand for the better materials in day-to-day applications like electrochemical devices such as solar cells, super capacitors, fuel cells, electrochromic devices, energy storage devices like batteries, etc. [1]. The polymer blend-based electrolytes play an important role in increasing the storage capacity of the battery and the efficiency of the device. The polymer-based electrolytes have high stability, flexibility and high-ionic conductivity. The main advantages of polymer-based films are easy in processability, low cost, having high-chemical resistance from environmental impact and high-mechanical strength [2, 3]. The best compatibility for high-standard application like solar cell, battery and sensing applications [4–7]. By blending two or more polymer results, the best mechanical strength, and to attain high-thermal stability which is very essential for high-standard applications. The suitable composite polymer blending is the most promising and very attractive for its simplicity, versatility and inexpensiveness. The new polymeric material with modified properties like thermal, mechanical and electrical with low degradation, long life and high sustainability can be established for new technical advancement. The interaction between two polymer interface characterisation reveals the mechanical, chemical and electrical stability and compatibility for various technical applications [8, 9].

In recent years, the research work has been done on several host polymers, e.g., poly(ethylene oxide) (PEO), poly(methyl methacrylate) (PMMA), poly(vinyl chloride) (PVC), poly(vinylidene fluoride-co-hexafluoropropylene) (PVdF-HFP) and poly(vinyl acetate) (PVA), etc. It is understood that some conducting polymers were investigated in depth. Some conducting polymers were investigated rarely. In the present study on host polymer, PMMA blended with PVdF-HFP films is prepared. PMMA is highly transparent, high amorphousness, good mechanical strength and abundant of oxide element which is main for electrical conductivity. The existence C–O and C = O functional group provides best electrochemical properties with blending PVdF-HFP. The blended polymer PVdF-HFP is having good electrochemical stability due to –C–F– and VdF unit and crystalline nature of PVdF and amorphous nature of HFP which will improve conductivity. The amorphous nature of PVdF-HFP is obtained by –CF₃ pendent group in HFP. The interaction between two polymer functional group of C–O, CH₃ and C = O in PMMA, and –C–F and –CF₃ in PVdF-HFP are main cause for perfect blending of two polymers and to improve good conductivity [10, 11]. Therefore, PVdF-HFP was chosen as the co-polymer for preparing the polymer blend with PMMA.

2 Experimental

2.1 Materials

PMMA (Poly(methyl methacrylate)) with molecular weight 1,20,000 CAC: 9011-14-7, Aldrich used as host polymer, PVdF-HFP (poly(vinylidene fluoride-co-hexafluoropropylene)) with average molecular weight 4,00,000 CAC: 14,283-07-9, Aldrich used as second polymer and a solvent THF (Tetra Hydro Furan) [Emparta] from Merck Millipore, Germany was used directly. All the materials used without any further purification.

2.2 Process of Films Preparation

Composite solid polymer blend (CSPB) films have been prepared by the solution cast method. The polymer PMMA and different weight percentages of PVdF-HFP were added accordingly and dissolved in solvent THF. Using magnetic stirrer, the solutions were continuously stirred at 60 °C for 2 h and then at room temperature for another 24 h till homogeneous solutions were obtained. The resulting solutions were then cast into glass petri dish, where the solvent was allowed to evaporate and dried in vacuum oven for 48 h at 60 °C. This method results in mechanically stable and free standing films. All the films were kept in a desiccator for protection from moisture and further use for analysis. The prepared polymer films and their blend films are labeled and tabulated in Table. 1, and Fig. 1. shows the flow diagram of solution casting method.

Table 1 Pure PMMA, Pure PVdF-HFP and PMMA / PVdF-HFP polymer blends of different concentrations

SNO	Sample code	Sample	PMMA (wt%)	PVdF-HFP (wt%)
(a)	PM1	Pure PMMA	100	0
(b)	PHP1	Pure PVdF-HFP	0	100
(c)	PM1PHP050	PMMA + PVdF-HFP	100	5
(d)	PM1PHP100	PMMA + PVdF-HFP	100	10
(e)	PM1PHP150	PMMA + PVdF-HFP	100	15
(f)	PM1PHP200	PMMA + PVdF-HFP	100	20
(g)	PM1PHP250	PMMA + PVdF-HFP	100	25

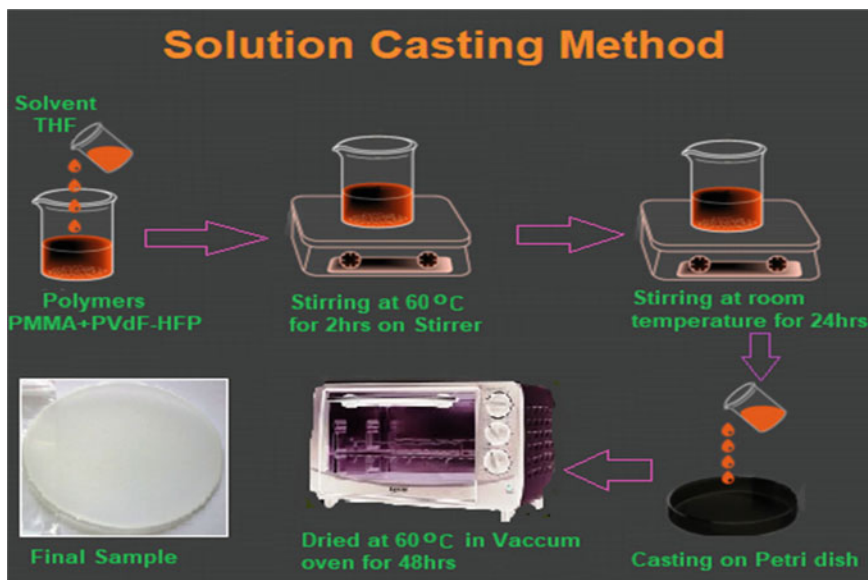


Fig. 1 Solution casting flow method

2.3 Characterization Techniques

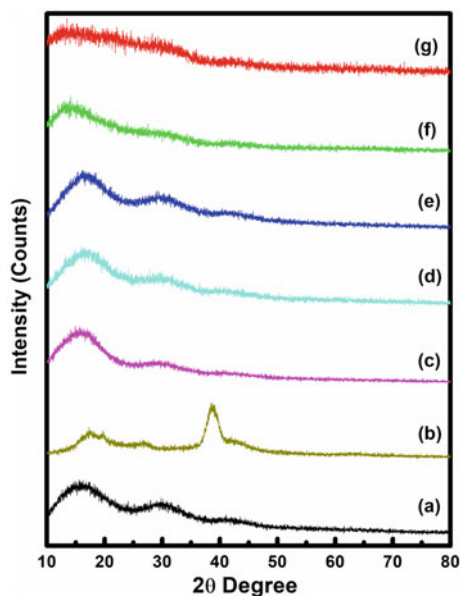
The XRD patterns of the polymer blend films were recorded using SHIMADZU-XRD(6100/7000) X-ray diffractometer at room temperature with the Bragg's angles (2θ) varying from 10 to 80°. The FT-IR spectral data was collected using SHIMADZU-FTIR(8400S) spectrometer in the frequency range from 400 to 4000 cm^{-1} with scan resolution of 5 cm^{-1} . The surface morphology of these polymer blend films was studied by using a Hitachi (Model 3700 N) instrument and gold-sputtered coated films. The absorption spectra of polymer blends have been recorded in the length range 200–1000 nm using SHIMADZU-UV-1800 spectrometer.

3 Results and Discussion

3.1 XRD Analysis

The XRD patterns for pure PMMA, pure PVdF-HFP and their blends with different concentrations are shown in Fig. 2. The diffraction angle of XRD at 15.54° and 29.76° reveals the broad humps which indicating semicrystalline nature of pure PMMA polymer. The broad hump in the region 5–20° corresponding to the organic phase present in the PMMA. The diffraction angle of pure PVdF-HFP reveals three

Fig. 2 XRD patterns of PMMA/PVdF-HFP polymer blends **a** PM1, **b** PHP1, **c** PM1PHP050, **d** PM1PHP100, **e** PM1PHP150, **f** PM1PHP200 and **g** PM1PHP250



prominent peaks 17.60° , 19.52° and 38.76° indicate the semicrystalline nature. The three peaks in XRD pattern of PVdF-HFP reveal α , β and γ phases of semicrystalline nature of polymer [12]. However, it is observed that broadened peak with lowered intensity by blending of PMMA and PVdF-HFP, and it is increased increasing the weight percentage of PVdF-HFP [13]. It is observed the highest 'd' spacing 6.722 reveals the existence of PMMA by the blending of PVdF-HFP. The peaks of PMMA are disappear gradually with blending of PVdF-HFP which is revealed by XRD graphs from Fig. 2a-g.

The two peaks of PMMA 15.54° , 29.76° and three peaks of PVdF-HFP 17.60° , 19.52° and 38.76° by broadening of peaks and decreasing of intensity in further increase in PVdF-HFP to PMMA and no peaks or broad humps revealing the amorphous nature of blended PMMA/PVdF-HFP films. An amorphous broad centered around 29.76° corresponding to PMMA is appeared with decreased intensity and increases bandwidth of the polymer when blended with PVdF-HFP polymer [14]. It indicates the complexation of the PMMA and PVdF-HFP within the missibility range, which is observed clearly in Fig. 2f.

3.2 Morphology and Structure

SEM micrographs advance the morphological investigations of polymer blend films under consideration. In the present work, a comparison of pure PMMA, pure PVdF-HFP and their blend with different concentrations of PMMA and PVdF-HFP blend

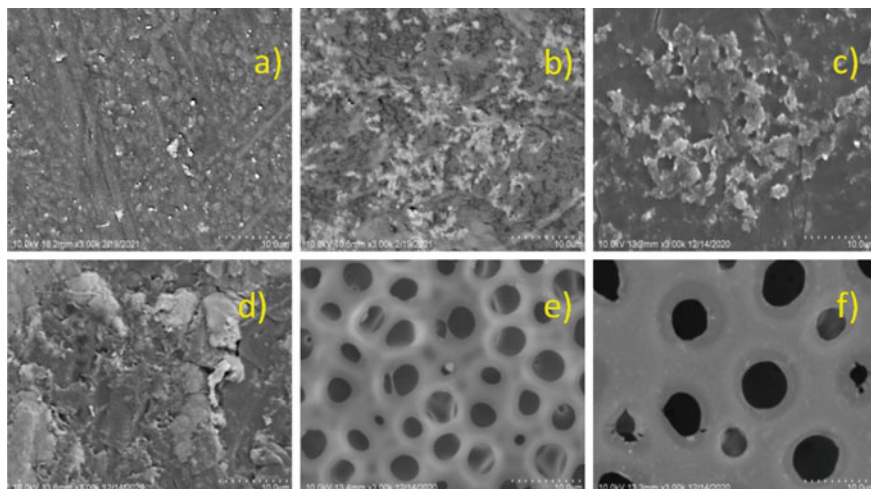


Fig. 3 SEM images of PMMA/PVdF-HFP polymer blends **a** PM1, **b** PHP1, **c** PM1PHP050, **d** PM1PHP100, **e** PM1PHP200 and **f** PM1PHP250

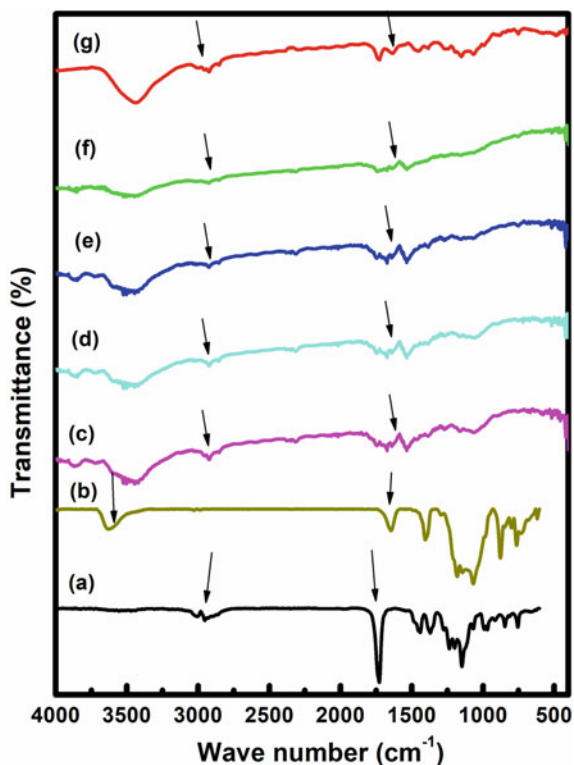
films as shown in Fig. 3a–g. From the SEM, it is observed that pure PMMA Fig. 3a has amorphous nature with no pores network. The PVdF-HFP polymer film has rough, granular, uneven surface having dark micro pores with lamellar distribution confirms the semicrystalline behavior [15].

As evident from the images, PMMA surface morphology is substantially modified due to the addition of PVdF-HFP. Both polymers are prominently blended and found without having any phase separation. Addition of PVdF-HFP, the morphology becomes smoother and interconnected more number of pores are observed on the surface of the blended polymer films. This confirms the reduction in the semicrystalline nature leading to increase in amorphous nature [16]. The amorphous nature revealed by SEM results is corroborates with XRD data.

3.3 FT-IR Spectra Analysis

The specific interaction between the polymers is studied by infrared spectroscopy. This method can be used both qualitatively and quantitatively evaluate the process of interpolymer miscibility by hydrogen bonding formation [17–19]. The FT-IR patterns of PMMA, PVdF-HFP and their blends with different concentrations is shown in Fig. 4. The PMMA explores Infra Red bands at 2937 cm^{-1} (C–H stretching band), 1724 cm^{-1} (C–H and O–H bending), 1448 cm^{-1} , 1359 cm^{-1} (C–C stretching), 1149 cm^{-1} (C–O stretching), 854 cm^{-1} and 742 cm^{-1} (C–C and C–O bending) [20], on the other hand peaks in FTIR spectra of pure PVdF-HFP provided that IR bands at 3500 cm^{-1} of CH_2 symmetrical stretching, 1350 cm^{-1} of crystalline phase,

Fig. 4 FT-IR spectra of PMMA/PVdF-HFP polymer blends **a** PM1, **b** PHP1, **c** PM1PHP050, **d** PM1PHP100, **e** PM1PHP150, **f** PM1PHP200 and **g** PM1PHP250



750 cm^{-1} and 600 cm^{-1} were CF_2 bending and wagging, respectively. It is observed that the bands in all blend films of PMMA and PVdF-HFP were broadened and shifted to higher wave number side and also observed that intensity of crystalline phase peaks reduces with increasing concentration of PVdF-HFP to PMMA polymer. The disappearance of some known peaks and appearance of some new peaks and also shifting of peaks in the spectra of blend films indicated that blending is compatible, occurrence of strong interaction between two polymers PMMA and PVdF-HFP.

3.4 Optical Property Analysis Using UV–Visible Spectroscopy

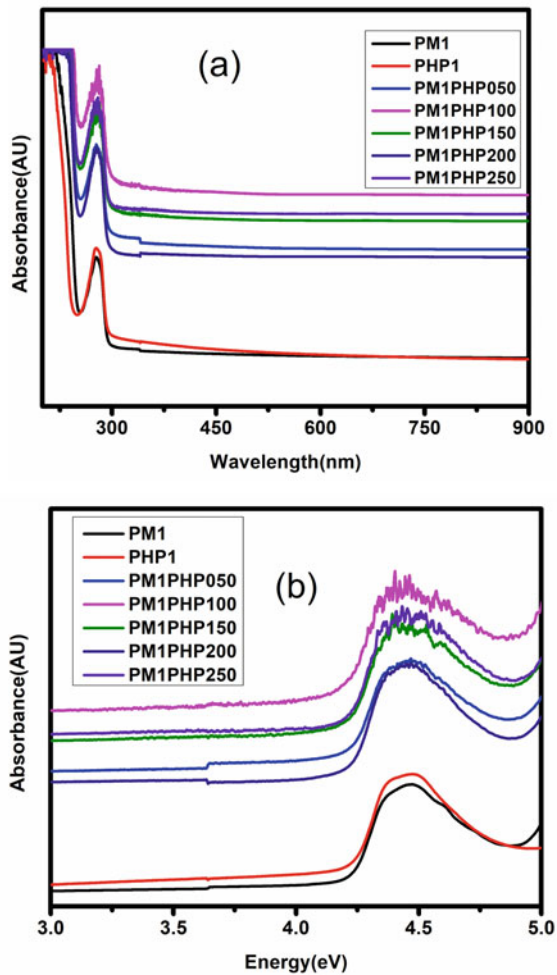
The optical property of the prepared samples can be understood from its absorption spectroscopy analysis in the UV–visible range. Absorption coefficient, a measure of the absorbance taken over the given UV–visible range of 200–1000 nm, is related by Eq. 1.

$$\alpha(\nu) = 2.303(A/t) \quad (1)$$

where, A is the optical absorbance for the given sample with thickness t . Figure 5a, b shows the absorbance spectra of samples taken for study. From the spectra, it is clearly understood that there is both hyperchromic and bathochromic shift as the concentration of PVdF-HFP increased to PMMA. Also the increase in the absorbance value indicates that the molar absorptivity has also increased with increase in PVdF-HFP concentration. The absorption edge calculated from the extrapolation of linear portion to the zero absorbance in the absorbance versus $h\nu$ plot (Fig. 5b) shows a red shift with increase in PVdF-HFP concentration.

The optical band gap values gives a clear picture of the possible optical transitions in the polymer blend films. Davis et al. have reported the possible existence of both the direct and indirect band transitions near fundamental band edge that can be calculated from the Tauc relations given by Eqs. 2 and 3 [21, 22].

Fig. 5 a Absorbance spectra along the UV–Visible wavelength range for PMMA, PVdF-HFP, PMMA/PVdF-HFP polymer blends, b absorbance versus energy for PMMA, PVdF-HFP, PMMA/PVdF-HFP polymer blends



$$\alpha h\nu = C(h\nu - E_g)^{1/2} \tag{2}$$

$$\alpha h\nu = A(h\nu - E_g + E_p)^2 + B(h\nu - E_g - E_p)^2 \tag{3}$$

where, E_g is the optical bandgap, C is a constant, ν is the frequency, and h is a Planck's constant in case for direct band gap. For indirect transition, phonon assistance is necessary, and equation is given as in Eq. 3, where E_p is associated with phonon energy and A, B are constants. Thus, the direct bandgap was calculated from the linear extrapolation of $(\alpha h\nu)^2$ versus $h\nu$ to the zero absorption coefficient as shown in Fig. 6a, and the calculated direct bandgap values are found to be 4.26, 4.24,

Fig. 6 **a** Tauc plot for determination of direct optical bandgap for pure PMMA, pure PVdF-HFP, PMMA/PVdF-HFP polymer blends, **b** Tauc plot for determination of Indirect bandgap for pure PMMA, pure PVdF-HFP, PMMA/PVdF-HFP polymer blends

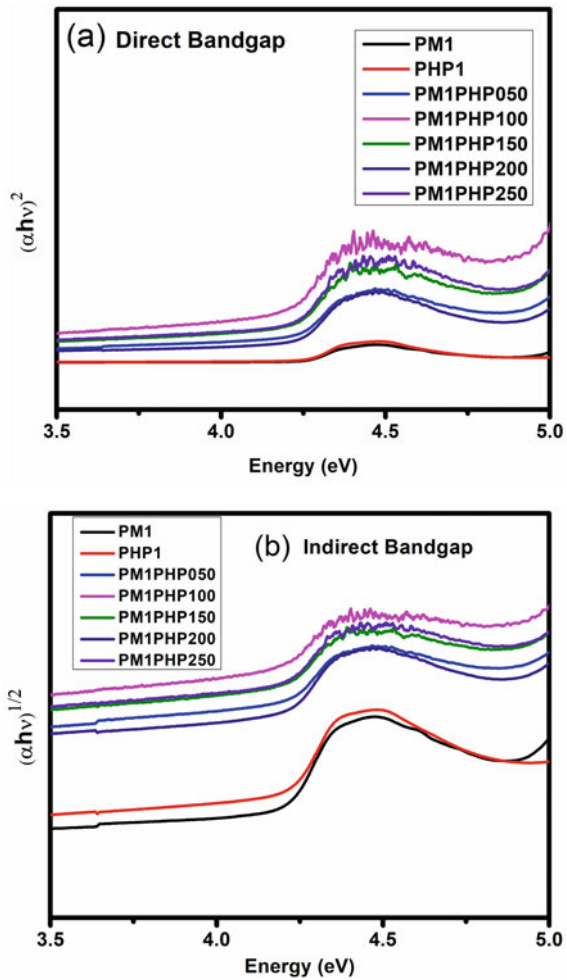


Table 2 Absorption edge, direct and indirect bandgap values of pure PMMA, pure PVdF-HFP, PMMA/PVdF-HFP polymer blends

Sample	Absorption edge eV	Direct bandgap eV	Indirect bandgap eV
PM1	4.20	4.26	4.09
PHP1	4.18	4.24	4.07
PM1PHP050	3.96	4.13	3.89
PM1PHP100	3.93	4.05	3.81
PM1PHP150	3.94	4.03	3.78
PM1PHP200	4.05	4.10	3.84
PM1PHP250	3.92	4.09	3.83

4.13, 4.05, 4.03, 4.10 and 4.09 eV for PM1, PHP1, PM1PHP050, PM1PHP100, PM1PHP150, PM1PHP200 and PM1PHP250, respectively.

Indirect bandgap values are estimated from the linear portion extrapolation of the $(\alpha h\nu)^{1/2}$ versus $h\nu$ to the zero absorption value shown in Fig. 6b. The indirect bandgap values are found to be 4.09, 4.07, 3.89, 3.81, 3.78, 3.84 and 3.83 eV corresponding to PM1, PHP1, PM1PHP050, PM1PHP100, PM1PHP150, PM1PHP200 and PM1PHP250, respectively, and these values also tabulated in Table 2. From the obtained results, it is found that the PVdF-HFP has contributed to decrease in the bandgap energy value when the PM1, PHP1 bandgap values are compared [23]. However, comparing the bandgap values of PM1, PHP050–250, the increase in the concentration of PVdF-HFP beyond 150 has shown decrease and then slight increase.

4 Conclusions

The polymer PMMA and PVdF-HFP blend films are investigated by XRD analysis which confirmed that there is a change from semicrystalline to amorphous phase. SEM revealed that when PVdF-HFP added to PMMA polymer, the surface morphology changes dramatically indicating that the two matrixes of PMMA, and PVdF-HFP polymers are fairly complexed. FT-IR data of PMMA/PVdF-HFP blend films suggested the fair complexation between PMMA and PVdF-HFP matrixes. From UV–visible spectroscopy analysis, it is found that the PVdF-HFP has contributed to the decrease in the energy direct and indirect bandgap values when compared to pure PMMA and pure PVdF-HFP.

Acknowledgements The authors would like to express their gratitude to the Head, BOS, Department of Physics, Osmania University. One of the author MMR express his gratitude to the Principal, Head (Science & Humanities), SNIST for their unwavering help in carrying out this work.

References

1. Aziz SB, Brza MA, Dannoun E, Hamsan MH, Hadi JM, Kadir MF, Abdulwahid RT (2020) The study of electrical and electrochemical properties of magnesium ion conducting CS: PVA based polymer blend electrolytes: role of lattice energy of magnesium salts on EDLC performance. *Molecules* 25:4503
2. Nidhi SP, Kumar R (2019) Synthesis and characterization of magnesium ion conductivity in PVDF based nanocomposite polymer electrolytes disperse with MgO. *J Alloy Compd* 789:6–14
3. Qi K, Li L, Chang K-C, Lin X, Liu H-J, Lai Y-C, Zheng H, Huang G, Kuo T-P (2020) A supercritical removal method: the rapid elimination of impurities in polymethylmethacrylate at near room temperature and a mechanism investigation of insulating property improvements. *J Mater Chem C* 8:15664–15668
4. Ponrouch A, Monti D, Boschini A, Steen B, Johansson P, Palacin MR (2015) Non-aqueous electrolytes for sodium-ion batteries. *J Mater Chem A* 3:22–42
5. Xue Y, Li X, Quesnel David J (2017) Electrochemical and mechanical properties of sodium-ion conducting cross-linked polymer gel electrolyte. *Intern. J Electrochem Sci* 12:10674–10686
6. Zhu Y, Yang Y, Fu L, Wu Y (2017) A porous gel-type composite membrane reinforced by nonwoven: promising polymer electrolyte with high performance for sodium ion batteries. *Electrochim Acta* 224:405–411
7. Xue Y, Quesnel DJ (2016) Synthesis and electrochemical study of sodium ion transport polymer gel electrolytes. *RSC Adv* 6:7504–7510
8. Cisnerosa CSM, Levenfelda B, Vareza A, Sancheza JY (2016) Development of sodium-conducting polymer electrolytes: comparison between film-casting and films obtained via green processes. *Electrochim Acta* 192:456–466
9. Przyłuski J, Wiczeorek W (1989) Increasing the conductivity of polymer solid electrolytes: a review. *Solid State Ionics* 36:165–169
10. Choe HS et al (1995) Preparation and characterization of poly(vinyl Zulfone)- and poly(vinylidene fluoride)-based electrolytes. *Electrochim, Acta* 40:2289
11. Saikia D, Kumar A (2004) Ionic conduction in P(VDF-HFP)/PVDF-(PC + DEC)-LiClO₄ polymer gel electrolytes. *Electrochim, Acta* 49:2581
12. Remskabr M, Iskra I, Jelenc J, Skapin SD, Visic B, Varlec A, Krzan A (2013) A novel structure of polyvinylidene fluoride (PVDF) stabilized by MoS₂ nanotubes. *Soft Matter* 9:8647–8653
13. Leo CJ, Subba Rao GV, Chowdary BVR (2002) Studies on plasticized PEO-lithium triflate-ceramic filler composite electrolyte system. *Solid State Ion* 148:159
14. Tripathi SK, Gupta A, Kumari M (2012) Studies on electrical conductivity and dielectric behaviour of PVdF-HFP-PMMA-NaI polymer blend electrolyte. *Bull Mater Sci* 35(6):969–975
15. SivaKumar M, Subhadev R, Rajendran S, Wu HC, Wu NL (2007) Compositional effect of PVdF-PEMA blend gel polymer electrolytes for lithium polymer batteries. *Eur Polymer J* 43(10):4466–4473
16. Jaipal Reddy M, Chu PP, Siva Kumar J, Subba Rao UV (2006) Inhibited crystallization and its effect on conductivity in a nano-sized Fe oxide composite PEO solid electrolyte. *J Power Sour* 161(1):535–540
17. Gohel K, Kanchan DK (2018) Ionic conductivity and relaxation studies in PVDF-HFP:PMMA-based gel polymer blend electrolyte with LiClO₄ salt. *J Adv Dielectr* 8(1):1850005
18. Arvindan V, Vickraman P (2008) Characterization of SiO₂ and Al₂O₃ incorporated PVdF-HFP based composite polymer electrolytes with LiPF₃ (CF₃CF₂)₃. *J Appl Polym Sci* 108:1314
19. Deka M, Kumar A (2010) Enhanced electrical and electrochemical properties of PMMA-clay nanocomposite gel polymer electrolytes. *Electrochimica Acta* 55(5):1836–1842
20. Ravindar Reddy M, Subrahmanyam AR, Maheshwar Reddy M, Siva Kumar J, Kamalaker V, Jaipal Reddy M (2016) X-RD, SEM, FT-IR, DSC studies of polymer blend films of PMMA and PEO. *Mater Today: Proc* 3:3713–3718
21. Davis PW, Shalliday TS (1960) Some optical properties of cadmium telluride. *Phys Rev* 118:1020

22. Mott NF, Davis EA (1979) *Electronic processes in non-crystalline materials*, 2nd edn, p 437. Clarendon, Oxford
23. Ramamohan K, Achari VBS, Sharma AK et al (2015) Electrical and structural characterization of PVA/PEG polymer blend electrolyte films doped with NaClO₄. *Ionics* 21:1333–1340

Chapter 27

Theoretical Analysis of Functional Materials and Finishes for Anti-Ballistic Fabrics



Gurumurthy B. Ramaiah, Asmamaw Tegegne, Bahiru Melese, Seblework Mekonnen, Eshetu Solomon, Kidist Tadesse, and Robel Legese Meko

Abstract Anti-ballistic fabrics find numerous technical applications in research areas of defense, firefighting aviation, aerospace, police, civil defense and other day-to-day applications. These fabrics basically provide protection against high impact causing objects like sharp knives, bullets, stones, etc. The design and selection of fabrics should be coupled with functional finishes which would provide protection and comfort for the wearer. The prime objective of this work is to evaluate and carry out a theoretical analysis on functional aspects of anti-ballistic fabrics and functional finishes. In this work, certain properties of Kevlar fabrics and shear thickening fluid are heated. The methodology involved consideration and understanding their technical aspects and its application methods used to make protective materials and functional finishes. The outcome shows that proper selection of functional materials, design, concept, testing the functionality parameters and application procedures play a vital role in making a successful anti-ballistic fabric. The application of shear thickening fluid increases the impact resistance values in anti-ballistic fabrics.

Keywords Anti-ballistic fabrics · Shear thickening fluid · Antimicrobial finish · Body armor · Softener finish · Impact resistance

1 Introduction

Anti-ballistic fabric is a class of technical textiles which covers materials, including textile fabrics used for protection against objects that impact at very high speed. Examples include bullets, sharp objects, etc. And hurt the human body and, in some instances, may lead to serious injuries or death. So in order to safeguard the user from such situations, anti-ballistic fabrics are used as a defensive layer over the body that is technically termed as armor in the normal usage. These fabrics are used by military personnel, police officers or any other applicants who wish to take cover under various threats which may result in severe trauma. However, some of

G. B. Ramaiah (✉) · A. Tegegne · B. Melese · S. Mekonnen · E. Solomon · K. Tadesse · R. L. Meko
Ethiopian Technical University, Addis Ababa, Ethiopia

© The Author(s), under exclusive license to Springer Nature Singapore Pte Ltd. 2022
V. Bindhu et al. (eds.), *Proceedings of Fourth International Conference on Inventive Material Science Applications*, Advances in Sustainability Science and Technology,
https://doi.org/10.1007/978-981-16-4321-7_27

307

the personal protective equipments including clothing are being made using these fabrics and used by defense personnel regularly.

In military usage, these fabrics are used in seating systems, vehicle internal panels, linings etc. In addition, they are also imparted with specific finishes so that these fabrics can keep the wearer in a comfortable position without having to think of protection against forces that may cause discomfort to the wearer or due to some of the attacks that can come from biological microbes, flames, harsh environmental conditions, etc. In this paper, detail evaluation is conducted on the functional materials, theoretical analysis on the design and development aspects of anti-ballistic fabrics coupled with review on the function finishes that may help to develop these anti-ballistic fabrics.

Ballistic fabrics are usually subjected to sudden impact and continuous wear and tear during its life cycle. Many external forces and environmental situations also affect the overall performance of anti-ballistic materials. In numerous applications, the fabrics are subjected to high-speed impact of the object of varying sizes and higher magnitude of frictional force that is generated at the point of impact. Due to these technical reasons, the ballistic fabrics need to have multifunctional properties and also protect the wearer from further thermal and chemical degradation. In some instances, the influence of fire flames and unexpected variation in heat and pressure may also result in a change in material properties.

The secondary characteristic property should also be monitored when engineering specific utility of fabrics when used with ceramics and nanocomposite materials so as to augment the performance of the armor fabrics. Some armor fabrics are designed based on the level of threat and the kind of protection levels that may be required in the present scenario. Numerous scientific and technological development has progressed in making the fibers and yarns that are used as anti-ballistic fabrics. The introduction of Kevlar with high impact strength value is reported to be greater than steel. This has enabled researchers to choose it as one of the best preferred fabrics for making bullet-proof vests in recent years; there are some new fibers like Tawaron, Zylon and Dyneema, being selected for armor making due to its flexibility and lightweight. This work tries to evaluate and do a theoretical technical analysis of anti-ballistic fabrics, since there is no such specific analysis being reported on the functionality of anti-ballistic fabrics and finishes used on these fabrics. This works also look into design development, testing and application aspects of anti-ballistic fabrics. Further, in this research evaluation is also carried on the anti-ballistic fabric requirements and their functional finish methods.

2 Methodology Followed in This Research

In this work which is presented, the concept mainly focuses on the analysis of anti-ballistic materials, the use of shear thickening fluid and its advantages. The research also addresses the importance of using functional textile and nanomaterials for the development of anti-ballistic fabrics. Kevlar 29 fabric properties and shear thickening

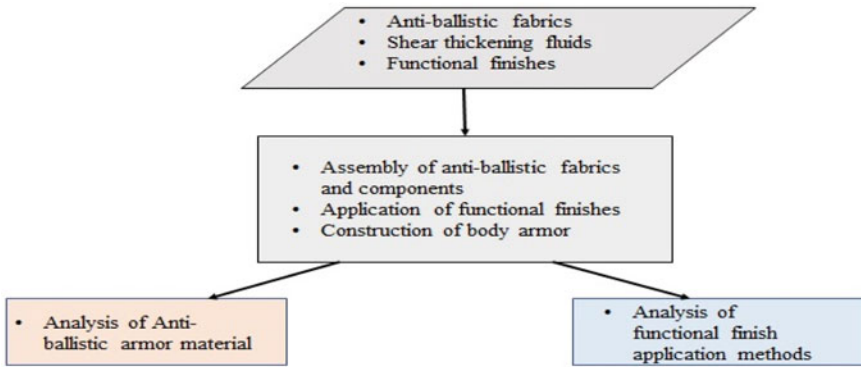


Fig. 1 Work method flowchart

fluid anti-ballistic properties are also discussed based on the scientific data which is published by Talreja et al. [1] and Aidy [2]. Figure 1 shows the flowchart of the work methodology that is followed in this research.

3 Protective Textiles and Its Functionality

Synthetic high-performance fibers based on materials are used due to their high tensile and impact resistance properties. These synthetic fabrics show good resistance to chemical treatments and anti-microbes. They also possess good resistance to flammability and UV (ultraviolet) radiation. Due to the limitation in the properties of the high-performance fabrics, the design and fabrication of anti-ballistic fabrics pose a stiff challenge to meet the specifications and standards as laid out by NIJ (National Institute of Justice) for armor fabrics. The finish required to be imparted for such fabrics should also be aimed at defense applications (Table 1).

Park and Jayaraman [3] carried out extensive work on the engineering design of intelligent protective textiles and clothing. In their research work, they carried analysis on the types of hazard levels of threats coupled with vulnerability of these fabrics. The authors conclude on the basic design strength and fabric properties that have to be evaluated before deploying it as an anti-ballistic fabric. Joshi et al. [4], in their research work on the design and development of functional finishes using activated zeolites obtained from natural sources on textiles to protect the user from exposure to radioactive substances in military operations. They conclude that salts obtained from natural sources provide good UV resistance and safeguard the user against microbes. They have also attempted to surface treat the fabric made from cotton fibers by using nanoparticles and natural salts which can safeguard the wearer from radioactive substances. Joshi [5], and Wazid et al. [6] in their work on nanomaterials and material science indicate that in order to obtain improved properties and multi-functionalities in textiles, use of nanofibers spun using electrospinning technology,

Table 1 Protective textiles and its functionality

Protective textile category	Functional materials
NBC (nuclear, biological and chemical) protection ballistic protection	Activated carbon, protective composite membranes, electrospun nanofibers
	Aramid fibers
	Shear thickening fluids
	Super-aligned carbon
	Nanotube yarns
Smart textiles	Self-cleaning property
	Self-healing property
	Thermoregulating textiles
	Electronic textiles
	Electro- and thermoactive textiles
	Shape-memory nanofibers
	PH-sensitive fibers
Conductive textiles	

nanocomposites nanocoatings and nanofinishing's are essential. These materials and processes help to obtain new functionality in textile such as self-cleaning surfaces conducting textile antimicrobial properties-controlled hydrophilicity or hydrophobicity protection against fire, UV radiation, etc. Antosik et al. [7], studied on the rheological properties of thickening fluids prepared from polypropylene glycol and silica powder. They have studied the physiochemical properties of these materials and the onset of maximum shear thickening and the dilution effect on ballistic fabrics. They have found that the length of the polypropylene glycol chain and size of silica particles has a significant effect on the control of onset and maximum shear thickening as well as the high values of the dilution effect.

Meng and Guangyin [8], and Wetzel et al. [9], conducted a study on the shear thickening fluid made from nanosilica and polyethylene glycol, and their study focused on the effect of different concentrations of shear thickening fluid, different temperatures on the static rheological properties of shear thickening fluids. They conclude that the shear thickening fluids show good reversibility in their phase change when stress is applied to the shear fluid. Holmberg [10] demonstrated the development of protective fabrics using shear thickening fluids in their laboratory at University of Delaware, USA. Sabit and Ashutosh [11] from university of auburn (USA) reviewed the application of textile materials in the development of military fabrics using other engineering materials of the nanoscale. Decker et al. [12] Egress et al. [13] and Xuhang et al. [14] focused their research on the development of stab resistance fabrics using different substrates including Kevlar fabric. Liu [15] in their research (orifice coagulation bath method) to encapsulate shear thickening fluid and form capsules in order to strengthen the flexibility of composite material reveals the improvement in thermal properties of the composite material. They have prepared the shear thickening fluid

using polyethylene glycol and silica and dipped in anhydrous ethanol. Capsules of STF were prepared by dipping the STF solution in the liquid paraffin solution. The resultant solution is mixed with sodium alginate solution to form a multiple emulsion. This multiple blend solution is then pumped through a syringe of specified orifice diameter dropping droplets of the emulsion into a solution containing calcium chloride to form spherical objects. Subsequently, the cross-linking of sodium alginate and calcium chloride results in the formation of a hard STF capsule. Zhang et al. [16] also carried research in STF fluid encapsulation and found interesting methods to encapsulate these STF fluids. Song et al. [17], in their research work developed new generation shear thickening fluid materials in the U.S. Army Research Laboratory and the State University of Delaware synthetic research center for creating new generation military suits. Song reviews the available theories and different approaches to understand the behavior of shear thickening materials and its applications. Vijaya et al. [18] in their research in preparation of STF using the sonar chemical method used silica nanoparticles and polyethylene glycol, which are dispersed in ethanol and irradiated with high power ultrasound for 5 h. The ethanol is completely removed by vacuum and heat. Their results clearly show that the snow chemical mixing before evaporation drastically improves the shear thickening effect.

4 Theory and Design of Soft Body Armor

Ballistic vests are made from layers of strong fibers that can catch and deform a bullet. The mechanism involved at the time of impact involves the mushroom structure formation and helping the force to be dissipated to a larger portion of the vest fiber. The bullet speed and kinetic energy of the bullet is absorbed by the layers of fabrics and prevents the penetration of the bullet from the textile matrix. Figure 2 shows the overview of bullet-proof vest. The textile matrix can be augmented with the use of additional protective materials like metal (steel or titanium), ceramics,



Fig. 2 Anti-ballistic fabric used for making bullet-proof vests (Source [19])



Fig. 3 a Hard armor, b soft armor (Source [21])

polyethylene plates that absorb extra energy from the bullet. There are two categories of body armor, namely the soft armor vests and liquid armor vest. When we use metal plates or ceramics, the armor body is called as hard armor vests which are designed for specifically for bladed weapons and sharp objects. Some of the important mechanical properties that influence the performance of the bullet-proof vest include strength, modulus and elongation at break. The interaction of impact forces with these protective systems plays a key role in the performance of the ballistic vest.

4.1 Designing a Soft Armor

Many soft armors are constructed from multiple layers of woven fabrics like Kevlar and carbon without using a resin binder. All the layers of woven fabrics are stitched together with meander and crosswise seams. The range of stitches/cm² should be less than 10, else this will reduce the fabric, yarn tenacity by up to 40%. The resin content should be minimized and kept in-between 20 and 25%. If the ballistic material has been given fire resistance, smoke resistant and nonconductive and self-supporting and enough stiffness properties would result in better performance of the ballistic vest. This is due to the interaction of these variables at the time of dissipation of energy absorbed by fabric layers. Carbon and graphene materials can also be used as fillers in STF so that they can enhance the strength properties of armor materials [20]. Figure 3 shows the picture of a hard armor and soft armor part of a bullet-proof vest.

4.2 Hard Armor Bullet-Proof Vest

Hard armor bullet-proof vests are made from multilayered fabrics, along with the usage of resin binder. In some cases, use of ceramics and fiber-reinforced plastics (FRP) of 10 mm thickness is reported. Many combinations of materials and resin can be worked out to design hard armor ballistic vests.

4.3 Shear Thickening Fluid for Soft Body Armor

Shear thickening fluid possesses the ability to change its phase when stress is applied to the medium. This phase change property results in drastic changes in its material properties. Due to this phase transition behavior from liquid to solid, the viscosity of the material increases and there is an ultimate increase in impact resistant property of the material. Due to this behavior of STF, they are used in the design and development of anti-ballistic fabrics. These STF are made from colloidal particle dispersions. Examples of prominent STF fluids are starch solutions, solutions made from ethylene glycol and silica particles, multiwalled carbon nanotubes dissolved in polypropylene glycol. Their properties are similar to the behavior on non-Newtonian fluids. Figure 4 shows the algorithm used in making anti-ballistic fabrics using STF solutions. The introduction of shear stiffening polymer and fluid into Kevlar fabric gives a novel flexible body armor material with excellent mechanical performance (Table 2). When

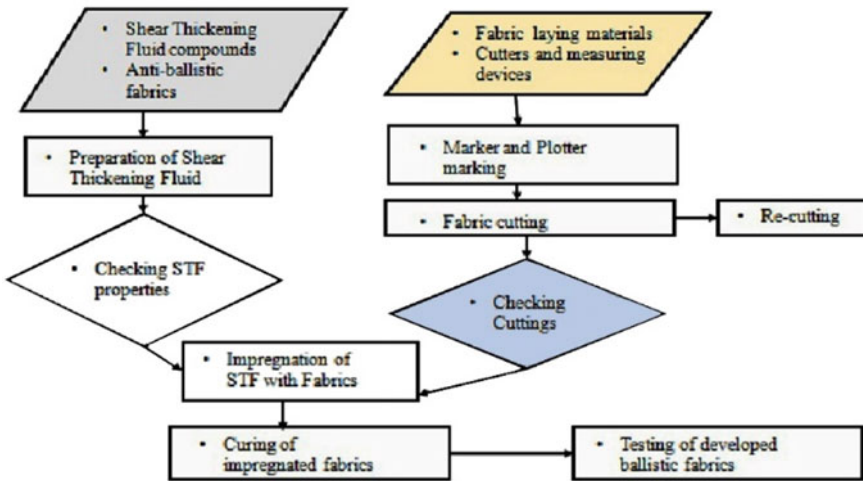


Fig. 4 Flowchart explaining the method followed in developing anti-ballistic fabrics

Table 2 Salient features of Kevlar-29 anti-ballistic fabrics [2]

Material property	Value
Denier/filament	1.5–2.5
Filament diameter (cm)	0.00012–0.0015
Cross-sectional shape	Circular
fiber density (g/cc)	1.44
Strength (yarn) (Tenacity) (GPA)	2.5–3
Elongation of yarns, %	3.6
Thermal conductivity w/m x K	0.04

Table 3 Impact testing results of Kevlar 29 fabrics treated with different shear thickening fluids [1]

Type of STF applied to the fabric	Peak viscosity of STF	Peak energy (Joules)	Peak force (Newton)	Total energy (Joules)	
without STF		9.2	1233.3	23.5	
with STF (silica particles + ethanol + polyethylene glycol)	Medium	97.4	4766.4	120.7	

carbon nanotubes are introduced into the composite, it gives the material excellent force sensing capability. The formation of a conductive network within the composite of the fabric enables the fabric to detect impacts instantly. This results in a smart fabric that offers excellent ballistic protection, much superior than Kevlar alone (Table 3).

5 Functional Materials and Its Importance

Turaga et al. [22] in their work on functional materials have brought about important technical information on the synthesis and application of functional materials. Functional materials are characterized by their properties and response to magnetic, chemical and electrical stimuli. These materials are used in applications like computing, sensing, energy conversion, etc. They possess unique structural and chemical properties and respond to externally induced magnetic, thermal and electric fields. Their phase diagrams are reported to be very complex in nature. Another important feature of these materials is that they can be modified with respect to their structure–property relationship which can again complicate the characteristics of the material phase diagram.

5.1 Functional Finishes for Protective Textiles

Functional finishes are also used for protective textiles like anti-ballistic fabrics. Table 4 provides a summary of functional materials used in textile applications.

Silicon carbide and silicon blended ceramic-based materials are used regularly as anti-ballistic materials. Silicon-based materials offer excellent resistance to penetration of sharp objects and sudden impact of bullets. The material also cuts down the trauma levels that a wearer can experience due to the high impact of bullets. Some fabrics made from polyethylene and emails are also used as anti-ballistic fabrics. Among the many natural and synthetic fibers aramid (Kevlar), carbon, ultrahigh molecular weight polyethylene (UHMWPE) fabrics are also used as anti-ballistic

Table 4 Summary of functional materials used for textile application

Sl. No.	Functional materials	Application
1	Silver nanoparticles	Antibacterial finishes
2	Fe (iron) nanoparticles	Conductive magnetic properties, remote heating
3	Zinc oxide (ZnO) and titanium dioxide (TiO ₂)	UV protection, fire protection, Oxidative catalysis
4	Titanium dioxide (TiO ₂) and magnesium oxide (Mgo)	Chemical and biological protective performance, provide self-sterilizing function
5	Silicon dioxide (SiO ₂) and aluminum oxide (Al ₂ O ₃) Nanoparticles with polypropylene (PP) or polyethylene (PE) coating	Super-water-repellent finishing
6	Indium-tin oxide nanoparticles	Electromagnetic/Infra-red protective clothing
7	Ceramic nanoparticles	Increasing resistance to abrasion
8	Carbon black nanoparticles	Increasing resistance to abrasion, chemical resistance and impart electrical conductivity, coloration of some textiles
9	Clay nanoparticles	Highly electrical, heat and chemical resistance
10	Cellulose nanowhiskers	Wrinkle resistance and water repellency

fabrics. These materials are superior in their structural behavior with crystallinity levels higher than 95% as compared to conventional fibers. The higher crystallinity level results in excellent strength and elongation properties.

5.2 Repellency Finishes

Water repellency is one of the important properties of protective textiles. The chemistry behind water repellent is to create a surface of the fabric which is water repellent by changing the surface tension forces and contact angle formed (Fig. 5). Silva et al. [23] reported few of the enzymatic finishes for textile fabrics and more information can be sought by referring to their published work. The repellent mixture is attracted to the hydrophobic regions, while the polar ends of the fatty acid are attracted to the metal salts at the fiber surface. Paraffin repellents, stearic acid melamine repellents, silicone water repellents like polydimethylsiloxane products are useful as water repellents. Fluorocarbons (FC) provide fiber surfaces with the lowest surface energies of all the repellent finishes in use. Application of these water-repellent functional finishes on textiles can be achieved by pad-dry-cure or by exhaustion method.



Fig. 5 Functional water-repellent finish on textile fabrics (Source [24])

5.3 Resin Finishes

Masamichi et al. [25] and Venneste et al. [26] reported few important findings by conducting research on easy-care finish on textiles. These easy-care finishes are achieved through resin finish treatment. Synthetic organic smaller complex molecular compounds combine together to form a high molecular weight compound resulting in the formation of resin. These molecular compounds are cross-linked and form the functional groups which, when applied to textiles will block the amorphous groups and block the formation of hydrogen bond formation resulting in resin finishing of textiles. These resin compounds improve the resilience, crease and draping properties of protective textiles when applied in a controlled manner. Some of the important cross-linking agents are.

The most important cross-linking agents used are urea formaldehyde, tetramethylol acetylene DI urea (TMADU), dimethyl ethylene urea (DMEU), dimethylol dihydroxy ethylene urea (DMDHEU). Resins are applied/deposited on textiles using padding mangles with the aid of cross-linking agents. Curing is done to cross-link the resin material and obtain a permanent finish. The durability and repellency values can be improved by using highly ordered polymer chains and following the application method that can form covalent bond and provides uniform deposition on the surface of the fiber. The fabric can be impregnated with the water-repellent compound and cured in an oven at high temperature so that there is uniform bonding with water-repellent nanoparticles and the fiber.

5.4 Softener Finishes

Protective textiles undergo various mechanical and chemical processes until it is used actually by the consumer. The process of after treating textiles using a suitable softening agent is called softening. Teli [27] has conducted experiments on the effect of different softeners in textiles. His work is reported in the reference cited. The

reader is suggested to refer his work which can give in depth information on the utility of softeners in textiles. The application of chemical softeners ensures that the fabrics used for making protective textiles are smoother, more flexible and better drape and pliability.

5.4.1 Anionic Softeners

Anionic softeners are used for cotton and other cellulosic blends. These softeners are not suitable for washing and do not possess high affinity to cellulosic. Oil, wax, fat, etc., are examples of these anionic softeners. They are applied to the fabric surface by pad-dry cure or exhaust method. Anionic softeners are stable to the application of direct dyes, starch, resins and optical brighteners. However, they possess poor fastness properties and are a temporary finish.

5.4.2 Cationic Softeners

Cationic softeners are a class of softeners that is used to impart smooth, bulky and soft hand feel to the fabrics. These softeners do not affect the color and increase strength of the fabric when finished. Most of the softeners are suitable for any kind of fabric background. They are basically silicone based and are amine free. Examples include amino-esters, quaternary ammonium salts and amino-amides. The cationic group present in the softened forms a negative electric potential and in the presence of anions will form reasonably good bonding with the fiber resulting in better durability. They are applied by exhaust process from a water bath with high liquor ratio.

5.4.3 Nonionic Softeners

These softeners do not have any charged molecules like what is seen in cation and anionic softeners. They can withstand harsh treatment and are stable. Examples include ethoxylated products, fats and paraffin's. They are applied by padding methods with proper control over pressure and temperature during the process.

5.4.4 Silicone Softeners

Silicone softeners are used on fabrics after diluting and dissolving them in organic solvents. These silicone softeners show good fastness properties and are used in lubrication and waterproof applications. Silicones have an alternating oxygen and silicon atoms which are flexible and have freedom to move at bonding points. Silicone softeners help in good sewing properties, result in better crease recovery, enhance tear strength and abrasion resistance and provide unique hand characteristics. Examples

of silicone softeners include diamino-silicone, amino-functional silicone, organo-functional silicone and amino-functional silicone.

5.4.5 Reactive Softeners

Reactive samples are used for all types of fibers. The hydroxyl group of the cellulose molecules reacts with the chemical groups present in the softener and form covalent bonds. They possess good fastness values, easy to apply from water bath. Pad-dry-calendar or exhaust process is normally followed while applying for reactive surfaces. These softeners provide permanent finish and excellent water repellency effect. Example of reactive softener is sterile amino-methyl pyrimidine chloride.

5.4.6 Softeners and Its Application Methods

Many of the softeners are applied by spraying or padding methods. They transfer onto fabric by using coating techniques or by exhaust method. Batch processes make use of the exhaustion process of application. Application of softeners also makes use of machineries like jet, winch or overflow machines. Sometimes foam applicator is also used when the substrate is a garment. One of the popular methods of application of softener is the pad-wetting method. After this process, the padded fabric is then passed to a center where the dimensional.

5.5 Antimicrobial Finishes

Nayaka et al. [28], have focused his research on the development of antimicrobial finishes for textile materials. The inspiration which they get is basically to do with the loss of textile properties due to antimicrobial attacks. Antimicrobial treatment for protective textiles is a special treatment given to safeguard the wearer against attack by microorganism. The mechanism of the application of antimicrobial agent depends on the approach used. There are two different approaches reported so far. One is by contact method and another is the diffusion method. In the contact method, the agent is coated on the surface of the fiber and will not disperse into the fiber. In case a microorganism touches the fiber surface, antimicrobial activity occurs. However, in case of diffusion method the antimicrobial agent migrates from the textile polymer matrix into the external medium to attack the microorganism. Some of the effective antimicrobial agents used for protective textiles are monoquaternary ammonium salt: alkyltrimethylammonium bromide usually applied on cotton, polyester, nylon and wool fibers. Triclosan applied on polyester, nylon, polypropylene, cellulose acetate, acrylic. Metals and metallic salts applied on cotton, wool, polyester, nylon. Chitosan applied on cotton, polyester and wool. Antimicrobial agents can be applied by padding–drying–curing process. However, nowadays they

are also applied on fabrics using a coating or foaming or by spray method. Recently, researchers have also developed techniques where the antimicrobial agents can be added by mass coloration process also. They can be applied in the fiber matrix using a microcovers technique or by finishing process. Some fibers are also applied using surface modification and enabling the chemical structure present in the fiber to make a covalent bond. Nanopolymers and co-polymers are also developed with an antimicrobial agent.

5.6 Soil-Release Finish

Soiling of textiles during usage is a common phenomenon. Textiles get soiled by different mechanism like mechanical adhesion, adhesion of dirt particles due to electrical forces and redeposition of soil particles during washing. Schindler and Hauser [29] have conducted in-depth research on the chemical structure, application and change in fabric properties after the application of soil release chemicals on textile fabrics. Soil release finish is a term applied to textiles where the surface is rendered for easy removal of soils using simple laundering techniques and chemicals which make the fibers more absorbent and hence increasing the usability of the fabric, thus ensuring effective soil removal. A different method is being developed for application of soil-release finish based on their chemical structures. Earlier methods were to apply polyglycols on polyester textiles. These polyglycolates interact with the chemical structure of polyester through ester reaction. This reaction is temperature and moisture sensitive. However, this method is not so frequently followed nowadays. Carboxy, ethoxy and fluorine-based cross-linking agents are regularly used today. Few examples are ethyl cellulose, methyl cellulose or acetates. They are applied through the padding process.

5.7 Flame-Proofing Finish

Firefighters and emergency personnel require protection. The flame retardants are classified into categories, namely phosphorous-based primary flame retardants (condensed phase mechanism) and halogens (gas phase mechanism). Flame retardants that exhibit their activity through physical effects (borates, alumina trihydrate and calcium carbonate) are called as adjunctive flame retardants. A simple pad-dry method is used for application of ammonium phosphates and other flame-retardant finish on textiles, using the pad-dry technique most nondurable and water-soluble finishes such as the ammonium phosphates and similar finishes. Koichi [30] has reported on the flame-retardant chemicals, its additives and other application procedures for textiles in their research work.

5.8 *Antistatic Finish*

Antistatic finish for protective textiles functions to remove any chances of accumulation of static charges on the surface of the fabric. The principal mechanism of static electricity is to prevent the accumulation of static charges by increasing the electrical conductivity of the fiber surface. The application of these anti-static agents on the surface of the fabric forms an intermediate layer on the surface. Seyam et al. [31] provide the various methods of anti-static treatment procedures involved in textiles. Chemical surfactants like organic salts like glycols, polyethylene glycols, polyelectrolytes, quaternary ammonium salts with fatty alkyl chains, polyethylene oxide compounds and esters of salts of alkyl phosphonium acids are used for textile materials. Antistatic materials are very useful in making conductive fibers. These conductive fibers are produced using antistatic agents which are incorporated into the polymer melt during the extrusion process. Some electroconductive materials like carbon or nanosilver are deposited on the fiber surface by coating method. Excellent control and durability over static electricity can be attained by incorporating these methods.

5.9 *UV Protection Finish*

Sarkar [32] reports UV protection finish which can be used effectively for textiles. UV-protective finish for protective textiles basically involves the protection of human skin under solar radiations. The damage to human skin due to UV radiation is a function of wavelength of incident radiation with most of the damage done at a wavelength of 300 nm. A solar protective factor known as SPF is the ratio of potential erythema effect to the transmitted erythema effect transmitted through the fabric by radiation and can be calculated from spectroscopic methods. This parameter is used for evaluating the effectiveness of UV protection.

6 **Conclusion**

In this research, the design and development aspects of anti-ballistic fabrics are discussed. The minimum material properties have to be kept in mind while selecting and developing an anti-ballistic material. Further the functional finishes are useful to enhance the performance and comfort characteristics. The method of application should be optimized based on the finish type. This paper acts as theoretical guidance to further enhance the experimental attempts to develop and innovate materials to meet anti-ballistic and functional requirements. The use of shear thickening fluid enhances the impact resistance properties of anti-ballistic fabrics. One of the technical

drawbacks of Kevlar's flexibility is that when it stops a bullet, the energy is transferred directly to the wearer at the point of impact, which causes trauma.

Acknowledgements The authors wish to acknowledge Ethiopian Technical University (Federal TVET Institute), Addis Ababa, Ethiopia, for providing support and assistance in carrying out department research activity and community research work related to COVID-19.

References

1. Talreja K, Chauhan I, Ghosh A, Majumdar A, Butola BS (2017) Functionalization of silica particles to tune the impact resistance of shear thickening fluid treated aramid fabrics 7(78):49787–49794. <https://doi.org/10.1039/c7ra09834k>
2. Aidy A, Shaker AR, Khalina A, Sapuan SM (2011) Development of anti-ballistic board from ramie fiber. *Polym-Plast Technol Eng* 50(6):622–634. <https://doi.org/10.1080/03602559.2010.551381>
3. Park S, Jayaraman S, Kiekens P (2012) The engineering design of intelligent protective textiles and clothing, pp 1–27. Springer, Netherlands. https://doi.org/10.1007/978-94-007-0576-0_1
4. Joshi M, Bhattacharyya A (2011) Nanotechnology a new route to high performance and functional textiles. *Text Prog* 43(3):155–233. <https://doi.org/10.1080/00405167.2011.570027>
5. Joshi M (2008) The impact of nanotechnology on polyesters, polyamides and other textile—advances in polyesters and polyamides, pp 354–415. Woodhead Publishing, Ltd. Cambridge, UK. <https://doi.org/10.1533/9781845694609.2.354>
6. Wazed AS, Rajendran S, Joshi M (2010) Effect of process parameters on layer-by-layer self-assembly of polyelectrolytes on cotton substrate. *Polym Polym Compos* 18(5):237–249. <https://doi.org/10.1177/096739111001800501>
7. Antosik A, Głuszek M, Żurowski RM, Szafran M (2016) Effect of SiO₂ particles size and length of poly(propylene glycol) chain on rheological properties of shear thickening fluids. *Arch Metall Mater* 61(3):1511–1514. <https://doi.org/10.1515/amm-2016-0247>
8. Meng B, Guangyin X (2016) Study of preparation and rheological properties of shear thickening fluid. In: 4th International conference on sustainable energy and environmental engineering (ICSEEE), pp 1033–1038. Shenzhen, China. <https://doi.org/10.2991/icseee-15.2016.183>
9. Wetzel ED, Wagner et al (2004) The effect of rheological parameters on the ballistic, properties of shear thickening fluid (stf) -kevlar composites. *AIP Conf Proc* 712, 288. <https://doi.org/10.1063/1.1766538>
10. Holmberg RA (1988) Composite fabrics for protective clothing. *J Coated Fabrics* 18(1):64–70. <https://doi.org/10.1177/152808378801800106>
11. Sabit A, Ashutosh T (1997) An overview of military textiles. *Indian J Fiber Text Res* 22:348–352
12. Decker MJ, Halbach CJ, Nam CH, Wagner NJ, Wetzel ED (2007) Stab resistance of shear thickening fluid (STF) -treated fabrics. *Compos Sci Technol* 67(3):565–578. <https://doi.org/10.1016/j.compscitech.2006.08.007>
13. Egress RG, Decker MJ, Halbach CJ, Lee JY, Kirkwood JE, Kirkwood KM, Wagner NJ, Wetzel ED (2006) Stab resistance of shear thickening fluid (STF)—Kevlar composites for body armor applications. *Transf Scie Techn Curr Fat Force* 264–271. https://doi.org/10.1142/9789812772572_0034
14. Xuhong M, Xiangyong K, Gaoming J (2013) The experimental research on the stab resistance of warp-knitted spacer fabric. *J Ind Text* 43(2):281–301. <https://doi.org/10.1177/1528083712464256>
15. Liu X, Huo JL, Li TT, Peng HK, Lin JH, Ching-Wen L (2019) Investigation of the shear thickening fluid encapsulation in an orifice coagulation bath. *Polymers* 11:519. <https://doi.org/10.3390/polym11030519>

16. Zhang H, Zhang X, Chen Q, Li X, Wang P, Yang E-H, Duan F, Gong X, Zhang Z, Yang J (2017) Encapsulation of shear thickening fluid as an easy-to-apply impact-resistant material. *J Mater Chem A* 5:22472–22479. <https://doi.org/10.1039/C7TA04904H>
17. Song K, Huang W, Wan H, Huang H (2017) Development of shear thickening material ACMME 2017. *IOP Conf Series Mater Sci Eng* 207: 012024. <https://doi.org/10.1088/1757-899X/207/1/012024>
18. Vijaya KR, Tarig AH, Mahfuz H, Jeelani S (2010) Sonochemical synthesis and rheological properties of shear thickening silica dispersions. *Ultrason Sonochem* 17(5):947–952. <https://doi.org/10.1016/j.ultsonch.2010.02.001>
19. <https://www.thomasnet.com/insights/how-textiles-are-used-for-ballistic-materials/>
20. Research. Look. to Carbon Nanotubes for New Body Armor. <https://eden.fm/2007/11/07/researchers-looking-to-carbon-nanotubes-for-new-body-armor/>
21. <https://caliberarmor.com/nij-body-armor-ballistic-levels/>
22. Turaga U, Singh V, Ramkumar S (2015) Biological and chemical protective finishes for textiles. In: *Functional finishes for textiles*, pp 555–578. Woodhead Publishing. <https://doi.org/10.1533/9780857098450.2.555>
23. Silva C, Cavaco-Paulo AM, Fu JJ (2015) Enzymatic biofinishes for synthetic textiles. In: *Functional finishes for textiles*, pp 153–191. Woodhead Publishing. <https://doi.org/10.1533/9780857098450.1.153>
24. https://www.just-style.com/management-briefing/functional-finishes-meet-environmental-concerns_id126337.aspx
25. Masamichi M, Hiroko O, Motonobu K (2015) Easy care finish for textiles, pp 227–256. Woodhead Publishing. <https://doi.org/10.1533/9780857098450.1.227>
26. Vanneste M (2015) Easy care finish for textiles. In: *Functional finishes for textiles*, pp 227–256. Woodhead Publishing. <https://doi.org/10.1533/9780857098450.1.227>
27. Thalia MD (2015) Softening finishes for textiles and clothing. In: *Functional finishes for textiles*, pp 123–152. Woodhead Publishing. <https://doi.org/10.1533/9780857098450.1.123>
28. Nayak R, Padhye R (2015) Antimicrobial finishes for textiles. In: *Functional finishes for textiles*, pp 361–385. Woodhead Publishing Series in Textiles. <https://doi.org/10.1533/9780857098450.2.361>
29. Schindler WD, Hauser PJ (2004) Soil-release finishes. In: *Chemical finishing of textiles*, pp 87–97. Woodhead Publishing Series in Textiles. <https://doi.org/10.1533/9781845690373.87>
30. Koichi F (1968) A review of the flame-proofing for textiles 1(5):257–262. <https://doi.org/10.2115/fiber1968.1.257>
31. Seyam AM, Oxenham W, Tyson T (2015) Antistatic and electrically conductive finishes for textiles. In: *Functional finishes for textiles*. Woodhead Publishing. <https://doi.org/10.1533/9780857098450.2.513>.
32. Sarkar AK (2005) Textiles for UV protection. In: *Textiles for protection*, pp 355–377. Woodhead Publishing Series in Textiles. <https://doi.org/10.1533/9781845690977.2.355>

Chapter 28

Rayleigh-Bénard Convection in the Presence of Synchronous and Asynchronous Thermal Rigid Boundary Conditions



Palle Kiran 

Abstract This paper investigates the effect of time-periodic temperature modulation on Rayleigh-Benard convection using rigid isothermal boundary conditions. The time-periodic temperature modulation has been considering in three different modes, out-of-phase (OPM), lower boundary (LBMO), and in-phase modulation (IPM). Heat transfer results are calculated in terms of the Nusselt and mean Nusselt numbers through the finite amplitude of convection which is derived from the Ginzburg-Landau equation (GLE). The Ginzburg-Landau equation has been derived from the Fredholm solvability condition at third. The GLE is a function of the system parameters and solved numerically. The present study shows that heat transfer results are controlled effectively by out-of-phase and lower boundary modulations. The modulated amplitude of convection enhances heat transfer for low frequencies and diminishes for high frequencies. Further, it is found that rigid boundary conditions are diminishing heat transfer than free boundaries. Finally, it is concluded that heat transfer results are controlled by rigid isothermal boundary conditions and modulation.

Keywords Thermal modulation · Weakly nonlinear theory · Rigid boundary · Heat transport · GL equation.

1 Introduction

Dynamic stabilization and destabilization of any mechanical system and its periodic state lead to dramatic modifications of behavior depending on the modulation. The concept of modulation to stabilize or destabilize stability analysis was introduced by many authors. A cellular regime of steady convection is formed at critical Rayleigh number of RBC. This critical regime needs to control to stabilize or destabilize the system to enhance its performance. Numerous studies on Rayleigh-Bénard convec-

P. Kiran (✉)

Chaitanya Bharathi Institute of Technology, Hyderabad 500075, India
e-mail: pallekiran_maths@cbit.ac.in

© The Author(s), under exclusive license to Springer Nature Singapore Pte Ltd. 2022
V. Bindhu et al. (eds.), *Proceedings of Fourth International Conference on Inventive Material Science Applications*, Advances in Sustainability Science and Technology,
https://doi.org/10.1007/978-981-16-4321-7_28

323

tion have been reported since the 19th century with various physical configurations. Let us discuss some relevant studies on Rayleigh-Bénard convection and its developments.

The nonlinear regime of the problem was discussed based on the linear problem by Malkus and Veronis [1]. It was found that initial heat transport due to (basic temperature) convection depends linearly on the Rayleigh number (critical state); the heat transport at higher Rayleigh numbers departs only slightly from this linear dependence. Sparrow et al. [2] investigated onset convection under internal heating effect on RBC for free-free and rigid boundary conditions. It was concluded that critical Rayleigh numbers marking the onset convection and internal heating generate the nonlinear temperature. The effect of internal heating is prone to instability as critical Rayleigh number decreases. The RBC was investigated under mean thermal modulation by Krishnamurti [3]. The stability analysis was examined in terms of mean temperature variation η and amplitude. It was found that hexagons are shown to be the stable solution near R_{0c} . The effect of time-dependent sinusoidal wall temperatures, i.e., temperature modulation on RBC was given by Venezian [4]. The shift in the critical Rayleigh number (R_{0c}) had been calculated as a function of frequency and wavenumber. It was found that modulated wall temperature can be used to advance or delay the onset of convection. The linear stability analysis of RBC under thermal modulation was given by Rosenblat and Tanaka [5]. It was found that the oscillatory gradient of basic temperature controls the critical Rayleigh number. The Stuart–Watson technique was extended to nonlinear hydrodynamic instability of Bénard convection under thermal modulation by Davis [6].

An excellent review of periodic flows was given by Davis [7]. Three main problems time-periodic flows, sinusoidal time variation, parallel shear flows, convective, and centrifugal instabilities had been well documented in his studies. The effect of internal heating on RBC for rigid thermal boundary conditions was given by Clever [8]. Instability of the quiescent state and heat transfer is obtained over a region in the dual Rayleigh number of stationary convection. The finite amplitude equation was obtained near to the threshold of onset convection by Ahlers et al. [9]. It was found that the onset of convection in steady-state not by roll pattern but by the stable in steady-state. But it was concluded that hexagonal configuration arrived in the intermediate state and adjusted with amplitude equation. The effect of thermal modulation on weakly nonlinear stability (RBC) was reported by Roppo et al. [10]. The study reveals that modulation produces a range of stable hexagons near the critical Rayleigh number and its size decreases with modulation frequency.

Venezian was the first person who investigated thermal modulation on RBC for free-free boundaries of linear convection. A similar problem has been extended to gravity modulation by Gresho and Sani [11]. The problem of [4, 7] was studied by Finucane and Kelly [12] experimentally and analytically for free boundary conditions. They found the low frequency modulation is to destabilize the system and higher frequency modulation stabilizes the system. The temperature modulation effect on Helium-I fluid layer was given by Niemela and Donnelly [13]. It was found that +tive and –ve shifts of the convective threshold are compared to the unmodulated case. The effect of thermal modulation on the rotating fluid layer (using the

Venezian approach) was given by Malashetty and Mahantesh [14]. The effect of thermal modulation of the free-boundary temperatures in the RBC, Boussinesq fluid layer has been studied using Floquet theory by numerically Jitender and Renu [15]. Most of the above studies are considered free isothermal boundary conditions and linear theories. In the 19th century, Pellew and Southwell [16] investigated the stability of viscous fluids which was given experimentally and theoretically by Jeffreys [17] and Low [18]. Among three boundary conditions, the critical value R_{0c} depends on ideal boundaries free (top) and rigid (bottom) conducting surfaces.

Using the complex Ginzburg-Landau equation, the effect of temperature modulation on viscoelastic fluid saturating porous convection has been investigated by Bhadauria and Kiran [19]. It was found that an oscillatory mode of thermal modulation transport heat transfer more than stationary mode. The model of [19] has been extended to binary viscoelastic fluid layer subjected to temperature modulation at the boundaries by Bhadauria and Kiran [20]. They have investigated an oscillatory mode of weakly nonlinear convection for free-free thermal boundary conditions. The effect of nonlinear throughflow and thermal modulated porous media was given by Kiran [21]. It was found that the effect of throughflow has dual nature either stabilizing or destabilizing depending on inflow and outflow in the presence of modulation. The similar results of throughflow under thermal modulation have been reported by Kiran [22, 23]. While using the complex Ginzburg-Landau equation, the effect of thermal modulation on oscillatory convection has been reported a series of works by Bhadauria et al. [24, 25]. It is found that complex Ginzburg-Landau model enhances heat and mass transfer results than GLE for stationary convection (reported by Bhadauria et al. [26–28]). The reason is that the oscillatory convective amplitude is a function of the growth rate of the disturbances. This growth rate (ω^2) contributes an additional strength to the heat/mass transfer. Using the linear stability analysis and free boundaries, the combined effect of magnetic field and temperature modulation on the porous stability has been investigated Bhadauria et al. [29]. The influences of the magnetic field and the Vadasz number have been studied through proper tuning of the frequency of modulation.

The effect of thermal modulation on linearly stability of Rayleigh-Benard convection for rigid boundaries is investigated by Jitender et al. [30]. The linear stability analysis of Rayleigh-Benard convection for rigid boundary conditions was investigated by Raju and Bhattacharyya [31]. It was found that the change from harmonic to subharmonic critical instability occurs via a bicritical state which depends on modulation and the Prandtl number. The exact solutions are obtained even when the boundaries are rigid. Three different modulations have been investigated and found that by suitably adjusting Pr and frequency of modulation the system either stable or un-stable. The linear double-diffusive convection in a porous medium under thermal modulation reported by Bhadauria and Sherani [32]. Using Galerkin method and the Floquet theory, stability criteria has been performed for rigid plates.

The literature on the weakly nonlinear analysis of RBC for rigid isothermal boundaries is very sparse and that of heat transfer. From the literature, no nonlinear study is available in which rigid boundaries are considered under thermal modulation. Hence, in this article, we study a weakly nonlinear thermal convection under thermal modulation using Ginzburg-Landau model with rigid boundaries.

2 Mathematical Model of the Problem

We have been considered an infinitely extended horizontal fluid layer confined between two parallel plates at $z = -\frac{d}{2}$ and $z = \frac{d}{2}$ is considered. The plates are maintained at oscillating temperature, and the fluid layer is heated from below. The temperature profiles at plates are given by:

$$\begin{aligned}
 T &= T_0 + \Delta T [1 + \delta_T \chi^2 \text{Re}\{e^{i\omega_T t}\}] && \text{at } -\frac{d}{2} \\
 &= T_0 + \Delta T \delta_T \chi^2 \text{Re}\{e^{i(\omega_T t + \theta)}\}. && \text{at } \frac{d}{2}
 \end{aligned} \tag{1}$$

A physical configuration of the problem is given in Fig. 1. The mathematical equations are simplified by Oberbeck-Boussinesq approximation. The Navier-Stokes equations under these conditions are given by:

$$\nabla \cdot \mathbf{q} = 0, \tag{2}$$

$$\left(\frac{\partial \mathbf{q}}{\partial t} + (\mathbf{q} \cdot \nabla) \mathbf{q} - \frac{1}{\rho_0} \nabla P + \frac{\rho}{\rho_0} \mathbf{g} \right) - \nu \nabla^2 \mathbf{q} = 0, \tag{3}$$

$$\partial T / \partial t + (\mathbf{q} \cdot \nabla) T = \kappa_T \nabla^2 T, \tag{4}$$

$$\rho = \rho_0 [1 - \alpha_T (T - T_0)], \tag{5}$$

where the physical variables have their usual meanings and are given in Nomenclature. In Eq. (1), χ is the smallness of amplitude of modulation, δ_T , ω_T are amplitude and frequency of modulation.

3 Basic State

The basic state is assumed to be quiescent, and the quantities in this state are given by

$$\mathbf{q}_b = 0, p = p_b(z, t), T = T_b(z, t), \rho = \rho_b(z, t). \tag{6}$$

In the quiescent state, the boundary conditions are: $\mathbf{q}_b = 0$ at $z = \pm \frac{d}{2}$, $T_b = T_0 + \nabla T$ at $z = -\frac{d}{2}$ and $T_b = T_0$ at $z = \frac{d}{2}$. Substituting Eq. (6) in Eqs. (2)–(5), we get the following relations, which helps us to define basic state pressure and temperature:

$$\frac{\partial p_b}{\partial z} = -\rho_b \mathbf{g} \left[1 - \alpha_T \Delta T \left(\frac{1}{2} - \frac{z}{2d} \right) \right] + c, \quad (7)$$

$$\kappa_T \frac{d^2 T_b}{dz^2} = \frac{\partial T_b}{\partial t}, \quad (8)$$

$$\rho_b = \rho_0 \left[1 - \alpha_T \Delta T \left(\frac{1}{2} - \frac{z}{d} \right) \right]. \quad (9)$$

Solution of Eq. (8), subjected to the condition (1), is given by

$$T_b(z, t) = T_s(z) + \chi^2 \text{Re}[T_0(z, t)], \quad (10)$$

where

$$T_s(z) = T_0 + \Delta T \left(\frac{1}{2} - \frac{z}{d} \right), \quad (11)$$

$$T_0(z, t) = \frac{\Delta T}{\sin h(\lambda)} \left(e^{i\theta} \sin h(\lambda) \left(\frac{1}{2} + \frac{z}{d} \right) + \sin h(\lambda) \left(\frac{1}{2} - \frac{z}{d} \right) \right) e^{i\omega t} \quad (12)$$

and $\lambda^2 = \frac{i\gamma\omega_T d^2}{\kappa_T}$.

$$\frac{\partial T_b}{\partial z} = -1 + \chi^2 \text{Re}[g(z)e^{i\omega t}], \quad (13)$$

where

$$g(z) = \frac{\lambda}{\sinh \lambda} \left(e^{i\theta} \cosh \lambda \left(\frac{1}{2} + z \right) - \cosh \lambda \left(\frac{1}{2} - z \right) \right) \quad (14)$$

and $\lambda = i\gamma\omega_T$. The finite amplitude perturbations on the basic state are superposed in the form:

$$\mathbf{q} = \mathbf{q}_b + \mathbf{q}', \quad \rho = \rho_b + \rho', \quad p = p_b + p', \quad T = T_b + T'. \quad (15)$$

Use Eq. (15) in Eq. (10), then non-dimensional physical variables; $(x, y, z) = d(x^*, y^*, z^*)$, $t = \frac{d^2}{\kappa_T} t^*$, $p' = \frac{\kappa_T \nu}{d^2} p^*$, $T' = \Delta T T^*$, and $\omega_T = \frac{\kappa_T}{d^2} \omega_T^*$.

$$\frac{\partial u}{\partial x} + \frac{\partial w}{\partial z} = 0, \quad (16)$$

$$\frac{1}{Pr} \frac{\partial \mathbf{q}}{\partial t} + \nabla p = \nabla^2 \mathbf{q} + Ra_T T \hat{k}, \tag{17}$$

$$\frac{\partial T}{\partial t} + \frac{\partial T_b}{\partial z} w = \nabla^2 T - \left(u \frac{\partial T}{\partial x} + w \frac{\partial T}{\partial z} \right). \tag{18}$$

where $\mathbf{q} = (u, w)$. Now while operating curl twice on Eq. (17), we obtain the following equation:

$$\frac{1}{Pr} \frac{\partial}{\partial t} \nabla^2 w - Ra_T \frac{\partial^2 T}{\partial x^2} - \nabla^4 w = 0, \tag{19}$$

The boundary conditions to solve the Eqs. (18) and (19) are those of rigid isothermal upper and lower plates, and thus, we take:

$$(u, w) = (0, 0), \left(\frac{\partial u}{\partial x}, \frac{\partial w}{\partial z} \right) = (0, 0), T = 0 \text{ at } z = \pm \frac{1}{2}. \tag{20}$$

Also along the x variable, we have the periodicity for both T and w as $T(x \pm 2\pi k_c^{-1}, z) = T(x, z)$ and $w(x \pm 2\pi k_c^{-1}, z) = w(x, z)$ where k_c is the critical wavenumber, $Ra = \frac{\alpha_T g \Delta T d^3}{\nu \kappa_T}$ is thermal Rayleigh number, $\nu = \frac{\mu}{\rho_0}$ is kinematic viscosity.

The parameter χ is a perturbed quantity shows deviation from onset of convection, and the variables are expanded as power series of χ :

$$Ra_T = R_0 + \chi^2 R_2 + \chi^4 R_4 + \dots, \tag{21}$$

$$(u, w, T) = \chi(u, w, T)_1 + \chi^2(u, w, T)_2 + \chi^3(u, w, T)_3 + \dots, \tag{22}$$

where R_0 is the critical value of the critical Rayleigh number at which the onset of convection takes place. For small amplitude of Rayleigh-Benard convection, we use slow time scale $t = \chi^2 \tau$. The boundary conditions are taken to solve the system Eqs.(18, 19) are:

$$w = \frac{dw}{dz} = T = 0, \text{ at } z = \pm \frac{1}{2}, \tag{23}$$

$$w(x \pm 2\pi k_c^{-1}, z) = w(x, z), T(x \pm 2\pi k_c^{-1}, z) = T(x, z), \tag{24}$$

4 Ginzburg-Landau Equation

The coupled system of Eqs. (18, 19) is solved using Eq. (22) and (24) at every order of χ .

4.1 Lowest Order

In this order, we have

$$\begin{bmatrix} \nabla^4 & R_0 \frac{\partial^2}{\partial x^2} \\ -\frac{\partial T_b}{\partial z} & \nabla^2 \end{bmatrix} \begin{bmatrix} w_1 \\ T_1 \end{bmatrix} = \begin{bmatrix} 0 \\ 0 \end{bmatrix} \tag{25}$$

The solution of the lowest order system subjected to the boundary conditions Eq. (24) is assumed to be

$$\begin{aligned} w_1 &= A(\tau) \cos(kx) f(z), \\ T_1 &= B(\tau) \cos(kx) \sin \left[\pi \left(z + \frac{1}{2} \right) \right]. \end{aligned} \tag{26}$$

The amplitudes are functions of slow time scale and are connected by:

$$B(\tau) = \frac{2I_1}{c} A(\tau), \tag{27}$$

where $I_1 = \int_{\frac{1}{2}}^{-\frac{1}{2}} f(z) \cos(\pi z) dz$ and $c = k^2 + \pi^2$. The function $f(z)$ is known as Chandrasekhar function, and it is given by Chandrasekhar [33]:

$$f(z) = \frac{\cosh(\mu_1 z)}{\cosh\left(\frac{\mu_1}{2}\right)} - \frac{\cos(\mu_1 z)}{\cos\left(\frac{\mu_1}{2}\right)}, \tag{28}$$

where $\mu_1 = 4.73004074$. Substituting the Eqs. (26–28) in Eq. (25) and using the orthogonality condition with the eigenfunctions and leading to the condition of occurrence of trivial solution, we obtain the critical Rayleigh number:

$$R_0 = \frac{c(\pi^4 - \mu_1^4)^2 \left[(k^2 + \mu_1^2) \left(\mu_1 \sec^2\left(\frac{\mu_1}{2}\right) - 2 \tan h\left(\frac{\mu_1}{2}\right) \right) + (k^2 - \mu_1^2) \left(\mu_1 \sec h^2\left(\frac{\mu_1}{2}\right) - 2 \tan\left(\frac{\mu_1}{2}\right) \right) \right]}{64\pi^2 k^2 \mu_1^5}, \tag{29}$$

for free-free case

$$R_0 = \frac{c^3}{k^2}, \tag{30}$$

The values are obtained by $k_c = 3.09$, $R_{0c} = 1728.38$ and $k_c = 2.22$, $R_{0c} = 657.51$ for free-free boundary conditions.

4.2 2nd Order

We arrive at:

$$\begin{bmatrix} \nabla^4 & R_0 \frac{\partial^2}{\partial x^2} \\ -\frac{\partial T_b}{\partial z} & \nabla^2 \end{bmatrix} \begin{bmatrix} w_2 \\ T_2 \end{bmatrix} = \begin{bmatrix} R_{21} \\ R_{22} \end{bmatrix} \tag{31}$$

where $R_{21} = -R_1 \frac{\partial^2 T_1}{\partial x^2}$ and $R_{22} = u_1 \frac{\partial T_1}{\partial x} + w_1 \frac{\partial T_1}{\partial z}$. Under the Fredholm solvability condition, we obtain the solutions of the form:

$$w_2 = 0, \tag{32}$$

$$T_2 = \frac{2 \operatorname{sech} h\left(\frac{\mu_1}{2}\right)}{(\pi^2 + \mu_1^2)^2} \left[2\pi \mu_1 \cos(\pi z) \sin h(\mu_1 z) + (\pi^2 - \mu_1^2) \sin(\pi z) \cos h(\mu_1 z) \right] \tag{33}$$

$$+ 1.37137z - \operatorname{sech}\left(\frac{\mu_1}{2}\right) \left(\frac{\sin((\pi - \mu_1)z)}{(\pi - \mu_1)^2} + \frac{\sin((\pi + \mu_1)z)}{(\pi + \mu_1)^2} \right)$$

The plane averaged Nusselt number, $Nu(\tau)$, for the stationary convection:

$$Nu(\tau) = 1 + \left[\frac{k_c}{2\pi} \int_0^{\frac{2\pi}{k_c}} \left(\frac{\partial T_2}{\partial z} \right) dx \right]_{z=0} / \left[\frac{k_c}{2\pi} \int_0^{\frac{2\pi}{k_c}} \left(\frac{\partial T_b}{\partial z} \right) dx \right]_{z=0} \tag{34}$$

The above equation is solved numerically and quantified heat transfer.

4.3 3rd Order

At this order, we get

$$R_{31} = \frac{1}{Pr} \frac{\partial}{\partial \tau} \nabla^2 w_1 - R_2 \frac{\partial^2 T_1}{\partial x^2}, \tag{35}$$

$$R_{32} = \frac{\partial T_1}{\partial \tau} + w_1 \frac{\partial T_2}{\partial z} + \delta_T g(z) w_1. \tag{36}$$

Under the Fredholm solvability condition:

$$\int_0^{\frac{2\pi}{k}} \int_{-\frac{1}{2}}^{\frac{1}{2}} (R_{31}w_1^* + R_{32}T_1^*) dx dz = 0 \tag{37}$$

where (w_1^*, T_1^*) are the solutions of adjoint system of Eq. (25). On simplifying, we get the Ginzburg-Landau equation in terms of the amplitude $A(\tau)$.

$$\left(\frac{\beta^2}{Pr} I_2 - \frac{4R_0 k^2 I_1^2}{c^2} I_3 \right) \frac{\partial A(\tau)}{\partial \tau} - \left(\frac{2R_2 I_1 k^2}{c} I_4 + \frac{2R_0 I_1 k^2}{c} \delta_T I_5 \right) A(\tau) - \frac{2R_0 k^2 I_1}{c} I_6 A(\tau)^3 = 0, \tag{38}$$

where the coefficients are $\beta^2 = k^2 + \mu_1^2, I_2 = -\int_0^{\frac{2\pi}{k}} \int_{-\frac{1}{2}}^{\frac{1}{2}} A^* \nabla^2 f(z) * f(z) dx dz$. where

$$f_1(z) = \frac{\cosh(\frac{\mu_1 z}{2})}{\cosh(\frac{\mu_1}{2})} + \frac{\cos(\frac{\mu_1 z}{2})}{\cos(\frac{\mu_1}{2})}. I_3 = \int_0^{\frac{2\pi}{k}} \int_{-\frac{1}{2}}^{\frac{1}{2}} A^* \cos^2(kx) \cos^2(\pi z) dx dz.$$

$$I_4 = \int_0^{\frac{2\pi}{k}} \int_{-\frac{1}{2}}^{\frac{1}{2}} A^* \cos^2(kx) \cos(\pi z) f(z) dx dz.$$

$$I_5 = \int_0^{\frac{2\pi}{k}} \int_{-\frac{1}{2}}^{\frac{1}{2}} A^* \cos^2(kx) \cos(\pi z) g(z) f(z) dx dz.$$

$I_6 = \int_0^{\frac{2\pi}{k}} \int_{-\frac{1}{2}}^{\frac{1}{2}} A^* \cos^2(kx) \cos(\pi z) f(z) \frac{\partial T_2}{\partial z} dx dz$. The Ginzburg-Landau equation is given by:

$$\left(\frac{c}{Pr} + \frac{R_0 k^2}{c^2} \right) \frac{\partial A(\tau)}{\partial \tau} - \frac{R_0 k^2}{c} (1 - 2\delta_T I_7) A(\tau) + \frac{R_0 k^2}{8c^2} A(\tau)^3 = 0, \tag{39}$$

where

$$f_2(z, t) = \text{Re} (f(z) e^{(-i\Omega_T t)}), \tag{40}$$

$$f(z) = (A(\zeta) e^{\zeta z} + A(-\zeta) e^{-\zeta z}), A(\zeta) = \frac{\zeta}{2} \frac{(e^{-i\theta} - e^{-\zeta})}{(e^\zeta - e^{-\zeta})} \& \zeta = (1 - i) \sqrt{\frac{\Omega_T}{2}}. \tag{41}$$

$$I_7 = \int_{-\frac{1}{2}}^{\frac{1}{2}} \sin^2(\pi z) f_2 dz.$$

5 Results

The effect of thermal modulation on weak nonlinear thermal instability has been investigated for the case of rigid isothermal boundaries. We have consider the following three cases for temperature modulation:

1. Two walls are in-phase (IPM) temperature modulation, i.e., $\theta = 0$,
2. Two walls are in out-of-phase (OPM) temperature modulation, i.e., $\theta = \pi$ and,

3. Lower wall only modulated (LBMO) then $\theta = i\infty$, the upper wall is held at constant temperature.

The cubic Ginzburg-Landau Eqs. (38) and (39) are obtained under Fredholm solvability condition [19, 21–24] at third order. The results of thermal modulation has been depicted in Figs. 1 and 2 where the figures of Nu with respect to the slow time τ are depicted. It can be seen that Nu (in Eq. 34) is a function of A and obtained from Eq.(39) numerically. The values of Nu start with 1, thus showing the conduction state. The values of Nu enhance for intermediate values of τ thus showing convection in progress. For further in time, an oscillatory mode is achieved. The parameters of our problem are $A, Pr, \delta_T, \Omega_T$, finite amplitude, Prandtl number, amplitude (δ_T), and frequency (Ω_T) of modulation. At first, we present our results corresponding to out-of-phase modulation late other phases will be compared.

In Fig. 1a, we have compared the results of free isothermal and rigid isothermal boundary conditions. For free isothermal boundary conditions, there are many studies which have been reported by Bhadauria et al. [19], Kiran et al. [21], and Bhadauria et al. [26, 28, 28, 31]. But for the current study, no data is found till today. From the figure, it is clear that heat transfer is more for free boundary conditions than rigid boundary conditions. It can be written clear as $Nu_{\text{freeboundary}} > Nu_{\text{rigidboundary}}$. Due to rigid surface, the plate needs high energy for the onset of convection and same for the heat transfer. One way rigid isothermal boundary conditions are useful to reduce heat transfer. Since no study reported on this particular case of nonlinear theory with thermal modulation we have developed this work. The reader may observe from thee studies of Bhadauria and Sharani [32] and Chandrasekhar [33] and Raju and Bhattacharyya [31] that they have investigated linear stability analysis. It can be observed that

$$Nu^{\text{freeboundary}} > Nu^{\text{rigidboundary}} \tag{42}$$

for the same wave number. This implies that free boundary case instabilities can set in before rigid boundary case.

The effect of Prandtl number Pr on heat transport is presented in Fig. 1b. Upon increasing Pr , Nu increases which shows that heat transfer increases. Due to the low thermal diffusivity or high momentum rates, Pr enhances heat transfer. These are the results compatible with the results obtained by Bhadauria et al. [19], Bhadauria and Kiran [20, 28] and Kiran and Bhadauria [32] for free isothermal boundary conditions. The nature of Pr on shift in the critical Rayleigh number R_{ac} versus σ the wavenumber given by Raju et al. [31]. It is found that R_{ac} decreases as Pr takes values from 1 to 1000 and showing destabilizing effect for rigid isothermal boundaries. Our results are quietly agrees with Raju et al.[31] for rigid isothermal boundaries. The moderate values of Pr have been considered to retain the effect of acceleration term in Eqs. (38) and (39).

Effects of Ω_T and δ_T on heat transport have been presented in Fig. 1c, d, respectively. In Fig. 1a, amplitude of modulation increases the magnitude of Nu, heat transfer increases. These results are comparable with the studies of Siddheshwar et al. [34], Bhadauria et al. [19, 29] and Bhadauria, and Kiran [26, 28, 28, 29, 31]. The effects

of frequency Ω_T on Nu have been observed an opposite results due to amplitude δ_T presented in Fig. 1d. We found that g-jitter diminishes heat transfer confirming the results of Venezian [4] and Kiran et al. [21–24]. Thus from the figures, it is concluded that the effect of thermal modulation on heat transport is more for low frequency and moderate values of δ_T . This confirms the results of [19, 20, 28, 32].

We have drawn the figure for mean Nusselt number (\overline{Nu}), which was given by Bhadauria and Kiran [19] to see that effects of δ_T, Ω_T on (\overline{Nu}). We have drawn the figures of (\overline{Nu}) versus θ, Ω_T and δ_T in Fig. 2. In Fig. 2a, the effect of δ_T on (\overline{Nu}) versus θ is presented. When the values of δ_T varies from 0.1 to 0.3 figures show enhancement of heat transfer. In Fig. 2b, the same results are presented for particular range of Ω_T and can be observe its effect clearly. In Fig. 2c, the effect of Pr presented on (\overline{Nu}) as a function of δ_T . The values of δ_T taken from 0.0 to 0.4 and found that Pr enhances heat transfer. These are the results comparable wit the studies of [34] for thermal modulation.

Here we are not interested to present results corresponding to LBMO and IPM due to repetition of the figures. In Fig. 2d, we have compared three different modulations. It is found that the following relation among three types of modulation:

$$Nu_{IPM} < Nu_{LBMO} < Nu_{OPM} \tag{43}$$

The in-phase modulation of the boundaries does not alter temperature gradient across the porous medium, therefore no difference on heat transfer. However, in the cases

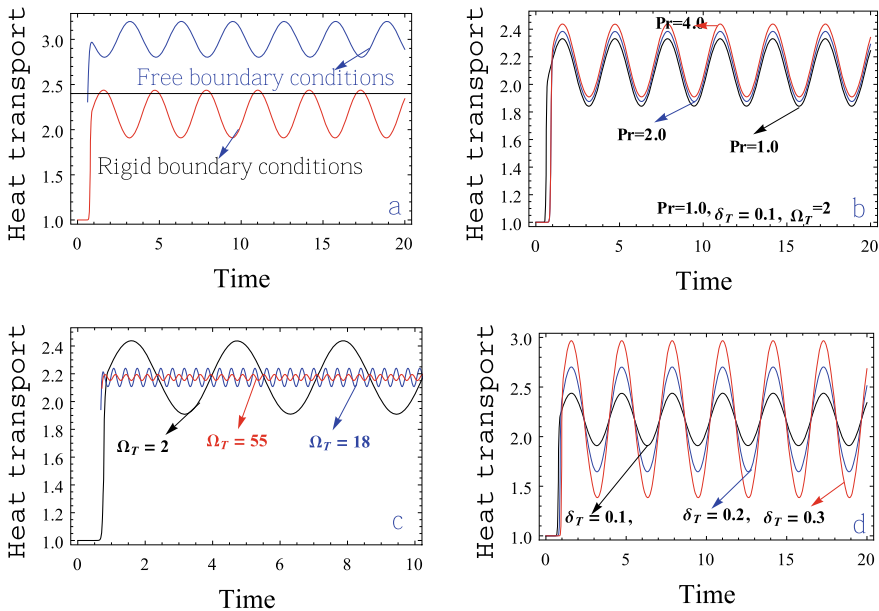


Fig. 1 Effect of various parameters on Nu

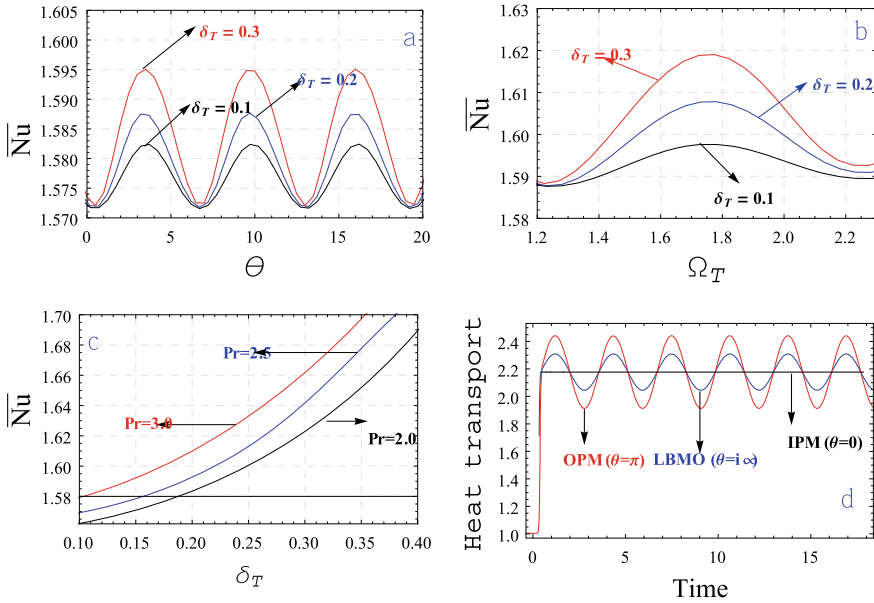


Fig. 2 Effect of thermal modulation on mean Nusselt number \overline{Nu}

of OPM and LBMO, the effect of temperature modulation on heat transfer is quite visible with oscillatory in nature. These are the results comparable with the studies of Bhadauria et al. [19] and Siddheshwar et al. [34].

6 Conclusions

The following conclusions are made based on our study:

1. The effect of (δ_T) is to enhance the heat transfer.
2. The effect of modulation frequency (Ω_T) is to diminish the heat transfer.
3. Thus, showing the both enhancement and decrement in heat transfer due to thermal modulation.
4. These boundaries (rigid isothermal) are more ideal to diminish or enhance heat transfer.
5. Free boundaries transport more heat transfer than rigid isotherms boundaries.
6. These boundaries are more ideal to stabilize or destabilize the system.
7. Both OPM and LBMO showing their effect on heat transfers and IPM has negligible effect on heat transfer.

Acknowledgements Author Dr. Palle Kiran acknowledge CBIT, Hyderabad, India for providing research specialities in the Department.

References

1. Malkus WVR, Veronis G (1958) Finite amplitude cellular convection. *J Fluid Mech* 4:225–260
2. Sparrow EM, Goldstein RJ, Jonsson VK (1964) Thermal instability in a horizontal fluid layer: effect of boundary conditions and non-linear temperature profile. *J Fluid Mech* 18:513–528
3. Krishnamurti R (1968) Finite amplitude convection with changing mean temperature, Part 1. Theory *J Fluid Mech* 33:445–455
4. Venzian G (1969) Effect of modulation on the onset of thermal convection. *J Fluid Mech* 35:243–254
5. Rosenblat S, Tanaka GA (1971) Modulation of thermal convection instability. *Phys Fluids* 14:1319
6. Davis SH (1971) Finite amplitude instability of time-dependent flows. *J Fluid Mech* 45:33–48
7. Davis SH (1976) The stability of time-periodic flows. *Ann Rev Fluid Mech* 8:57–74
8. Clever RM (1977) Heat transfer and stability properties of convection rolls in an internally heated fluid layer. *J Appl Math Phys (ZAMP)* 28:585–597
9. Ahlers G, Cross MC, Hohenberg PC, Safran S (1981) The amplitude equation near the convective threshold: application to time-dependent heating experiments. *J Fluid Mech* 110:297–334
10. Roppo MH, Davis SH, Rosenblat S (1984) Benard convection with time periodic heating. *Phys Fluids* 27:796–803
11. Gresho PM, Sani RL (1970) The effects of gravity modulation on the stability of a heated fluid layer. *J Fluid Mech* 40:783–806
12. Finucane RG, Kelly RE (1976) Onset of instability in a fluid layer heated sinusoidally from below. *Int J Heat Mass Transf* 19:71–85
13. Niemela JJ, Donnelly RJ (1987) Externally modulation of Rayleigh-Benard convection. *Phys Rev Lett* 59(21):2431–2434
14. Malashetty MS, Mahantesh S (2008) Effect of thermal modulation on the onset of convection in a rotating fluid layer. *Int J Heat Mass Transfer* 51:2814–2823
15. Jitender S, Renu B (2008) Temperature modulation in rayleigh-bénard convection. *ANZIAM J* 50:231–245
16. Pellew A, Southwell RV (1940) On maintained convective motion in fluid heated from below. *Proc R Soc Lond A* 176:312–343
17. Jeffreys H (1926) The stability of a layer of fluid heated below. *Philosoph Mag* 2:833–844
18. Low AR (2012) On the criterion for stability of a layer of viscous fluid heated from below. *Proc R Soc Lond A* 123(1929):180–195. temperature or gravity modulation using Ginzburg-Landau model. *Int J Non Linear Mech* 47(2012):418–425
19. Bhadauria BS, Kiran P (2014) Weakly nonlinear oscillatory convection in a viscoelastic fluid saturating porous medium under temperature modulation. *Int J Heat Mass Transf* 77:843–851
20. Bhadauria BS, Kiran P (2014) Heat and mass transfer for oscillatory convection in a binary viscoelastic fluid layer subjected to temperature modulation at the boundaries. *Int Comm Heat Mass Transf* 58:166–175
21. Kiran P (2016) Throughflow and non-uniform heating effects on double diffusive oscillatory convection in a porous medium. *Ain Shams Eng J* 7:453–462
22. Kiran P, Bhadauria BS (2015) Nonlinear throughflow effects on thermally modulated porous medium. *Ain Shams Eng J* 7(1):473–482
23. Kiran P (2015) Throughflow and g-jitter effects on binary fluid saturated porous medium. *Appl Math Mech* 36(10):1285–1304
24. Kiran P, Bhadauria BS (2016) Weakly nonlinear oscillatory convection in a rotating fluid layer under temperature modulation. *ASME J of Heat Transf* 138:051702
25. Bhadauria BS, Kiran P (2015) Chaotic and oscillatory magneto-convection in a binary viscoelastic fluid under g-jitter. *Int J of Heat and Mass Transfer* 84:610–624
26. Kiran P, Bhadauria BS, Narasimhulu Y (2017) weakly nonlinear and nonlinear magneto-convection under thermal modulation. *J Appl Nonlinear Dynam* 6(4):487–508
27. Bhadauria BS, Kiran P (2013) Heat transport in an anisotropic porous medium saturated with variable viscosity liquid under temperature modulation. *Transp Porous Media* 100:279–295

28. Bhadauria BS, Kiran P (2014) Weak nonlinear double diffusive magneto-convection in a Newtonian liquid under temperature modulation. *Int J Eng Math* 2014:01–14
29. Bhadauria BS, Sherani A (2008) Onset of darcy-convection in a magnetic-fluid saturated porous medium subject to temperature modulation of the boundaries. *Transp Porous Med* 73:349–368
30. Jitender S, Renu B, Puneet K (2015) Bicritical states in temperature-modulated Rayleigh-Bénard convection. *Phys Rev E* 92:013005
31. Raju VRK, Bhattacharyya SN (2010) Onset of thermal instability in a horizontal layer of fluid with modulated boundary temperatures. *J Eng Math* 66:343–351
32. Bhadauria BS, Sherani A (2008) Onset of double diffusive convection in a thermally modulated fluid saturated porous medium. *Z Naturforsch* 63a(2008):291–300
33. Chandrasekhar S (1961) *Hydrodynamic and Hydromagnetic stability*. Oxford University Press, New York
34. Siddheshwar PG, Bhadauria BS, Suthar OP (2013) Synchronous and asynchronous boundary temperature modulations of Bénard-Darcy convection. *Int J Nonlinear Mech* 49(2013):84–89

Chapter 29

Prediction of Aluminum Alloys Composition for Industrial Requirement Using Data Analysis Techniques



M. Arunadevi, C. P. S. Prakash, Venugopal Prasanna Joshi,
Rohit Shanakar Palada, Ravut Dixit, and Rahul Pandappa Chinnannavar

Abstract Traditional methods of developing new materials, such as observational trial and error and density functional theory (DFT)-based methods, often take enormous time and energy and are constrained by laboratory environments and theoretical foundations. As a result, it is important to formulate a new approach for speeding the process of developing the new materials for the industrial needs. Discovering new material using data analysis techniques has recently received increased interest, with significant increases in prediction accuracy and also time efficiency. So, this paper proposes algorithms for predicting the aluminum composites using various data analysis techniques like linear regression, random forest regressor, K-nearest neighbor (KNN) and decision tree for the required mechanical properties like yield strength, tensile strength, density and thermal conductivity.

Keywords Aluminum alloys · Linear regression · Random forest regressor · KNN · Decision tree

1 Introduction

The conventional method of discovering new materials was not matching the pace with advancement in material science. So, machine learning was introduced to discover and develop new materials as it was cost-effective and had short development cycles [1]. In the field of material science, finding the new material with high accuracy has become more challenging for the research works. Nowadays, data analysis is playing a significant role in the field of material science in discovery of new materials. Machine learning algorithm can be applied in development and validation of new materials [2]. Industries face challenges during the production of aluminum components that is achievement of the necessary properties of aluminum alloys. There is a lot of time and energy is wasted in experimentation and also in testing of their properties in modern aluminum composites [3].

M. Arunadevi (✉) · C. P. S. Prakash · V. P. Joshi · R. S. Palada · R. Dixit · R. P. Chinnannavar
Department of Mechanical Engineering, Dayananda Sagar College of Engineering, Bangalore,
India

As automation in the mechanical industry era has been more emulative since the 20s, predictive machine status management is a key challenge for machine industries where a variety of large-scale machines work [4]. Application of machine learning algorithms is establishing a relationship between the elementary structure and their properties (mechanical) due to the hydrogen presence [5].

The main objective of unsupervised learning is to explore data representations that are useful for subsequent assignments, without reference to supervised labeling during pr of separation [6]. Artificial neural networks (ANN) is an approach to the creation of an effective model for predicting DC motor speed based on a series of input conditions [7]. Artificial neural network (ANN) is an approach to the creation of an effective model for predicting DC motor speed based on a series of input conditions [8]. The material database showing various properties was created. In order to estimate influence of alloying elements, ANN model is used [9]. In this paper, ANN is used to optimize the mechanical properties of developed MMCs for different SiC particles size spectrum [10]. Neural network pruning strategies can reduce the number of parameters of qualified networks by more than 90%, reduce storage requirements and improve statistical inference efficiency without losing accuracy [11]. In this paper, progress in the applications of data analysis techniques in the different fields like building technology, earthquake engineering is discussed [12]. Results indicate that the Gaussian process regression methodology provides very accurate predictions for all three datasets studied. It was found that the modular Gaussian method methodology has been able to sustain the high precision of the forecasts while significantly increasing the pace of online learning [13]. Considering the analogy of biological evolution, a model was created using machine learning, i.e., genetic algorithm.

The mechanical properties of aluminum matrix were found experimentally and also by using ANN-GA model [14]. For 7017 aluminum alloy, an artificial neural network (ANN) and Johnson–cook model were developed in order to predict the various properties of strain rates and temperatures [15]. The prediction of weight loss after wear test is done using ANN model, and the influence of aging parameters on PM Inconel 706 wear behavior is investigated experimentally [16]. The present thesis examines the feasibility of the friction stir welding process for joining NiTi form memory alloys, the impact of the process on the mechanical properties of the material has been calculated in order to analyze the welding process [17]. The quantitative structure property relationship (QSPR) technique was used to estimate the cetane number (CN) of hydrocarbons likely to be present in diesel fuels [18]. Statistical learning approach using chemical bonding and atomic radii of elements in alloys facilitates to predict transformation temperatures [19]. A novel hypothesis of the Fermat paths of light was proposed. The method enables, for the first time, precise shape recovery of complex materials, ranging from diffuse to specular, concealed around the corner, as well as hidden behind a diffuser [20]. Considering the references, it was found that industries were facing difficulties in the process of discovery, development and selection of aluminum alloys that consumed much expense and time so we found solving this problem was necessary.

2 Problem Description

Main objective of this paper is to concentrate on one of the key issues that industries face while producing aluminum parts with the necessary properties. Experimenting with and checking the properties of different aluminum alloys take a significant amount of time and resources. It wastes a lot of money and often produces no effects at all. When the available data are huge, the machine learning is the best option for the better predictions.

2.1 Material Selection

Aluminum has been used to produce vehicles for well over a hundred years. Aluminum is a metallic material. Aluminum mixes quickly to produce lightweight yet solid alloys. As aluminum composites are thin and lightweight, they absorb large amount of heat energy and easy to work. So, in this study, aluminum composites are considered for the research.

2.2 Material Properties

Tensile Strength. Among the mechanical properties of a material, the breaking load is identified as the highest load it can undergo without breaking. It is not possible to find a particular data on the breaking load of aluminum because it depends on the alloy to which it refers: It is equivalent to one third relative to the steel.

Yield Strength. One of the most significant mechanical properties is the yield power, which specifies the point after which a material deforms under the action of the load. In aluminum, the yield intensity is conventionally defined as the force that induces, in the stress/deformation curve, a divergence from the proportionality of 0.2% of the original length.

Density. Aluminum's density is special in a variety of ways, making it a common alternative for a variety of applications. Aluminum has a low density, making it light and simple to transport. As a result, it is the chosen metal for aircraft construction. The material is both lightweight and solid, as well as easy to form, making it an excellent choice for manufacturing.

Thermal conductivity. Aluminum has good thermal conductivity, and it is ideal for making utensils in large scale. Aluminum is a good conductor of heat and electricity so aluminum heat exchangers are used in food, chemical and aerospace industries. Thermal conductivity refers to the transfer of heat from one medium to another; for

example, heat exchangers made of aluminum are used in the chemical, food and aerospace industries.

2.3 Algorithm Selection

Machine learning is classified into Supervised and Unsupervised learning. Considering the Supervised learning it is categorized into: (i) Regression (E.g., Linear Regression and Random forest Regression) and (ii) Classifier (E.g., K-nearest neighbor and Decision Tree) which is shown in Fig. 1.

Linear Regression. It is used to measure real values (house prices, phone calls, overall sales and so on) using continuous variables (s). By fitting the best line, relationship between the input and output variables is created. The aim of regression is to look at two things such as possibility of predicting an outcome (output) variable using a set of input variables and the influence of input variables on the output variables. These regression estimates are used to describe how one dependent variable interacts with one or more independent variables.

Random Forest Regressor. An ensemble of decision trees is referred to as a random forest. In this, set of decision trees is called as forest. Each tree gives a classification to the new object and claiming the “votes” for that class from the tree. The classification with the maximum votes is chosen by the forest (over all the trees in the forest). Random forests, in general, yield better outcomes, perform well on large datasets and can work with missing data by generating estimates. It does, however, face a significant challenge in that they are unable to extrapolate data from unknown sources.

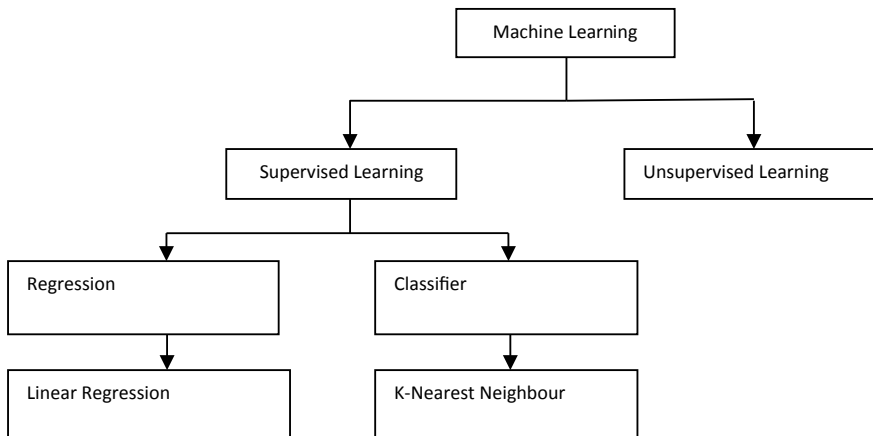


Fig. 1 Classification of machine learning

K-Nearest Neighbor. KNN is used for solving regression and classification problems. The KNN algorithm classifies the new cases based on average of K neighbors in case of regression and maximum occurrence in case of classification. Nearest neighbors are determined by distance function.

Decision Tree. Decision tree algorithm, which is a type of supervised learning, is used to create a model to predict the output variable by the decision rules from the training data. In decision tree algorithm, the model is in the form of tree-like structure which is used for decision-making.

3 Objectives

To overcome the above problem, the goals of this research are as follows:

- Accurately finding the composition of aluminum alloy using data analysis techniques.
- Use a data analysis technique to minimize the expense of the experiment.
- To reduce experimentation time by using a data analysis technique.

4 Methodology

4.1 Processing of Data

The process of transforming unsuitable data into desired form to get useful information out of it. The important phase in machine learning is data processing as the output of a data analysis model is dependent on processing of data. Processing of data includes two steps: selection of data and feature engineering.

Selection of data. A total of 129 datasets were collected from mat match for this analysis, which include various compositions of aluminum alloys containing mechanical properties like strength of material, thermal conductivity and density of aluminum composites, as in Tables 1 and 2.

Feature Engineering. The process of extracting the appropriate characteristics for target prediction. Different mechanical properties of aluminum alloy are used as features in this to predict aluminum composites. The features can be utilized to enhance the accuracy of machine learning algorithms.

Table 1 Aluminum alloys composition

Sl no.	Al (%)	Fe (%)	Mn (%)	Others (%)
1	95.7	0.7	1.5	2.1
2	96.1	0.7	0.8	2.4
3	96.1	0.7	0.8	2.4
.
.
127	95.85	0.7	1.5	1.95
128	95.85	0.7	1.5	1.95
129	83.05	0.2	0.6	16.15

Table 2 Mechanical properties of above aluminum alloy compositions

Sl no.	Tensile strength (MPa)	Yield strength (MPa)	Density (g/cc)	Thermal conductivity (W/m K)
1	235	160	2.72	190
2	150	40	2.71	190
3	255	185	2.71	190
.
.
127	240	185	2.72	200
128	180	80	2.72	200
129	400	350	2.7	160

4.2 Modeling

An algorithm is used to analyze the data after processing of data. The algorithm modeling involves selection of algorithm, training, testing and making predictions. For modeling the above data, four machine learning algorithms, like random forest regressor, linear regression, KNN and decision tree were chosen based on continuous and discrete data and predictions were made using Python.

4.3 Model Validation

To evaluate the performance and accuracy of developed model, validation is conducted. The original data are split into test set and training set in every data analysis technique. The training set of data is used to train the model, and the validation set of data is used to validate the model. The difference between the predicted values and actual values gives error of each data in different attributes. The model

is validated based on finding accuracy and random mean square error of data for different attributes on regression and classification models.

5 Results and Discussion

In this study, there are two regression (LR, RFR) and two classifier (KNN, DT) algorithms are selected, modeled and prediction made from the four algorithms are compared using accuracy and RMSE values for the different percentage of testing data.

In Fig. 2, the percentage of test date versus root-mean-square error (RMSE) is plotted for above four algorithms in prediction of aluminum composition. It is observed that, by comparing all the four algorithms predictions for the proportion of aluminum, random forest regression is giving better or less RMSE values for all percentage of training data. Next to the radom forest regression, linear regression is the second-best algorithm which gives better results compared to other two algorithms. Compared to classifier algorithms, the regression algorithms are able to produce better results in this prediction. It shows that the relation between input and output is linear and easily predictable.

In Fig. 3, the percentage of test date versus root-mean-square error (RMSE) for different algorithms is plotted while predicting the amount of iron present in the composition. It is observed that, by comparing all the four algorithms predictions for the proportion of iron, random forest regression is giving better or less RMSE values for all percentage of training data. Next to the random forest regression, linear regression is the second-best algorithm which gives better results compared to other two algorithms. Again, this proves that the regression algorithms are better compared to classifier algorithms and the linear relation between iron composition and the mechanical properties of the composites.

In Fig. 4, the percentage of test date versus root-mean-square error (RMSE) for different algorithms is plotted while predicting the amount of manganese present in the composition. It is observed that, by comparing all the four algorithms predictions

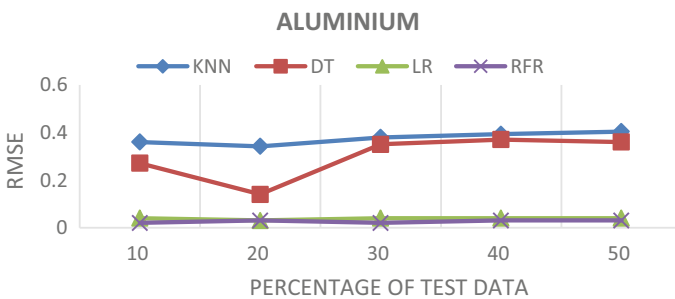


Fig. 2 Prediction of aluminum (Al) composition

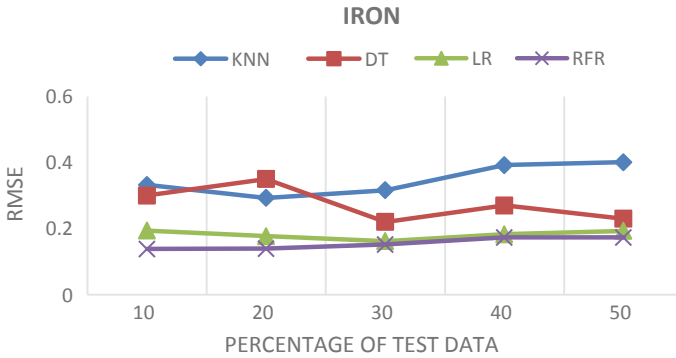


Fig. 3 Prediction of iron (Fe) composition

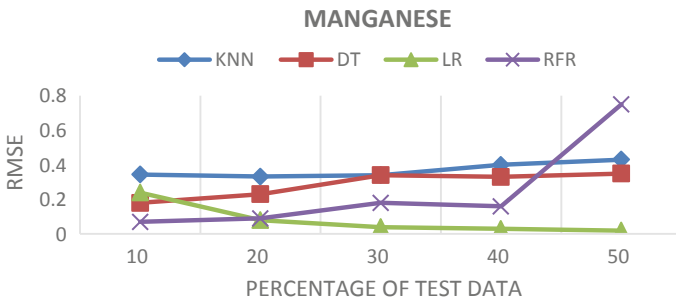


Fig. 4 Prediction of manganese (Mn) composition

for the proportion manganese, if the training data are more than 80%, random forest regression is having less error or better (less) RMSE value. If training data are less than 80%, linear regression is having less RMSE value.

In Fig. 5, the percentage of test date versus root-mean-square error (RMSE) for different algorithms is plotted while predicting the amount of other metals present in

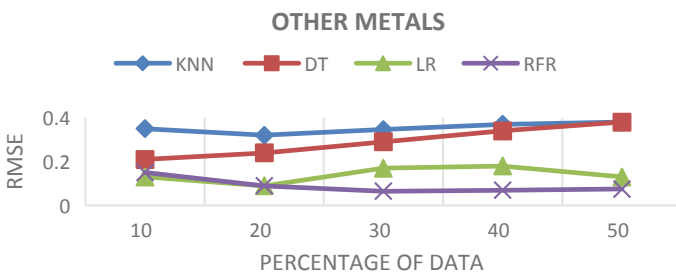


Fig. 5 Prediction of other metals in composition

the composition. It is observed that, by comparing all the four algorithms predictions for the proportion of other metals. If the training data are more than 80%, linear regression is having less error or better (less) RMSE value. If training data are less than 80%, the random forest regression is the best-chosen algorithm for the manganese prediction. In manganese prediction also, regressor is giving better results compared to classifier. The accuracy of all the algorithms is for the different output predictions that are given in Table 3. By comparing the accuracies of all algorithm, linear regression (LR) and random forest regression (RFR) are better than other two algorithms. So the actual versus predictions graphs are plotted for LR and RFR which is shown in Figs. 6, 7, 8 and 9.

It is observed from Figs. 6, 7, 8 and 9 that always random forest regression predictions are very closer to actual values compared to linear regression.

Table 3 Comparison of algorithms

Sl. No.	Algorithm	Accuracy (%)			
		Al	Fe	Mn	Others
1	KNN	65.38	61.53	57.69	65.38
2	DT	88.48	76.92	80.76	69.23
3	LR	99.98	99.59	96.18	99.02
4	RFR	99.99	99.64	98.92	99.19

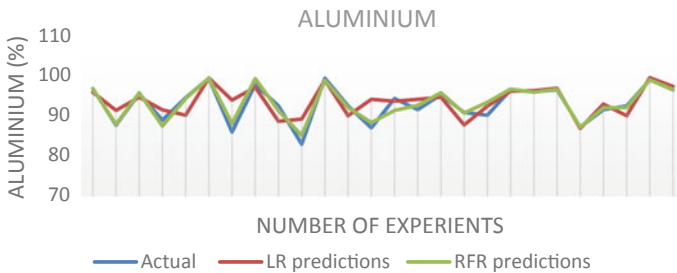


Fig. 6 Actual versus predictions for Al%

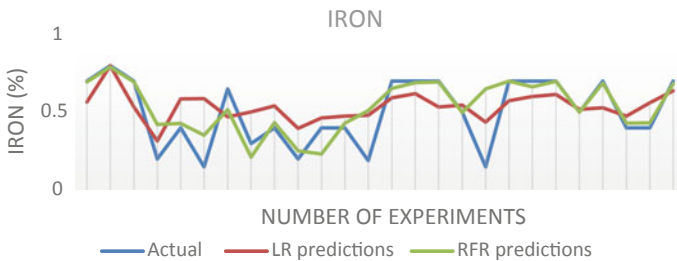


Fig. 7 Actual versus predictions for Fe%

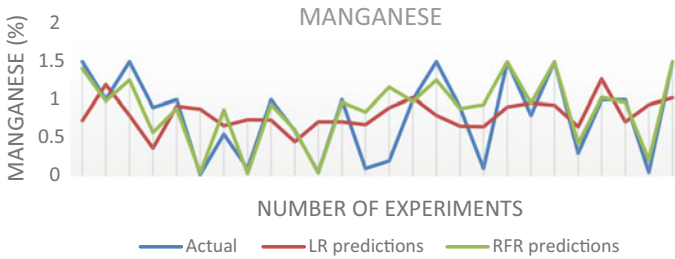


Fig. 8 Actual versus predictions for Mn%

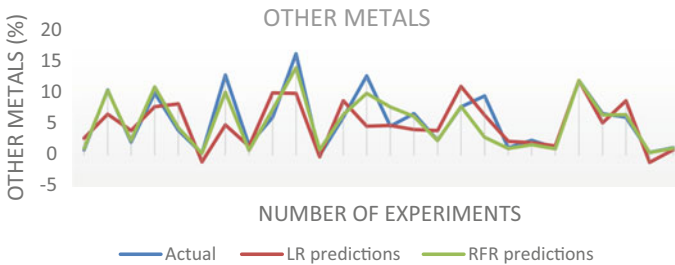


Fig. 9 Actual versus predictions for other metals %

6 Conclusion

In this study, there are two regression (LR, RFR) and two classifier (KNN, DT) algorithms selected, modeled and prediction made from the four algorithms are compared using accuracy and RMSE values for the different percentage of testing data. By comparing all the algorithms, regression algorithms are giving better results compared to classifier algorithms. On overall comparisons, random forest regression predictions are more accurate compared to all other algorithms. In aluminum composites research, this paper gives impact in the form of predicting the composition requirements for alloys without experimentation. It saves lot of energy and time for the manufacturing industries. Future work of this paper is to apply same methodology for the other composites for the predictions.

References

1. Wei J, Chu X, Sun X-Y, Kun Xu, Deng H-X, Chen J, Wei Z, Lei M (2019) Machine learning in materials science. *InfoMat*. 1:338–358
2. Rajiv Kumar A, Mishra PK (2020) An intelligent computing system to detect material. *Mater Today Proc*

3. Aruna Devi M, Prakash CPS, Chinnannavar RP, Joshi VP, Palada RS, Dixit R (2020) An informatic approach to predict the mechanical properties of aluminum alloys using machine learning techniques. In: International conference on smart electronics and communication (ICOSEC)
4. Lin YC, Zhang J, Zhong J (2008) Application of neural networks to predict the elevated temperature flow behavior of a low alloy steel. *Comput Mater Sci* 43(4):752–758
5. Titus Thankachana K, Prakash S, Pleass CD, Rammasamy D, Prabakar B, Jothi S (2017) Artificial neural network to predict the degraded mechanical properties of metallic materials due to the presence of hydrogen. *Int J Hydrogen Energy* 42(47):28612–28621
6. Metz L, Maheswaranathan N, Cheung B, Sohl-Dickstein J (2019) Meta-learning update rules for unsupervised representation learning. In: ICLR 2019 conference blind submission
7. Bobbili R, Ramakrishna B, Madhu V, Gogia AK (2015) Prediction of flow stress of 7017 aluminium alloy under high strain rate compression at elevated temperatures. *Defence Technol* 11(1):93–98
8. Wei J, Chu X, Sun X-Y, Xu K, Deng H-X, Chen J, Wei Z, Lei M (2019) Machine learning in materials science. *Wiley J InfoMat* 1:338–358
9. Palavar O, Ozyurek D, Kalyon A (2015) Artificial neural network prediction of aging effects on the wear behavior of IN706 super alloy. *Mater Design* 82:164–172
10. Kumar R, Pradeep Kumar M (2020) An intelligent computing system to detect material. *Mater Today Proc* 34(3):563–880
11. Frankle J, Carbin M (2019) The lottery ticket hypothesis: finding sparse, trainable neural networks
12. Mangalathu S, Jeon J-S (2020) Regional Seismic risk assessment of infrastructure systems through machine learning: active learning approach. *J Struct Eng* 146(12):1–11
13. Shabani MO, Mazahery A (2012) Optimization of process conditions in casting aluminium matrix composites via interconnection of artificial neurons and progressive solutions. *Ceram Int* 38(6):4541–4547
14. Xue D, Xue D, Yuan R, Zhou Y, Balachandran PV, Ding X, Sun J, Lookman T (2017) An informatics approach to transformation temperatures of NiTi based shape memory alloy. *Acta Mater* 125(47):532–541
15. Kessler T, Sacia ER, Bell AT, Hunter Mack J (2017) Artificial neural network based predictions of cetane number for furanic biofuel additives. *Fuel* 206:171–179
16. Krajewski S, Nowackin J (2014) Dual-phase steels microstructure and properties consideration based on artificial intelligence techniques. *Arch Civil Mech Eng* 14(2):278–286
17. Mangalathua S, Jeonb J-S (2018) Classification of failure mode and prediction of shear strength for reinforced concrete beam-column joints using machine learning techniques. *Eng Struct* 160:85–94
18. Khobragade S, Pakle GK (2014) A neural network based approach to predict machine status for big data using R. *Int J Curr Eng Technol* 5(4):2383–2389
19. Xue D, Xue D, Ruihaoyuan, Zhou Y, Prasanna V, Ding X, Juan L, Lookman T (2017) An informatics approach to transformation temperatures of NiTi-based shape memory alloys. *Acta Mater* 125(47):532–541
20. Xin S, Nousias S, Kutulakos KN, Sankaranarayanan AC, Narasimhan SG, Gkioulekas I (2019) A theory of ferret paths for non-line-of-sight shape reconstruction. In: 2019 IEEE/CVF conference on computer vision and pattern recognition (CVPR), pp 6793–6802

Chapter 30

Design of an Adaptive Fuzzy Logic Controller for Solar PV Application with High Step-Up DC–DC Converter



CH Hussaian Basha , P. Akram, M. Murali, T. Mariprasath, and T. Naresh

Abstract In this article, a fuzzy logic controller is developed for the proposed three-phase inverter system to extract the peak power of the solar panel-based generation system. Also, it is useful to maintain the constant grid voltage and frequency. The features of the two-leg three-phase inverter are fast controlling in action, wide-range input, and output operations. A slider controller functionally depended on a small signal model with a low-pass filter is connected to the coupled inductor boost converter (CIBC) to enhance the system dynamic response, infinite switching, and voltage gain at diverse solar irradiation conditions. An adaptive power point tracing controller is applied to the solar photovoltaic (PV)-fed boost converter system to track the peak power of the solar PV.

Keywords Duty cycle · Fuzzy logic · High-voltage gain boost converter · Slider controller · Two-leg inverter

1 Introduction

From the last few years, the usage of renewable sources is increased to a greater extent level. Amidst the availability of many renewable sources, PV energy is the predominant natural source of energy and it is converted to electrical energy with the help of the photovoltaic effect [1]. The features of PV systems are less environmental pollution and excess availability in nature. The disadvantages of photovoltaic are high installation cost and less efficiency. However, the PV cost is limited by using different manufacturing semiconductor technologies [2, 3].

The classifications of semiconductor technologies are monocrystalline, polycrystalline, and thin-film technologies. The mono- and polycrystalline PV cells are designed by applying a microelectronic method, and thin-film-based PV cells are implemented by using CdTe, a-Si materials. From [4], thin-film technologies give high efficiency when compared to mono- and poly cell technologies. The voltage output of the single PV cell is 0.7 V which is insufficient for the consumer power

CH Hussaian Basha (✉) · P. Akram · M. Murali · T. Mariprasath · T. Naresh
Department of EEE, K.S.R.M. College of Engineering, Kadapa, India

demand. To supply the power demand of consumers, the PV cells are connected in parallel and series to improve the power supply of the solar PV system. The series interconnection of PV cells improves the profile of operating voltage of the PV system, and parallel connection improves the operating current of solar PV [5].

From the literature survey, some of the researchers are focusing on single-diode circuit-based PV cells to design the solar PV module, and the remaining are focusing on solar PV cells which are double-diode circuit-based. In [6], the comparative analysis of single-diode circuit PV cell and double-diode circuit PV cell technologies have been carried in terms of maximum power extraction, efficiency, and fill factor. From the simulative performance analysis, the authors say that the double-diode circuited PV cell technology gives good performance when matched to the single-diode circuit-type PV cell. Here, in this article, a double-diode-based PV cell technology is proposed to obtain the peak power of the solar PV panel.

From the literature survey, solar PV power is used in many industrial usages listed as automotive, hybrid electric vehicles, batteries headlamps, and fuel cells. The utilization of PV power has been increased by interfacing a wide input operation-based DC–DC converter and it is a challenging task in hybrid power generation and distribution systems [7–9]. At present, most of the PV power is used in urban areas and it is a quick-rising path due to the lack of firewood power. The per-unit electricity generation cost of the solar systems is very high and it is reduced by improving the fill factor and continuous peak power extraction from the solar PV cell.

The DC–DC converters are classified as isolated and non-isolated converters. The isolated DC-to-DC converters output voltage and supply power is increased by improving the turns ratio of the transformer inductors. In addition to that, it is useful for high-switching-power applications. But, it has a drawback of high design cost and high implementation complexity [10]. The drawbacks of the isolated converters are overcome by using a non-isolated DC-to-DC converter.

The most popular non-isolated DC-to-DC converter is the conventional boost converter. The advantages of a basic boost converter are ease in designing, less cost in implementation, and high robustness. But, it has the drawbacks of less static voltage gain and less overcurrent protection. The single-ended primary inductance converter is used in the [11] to improve the performance of the solar PV modules. But, it does not consist of any external short-circuit current protection.

To seize the limitations of the above-explained conventional DC–DC converters, a single-switch inductor-coupled boost converter is proposed to step up the voltage output of solar PV in this article. The voltage gain of the proposed boost converter is very high. Here, the voltage improving is mainly depending on the coupled inductor turns ratio. The solar PV system I–V and PV characteristics are nonlinear behaviour in addition to that its operating point is varied continuously at drive's atmospheric temperature conditions.

In the process of extracting the maximum power from the solar PV, an MPPT process is used to find out the peak position of the operating point as shown in Fig. 1. From the literature review, different types of MPPT techniques are used to trace the maximum power deliver position which is classified as conventional, meta-heuristic, and soft computing tracing techniques [12]. The most popular conventional and

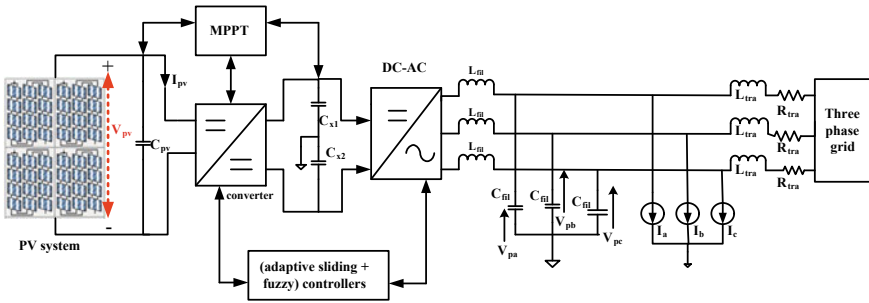


Fig. 1 Block diagram of PV-fed high-voltage gain boost converter with three-phase inverter

commonly used peak power point tracking technique is Perturb & Observe (P&O). In this P&O method, the PV power is varied continuous along with the corresponding voltage. If the variation of power gives a positive sign, then it perturbs the positive direction. Otherwise, it starts to vary negatively [13]. But, it has a drawback of high power losses at the time of perturbation. An incremental conductance (IC)-based power point tracking technique is used in the [14] to trace the MPP at adverse atmospheric temperature conditions. Here, the variation of PV current along with the corresponding voltage is observed. When the variation of inductance gives a positive sign, then the inductance of PV starts to vary in the same direction, or else, it varies in an opposite direction. However, it has a drawback of high complexity in implementation.

In [15], the state flow power point tracing controller is used to overcome the drawbacks of HC and IC MPPT techniques. The advantages of the state flow controller are stress-free to design, minimal steady-state oscillations, and good accuracy in MPP tracing. But, it gives the dithering effect. These results to noise problems in the overall system. The disadvantages of all conventional peak power point tracking techniques are mitigated by using an adaptive MPPT technique.

From the literature review, the diverse pulse width modulation techniques helps in the generation of switching pulses to the PV-fed three-phase inverter system. The most popular pulse width modulation technique is sine pulse width modulation. The advantages of this technique are fewer switching losses and give high constant output voltage to the grid. In [16], the space vector pulse width modulation method is applied to gives the switching pulses to the hybrid PV systems. The advantages of this method are minimal inverter output voltage ripples, fast controlling action, and good modulation index.

From the literature review, artificial intelligence techniques are used for computational system design and nonlinear problem-solving applications. The attractive features of artificial neural network techniques are easy to understand and less complex to implement. In [17], a neural network-based pulse width modulator is applied to the PV-fed grid-connected network to eliminate the lower-order harmonics of the inverter phase voltages. The only drawback of a neural network controller is

that it needed a high-knowledge person to train the complex networks. In this article, a fuzzy controller is implemented to generate the switching pulses to the inverter.

2 Double-Diode Model-Based PV Cell

The parameters required for the designing of a double-diode PV cell are seven which are classified as open-circuit voltage ($V_{oc} = 497.8$ V), peak-to-peak voltage ($V_{MPP} = 402$ V), short-circuit current ($I_{sc} = 14.15$ A), peak-to-peak current ($I_{MPP} = 12.05$ A), series resistance ($R_{sc} = 0.278$ Ω), parallel resistance ($R_{sh} = 86.83$ Ω), and two diodes ideality factors (a_x , and a_y) [18]. At different lower irradiances and temperature conditions, the double-diode PV cell gives accurate current versus voltage characteristics. In addition to that, it gives high efficiency when compared to the other PV cell technologies.

3 Design and Analysis of High-Voltage Gain Boost Converter

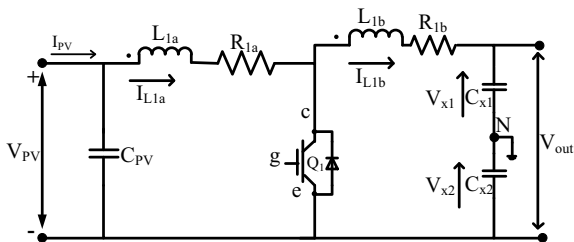
From the literature review [19, 20], there are different types of inductor-coupled boost converters that are employed to boost the PV output voltage to supply the consumer power requirements. The coupled inductor concept is the upcoming method for many industrial and non-industrial applications which are central processing units and signal development.

In [21], a modified three winding integrated coupled inductor topology is designed to obtain the maximum PV module voltage. Here, by the integration of inductors, the converter gives continuous input current with less ripple. Also, the leakage inductor stored is restored by using a passive voltage clamping circuit. Also, the clamping circuit reduces the voltage strain across the switch. This results in the reduction of the switch conduction losses extensively. But, it has a drawback of high complexity in design, excessive design cost, and high current stress.

Here, a single-switch high step-up DC–DC converter is designed to limit the above-coupled inductors converters' drawbacks. This proposed converter gives good static and dynamic responses at different atmospheric temperatures and irradiation conditions. The block diagram of the designed step-up converter is shown in Fig. 2. From Fig. 2, switch (Q_1) is used for high-power solar PV application and a diode is applied to limit the reverse recovery voltage of the supply. The advantages of the proposed converter are highly robust, less electromagnetic interference, less design cost, and lower switching and conduction losses.

A. Small signal-based sliding controller

Fig. 2 Block diagram of single-switch high-voltage gain boost converter



From the literature review [22], the sensing of all state variables in the basic boost converter is not mandatory for the generation of optimum switching pulses. Generally, the error and variations in error values are measured and applied to the MPPT controller. The output signal of the MPPT controller is connected to the converter switch to obtain the constant output voltage and current of the load. The input side boost converter design resistances are ($R_{1a} = 0.244 \Omega$), and ($R_{1b} = 0.07 \Omega$). Similarly, the capacitors and inductors are $C_{dy} = 0.01$ F, $C_{PV} = 0.122$ F, $L_{1b} = 0.0144$ H, and $L_{1a} = 15.60$ mH, respectively. Here, in this work, a low-pass circuit-based sliding method is designed to control the nonlinear behaviour of the DC–DC converter. Also, it provides the converter to work at wide input–output operation.

B. An adaptive power point tracing method

The main drawback of solar power generation is nonlinear power versus voltage characteristics. To solve the nonlinear behaviour, in this work, an adaptive power point tracing method is proposed. This method is majorly utilized in tracing the rapid changes of solar insolation conditions. Also, this method is used for lower-order harmonic reduction purposes.

The interconnection of integrator and low-pass filter is the optimum solution for the reduction of high-frequency-based noise components in the multidimensional wave. Here, the gradient value is obtained based on the dimension of the signal. From the MPPT method, the resultant error signal is summed with the sine signal to trace out the peak power point. The main goal of an adaptive controller is to obtain the peak power from the converter output DC link. The peak voltage of the solar PV is given to the MPPT controller to find out the PV sliding surface and it is added to the constant of the sliding controller. The continuous variation of PV voltage and current is supplied to the sliding controller to obtain the regulated peak voltage and current.

4 Operation of a Two-Leg Three-Phase Inverter

From the literature review, different types of inverters are used to convert DC to AC. In [23], the conventional three-leg three-phase inverter is used in PV-fed water pumping applications. The attractive feature of this inverter, when compared with the

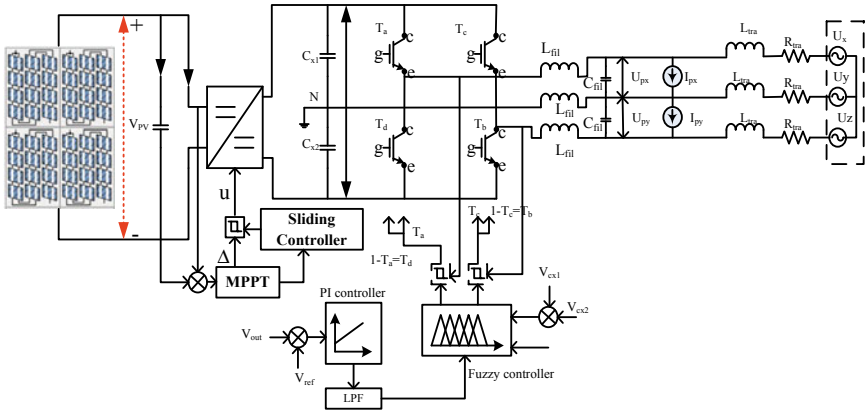


Fig. 3 Schematic diagram of the two-leg three-phase conversion system

single-phase inverter, is less power-to-weight ratio and it is used for high-power-rated applications. However, it has a limitation of high switching ripples in the inverter output voltage. In addition to that, if any one of the legs fails in the bridge-type three-phase inverter then the entire supply to the load is getting shut down.

Here, a two-leg bridge-type inverter is used to convert the PV output to the grid as shown in Fig. 3. In this inverter, the selected DC-link capacitor values are maintained constant to obtain the balanced neutral point. The grid line voltages are U_j and U_k . The root mean square of the line voltage is U . Similarly, the currents are indicated as I_j and I_k . The attractive features of this inverter are minimum lower-order ripples and sinusoidal output voltage. Also, it supplies the power with less number of power semiconductor switches. The mathematical modelling of the inverter system is followed as,

$$\frac{dI_j}{dt} = \frac{2}{3L_{tra}}(U_j - 2R_{tra}I_j - V_{pj} - I_k R_{tra}) - I_F \tag{1}$$

$$I_F = \frac{1}{3L_{tra}}(U_k - 2R_{tra}I_k - V_{pk} - I_j R_{tra}) \tag{2}$$

$$\frac{dI_{inaj}}{dt} = \frac{1}{C_{fill}}(I_j + I_{inaj} - I_{pj}) \tag{3}$$

$$\frac{dV_{cx1}}{dt} = \frac{-1}{C_{x1}}(U_{sx} I_{ina} + U_{sy} I_{inb}) + \frac{I_{mag}(1-u)}{C_{x1}(1+N)} \tag{4}$$

$$\frac{dV_{cx2}}{dt} = \frac{1}{C_{x2}}((1 - U_{sa})I_{ina} + (1 - U_{sb})I_{inb}) + \frac{I_{mag}(1-u)}{C_{x2}(1+N)} \tag{5}$$

In [24], a sliding-based controller is applied to produce the appropriate switching pulses to inverting device. But, it requires several sensing devices to sense the

converter and inverter variables. It results in an excessive increment of overall system implementation. Also, its size is very high. In [25], an artificial neural network is designed for the optimization of the size of a hybrid power generation system. The merits of the ANN are high nonlinear behaviour handling capability, easy implementation, and understanding. But, it requires highly trained data to give the pulses to the network. Also, it requires high training time when the network is having multiple layers. Here, a fuzzy logic controller is designed to generate the switching signals to the PV-based inverter system. The switching behaviour of the inverter is shown in Table 1.

The fuzzy system has three operations which are fuzzification, inference, and finally defuzzification. The fuzzification concept is useful for transferring real parameters into linguistic variables, and the inference controller is applied for controlling the surface-related issues. The rules of the proposed fuzzy logic controller and its working behaviour for generating the switching signals are shown in Fig. 4. The final process in the fuzzy logic controller is defuzzification which is applied to transfer the linguistic variables to real functions.

Table 1 Operation of PV-fed three-phase inverter system

Nodes	Switching condition					Inverter o/p voltage		
	y	T_a	T_b	T_c	T_d	V_{in_x}	V_{in_y}	V_{in_z}
0	0	0	1	0	1	$-V_{out}/3$	$-V_{out}/3$	$2V_{out}/3$
1	0	1	1	0	0	V_{out}	$-V_{out}$	0
0	1	0	0	1	1	$-V_{out}$	V_{out}	0
1	1	1	0	1	0	$V_{out}/3$	$V_{out}/3$	$-2V_{out}/3$

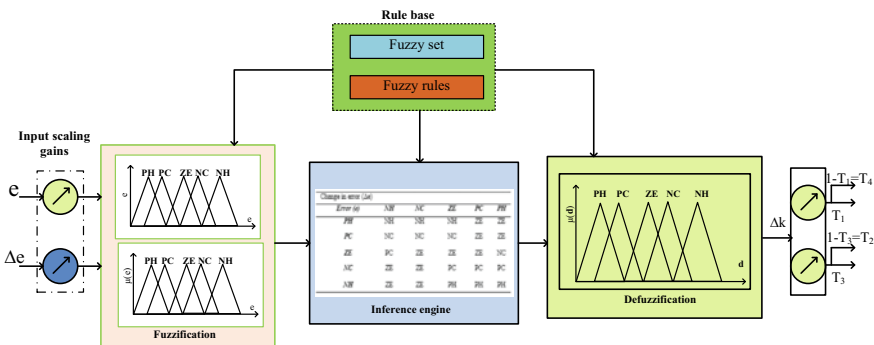


Fig. 4 Fuzzy logic-based switching pulse generation

5 Simulation Results and Discussion

From Section II, the PV module is designed by using a two diode circuit topology which has nonlinear I–V and power versus voltage characteristics. From the nonlinear curves, it is keenly observed that the peak voltage, peak current, and peak power of the PV at 1000 W/m^2 are 415.0 V, 23.33 A, and 9.68 kW. Similarly, the maximum voltage, current, and power of the PV module at 800 W/m^2 are 406.0 V, 16.82 A, and 6.828 W, respectively. Finally, at 500 W/m^2 , the corresponding voltage, current, and power of PV are 402.0 V, 12.89 A, and 5.18 W, respectively.

At diverse irradiation conditions, the PV module output power is displayed in Fig. 5. From Fig. 5, the PV power is increased linearly up to the time duration of 0.2 s. After that, it is constant at 1000 W/m^2 . The constant time period of the power at 1000 W/m^2 is 4 s. When the irradianations step down from 1000 to 750 W/m^2 , the PV output power starts decreasing up to the time period of 0.3 s. After that, it has been constant and it is equal to 6.12 kW. Finally, at 500 W/m^2 , the power generated by the solar PV is 4.9 kW.

Figure 6 shows that the high step-up DC–DC converter gives constant output voltage with fewer distortions. From that, the adaptive power point tracing controller tracks the peak operating point of the solar PV with high accuracy. At the origin point, the converter gives small fluctuations in the voltage; after that, it is reduced by using the low-pass filter.

Similarly, the single-switch DC–DC converter DC-link voltages are given in Fig. 7. Figure 7 shows that the two DC capacitor voltages are the same and are equal to 600 V. Also, these voltages are distorted at diverse atmospheric conditions.

The three-phase balanced currents are obtained from the two-leg inverter which is shown in Fig. 8. At 1000 W/m^2 , the grid is equal to the 13 A. After that, it is reduced to 10 A at 750 W/m^2 . Finally, at 500 W/m^2 , the current is stepped down to 7.5A. The inverter output voltages are given to the grid by using a L_{fil} C_{fil} filter and which are given in Fig. 9. From Fig. 9, at 1000, 750, and 500 W/m^2 , the per-unit three-phase

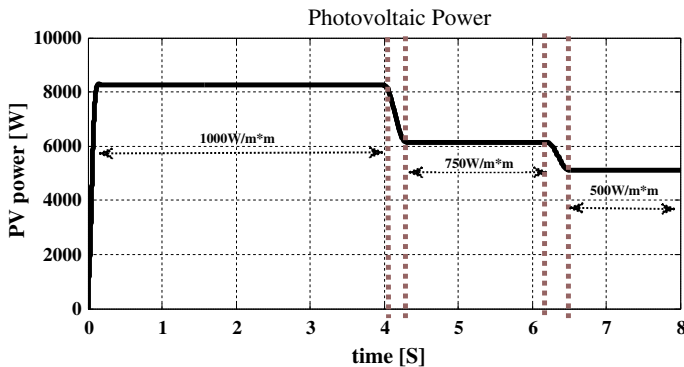


Fig. 5 PV Module output power at diverse irradianations

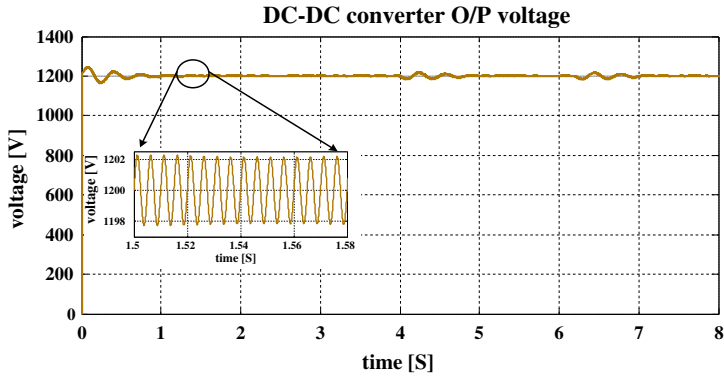


Fig. 6 Output voltage of single-switch non-isolated boost converter

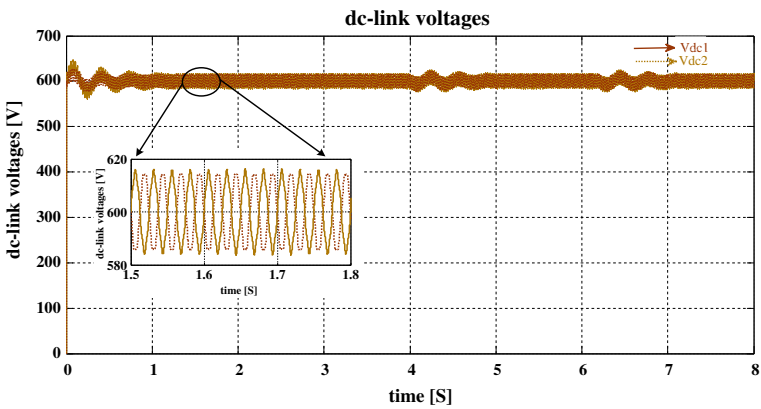


Fig. 7 DC-link voltages of coupled inductor-based high step-up boost converter

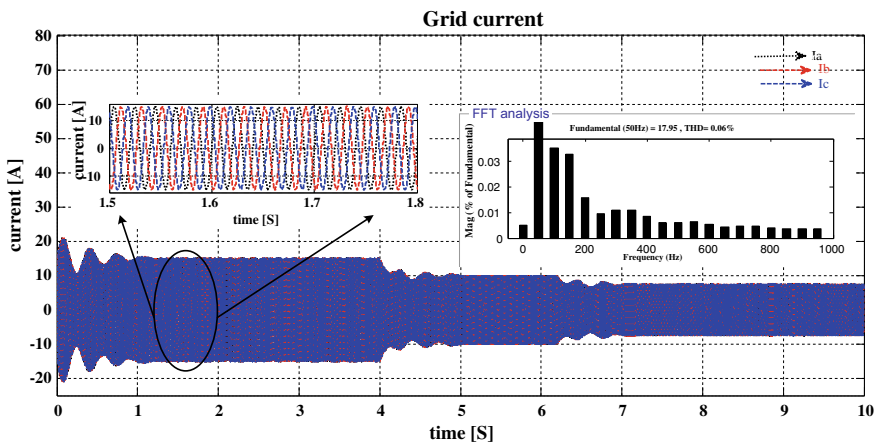


Fig. 8 Non-isolated three-phase currents at diverse irradiation conditions

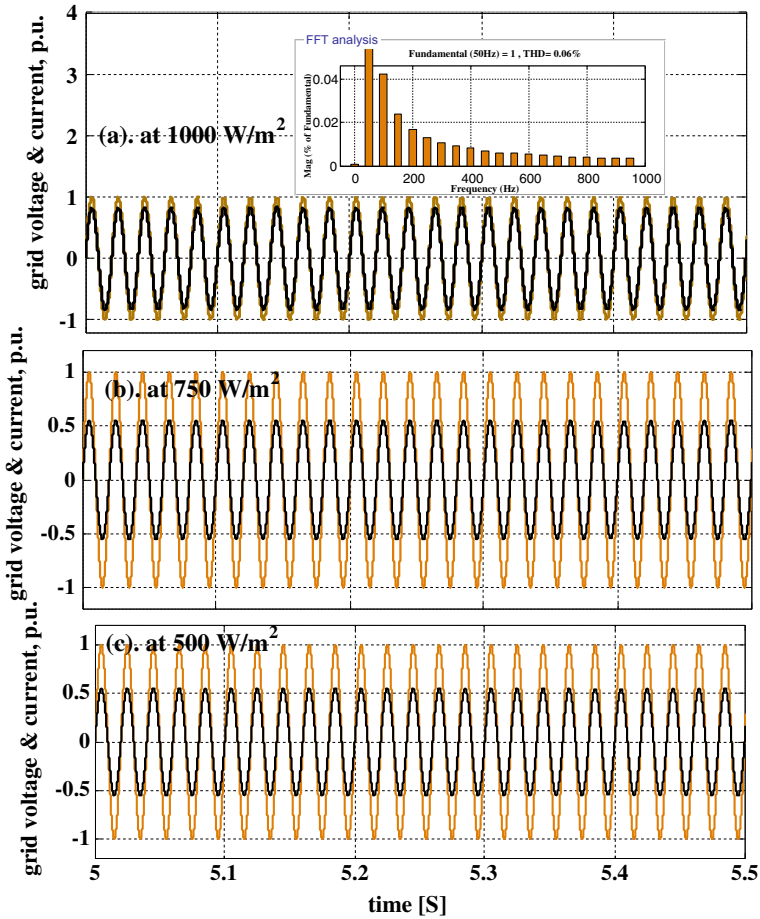


Fig. 9 Per-unit three-phase grid voltages at 1000, 750, and 500 W/m²

grid voltages are the same and it is equal to one. Similarly, the per-unit grid currents are 0.85, 0.7, and 0.5, respectively.

6 Conclusion

The PV-connected high step-up boost converter grid-connected system is simulated successfully by using MATLAB/Simulink window. From the simulation results, the converter is giving high-voltage conversion, less voltage stress on power switching devices, and continuous output voltage. The boost converter optimum duty value is obtained by using an adaptive power point tracing controller. Also, the proposed

MPPT technique advantages are high accuracy, lower steady-state oscillations, high efficiency, and fast tracing speed. The two-leg inverter circuit is connected to the PV-fed coupled inductor DC–DC converter to supply three-phase power to the load. The fuzzy logic controller is giving the optimum switching pulses to the inverter. These result in the reduction of the entire system size and complexity.

Acknowledgements We would like to thank the management of K.S.R.M. College of Engineering (Autonomous) for providing the facilities for the research.

ORCID: *Chakarajamula Hussaian Basha*, <https://orcid.org/0000-0002-9858-8353>

References

1. Yan J et al (2020) Parametric life cycle assessment for distributed combined cooling, heating and power integrated with solar energy and energy storage. *J Cleaner Prod* 250:119483
2. Basha CH, Rani C (2020) Different conventional and soft computing MPPT techniques for solar PV systems with high step-up boost converters: a comprehensive analysis. *Energies* 13(2):371
3. Mohammed SS, Devaraj D, Imthias Ahamed TP (2021) Learning automata and soft computing techniques based maximum power point tracking for solar PV systems. *Intelligent paradigms for smart grid and renewable energy systems*. Springer, Singapore, pp 227–262
4. Basha CHH et al (2020) Development of Cuckoo search MPPT algorithm for partially shaded solar PV SEPIC converter. *Soft computing for problem solving*. Springer, Singapore, pp 727–736
5. Wagner L et al (2020) Integrated series/parallel connection for photovoltaic laser power converters with optimized current matching. *Progress in photovoltaics: research and applications*
6. Cavalcanti MC et al (2020) Hybrid maximum power point tracking technique for PV modules based on a double-diode model. *IEEE transactions on industrial electronics*
7. Basha CHH, Rani C, Odofin S (2017) A review on non-isolated inductor coupled DC-DC converter for photovoltaic grid-connected applications. *Int J Renew Energy Res (IJRER)* 7.4:1570–1585
8. Basha CHH, Rani C, Odofin S (2018) Analysis and comparison of SEPIC, landsman and zeta converters for PV fed induction motor drive applications. In: 2018 international conference on computation of power, energy, information and communication (ICCPEIC). IEEE
9. Basha CHH, Rani C (2020) Performance analysis of MPPT techniques for dynamic irradiation condition of solar PV. *Int J Fuzzy Syst* 22.8:2577–2598
10. Basha CHH et al (2019) Design of an LPF based slider controller for THD reduction in solar PV B-4 inverter. In: 2019 IEEE international conference on electrical, computer and communication technologies (ICECCT). IEEE
11. Sankar VU et al (2020) Application of WDO for decision-making in combined economic and emission dispatch problem. *Soft computing for problem solving*. Springer, Singapore, pp 907–923
12. Sankar VU et al (2020) Application of wind-driven optimization for decision-making in economic dispatch problem. *Soft computing for problem solving*. Springer, Singapore, pp 925–940
13. Salman S, Xin AI, Zhouyang WU (2018) Design of a P-&-O algorithm based MPPT charge controller for a stand-alone 200W PV system. *Prot Control Mod Power Syst* 3.1:1–8
14. Harrag A, Messalti S (2019) IC-based variable step size neuro-fuzzy MPPT Improving PV system performances. *Energy Procedia* 157:362–374

15. Maher RA et al (2019) High performance state-flow based MPPT technique for micro WECS. *IET Renew Power Gener* 13.16:3009–3021
16. Ronanki D, Williamson SS (2018) A simplified space vector pulse width modulation implementation in modular multilevel converters for electric ship propulsion systems. *IEEE Trans Transp Electrification* 5(1):335–342
17. Messalti S, Harrag A, Loukriz A (2017) A new variable step size neural networks MPPT controller: Review, simulation and hardware implementation. *Renew Sustain Energy Rev* 68:221–233
18. Basha CH, Rani C (2020) Design and analysis of transformerless, high step-up, boost DC-DC converter with an improved VSS-RBFA based MPPT controller. *Int Trans Electrical Energy Syst* 30.12:e12633
19. Chowdary VG et al (2020) Hybrid fuzzy logic-based MPPT for wind energy conversion system. *Soft computing for problem solving*. Springer, Singapore, pp 951–968
20. Basha CHH et al (2020) Simulation of metaheuristic intelligence MPPT techniques for solar PV under partial shading condition. *Soft computing for problem solving*. Springer, Singapore, pp 773–785
21. Bindhu V (2020) Constraints mitigation in cognitive radio networks using cloud computing. *J Trends Comput Sci Smart Technol (TCSST)* 2(01):1–14
22. Raj JS (2020) Machine learning implementation in cognitive radio networks with game-theory technique. *J IRO J Sustain Wireless Syst* 2:68–75
23. Basha CHH, Rani C, Odofin S (2018) Design and switching loss calculation of single leg 3-level 3-phase VSI. In: 2018 international conference on computation of power, energy, information and communication (ICCPEIC). IEEE
24. Khan IU et al (2021) Neuro-adaptive backstepping integral sliding mode control design for nonlinear wind energy conversion system. *Turkish J Electr Eng Comput Sci* 29.2:531–547
25. Ali MN et al (2021) Promising MPPT methods combining metaheuristic, fuzzy-logic and ANN techniques for grid-connected photovoltaic. *Sensors* 21.4:1244

Chapter 31

Nonlinear Thermal Instability of Couple-Stress Fluids in Porous Media Under Thermal Modulation



S. H. Manjula and Palle Kiran

Abstract Temperature modulation effect on chaotic convection in a porous media saturated with couple stress fluid has been investigated. Three different profiles of thermal modulations, OPM (out of phase modulation), LBMO (lower boundary modulation), IPM (in phase modulation) have been investigated. The Darcy-Brinkman model has been employed for the porous media. The transition from stable mode to the unstable mode in terms of chaos analyzed with modulation and couple stress parameter. Lorenz system of equations Lorenz (Deterministic non-periodic flow in J Atmos Sci 20:130–142 1963 [1]) derived based on the critical Rayleigh number and initial conditions. For choosing the suitable thresholds of the modulation parameters, one can easily control the nonlinear nature of the solutions. It is observed that thermal modulation can be applied to control the system in three different profiles than gravity modulation. For fixed values of R near the threshold of convection, whilst adjusting suitable ranges of modulation parameters, and couple stress parameters, one can control the chaos. It is clearly found that thermal modulation with couple stress parameter the periodic and non-periodic solutions are controlled. The heat transfer analysis has been quantified with couple stress parameter and modulation.

Keywords Chaotic convection · Couple-stress fluids · Modulation · Nonlinear theory

1 Introduction

Studies on chaotic convection with relation to different types of parameters like Rayleigh and Prandtl numbers largely investigated by the subsequent studies. Most of the chaotic convective models associated with the RBC area obtained in three-

S. H. Manjula (✉)

Division of Mathematics, Department of S&H, VFSTR, Guntur, AP 522213, India

P. Kiran

Chaitanya Bharathi Institute of Technology, Hyderabad 500075, India

e-mail: pallekiran_maths@cbit.ac.in

dimensional space (similar to Lorenz system [1]) arising from the truncation of the classical Darcy Bénard convection. Some applications of chaotic convection are production of crystals, oil reservoir modelling, and chemical process packed-bed filtration. Vadasz and Olek [2] study the transition from steady convection to chaos as a result of a subcritical Hopf bifurcation producing a solitary cycle that can be associated to a homoclinic explosion for low Prandtl range. Vadasz [3] study provides proof for the solitary limit cycle via native analytical data. Mahmud and Hashim [4] examined the effect of a magnetic field on chaotic convection in a fluid layer. They discovered that the shift from chaotic to steady convection occurs via a subcritical Hopf bifurcation, which results in a homoclinic explosion, which can be a limit cycle as the Hartman range increases. For the values that are moderate. They discovered that the shift from chaotic to steady convection occurs via a subcritical Hopf bifurcation, which results in a homoclinic explosion, which can be a limit cycle as the Hartman range increases. For moderate Prandtl values, the path to chaos is taken by a period-doubling sequence of bifurcations described by Vadasz and Olek [5]. Feki [6] proposed a simple adaptive controller to manage chaotic systems as an alternative. The controller's linear structure can be employed for chaos control.

Yau and Chen [7] discovered that the Lorenz model can be stabilized even in the presence of system external distraction. Sheu et al. [8] and Vadasz [9] have demonstrated that stress relaxation tends to expedite the development of chaos in non-Newtonian fluid conditions. Narayana et al. [10] examined heat and mass transmission using the truncated Fourier series approach. Chuanshi et al. [14] studied the bifurcations of Rayleigh Benard convection in a cylindrical container. Their findings indicate that the commencement of axisymmetric convection happens via a transcritical bifurcation. They also got two qualitatively distinct steady axisymmetric solutions. Magyari [16] examined the influence of feedback control on chaotic convection in a porous media with a moderate Prandtl number. In the presence of feedback control, the suppression or augmentation of chaotic convection is considered. Sheu et al. [18] present a study of chaotic convection in a porous media of Oldroydian-type fluids. The stress relaxation parameter has the tendency to hasten the emergence of chaos.

In addition to the convective model, the concept of modulation has been introduced by many authors. The temperature modulation by Venezian [14], Siddheshwar et al. [15], Bhadauria et al. [16], gravity modulation by Gresho and Sani [17] and Bhadauria et al. [18, 19], rotation modulation by Donnelly [20], Kiran et al. [21], and magnetic field modulation by Kiran et al [22] and Sharma et al. [23]. The majority of their research focuses on thermal convection in a fluid or porous medium. Their plan is to find an external regulator for the device in order to regulate instability and track heat mass transfer. But what happens when we apply these configurations to the problem of Lorenz system [1]. Looking into this kind of problems, the following studies are very few investigated external modulation on chaotic convection. Jawdat and Hashim [24] and Vadasz and Olek [2] analyzed the transition from steady motion to chaos is sudden and occur by a subcritical Hopf bifurcation producing a solitary limit cycle which may be associated with low Prandtl number. Mahmud et al. [25] investigated the effect of magnetic field on chaotic convection in a fluid layer. The centrifugal force effect on

chaos was given by Gupta et al. [26] without any modulation. They found that rotation has delayed in chaos and controls nonlinearity. It is also concluded there is a suitable range over Ta and R to reduce chaos in the system. Chaos phenomena and bifurcation analysis in terms of strong nonlinearities are investigated by Ming et al. [27]. The Runge-Kutta fourth-order method is used to investigate the transformation of airfoil motion from equilibrium, phase, and period-doubling bifurcations to chaos.

The above paragraph demonstrated that the earlier work on chaotic convection with different types of configurations and models to control the chaos. Till today, no data is found which describes the modulation effect on chaotic convection in porous layer saturated with couple-stress fluid. It is due to the studies of [28, 29] modulation effect on chaotic convection in a porous medium has been investigated. Their results found that scaled Rayleigh number control chaos in the presence modulation. The study of chaotic and oscillatory magneto-convection in a binary viscoelastic fluid under the effect of gravity modulation is investigated by Bhadauria et al. [30]. The study of heat mass transfer is discussed in terms of finite-amplitude through Nusselt and Sherwood numbers. It is found that chaos is controlled by suitably tuning of g-jitter amplitude and frequency. The effect of internal heating and thermal modulation effects on chaotic convection in a porous medium by Kiran et al. [31]. Looking into both the papers, three types of phase angle are discussed on chaotic convection. It is shown that irrespective of the value of R and initial conditions, OPM and LBMO have their effects on chaos. It can be observed there will be a nonperiodic solution for lower values of amplitude and frequency of modulation near to R for small variation in amplitude there will be periodic solutions that arise around two critical points. Recently, the effect of g-jitter on chaotic convection in a rotating fluid layer is given by Kiran [32]. The time-periodic gravitation force concerning small amplitude and high resonance being discussed on chaos.

Although the study of Moli et al. [33] is available and investigated g-jitter on chaotic convection with a low amplitude of modulation. But the study of thermal modulation on thermal instability of couple stress fluid-saturated porous media is not done. In their work, they have discussed the gravity modulation effect on chaotic convection. They found a suitable adjustment of the g-jitter parameter with a couple stress parameter to control chaos in the system. In the above literature, it is found that nowhere temperature modulation on chaotic convection is investigated due to its difficult nature and insufficient data. With this, we would like to investigate the effect of temperature modulation with couple stress parameters on chaotic convection. In this article, we consider three types of thermal modulations (OPM, LBMO, and IPM) on chaotic convection in the presence of a couple-stress parameter.

2 Governing Equations

Under Oberbeck approximations and Brinkman Darcy law the dimension less mathematical model (see in Fig. 1) which describes the problem are (for similar model see Moli et al. [33]):

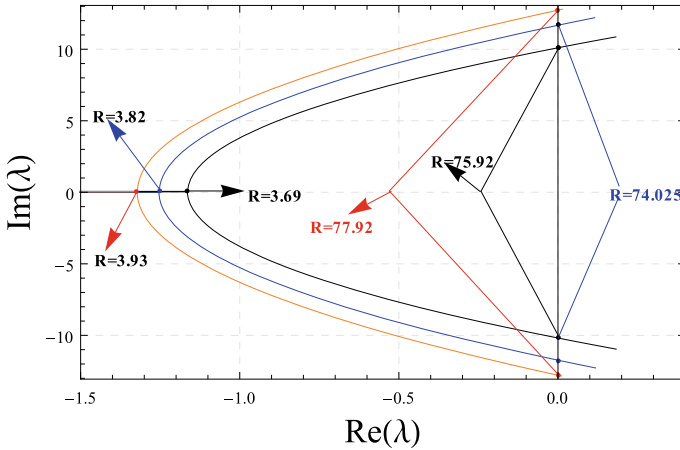


Fig. 1 The evolution of the complex eigenvalues as Rayleigh number increases

$$\left(\frac{1}{PrD} \frac{\partial}{\partial t} + (1 - C\nabla^2) \right) (\nabla^2 \psi) = RaD \frac{\partial T}{\partial x} \tag{1}$$

$$- \frac{\partial T_b}{\partial z} \frac{\partial \psi}{\partial x} + \left(\frac{\partial}{\partial t} - \nabla^2 \right) T = \frac{\partial(\psi, T)}{\partial(x, z)}, \tag{2}$$

where $RaD = \frac{\alpha_T g \Delta T K d}{\nu \kappa_T}$ is thermal Darcy-Rayleigh number, $\nu = \frac{\mu}{\rho_0}$ is kinematic viscosity, $PrD = \frac{\gamma \nu e d^2}{\kappa_T K}$ is the Darcy Prandtl number and $C = \frac{K \mu_c}{\mu d^2}$ couple stress parameter. The basic state solution which appears in Eq. (2), influences the stability problem through the factor $\frac{\partial T_b}{\partial z}$ which is given by

$$\frac{\partial T_b}{\partial z} = -1 + \delta_T (f_2(z, t)), \tag{3}$$

where

$$f_2(z, t) = \text{Re} (f(z) e^{(-i\Omega t)}), \tag{4}$$

$$f(z) = (A(\zeta) e^{\zeta z} + A(-\zeta) e^{-\zeta z}), \quad A(\zeta) = \frac{\zeta (e^{-i\phi} - e^{-\zeta})}{2 (e^\zeta - e^{-\zeta})} \quad \& \quad \zeta = (1 - i) \sqrt{\frac{\Omega}{2}}. \tag{5}$$

These are the governing equations of the flow of Darcy convection in an horizontal porous layer saturated with couple stress fluid. The layer was vibrated up and down. To obtain the solution of Eqs. (1) and (2), we assume the following Fourier series (given in [2, 12, 28]):

$$\psi = A_{11}(\tau) \sin\left(\frac{\pi x}{L}\right) \sin(\pi z) \tag{6}$$

$$T = T_b + B_{11}(\tau) \cos\left(\frac{\pi x}{L}\right) \sin(\pi z) + B_{02}(\tau) \sin(2\pi z), \tag{7}$$

here $A_{11}(\tau)$, $B_{11}(\tau)$, $B_{02}(\tau)$ are the functions of time τ . Substitute Eqs. (6) and (7) in Eqs. (1) and (2), Taking into account the orthogonality condition with eigen functions Eqs. (6) and (7), and integrate through the different domain yields with the set of 3 differential equations:

$$\frac{dA_{11}(\tau)}{d\tau} = -\text{Pr} \left[\left(1 + C \frac{\pi^2}{\gamma} \right) A_{11} + \frac{\text{RaD}}{\pi\theta} B_{11} \right], \tag{8}$$

$$\frac{dB_{11}(\tau)}{d\tau} = - \left[A_{11} \frac{1}{\pi\theta} (1 + \delta I_1) + \frac{1}{\theta} A_{11} B_{02} + B_{11} \right], \tag{9}$$

$$\frac{dB_{02}(\tau)}{d\tau} = \frac{1}{2\theta} A_{11} B_{11} - 4\gamma B_{02}, \tag{10}$$

The following notations are introduced $\tau = \frac{(L^2+1)\pi^2}{L^2} t$, $\theta = \frac{(L^2+1)}{L}$, $\gamma = \frac{L}{\theta}$, $I_1 = \int_0^1 \sin^2(\pi z) f_2 dz$ and $\Omega_T = \frac{L^2}{(L^2+1)\pi^2} \Omega$. It is convenient to introduce the following further notations: $R = \frac{\text{RaD}}{\pi^2\theta^2}$, $\text{Pr} = \frac{\text{Pr}_D\gamma}{\pi^2}$ and $\frac{\partial}{\partial t} = \frac{\pi^2}{\gamma} \frac{\partial}{\partial \tau}$. Now introducing the following further notations for convenience: $X = -\frac{A_{11}}{2\theta\sqrt{2\gamma(R-1)}}$, $Y = \frac{\pi R B_{11}}{2\sqrt{2\gamma(R-1)}}$, and $Z = -\frac{\pi R B_{02}}{(R-1)}$, to get the following set of scaled equations which are equivalent to Eqs. (8)–(10):

$$\frac{dX}{d\tau} = \text{Pr} \left(Y - \left(1 + C \frac{\pi^2}{\gamma} \right) X \right), \tag{11}$$

$$\frac{dY}{d\tau} = R(1 + \delta_T I_1) X - Y - (R - 1) X Z, \tag{12}$$

$$\frac{dZ}{d\tau} = 4\gamma (X Y - Z). \tag{13}$$

Equations (11)–(13) are equivalent to Lorenz equations [4] with $C=0$ and unmodulated case. The results for $\delta_T = 0$ and $C = 0$ presented in [29], which is a special case Eqs. (11)–(13). According to [28], the fixed points for motionless $(X_1, Y_1, Z_1) = (0, 0, 0)$, and $(X_{2,3}, Y_{2,3}, Z_{2,3}) = [\pm\sqrt{\frac{Z}{c}}, \pm c\sqrt{\frac{Z}{c}}, \frac{(R I_1 - c)}{(R-1)^2}]$, corresponding to convection solution. The critical R , where the unstable solution takes over, is obtained as $R_{cr} = \frac{c}{I_1}$, which is corresponding to $Ra = 4\pi^2 \frac{c}{I_1}$ where $c = \left(1 + C \frac{\pi^2}{\gamma} \right)$ and $I_1 = \int_0^1 \sin^2(\pi z) f_2 dz$. This pair points are stable if $R < \sqrt{\frac{Z}{c}}$, beyond this periodic, quasi-periodic, or chaotic solutions takes over at $R > \sqrt{\frac{Z}{c}}$. Instability nature, of motionless solution $(X_1, Y_1, Z_1) = (0, 0, 0)$, is controlled by the following:

$$\lambda^2 + (1 + PrDc)\lambda + PrD(C - R(1 + \delta_T I_1)) = 0. \tag{14}$$

The first eigenvalue of Eq. (14), $\lambda_1 = -4\gamma$ is always negative. The other two eigenvalues are $\lambda_{2,3} = \frac{-(1+cPrD) \pm \sqrt{(1+PrDc)^2 - 4Pr(c-R(1+\delta_T I_1))}}{2}$. For motionless solution, both the eigen values are negative which leads to $R < \sqrt{\frac{Z}{c}}$ therefore, critical R_{cr} is given by $\sqrt{\frac{Z}{c}}$. The stability of $(X_{2,3}, Y_{2,3}, Z_{2,3})$ is governed by the eigen values of:

$$\lambda^3 + (m_1 + 4\gamma + 1)\lambda^2 + 4\gamma \left(m_1 + \frac{R}{R_{cr}}\right)\lambda + 8\gamma m_1 \left(\frac{R}{R_{cr} - 1}\right) = 0. \tag{15}$$

where $m_1 = PrD(1 + \frac{C\pi^2}{\gamma})$. From the above equation, three eigen values can be calculated. One is still genuine and pessimistic. At slightly supercritical values of R , the other two are real and negative, indicating that the convection fixed points are stable. For $PrD = 5, \gamma = 0.5, C = 0.1, \delta_T = 0.1$ these roots become equal at $R = 3.69, 3.82, 3.93$ for OPM case, LBPM and IPM (given in Fig. 1b). At these points two roots becomes complex conjugate. The system is stable at these points due to their negative real pieces. The imaginary and real parts of these two complex parts of eigenvalues both increase when R are used. The two eigenvalues have the same real part at R , according to the Routh-Hurwitz condition:

$$R_{c2} = \frac{m_1 R_{cr}(m_1 + 4\gamma + 3)}{m_1 - 4\gamma - 1}. \tag{16}$$

For $PrD = 5, \gamma = 0.5, C = 0.1, \delta_T = 0.1$, we can evaluate the loss of stability of the convection fixed points as $R_{c2} = 72.6841$ (OPM), 73.3487 (LBPM), 74.0256 (IPM), ($R_{c2} = 67.3$ for gravity, $R_{c2} = 74.0256$ for un-modulated case)

3 Heat Transfer

Heat transport takes place through conduction in the steady state. The Nusselt number (Nu) is defined (see [10]), from Eqs. (11)–(13):

$$Nu = 1 - 2\pi B_{02} = 1 + \frac{2(R - 1)}{R} Z(\tau). \tag{17}$$

The following Nusselt number is obtained from Ginzburg-landau model [18, 19].

$$Nu(\tau) = 1 + \frac{k^2}{4\delta^2} A^2(\tau). \tag{18}$$

To simplify Eq. 18, the finite amplitude $A^2(\tau)$ is calculated from Eq. 17.

4 Results

The governing system of Eqs. (11)-(13) is solved by using a Matlab (ODE 45) and Mathematica (NDSolve). In the bifurcation diagram, there is a sudden transition from smooth convection to chaos. $Rc2=72.6841$ (OPM), 73.3487 (LBPM), 74.0256 (IPM), ($Rc2= 67.3$ for gravity, $Rc2=74.0256$ for un-modulated case). The numerical results for trajectories projections on $X - Y - Z$ planes are discussed. The evolution of $X - Y - Z$ trajectories over a time scale of 0–100 is graphically depicted.

$$Nu^{IPM} < Nu^{LBMO} < Nu^{OPM}$$

In Fig. 2 ($R = 1.41$ and 5.41) When the Rayleigh number is slightly higher than the stability value for the motionless solution for out of phase modulation, the solution trajectories transition to steady convection. Figure 2a, b shows (trajectory $X = Y$) the solution of the system of Eqs. (11)–(13). As R increases, the trajectories try to shift around the fixed points. When the Rayleigh number is slightly above the stability value for the motionless solution, the trajectory transitions to steady convection. It is also observed that the time series solution presented in Figs. 2C and 2D are in steady motion stating the conduction state.

It is observed that the periodic solutions presented in Fig. 3 and acquired with the increasing the value of R higher than $R = 72.6841$. It is discovered that the envelop of the function X, Y, Z does not converge or diverge, but instead exhibits a periodic behaviour known as chaotic behaviour. The value of R , as well as modulation parameters, are linked to the occurrence of periodic solutions (Ω_T, Δ) and couple stress parameter C , which can be seen from the bifurcation diagram later. The projections

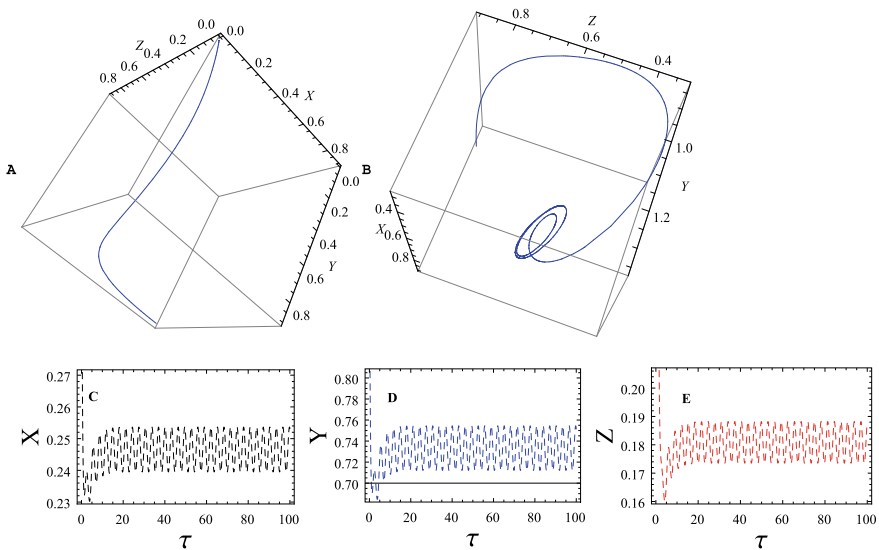


Fig. 2 The solution for ($\phi = \text{Pi}$; $\Omega_T = 2.$; $\delta_T = 0.1$; $C = 0.1$; $R = 1.41$ and $R = 5.41$), the projection of trajectories on the $Y - Y - Z$ planes

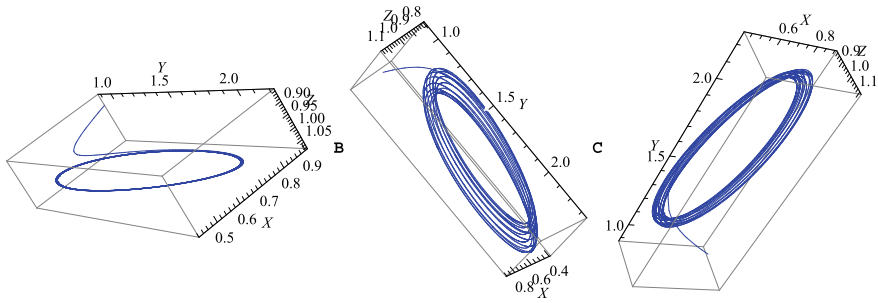


Fig. 3 The solution for ($\Omega_T = 2; \delta_T = 0.1; C1 = 0.1; R = 72.4841, \phi = 0, Pi, -I$ Infinity). The projection of trajectories on the $Y - Y - Z$ planes, respectively

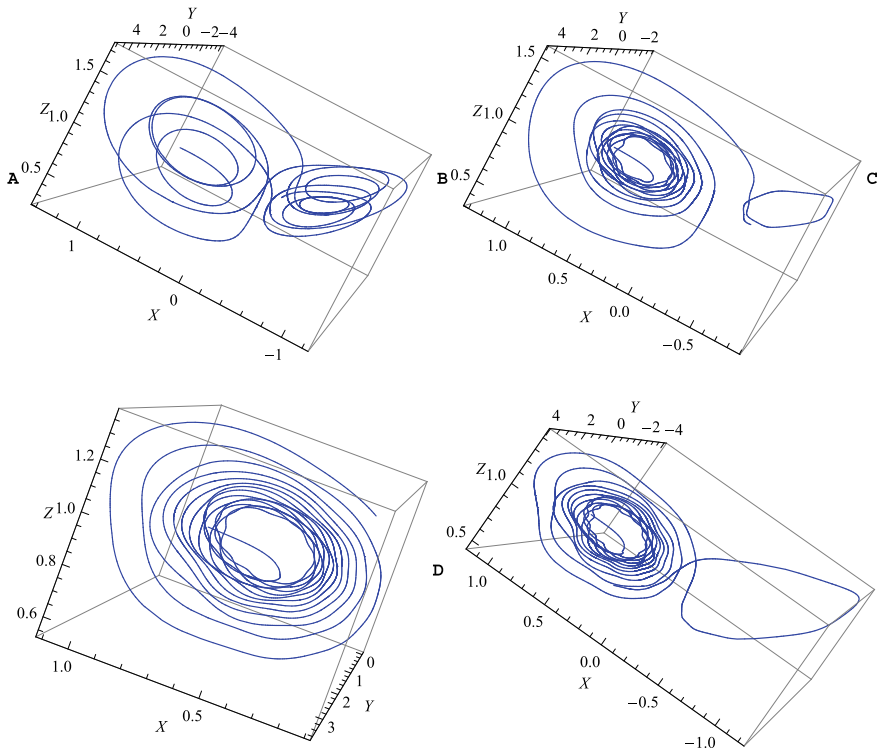


Fig. 4 Projections and evolution of trajectories over the planes $X - Y - ZR = 85.6841, \delta t = 0.3, \omega = 2.00, 40, 60 (R = 85.6841, \Omega_T = 60; \delta_T = 0.6; \text{fig. D})$

and evolution of trajectories over the planes $X - Y - Z$ and a time domain of solutions for $R = 85.6841$ is given in Fig. 3. For a periodic nature of solutions in the time domain easily observed.

Now it is explained how the modulation and couple stress parameter can be used to alternate the chaos, from steady to unsteady state. There are several cases where the suitable parameter values can rewind the system into its stable manifolds. From the Fig. 4, the projections and evolution of trajectories over the planes $X - Y - Z$, for $R = 85.6841$, $\delta_T = 0.3$ and varying the value of $\Omega_T = 2, 40, 60$. It is clear that for $\delta_T = 0.3$, as Ω_T varies the periodic solutions become stable, which means that the frequency of thermal modulation rigorously controls the chaos in the system. It is evident that frequency of modulation reduces heat transfer and bring back the system from unstable to stable. One can also immediately observe that for the same values of $R = 85.6841$, $\Omega_T = 60$ the values δ_T varies from 0.3 to 0.6 again there is an un-steady motion exist in the system for $C = 0.1$. These are the new results states that with modulation parameters, one can easily get control chaos. The similar nature of the results can observed for the cases of LBMO and IPM.

The effect C is presented in Fig. 5a–f. For the value of $C = 0.1$, $R = 77.92$, it is found that modulation adapt the chaotic solutions and the thermal modulation adapt steady solutions. It is clear form the studies of Moli et al. [33] that lower values of gravity modulation required for chaotic solution than thermal modulation.

When the value of C varies from 0.1 to 0.3, then the trajectories of X, Y, Z oscillate in a wider intervals and the R values varies rapidly from 72.92 to 315.94, ($R = 27.75, 44.74, 77.91, 176.24, 315.94$ for $C = 0.01, 0.05, 0.1, 0.2, 0.3$). In this case, the chaotic solutions are exhibit chaotic behaviour. For a very small change in C , there is large difference in R and leads to chaotic solutions. Thus, the couple stress parameter C along with thermal modulation gives a better control on the system. It is clear that when R takes 150 (in same nature of Fig. 4) and $\delta_T = 0.1$, $\Omega_T = 45$ chaotic solutions are recovered from the Fig. 4.

In both Fig. 5g it is observed that the effect of couple stress parameter C is to reduce heat transfer in the medium. The comparison of thermal and gravity modulation is presented in the Fig. 5h. It is found that thermal modulation enhances the heat transfer than gravity modulation. It is also noticed that the gravity modulation acts like only lower boundary modulation. These results are compared with the results of Kiran et al. [29, 31]. It is observed that the values of δ_T and Ω_T are taken near by 0.1 and 3 which do not affect the system.

5 Conclusions

It is proven that the chaotic behaviour of convection connected with thermal modulation and couple stress parameter C . The following findings are drawn:

1. The effect of (δ_T) is to enhance the heat transfer, and frequency (Ω_T) is to diminish the heat transfer.
2. The effect of (δ_T) is to encourage chaotic solutions in the presence of frequency and phase angle.

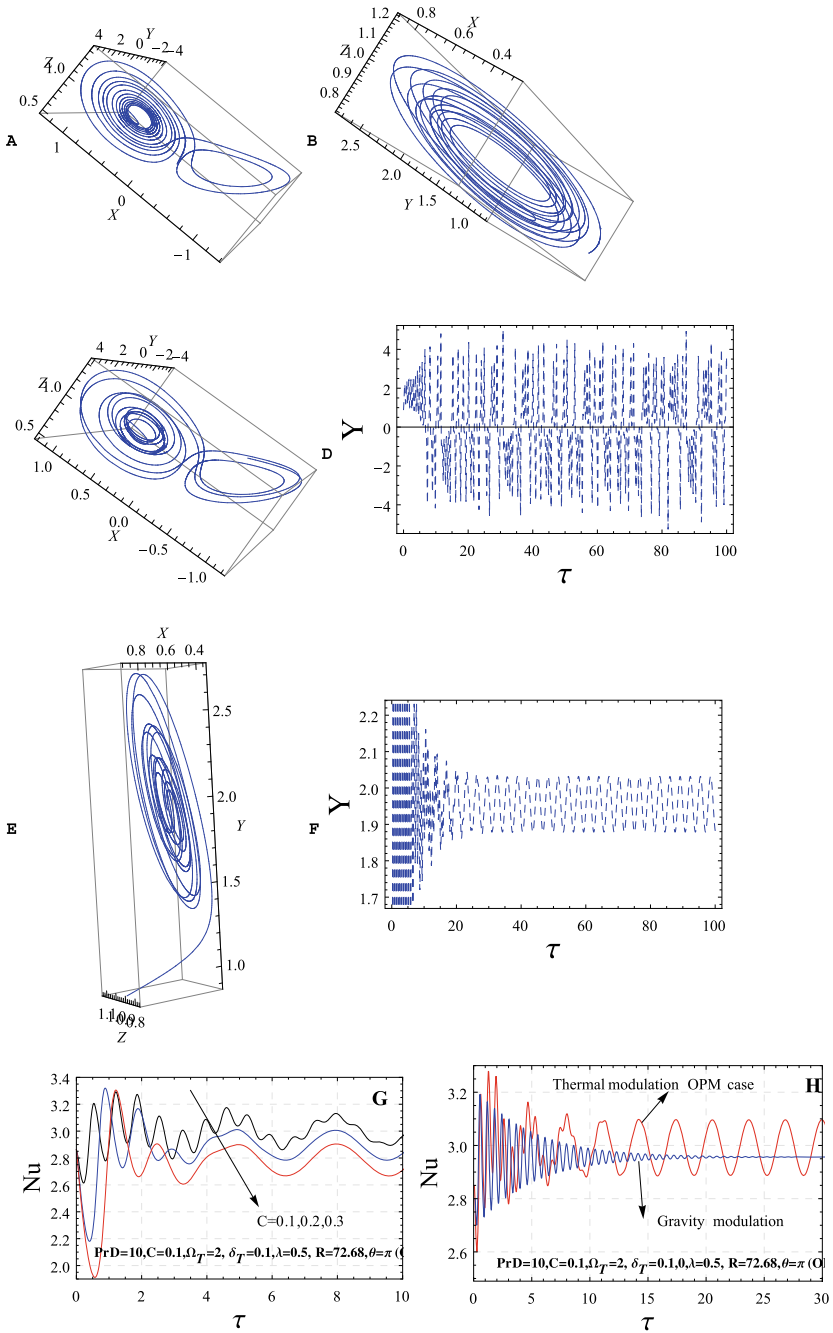


Fig. 5 Projections and evolution of trajectories over the planes $X - Y - Z$ for $R = 77.92 : C = 0.1$ (a) $\delta_g = 0.1$ ($\delta_T = 0.0$) (b) $\delta_T = 0.1$ ($\delta_g = 0.0$) $R = 77.92$ $C = 0.1$ for, (c, d): $R = 77.92$ $C = 0.15$ for (e, f)

3. The results are obtained computational and found that the C reduces heat transfer and thermal modulation enhances heat transfer.
4. The couple stress parameter C admits chaotic solutions faster than modulation.
5. Whilst the suitable combinations of C and modulation parameters one can have better understanding in chaos.
6. Three types of modulations have usual effects on heat transfer, and with couple stress parameter C there is relevant effect on chaos.
7. The critical value of R near to threshold of chaos is controlled by modulation parameters ϕ , δ_T , Ω_T .

Acknowledgements The author MJ would like to acknowledge the support of VFSTR for providing research specialties in the department. The author Dr. Palle Kiran is gratefully acknowledged CBIT, Hyderabad, India for providing research specialties in the Department.

References

1. Lorenz EN (1963) Deterministic non-periodic flow. *J Atmos Sci* 20:130–142
2. Vadasz P, Olek S (1999) Weak turbulence and chaos for low Prandtl number gravity driven convection in porous media. *Trans Porous Media* 37:69–91
3. Vadasz P (1999) Local and global transitions to chaos and hysteresis in a porous layer heated from below. *Trans Porous Media* 37:213–245
4. Mahmud MN, Hashim I (2011) Effect of magnetic field on chaotic convection in fluid layer heated from below. *Int Commun Heat Mass Transfer* 38:481–486
5. Vadasz P, Olek S (2000) Route to chaos for moderate Prandtl number convection in a porous layer heated from below. *Trans Porous Media* 41(2):211–239
6. Moez F (2003) An adaptive feedback control of linearizable chaotic systems. *Chaos, Solitons and Fractals* 15:883–890
7. Yau HT, Chen CK, Chen CL (2000) Sliding mode control of chaotic systems with uncertainties. *Int J Bifurcation Chaos* 10:1113–1147
8. Sheu LJ, Tam LM, Chen JH, Chen HK, Kuang-Tai L, Yuan K (2008) Chaotic convection of viscoelastic fluids in porous media. *Chaos, Solitons and Fractals* 37:113–124
9. Vadasz P (2010) Analytical prediction of the transition to chaos in Lorenz equations. *Appl Math Lett* 23:503–507
10. Narayana M, Gaikwad SN, Sibanda P, Malge RE (2013) Double diffusive magneto-convection in viscoelastic fluids. *Int J Heat Mass Transf* 67:194–201
11. Chuanshi S, Liu S, Wang Q, Wan Z, Sun D (2019) Bifurcations in penetrative Rayleigh-Bénard convection in a cylindrical container. *Appl Math Mech* 40:695–704
12. Magyari E (2010) The butterfly effect in a porous slab. *Trans Porous Media* 84(3):711–715
13. Sheu LJ, Tam LM, Chen JH, Chen HK, Lin KT, Yuan K (2008) Chaotic convection of viscoelastic fluids in porous media. *Chaos Solitons Fractals* 37:113–124
14. Venezian G (1969) Effect of modulation on the onset of thermal convection. *J Fluid Mech* 35:243–254
15. Siddheshwar PG, Uma D, Bhavya S (2019) Effects of variable viscosity and temperature modulation on linear Rayleigh-Bénard convection in Newtonian dielectric liquid. *Appl Math Mech* 40:1601–1614
16. Bhadauria BS, Kiran P (2014) Weak nonlinear analysis of magneto-convection under magnetic field modulation. *Phys Scripta* 89(9):095209
17. Gresho PM, Sani RL (1970) The effects of gravity modulation on the stability of a heated fluid layer. *J Fluid Mech* 40:783–806

18. Bhadauria BS, Kiran P (2014) Weak nonlinear oscillatory convection in a viscoelastic fluid saturated porous medium under gravity modulation. *Trans Porous Media* 104(3), 451–467
19. Bhadauria BS, Kiran P (2014) Weak nonlinear oscillatory convection in a viscoelastic fluid layer under gravity modulation. *Int J Non-linear Mech* 65:133–140
20. Donnelly RJ (1964) Experiments on the stability of viscous flow between rotating cylinders III: enhancement of hydrodynamic stability by modulation. *Proc R Soc Lond Ser A* 281:130–139
21. Kiran P, Bhadauria BS (2016) Weakly nonlinear oscillatory convection in a rotating fluid layer under temperature modulation. *J Heat Transfer* 138(5):051702
22. Kiran P, Bhadauria BS, Narasimhulu Y (2017) Oscillatory magneto-convection under magnetic field modulation. *Alexandria Engg J* 57:445–453
23. Sharma GC, Madhu J, Chandra M (2003) The effect of magnetic fields on low frequency oscillating natural convection with pressure gradient. *Appl Math Mech* 24:274–283. <https://doi.org/10.1007/BF02438265>
24. Jawdat JM, Hashim I (2010) Low Prandtl number chaotic convection in porous media with uniform internal heat generation. *Int Comm in Heat and Mass Transfer* 37:629–636
25. Mahmud MN, Hashim I (2011) Effect of magnetic field on chaotic convection in fluid layer heated from below. *Int Commun Heat Mass Trans* 38:481–486
26. Gupta VK, Bhadauria BS, Hashim I, Jawdat J, Singh AK (2015) Chaotic convection in a rotating fluid layer. *Alexandria Eng J* 54:981–992
27. Ming C, Liu WF, Liu JK (2013) Bifurcation and chaos of airfoil with multiple strong nonlinearities. *Appl Math Mech* 34:627–636. <https://doi.org/10.1007/s10483-013-1696-x>
28. Vadasz JJ, Govender Meyer JP, S, (2014) Chaotic and periodic natural convection for moderate and high prandtl numbers in a porous layer subject to vibrations. *Trans Porous Media* 103:279–294
29. Kiran P, Bhadauria BS (2015) Chaotic convection in a porous medium under temperature modulation. *Trans Porous Media* 107:745–763
30. Bhadauria BS, Kiran P (2015) Chaotic and oscillatory magneto-convection in a binary viscoelastic fluid under G-jitter. *Int J Heat Mass Transf* 84:610–624
31. Kiran P, Narasimhulu Y (2018) Internal heating and thermal modulation effects on chaotic convection in a porous medium. *J Nanofluids* 7(3), 544–555
32. Kiran P (2020) G-jitter effects on chaotic convection in a fluid layer. *Condensed Matter Phys* 01–23. <https://doi.org/10.5772/intechopen.90846>
33. Moli Z, Wang S, Li SC, Zhang QY, Mahabaleshwar US (2018) Chaotic Darcy-Brinkman convection in a fluid saturated porous layer subjected to gravity modulation. *Results Phys* 9:1468–1480

Chapter 32

Effect of Ceramic Particles on AMMC Through Stir Casting Method—A Review



Ramesh Kurbet, Basavaraj, C. M. Amruth, and S. L. N. Jayasimha

Abstract Metals are the basic need for any manufacturing industry and currently it plays an indispensable role in human lives. Humans need some improved quality metals and it is also attempted to enhance the properties and thus they found alloys. Further, to extend the study, composite materials, which shows better-desired properties when compared with the base materials are considered. This research work is a clear cut review on different ceramic reinforcement materials and the results of variation of reinforcement material and their proportion. After a detailed study, it has been found that with the increase in reinforcement, hardness and ultimate tensile strength of material increase with the decrease in percentage elongation of the material.

Keywords Aluminium MMC · Stir casting · Silicon carbide · Titanium carbide · Boron carbide · Titanium diboride

1 Introduction

Metals are the the good conductor of electricity and also they are available in atmospheric dust, where the durability property of the metal is strong. Therefore it is used in various applications like aerospace, automobile and transportation. They may contain carbon and based on it they will have a cluster of shining property along with ductility i.e. they can be drawn into wire and malleability i.e. it can stretch into sheets, which are used in aerospace applications. Metal produces a different type of gas by reacting with the water acids and oxygen like magnesium oxide is formed by burning magnesium strips in the presence of oxygen. Alloy can be prepared by mixing two or more metals, alloys that are prepared to enhance properties like hardness, tensile strength and corrosion resistivity material, there are several commonly used alloy elements like chromium, carbon, Nickel and others, which are used to enhance the corrosion resistance, hardness, strength and toughness. An example of an alloy is steel which is the combination of iron and carbon and is stronger, lighter, and more workable when compared to pure alloy. Different materials will

R. Kurbet (✉) · Basavaraj · C. M. Amruth · S. L. N. Jayasimha
Department of Mechanical Engineering, PES College of Engineering, Mandya, India

have different physical properties and chemical properties such type of materials are combined to prepare a composite material and these composite materials are specified to do a certain job, Different type of composite materials are prepared by adding the ceramics particle, concrete, and glass fibre. To prepare polymer-metal Matrix composite the plastic materials are mixed with the different material, not all the plastics are capable to prepare a polymer-metal Matrix composite material. There are several plastic materials used to prepare polymer-metal Matrix composite. Ceramic Metal Matrix Composite can be prepared by spreading the ceramics particles in the matrix since ceramic material is harder the prepared composite material will have more hardness. Reinforcement used in ceramic metal matrix composite is TiC, $B_4C \cdot Al_2O_3$, ZrO_2 .

2 Experimental or Computational Details

2.1 SiC

Ashok et al. [1] had a detailed study on Mechanical properties of Aluminium 6065 without reinforcement and with reinforcement materials like Sic and Al_2O_3 produced by modified stir casting method. The authors concluded that hardness is directly proportional to the quantity of Sic particles. By adding 6wt% of Sic and Fly ash 106 BHN hardness was obtained and the tensile strength of hybrid composite was observed as 314 MPa, also a Yield strength of 173 MPa is obtained. Toughness is observed as 3.6 J, 3.2 J and 2.6 J, respectively, for Al6065-6wt% Sic-Fly ash, Al6065-6wt% Fly ash and Al6065-6wt% sic. Bhat and Kakandikar [2] studied on Preparation of MMC by adding Sic to Al 6065 to Enhance the sliding wear properties by the stir casting method. Wear test is carried out by surface methodology, after successful completion of wear test in 9 attempts by varying load and speed the authors concluded that adding 5% of sic increases the wear resistance. By load variation and at constant Speed and vice-versa causes an increase in the wear rate of the material. The minimum wear rate is 316 μm and the maximum wear rate is 948 μm is obtained for the load of 20 N and 200 N, respectively. The hardness of the material also increases from 81 to 135 HB as we increase the load. David et al. [3–5] studied the preparation of Al MMC with reinforcement of SiC particle by a stir casting technique and analysed ductility and fracture characteristics of the MMC. And the authors found that the yield and tensile strength of MMC are increased by 60% when compared to base Al alloy and found that yield and Ultimate Tensile Strength depend mainly on the reinforcement content and temperature of the matrix alloy Alip Kumar et al. [6, 7] studied the mechanical, microstructural and tribological properties of Aluminium hybrid matrix composite with SiC-TiC particles by fixing the composition of SiC at 1 wt% and varying the wt% of TiC from 1–2.5 in the step of 0.5 experiment was carried out with stir casting. Authors concluded that with increasing the composition of reinforcement there will be an increment in hardness and wear rate of the material

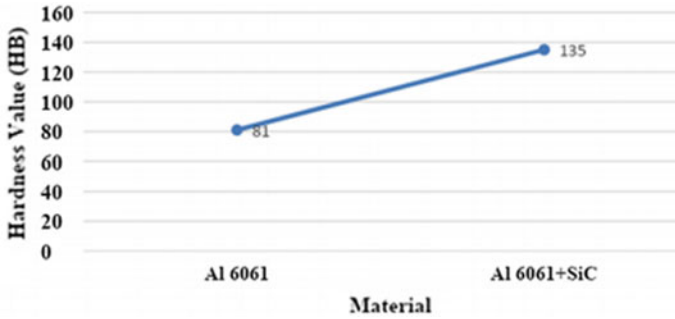


Fig. 1 Hardness of Al 6061 compared with Al6061 + SiC

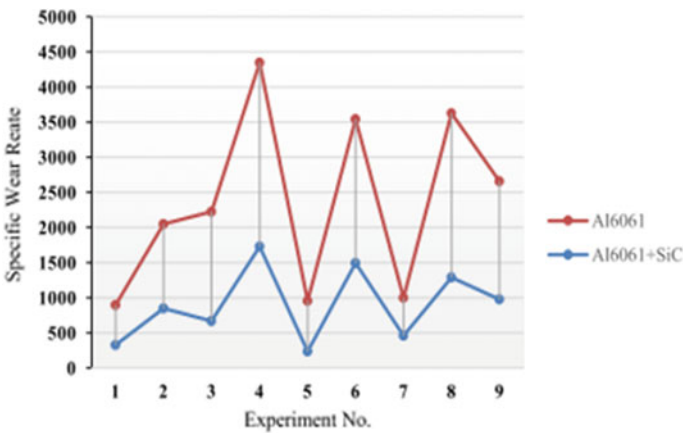


Fig. 2 Comparison of specific wear rate of Al6061 and Al6061 + SiC

along with the decrease in the density. For AST05 the maximum hardness of 138HV and low density are obtained (Figs. 1, 2 and 3).

2.2 Al₂O₃

Bharath et al. [8] studied on mechanical and wear properties of AMMC with the reinforcement of Al₂O₃ produced by the stir casting. The authors concluded that as the addition of Al₂O₃ increases 178.91 MPa of yield strength and 193.47 MPa of tensile strength was obtained. And the minimal wear rate is observed at Al+12% of Al₂O₃ of the composition of which is less than the Al matrix. Increase in the wt% of reinforcement reduces the ductility of the material which leads to an increment in the fracture strength. Karbalaee Akbari et al. [9, 10] studied the preparation of Aluminium composite with nano-sized Al₂O₃ particles by a stir casting process. And

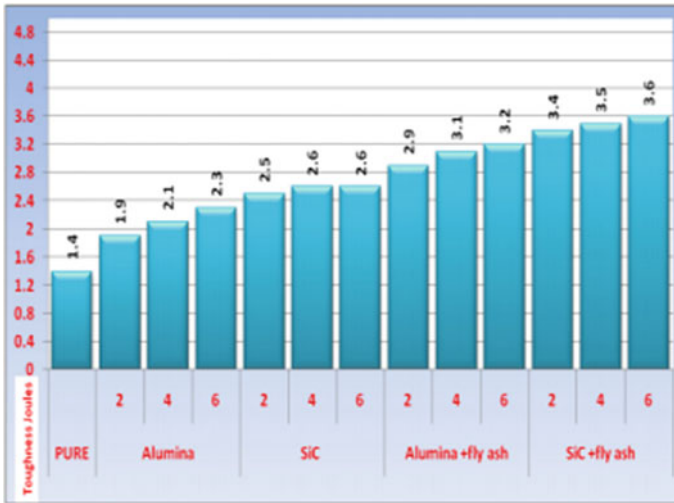


Fig. 3 Toughness of Al6065-SiC Al6065- Al_2O_3 , Al6065-hybrid composites

authors concluded that milling time will affect the mechanical properties, and with the composition of Al356 and 1.5 vol.% Al_2O_3 Using Cu Particle with milling time of 24 h, the yield strength, young's modulus, and percentage of porosity is increased from 122 to 169 GPa, 65.45 to 78.48, and 1.6% to 3.6%, respectively, and the grain size is decreased from 48 to 24 μm . Mohanavel et al. [11] worked on mechanical properties of alumina (Al_2O_3) reinforced with AMMC and the author observed a homogeneous mixture of alumina particulate in the composite. Tensile strength along with hardness of the composites increases with the increase in alumina content, 3% volume fraction composite shows the maximum tensile strength of 181 MPa and hardness of 68 HV because of good interfacial bonding between Al6082 and alumina particulates. Pratap Singh et al. [12, 13] studied on properties of $\text{ZrO}_2/\text{Al}_2\text{O}_3/\text{Gr}$ reinforced with hybrid metal matrix by casting technique and study evidence by adding various wt% of ceramic particulates tensile strength and hardness of the hybrid metal matrix improves. Maximum tensile strength of 157.36 MPa and hardness of 158 HV of the composite were found by adding 10 wt% of $\text{ZrO}_2/\text{Al}_2\text{O}_3/\text{Gr}$. But maximum porosity of composite found for 4 wt% of $\text{ZrO}_2/\text{Al}_2\text{O}_3/\text{Gr}$ (Figs. 4 and 5).

2.3 ZrO_2

Boppana et al. [14] experimented on the Preparation and characterization of Aluminium 6061 MMC with ZrO_2 and nanographene particles as reinforcement with stir casting technique. By their experimentation, they concluded that the ZrO_2 particles show a high wear property and by addition of 0.75% of nanographene

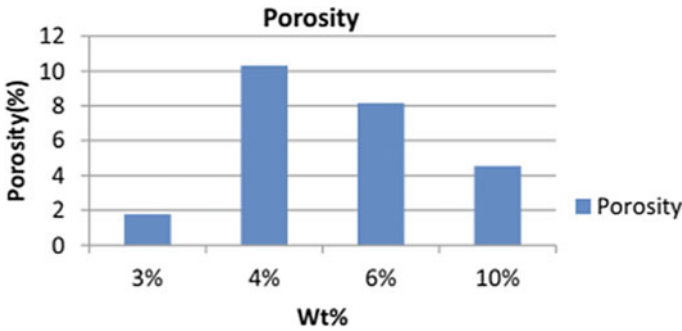


Fig. 4 The variation of porosity of the HMMCs with different weight fraction of Al₂O₃/ZrO₂/Gr

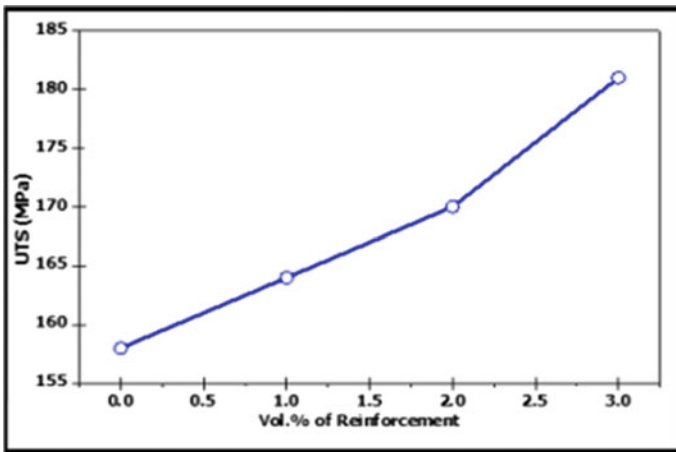
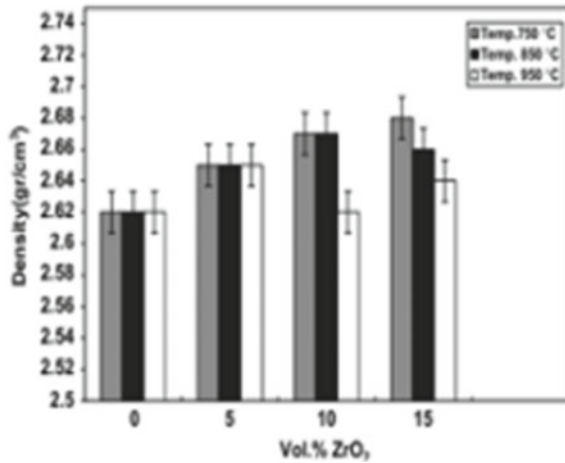


Fig. 5 Ultimate tensile strength of the AMMCs

particles dendritic structure was observed in the sample, and increment in yield and tensile. Ravi Kumar et al. [15] studied on the mechanical properties and characterization of Al metal matrix composite with ZrO₂ and coconut shell ash as reinforcement by stir casting technique. By experimentation, the authors concluded that 11.1% higher density was obtained in the composite when compared with Al alloy. By adding coconut shell ash the hardness of the material is decreased but it is overcome by adding ZrO₂ particles and obtained 31.5% higher hardness than the Al Alloy, and increase in impact strength was occurred by adding the 10% of ZrO₂ particles. Abdizadeh and Baghchesara [16] studied fracture property and mechanical properties of Zirconium oxide (ZrO₂) reinforced with A356 aluminium composite and the study pieces of evidence that maximum tensile strength (232 MPa) and hardness (70 HBN) are observed on adding 15% of B₄C since the mechanical properties of the composites increase with increase in ZrO₂ wt%. Optimum value for the composite observed when it is fabricated at 750 °C by reinforcing with 15% of ZrO₂. It is

Fig. 6 The density of the aluminium alloy and the composite specimen containing 5, 10, 15 wt% ZrO_2 fabricated at 750, 850 and 950 °C



observed that fracture of the composite occurs due to interdendritic cracking and on the fracture surface, more dimples were found as a result of coalescence and void nucleation. Udayashankar and Ramamurthy [17] has conducted an experiment on properties of ZrO_2 with Al6061 as reinforcement and concluded that uniform distribution of zirconia was observed which results in zero voids and porosity. The hardness and ultimate tensile strength of the composite material increased to 9 wt% of reinforcement above that the values declined due to poor bonding and wettability of particulate with the base material. Optimum values of the ultimate tensile strength was found to be 144 MPa and hardness is of 98 BHN were observed by adding 9% of zirconia. Kumar [18] studied tribological and mechanical properties of ZrO_2 reinforced with Al6061 metal matrix composite and the study indicates that hardness, tensile strength and wear resistance of the composite increases on increasing wt% of the ZrO_2 however % elongation and the ductility decreases. For 6 wt% of ZrO_2 maximum hardness of 67.8 BHN and tensile strength of 174.9 MPa is observed as a result of good bonding between the Al6061 and ZrO_2 with dendrite areas (Figs. 6 and 7).

2.4 B_4C

Kalaiselvan et al. [19] studied on Preparation and properties of the Al metal matrix composite reinforced by B_4C the stir casting technique, and conveyed that, After adding the B_4C there is an increase in microhardness of the metal matrix composite from 51.3 to 80.8 HV and macrohardness from 34.4 to 58.6 BHN. After adding B_4C particle there will be a gradual increment in ultimate tensile strength from 185 to 215 MPa. And wettability is increased by adding K_2TiF_6 . Venkatesh et al. [20] studied the mechanical and micro-structural properties of Al metal matrix composite

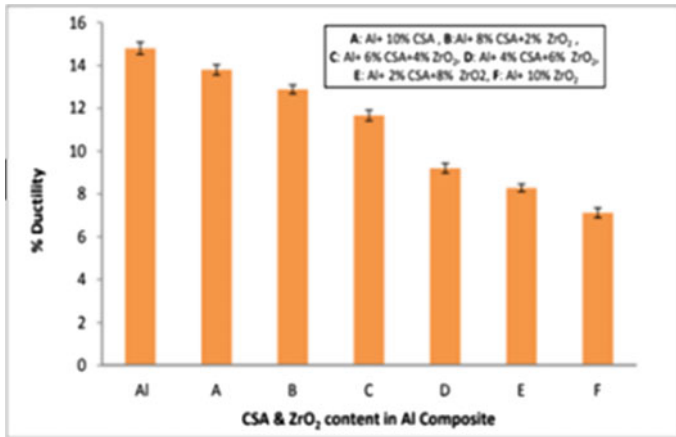


Fig. 7 Effect of ZrO₂ and CSA on elongation

with the reinforcement of B₄C and ground nutshell ash by squeeze casting method (the combination of stir casting and forging). Reinforcement varied between 0 and 7.5%. successful conduction of work yields that with the addition of 2.5% of GSA (Groundnut shell ash) the increment in hardness and tensile strength and observed as 17% and 18.32%, respectively, but if the wt% of GSA is 7.5% then the hardness, tensile strength, and impact strength will be decreased. Auradi et al. [21, 22] studied on Preparation of Al MMC with B₄C particles as reinforcement by the two-step addition of the stir casting technique. the composition of B₄C particles is 11%. The authors concluded that the wettability is enhanced with a two-step addition process and with the addition of 11% of B₄C the ultimate tensile strength along with yield strength are increased by 42.6% and 44.35%, respectively, although the percentage elongation of material decreases. And the hardness is increased from 70.4 VHN to 157.3 VHN along with porosity also increases. Mazaheri et al. [23, 24] studied the comparative study on mechanical and microstructural properties of Aluminium metal matrix composites with the reinforcement of TiC, B₄C, TiC + B₄C, prepared by stir casting technique. And authors concluded that the wettability can be overcome with the addition of TiC and also by heat treating of B₄C particles with the flux. With the composition of Al+5%TiC+5%B₄C, Al+10%B₄C and Al+10%TiC the maximum hardness, UTS, yield strength and maximum elongation of the material obtained. Al+10%B₄C will show a lower wear rate. Kerti and Toptan [25] studied the microstructural variation in Al-B₄C composites and the study evidence that by adding flux such as K₂TiF₆, a homogeneous mixture of B₄C particles was observed and it should be nearly equal to the content of B₄C reinforcement. Agglomeration of B₄C particulates is less when their size is more than 20 μm and more when their size less than 10 μm. Chellapandi [26] studied the influence of SiC, B₄C and Mg reinforced with aluminium metal matrix composite and found that distribution of SiC in Al matrix is uniform hence tensile strength of the composite material was

found to be in increasing pattern with an increase in SiC particulate. The author observed that the maximum compressive strength found by adding 9% of SiC and 9% of B₄C into the composite. Boron carbide reinforced composite shows higher compressive strength than Silicon Carbide reinforced composite, this is due to the restriction of particle dislocation in the pure aluminium alloy by the mechanism of dispersion strengthening. An increase in B₄C content in the composite increases the brittleness thereby altering impact strength of the composite material, which is found to be reduced. The addition of both SiC and B₄C will increase the hardness of the material but adding them more than 20% makes the composites more brittle (Figs. 8 and 9).

Fig. 8 Influence on impact strength

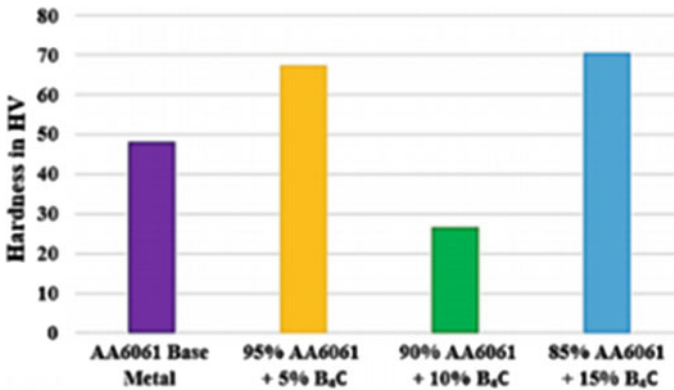
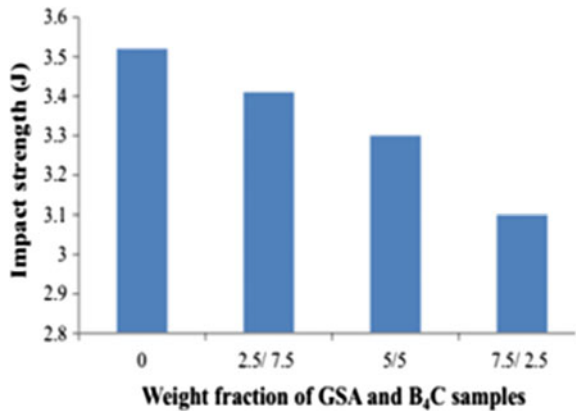
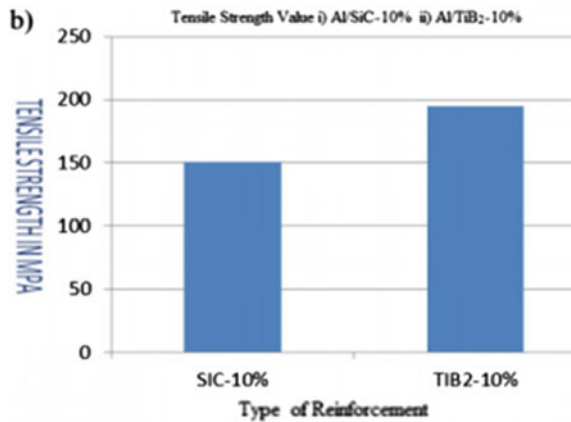


Fig. 9 Hardness value of the specimen

Fig. 10 Comparative tensile strength chart



2.5 TiB₂

Tan et al. [27] studied on the preparation of Al hybrid metal matrix composite with the nano and microparticles of SiC and TiB₂ as reinforcement, respectively, by powder metallurgy technique to increase the desired mechanical properties of the material chosen. After the experiment, the authors concluded that enhancing the mechanical properties of material TiB₂ nanoparticle performs a very important role, and there will be an increase in yield strength of the material by 64% and ultimate tensile strength was found to be increased by 23%. Suresh and Moorthi [28] reviewed the aluminium metal matrix composite prepared with the reinforcement of TiB₂ particles and the authors provided the information that thermal, microstructural along with mechanical properties of the material will directly effect by the addition of TiB₂ particles, and the wear rate of the composite material is increased by the addition of TiB₂ reinforcement. Kumar et al. [29] studied the corrosion properties of aluminium metal matrix composite with the reinforcement of TiB₂, and the authors concluded that by the addition of TiB₂ reinforcement decrement in weight loss is observed and the corrosion resistance of the material will increases. Johny James et al. [30] studied the fabrication and comparative study on aluminium hybrid matrix composite with SiC and TiB₂ particles as the reinforcement and the authors conveyed the information that the tensile strength of the metal matrix composite will be more compared to pure alloy and with the increase in the addition of TiB₂ wear resistance property of the material will increase (Fig. 10).

2.6 Graphite

Gowrishankar et al. [31] worked on the preparation of an Al hybrid metal matrix composite by the reinforcement of Graphite and TiC particles by stir casting

technique. Upon successful conduction of stir casting by adding 5% of graphite throughout the process and varying the wt% of Tic from 0 to 8% in step of 2% and the authors concluded that the hardness of the material found to be decreased along with the addition of only graphite particle, and with the addition of TiC and graphite particles there is a 60% increment in wear resistance compared to Al Alloy, and with the composition of Al6061+5%Gr+4%TiC, the ultimate tensile strength of the material and yield strength of the material were increased by 37.5% and 32%, respectively. Amrendra Pratap Singh et al. studied on properties of $ZrO_2/Al_2O_3/Gr$ reinforced with hybrid metal matrix by casting technique and study evidence by adding various wt% of ceramic particulates tensile strength and hardness of the hybrid metal matrix improves. Maximum tensile strength (157.36 MPa) and hardness (158 HV) of the composite were found by adding 10 wt% of $ZrO_2/Al_2O_3/Gr$. But maximum porosity of composite found for 4 wt% of $ZrO_2/Al_2O_3/Gr$. Mohanavel et al. [32] studied on the fabrication and mechanical behaviour of Al MMC with the reinforcement of Graphite particle by stir casting technique 0–12% of reinforcement is added by step of 4%. And the authors conveyed the information that through the addition of graphite particle the hardness along with the ultimate tensile strength of the material will get increases since graphite particles have low density and brittle it causes a reduction in the mechanical properties in the material. Kumari [33] analysed the aluminium metal matrix composite prepared with the reinforcement of graphite particles by a stir casting technique and the authors provided the information that the addition of graphite particles leads to an increment in the ultimate tensile strength and hardness till at an optimum level, in the same case the wt% of graphite particle 4% and greater than 4% causes decrement in hardness and ultimate tensile strength (Figs. 11 and 12).

Fig. 11 Variation of hardness with weight percentage of Gr addition

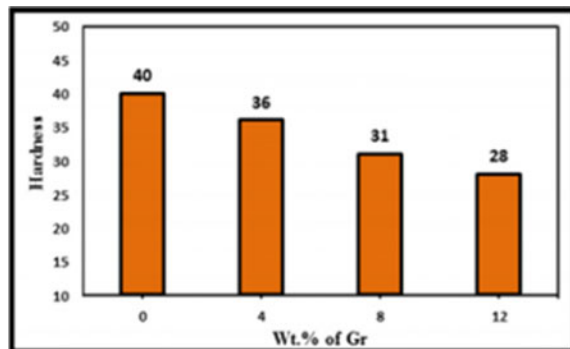
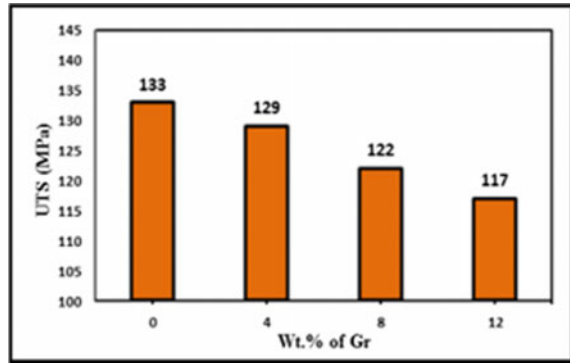


Fig. 12 Variation of UTS with weight percentage of Gr addition



2.7 TiC

Pandey et al. [34] studied on the mechanical properties of the Al MMC with the reinforcement of TiC particles by the stir casting technique method. The authors have concluded by the addition of the 40 wt% of TiC particle the hardness of the MMC observed as 55 HRC. The rate of wear and the friction coefficient of MMC are decreased gradually with the increase in volume fraction of TiC particles. Amanda Murthy and Singh [35] studied on the preparation of Aluminium MMC with the reinforcement of TiC particles by Stir casting technique to investigate the corrosion property of the MMC. After successful conduction of the experiment, authors concluded that the Al+TiC composition has more corrosion resistance and pitting resistance when compared with the Al alloy so this composition has more opportunities in the future days. Jebeen Moses et al. [36] Studied on the preparation, characterization of Aluminium metal matrix composite reinforced with TiC produced by stir casting technique. Reinforcement was given in a step of 5% from 0 to 15%. successful conduction of work yielded better bonding of matrix with the help of refined grains. And by adding 15% of TiC the microhardness and ultimate tensile strength are increased by 134.4% and 70.5%, respectively, when compared to Al alloy, and the wear resistance of the prepared material is increased by 30.5%. but the ductility and percentage elongation decreases with an increase in the TiC particles. Ravi Kumar et al. [37, 38] studied on the mechanical properties and micro-structure behaviour of the Al MMC reinforced with TiC through the stir casting method. 0–10% of TiC was varied in a step of 2% and concluded that the addition of TiC particle enhances the density of the MMC by 11.1% by comparing to Al alloy. Plastic deformation was observed with the addition of TiC particle which causes the conversion of failure mode to a brittle mode of the material, with the addition of TiC the impact strength and elongation and density is decreased by 7.8%, 20% and 19.55%, respectively. Tahamtan et al. [39] studied on the preparation of Aluminium metal matrix composite with Al_2O_3 as reinforcement by combining ball milling and stir casting method. The authors with clear cut information found that the tensile strength of the prepared composite is increased by decreasing the size of the alumina particles

from micrometre to nanometer, further porosity and interfacial reaction products are decreased by reducing the temperature of stirring. Agarwal and Tungikar [40] studied on the wear properties of titanium carbide (TiC) reinforced with aluminium metal matrix using the Taguchi method and the study evidence that the friction coefficient and wear rate of the composite improve by increasing the weight percentage of TiC and it highly influences coefficient of friction and wears rate factors by 53.450 and 54.401%. And the optimum value of the coefficient of friction and wear rate found at 7.5 wt%.

3 Pros and Cons

Due to the density difference observed in composite materials produced through stir casting it is suggested to prepare the composite material through powder metallurgy technique [41, 42]. Ceramic particle reinforcement plays a vital role in properties of composite material, hence reinforcement material has to be chosen wisely [43]. Joining of composite material for the various application need to be carried out wisely, friction stir welding is one such technique which joins composite material to well extent [44]. If proper reinforcement is chosen we can have great corrosion resistance for composite material [45]. Even shape memory alloys which are used predominantly in advanced medical industry is a composite material of various materials [46].

4 Conclusion

- By reviewing the SiC papers we conclude that greater hardness, yield strength and toughness are obtained. Increasing the percentage of reinforcement leads to an increase in wear resistance and a decrease in density.
- By reviewing the Al₂O₃ papers we conclude that poor wettability property can be overcome, molten stage wettability improved by decreasing particulate size and increase in particulate content. Increasing the addition of reinforcement leads to a decrease in ductility, percentage elongation and grain size. An increment in wear rate, fracture strength and percentage of porosity, Tensile strength is obtained
- By reviewing the ZrO₂ papers we conclude that increasing the particle of reinforcement dendrite region and density of the composite material increases with zero voids and porosity, more corrosion resistance can be obtained, pitting resistance also increases due to less tendency towards corrosion.
- By reviewing the papers B₄C we conclude that wettability can be overcome by the addition of K₂TiF₆ and an increase in groundnut shell ash the impact strength is decreased. With the increase, the percentage of reinforcement compression strength and brittleness, and hardness is increases but percentage elongation and impact strength are decreased.

- By reviewing all the TiB₂ papers we conclude that the addition of TiB₂ will act a crucial role, and it is found that the mechanical properties of the material will increase such as yield strength, ultimate tensile strength and corrosion resistance. But the decrement in weight loss was observed.
- By reviewing all the Graphite paper we concluded that by adding graphite particles as reinforcement the properties such as hardness, yield strength, ultimate tensile strength and wear resistance of the material are found to be increased when compared with the pure aluminium alloy.
- By reviewing all thetic papers we conclude that with the increasing percentage of TiC particles corrosion and pitting resistance is increased, wettability can overcome but wear rate, friction coefficient, density and impact strength is decreased.

properties	Yield strength	hardness	Percentage elongation	wettability
Al6065	115 MPA	54 BHN	-	-
Al6065 + 6 % SiC	156 MPA	89 BHN	-	-
Al6065 + Al ₂ O ₃	-	-	Decreases	Increases
Al6065 + Graphiite	Increases	61VHN	-	-
Al6065 + 20% B ₄ C	Increases	74.1HV1	Decreases	-

References

1. Ashok N, Mulu A (2021) Effect of reinforcement of particles on the mechanical properties of Al6065-SiC, Al6065-Al₂O₃. Hybrid Compos Modified Stir Cast Method 3(1):31–36
2. Bhat A, Kakandikar G (2019) Manufacture of silicon carbide reinforced aluminium 6061 metal matrix composites for enhanced sliding wear properties. *Manuf Rev* 6:4–9. <https://doi.org/10.1051/mfreview/2019021>
3. McDanel DL (1985) Analysis of stress-strain, fracture, and ductility behavior of aluminum matrix composites containing discontinuous silicon carbide reinforcement. *Metall Trans A* 16(6):1105–1115. <https://doi.org/10.1007/BF02811679>
4. Tham LM, Gupta M, Cheng L (2001) Effect of limited matrix-reinforcement interfacial reaction on enhancing the mechanical properties of aluminium-silicon carbide composites. *Acta Mater* 49(16):3243–3253. [https://doi.org/10.1016/S1359-6454\(01\)00221-X](https://doi.org/10.1016/S1359-6454(01)00221-X)
5. Kumar A, Yeasin Arafath M, Gupta P, Kumar D, Mustansar Hussain C, Jamwal A (2020) Microstructural and mechano-tribological behavior of Al reinforced SiC-TiC hybrid metal matrix composite. *Mater Today Proc* 21(xxx):1417–1420. <https://doi.org/10.1016/j.matpr.2019.08.186>

6. Hossain S et al (2020) Fabrication, microstructural and mechanical behavior of Al-Al₂O₃-SiC hybrid metal matrix composites. *Mater Today Proc* 21(xxxx):1458–1461. <https://doi.org/10.1016/j.matpr.2019.10.089>
7. Bharath V, Nagaraal M, Auradi V, Kori SA (2014) Preparation of 6061Al-Al₂O₃ MMC's by Stir casting and evaluation of mechanical and wear properties. *Proc Mater Sci* 6(Icmpc):1658–1667. <https://doi.org/10.1016/j.mspro.2014.07.151>
8. Sivananthan S, Rajalaxman Reddy V, Samson Jerold Samuel C (2020) Preparation and evaluation of mechanical properties of 6061Al-Al₂O₃ metal matrix composites by stir casting process. *Mater Today Proc* 21(xxxx):713–716. <https://doi.org/10.1016/j.matpr.2019.06.744>
9. Su H, Gao W, Feng Z, Lu Z (2012) Processing, microstructure and tensile properties of nano-sized Al₂O₃ particle reinforced aluminum matrix composites. *Mater Des* 36:590–596. <https://doi.org/10.1016/j.matdes.2011.11.064>
10. Kane SN, Mishra A, Dutta AK (2016) Preface: international conference on recent trends in physics (ICRTP 2016). *J Phys Conf Ser* 755(1). <https://doi.org/10.1088/1742-6596/755/1/011001>
11. Mohanavel V, Suresh Kumar S, Mariyappan K, Ganeshan P, Adithiyaa T (2018) Mechanical behavior of Al-matrix nanocomposites produced by stir casting technique. *Mater Today Proc* 5(13):26873–26877. <https://doi.org/10.1016/j.matpr.2018.08.170>
12. Sajjadi SA, Ezatpour HR, Beygi H (2011) Microstructure and mechanical properties of Al-Al₂O₃ micro and nano composites fabricated by stir casting. *Mater Sci Eng A* 528(29–30):8765–8771. <https://doi.org/10.1016/j.msea.2011.08.052>
13. Pratap Singh A et al (2020) Processing and characterization mechanical properties of AA2024/Al₂O₃/ZrO₂/Gr reinforced hybrid composite using stir casting technique. *Mater Today Proc*. <https://doi.org/10.1016/j.matpr.2020.07.156>
14. Boppana SB, Dayanand S, Anil Kumar M, Kumar V, Aravinda T (2020) Synthesis and characterization of nano graphene and ZrO₂ reinforced Al 6061 metal matrix composites. *J Mater Res Technol* 9(4):7354–7362. <https://doi.org/10.1016/j.jmrt.2020.05.013>
15. Ravi Kumar K, Pridhar T, Sree Balaji VS (2018) Mechanical properties and characterization of zirconium oxide (ZrO₂) and coconut shell ash (CSA) reinforced aluminium (Al 6082) matrix hybrid composite. *J Alloys Compd* 765(6082):171–179. <https://doi.org/10.1016/j.jalcom.2018.06.177>
16. Abdizadeh H, Baghchesara MA (2013) Investigation on mechanical properties and fracture behavior of A356 aluminum alloy based ZrO₂ particle reinforced metal-matrix composites. *Ceram Int* 39(2):2045–2050. <https://doi.org/10.1016/j.ceramint.2012.08.057>
17. Udayashankar S, Ramamurthy VS (2018) Development and characterization of Al6061-Zirconium dioxide reinforced particulate composites. *Int J Eng Technol* 7(3):128–132. <https://doi.org/10.14419/ijet.v7i3.12.15901>
18. Kumar GBV (2019) Heliyon investigation of physical, mechanical and tribological properties of Al6061-ZrO₂ nano-composites 5:0–7
19. Kalaiselvan K, Murugan N, Parameswaran S (2011) Production and characterization of AA6061-B4C stir cast composite. *Mater Des* 32(7):4004–4009. <https://doi.org/10.1016/j.matdes.2011.03.018>
20. Venkatesh L, Arjunan TV, Toptan F, Kilicarslan A, Ravikumar K (2019) Microstructural characteristics and mechanical behaviour of aluminium hybrid composites reinforced with groundnut shell ash and B₄C. *J Brazilian Soc Mech Sci Eng* 41(7):1–13. <https://doi.org/10.1007/s40430-019-1800-1>
21. Auradi V, Rajesh GL, Kori SA (2014) Processing of B₄C particulate reinforced 6061Aluminum matrix composites by melt stirring involving two-step addition. *Proc Mater Sci* 6(Icmpc):1068–1076. <https://doi.org/10.1016/j.mspro.2014.07.177>
22. Hynes NRJ, Raja S, Tharmaraj R, Pruncu CI, Dispinar D (2020) Mechanical and tribological characteristics of boron carbide reinforcement of AA6061 matrix composite. *J Brazilian Soc Mech Sci Eng* 42(4):1–11. <https://doi.org/10.1007/s40430-020-2237-2>
23. Mazaheri Y, Meratian M, Emadi R, Najarian AR (2013) Comparison of microstructural and mechanical properties of Al-TiC, Al-B₄C and Al-TiC-B₄C composites prepared by casting techniques. *Mater Sci Eng A* 560:278–287. <https://doi.org/10.1016/j.msea.2012.09.068>

24. Gopal Krishna UB, Sreenivas Rao KV, Vasudeva B (2013) Effect of boron carbide reinforcement on aluminium matrix composites. *Int J Metall Mater Sci Eng* 3(1):41–48
25. Kerti I, Toptan F (2008) Microstructural variations in cast B₄C-reinforced aluminium matrix composites (AMCs). *Mater Lett* 62(8–9):1215–1218. <https://doi.org/10.1016/j.matlet.2007.08.015>
26. Chellapandi P, SKA, AVS (2015) *Carbon Sci Technol* 1:59–68
27. Tan A, Teng J, Zeng X, Fu D, Zhang H (2017) Fabrication of aluminium matrix hybrid composites reinforced with SiC microparticles and TiB₂ nanoparticles by powder metallurgy. *Powder Metall* 60(1):66–72. <https://doi.org/10.1080/00325899.2016.1274816>
28. Suresh S, Moorthi NSV (2012) Aluminium-titanium diboride (Al-TiB₂) metal matrix composites: challenges and opportunities. *Proc Eng* 38:89–97. <https://doi.org/10.1016/j.proeng.2012.06.013>
29. Kumar GSP, Keshavamurthy R, Kumari P, Dubey C (2016) Corrosion behaviour of TiB₂ reinforced aluminium based in situ metal matrix composites. *Perspect Sci* 8:172–175. <https://doi.org/10.1016/j.pisc.2016.04.025>
30. Johny James S, Venkatesan K, Kuppan P, Ramanujam R (2014) Comparative study of composites reinforced with SiC and TiB₂. *Proc Eng* 97:1012–1017. <https://doi.org/10.1016/j.proeng.2014.12.378>
31. Gowrishankar TP, Manjunatha LH, Sangmesh B (2019) Mechanical and wear behaviour of Al6061 reinforced with graphite and TiC hybrid MMC's. *Mater Res Innov* 00(00):1–7. <https://doi.org/10.1080/14328917.2019.1628497>
32. Mohanavel V, Rajan K, Suresh Kumar S, Vijayan G, Vijayanand MS (2018) Study on mechanical properties of graphite particulates reinforced aluminium matrix composite fabricated by stir casting technique. *Mater Today Proc* 5(1):2945–2950. <https://doi.org/10.1016/j.matpr.2018.01.090>
33. Kumari UPP (2018) Analysis of graphite reinforced aluminium-6061 metal matrix composite using stir casting method. *Int J Appl Eng Res* 13(6):189–193 [Online]. Available: <http://www.ripublication.com>
34. Pandey U, Purohit R, Agarwal P, Dhakad SK, Rana RS (2017) Effect of TiC particles on the mechanical properties of aluminium alloy metal matrix composites (MMCs). *Mater Today Proc* 4(4):5452–5460. <https://doi.org/10.1016/j.matpr.2017.05.057>
35. Ananda Murthy HC, Singh SK (2015) Influence of TiC particulate reinforcement on the corrosion behaviour of Al 6061 metal matrix composites. *Adv Mater Lett* 6(7):633–640. <https://doi.org/10.5185/amlett.2015.5654>
36. Kilerci I, Koksall NS (2013) <53_1_ULU.pdf>, no. January, 2013, , doi: 10.4149/km
37. Ravi Kumar K, Kiran K, Sreebalaji VS (2017) Micro structural characteristics and mechanical behaviour of aluminium matrix composites reinforced with titanium carbide. *J Alloys Compd* 723:795–801. <https://doi.org/10.1016/j.jallcom.2017.06.309>
38. Nayim SMTI et al (2020) Effect of CNT and TiC hybrid reinforcement on the micro-mechanotribehaviour of aluminium matrix composites. *Mater Today Proc* 21(xxxx):1421–1424. <https://doi.org/10.1016/j.matpr.2019.08.203>
39. Tahamtan S, Halvae A, Emamy M, Zabihi MS (2013) Fabrication of Al/A206-Al₂O₃ nano/micro composite by combining ball milling and stir casting technology. *Mater Des* 49:347–359. <https://doi.org/10.1016/j.matdes.2013.01.032>
40. Agrawal E, Tungikar V (2019) Study on tribological properties of Al-TiC composites by Taguchi method. *Mater Today Proc* 26(xxxx):2242–2247. <https://doi.org/10.1016/j.matpr.2020.02.486>
41. Shivaprakash YM, Gurumurthy BM, Siddhartha MA, Siddesh Kumar NM, Dutta A (2019) Studies on mild steel particulates reinforced Duralumin composite fabricated through Powder metallurgy route. *Int J Mech Prod Eng Res Develop* 9:2:903
42. Gowri Shankar MC, Shivaprakash YM, Siddesh Kumar NM, Siddhartha MA, Dutta A (2019) Experimental investigation on silicon carbide reinforced Duralumin based mmc produced by cold compacting. *Int J Mech Prod Eng Res Develop* 9(2):507–524

43. Siddesh Kumar NM, Shashank TN, Dhruthi (2021) Different ceramic reinforcements in aluminum metal matrix composites. *ECS J Solid State Sci Technol* 10
44. Kurbet R, Karthikreddy G, Monica J, Siddesh Kumar NM, Avinash M, Addamani R (2021) A review on friction stir welding over other welding techniques of aluminium alloys. *Solid State Technol* 64(2):3713–3729
45. Siddesh Kumar NM, Monica J, Karthik reddy G, Sadashiva M, Ganapathy B (2021) Comparative study on methods used to improve the corrosion resistance property of aluminum alloys-a review. *Solid State Technol* 64(1)
46. Sadadhiva MM, Yunus sheikh, Nouman Khan, Ramesh Kurbet, Devegowda TM (2021) A review on application of shape memory alloys. *A Rev Appli Shape Mem Alloy* 9(6)

Chapter 33

Preparation of Si-Graphite Composites as Anode Material in Li Ion Batteries



Kevin Vattappara, Sushmit Bhattacharjee, Yashdeep Srivastava,
Benson K. Money, and Parvati Ramaswamy

Abstract This research paper is based on reducing the particle size of submicron silicon by using low-cost size reduction method of ball milling (BM) and enhancing the electronic conductivity of finer silicon powder with the addition of nanographite platelets for anode materials synthesis for eventual use in batteries. Spray drying was employed for preparing silicon@C@graphite composites, using the ball-milled sub-micron silicon as precursor. Calcination of the spray-dried silicon-sucrose-graphite composites in inert atmosphere resulted in silicon@C@graphite powder with uniform consistency and morphology, as confirmed via particle size, scanning electron microscope (SEM) and X-ray diffraction (XRD) analysis. The electronic conductivity values show improvement from 10^{-7} S cm^{-1} for sub-microsilicon to 10^{-3} S cm^{-1} for the composite powder. Results are presented in the light of powder synthesis methods, structural phase, powder size and morphological analysis and electrical conductivity measurements.

Keywords Silicon · Graphite · Spray drying · Ball milling · Electronic conductivity

1 Introduction

In the past few decades, electrochemical batteries have paved the way for innovations such as mobiles, smartphones, tablets, laptops. Also, the battery market has been viewed to gain immense traction from the new wave of electric vehicles. Compared to

K. Vattappara · S. Bhattacharjee · P. Ramaswamy
Department of Mechanical and Automobile Engineering, School of Engineering and Technology,
CHRIST (Deemed to be University), Kengeri Campus, Bangalore 560074, India

Y. Srivastava
Department of Electrical and Electronics Engineering, School of Engineering and Technology,
CHRIST (Deemed to be University), Kengeri Campus, Bangalore 560074, India

B. K. Money (✉)
Department of Science and Humanities, School of Engineering and Technology, CHRIST
(Deemed to be University), Kengeri Campus, Bangalore 560074, India
e-mail: benson.money@christuniversity.in

IC engines, as more numbers of EV's are expected to hit the roads by 2040, the electric vehicles trend has become the newest catalyst for investigation in long-lasting, safer, compact, lightweight batteries [1–4]. Recommended as the most important component, lithium ion batteries (LiBs) introduction in the early 1990s has revolutionized the electronics market. LiBs promised higher energy density, better charge retention and cycling life as compared to lead acid and metal hydride batteries. The electrochemical performance of the LiBs is greatly determined by the electrode materials of batteries. Conventionally, the commercially available LiBs use graphite as the anode material which has a specific capacity of around 300 mAh/g. Graphite's high electronic conductivity allows the electrons from the external circuit to pass through it and recombine with Li ions easily allowing for higher power density. Whereas the energy density of the battery is limited by the relatively low specific capacity of graphite, this demands investigations into new anode materials with higher specific capacity.

Alloying-type materials such as silicon, germanium, magnesium offer higher specific capacity than intercalation-type materials, as they are able to hold more amount of Li by forming an alloy with lithium. These Li-mixed alloy anodes exhibit desirable properties such as preventing lithium dendrite growth, inhibiting interfacial reactions and enhancing the Coulombic efficiency (CE) as well as cycle life [5–7]. However, the presence of additional metals results in increased weight and volume and thus reduces the specific energy density as compared to the pure lithium or binary lithium alloy anodes. Silicon comes across as the most promising anode material as it offers a higher specific capacity of ~3600 mAh/g than most alloying-type materials. Also, silicon is one of the most abundant materials present on earth's crust which reduces the procurement costs and provides a sustainable solution [8–12].

However, the development of silicon as an anode material for commercial battery application, has been hampered by two of the major problems, i.e., (a) huge volumetric expansion and (b) low electronic conductivity. Silicon undergoes severe volumetric changes (upto 300%) under lithiation and delithiation with Li ion, resulting in pulverization of silicon particles in the anode. This leads to the deterioration of the anode as the pulverized silicon particles get separated from the bulk anode resulting in electronic isolation of silicon and therefore reduce the battery's capacity over time as the amount of silicon participating in charging and discharging process reduces over cycling [9]. Second, silicon is a semiconductor material, i.e., it has low electronic conductivity which hampers the rate at which the lithiation and delithiation occur and therefore result in reduced power density of the battery [11].

Appropriate processing of silicon is required to overcome the above-mentioned drawbacks before used in LiBs. The extent of pulverization and cracking of silicon particles due to volumetric changes is dependent on the particle size and morphology. It has been reported that below the critical particle size of 150 nm, the crystalline silicon particles do not crack or crumble under volumetric changes [8]. The specific surface area of silicon particles increases as the particle size decreases which allows for faster lithiation and delithiation. It is evident that smaller particle size is desirable for the anode material, making nano-silicon a preferred choice as a precursor, but the higher manufacturing cost results in increased cost of the nano-powder materials. To

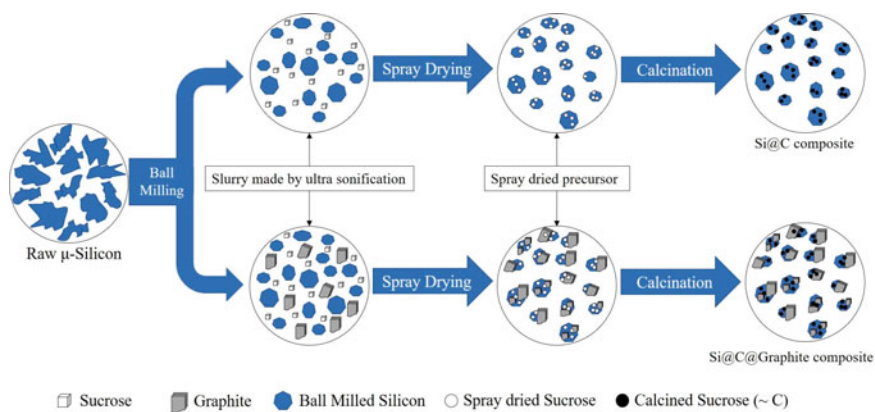


Fig. 1 Schematic illustration of the preparation of Si@C@Graphite

overcome this, several researchers have investigated sub-micron silicon powder as the precursor for the anode material, prepared from micro-silicon using various size reduction techniques [11].

Recently, the use of carbon and silicon composites with different morphologies such as spherical, yolk shell, has been investigated extensively in order to stabilize the volume expansion and hence to improve the electrochemical properties of silicon for anode applications [9–12]. Using spray drying technique, individual silicon particles are carbon-coated, to provide an electronic conductive network of carbon around silicon particles. The spherical carbon-coated silicon particles can also be wrapped with graphene sheets to further improve electronic conductivity to allow faster lithiation and delithiation [11, 12].

The present work mainly focuses on ball milling for size reduction of the micron size silicon particles and utilizing spray drying toward preparation of submicron silicon-based anode composites. Figure 1 shows the schematic illustration for the proposed work. The purpose of the current work is to ensure a balance between cost-effectiveness with scalability and improved electronic performance of the prepared composites.

2 Experimental

2.1 Material Preparation

Micron silicon was wet ball-milled using Retsch 4000 Planetary ball milling machine for 2, 4 and 6 h, respectively, to achieve sub-micron-sized silicon particles. In this work, wet ball milling was preferred over dry milling as wet milling requires less

energy, consumes less power and can achieve a higher degree of size reduction compared to dry milling [13].

The ball to powder was taken in the ratio of 10:1 by weight, and ethanol was used as the wet media. After each hour, the machine was stopped for 10 min to prevent cold welding of particles [14]. The powder solution obtained after ball milling was transferred to an open container and was dried at normal room temperature. The obtained powder was analyzed using SEM and particle size analyzer.

Spray drying was carried out by using a lab-scale spray dryer (Technosearch). Slurry for spray drying was prepared by using sucrose, silicon and graphite in the weight ratio of 15:10:2 [11]. The slurry was spray dried with a graphite to water ratio of 3 mg/ml. The inlet temperature was taken to be 220 °C. The pressure was set to 1.1 Bar. The spray-dried powders were heat-treated at 750 °C for 3h under Nitrogen atmosphere in a tube furnace to yield the silicon@C@graphite composite. For the purposes of comparison of electrical properties, silicon@C composite was also prepared using the same procedure. The sprayed particles were collected and characterized by using SEM, particle size analyzer, and XRD and the results obtained were analyzed.

2.2 Characterization

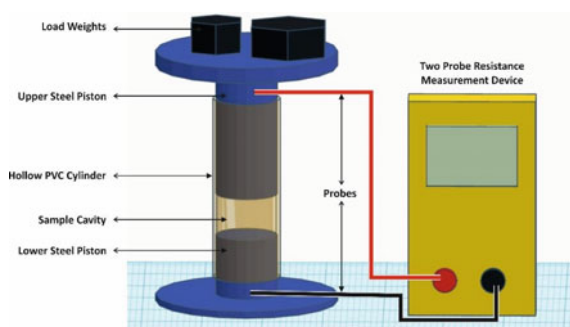
The X-ray diffraction patterns have been recorded for the investigated systems using a PANalytical X-ray diffractometer (X'pert Highscore plus) using Cu-K radiation ($\lambda = 1.5418 \text{ \AA}$) in the range 10–80° at a scanning rate of 2° per minute. The particle size was analyzed for as-received silicon powder and ball-milled silicon using a Particle Size Analyzer (Microtec Zetatrac) where the measurement principle is based on dynamic light scattering (DLS). The particle size analyzer measurement range is from 10 nm to 10 μm , and the statistical analysis of the particles size distribution was carried out using FLEX software. The morphology of the powders was observed by scanning electron microscope (SEM—TESCAN-VEGA3 LMU) at magnification of 10000X. The detector used was for secondary electrons (SE) at 25 kV with a working distance close to 5 mm.

2.3 Electrical Conductivity Measurements

The electronic conductivity of powdered materials mainly depends on two factors, i.e., the intrinsic electronic conductivity of individual grains and the contacts between the grains.

In order to measure conductivity of powdered materials, an adequate amount of pressure has to be applied to ensure proper electrical contact between particles and to prevent crushing of the composite particles [15]. The scheme of the setup used for this experiment is shown in Fig. 2. A hollow cylinder of PVC material with an inner

Fig. 2 Conductivity measurement setup



diameter of 10 mm is used to hold the sample. Two steel pistons of the same cross-sectional dimension are placed on the both ends of the cylinder. These pistons have two functions, first, to apply pressure on the sample and second to provide galvanic contacts for measuring the resistance of the sample. The sample is weighed and placed inside the cylinder along with the pistons; then, known pressure values in the range of 250–500 kPa are applied at the cross section of the sample. The height of the column of the sample powder is measured using a Vernier's calliper. The resistance offered by the probes and pistons can be assumed negligible when compared to that of the sample. The DC electronic conductivity of the sample is then calculated using the equation, with the height and the cross-sectional area of the powder column. The same steps were repeated for different samples.

$$\rho = \frac{A \times R}{L} \quad (1)$$

$$\sigma = \frac{1}{\rho} \quad (2)$$

where

- ρ is the resistivity of the sample,
- A is the cross-sectional area,
- L is the height of the powder column,
- σ is the electronic conductivity of the sample.

3 Results and Discussion

The XRD pattern for (a) as-received sub-microsilicon, (b) graphite, (c) sucrose, (d) spray-dried composite and (e) calcined composite is shown in Fig. 3. The diffraction peaks of the as-received silicon powder coincide well with pristine Si ($2\theta = 28.4^\circ, 47.3^\circ, 56.1^\circ, 69.1^\circ$ and 76.4°) (JCPDS No. 27–1402) [16]. The major peak for graphite was observed at $2\theta = 26.7^\circ$ [17]. In the spray-dried composite (shown

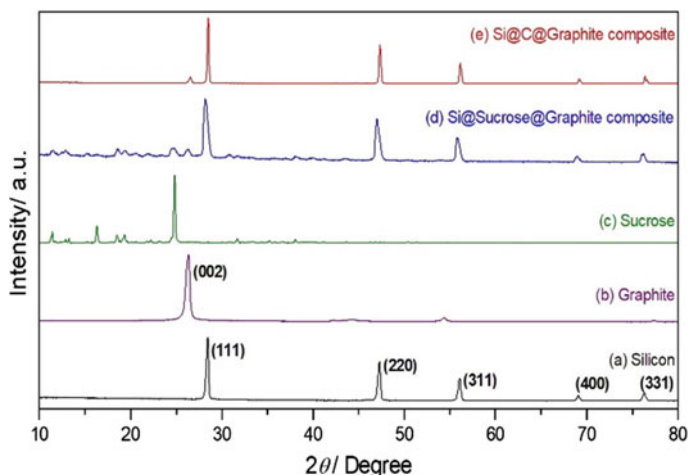


Fig. 3 X-ray diffraction pattern of **a** silicon, **b** graphite, **c** sucrose, **d** Si@sucrose@graphite composite, **e** Si@C@graphite composite

in Fig. 3e), there is no shift in the 2θ values (from Fig. 3a, b), which shows that the presence of graphite does not influence the crystal structure of silicon. There were no other peaks associated with impurities that can be seen in the XRD patterns.

Figure 4 shows the SEM micrographs of (a) as-received microsilicon (b) 2-h, (c) 4-h, and (d) 6-h ball-milled silicon. The micrographs depict a qualitative reduction in size of the as-received microsilicon. This particular result is further supported by particle size analysis (shown in Fig. 5).

The particle size analysis as shown in Fig. 5 provides a better understanding of the effect of ball milling time on the particle size distribution of the powder. The particle size distribution curve depicts a trend of size reduction in individual particles of the ball-milled powders as the ball milling time increases. The particle size distribution of the as-received submicron silicon is consistent with the observations in the SEM micrographs, with the highest percentage of particles that are found in the 1000–2000 nm range. The 2-h ball-milled sample shows minimal size reduction, but a significant amount of change in particle size distribution can be observed in the 4-h and 6-h ball-milled powders. The highest percentage of the particles for the 4-h and 6-h ball-milled powders is seen in the ranges of 400–800 nm and 200–400 nm, respectively. The average particle sizes for all the samples are shown in Table 1.

For the higher size ranges (Fig. 6a), there is a decreasing trend in the percentage of particles present, as we increase the ball milling time and for smaller size ranges this behavior gets reversed as shown in Fig. 6b.

The reduction in the particle size of silicon allows uniform distribution of carbon and graphite particles around individual silicon particles while spray drying. This ensures a uniform conductive network of carbon and graphite particles around the silicon particles and therefore should significantly increase the electronic conductivity of the prepared composite [10, 18, 19].

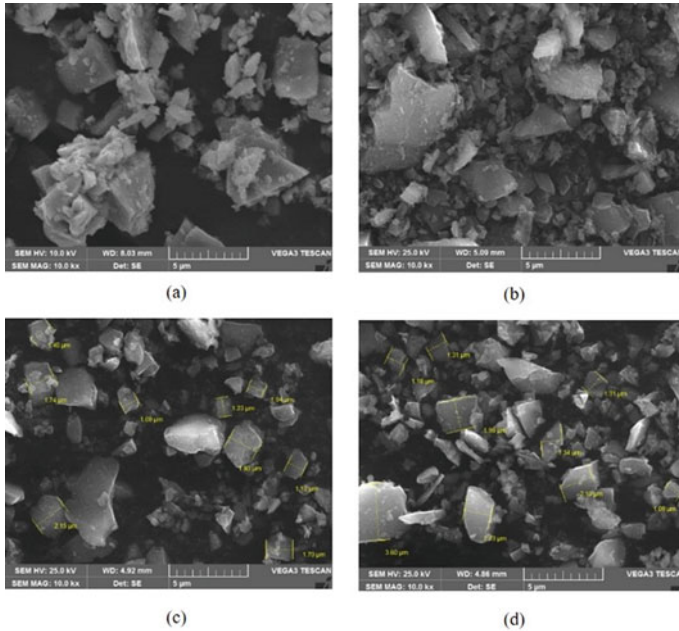


Fig. 4 SEM micrographs of **a** as-received submicron silicon, **b** 2-h BM silicon, **c** 4-h BM silicon, **d** 6-h BM silicon

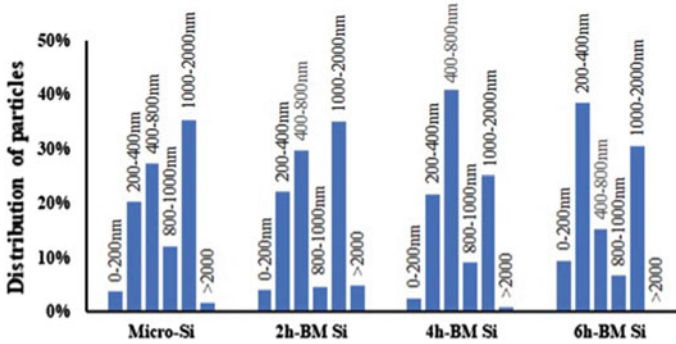


Fig. 5 Particle size distribution for as-received submicron silicon and ball-milled silicon powders

Table 1 Average size for as-received and ball-milled silicon

Specimen details	Average particle size (nm)
As-received sub-micron Si	~860
2-h ball-milled Si	~870
4-h ball-milled Si	~720
6-h ball-milled Si	~640

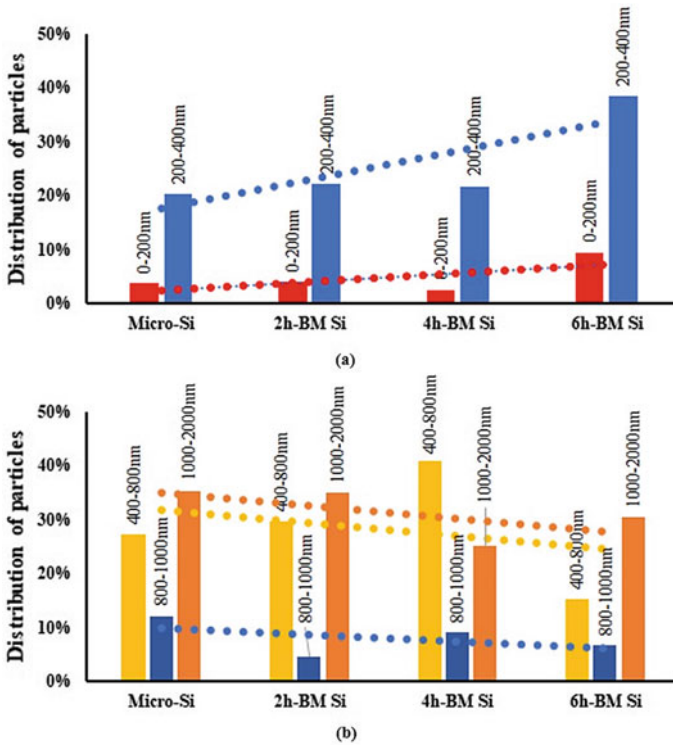


Fig. 6 Behavioral trends for the ball-milled silicon powder **a** bigger size classes, **b** lower size classes

The electronic conductivities of as-received submicron silicon and prepared composites were measured using the setup described in Sect. 2.3 and are shown in Fig. 7. The compact powder samples at medium pressure values of 250, 300 and 500 kPa ensure proper galvanic contact between each particle and also prevent

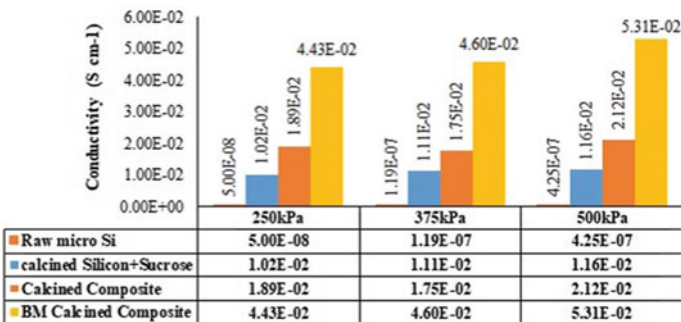


Fig. 7 Electronic conductivity measurements for as-received silicon and prepared composites

any morphological change of the prepared composite due to crushing of particles. The electronic conductivity for the as-received submicron silicon was measured to be in the order of 10^{-7} S cm⁻¹, which is consistent with the reported value [20]. A significant improvement in the measured electronic conductivity values of prepared composites was observed when compared to that of as-received submicron silicon. This occurs due to the coating of individual silicon particles with carbon and graphite during the spray drying process. Si@C@Graphite exhibits higher conductivity than Si@C due to the introduction of graphite particles into the composite. The 6-h ball-milled Si@C@Graphite exhibits superior conductivity among all the prepared composites, owing to its highly uniform network of conductive carbon particles, enabled by the small particle size of 6-h ball-milled silicon as predicted and discussed above. The spray-dried composites are seen to exhibit improved electronic conductivity compared to raw silicon. This requires further studies with electrochemical characterizations. The future work could also focus on morphological studies, surface modifications and using other dopants in graphite for the usage of Si@C@Graphite as anode material for use in Lithium ion batteries.

4 Conclusions

This study investigates a scalable and low-cost processing technique for Si@C@Graphite composite for battery anode applications. This process is initiated by the size reduction of submicron silicon by high-energy ball milling technique, followed by spray drying of sub-micron silicon, sucrose and graphite and further subjecting it to low-temperature reduction methods. Through these investigations the following conclusions can be made.

- (a) The effects of the ball milling time with respect to as-received commercial silicon powder in further reducing the particle size while maintaining uniform morphology were established. The increase in the duration of ball milling as expected decreased the particle sizes. A limitation with this method is the oxidation of silicon particles which can be overcome by carrying out the ball milling process under an inert atmosphere.
- (b) The spray drying of the constituents such as silicon, graphite and sucrose resulted in the formation of composite compositions, i.e., the individual silicon particles were overlaid with the dopants which were eventually calcined into Si@C@Graphite. Changes in parameters such as temperature, feed rate were found to influence the spray-dried powder characteristics.
- (c) Si@C@Graphite composite exhibited enhanced electrical conductivity compared with undoped silicon, thereby confirming the potential of spray drying method to process battery anode materials.

The two methods, i.e., ball milling and spray drying, used in this work for the preparation of the Si composite have their merits and limitations. The common merit for both the methods is the ease of scaling up to an industrial-level facility and the

low cost associated with it. Ball milling can be effectively utilized to reduce particle sizes to sub-micron and also to nanoscale. Spray drying can be utilized to prepare composites from the ball-milled raw materials with ease as compared to chemical synthesis routes such as sol-gel method. It is important to optimize the parameters for both ball milling and spray drying to carry out effective synthesis of composites for battery applications.

References

1. Fotouhi A, Auger DJ, Propp K, Longo S, Wild M (2016) A review on electric vehicle battery modelling: From Lithium-ion toward Lithium-Sulphur. *Renew Sustain Energy Rev* 56:1008–1021
2. Zhang Y, Li Y, Tao Y, Ye J, Pan A, Li X, Liao Q, Wang Z (2020) Performance assessment of retired EV battery modules for echelon use. *Energy* 193:116555
3. Zhu L, Xiong F, Chen H, Wei D, Li G, Ouyang C (2020) Thermal analysis and optimization of an EV battery pack for real applications. *Int J Heat Mass Transfer* 163:120384
4. Akinlabi AAH, Solyali D (2020) Configuration, design, and optimization of air-cooled battery thermal management system for electric vehicles: a review. *Renew Sustain Energy Rev* 125:109815
5. Wu Y, Yao Y, Wang L, Yu Y (2021) Recent progress on modification strategies of alloy-based anode materials for alkali-ion batteries. *Chem Res Chin Univ* 37:200–209
6. Ma W, Yin K, Gao H, Niu J, Peng Z, Zhang Z (2018) Alloying boosting superior sodium storage performance in nanoporous tin-antimony alloy anode for sodium ion batteries. *Nano Energy* 54:349–359
7. Kong LL, Wang L, Ni ZC, Liu S, Li GR, Gao XP (2019) Lithium–magnesium alloy as a stable anode for lithium–sulfur battery. *Adv Func Mater* 29:1808756
8. Ozanam F, Rosso M (2016) Silicon as anode material for Li-ion batteries. *Mater Sci Eng B* 213:2–11
9. Liu N, Wu H, McDowell MT, Yao Y, Wang C, Cui Y (2012) A yolk-shell design for stabilized and scalable Li-ion battery alloy anodes. *Nano Lett* 12:3315–3321
10. Ashuri M, He Q, Liu Y, Shaw LL (2020) Investigation towards scalable processing of silicon/graphite nanocomposite anodes with good cycle stability and specific capacity. *Nano Mater Sci* 2:297–308
11. Pan Q, Zuo P, Lou S, Mu T, Du C, Cheng X, Ma Y, Gao Y, Yin G (2017) Micro-sized spherical silicon@carbon@graphene prepared by spray drying as anode material for lithium-ion batteries. *J Alloy Compd* 723:434–440
12. Su M, Liu S, Tao L, Tang Y, Dou A, Lv J, Liu Y (2019) Silicon@ graphene composite prepared by spray-drying method as anode for lithium ion batteries. *J Electroanal Chem* 844:86–90
13. Fuerstenau D, Abouzeid A-Z (2002) The energy efficiency of ball milling in comminution. *Int J Miner Process* 67:161–185
14. Nilssen BE, Kleiv RA (2020) Silicon powder properties produced in a planetary ball mill as a function of grinding time, grinding bead size and rotational speed. *Silicon* 12:2413–2423
15. Celzard A, Marêché J, Payot F, Furdin G (2002) Electrical conductivity of carbonaceous powders. *Carbon* 40:2801–2815
16. Su M, Wang Z, Guo H, Li X, Huang S, Xiao W, Gan L (2014) Enhancement of the cyclability of a Si/Graphite@ Graphene composite as anode for Lithium-ion batteries. *Electrochim Acta* 116:230–236
17. Popova A (2017) Crystallographic analysis of graphite by X-ray diffraction. *Coke Chem* 60:361–365

18. Park J-H, Kang S-W, Kwon T-S, Park HS (2018) Spray-drying assisted synthesis of a Li₄Ti₅O₁₂/C composite for high rate performance lithium ion batteries. *Ceram Int* 44:2683–2690
19. Dhar S, Dash T, Palei B, Rout T, Biswal S, Mitra A, Sahu A (2020) Silicon-graphene composite synthesis: Microstructural, spectroscopic and electrical conductivity characterizations. *Mater Today Proc* 33:5136–5142
20. Neuberger M (1963) Silicon: electrical conductivity data sheets. HUGHES AIRCRAFT CO CULVER CITY CA

Chapter 34

Morphological, Spectroscopic, Structural and Electrical Properties of Mg⁺² Ion Conducting PMMA: PVDF-HFP Blend Polymer Electrolytes



A. Mallikarjun, M. Sangeetha, Maheshwar Reddy Mettu, M. Vikranth Reddy, M. Jaipal Reddy, J. Siva Kumar, and T. Sreekanth

Abstract Blended polymer electrolytes composed of (PMMA: PVDF-HFP) and Mg (ClO₄)₂ salt were prepared using the solution casting technique. The morphological, spectroscopic and structural changes were studied by scanning electron microscopy (SEM), Fourier transform infrared spectroscopy (FTIR) and X-ray diffraction (XRD) characterizations. SEM and XRD analysis reveal an increase in amorphous nature of (PMMA: PVDF-HFP) blended polymer with the incorporation of compatible concentration of Mg (ClO₄)₂ salt and a network of homogenous dark micro-pores initiates quick mobility of Mg-ions. Incorporation of various concentration ratios of (01wt, 02wt, 03wt) Mg (ClO₄)₂ salt, the diminished intensity of XRD peaks

A. Mallikarjun
Department of Physics, JNTUH, Kukatpally, Telangana, Hyderabad, India

Department of Physics, Vignana's Institute of Management and Technology for Women,
Telangana, Hyderabad, India

A. Mallikarjun
e-mail: mallikarjun.a@saimail.com

M. Sangeetha
Department of Physics, Guru Nanak Institutions Technical Campus, Ibrahimpatnam, Hyderabad,
India

M. Reddy Mettu · J. Siva Kumar (✉)
Department of Physics, Osmania University, Telangana, Hyderabad, India

M. Reddy Mettu
Department of Science and Humanities, Sreenidhi Institute of Science and Technology,
Telangana, Hyderabad, India

M. Vikranth Reddy
Nilima Organics Private Ltd., Plot No. 105 & 106, IDA Uppal, Hyderabad, India

M. Jaipal Reddy (✉)
Department of Physics, Palamuru University, Mahabubnagar, Telangana, India

T. Sreekanth
Department of Physics, JNTUH College of Engineering Jagtial, Jagtial, Telangana, India

that provokes an increase in the amorphous phase of the polymer blend composition ratio (07:03) (PMMA: PVDF-HFP). But for excess concentration (04wt) of salt reduced amorphosity and the smooth texture slightly becomes crystalline due to aggregation of excess salt on the surface of the polymer. The FTIR absorption peaks showed a shift of band of various functional groups to higher wavenumber and disappear of certain peaks manifests due to chemical interaction, proper blending and complexation of polymer–salt electrolytes. Electrical impedance spectroscopy (EIS) of polymer electrolytes attained the highest ionic conductivity of 1.89×10^{-4} S cm⁻¹ at room temperature for a compatible significant composition ratio of (07: 03: 03) (PMMA: PVDF-HFP: Mg(ClO₄)₂) polymer blend salt matrix and the results are corroborated with SEM, FTIR and XRD studies. Finally in this paper, it is observed that blending of two polymers and an appropriate optimum concentration of Mg (ClO₄)₂ salt to PMMA: PVDF-HFP blended polymer, reduced the crystallite size to a minimum value of 2.65672×10^{-9} nm which is the best compatibility to attain the highest ionic conductivity in solid polymer electrolytes.

Keywords Poly(vinylidene fluoride-hexafluoropropylene) · Scanning electron microscopy · X-ray diffraction · Fourier transform infrared spectroscopy · Electrical impedance spectroscopy · Poly(methylmethacrylate) · Solution casting technique

1 Introduction

Polymer electrolytes have been focused extensively due to their commercial usage in a variety of electrochemical devices such as rechargeable batteries, electrochemical cells, supercapacitors and sensors. In the emerging advanced technological applications, there is a huge demand of rechargeable battery systems of high specific energy density, high power, good electrode–electrolyte interface and high electrochemical stability. Even though Li-ion electrolytes are used in lithium-ion batteries, still there is a necessity to improve their physical, electrochemical and electrical properties [1]. In contrast to Li-ion batteries, Mg-ion rechargeable batteries had a wide range of applications because of its significant characteristics such as high safety, low cost, low toxic in nature, high stability, high melting point and high negative standard potential. Magnesium metal is the most abundant element than lithium metal has strong interaction with the polymer host and has good electrochemical stability, low interfacial impedance, good thermal stability and adequate mechanical properties. Few studies showed proper Mg salt complexation and transport in polymers employ Mg-ion polymer batteries. Researchers have synthesized and characterized different polymer–salt complexes to find a polymer electrolyte with adequate ionic conductivity and thermal stability at ambient and sub-ambient temperature [2]. Many polymers such as poly(ethylene oxide)(PEO), poly(methyl methacrylate) (PMMA), poly(vinyl pyrrolidone) (PVP), poly(acrylonitrile) (PAN),

poly(vinyl acetate) (PVAc), poly(vinylidene fluoride) (PVDF), and poly(vinylidene fluoride-co-hexafluoropropylene) (PVDF-HFP). It is studied that PVDF-HFP polymer has excellent properties such as semicrystalline nature, excellent thermal stability, good mechanical, wider electrochemical stability, high dielectric constant ($\epsilon = 8.4$), low glass transition temperature ($T_g = -62$ °C). More over, PMMA is blended to strengthen the mechanical integrity and chemical cross-linking of PMMA will increase the electrolyte solution retention ability of solid polymer electrolytes. In this part of the research, a polymer electrolyte of PMMA: PVDF-HFP with the variation of $\text{Mg}(\text{ClO}_4)_2$ was prepared and characterized to enhance potential ionic conductivity with thermal stability at ambient and sub-ambient temperature. PMMA and PVDF-HFP blending also enhances the polymer properties like thermal stability, mechanical strength and electrical stability. In $\text{Mg}(\text{ClO}_4)_2$, Mg^{+2} ions have the same surface area as compared with Li^+ ion. Hence, the addition of Mg salt in the blend (PMMA: PVDF-HFP) polymer complex manifests the thermal, electrical and mechanical stability of the polymer. There is a very high demand for complex polymer blends for its development in reusable electrical devices to meet the needs of present advanced technology. As a part of this, PVDF-HFP has good properties in terms of chemical, thermal stability, along with oxidation, UV resistant and good mechanical strength owing to the existence of “F” element in the host polymer chain. On the other hand, PMMA polymer has many advantages such as good optical properties, low molecular weight, good chemical resistant, good electrical compatibility, and when blended with PVDF-HFP improves mechanical stability, increases electrical and good Flory–Huggies interaction parameter which indicates free energy mixing [3]. The miscibility of two grains of different polymer to form homogeneous mixture enhances the amorphous nature and hence there is a progress in the characteristic properties of blended polymer electrolyte (PVDF-HFP:PMMA:Mg(ClO_4)₂). The proper miscibility may also lead to disassociation of $\text{Mg}(\text{ClO}_4)_2$ salt as Mg^{2+} & ClO_4^- ions and also attains the highest conductivity [2, 4–6]. Moreover, blend polymer electrolyte composed of (PMMA: PVDF-HFP) is expected to have good electrical conductivity and non-combustibility owing to the strong with drawing functional group (–C–F–) in VDF unit and plasticity due to steric hindrance provided by –CF₃– pendent group in HFP monomers. PVDF-HFP has both a crystalline phase due to VDF units and an amorphous phase due to its HFP monomer. The amorphous phase of PVDF-HFP facilitates the trapping of a large amount of liquid electrolyte providing mobility cations due to more free volume and hence helps in enhancing ionic conductivity, whereas the crystalline phase acts as structural support for the formation of free-standing polymer film. The blended polymer electrolytes PMMA:PVDF-HFP: $\text{Mg}(\text{ClO}_4)_2$ are characterized by XRD, FTIR, SEM, electrical impedance spectroscopy (EIS).

2 Experimental

2.1 Preparation of Solid Polymer Electrolytes

The preparation of (PMMA:PVDF-HFP: $\text{Mg}(\text{ClO}_4)_2$) solid polymer electrolytes is shown in Fig. 1. Poly(methyl methacrylate) (PMMA) of average molecular weight 1.2×10^5 /mol, (Aldrich, USA) and poly(vinylidene fluoride-hexa fluoropropylene) (PVDF-HFP) (Aldrich, USA) of average molecular weight 4×10^5 g/mol were dried at 70°C and $\text{Mg}(\text{ClO}_4)_2$, (Aldrich, USA) was dried at 100°C under vacuum conditions for about 8 h to eliminate moisture present in it. The anhydrous THF solvent (Merck) was used for the preparation of polymer electrolyte films by the solution casting technique. Initially a compatible concentration wt. ratio of (07:03) (PMMA:PVDF-HFP) two polymers are dissolved in THF for about 5 h and stirred continuously for about 10–12 h to get a uniform blended polymer solution. Now different concentration ratio of (01wt, 2wt, 3wt, 4wt) $\text{Mg}(\text{ClO}_4)_2$ salt is mixed in the desired concentration ratio of (07:03) (PMMA:PVDF-HFP) blended polymer. The mixture of blended polymer (PMMA: PVDF-HFP) and $\text{Mg}(\text{ClO}_4)_2$ salt solution is continuously stirred for 24 h at ambient temperature, so that a uniform polymer–salt electrolyte gel is formed. This homogenous solution is poured in Petri dishes and dried at 323 K (50°C) for 24 h in a controlled vacuumed oven. The nice dried blended

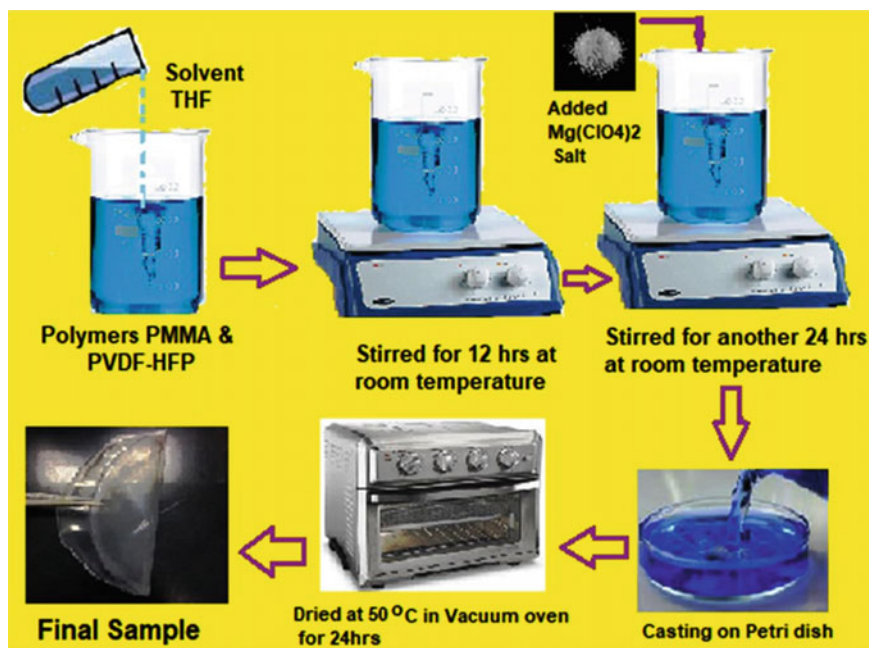


Fig. 1 Preparation of (PVDF-HFP: PMMA: $\text{Mg}(\text{ClO}_4)_2$) blended polymer–salt electrolytes

polymer–salt electrolyte films formed under this controlled vacuumed condition are preserved for various characterization.

2.2 Sample Characterization

Blended polymer–salt electrolyte samples of (PMMA: PVDF-HFP:Mg(ClO₄)₂) were sputtered with gold coating, and the surface morphology of the samples is examined under vacuum conditions by scanning electron microscopy with Carl Zeiss SEM. The SEM analysis clearly shows the microporous amorphous nature of the blended (PMMA:PVDF-HFP) polymer samples on the addition of Mg (ClO₄)₂ salt as shown in Fig. 2. XRD studies were carried with a PHILIPS X'pert diffractometer of an operating voltage 40 kV at the glancing angle ranging from $2\theta = 10^\circ$ to 80° . The effect of Mg (ClO₄)₂ salt diminishes the intensity of XRD peaks which illustrates the amorphosity of the blended polymer matrix. The FTIR transmittance band spectra of PMMA: PVDF-HFP:Mg(ClO₄)₂ polymer electrolytes were carried out to investigate the complexation behavior and the presence of functional groups with a Perking-Elmer spectrometer. The dissociation of Mg(ClO₄)₂ salt in PVDF-HFP polymer and the host polymer PMMA represents structural changes, ion mobility, a hoping mechanism in the polymer chain. The electrical impedance spectroscopic studies (EIS) are characterized with E4980A Precision LCR Meter. Blending of two polymers (PMMA: PVDF-HFP) with Mg(ClO₄)₂ salt affirms the interconnecting network of micro-pores of the polymer matrix which provides the favorable condition to absorb a good amount of electrolyte and faster ion mobility to enhance the dc and ac ionic conductivity of the polymer matrix.

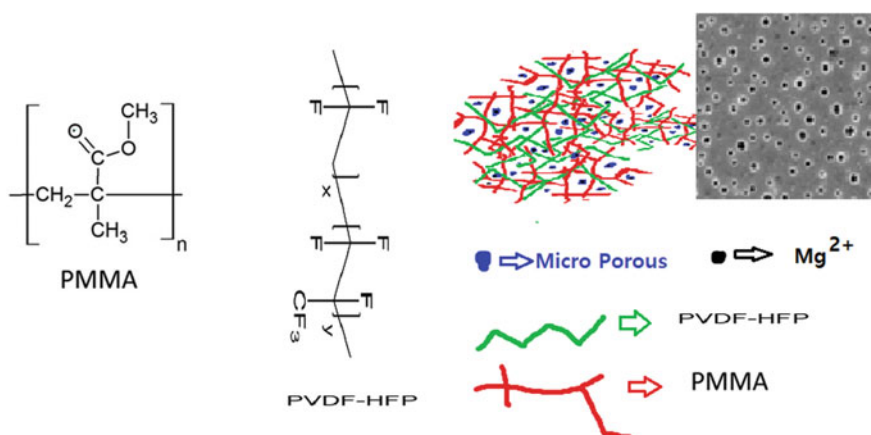


Fig. 2 Illustrates the blending of PMMA: PVDF-HFP with various concentration of Mg (ClO₄)₂ salt

3 Results and Discussion

3.1 SEM

The SEM micrographs of (PMMA: PVDF-HFP: $\text{Mg}(\text{ClO}_4)_2$) polymer films are shown in Fig. 3. The SEM images do not possess spherulites which discloses the amorphous nature of polymer electrolytes. As the concentration of salt increases, the porosity of polymer electrolyte gradually appears on the surface which favors increasing in its ionic conductivity. It is observed that for an optimum concentration of (07:03:03) (PMMA: PVDF-HFP: $\text{Mg}(\text{ClO}_4)_2$) polymer electrolyte, a large number of the interconnecting network of micro-pores as shown in Fig. 3f aids for the mobility of ions to enhance its ionic conductivity. Further higher concentration of salt fades the porous structure and the bright scratches of the polymer illustrate a slight increase in crystalline nature as shown in Fig. 3g. The blending of polymers PMMA: PVDF-HFP and $\text{Mg}(\text{ClO}_4)_2$ salt leads to good microporous structure as Mg-ion interacts with 'F' element of PVDF-HFP and 'O' element of PMMA with gradual evaporation of

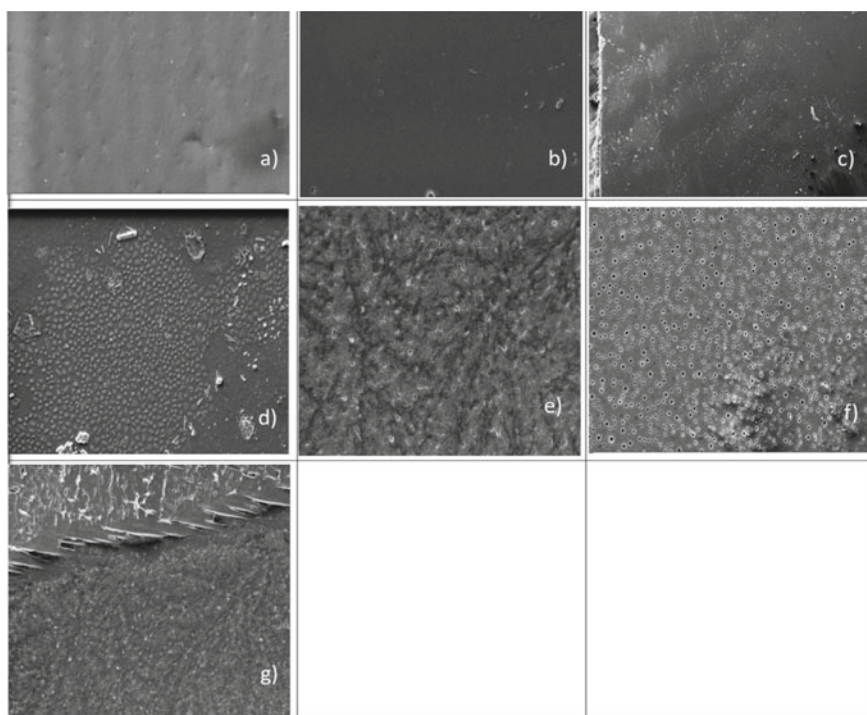


Fig. 3 SEM micrographs of **a** Pure PMMA, **b** Pure PVDF-HFP, **c** (07:03) PMMA: PVDF-HFP, **d** (07:03:01) PMMA: PVDF-HFP: $\text{Mg}(\text{ClO}_4)_2$, **e** (07:03:02) PMMA: PVDF-HFP: $\text{Mg}(\text{ClO}_4)_2$, **f** (07:03:03) PMMA: PVDF-HFP: $\text{Mg}(\text{ClO}_4)_2$, **g** (07:03:04) PMMA: PVDF-HFP: $\text{Mg}(\text{ClO}_4)_2$

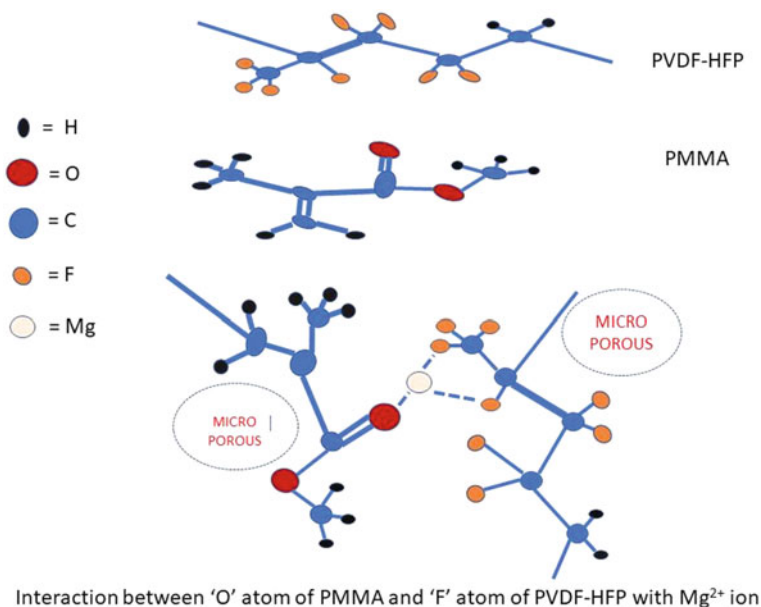


Fig. 4 Representation of interaction between 'O' atom of PMMA and 'F' atom of PVDF-HFP with Mg²⁺ ion

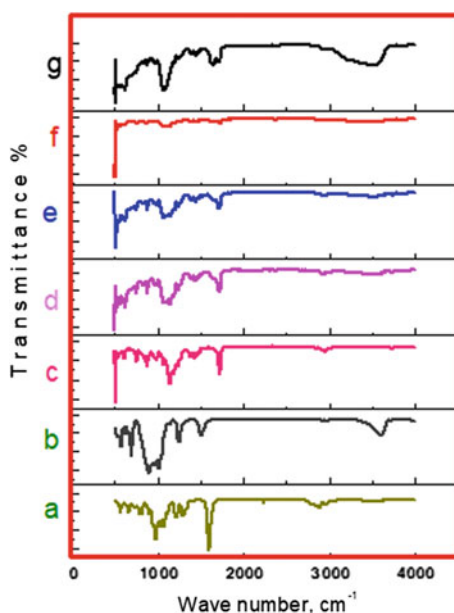
the solvent under vacuumed conditions as represented in Fig. 4. As the concentration of Mg (ClO₄)₂ increases the structural changes in polymer become compatible to ion migration and pore size is sufficient for ion mobility in the polymer electrolyte. The F atom in PVDF-HFP and O atom of PMMA may interact with interconnecting Mg-ion which acts as an electrolyte for conducting nature of the polymer. The interaction of Mg-ions also leads to the flexibility and the amorphous nature of polymer electrolytes. It is observed that there is no presence of lamellar structure in any of the polymer samples which strictly indicates perfect blending of PMMA and PVDF-HFP along with Mg (ClO₄)₂ salt [7]. Moreover, perfect blending and better microporous structure confirms good electrolyte absorption to obtain high ionic conductivity. This blended polymer is applicable in rechargeable batteries to enhance the power densities of energy storage systems. Also, the dark and smooth texture of micro-pores shows evidence of amorphous nature and capability of absorption of more electrolyte. The uniformity in the porous nature indicates proper evaporation of solvent at a constant rate without the intact of Mg-ion.

3.2 FTIR

FTIR spectroscopy is a powerful tool to study the structural details of material and to analyze the molecular interaction in polymer blend with the effect of salt. The individual behavior cannot be recognized in flawlessly blended polymer but the intricate behavior can be understood. The atomic and molecular interaction or chemical interaction may appear in band shifting, broadening and disappearance of FTIR absorption peak. The surrounding 483 cm^{-1} absorption peaks of PMMA and 484 cm^{-1} absorption peaks of PVDF-HFP disappears after blending. This is due to (a) the perfect miscibility of two polymers (b) dissociation of various concentrations of $\text{Mg}(\text{ClO}_4)_2$ salt attains the amorphous phase in the polymer. The peak at 658 cm^{-1} of PMMA and 689 cm^{-1} of PVDF-HFP represent α -phase of polymorphous nature of PVDF (Fig. 5).

The perfect incorporation of salt with blended polymers indicates a shift of peak to a low wavenumber 600 cm^{-1} and disappearance of 600 cm^{-1} peak indicate α -phase transition to δ -phase transition. The amorphous phase increases in blended polymers due to faster dissociation of Mg^+ and $(\text{ClO}_4)_2^-$ ions. The α , β , γ and δ polymorphous phases are the four types of phases. The amorphous phase is contributed by HFP units of PVDF-HFP polymer [8, 9]. Compatible blending of PVDF-HFP polymer with host polymer PMMA dissociation of $\text{Mg}(\text{ClO}_4)_2$ salt, affects the PVDF-HFP α polymorphous phase transition to δ polymorphous phase which is very close to amorphous nature. The δ polymorphous phase being polar due to the different order of the monomer dipole moments. A similar structural change for PVDF is expressed

Fig. 5 FTIR spectra of (a) Pure PMMA (b) Pure PVDF-HFP (c) (07:03) PMMA: PVDF-HFP (d) (07:03:01) PMMA: PVDF-HFP: $\text{Mg}(\text{ClO}_4)_2$ (e) (07:03:02) PMMA: PVDF-HFP: $\text{Mg}(\text{ClO}_4)_2$ (f) (07:03:03) PMMA: PVDF-HFP: $\text{Mg}(\text{ClO}_4)_2$ (g) (07:03:04) PMMA: PVDF-HFP: $\text{Mg}(\text{ClO}_4)_2$



in Sun et al. [9]. The absorption peak at 806 cm^{-1} of PMMA shifts to 717 cm^{-1} and disappears with a blending of PVDF-HFP polymer and with the addition of $\text{Mg}(\text{ClO}_4)_2$ salt. This influences symmetrical stretching of CH_3 and bending of CH_3 of PMMA [9]. The C-O-CH_3 rocking vibration at 806 cm^{-1} shifts and disappears which reveals proper blending and better incorporation of $\text{Mg}(\text{ClO}_4)_2$ salt in PVDF-HFP:PMMA confirming its amorphous nature. The shift and disappearance of vibration band from 745 cm^{-1} to 1159 cm^{-1} of pure PVDF-HFP indicates α to γ phase transition due to amalgamation of PMMA, PVDF-HFP and $\text{Mg}(\text{ClO}_4)_2$. And the vibration band of PMMA from 836 cm^{-1} to 1159 cm^{-1} belongs to the skeletal rocking of polymer backbone of -C-O-CH_3 and C-O-C symmetric stretching. The complete disappearance of this absorption band also indicates a more amorphous nature with the incorporation of $\text{Mg}(\text{ClO}_4)_2$ salt. It is evidence of higher dissociation of $\text{Mg}(\text{ClO}_4)_2$ salt. The dissociation of $\text{Mg}(\text{ClO}_4)_2$ scatters over and interconnecting polymer functional groups. Hence, the absorption peaks shift to higher wavenumber [9–11].

$$C = \vartheta \lambda \quad (1)$$

$$\omega = \frac{1}{\lambda} \quad (2)$$

ω wavenumber in cm^{-1}

λ wavelength of the infrared radiation

C velocity of infrared radiation

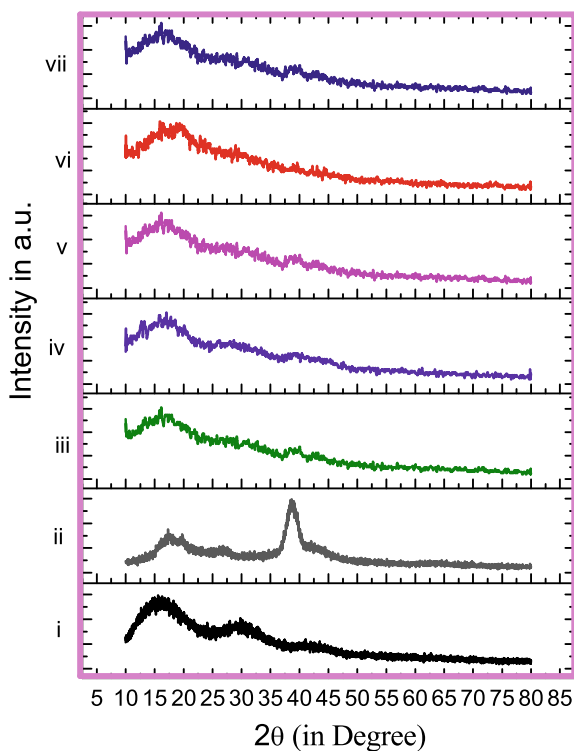
The FTIR absorption band of PMMA from 1159 cm^{-1} to 1248 cm^{-1} represents C-C-C and C-O symmetric stretching, respectively. The band at 1248 cm^{-1} to 1365 cm^{-1} is due to the C-O-C stretching of PMMA may be influenced by β -phase of PVDF polymorphous. The shift of 1248 cm^{-1} to 1365 cm^{-1} vibration band to higher wavenumber is due to stretching of a functional group because the degree of freedom of functional group decreases the frequency of vibration increases [9–14]. The absorption peak of PVDF-HFP at 1498 cm^{-1} represents CH_2 and 1069 cm^{-1} corresponds to C-C-C bending. These peaks gradually disappear while merging of PVDF-HFP with PMMA and dispersion of $\text{Mg}(\text{ClO}_4)_2$ salt. This can be seen in Fig. 5a–f. The peak at 1586 cm^{-1} of PMMA intended to get stabilized polymer by bending of C-H bonds in CH_3 . The C-H bond vibration in CH_3 is a sign of amorphous nature of PMMA [10–15]. But due to the blending of PVDF-HFP on the host polymer, PMMA shifts the peak to a higher wavenumber. The rise in the concentration of $\text{Mg}(\text{ClO}_4)_2$ salt to the blend polymer causes a shift to higher wavenumber and disappears of absorption peak. The shift and disappearance of absorption peaks are the evidence of complete disassociation of $\text{Mg}(\text{ClO}_4)_2$ salt and perfect blending of PMMA with PVDF-HFP. The absorption peaks at 2880 and 2939 cm^{-1} reveal aliphatic stretching vibration of CH_2 . These peaks also disappear for ample concentration of $\text{Mg}(\text{ClO}_4)_2$ salt disassociation.

3.3 XRD

The XRD spectra investigate structural changes of pure PMMA, pure PVDF-HFP and PMMA: PVDF-HFP:Mg(ClO₄)₂ (07:03:00, 07:03:01, 07:03:02, 07:03:03, 07:03:04) of polymer films. The XRD spectra of pure PMMA has three major peaks at different diffraction angles $2\theta = 15.92^\circ$, 29.38° and 30.75° , respectively. The broadening of these peaks may stand for the low degree of crystallinity in pure PMMA [16]. It reveals an increase in the amorphous nature of polymer with the incorporation of optimum concentration of Mg(ClO₄)₂ salt as shown in Fig. 6(vi). The gradual reduction and broadening of XRD peaks support proper structural changes which enhance ionic conductivity and mechanical properties [17]. The alignment of polymer chains at a specific distance is maintained by sufficient crystalline phase of polymer electrolyte. It also ropes to exchange strong interaction between the polymer [17].

The low crystalline phase interaction with polymer is shown in Fig. 9. The pure PMMA and pure PVDF-HFP crystallite size are almost similar to each other. It is observed that the crystallite size increases as the host polymer PMMA is blended with PVDF-HFP polymer. And by the addition of Mg(ClO₄)₂ salt to blended PMMA:PVDF-HFP polymer, it further increases from 3.03999×10^{-9} nm to 3.18022×10^{-9} nm.

Fig. 6 XRD diffraction pattern of (i) Pure PMMA (ii) Pure PVDF-HFP (iii) (07:03) PMMA: PVDF-HFP (iv) (07:03:01) PMMA: PVDF-HFP:Mg(ClO₄)₂ (v) (07:03:02) PMMA: PVDF-HFP: Mg(ClO₄)₂ (vi) (07:03:03) PMMA: PVDF-HFP: Mg(ClO₄)₂ (vii) (07:03:04) PMMA: PVDF-HFP: Mg(ClO₄)₂



But at an appropriate optimum concentration of $\text{Mg}(\text{ClO}_4)_2$ salt to PMMA: PVDF-HFP blended polymer, the crystallite size decreases to a minimum value of 2.65672×10^{-9} nm. The domination of polymer–polymer interaction over polymer–crystallite interaction results in low crystallite size. This size of crystallite is the best compatibility to attain the highest ionic conductivity in the polymer electrolyte. The optimum nanosize of crystallite is obtained for a concentration ratio of (07:03:03) (PMMA: PVDF-HFP: $\text{Mg}(\text{ClO}_4)_2$) blended polymer–salt electrolyte. Further addition of higher concentration of $\text{Mg}(\text{ClO}_4)_2$ salt in PMMA: PVDF-HFP blended polymer increases the crystallite size. Since the polymer–polymer interaction is less than the polymer–crystallite interaction that may lead to more crystallite nature which is not recommended for good ionic conductivity. The variation of crystallite size for different concentrations of $\text{Mg}(\text{ClO}_4)_2$ salt in blend polymer (PMMA: PVDF-HFP) is shown in Fig. 7.

In Fig. 8, the area under peak 1, peak 2 and peak 3 are calculated by linear curve fitting of XRD diffraction pattern for the various concentration of PMMA: PVDF-HFP: $\text{Mg}(\text{ClO}_4)_2$. It is observed that area of the three major XRD peaks 1, 2, 3 of pure PMMA (10:00:00) is found at $2\theta = 15.92^\circ$, 29.38° and 30.75° , respectively, and the area of these peaks 1, 2, 3 decreases with the addition of various composition ratio of pure PVDF-HFP polymer (00:10:00) and different concentrations of ($X = 1\text{wt}$, 2wt , 3wt , 4wt) $\text{Mg}(\text{ClO}_4)_2$ salt in (07: 03) concentration ratio of blended (PMMA: PVDF-HFP) polymer. The depression of the peak 1, peak 2 and peak 3 areas with a concentration of salt variation in the blended polymer is shown in Fig. 8. The

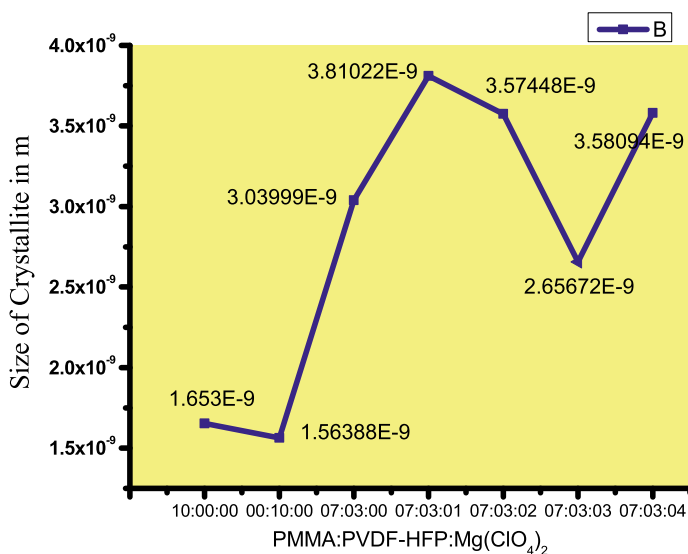


Fig. 7 Represents variation of crystallite size of pure PMMA polymer (10:00:00), pure PVDF-HFP polymer (00:10:00) and various concentrations of ($X = 1\text{wt}$, 2wt , 3wt , 4wt) $\text{Mg}(\text{ClO}_4)_2$ salt in (07: 03) concentration ratio of blended PMMA: PVDF-HFP polymer

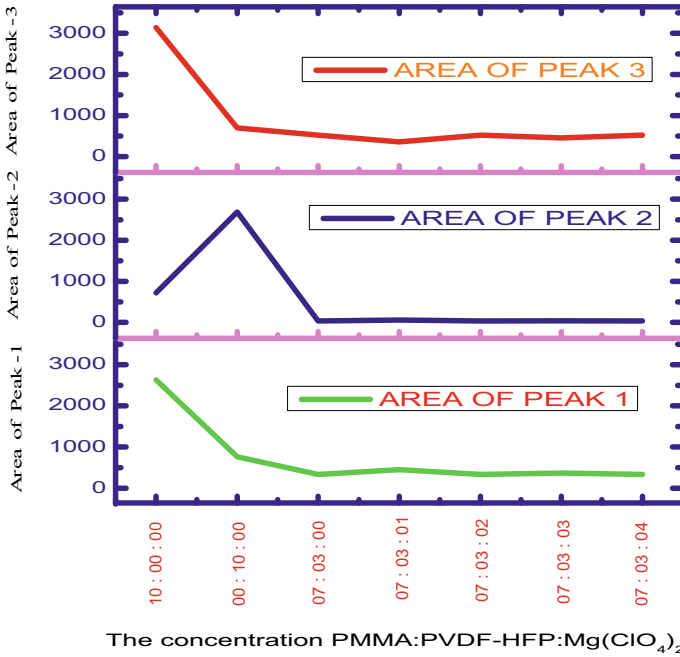


Fig. 8 Represents variation of area of the three major XRD peaks 1, 2, 3 of pure PMMA (10:00:00) at $2\theta = 15.92^\circ, 29.38^\circ$ and 30.75° with various composition of pure PVDF-HFP polymer (00:10:00) and various concentrations of ($X = 1\text{wt}, 2\text{wt}, 3\text{wt}, 4\text{wt}$) $\text{Mg}(\text{ClO}_4)_2$ salt in (07: 03) concentration ratio of blended PMMA: PVDF-HFP polymer

depression of the peaks area reveals an increase in the amorphous nature of polymer electrolytes. And it may initiate the best ionic conductivity of the polymer electrolytes (Fig. 9).

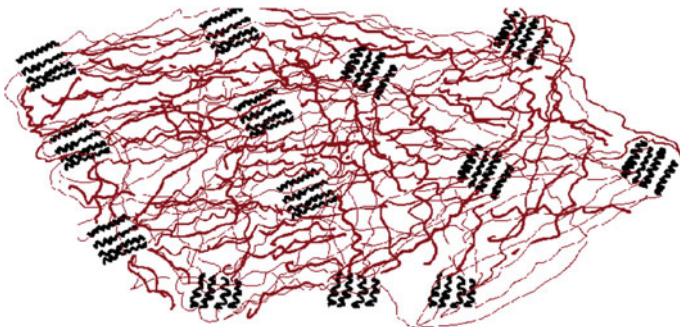


Fig. 9 Represents the supportive behavior of crystallites that favors the amorphous nature to attain high degree of polymer chain in polymer electrolyte

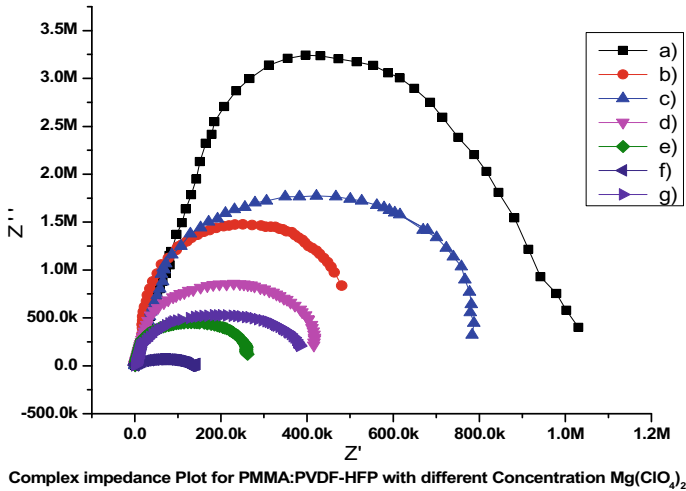


Fig. 10 Complex impedance plot of (a) Pure PMMA (b) Pure PVDF-HFP (c) (07:03) PMMA: PVDF-HFP (d) (07:03:01) PMMA: PVDF-HFP: $Mg(ClO_4)_2$ (e) (07:03:02) PMMA: PVDF-HFP: $Mg(ClO_4)_2$ (f) (07:03:03) PMMA: PVDF-HFP: $Mg(ClO_4)_2$ (g) (07:03:04) PMMA: PVDF-HFP: $Mg(ClO_4)_2$

3.4 Electrical Impedance Spectroscopic Studies (EIS)

The electrical impedance spectra of real Z' and imaginary Z'' part of impedance are recorded in Fig. 10. From electrical impedance spectra of individual polymer sample, bulk resistance R_b is measured to calculate the dc ionic conductivity using Eq. 3.

$$\sigma_{dc} = \frac{t}{AR_b} \quad (3)$$

The variation of dc ionic conductivity σ_{dc} with various concentrations of PMMA: PVDF-HFP: $Mg(ClO_4)_2$ salt is shown in Fig. 11.

The experimental results of dc ionic conductivity with the various compositions of blended (PMMA: PVDF-HFP) polymer and $Mg(ClO_4)_2$ salt are well correlated and confirmed with SEM, FTIR and XRD characterizations. In Fig. 10, pure host polymer PMMA has high impedance and low conductivity comparative to PVDF-HFP polymer, but it possesses feasible mechanical strength and flexibility which do not favor in various technical applications. Hence, to increase the good mechanical strength of PMMA, PVDF-HFP polymer is blended in PMMA to develop a significant polymer electrolyte. It is observed that with the blending of PMMA in PVDF-HFP, there is a slight increase of conductivity. But as the $Mg(ClO_4)_2$ salt concentration raises in PMMA:PVDF-HFP polymer, the conductivity increases gradually and attains the highest conductivity which is clearly shown in Fig. 11.

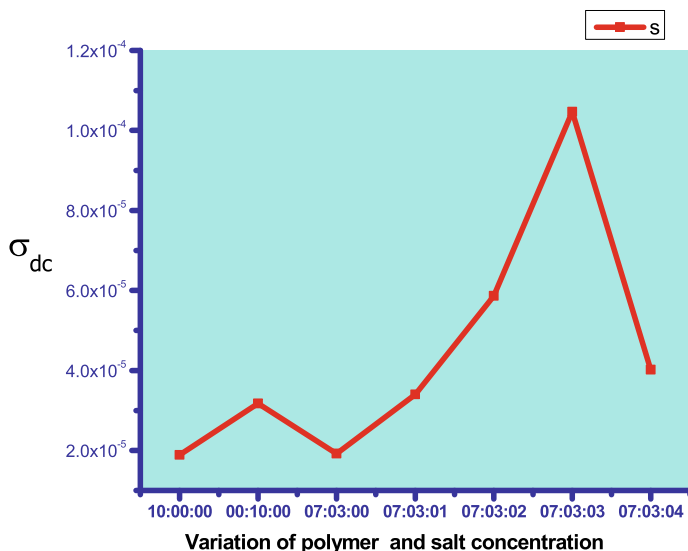


Fig. 11 Variation of dc ionic conductivity with different compositions of (PMMA: PVDF-HFP: Mg (ClO₄)₂) blended polymer–salt electrolytes

The highest conductivity of $1.89 \times 10^{-4} \text{ S cm}^{-1}$ is noted for a compatible concentration of (07:03:03) (PMMA:PVDF-HFP: Mg (ClO₄)₂) blended polymer–salt electrolyte. The mechanical strength of blended polymer PMMA: PVDF-HFP increases by the effect of PVDF crystalline phase transition in between α , β and γ phase of PVDF-HFP. The transition of α , β and γ may also lead to an increase amorphous nature in blended polymer electrolytes. The raising of Mg(ClO₄)₂ salt concentration may also increase the amorphous nature in the polymer blend, due to phase transitions in PVDF-HFP and stretching of the blended polymer chain. Hence, the (07:03:03) (PMMA:PVDF-HFP: Mg (ClO₄)₂) polymer electrolyte represents the highest conductivity and it is a compatible composition ratio for various technical applications. Further for the higher concentration of Mg (ClO₄)₂ salt in the polymer blend decreases the ionic conductivity to $4.196 \times 10^{-5} \text{ S cm}^{-1}$. It reveals the aggregation of Mg⁺ and (ClO₄)₂⁻ ions in the microporous structure which interconnects the network of polymer blend.

4 Conclusion

(PMMA: PVDF-HFP: Mg (ClO₄)₂) blended polymer–salt electrolyte films are synthesized by the solution casting technique method. The morphological (SEM) and structural (XRD) characterization conclude the formation of a sufficient number of the interconnected network of uniform-sized micro-pores for faster ion mobility,

absence of spherulites and dark smooth texture confirms increase in amorphous nature of (PMMA: PVDF-HFP) blended polymer with the incorporation of appropriate composition of Mg (ClO₄)₂ salt. The blended polymers find application in energy storage devices such as Mg⁺² ion rechargeable batteries to improve their energy power densities. The broadening of XRD peaks and decrease in the size of crystallites provokes an increase in the amorphous phase of polymer electrolyte. And drop in the area of three major peaks of host polymer PMMA with the addition of various composition ratio of PVDF-HFP polymer and Mg (ClO₄)₂ salt strictly results in the raise of the amorphous phase of polymer samples. FTIR spectroscopic studies manifest eminent interaction of the blended polymer with salt illustrates proper complexation, the phase transition of (PMMA: PVDF-HFP) with Mg (ClO₄)₂ and dissociation of salt results in the shift of peaks to higher wavenumber and disappearance of few peaks leads to the inference of amorphous nature of the polymer electrolyte. The incorporation of PVDF-HFP in the host PMMA improved the mechanical strength and flexibility. The electrical impedance spectroscopic studies (EIS) finally conclude enhancement in the dc conductivity of the blended (PMMA: PVDF-HFP) polymer for an appropriate optimum concentration of Mg (ClO₄)₂ salt and the highest conductivity of $1.89 \times 10^{-4} \text{ S cm}^{-1}$ is reported for a compatible concentration of (07:03:03) (PMMA:PVDF-HFP: Mg (ClO₄)₂) blended polymer–salt electrolyte. Moreover, the experimentally obtained results of ionic conductivity are well correlated and confirmed with SEM, FTIR and XRD studies.

References

1. Croce F, Sacchetti S, Scrosati B (2006) *J Power Sour* 162:685
2. Gebreyesus MA, Purushotham Y, Kumar JS (2016) Preparation and characterization of lithium ion conducting polymer electrolytes based on a blend of poly(vinylidene fluoride-co-hexafluoropropylene) and poly(methyl methacrylate). *Heliyon* 2(7):e00134. <https://doi.org/10.1016/j.heliyon.2016.e00134>
3. Aid S, Eddhahak A, Khelladi S, Ortega Z, Chaabani S, Tcharkhtchi A (2018) On the miscibility of PVDF/PMMA polymer blends: thermodynamics, experimental and numerical investigations. *Polym Testing* S0142941818306615. <https://doi.org/10.1016/j.polymertesting.2018.11.036>
4. Bellehumeur CT, Bisaria MK, Vlachopoulos J (1996) An experimental study and model assessment of polymer sintering. *Polym Eng Sci* 36:2198–2207
5. Bellehumeur CT, Kontopoulou M, Vlachopoulos J (1998) The role of viscoelasticity in polymer sintering. *Rheol Acta* 37:270–278
6. Ghosh S, Ohashi H, Tabata H, Hashimasa Y, Yamaguchi T (1995) Microstructural pore analysis of the catalyst layer in a polymer electrolyte membrane fuel cell: a combination of resin pore-filling and FIB/SEM. *Int J Hydrogen Energy* 40(45):15663–15671. <https://doi.org/10.1016/j.ijhydene.2015.09.080>
7. Pandey GP, Hashmi SA, Agrawal RC (2008) Hot-press synthesized polyethylene oxide based proton conducting nanocomposite polymer electrolyte dispersed with SiO₂ nanoparticles 179(15–16):543–549. <https://doi.org/10.1016/j.ssi.2008.04.006>
8. Sim LN, Majid SR, Arof AK (2012) FTIR studies of PEMA/PVdF-HFP blend polymer electrolyte system incorporated with LiCF₃SO₃ salt 58(none):57–66. <https://doi.org/10.1016/j.vibspec.2011.11.005>

9. Sun F-C, Dongare AM, Asandei AD, Pamir Alpay S, Nakhmanson S (2015) Temperature dependent structural, elastic, and polar properties of ferroelectric polyvinylidene fluoride (PVDF) and trifluoroethylene (TrFE) copolymers. *J Mater Chem C* 3(32):8389–8396. <https://doi.org/10.1039/C5TC01224D>
10. Huszank R, Szilágyi E, Szoboszlai Z, Szikszai Z (2018) Investigation of chemical changes in PMMA induced by 1.6 MeV He⁺ irradiation by ion beam analytical methods (RBS-ERDA) and infrared spectroscopy (ATR-FTIR). *Nuclear instruments and methods in physics research section B: beam interactions with materials and atoms* S0168583X18303240. <https://doi.org/10.1016/j.nimb.2018.05.016>
11. Bournel F, Laffon C, Parent Ph (1996) G Tourillon Adsorption of some substituted ethylene molecules on Pt (111) at 95 K II. A FT-RAIRS study. 359(1–3):16. [https://doi.org/10.1016/0039-6028\(96\)00024-6](https://doi.org/10.1016/0039-6028(96)00024-6)
12. Zheng X-F, Lian Q, Yang H, Wu H-X, Cheng C, Yin G, Zhang W (2016) Preparation and characterization of temperature-memory nanoparticles of MIP-CS-g-PMMA. *RSC Adv* 6(112):110722–110732. <https://doi.org/10.1039/C6RA22730A>
13. Buckley J, Cebe P, Cherdack D et al (2006) Nanocomposite of poly (vinylidene fluoride) with organically modified silicate. *Polymer* 47:11
14. Sahoo G, Sarkar N, Sahu D, Swain SK (2017) Nano gold decorated reduced graphene oxide wrapped polymethylmethacrylate for supercapacitor applications. *RSC Adv* 7(4):2137–2150. <https://doi.org/10.1039/C6RA26930C>
15. Soman VV, Kelkar DS (2009) FTIR studies of doped PMMA—PVC blend system. *Macromol Symp* 277(1):152–161. <https://doi.org/10.1002/masy.200950319>
16. Shahzada A, Sharif A, Agnihotry SA (2007) Synthesis and characterization of insitu prepared poly (methyl methacrylate) nanocomposites 30(1):31–35. <https://doi.org/10.1007/s12034-007-0006-9>
17. Worgull M (2009) Hot embossing molding materials for hot embossing 57–112. <https://doi.org/10.1016/b978-0-8155-1579-1.50009-4>
18. Ganta KK, Jeedi VR, Vijaya Kumar K, Laxmi Narsaiah E (2020) *International journal of polymer analysis and characterization*. Taylor & Francis. <https://doi.org/10.1080/1023666X.2020.1860396>
19. Choe HS et al (1995) *Electrochim Acta* 40:2289

Chapter 35

Modelling of Acetaminophen Removal from Wastewater Using Response Surface Methodology



P. Varshini, P. Chinnaiyan , K. Abinaya, R. Karthikeyan, and V. Manirajasekaran

Abstract Sewage sludge and wastewater from urban areas are usually filled with various forms of environmental/emerging contaminants which include personal care products (PPCPs) and pharmaceuticals, pesticides, manufactured nanomaterials, heavy metals, pathogens, surfactants and metalloids (Sarkar et al. in *Industrial and municipal sludge: emerging concerns and scope for resource recovery*. Elsevier, pp. 553–571, 2019, [1]). Newly located/discovered groups of chemicals found in groundwater or surface water are termed as contaminants of emerging concern or in other words emerging contaminants. Pharmaceutical chemicals are widely present in water and wastewater effluents (Stefanakis and Becker in *A review of emerging contaminants in water: classification, sources, and potential risks*, 2015, [2]). These pharmaceutical chemicals are traced commonly in natural wastewater bodies and sometimes even in drinking water, have high toxicity and are non-biodegradable substances (Kanakaraju et al. in *J Environ Manage* 1:189–207, 2018, [3]). It vividly leads to many health compromises, diseases and environmental risks which are drastic and not adaptable. The existence of active pharmaceutical ingredients (APIs) in water bodies in recent years has led to a rapid expansion in the field of examining environmental contaminants existence (Daughton and Brooks in *Environ Contam Biota Interpreting Tissue Concentrations* 281–341, 2011, [4]). These pharmaceuticals have their own characteristics which cannot be altered by other chemical organic contaminants. Hence, they fall under a unique category of pollutants (Fatta-Kassinos et al. in *Anal Bioanal Chem* 399:251–275, 2011, [5]). These pharmaceuticals are very well tackled by the advanced oxidation process. Many processes are being adopted for removing pharmaceutical contaminants such as electrochemical oxidation, sonolysis, photo-Fenton, radiation and ozonation (Kanakaraju et al. in *J Environ Manage* 1:189–207, 2018, [3]). The study concentrates on modelling the removal of pharmaceutical contaminants using response surface methodology with the help of Minitab software.

Keywords Emerging contaminants · Acetaminophen · Response surface methodology

P. Varshini · P. Chinnaiyan (✉) · K. Abinaya · R. Karthikeyan · V. Manirajasekaran
Department of Civil Engineering, Amrita School of Engineering, Coimbatore, India
e-mail: c_prakash@cb.amrita.edu

1 Introduction

The increase in the industries and hospitals has caused disastrous damage to the water bodies. The release of hospital wastewater contains a high amount of pharmaceutical contaminants which cause damage to the aquatic organisms as well as human beings in either perspective. The concentrations of emerging contaminants range from $\mu\text{g/L}$ to a few ng/L which are widely present in the environment which includes sewage water, groundwater and surface water [6]. Acetaminophen is the major constituent compound in paracetamol. Paracetamol is a type of analgesic which mitigates pain and helps in reducing fever [7]. It is one of the world's widely consumed analgesics. In certain areas, paracetamol is referred to as acetaminophen. On the basis of our strong analysis and reference of certain literature papers based on removal of acetaminophen, we preferred to follow advanced oxidation process in our study. Advanced oxidation processes (AOPs), in a broad sense, include a chemical process which is meant to remove organic materials in water and wastewater through an oxidation process with hydroxyl radicals [8–10]. This process contains ozone, hydrogen peroxide and UV light in real applications to treat wastewater. The parameters considered for the study include reaction time ranging between 15 and 60 min, pH ranging between 3 and 11, acetaminophen initial concentration ranging from 20 to 50 mg/L and concentration of catalyst, i.e. TiO_2 and H_2O_2 , ranging between 5 and 15 mg/L. DoE was used for designing the experiment. The data obtained from literature papers were utilized for executing the regression analysis with the help of Minitab software. Response surface methodology was performed for regression analysis. With the help of Minitab software, an empirical equation has been generated correlating the parameters chosen in the study and removal of acetaminophen [11].

2 Methodology

Removal efficiency of acetaminophen through advanced oxidation process from water/wastewater has been explored in this study by comprehending the data researched from various literature papers. Four parameters were taken into consideration for this study which are pH from 3 to 11, reaction time in the span of 15 to 60 min, concentration of catalyst, i.e. TiO_2 and H_2O_2 , ranging from 5 to 10 mg/L and concentration of acetaminophen at initial varying from 20 to 50 mg/L [12]. Experiment was designed using design of experiment (DoE). The Minitab software is adopted for generating the regression analysis using the comprehended data provided. To model and optimize the parameters involved, response surface methodology (RSM) was used [13]. The response surface design was analysed, and the following tables and regression equations (Eqs. 1 and 2) show the parameters involved in the design. The coefficients and P values (in the range 0–1) of various terms are shown in Tables 1 and 3 for catalysts TiO_2 and H_2O_2 , respectively. The design was further fine-tuned

Table 1 Coded coefficient table for TiO₂ catalyst

Term	Coef.	SE coef.	T-value	P-value	VIF
Constant	59.62	2.73	21.83	0	
ACT Conc. (mg/L)	-6.17	2.11	-2.92	0.01	1
pH	-0.72	2.11	-0.34	0.736	1
Time (min)	4.33	2.11	2.05	0.057	1
Catalyst Conc. (mg/L)	4.89	2.07	2.36	0.031	1.01
ACT Conc. (mg/L) * ACT Conc. (mg/L)	-3.25	5.46	-0.59	0.561	2.81
pH * pH	-6.25	5.46	-1.14	0.27	2.81
Time (min) * Time (min)	7.25	5.46	1.33	0.203	2.81
Catalyst Conc. (mg/L) * Catalyst Conc. (mg/L)	-9.74	4.89	-1.99	0.064	2.2
ACT Conc. (mg/L) * pH	1.12	2.24	0.5	0.622	1
ACT Conc. (mg/L) * Time (min)	-0.13	2.24	-0.06	0.956	1
ACT Conc. (mg/L) * Catalyst Conc. (mg/L)	-0.37	2.24	-0.17	0.869	1
pH * Time (min)	1.63	2.24	0.73	0.478	1
pH * Catalyst Conc. (mg/L)	0.12	2.24	0.06	0.956	1
Time (min) * Catalyst Conc. (mg/L)	0.38	2.24	0.17	0.869	1

with respect to the *P*-values such that the terms with *P*-value less than 0.1 were considered for the design and the other terms were neglected as shown in Tables 2 and 4 for catalysts TiO₂ and H₂O₂, respectively.

Regression equation for TiO₂ catalyst:

$$\begin{aligned} \text{ACT removal (\%)} = & 11.4 + 0.53 \text{ ACT Conc (mg/L)} + 3.89 \text{ pH} - 1.029 \text{ Time (min)} \\ & + 8.78 \text{ Catalyst Conc (mg/L)} - 0.0144 \text{ ACT Conc (mg/L)} \\ & * \text{ACT Conc (mg/L)} - 0.390 \text{ pH} * \text{pH} + 0.0143 \text{ Time (min)} \\ & * \text{Time (min)} - 0.390 \text{ Catalyst Conc (mg/L)} \\ & * \text{Catalyst Conc (mg/L)} + 0.0188 \text{ ACT Conc (mg/L)} * \text{pH} \\ & - 0.00037 \text{ ACT Conc (mg/L)} * \text{Time (min)} \end{aligned}$$

Table 2 Coded coefficient table for TiO₂ catalyst after fine tuning

Term	Coef.	SE coef.	T-value	P-value	VIF
Constant	58.86	2.36	24.91	0	
ACT Conc. (mg/L)	-6.17	1.86	-3.32	0.003	1
Time (min)	4.33	1.86	2.33	0.028	1
Catalyst Conc. (mg/L)	4.69	1.82	2.58	0.016	1.01
Time (min) * Time (min)	2.33	3.86	0.6	0.022	1.82
Catalyst Conc. (mg/L) * Catalyst Conc. (mg/L)	-12.84	3.91	-3.28	0.003	1.81

Table 3 Coded coefficients for H₂O₂ catalyst

Term	Coef.	SE coef.	T-value	P-value	VIF
Constant	45.7	2.88	15.88	0	
ACT Conc. (mg/L)	-6	2.29	-2.62	0.018	1
pH	-1.22	2.29	-0.53	0.6	1
Time (min)	3.44	2.29	1.51	0.152	1
Catalyst Conc. (mg/L)	3.33	2.29	1.46	0.164	1
ACT Conc. (mg/L) * ACT Conc. (mg/L)	0.14	6.02	0.02	0.982	2.91
pH * pH	-7.86	6.02	-1.3	0.21	2.91
Time (min) * Time (min)	8.14	6.02	1.35	0.195	2.91
Catalyst Conc. (mg/L) * Catalyst Conc. (mg/L)	-9.86	6.02	-1.64	0.121	2.91
ACT Conc. (mg/L) * pH	0.19	2.43	0.08	0.939	1
ACT Conc. (mg/L) * Time (min)	0.81	2.43	0.33	0.742	1
ACT Conc. (mg/L) * Catalyst Conc. (mg/L)	-0.94	2.43	-0.39	0.704	1
pH * Time (min)	2.06	2.43	0.85	0.408	1
pH * Catalyst Conc. (mg/L)	0.06	2.43	0.03	0.98	1
Time (min) * Catalyst Conc. (mg/L)	0.44	2.43	0.18	0.859	1

Table 4 Coded coefficients for H₂O₂ catalyst after fine tuning

Term	Coef.	SE coef.	T-value	P-value	VIF
Constant	45.02	2.46	18.32	0	
ACT Conc. (mg/L)	-6	2	-3	0.006	1
Time (min)	3.44	2	1.72	0.098	1
Catalyst Conc. (mg/L)	3.33	2	1.67	0.098	1
Time (min) * Time (min)	4.87	4.56	1.07	0.295	2.18
Catalyst Conc. (mg/L) * Catalyst Conc. (mg/L)	-13.13	4.56	-2.88	0.008	2.18

$$\begin{aligned}
& - 0.0050 \text{ ACT Conc (mg/L) * Catalyst Conc (mg/L)} \\
& + 0.0181 \text{ pH * Time (min) + 0.006 pH * Catalyst Conc (mg/L)} \\
& + 0.0033 \text{ Time (min) * Catalyst Conc (mg/L)}. \quad (1)
\end{aligned}$$

Regression equation for H₂O₂ catalyst:

$$\begin{aligned}
\text{ACT removal (\%)} = & 16.6 - 0.43 \text{ ACT Conc (mg/L) + 5.57 pH - 1.337 Time (min)} \\
& + 8.82 \text{ Catalyst Conc (mg/L) + 0.0006 ACT Conc (mg/L)} \\
& * \text{ACT Conc (mg/L) - 0.491 pH * pH + 0.0161 Time (min)} \\
& * \text{Time (min) - 0.394 Catalyst Conc (mg/L)} \\
& * \text{Catalyst Conc (mg/L) + 0.0031 ACT Conc (mg/L) * pH}
\end{aligned}$$

Table 5 DoE observed data for the ACT removal for TiO₂ and H₂O₂ catalyst [16–18]

ACT Conc. (mg/L)	pH	Reaction time (min)	Catalyst conc. (mg/L)	ACT removal efficiency % employing TiO ₂	ACT removal efficiency % employing H ₂ O ₂
35	7	37.5	5	46	36
20	11	60	15	67	52
35	7	37.5	5	48	38
50	3	60	5	41	31
50	3	15	15	39	25
35	7	37.5	10	56	46
35	7	37.5	10	61	47
50	7	37.5	10	44	34
50	11	15	5	34	22
35	7	15	10	51	41
35	7	37.5	10	57	42
20	3	15	15	69	59
50	3	15	5	37	32
20	3	15	5	46	36
50	11	15	15	48	33
50	3	60	15	53	43
35	7	37.5	10	68	53
35	7	37.5	10	70	61
35	3	37.5	10	49	34
20	11	60	5	50	40
20	3	60	5	51	38
35	7	60	10	83	68
50	11	60	5	37	21
20	3	60	15	56	41
20	7	37.5	10	69	59
35	11	37.5	10	58	43
20	11	15	5	42	32
35	7	37.5	15	51	35
35	7	37.5	10	45	31
50	11	60	15	49	35
20	11	15	15	43	33

$$\begin{aligned}
 &+ 0.00241 \text{ ACT Conc (mg/L)} * \text{Time (min)} \\
 &- 0.0125 \text{ ACT Conc (mg/L)} * \text{Catalyst Conc (mg/L)} \\
 &+ 0.0229 \text{pH} * \text{Time (min)} + 0.003 \text{ pH} * \text{Catalyst Conc (mg/L)} \\
 &+ 0.0039 \text{Time (min)} * \text{Catalyst Conc (mg/L)}. \quad (2)
 \end{aligned}$$

With the help of Minitab software, an empirical equation has been generated correlating the parameters chosen in the study and removal of ACT after fine tuning the P value of terms involved (Eqs. 3 and 4) [14, 15].

3 Results and Discussion

3.1 Removal of ACT

The results observed from the literature papers and the criteria varying through the design of experiment are shown in Table 1. With the previous results obtained, analysis was performed with the help of Minitab software and equations obtained are presented in Eqs. 1 and 2 for TiO_2 and H_2O_2 catalysts, respectively. The elimination of ACT varied between 83 and 34% for TiO_2 , and for H_2O_2 , the ACT elimination differs between 68 and 22% for the different combinations of the chosen four parameters in the analysis.

Equation 1 (TiO_2):

$$\begin{aligned}
 \text{ACT removal (\%)} &= 11.8 - 0.411 \text{ ACT Conc (mg/L)} \\
 &- 0.152 \text{Time (min)} + 11.21 \text{Catalyst Conc (mg/L)} \\
 &+ 0.00460 \text{Time (min)} * \text{Time (min)} \\
 &- 0.514 \text{Catalyst Conc (mg/L)} * \text{Catalyst Conc (mg/L)}. \quad (3)
 \end{aligned}$$

Equation 2 (H_2O_2):

$$\begin{aligned}
 \text{ACT removal (\%)} &= 7.6 - 0.400 \text{ ACT Conc (mg/L)} \\
 &- 0.569 \text{Time (min)} + 11.17 \text{Catalyst Conc (mg/L)} \\
 &+ 0.00962 \text{Time (min)} * \text{Time (min)} \\
 &- 0.525 \text{Catalyst Conc (mg/L)} * \text{Catalyst Conc (mg/L)}. \quad (4)
 \end{aligned}$$

3.2 Removal of ACT for Variation in Concentration of ACT and Catalysts TiO_2 and H_2O_2

The impact of different parameters on the removal of ACT (Fig. 1a, b) infers the response surface plots (RSPs) derived from Eqs. 1 and 2 from Minitab software. By analysing the response surface plots obtained (Fig. 1a, b), it can be observed that the removal of ACT is driven by the factors such as concentration of ACT, TiO_2 and H_2O_2 . From the response surface plots, maximum removal percentage of ACT is observed at low concentration of ACT and high concentration of photocatalysts TiO_2 and H_2O_2 . Maximum removal of ACT of around 60–70% was noticed when the concentration of TiO_2 is 7.5–14 mg/L and around 45–55% with H_2O_2 concentration of 20–35 mg/L. Hence, the highest removal of ACT is observed to be 70% with TiO_2 catalyst comparatively. The RSP shows that TiO_2 shows higher removal compared to H_2O_2 which has a removal efficiency of 55%. As the concentration of contaminant increases to 50 mg/L, removal of ACT decreases to 35% for TiO_2 catalyst and 22% for H_2O_2 catalyst.

3.3 Removal of ACT for Variation in Concentration of ACT and Reaction Time

The impact of different parameters on the removal of ACT (Fig. 2a, b) infers the response surface plots (RSPs) derived from Eqs. 1 and 2 from Minitab software. By analysing the response surface plots obtained (Fig. 2a, b), it can be observed that the removal of ACT is driven by the factors such as concentration of ACT and reaction time. For TiO_2 catalyst, it is seen that the removal efficiency increases with respect to an increase in reaction time for lower concentration of acetaminophen. But on the contrary for H_2O_2 catalyst, the ACT removal efficiency is seen to be decreasing up to a reaction time of 40 min and then steadily increasing till 60 min.

3.4 Removal of ACT for Variation in Reaction Time and Concentration of Catalyst, i.e. TiO_2 and H_2O_2

The impact of different parameters on the removal of ACT (Fig. 3a, b) infers the response surface plots (RSPs) derived from Eqs. 1 and 2 from Minitab software. By analysing the response surface plots obtained (Fig. 3a, b), it can be observed that the removal of ACT is driven by the factors such as reaction time and concentration of catalyst, i.e. TiO_2 and H_2O_2 . For TiO_2 catalyst, from RSP it is inferred that high removal efficiency of ACT falls between reaction time in the range 40–60 min and catalyst concentration in the range 7.5–14 mg/L. For H_2O_2 catalyst, from RSP it is inferred that removal efficiency of ACT falls between reaction time up to 20 min

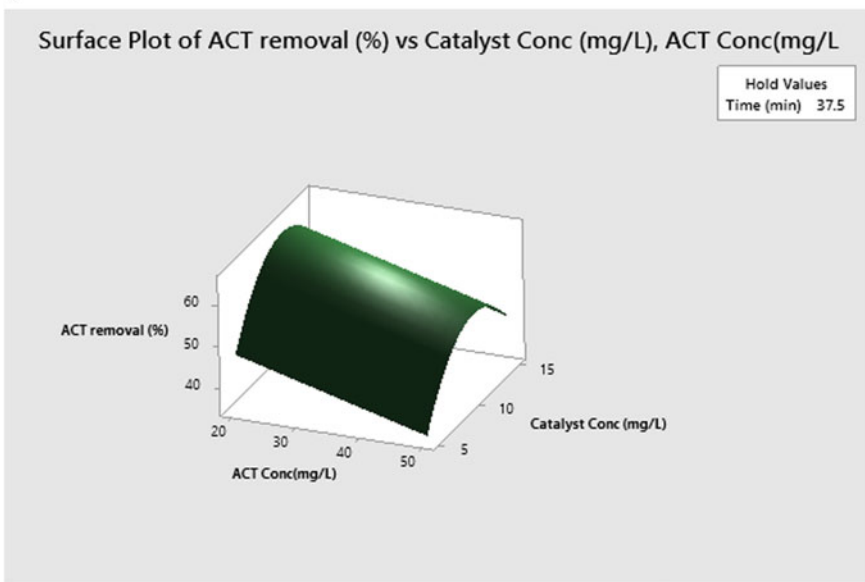
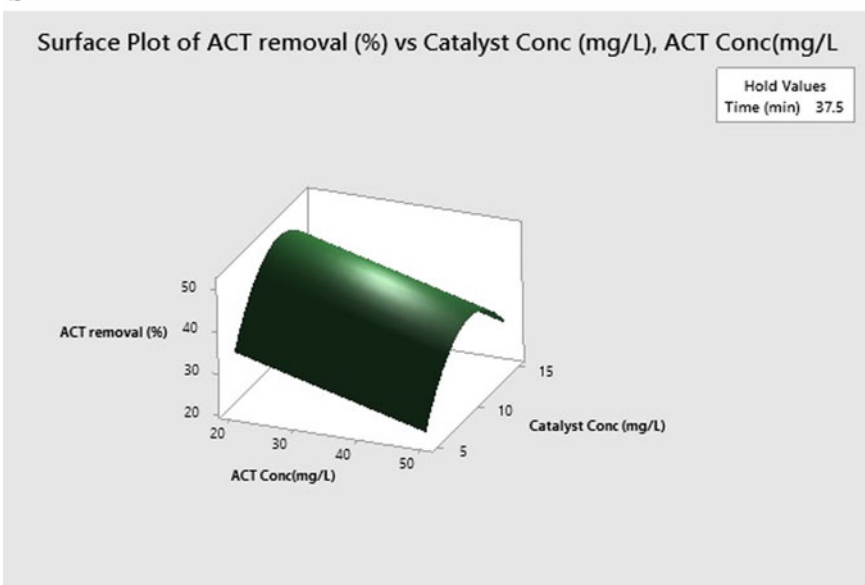
a**b**

Fig. 1 **a** Response surface plot for removal of ACT with respect to variation in concentration of ACT and TiO_2 . **b** Response surface plot for removal of ACT with respect to variation in concentration of ACT and H_2O_2

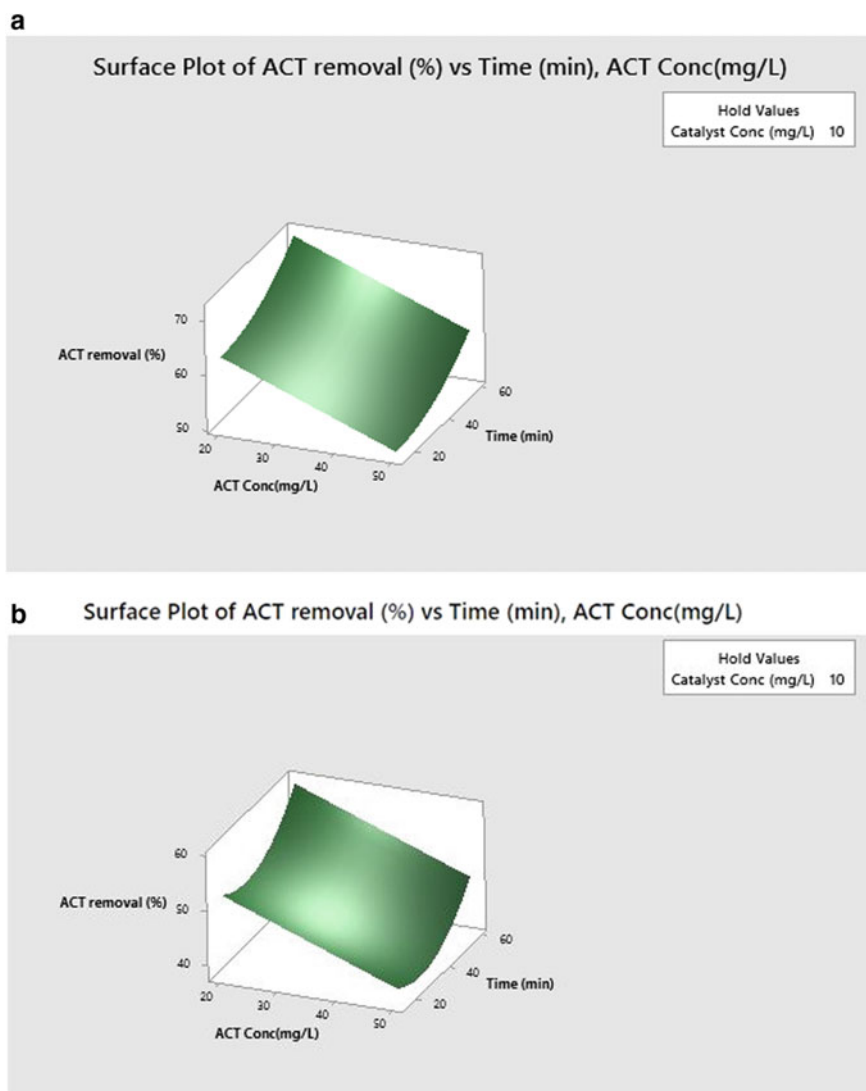


Fig. 2 **a** Response surface plot for removal of ACT with respect to variation in ACT and time for TiO_2 catalyst. **b** Response surface plot for removal of ACT with respect to variation in ACT and time for H_2O_2 catalyst

for catalyst concentration in the range 9–12.5 mg/L, and the maximum removal efficiency falls in the range 35–60 min and catalyst concentration in the range 7.5 to 14.5 mg/L. Hence, the removal percentage of ACT is inferred as 45–50%.

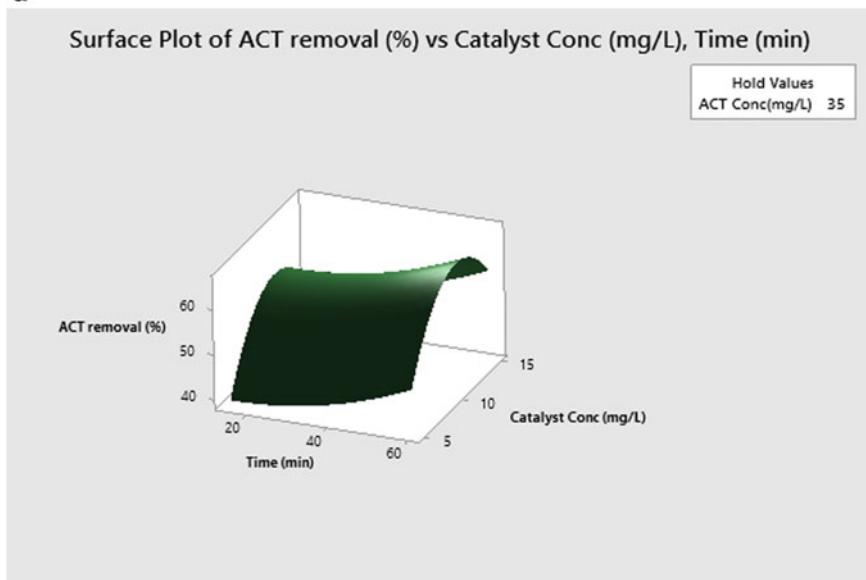
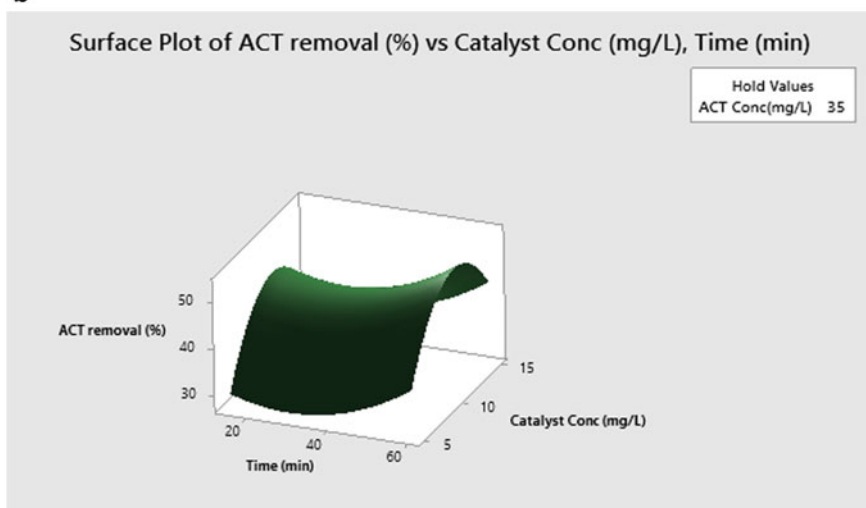
a**b**

Fig. 3 **a** Response surface plot for removal of ACT with respect to variation in reaction time and catalyst conc. TiO_2 . **b** Response surface plots for removal of ACT with respect to variation in reaction time and catalyst conc. H_2O_2

4 Conclusion

Pretreatment of removal of acetaminophen (ACT), a major pharmaceutical contaminant in India, is studied and investigated. Four factors were considered in this study, which are reaction time, concentration of ACT, concentration of catalyst, i.e. TiO_2 and H_2O_2 , and pH. The comprehended data were used for generating the regression analysis and were obtained using Minitab software. From the study, it is inferred that maximum removal of ACT is found during lower concentration of ACT, that is, 20 mg/L, and higher concentration of catalyst, that is, 15 mg/L. From our analysis, TiO_2 showed higher removal efficiency of 75% as compared to H_2O_2 which showed a removal efficiency of 55%. Hence, TiO_2 catalyst is more suitable for higher efficiency in ACT removal. The R-square value for TiO_2 is 68.02% and for H_2O_2 is 50.3%. The proposed model was able to efficiently predict the removal efficiency of acetaminophen using advanced oxidation process through response surface methodology.

References

1. Sarkar B, Mandal S, Tsang YF, Vithanage M, Biswas JK, Yi H, Dou X, Ok YS (2019) Sustainable sludge management by removing emerging contaminants from urban wastewater using carbon nanotubes. In: Industrial and municipal sludge: emerging concerns and scope for resource recovery. Elsevier, pp 553–571. <https://doi.org/10.1016/B978-0-12-815907-1.00024-6>
2. Stefanakis A, Becker J (2015) A review of emerging contaminants in water: classification. *Sour Potential Risks*. <https://doi.org/10.4018/978-1-4666-9559-7.ch003>
3. Kanakaraju D, Glass BD, Oelgemöller M (2018) Advanced oxidation process-mediated removal of pharmaceuticals from water: a review. *J Environ Manage* 1(219):189–207. <https://doi.org/10.1016/j.jenvman.2018.04.103> Epub 2018 May 7 PMID: 29747102
4. Daughton C, Brooks B (2011) Active pharmaceutical ingredients and aquatic organisms. *Environ Contam Biota Interpreting Tissue Concentrations* 281–341. <https://doi.org/10.1201/b10598-10>
5. Fatta-Kassinos D, Meric S, Nikolaou A (2011) Pharmaceutical residues in environmental waters and wastewater: current state of knowledge and future research. *Anal Bioanal Chem* 399(1):251–275. <https://doi.org/10.1007/s00216-010-4300-9> Epub 2010 Nov 10 PMID: 21063687
6. Ngo TH, Van DA, Tran HL et al (2021) Occurrence of pharmaceutical and personal care products in Cau River, Vietnam. *Environ Sci Pollut Res* 28:12082–12091. <https://doi.org/10.1007/s11356-020-09195-0>
7. Maroon JC, Bost JW, Maroon A (2010) Natural anti-inflammatory agents for pain relief. *Surg Neurol Int* 1:80. <https://doi.org/10.4103/2152-7806.73804>
8. Covicich LG, Bengoechea DI, Fenoglio RJ, Area MC (2014) Advanced oxidation processes for wastewater treatment in the pulp and paper industry: a review. *Am J Environ Eng* 4(3):56–70. <https://doi.org/10.5923/j.ajee.20140403.03>
9. Akshaya A, Chinnaiyan P, Unni D, Keerthana G (2018) Use of TiO_2 and rice husk ash to study the removal of reactive yellow dye as contaminant in water. *Mater Today Proc* 5(11):24268–24276

10. Swarnalakshmi KS, Chinnaiyan P, Nivetha S, Nair AS (2018) Use of rice husk ash as an adsorbent to remove contaminants in water and comparison with advanced oxidation process—a study. *Mater Today Proc* 5(11):24248–24257
11. Chinnaiyan P, Thampi SG, Prakash EL, Abinaya K, Varshini P (2020) A study on emerging contaminant amiodarone removal in water—experimental investigations and modeling. *IOP Conf Series Mater Sci Eng* 872(1):012143
12. Chinnaiyan P, Thampi SG, Ananthkumar M et al (2020) Heterogeneous photo catalytic process using TiO_2 for removing Levetiracetam in water—a study. *IOP Conf Series Mater Sci Eng* 872(1):012134
13. Chinnaiyan P, Thampi SG, Kumar M, Balachandran M (2019) Photocatalytic treatment of amiodarone and levetiracetam in pharmaceutical industry effluent: process optimization using response surface methodology. *Desalin Water Treat* 170:253–264
14. Chinnaiyan P, Thampi SG, Bharath Krishnaa AC, Sasi M (2019) Use of TiO_2 for removing emerging contaminant in water—amoxicillin as a case study. *IOP Conf Series Mater Sci Eng* 561(1):012091
15. Chinnaiyan P, Thampi SG, Bharath Krishnaa AC, Sasi M, Tejashwi L (2019) Optimisation of system parameters for the removal of Metformin in a photocatalytic reactor employing TiO_2 . *IOP Conf Series Mater Sci Eng* 561(1):012087
16. Abdel-Wahab A-M, Elsherbini A, Mohamed O, Nasr O (2017) Photocatalytic degradation of paracetamol over magnetic flower-like $\text{TiO}_2/\text{Fe}_2\text{O}_3$ core-shell nanostructures. *J Photochem Photobiol A Chem.* 347. <https://doi.org/10.1016/j.jphotochem.2017.07.030>
17. Wang S, Wu J, Lu X, Xu W, Gong Q, Ding J, Dan B, Xie P (2018) Removal of acetaminophen in the Fe^{2+} /persulfate system: kinetic model and degradation pathways. *Chem Eng J* 358:1091. <https://doi.org/10.1016/j.cej.2018.09.145>
18. Ahmadzadeh S, Dolatabadi M (2018) Removal of acetaminophen from hospital wastewater using electro-Fenton process. *Environ Earth Sci* 77:53. <https://doi.org/10.1007/s12665-017-7203-7>

Chapter 36

Speculative Testament of Corrosive Behaviour of Aluminium Composite Welded by FSW



N. M. Siddesh Kumar, M. Sadashiva, and J. Monica

Abstract Corrosion plays a very important role in the modern world, and there are many causes for the corrosion, in which welded joint is one of the cruiser parts, where the material undergoes corrosion. Current investigation focuses on the study of the corrosion behaviour of welded and unwelded zone in hybrid aluminium metal matrix composite. Aluminium 7075 alloy is known for its high strength and good corrosion resistance property; thus, it has a wide range of applications in building bridges, aerospace, industries, defence equipment, transport industries, railway transports and aircraft industries. An attempt is made to study the corrosion behaviour of hybrid composite aluminium alloy 7075 metal matrix prepared with fine greenish SiC of 7% along with chopped E-glass fibre and AA7075 of about 90% was produced by stir casting method with the help of graphite crucible furnace. Then the process was followed by (FSW) friction stir welding process for joining, where two hybrid MMC metals are joined with the help of a cylindrical tapered tool, with different welding parameters like transverse speed and tool spindle rotational speed of about 600, 900, 1200 rpm and feed rate is about 40, 80, 120 mm/min. Impetus gives normal force, effects of torque and the transverse force which is affecting the plate while welding. The corrosion is mainly contingent on environmental conditions, and thus the test followed by the specimen was placed in sodium chloride solution for 24 h, the flow of the election was determined between the standard electrons and sample metal piece concerning corrosion rate. The main objective is to study and evaluate the result compared with a hybrid MMC plate with aluminium 7075 base metal and weld zone. We observed that the corrosion resistance of welded composite material exhibits very high resistance to corrosion because of the uniform distribution of atoms and the compaction of atoms at the welding zone. When compared to base material welded zone exhibits a better corrosion resistance property and also changes in grain size and grain shape the effects of corrosion behaviour of a welded joint by FSW process when compared to aluminium 7075 base material.

Keywords Corrosion · FSW · Stir casting · Silicon carbide · E-glass fibre

N. M. Siddesh Kumar (✉) · M. Sadashiva · J. Monica
Department of Mechanical Engineering, PES College of Engineering, Mandya, India

1 Introduction

The aluminium 7 series has outstanding mechanical properties comparatively with other series, and 7 series aluminium material is much better in resistance to corrosion and other mechanical properties. It has a high strength; thus, it is used in structural applications and is also extremely used in the aircraft industries in the building of aircraft parts. The material's mechanical property shows a direct reflection on tempering. In the whole world for the first time, mass production of any alloying material is done means, that is, aluminium alloy 7075 only because of its outstanding manoeuvrability compared to other alloying elements, because of its excellent specific strength, mechanical properties like low density, high polishability, strength and thermal properties. Strength, electrical resistance property, corrosion resistance, wear resistance, AA7075 is used in the manufacturing of mould tools. Mechanical properties can be increased by grain size of reinforcement methods like plastic deformation operation in this method gives equal angular channels between the micro-structure [1]. Friction stir processing (FSP) method is well known as the fastest emerging technologies in a solid-state process [2]. In FSP method, the metal and alloy improve the mechanical properties of material that are ductility corrosion resistance wire resistance and fatigue resistance [3]. Mechanical property of a material is improved by achieving the reinforcing grain structure and removes the defects of work-piece material [4]. Mechanical property of the material is been increased by increasing the welding and frictional speed [5]. Hardness, strength and resistance to corrosion were found excellent correlation [6]. The casting method gives an equal distribution of reinforcement of base material and thus helps in reducing cracks [7]. This hybrid composite alloy was developed by using a friction stir casting method; here, Gr was a primary composite material that helped improve the wear resistance of a material and later SiC was added as secondary composite material [8]. Inter-molecular bonding is been improved and thus results in the improvement of strength between the reinforcement and matrix [9]. The extreme increases of the elongation near crack are because of the addition of polyurethane in E-glass fibre [10]. As the sliding speed and load increases the co-efficient of Friction reduces [11]. AA7075 MMC had a uniform distribution of SiC particles [12] that reinforcement gives more attractive strength, lightweight and stiffness property [13]. AA7075 gives better corrosion properties, increased hardness, and increases in wear rate when a load is applied, decreases in the density of a material and found that AA7075 MMC has high elastic modulus [14]. Remarkable drop in the tensile properties and hardness of a material [15]. Addition of E-glass fibre material and also compressive stress of a material have been increased with addition percentage of an E-glass fibre that was proven [16]. SiC and E-glass fibre MMC have uniform distribution matrix which was found and increases the hardness and the corrosion resistance property [17]. 1.5 wt% of silicon carbide gives an outstanding increment in mechanical properties [18]. Composite material surface was found with the addition of silicon carbide material [19]. Hybrid material is obtained by both the heat treatment and casting conditions [20]. Wear rate is increased when the load is increased and changing the load will

show a significant increase in wear property [8]. Increases in 15% of hardness at the same time corrosion behaviour is been increased for 15% with reinforcement SiC and E-glass fibre material [21]. E-glass fibre increases mechanical property by about 0% to 5% and found a data decrement in the percentage of elongation [22]. The corrosion property depends on the addition of silicon carbide percentage in Al7075 corrosion resistance which is increased because of the passive layer and the protective layer which is formed on the surface material [23].

The evidence of the above literature review focuses on the physical and mechanical behaviour of AA7075 with reinforcement of materials like E-glass fibre and SiC. SiC with AA7075 and E-glass fibre with AA7075, and other reinforcement with SiC and E-glass is been discussed in the literature review and this made a motivation for the current work, availability and form-ability of AA7075 that gives a suitable application. AA7075 is known for its high strength and good corrosion resistance; hence, it is particularly used in building bridges, aerospace industries, defence equipment, transport industries, railway transports and aircraft industries. Here AA7075 is being used as a primary alloy with the reinforcement of E-glass fibre and SiC by the friction stir casting process and studies the corrosion behaviour of a material. Furthermore, the effects of corrosion behaviour of the hybrid composite of AA7075 with SiC and E-glass are studied.

2 Methodology

The study focus is on AA7075 base material of 90% metal matrix with a hybrid composite of silicon carbide particles of 7% and E-glass fibre of 3%. The percentage composition of the reinforcement is taken from the literature review. The MMC is produced by using the stir casting method. The hybrid composite material plate was fabricated, and it is welded with the help of the FSW method. The welding parameters of the friction stir welding method are speed of the spindle which is about 600, 900, 1200 rpm and the welding speed is about 40, 80, 120 mm/min. The study focuses on the corrosion resistance property of AA7075 reinforced with hybrid material silicon carbide and E-glass fibre. Particle in composite aluminium is aluminium 7075 + SiC + S-glass fibre material.

2.1 Steps Involved

- Selection of matrix and reinforcement.
- Preparation of composite material.
- Welding of composite material.
- Corrosion test of welded and unwelded zones.
- Analysis result and discussion.



Fig. 1 **a** Fine greenish silicon carbide powder and **b** Chopped E-glass fibre

Table 1 Elements compounded in E-glass fibre: as revised

SiC (%)	Al ₂ O ₃ (%)	CaO (%)	MgO (%)	B ₂ O ₂ (%)
54.5	15.3	17.1	0.6	8

2.1.1 Selection of Matrix and Reinforcement

Silicon carbide is a semiconductor material in which it is a composite of carbon and silicon. Here material properties of silicon carbide are known for low density, low thermal expansion, and also, it has the highest strength, hardness, endurance and good thermal conductivity. These are some properties of silicon carbide material. Further, study is on E-glass fibre and its properties. The mechanical properties of the E-glass fibre are given here, and the chopped E-glass fibre is also called “electrical grade-glass”. Here E-glass fibre material has a major reinforcement. It has a better corrosion resistance property, a good strength-to-weight ratio, outstanding stiffness and acts as electrical insulators. Chopped R-glass has better stiffness to the moisture observation. It has epoxy of different percentages which influences the mechanical behaviour of material. Some more properties have given more popularity to E-glass fibre material; they are: it includes high stiffness, lightweight, high modulus, the highest strength, relatively low density and low cost. Because of these advantages of E-glass fibre has more application, it is used in the aerospace/defence sector, building construction, transportation sectors and composite applications and also used in the medical products (Fig. 1; Table 1).

2.1.2 Preparation of Composite Material

Metal Matrix and Reinforcement

AA7075 base metals reinforcement with hybrid materials with the weight fraction of silicon carbide 7%, 25 microns of very fine greenish particles is added with 3% of E-glass very fine micron with the length of 2–3 mm and diameter having 10–14 μ .

Table 2 Chemical composition Al7075

Si	Fe	Zn	Mg	Mn	Cu	Cr	Al	Ti
0.4	0.5	5.1 to 6.1	2.1 to 2.9	0 to 0.3	0.12 to 2	0.2 to 0.28	Balance	0.2

Table 3 Stir casting process parameters

Parameters	Values
Speed	400–600 rpm
Time	3 min
Temperature	800 °C

of E-glass fibres is been used. The current study focuses to enhance the mechanical property and increase the corrosion resistance behaviour of composite material (Table 2).

Stir Casting Process

AA7075 is taken for a particular composite; the molten metal mixture is placed inside the graphite crucible furnace. The furnace temperature is maintained at 800 °C, aluminium starts melting at around 660 °C, and it reaches a liquid state. The Al7075 molten liquid state was taken out from the ladle and poured into mould cavity for the formation of hybrid composite material; first preheating the furnace is done, and the aluminium 7075 ingots were heated up to 800 °C; after that 7% fine Greenish SiC was heated up to 700 °C, and chopped E-glass fibre was heated up to 500 °C. The molten state AA7075 is bought out from the furnace and poured into the preheated reinforcement furnace. The mixture was stirred by an electric stirrer, for 10 min at the speed of 600 rpm to achieve a homogenous distribution of matrix and then metal let to solidify for 15 min. Table 3 is the properties of site casting operation.

After the casting process, the hybrid composite material was cut with the help of the machining process according to ASTM standard, the plate dimension is 100 * 50 * 6 mm (length * width * thickness). The plate is welded using the FSW method. The FSW method was conducted at IISC, Bangalore, India (Fig. 2).

2.1.3 Welding of Composite Material

FSW method is suitable only for low melting point metals, while welding three loads and three forces are acted on the working tool. The welded metal plate is cut; according to 100 * 50 * 6 mm by using wire, EDM process for ASTM standards and the corrosion test were conducted. FSW is carried out at IISC, Bangalore; the test is carried out for two different conditions of tool speed, and tool feed is carried for 3 different parameters S1, S2, S3, F1, F2 and F3 (Speed1, Speed2, Speed3, Feed1, Feed2 and Feed3) (Fig. 3; Table 4).

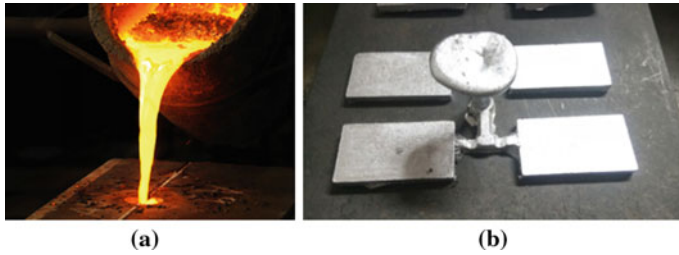


Fig. 2 a Pouring of molten metal, b Metal plates cut for ASTM standards

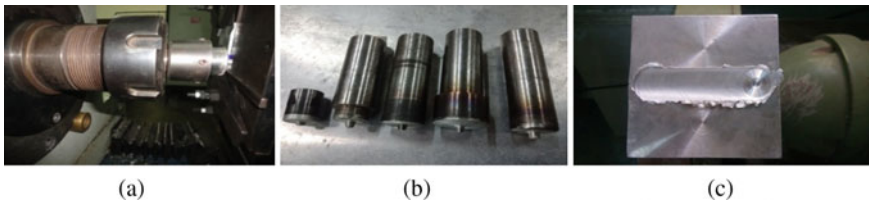


Fig. 3 a Friction stir welding spindle. b Friction stir welding tool. c Material welded plate

Table 4 Material welding parameter

Welding	Tool speed	Tool feed	Plunge depth
Parameters	S1 = 500 rpm S2 = 800 rpm S3 = 1100 rpm	F1 = 40 mm/min F2 = 80 mm/min F3 = 120 mm/min	5.5 mm

2.1.4 Corrosion Test of Welded and Unwelded Zone

Corrosion means impulsively destruction of material, the microstructure changes to chemical, electrochemical and biochemical in the environment. The corrosion is mainly contingent on environmental conditions. The test was conducted; at very first step, the specimen was cleaned from dust and grease particles followed by the specimen which was placed in NaCl solution for 24 h, by using NaCl solution “hexamine”, which enhances the resistance of corrosion. The flow of the election was determined between the standard electrons and sample metal piece. The electrons flow is given by $Q = I * T$, whereas Q changes in density, I is flow of current, and T is time taken in hours (Table 5).

2.1.5 Test Result and Discussion

The corrosion rate of aluminium 7075 base material, composite material, welded and unwelded part is taken into consideration. The result of the values is shown in the

Table 5 Specification of tested sample AA7075

Specimen	AA7075 matrix in percentages (%)	Reinforcement (SiC) in (%)	Reinforcement (E-glass fibre) in (%)	Welding parameter rotational speed in rpm	Welding parameter tool feed in mm/min
7075 (BM)	100	–	–	Unwelded	Unwelded
70S1F1	100	–	–	600	40
70S1F2	100	–	–	600	80
70S1F3	100	–	–	600	120
7075 (CM)	90	7	3	Unwelded	Unwelded
7S1F1	90	7	3	600	40
7S1F2	90	7	3	600	80
7S1F3	90	7	3	600	120
7S2F1	90	7	3	900	40
7S2F2	90	7	3	900	80
7S2F3	90	7	3	900	120
7S3F1	90	7	3	1200	40
7S3F2	90	7	3	1200	80
7S3F3	90	7	3	1200	120

tabular column; further, it shows that as the percentage of reinforcement increases, corrosion rate of aluminium 7075 composite material also increases due to the addition of composite material silicon carbide and E-glass fibre of aluminium material. The composition forms a very thin inhibitions layer that resists corrosion (Fig. 4; Table 6).

The composite aluminium material has a good corrosion resistance property when it is compared with aluminium alloy 7075 base metal. In composite material, we

Fig. 4 Graphical representation of corrosion rate of unwelded material AA7075

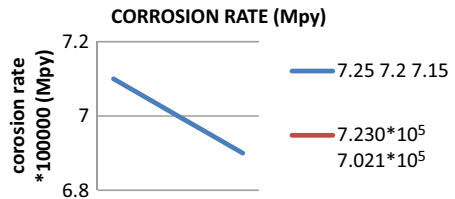


Table 6 Corrosion rate composite unwelded material AA7075

Specimen	Current	Voltage	Corrosion rate
AA7075 (base metal)	3.954×10^{-3}	-0.584	7.230×10^5
Composite material	3.754×10^{-3}	-6.000	7.021×10^5

noticed that addition of E-glass fibre and silicon carbide material to aluminium 7075, properties like interstitial compound and chemistry of compound play a significant role in increase of corrosion resistance and corrosion rate. 7.230×10^5 base metal corrosion rate was noted for unwelded aluminium 7075 base metal with current of 3.954×10^{-3} and voltage of -0.584 (Fig. 5; Table 7).which is greater than AA7075 composite material, corrosion rate 7.021×10^5 was noted for an unwelded metal samples. The corrosion rate of aluminium alloy 7075 is been increased for 3% when it is compared to base metal. 4.1287×10^5 mpy lowest corrosion rate of AA7075 base metal was noticed at the speed of 600 RPM and 120 mm/min feed rate, whereas in AA7075 composite material 2.6525×10^5 mpy was noticed. Thus, it influences new atomic bonding, molecular diffusion and surface modification due to FSW process. Corrosion rate is decreased when it is compared with unwelded Al7075 base metal (Fig. 6).

The corrosion rate of AA7075 welded and unwelded material specimen is reinforcement with 7% silicon carbide and 3% E-glass fibre. Here we noticed that decrease of corrosion rate related to FSW process gives better performance compaction of corrosion resistance property, and the opposing composite films were formed by the chemical reaction between silicon carbide and E-glass fibre (Fig. 7; Table 8).

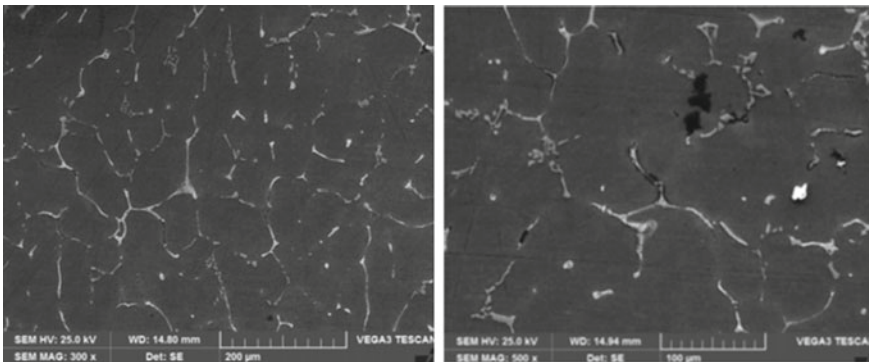


Fig. 5 SEM image of welded and unwelded base metal AA7075 corrosion rate

Table 7 Welded and unwelded base metal AA7075 corrosion rate

Specimen	Current (A)	Voltage (V)	Corrosion rate (mpy)
Unwelded base metal	3.954×10^{-3}	-0.584	7.230×10^5
70S1F1	3.85×10^{-3}	-0.852	5.25×10^5
70S2F2	3.955×10^{-3}	-0.584	6.252×10^5
70S3F3	2.585×10^{-3}	-0.524	4.129×10^5

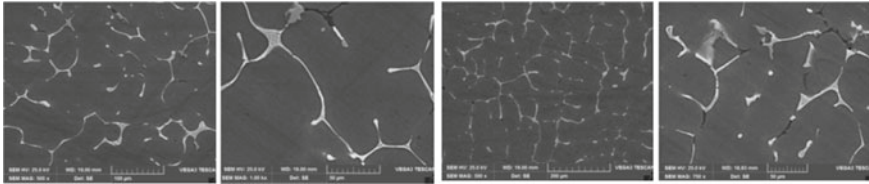


Fig. 6 Corrosion rate of composite material AA7075

Fig. 7 Graphical representation of corrosion rate of composite material AA7075

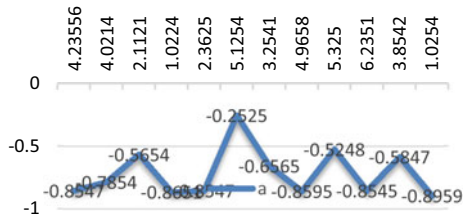


Table 8 Corrosion rate of composite material AA7075

Specimen	Current (A)	Voltage (V)	Corrosion rate (mpy)
Unwelded composite metal	3.754×10^{-3}	-0.600	7.021×10^5
7S1F1	1.254×10^{-3}	-0.854	4.024×10^5
7S1F2	2.125×10^{-3}	-0.652	6.931×10^5
7S1F3	2.355×10^{-3}	-0.526	5.224×10^5
7S2F1	3.568×10^{-3}	-0.585	4.125×10^5
7S2F2	3.221×10^{-3}	-0.565	4.252×10^5
7S2F3	2.658×10^{-3}	-0.895	4.125×10^5
7S3F1	2.254×10^{-3}	-0.584	2.121×10^5
7S3F2	4.154×10^{-3}	-0.965	3.251×10^5
7S3F3	3.225×10^{-3}	-0.876	2.652×10^5

When compared to base metal, AA7075 composite plate shows the lowest corrosion rate of about 2.121×10^5 mpy and due to homogenous distribution of composite reinforce matrix is achieved by at the speed of 1200 RPM and 40 mm/min feed rate. It shows the properties of opposing wear, and these barriers are called as corrosion. The friction stir welding process reduces the corrosion rate with modification of surface (Fig. 8).

In this tabular column, it shows that complete comparative result of aluminium 7075 welded and unwelded metal. Here we observe that decrease in corrosion rate is achieved due to the friction stir welding method (Table 9).

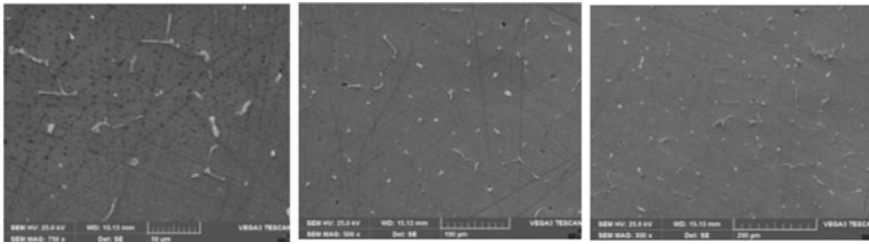


Fig. 8 SEM image of AA7075 FSW material surface modification

Table 9 Comparative result of aluminium 7075 welded and unwelded metals

Specimen AA7075	Current (A)	Voltage (V)	Corrosion rate (mpy)
Unwelded base metal	3.954×10^{-3}	-0.584	7.230×10^5
70S1F1	3.85×10^{-3}	-0.852	5.25×10^5
70S2F2	3.955×10^{-3}	-0.584	6.252×10^5
70S3F3	2.585×10^{-3}	-0.524	4.129×10^5
Unwelded composite metal	3.754×10^{-3}	-0.600	7.021×10^5
7S1F1	1.254×10^{-3}	-0.854	4.024×10^5
7S1F2	2.125×10^{-3}	-0.652	6.931×10^5
7S1F3	2.355×10^{-3}	-0.526	5.224×10^5
7S2F1	3.568×10^{-3}	-0.585	4.125×10^5
7S2F2	3.221×10^{-3}	-0.565	4.252×10^5
7S2F3	2.658×10^{-3}	-0.895	4.125×10^5
7S3F1	2.254×10^{-3}	-0.584	2.121×10^5
7S3F2	4.154×10^{-3}	-0.965	3.251×10^5
7S3F3	3.225×10^{-3}	-0.876	2.652×10^5

Hybrid AA7075 is reinforced with silicon carbide 7%, and E-glass fibre 3% is validated the result table of corrosion and noticed that decrease in corrosion rate with friction stir welding process. In AA7075, composite silicon carbide and E-glass fibre material give minimum of 600 RPM to 40 mm/min with FSW process; however, welding parameters rise upto 600–1200 rpm and rotational speed rise upto 40–120 mm/min feed rate. Eventually, it reduces the corrosion rate of composite metal with friction stir welding method; this is achieved due to stirring action, and thus, it decreases the oxidation of the metal inner surface and subsurface. Decreased corrosion rate of composite metal specimen 7S3F1 with the speed of 1200 RPM and 40 mm/min feed rate is achieved, and decreased corrosion rate of a composite material with higher rotational speed and lesser feed rate is obtained. FSW welding

process can be done for ferrous and non-ferrous metal, and also, we can use other rein format fibre like R-glass fibre and S-glass fibre.

3 Conclusion

After throughout investigation and evaluation of parameter, the effects of corrosion behaviour of the hybrid composite of aluminium 7075 alloy with reinforcement of SiC 7% and E-glass fibre 3% are considered; for this work, the experiment trials were carried out for different tool speed (600, 900, 1200 rpm) and different feed rate (40, 80, 120 mm/min). The welded composite material exhibits very high corrosion resistance rate because of uniform distribution of atoms and the compaction of atoms at the welding zone. When compared to base material, welded zone exhibits a better corrosion resistance property and also changes in grain size and grain shape. In addition to silicon carbide and E-glass fibre to aluminium material, they form a very thin inhibitions layer that resists corrosion. We noticed that with addition of E-glass fibre and silicon carbide material to aluminium 7075 alloy, properties like interstitial compound and chemistry of compound play a significant role in increase of corrosion resistance. Hybrid AA7075 reinforced with silicon carbide 7% and E-glass fibre 3% is validating the result table of corrosion, and we noticed that decrease in corrosion rate with friction stir welding process. The corrosion rate of aluminium alloy 7075 is been increased by 3% when it is compared to base metal. The decreased corrosion rate of composite metal is found in 7S3F1 with the speed of 1200 RPM and 40 mm/min feed rate and decreases corrosion rate of a composite material with higher rotational speed and lesser feed rate which is obtained.

References

1. Zhao YH, Liao XZ, Jin Z, Valiev RZ, Zhu YT (2004) Microstructures and mechanical properties of ultrafine grained 7075 Al alloy processed by ECAP and their evolutions during annealing. *Acta Mater* 52:4589–4599
2. Mishra RS, Mahoney MW (2001) Friction stir processing: a new grain refinement technique to achieve high strain rate super plasticity in commercial alloys. *Mater Sci Forum* 357–359:p507-514
3. Kwon YJ, Shigematsu I, Saito N (2003) Mechanical properties of fine grained aluminum alloy produced by friction stir process. *Scr Mater* 49:785–789
4. Surekha K, Murty BS, Prasad Rao K (2009) Effect of processing parameters on the corrosion behaviour of friction stir processed AA2219 aluminum alloy. *Solid State Sci* 11:907–917
5. Azimzadegan T, Serajzadeh S (2010) An investigation into microstructures and mechanical properties of AA7075-T6 during friction stirwelding at relatively high rotational speeds. *J Mater Eng Perform* 19:1256–1263
6. Clark R Jr, Coughran B, Traina I, Hernandez A, Scheck T, Etuk C (2005) On the correlation and physical properties of 7075-T6 Al alloy. *Eng Failure Anal* 12:520–526
7. Idrisi AH, Mourad A-HI (2019) Conventional stir casting versus ultrasonic assisted stir casting process: mechanical and physical characteristics of AMCs. *J Alloys Compd* 805:502 26,1,1,2,

8. Kumar R, Dhiman S (2013) A study of sliding wear behaviors of Al-7075 alloy and Al-7075 hybrid composite by response surface methodology analysis. *Mater Des* 50:351–359
9. Kumar A, Pal K, Mula S (2017) Simultaneous improvement of mechanical strength, ductility and corrosion resistance of stir cast Al7075-2% SiC micro-and nanocomposites by friction stir processing. *J Manuf Process* 30:1–13. <https://doi.org/10.1016/j.jmapro.2017.09.005>
10. Suresh G, Stephen Bernard S, Vivek S, Sai Krishnan G, Ashwin Kishore V, Ivon Paul A, Mohideen Fowzan K (2020) Study of mechanical performance of E-Glassfiber reinforced (IPN) interpenetrating polymer networks. *Mater Today Proc.* <https://doi.org/10.1016/j.matpr.2020.02.332.2121212>
11. Santhosh Kumar BM, Girish DP (2018) Friction and wear behaviour of Tungsten Carbide and E glass fibre reinforced Al7075 based hybrid composites. *IOP Conf Series Mater Sci Eng* 390:012002. <https://doi.org/10.1088/1757-899X/390/1/012002>
12. Hanumanthe G (2015) Study on mechanical properties of Al 7075 based metal matrix composites. ISSN: 2278–0181. Published by, www.ijert.org NCERAME-2015 conference proceedings
13. Nandini MC, Balakrishna G, Praveen Kumar BC, Veena Dinesh (2018) A study of tribological properties and corrosion behavior of short E glass fiber and fly ash reinforced with aluminum 7075 composite 04(04). ISSN(online): 2455-1457; [ISSN: 2455-1457]
14. Krishnamoorthi K, Balasubramanian P (2015) Review the properties of Al7075 matrix composites 2(1):85–90. Krishi Sanskriti Publications. Print ISSN: 2393-9095; Online ISSN: 2393-9109
15. Ahmed A, Neely AJ, Shankar K, Nolan P (2010) Synthesis, tensile testing, and microstructural characterization of nanometric SiC particulate-reinforced Al 7075 matrix composites. *Metall Mater Trans A* 1582:41
16. Kammer P, Shivanand HK (2012) Experimental studies on mechanical properties of E-glass short fibres & fly ash reinforced Al 7075 hybrid metal matrix composites. *Int J Mech Ind Eng (IJMIE)* 1(4). ISSN: 2231-6477
17. Haridas A, Ravikumar M, Uvaraja VC (2013) Production and wear analysis of aluminium metal matrix composite. *Int J Innov Res Develop* 2(3)
18. Gopalakannan S, Senthilvelan T (2013) Application of response surface method on machining of Al–SiC nanocomposites. *ELSEVEIR Measur* 46:2705–2715
19. Sert A, Cellik ON (2014) Wear behaviour of Sic reinforced surface composite Al7075-T651 aluminium alloy produced using friction stir processing. *Ind J Eng Mater Sci* 21:35–43
20. Kalkanlı A, Yılmaz S (2008) Synthesis and characterization of aluminum alloy 7075 reinforced with silicon carbide particulates. *Mater Des* 29(4):775–780
21. Sambathkumar M, Navaneethakrishnan P, Ponappa K, Sasikumar KSK Mechanical and corrosion behavior of Al7075 (hybrid) metal matrix composites by two step stir casting process. <https://doi.org/10.1590/1679-78253132>
22. Beffort O, Long S, Cayron C, Kuebler J, Buffat P-A (2007) Alloying effects on microstructure and mechanical properties of high volume fraction SiC-particle reinforced Al-MMCs made by squeeze casting infiltration. *Compos Sci Technol* 67(3–4):737–745
23. Manoharan EK, Singanan M (2020) Studies on the corrosion resistance of Al7075 / SiC metal matrix composites in an alkaline environment. *Int Res J Pharm Appl Sci* 10(4)

Chapter 37

Electrifying the Future with Green Vehicle: A Review on Prospects and Issues of Electric Vehicle in India



Abhaysinha G. Shelake and Pravin R. Minde

Abstract In recent years, a significant research attention has been given for the protection of the environment with an increase in environmental pollution and a continuous increase in global warming. Due to these issues, renewable energy sources such as solar and wind energy and the latest technologies such as electric vehicles have received an increased research attention. The transport sector accounts for 18% of total energy consumption in India. In the last few years, the Indian Segment of Electric Vehicles has been increased. However, the growth rate has been slow; the support for policy was not enough to fully realize the potential of the electricity market. When compared to internal combustion engine (ICE) vehicles, sales of EVs are still low. Electric vehicles have benefits such as environmental friendly, as they have the advantageous characteristics such as non-polluting, reducing dependency on conventional fuel, and low running cost. High price, charging infrastructure, and limited range are some of the major issues involved with electric vehicles. When renewable energy sources are not available, the development of new technologies in the EV sector creates an additional power source. Industry leaders believe that electric vehicles will be the best option for the Indian public to develop a sustainable future.

Keywords Electric vehicles · Environment · Renewable energy · New technologies

1 Introduction

The concept of green vehicles or eco-friendly vehicles implies to produce motor vehicle, which will create reduced harmful impacts on the environment as compared to the widely used internal combustion-based vehicles. In European countries, the

A. G. Shelake (✉) · P. R. Minde
Dr. Vishwanath Karad MIT World Peace University, Pune, Maharashtra, India
e-mail: abhaysinha.shelake@mitwpu.edu.in

P. R. Minde
e-mail: pravin.minde@mitwpu.edu.in



Fig. 1 Rise in fossil fuel production in world [1]

definition of green vehicles has become more accurate as European emission standards now jump in green vehicle standard levels. By them vehicles complying or surpassing Euro6, California zero-emission vehicle standards, then it is considered as Green Vehicle.

The UNFCCC (United Nation Framework Convention on Climate Change) was founded in 1992 for coping up with climate change especially raising the concentration of carbon dioxide level in the atmosphere. It is a better step in today's world to shift from gasoline-based fuel vehicles to green vehicles. The current status of fossil fuel emission in the world shows some serious rise from 1970 in fossil fuel production which shows worrying signs in the context of a sustainable environment. The prospects of an electrified future are exciting, as the element is rapidly expanding on a global scale. However, while most consumers, businesses, and governments around the world are actively promoting e-mobility, EV acquisition rates in many countries, including India, paint a bleak picture (Fig. 1).

With the upsurge in production of fossil fuel, consumption of fossil fuel is also increased. Following figure gives valuable information regarding fuel consumption in 2019. Considering the data, India is one of the major fossil fuel consuming countries in the world (Fig. 2).

1.1 Electric Vehicle as Green Vehicle

As described earlier these are the vehicles which run on low carbon emission fuels and thus keeping the environment sustainable. An electric vehicle runs on an electric drive rather than an internal combustion engine that produces energy through the

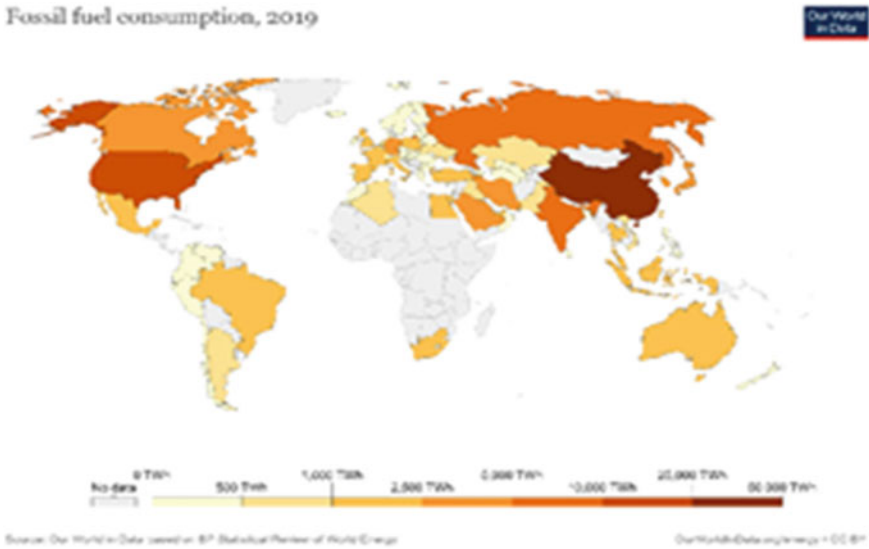


Fig. 2 Fossil fuel consumption in world [1]

combustion of fuel and gas. As a result, such a vehicle is viewed as a potential alternative for current-generation automobiles in order to address issues such as increasing pollution, global warming, and depleting natural resources. Though the concept of electric vehicles was old one, it has gained a lot of attention in the last decade due to rising carbon footprints and other environmental impacts of fuel-driven vehicles. Also, use of fuel cell vehicles has cost, efficiency and durability problem as compared to electric vehicles [2]. Following diagram gives the idea regarding different types of fuel used in green vehicles (Fig. 3).

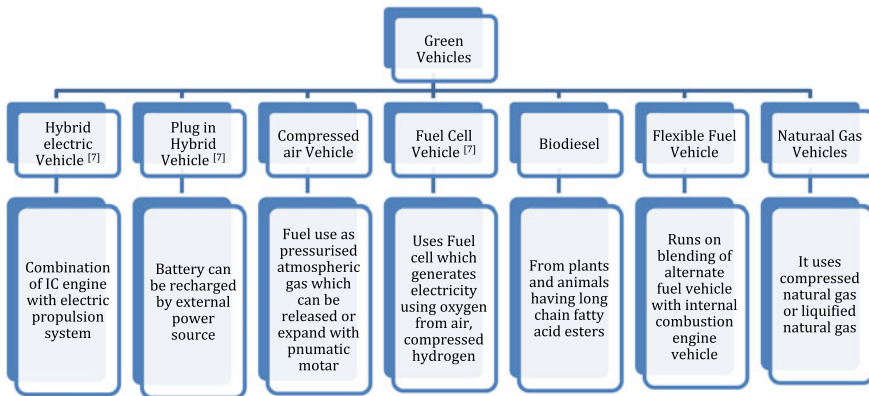


Fig. 3 Green vehicle types and their fuel consumption

2 Literature Review

A review on barriers and challenges of electric vehicles in India and vehicle to grid optimization by Goel et al. [3] states that a summary of the barriers and problems associated with electric vehicles in Indian scenario. Hybrid, Plug-in Hybrid, and Electric Vehicles are proficient for growing vehicle fuel economy, but at a higher cost of purchase when equated to traditional vehicles. In general, their lower petroleum consumption and increased productivity provide long-term economic benefits to buyers, society, automakers, and policymakers. This paper provides a comprehensive review of the literature, as well as an overview and guidelines for HEV, PHEV, and BEV penetration rate studies in the Indian market. Green Transportation in India: Need Analysis and Solution by Panday and Bansal [4] is another paper. According to this paper, it is critical to find an alternative mode of transportation. Because of their lower petroleum consumption and toxic emissions, hybrid vehicles have the potential to change the face of the market, but they are not preferred due to their niche pricing. Improved battery technology and cost reductions will make PHEVs/EVs more widely available on the road. New factory setups are required for mass production of these to lessen end-user buying costs, which will generate new job opportunities.

Struggles faced in the research and development of electric vehicles in India: present scenario by Luthra [5] states that the high price tag and limited range are some of the issues associated with E.Vs, which give them a serious disadvantage when compared to conventional vehicles. As a result, the time has come to familiarize pollution-free E.Vs. However, the main challenge is achieving customer satisfaction, which will only be possible if issues such as high cost, limited range, and so on are addressed through research. Finally, it is necessary to modify the current Indian industry and power generation sector in order to develop and commercialize electric and hybrid vehicles for public transportation. Addressing the challenges to electric vehicle adoption via sharing economy: an Indian perspective by Kumar et al. [6]. The study's findings show the critical roles of the economy-sharing and public service in promoting EV adoption given Indian clients' high cost of EV, lack of infrastructure and poor buying power. The economic sharing perspective offers the government different possibilities for optimal resources management (electrical transport system). The study also compares the global outlook in assigning target numbers.

Also, Bindhu [7] and Manoharan [8] proposed system of an Enhanced Safety System for Auto Mode E-Vehicles through Mind Wave Feedback and an improved safety algorithm for artificial intelligence enabled processors in self-driving cars. In case of electric vehicles, these ideas whether possible to implement or not are also one of the considerations of the author.

In short, in this paper high initial price of electric vehicle in comparison with traditional vehicle, concerned of economic, environmental benefits of electric vehicle over IC engine vehicles, need to identify alternative mode of transportation which reduce emission of CO₂ to complement try of making earth again greener and safe, proposed infrastructure required for making electrical vehicle operational, use of

recent advancement in automobile in electrical vehicle to maintain or to improve ease of driving is a scope of discussion.

3 Methodology

The basic idea is making environment pollution free. As one of the biggest modes of increase in pollution in transportation is internal combustion engine running on fossil fuel, it is need of hour to replace them. Author discusses a suitable alternative of electrical vehicle as green vehicle by putting prospects and challenges in use of electric vehicles. Several research papers are studied and outcomes are discussed. A survey has been carried out regarding utilization prospects and challenges for electric vehicle as green vehicle and internal combustion vehicles in Indian context. Conclusions are developed at the end of survey for finalizing prospects and issues for electric vehicle utilization in India.

3.1 Survey Statistics

In order to have generic opinion of end user about electric vehicle, a survey is carried out. The goal is to understand public sentiment for use of electric vehicle instead of IC engine vehicle. Several questions are asked based on fuel price, economy, initial cost, environmental viability. This survey is carried out with Google form [9] and randomly sending to people for giving their opinion. The results obtained from the survey are tabulated as below with author perspective mentioned in conclusion. However, author tries to find out common public opinion about utilization of green vehicles using this survey. Majorly it is concluded that for most of the factor people needs clarification for beneficial utilization of electric vehicles. Through this research paper author tries to prove applicability of electric vehicle in India while considering several contexts like fuel consumption, CO₂ emissions, environmental pollution, ease of driving in electric vehicle, installation modern days gadgets in electric vehicles, use of renewable energy sources and charging infrastructures. Also, at the end of paper it is concluded that several advance techniques like cloud computing and implementation of machine learning in easing operation of vehicle are also possible (Table 1).

4 Energy Requirements of EV's in India

As per Bureau of Energy Efficiency [10], India is country where transport sector accounts 18% of total energy consumption. To fulfill this large amount of energy demand, importing crude oil is the current option but with this by 2030, high energy

Table 1 Survey statistics for electrical vehicles [9]

Sr. No.	Parameters	Survey statistics			Conclusion
1	Rise in fuel price in IC engine Vehicles	Low (0%)	Moderate (7.7%)	High (92.3%)	Green vehicles fuel price rise is less
2	Rise in fuel price in Electric Vehicles	Low (50%)	Moderate (46.2%)	High (3.8%)	
3	Travelling safety in IC engine Vehicles	Low (11.5%)	Moderate (15.4%)	High (73.1%)	There is no as such impact of fuel type on safety if travelling by electric vehicle
4	Travelling safety in Electric Vehicles	Low (7.7%)	Moderate (61.5%)	High (30.8%)	
5	Is driving by IC engine vehicle economical?	Low (42.3%)	Moderate (26.9%)	High (30.8%)	Driving by electric vehicle is economical
6	Is driving by electric vehicle economical?	Low (15.4%)	Moderate (50%)	High (34.6%)	
7	Maintenance cost of IC engine vehicle ?	Low (3.8%)	Moderate (57.7%)	High (38.5%)	Maintenance cost of EV is moderately high
8	Maintenance cost of electric vehicle?	Low (30.8%)	Moderate (46.2%)	High (23.1%)	
9	Initial cost of IC engine vehicle	Low (15.4%)	Moderate (50%)	High (34.6%)	Electric vehicles Initial cost is higher than IC engine vehicles
10	Initial cost of electric vehicle	Low (15.4%)	Moderate (38.5%)	High (46.2%)	
11	Ease of refueling if fuel points are provided just like IC engine vehicles fuel points	Low (23.1%)	Moderate (19.2%)	High (57.7%)	Peoples found it is highly unsuitable if fuel point structure of electrical vehicles is similar to IC engine fuel point structure
12	Possibility of utilization of renewable source of energy in IC engine vehicles	Low (42.3%)	Moderate (15.4%)	High (42.3%)	More chances with electric vehicles to use fuel from renewable source of energy
13	Possibility of utilization of renewable source of energy in electric vehicles	Low (15.4%)	Moderate (15.4%)	High (69.2%)	

(continued)

Table 1 (continued)

Sr. No.	Parameters	Survey statistics			Conclusion
14	Ease of driving with electric vehicle	Low (3.8%)	Moderate (38.5%)	High (57.7%)	High ease of driving in electric vehicles

demands make this sector vulnerable to the volatile International crude oil prices. Even today in 2021, the prices of petrol and diesel are continuously rising and with that CO₂ level as well [11]. Interestingly transport sector accounts 142 million tonnes of CO₂ emissions out of which road transportation shares value of 123 million tonnes. Considering environmental impact of these emissions, it is a need of hour to use fuel source having zero or minimum CO₂ emission (Fig. 4).

Electric vehicles running on renewable source of energy are viable option here. As on 31st January 2021, central electricity authority under Ministry of Power (GOI) [13], following is the statistic of installed capacity in India for production of electricity (Table 2).

Looking these recent statistics to make greater impact of electric vehicle as green vehicle government of India needs to give a boost to use renewable source of energy for electricity production. As per statistic in table, around 36.8% of total energy need comes from renewable source of energy. Utilizing electricity produced from non-renewable source of energy means defying concept of electric vehicle as green vehicle. Moreover, as per researcher tremendous hydroelectric potential yet remains to be tapped [14]. Following chart will give exact idea of this untapped potential (Fig. 5).

From the figure around 90,000 MW is yet to be taken under construction which if implemented surely satisfy approximately extra 25% electricity requirement. This

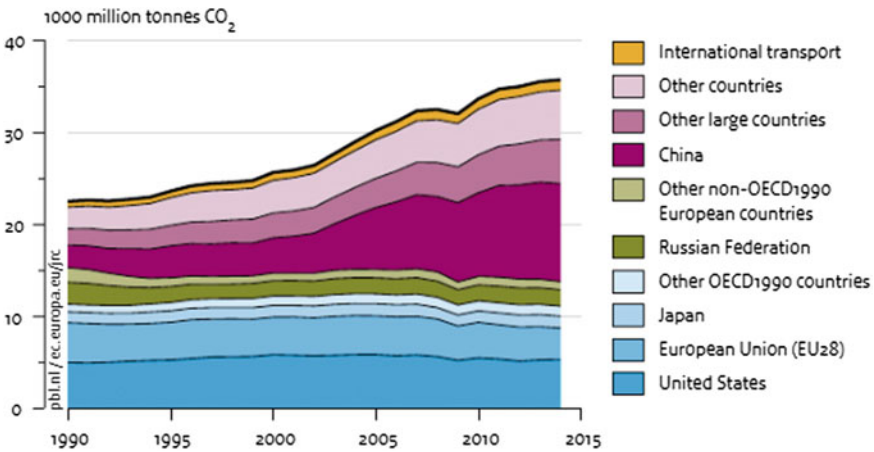


Fig. 4 Global CO₂ emission [12]

Table 2 Actual installed capacity by source in India

Sr. No.	Source type	Percentage share in electricity	Renewable or non-renewable
1	Coal	200,248.5 MW (53.1%)	Non-renewable
2	Lignite	6120 MW (1.6%)	Non-renewable
3	Large hydroelectric	46,059.22 MW (12.2%)	Renewable
4	Small hydroelectric	4758.46 MW (1.3%)	Renewable
5	Solar power	38,794.07 MW (10.3%)	Renewable
6	Wind power	38,683.65 MW (10.3%)	Renewable
7	Natural gas	24,956.51 MW (6.6%)	Non-renewable
8	Biomass	10,314.56 MW (2.7%)	Renewable
9	Nuclear power	6780 MW (1.8%)	Non-renewable
10	Diesel	509.71 MW (0.1%)	Non-renewable

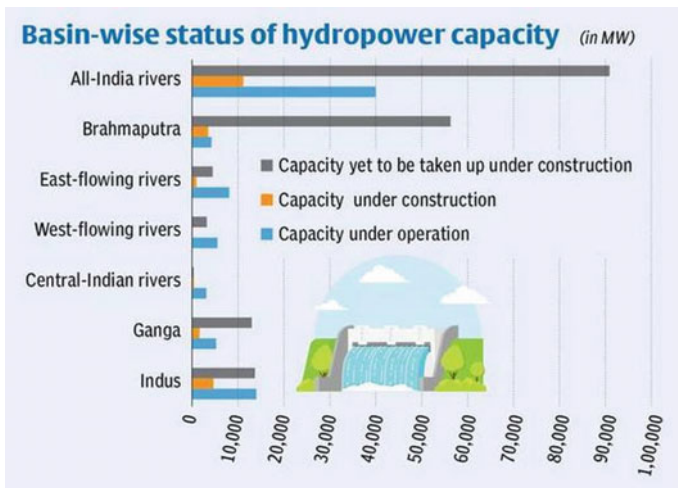


Fig. 5 Hydropower capacity of India [15]

can be good renewable source which can fulfil demand of electricity for electric vehicles.

5 Prospects of Electric Vehicle in India

India has undoubtedly focused on next-generation mobility under the present government, but the NEMMP [16] was actually launched in 2013 under the previous government. It is anticipated that the next decade will be the full electric vehicle. The widespread use of e-mobility has much in India. The Make In India programmed is expected to raise the share of manufacturing e-vehicles and related components in Indian GDP to 25% by 2022. The economic front is projected to save 60 billion dollars in oil imports by 2030 by means of the large-scale adoption of energy vehicles—82% of India's oil demand is currently met by imports.

5.1 Zero Emissions and Pollution

E-cars do not release greenhouse gases that are harmful to the environment or nitrogen oxide that is harmful to one's health. While it is a diverse story from the well to the wheel for these vehicles, the bottom line is that an EV has no final emissions. This allows them to run cleanly. As a result, these are considered non-polluting vehicles. Ideal for situations such as Delhi's own odd-even and those puffing for air.

5.2 Low Operating Cost

A car or two-wheeler that runs on electricity would often have lower operating costs. After all, the government must import oil, which affects fuel prices. The cost of electricity has nearly remained constant. If you do the math, the cost of running an EV is less than 60 paisa/km. That is a significant savings when compared to the cost of operating your own petrol/diesel vehicle, which will be at least ten times higher.

5.3 Low Registration Charges & Cost

It reduced registration fees, or even none at all. A few states provide free registration and other perks if you buy an electric vehicle. Furthermore, municipally reserved parking spaces are open for EVs. Although it is less expensive, PUC certificates are not needed.

5.4 The Simplest Driving Operation

In the world of vehicles, electric cars have the simplest driving form. Commercial electric vehicles have a transmission with only one extremely long gear. They also do not have the stalling issue that petrol cars do. This fundamentally removes the need for a clutch system to prevent stalling from occurring. This simply means that you can drive an electric vehicle using solitary the accelerator pedal, brake pedal, and steering wheel. Regenerative braking is another extremely useful function of electric vehicles. In most vehicles, the braking mechanism wastes all of the kinetic energy that is emitted as frictional heat. In an electric car, though, instead of being lost to heat, the same energy is used to charge the batteries.

6 Difficulties in India EV Adoption

In the quick acceptance of EVs in India, many factors act as a major obstacle. This involves inadequate charging facilities, a reliance on manufacturing incentives, higher battery costs and import reliance, high EVs currently in a state where electricity is insufficient in many parts of the country, insufficient quality repairs options, a failure to maintain quality, a dependency on component and part imports, a lack of high-quality features. The average on-road price of electric vehicles in India is high. In addition to these challenges, a change in e-mobility can bring about a significant change in the future, as e-mobility is strongly linked to environmental benefits. EVs will offer many companies willing to develop and remain at the forefront of the industry. Some of the key issues are as follows:

6.1 The Expensiveness of Electric Vehicles

The average on-road electric vehicle prices for India are not sufficiently attractive to consumers. Moreover, in India, the average cost in electric cars for economical cars run on traditional fuel is about Rs. 13 Lakh, which is far higher than the average Rs. 5 Lakh. The price of electric scooters in India is also high.

6.2 Charging Infrastructure

In 2018, 650 charging stations were there in India, while in the same year China had over 456,000 charging points. Apart from charging points, the absence of private parking spaces also impedes the adoption of electric cars, and the lack of affordable

energy to charge electricity generators imposes a charge on the existing stressed coal-fired electricity grid. EVs take a great deal of time to be charged. In today's scenario, it takes up to sixty minutes to charge even if the charge technology is most advanced. It's a lot of time to spend with a lot of stuff. This makes it clear that charging stations are no longer necessary as fuel stations and charging stations can consist of cafes, movie halls or even malls that allow people to relax or recharge.

6.3 Lack of Quality Maintenance and Repair Options

For EVs, the exact service costs are still unknown. Many service centers are known for duping customers by mentioning false car problems. In this area, EVs can only cause additional problems. In case of electric car breakdown, you cannot call just a normal mechanic for a normal vehicle like you would. You will only have to call some authorized service staff from the company to lead me to my next item. As a result, until a significant number of them are no longer on the road, most mechanics will be unaware of their complete systems, causing inconvenience for the consumer.

6.4 Battery Scrapping

It is anticipated that electric vehicles will enter the market enormously by 2030. The battery life is estimated at approximately one thousand charge cycles of a well picked up lithium battery two-wheel drive. Because of the fact that the use of these batteries will take two to five years to replace them. Your past batteries can, however, be used to compose power banks that can make use of disused batteries and store energy for various purposes while you decide to change your batteries.

It still has the ability to achieve optimum benefit such as for wind and solar power sources and can be recycled for metals like copper, steel or aluminum once the batteries lose their full loading.

6.5 Lack of Assured Government Policy

For years, electric vehicles have been welcomed in many European countries through reductions in their taxes and subsidies in some ways. In particular for electric vehicles, clear rules and policies are made to promote buyers. Some even plan to only sell EVs at long last. In India, however, this is another storey, since the administration had never been clear from the beginning about its EV policy. This has confused the car manufacturers about their electric vehicle plans. The fact that you pay more for electric vehicles is, as it does, for consumers.

However, the challenges associated with EV deployment have become more controllable in recent years, but they remain significant. The life cycle cost of ownership of EVs has decreased significantly, with further decreases in installed battery prices expected. Below \$300 per kWh may result in genuine parity with ICEs within the next 5–7 years.

7 Architectural Overviews of Electric Vehicle

The basic block diagram of electric vehicles is as given below. An electric source provides required power to electric power convertor which can be used by electric motor and vehicle control unit to run vehicle. Auxiliary power unit is also there to supply power to cooling and power steering unit. Though basic but one can understand except additional electric units basic working of vehicles remains same. This is in fact good thing as much lesser variation in design of electric vehicle as compared with IC engine vehicles. Actual diagrammatic representation of vehicle is also shown. In the today's world of artificial intelligence by studying electric vehicle architecture, one can say implementation of AI in self-driving cars [8] and auto-mode E-vehicle [7] is possible in electric vehicle as basic architecture remains same and there is surely no impact on ease of driving on electric vehicles. Also, techniques like cloud computing [17] and machine learning [18] will make electric vehicle safest and easiest in its operation (Figs. 6 and 7).

Fortunately, as per revised guidelines issued by Ministry of Power the electric stations which are required to charge batteries of electric vehicles are de-licensed activity unlike to conventional IC engine fuel charging stations [20]. This actually creates additional opportunities in employment/business generation and boosting economy.

8 Conclusion

From the discussion authors concluded that EV has more promising future in India. In order to compensate pollution caused because of IC engine vehicles EV plays promising role in all green vehicles. As per IEA report 2009, fossil fuel-based vehicles are second largest origin of CO₂ emitter and in addition to that from 2006 to 2030 the energy consumption of world on fossil fuel is susceptible to rise by 53% resulting in tremendous damage to environment.

Twentieth century in mankind is a century of IC engine-based vehicles, but twenty-first century will be century of electric vehicles. Countries like India and USA are taking major initiatives to encourage use of electric vehicles through their vehicle emission standards. More recent technologies in electric cars help in bringing down initial cost of electric vehicle. The study's goal was to bring together all of the pieces of information that contribute to a complete picture of the potential significance of

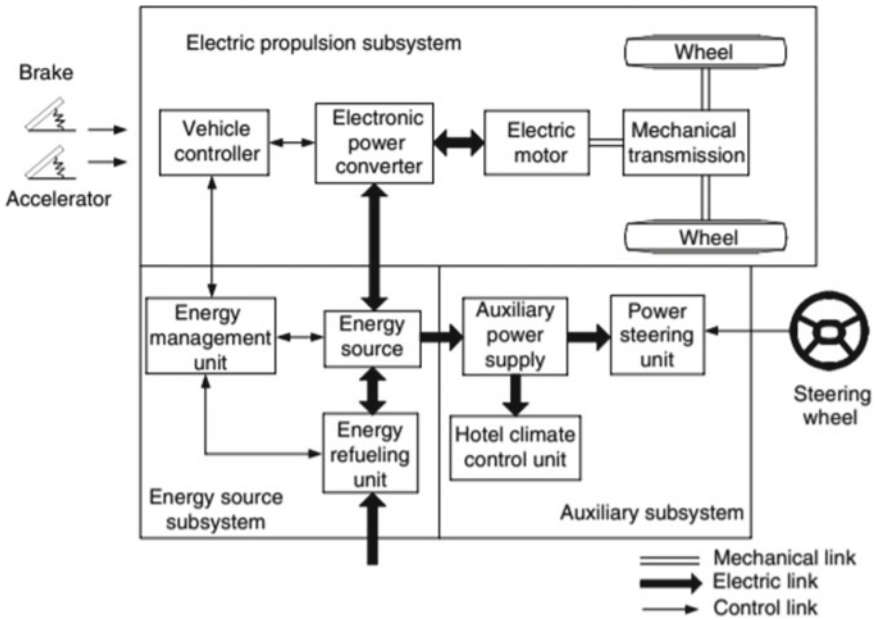


Fig. 6 Block diagram of electric vehicle [19]

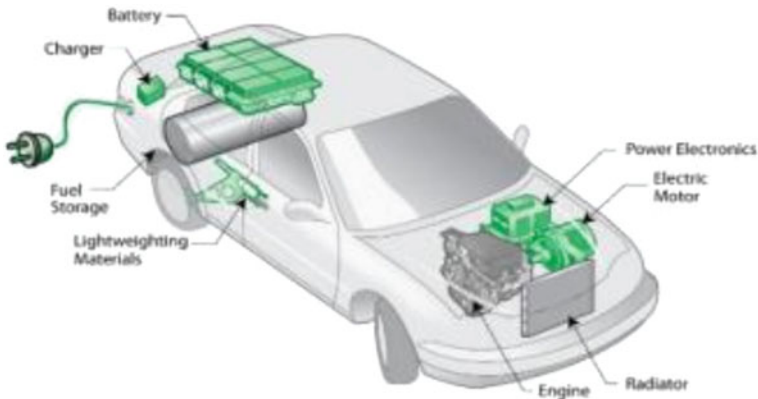


Fig. 7 Implementing block diagram in actual architecture of electric vehicle [10]

this technology. While electric vehicles are making a difference now, their impact could be amplified if the government and lobbying groups make a concerted effort to boost more policy change, research, and manufacture of electric vehicles.

The criteria for determining whether public ownership and cost-based charging infrastructure is the best tool for developing this market, or whether charging infrastructure should be left entirely to the private sector is a key feature in popularizing

EV in India. However, decentralize private station at several service section in the community may produce ease of refueling and additional income to private vendors which is supported by recent guidelines issued by Ministry of Power.

In order to make this difficult but achievable task, it is now right time for governments to take a lead and encourage businessman and common people to use EV by providing subsidies and established centers for complete technical guidance for manufacturing and use of EV. Consideration of renewable source of energy for providing electricity for EV is also one of the main tasks in front of Indian government. Government can take option like solar energy, wind energy for remote decentralize charging station in order to make EV successful in India. But, most importantly trapping unused potential of hydroelectric power is key aspect for electric vehicle future in India.

Just because of architectural similarity, merely change in fuel the ease of driving and operating vehicle is not reduced. Also, utilization of recent smart gadgets in electric vehicle is as similar as IC engine vehicles which makes electric vehicle as comfortable in its operation as IC engine vehicles.

Electric vehicles initial cost is higher and this could be only possible disadvantage in front of IC engine vehicle. Also, considering the lower maintenance cost, lower refueling cost, reduction in environmental degradation and long-term prospect of creating additional boost to existing economy makes electric vehicle most viable option to IC engine vehicle.

References

1. <https://ourworldindata.org/fossil-fuels>
2. Chalk SG, Miller JF (2006) Key challenges and recent progress in batteries, fuel cells and hydrogen storage for clean energy systems. *J Power Sources* 159(1):73–80
3. Goel S, Sharma R et al (2021) A review on barriers and challenges of electric vehicles in India and vehicle to grid Optimisation. Elsevier Jan 2021, vol 4
4. Panday A, Bansal HO (2013) Green transportation in India: need analysis and solution. In: International conference on control automation robotics and embedded system (CARE)
5. Luthra G (2017) Struggles faced in the research and development of electric vehicles in India: present scenario. *Int J Mech Prod Eng* 5(6)
6. Kumar R, Jha A et al (2020) Addressing the challenges to electric vehicle adoption via sharing economy: an Indian perspective. *Manag Environ Qual Int J*
7. Bindhu V (2020) An enhanced safety system for auto mode E-vehicles through mind wave feedback. *J Inf Technol* 2(03):144–150
8. Manoharan S (2019) An improved safety algorithm for artificial intelligence enabled processors in self driving cars. *J Artif Intell* 1(02):95–104
9. Author Google Form Survey Link: https://docs.google.com/forms/d/1mWEHjPOGrTKArja414d7NjmOdfxzXtWEEVe5qiW0w_c/edit#responses
10. <https://beeindia.gov.in/content/emobility#:~:text=If%20India%20were%20to%20follow,the%20demand%20of%20this%20sector.>
11. Kamyotra JS et al (2010) Status of the vehicular pollution control programme in India. Central pollution control board (Ministry of Environment and Forests, Government of India)
12. Olivier JGJ, Peters JAHW (2012) Trends in global CO₂ emissions. PBL Netherlands environmental assessment agency

13. https://cea.nic.in/wp-content/uploads/installed/2021/01/installed_capacity.pdf
14. Malhan P, Mittal M (2021) Evaluation of different statistical techniques for developing cost correlations of micro hydro power plants. *J Sustain Energy Technol Assess* 43:100904
15. <https://www.thehindubusinessline.com/opinion/indias-true-hydropower-potential-remains-untapped/article31580979.ece>
16. National electric mobility mission plan 2020
17. Bindhu V (2020) Constraints mitigation in cognitive radio networks using cloud computing. *J Trends Comput Sci Smart Technol (TCSST)* 2(01):1–14
18. Raj JS (2020) Machine learning implementation in cognitive radio networks with game-theory technique. *IRO J Sustain Wirel Syst* 2:68–75
19. Ehsani M, Gao Y, Emadi A (2010) *Modern electric, hybrid electric and fuel cell vehicles-fundamentals, theory and design*, 2nd edn. CRC Press, New York, USA, pp 1–18
20. Charging infrastructure for Electric Vehicles (EVs)-Revised Guidelines and Standards issued on 01.10.2019

Chapter 38

Multi-layered Epoxy Composites of Micro and Nano Bi₂O₃ and Ta₂O₅ for γ -ray Shielding



Srilakshmi Prabhu, Ajith Geejo, Rohit Dagar, Divyasree Chakraborty, Andrews Jacob, Sriya Paul, S. G. Bubbly, and S. B. Gudennavar

Abstract In this work, we have developed lead-free multi-layered epoxy polymer composites to effectively shield personnel and equipment against high energy γ -rays. Multi-layered shield, consisting of several layers of different materials, not only contributes to weight and cost reduction but also offers solution to inconsistent shielding performance. Compared to single layer of one type of shielding material, the probability of radiation absorption and scattering is higher in multi-layered configuration, thus enhancing shielding efficiency. However, there is a need to investigate the effect of stacking sequence and properties (dispersion of fillers, density of composites, etc.) of multi-layered materials on shielding performance. In view of this, several combinations of epoxy multi-layered composites containing micro and nano particles of both bismuth (III) oxide and tantalum (V) oxide were prepared to study the attenuation of γ -rays from ¹³⁷Cs (662 keV) radioactive source. Attenuation experiments showed that the layered epoxy composites loaded with 30 wt% Bi₂O₃ nanoparticles alone showed around 30% γ -ray attenuation. 19-mm-thick multi-layered shield composed of two layers of n-Ta₂O₅/epoxy at the outer side, and two layers of n-Bi₂O₃/epoxy layer at the inner side were found to be as effective with almost same shielding efficiency. At around similar thickness, the epoxy composite containing n-Bi₂O₃/m-Bi₂O₃/n-Ta₂O₅/m-Ta₂O₅ layer-by-layer showed 28% attenuation, demonstrating the synergistic effect of combining micro and nano sized particles. Enhancement in attenuation on use of multi-layered structures would be attributed to the fact that epoxy composites containing different fillers of varying size will probably attenuate radiations more efficiently than those with one type of filler of a particular size. This work demonstrates that the multi-layered high-Z metal oxide-polymer composites may be as reliable as conventional lead-based materials in attenuating γ -rays.

S. Prabhu · A. Geejo · R. Dagar · D. Chakraborty · A. Jacob · S. Paul · S. G. Bubbly (✉) · S. B. Gudennavar

Department of Physics and Electronics, CHRIST (Deemed to be University), Bangalore Central Campus, Bengaluru, India

e-mail: bubbly.sg@christuniversity.in

Keywords γ -ray shielding · Multi-layered configuration · Lead-free composites · DGEBA epoxy matrix · High-Z metal oxides · Nanofillers · Size-dependent shielding · Stacking sequence

1 Introduction

Progress in nuclear science and technology has immensely influenced medical and healthcare industry, agriculture, food sterilization, industrial gauging and aerospace, making the world a better place. Undesirable exposure to high energy radiations, such as X-rays or γ -rays in these sectors, can have adverse effect on human health due to accumulation of radiation dosage. Therefore, the use of appropriate shielding material for radiation protection is crucial to mitigate any kind of radiation damage. Lead (Pb) and lead-based shielding materials are most commonly preferred owing to their superior radioprotective characteristics. However, the use of these Pb-based materials not only present an insidious health hazard but also make the protective gears clumsy, thus limiting its application. In view of developing light weight and eco-friendly shielding materials, polymer-based metal/metal oxide composites (PMCs) are considered to be propitious candidates. Particularly, polymer nanocomposites are found to be more efficient owing to the large surface-to-volume ratio of nanofillers and their consequent ability to attenuate more radiations [1]. In general, the shielding efficiency of these PMCs is mainly dependent on the type of filler and uniformity in dispersion of fillers in the matrix, as the polymer matrix alone lacks shielding ability. Shielding performance of these PMCs can be substantially enhanced by designing densely packed structures, leaving no pinholes in the composites, to ensure greater probability of radiation—matter interaction. Therefore, exploiting the properties of multi-layered structuring in PMCs can greatly extend the utility of these materials.

A multi-layered shield basically consists of two or more layers of different materials stacked together, such that the incident radiations have more chances to be scattered and absorbed by the shield. Stacking of several layers of PMCs, with each layer having uniform distribution of fillers, would reduce void paths for photons to penetrate, thus increasing radiation attenuation probability [2, 3]. Materials with different shielding properties can be layered in various configurations to achieve optimal shielding design. In this regard, different types of PMCs and their combinations have been tested for their radiation shielding efficiency. McCaffrey et al. investigated theoretically the X-ray shielding ability of three low-Z/high-Z bilayer (Sb/W, Sb/Bi and Ba/Bi) metal powders embedded in elastomer layers using MCNP simulations [4]. The low-Z upstream/high-Z downstream ordering of these metal bilayers was reported to be 5 times more efficient than the reverse order at 50 kVp, with the effect gradually diminishing at 150 kVp. Kim et al. reported that the shielding ability was greater when 150 kVp photons passed through W layer first and Sendust/polymer composite layer next, suggesting that high-Z/low-Z order is better than the reverse arrangement [5]. Multi-layered composites of lead acrylate/erbium oxide/epoxy and tungsten oxide/erbium oxide/epoxy investigated for shielding at 79.9, 167.6 and

662 keV by Zhang et al. suggested that these composites exhibited higher shielding ability for low energy γ -rays [6]. Kim et al. reported that 20-mm-thick multi-layered material composed of BiSn/polymer composite laminated to W sheet achieved complete attenuation of γ -rays of 662 keV [3]. Thin and flexible multi-layered nanocomposites of lead/polyimide (PI) were synthesized for radiation protection, in particular, against X-ray bremsstrahlung in outer space [7]. Nano dispersed metallic lead was first filled into 200-nm-diameter pores of PI films, and these lead-filled PI track membranes were then assembled into a sandwich of required thickness to form multi-layered shields. The X-ray attenuation studies carried out in the energy range of 10–88 keV via the mathematical simulation, showed that the attenuation coefficients of the proposed composite structures were 22–24% lower than pure lead. Recently, Li et al. [8] studied the effect of direction of X-ray incidence, number of layers and layer thickness ratio of (tungsten/ethylene-octene copolymer)/(bismuth/ethylene-octene copolymer) layered composites on their shielding efficiency. In the energy range of 70–90 keV, they found that the shielding ability significantly improved when layer containing fillers with higher absorption edge was arranged in front. However, there is no clear trend observed on various aspects of multi-layered structuring and its effect on shielding efficiency.

In the present study, we have evaluated the γ -ray shielding efficiency of epoxy resin-based composites, containing both micro and nano sized fillers of bismuth (III) oxide (Bi₂O₃) and tantalum (V) oxide (Ta₂O₅), at 662 keV γ -rays from ¹³⁷Cs radioactive source. We have employed multi-layer structuring to investigate the effect of filler size and stacking sequence on shielding properties. The thermosetting epoxy resin, diglycidyl ether of bisphenol A (DGEBA), was used as matrix owing to its good engineering properties such as chemical and corrosion resistance, good workability, high stiffness and creep resistance. Both Bi₂O₃ and Ta₂O₅ fillers are non-toxic and non-carcinogenic, making the composite systems benign. The multi-stacked structure of epoxy/Bi₂O₃/Ta₂O₅ is expected to provide effective γ -ray shielding for further design and development of protective gears, disposal containers for radioactive wastes and units for storage of radioactive sources.

2 Materials and Methods

2.1 Materials

Bisphenol A diglycidyl ether-based (Araldite LY556) epoxy resin (DGEBA) and triethylenetetramine (TETA)-based (Aradhur HY951) curing agent were procured from S & S Polymers, Bengaluru, India. Tantalum (V) oxide nanopowder having average particle size (APS) of 80 nm and bismuth (III) oxide of APS 20 nm were supplied by Nanoshel LLC, USA. Micron-sized Ta₂O₅ and Bi₂O₃ were purchased from Laboratory Traders, Bengaluru, India.

2.2 Preparation of Epoxy Composites

Neat and $\text{Bi}_2\text{O}_3/\text{Ta}_2\text{O}_5$ filled epoxy composite films were prepared by room temperature solution casting technique. For the preparation of neat epoxy film, DGEBA epoxy resin was mixed with curing agent triethylenetetramine (TETA) in the mass ratio 100:10 by ultrasonication followed by vigorous stirring for 30 min. The mixture was degassed and poured into appropriate mold and left for curing at room temperature for 24 h. This was followed by heating at $130\text{ }^\circ\text{C}$ for 6 h in a hot air oven.

Epoxy/ $n\text{-Ta}_2\text{O}_5$ composite (Layer A) was prepared as follows: 30 wt% $n\text{-Ta}_2\text{O}_5$ was dispersed into epoxy matrix via mechanical stirring, and the slurry was subjected to ultrasonic vibrations for 1 h to ensure uniform dispersion of fillers. During ultrasonication, the beaker containing epoxy/filler mixture was submerged in an ice water bath for external cooling to avoid temperature rise. This semi-viscous slurry was again vigorously stirred for 1 h to prevent any possible sedimentation. Post addition of stoichiometric amount of hardener, the mixture was degassed and poured into molds for curing. Curing cycle for the composites was similar to that of neat epoxy. Other layers, namely, Layer B containing 30 wt% $n\text{-Bi}_2\text{O}_3$ /epoxy, Layer C containing 30 wt% $m\text{-Ta}_2\text{O}_5$ /epoxy and Layer D containing 30 wt% $m\text{-Bi}_2\text{O}_3$ /epoxy were prepared in a similar manner. Schematic illustration of sample preparation is presented in Fig. 1. High resolution SEM images of the composites were obtained using JEOL Model JSM-6390LV.

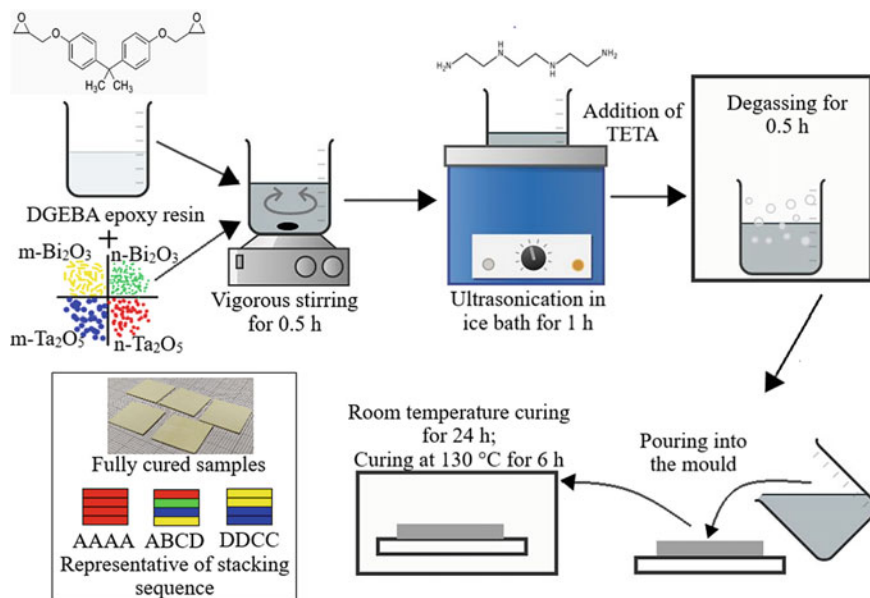


Fig. 1 Schematic illustration of epoxy composite synthesis and stacking

Eighteen different multi-layer configurations of composites with Layer A, Layer B, Layer C and Layer D were prepared layer-by-layer and designated as AAAA, BBBB, CCCC, DDDD, AABB, ABAB, BABA, BBAA, CCDD, CDCD, DCDC, DDCC, BDAC, BADC, ACBD, ABCD, CADB and CDAB. The shielding efficiency of all the 4-layered composites were investigated at 662 keV γ -rays from ¹³⁷Cs radioactive source.

2.3 γ -Ray Attenuation Measurements

γ -Ray shielding measurements were performed on a well-calibrated 2'' \times 2'' NaI(Tl) detector coupled to 8 k multichannel analyzer (MCA). ¹³⁷Cs radioactive source (662 keV) with activity of 2.40 μ Ci (as on December 2020) was procured from Board of Radiation and Isotope Technology (BRIT), Mumbai, India. γ -ray shielding properties of the composites were determined in terms of mass attenuation coefficients (μ/ρ) by measuring the incident (I_0) and transmitted (I) intensities of γ -rays. Attenuation experiment was carried out adopting narrow beam geometry, the experimental setup being similar to that used in our previous study (Fig. 2) [9]. The γ -ray photons emitted from ¹³⁷Cs were collimated through two cylindrical lead collimators, each of height 3 cm and hole diameter of 3 mm. These collimators were spaced 2 cm apart from each other to accommodate the stacking of samples. Collimated γ -ray photons before and after passing through the sample were detected by NaI(Tl) detector spectrometer with a suitable acquisition time set in MCA. The live acquisition time of MCA was fixed such that the area under the photopeak of interest was sufficient (>10,000) to keep the contribution of statistical uncertainty to the results less than 1%. The 'background spectrum' and the 'incident plus background spectrum' were acquired for a suitable preset live time of the MCA without and with

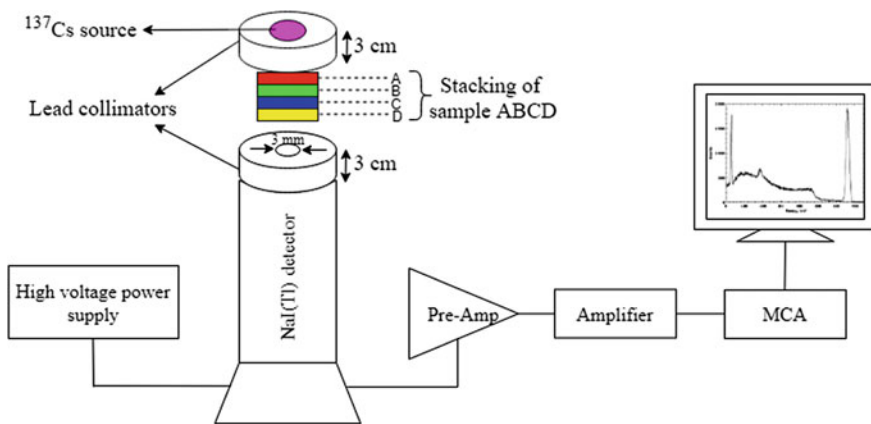


Fig. 2 Schematic diagram of γ -ray attenuation experimental setup

placing the source in the prefixed position in front of the collimator, respectively. The ‘background corrected incident spectrum’ was obtained by subtraction of ‘background spectrum’ from the ‘incident plus background spectrum’. This was followed by acquisition of the ‘background plus transmitted spectrum’ for the same live time but by inserting the composite films in between the collimators with the source in prefixed position. Again, ‘background corrected transmitted spectrum’ was obtained by subtraction of ‘background spectrum’ from the ‘background plus transmitted spectrum’. The background corrected incident and transmitted spectra, respectively, were used for obtaining I_0 and I , which are further required to determine the μ/ρ values. Using the OriginPro 2017 program, the area under ^{137}Cs photopeak was obtained by fitting with Gaussian function to determine I_0 and I at various thicknesses of the samples. However, before starting the radiation studies for the samples under study, the detector spectrometer was calibrated using various γ -ray sources (^{133}Ba , ^{22}Na , ^{137}Cs and ^{60}Co). Linearity and stability of the spectrometer were checked often throughout the experiment. Standardization of the experimental procedure was carried by determining the μ/ρ values for aluminum (Al) foils as its theoretical μ/ρ value is well-known. By varying the thickness of Al foils, I_0 and I of 662 keV γ -ray photons were measured, and μ/ρ value was obtained from the slope of $\ln(I)$ versus mass thickness (t) plot. The experiment was repeated thrice, and weighted average of μ/ρ values was compared with standard theoretical value obtained using WinXCom program [10]. The experimental and WinXCom μ/ρ values for Al agreed within 3%, and therefore, the same procedure was extended to all the epoxy composites used in the study. For different combinations and stacking arrangements, the μ/ρ values were determined with at least four different sample thicknesses (up to maximum thickness of 1.960 ± 0.002 cm). Further, the shielding efficiency (η) was determined as $\eta = 1 - (I/I_0)$, where I/I_0 is known as transmittance or dose ratio [3]. While stacking the different layers in a particular configuration, say ABCD, the Layer A was placed toward the radioactive source and Layer D toward the detector window (refer Fig. 2).

3 Results and Discussion

The shielding efficiency of the 30 wt% micro/nano $\text{Bi}_2\text{O}_3/\text{Ta}_2\text{O}_5$ filler loaded epoxy composites AAAA, BBBB, CCCC and DDDD were investigated first. Figure 3 shows an exponential decrease in transmittance of γ -rays for the 4-layered composites as the number of stacks increased. In particular, ~ 1.960 -cm-thick 4-layered sample BBBB showed highest shielding efficiency ($\sim 30\%$). For this sample BBBB, transmitted intensity (I) showed an exponentially decreasing behavior, consistent with decay law as $I/I_0 = \exp(-0.184 \times x)$, where x is the thickness of the composite in centimeter (cm) (Fig. 3b). This expression fits the data with a correlation of 1. With the increase in number of stacks of these composites, the dose ratio decreased, and the shielding effect increased. The shielding efficiency of the samples increased in the order BBBB

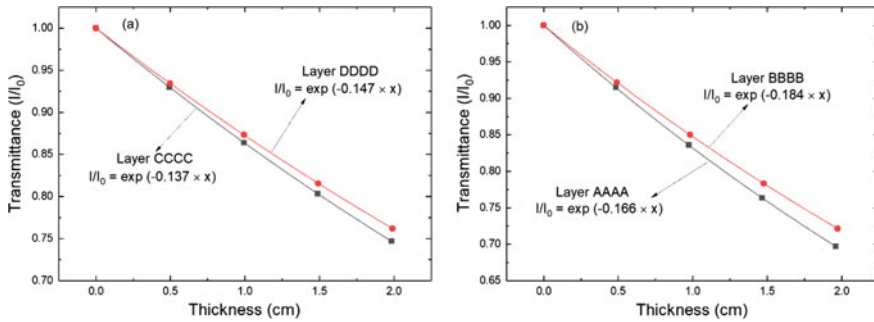


Fig. 3 γ -Ray transmittance through 4-layered composite of **a** Layer CCCC and Layer DDDD and **b** Layer AAAA and Layer BBBB

(30%) > AAAA (27%) > DDDD (25%) > CCCC (23%). These observations demonstrate that the nanocomposites have higher shielding efficiency when compared to their micro-counterparts. In particular, 30 wt% n- Bi_2O_3 /epoxy composites (BBBB) show enhanced shielding efficiency than epoxy composites containing 30 wt% n- Ta_2O_5 (AAAA). This could be attributed to (a) the difference in atomic number of fillers and (b) size-dependent shielding behavior. Owing to the higher atomic number of Bi ($Z = 83$) over Ta ($Z = 74$), Bi-based compounds have μ/ρ values greater than Ta-based. Secondly, the difference in sizes of Bi_2O_3 (~20 nm) and Ta_2O_5 (~80 nm) nanoparticles might have considerably influenced the shielding performance. With decrease in filler size, the surface-to-volume ratio increases, which not only ensures their uniform distribution over a larger surface area within matrix, but also tends to increase the volume fraction of fillers at surfaces or interfaces [11]. This in turn, increases the packing density of the composites, thus enhancing the interaction probability of photons with nano particles in nanocomposites compared to their micro-counterparts. In general, the distribution of fillers in the matrix plays crucial role in determining the shielding efficiency, such that, greater the homogeneity in distribution, higher is the probability of radiation attenuation. SEM images of single layer of each composite have been observed as shown in Fig. 4. Figure 4a, c shows fairly uniform distribution of spherical Ta_2O_5 fillers in epoxy matrix. The Bi_2O_3 nanoparticles are homogeneously dispersed in epoxy matrix, with composite films showing no phase separation or voids (Fig. 4b). Figure 4d shows the distribution of rod-shaped m- Bi_2O_3 fillers in epoxy.

Two layers each of two nanocomposites, 30 wt% n- Ta_2O_5 /epoxy (Layer A) and 30 wt% n- Bi_2O_3 /epoxy (Layer B), were arranged in 4 different combinations as AABB, ABAB, BABA and BBAA to study their shielding rates at 662 keV. The total thickness of stacked layers for these combinations was 1.850 ± 0.004 cm. It was observed that the multi-layer BBAA showed shielding performance close to that of BBBB and higher than other combinations. For BBAA, every photon passing through two layers of B would first encounter densely packed atoms in n- Bi_2O_3 /epoxy layers with incident photons losing their energy sufficiently. With decrease in energy of incident photons, they can be easily attenuated by two layers of n- Ta_2O_5 /epoxy composites.

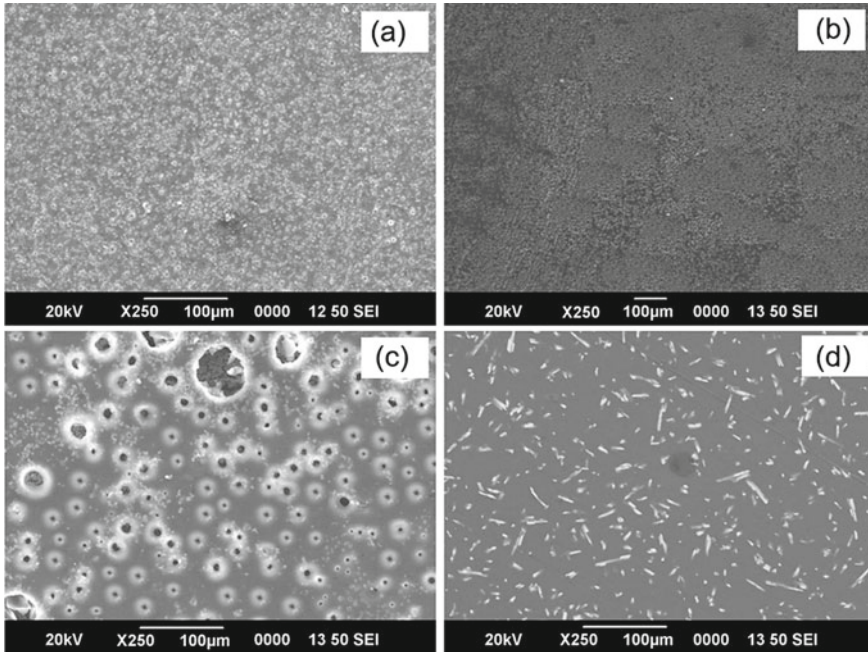
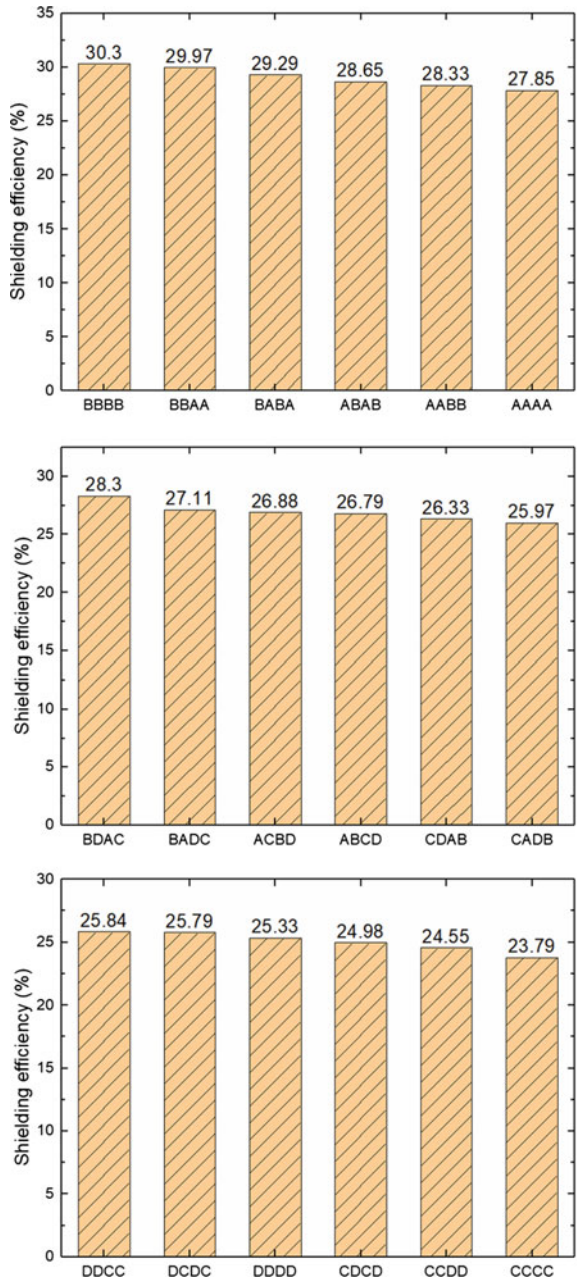


Fig. 4 SEM images **a** 30 wt% n-Ta₂O₅/epoxy (Layer A), **b** 30 wt% n-Bi₂O₃/epoxy (Layer B), **c** 30 wt% m-Ta₂O₅/epoxy (Layer C) and **d** 30 wt% m-Bi₂O₃/epoxy (Layer D)

On other hand, for AABB, the incident photons would not be attenuated as much as in BBAA while first passing through two layers of n-Ta₂O₅/epoxy composites because of relatively lower Z fillers. The remaining photons that still maintain their high energy would interact with two denser layers of n-Bi₂O₃/epoxy, thus implying that BBAA arrangement has better shielding performance compared to AABB. However, the shielding efficiency of these combinations is in between that of AAAA and BBBB in the order as follows: BBBB > BBAA > BABA > ABAB > AABB > AAAA. It is interesting to note that combining layers A and B would yield γ -ray attenuation to almost same extent as that of using stacks of single type of layer. This could be probably attributed to the synergistic effect of using nanofillers of different sizes and different atomic numbers. Also, in the multi-layered shield design, the subsequent layer is most probable to absorb the scattered radiation of lower energy emerging out from the preceding layer, yielding better results than that of when using them separately. On similar grounds, for several combinations of multi-layered micro-composites, we observed that the combinations DDCC, DCDC and DDDD have similar shielding properties. Also, the shielding efficiency exhibited by various combinations of micro-composites at 662 keV is significantly greater than the multi-layered epoxy composites containing particles of lead oxide, erbium oxide and tungsten oxide [2]. These results suggest that interlayering composites containing micro and nanoparticles of different atomic numbers would help achieve

attenuation as high as nanocomposites alone, thus making the composite systems cost effective. The comparison of shielding efficiency of different combinations studied in the present work is represented in Fig. 5.

Fig. 5 Radiation shielding efficiency of multi-layered composites for γ -rays at 662 keV



To further understand the effect of filler size and stacking sequence on shielding, both nano- and micro-composite layers containing Bi_2O_3 and Ta_2O_5 were intermixed in several ways as BDAC, BADC, ACBD, ABCD, CADB and CDAB. The shielding efficiency of these layers was significantly higher than that of multi-layered micro-composites. The combination in which two layers of epoxy containing high-Z fillers arranged in front of two layers of epoxy containing low-Z fillers, irrespective of filler size, seems to display considerably good shielding rate. In the present case, the shielding efficiency follows as $\text{BDAC} > \text{BADC} > \text{ACBD} > \text{ABCD}$. Also, BDAC shows shielding (~28.30%) on par with multi-layered nanocomposites of AABB and AAAA. This could be probably attributed to less prominence of filler size effect at 662 keV γ -rays. In any case, there is no large difference between the shielding efficiency of various combinations. Composite stacks containing intermixed layers of A, B, C and D could be used in place of nanocomposite stacking so as to yield similar shielding performance at relatively lower cost. However, there was no significant change in shielding performance among these hybrid multi-layered structures, suggesting the need for detailed investigation on multi-layer designs in future.

Altogether, we couldn't derive definite conclusion on effect of stacking sequence on the shielding performance, although some of the previous studies claim that there was significant difference in shielding on interchanging the layers [12]. These differences in observations could be attributed to error in shielding calculations arising from build-up factor (B). On absorption or scattering of radiations from interacting medium, secondary radiations such as β particles or low energy γ -ray photons are produced. Also, the direction of the radiation particles may also change during scattering process, and these scattered particles get transmitted through the shielding material. This phenomenon is referred to as 'build-up' and is represented by build-up factor (B), neglecting which may give rise to inaccurate results. Therefore, there is a need to study different kinds of multi-layer shield designs and layer arrangements as function of energy to clearly understand the shielding effects. These studies must also be accompanied with build-up factor calculations either experimentally or theoretically using photon transport simulation codes such as Monte Carlo or GEANT4. With thorough investigation, it is possible to optimize multi-layer shielding design so as to improve the efficiency radioprotective materials.

4 Conclusions

The new Bi_2O_3 /epoxy and Ta_2O_5 /epoxy micro and nanocomposites were found to be effective materials in shielding high energy γ -rays (662 keV from ^{137}Cs source). The multi-layered composites showed fairly good shielding ability against high energy γ -rays. 4-layered nanocomposites of epoxy, each layer containing 30 wt% n- Bi_2O_3 fillers, showed highest shielding efficiency of 30%, probably owing to nano effect. At similar thickness, multi-layered structuring with epoxy layers containing nanoparticles of different sizes and different atomic numbers yielded almost same shielding, attributed to multiple scattering events. On similar grounds, combining

layers of epoxy composites containing different micron-sized fillers of different atomic number enhanced attenuation over single type. On the other hand, the 4-layered hybrid composites, each of which contains one of either n-Bi₂O₃, m-Bi₂O₃, n-Ta₂O₅ or m-Ta₂O₅ fillers, showed shielding efficiency on par with multi-layered nanocomposites with different fillers. However, there was no significant difference in the shielding performance due to change in layer arrangement and stacking sequence at 662 keV. Future studies on such multi-layered shielding designs and their performance dependence on energy of incident radiations, stacking sequence and layer arrangement would be helpful in improving their design for efficient radiation protection.

References

1. More CV, Alsayed Z, Badawi MS, Thabet AA, Pawar PP (2021) Polymeric composite materials for radiation shielding: a review. *Environ Chem Lett* 19:2057–2090
2. Sazali MA, Rashid NKAM, Hamzah K (2019) A review on multilayer radiation shielding. *IOP Conf Ser Mater Sci Eng* 555:012008–012016
3. Kim H, Lim J, Kim J, Lee J, Seo Y (2020) Multilayer structuring of nonleaded metal (BiSn)/polymer/tungsten composites for enhanced γ -ray shielding. *Adv Eng Mater* 22:1901448–1901455
4. McCaffrey JP, Mainegra-Hing E, Shen H (2009) Optimizing non-Pb radiation shielding materials using bilayers. *Med Phys* 36:5586–5594
5. Kim Y, Park S, Seo Y (2015) Enhanced X-ray shielding ability of polymer–nonleaded metal composites by multilayer structuring. *Ind Eng Chem Res* 54:5968–5973
6. Zhang HX, Chang SQ, Kang B, Sheng B, Dai YD (2014) Preparation of functional particles modified epoxy multilayer composite and their radiation shielding properties. *Adv Mater Res* 900:150–153
7. Cherkashina NI, Pavlenko VI, Noskov AV, Novosadov NI, SamoiloVA ES (2020) Using multilayer polymer PI/Pb composites for protection against X-ray bremsstrahlung in outer space. *Acta Astronaut* 170:499–508
8. Li Z, Zhou W, Zhang X, Gao Y, Guo S (2021) High-efficiency, flexibility and lead-free X-ray shielding multilayered polymer composites: layered structure design and shielding mechanism. *Sci Rep* 11(1):1–13
9. Prabhu S, Bubbly SG, Gudennavar SB (2021) Sodium alginate/bismuth (III) oxide composites for γ -ray shielding applications. *J Appl Polym Sci* 138:50369–50388
10. Gerward L, Guilbert N, Jensen KB, Levring H (2004) WinXCom—a program for calculating X-ray attenuation coefficients. *Radiat Phys Chem* 71:653–654
11. Mahmoud ME, El-Khatib AM, Badawi MS, Rashad AR, El-Sharkawy RM, Thabet AA (2018) Fabrication, characterization and gamma rays shielding properties of nano and micro lead oxide-dispersed-high density polyethylene composites. *Radiat Phys Chem* 145:160–173
12. Fuse T, Yamaji A, Miura T (1970) The optimum arrangement of laminated iron-water shields. *Nucl Eng Des* 13:390–394

Chapter 39

Carbon-Related Materials for Tribological Application



Nitish Singh Jammoria, Mir Irfan Ul Haq, and Ankush Raina

Abstract A lot of focus has been laid on the studies of carbon-related materials (CRMs). Owing to self-lubricating properties, high strength, high density, high hardness, and good electrical conductivity, CRMs find a variety of applications. Recent studies have shown that the carbon-related materials have been successfully incorporated in the Al, Mg, Cu and their alloys. Also, they serve as additives in different lubricating oils in order to obtain the improved tribological properties. Further, their use as coating materials also resulted in the enhancement of wear resistant capability of different materials. The aim of this paper is to discuss the recent developments in related to CRMs in field of tribology.

Keywords Carbon · Composites · Lubrication · Coatings · Tribology

1 Introduction

Energy conservation is the most important aspect of sustainable development [1]. Lot of energy is consumed due to the friction between materials under sliding contact. In automobiles, one-third of the losses are incurred in overcoming the friction itself and only one-fifth of the total fuel energy is effectively used to propel the vehicles [2, 3]. Tribological studies are aimed at controlling the friction and wear of not only the macro-sized materials but also of the micro-/nano-sized materials [4]. Coatings and surface texturing on the other hand are also the potential ways that can help in reducing the friction [5].

For further reducing of frictional coefficient and wear loss of the materials, small concentration of different additives (anti-wear, extreme pressure, anti-friction, anti-corrosion) are added in lubricants to improve the overall behavior of the lubricating oils. [6, 7]. The use of nanoparticles in composite materials is also an important aspect of material development as it results in improved properties (mechanical & tribological) in contrast to the bulk materials [8]. The size and volume fraction of the nanoparticles are key components in this aspect.

N. S. Jammoria · M. I. Ul Haq · A. Raina (✉)

School of Mechanical Engineering, Shri Mata Vaishno Devi University, Katra, J&K 182320, India

Carbon materials are most widely used as additives in bulk material as well as in lubricants because of good corrosion behavior, good mechanical properties, high thermal conductivity and good lubricating properties [9]. Figure 1 shows the number of articles published related to carbon materials in the field of tribology. The data were extracted from SCOPUS database by using the three set of keywords such as carbon + tribology + composites, carbon + tribology + lubrication and carbon + tribology + coatings. Diamond and graphite are the naturally occurring allotropes of the carbon, but they can be synthesized in any size, shape and properties by various physical and chemical methods. Carbon nanomaterials are regarded as most attractive materials for minimizing energy consumption. Apart from the lubricant additives, they can be used as additives in bulk material and for the development of coatings in order to attain the better tribological properties.

Carbon atoms have the ability to form three types of hybridizations and on the basis of that the carbon allotropes are classified in three categories— sp^3 hybridization, sp^2 hybridization and sp hybridization (Fig. 2). Another classification is on the dimensionality—zero-, one-, two- and three-dimensional (Fig. 3). Each of these

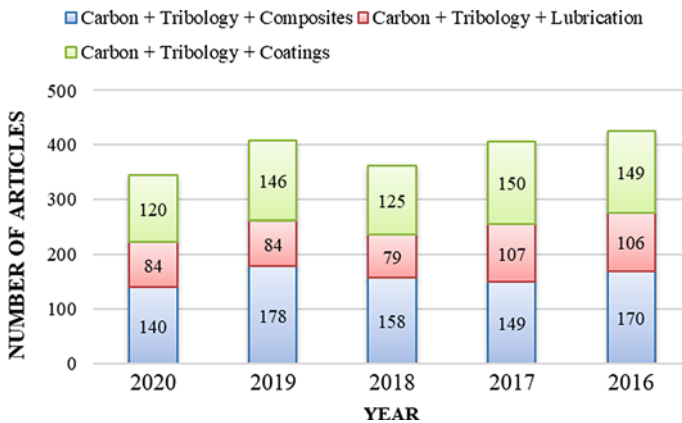


Fig. 1 Number of articles published related to the use of carbon-related materials in last five years. Source SCOPUS

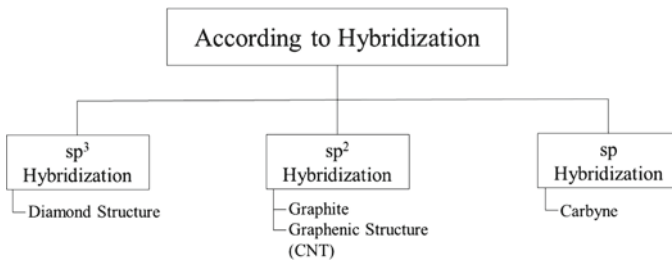


Fig. 2 Classification according to hybridization

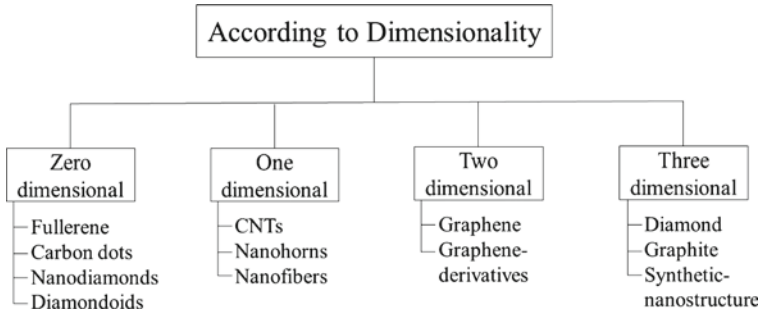


Fig. 3 Classification according to dimensionality

carbon atoms has its own distinct advantages due to which they find their specific application in each field. A brief description of the various carbon atoms used along with their classifications has been presented in Table 1. This paper presents an insight into the different studies carried with the use of carbon related materials. The paper is structured to present the studies related to the use of CRMs in different metal matrix composites. In the next section, their use as lubricant additives in different oils has been presented. Further, their use as coating materials has also been discussed in detail.

2 CRMs as Additives in Metal Matrix Composites (MMCs)

When one or more materials are added in a metal to enhance or tailor its certain properties, it is termed as MMCs. Different types of additives are added to the base matrix for enhancing its mechanical (yield strength, tensile strength, compressive strength, toughness, hardness) and tribological properties (coefficient of friction, wear resistance). In this section, a discussion on the various carbon-based materials in Al-, Mg- and Cu-based matrix has been made.

2.1 Aluminum Matrix Composites (AMCs)

The use of AMCs is one of the active areas in the material development. There is need for the lightweight materials with high mechanical strength and improved wear resistance properties, and different studies have been carried out in this direction [22, 23]. Slathia et al. [24] fabricated hybrid composite of AA 2024 reinforced with ZrO₂ (6 wt%) and graphite (1.5, 3 and 4.5 wt%). Density and microhardness decreased while ultimate compressive strength increased with increasing wt% of graphite.

Xiong et al. [25] fabricated graphene nanoplatelets (GNPs)-reinforced AMCs at four different compositions from 0.3 to 1.2 vol.% by spark plasma sintering (SPS).

Table 1 Brief description of the various carbon atoms used along with their applications

Types of carbon atoms	Structure/shape	Hybridization	Particle size (nm)	Advantages & applications
Fullerene (C60)	Spherical with 60 carbon atoms	In between sp^2 and sp^3	0.7 nm	Engineering and Medical industry Offers better lubricating conditions [10]
Carbon dots (CDs)	Quasi-spherical shape	Combined hybridization of sp^2 and sp^3	Below 10 nm	Less toxic, chemically stable and biocompatible Applications in medical and optical industry [11]
Nanodiamonds (nD)	Crystalline	sp^3 hybridized	4–5 nm	Chemically stable, biocompatible & non-toxic Best additive for improving lubricating properties of engine oils
Diamondoids	Cage structure	sp^3 hybridized	1–2 nm	Chemically & thermally stable and biocompatible Good mechanical properties [12]
Single-walled carbon nanotubes (SWCNT)	Single cylinder	sp^2 hybridized	1–2 nm	Energy storage and biomedical applications Thermally stable and conductive [13, 14]
Multi-walled carbon nanotubes (MWCNT)	Several concentric tubular structure	sp^2 hybridized	10–200 nm	Chemically stable and good thermal conductivity Best mechanical and electrical properties Mostly used in energy storage industry [15]

(continued)

Table 1 (continued)

Types of carbon atoms	Structure/shape	Hybridization	Particle size (nm)	Advantages & applications
Carbon nanohorns	Conical cage shapes	sp^2 hybridized	2–3 nm	Porous in nature Improves mechanical properties of nanocomposite Used in biomedical, fuel cells and gas storage industry [16]
Carbon nanofibers	Cylindrical structure	sp^2 hybridized	3–100 nm	Electrochemically stable and porous nature Excellent composite material [17]
Graphene	Hexagonal shape	sp^2 hybridization	25 μm	Chemically inert High Thermal and electrical conductivity Applications in medical industry [18, 19]
Graphene oxide (GO)	Sheet like structure	sp^2 hybridization	1–1.3 nm	Good coating material Biocompatible and highly functionalized [20]
Diamond	Cubic structure	sp^3 hybridized		Best mechanical, lubricating and coating properties Chemically stable and electrically conductive Excellent lubricating and coating material [21]

Chemical bonding improved between the reinforcement material and Al matrix and the load transfer efficiency of the interface has increased. Turan [26] fabricated MWCNT, GNPs and fullerene (C60)-reinforced AMC using semi-powder technique at 0.25 wt% of reinforcement. Enhancement in the yield strength and tensile strength of the composites was observed with the addition of carbon materials. The C60 reinforcement resulted in maximum hardness, tensile strength and yield strength.

Tsemenko et al. [27] fabricated carbon nanostructure (CNS)-reinforced AMC by using powder metallurgy technique and studied the effect of particle size of aluminum powder on the fused carbon nanofibers. It was observed that prepared matrix resulted in the enhancement of mechanical properties. Liu et al. [28] fabricated graphene nanosheets (GNS)-reinforced AMC by in situ technique. 200% improvement in tensile strength was observed at 2.5 vol.% of GNS. Cavaliere et al. [29] studied the microstructure and the mechanical properties of the AMC reinforced with CNT fabricated by SPS technique at 0.5 and 1 wt%. Higher density was observed at lower wt% of CNT, while the porosity and the tensile strength increased at higher concentration of reinforced material. Kwon et al. [30] fabricated single and dual reinforced AMC with nanodiamond (nD) and MWCNT by mechanical milling and hot pressing technique. Vickers hardness increased by five times, and the flexural strength increased by seven times. From the above studies carried out, it can be observed that addition of various reinforcements can result in the improved mechanical and tribological properties.

2.2 Magnesium Matrix Composites

The use of magnesium matrix composites has also remained an active area of research. In this direction, Say et al. [31] successfully fabricated AZ61/CNT- and AZ91/CNT-reinforced composite by chemical vapor deposition technique. Authors used the different reinforcement at 0.1, 0.2 and 0.5 wt% conc. Increased value of strength was observed with the increase in reinforcement. Further, the maximum corrosion resistance was observed for 0.2 wt% reinforcement. Du et al. [32] fabricated GNPs-reinforced ZK60 magnesium matrix composite at 0.05 and 0.1 wt% reinforcement by melt stirring, casting and hot extrusion process. Maximum value of hardness was observed at 0.05 wt% reinforcement. Further, it was also observed that yield strength (tensile and compressive both) also increased.

In another study, Yuan et al. [33] fabricated AZ91-GNS magnesium matrix composite by thermal reduction process at 0.1, 0.3, 0.5, 0.8 and 1.2 wt% of reinforcement. Maximum value of hardness, ultimate tensile strength, yield strength and elongation were observed at 0.5 wt% reinforcement. Turan et al. [34] fabricated fullerene (C60)-reinforced composite using the semi-powder metallurgy technique at 0.5 wt% of reinforcement and studied the microstructure, wear, corrosion and mechanical properties of the reinforced composite. Hardness, yield strength and the ultimate strength increased in comparison with the unreinforced magnesium. Wear rate and COF decreased, while the corrosion rate increased for the reinforced magnesium. In another study, Turan et al. [35] fabricated composite reinforced with MWCNT, GNPs and C60 reinforcements at 0.5 wt% by semi-powder metallurgy. Highest hardness observed for C60 and the MWCNT-reinforced composite exhibited poor corrosion resistance. Thus, from the above studies, it can be determined that addition of reinforcements leads to an improvement in properties (both mechanical

& tribological), but the issues related to corrosion resistance need to be explored further.

2.3 *Copper Matrix Composites*

Different studies have been carried out with regard to the copper matrix composites. In this direction, Zhang et al. [36] fabricated hybrid composite reinforced with graphene and carbon fiber with fixed 0.5 wt% CF and two contents 0.1 and 0.4 wt% of G reinforcements. Hardness and yield strength increased with increasing wt% of G reinforcement, while elongation decreased. Shao et al. [37] fabricated Cu/GNP-reinforced composite at 0.1, 0.2 and 0.3 wt% reinforcement by electrostatic self-assembly and SPS technique. Mechanical properties increased up to 0.2 wt% reinforcement. Tensile strength and Vickers hardness at 0.2 wt% increased by 27 and 19% as compared to pure Cu. Zhang et al. [38] studied the corrosion and wear behavior of the Cu/GNP-reinforced composite at 0.1, 0.2 and 0.4 wt% reinforcement fabricated by electrostatic self-assembly and SPS technique. Best antifriction properties and corrosion resistance observed at 0.4 wt% reinforcement. Salvo et al. [39] synthesized 1 wt% GNS-reinforced copper matrix composites by sintering technique. 22% improvement in electrical conductivity was observed for composite when compared with base material. At 600 °C sintering temperature, significant improvement in electrical conductivity was observed with insignificant change in mechanical property, but at 700 °C sintering temperature a significant improvement in mechanical properties was observed with a minute decrease in electrical conductivity.

Kumar and Mondal [40] fabricated graphite-reinforced copper matrix composites at 5, 10 and 15 wt% reinforcement by powder metallurgy technique. Wear rate, friction coefficient and density decreased with increasing wt% of reinforcement. Maximum value of hardness for all concentrations of graphite observed at 1000 °C. Compression strength increased up to 5 wt% reinforcement, and after that a decreasing trend was observed. Liu et al. [41] successfully fabricated MWCNT-reinforced copper matrix composites by flake powder metallurgy technique at 0.5 and 1 vol.% reinforcement. 87% increase in tensile strength and 20% in elongation rate for 1 vol.% reinforcement when compared to coarse-grained Cu.

Thus, from the above studies related to the use of CRMs in the MMCs, it can be ascertained that various reinforcements resulted in the improvement of behavior of material. However, magnesium matrix composites resulted in poor corrosion resistance.

3 **As Additives in Liquid Lubricants**

Reducing frictional and wear behavior of mechanical systems is the major concern in recent studies. For enhancing lubricating properties, certain nanoparticles are added

to the base oil. These nanoparticles help in reducing the friction and wear of the machine elements and thus help in improving the life of the sliding components. In this section, the recent studies of various carbon-based additives in different types of oils have been discussed.

3.1 Vegetable Oils

Vegetable oils used for lubrication purpose have resulted in better tribological properties [42]. Different studies have been carried out in this regard [6, 43]. Omrani et al. [44] used GNP as nanoadditive in canola oil and studied the COF and wear rate at different concentrations corresponding to varying loads. Anand et al. [19] studied the friction reduction mechanism of rice bran oil with nanoadditives of GNP and TiO₂ and observed the improvement in tribological and thermophysical properties. COF and wear rate were improved by adding the nanoadditives. Zhang et al. [45] used rapeseed oil (RSO) as base and used two additives GO-D (graphene oxide 1-dodecanethoil) and GO-T (graphene oxide tert-dodecyl mercaptan). Coefficient of friction and wear scar diameter decreased by 44.5 and 40.1% at 0.2 wt% GO-D. Krishna et al. [46] formulated a cutting fluid for machining by adding CNT in coconut oil with varying % of nanoparticles inclusions and observed the reduction in cutting force, cutting temperature, tool wear and surface roughness. Sadiq et al. [47] studied the lubricating and thermal properties of coconut oil with nanoparticles of exfoliated nanographene (XnG) at 0.35, 0.7 and 1.05 wt%. It was observed that with the increase in concentration of nanoparticles thermal conductivity and viscosity increased. At 0.35 wt%, minimum value of friction coefficient was observed. Bhaumik et al. [48] used castor oil as base and used micro- and nano-sized additives of graphite, MWCNT and multilayered graphene. Graphene-based oil showed the best anti-wear and extreme pressure properties. Kiu et al. [49] studied the tribological properties of the vegetable oil with additives of GNS, CNT and graphene oxide (GO) at 50 and 100 ppm. Lowest value of coefficient of friction and wear was observed at 50 ppm of GNS. GO at both conc. showed an increase in wear and friction as compared to base vegetable oil.

3.2 Synthetic Oils and Mineral Oils

The use of synthetic oils has resulted in much better lubricating properties owing to their better physical and chemical properties. Lv et al. [50] added 0.5 wt% carbon sphere as additive in 5W30 engine oil and observed the improvement in wear and COF. Pico et al. [51] studied the performance of polyol ester (POE) synthetic oil with 0.1 and 0.5 wt% of diamond nanoparticles and observed an improvement in coefficient of friction and cooling capacity with 4% reduction in friction and 30% reduction in wear.

Paul et al. [52] studied the tribological properties of the dodecylamine-functionalized graphene in 5w-30 engine oil. Coefficient of friction reduced at low speeds for oil with additives, but at higher speeds engine oil served as good lubricant. Raina and Anand [53] studied the friction and wear behavior of PAO (poly-alpha-olefin) synthetic oil containing 0.2% nanodiamond (nD) along with nanoparticles of MoS₂ and WS₂. Coefficient of friction and wear volume decreased by two times as compared to base oil. Raina and Anand [54] studied the influence of various concentration (0.2, 0.4, 0.6 and 0.8 wt%) of nD additives in PAO oil on friction and wear rate. Minimum value of coefficient of friction and wear rate was observed at 0.2 wt% nD additives. Raina and Anand [55] studied the effect of surface roughness and nD concentration on the friction and wear rate of PAO base oil. Minimum value of coefficient of friction observed at higher concentration of nD for rough surfaces, but for smooth surfaces lower concentration of nD showed reduced friction value. In another study by Raina and Anand [56], the influence of nD additives along with copper oxide (CuO) and hexagonal boron nitride (h-BN) in PAO oil was studied. Better frictional characteristics were observed for CuO/nD oil and h-BN/nD oil as compared to single additives in oil. Azman et al. [57] studied the effect of different concentrations of GNP in blended lubricant containing 95 vol.% PAO oil and 5 vol.% palm oil trimethylolpropane ester. 5 and 15% reduction in friction and wear observed for 0.05 wt% of GNP.

Vats and Singh [58] studied the tribological behavior of paraffin oil with GO additives at 0.2 wt% under varying load conditions. GO improved the friction, anti-wear and dynamic viscosity of the oil. COF decreased by 75 and 61.8% in EHD and boundary regime. Majeed et al. [59] studied the tribological properties to improve friction and corrosion resistance of XGNP and Fe₂O₃ nanoparticles in paraffin oil. Yunusov et al. [60] studied the friction and wear behavior of MS-20 mineral oil with nanostructure additives of GO and fullerene soot. Friction force reduced when fullerene soot concentration increased from 0.5 to 2%, but the addition of GO showed no change in the friction force. Khalil et al. [61] studied the tribological properties of paraffinic mineral oil with MWCNT additives at 0.1, 0.5, 1 and 2 wt%. Wear rate decreased by 38% and friction by 49% for mineral oil with MWCNT additives when compared with base mineral oil. Marko et al. [62] added 0.01 wt% nD particles in mineral oil and observed that the average friction coefficient and wear decreased significantly. Peng et al. [63] studied the tribological properties of liquid paraffin with diamond nanoparticles and observed that best values of friction and wear scar diameter observed at 0.5 wt%. Thus, the studies related to the use of mineral and synthetic oils resulted in better tribological properties with the use of different nanoadditives.

4 As Coating Materials

Coatings are deposition of thin films to achieve properties that are not achievable by the base material. Hard coatings are used when the aim is to reduce the wear of the material, and the soft coatings are used when the aim is to reduce the friction.

Multilayered coatings are often used for improving the chemical, mechanical and tribological properties of the materials, and each layer of the multilayered coating has its own distinct function.

Toosinezhad et al. [64] used graphene particles to study the tribological behavior of cobalt-graphene coating. Microhardness increased by 1.6 times as compared to pure cobalt coating and 2.9 times as compared to steel substrate. Mura et al. [65] studied the tribological performance of C40 steel samples with graphene coating using two coatings techniques. Direct growth coated samples for 10 min showed the best wear resistance, and Transferred coated samples gave the least value of COF. Vinoth et al. [66] studied the tribological behavior of vehicle piston rings with DLC coating at different radio frequencies (RF). Better hardness and tribological properties were achieved for DLC at 150 W RF. Siddaiah et al. [67] studied the tribological effect of nickel-graphite (Ni-Gr) coating on steel and found that the presence of Gr in coating aided in reducing the wear and also lowered the friction value. Kim and Kim [68] found that the friction between the 440 C stainless steel ball and plate reduced by 6 times by coating with reduced graphene oxide (rGO) (Table 2).

5 Conclusions

Each carbon nanomaterial has its own properties that help in either one or other way depending on hybridization, dimensionality or uniform dispersion of these nanoparticles in different materials for improving the tribo-mechanical properties of the materials. CNTs, graphite and fullerene are among the most promising materials as nanoadditives for MMCs. They help in improving the strength, hardness and coefficient of friction of the MMCs. Nanodiamonds, CNT and graphene as nanoadditives in oils aimed at achieving the superlubricity. Among the various CRMs fullerene, CNTs, nanodiamonds and graphene are most widely used nanomaterials as they are stable, non-toxic and biocompatible. Carbon-based materials owing to their excellent properties can be explored further for use in different tribological applications. The concept of hybridization with other materials and developing materials, coatings and additives can yield good results. The effect of various parameters, underlying theories and mechanisms needs to be studied further to widen the application area of the carbon-based materials.

Table 2 Comparison of the different studies carried out using different techniques

Author	Material & method	Study purpose	Outcomes
Ogawa et al. [69]	Carbon nanofiber (CNF)-reinforced AMC by ball milling and SPS technique & powder extrusion at 0.5, 1, 2, 3, 4 & 5 vol.% CNF	Study & compare the thermal conductivity & tensile strength of the AMC fabricated by two techniques	Higher thermal conductivity observed for AMCs fabricated by powder extrusion and decreases with increasing vol.% of CNF Lower tensile strength by SPS technique
Yuan et al. [70]	AMC reinforced with CNTs at 0, 1.5 and 3 wt. % by flake powder metallurgy technique	Study the mechanical properties of the fabricated AMCs	Hardness, yield strength and ultimate tensile strength increased with increasing wt. % of CNTs
Ghasali et al. [71]	Fabricate AMC reinforced with graphene (1 wt%) & CNT (1 wt%) by SPS, microwave and conventional method	Study and compare the bending strength and microhardness of composites fabricated by all techniques	Maximum bending strength and density observed for AMC fabricated by SPS technique Maximum microhardness observed by AMC fabricated by microwave technique
Meng et al. [72]	Fabricate AMC reinforced with graphene by hot-press sintering at 580, 590 & 600 °C	Study the microhardness, wear & COF of fabricated AMC samples	Highest microhardness observed at 600 °C sintering temp COF & wear rate decreased with increase in sintering temp
Sedlák et al. [73]	Fabricate B ₄ C/GPLs composite by sintering technique	Study the effect of graphene platelets (GPLs) reinforcement (0.5, 1, 2, 4 & 6 wt%) on B ₄ C composites	Highest value of hardness observed at 0.5 wt% GPLs and lowest at 4 wt% COF have not varied much but wear rate decreased with increasing wt% of GPLs
Li et al. [74]	Fabricate CNT-reinforced Mg matrix composite by in situ synthesis and powder metallurgy process at 2, 4, 6 & 8 wt% reinforcement	Study the mechanical properties of the fabricated composite	Breaking elongation, UTS & microhardness by in situ process composite increased by 31.3, 33.4 & 43.5% Mechanical properties of composite fabricated by in situ process were superior than traditional process

(continued)

Table 2 (continued)

Author	Material & method	Study purpose	Outcomes
Wang et al. [75]	Fabricate graphene nanocrystallite embedded carbon nitride (GNECN) coating by plasma sputtering system	Study the friction behavior of graphene coating in ambient and Nitrogen gas	High friction coefficients observed in ambient air while very low friction coefficients observed in N ₂ gas
Song et al. [76]	Fabricate MoS ₂ -GO composite by simple hydrothermal method	Study the tribological properties of fabricated composite in sunshine oil	Lubricity improved (friction & wear reduced) by adding MoS ₂ /GO composite in sunshine oil MoS ₂ /GO composite protected the contact interfaces from damaging
Gupta et al. [77]	Mixed the particles in modified canola oil	Effect of MoS ₂ particles in canola oil	Improvement in COF and wear by the addition of particles Film formation led to the improvement in tribological properties

References

1. Anand A, Haq MIU, Vohra K, Raina A, Wani MF (2017) Role of green tribology in sustainability of mechanical systems: a state of the art survey. *Mater Today: Proc* 4(2):3659–3665
2. Baba ZU, Shafi WK, Haq MIU, Raina A (2019) Towards sustainable automobiles—advancements and challenges. *Prog Ind Ecol Int J* 13(4):315–331
3. Holmberg K, Andersson P, Erdemir A (2012) Global energy consumption due to friction in passenger cars. *Tribol Int* 47:221–234
4. Singh N, Mir IUH, Raina A, Anand A, Kumar V, Sharma SM (2018) Synthesis and tribological investigation of Al-SiC based nano hybrid composite. *Alex Eng J* 57(3):1323–1330
5. Aziz R, Haq MIU, Raina A (2020) Effect of surface texturing on friction behaviour of 3D printed polylactic acid (PLA). *Polym Test* 85:106434
6. Shafi WK, Raina A, Haq MIU (2018) Tribological performance of avocado oil containing copper nanoparticles in mixed and boundary lubrication regime. *Ind Lubr Tribol*
7. Kerni L, Raina A, Haq MIU (2019) Friction and wear performance of olive oil containing nanoparticles in boundary and mixed lubrication regimes. *Wear* 426:819–827
8. Bakunin VN, Suslov AY, Kuzmina GN, Parenago OP, Topchiev AV (2004) Synthesis and application of inorganic nanoparticles as lubricant components—a review. *J Nanopart Res* 6(2):273–284
9. Dresselhaus MS, Avouris P (2001) Introduction to carbon materials research. *Carbon Nanotubes* 1–9
10. Kroto HW, Heath JR, O'Brien SC, Curl RF, Smalley RE (1985) C₆₀: buckminsterfullerene. *Nature* 318(6042):162–163
11. Li H, Kang Z, Liu Y, Lee ST (2012) Carbon nanodots: synthesis, properties and applications. *J Mater Chem* 22(46):24230–24253
12. Legoas SB, Dos Santos RPB, Troche KS, Coluci VR, Galvao DS (2011) Ordered phases of encapsulated diamondoids into carbon nanotubes. *Nanotechnology* 22(31):315708

13. Iijima S, Ajayan PM, Ichihashi T (1992) Growth model for carbon nanotubes. *Phys Rev Lett* 69(21):3100
14. Ajayan PM, Zhou OZ (2001) Applications of carbon nanotubes. *Carbon Nanotubes* 391–425
15. Mittal G, Dhand V, Rhee KY, Park SJ, Lee WR (2015) A review on carbon nanotubes and graphene as fillers in reinforced polymer nanocomposites. *J Ind Eng Chem* 21:11–25
16. Yudasaka M, Iijima S, Crespi VH (2007) Single-wall carbon nanohorns and nanocones. *Carbon Nanotubes* 605–629
17. De Jong KP, Geus JW (2000) Carbon nanofibers: catalytic synthesis and applications. *Catal Rev* 42(4):481–510
18. Choi W, Lahiri I, Seelaboyina R, Kang YS (2010) Synthesis of graphene and its applications: a review. *Crit Rev Solid State Mater Sci* 35(1):52–71
19. Anand R, Raina A, Ul Haq MI, Mir MJ, Gulzar O, Wani MF (2020) Synergism of TiO₂ and graphene as nano-additives in bio-based cutting fluid—an experimental investigation. *Tribolo Trans* 1–21
20. Pei S, Cheng H-M (2012) The reduction of graphene oxide. *Carbon* 50(9):3210–3228
21. Georgakilas V, Perman JA, Tucek J, Zboril R (2015) Broad family of carbon nanoallotropes: classification, chemistry, and applications of fullerenes, carbon dots, nanotubes, graphene, nanodiamonds, and combined superstructures. *Chem Rev* 115(11):4744–4822
22. Kerni L, Raina A, Haq MIU (2018) Performance evaluation of aluminium alloys for piston and cylinder applications. *Mater Today: Proc* 5(9):18170–18175
23. Singh H, Raina A, Haq MIU (2018) Effect of TiB₂ on mechanical and tribological properties of aluminium alloys—a review. *Mater Today: Proc* 5(9):17982–17988
24. Slathia S, Haq MIU, Raina A (2018, August) Fabrication and mechanical characterization of AA2024-ZrO₂-Gr hybrid composite. In: AIP conference proceedings, vol 2006, No. 1, p 030047. AIP Publishing LLC
25. Xiong B, Liu K, Xiong W, Wu X, Sun J (2020) Strengthening effect induced by interfacial reaction in graphene nanoplatelets reinforced aluminum matrix composites. *J Alloys Compd* 845:156282
26. Turan ME (2019) Investigation of mechanical properties of carbonaceous (MWCNT, GNPs and C60) reinforced hot-extruded aluminum matrix composites. *J Alloy Compd* 788:352–360
27. Tsemenko VN, Tolochko OV, Kol'Tsova TS, Ganin SV, Mikhailov VG (2018) Fabrication, structure and properties of a composite from aluminum matrix reinforced with carbon nanofibers. *Metal Sci Heat Treat* 60(1):24–31
28. Liu X, Li J, Sha J, Liu E, Li Q, He C et al (2018) In-situ synthesis of graphene nanosheets coated copper for preparing reinforced aluminum matrix composites. *Mater Sci Eng A* 709:65–71
29. Cavaliere P, Sadeghi B, Shabani A (2017) Carbon nanotube reinforced aluminum matrix composites produced by spark plasma sintering. *J Mater Sci* 52(14):8618–8629
30. Kwon H, Lee GG, Kim SG, Lee BW, Seo WC, Leparoux M (2015) Mechanical properties of nanodiamond and multi-walled carbon nanotubes dual-reinforced aluminum matrix composite materials. *Mater Sci Eng A* 632:72–77
31. Say Y, Guler O, Dikici B (2020) Carbon nanotube (CNT) reinforced magnesium matrix composites: the effect of CNT ratio on their mechanical properties and corrosion resistance. *Mater Sci Eng A* 798:139636
32. Du X, Du W, Wang Z, Liu K, Li S (2018) Ultra-high strengthening efficiency of graphene nanoplatelets reinforced magnesium matrix composites. *Mater Sci Eng A* 711:633–642
33. Yuan QH, Zhou GH, Liao L, Liu Y, Luo L (2018) Interfacial structure in AZ91 alloy composites reinforced by graphene nanosheets. *Carbon* 127:177–186
34. Turan ME, Sun Y, Akgul Y (2018) Mechanical, tribological and corrosion properties of fullerene reinforced magnesium matrix composites fabricated by semi powder metallurgy. *J Alloy Compd* 740:1149–1158
35. Turan ME, Sun Y, Aydin F, Zengin H, Turen Y, Ahlatci H (2018) Effects of carbonaceous reinforcements on microstructure and corrosion properties of magnesium matrix composites. *Mater Chem Phys* 218:182–188

36. Zhang X, Yang W, Zhang J, Ge X, Liu X, Zhan Y (2019) Multiscale graphene/carbon fiber reinforced copper matrix hybrid composites: microstructure and properties. *Mater Sci Eng A* 743:512–519
37. Shao G, Liu P, Zhang K, Li W, Chen X, Ma F (2019) Mechanical properties of graphene nanoplates reinforced copper matrix composites prepared by electrostatic self-assembly and spark plasma sintering. *Mater Sci Eng A* 739:329–334
38. Zhang K, Shao G, Li W, Chen X, Ma F, Liu P (2019) Wear and corrosion behavior of graphene-nanoplate-reinforced copper matrix composites prepared through electrostatic self-assembly. *J Mater Eng Perform* 28(3):1650–1660
39. Salvo C, Mangalaraja RV, Udayabashkar R, Lopez M, Aguilar C (2019) Enhanced mechanical and electrical properties of novel graphene reinforced copper matrix composites. *J Alloy Compd* 777:309–316
40. Kumar J, Mondal S (2018) Microstructure and properties of graphite-reinforced copper matrix composites. *J Braz Soc Mech Sci Eng* 40(4):1–10
41. Liu J, Xiong DB, Tan Z, Fan G, Guo Q, Su Y et al (2018) Enhanced mechanical properties and high electrical conductivity in multiwalled carbon nanotubes reinforced copper matrix nanolaminated composites. *Mater Sci Eng A* 729:452–457
42. Shafi WK, Raina A, Haq MIU (2019) Performance evaluation of hazelnut oil with copper nanoparticles—a new entrant for sustainable lubrication. *Ind Lubric Tribol*
43. Anand R, Haq MIU, Raina A (2020) Bio-based nano-lubricants for sustainable manufacturing. In: *Nanomaterials and environmental biotechnology*, pp 333–380. Springer, Cham
44. Omrani E, Siddaiah A, Moghadam AD, Garg U, Rohatgi P, Menezes PL (2021) Ball milled graphene nano additives for enhancing sliding contact in vegetable oil. *Nanomaterials* 11(3):610
45. Zhang G, Xu Y, Xiang X, Zheng G, Zeng X, Li Z et al (2018) Tribological performances of highly dispersed graphene oxide derivatives in vegetable oil. *Tribol Int* 126:39–48
46. Krishna PV, Srikant RR, Parimala N (2018) Experimental investigation on properties and machining performance of CNT suspended vegetable oil nanofluids. *Int J Automot Mech Eng* 15(4):5957–5975
47. Sadiq IO, Sharif S, Suhaimi MA, Yusof NM, Shayfull Z (2018, November) Influence of XGnP as additives on properties of vegetable oil nanolubricant for machining process. In: *AIP conference proceedings*, vol 2030, No. 1, p 020085. AIP Publishing LLC
48. Bhaumik S, Datta S, Pathak SD (2017) Analyses of tribological properties of castor oil with various carbonaceous micro-and nano-friction modifiers. *J Tribol* 139(6)
49. Kiu SSK, Yusup S, Chok VS, Taufiq A, Kamil RNM, Syahrullail S, Chin BLF (2017, June) Comparison on tribological properties of vegetable oil upon addition of carbon based nanoparticles. In: *IOP conference series: materials science and engineering*, vol 206, No. 1, p 012043. IOP Publishing
50. Lv X, Cao L, Yang T, Wan Y, Gao J (2020) Lubricating behavior of Submicrometer carbon spheres as lubricant additives. *Part Sci Technol* 38(5):568–572
51. Pico DFM, da Silva LRR, Mendoza OSH, Bandarra Filho EP (2020) Experimental study on thermal and tribological performance of diamond nanolubricants applied to a refrigeration system using R32. *Int J Heat Mass Transfer* 152:119493
52. Paul G, Shit S, Hirani H, Kuila T, Murmu NC (2019) Tribological behavior of dodecylamine functionalized graphene nanosheets dispersed engine oil nanolubricants. *Tribol Int* 131:605–619
53. Raina A, Anand A (2018) Effect of nanodiamond on friction and wear behavior of metal dichalcogenides in synthetic oil. *Appl Nanosci* 8(4):581–591
54. Raina A, Anand A (2018) Lubrication performance of synthetic oil mixed with diamond nanoparticles: Effect of concentration. *Mater Today: Proc* 5(9):20588–20594
55. Raina A, Anand A (2018) Influence of surface roughness and nanoparticles concentration on the friction and wear characteristics of PAO base oil. *Mater Res Express* 5(9):095018
56. Raina A, Anand A (2017) Tribological investigation of diamond nanoparticles for steel/steel contacts in boundary lubrication regime. *Appl Nanosci* 7(7):371–388

57. Azman SSN, Zulkifli NWM, Masjuki H, Gulzar M, Zahid R (2016) Study of tribological properties of lubricating oil blend added with graphene nanoplatelets. *J Mater Res* 31(13):1932
58. Vats BN, Singh M (2020) Evaluation of tribological properties of graphene oxide dispersed paraffin oil. *Mater Today: Proc* 25:557–562
59. Majeed FSA, Yusof NBM, Suhaimi MA, Elsiiti NM (2020) Effect of paraffin oil with XGnP and Fe₂O₃ nanoparticles on tribological properties. *Mater Today: Proc* 27:1685–1688
60. Yunusov FA, Breki AD, Vasilyeva ES, Tolochko OV (2020) The influence of nano additives on tribological properties of lubricant oil. *Mater Today: Proc* 30:632–634
61. Khalil W, Mohamed A, Bayoumi M, Osman TA (2016) Tribological properties of dispersed carbon nanotubes in lubricant. *Fullerenes Nanotubes Carbon Nanostruct* 24(7):479–485
62. Marko M, Kyle J, Branson B, Terrell E (2015) Tribological improvements of dispersed nanodiamond additives in lubricating mineral oil. *J Tribol* 137(1)
63. Peng DX, Kang Y, Chen CH, Shu SKCFC (2009) The tribological behavior of modified diamond nanoparticles in liquid paraffin. *Ind Lubric Tribol*
64. Toosinezhad A, Alinezhadfar M, Mahdavi S (2020) Cobalt/graphene electrodeposits: characteristics, tribological behavior, and corrosion properties. *Surf Coatings Technol* 385:125418
65. Mura A, Wang H, Adamo F, Kong J (2019) Graphene coatings to enhance tribological performance of steel. *Mech Adv Mater Struct*
66. Vinoth IS, Detwal S, Umasankar V, Sarma A (2019) Tribological studies of automotive piston ring by diamond-like carbon coating. *Tribol Mater Surf Interfaces* 13(1):31–38
67. Siddaiah A, Kumar P, Henderson A, Misra M, Menezes PL (2019) Surface energy and tribology of electrodeposited Ni and Ni-graphene coatings on steel. *Lubricants* 7(10):87
68. Kim HJ, Kim DE (2015) Water lubrication of stainless steel using reduced graphene oxide coating. *Sci Rep* 5(1):1–13
69. Ogawa F, Yamamoto S, Masuda C (2019) Thermal conductivity and tensile properties of carbon nanofiber-reinforced aluminum-matrix composites fabricated via powder metallurgy: effects of ball milling and extrusion conditions on microstructures and resultant composite properties. *Acta Metallurgica Sinica (English Letters)* 32(5):573–584
70. Yuan C, Tan Z, Fan G, Chen M, Zheng Q, Li Z (2019) Fabrication and mechanical properties of CNT/Al composites via shift-speed ball milling and hot-rolling. *J Mater Res* 34(15):2609–2619
71. Ghasali E, Sangpour P, Jam A, Rajaei H, Shirvanimoghaddam K, Ebadzadeh T (2018) Microwave and spark plasma sintering of carbon nanotube and graphene reinforced aluminum matrix composite. *Arch Civil Mech Eng* 18:1042–1054
72. Meng J, Shi X, Wang M, Zhang S, Kong X (2018) Microstructure and wear resistance of graphene-reinforced aluminum matrix composites. *Mater Res Express* 6(2):026517
73. Sedlák R, Kovalčíková A, Balko J, Rutkowski P, Dubiel A, Zientara D et al (2017) Effect of graphene platelets on tribological properties of boron carbide ceramic composites. *Int J Refract Metal Hard Mater* 65:57–63
74. Li H, Dai X, Zhao L, Li B, Wang H, Liang C, Fan J (2019) Microstructure and properties of carbon nanotubes-reinforced magnesium matrix composites fabricated via novel in situ synthesis process. *J Alloy Compd* 785:146–155
75. Wang P, Zhang W, Diao D (2017) Low friction of graphene nanocrystallite embedded carbon nitride coatings prepared with MCECR plasma sputtering. *Surf Coat Technol* 332:153–160
76. Song H, Wang B, Zhou Q, Xiao J, Jia X (2017) Preparation and tribological properties of MoS₂/graphene oxide composites. *Appl Surf Sci* 419:24–34
77. Gupta G, Haq MIU, Raina A, Shafi WK (2021) Effect of epoxidation and nanoparticle addition on the rheological and tribological properties of canola oil. In: *Proc Inst Mech Eng Part J: J Eng Tribol* 13506501211016181
78. Ho DN (2010) *Applications in biology and nanoscale medicine*. Springer US, 10, 978-1

Chapter 40

Cobalt Extraction Mechanisms



Marcelo Rodríguez, Kevin Pérez, Luís Ayala, Rossana Sepúlveda,
and Edelmira Gálvez

Abstract Cobalt (Co) is a potentially critical mineral. Most of its extraction is associated with a by-product of other mineral species such as copper, nickel and manganese, where it is a fundamental piece for activities that have increased their development in recent times such as electromobility, industrial and military applications. The cobalt minerals of interest for industrial production are reduced and can be in the form of sulfates, carbonates, arsenates, sulfides, arsenides, selenides and oxides. Its processing is of a moderate cost, being the mixed processes (pyro-hydrometallurgical) the most used. In addition, it is important to mention that cobalt dissolves at a low oxidation potential and low pH, which facilitates its processing.

Keywords Cobalt · Temperature · Dissolution · Process · Mineral · Metallurgy

1 General Aspects

Although there have been findings of the use of cobalt in ancient times, the so-called (in the sixteenth century) goblin metal [1] was discovered by the Swedish chemist George Brandt in 1730–1737 (the sources differ) who showed through an analysis of the blue color of glasses that cobalt was a new element different from bismuth and other metals. Cobalt is a strategic metal [2–4] that in recent times has increased its importance, being named in 2017 as the “most popular product” [5], it is bluish-white in color, its atomic weight is 58.933195 u and atomic number 27. It is found on the earth’s surface chemically combined with various elements, belonging to the

M. Rodríguez · E. Gálvez (✉)

Departamento de Ingeniería Metalúrgica y Minas, Universidad Católica del Norte, 1270709
Antofagasta, Chile

e-mail: egalvez@ucn.cl

K. Pérez · L. Ayala

Facultad de Ingeniería y Arquitectura, Universidad Arturo Prat, 1244260 Antofagasta, Chile

R. Sepúlveda

Departamento de Ingeniería en Metalurgia, Universidad de Atacama, 1531772 Copiapó, Chile

transition metals of the periodic table, more precisely belonging to group 9 and period 4 [6].

Properties: The density of cobalt is 8.9 g/mL. It has characteristics very similar to iron and nickel, characteristics such as hardness, resistance, thermal properties and electrochemical behavior. It is not considered an inert element due to its stability against conditions caused by water or humid air at room temperature. Cobalt metal powder is soluble in different acids (sulfuric, hydrochloric and dilute nitric acids stand out) and is weakly attacked by sodium or ammonia hydroxides. It is very reactive against halogens and carbon oxides, but it has low chemical activity against nitrogen [7]. Cobalt at temperatures below 417 °C is very stable and compact, presenting a hexagonal-type crystal structure, but at temperatures close to the melting point (usually around 1495 °C) it behaves differently, reaching stability to form a face-centered cubic-type crystal structure. Another noteworthy point is that it has 12 radioactive isotopes, none of which are produced naturally, the most influential today being cobalt-60 since it has a wide range of uses in the medicine industry [8]. Cobalt melts at 1495 °C and boils at 2900 °C [8].

Compounds: It usually has oxidation states of +3 and +2, but states of +4, +1, 0 and -1 are still known, being very particular cases, such as the formation of nitroxyl or carbonyl complexes, where you can have an oxidation state of +1. Due to its similarity to other ions such as Mg^{2+} , Mn^{4+} and Fe^{2+} , with respect to ionic radius, it can easily replace them in mineral structures [8]. The main properties of this element are found in Table 1 (Data from: [9]).

Table 1 Properties of cobalt

Atomic number	27
Electronegativity	1.88
Covalent radius (Å)	1.26
Ionic radius (Å)	0.63
Electronic configuration	[Ar]3d ⁷ 4s ²
First ionization potential (eV)	7.90
Atomic mass (g/mol)	58.933.195
Density (g/mL)	8.9
Melting point	1495 °C
Boiling point	2900 °C
Heat of fusion	169 kJ/mol
Specific heat	420 J/(k Kg)
Thermal conductivity	100 (km)

2 Applications

Cobalt is useful for forming alloys and therefore can be present in various industries and applications. These industries take advantage of cobalt for its properties such as ferromagnetism, resistance to corrosion, wear and high temperatures [10]. It can form alloys with metals such as aluminum, nickel or iron [8]. We can find cobalt in the formation of super alloys for aeronautical engines, magnetic alloys for high power permanent magnets, hard alloys for cutting tools, alloys with high resistance to wear and corrosion [11]. In this sense, the cobalt chromium alloy should be highlighted, which is recognized as an attractive material in the application of many engineering fields, such as aero-engines, nuclear, biomedical and gas turbines. This alloy also has the presence of molybdenum, which has the function of reducing the size of the grain, and, therefore, improving the strengthening of the solid solution and improving the mechanical properties of the alloy [12]. Among the best known alloys, we have [13]:

- Alnico with 5–35% of Co.
- Remalloy with 12% of Co.
- Vicalloy with 52% or 14% of Co.
- Cunico with 29–41% of Co.
- Cobalt–phosphorous with 50% of Co.
- Permendur with Co–Fe 50%.
- Hiperco with 35% Co, 64% Fe and 1% Cr.

3 Productive Process

The processes that Young [8] define, to obtain cobalt, are a pyrometallurgical and chemical combination. Considering that the largest amount of cobalt obtained worldwide comes as a by-product of other production processes (copper and nickel), the extraction of cobalt will depend especially on the main metal that is being treated, the mineralogy that is being worked and the product end that you want to obtain. In polymetallic deposits, in order to determine the best cobalt recovery process, the potential of the deposit with the different metals (Cu, Ni and Co) and the ratio of the content of the concentrate between the metals must be taken into account. Currently, approximately 70% of the world's cobalt is produced under hydrometallurgical methods [1] (Fig. 1).

Next, we will detail the metallurgical processes that involve the extraction of cobalt.

Concentration processes.

The cobalt concentration processes will depend on the characteristics of each mineral.

- Gravitational concentration
Generally, it is used as a pre-concentration process in order to reduce the gangue load to the plant. This process includes separation in jiggs, vibrating tables, spirals

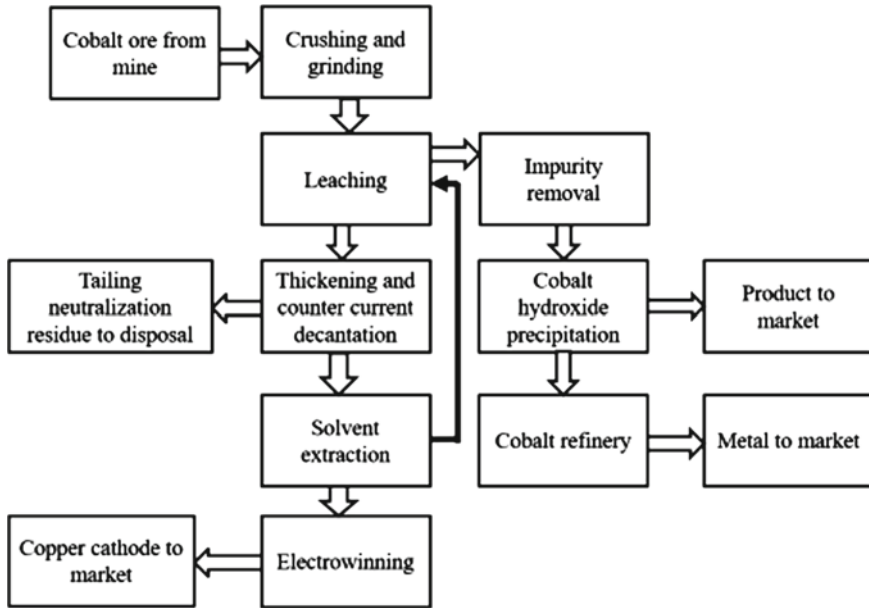


Fig. 1 Cobalt metal extraction process flow sheet [14]

and dense media. Jigging and vibrating tables are ideal for cobalt arsenides, and dense media plants are used to produce a salable concentrate [15].

- Flotation of sulfides and cobalt oxides

It is a difficult method for arsenides and sulfo-arsenides, since these ores contain chalcopyrite and iron sulfides such as pyrite and pyrrhotin. Cobalt can be depressed and chalcopyrite float as long as both species are clearly separated. In the case of the separation of the cobaltiferous species from the iron ores, difficulties arise because both species have similar behavior toward flotation, especially in the case of cobaltite.

Cobalt recovery by flotation is typically poor, generally below 60%, and in many cases well below this value. For cobalt associated with sulfides, the flotation process is easier since Co floats easily together with copper sulfides using xanthate-type collectors. Here, a single sulfide concentrate or a copper-rich and cobalt-rich concentrate can be produced. For the latter, a differential flotation is carried out as follows [15]:

1. Global flotation of copper–cobalt, from a pre-concentrate obtained by gravitational means.
2. Selective flotation of copper, depressing cobalt, from the global concentrate obtained in the previous global flotation.

Regarding the parameters of this differential flotation, some companies after floating copper and cobalt together, the pH is increased to 9.5 using lime and cyanide is used as a depressant. The perfect separation of copper and cobalt under this route has not been achieved.

For oxide minerals (mainly malachite and heterogenite), it is first conditioned by sulfidation using NaHS or $\text{Na}_2\text{S} \cdot 9\text{H}_2\text{O}$ and then flotation using xanthate collectors or a combination of xanthate and hydroxamate collectors. Like any flotation process, the gangue species has a fundamental role to consider, such is the case, for example, of the flotation of a dolomitic matrix, for which more efforts are required, and therefore, it is more difficult than flotation of the same minerals, but of a siliceous matrix, it is believed that crystalline CoOOH does not respond to sulfidation techniques, making it difficult for the cobalt present to float, while the more amorphous or cryptocrystalline forms of heterogenite and absollane respond slightly better. Finally, studies reveal that small amounts of copper in cobalt ores help it to float [15].

- Magnetic separation

As its name says, it is a process that takes advantage of the high magnetic susceptibility that some minerals have, to be separated from others that do not have this quality. Minerals such as pyrite [which may be associated with a considerable cobalt content (22%)] that are a non-magnetic species of iron can be separated from other iron species that do present this quality to a greater or lesser degree, such as pyrrhotin, magnetite and hematite. In general, cobaltiferous minerals treated in this way are also usually associated with other copper species such as chalcopyrite, chalcosine and bornite, in different proportions. By treating these minerals in this way, a useful product can be obtained with a lower weight and higher grade, with respect to the original head. Another case where this technique can be used is when there is the presence of erythrine (or another oxidized species of cobalt) which may be present in a large proportion due to alterations in the primary ores [15].

Pyrometallurgical process.

- Foundry

The concentrate obtained in previous processes (mixed with coke and warm coal) is roasted proportionally and then melted in electric furnaces [16]. The mat obtained (copper–cobalt and in some cases nickel–cobalt) passes to the converters where metallic copper and a cobalt-rich slag are obtained. Cobalt can be recovered in a slag cleaning furnace or in specific furnaces for this process, adding coke, reversals and concentrate, in order to achieve the alloy of the metals present in the slag in addition to Co, such as copper and iron. Under this process, around 60% of Co is recovered [15].

In the case of treating minerals containing cobalt, an electric arc furnace is used and in the process limestone is added as a flux and carbon as a reducing agent, obtaining as a product, a metallic phase and a slag phase. Subsequently, a slow cooling is carried out and the metallic phase is separated into a red alloy (containing approximately 85% copper) and a white alloy (containing approximately 15–20% copper, 40–45% cobalt and 20–35% iron), the latter being the form in which cobalt is produced. It should be noted in some operations, slow cooling is not used, producing a single dark purple alloy [15].

Operations have also been recorded where a DC electric arc furnace has been used to treat slags with cobalt content, where cobalt was found as CoO , and for which a

carbon source was used to reduce it to a temperature 1500–1600 °C. This process recovers the cobalt in an iron-rich alloy, which is extracted and later atomized and then sent to leaching processes using oxygen under pressure [15].

In other operations, slags rich in cobalt (approximately 2.1%) are processed in a 34 MW electric arc furnace. The process consists in that first, the slag is dried and fed to the furnace, where coke is added as a reducing agent. Subsequently, the metal is extracted and fed to a 20 MW furnace and then atomized with a jet of water to fine white alloy powder or “alliage blanc”. Finally, the “alliage blanc” is exported for its treatment under the hydrometallurgical route [15].

- Roasting

The roasting process of high cobalt sulfide concentrates is carried out in a fluidized bed at a temperature of 650 and 710 °C. If the temperature range is well controlled, it is possible to obtain basic sulfates and sulfates. This is achieved since, above 650 °C, the dominant iron product is Fe_2O_3 and at 680 °C, 93% of copper is formed as copper sulfate. If 720 °C is reached, only 50% of the copper will be formed as sulfate, but about 90% of the cobalt will remain in the sulfate form. From this process, dust can be recovered by gas escaping from the operation. This can be achieved by a series of cyclones or venturi scrubbers for dust recovery. Later, the powder is sent to the acid plant [15].

If concentrates with high copper content and low sulfur content are used, the roasting process could have its complications. If this is the case, additional fuel is required, usually in the form of coal or sulfur which is mixed with the ore and fed to the roaster using a screw feeder. Some other operations have experienced problems with sulfur simply as it sublimates during the gas phase, causing no thermal benefit to be achieved. To minimize this problem, direct injection has been used as an alternative [15].

Hydrometallurgical processes.

- Leaching of copper and cobalt ores

Cobalt minerals by themselves are difficult to leach because the cobalt present in sulfide and oxide minerals is in the trivalent state (Co^{3+}), which has a low solubility in aqueous solutions, which makes the leaching rate of Co minerals low. For this reason, it was sought to reduce Co^{3+} to Co^{2+} , and for that, a reducing agent is added, such as sodium metabisulfite or gaseous sulfur dioxide [17].

The process is generally carried out in a series of atmospheric tanks that are mechanically agitated and the residence time can vary between 4 and 8 h, with acid and reducers added to the first tank, although reducers can be added later in the process to optimize the recovery and reagent consumption [15].

In the case of concentrated tailings, copper and cobalt are easily mined with a low cost of acid waste [18]. Here, a two-stage leaching process is carried out, one for copper (the first) and another for cobalt (the second), allowing the leaching efficiencies of copper and cobalt to be independently optimized. Carrying out the process in one stage significantly affects the leaching efficiency of copper [15].

- Solvent extraction

If copper and cobalt-containing ores are processed, solvent extraction is the most effective method for separation. In this case, since copper is the main mineral, the aim is to eliminate the cobalt present from the circuit, which ends up in refining together with the rest of the impurities. The process itself is quite similar to copper mining both in equipment and procedures; it only differs in the working conditions, be it pH or organic reagent. Another approach that has been given to this process is to treat the nodules for cobalt recovery [15].

Purification processes.

- Precipitation

It depends mainly on the previous process used, as well as the rest of the impurities present. Among the impurities present, we can find manganese [19], aluminum, copper, iron, nickel, zinc, etc. Although the precipitation process is one of the most used for the removal of impurities, modern circuits that remove impurities also include SX and ion exchange processes [20], either the product to be obtained (impure cobalt hydroxide, cobalt hydroxide pure or metallic cobalt) [15].

In the case that the source is refined from SX processes; in general, iron and aluminum are precipitated first, then copper, nickel and then zinc; from this process, cobalt is recovered as cobalt hydroxide which then it goes through a refining process to obtain metallic cobalt. It must be taken into consideration that the process of elimination of impurities will depend on the levels of these present, such is the case, for example, of nickel that in some operations is eliminated through an ion exchange process present between the unit operations of the process of refining to obtain metallic cobalt [15].

If the final product is intended to be impure cobalt hydroxide, the iron and aluminum precipitation processes are simply carried out, although clearly the operating parameters, conditions and yields change.

In the case of copper, removal is achieved by raising the pH to about 6, obtaining copper in the form of basic copper–cobalt sulfate and a liquor that can be passed through a bed of cobalt granules to reduce the copper concentration by cementation. Generally, the precipitate is recycled in the leaching circuit.

In the case of zinc, removal is carried out by solvent extraction using D2EHPA as reagent and in other operations zinc is removed by sulfide precipitation with considerable cobalt co-precipitation.

In the case of cobalt, the precipitation of cobalt may include one or more stages. If working in one stage, it should be at a pH of approximately 8.4. If you work in two stages, the pH of the first should be approximately 7.5 and the pH of the second stage should be approximately 8.2–8.5.

Working in multiple stages has its benefits. We must mention that the first stage fulfills two functions; first, it decreases the amount of reagent needed, and, secondly, it limits the amount of magnesium and manganese that enters the cobalt product, although this is not perfect since it is presented in the same way magnesium and manganese in the product. The form of the cobalt precipitate is like a basic sulfate.

Among the reagents that can be used for cobalt precipitation, we find hydrated lime ($\text{Ca}(\text{OH})_2$), sodium carbonate (Na_2CO_3), sodium hydroxide (NaOH) and magnesia (MgO), although the most used are lime and magnesia [15].

- Refinery and electroplating

The cobalt metal refinery consists of the redissolution of cobalt hydroxide (in a series of tanks stirred at pH 6.4) to produce a concentrated solution of cobalt sulfate. El proceso de electrodeposición, dependiendo del circuito a utilizar y de las características del mineral y la solución obtenida previamente, puede ser ejecutado con diferentes parámetros, pero acorde a las plantas de cobalto a nivel mundial, por lo general se trabaja a un voltaje de 4,0–4.8 V, con una densidad de corriente de 280–400 A y un electrolito con una concentración de Co de entre 30–40 g/L. Under this system, the cobalt product is a standard grade cathode (greater than 99.3% purity). Ideally, to achieve these results, the cobalt concentration should be approximately 30–45 g/L of Co. One of the main considerations when producing cathodes is the cobalt–nickel ratio which must be greater than 250. To control and eliminate the charge of nickel in the advanced electrolyte, in some facilities, as mentioned above, a continuous ion exchange process was implemented before the electrolytic extraction of cobalt (Bailey et using the Dow M4195 as resin). Currently, the ion exchange process has also been tested to remove zinc, leaving the cobalt refining unit operations such as hydroxide dissolution, iron removal, copper removal, zinc ion exchange, nickel ion exchange and cobalt electrowinning.

As mentioned, metallic cobalt is produced by electrodeposition in which a sulfate electrolyte is used in a complete cell. The working parameters are generally a cell voltage of 4.0–4.8 V, current density 300–400 A / m² and an efficiency of 60–80%. The cathodes can be made of stainless steel or carbon steel [15].

- Challenges ahead in processing

Although the cobalt industry and market today are on the rise, there are various challenges ahead which must be addressed as soon as possible. Among these challenges, we find: improvements in metal processing technologies and improvement in the final product delivered, this in relation to the fact that today, consumers only buy impure cobalt hydroxide, which means less profit and a high cost of transport. Another important challenge is the cobalt losses due to the fact that the cobalt in the minerals is present in the form of sulfide and oxide, and depending on the process, it is difficult to recover cobalt in the form of sulfide if the oxide is worked and vice versa. In addition, cobalt losses in precipitation due to iron and manganese must be considered. The elimination of impurities is another challenge to consider because not all impurities always have the same characteristics; in addition, this brings with it another challenge and that is that the agents to carry out the correct precipitation (elimination of impurities) turn out to be quite expensive in some cases [14].

The control of water in the hydrometallurgical circuit is essential for the successful operation of the plant [21], so it is an important challenge to consider in the future; it must come up with a way to be able to use a lesser amount of water in the process

hydrometallurgical because when large quantities are used in countercurrent decantation, the water ends up transporting impurities to the electrodeposition process. Lastly, due to the constant changes in the copper–cobalt market, the processing circuits keep changing over time. It is necessary to start thinking about new ways or technologies to process cobalt copper, due to the future challenges ahead, such as mixed minerals that arise as mining moves toward the transition zone between the zone of degraded oxide and the zone of sulfur not weathered [14, 22, 23].

4 Conclusion

Cobalt is a critical mineral, rare and of high economic value. Its processing is of a moderate cost, being the mixed processes (pyro-hydrometallurgical) the most used. In addition, it is important to mention that cobalt dissolves at a low oxidation potential and low pH, which facilitates its processing.

References

1. Huang Y et al (2020) Overview of cobalt resources and comprehensive analysis of cobalt recovery from zinc plant purification residue—a review. *Hydrometallurgy* 193:105327. <https://doi.org/10.1016/j.hydromet.2020.105327>
2. Xu JN, Yang HY, Tong LL, Jin ZN, Song Y (2017) The mechanism of Skutterudite acid leaching: a DFT study of H⁺ effect on CoO (010) Surface. *Solid State Phenom* 262:408–412. <https://doi.org/10.4028/www.scientific.net/SSP.262.408>
3. Toro N, Robles P, Jeldres RI (2020) Seabed mineral resources, an alternative for the future of renewable energy: a critical review. *Ore Geol Rev* 103699. <https://doi.org/10.1016/j.oregeorev.2020.103699>
4. Toro N, Jeldres RI, Órdenes JA, Robles P, Navarra A (2020) Manganese nodules in Chile, an alternative for the production of Co and Mn in the future—a review. *Minerals* 10(8):674. <https://doi.org/10.3390/min10080674>
5. Banza Lubaba Nkulu C et al (2018) Sustainability of artisanal mining of cobalt in DR Congo. *Nat. Sustain* 1(9):495–504. <https://doi.org/10.1038/s41893-018-0139-4>
6. Cifuentes C (2019) Chile, minería más allá del cobre. [Online]. Available: https://www.cochilco.cl/Presentaciones/2019_08_22_Chile_-_miner%C3%ADa_m%C3%A1s_all%C3%A1_del_cobre_CCG.pdf
7. Rubio J (2003) Monografía sobre recursos minerales de cobalto en España. <https://www.yumpu.com/es/document/view/17512955/monografia-sobre-recursos-minerales-de-cobalto-en-espana>
8. Young RS (2021) Cobalt processing. <https://www.britannica.com/technology/cobalt-processing>
9. Greenwood NN, Earnshaw A (1997) *Chemistry of the elements*. Butterworth
10. Safarzadeh MS, Dhawan N, Birinci M, Moradkhani D (2011) Reductive leaching of cobalt from zinc plant purification residues. *Hydrometallurgy* 106(1–2):51–57. <https://doi.org/10.1016/j.hydromet.2010.11.017>
11. Habashi F (1997) *Handbook of extractive metallurgy*. Wiley-VCH
12. Zaman HA, Sharif S, Kim D-W, Idris MH, Suhaimi MA, Tumurkhuayag Z (2017) Machinability of cobalt-based and cobalt chromium molybdenum alloys—a review. *Procedia Manuf* 11:563–570. <https://doi.org/10.1016/j.promfg.2017.07.150>

13. D'Aubarede G (1969) Evaluación de los conocimientos existentes sobre Cobalto, Manganeso, Mercurio, Perlita, Plomo, Zinc, Zirconio. <http://bibliotecadigital.ciren.cl/handle/123456789/19453>
14. Farjana SH, Huda N, Mahmud MAP (2019) Life cycle assessment of cobalt extraction process. *J Sustain Min* 18(3):150–161. <https://doi.org/10.1016/j.jsm.2019.03.002>
15. Crundwell FK, du Preez NB, Knights BDH (2020) Production of cobalt from copper-cobalt ores on the African Copperbelt—an overview. *Miner Eng* 156:106450. <https://doi.org/10.1016/j.mineng.2020.106450>
16. Navarra A et al (2020) Quantitative methods to support data acquisition modernization within copper smelters. *Processes* 8(11):1478. <https://doi.org/10.3390/pr8111478>
17. Mwema MD, Mpoyo M, Kafumbila K (2002) Use of sulphur dioxide as reducing agent in cobalt leaching at Shituru hydrometallurgical plant. *J South African Inst Min Metall* 102(1):1–4
18. Torres D et al (2020) Leaching of pure chalcocite with reject brine and MnO₂ from manganese nodules. *Metals (Basel)* 10(11):1426. <https://doi.org/10.3390/met10111426>
19. Toro N, Rodríguez F, Rojas A, Robles P, Ghorbani Y (2021) Leaching manganese nodules with iron-reducing agents—a critical review. *Miner Eng* 163:106748. <https://doi.org/10.1016/j.mineng.2020.106748>
20. González Y, Navarra A, Jeldres RI, Toro N (2021) Hydrometallurgical processing of magnesium minerals—a review. *Hydrometallurgy* 201:105573. <https://doi.org/10.1016/j.hydromet.2021.105573>
21. Alexander D, van der Merwe C, Lumbule R, Kgomo J (2018) Innovative process design for copper-cobalt oxide ores in the Democratic Republic of Congo. *J South African Inst Min Metall* 118(11). <https://doi.org/10.17159/2411-9717/2018/v118n11a6>
22. Pérez K, Toro N, Gálvez E, Robles P, Wilson R, Navarra A (2021) Environmental economic and technological factors affecting chilean copper smelters – a critical review. *J Materi Res Technol.* <https://doi.org/10.1016/j.jmrt.2021.08.007>
23. Moraga C, Cerecedo-Saenz E, González J, Robles P, Carrillo-Pedroza FR, Toro N (2021) Comparative study of MnO₂ dissolution from black copper minerals and manganese nodules in an acid medium. *Metals* 11(5):817. <https://doi.org/10.3390/met11050817>

Chapter 41

Magnesium Extraction Mechanisms



Yessica González, Edelmira Gálvez, Jonathan Castillo, and Norman Toro

Abstract Metallic magnesium can be obtained from seawater, brines, minerals, in recycled scrap, and in alloys. It is the eighth most abundant element on the planet, using 2% of the earth's crust, and it is the third most abundant element in the sea with approximate contents of 1.3% of magnesium, on the other hand, brines have around 0.3–1% magnesium. Also, it is considered the third most used structural metal after aluminum and iron. Regarding its extraction mechanisms, leaching is the most crucial stage for Mg extraction, the most common lixiviants being inorganic and organic acids and ammonium salts. The choice of the leaching agent depends on the raw material to be used. Organic acids are more selective in dissolving Mg, although with less dissolving power. While inorganic acids are more dissolving, they nevertheless generate greater corrosion of the equipment to be used.

Keywords Magnesium · Organic acid · Inorganic acid · Leaching

1 General Aspects

Magnesium is a chemical element with the symbol Mg, atomic number 12, and its most common oxidation number being +2, belongs to alkaline earth minerals, has a melting point of 650 °C and a boiling point of 1107 °C [1]. Its discovery is attributed to Sir H. David in 1808 [2]. It was produced for the first time as metallic magnesium by a Frenchman in 1829 and its use at an industrial level began at the end of the nineteenth century [1], however, the high price in its production has prevented its great use despite its physical properties [3, 4].

Y. González · N. Toro (✉)

Facultad de Ingeniería y Arquitectura, Universidad Arturo Prat, 1244260 Antofagasta, Chile
e-mail: ntoro@ucn.cl

E. Gálvez

Departamento de Ingeniería Metalúrgica y Minas, Universidad Católica del Norte, 1270709 Antofagasta, Chile

J. Castillo

Departamento de Ingeniería en Metalurgia, Universidad de Atacama, 1531772 Copiapó, Chile

Table 1 Characteristics of magnesium

Properties	Magnesium
Chemical symbol	Mg
Crystal structure	Hcp hexagonal
Density at 20 °C (g/cm ³)	1.74
Coefficient of thermal expansion 20–100 °C ($\times 10^6/C$)	25.2
Elastic modulus [Young's modulus of elasticity] (106 Mpa)	44.126
Tensile strength (Mpa)	240 (AZ91D)
Melting point (°C)	650
Boiling point (°C)	1107
Atomic number	12
Atomic diameter (nm)	0.32

Metallic magnesium can be obtained from seawater, brines, minerals, in recycled scrap, and in alloys [5]. It is a light metal with a density of 1.74 g/cm³; 1.6 times less than aluminum (2.7 g/cm³) and 4.5 times less than steel (7.86 g/cm³) [6]. It is the eighth most abundant element on the planet, using 2% of the earth's crust [7], and it is the third most abundant element in the sea with approximate contents of 1.3% of magnesium, on the other hand, brines have around 0.3–1% magnesium [4–8]. It is considered the third most used structural metal after aluminum and iron [9]. The main characteristics of magnesium are that it has low density, good ductility and advantages of noise and vibration damping [8]. Its characteristics are shown in Table 1.

2 Alloys

Magnesium is available with purity higher than 99.8%. However, it is mostly used in alloys, since its properties improve [10], both its hexagonal crystalline shape, its atomic diameter of 0.32 nm and its light nature, make it favorable for alloying it with different metals [10], which is why it is considered the best alloy of the twenty-first century [6]. Its lightweight nature has caused an increase in demand in the manufacture of alloys for use in motorized equipment [11]. Magnesium alloys have excellent physical and chemical properties such as low density, high specific resistance, superior hydrogen storage capacity, light for transport, biocompatibility and good damping performance, and it is considered to be used in aerospace, transportation, electronics especially 3C products (Computing, communication and electronics), energy and biomedical (orthopedics, cardiology, urology), however, studies are still lacking since it presents low resistance to corrosion, and rapid degradation rate [12–14]. It is common to find magnesium in alloys with aluminum, zinc, cerium, silver,

thorium, yttrium and zirconium [10]. And as mentioned by Harraz [1], zirconium or rare earths can be added to strengthen the alloys.

Advantages of alloys [15].

- Low density in construction materials.
- High specific resistance.
- Molding capacity, suitable for high pressure casting.
- Good weldability.
- Corrosion resistance can be improved with high purity magnesium.
- Availability.
- Better mechanical properties.
- Better electrical and thermal conductivity.
- Recyclable.

However, it still has some disadvantages that must be overcome:

- Low elastic modulus, low ductility.
- Limited cold work.
- High chemical reactivity.
- Limited resistance to corrosion.
- Some limited mechanical properties (stress, deformation and wear).

3 Applications

Magnesium was used in large quantities in the First and Second World War, in the nuclear industry and military aircraft [2]. However, both magnesium and its alloys have been used in various fields, such as refractory and insulating materials, in the manufacture of rubber, printing ink, pharmaceutical and toilet products, agriculture, fertilizers, pyrotechnics, aerospace, construction materials, industry, chemistry, and among others. Magnesium alloys are also used as sacrificial anodes when contacting a less reactive metal. Pure magnesium is used as an additive in alloys such as in the aluminum industry mainly and can also be seen in the titanium industry. More details can be seen as follows [16–19]:

- Magnesium sulfate: Epsom salts and as a fire retardant agent.
- Magnesium chloride: Application in ceramics, cement.
- Magnesium carbonate: Clinical area, filling ink, paints and varnish.
- Magnesium peroxide: Antiseptics and bleach.
- Magnesium silicates: Fertilizer production, civil construction, steel market, carbon sequestration, silica production.

4 Productive Process

There are various technologies for the extraction of magnesium depending on the source, and these are the electrolytic process, the Pidgeon process, and the thermal reduction process; generally, magnesium from seawater and brine are extracted by electrolytic processes; in the case of extraction of magnesium from minerals of magnesite, dolomite and carnalite, the Pidgeon process is applied, and in the case of secondary sources such as waste and some primary sources such as dolomite and magnesite, the pyrometallurgical process of thermal reduction is used; and however, these methods require high energies for its process and produce toxic emissions to the environment, so new technologies or alternative sources are sought for a more economical extraction [4].

Electrolytic process: This process requires 10.5–13.2 kWh/kg [9], here, the molten magnesium is produced by the chlorination of magnesium oxide [20]. This method includes mineral preparation, magnesium chloride dehydration and electrolysis, involving two stages: the first is the production of pure magnesium chloride from seawater or brine, and the second corresponds to the electrolysis of fused magnesium chloride, delivering as products magnesium and gaseous chlorine, where the magnesium is added to ingots and the gaseous chlorine is recycled to the chlorination furnace [4]. 75% of the world's magnesium production is through this method [11]. The important parameters to carry out this method are as follows: voltage, current density, electrolyte temperature, selection of refractories and an efficient method for collecting magnesium and chlorine gas [9].

Pidgeon process: This process requires temperatures between 1000 and 1300 °C [9]. It is a thermal reduction process; here, the dolomite is calcined to MgO and CaO under vacuum pressure (10 Pa), then reduces it with silicon or ferrosilicon and later produce magnesium gas [20]; this steam is condensed obtaining high purity magnesium reaching 99.68%; and the process presents a slow kinetics due to the temperature used, which produces a deficient heat transfer so the production is lower with this method [21].

Mintek process: This process requires temperatures between 1700 and 1750 °C. Corresponds to a silicothermic process, which is carried out in large-scale batches, slag, aluminum and ferrosilicon are used to reduce magnesium oxide, as it presents higher temperature and pressure than the Pidgeon process (0.85 atm.), it obtains a production higher, but with higher levels of impurities, reaching 97.86%, which requires the addition of a subsequent refining stage [4].

Thermal reduction process: This process requires temperatures between 1160 and 1700 °C [9], it involves the reduction of the mineral by means of reagents, the mineral is crushed and calcined in furnaces to produce a mixture of calcium and magnesium oxide, then it is reduced with ferrosilicon, to later condense the magnesium and then it is molded into ingots, leaving it with a purity of 99.99% and on the other hand calcium oxide slag [4].

Leaching process: This process requires temperatures between 70 and 90 °C in stirred reactors [17], for the dissolution of magnesium minerals, both inorganic

and organic acid or base solvents are used depending on the characteristics of the mineral to be treated, organic solvents are less abrasive and more selective, but present greater difficulty in handling, on the other hand, inorganic reagents present faster leaching kinetics, since they can operate at higher temperatures, but produce greater deterioration in reactors [22]. The dissolution kinetics of magnesium is controlled by the slowest process that occurs between; diffusion through the fluid or the layer of inert solid, or by surface chemical reaction [16]. There are 3 sub-processes during leaching, the first is the external diffusion of the acid to the solid surface, then the internal diffusion in the porous layer from the solution to the core surface and lastly, the leaching reaction at the core surface [23]. Various studies have been carried out with organic acid solvents such as citric, lactic, gluconic, acetic and succinic acids, inorganic acids such as hydrochloric, nitric and sulfuric, and ammonium salts such as ammonium chloride and ammonium sulfate. On the other hand, the parameters with the greatest influence on the leaching of magnesium minerals are the temperature and the concentration of the reagent, both presenting a direct relationship with the extraction of magnesium, and the particle size, which presents an inverse relationship with the extraction [4].

In Table 2 you can see some processes used for the production of magnesium for both the electrolytic process and the thermal reduction process, these are specified according to the feed material used, defining the reactions that occur and the temperature and pressure required to carry them finished.

5 Conclusions

Among the proposed methods, the hydrometallurgical is the most striking for the extraction of Mg since it is less polluting than the pyrometallurgical and electrolysis processes; in addition, it is more profitable.

Different physical and chemical properties of materials with different crystalline structures influence their degree of solubility and the choice of leaching media. Inorganic solvents have a higher dissolving power and are preferred for difficult-to-leach raw materials; inorganic solvents can also operate at higher temperatures. For raw materials that are relatively easy to dissolve, more selective organic solvents are favored, as these solvents operate at lower temperatures and cause less corrosion. Furthermore, inorganic solvents are inexpensive.

Table 2 Selected magnesium production processes. Modified from: [4]

Process	Feeding material	Route	Reactions present	Temperature and pressure
Electrolytic process				
DOW process	Brine and sea water	Neutralization, purification and dehydration	Electrolytic $\text{MgCl}_{2(s)} = \text{Mg}_{(l)} + \frac{1}{2} \text{Cl}_{2(g)}$	$T = 700\text{--}800\text{ }^\circ\text{C}$ $P = 1\text{ atm.}$
AM Process	Magnesite	Mining, HCl leaching and dewatering	Cathode $\text{Cl}^- = \text{Cl}_{2(g)} + 2e$ Anode $\text{Mg}^{+2} + 2e = \text{Mg}_{(l)}$	
IG Farben Process	Brine and sea water	Neutralization, dehydration and chlorination		
Thermal reduction process				
Silicothermic	Dolomite, FeSi	Calcination, FeSi manufacturing, palletizing	$\text{MgO} + \text{CaO} + \text{FeSi} = \text{Mg}_{(g)} + \text{Ca}_2\text{SiO}_4(s) + \text{Fe}$	$T = 1160\text{ }^\circ\text{C}$ $P = 67\text{ Pa}$
Carbothermic	Magnesite, coal	Calcination, palletizing	$\text{MgO} + \text{C} = \text{Mg}_{(g)} + \text{CO}_{(g)}$	$T = 1700\text{ }^\circ\text{C}$ $P = 1\text{ atm.}$
Magnetothermic	Dolomite, bauxite FeSi	Calcination, manufacture of FeSi	$2\text{CaO MgO} + (x\text{Fe})\text{Si} + n\text{Al}_2\text{O}_3 = 2\text{CaO SiO}_2 + n\text{Al}_2\text{O}_3 + 2\text{Mg} + x\text{Fe}$	$T = 1550\text{ }^\circ\text{C}$ $P = 0,05\text{ atm.}$
Thermal-aluminum	Dolomite, Al scrap	Calcination	$4\text{MgO}_{(s)} + 2\text{Al}_{(s)} = 3\text{Mg}_{(g)} + \text{MgAl}_2\text{O}_4(s)$	$T = 1700\text{ }^\circ\text{C}$ $P = 0,85\text{--}1\text{ atm.}$
Mintek7	Dolomite, Bauxite, FeSi, Al scrap	Calcination	$2\text{CaO MgO} + (x\text{Fe})\text{Si} + n\text{Al}_2\text{O}_3 = 2\text{CaO SiO}_2 + n\text{Al}_2\text{O}_3 + 2\text{Mg} + x\text{Fe}$ $\text{MgO}_{(s)} + \text{Al}_{(s)} = 3\text{Mg}_{(g)} + \text{MgAl}_2\text{O}_4$	$T = 1700\text{ }^\circ\text{C}$ $P = 1\text{ atm.}$

References

- Harraz HZ (2017) Beneficiation and mineral processing of magnesium minerals
- King JF (2007) Materials perspective magnesium: commodity or exotic? Mater Sci Technol 23
- Amasaka K (2004) Production process. In: Science SQC, new quality control principle, pp 285–295
- González Y, Navarra A, Jeldres RI, Toro N (2021) Hydrometallurgical processing of magnesium minerals—a review. Hydrometallurgy 201:105573. <https://doi.org/10.1016/j.hydromet.2021.105573>
- Liu T, Yang Q, Guo N, Lu Y, Song B (2020) Stability of twins in Mg alloys—a short review. J Magnes Alloy [Internet] 8(1):66–77. Available from: <https://doi.org/10.1016/j.jma.2020.>

02.002

6. Shao Y, Zeng RC, Li SQ, Cui LY, Zou YH, Guan SK et al (2020) Advance in antibacterial magnesium alloys and surface coatings on magnesium alloys: a review [Internet]. *Acta Metallurgica Sinica (English Letters)*. Chin Soc Metals. Available from: <https://doi.org/10.1007/s40195-020-01044-w>
7. Ghimire S, Flury M, Scheenstra EJ, Miles CA (2019) Recycling of magnesium waste into magnesium hydroxide aerogels. *Sci Total Environ* [Internet] 135577. Available from: <https://doi.org/10.1016/j.scitotenv.2019.135577>
8. Kulekci MK (2008) Magnesium and its alloys applications in automotive industry. *Int J Adv Manuf Technol* 39(9–10):851–865
9. Nagesh CR, Prasad MRS, Prasad VVS (2018) Developments in magnesium production by fused salt electrolysis of anhydrous magnesium chloride (December)
10. Stjohn D, Nie J (2017) Magnesium alloys. In: *Light Alloys*, 287–366
11. Tshuma B, Hlabangana N, Tshuma J (2018) Extraction of magnesium from chorme slag by sulphuric acid
12. Liang Q, Shuping G, Chenyu L, Dongyu J, Guixue W, Tieying Y (2020) Impact of a bioactive drug coating on the biocompatibility of magnesium alloys. *J Mater Sci* [Internet] 55(14):6051–6064. Available from: <https://doi.org/10.1007/s10853-020-04365-4>
13. Song J, She J, Chen D, Pan F (2020) Latest research advances on magnesium and magnesium alloys worldwide. *J Magnes Alloy* [Internet] 8(1):1–41. Available from: <https://doi.org/10.1016/j.jma.2020.02.003>
14. Yin ZZ, Qi WC, Zeng RC, Chen XB, Gu CD, Guan SK et al (2020) Advances in coatings on biodegradable magnesium alloys. *J Magnes Alloy* 8(1):42–65
15. Mordike BL, Ebert T (2001) *Magnesium Properties—applications—potential*, vol 302. *Mater Sci Eng A* 37–45
16. Gao W, Wen J, Li Z (2014) Dissolution kinetics of magnesium from calcined serpentine in NH₄Cl solution. *Ind Eng Chem Res* 53(19):7947–7955
17. Royani A, Sulistiyono E, Prasetyo AB, Subagja R (2018) Extraction of magnesium from calcined dolomite ore using hydrochloric acid leaching. In: *AIP conf proc.* 2018;1964
18. Hu Y (2020) Constructing grey prediction models using grey relational analysis and neural networks for magnesium material demand forecasting [Internet]. *Appl Soft Comput J.* Elsevier B.V.93. Available from: <https://doi.org/10.1016/j.asoc.2020.106398>
19. Carmignano ORRD, Vieira SS, Brandão PRG, Bertoli AC, Lago RM (2020) Serpentinites: Mineral structure, properties and technological applications. *J Braz Chem Soc* 31(1):2–14
20. Lee Y, Yang JK, Park JH (2018) Thermodynamics of fluoride-based molten fluxes for extraction of magnesium through the low temperature solid oxide membrane (LT-SOM) process. *Calphad Comput Coupling Phase Diagrams Thermochem* [Internet]. 62(March):232–237. Available from: <https://doi.org/10.1016/j.calphad.2018.07.006>
21. Du J, Han W, Peng Y (2010) Life cycle greenhouse gases, energy and cost assessment of automobiles using magnesium from Chinese Pidgeon process [Internet]. *J Cleaner Prod.* Elsevier Ltd. 18. Available from: <http://dx.doi.org/https://doi.org/10.1016/j.jclepro.2009.08.013>
22. Demir F, Dönmez B (2019) The determination of the optimum conditions upon the leaching performance of calcined magnesite, vol 5, *Heliyon*
23. Didyk-Mucha A, Pawlowska A, Sadowski Z (2016) Application of the shrinking core model for dissolution of serpentinite in an acid solution. *E3S Web Conf.* 8

Chapter 42

Machinability Study of IS2062 Steel During Milling Using Different Coated Tools: A Review



Atul P. Kulkarni, Kedar Ramdasi, Omkar Kulkarni, Priya Murkewar, and Sampada Dravid

Abstract IS 2062 steel is a low-carbon steel. It meets all the requirements of high-strength steel when it is hot rolled. Hence, it is one of the popular steels for structure and machining application in various industries worldwide. Despite excellent mechanical properties, high-speed machining of IS 2062 is still challenging for the manufactures to increase material removal rate, tool life and improved surface finish. In the present study, the challenges, solutions proposed by several researchers, cutting tool and coating manufacturers are presented during milling of IS 2062 steel. It is observed that the uncoated carbide tool is not suitable for high-speed machining due to its low hot hardness. However, prominent results are shown using AlTiN PVD-coated carbide tools during high-speed milling of IS 2062. CVD multilayer TiN/Al₂O₃/TiC-coated tool can also be a suitable option for high-speed milling. However, CVD process reported some ecological and environmental challenges. There is a need to investigate more on high-speed machining of IS 2062 steel using coated tools.

Keywords IS2062 · Milling · PVD · CVD · Coating · Insert

A. P. Kulkarni (✉) · K. Ramdasi · O. Kulkarni · P. Murkewar · S. Dravid
Department Mechanical Engineering, VIIT, Pune, India
e-mail: atul.kulkarni@viit.ac.in

K. Ramdasi
e-mail: kedar.17u477@viit.ac.in

O. Kulkarni
e-mail: omkar.17u051@viit.ac.in

P. Murkewar
e-mail: priya.21820052@viit.ac.in

S. Dravid
e-mail: sampada.dravid@viit.ac.in

1 Introduction

The machining industries have been growing significantly, and the project growth of it till 2025 is around \$100B to \$120B [1]. It is mainly due to the increasing demands of high-quality products. CNC machines help manufactures to produce good-quality products at high-speed machining capability. A large demand for precision high-strength steel machining can be seen in the industry [2]. IS 2062-grade steel is a low-carbon steel. The main alloying elements are vanadium, manganese and silicon with different proportions. The primary function of these elements is to increase the strength-to-weight ratio, formability, weldability and toughness of that material. At high temperatures, IS 2062 steel has high strength. It also states standards that have been set for hot-rolled and high-strength structure steel [3–5]. Due to such excellent properties, it became very attractive material for structural fabrication, machining and casting. It is widely used in many industries like automobile, petrochemical, oil & gas, sugar, defence, shipbuilding, nuclear mining, etc. IS 2062 E 250-grade steel rusts faster in comparison with other steels due to the lower resistance of corrosion. However, close tolerance can be achieved on the specified dimensions after machining. It can also sustain high pressure and temperature loads leading to excellent stress distribution across the surface [5–7]. Table 1 shows the typical chemical composition of the material. It is obtained after using Spark Atomic Emission Spectrometry as per ASTM E415–17. The mechanical properties of the material are also given in Table 2.

Table 1 Chemical composition of IS 2062 steel

Components	Percentage
C %	0.20
Mn %	0.75
Si %	0.20
S %	0.032
P %	0.019

Table 2 Mechanical and physical properties of IS 2062 steel

Properties	Value
Hardness (ASTM E 381)	137 (BHN)
Yield stress	302 Mpa
Ultimate tensile stress	486 Mpa
0.2% proof stress	297 Mpa
Elongation	12% min

2 Milling Performance

In milling process, cutting tool is rotating and workpiece is stationary. In this machining process, straight surface or planar surface is generated using rotating tool having multiple cutting edges working across the stationary workpiece. Different cutting tools with different materials like HSS, cemented carbide, ceramic, cermet, etc. are extensively used for low-speed to high-speed milling [8]. High-speed machining (HSM) has made revolutionary changes by drastically increasing the productivity, and it became one of the important reasons for different machine manufacturers to showcase their capability to improve chatter-less HSM. This means that, by increasing in quick milling passes, the material removal rate (MRR) increases. As per the chart, it is from Dr. Herbert Schulz's "History of High machining speed" [9]. It was stated that with the increase in cutting speed, cutting temperature also increases. However, after a particular cutting speed, there was a decrease in cutting temperature that was observed in nearly all the experimental materials. Cutting temperature reduced primarily because of low cutting forces and very low chip thickness recorded during the experimentation [10]. HSM conditions are more suitable for improvement in tool life and increase in productivity. In case of milling machine, HSM range is range of cutting speed from 400 to 1600 m/min. HSM can be done for roughing as well as finishing operations. For finishing operation, it is recommended to use multiflute cutter with higher feed rate. Since plenty of chip clearance is available, it helps to remove chip easily at higher feed rate thereby increasing material removal rate. IS 2062 E 250-grade steel shows work hardening at sudden rise in temperature. It was majorly observed during milling operation [11, 12].

Dennison et al. [13] did research on the face milling operation of low-carbon steel by carbide insert coated with zinc. Optimization was performed using Taguchi technique. A design of experiment of L9 array was made for experimentation purpose where cutting speed, number of passes, feed rate and depth of cut were varied for different trials. It was reported that cutting speed has greater impact on cutting force, whereas feed rate showed influence on surface roughness. Higher roughness values were observed at high feed rate. Regression model was prepared, and the results comparison was done experimentally with optimized results. The results are in line with each other with acceptable error of 4.624%. Choubey et al. [14] studied the process parameter optimization for machining mild steel on CNC milling machine with the use of Taguchi design and analysing signal-to-noise ratio', HSM tool is used for surface finish operations of mild steel using CNC milling machine, and to identify optimum process parameters, signal-to-noise ratio method is used. Analysis of variance (ANOVA) method and a L9 orthogonal array are used to study the machining parameters' performance like spindle speed (200–2000 rpm), feed (200–2000 mm/min), depth and width of cut 0.01–0.1 mm and 0.1–0.4 mm, respectively, taking into account a very good surface finish and large material removal rate (MRR). The surface finish of workpiece and MRR have been taken into consideration as they are directly related to productivity improvement. Feed is the most effective factor for MRR as per the results analysed that were obtained from Taguchi method and

signal to noise which nearly matches with (ANOVA). Also, spindle speed is one of the most impactful factors on surface roughness. From the paper, the viability of machining of mild steel by CNC finishing machine using a HSS tool can be understood. It was observed that the surface roughness of material is majorly impacted by speed of spindle and MRR by feed rate. Nadaf et al. [15] carried out research experiment on IS 2062:2011 E250-grade material using Taguchi method for experimental trials designed on L27 orthogonal array. They studied that process parameters like feed rate, depth of cut and spindle speed are optimized using various performance measuring parameters like surface roughness (Ra) and material removal rate (MRR). The machining was done on machine having vertical machining centre, coolant was used, and cutter having 63 mm diameter was used. The analysis was done on insert having AlTiN PVD coating. It is noted that the surface roughness was affected by spindle speed, feed and depth of cut with around 4.58%, 85.51% and 7.72% proportion, respectively. Results of MRR showed that maximum MRR that was obtained is 43.1 gm/min and minimum was 9.9 gm/min. It is majorly affected by spindle speed 10.10%, feed rate 50.13%, and depth of cut 31.46% contribution, respectively.

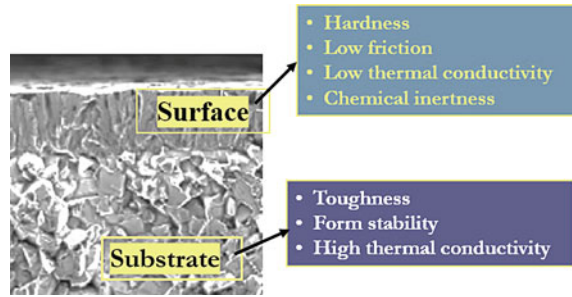
Ojolo et al. [16] studied the tool life under dry machining environment and the effects of machining on it. Three materials, namely medium carbon steel with 0.4 wt% of carbon (C), mild steel 0.29 wt% of carbon (C) and brass C330, were selected and used as the materials for testing. The cutting tools used were HSS tool M2 C66, P-10-grade tungsten carbide insert and 150412-SA grade DMNG carbide insert tool. The parameters selected for experiment are speeds of spindle as (900, 1120, 1400 rpm), feed rates of (0.1, 0.2, 0.3 mm/rev) and depth of cut (0.5, 1.0, 1.5 mm). It was reported that spindle speed had greatest impact on tool life, with depth of cut and feed rate following it. Tungsten carbide tool lasted 480 s, 726 s and 1028 s for three materials, respectively. DMNG carbide tool lasted was 782 s, 864 s, 1183 s for three materials, respectively. HSS tool gave tool life of 161 s, 321 s and 386 s for three materials, respectively. Lesser tool life was obtained at these parameters (1400 rev/min), feed rate (0.3 mm/rev) and depth of cut (1.5 mm). Increase in spindle speed, depth of cut and feed rate affected the tool life significantly. Filho et al. [17] studied the influence that cutting conditions have on tool life, tool wear and surface finish achieved during face milling process. The study involves the influence of cutting conditions on tool life and surface roughness of the material on which face milling operation is being performed for flat surfaces like cutting speed, feed velocity and feed per tooth. In the first stage of the experiments, a variation in feed per tooth (0.12, 0.15, 0.10 mm) is observed which is caused by the cutting speed (240, 192.4, 288.6 m/min) which was varied without varying feed rate (587 mm/min). In the second stage of the trials, cutting speed (288.6, 331.4 m/min) and feed rate (705, 810 mm/min) were fluctuated in such manner that feed/ tooth (0.12 mm) was kept constant. Tool flank wear and surface finish of the workpiece were measured at regular interval. It was observed that tool life is greatly impacted by cutting speed, irrespective of whether feed rate or feed per tooth is fluctuated. In addition, it is also observed that tool wear increases with primary machining edge; it does not have influence on increasing the surface finish of the workpiece material. Nath et al. [18] did research study on machinability and optimization of face milling process of steel alloys using indexable milling inserts.

As per their observations, stainless steels and nickel-based super alloys are hard to cut materials that could be used in different critical and important areas like chemical plants, aerospace and automotive components. Parts with different complexity were used for milling with indexable inserts. Machinability and process cost optimization of alloys like stainless steel SS 403cb+ , Inconel 718 and Inconel 625 were one of the main focuses of their research. The machining trials for the same were performed using different combinations of cutting parameters like feed rate and cutting speed. They stated their observations on machinability based on tool life and tool wear, MRR and cutting forces. They concluded that Inconel 625 has poorest machinability and Inconel 718 followed it. The MRR and tooling life of material SS 403cb+ were obtained to be almost 7 to 10 times greater when we compare it to that of the 2 nickel alloys when the cutting speed and the feed rate used are same. They found that feed rate showed higher effect and was found to be of higher significance with a nonlinear relation on tool life. They also found out that the parameter recommended by the method of optimization of cost is different as compared to the tool life method. Machining the workpiece with the optimized values of speed and feed rate variations for equal amount of material to be machined, it was found that the cost of machining was an estimate of about 6 and 5 folds for Inconel 625 and Inconel 718, respectively, compared to that for SS403cb+ . Pimenov et al. [19] did research on the effect that the face milling tool's relative position has towards surface roughness of machined workpiece and dynamics of milling. One of the most significant factors in the process of face milling quality is the surface roughness achieved of the machined workpiece surface. It is observed that surface roughness and cutting force are more influenced by spindle speed during face milling. It also depends on the position of face mill with respect to the workpiece. For the experiment purpose, cutting speed (100 m/min), feed per tooth (0.1 mm/tooth), depth of cut (1 mm) and different relative positions of the cutter, a' (0, 0.3, 0.8, 3.3 6.3, 9.3, 11.8, 12.3, 12.6 mm) were taken. By the experiments, the work was focussed on the influence of relative position of the face mill on technological effects of the process and towards the workpiece on milling dynamics. When the value of $a = 0$, mostly during up milling, X and Z directions have the lowest forces and Y direction vibrations are reached. Thus, the slow but steady increment of uncut chip thickness can be reached in the function of rotation angle of tool. Depending on the determination of total desirability function decides the performed multicriteria optimization. The optimal a' factor equalled to 3.15 mm is obtained from this. In the face milling, the reduction in cutting forces, vibrations and surface roughness parameters is affected by the selection of optimal a' factor. Majority operations were observed during low-to-medium speed machining.

3 Tool Coating

In case of high-speed milling, some challenges like tensile residual stresses were observed on the surface of the part produced. It was mainly due to the thermal shock was observed during machining. This phenomenon can be reduced using coated

Fig. 1 Cross-sectional view of coated tool



carbide tools. Tool coating serves mainly two ways; initially, it helps to carry away maximum heat along with the chip; coating also protects tool acting as a thermal barrier eventually improving tool life [2, 20]. The function requirement of tool coating and substrates is different and conflicting which are shown in Fig. 1. Tool coating mainly acts as a thermal barrier and protects the substrate from overheating. In addition, due to low coefficient of friction, it helps in rapid movement of chip. However, toughness of the substrate protects the tool from premature failure and provides good form stability [21].

There are mainly two types of coating deposition techniques, Physical Vapour deposition Technique (PVD) and Chemical Vapour Deposition Technique (CVD). Titanium nitride (TiN) was the first PVD coating produced in 1960. It holds very abrasive wear resistance and good hardness [17]. TiN and CrN coating has been used as protective hard and wear resistance coating for cutting tools and moulding dies wear components, respectively [18]. Kawate et al. [19] mentioned that CrN coating is better than TiN in corrosion, wear resistance, friction behaviour and toughness. However, the oxidation resistance of TiN and CrN is limited up to 500 °C and 600 °C, respectively [20]. Barshilia et al. [21] reported that during machining, tool coating is exposed to exothermic environment like high temperature and it can be sustained only if the coatings have high thermal stability. Thermal stability of the coating can be improved by adding different elements like Si, Ti, B, Al, and C into TiN and CrN coatings. The coating TiAlN and AlTiN has been classified based on the percentage of Al. It is reported that these two coatings have high abrasive wear resistance and Al₂O₃ oxide layer formed that helps to improve their thermal stability [22, 23]. AlTiN coating has higher microhardness, and it is due to high percentage of Al. It was reported that the microhardness of the coating increases with the increase of Al. This happens due to the effect of solid solution hardening and effect produced by grain boundary hardening because of smaller size crystal [24]. Various researchers reported that (Ti, Al)N-based coatings produced sputtering due to cathodic arc (PVD) technique. High hot hardness, chemical inertness and low thermal conductivity make (Ti, Al)N coatings a great option for high-speed dry machining of different alloys [25]. The previous literature shows that there are some other effective coatings as well with better properties. These coatings are recommended for HSM of IS 2062. Based on this literature, properties of different coatings are listed in Table 3.

Table 3 Shown below are the properties of various single layered and multilayered PVD coatings reported in the literature [24, 26–32]

Coating material(s)	Microhardness (GPa)	Maximum temperature (°C)	Young's modulus (GPa)	Thermal conductivity (W/m K)	Coefficient of friction
TiAlN	26–32	700–900	344–460	6.70	0.40–0.93
AlTiN	32–38	800–900	470–550	4.50	0.30–0.80
CrN	26–32	600	245–436	4.80	0.50–0.65
TiN	20–31	500	380–562	22.0	0.30–0.86
TiAlN/TiN	21–29	500–700	366	5.10	0.25–0.70

Tool manufacturing companies like Sandvik Coromant, Kennametal Inc., Mitsubishi Materials Corporation, Tungaloy, ISCAR Cutting Tools, KYOCERA Precision Tools, Inc. etc. have been in the cutting tool manufacturing industry for numerous years. These companies also recommended the cutting tools for machining of IS 2062 subject to the cutting parameters. A short summary of the cutting tool along with some information related to coated or uncoated grade is given in Table 4. This information is based on the experimental available on official Web site of respective company. Lot of development is going in the field of development of new high wear resistance coating. Many researchers are focussing on mainly PVD technique because of ecological limitation on CVD technique. Table 5 shows the tool coating recommendation for high-speed machining of low-carbon steel. These data are also available on official Web site of the companies.

4 Conclusion

IS 2062 steel being the most recommended steel is used in various industries. Many researchers have studied the machinability of IS 2062 using coated and uncoated tools. Following are the major concluding remarks for the reviews of IS 2062 for its machinability during milling.

- Majority study has been reported for low and medium machine optimization of IS 2062. It mainly showed that feed rate has significant effect on surface quality followed by spindle speed. It is also observed that in high-speed machining, as cutting speed increases, the cutting temperature rises up to some certain limit, and after that, it reduces due to rapid movement of chip. Chip carries maximum heat along with it.
- The literature related to experimental trials using PVD- and CVD-coated tools is rarely reported. However, good literature is available using uncoated tools during machining of IS 2062 steel.
- Experimental results in the literature related to high-speed milling of IS 2062 using single-layer and multilayer coated tools are not reported.

Table 4 Shown below are particulars of coated and uncoated cutting tools recommended by various manufacturers of cutting tools for machining of IS 2062 steel [33–37]

Company name	Grade	ISO	Hardness	Coated/Uncoated	Coating	Coating composition	Coating thickness (μm)
Tungaloy	AH3135	P	200–300 HB	Coated	PVD	TiAlN	4
	T3225	P	200–300 HB	Coated	CVD	TiCN-Al ₂ O ₃	10
	AH120	K	150–250 HB	Coated	PVD	TiAlN	
Mitsubishi	HTi05T	K	92.5 HRA	Uncoated	–	–	–
	HTi10	K	92 HRA	Uncoated	–	–	–
	UTi20T	K	90.5 HRA	Uncoated	–	–	–
	VP15TF	P	91.5 HRA	Coated	PVD	(Al,Ti)N	Thin
	MP6120	P	91.5 HRA	Coated	PVD	(Al,Ti,Cr)N	Thin
	MP6130	P	90.5 HRA	Coated	PVD	(Al,Ti,Cr)N	Thin
	F7030	P	88.8 HRA	Coated	CVD	TiCN-Al ₂ O ₃ -TiN	Thin
Kyocera	PR1225	P		Coated	PVD	Megacoat	
	KW10	K		Uncoated	–	–	–
	GW25	K		Uncoated	–	–	–
Sumitomo	ACP200	P	89.5 HRA	Coated	PVD	TiAlN/AlCrN	3
	ACP100	P	89.3 HRA	Coated	CVD	Al ₂ O ₃	6
	ACP300	P	89.3 HRA	Coated	PVD	AlCrN / TiAlN	3
	G10E	K	91.1 HRA	Uncoated	–	–	–

- Commonly recommended PVD coating is AlTiN coating, and it is mainly due to better thermal stability at elevated temperature. Its oxidation temperature is between 800 and 1100 °C. Most of the coating manufacturers also recommended the same tool coating.
- In-depth analysis of cutting temperature, tool life, surface finish and surface integrity have not been carried out along with high-speed milling. Chip characteristics need more detailed investigation.

Table 5 Particulars of coated and uncoated cutting tools recommended by various manufacturers of cutting tools for machining of IS 2062 steel [38–40]

Company name	Coating name	Coating material	Coating technology	Operating temperature (°c)	Micro-hardness (gpa)
Balzer	Balinit Latuma	AlTiN	PVD	1000	35
	Balinit Alcrona	AlTiN	Arc	1100	36
Cemecon	FerroCon quadro	AlTiN	HiPIMS	1100	–
	Hyperlox	AlTiN	Sputtering	1100	30
	TyAlox	TiAlN	HiPIMS	1100	–
Ion Bond	Crosscut	AlCrN	PVD	1050	–

- Many researchers proposed different optimized solutions; however, reliability analysis is rarely observed. It also requires a need for optimization of cutting parameters at high-speed milling.

References

1. CNC Machining Projected to be \$100B Industry by 2025. Available online: <https://www.thomasnet.com/insights/cnc-machining-projected-to-be-100b-industry-by-2025/>
2. Sousa VFC, Silva FJG (2020) Recent advances on coated milling tool technology—a comprehensive review. *Coatings* 10:235. <https://doi.org/10.3390/coatings10030235>
3. Properties and selection: irons, steels, and high-performance alloys. ASM handbook, vol 1
4. Indian standard hot rolled medium and high tensile structural steel—specification, IS 2062 : 2011 (seventh revision), bureau of Indian Standards (2011)
5. Sen G, Mondal SC (2020) Investigation of the effect of copper, brass and graphite electrode on electrical discharge machining of mild steel grade IS2062. *AIP Conf Proc* 2273:050054. <https://doi.org/10.1063/5.0024672>
6. Rizvi SA, Tewari A, Al W (2017) Application of Taguchi technique to optimize the process parameters of MIG welding on IS 2062 steel. *Int J Emerg Trends Mech Prod Eng* 1(1):1–17
7. Dhameliya K, Desai J, Gandhi M, Dave D (2014) Experimental investigation of process parameters on MRR and Surface roughness in turning operation on CNC Lathe machine for Mild Steel—E250: IS 2062. *Int J Eng Res Technol (IJERT)* 3(5): 742–750
8. Boothroyd G (1997) *Fundamentals of machining and machine tools*. Marcel Dekker, New York, USA
9. Nagaraj M, Ravisankar B (2018) Investigation on ECAPed structural steel IS2062 and evaluation of strengthening mechanisms. *Mater Res Express* 6(3). <https://doi.org/10.1088/2053-1591/aaf2fb>
10. Chinchanikar S, Kulkarni AP, Choudhury SK (2015) Hard turning under dry and minimum quantity lubrication (MQL): comparative assessment through multi-objective optimization. *J Prod Eng* 18(2):16–20
11. Pawar S, Salve A, Chinchanikar S, Kulkarni A, Lamdhade G (2017) Residual stresses during hard turning of AISI 52100 steel: Numerical modelling with experimental validation. *Mater Today: Proc* 4(2):2350–2359

12. Nizamuddin M, Agrawal SM, Patil N (2018) The effect of Karanja based soluble cutting fluid on chips formation in orthogonal cutting process of AISI 1045 steel. *Procedia Manuf* 20:12–17
13. Selvam MD, Dawood DAS, Karuppusami DG (2012) Optimization of machining parameters for face milling operation in a vertical CNC milling machine using genetic algorithm. *Eng Sci Technol Int J* 2(4):544–548
14. Choubey A, Chaturvedi V, Vimal J (2012) Optimization of process parameters of CNC Milling machine for mild steel using Taguchi design and Single to Noise ratio Analysis. *Int J Eng Res Technol (IJERT)* 1(6). ISSN: 2278-0181
15. Nadaf SS, Shinde MY (2020) Optimization of process parameters on CNC milling machine for Mild steel IS 2062:2011 E250 Gr. A with AlTiN coated tool insert in wet condition. *Mater Sci Eng* 748
16. Ojolo SJ, Ogunkomaiya O (2014) A study of effects of machining parameters on tool life. *Int J Mater Sci Appl* 3(5):183–199. <https://doi.org/10.11648/j.ijmsa.20140305.19>
17. Caldeirani Filho J, Diniz AE (2002) Influence of cutting conditions on tool life, tool wear and surface finish in the face milling process. *J Braz Soc Mech Sci* 24(1). Print version ISSN 0100-7386 (Rio de Janeiro Mar. 2002)
18. Nath C, Brooks Z, Kurfess TR (2015) On machinability study and process optimization in face milling of some alloys with indexable copy face mill inserts. *J Manuf Process* 20(1):88–97
19. Pimenov DY, Hassui A, Wojciechowski S, Mia M, Magri A, Suyama DI, Bustillo A, Krolczyk G, Gupta MK (2019) Effect of the relative position of the face milling tool towards the workpiece on machined surface roughness and milling dynamics. *MDPI Appl Sci* 9:842
20. Bunshah RF (2001) *Handbook of hard coatings*. Noyes Publications, New Jersey
21. Huddedar S, Kulkarni AP, Joshi G, Sargade VG (2012) Microstructure and mechanical properties of AlTiCrN, AlCrN coatings deposited by cathodic arc evaporation (PVD) technique. In: *Proc. 21st Int. conf. process. fab. adv. mater, vol 1*, pp 514–520
22. Kulkarni A, Joshi G, Patil N, Sargade V (2016) Investigation of microstructure and mechanical properties of AlTiCrN, AlCrN coatings deposited by advance sputtering technique. In: *International conference on communication and signal processing 2016 (ICCASP)*
23. Kulkarni AP, Sargade VG (2015) Characterization and performance of AlTiN, AlTiCrN, TiN/TiAlN PVD coated carbide tools while turning SS 304. *Mater Manuf Process* 30(6):748–755
24. Chauhana KV, Rawal SK (2014) A review paper on tribological and mechanical properties of ternary nitride based coatings. *Procedia Technol* 14:430–437
25. Kalss W, Reiter A, Derfinger V, Gay C, Endrino JL (2006) Modern coating in high performance cutting applications. *Int J Refract Metal Hard Mater* 24:399–404
26. Hovsepian P, Ehiasarian AP, Petrov I (2010) TiAlCN/VCN nanolayer coatings suitable for machining of Al and Ti alloys deposited by combined high power impulse magnetron sputtering/unbalanced magnetron sputtering. *Surf Eng* 26(8):610–614
27. PalDey S, Deevi SC (2003) Single layer and multilayer wear resistant coatings of (Ti, Al)N: A review. *Mater Sci Eng A* 342:58–79
28. Mo JL, Zhu MH (2009) Sliding tribological behaviors of PVD CrN and AlCrN coatings against Si₃N₄ ceramic and pure titanium. *Wear* 267:874–881
29. Kalss W (2010) Latest developments and applications in coating technologies. UniaxisBalzers Ltd
30. Lukaszewicz K, Dobrzański LA, Kwaśny W, Labisz K, Pancielejko M (2010) Microstructure and mechanical properties of nanocomposite coatings deposited by cathodic arc evaporation. *J Achievements Mater Manuf Eng* 42(1–2):156–163
31. Śliwa A, Dobrzański LA, Kwaśny W, Sitek W (2009) The computer simulation of internal stresses on the PVD coatings 1(3):183–188
32. Braic M, Braic V, Balaceanu M, Pavelescu G, Vladescu A, Tudora I, Popescu A, Borsos Z, Logofatu C, Negrița CC (2005) Microchemical and mechanical characteristics of arc plasma deposited TiAlN and TiN/TiAlN coatings. *J Optoelectron Adv Mater* 7(2):671–676
33. Kyocera Asia Pacific <https://asia.kyocera.com/products/cuttingtools/catalogs/>
34. Tungaloy <https://www.imc-companies.com/Tungaloy/tungaloycatalog/Index.aspx>

35. Sumitomo-<https://www.sumitool.com/en/downloads/cutting-tools/>
36. Mitsubishi-<https://www.mitsubishicarbide.com/mmus/en/product/catalog/index.html>
37. Sandvik coromant-<https://www.sandvik.coromant.com/en-gb/downloads>
38. Ionbond-<https://www.ionbond.com/coating-services/cutting-tools/>
39. Oerlikonbalzers-<https://www.oerlikon.com/balzers/in/en/portfolio/coating-technologies/>
40. Cemecon-<https://www.cemecon.de/cn-en/coating-materials>

Chapter 43

Post-combustion Effect on Nickel and Cobalt Extractions from the Caron Process



Hugo Javier Angulo Palma, Angel Legrá Legrá, Alisa Lamorú Urgellés, Edelmira Gálvez, and Jonathan Castillo

Abstract Lateritic ores are currently considered as the fundamental raw material for the extraction of Ni and Co through the Caron process. This directly affects the temperature control of the hearth 6 of reduction furnaces from the injection of the post-combustion air into the metallurgical process. To date, there is no consensus on the part of the researchers about the positive or negative effect that this variable generates in Ni and Co extractions; therefore, this research reports the results obtained by reducing a lateritic ore on a pilot plant scale, evaluating different temperature levels in the hearth 6, as the post-combustion air was fed. It was found that the injection of the post-combustion air in the reduction furnaces decreases the Ni extractions with respect to the Co extractions, the behavior is becoming more irregular by showing maximum and minimum values. The best result of the present study is obtained when working in an operational condition without the injection of post-combustion air with a temperature of 495 °C in hearth 6 of the reduction furnace.

Keywords Nickel and cobalt extractions · Reduction furnaces · Post-combustion · Caron process

1 Introduction

Nickel (Ni) and cobalt (Co) are very important metals in the production of special alloys [1]. The main sources of Ni are lateritic and sulfurous ores. Although 70% of

H. J. A. Palma (✉) · A. L. Legrá · A. L. Urgellés
Centro de Investigaciones del Níquel (CEDINIQU), Moa, Holguín, Cuba
e-mail: hangulo@cil.moa.minem.cu

H. J. A. Palma
Departamento de Metalurgia y Materiales, Universidad de Moa, Holguín, Cuba

E. Gálvez
Departamento de Ingeniería Metalúrgica y Minas, Universidad Católica del Norte, 1270709
Antofagasta, Chile

J. Castillo
Departamento de Ingeniería en Metalurgia, Universidad de Atacama, 1531772 Copiapó, Chile

the Ni in the world is contained in lateritic ores, only 40% of production comes from this source [2, 3]. There is an increasing interest and research on lateritic ores because they contain commercially viable levels of cobalt (Co), while the availability of high-grade Ni in sulfur ores gets decreased. In contrast to Ni, the Co in lateritic ores is potentially significant for the scarcity of cobalt and current demand levels. Currently, lateritic ores are considered as the main supplier of these metals, by concentrating Ni in more than 1.0% by weight. These deposits are produced by prolonged and deep weathering of Ni silica by including ultramafic rocks, usually in humid tropical or subtropical climates. Lateritic ores can be classified as hydrated silicate deposits, clay silicate deposits and oxide deposits; the latter being processed by different technologies, among which is the Caron process [4–6].

The decision to feed lateritic ores to the Caron process is known to depend on their composition, particularly on the relationship between Fe/Ni and SiO₂/MgO. When the Mg contents exceed 2%, where the use of hydrometallurgical process, before the Caron process, is not convenient due to the considerable increase in solvent consumption, since MgO is soluble in acid. In the case of using pyrometallurgical process, the SiO₂/MgO ratio in the lateritic ores must not exceed two, and the FeO must not exceed 25% [7].

The Caron process is a technology that combines the pyrometallurgical and hydrometallurgical process, and it is based on the leaching of previously reduced lateritic ores with ammoniacal ammonium carbonate solution; the reduction being one of the stages that most influences the final extractions [8–15].

In the Caron process, the reduction of lateritic ores has carried out in a multiple hearth furnace of the Herreshoff type. These metallurgical furnaces ensure that the ore is dried, heated and reduced properly by contacting the reducing gases that flow counter currently. In order to generate these gases, the furnace has the coupled combustion chambers and a quantity of oil have added directly to the mineral, which has the function of reducing additive that enriches the reducing atmosphere [16, 17].

Different researchers have studied the reduction of lateritic ores; all agree that the temperature profile and the concentration of the reducing atmosphere are the most important variables of the process, which is why the control of the temperature from the post-combustion air supply in hearth 4 and 6 is decisive in the metallurgical efficiency of the Herreshoff furnace [18–25].

Post-combustion has called secondary air injection in the upper part of the Herreshoff furnace with the aim of burning the reducing compounds (CO and H₂) in excess. The process is important for controlling the composition of the exhaust gases by preserving the mechanical integrity of the furnace and for energy recovery [26, 27].

In spite of the energy benefits of the post-combustion process, it is necessary to have a strict control of the air supply in hearths 4 and 6, as nickel and cobalt extractions may decrease due to changes in temperature and the reducing atmosphere [28].

There is no consensus by researchers regarding the positive [27] or negative [16] effect that the variation in the post-combustion airflow can generate Ni and Co extractions from laterites. The main investigations reported are focused on modeling the process with artificial neural networks [29–31], presenting as a limitation that they

have not determined the influence of the temperature in the hearth six in the nickel and cobalt extractions in multiple hearth furnaces. To determine the influence of this variable, different temperature profiles were evaluated, which were controlled from the post-combustion supply in hearths 4 and 6 in a pilot plant-scale multiple hearth furnace, determining the nickel and cobalt extractions in each of the experiments to determine its effect on the efficiency of the metallurgical process.

2 Materials and Experimental Design

This research was carried out at the pilot plant, which simulates the Caron process, of the Centro de Investigaciones del Niquel: Capitan Alberto Fernandez Montes de Oca (CEDINIQ). The reduction process was carried out in a Herreshoff furnace (Fig. 1) composed of 17 hearths, listed from top to bottom from hearth 0 (H0) to 16 (H16), enclosed in a metal cylinder 11 m high and 2,51 m in diameter, coated internally by

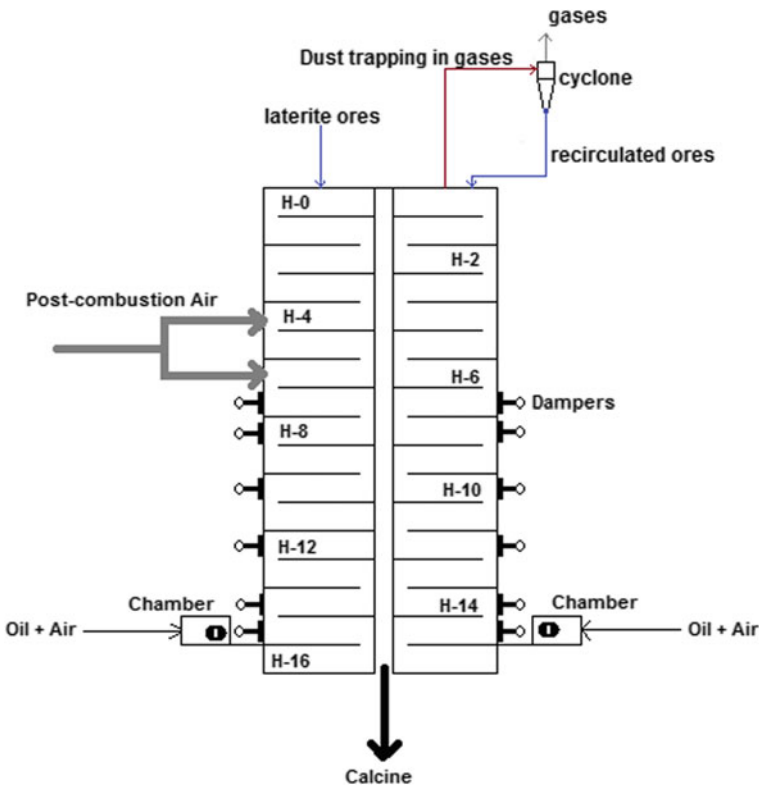


Fig. 1 Pilot plant-scale reduction furnace

a refractory material; the post-combustion air being fed by furnace hearth 4 (H4) and 6 (H6).

2.1 Physical Chemistry Characteristics of the Fed Lateritic Ore

Lateritic ore with a degree of homogenization greater than 89% was fed to the furnace at a rate of 625 kg/h, after being dried and ground until its humidity was less than 5% and presented a percentage of 86 to 88 for the fraction smaller than 75 μm . Table 1 shows its main characteristics.

2.2 Mineralogical Characteristics of the Fed Lateritic Ore

The mineralogical characteristics were determined by X-ray diffraction (PANalytical X'PERT3 –Diffractionmeter with Gonio-type scan at [$^{\circ}2\theta$]) and the Panalytical High-Score software by processing two competing samples. Figure 2 and Table 2 present the mineralogical characteristics of the lateritic ore fed to the reduction process. It observed that the samples correspond to iron minerals with a predominance of oxides and oxy-hydroxides goethite and maghemite, as well aluminum hydroxide. The low silicon and magnesium contents were found in the lizardite and quartz phases.

2.3 Temperature Profile of the Reduction Process

In the investigation, six experiments were performed (Fig. 3). In five of them, the influence of the effect of post-combustion on Ni and Co extractions was evaluated, feeding secondary air in the H4, until a temperature between 660 and 670 $^{\circ}\text{C}$ was achieved; and in the H6 until reaching the temperatures of 660, 720, 780, 810 and 850 $^{\circ}\text{C}$. The seventh experiment was characterized by the elimination of the post-combustion air supply in hearths four and six of the reduction furnace. Temperature measurements inside the different hearths were made using K-type thermocouples.

2.4 Nickel and Cobalt Extractions

To determine nickel and cobalt extractions, the reduced mineral (for 75 min in each of the experiments) was leached with an ammonia carbonate solution with an NH_3 concentration of 80–85 g/L and CO_2 of 40–42 g/L for two hours with a liquid/solid

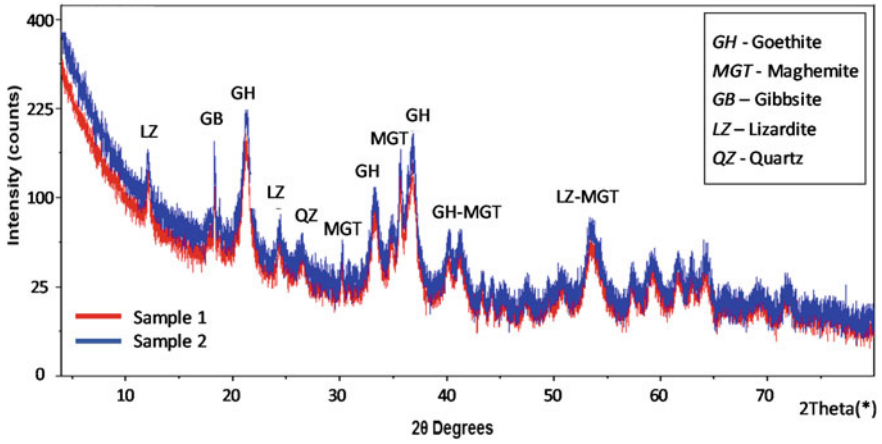


Fig. 2 X-ray diffraction diagram of samples

Table 2 Initial mineral composition

Mineral	Formula	Score
Goethite	$Fe^{+3}O(OH)$	40
Maghemite	$Fe_{21.16}O_{31.92}$	26
Lizardite-1\ITTRG	$Mg_3Si_2(OH)_4O_5$	15
Gibbsite	$Al(OH)_3$	10
Quartz	SiO_2	8

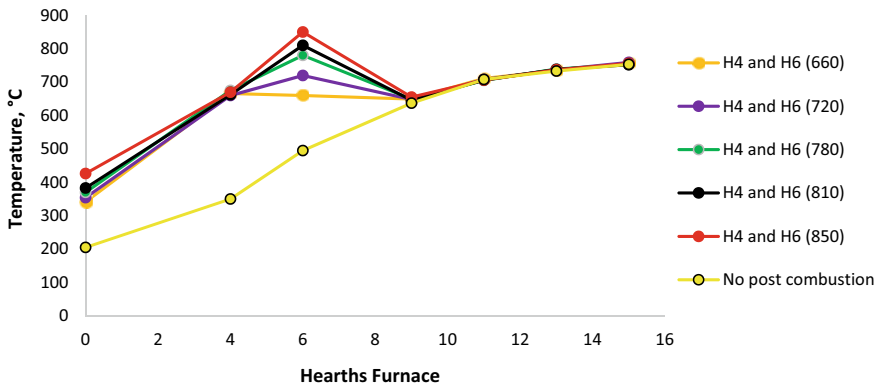


Fig. 3 Temperature profile in the reduction furnace

ratio (L/S) of 10/1. Ni and Co extractions were determined by Eq. 1, with an estimate of the error for Ni and Co of ± 1.5 and 2.5, respectively.

$$\%Ext_{Met} = \left(1 - \frac{Met_{leached\ ore} * Fe_{fed}}{Met_{fed} * Fe_{leached\ ore}} \right) * 100 \quad (1)$$

where:

- % Ext Met is the percentage of extractable metal under analysis, Ni or Co
- Met leached ore is the percentage of the Ni or Co in the ore after leaching
- Met fed is the percentage of Ni or Co in the ore fed to the reduction furnaces
- Fe fed is the percentage of iron in the ore fed to the reduction furnaces
- Fe leached ore is the percentage of iron in the ore after leaching

2.5 Reducing Atmosphere

The CO₂/CO ratio for each experiment ranged from 0.5 to 3.0 and evaluated from the combustion chambers to the chimney. All the experiments were carried out under the same reduction conditions in the reduction chambers and in the lower furnace hearths (from H9 to H16) with the objective of evaluating the effect of the temperature control of hearth 6 of the reduction furnace from injection of the post-combustion air. Table 3 shows the CO₂, O₂ and CO values in volumetric percentages in different areas of the furnace.

Table 3 Gaseous profile of the reduction furnace

Volumetric (%)									
Experiments	Combustion chamber			H10			Chimney		
	CO ₂	O ₂	CO	CO ₂	O ₂	CO	CO ₂	O ₂	CO
H4 and H6 (660)	6.9	0.0	13.0	9.5	0.0	8.8	10.5	0.4	5.6
H4 and H6 (720)	7.0	0.0	13.1	9.8	0.0	8.9	11.0	0.5	5.4
H4 and H6 (780)	6.6	0.0	13.6	8.9	0.0	8.8	11.3	0.7	5.3
H4 and H6 (810)	6.8	0.0	13.2	9.0	0.0	8.4	12.0	0.8	4.6
H4 and H6 (850)	6.5	0.0	13.5	9.5	0.0	8.6	12.5	1.0	4.1
No post-combustion	7.1	0.0	13.3	9.3	0.0	8.7	10.7	0.1	6.0

3 Results and Discussion

3.1 Effect of Post-Combustion Air on Ni Extractions

The Ni extractions are obtained during five days of continuous operation, in each of the experiments is shown in Fig. 4. They were obtained by using Eq. 1, and the methodology reported by Angulo et al. [16], taking a sample every six hours of the lateritic ore fed and reduced in the furnace.

It can be seen that the percentage of Ni extractions ranged in the range of 81.27–91.12 for the different temperature profiles evaluated. De Graaf [18] recognizes that when lateritic ores are processed with a predominance of limonitic minerals in reduction furnaces, extractions can reach up to 95%. Chang et al. [31] report similar extractions of Ni, at the Punta Gorda plant in Moa, which ranged from 76.56 to 88.07% in lateritic ores processed without homogenization.

The behavior presented by the average Ni extractions as a function of the temperature increase in H6 is presented in Fig. 5.

Judging by its behavior, it can be concluded that the temperature increase in H6, due to the feeding of the post-combustion air in the reduction furnace, exerts a negative influence on the Ni extractions that are achieved in the pyrometallurgical process, decreasing it by 1.3% for every 71 °C that increases. The maximum values of Ni extractions were achieved by processing the lateritic ores in the reduction furnace without introducing the post-combustion air. This behavior is logical and is justified because when the temperature of the hearth 6 increases, the nickel more easily changes place with magnesium in the silicates [32–35], which increases the non-leached phases of Ni in the form of olvines and complex spinels Mg, Fe, Al and Si that hinder the reduction process regardless of the reducing agent used [36].

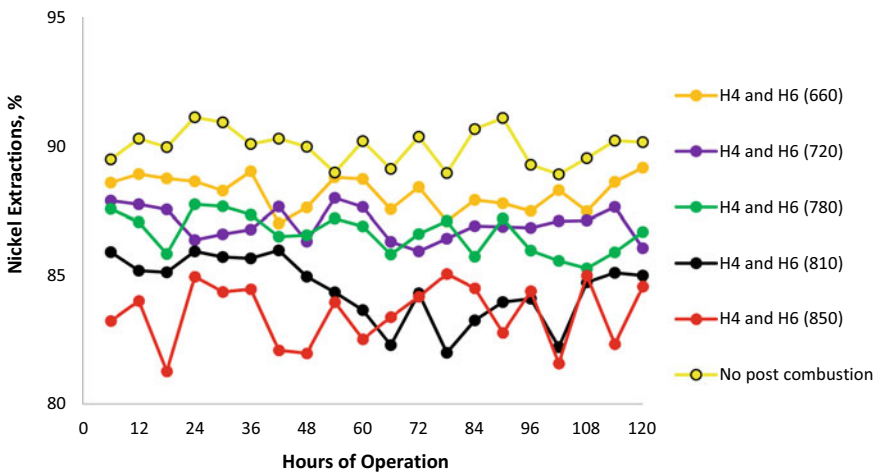


Fig. 4 Behavior of Ni extractions in each experiment

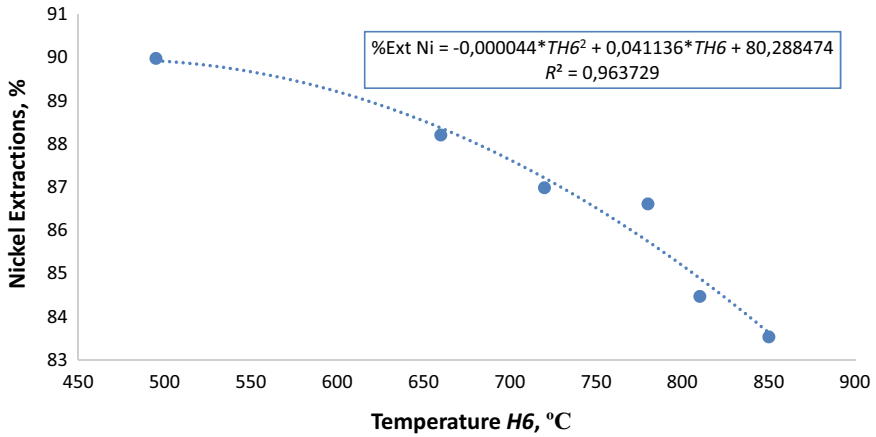


Fig. 5 Relationship between Ni extractions and temperature in H6

The mathematical model that describes this relationship corresponds to a polynomial of order two with a coefficient of determination greater than 0.96 and an error of estimation less than 0.5%.

3.2 Effect of Post-combustion Air on Co Extraction

Ni and Co extractions were determined using the same methodology. Co extractions (Fig. 6) ranged from 59 to 75%, during the five days of operation of each experiment.

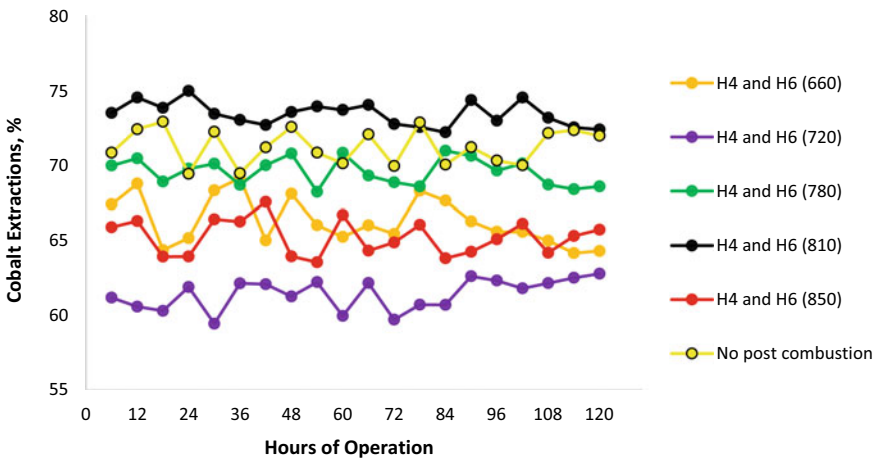


Fig. 6 Behavior of Co extractions in each experiment

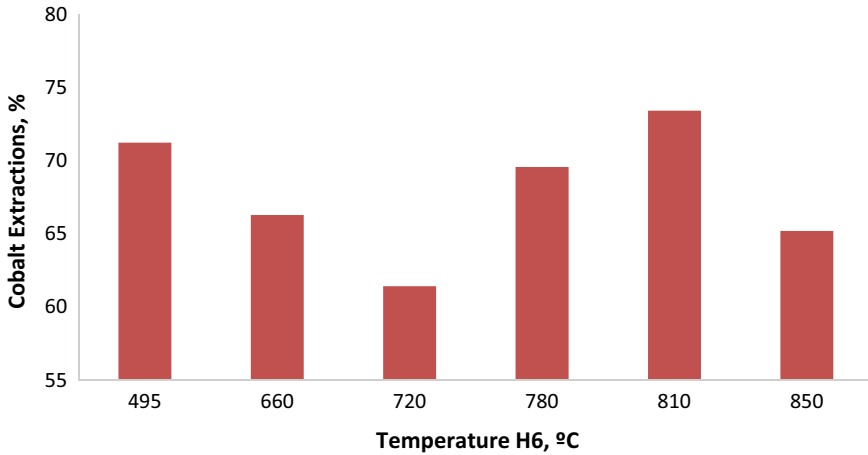


Fig. 7 Relationship between Ni extractions and temperature in H6

Kawahara, Toguri and Bergman [20] and Chang [35] report Co extractions between 40 and 75% depending on the Fe content and the mineral mineralogy, as well as the reduction temperature [37, 38].

The maximum values of Co extractions were reached by feeding the post-combustion air into H6 until a temperature of 810 °C was reached, followed by the experiment in which post-combustion air is not fed.

The effect of average Co extractions on the increase in H6 temperature is observed in Fig. 7, where irregularities are shown with respect to the behavior presented by Ni extractions. Two zones are observed in Co extractions by varying the temperature of H6 range from 495 to 850 °C.

The first zone, in the temperature range of 495–720 °C (Fig. 7), tends to show a behavior similar to that achieved by Ni extractions, characterized by a decrease of 2.1% for every 45 °C of temperature increased by the H6. The second zone, from 720 to 850 °C, was characterized by increasing Co extractions as household temperature increased to 810 °C, followed by a sharp decrease in extractions as temperature reached the highest level evaluated.

At present, the phenomena that cause the decrease in Co extractions in multiple hearth furnaces are unknown. The most correct hypothesis that allows it to be explained is the fact that at hearth 6 temperatures of 810 and 495 °C, the process of exchange of positions between Co^{2+} and Fe^{2+} decreases, forming less solid solutions that lead to a better reductibility.

4 Conclusion

The supply of the post-combustion air in the reduction furnaces of the Caron process generates variations in the Ni and Co. extractions. In the case of Ni, the increase in the temperature of the hearth 6 causes a decrease in the extractions, while the Co extractions show an irregular behavior with the presence of maximum and minimum. The best result of the study was achieved when working in an operational condition without injection of the post-combustion air with a temperature of 495 °C in hearth 6 of the reduction furnace by keeping the other variables of the pyrometallurgical process constant.

References

1. Crundwell F, Moats M, Ramachandran V, Robinson T, Davenport WG (2011) Extractive metallurgy of nickel, cobalt and platinum-group metals. Elsevier, pp 1–18. ISBN: 978-0-08-096809-4
2. Chen GJ, Hwang WS, Liu SH, Shiau JS (2015) The effect of bio-coal on the carbothermic reduction of laterite ores. *Mater Trans* 56(4):550–555
3. Dong J, Wei Y, Lu C, Zhou S, Li B, Ding Z, Wang C, Ma B (2017) Influence of calcium chloride addition on coal-based reduction roasting of low-nickel garnierite ore. *Mater Trans* 58(8):1161–1168
4. Charles B, Dominique C (2013) Nickel laterite ore deposits: weathered serpentinites. *Elements* 9(2):123–128
5. Al-Khribash S (2015) Genesis and mineralogical classification of Ni-laterites, Oman Mountains. *Ore Geol Rev* 65:199–212
6. Domenech C, Galí S, Villanova-de-Benavent C, Soler J, Proenza J (2017) Reactive transport model of the formation of oxide type Ni-laterite profiles (Punta Gorda, Moa Bay, Cuba). *Mineralium Deposita* 52(7):993–1010
7. Díaz Bello S (2016) Modelamiento cinético del procesamiento de minerales lateríticos por vía pirometalúrgica. (Tesis Doctoral) Universidad Nacional de Colombia, pp 105
8. Caron MH (1950a) Fundamental and practical factors in ammonia leaching of nickel and cobalt ores. *JOM-J Miner Metals Mater Soc* 2:67–90
9. Caron MH (1950b) Separation of nickel and cobalt. *JOM-J Miner Metals Mater Soc* 2:91–103
10. Keskinilic E, Pournaderi S, Geveci A, Topkay YA (2011) Calcination behavior of sivrihisar laterite ores of Turkey. In: 2nd international symposium on high-temperature metallurgical processing. Wiley, The Minerals, Metals & Materials Society, pp 319–326
11. Yucel O, Turan A, Yildirim H (2012) Investigation of pyrometallurgical nickel pig iron (NPI) production process from lateritic nickel ores. In: 3rd international symposium on high-temperature metallurgical processing, Wiley Online Library and The Minerals, Metals & Materials Society, pp 17–23
12. Nikoloski AN, Nicol MJ (2010) The electrochemistry of the leaching reactions in the Caron process II. Cathodic processes. *Hydrometallurgy* 105(1–2):54–59
13. Oxley A, Smith M, Caceres O (2016) Why heap leach nickel laterites? *Miner Eng* 88:53–60
14. Graeme T, Gamini S (2018) Effect of iron (II) and manganese (II) on oxidation and coprecipitation of cobalt (II) in ammonia/ammonium carbonate solutions during aeration—An update and insight to cobalt losses in the Caron process for laterite ores. *Hydrometallurgy* 181:53–63
15. Rodríguez R (2004) Reduction in energy cost in Cuban Caron process plants. In: Imrie W, Lane D, International laterite nickel symposium 2004 (as held during the 2004 TMS Annual Meeting). The Minerals, Metals & Materials Society, pp 657–664. ISBN: 0-87339-550-6

16. Angulo-Palma HJ, Merencio-Guevara PL, Legrá-Legrá A, Videaux-Arcia L (2016) Análisis especiales en un horno de reducción de níquel a escala de Planta Piloto. *Tecnología Química* 37(3):445–460
17. Angulo-Palma HJ, Legrá-Legrá, A, Hernández-Pedrerá C, Lamorú-Urgellés A, Vega-Cala JR (2018) Efecto de la sustitución del petróleo aditivo por carbón bituminoso en el proceso de reducción de lateritas. *Tecnología Química* 38(3):613–625
18. De Graaf JE (1979) The treatment of lateritic nickel ores—a further study of the Caron process and other possible improvements. Part I. Effect of reduction conditions. *Hydrometallurgy* 5(1):47–65
19. Chander S, Sharma VN (1981) Reduction roasting/ammonia leaching of nickeliferous laterites. *Hydrometallurgy* 7(4):315–327
20. Kawahara M, Toguri JM, Bergman RA (1988) Reducibility of laterite ores. *Metall Trans B* 19(2):181–186
21. Utigard T, Bergman RA (1993) Gaseous reduction of laterite ores. *Metall Trans B* 24(2):271–275
22. Antola O, Holappa L, Paschen P (1995) Nickel ore reduction by hydrogen and carbon monoxide containing gases. *Miner Process Extr Metall Rev* 15(1–4):169–179
23. Pickles CA, Elliott R (2015) Thermodynamic analysis of selective reduction of nickeliferous limonitic laterite ore by carbon monoxide. *Miner Process Extr Metall* 124(4):208–216
24. Pickles CA, Anthony W (2018) A thermodynamic study of the reduction of a limonitic laterite ore by methane. *High Temp Mater Process (London)* 37(9–10):909–919
25. Pickles CA, Anthony W (2018) Thermodynamic modelling of the reduction of a saprolitic laterite ore by methane. *Miner Eng* 120:47–59
26. Ramírez-Mendoza M (2002) Modelación del proceso de postcombustión en un horno de reducción de níquel. *Rev Metal* 38(2):150–157
27. Montero-Góngora D, Ramírez-Mendoza M, Gilbert-Hernández A, Campos-Perdices S (2015) Modelación matemática para el control de la postcombustión en un horno de reducción de níquel. *Ingeniería Electrónica Automática y Comunicaciones* 36(3):21–34
28. Reid JG (1987) Improvements in the greenvale operations. *Int J/Miner Process* 19:263–272
29. Montero-Góngora D, Góngora-Leyva E, Ramirez-Mendoza M (2019) Identification of post-combustion sub-process using artificial neural networks. *Biomed J Sci Tech Res* 21(4):16031–16039
30. Montero-Góngora D, Van-Caneghem J, Haeseldonckx D, Góngora-Leyva E, Ramirez-Mendoza M, Dutta A (2020) Post-combustion artificial neural network modeling of nickel-producing multiple hearth furnace. *Int J Chem Reactor Eng* 18(7):20190191
31. Chang-Cardona AR, Rojas-Puron AL, Aece-Molina J (2014) Influencia sobre el extractable de níquel de los minerales oxidados del yacimiento de Punta Gorda. *Minería y Geología* 30(4):70–88
32. Toro N, Ayala L, Pérez K, Castillo J, Navarra A (2020) Environmental analysis of the current situation of Chilean copper smelters. In: AIP conference proceedings 2281, p 020009
33. Navarra A et al (2020) Quantitative methods to support data acquisition modernization within copper smelters. *Processes* 8(11):1478
34. González Y, Navarra A, Jeldres RI, Toro N (2021) Hydrometallurgical processing of magnesium minerals—a review. *Hydrometallurgy* 201:105573
35. Chang-Cardona AR, Aece-Molina J, Toirac-Suárez MM (2005) Modelos multivariados para predecir el extractable de níquel por la composición mineralógica de la mena tecnológica en el Proceso Caron. *Minería y Geología* 21(1):1–32
36. Pérez K, Toro N, Gálvez E, Robles P, Wilson R, Navarra A (2021) Environmental economic and technological factors affecting Chilean Copper Smelters – a critical review. *J Mater Res Technol.* <https://doi.org/10.1016/j.jmrt.2021.08.007>
37. Toro N, Rodríguez F, Rojas A, Robles P, Ghorbani Y (2021) Leaching manganese nodules with iron-reducing agents – A critical review. *Miner Eng* 163:106748. <https://doi.org/10.1016/j.mineng.2020.106748>

38. Toro N, Jeldres RI, Órdenes JA, Robles P, Navarra A (2020) Manganese nodules in Chile, an alternative for the production of Co and Mn in the future—A review. *Minerals* 10(8):674. <https://doi.org/10.3390/min10080674>

Chapter 44

Design and Analysis of Neural Network-Based MPPT Technique for Solar Power-Based Electric Vehicle Application



M. Murali, CH Hussaian Basha , Shaik Rafi Kiran, and K. Amaresh

Abstract At present, solar power is the major concern for the most industrial as well as domestic applications. The solar power is having the demerit of nonlinear output power generation. As a result, it gives less operating efficiency and high oscillated output voltage. Here, the perceptron-based feed forward neural network is used for generating the duty cycle of the high step-up boost converter and solving the nonlinear behavior of the solar PV. The attractive features of the neural network-based MPPT controller are easy design, less implementation complexity, and high accuracy. The boost converter is used in the PV-based dc-dc converter system to improve the voltage profile of input supply. The MATLAB/Simulink window is used for the analysis of neural network-based power point tracing controller.

Keywords Double-diode PV cell · Diverse temperature conditions · High-voltage gain converter · Irradiation conditions · I-V and P-V characteristics · Neural network

1 Introduction

In nineteenth century, most of the power generation systems are thermal, oil, nuclear energy, and natural gas. Thermal power is generated based on fuel. The fuel is availed only in the earth and which is formed due to the dead plants over the trillion of the years. The disadvantage of thermal power generation systems is less operating efficiency, high maintenance cost, required huge amount of power for handling temperature, and high manpower. In addition, it produces the inflammable gasses

M. Murali · CH Hussaian Basha (✉) · K. Amaresh
Department of Electrical and Electronics Engineering, K.S.R.M. College of Engineering, Kadapa, India

K. Amaresh
e-mail: amaresh@ksrmce.ac.in

S. R. Kiran
Department of Electrical and Electronics Engineering, Sri Venkateswara Engineering College, Tirupati, India

and smoke [1]. As a result, the atmosphere temperature is increasing excessively. The drawbacks of the thermal power plants are overcome by using the oil power production. The attractive features of the oil power plants are high energy density, using for different industrial applications, easily available, and gives constant power to the load. But it is having the drawbacks of greenhouse gas emission and produces highly inflammable toxic substances. In addition, it pollutes the water source [2].

The drawbacks of oil-based power generation systems are overcome by using the renewable energy sources. The major renewable energy sources are wind, tidal, geothermal, hydro, solar, and biomass energy. The output power of wind is mainly depending on kinetic energy, and it is converted mechanical energy by using wind forms. After that the mechanical energy is transferred to electrical energy by using the generator [3]. The wind is occurred due to the overheating of the atmospheric air. Most of the wind plants are installed at mountains. At high intensity air condition, the wind plants give high output power. The advantages of wind power generation are cost effective, clean energy, naturally available, and it is used for the most of domestically applications [4]. The demerits of the wind systems are inconsistent, visual impact on turbines, requires high capital investment, noise problems, and less safety hazard. In addition, it affects the bird's population. In hydraulic power plants, the power is generated based on the water head. Here, the water kinetic energy is transformed to electrical supply by using the hydro turbines. The advantages of hydropower stations are flood controlling, continuous water supply, and less pollutant. However, it gives a social threat. As a result, it harmed the water quality [5].

However, the drawbacks of above renewable power generation systems are overcome by using the solar power. Solar is the natural source of energy, and it is available most of the times. Solar power is mainly contingent on the sun insolation conditions and atmospheric temperature conditions [6]. The applications of solar power generation systems are water heating, electric drives, satellite communication systems, battery charging, and electric vehicle applications. The advantages of solar photovoltaic (PV) systems are high robust, high flexible, less maintained cost, excess availability with free of cost, and less environmental pollution. In addition, it is useful for reducing the electricity consumption cost [7].

The working behavior of solar PV is similar to the working condition of P-N diode. The PV cell generated voltage is 0.7–0.8 and it is not sufficient for the high industrial load applications. So, the PV cells are interconnected with each other in series manner and parallel manner.

The voltage rating of the PV system is mainly depending on the series condition of cell [8]. Similarly, the current supplied by the solar system is improved by applying the parallel connection in the PV system. As a result, the PV module is formed, and its sunlight incident area is improved. The PV cells are designed by using different manufacturing technologies which are mono-crystalline, poly-, and thin-film-based technology. Among all of that, thin film is used because of its high output efficiency [9]. The block diagram of the PV-fed boost converter topology is given in Fig. 1.

The solar PV systems output voltage is stepped-up by using the boost converter and its optimum duty is obtained by using the different and highly efficient conventional and artificial intelligence-based Maximum Power Point Tracking techniques.

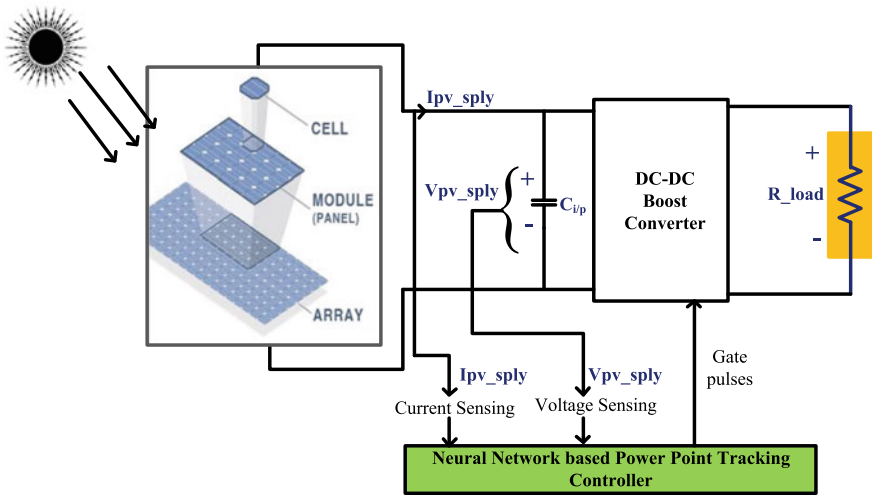


Fig. 1 PV-fed high-voltage gain boost converter

From the literature survey, the most frequently used power point tracking techniques are fractional open-circuit voltage power point tracking technique [10]. This method is easy to design, less implementation complexity, and general method. The disadvantage of this technique is less accuracy at the time of MPP tracking. In addition, it cannot give the exact position of the operating point of the solar PV.

The fractional short-circuit current-based power point tracing method is used in article [11] to transfer the peak power of the solar PV from supply to load. In this technique, the maximum peak-to-peak current is evaluated based on the separate switch. The drawback is high-power loss at the time of measurement of short-circuit current. In addition, it requires additional circuit for evaluating the proportionality constant. However, the drawbacks of the above MPPT techniques are overcome by using the perceptron neural network-based MPPT technique and it is compared with the different step size-based Perturb and Observe (DSS-P&O) peak power point tracing method and modified different step size-based incremental conductance (DSS-IC) technique [12].

The remaining part of the article is explained as the design and analysis of triple-diode model-based PV panel is explained in Sect. 2 and the detailed design and analysis of different power point tracing methods in terms maximum extracted power, accuracy of tracing, dependency on the type of PV module is selected, steady-state oscillations, and number of sensors used for determining the PV voltage and current are illustrated in Sect. 3. The design of boost converter, simulation results of power point techniques and their corresponding conclusions are given Sects. 4–6.

2 Three-Diode Model-Based Solar PV Cell

From the literature survey [13], different researchers utilizing different PV cell topologies which are single, two, and three-diode-based solar PV cells. The design of ideal diode PV cell has been done by connecting a diode in parallel with the ideal current source. The design of ideal diode solar cell is easy, less implementation cost, and easy understanding. But it is not applicable where the accuracy of the MPP tracking is high. The ideal cell-based PV system drawbacks are overcome by using the single-diode cell and it is implemented by involving a parallel resistance, and series resistance. The demerit of this topology is that it gives approximated current versus voltage curves.

The three-diode-based solar PV cell is implemented by including an additional diode with the two-diode-based solar PV array. The ideal, and single-diode model-based PV cells designing has been done by considering four major parameters which are defined as, open-circuit voltage (V_{oc}), maximum peak-to-peak voltage (V_{mpp}), short-circuit current (I_{sc}), and peak-to-peak current (I_{mpp}). For the designing of two-diode PV cell requires an additional two more parameters which are diode ideality factor (a), reverse saturation current (I_{revs}). Similarly, the triple-diode model requires two more parameters when compared to the two-diode cell. The designing of triple-diode PV cells without series resistance and with series resistance are given in Fig. 2. From Fig. 2a, the PV cell output current is derived as,

$$I_{cell_o} = I_{PV_sply} - I_{D1} - I_{D2} - I_{D3} \tag{1}$$

$$I_{cell_o} = I_{PV_sply} - i_{revs_1} \left(e^{\frac{q(V_{cell_o} + I_{cell_o} R_s)}{\eta_1 K T}} - 1 \right) - I_x \tag{2}$$

$$I_x = i_{revs_2} \left(e^{\frac{q(V_{cell_o} + I_{cell_o} R_s)}{\eta_2 K T}} - 1 \right) + i_{revs_3} \left(e^{\frac{q(V_{cell_o} + I_{cell_o} R_s)}{\eta_3 K T}} - 1 \right) \tag{3}$$

$$I_{PV_sply} = (I_{PV_splySTC} + K_i \Delta T) * \frac{G}{G_{STC}} \tag{4}$$

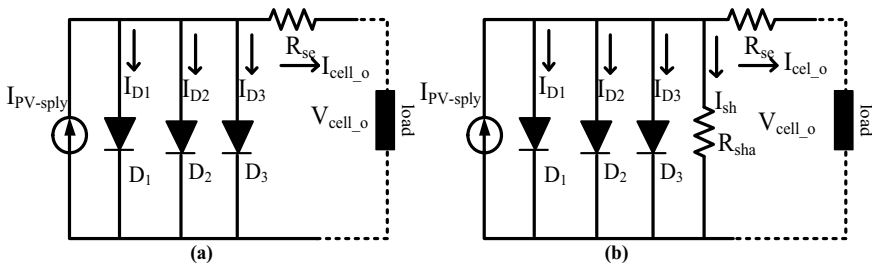


Fig. 2 Three-diode PV cells a Without shunt resistance. b With shunt resistance

If the series connected cells are increased with n_s , then the generation of PV cell current is expressed as,

$$I_{\text{cell}_o} = I_{\text{PV_sply}} - i_{\text{revs}_1} \left(e^{\frac{q(V_{\text{cell}_o} + I_{\text{cell}_o} R_s)}{\eta_1 K T n_s}} - 1 \right) - I_x \quad (5)$$

$$I_x = i_{\text{revs}_2} \left(e^{\frac{q(V_{\text{cell}_o} + I_{\text{cell}_o} R_s)}{\eta_2 K T n_s}} - 1 \right) + i_{\text{revs}_3} \left(e^{\frac{q(V_{\text{cell}_o} + I_{\text{cell}_o} R_s)}{\eta_3 K T n_s}} - 1 \right) \quad (6)$$

From Fig. 2b, the triple-diode PV cell consists of series resistance and parallel resistance. The cell current is derived as,

$$I_{\text{cell}_o} = I_{\text{PV_sply}} - I_{D1} - I_{D2} - I_{D3} - I_{sh} \quad (7)$$

$$I_{\text{cell}_o} = I_{\text{PV_sply}} - i_{\text{revs}_1} \left(e^{\frac{q(V_{\text{cell}_o} + I_{\text{cell}_o} R_s)}{\eta_1 K T}} - 1 \right) - i_{\text{revs}_2} \left(e^{\frac{q(V_{\text{cell}_o} + I_{\text{cell}_o} R_s)}{\eta_2 K T}} - 1 \right) - I_y \quad (8)$$

$$I_z = i_{\text{revs}_3} \left(e^{\frac{q(V_{\text{cell}_o} + I_{\text{cell}_o} R_s)}{\eta_3 K T}} - 1 \right) + \frac{V_{\text{cell}_o} + I_{\text{cell}_o} R_s}{R_{sh}} \quad (9)$$

$$I_{\text{revs}_1} = I_{\text{revs}_2} = I_{\text{revs}_3} = I_{\text{on}} \left(\frac{T}{T_N} \right)^3 e^{\frac{qE_g}{nk} \left(\frac{1}{T_N} - \frac{1}{T} \right)} \quad (10)$$

$$I_{\text{on}} = I_{\text{on}_1} = I_{\text{on}_2} = I_{\text{on}_3} = \frac{I_{SC,n}}{e^{\left(\frac{V_{oc,n}}{\eta V_{Tn}} \right)}} \quad (11)$$

3 Design and Investigative Analysis of MPPT Techniques

From the literature review, the PV-fed boost converter systems are analyzed by using the different soft computing MPPT techniques. Here, a neural network controller is proposed, and it is successfully compared with other high efficient power point tracing controller which are P&O, and IC-based peak power point tracing techniques. From article [14], P&O is the most popular power point tracing controller because of its attractive features are moderate power point tracing speed, easy implementation and understanding. The P&O MPPT controller is used for low and moderate power usage applications. In addition, it's not applicable for high-power rated solar PV systems.

To limit the disadvantages of the basic P&O technique, a step change of duty cycle is considered. If the operating is on the right side of the curve, then the duty cycle is reduced. After that, if the working behavior of the PV cell is left side of the MPP then the duty of the boost converter is improved. The duty of the boost converter is

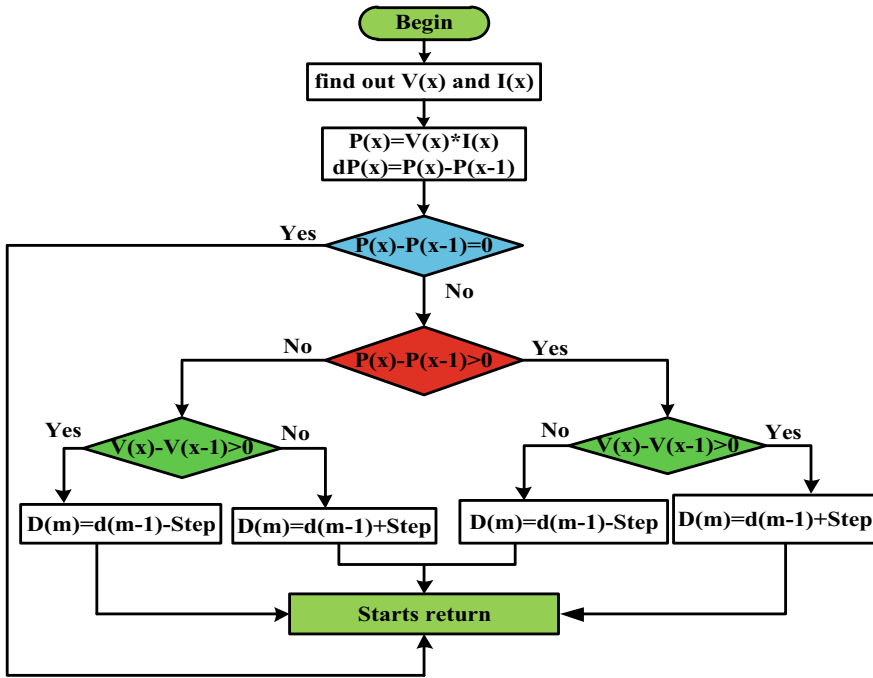


Fig. 3 Working behavior of P and O MPPT controller

updated by using Eq. (12) and its corresponding block diagram is given in Fig. 3

$$D(m) = D(m - 1) \pm k \frac{P(x) - P(x - 1)}{V(x) - V(x - 1)} \tag{12}$$

From Eq. (12), the scaling factor ‘k’ is used to improve the tracking speed of the MPP. The duty $D(m)$, and $D(m - 1)$ are the present and previous duty cycles. Similarly, $P(x)$, and $P(x - 1)$ are the present and previous PV powers. However, the P&O controller is not suitable high-power solar PV application. In article [15], an IC-based power point tracking controller is used to equalize the source resistance with the load resistance. Based on the equalized resistance of the solar PV, the duty is varied continuously. The advantages of the IC power point tracking controller are high robust, less steady-state oscillations, constant converter output voltage. But it is having a drawback of high design cost when compared to P&O. The working condition of IC controller is given in Fig. 4 and the duty cycle is updated by using Eq. (13) when the incremental conductance of the solar PV is very high. If the operating incremental conductance is low, then Eq. (14) is applied to trace out the peak point of MPP.

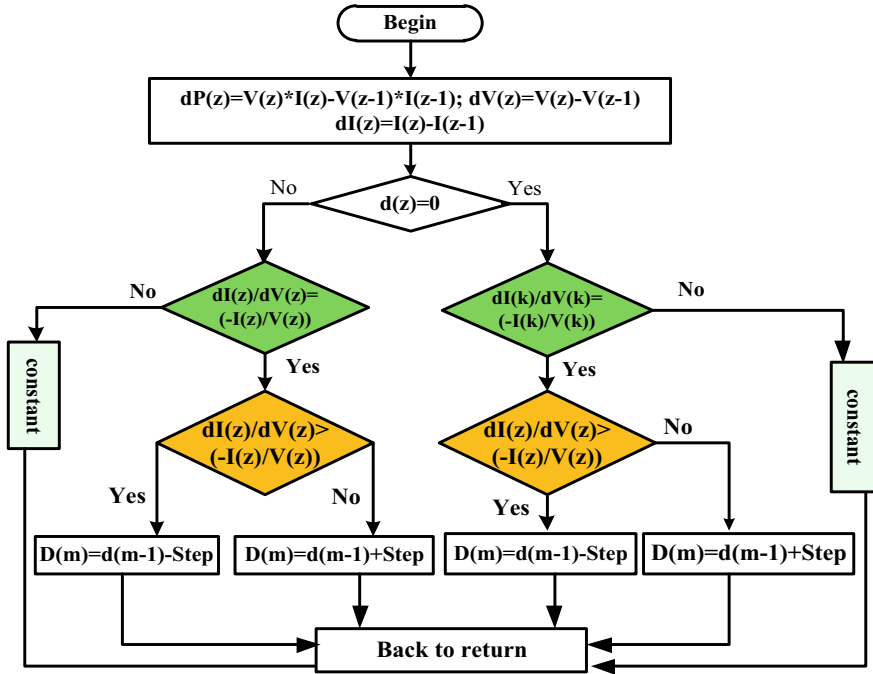


Fig. 4 Working behavior of incremental conductance MPPT technique

$$D(m) = D(m - 1) + D_{step} * \text{sig}\left(\frac{\Delta I}{\Delta V} + \frac{I}{V}\right) \tag{13}$$

$$D(m) = D(m - 1) - D_{step} * \text{sig}\left(\frac{\Delta I}{\Delta V} + \frac{I}{V}\right) \tag{14}$$

$$D_{step} = \zeta * \frac{\Delta P}{\Delta V}; \tau = \frac{\Delta P}{\Delta V} \tag{15}$$

where the term D_{step} is used to reduce the tracing time of peak power point controller. The term τ is the scaling parameter which is used for the reduction of high oscillations across operating point of solar PV system. In addition, it is useful for achieving the high accurate I-V and P-V characteristics.

The drawbacks of the conventional MPPT methods are limited by applying an artificial intelligence-based MPPT techniques. Artificial intelligence power point tracking controllers are used in many industrial and non-industrial applications in order to solve the nonlinear behavior of the solar PV. Neural networks are the series of algorithms and which are used to find out the relationship between the different types of data. The neural networks are having the capability of handling the change of input parameters and it is used for computational system design. In addition, neural

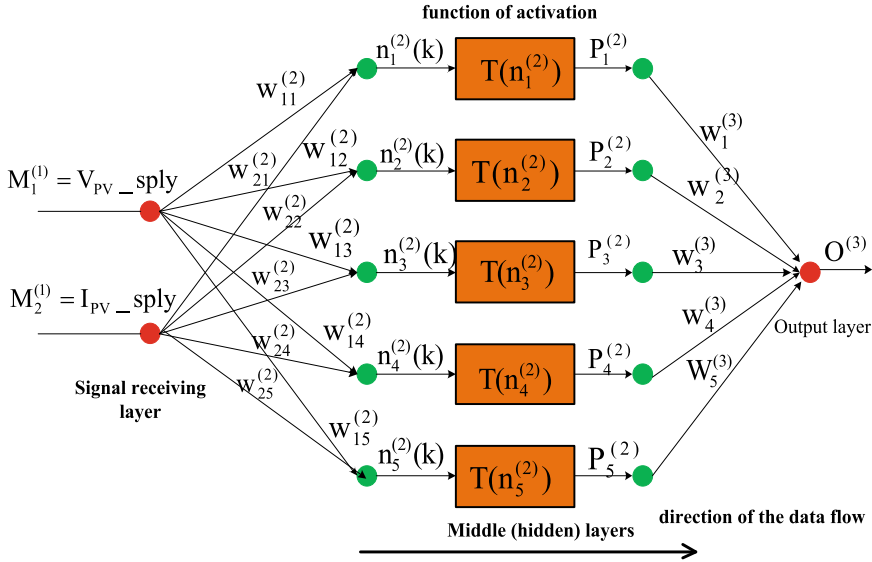


Fig. 5 Multiple layer perceptron neural network-based power point tracing controller

networks are act as soft computing techniques. The attractive features of the neural networks are easy to train the data, and less size of the system. As a result, the overall system design cost is reduced.

Here, a multiple layer neural network is used for the design of the MPPT controller, and its block diagram is given in Fig. 5. From Fig. 5, the number of nodes in the input side are double which are processed with the help of PV module output parameters such as voltage and current. The output signals of the input nodes are given to the middle layer nodes. The sigmoidal function is applied to the middle layer neurons in order to obtain the output signals. Finally, the output layer has one node which is used to generate the switching signals to the boost converter.

From Fig. 5, the input, middle, and output layers nodes out signals are derived as,

$$n_t^{(2)}(k) = \sum_{s=1}^2 w_{ts}^{(2)} * M_s^1; t = 1, 2, 3, 4, 5 \dots k \tag{16}$$

$$P_t^{(2)}(k) = T(n_s^{(2)}(k)) \tag{17}$$

$$O^3(t) = \sum_{t=1}^5 w_t^{(3)} * P_t^{(2)} \tag{18}$$

From Eq. (16), the delta method is applied to the three layers nodes in order to obtain the updated weights.

$$w_{ts}^{(2)} = w_{ts}^{(2)} + \Delta w_{ts} \tag{19}$$

$$w_t^{(3)} = w_{t3}^{(3)} + \Delta w_t \tag{20}$$

$$\Delta w_{ts} = u * \frac{\partial e}{\partial w_{ts}^{(2)}}, \quad \text{and} \quad \Delta w_t = u * \frac{\partial e}{\partial w_t^{(3)}} \tag{21}$$

The resultant error signal from the neural network controller is obtained as follows,

$$e = \frac{1}{2} (O_{\text{desired}} - O^{(3)})^2 \tag{22}$$

4 Design of DC–DC Boost Converter System

From the literature review, most of the DC–DC converters are used to control the input supply voltage for different load applications. Here, the boost converter is used to reduce the PV system installation cost and its step-up has been done at different irradiation and atmospheric temperature conditions. The block diagram of DC–DC boost converter is shown in Fig. 6 and the advantages of boost converter are easy design, high flexibility and reliability when compared to the switched capacitor converter, and inductor-coupled converter.

In addition, the boost converter works in two different modes of operations which are continuous mode, and discontinuous mode. In the continuous output voltage condition, the metal oxide semiconductor field effect transistor switch acts as working state. As a result, there is no supply voltage from PV system to the standalone load. In this condition, the diode 'D' work as blocking condition and the inductor 'L' is in charging condition. Similarly, in the blocking state, the switch is in off condition and the input inductor stored energy is transferred to the variable resistive load.

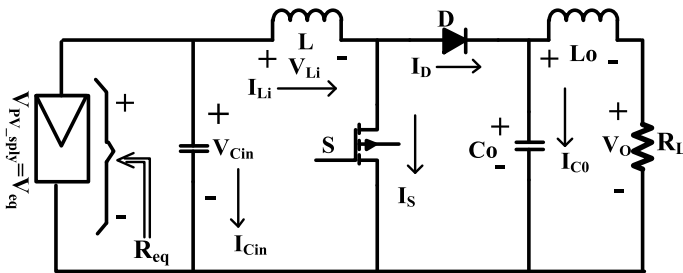


Fig. 6 PV-fed DC–DC boost converter for EV application

5 Discussion of MATLAB/ Simulation Results

The performance investigation on PV-fed boost converter system for solar electric vehicle application has been done at different sun irradiation and temperature conditions. Here, the 259 W three-diode cell-based PV module is proposed for the investigation of the neural network controller. The design parameters selected for triple-diode cell are open-circuit voltage ($V_{oc} = 38.6$ V), peak-to-peak voltage ($V_{MPP} = 31.6$ V), peak-to-peak current ($I_{MPP} = 8.21$ A), and short-circuit current ($I_{sc} = 8.93$ A). In addition to that there are few more parameters selected to design the PV module which are classified as, series resistance ($R_{se} = 0.27126$ Ω), and parallel resistance ($R_{sha} = 108.7$ Ω) respectively.

(a) At various irradiation conditions (1000, 800, 600, 400 W/m²).

The design parameters of DC-DC boost converter are, PV side capacitor ($C_{in} = 100$ μ F), input inductor ($L = 1$ mH), output capacitor ($C_0 = 250$ μ F), and output side inductor ($L_0 = 3$ mH). The PV side capacitor is suitable for reducing the fluctuations in the output voltage and the input inductor is useful for smoothening the PV current. Similarly, the output side inductor is applied to the load for improving the voltage profile and the load side capacitor is useful to stabilize the converter output voltage. From the above parameters of PV system and boost converter, the PV-fed standalone system is analyzed at diverse atmospheric circumstances. The PV output generated I-V and P-V characteristics are shown in Fig. 7a, b.

From Fig. 7a, c, d, the maximum peak-to-peak voltages and powers at 1000, 800, 600, 400 W/m² are 31.6 V, 31.53 V, 31.41 V, and 31.37 V, 259 W, 208.2 W, 156.15 W, and 103.52 W, respectively. At 1000 W/m², the obtained boost converter output voltages by using IC, P&O, and neural network controllers are 74.6 V, 72.5 V, and 76 V, respectively. Similarly, the P&O, IC, and neural network-based power point tracing-based converter output powers at 800 W/m² are 192 W, 203 W, and 207 W respectively. Finally, at 400 W/m², the boost converter output voltages and powers by using neural network, IC, and P&O-based MPPT controllers are 47.3 V, 46.2 V, and 42.5 V respectively.

From Fig. 8a–d, the solar PV power various based on the reverse saturation current of the diode, and different sun insolation conditions. The PV power and voltages are reduced based on the step-up of the temperature. At 45 °C, the IC, P&O, and neural network-based boost converter output voltages and powers are 57 V, 48 V, and 63 V, 158 W, 132 W, and 175 W respectively. Similarly, the neural network-based boost converter output voltage and powers at 65 °C are 53 V, and 130 W, respectively. In addition, the proposed neural network controller gives optimum duty cycle, less oscillations across MPP, and high accurate output voltage.

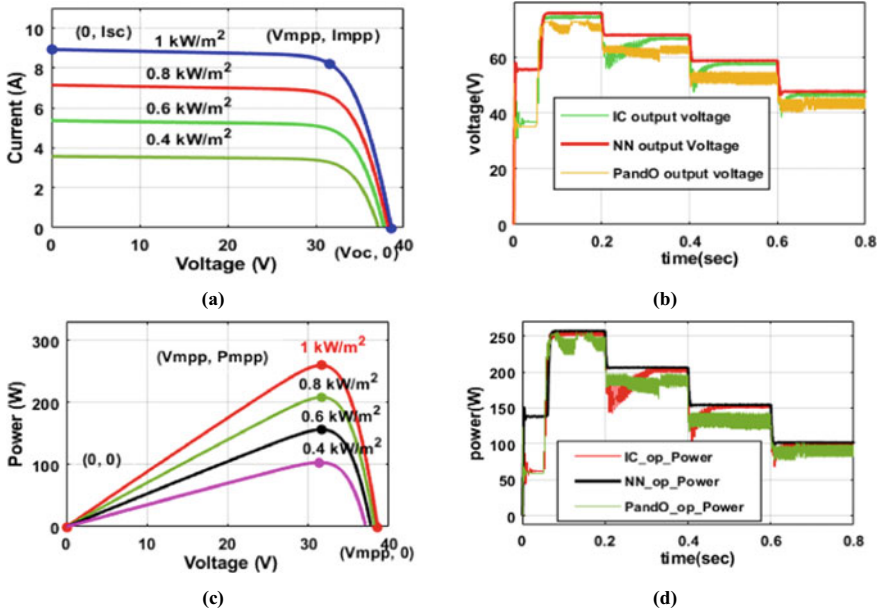


Fig. 7 a I-V Curve. b Converter O/P voltage. c P-V curve, and d Converter O/P power at different irradiances

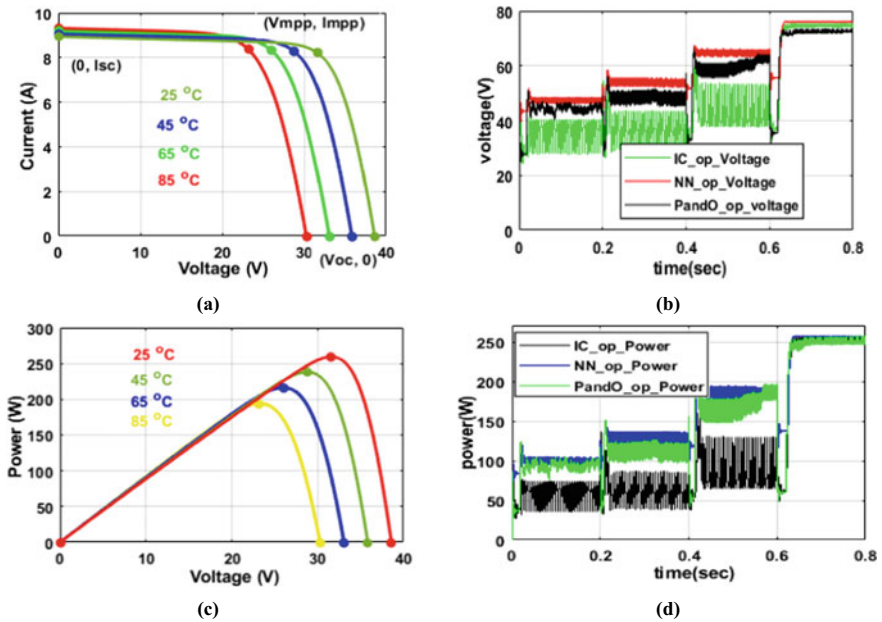


Fig. 8 a I-V Curve. b Converter O/P voltage. c P-V curve, and d Converter O/P power at different temperatures

6 Conclusion

The proposed PV-fed DC-DC converter system is implemented successfully. From the simulative performance results, the proposed neural network-based MPPT technique is giving high accurate converter output voltage and power when compared to the IC and P&O MPPT algorithms. In addition, it is giving constant converter output voltage with less steady state and dynamic distortions at different irradiances and temperature conditions. The advantages of the perceptron neural network-based controller are less implementation complexity, easy design, and fast MPP tracking speed.

Acknowledgements We would like to thank the management of K.S.R.M. College of Engineering (Autonomous) for providing all the facilities to carry out our research work.

References

1. Faraji H et al (2021) Emerging applications of phase change materials: a concise review of recent advances. *Heat Transfer* 50.2:1443–1493
2. Yaqoob H et al (2021) Current status and potential of tire pyrolysis oil production as an alternative fuel in developing countries. *Sustainability* 13.6:3214
3. Ghoushchi SJ et al (2021) An extended new approach for forecasting short-term wind power using modified fuzzy wavelet neural network: a case study in wind power plant. *Energy* 223:120052
4. Koivisto M et al (2021) Application of microscale wind and detailed wind power plant data in large-scale wind generation simulations. *Electric Power Syst Res* 190:106638
5. Huangpeng Q, Huang W, Gholinia F (2021) Forecast of the hydropower generation under influence of climate change based on RCPs and developed crow search optimization algorithm. *Energy Rep* 7:385–397
6. Basha CH, Rani C (2020) Different conventional and soft computing MPPT techniques for solar PV systems with high step-up boost converters: a comprehensive analysis. *Energies* 13(2):371
7. Basha CH et al (2020) Development of cuckoo search MPPT algorithm for partially shaded solar PV SEPIC converter. *Soft computing for problem solving*. Springer, Singapore, pp 727–736
8. Basha, CH, Rani C (2020) Performance analysis of MPPT techniques for dynamic irradiation condition of solar PV. *Int J Fuzzy Syst* 22.8:2577–2598
9. Xiao K et al (2020) Residual stress analysis of thin film photovoltaic cells subjected to massive micro-particle impact. *RSC Adv* 10.23:13470–13479
10. Bu L et al (2020) On-site traversal fractional open circuit voltage with uninterrupted output power for maximal power point tracking of photovoltaic systems. *Electronics* 9.11:1802
11. Nadeem A et al (2021) Online current-sensorless estimator for PV open circuit voltage and short circuit current. *Solar Energy* 213:198–210
12. Ali MN et al (2021) An efficient fuzzy-logic based variable-step incremental conductance MPPT method for grid-connected PV systems. *Ieee Access* 9:26420–26430
13. Basha CH et al (2020) Mathematical design and analysis of photovoltaic cell using MATLAB/Simulink. *Soft computing for problem solving*. Springer, Singapore, pp 711–726
14. Mokhlis M et al (2020) Comparative study between the different MPPT techniques. In: 2020 5th international conference on renewable energies for developing countries (REDEC). IEEE

15. Javed MR et al (2020) Comparison of the adaptive neural-fuzzy interface system (ANFIS) based solar maximum power point tracking (MPPT) with other solar MPPT methods. In: 2020 IEEE 23rd international multitopic conference (INMIC). IEEE

Chapter 45

Mechanical and Durability Properties of High Strength Concrete Incorporating Different Combinations of Supplementary Cementitious Materials: A Review



B. Sankar and P. Ramadoss

Abstract Ever since the concept of high strength concrete has been first derived, supplementary cementitious materials have been an essential part of its production. The addition of such finer particles in the cementitious matrix not only enhances its mechanical property, but also improves its pore structure, resulting in a more durable and sustainable matrix. In recent years, the effects of using a combination of two SCMs instead of a single SCM are being deeply studied considering the synergy between different SCMs. Higher cement replacement levels keeping in view of sustainability and reduced carbon footprint in concrete are possible only through the usage of combined SCMs. This paper reviews the influence of different SCMs such as fly ash, GGBS, silica fume and metakaolin on both the mechanical properties and durability properties of ternary blended high strength concrete. A comparative perspective is used to present the works studied from the collected literatures.

Keywords Supplementary cementitious materials · Binary blend · Ternary blend · Hybrid cement · High strength concrete

1 Introduction

Over the last 60 years, concrete has evolved drastically from its conventional use. Increased knowledge about the materials used in concrete lead to the understanding of material modification, and how to modify in order to attain a particular set of results. The exquisite versatility of the concrete has made possible the composite stronger than before, more durable than before and almost irreplaceable. Nowadays, concrete

B. Sankar (✉) · P. Ramadoss
Department of Civil Engineering, PEC, Puducherry 605014, India
e-mail: samkarboomibalan180@pec.edu

P. Ramadoss
e-mail: dosspr@pec.edu

is being used in critical structures like high-rise buildings and more hostile environments such as offshore piers, seafloor tunnels, toxic chemical containers and radioactive wall linings [1]. The only drawback being the amount of CO₂ emitted during the production of the clinker and the indirect environmental effects that contribute to climate change [2].

High strength and high-performance concrete require more quantity of cement with a lesser water-cement ratio. Replacement of cement with supplementary cementitious materials like fly ash, silica fume, GGBS not only provides denser microstructure, increased durability and higher strength; rather, these are more environmentally friendly and improves the sustainability of concrete [3]. Blended cement containing such pozzolanic admixtures is commercially available all around the world. In recent years, studies have shown that combinations of cement additions can provide more benefits compared to that of a single additive. The practice of using two cementitious materials is often termed ternary blended concrete. The presence of two cementitious materials in such ternary blended concrete can make use of the synergistic effect, where the shortcomings of one SCM are overcome by the other SCM. In order to maintain strength and durability of concretes containing high volume cement replacements, exploiting potential synergy between SCMs might come in hand. Despite the advantages of ternary blended concrete over binary blending, it has some drawbacks too such as increased water requirement due to higher surface area of the SCMs, workability and reactivity problems based on the chemical compositions of the materials available [4]. Further research has to be done to better understand the role of SCMs in a ternary blended concrete. Compiled study of the research works in order to facilitate implementation and to arrive at a standard specification for casting, is a major concern.

This paper presents a part of wide research involving the ternary blending of cementitious material in high-performance concrete. The information provided in this paper through research involves mechanical and durability studies of concretes containing binary and ternary blending of cementitious materials in a comparative perspective.

2 Supplementary Cementitious Materials

Supplementary cementitious materials (SCMs) such as fly ash, GGBS, silica fume, metakaolin are by-products of production industries that are highly silicious with lesser lime content compared to cement. SCM replacement in cement has environmental benefits such as eliminating an equivalent mass of CO₂ released during cement production, recycling of industrial by-products and prevents huge waste dumping [5]. The data for worldwide annual production of cement and its corresponding CO₂ emission levels over the years are shown in Fig. 1. The worldwide availability of SCMs per year is shown in Table 1. Despite the utility percentage of these SCMs is being increased over the years, utility to availability ratio must be increased further, since the demand for cement will increase in the near future. SCMs are classified with respect

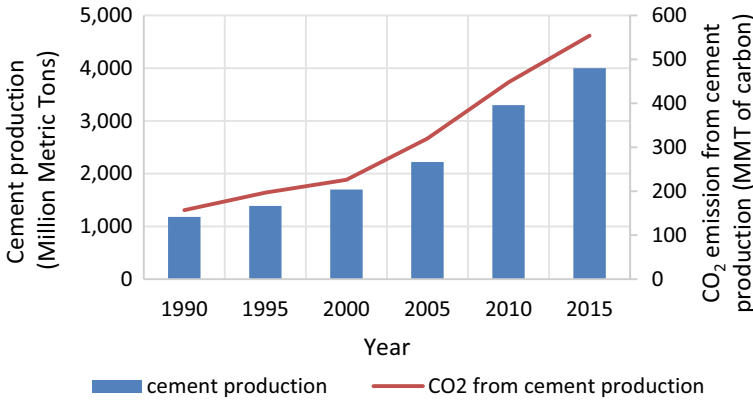


Fig. 1 Cement production and CO₂ emission throughout the years. *Source* USGS, CDIAC

Table 1 Annual worldwide availability of supplementary cementitious materials

Cementitious material	Availability (tonnes/year)
Fly ash	2 billion
GGBS	30–70 million
Silica fume	1.5 million
Rice husk ash	20 million
Metakaolin	1 million

to their chemical composition, particle size and most importantly through their ability to consume portlandite (CH) and form calcium silicate hydrate gel generally referred to as pozzolanicity [6]. The chemical composition of different SCMs is presented in Table 2. Several studies have recorded detrimental effects of pozzolanicity over strength (strength-activity index), durability properties and microstructural integrity of concrete [7, 8]. Detailed study on the degree of reaction of SCMs through different methods such as dissolution, backscattered electron (BSE) image analysis and NMR spectroscopy is done by Scrivener et al. [9]. Pozzolanic reactivity of different SCMs measured through Fratini test is presented in Table 3 [10].

3 Ternary Blending of Cementitious Materials

High-performance concrete necessarily contains one supplementary cementitious material in order to make the pore structure denser and more durable. The concept of adding more than one cementitious material as cement replacement in a concrete matrix is referred to as ternary or quaternary blended concrete shown in Fig. 2.

The primary objective of ternary blended concrete is higher SCM utilization and to make use of the synergy when used in combination by overcoming the shortfalls

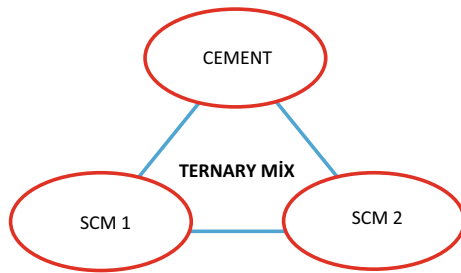
Table 2 Chemical composition and physical properties of different SCMs

	PC	SF	FA	GGBS	MK	Limestone filler	POFA
<i>Chemical Composition (%)</i>							
SiO ₂	20.54	92.0	63.5	35.76	52.68	10.63	64.81
Al ₂ O ₃	6.06	0.7	11.1	13.96	36.34	1.20	5.66
Fe ₂ O ₃	2.77	1.2	5.2	0.25	2.14	0.78	4.73
CaO	64.49	0.3	14.7	41.21	0.78	47.16	8.24
MgO	1.72	0.2	1.98	8.18	0.16	0.39	4.63
Na ₂ O	0.14	1.5	0.48	–	0.26	–	0.063
K ₂ O	0.61	1.80	0.4	–	0.62	0.34	6.37
SO ₃	3.03	0.30	0.35	–	–	0.16	0.36
Loss on ignition	0.64	2.0	2.1	0.64	0.98	37.50	2.55
<i>Physical Properties</i>							
Specific gravity	3.18	2.10	2.43	2.91	2.5	2.73	2.56
Specific surface area (m ² /kg)	322	2000	565	600	1248	710	1775

Table 3 Pozzolanic activity of different pozzolans

Pozzolan	SF	FA	MK
Reactivity (mg) Ca (OH) ₂ /g pozzolan	427	875	1050

Fig. 2 Concept of ternary blended concrete



of concrete containing single SCM. For example, fly ash binary matrix despite its advantages, such as low heat of hydration, increased workability due to its finer particle size, higher long-term strength and sustainability, has shortfalls such as low early strength and slow rate of reaction [11, 12]. Addition of ternary cementitious materials like silica fume or metakaolin in such composite can help to compensate for such weaknesses [13, 14]. Some negative effects of using ternary cementitious mixture are increased water demand and superplasticizer dosage due to the higher surface area of cementitious materials.

In a concrete mixture, when the number of components increases, as in the case with ternary blended concrete, striking a balance between mechanical property, workability, durability and economy is a tedious and time-consuming process. Major research work focused on trial-and-error methods and single factor variable methods to attain the desired performances. Optimization using mathematical and statistical modeling, algorithms based on artificial neural networks and Taguchi methods proved successful to some extent [15–17]. In a most recent study, simplex centroid design method is used for optimization of ternary blended concrete, and the optimum cementitious material content has arrived for desired workability and mechanical performance [18, 19]. A vast amount of research has been carried out to quantify the percent replacement of different SCMs for every water to binder ratio which gives the ultimate results for ternary blended concretes [20–23]. A comparative perspective is necessary to estimate the behavior of different SCMs when used in combination.

3.1 Effects on Mechanical Properties

For SCMs, the factors that greatly influence their mechanical performance in a ternary matrix are the amount of secondary C–S–H gel produced which in turn densifies the matrix, water-binder ratio and percentage of replacement. The possible variations of percentage of replacements differ for every SCMs. For instance, fly ash and slag are known to exhibit good mechanical performance even for higher percentages such as 40 and 50% [24]. From numerous studies, it was found out that a replacement of 10% is acceptable for all types of SCMs. A graph has been drawn containing different SCMs with an equal percentages of cement replacement, and an equal water-binder ratio to understand the behavior of SCMs is shown in Fig. 3 [25, 26].

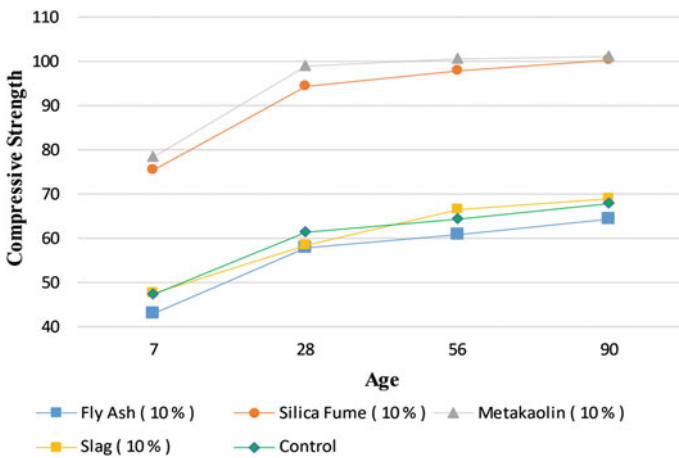


Fig. 3 Performance of HSC containing SCMs at 10% replacement levels

From the figure, it is evident that surface area and reactivity are major factors influencing the mechanical performance of HSC, where the low surface area and less reactive fly ash and slag perform lower than ultrafine silica fume and metakaolin, but in par with the control specimens. When it comes to higher replacement, ultrafine particles show weakness, as high surface area increases water demand. The solution pointed out to increase the SCM utilization and to reduce the shortfalls of a single SCM is to use a combination of fine and ultrafine cementitious materials, less reactive and a highly reactive cementitious material [27]. The resultant was ternary blended concrete. Numerous researchers have pointed out the combined usage of SCMs improving the compressive strength of matrix. Since the compressive strength is the major player for concrete, a comparative evaluation of compressive strength of both binary and ternary mix investigated by several researchers is presented in Table 4. The relative compressive strength for ternary and binary mixes with reference to the control mix is shown in Fig. 4. From the figure, a clear improvement of strength for ternary mixes over control and binary mixes is evident for different combinations of SCMs.

The ternary blending of fly ash and slag is reported to have increased compressive strengths for almost all ages compared to its binary counterpart [36]. Similarly, short-term and long-term mechanical performance improvements are identified for FA and slag [34]. Erdem et al. [28] in their study observed a 14.16% increment in the strength of ternary mixes over binary mixes. In mixes containing limestone fillers, rapid depletion of cementing materials due to increased hydration rates is observed, commonly referred to as the dilution effect. This leads to early strength gain and loss of strength in later ages. GGBS known for its slower reactivity and formation of secondary cementing material in the presence of water can compensate for the negative effects of limestone fillers. In ternary mixes containing metakaolin

Table 4 Comparison of mechanical properties of ternary and binary mix from previous studies

References	Compressive strength			Relative compressive strength w.r.t control mix		Improvement of strength of ternary mix w.r.t binary mix (%)
	Control	Binary	Ternary	Binary	Ternary	
[28]	55.1	72.0	82.2	130.67	149.18	14.16
[29]	46.8	47.2	50.6	100.85	108.119	7.20
[30]	62.5	74	70	118.4	112	-5.40
[31]	80	81.5	93	101.875	116.25	14.11
[32]	55	50	63	90.9	114.54	26
[26]	110	85	94	77.27	85.4	10.58
[33]	35	36	37	102.85	105.71	2.77
[34]	81.1	65.2	80.6	80.39	99.38	23.61
[24]	83	81.3	89	97.95	107.23	9.47
[35]	66	62	72.5	93.94	109.84	16.93

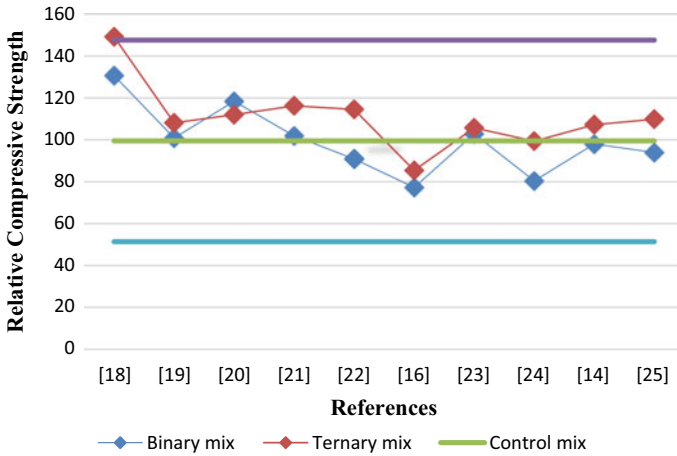


Fig. 4 Relative compressive strength variation of ternary and binary mixes from various studies

and red mud, the presence of red mud provides a good pH environment for the high alumina MK [30]. A 30% total replacement of cement by fly ash and limestone produces comparatively similar hydration products to that of 100% cement, increases early age compressive strength and reduces mass loss [37]. Mechanical properties of raw silica fume-fly ash compared to that of densified silica fume-fly ash showed slight deviation in the early age strengths and microstructure but reaches somewhat similar results in the later ages [38]. Another study with mass loss and mechanical properties in elevated temperatures shows reduced mass loss and increased strength performance for ternary mixes with fly ash, silica fume and MK [39]. Gao et al. [40] investigated the interfacial transition zone characteristics such as porosity and C-S-H gel formation around the aggregates of ternary blended concrete incorporating slag and filler through image techniques and found a strong correlation with compressive strength. In studies with palm oil fuel ash (POFA), the maximum replacement percentage in earlier times was limited to 20% in high strength concrete [41], above which significant strength loss is observed due to coarser particles. Now with the ultra-grinding and heat-treating techniques, higher replacement with improvement in strength upto 30% replacement is made possible [42]. Alani et al. [31] in their study used ultrafine palm oil fuel ash along with densified SF and observed a strength improvement of 14.11% for ternary mixes over binary mixes. Higher replacement of slag along with SF exhibited an increment of 10.58% and 9.47% strength than the binary mixes [24, 26].

In recent years, studies with fiber-reinforced concrete and hybrid fiber-reinforced concrete containing two cementitious materials showed improved flexural strength and reduced crack propagation, which is a direct result of the finer particle size of the SCMs leading to an even distribution of fibers [43, 44].

3.2 Effects on Durability Properties

Fly ash in ternary blend. Fly ash addition in a ternary blended matrix significantly improves the pore size distribution, chloride ingress and sulfate resistance without much increase in the water demand [45, 46]. In fly ash, replaced ternary blended concrete synergy is associated with both physical effects and chemical effects. Physical effects arise from the higher packing density and denser filler effect. Chemical effects manifest themselves through the pozzolanicity, and the chemical compatibility of the SCMs presents in the mix. Positive synergies have been reported for permeation properties, chloride ion permeability, plastic shrinkage and resistance to sulfate action [32]. Radlinski and Olek [32] in their study with FA and SF noted an increase in chloride ion permeability and sorptivity at an early age of binary mix with 20%FA. But in later ages, the ternary mix shows a much-reduced chloride permeability, sorptivity and heat of hydration than the binary mixes containing FA and SF, shown in Fig. 5. Higher replacement levels of FA of 38% along with small quantities of nano-silica (NS) 2% provide denser microstructure due to increased calcium hydroxide levels in the paste, which then forms C-S-H gel in the presence of silica from the NS addition [33]. Results for chloride ion permeability for quaternary blend of fly ash-palm oil ash and nano-silica showed significant improvement over ternary and binary blends of fly ash and palm oil ash [47].

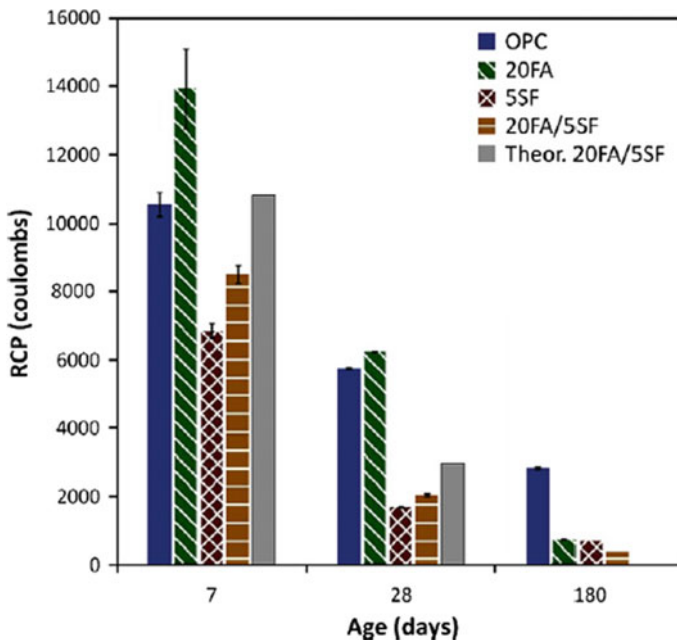


Fig. 5 Chloride ion permeability of ternary and binary blend containing fly ash [32]

GGBS in ternary blend. GGBS known to produce hydration products very similar to that of Portland cement shows reduced permeability of chloride ions and reduced sulfate attack regardless of its chemical composition and replacement levels [29]. Durability studies with higher replacement of GGBS and SF result in much better air permeability and sorptivity results, and the values reduced upto 10.87 and 6.1% compared to that of binary mix [24]. A 50% replacement of GGBS and 7.5% of SF exhibit reduced water absorption and low chloride ingress. Similar studies with high replacement GGBS in ternary mix showed reduced adiabatic heat rise [26]. The scanning electron microscope studies with GGBS and FA presented a finer and denser microstructure, especially in later ages, which explains the superior performance against H_2SO_4 [34]. Synergy studies have also been carried out with GGBS and FA to arrive at an optimized mixture proportion through factorial design method [48].

Silica fume in ternary blend. Despite silica fume being the best player among different SCMs, achieving higher replacement levels is not possible because of increased water demand due to increased surface area and higher rate of consumption of portlandite leading to workability problems and causes dilution effect. Numerous studies have reported better pore structure and reduced autogenous and drying shrinkage of high strength concrete incorporating SF [49]. Durability studies on porosity, water absorption and drying shrinkage of quarternary blends containing fly ash, bottom ash, silica fume show promising results [50]. In a mixture containing ultrafine palm oil fuel ash at 40%, an increase in the SF content reduced its pore volume which in turn lead to reduced air, water and chloride ion permeability. Porosity and water absorption of ternary mix containing 15% SF reduced upto 41.9 and 50% compared to that of the binary mix [31]. Durability studies on electrical resistivity and mass loss in sulphuric acid solution for silica fume-metakaolin incorporated ternary mixes exhibited significant improvement over binary mixes for a total of 20% replacement [51]. Lime sludge, a waste from the paper industry is estimated to be generated around 5 tons per annum in India. Cement replacement of 10% with lime sludge showed equivalent strength compared to control mix. Ternary mixes containing lime slag 20% and silica fume 6% showed improved compressive strength, reduced mass loss and increased formation of ettringite and C-S-H gel at both room and elevated temperature [52]. In addition, SF reduced carbonation in concrete preventing corrosion of embedded steel reinforcements.

Metakaolin in ternary blend. Metakaolin also known as calcined clay is greatly influenced by the calcination temperature and the duration of the calcination process [25]. Through researches it is pointed out that a 10% replacement level is optimum for its durability. The diffusion properties or transport properties such as water absorption, chloride ion penetration, carbonation, electrical resistivity for MK replaced concretes are suggested by various researchers [54]. A study in ternary blended concrete containing FA and MK showed reduced sorptivity and chloride permeability compared to the binary mix containing FA [35]. In the same study, the water absorption for ternary mix containing 20% FA and 10% MK is less than binary mix of 20% FA but more than the binary mix of 10% MK, but as the age of specimens increases the ternary mix exhibited much lesser values for water absorption compared

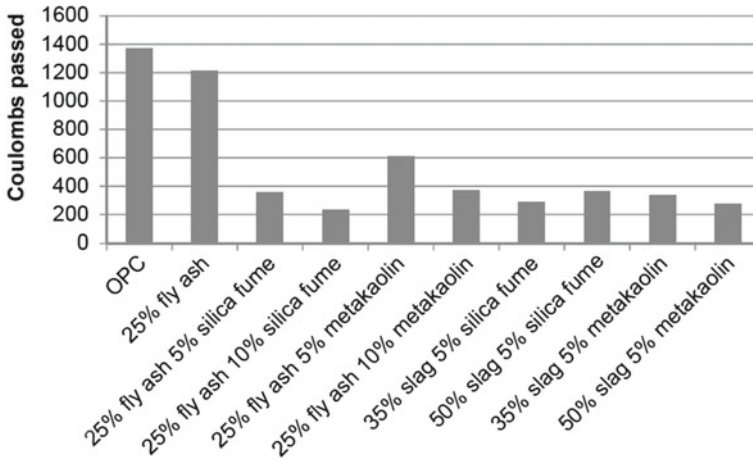


Fig. 6 Chloride ingress of ternary blend containing combinations of SCMs [53]

to every binary mixes, shown in Fig. 7. Ternary blending of MK with limestone and red mud shows early age durability properties due to rapid gel formation and provides a denser composite. Since both SF and MK are ultrafine particles, a comparison of both SCMs in the ternary mixes can shed light on the superior performer among both, one such study has been carried out by holland [53] shown in Fig. 6, where the chloride ion diffusivity of MK and FA replaced ternary blend is higher for an equal volume of SF and FA, but in case of slag and MK, the ternary blend shows reduced chloride ingress compared to SF and slag.

4 Summary

The following conclusions are drawn and summarized from the studies incorporating ternary blends of cementitious materials.

- Mineral additions in concrete densify microstructure, increases concrete compressive strength, improves transition zone characteristics, provides durability and sustainability in the long run.
- Concretes containing combination of SCMs can produce interesting advantages over concretes containing a single SCM. A combination of fine and ultrafine cementitious materials can make use of the synergy by overcoming the drawbacks of SCMs when used individually.
- Higher replacement levels for FA and GGBS are possible when used along with ultrafine particles like MK and SF. Higher replacement of SF and MK leads to increased water demand and affects later age strength. A replacement of 10% is found optimum.

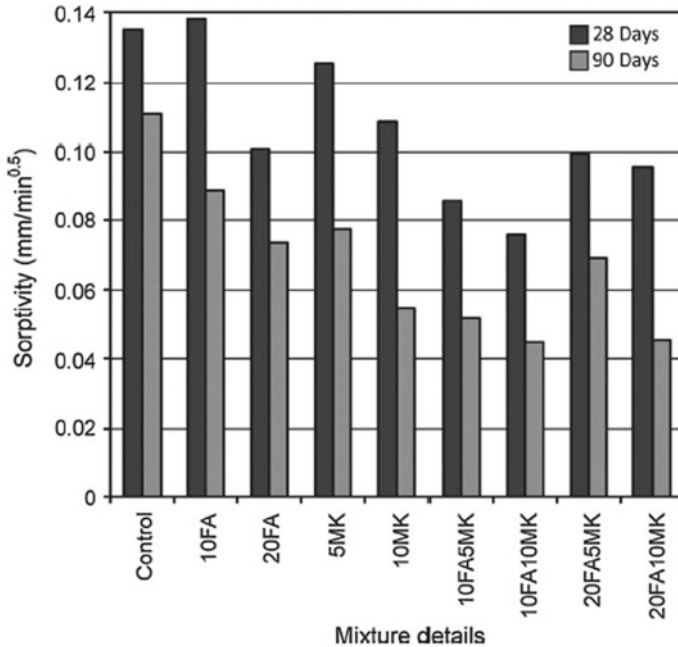


Fig. 7 Sorptivity of ternary and binary blend containing fly ash and MK [35]

- Ternary blending of SCMs improves mechanical properties. In most cases, relative compressive strength of ternary mixes is higher than that of both control and binary mixes. Durability studies on chloride ion permeability, water absorption, sorptivity, carbonation, sulfate attack resistance, porosity shows improvement for ternary mixes over binary mixes.
- There still exist limitations in some cases, increased water demand and early age cracking due to insufficient strength development in ternary blended concretes. Some studies have also shown negative synergies in case of slag-high calcium fly ash and slag-silica fume [55, 56].
- Optimization of mixture proportions of cementitious materials in a ternary blended concrete to attain desired mechanical and durability properties is a subject of much interest and need further research.
- More future works should be focused on the effects of ternary blending of cementitious materials on mechanical properties of fiber-reinforced concrete and hybrid fiber-reinforced concrete.
- Higher utilization potentials of SCMs should be explored in view of the drastic construction developments that are going to take place in the near future.

Acknowledgements The authors wish to acknowledge National Doctoral Fellowship, AICTE for providing facilities and funding during the Doctoral work of the corresponding author. The authors

would also like to thank Head of the Department and the Principal, Pondicherry Engineering College for providing moral support.

References

1. Khan MI, Lynsdale CJ, Waldron P (2000) Porosity and strength of PFA/SF/OPC ternary blended paste. *Cem Concr Res*. [https://doi.org/10.1016/S0008-8846\(00\)00307-0](https://doi.org/10.1016/S0008-8846(00)00307-0) Published online
2. Habert G (2013) Assessing the environmental impact of conventional and “green” cement production. <https://doi.org/10.1533/9780857097729.2.199>
3. Mehta PK (1989) Pozzolanic and cementitious by-products in concrete—another look. *ACI Spec Publ* 114 (Published online)
4. Khatri RP, Sirivivatnanon V, Gross W (1995) Effect of different supplementary cementitious materials on mechanical properties of high performance concrete. *Cem Concr Res*. [https://doi.org/10.1016/0008-8846\(94\)00128-L](https://doi.org/10.1016/0008-8846(94)00128-L) Published online
5. Aitcin PC (2016) Supplementary cementitious materials and blended cements. Elsevier Ltd. <https://doi.org/10.1016/B978-0-08-100693-1.00004-7>
6. Juenger MCG, Siddique R (2015) Recent advances in understanding the role of supplementary cementitious materials in concrete. *Cem Concr Res* 78:71–80. <https://doi.org/10.1016/j.cemconres.2015.03.018>
7. Adu-Amankwah S, Zajac M, Stabler C, Lothenbach B, Black L (2017) Influence of limestone on the hydration of ternary slag cements. *Cem Concr Res* 100(May):96–109. <https://doi.org/10.1016/j.cemconres.2017.05.013>
8. Kocaba V, Gallucci E, Scrivener KL (2012) Methods for determination of degree of reaction of slag in blended cement pastes. *Cem Concr Res* 42(3):511–525. <https://doi.org/10.1016/j.cemconres.2011.11.010>
9. Scrivener KL, Lothenbach B, De Belie N et al (2015) TC 238-SCM: hydration and microstructure of concrete with SCMs: State of the art on methods to determine degree of reaction of SCMs. *Mater Struct Constr* 48(4):835–862. <https://doi.org/10.1617/s11527-015-0527-4>
10. Siddique R, Klaus J (2009) Influence of metakaolin on the properties of mortar and concrete: a review. *Appl Clay Sci* 43(3–4):392–400. <https://doi.org/10.1016/j.clay.2008.11.007>
11. Thomas MDA, Shehata MH, Shashiprakash SG (1999) The use of fly ash in concrete: classification by composition. *Cem Concr Aggregates*. <https://doi.org/10.1520/cca10423j> Published online
12. Lam L, Wong YL, Poon CS (1998) Effect of fly ash and silica fume on compressive and fracture behaviors of concrete. *Cem Concr Res*. [https://doi.org/10.1016/S0008-8846\(97\)00269-X](https://doi.org/10.1016/S0008-8846(97)00269-X) Published online
13. Shehata MH, Thomas MDA (2002) Use of ternary blends containing silica fume and fly ash to suppress expansion due to alkali-silica reaction in concrete. *Cem Concr Res*. [https://doi.org/10.1016/S0008-8846\(01\)00680-9](https://doi.org/10.1016/S0008-8846(01)00680-9) Published online
14. Bai J, Wild S (2002) Investigation of the temperature change and heat evolution of mortar incorporating PFA and metakaolin. *Cem Concr Compos*. [https://doi.org/10.1016/S0958-9465\(01\)00042-7](https://doi.org/10.1016/S0958-9465(01)00042-7) Published online
15. Bektas F, Wang X (2015) Statistical mixture design of ternary blends for controlling ASR. *Mag Concr Res* 67(2):63–70. <https://doi.org/10.1680/mac.14.00149>
16. Özbay E, Erdemir M, Durmuş HI (2016) Utilization and efficiency of ground granulated blast furnace slag on concrete properties—A review. *Constr Build Mater* 105:423–434. <https://doi.org/10.1016/j.conbuildmat.2015.12.153>
17. Dvorkin L, Bezusyak A, Lushnikova N, Ribakov Y (2012) Using mathematical modeling for design of self compacting high strength concrete with metakaolin admixture. *Constr Build Mater* 37:851–864. <https://doi.org/10.1016/j.conbuildmat.2012.04.019>

18. Jiao D, Shi C, Yuan Q, An X, Liu Y (2018) Mixture design of concrete using simplex centroid design method. *Cem Concr Compos* 89:76–88. <https://doi.org/10.1016/j.cemconcomp.2018.03.001>
19. Shi Z, Shi C, Zhao R, Wang D, He F (2016) Factorial design method for designing ternary composite cements to mitigate ASR expansion. *J Mater Civ Eng* 28(9):04016064. [https://doi.org/10.1061/\(asce\)mt.1943-5533.0001568](https://doi.org/10.1061/(asce)mt.1943-5533.0001568)
20. Nazerigivi A, Najigivi A (2019) Study on mechanical properties of ternary blended concrete containing two different sizes of nano-SiO₂. *Compos Part B Eng* 167:20–24. <https://doi.org/10.1016/j.compositesb.2018.11.136>
21. Benli A, Karataş M, Gurses E (2017) Effect of sea water and MgSO₄ solution on the mechanical properties and durability of self-compacting mortars with fly ash/silica fume. *Constr Build Mater* 146:464–474. <https://doi.org/10.1016/j.conbuildmat.2017.04.108>
22. Younes MM, Abdel-Rahman HA, Khattab MM (2018) Utilization of rice husk ash and waste glass in the production of ternary blended cement mortar composites. *J Build Eng* 20:42–50. <https://doi.org/10.1016/j.jobbe.2018.07.001>
23. Schöler A, Lothenbach B, Winnefeld F, Zajac M (2015) Hydration of quaternary Portland cement blends containing blast-furnace slag, siliceous fly ash and limestone powder. *Cem Concr Compos* 55:374–382. <https://doi.org/10.1016/j.cemconcomp.2014.10.001>
24. Elahi A, Basheer PAM, Nanukuttan SV, Khan QUZ (2010) Mechanical and durability properties of high performance concretes containing supplementary cementitious materials. *Constr Build Mater*. <https://doi.org/10.1016/j.conbuildmat.2009.08.045> Published online
25. Shafiq N, Nuruddin MF, Khan SU, Ayub T (2015) Calcined kaolin as cement replacing material and its use in high strength concrete. *Constr Build Mater* 81:313–323. <https://doi.org/10.1016/j.conbuildmat.2015.02.050>
26. Domone PL, Soutsos MN (1997) Properties of high-strength concrete mixes containing PFA and ggbs. *Mag Concr Res* 49(180):263–265. <https://doi.org/10.1680/macr.1997.49.180.263>
27. Mehta PK, Gjörv OE (1982) Properties of portland cement concrete containing fly ash and condensed silica-fume. *Cem Concr Res*. [https://doi.org/10.1016/0008-8846\(82\)90019-9](https://doi.org/10.1016/0008-8846(82)90019-9) Published online
28. Erdem TK, Kirca Ö (2008) Use of binary and ternary blends in high strength concrete. *Constr Build Mater* 22(7):1477–1483. <https://doi.org/10.1016/j.conbuildmat.2007.03.026>
29. Menéndez G, Bonavetti V, Irassar EF (2003) Strength development of ternary blended cement with limestone filler and blast-furnace slag. *Cem Concr Compos* 25(1):61–67. [https://doi.org/10.1016/S0958-9465\(01\)00056-7](https://doi.org/10.1016/S0958-9465(01)00056-7)
30. Raj RR, Pillai EBP, Santhakumar AR (2013) Evaluation and mix design for ternary blended high strength concrete. *Procedia Eng* 51(NUI CONE 2012):65–74. <https://doi.org/10.1016/j.proeng.2013.01.012>
31. Alani AH, Johari MAM, Aldahdooh MAA, Muhamad Bunnori N (2019) Development of engineering and transport properties of green high strength concrete utilizing ternary blended binders. *Eur J Environ Civ Eng* 0(0):1–17. <https://doi.org/10.1080/19648189.2019.1573381>
32. Radlinski M, Olek J (2012) Investigation into the synergistic effects in ternary cementitious systems containing portland cement, fly ash and silica fume. *Cem Concr Compos*. <https://doi.org/10.1016/j.cemconcomp.2011.11.014> Published online
33. Shaikh FUA, Supit SWM, Sarker PK (2014) A study on the effect of nano silica on compressive strength of high volume fly ash mortars and concretes. *Mater Des*. <https://doi.org/10.1016/j.matdes.2014.04.025> Published online
34. Li G, Zhao X (2003) Properties of concrete incorporating fly ash and ground granulated blast-furnace slag. *Cem Concr Compos*. [https://doi.org/10.1016/S0958-9465\(02\)00058-6](https://doi.org/10.1016/S0958-9465(02)00058-6) Published online
35. Güneysi E, Gesoğlu M, Algin Z, Mermerdaş K (2014) Optimization of concrete mixture with hybrid blends of metakaolin and fly ash using response surface method. *Compos Part B Eng*. <https://doi.org/10.1016/j.compositesb.2014.01.017> Published online
36. Tan K, Pu X (1998) Strengthening effects of finely ground fly ash, granulated blast furnace slag, and their combination. *Cem Concr Res*. [https://doi.org/10.1016/S0008-8846\(98\)00158-6](https://doi.org/10.1016/S0008-8846(98)00158-6) Published online

37. Thongsanitgarn P, Wongkeo W, Chaipanich A (2014) Hydration and compressive strength of blended cement containing fly ash and limestone as cement replacement. *J Mater Civ Eng* 26(12):04014088. [https://doi.org/10.1061/\(asce\)mt.1943-5533.0001002](https://doi.org/10.1061/(asce)mt.1943-5533.0001002)
38. Zhang Z, Zhang B, Yan P (2016) Hydration and microstructures of concrete containing raw or densified silica fume at different curing temperatures. *Constr Build Mater* 121:483–490. <https://doi.org/10.1016/j.conbuildmat.2016.06.014>
39. AzariJafari H, Taheri Amiri MJ, Ashrafian A, Rasekh H, Barforooshi MJ, Berenjani J (2019) Ternary blended cement: an eco-friendly alternative to improve resistivity of high-performance self-consolidating concrete against elevated temperature. *J Clean Prod* 223:575–586. <https://doi.org/10.1016/j.jclepro.2019.03.054>
40. Gao Y, De Schutter G, Ye G, Huang H, Tan Z, Wu K (2013) Characterization of ITZ in ternary blended cementitious composites: experiment and simulation. *Constr Build Mater* 41:742–750. <https://doi.org/10.1016/j.conbuildmat.2012.12.051>
41. Tangchirapat W, Jaturapitakkul C, Chindaprasit P (2009) Use of palm oil fuel ash as a supplementary cementitious material for producing high-strength concrete. *Constr Build Mater*. <https://doi.org/10.1016/j.conbuildmat.2009.01.008> Published online
42. Sata V, Jaturapitakkul C, Kiattikomol K (2007) Influence of pozzolan from various by-product materials on mechanical properties of high-strength concrete. *Constr Build Mater* 21(7):1589–1598. <https://doi.org/10.1016/j.conbuildmat.2005.09.011>
43. Nguyen H, Staudacher M, Kinnunen P, Carvelli V, Ilikainen M (2019) Multi-fiber reinforced terringite-based composites from industrial side streams. *J Clean Prod*. <https://doi.org/10.1016/j.jclepro.2018.11.241> Published online
44. Teng S, Afroughsabet V, Ostertag CP (2018) Flexural behavior and durability properties of high performance hybrid-fiber-reinforced concrete. *Constr Build Mater*. <https://doi.org/10.1016/j.conbuildmat.2018.06.158> Published online
45. Ozyildirim C, Halstead WJ (1994) Improved concrete quality with combinations of fly ash and silica fume. *ACI Mater J*. <https://doi.org/10.14359/1379> Published online
46. Lane DS, Ozyildirim C (1999) Preventive measures for alkali-silica reactions (binary and ternary systems). *Cem Concr Res*. [https://doi.org/10.1016/S0008-8846\(98\)00242-7](https://doi.org/10.1016/S0008-8846(98)00242-7) Published online
47. Sneh K, Das BB, Akanksha M (2020) Early age, hydration, mechanical and microstructure properties of nano-silica blended cementitious composites. *Constr Build Mater* 233:117212. <https://doi.org/10.1016/j.conbuildmat.2019.117212>
48. Hu X, Shi Z, Shi C et al (2017) Drying shrinkage and cracking resistance of concrete made with ternary cementitious components. *Constr Build Mater*. <https://doi.org/10.1016/j.conbuildmat.2017.05.113> Published online
49. Mazloom M, Ramezaniapour AA, Brooks JJ (2004) Effect of silica fume on mechanical properties of high-strength concrete. *Cem Concr Compos* 26(4):347–357. [https://doi.org/10.1016/S0958-9465\(03\)00017-9](https://doi.org/10.1016/S0958-9465(03)00017-9)
50. Wongkeo W, Thongsanitgarn P, Chaipanich A (2012) Compressive strength and drying shrinkage of fly ash-bottom ash-silica fume multi-blended cement mortars. *Mater Des* 36:655–662. <https://doi.org/10.1016/j.matdes.2011.11.043>
51. Khodabakhshian A, Ghalehnovi M, de Brito J, Asadi Shamsabadi E (2018) Durability performance of structural concrete containing silica fume and marble industry waste powder. *J Clean Prod* 170:42–60. <https://doi.org/10.1016/j.jclepro.2017.09.116>
52. Maheswaran S, Iyer NR, Palani GS, Pandi RA, Dikar DD, Kalaiselvam S (2015) Effect of high temperature on the properties of ternary blended cement pastes and mortars. *J Therm Anal Calorim* 122(2):775–786. <https://doi.org/10.1007/s10973-015-4817-4>
53. Holland RB, Kurtis KE, Kahn LF (2016) Effect of different concrete materials on the corrosion of the embedded reinforcing steel. Elsevier Ltd. <https://doi.org/10.1016/B978-1-78242-381-2.00007-9>
54. Ayub T, Shafiq N, Khan S, Nuruddin M (2013) Durability of concrete with different mineral admixtures: a review. *Int J Civil Archit Struct Constr Eng* 7(8):273–284. <http://www.waset.org/publications/9996810>

55. Shi C, Wang D, Wu L, Wu Z (2015) The hydration and microstructure of ultra high-strength concrete with cement-silica fume-slag binder. *Cem Concr Compos* 61:44–52. <https://doi.org/10.1016/j.cemconcomp.2015.04.013>
56. Kandasamy S, Shehata MH (2014) The capacity of ternary blends containing slag and high-calcium fly ash to mitigate alkali silica reaction. *Cem Concr Compos* 49:92–99. <https://doi.org/10.1016/j.cemconcomp.2013.12.008>

Chapter 46

Fabrication of Rechargeable Lithium Ion Coin Cell Using a Biopolymer Electrolyte (Cellulose Acetate)



R. Venkata Jyotsna, M. Vengadesh Krishna, Selvasekarapandian, P. Chandrasekar, and S. Monisha

Abstract The naturally occurring polymer cellulose acetate with tetrahydrofuran (THF) as solvent was used as base agents to develop the electrolyte for a rechargeable lithium ion cell. The biopolymer electrolyte was developed and by the popular solution casting technique. Maximum elevated conductivity of this biopolymer electrolyte was recorded at 2.136×10^{-2} Scm⁻¹ at room temperature for the concentration of 10:90 weight proportion of CA: LiCl. The cell has been constructed with a configuration of charcoal || 10 m% cellulose acetate/90 m% LiCl, and a maximum cell potential of 3.55 V has been accomplished. This affirms the applicability of the membrane as a feasible choice of electrolyte for solid-state lithium ion batteries.

Keywords Biopolymer · Solution casting technique · Lithium · Electrolyte · Discharge · Conductivity · Cellulose acetate · Impedance spectroscopy · Amorphousness

1 Introduction

The current investigation aims to reach one of the major green revolution goals—clean energy . To present the scenario in this aspect, it would be necessary to

R. Venkata Jyotsna (✉) · P. Chandrasekar
Department of Electrical and Electronics Engineering, Veltech University, Chennai, Tamil Nadu, India

S. Monisha
Department of Physics, Veltech University, Chennai, Tamil Nadu, India

R. Venkata Jyotsna · M. Vengadesh Krishna · Selvasekarapandian
Materials Research Center, Coimbatore, Tamil Nadu, India

Selvasekarapandian
Department of Physics, Bharathiar University, Coimbatore, Tamil Nadu, India

M. Vengadesh Krishna
Department of Chemistry, Bharathiar University, Coimbatore, Tamil Nadu, India

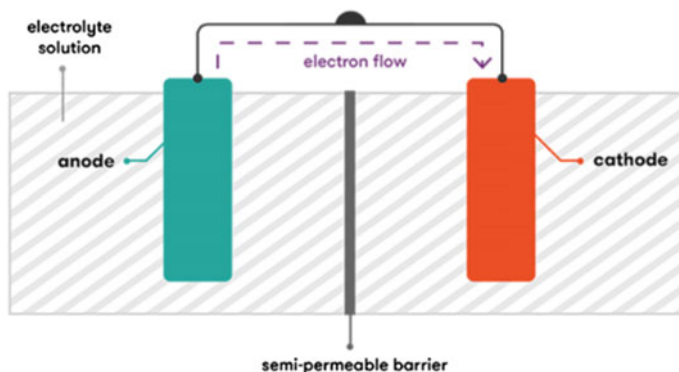


Fig. 1 Parts of a battery

consider the fundamental parts of a battery—anode, cathode and the electrolyte [shown in Fig. 1]. The three components are normally inorganic in nature, making them difficult to dispose and effectively chemically polluting. The investigation taken up aims to alleviate the environmental impact of one of these components—the electrolyte. While achieving completely green batteries may not be feasible industrially at present, extensive research has proven that there is hope in trying to lessen the impact by using a biopolymer based electrolyte instead of the metal oxide variants. The scope of this work is to fabricate a rechargeable battery based on a clean electrolyte with a working voltage of over 2.5–3 V.

New materials following the fundamental green chemistry principles are under extensive focus due to the lower release of pollutants into the environment. Two strong alternatives, namely batteries and super-capacitors as energy storage devices, seem to supplant other non-sustainable energy sources like oil and fossil fuels [1]. Solid electrolytes have been under research to analyze their application to large-scale production. Polymer electrolytes are membranes for the ion transport mechanism [2, 3]. For example, a cellulose acetate (CA) polymer host is assumed to be one of the cornerstones for the preparation of various types of polymer electrolytes, because of its capability of dissolving a number of inorganic salts and also its biodegradability.

The chosen battery type is that of the lithium ion, owing to its high energy density and specific energy values than historic chemistries [4]. Also, it is noteworthy to mention that the abundance of lithium supply across the world makes it the best economically and chemically feasible choice of material for a battery. Often a single lithium ion cell can be used in place of multiple NiMH or NiCd cells. The various energy densities of the popular chemistries globally are presented in Fig. 2.

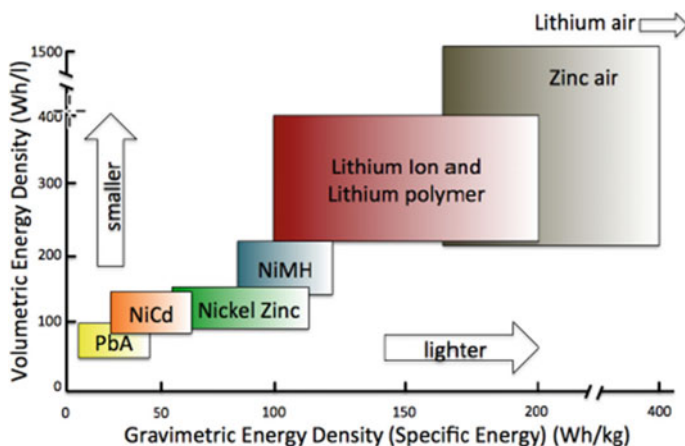


Fig. 2 Energy densities across popular industrial battery chemistries

2 Experimental Method

2.1 Fabrication

In the present study, polymer CA, and salt LiCl were used as the raw materials. Tetrahydrofuran (THF) is utilized for the solvating agent. The polymer complex CA:LiCl with various molecular weight proportions of 60:40, 50:50, 40:60, 30:70, 20:80, 15:85 and 10:90 was mixed and stirred persistently until a homogeneous combination was obtained. The acquired arrangement was of Petri dishes that consisted of these homogeneous solutions, which were then dried at 60 °C using a hot oven to guarantee that none of the solvent traces were present. Subsequently, this produced films that were flexible and transparent, of around 0.22 to 0.16 μm thickness. The process can be understood from Fig. 3.

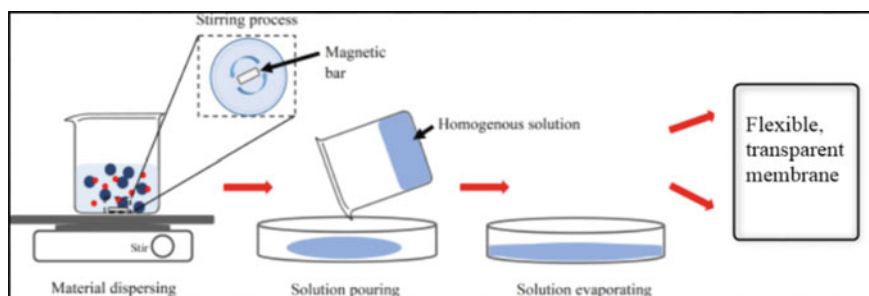


Fig. 3 Membrane preparation using solution casting technique

Typically, the CA and LiCl solutions prepared using with the THF solvent are mixed by pouring one into the other—however, in this investigation, the LiCl solution, which happens to be the salt solution was thoroughly homogenized and poured in increments into the CA solution beaker. This method has effectively resulted in a higher conductivity for the developed membrane, since cellulose acetate as an organic substance is more viscous than Lithium Chloride.

2.2 Characterization

X-ray diffraction patterns were recorded using the X' pert pro diffractometer system room temperature [1, 3, 5]. The copper- α radiation was utilized across a scope of $2\theta = 10^\circ\text{--}60^\circ$ for the same. Fourier transform infrared spectroscopy analysis was performed utilizing the BRUCKER spectrophotometer over the $2300\text{--}600\text{ cm}^{-1}$ range. DSC estimates were recorded utilizing the DSC-Q20 V24.10 Build 122, TA Instruments device. Conductivity investigation of the biopolymer electrolytes was performed using the HIOKI 3523 LCR Meter across the frequency range of 42 Hz to 1 M Hz by sandwiching them using aluminum as the impeding electrodes.

2.3 Operational Aspects

Resistance values [EIS parameters] of the electrolyte membrane are achieved through the conductivity study [also known as impedance spectroscopy analysis] performed using the Hioki 3525 LCR Meter [Fig. 4]. This device makes use of an LCR meter which consists of a Wheatstone bridge performing the LCR function. The LCR function allows to measure the impedance, phase angle and other items by applying any frequency or level (effective value) signal to the element under consideration.



Fig. 4 Hioki 3523 LCR meter

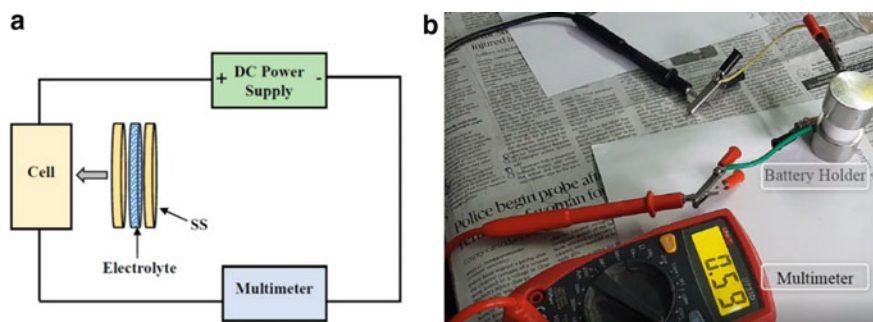


Fig. 5 a Setup for measurement of primary quantities. b Setup for voltage/current measurement



Fig. 6 Illustration of the setup—crimper; used to fix the cells together, battery holder, the prepared anode, cathode and solid biopolymer electrolyte

Other quantities like voltage and current are measured using a multimeter. The performance metrics [energy density, specific energy, energy capacity] are derived from these primary quantities using electrical laws (Figs. 5, 6, 7).

3 Results

(i) EIS Analysis [Impedance plot] of the biopolymer

The ionic conductivity primarily relies upon the conducting specimen and its mobility [6, 7]. Figure 9 shows the Cole–Cole plot (Z' vs. Z'') for the considered

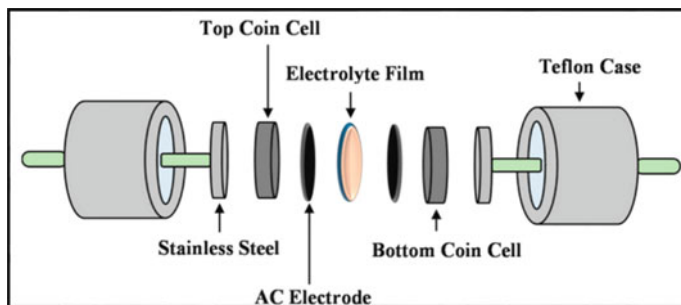


Fig. 7 Component view of the parts as assembled from Fig. 6

biopolymer electrolyte [Cellulose Acetate] doped with different concentrations of LiCl at standard temperature and pressure conditions. The impedance plot or the Cole–Cole plot is commonly used to represent the EIS data, where in the imaginary part of impedance is plotted against the real part of impedance. Each plot corresponds to the impedance behavior at a particular frequency and is also represented by an equivalent circuit model.

Typically, an impedance plot comprises of a contorted semicircle within the high frequency area followed by a slanted spike in the low frequency area [8, 9]. The high frequency crescent is because of the blend of bulk resistance (caused by ion relocation) and bulk capacitance (caused by stationary polymer chains). The low frequency spike addressed by a steady-state component is because of the arrangement of a twofold layer capacitance at the interface of the electrode and electrolyte.

In the current examination, the CA:LiCl polymer electrolytes comprise only of the slanted spike. The semicircle was not present, which indicates that the CA:LiCl membrane has a resistive nature only and the capacitive nature of electrolyte vanished, which can be attributed to the movement of charge carriers in the biopolymer electrolyte. The equivalent circuit can be seen in Fig. 8. Electrochemical impedance spectroscopy (EIS) parameters were derived from the Cole–Cole plot through the EQ software program and are recorded in Table 1 (Fig. 9).

Pure CA has a resistance value of 61.2 k Ω [8]. Upon addition of LiCl with the cellulose acetate electrolyte, the resistance value diminished from 2574.4 to 0.5095 Ω . The constant phase element (CPE) value for pure CA is 2.66×10^{-4} μF . The most noteworthy of the polymer electrolytes which is the 10CA:90LiCl has an $R_b = 0.5095$ Ω . The ionic conductivity (σ) of the polymer electrolyte is determined using the equation

Fig. 8 Equivalent circuit



Table 1 EIS parameters for all concentrations of the polymer electrolytes

Polymer composition (molar %)	R [Ohm]
60CA:40LiCl	2574.4
50CA:50LiCl	427.23
40CA:60LiCl	11.1
30CA:70LiCl	11.22
15CA:85LiCl	2.74
10CA:90LiCl	0.5095

$$\sigma = \frac{L}{AxR_b} \text{Scm}^{-1}$$

where L is the thickness, R_b is the bulk resistance and A is the contact area of the electrolyte film. Among various weight ratios of CA:LiCl polymer electrolyte, the 10CA:90LiCl electrolyte has the maximum ionic conductivity ($2.1366 \times 10^{-2} \text{Scm}^{-1}$) at STP. The elevation in the ionic conductivity of 10CA:90LiCl can be attributed to the transition from semicrystalline to amorphous phases of polymer complex and increase in charge carrier concentration. The conductivity is observed to be directly proportional to the concentration of salt content. The causative factor for the conductivity enhancement hence is the polymer–salt interaction.

(ii) *Charging-Discharging characteristics of the coin cell*

The fabricated cell is subjected to DC supply of 5 V. Open circuit cell potential of 3.5 V has been observed for the first cycle, and then, the cell has been charged for one hour. The discharge of the cell takes 4 h to reach the deep discharge voltage point of 0.6 V. At the 10th cycle, the cell reached a maximum of 1.41 V and the same discharge time is observed for this cycle too. The value of the cell resistance has been found to increase with charging cycles owing to interface resistance between electrodes and electrolyte of the cell. The photograph of the fabricated cell potential is shown in Fig. 10.

4 Conclusion

A solid biopolymer electrolyte imbibing cellulose acetate for the concept of a clean fuel through the successful lithium ion rechargeable battery has been fabricated through the solution casting technique. A high conductivity value of $2.1366 \times 10^{-2} \text{Scm}^{-1}$ is obtained through the composition of 10 wt% CA: 90 wt% LiCl. The expansion of lithium chloride content in the cellulose acetate membrane can disturb the intermolecular interactions inside the host polymers to make new connections between molecules leading to the increment in the amorphousness of the membrane. The choice of salt [Lithium Chloride] for a rechargeable battery distinguishes this work from the research projects done so far in the domain of battery fabrication. The

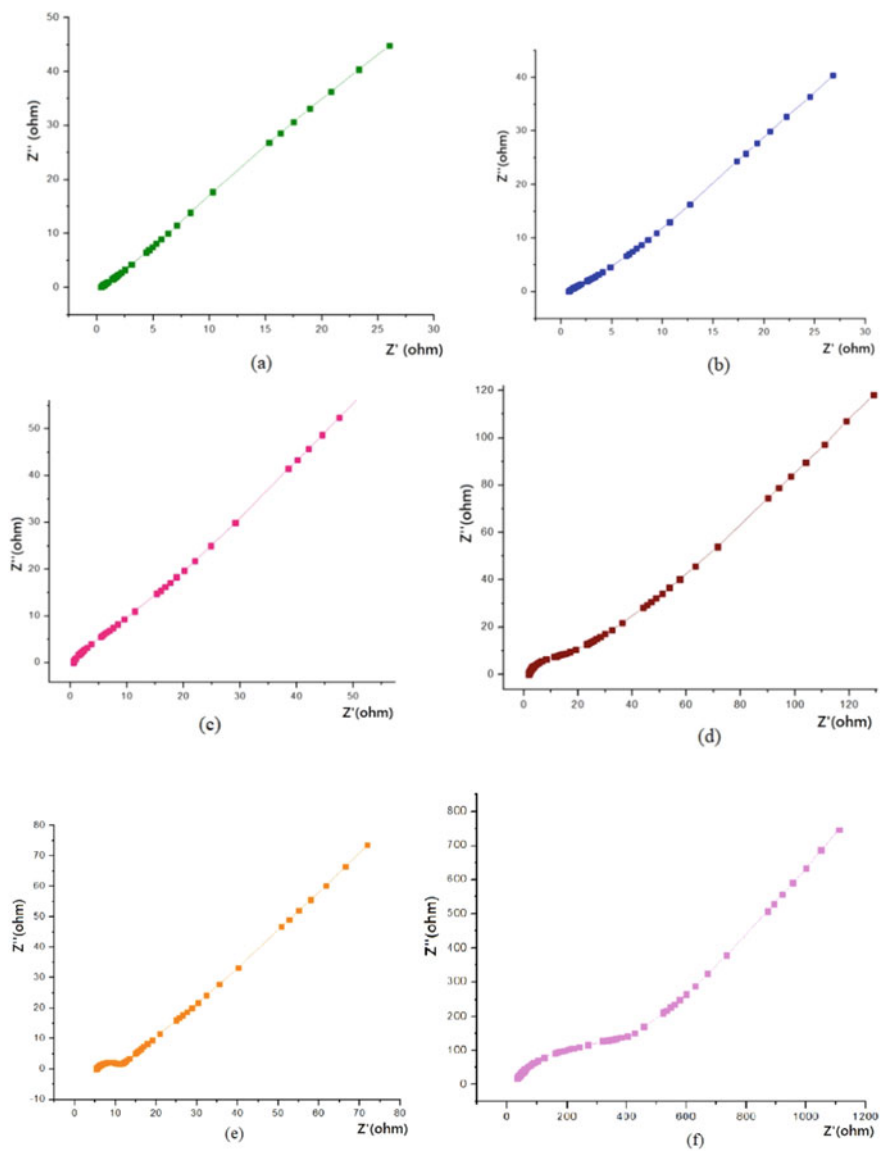


Fig. 9 Cole–Cole plot for **a** 10CA:90LiCl, **b** 15CA:85LiCl, **c** 20CA:80LiCl, **d** 30CA:70LiCl, **e** 40CA:60LiCl, **f** 50CA:50LiCl

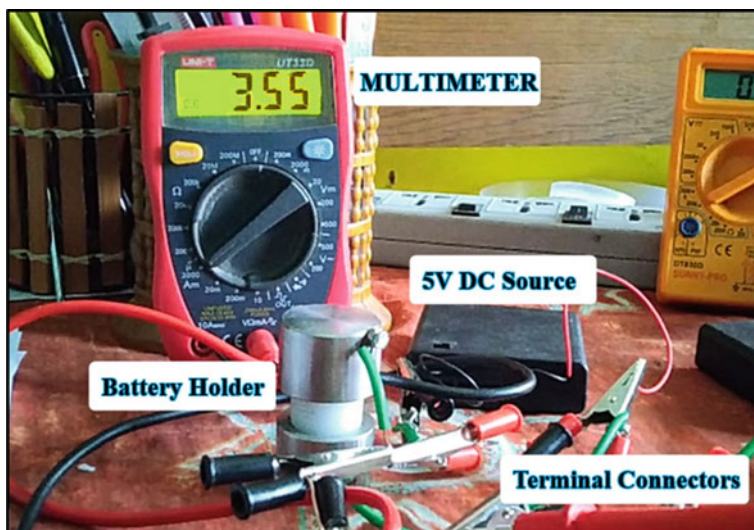


Fig. 10 Photograph of the coin cell potential

lithium ion batteries which use a biopolymer electrolyte has thus far shown nominal working voltage range between 1 and 2.8 V only. Majority of the biopolymer electrolyte based batteries are of primary type. The current investigation has allowed to fabricate a rechargeable lithium ion battery which provides nominal voltage of 3.55 V.

References

1. Kiruthika S, Malathi M, Selvasekarapandian S, Tamilarasan K, Moniha V, Manjuladevi R (2019) Eco-friendly biopolymer electrolyte, pectin with magnesium nitrate salt, for application in electrochemical devices
2. Rayung M, Aung MM, Azhar SC, Abdullah LC, Su'ait MS, Ahmad A, Jamil SNAM (2020) Bio-based polymer electrolytes for electrochemical devices: insight into the ionic conductivity performance
3. Karthikeyan S, Selvasekarapandian S, Premalatha M, Monisha S, Boopathi G, Aristatil G, Arun A, Madeswaran S (2016) Proton conducting I-carrageenan-based biopolymer electrolyte for fuel cell application. *Ionics* 23:2775–2780
4. Venkatasetty HV, Jeonga YU (2002) Recent advances in lithium-ion and lithium-polymer batteries
5. Anbazhakan K, Selvasekarapandian S, Monisha S, Premalatha M, Neelaveni A (2017) Lithium ion conductivity and dielectric properties of P(VdCl-co-AN-co-MMA)-LiCl-EC triblock copolymer electrolytes (2016). Springer-Verlag, Berlin Heidelberg
6. Vengadesh Krishna M, Chitra R, Selvasekarapandian S (2020) Fabrication of rechargeable lithium ion coin cell using triblock polymer electrolyte poly (Vinylidene Chloride-Co-Acrylonitrile-Co-Methyl Methacrylate) with lithium perchlorate

7. Premalatha M, Vijaya N, Selvasekarapandian S, Selvalakshmi S (2016) Characterization of blend polymer PVA-PVP complexed with ammonium thiocyanate. *Ionics* 22(8):1299–1310
8. Monisha S, Selvasekarapandian S, Mathavan T, Milton Franklin Benial A, Sindhuja Manoharan, Karthikeyan S (2016) Preparation and characterization of biopolymer electrolyte based on cellulose acetate for potential applications in energy storage devices
9. Boopathi G, Pugalendhi S, Selvasekarapandian S, Premalatha M, Monisha S, Aristatil G Development of proton conducting biopolymer membrane based on agar–agar for fuel cell
10. Muhamaruesa NHM, Isa MINM (2020) Chapter 19—Biopolymer membranes for battery applications
11. Li X, Ding C, Li X, Yang H, Liu S, Wang X, Zhang L, Sun Q, Liu X, Chen J (2020) Electronic biopolymers: from molecular engineering to functional devices
12. Laffly E, P'era M-C', Hissel D, Senior Member IEEE (2007) Polymer electrolyte membrane fuel cell modelling and parameters estimation for ageing consideration
13. Liu W, Lin D, Sun J, Zhou G, Cui Y (2016) Improved lithium ionic conductivity in composite polymer electrolytes with oxide-ion conducting nanowires. *ACS Nano* 10(12):11407–11413
14. Zulkefli FN, Navaratnam S, Ahmad AH (2015) Proton conducting biopolymer electrolytes based on starch incorporated with ammonium thiocyanate. *Adv Mater Res* 1112:275–278
15. Sohaimy MIH, Isa MIN (2017) Ionic conductivity and conduction mechanism studies on cellulose based solid polymer electrolytes doped with ammonium carbonate. *Polym Bull* 74(4):1371–1386
16. Selvalakshmi S, Vijaya N, Selvasekarapandian S, Premalatha M (2017) Biopolymer agar-agar doped with NH₄SCN as solid polymer electrolyte for electrochemical cell application. *J Appl Polym Sci* 134:44702
17. Mohnen D (2008) Pectin structure and biosynthesis. *Curr Opin Plant Biol* 11(3):266–277
18. Srivastava P, Malviya R (2011) Sources of pectin, extraction and its applications in pharmaceutical industry—an overview. *Indian J Nat Prod Resour* 2:10–18
19. Jia X, Yang Y, Wang C, Zhao C, Vijayaraghavan R, MacFarlane DR, Wallace GG (2014) Biocompatible ionic liquid–biopolymer electrolyte-enabled thin and compact magnesium–air batteries. *ACS Appl Mater Interfaces* 6(23):21110–21117
20. Nirmala Devi G, Chitra S, Selvasekarapandian S, Premalatha M, Monisha S, Saranya J (2017) Synthesis and characterization of dextrin-based polymer electrolytes for potential applications in energy storage devices. *Ionics* 23(12):3377–3388

Chapter 47

Building Knowledge Graph End to End: Data Integration with Semantic Web



M. Lissa and V. Bhuvaneshwari

Abstract The data are evolved from heterogeneous sources as structured, unstructured, and semi-structured in varied formats from various platforms and applications, extending data integration difficulty. Data heterogeneity in varied formats and representation leads to a standardization gap that has to be addressed on enabling common data representation. Semantic web technologies are used to address the gap of data interoperability by representing data in a machine-understandable format for knowledge inference defined as taxonomy, thesaurus, and ontology to infer knowledge. An end-to-end knowledge graph is proposed to integrate diverse data generated from heterogeneous data sources in this work. A brief view of the data integration process and NLP techniques are discussed to identify concepts from unstructured data inputs to the knowledge representation ontology. The concepts for knowledge modeling are described as a logistic domain for shipping processes. Logistic information is extracted for conceptualization and represented as taxonomy. Ontology is modeled for managing logistic shipping containers to infer knowledge of containers used in the logistic shipping process. The proposed knowledge base is evaluated with a specific use case to infer knowledge for cargo tracking in shipment processes.

Keywords Logistics · Ontology · Semantic web · Data integration · Knowledge graph · Data heterogeneity · Natural language processing

1 Introduction

In the current data era, the data evolve from multiple heterogeneous systems in varied formats and structures. Data integration is essential to connect system functionalities to enable data exchange for implementing business decisions. The business domains accumulate data from the data-centric application systems such as ERP, CRM, MDM in a standardized format. They need to integrate data from machinery deployed at manufacturing units from sensors, RFID tags. Unstructured data sources such as business reports, feedback, and social media data from chat applications are also

M. Lissa (✉) · V. Bhuvaneshwari
Department of Computer Applications, Bharathiar University, Coimbatore, India

considered vital inputs. Domain knowledge of individuals who process information based on experience must be modeled to the machines for automatic knowledge inference. AI-based techniques are under development to enable data integration from diverse data pools inculcating domain knowledge. This paper addresses data integration issues related to data heterogeneity and data standardization using the semantic web.

The semantic web is used for addressing the problem of semantic integration through knowledge representation in the domain of knowledge-based systems. Researchers from natural language processing and logistics management communities have taken advantage of these developments with reasonable success [1].

The data integration process is described for the logistic domain in this paper. The logistic domain is interdisciplinary requiring coordinated efforts among various fields of logistic activities from internal and external sources such as production, transport, storage, finance, marketing (customer services), and external services such as suppliers, freight carriers, freight forwarders, logistic providers, manufacturers, distribution centers, wholesalers, business management, information technology, cargo and designing transit, warehousing, and other engineering fields [2]. The logistic management process needs to be integrated with the dynamic network of manufacturing units, product services, transportation, and logistics with e-commerce systems. The digital data that evolve from diverse logistic planning processes and functionalities are available in heterogeneous systems, leading to data integration challenges. The data interoperability challenge arises due to data heterogeneity due to data varied formats and standards. Ontology provides semantic primitives to represent and share the domain knowledge. This paper presents a generic methodological approach for building a knowledge graph by constructing logistic ontology using natural language processing techniques for conceptualization.

This paper presents an end-to-end approach required in building a knowledge graph for the domain of logistics. The paper is organized as follows: Knowledge acquisition related to literature and approaches for logistic ontologies and text mining algorithms are reviewed in Sect. 2. The logistic data ecosystem and the natural language processing techniques to extract the concepts and the entities are presented in Sect. 3. The particular focus is placed on building knowledge graphs for the domain logistics with ontology in Sect. 4. The generic architecture using knowledge modeling for a shipping container as a usecase for integrating multiple datasets with knowledge inference is presented in Sect. 4.1, followed by Sect. 5.

2 Related Work

Logistic shipment processes are related to transportation and supply chain systems connected to the organizations both internally and externally. The semantic-based knowledge model enables identifying and tracking the shipment with geo-location tagging connects multiple information systems to determine the status of the cargo

shipment ports. This section discusses the related work specific to knowledge modeling, data integration, natural language processing techniques, and ontology.

The importance of paradigm shift for information representation in the context of knowledge is discussed by Mendes et al. [3], Seedah et al. [4]. Mendes, Arsenio et al. [5] presented a study on incorporating data from multiple sources and mapping numerous heterogeneous sources, mobility patterns, time-series data. Dimou [6] discusses the conceptual development required for rich interlinking among resources due to high integrity within data.

Gruber [7] discussed the translation approach for sharing and reusing the represented knowledge formally with common vocabulary that shares the knowledge among systems. Zhang et al. [8], Borgi et al. [9] reviewed the concept of interlinking the fields of transport and logistics with multiple resources. They addressed a critical data integration approach based on resolving the data ambiguity issues to improve reproducibility. Chung and Kwon [10], Ali et al. [11] stated the impact of product perishability on manufacturers, distribution centers, wholesalers, and demand markets in logistics to build an integrated supply chain management framework to support and store a comprehensive using a centralized RDF engine.

Dudaš et al. [12] briefed Protégé tool for the ontology visualization. The author proposed various visualization tools using a different classification of ontology visualization methods and accompanied a list of interaction techniques. Augenstein et al. [13] discussed the approach of LODifier to extract information from text through deep semantic analysis with named entity recognition, word sense disambiguation, controlled semantic web vocabularies, due to the massive evolution of textual data existence in textual databases like PubMed. Abulaish et al. [14] explained the methods of phrasing a deep text mining system's processes to automatically identify and extract key phrases from text documents. Chuang and Chien [15] briefed on the clustering-based method to generate topic hierarchies from the segmentation of text documents. Lau et al. [16] discussed encoding the knowledge in a minimal hierarchical structure or a vocabulary with the machine-understandable standard domain ontology extraction. Cali et al. [17] summarized the importance of unifying the classical database constraints with the description logics of ontology language related to the ontological database management system. O'Leary [18] addressed facilitating communication between multiple knowledge bases using artificial intelligence and ontological modeling with knowledge graphs in the explicit use of ontologies for knowledge development.

3 Logistic Data Ecosystem

The architecture discusses the data heterogeneity of logistic stack domain platform, domain functionalities to understand the complexities of data integration and the need for knowledge modeling.

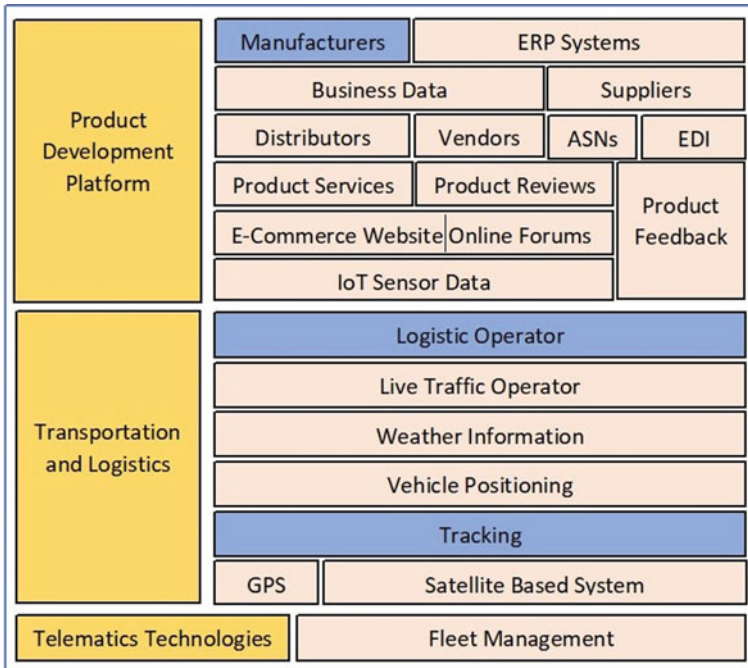


Fig. 1 Data architecture stack for disparate logistic data sources

The data architecture shows the stack of fundamental digital data cap elements—turned across the various information systems used in the logistic management activities, as shown in Fig. 1. This helps as an information base to integrate and reuse by all other applications as a standard model using ontology as a key element. The logistic paper is classified as a product development prototype, telematics technology to monitor the fleet.

Product Development Platforms Requirements

The product platform integrates multiple logistic activity fields generating a massive amount of data from transactional sources and originates from the logistic process connected with the enterprise resource planning system. The platform needs to collaborate and share data among different systems. In the channel of supplier portals, the external data from product reviews, feedback, and environmental data must be integrated to verify information in the supply chain management system. The product delivery tracking and real-time order filling have to be combined with the back-end inventory management information system.

The transportation interlinked with logistic operations receives data from disparate data sources such as live traffic updates, weather information, location data through GPS and satellite-based systems. Logistic decisions require route planning which is implemented through telematics technologies. The different logistic applications that

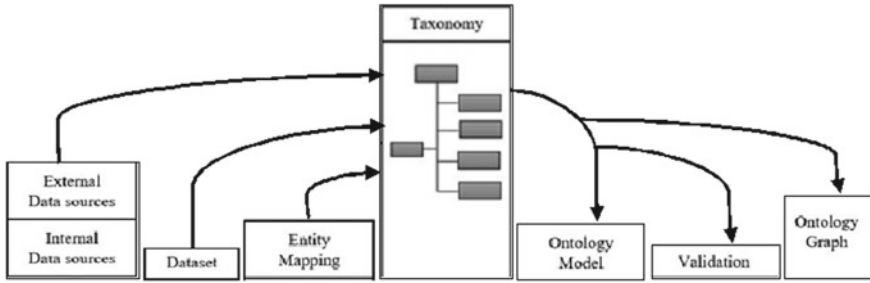


Fig. 2 Prototype knowledge model mapping of shipping

need to communicate with each other suffer from data interoperability due to varied data standardization. The issues in the existing models of data standardization of unstructured, structured, and semi-structured in existing systems are managed using codes like ASN and EDI within internal systems. The issue of data standardization is addressed by representing data.

In machine-readable format, RDF and communication among systems are addressed by designing a knowledge model for a logistic domain for the shipping use case (Fig. 2).

Domain Conceptualization from Unstructured Data

The unstructured data are providing groundbreaking values when data formats are standardized and structured. A vast amount of data are generated in social networks, e-commerce systems, different networking systems, applications, online forums, search engines, web portals, and other smart devices connected to the essential online factors. That helps to generate potential entities, histories with patterns of surveys on business data. Based on these retrievals of concepts from the pool of unstandardized data groups, domain concept is extracted with natural language processing techniques in text mining. NLP techniques are used as middleware for domain concept extraction for knowledge representation. The primary tasks are tokenization, lemmatization, part of speech tagging and term document frequency, named entity recognition. The process of entity extraction through the NLP pipeline is shown in Fig. 3.

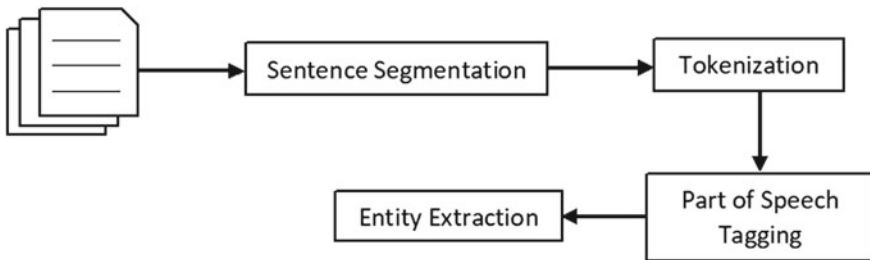


Fig. 3 Entity extraction pre-processing pipeline

NLP Pipeline

The unstructured data are providing groundbreaking values when the formats of data are standardized and structured. A vast amount of data are generated in the social networks, e-commerce systems, different networking systems, applications, online forums, search engines, web portals, and other smart devices connected to the essential online factors. It generates potential entities, histories with patterns of surveys on business data. Based on these retrievals of concepts from the pool of un-standardized data groups, domain concept is extracted using natural language processing techniques in text mining.

Sentence Segmentation

Sentence tokenization (also called sentence segmentation) is dividing a string of written language into its component sentences, and in the proposed design, the sentences are segmented semi-automatically, manually with the help of domain experts or subject engineer.

Part of Speech tagging: POS is the technique to convert the sentence and splits it into word lists and tuple lists. The tag is a part-of-speech tag and signifies whether the word is a noun, adjective, verb. Domain-specific tagging can also be created for a specific domain that serves as knowledge-based by creating a corpus.

Entity extraction: Entity recognition is an important phase for identifying meaningful concepts from unstructured data sources. Text tokens are based on language semantics such as Nouns, Verbs, Conjunctions, Adjectives, and Adverbs. Named Entity Recognition is applied to extract entities from tokens such as name, person, organization, location names, and numeric expressions such as time, data, money, and percentages. Named entity recognition is used to create a domain-specific corpus.

The NLP pipeline is applied to extract entities for knowledge representation in the knowledge modeling process.

4 Methodology: Tabular Data Integration

A methodology is proposed and designed with a generic architecture for the logistic shipping model to integrate the multiple datasets through ontology to model knowledge graph. The knowledge modeling is classified into three phases: taxonomy creation for concept identification, building ontology for knowledge modeling, and validation.

Taxonomy

Taxonomy defines concepts that relate metadata semi-automatically and tags the annotation under specific concepts for enriching consistent vocabulary. The relevant entities from structured data are used to create a taxonomy. The domain concepts (entities) are identified from unstructured data through the text mining process using

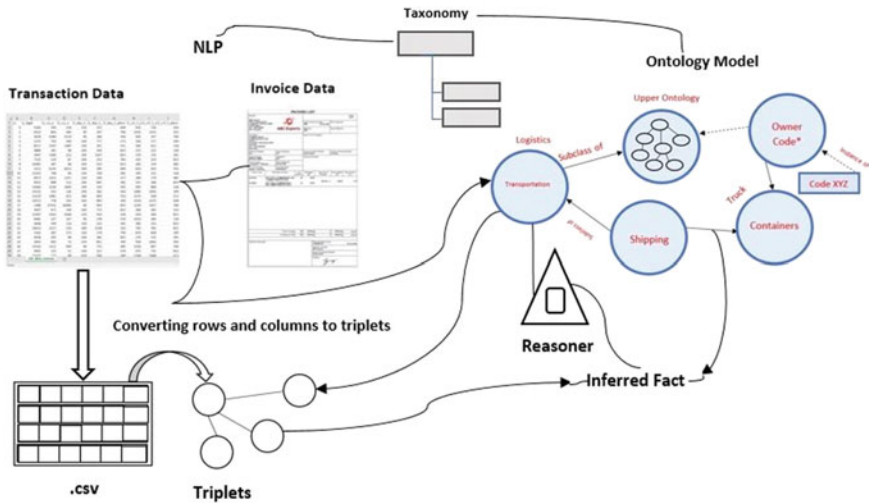


Fig. 4 Generic architecture workflow for tabular data integration

the NLP pipeline to create a related conceptual vocabulary. The identified concepts are represented as term lists with domain-specific consistent tagging in a hierarchical structure for knowledge modeling (Fig. 4).

The Operational difference between IRI and URI

Uniform Resource Identifier (URI) identifies a resource either by location, or a name, or both. A URI has two specialization known as URL and URN. The web links are now referred to a Uniform Resource Locator (URL) or named as Internationalized Resource Identifiers.

Internationalized Resource Identifiers (IRI)

It has several components like host (resource: as name of the organization), sub-domain (reference: sub-group within the host organization), path (reference: directories of the documents on the host), scheme (reference: description to map by the internet to get the document) which includes as http://, query (reference method call: request for the resource to identify with the symbol “?”), query parameters (details of the query—keys and values separated by “=” and “&”, port (connects the host), authentication for the schemes (username & password) and IRI also helps to find the networked resources around the global internet.

Requirements to recognize before creating Ontology

- Create IRI on the following basic schemes to identify the modeled ontology on the web.
- Specify the ontology file and name with a stable format like RDF/XML.
- Add Metadata about the ontology.
- Create a class with preferred IRI.

- Each entity in an ontology should be assigned a separate name and ID. The title should be represented as annotation, values as labels, and IDs are specified with tagging IRIs. Create a class hierarchy with related subclasses and sibling classes. The entity of a class can be an identifier such as URIs.
- Uniform Resource Identifier (URI) defines as globally unique identifiers that identify to map and access the resource.
- An entity of each class is assigned with a unique static URI as a base.
- Each URI identifies a unique concept or an individual.
- The static URI specified will be followed by a separator character (# or /), user-supplied name, and ended with the auto-generated ID.
- The URI reference each class to support machine processing and Interoperability.
- Create Object Property to assert relationship among the individuals (or instances).

Create IRI for Ontology

The ontology creator or publisher should construct the IRI in a semantically meaning pattern to avoid semantic mapping issues of the identifiers and concepts over the web resource, as mentioned in Fig. 5.

Knowledge Modeling: Ontology

Ontology is the integration of data acquisition from the heterogeneous system in multiple formats required to map related concepts of domain and recommended as standards by W3C for knowledge representation and vocabularies helps organize the terms with explicit semantics for reasoning and infer information about associated associations. Ontologies are detailed specifications of conceptualizations [7]. Typically, these information-based specifications identify a taxonomy of the tasks that characterize the knowledge. Ontologies are discourse requirements in the form of a common vocabulary in the context of knowledge-management systems. They can vary depending on the developer and industry. Every consulting firm we have looked at has developed or is developing an ontology. Since enterprise ontologies are so expensive to create and maintain, and since they are continuously evolving,

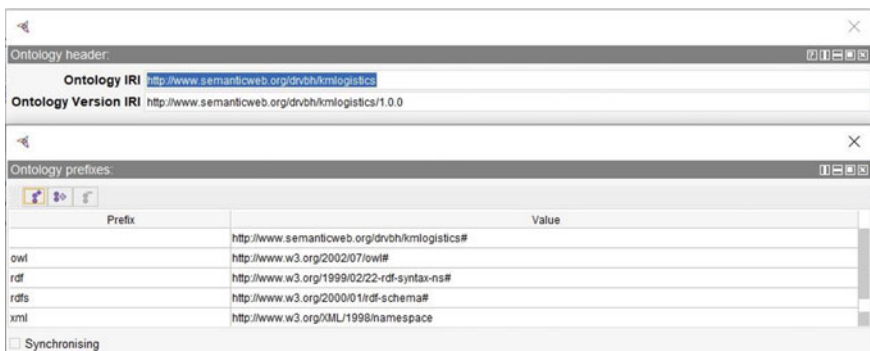


Fig. 5 Naming IRI for an ontology

Table 1 Classes and their properties

Class	Object properties	Data properties
Logistic	hasCarrier, hasContainer	hasFreightforwarders
Shipper	hasService, hasProduct	hasProductTypeAs, BillOfLanding
Transportation	hasShipment, hasTransported	Consignee, hasShipper
Warehouse	hasDistributionCentres	StorageMethod
Goods transport agencies	hasInsurance, isLocatedAt	dateOfIssue, belongstoTaxReturns

ontology or taxonomy issues are emerging as some of the most critical problems in knowledge management [18, 19]. These definitions include classes, subclasses, inheritance, relations, properties, and instances.

Ontology Modeling for Logistic Management System

This section provides an overview of entities involved in the logistic management system. The logistics are the base and main class. All other classes are represented as a subclass. The ontology representation with ontology terminologies is presented as classes, object properties, and data properties. Figure 5 shows the class hierarchy with mapping object property, data property to the logistic class; Table 1 shows the classes and their properties.

Knowledge Representation Language: RDF

The Resource Description Framework (RDF) is a simple triple-based data model (Subject, Predicate, and Object) for interchanging the data over the web with varied data schemas. RDF data represented triplets as a graph-based formalism for defining metadata, as shown in Fig. 7. Individual things are given unique identifiers and XML serialization (RDF/XML) to ease data exchange with various textual representations for ease of human understanding (Fig. 6).

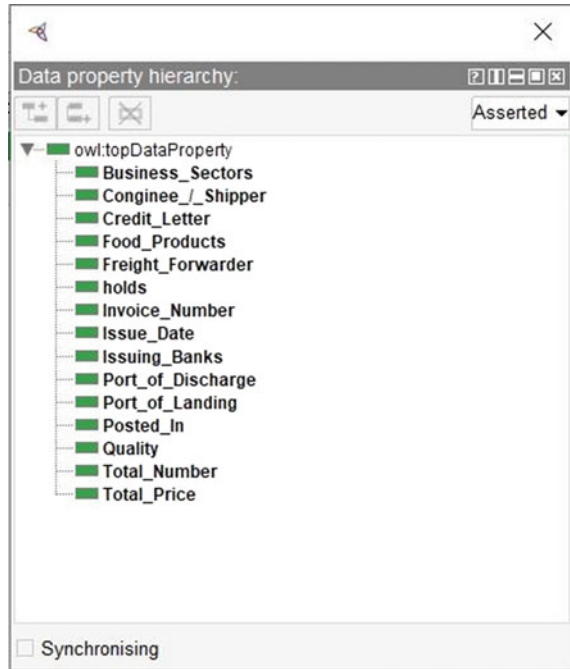
Graph visualization of the relationship between classes, subclasses, and individuals

The logistic information is viewed using graph visualization by using OntoGraf with protégé tool.

RDF Serialization

RDF Serialization is the process of converting the RDF graphs into a machine-readable format. Various RDF serialization formats resolve the overall performance and the scalability issues. The RDF model describes the previous concepts using an abstract syntax. Therefore, RDF data can be written in different ways. Table 2 shows the RDF serialization formats (Figs. 8, 9 and 10).

Fig. 6 Hierarchy of data property



RDF Serialization formats

Different tools to convert RDF data between other serializable formats

There exist many tools online to convert the serialized formats between the RDF. The tools for offline converters are also made online as web services. Others are pure web services to offer conversion between various data formats, as shown in Table 3.

The different RDF translator tools with web services are bidirectional conversion between various RDF data formats like RDFa, Microdata, RDF/XML, Notation 3, N-Triples, RDF/JSON, and JSON-LD.

4.1 Use Case: Knowledge Inference for Logistic Asset Positioning System

The logistic knowledge model aims to develop a logistic asset positioning network, improve the monitoring of the shipping container, provide information in prior as before it impacts the system's unplanned downtime, analyze and identify the issue of product transporting system services. Here, the use case of knowledge inference for logistic asset positioning system depicts the knowledge inference generated through the logistic ontology model, which solves to position the asset in real time to avoid

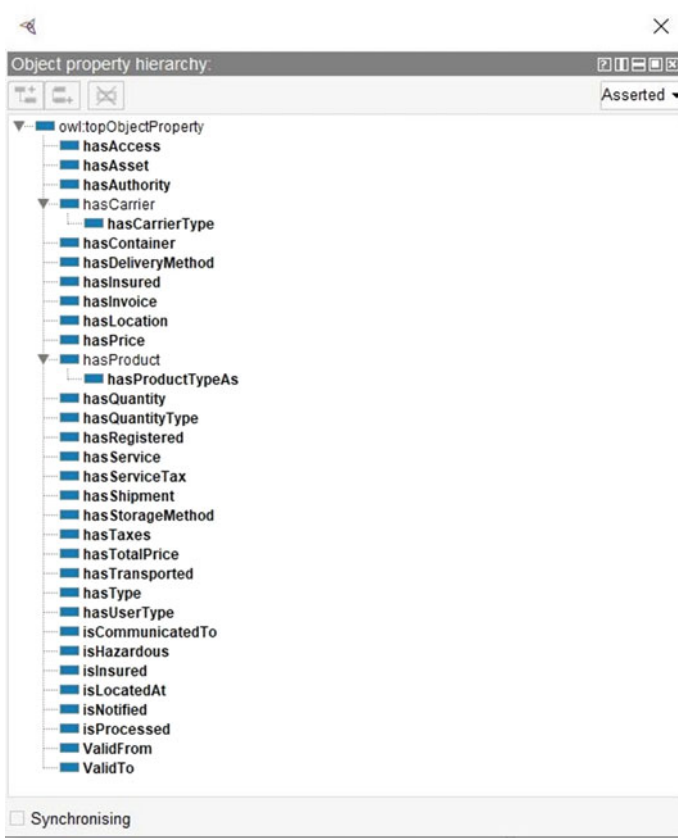


Fig. 7 Hierarchy of object property

Table 2 RDF serialization formats

List of various RDF	Serialization format names
<ul style="list-style-type: none"> • TriG • Tri x • N3 • Turtle • N-Triples • RDF/XML 	<ul style="list-style-type: none"> • BinaryRDF • N-Quads • JSON-LD • RDF/JSON

the delay the product delivery to a customer in time. The inference generated from the model characterized the continuous positioning of assets of specific containers shipped from port v9 to port v8, as mentioned in the figure. The tracking of a container through GPS tagging of the route code to identify actual delay in departure and arrival at destination ports.

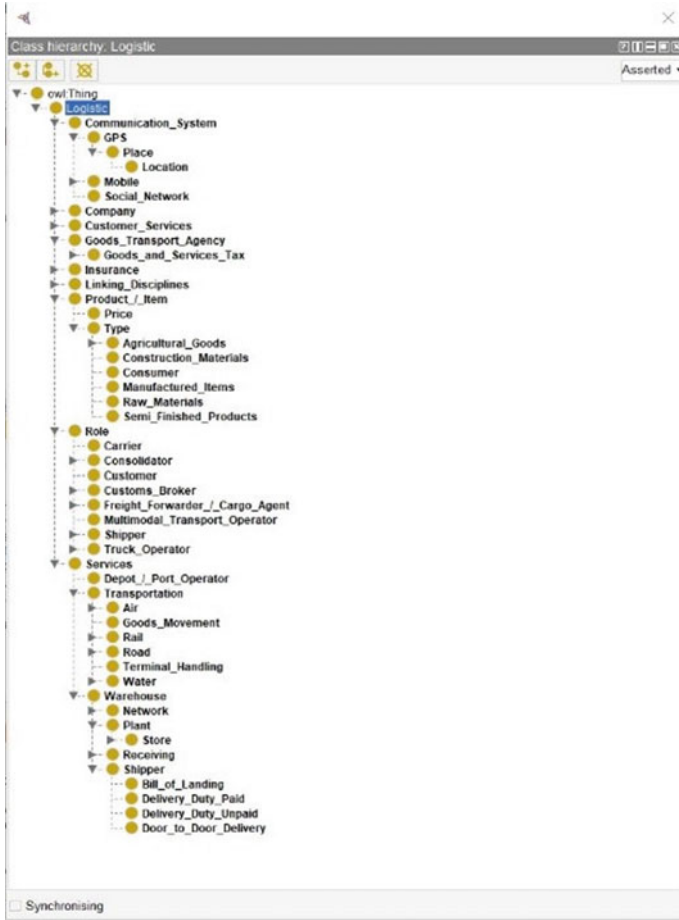


Fig. 8 Class hierarchy of the logistic entities

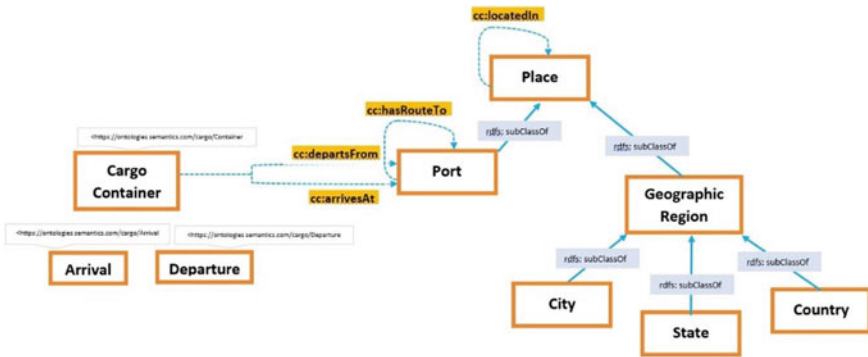


Fig. 9 Transportation knowledge model with unique identifier

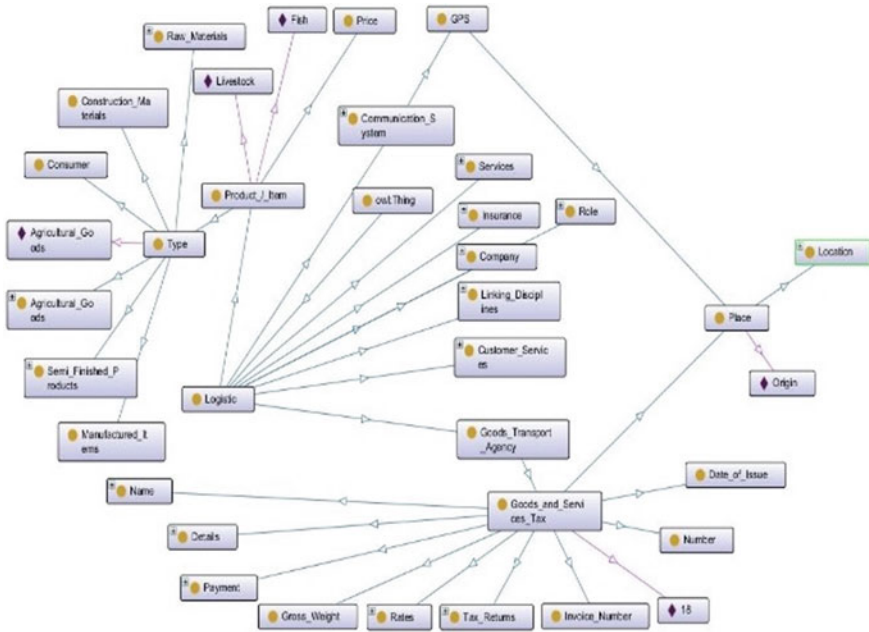


Fig. 10 Graph-based on grouping logistic shipping activities

Table 3 Tools for RDF data serialization

Tools	Services
Any23	REST-Style
Triplr	REST service
RDF distiller	Ruby Gem
Omnidator	Schema.org
RDFa online Parser	Node.js
RDFa Lite 2 RDF Extractor	Node.js
RDF2Microdata	Microdata

The shipping port has several routes with distances. Here, shipping ports are places located in various geographic regions such as city-states and countries or locations. As shown in Fig. 5, the knowledge model depicts different places and locations within other areas. For example, a State belongs to a district which is again a district that belongs to the same state as vice versa. Ontology terminologies are defined as a transitive relationship on validating these main ontology concepts with multiple datasets as an input with ontology to get the inference. The knowledge inference for the model is generated as new related triplets about assets with tagged information to notify as an alert system.

5 Conclusion

In this paper, a generic framework for heterogeneous mapping sources is presented for logistic transportation shipping activities and multiple datasets into RDF as converting all tabular data into triplets and stored in the triple stores. The proposed model integrates the tabular data and provides inference through the ontology model, which validates and checks the incoming triplets with framed constraints using validator engines and reasoners.

Acknowledgements This research paper is supported and funded by DST–ICPS Networked Project.

References

1. Ye Y, Yang D, Jiang Z, Tong L (2008) Ontology-based semantic models for the supply chain management. *Int J Adv Manuf Technol* 37(11–12):1250–1260. <https://doi.org/10.1007/s00170-007-1052-6>
2. Niine T, Koppel O (2015) Logistics systems engineer—interdisciplinary competence model for modern education. *Int J Eng Pedagogy (iJEP)* 5(2):54–54. <https://doi.org/10.3991/ijep.v5i2.4578>
3. Mendes P, Kapanipathi P, Cameron D, Sheth A (2010) Dynamic associative relationships on the linked open data web
4. Seedah DPK, Choubassi C, Leite F (2016) Ontology for querying heterogeneous data sources in freight transportation. *J Comput Civil Eng* 30(4):04015069–04015069. [https://doi.org/10.1061/\(asce\)cp.1943-5487.0000548](https://doi.org/10.1061/(asce)cp.1943-5487.0000548)
5. Arsenio E, Silva S, Iglésias HP, Domingues A (2020) Assessing multimodal mobility trends using heterogeneous data sources: a case study supporting sustainable policy goals within the region of Algarve. *Transp Res Proc* 49:107–118. <https://doi.org/10.1016/j.trpro.2020.09.010>
6. Dimou A (2014) RML: a generic language for integrated RDF mappings of heterogeneous data. In: *Proceedings of the 7th Workshop on Linked Data on the Web* 1184
7. Gruber TR (1993) A translation approach to portable ontology specifications. *Knowl Acquisition* 5(2):199–220. <https://doi.org/10.1006/knac.1993.1008>
8. Zhang H, Guo Y, Li Q (2018) An ontology-guided semantic data integration framework to support integrative data analysis of cancer survival. *BMC Med Inform Decis Mak* 18:41–41
9. Borgi T, Zoghalmi N, Abed M (2017) Big data for transport and logistics: a review. In: *International Conference on Advanced Systems and Electric Technologies (IC_ASET)*
10. Chung SH, Kwon C (2016) Integrated supply chain management for perishable products: dynamics and oligopolistic competition perspectives with application to pharmaceuticals. *Int J Prod Econ* 179, 117–129. <https://doi.org/10.1016/j.ijpe.2016.05.021>
11. Hogan A, Ali W, Saleem M, Yao B, Ngomo ACN (2020) Storage, indexing, query processing, and benchmarking in centralized and distributed RDF engines: a survey <https://doi.org/10.20944/preprints202005.0360.v1>
12. Dudáš M, Lohmann S, Svátek V, Pavlov D (2018) Ontology visualization methods and tools: a survey of state of the art. *Knowl Eng Rev* 33. <https://doi.org/10.1017/s0269888918000073>
13. Augenstein I, Padó S, Rudolph S (2012) LODifier: generating linked data from unstructured text. *Semantic Web: Res Appl* 7295, 210–224. https://doi.org/10.1007/978-3-642-30284-8_21
14. Abulaish M, Jahiruddin Dey L (2011) Deep text mining for automatic keyphrase extraction from text documents. *J Intell Syst* 20(4). <https://doi.org/10.1515/jisys.2011.017>

15. Chuang SL, Chien LF (2005) Taxonomy generation for text segments. *ACM Trans Inf Syst* 23(4):363–396. <https://doi.org/10.1145/1095872.1095873>
16. Lau RYK, Hao JX, Tang M, Zhou X (2007) Towards context-sensitive domain ontology extraction. In: 2007 40th Annual Hawaii International Conference on System Sciences (HICSS'07), pp 60–60. <https://doi.org/10.1109/HICSS.2007.570>
17. Cali' A, Gottlob G, Pieris A (2012) Towards more expressive ontology languages: the query answering problem. *Artif Intell* 193:87–128. <https://doi.org/10.1016/j.artint.2012.08.002>
18. O'leary D (1998) Using AI in knowledge management: knowledge bases and ontologies. *IEEE Intell Syst* 13(3):34–39
19. O'leary D (1997) Impediments in the use of explicit ontologies for KBS development. *Int J Hum Comput Stud* 46(2–3):327–337

Chapter 48

Ordered Pt₃M (M = Early d-Block Metals) Intermetallic Nanocrystals: Synthesis and Electrocatalysis



D. Saritha, N. Mahender Reddy, and Gubbala V. Ramesh

Abstract Ordered intermetallic nanocrystals have demonstrated significantly higher electrocatalytic activity and stability in fuel cell reactions such as cathodic oxygen reduction reaction (ORR) and anodic fuel oxidation reactions when compared to their counter disordered alloy nanocrystals. The improved electrocatalytic behavior may be attributed to definite structural, geometrical, and electronic structures. In this chapter, various Pt₃M (M = early d-block metals, Ti, Nb, Zr, Ta, Y, etc.) intermetallic nanocrystals will be introduced, and their recent developments in synthesis, characterization, and electrocatalytic activity will be discussed. Pt₃Ta intermetallic nanoparticles showed the highest activity in electrooxidation of ethanol by breaking C–C single bond, which was confirmed by in situ IR study. The activity of these materials can be improved further by reducing their sizes in the nanometer range. Finally, recent problems and future proposals are presented. As a result of this study, intermetallic nanoparticles will shed light on the future development of electrocatalysts for fuel cells.

Keywords Order intermetallic nanocrystals · Pt₃Ti · Pt₃Nb · Pt₃Zr · Pt₃Ta · Fuel cell · Small molecule oxidation · Oxygen reduction reaction (ORR)

1 Introduction

Catalytic metal nanoparticles (NPs) have become central for sustainable energy transition technologies because of a broader interest in renewable energies. While the nanocrystals consisting of single metal have been surprisingly effective, they clearly cannot fulfill all the criteria for a certain catalytic application. In addition to high activity and selectiveness, a catalyst should preferably have chemical and structural

D. Saritha · N. M. Reddy · G. V. Ramesh (✉)

Department of Chemistry, Chaitanya Bharathi Institute of Technology (A), Gandipet, Hyderabad, Telangana 500075, India

e-mail: venkataramesh_chm@cbit.ac.in

N. M. Reddy

e-mail: nmahenderreddy_chm@cbit.ac.in

stability [1–9]. The synergy that arises when a second metal is inserted to form bimetallic nanocrystals will theoretically satisfy all those critical criteria. By adding the second metal, the environment of the property would be extended considerably to increase catalytic efficiency and stability unprecedentedly. A significant example is a technique most commonly investigated to enhance Pt's performance against the ORR by incorporating it with other metals such as early and late d-block metals, e.g., Pt₃Ni, Pt₃Cu, Pt₃Mn [10]. It is infelicitous to designate bimetallic nanocrystals by the word “composition,” since their characteristics are extremely susceptible to the existence of the atomical order (i.e., alloy versus intermetallic).^R This disparity can be due to variations in the composition and structure of the crystal, which can influence the strength and effectiveness of the adsorption of chemical species in chemical reactions. In recent years, intermetallic nanocrystals have been subject to active research because of their extraordinary behavior, selectivity and durability against a wide variety of catalytic reactions [11–15]. In comparison, wet chemical synthetic routes are the main route for intermetallic nanocrystals with controlled size, shape and internal structure [16–20].

High power density, high energy transfer efficiencies and environmentally friendly nature made polymer exchange membrane fuel cell (PEMFC) are among the most promising and feasible devices for converting energy. The biggest barrier to commercialization of PEMFC technology is the development of active and stable electrocatalysts. Pt is currently used as an electrocatalytic material in both anodic and cathodic electrodes. The shortage of Pt, as well as its catalytic poisoning nature, precludes the hunt for substitute electrode catalytic materials. Pt alloys can improve both the resistance to poisoning and the catalytic performance of metals such as Co, Ni, Cu, and others, but they induce low catalyst stability due to surface segregation, and the Pt counterpart can easily migrate to the bulk or leach from the alloy during long-term operation [21, 22]. In fuel cells, Pt intermetallic NPs with early d-block metals were developed for stable and active electrodes. Nørskov and colleagues had predicted that in oxygen reduction reaction (ORR), Pt₃Y was more successful than pure Pt on the basis of the oxygen adsorption energy calculations for Pt overlayer on the intermetallics [5]. F. J. DiSalvo research group developed various Pt-based intermetallic NPs with early d-block metals such as Pt₃Ti, Pt₃V, and Pt₃Cr. This chapter provides a detailed discussion of Pt-based intermetallic NPs with early d-block metals.

2 Pt₃Ti Nanocrystals

Pt₃Ti has a Cu₃Au-type crystal structure with a space group of $Pm\bar{3}m$ ($a = 0.3898$ nm). Abe et al. reported the synthesis of Pt₃Ti nanoparticles (NPs) for the first time by co-reduction of cyclooctadienedichloroplatinum (Pt(COD)Cl₂) and titanium(IV) chloride tetrahydrofuran complex (TiCl₄·2THF) in THF solvent with sodium naphthalide (NaC₁₀H₈), which is a strong reducing agent with reduction potential around -2.5 V versus NHE [23]. The as-prepared NPs were in disorder or alloy phase; after annealing at 400 °C the ordered phase had obtained. The average

ordered particle sizes were 37 ± 23 nm. *p*XRD measurements demonstrated the dependence of annealing temperature on the transformation of the disordered to an ordered phase (Fig. 1). Pt₃Ti NPs, both ordered and disordered, showed lower onset potential and CO adsorption affinity for methanol and formic acid than pure Pt, Pt-Ru NPs. For ordered Pt₃Ti intermetallic NPs, disordered alloys Pt₃Ti NPs, and pure Pt, the onset potentials for electrooxidation of methanol were 0.05, 0.04, and 0.4 V, respectively, while the onset potentials for formic acid oxidation were -0.15 , -0.17 , and -0.09 V. However, atomically ordered Pt₃Ti NPs exhibited higher current density than pure Pt, Pt-Ru nanoparticles. Atomically ordered Pt₃Ti intermetallic NPs exhibit a CO-stripping peak at 0.5 V, which is almost similar to alloy Pt₃Ti NPs (Fig. 1). The CO-stripping peak of Pt₃Ti intermetallic NPs is weaker than that of alloy Pt₃Ti NPs and significantly weaker than that of pure Pt or Pt-Ru nanoparticles. Authors inferred that atomically disordered (alloy NPs) and ordered Pt₃Ti intermetallic NPs had significantly lower affinity for CO adsorption than pure Pt or Pt-Ru nanoparticles. Further, the size of the NPs was reduced successfully by KCl-nanoparticle method reported by Cui and coworkers. Ultrasmall Pt₃Ti intermetallic NPs were prepared by co-reduction of Pt precursor (PtCl₄) and Ti precursor (TiCl₄) in the presence of LiCl in THF solvent by potassium triethylborohydride (KEt₃BH) as a reducing agent as shown in the below equation.

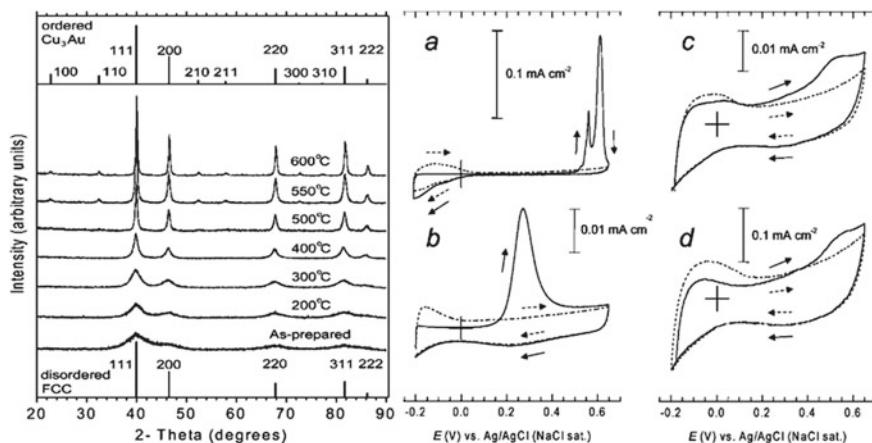
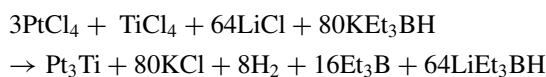


Fig. 1 *p*XRD profiles of vacuum-annealed Pt-Ti NPs at different temperatures. Simulated *p*XRD peaks are marked by solid markers in the lower and top of the figures for disordered FCC-type and ordered AuCu₃-type structures respectively. CO stripping profiles of (a) Pt NPs, (b) Pt-Ru NPs, (c) Pt₃Ti alloy NPs, and (d) Pt₃Ti intermetallic NPs. Full curves represent CO stripping profiles, whereas dashed lines represent before exposure to CO

The by-product KCl is insoluble in THF and encapsulates NPs formed during the synthesis process. Further, it prevents agglomeration during the annealing process by slowing down particle coalescence [24]. The average particle sizes are in the range of 6.1 ± 0.5 nm. Crystalline nature and structural orderity were confirmed by pXRD and HR-TEM. Ultrafine Pt₃Ti/C NPs showed high activity and durability in electrooxidation of methanol.

3 Pt₃Nb Nanocrystals

Gubbala et al. published the first-ever synthesis of Pt₃Nb intermetallic NPs in 2014 [25]. The stability/durability of the electrocatalyst in electrochemical cycles depends on the enthalpy of formation (ΔH_f) of intermetallics. The high value implies the material's high stability; for example, $\Delta H_f = 46.6$ kJ/mol for Pt₃Nb, while $\Delta H_f = 13.6$ kJ/mol for Pt₃Fe. Pt₃Nb NPs was synthesized under Ar-pressurized high-pressure (0.5 MPa) conditions at elevated temperatures. Both the Pt and Nb precursors in dry diglyme were reduced by superhydride at room temperature and after transferred to a stainless-steel pressure vessel. The vessel was heated in an oil bath at 200 °C for 2 h. The as-prepared NPs were Pt–Nb alloy NPs and converted to intermetallic NPs by annealing at 1000 °C under inert atmosphere. The pXRD profiles showed FCC (face-centered cubic) structure (Fm $\bar{3}$ m, $a = 3.93$ Å) similar to Pt crystal structure upto annealing temperature 500 °C. The intermetallic peak at 42.38° appeared when the annealing temperature rises to 600 °C. Perfect intermetallic phase (Cu₃Ti-type, Pmmn, $a = 4.564$ Å, $b = 5.534$ Å, $c = 4.873$ Å) of Pt₃Nb has obtained for the product annealed at 1000 °C (Fig. 2). Photoelectron spectra and TEM analysis have confirmed the formation of Pt₃Nb intermetallic NPs. Nb 3d_{5/2} and 3d_{3/2} peaks appeared at 203.95 and 206.75 eV, respectively, which matched with the bulk Pt₃Nb intermetallic compound. The NP sizes were not uniformly distributed; on average, they were less than 150 nm. Pt₃Nb intermetallic NPs showed better/lower onset potential (−0.1 V) than Pt–Nb alloy NPs (+0.1 V) and commercial Pt NPs (+0.1 V) for electrooxidation of ethanol. Furthermore, across the entire potential spectrum, Pt₃Nb intermetallic NPs exhibit higher current density than Pt–Nb alloy NPs and Pt NPs. Pt NPs showed a strong CO-stripping peak at +0.52 V, while Pt–Nb alloy NPs and Pt₃Nb intermetallic NPs had slightly lower peaks at +0.47 and +0.49 V, respectively. Furthermore, the CO-stripping onset potentials for Pt–Nb alloy NPs (+0.30 V) and Pt₃Nb intermetallic NPs (+0.43 V) are smaller than for Pt NPs (+0.47 V). Pt₃Nb intermetallic NPs and PtNb alloy NPs are more resistant to CO poisoning than Pt NPs. The improved catalytic efficiency of Pt₃Nb NPs can be attributed to changes in the valence electronic structure. The d-band centers in the valence region of Pt NPs (3.33 eV), Pt–Nb alloy NPs (3.70 eV), and Pt₃Nb intermetallic NPs (3.70 eV) were determined by using HX-PES spectra. The d-band center of Pt₃Nb intermetallic NPs was 0.37 eV less than Pt NPs because of the hybridization between Pt and Nb atoms. The adsorption of CO on the Pt₃Nb surface is weakened by the reduction in

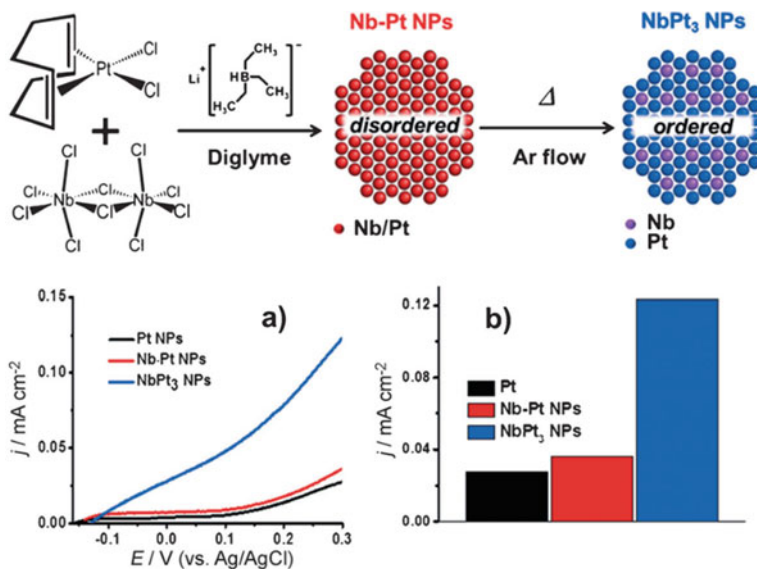


Fig. 2 **a** The synthetic method for Pt₃Nb intermetallic NPs is depicted schematically. **b** The electrocatalytic behavior of Pt₃Nb intermetallic NPs for ethanol electrooxidation was compared to that of Pt–Nb alloy NPs and Pt NPs

the d-band core of Pt₃Nb intermetallic NPs, resulting in tolerance to CO poisoning and electrooxidation activity for ethanol fuel.

4 Pt₃Ta Nanocrystals

Rajesh and coworkers made Pt₃Ta intermetallic NPs by co-reducing Pt and Ta precursors in diglyme solvent for 2 h at 200 °C in an oil bath in an argon atmosphere [26]. The as-prepared Pt–Ta alloy NPs were totally transformed to Pt₃Ta intermetallic NPs by annealing at 1000 °C for 15 h under vacuum. pXRD, HX-PES, and TEM were used to characterize the prepared intermetallic NPs. pXRD spectra of 1000 °C annealed sample is matched with reported crystal structure of Pt₃Ta, which is Pt₃Nb-type, P21/m, $\beta = 100.621$, $a = 4.869$ Å, $b = 5.537$ Å, $c = 9.269$ Å (Fig. 3). Pt₃Ta NPs showed clear emission peaks corresponding to Ta 4f_{7/2} and Ta 4f_{5/2} of Ta (0) at 23.57 eV and 25.47 eV, respectively, which matched with bulk Pt₃Ta. Figure 4a demonstrates a network structure of the prepared Pt₃Ta NPs. The Pt₃Ta NP STEM images and the respective fast Fourier transform (FFT) pattern suggested that the atoms in the Pt₃Ta NPs are in the monoclinical structure Pt₃Nb-type, as anticipated by pXRD (Fig. 4b and c). The Ta-to-Pt atomic ratio in the Pt₃Ta intermetallic NPs was 1:3 which is confirmed by the EDS spectrum analysis. Uniform distributions of Pt (red) and Ta (green) in Pt₃Ta NPs suggested the formation of Pt₃Ta

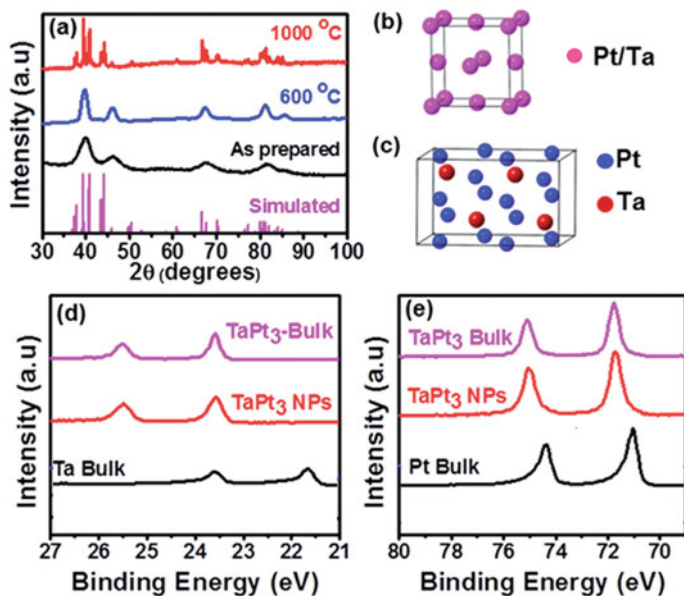


Fig. 3 a pXRD profiles of Pt–Ta NPs annealed at various temperatures. Simulated bulk Pt₃Ta intermetallic pXRD pattern shown at the bottom. **b, c** An atomic arrangement in Pt–Ta alloy and Pt₃Ta intermetallic NPs. **d** HX-PES spectra of Ta and Pt in the binding energy region of 4f for bulk, Pt–Ta alloy NPs and Pt₃Ta intermetallic NPs

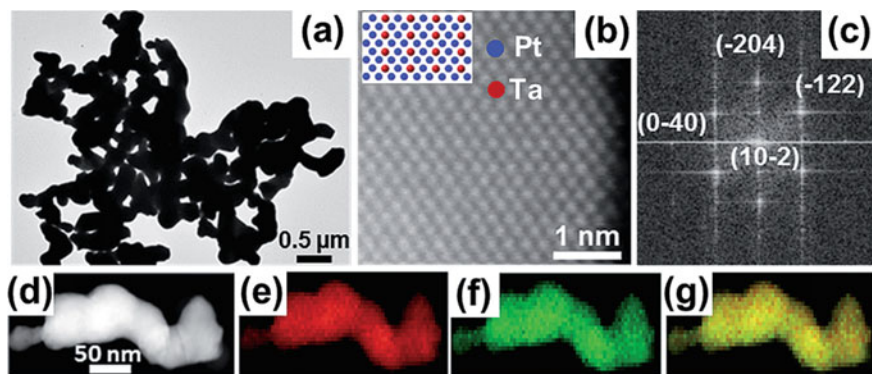


Fig. 4 a Bright-field TEM image of Pt₃Ta intermetallic NPs, **b** high-resolution STEM image of the Pt₃Ta intermetallic NPs. The simulated atomic arrangement of Pt and Ta atoms along (201) zone axis showed in the inset, **c** FFT pattern, **d** dark field image of Pt₃Ta, **e** EDS elemental mapping of Pt, **f** mapping of Ta, and **g** composite mapping of Pt₃Ta intermetallic NPs

intermetallic NPs (Fig. 4d–g). The potential of Pt₃Ta to electrooxidation of ethanol (EOR) was tested and compared with Pt NPs and a state-of-the-art EOR catalyst, carbon-supported Pt₃Sn NPs (Pt₃Sn/C), as well as Pt–Ta alloy NPs. The onset potential of Pt₃Ta (+0.27 V) is 0.17 V less than Pt NPs (+0.44 V). The Pt₃Ta intermetallic NPs showed excellent current density and very low onset potential as compared with commercial Pt₃Sn/C NPs. The probable reason was the formation of Ta–OH from the reaction between oxyphilic Ta and water that can further oxidize the intermediate reactions from alcohols chemisorbed in the adjacent Pt atoms.¹² Pt₃Ta intermetallic NPs effectively broke the C–C bond in the ethanol molecule and efficiently converted ethanol to carbon dioxide (CO₂), as evidenced by in situ infrared reflection–absorption spectroscopy (IRRAS). A range of IRRAS spectrums acquired with increased potential for Pt₃Ta NPs in the range of CO-stretching area. At +0.15 V, an anomaly appeared around 2070 cm⁻¹ due to the formation of CO molecule by C–C bond cleave in ethanol. CO-stretching peak increased upto 0.35 V, while the potential range from 0.40 V to 0.60 V peak was reduced and disappeared, which was due to the full conversion of CO to CO₂.

5 Pt₃Zr Nanocrystals

Currently, the majority of alloy NPs catalytic properties are governed by alloy composition, where the component atoms are dispersed in the FCC-type or FCC-originated crystal systems. Possible catalytic performance control by means of bulk-structure tuning has not been fully explored except for some of the pioneering works [27, 28], while various alloy functionalities like martensitic hardening and shape-memory effects [29, 30] are significantly influenced by the bulk structure. Such rational support could result in enhanced activity and long-term stability in bulk-structural transformation of the alloy NPs, which frequently is mutually exclusive because the bulk structure is not sensitive to surface segregation or contamination, which reduces catalytic/sensory surfaces efficiency. The catalytic efficiency of Pt₃Zr intermetallic NPs was tuned by changing its bulk crystal structure between cubic (c–Pt₃Zr NPs, space group Fm $\bar{3}$ m) and hexagonal (h–Pt₃Zr NPs, space group P63/mmc) (Fig. 5). c–Pt₃Zr NPs were prepared from their organometallic precursors by reduction with superhydride solution in diglyme. The c–Pt₃Zr NPs are converted to h–Pt₃Zr NPs, when the annealed temperature exceeded 900 °C under vacuum for 20 h [31]. HX-PES and the pXRD analysis suggested that the Pt–Zr bonds were stronger in the h–Pt₃Zr NPs than in the c–Pt₃Zr NPs, which resulted in an increase in surface energy in the h–Pt₃Zr NPs. This was further supported by the computational calculations. Indeed, the most stable surface energy of the h–Pt₃Zr NP, 1.47 J m⁻² has been shown to be superior to that of the c–Pt₃Zr NP, 1.34 J m⁻². High energy surfaces of metal NPs have superior catalytic activities as compared with low energy surfaces.

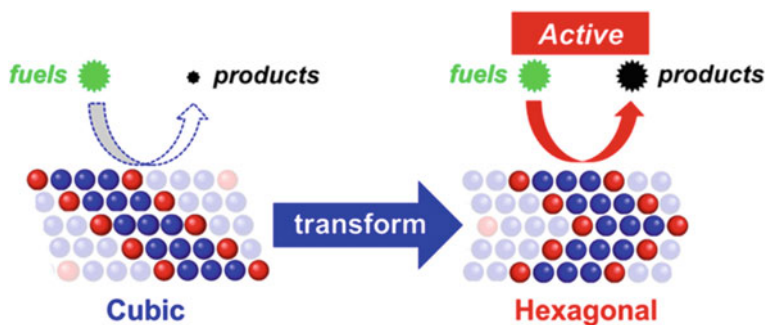


Fig. 5 Schematic representation of the surface activation of fuel oxidation catalysis is a result of the transformation of Pt_3Zr NPs from cubic to hexagonal bulk structures

6 Pt_3Cr Nanocrystals

Cui et al. developed the KCl matrix method with KEt_3BH as the reducing agent and successfully synthesized ordered Pt_3Cr intermetallic NPs with small particle size (5 nm and smaller) [32]. When the annealing temperature and time increase, the formation of ordered intermetallic phases increases. However, sintering of NPs occurs during the annealing process. KCl serves as a matrix to prevent Pt–M NPs agglomeration and coalescence by trapping particles during the annealing process. Pt_3Cr intermetallic NPs outperformed disordered Pt–Cr alloys and Pt/C in terms of activity and durability. A 4-week chemical stability test reveals that there is only minor Cr leaching and that the ordered structure is still preserved. The ordered crystal structure and small particle size of the ordered $\text{Pt}_3\text{Cr}/\text{C}$ can be attributed to its increased activity and longevity.

7 Conclusions and Future Perspective

Intermetallic nanocrystals are a fascinating and active area of study at the interface of materials science, catalysis, and nanotechnology. Intermetallic nanocrystals often outperform their alloy equivalents in terms of activity, selectivity, and longevity for a range of reactions. It has been demonstrated that Pt-based intermetallic NPs with early d-block metals are the best candidates for high catalytic activity, durability, and low Pt-loading electrocatalysts for fuel cell applications. Ultrasmall particles are the fundamental prerequisite for ordered Pt_3M intermetallic NPs for electrocatalytic applications and have received significant research attention in the development, which should also be achieved in engineering terms, particularly in large-scale applications. This chapter outlines the latest developments of anodic (oxidation) and cathodic (reduction) electrocatalytic reactions on Pt_3M intermetallic NPs in fuel cell applications. Pt_3Ta and Pt_3Nb intermetallic NPs are the best catalysts for ethanol

electrooxidation, and Pt₃Ti intermetallic NPs are the best catalysts for methanol and formic acid electrooxidation reactions. The electrochemical behavior and poisoning resistance of Pt₃M NPs were enhanced by their high surface energy and low d-band center. The formation of enthalpy of these intermetallic is very high as compared to late d-block and p-block elements, which is the key explanation for long-term stability in electrochemical cycling. Synthesis and/or crystal face regulated Pt₃M (M = early d-block metals, Ti, Nb, Zr, Ta, Y, etc.) intermetallic NPs are still being investigated, and their use as electrocatalysts opens up a wide range of catalytic applications.

References

1. Imada T, Iida Y, Ueda Y, Chiku M, Higuchi E, Inoue H (2021) Electrochemical toluene hydrogenation using binary platinum-based alloy nanoparticle-loaded carbon catalysts. *Catalysts* 11(3):1–14. <https://doi.org/10.3390/catal11030318>
2. Enache DI et al (2006) Solvent-free oxidation of primary alcohols to aldehydes using Au-Pd/TiO₂ catalyst. *Science* (80) 311(5759). <https://doi.org/10.1126/science.1120560>
3. Stamenkovic VR et al (2007) Improved oxygen reduction activity on Pt₃Ni(111) via increased surface site availability. *Science* (80) 315(5811). <https://doi.org/10.1126/science.1135941>
4. Kowal A et al (2009) Ternary Pt/Rh/SnO₂ electrocatalysts for oxidizing ethanol to CO₂. *Nat Mater* 8(4). <https://doi.org/10.1038/nmat2359>
5. Greeley J et al (2009) Alloys of platinum and early transition metals as oxygen reduction electrocatalysts. *Nat Chem* 1(7). <https://doi.org/10.1038/nchem.367>
6. Lim B et al (2009) Pd-Pt bimetallic nanodendrites with high activity for oxygen reduction. *Science* (80) 324(5932). <https://doi.org/10.1126/science.1170377>
7. Wang C, Markovic NM, Stamenkovic VR (2012) Advanced platinum alloy electrocatalysts for the oxygen reduction reaction. *ACS Catalysis* 2(5). <https://doi.org/10.1021/cs3000792>
8. Van Der Vliet DF et al (2012) Mesoporous thin films as electrocatalysts with tunable composition and surface morphology. *Nat Mater* 11(12). <https://doi.org/10.1038/nmat3457>
9. Strmcnik D et al (2013) Improving the hydrogen oxidation reaction rate by promotion of hydroxyl adsorption. *Nat Chem* 5(4). <https://doi.org/10.1038/nchem.1574>
10. Cui C, Sun M, Zhu X, Han J, Wang H, Ge Q (2020) Oxygen reduction reaction catalyzed by Pt₃M (M = 3d transition metals) supported on o-doped graphene. *Catalysts* 10(2). <https://doi.org/10.3390/catal10020156>
11. Delogu F (2007) The mechanism of chemical disordering in Cu₃Au nanometre-sized systems. *Nanotechnology* 18(23). <https://doi.org/10.1088/0957-4484/18/23/235706>
12. Fedorov PP, Volkov SN (2016) Au–Cu phase diagram. *Russ J Inorg Chem* 61(6). <https://doi.org/10.1134/S0036023616060061>
13. Yu W, Porosoff MD, Chen JG (2012) Review of Pt-based bimetallic catalysis: from model surfaces to supported catalysts. *Chem Rev* 112(11). <https://doi.org/10.1021/cr300096b>
14. Nørskov JK, Bligaard T, Rossmeisl J, Christensen CH (2009) Towards the computational design of solid catalysts. *Nat Chem* 1(1). <https://doi.org/10.1038/nchem.121>
15. Xin H, Holewinski A, Linic S (2012) Predictive structure-reactivity models for rapid screening of Pt-based multimetallic electrocatalysts for the oxygen reduction reaction. *ACS Catal* 2(1). <https://doi.org/10.1021/cs200462f>
16. Zhang H, Jin M, Xia Y (2012) Enhancing the catalytic and electrocatalytic properties of Pt-based catalysts by forming bimetallic nanocrystals with Pd. *Chem Soc Rev* 41(24). <https://doi.org/10.1039/c2cs35173k>

17. Cui C, Gan L, Li HH, Yu SH, Heggen M, Strasser P (2012) Octahedral PtNi nanoparticle catalysts: Exceptional oxygen reduction activity by tuning the alloy particle surface composition. *Nano Lett* 12(11). <https://doi.org/10.1021/nl3032795>
18. Motl NE, Smith AF, Desantis CJ, Skrabalak SE (2014) Engineering plasmonic metal colloids through composition and structural design. *Chem Soc Rev* 43(11). <https://doi.org/10.1039/c3cs60347d>
19. Porter NS, Wu H, Quan Z, Fang J (2013) Shape-control and electrocatalytic activity-enhancement of pt-based bimetallic nanocrystals. *Acc Chem Res* 46(8). <https://doi.org/10.1021/ar3002238>
20. Zhang L, Xie Z, Gong J (2016) Shape-controlled synthesis of Au-Pd bimetallic nanocrystals for catalytic applications. *Chem Soc Rev* 45(14). <https://doi.org/10.1039/c5cs00958h>
21. Xu C et al (2009) Electrodeposited PtCo and PtMn electrocatalysts for methanol and ethanol electrooxidation of direct alcohol fuel cells. *Electrochim Acta* 54(26). <https://doi.org/10.1016/j.electacta.2009.05.088>
22. Alayoglu S, Zavalij P, Eichhorn B, Wang Q, Frenkel AI, Chupas P (2009) Structural and architectural evaluation of bimetallic nanoparticles: a case study of pt-ru core-shell and alloy nanoparticles. *ACS Nano* 3(10). <https://doi.org/10.1021/nn900242v>
23. Abe H, Matsumoto F, Alden LR, Warren SC, Abruña HD, DiSalvo FJ (2008) Electrocatalytic performance of fuel oxidation by Pt₃Ti nanoparticles. *J Am Chem Soc* 130(16):5452–5458. <https://doi.org/10.1021/ja075061c>
24. Cui Z et al (2014) Synthesis of structurally ordered Pt₃Ti and Pt₃V nanoparticles as methanol oxidation catalysts. *J Am Chem Soc* 136(29):10206–10209. <https://doi.org/10.1021/ja504573a>
25. Ramesh GV et al (2014) NbPt₃ intermetallic nanoparticles: highly stable and CO-tolerant electrocatalyst for fuel oxidation. *ChemElectroChem* 1(4):728–732. <https://doi.org/10.1002/celec.201300240>
26. Kodiyath R et al (2015) Promoted C–C bond cleavage over intermetallic TaPt₃ catalyst toward low-temperature energy extraction from ethanol. *Energy Environ Sci* 8(6):1685–1689. <https://doi.org/10.1039/c4ee03746d>
27. Furukawa S, Suga A, Komatsu T (2014) Highly efficient aerobic oxidation of various amines using Pd₃Pb intermetallic compounds as catalysts. *Chem Commun* 50(25). <https://doi.org/10.1039/c4cc00024b>
28. Komatsu T, Takasaki M, Ozawa K, Furukawa S, Muramatsu A (2013) PtCu intermetallic compound supported on alumina active for preferential oxidation of CO in hydrogen. *J Phys Chem C* 117(20). <https://doi.org/10.1021/jp4007729>
29. Sato A, Chishima E, Soma K, Mori T (1982) Shape memory effect in $\gamma \rightleftharpoons \epsilon$ transformation in Fe-30Mn-1Si alloy single crystals. *Acta Metall* 30(6). [https://doi.org/10.1016/0001-6160\(82\)90011-6](https://doi.org/10.1016/0001-6160(82)90011-6)
30. Benafan O, Padula SA, Noebe RD, Sisneros TA, Vaidyanathan R (2012) Role of B19' martensite deformation in stabilizing two-way shape memory behavior in NiTi. *J Appl Phys* 112(9). <https://doi.org/10.1063/1.4764313>
31. Ramesh GV et al (2014) Stimulation of electro-oxidation catalysis by bulk-structural transformation in intermetallic ZrPt₃ nanoparticles. *ACS Appl Mater Interfaces* 6(18):16124–16130. <https://doi.org/10.1021/am504147q>
32. Cui Z, Chen H, Zhou W, Zhao M, Disalvo FJ (2015) Structurally ordered Pt₃Cr as oxygen reduction electrocatalyst: ordering control and origin of enhanced stability. *Chem Mater* 27(21):7538–7545. <https://doi.org/10.1021/acs.chemmater.5b03912>

Chapter 49

Modern Progression in Anode Materials for Lithium-Ion Batteries: Review



Gubbala V. Ramesh, N. Mahendar Reddy, and D. Saritha

Abstract Li-ion batteries are the dynamic energy storage device presently. Li-ion batteries have broadly explored an extensive variety of areas comprising electric, information technology, hybrid vehicles and aerospace. Nanostructure anode materials with superior reversible capacity and constant cycling life are vital for the great performance of Li-ion batteries. Consequently, various new anode materials have been projected as a substitution for graphite in modern years. Nanostructure electrodes have excellent properties including large surface area, small diffusion path and decent dimensional steadiness for Li-ion battery applications. Numerous categorizations of the anode resources including the insertion, alloy and conversion materials are demonstrated coherently. The utilization of the above materials in highly efficient Li-ion batteries for extensive energy storage applications is also emphasized. The current summary focused the latest research on the progress of nanostructured anode materials with impressive performance, excellent rates and excellent cycling perpetuity for the future-generation Li-ion batteries.

Keywords Li-ion batteries · Insertion · Anode · TiO₂

1 Introduction

Extreme exhaustion of fossil fuels and natural assets has produced severe ecological effluence. Fossil fuels including coal, oil and natural gas depletion and environmental issues are key to development in renewable energy storage systems [1]. The progress of battery expertise for extremely proficient energy conversion and storage is significant to overcome the energy and environmental crisis. Progressively severe ecological effluence problems have realized increased research activity regarding novel clean energy sources and effective energy storage and conversion methods. Li-ion batteries are the supreme and proficient devices for electrical energy storage among all the power sources. Li-ion batteries are the foremost effective energy storage devices and

G. V. Ramesh · N. Mahendar Reddy · D. Saritha (✉)

Department of Chemistry, Chaitanya Bharathi Institute of Technology, Hyderabad, Telangana 500075, India

e-mail: dsaritha_chm@cbit.ac.in

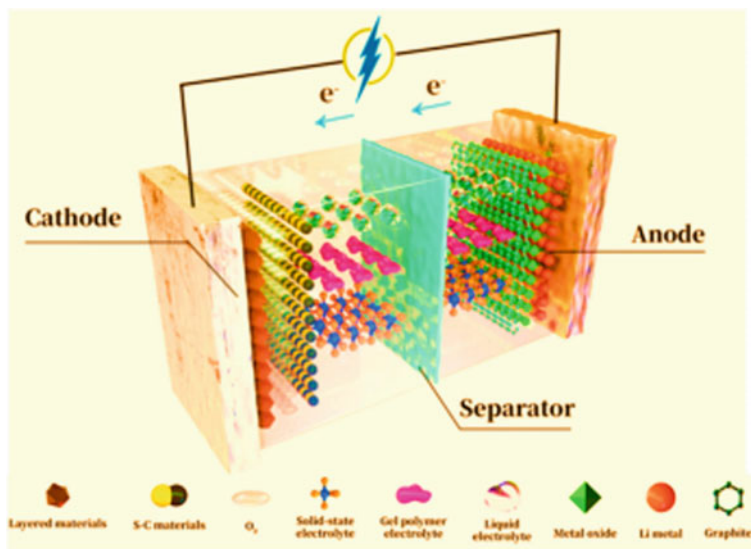


Fig. 1 Graphic description of working mechanism for Li-ion battery with numerous electrode materials [2]

are playing vital roles in contemporary society due to their great energy density, extensive lifetime and ecological openness [1]. The state of Li-ion battery is explicated via the significance of the electrodes. The progress of electrode material and electrolytes are the remarkable criteria for accomplishing higher energy densities in future-generation rechargeable Li-ion batteries. The graphic illustration of a Li-ion battery with various electrodes is shown in Fig. 1 [2].

The anode shows a vital role in the Li-ion battery as the appearances of the anode openly stimulus the battery's electrochemical performance. Material selection, preparation, suitable architectural alteration and design are essential for superior battery performance. The employment of lithium metal as an anode was restricted owing to the formation of dendrites through the reaction. Graphite is the remarkably exploited anode material in Li-ion batteries owing to its prominent parameters such as low working potential, low price and long cycle lifetime. The graphite capacity is 372 mAh/g as it permits the formation of stoichiometric LiC_6 due to the one lithium intercalation for six carbon atoms. Graphite materials have been explored as harmless and ecologically approachable negative electrode material. Low specific capacity and poor rate performance are the limitation of graphite electrodes. Graphite is generally explored as anodes in Li-ion cells due to its theoretical specific capacity. However, its lower working potential at 0.1 V causes the growth of lithium dendrite which raises safety issues and limits the graphite in high power applications [3]. Therefore, here is a tough ultimatum for developing novel anode materials with great reversible capacity and a steady lifecycle. Three sorts of anode materials such as insertion sort, conversion sort and alloy sort are explored in the literature founded

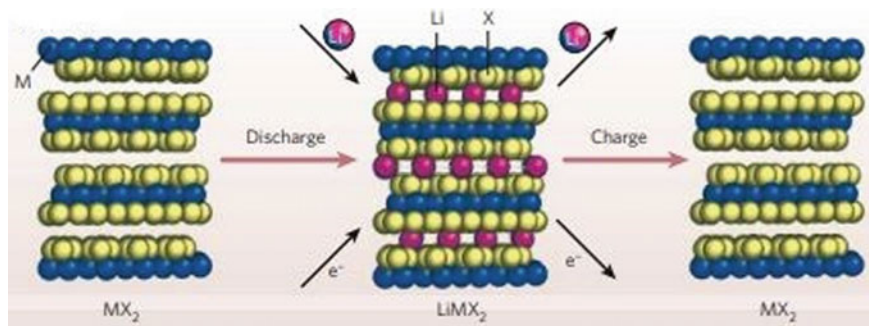


Fig. 2 Graphic sketch of insertion kind of anodes supported on the lithium storage mechanism [6]

on different mechanisms of storing lithium ions for the progress of high-efficiency Li-ion cells [4]. Insertion reaction sorts comprising carbon materials, Li₄Ti₅O₁₂ and various forms of TiO₂, etc., alloying reaction sorts covering Si, Ge, Sn, etc., and conversion reaction sorts like transition metal oxides, sulfides, etc., are observed [5]. The schematic diagram of insertion-kind materials chemical reaction execution is shown in Fig. 2. The retention of structure after complete cycle is distinctly seen from Fig. 2 during insertion mechanism. This review emphasized the insertion-kind materials with few illustrations as anode materials for Li-ion batteries and outlines the modern inclination and strategies to design materials and structures of anode materials toward future-generation rechargeable Li-ion batteries meeting the demands of current society.

2 Insertion-Type Materials

2.1 Graphene

The numerous morphologies of carbon-founded materials are measured as budding anode materials due to their auspicious material characteristics and are familiar as suitable anode materials for Li-ion batteries owing to their accessibility, regularity, low price and decent lithium insertion/deinsertion. Graphene gained attention as of its marvelous possessions and adaptability in chemical, physical, biological and engineering science fields. Graphene comprises sp² carbons in a network of honeycomb and joined into two-dimensional sheets with nanometer thickness. Literary studies advised that lithium ions favor producing clusters compared to the uniform distribution on the graphene surface. The expert specific capacity is 1116 mAh/g owing to the formation of Li₃C₆ compound [7]. If Li is absorbed on both sides and Li is trapped at the benzene rings then the capacity is 1116 mAh/g correspondent to the chemical formula Li₃C₆. The stoichiometric Li₂C₆ is produced since the Li is absorbed on the top of a carbon atom, and some other Li atoms in a primitive unit cell

under a different carbon atom match a specific capacity of 780 mAh/g [8]. Graphene theoretical capacity is 780 mAh/g similar to the chemical formula Li_2C_6 . N- and S-doped graphene with hierarchically porous morphology electrode exhibited great performance with an advanced power density (116 kWkg^{-1}) and energy density (322 Whkg^{-1}) at C rate 80 Ag^{-1} [9]. The estimable electrochemical performances of graphene-founded anode materials are ascribed to their exclusive physical and chemical possessions, immense surface area, great electrical conductivity and extra space for Li-ion storage [10].

2.2 Spinel $\text{Li}_4\text{Ti}_5\text{O}_{12}$

The $\text{Li}_4\text{Ti}_5\text{O}_{12}$ is recognized as distinguished anode material since it is a zero-strain material and the theoretical capacity is 175 mAh/g. Superior rate capability, power density, extended cycle lifespan and consistency are the rewards linked with it [11]. The growth of solid electrolyte interface layer is diminished since the $\text{Li}_4\text{Ti}_5\text{O}_{12}$ works at 1.55 V versus Li^+/Li potential. The structural regularity is decent. $\text{Li}_4\text{Ti}_5\text{O}_{12}$ has a spinel structure and described as $\text{Li}[\text{Li}_{1/3}\text{Ti}_{5/3}]\text{O}_4$. Li exists in completely tetrahedral 8a sites, whereas the 1:5 Li/Ti ratio occupies in the octahedral 16d sites. Still, the oxygen atoms dwell in 32e sites, correspondingly. Lithium and titanium atoms indiscriminately dispersed on one half of the octahedral sites and one-eighth of the tetrahedral sites also filled by lithium atoms inside the oxygen close packed lattice. Reduction of Ti^{4+} to Ti^{3+} happens as lithium is inserted into $\text{Li}_4\text{Ti}_5\text{O}_{12}$ which permits an alteration between $\text{Li}_4\text{Ti}_5\text{O}_{12}$ and $\text{Li}_7\text{Ti}_5\text{O}_{12}$ during discharge. Spinel to a rock salt structure $\text{Li}_7\text{Ti}_5\text{O}_{12}$ alteration takes place through a two-phase reaction mechanism as soon as 3 Li atoms at the 8a sites and peripheral lithium ions also transfer to the vacant 16c sites during Li insertion at 1.55 V (Fig. 3) [11].

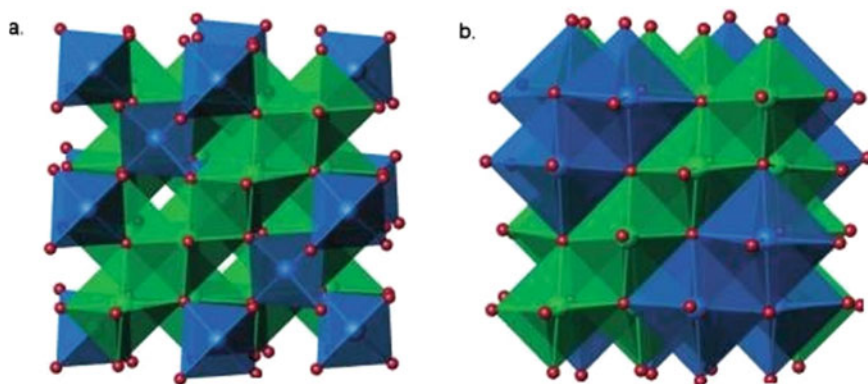


Fig. 3 $\text{Li}_4\text{Ti}_5\text{O}_{12}$ and $\text{Li}_7\text{Ti}_5\text{O}_{12}$ structures without volume variation after charge and discharge [12]

This process reveals admirable Li insertion/extraction reversibility to achieve a 175 mAh/g theoretical capacity. The reduced particle size increased the Li-ion diffusion rate. Heterogeneous nanostructured $\text{Li}_4\text{Ti}_5\text{O}_{12}$ has been effectively employed as anode and confirmed with better rate capability and cycling uniformity. The enhanced conductivity with carbon coating enriched the electrochemical possessions. The displayed capacity is 165 mAh/g with 99% preservation after 100 cycles at 1C rate for 5 wt% C-covered/ $\text{Li}_4\text{Ti}_5\text{O}_{12}$ (100 nm size) [13]. C-covered (1.5–3.0 nm thickness)/ $\text{Li}_4\text{Ti}_5\text{O}_{12}$ (90 nm size) preserved an 80% of capacity at a 60C rate. C-covered (1.0 nm thickness)/ $\text{Li}_4\text{Ti}_5\text{O}_{12}$ (90 nm size) composite boosts the diffusivity of the lithium through the coat. The attained capacity was 136 mAh/g at a 20C rate [14].

$\text{Li}_4\text{Ti}_5\text{O}_{12}$ has been measured as one of the auspicious options owing to its superior characters including a slight volume variation during charge/discharge procedure which permits an extensive and steady cycle lifespan, and a steady potential at 1.55 V versus Li, and prevents the reduction response of electrolyte. Furthermore, $\text{Li}_4\text{Ti}_5\text{O}_{12}$ has an exceptional Li^+ movement, therefore auspicious for battery applications. The $\text{Li}_4\text{Ti}_5\text{O}_{12}$ hollow microspheres prepared via the sol–gel method display an advanced Li storage capacity at greater C rates exclusively. Vast contact area and reduced diffusion length of Li among $\text{Li}_4\text{Ti}_5\text{O}_{12}$ electrode and electrolyte improved together the proficiency of Li^+ , electronic conductivity and the rate capacity. The exhibited specific capacity is 95 mAh/g at a 20C rate for hollow spherical $\text{Li}_4\text{Ti}_5\text{O}_{12}$ [15]. Eventually, the established even capacity is 140 mAh/g at a 2C rate above 500 cycles.

Spinel $\text{Li}_4\text{Ti}_5\text{O}_{12}$ (LTO) is measured as the supreme titanium-centered oxide material for lithium insertion because it displays estimable reversibility of Li-ion at the great working potential of 1.55 V versus Li^+/Li . Spinel $\text{Li}_4\text{Ti}_5\text{O}_{12}$ produces rock salt type $\text{Li}_7\text{Ti}_5\text{O}_{12}$ through the Li insertion. Low conductivity restricts the overall capacity at superior C rates and diminishes the diffusion of Li ions. Two strategies have been explored to overcome these concerns. One option is to boost the LTO electronic conductivity via surface cures, and another remarkable approach is to diminish the particle size to the nanoscale. 20–50 nm size LTO has been prepared via combustion method. The displayed capacity is 170 mAh/g at a 0.5 C rate, while the analogous capacities are 140 and 70 mAh/g at 10C and 100C, correspondingly.

Shen et al. hired a process for LTO nanowire's direct growth on titanium foil. The conductivity of LTO nanowires boosted via the introduction of Ti^{3+} ions through hydrogenation and confirmed via the XPS technique [16]. As-prepared self-supported H-LTO nanowire electrodes have big particular space that support the Li + ion quick transfer. Electronic conductivity is enhanced through hydrogenation by Ti^{3+} states introduction. All nanowires prepared via substrate accelerated electrochemical reaction. Binders or conducting additive material utilization is prevented in this specific electrode architecture. All of these factors impart to the efficient diffusion of Li^+ and e^- in the H-LTO NWA electrode architecture facilitating exceptional rate capability and cycling performance. As attained nanowires comprising Ti foil were explored as electrodes displayed estimable rate performance and displayed capacity is 121 mAh/g at 30C rate (Fig. 4). The better results are connected to the advancement of the hydrogenated-LTO electron conductivity compared to pure one. $\text{Li}_4\text{Ti}_5\text{O}_{12}$ – $\text{Li}_2\text{Ti}_3\text{O}_7$

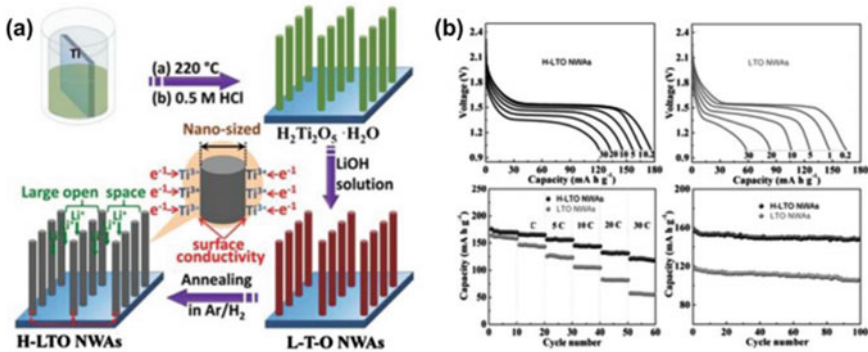


Fig. 4 a Diagram appearance of the assembly of hydrogenated LTO (H-LTO); b Electrochemical performance of H-LTO and LTO nanowires [16]

nanocomposite with lamellar-like morphology demonstrated superb capacity and cycling life [17].

2.3 Titanium Oxides (TiO_2)

Titanium oxides gained grandness in the Li-ion battery as they allow controls of designs. Moreover, they have optimistic properties specifically low toxic behavior, brilliant life span and reduced volume variation (2–3%) together during lithium insertion/deinsertion. Titanium-centered oxide's performance was fundamentally founded on its assembly, morphology and dimension. Advanced capacity preservation, enhanced capacity and extensive life period were accomplished in nanostructured titanium oxides as compared to the bulk materials. Titanium-centered oxides have drawn noteworthy thought as anode resource in Li-ion batteries. Titanium dioxide is explored as an anode in Li-ion battery applications. Titanium dioxide displays admirable protection and steadiness at the operating potential of 1.5 V versus Li^+/Li [18]. TiO_2 has marvelous rewards including high electro-activity, robust oxidation competence, decent chemical steadiness, great accessibility and structural variation. TiO_2 has numerous allotropic variations. Rutile, anatase and brookite are the most eminent forms. Although anatase TiO_2 has been measured in the supreme electroactive form and other allotropes including brookite, rutile is extensively explored for anode determinations [18]. The structure of rutile, anatase and TiO_2 -B is exposed in Fig. 5 [18]. TiO_6 octahedra are joining through edges along the c-direction and the corners are connecting along the ab-planes in rutile TiO_2 [19]. Li insertion is challenging in rutile TiO_2 owing to the difficult Li ions movement into the tetrahedral sites. TiO_2 -B comprises wrinkled sheets of edge and corner sharing TiO_6 polygons [19]. TiO_2 -B structure comprises of TiO_6 polygons connected through edge and corner sharing which supply unidimensional boundless channels and provide the

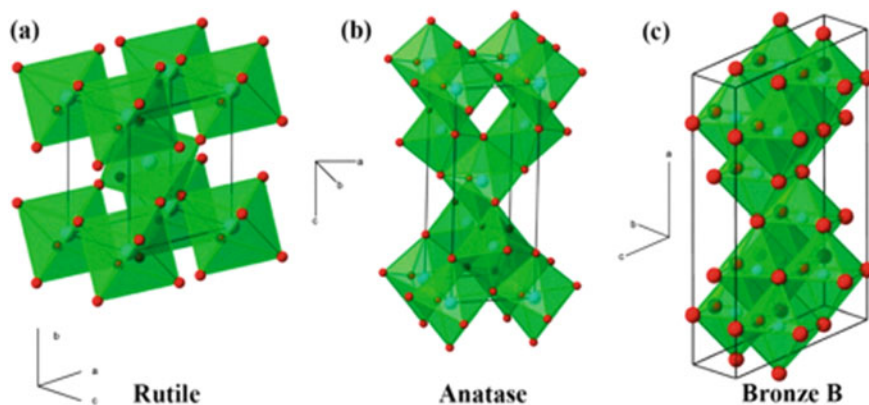
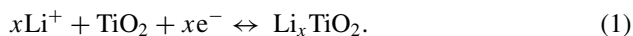


Fig. 5 Schematic outlook of **a** rutile, **b** anatase and **c** bronze B TiO_2 [18]

volume variations during lithium insertion without lattice alteration [19]. Anatase consists of distorted edge sharing TiO_6 octahedra that are built in one-dimensional zigzag chains [19].

Titanium oxide produces a changeable phase composition as a consequence of lithium intercalation.



TiO_2 exhibited a specific capacity of 335 mAh/g as one mole of Li intercalated into the one mole of TiO_2 . Titanium oxide occurs in numerous crystallographic variations comprising rutile, anatase, brookite and bronze structures and is explored as electrodes for Li-ion batteries. The progress is represented by Eq. 1. However, the shape of the discharge curve is varied during the insertion of Li in rutile and the potential variations effortlessly in the sort of 2.5 to 1 V. Fundamentally horizontal plateau remarked at 2 V potential as lithium intercalates into the anatase. Further plateaus are displayed on brookite and bronze structures [20]. To enhance the conductivity of titanium oxides, various morphologies such as nanoflakes, nanowires, nanotubes, hollow nanospheres and nanorods of titanium oxides are explored to enhance the conductivity and to progress the performance. Titanium oxide composites with various elements including carbon, silicon, silver and tin are also studied in the literature as electrode materials [20].

$\text{TiO}_2(\text{B})$ is a good host as electrode material for lithium insertion/extraction. Lithium insertion into TiO_2 occurs at great potential around 1.5 V versus Li^+/Li and offers brilliant protection to the battery. But then, it supplies considerably superior capacity (330 mAh/g) and accomplishing the theoretical capacity is exciting. TiO_2 electrochemical performance is profoundly centered on its morphology, crystal structure and particle dimension. Contemporary outcomes confirmed that regulating the shape and dimension of TiO_2 nanoparticles provides abundant rewards [11]. 40–60 nm diameter $\text{TiO}_2\text{-B}$ nanotubes or nanowires produced from an effortless aqueous

method revealed expressively boosted rate proficiency with advanced capacity (305 mAh/g analogous to $\text{Li}_{0.91}\text{TiO}_2\text{-B}$). Rutile TiO_2 shows that the capacities of the first and 20th cycle are 110 and 50 mAh/g correspondingly [21]. Rutile form of TiO_2 displays a 378 mAh/g capacity at initial discharge and steady capacity of 200 mAh/g above 20 cycles at 0.05 A/g C rate as the particle size reduced to 15 nm. The enhancement of the capacity and the Li-ion acceptance are connected to the nano-size characteristic and extraordinary surface area. 6 nm particle size of TiO_2 anatase retains a superior capacity of 200 mAh/g above 20 cycles at the 0.1 A/g current density [22]. The reduced particle size accelerates the diffusion of Li ions and short path length correspondingly. 12 nm pore size $\text{TiO}_2\text{-B}$ microspheres are prepared by Brown et al. and the displayed capacity is 120 mAh/g at 60C current rate. This enhanced rate performance is connected to fast kinetics. Nanostructures of titania mixed with conductive materials including carbon nanotubes, graphene and carbon improved the power density and cycling life of TiO_2 . The attained specific capacity of $\text{TiO}_2\text{-Graphene}$ composite was 300 mAh/g in the potential variation from 1.0 to 3.0 V versus Li^+/Li [23]. The auspicious results are promising to owe to the morphology of nanotubes and the electronic connections among the hybrid constituents.

2.4 Conclusions

In contemporary areas, numerous new anode materials have been established to replace graphite owing to its difficulty to encounter the necessities of forthcoming high-performance lithium-ion batteries. This review primarily explored the research happenings and accomplishments of insertion kind of anode materials. The significant remarks comprise the precise surface area, structure, alignment and morphology portrayed via the storing capacity of the Li-ion batteries. But then, various discriminates associated with nanostructured materials are side reactions, reduced thermodynamic steadiness and low volumetric energy density. Recently, progressive anode materials were expansively exemplified reliant on their reaction mechanism with the lithium. The instinctive investigation of the intercalation and deintercalation resources that comprise the graphene, spinel $\text{Li}_4\text{Ti}_5\text{O}_{12}$ and titanium oxides (TiO_2) was communicated. Technological accomplishment of these nanostructured electrodes requires basic progress in engineering of materials and building techniques to promote better performance.

References

1. Oh SH, Kwon OH, Kang YC, Kim J, Cho JS (2019) Highly integrated and interconnected CNT hybrid nanofibers decorated with α -iron oxide as freestanding anodes for flexible lithium polymer batteries. *J Mater Chem* 7:12480–12488

2. Kim HJ, Krishna TNV, Zeb K, Rajangam V, Gopi CVVM, Sambasivam S, Raghavendra KVG, Obaidat IMA (2020) Comprehensive review of Li-Ion battery materials and their recycling techniques. *Electronics* 9(7):1161
3. Arico AS, Bruce P, Scrosati B, Tarascon JM, Schalkwijk VW (2005) Nanostructured materials for advanced energy conversion and storage devices. *Nat Mater* 4:366–377
4. Saritha D (2019) A concise review on the advancement of anode materials for Li-ion batteries. *Mater Today Proc* 19:726–730
5. Lu J, Chen Z, Pan F, Cui Y, Amine K (2018) High-performance anode materials for rechargeable lithium-ion batteries. *Electrochem Energy Rev* 1:35–53
6. Armand M, Tarascon JM (2008) Building better batteries. *Nature* 451:652–657
7. Yoo E, Kim J, Hosono E, Zhou H, Kudo T, Honma I (2008) Large reversible Li storage of graphene nanosheet families for use in rechargeable lithium ion batteries. *Nano Lett* 8(8):2277–2282
8. Medeiros PVC, Mota FD, Mascarenhas AJS, de Castilho CMC (2010) Adsorption of monovalent metal atoms on graphene: a theoretical approach. *Nanotechnology* 21(11):115701
9. Wang ZL, Xu D, Wang HG, Wu Z, Zhang X (2013) In-situ fabrication of porous graphene electrodes for high performance energy storage. *ACS Nano* 7(3):2422–2430
10. Zhong M, Yan J, Wu H, Shen W, Zhang J, Yu C, Li L, Hao Q, Gao F, Tian Y, Huang Y, Guo S (2020) Multilayer graphene spheres generated from anthracite and semi-coke as anode materials for lithium-ion batteries. *Fuel Process Technol* 198:106241
11. Amine K, Belharouak I, Chen Z et al (2010) Nanostructured anode material for high-power battery system in electric vehicles. *Adv Mater* 22:3052–3057
12. Sorensen EM, Barry SJ, Jung HK, Rondinelli JR, Vaughey JT, Poeppelmeier KR (2006) *Chem Mater* 18:482–489
13. Jung HG, Myung ST, Yoon CS et al (2011) Microscale spherical carbon-coated $\text{Li}_4\text{Ti}_5\text{O}_{12}$ as ultra high power anode material for lithium batteries. *Energy Environ Sci* 4:1345–1351
14. Li B, Han C, He YB et al (2012) Facile synthesis of $\text{Li}_4\text{Ti}_5\text{O}_{12}/\text{C}$ composite with super rate performance. *Energy Environ Sci* 5:9595–9602
15. Huang J, Jiang Z (2008) The synthesis of hollow spherical $\text{Li}_4\text{Ti}_5\text{O}_{12}$ by macroemulsion method and its application in Li-Ion batteries. *Electrochem Solid State Lett* 11:A116–A118
16. Shen L, Uchaker E, Zhang X, Cao G (2012) Hydrogenated $\text{Li}_4\text{Ti}_5\text{O}_{12}$ nanowire arrays for high rate lithium ion batteries. *Adv Mater* 24(48):6502–6506
17. Zhu G-N, Chen L, Wang Y-G, Wang C-X, Che R-C, Xia Y-Y (2013) Binary $\text{Li}_4\text{Ti}_5\text{O}_{12}$ - $\text{Li}_2\text{Ti}_3\text{O}_7$ nanocomposite as an anode material for li-ion batteries. *Adv Funct Mater* 23(5):640–647
18. Yang Z, Choi D, Kerisit S, Rosso KM, Wang D, Zhang J, Graff G, Liu J (2009) Nanostructures and lithium electrochemical reactivity of lithium titanites and titanium oxides: a review. *J Power Sour* 192:588–598
19. Madian M, Eychmüller A, Giebeler L (2018) Current advances in TiO_2 -based nanostructure electrodes for high performance lithium ion batteries. *MDPI* 4(7):1–36
20. Kulova TL (2013) New electrode materials for lithium-ion batteries. *Russ J Electrochem* 49(1):1–25
21. Aricò AS, Bruce P, Scrosati B et al (2005) Nanostructured materials for advanced energy conversion and storage devices. *Nat Mater* 4:366–377
22. Rai AK, Anh LT, Gim J, Mathew V, Kang J, Paul BJ, Song J, Kim (2013) Simple synthesis and particle size effects of TiO_2 nanoparticle anodes for rechargeable lithium ion batteries. *J Electrochim Acta* 90:112–118
23. Wang J, Zhou Y, Xiong B, Zhao Y, Huang X, Shao Z (2013) Fast lithium-ion insertion of TiO_2 nanotube and graphene composites. *Electrochim Acta* 88:847–857

Chapter 50

Experimental Investigation of Sliding Wear Characteristics on Aluminium-Based Metal Reinforced with SiC, Al₂O₃ and Cadmium Sulphide



Sachin Pande, Ravindra G. Tikotkar, Asifiqbal M. Doddamani, and Syed Sameer Hussain

Abstract Aluminium oxide- and silicon carbide-alloyed MMC is an exceptionally helpful engineering MMC because of its high strength, structure, flexibility and great protection from wear. In this experimental study, the dry sliding wear pattern of hybrid aluminium composite is tested. An alloy of aluminium oxide, silicon carbide and cadmium sulphide along with other materials in a small percentage is used to strengthen the base aluminium (Al 1100); in order to prepare a basic or similar version of AA6061 T9 Al₂O₃/SiC/CdS, Mn composite metal matrix by using the stir casting process [ASM handbook in Properties and selection: nonferrous alloys and special-purpose materials. ASM International, Materials Park, Ohio, 1990, Tikotkar et al. in Int J Mech Automob Eng 1:2009, 2008], various parameters of a pin-on-disc apparatus are discussed in detail and further few more tests related to structure will be carried out. This experimentation shows the effect of load on sliding speed. This type of hybrid is the base aluminium with CdS in nanoparticles that were never tested, and cadmium bears good lubrication properties, which will help in reducing wear on material, and it is useful in applications such as cams, gears and pistons and journal bearing a feature of self-lubrication or at least reduced wear to study the decrease in wear rate in the newly fabricated composite is indicated. Further, the results obtained are validated by conducting confirmation test and errors detected will be kept minimum, below 9%. Wear attributes of aluminium MMC under various operational test scenarios were observed on the test rig apparatus by considering various loads from 4 N to 70N simultaneously by considering the sliding speeds of 0.50 up to 10.00 m per second, where constant sliding of 20,000 m was taken. Wear was seen as basically abrasive followed by oxidative.

S. Pande (✉) · A. M. Doddamani
B.L.D.E.A's V.P, P.G.H College of Engineering and Technology (SECAB.I.E.T), Vijayapur,
Karnataka, India

R. G. Tikotkar
Department of Mechanical Engineering, B.L.D.E.A's V.P, P.G.H College of Engineering and
Technology, Vijayapur, Karnataka, India

S. S. Hussain
SECAB Institute Engineering and Technology (SECAB.I.E.T), Vijayapur, Karnataka, India

Keywords Al 1100/SiC/Al₂O₃/CdS · Wear resistant with lubrication · Hybrid alloy composite · Load carrying · Action mechanics

1 Introduction

Since decades, Aluminium alloys have been used as an excellent alternative for steel. The conventional Al MMC alloys possess impeccable features and properties related to strength and wear properties. The alloying and mixing of other material to aluminium composite/MMC allow attaining good hardness and anti-wearing characteristics that have low density and malleability resulting in an exceptionally and dimensionally stable material with versatile applications ranging from engine components to spacecraft components. The researchers Niranjan and Lakshminarayanan showed that wear response of TiB₂-alloyed aluminium composite resulted in an increase in wear with the increase in particle size and sliding distance [1, 2]. Niranjan and Lakshminarayanan studied wear behaviour of TiB₂-reinforced aluminium composites and observed improved and enhanced wear features of Al/TiB₂, and this further with other organic/inorganic composition is tried in the present paper considering the best results in reducing wear due to the presence of cadmium compound and simultaneously considering the environmental and human safety.

The wearing process leading to material removal is observed in geared transmissions, follower and cam arrangement, piston, clutches and others where we can see the sliding of two parts. In these cases, the wear characteristics of aluminium alloy become meticulously critical. Sahin work on result of wearing characteristics of aluminium matrix using silicon carbide particles and the output shows a lesser rate of wearing as compared with conventional nonalloyed aluminium [3, 4], at the same time focusing on improvising the lubrication properties as mentioned in the similar research carried out by Jianqiang [5].

2 Literature Survey

Authors Jianqiang and Huanqin carried out various experiments to investigate the tribological properties and effects of organic cadmium composition in lubrication [5]. During this experimentation, an oil affinity-based cadmium composition was prepared and its effect was studied using a four-ball test rig and its result was compared with some standard additives, and the results showed that it exhibits far better antiwear and load carrying capacity than convention lubricants or base oil. Now, in the present analysis the same element, i.e. cadmium sulphide, is used in a very small percentage in the range of 0.3–0.5% in matrix form and a similar result is evaluated, i.e. improvement in load carrying capacity along with the reduction in wear.

Classification	Wear mechanism	Coefficient of wear 'K' (range)
Wear occurring by mechanical behaviour of composition	<ol style="list-style-type: none"> 1. Sharpness deformation and removal 2. Wear affected by plowing 3. Delimitation wear 4. Adhesive wear 5. Abrasive wear 6. Fretting wear 7. Wear by solid particle impingement 	10^{-4}
Wear due to chemical behaviour of materials	<ol style="list-style-type: none"> 1. Solution wear 2. Oxidation wear 3. Diffusion wear 4. Wear by melting of the surface 5. Layer 6. Adhesive wear at high temperature 	—

Nevillea et al.'s priority in this paper was concerned towards environment, and they synthesize a component or a lubricant that had little or no harm towards the environment, at the same time quality of performance is not compromised, and cost factor is considered [1], and in this paper, a study of the current situation in the form of application of modern material or treatments to mating surface in the form of coating on wear-effected parts like IC engine is analysed, and results from the experiment showed enhanced tribological features and effects on tribofilm and tribological reaction showing the synergies and antagonisms. This study mainly focused on engine components, especially piston ring.

Gurpreet Singh and Sanjeev Goyal synthesized a new MMC with the aim of fabricating an alloy having enhanced hardness, refractoriness, strength, less dense and better resistance to corrosion. The MMC was fabricated using stir casting technique. The compositions were altered for comparative studies, and further, the testing and experimentation were carried out on a pin-on-disc set-up at normal temperature using a response of top-layer method. The author considered five parameters for the research work, namely % reinforce, sliding speed, load, temperature and sliding distance, and the authors were able to conclude that the new MMC exhibits superior performance.

3 Objective of the Proposed Work

The present study concentrates on sliding wear characteristics of aluminium-based metal reinforced with SiC, Al₂O₃ and cadmium sulphide [5] in nano-particulate form along with other compositions, namely zinc, nickel, magnesium, copper and manganese, with a view of enhancing mechanical, chemical and thermal properties and through experimental study of different graphs obtained considering the variables

such as applied load, speed and time [6, 7]. The following study parameters are focused:

- Study the hardenability of material after wear.
- Study the wear mechanism of composite after wear.
- Plot the wear map for composite.

4 Study Area and Methodology

The experimentation is being conducted on equipment known as a pin-on-disc thick-plate apparatus, and at the same time, the frictional monitor is connected to PC with all necessary preinstalled software supplied from DUCOM India Ltd., basically a tribometer that will be used as test rig. The process of specimen preparation was started by first procuring base Al 1100, heating a fresh crucible and melting it at 800 °C, then the preheated mixtures, namely aluminium oxide, silicon carbide, and cadmium sulphide, at 200 °C were gradually added in a vortex-type stir casting set-up until uniform distribution occurs, and the stirring rate was maintained at approximately 350 rpm. Mn was added basically to improve wettability of composition with base aluminium. This composition was poured into moulds to obtain slabs of roughly 9 kg weight; these slabs were machined first on milling machine and later on lathe to obtain standard specimens. The specimen for pin on disc is of 25 mm length with 10 mm diameter which slides on the flat surface of the disc of 165 mm diameter and 8 mm thickness (Fig. 4b). Another for abrasion test is rectangular in shape with dimension 76.2 × 25.4 × 12.7 as per ASTM G-99, and it was tested using abrasion test rig as shown in Fig. 1. The wear volume of the pin specimen was determined from weight loss measurements by considering the density.

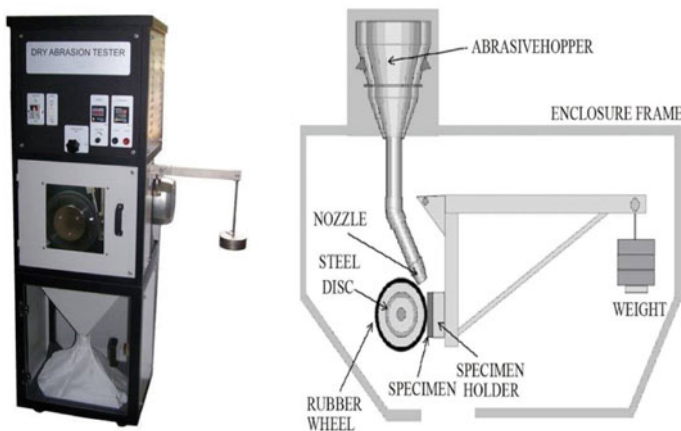


Fig. 1 Schematic view of set-up for abrasion test rig

5 Experimentation

The base material used is aluminium slab containing 99% of aluminium with other metals such as iron, copper, silicon, zinc, manganese and other residual forms [1]. The process of preparation of specimen was initiated by procuring the base aluminium (Al 1100) slabs obtained from M/S NDC Industry, Peenya Industrial Area, Bengaluru. Then, the process of alloying was done in M/S SVT Foundry Works, Bengaluru, at the appropriate temperature, making sure that the higher melting point elements, i.e. Al_2O_3 and SiC, are effectively alloyed to form the desired MMC with necessary structure.

5.1 Synthesis and Composition of Material

To obtain a component with properties mentioned in objective section, the specimen is synthesized in aluminium foundry, it is meticulous process to identify suitable composition, and hence, it is considered under experimentation. The metal matrix is synthesized by effectively dispersing and strengthening the base metal. The major task was to effectively blend the other materials such as Al_2O_3 , CdS and SiC to base aluminium so that necessary quality of composite is obtained [3]. The alloying of SiC, Al_2O_3 and cadmium sulphide in nano-form was carried out explained in the following (Fig. 2).

The aluminium ingots were cleaned and placed in stir casting set-up, shown in Fig. 3, where it was heated to superheating temperature of 755°C and then transferred to a three-phase electric furnace, SiC, CdS and Al_2O_3 were added by stirring intermittently at a gap of six to seven minutes, and borax powder was added to improve wettability of alloying particles. The final compositions obtained are represented in Tables 1 and 2 and shown in Fig. 3.

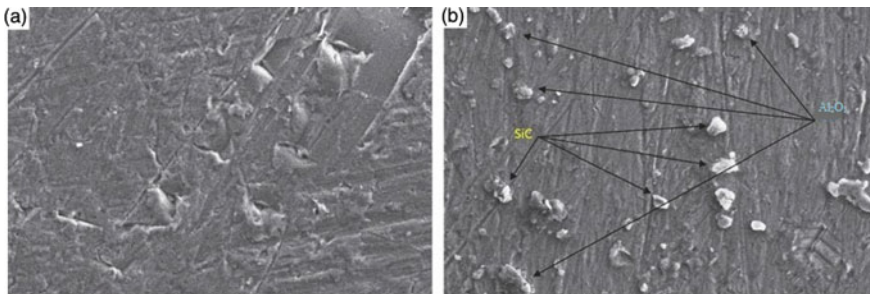


Fig. 2 SEM micrograph 31.40% of SiC and Al_2O_3 -reinforced hybrid composite

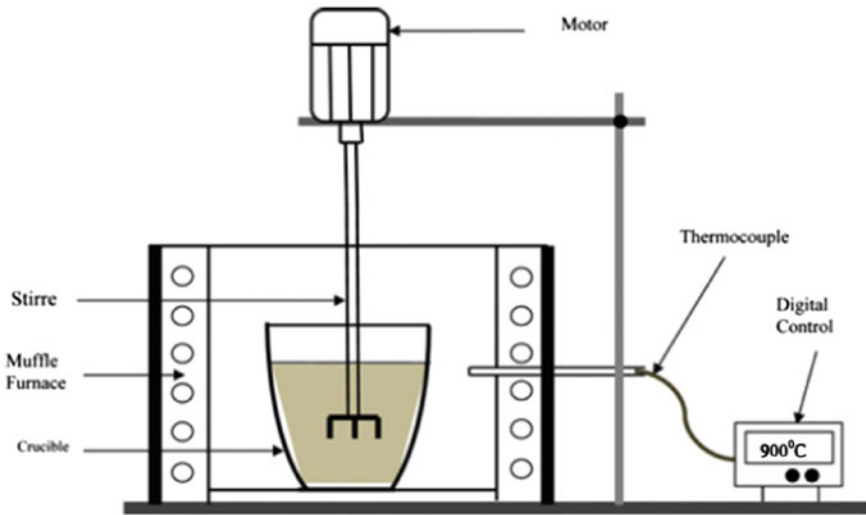


Fig. 3 Schematic view of set-up for stir casting

Table 1 Composition of test specimen of Al 1100 in percentage weight

Element	Al ₂ O ₃	Silicon carbide composition			CdS	Zn	Ni	Others
		Total carbon as 'C'	Metallic silicon as 'Si'	Si + C				
Weight %	0.92	0.05	31.05	31.40	0.019	0.25	0.024	Al

Table 2 Details of SiC in particulate and composite form

Reinforcement	Average particle size (nm)	Density (g/cm ³)	Melting point °C	Hardness (Kg/mm ²)
Total carbon as 'C'	40–75	2.26	3550	3000
Metallic silicon as 'Si'	30–50	3.30	2750	2900
Si + C	30–75	3.50	3660	3000

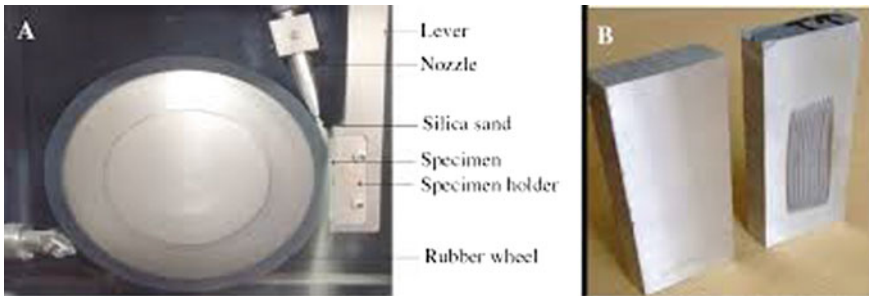


Fig. 4 Abrasion wear test rig and specimen

5.2 Specimen Dimension

After solidification and cooling of metal matrix composite, it was taken out in the form of small slabs and then machined to desired size as per standard specimens, one used in abrasion test and other used at room temperature upon a pin-on-disc set-up as shown in Fig. 4, the metal matrix was synthesized by evenly alloying and strengthening the base metal matrix [9], and these are generally prepared by powder metallurgy and casting techniques. There exist various difficulties in casting process, and yet obtaining a consistent mixture of even distribution of composites is one of many challenges effecting the performance quality and properties of composite matrix [10].

This composite of metals in base aluminium was characterized by high strength, sturdiness along with stiffness and also thermal stability, having corrosion as well wear resistance, and better life under fatigue conditions was achieved in this MMC [11].

Once the desired MMC was obtained, the same was machined on milling machine to make sure that the properties of metal are not altered, and basically, two types of specimen were prepared, one rectangular specimen and another specimen for pin on disc of dimensions 10 mm diameter with 25 mm length as shown in Fig. 5a. These will be used in two different test rigs as mentioned: one is pin on disc and other the abrasion test rig that uses sand as an abrasion material.

Tests were made upon a pin-on-disc set-up along with friction monitor test rig shown in Fig. 5 and the disc shown in Fig. 6 which causes the pin to lose its weight due to wearing caused by weights, i.e. 4.91, 9.81, 39.24 and 68.67 N, along with the speed of slide varying from a minimum value of 0.50 up to 8.0 m/s, leading to loss in weight of pin specimen, and the same was estimated in grams by an electronic balance.

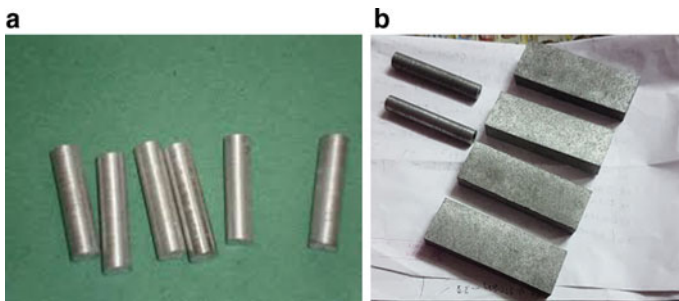


Fig. 5 a Pin-on-disc specimen. b Abrasive wear specimen

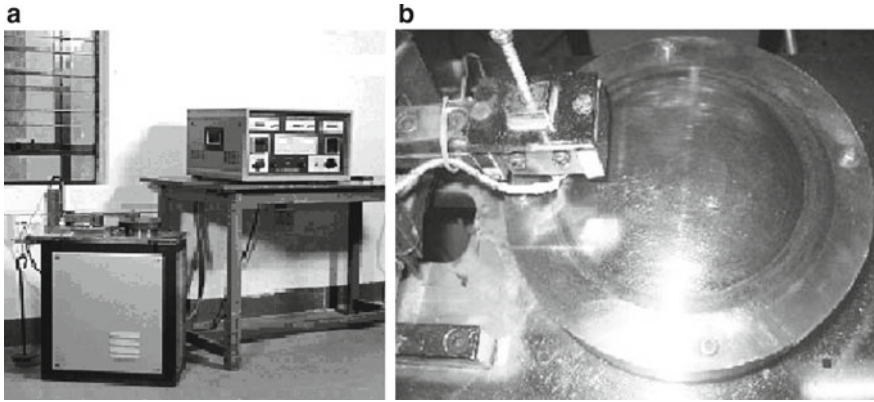


Fig. 6 a Wear testing m/c. b Disc driving the pin

6 Results and Discussion

The experimentations were completed with a pin-on-plate wear testing machine with a constant slide parameter of 21,000 m (distance). Figure 7a represents the impacts of wearing load on frictional powers for the diverse sliding rates, and the equivalent is expanded legitimately along with applied wear pressure for various numbers of sliding rates [12, 13].

Figure 7b represents the impacts of a sliding speed on frictional powers created due to the expansion in wear pressure. The generalized pattern shows that frictional

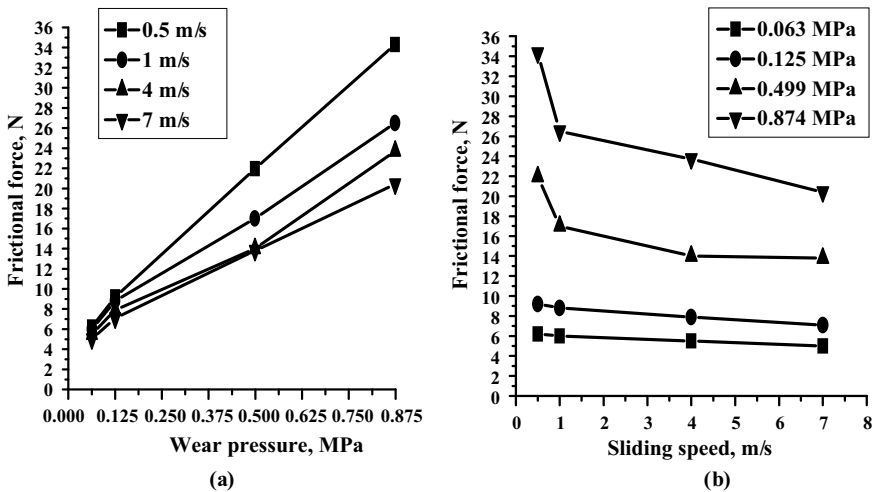


Fig. 7 a, b The effect on wear pressure on frictional force and speed of sliding

powers are diminished with the sliding velocities due to various wear tensions and comparing rates change straightforwardly with the wear pressure.

The power due to frictional force created during sliding is decreased consistently with sliding rates as shown in Fig. 7a, b, because of action mechanics and the frictional warming subsequently relaxing the wearing surface [4, 11]. The sliding due to high wear pressures produces high frictional temperatures [5]. The relating estimation of $\ln(m) \div \ln(t)$ turns out to be about equivalent to 0.5 and consequently affirms to oxidizing wear feature.

Most types of wear are the consequence of occasions happening at severity contacts. Wear coefficient or Archard coefficient is used to depict the particular wear rate ' k ' by Stachowiak and Batchlor [7] communicated as the proportion of wear volume (V) to the heap acting (W) and sliding-type separation (L). $k = V/W * L$, m^3/Nm .

It is obvious from graphical representation given in the following that the particular value ' k ' that is rate of wear has an estimation of 10^{-16} m^3/Nm or less as 10^{-17} or 10^{-18} m^3/Nm , which shows that the material has a great wear opposition property.

It is observed that a small welding action forms due to wearing and rubbing action and as the sliding reduces, so will be the reduction in this weld action, and that it is caused mainly due to the presence of CdS particle; thus, it also diminishes the wear rate.

It is seen that the rate of wear is marginally higher with a small speed of 0.4 m/s as compared with double sliding speed and the forces in terms of weight are in the range of 4.90 N and 9.90 N represented in graphs, and the wear features are viewed in Fig. 8a, b.

The wear rate is increasing due to the rough wear system. Under low sliding velocity and high burden, the development of miniaturized weld with the circle is observed, and also, the grating wear is described by profound valley, shown in Fig. 9a. For sliding rate 7 m/s under the heap load of 39.24 N as shown in Fig. 7, wear rate tumbles down because of the smooth surface shaped on the wearing surface. The

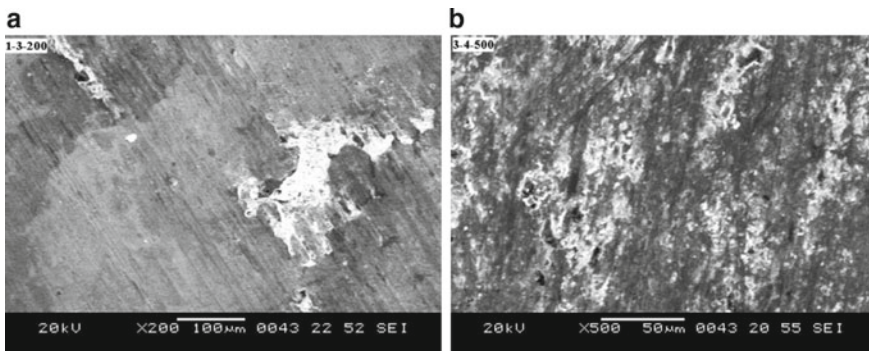


Fig. 8 **a** Oxidative wear (4.91 N, 0.5 m/s). **b** Abrasive wear (9.81 N, 1 m/s)

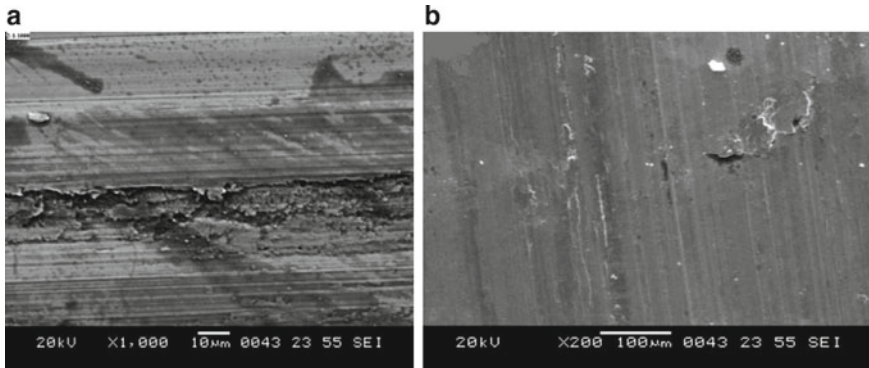


Fig. 9 **a** Abrasive wear (68.67 N, 0.5 m/s). **b** Laminative wear (39.24 N, 7 m/s)

smooth surface is framed because of overlays on the wearing surface; yet the covers are not isolated from the parent material as shown in Fig. 9b.

Thus, initial investigation and experimental analysis reveal that the presence of inorganic compound, i.e. cadmium sulphide, reduces the weld action caused by loading generated due to inertial force and simulated using the loads in the present experimentation, the profound valleys observed in Fig. 9a for a specimen without the addition of element and on other hand a smoother laminative surface for the newly formed MMC.

The matter of this journal paper has been the estimation of wear rate and examination with the particular wear rate under various loads and sliding velocities and also contemplation of the wear systems on the newly formed hybrid composite, with a view of developing a hybrid composite with reduced failures due to wearing, especially in mating components as discussed in Introduction.

7 Conclusion

The graphical representations in Figs. 7 and 8 are evident that there is a reduction in wear with the reinforcement in the hybrid composite, and also, it shows that there is a reduced wear rate with an increase in sliding speed, and the graph also shows improved mechanical properties, the mixture of aluminium oxide and silicon carbide with others offers opposition to roughness action due to abrasion wear, and at the same time it helps to reduce the wear. The wear coefficient value with a sliding speed is also negative, and it proves a decrease in wear with an increase in sliding speed, and this reduction in behaviour is possible due to the change in shear force at sliding surfaces. The following outcomes are confirmed:

- The Al hybrid MMC material synthesized behaves as a good wear-resistant material under high operational conditions.

- The oxidative type of wear mechanism is observed.
- For different sliding speeds, the frictional forces increase directly with wear pressure.
- Under low speed, 0.9 m/s, the wear rate is increased with the load.
- Wear rate decreases with a speed in the range of 0.7 to 1.3 m/s for all wear pressures.

References

1. Nevillea A, Morinaa A, Haquea T, Voonga M (2007) Corrosion and Surface Engineering Research Group, School of Mechanical Engineering, University 26 March 2007
2. Niranjana K, Lakshminarayanan PR (2013) Dry sliding wear behavior of Al-TiB₂ composites 47:167–173
3. Singh G, Goyal S (2018) Dry sliding wear behaviour of AA6082-T6/SiC/B4C hybrid metal matrix composites using response surface methodology, vol 232, pp 952–964. Issue published 1 Nov 2018
4. Ashby MF, Lim SC (1990) Wear-mechanism maps. *Metall Mater* 24:805–810
5. Jianqiang H, Huanqin Z, Li W, Xianyong W, Feng J, Zhiming Z (2005) Study on tribological properties and action mechanism of organic cadmium compound in lubricants. Chinese university of mining and technology, Xuzhou 221000, 10 May 2005
6. Smith RW, DeMonte A, Mackay WBF (2004) Development of high manganese steels for heavy duty cast-to-shape applications. *J Mater Process Tech* 153:589–595
7. Balogun SA, Esezobor DE, Agunsoye JO (2008) Effect of melting temperature on the wear characteristics of austenitic manganese steel. *J Miner Mater Charact Eng* 7(3):277–289
8. ASM handbook (1990) Properties and selection: nonferrous alloys and special-purpose materials, vol 2. ASM International, Materials Park, Ohio
9. Waterhouse RB (1977) The role of the adhesion and delamination in the fretting wear of metallic materials. *Wear* 45(3):355–364
10. Stachowiak GW, Batchlor AW *Engineering Tribology*. Third Edition. Elsevier.
11. Sahin Y (2003) Wear behavior of aluminum alloy and its composites reinforced by SiC particles using statistical analysis. *Mater Des* 24:95–105
12. Salib J, Kligerman AEY, Etsion AEI (2008) A model for potential adhesive wear particle at sliding inception of a spherical contact. Published online: 10 May 2008. Springer Science Business Media, LLC
13. Sarkar AD (2013) *Wear of metals*. Pergamon Press Elsevier Science. ISBN 978143140100
14. Tikotkar RG, Kabadi VR, Ganechari SM (2008) Effect of wear rate and specific wear rate on Hadfield steel. *Int J Mech Automob Eng* 1(1):2009

Chapter 51

Investigation of the Influence of Impeller Type, Speed and Vertical Height on the Mixing Efficiency of a Biogas Plant Stirrer



Temilola T. Olugasa, J. O. Omokayode, and N. Idusuyi

Abstract The condition of the substrate in biogas digesters is critical to biogas yield. Substrates used in most digesters are semi-solid and are prone to clogging which is a major cause of reduction of biogas yield and eventual stalling of biogas production process. Stirring in biogas digesters ensures the uniform distribution of the substrate in the biogas digester, formation of a homogeneous suspension, uniform heat distribution and easy gas lift from the fermentation substrate at high dry matter content. This study sought to investigate the effects of impeller speed and installation height on the mixing performance of different impellers. Pitched blade turbine and open flat blade were investigated in order to develop a suitable model of a stirrer. The appropriate velocity for the stirrer from the velocity profiles generated was also determined. A computational fluid dynamics (CFD) model was developed for solid–liquid mixing in a cylindrical tank equipped with a top-entering impeller. The multiple reference frame (MRF) technique, *k*-model and Eulerian–Eulerian approach were employed to simulate the flow pattern in the digester. It was observed that the six pitched blade impeller provided better mixing results compared to the flat blade impellers as well as the four and two pitched blade impellers. The installation height of about 1/25 of the height of the tank was found to be appropriate to prevent dead space at the bottom of the mixer. Stirring speed of 25 rpm was compared with other stirring speeds and was found to provide better mixing as it provided good mixing quality as well as preservation of the biological environment in the digester.

Keywords Biogas digester · Impeller · Velocity · Flow pattern · Model · Blades

1 Introduction

Biogas is a mixture of gases produced by the breakdown of organic matter in the absence of oxygen. Raw materials such as agricultural waste, manure, sewage or food waste can be used to produce biogas. The anaerobic digestion of these materials in a closed system results in the production of biogas [1]. With the emphasis on clean

T. T. Olugasa (✉) · J. O. Omokayode · N. Idusuyi
Department of Mechanical Engineering, University of Ibadan, Ibadan, Oyo, Nigeria

and renewable sources of energy, biogas is gaining prominence in many countries. Apart from supplying energy and manure, the use of biogas helps in the mitigation of green house gas (GHG) emissions and the reduction of global warming. The Clean Development Mechanism (CDM), a body under the Kyoto Protocol on emissions reduction project in developing countries, singled out biogas as a potential renewable energy replacement for kerosene in the rural areas [2]. Biogas also has been shown to possess qualities that surpass that of other renewable energy sources [3, 4].

Biogas production is enhanced by mixing the substrate in the digester daily [5, 6]. Mixing is a physical process carried out by agitators, stirrers or mixers. It is physically defined as a random distribution of materials in different phases into another, forming a homogenous dispersion. It is very crucial to the homogenization of organic matter [7]. This is done to prevent the formation of surface crusts which may be difficult to penetrate and may prevent the biogas generated from breaking through to the surface. Manual digesters are used in small-scale digesters, while motorized mixers are used in large-scale digesters. In this study, cow dung was used as the material to be mixed, owing to the fact that large mass of cow dung and other animal wastes are usually found in places where cows are confined such as in large farms or abattoirs. Large abattoirs are usually sited in the outskirts of every major town in Nigeria and would guarantee the availability of large deposits of cow dung. Cow dung was also focused on in this study because apart from being used solely to generate biogas, it is often added to other organic matter to kick start biogas production [8].

It is important to simulate the flow pattern of the cow manure used as a substrate to determine the suitable stirrer using computational fluid dynamics (CFD). This reduces dead spaces in the bioreactor and improves stirrer efficiency. Researchers, in recent times, tend to rely on advanced single-phase, multi-phase or dispersion-phase models to predict the hydrodynamics of the ever increasing complex systems, thus saving time as well as the cost of expensive experiments during the prototyping phase [9] Mohammadrezaei et al. [10] used computational fluid dynamics (CFD) to find an appropriate mechanical stirrer for a biogas plant and model the flow pattern of cow manure, comparing three types of stirrers: a six-blade turbine, a four-blade turbine and a six-flat-blade disc turbine. The simulations were carried out under steady-state settings using Fluent 18.1 software with a multiple reference frame method and the usual k -turbulence model. The six-blade turbine stirrer was found to be more suited than the other two stirrers. Zhang et al. [11] investigated the performance of different modes of mixing a biogas digester fed with cow manure and silage maize using CFD. The results indicated that the standard k - ϵ model outperformed other turbulence models. Jirout and Rieger [12] experimentally determined the critical speed and power consumption of various impellers and then numerically determined their efficiencies. He observed that pitched blade impellers had higher suspension efficiencies compared to the others. Kayode et al. [7] were able to design a new type of impeller called KIA for homogenization of food waste. A comparative analysis was carried out with three conventional impeller types (Rushton, Anchor and pitched blade) using computational fluid dynamics ANSYS CFX v.15.0. It was observed that the LIA impeller had improved performance in terms of reduction in dead zones and better heat transfer. Ahmad et al. [13] designed a mixing system for biodiesel

production using both analytical and numerical methods. The stress analysis and power requirements for a 45° pitched 2-blade impeller were evaluated analytically and numerically (finite element method). The experimental and numerical results were similar, and the geometry was within acceptable range. Meister et al. [14] used CFD simulations to compare the velocity contours obtained during induced mixing and that obtained during recirculation of the slurry. The models obtained were validated with the literature, and it was observed that higher velocities were obtained during induced mixing than when the slurry was recirculated in the digester.

This study investigated the effect of the impeller type, number, speed and vertical height on the mixing efficiency of a biogas plant stirrer using the velocity profiles generated by CFD.

2 Materials and Method

The design model used was a baffled-cylindrical tank with a volume of 500 L adopting the dimensions 900 cm by 421 cm.

2.1 Conservation Laws Applicable to the System

Mass, momentum and energy of a fluid in a system are conserved. The governing equations of flow can be based on any applicable conservation laws of physics. The general format of these laws in a controlled volume is:

(rate of an entity change) = (rate of entity in) – (rate of entity out) + (rate of entity generation).

Continuity equation [15]

$$\frac{\partial \rho}{\partial t} + \nabla \cdot (\rho \vec{u}) = S_m$$

Momentum equation

$$\frac{\partial \rho u}{\partial t} + \nabla \cdot (\rho \vec{u} \vec{u}) = -\nabla \cdot P + \nabla \cdot (\bar{\bar{r}}) + \rho \vec{g} + \vec{F}$$

where P is the static pressure, $\bar{\bar{r}}$ is the stress tensor (described below), and $\rho \vec{g}$ and \vec{F} are the gravitational body force and external body forces (e.g. that arise from interaction with the dispersed phase), respectively.

Energy equation [15]

Fig. 1 Pitched blade impeller (45°)

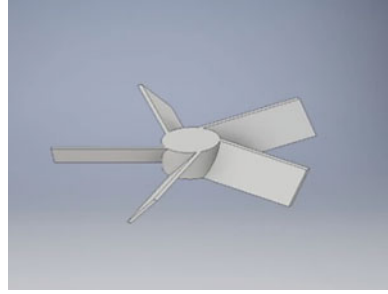
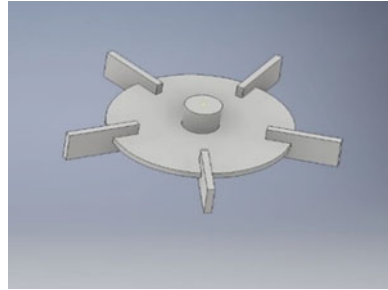


Fig. 2 Flat-blade-disc impeller



$$\frac{\partial \rho e}{\partial t} + \nabla \cdot (eu) = -\nabla \cdot (u \cdot P) - \nabla \cdot q$$

where ρ , e and q are the velocity components, density, total energy per unit volume and heat flux, respectively.

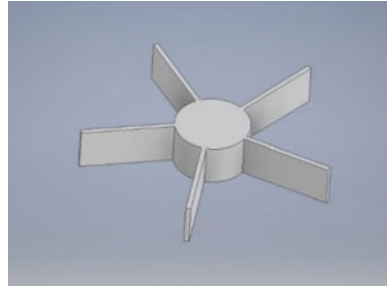
2.2 Design of Stirrer

For the purpose of this study, three types of impellers were designed using the Autodesk Inventor software, on which geometry subsequent analyses were based. Figures 1, 2 and 3 show three types of impellers designed which are the pitched blade turbine impeller, six-flat-blade disc turbine impeller and the radial flat blade impeller.

2.3 CFD Method

Computational fluid dynamics (CFD) is a computer-controlled approach for studying fluid flow systems using numerical methods and simulations. Engineers can easily

Fig. 3 Radial flat blade impeller



research new and complex models in virtual environments with CFD, determining design information, predicting potential failure causes and optimizing system operations.

2.3.1 Steps Followed in CFD Modelling

The model simulation was achieved using a three-dimensional, steady, implicit and pressure-based solver. After defining a turbulence model, the operational conditions were activated by gravity and the boundary conditions were defined. Thereafter, flow fields were selected, and the flow fields were solved until convergence was achieved.

The study of different materials saw that the time-averaged RANS model is one that provides a reasonable compromise between computational requirements, speed and accuracy of results [16].

$$\frac{\partial \rho}{\partial t} + \frac{\partial}{\partial x_i}(\rho U_i) = 0$$

$$\frac{\partial}{\partial t}(\rho U_i) + \frac{\partial}{\partial x_j}(\rho U_i U_j) = \frac{\partial p}{\partial x_i} + \frac{\partial}{\partial x_j} \left[\mu \left(\frac{\partial u_i}{\partial x_j} + \frac{\partial u_j}{\partial x_i} - \frac{2}{3} \delta_{ij} \frac{\partial u_l}{\partial x_l} \right) \right] + \frac{\partial}{\partial x_j} (-\rho \overline{u'_i u'_j})$$

The equations above are the Reynolds-averaged Navier–Stokes (RANS) equations. They have the same general form as the instantaneous Navier–Stokes equations, with the velocities and other solution variables now representing ensemble-averaged (or time-averaged) values.

2.3.2 CFD Summary

Mesh

- Model and grid were generated in design modeller
number of nodes 22,417

number of elements 110,541.

Water was chosen as a medium, and properties of glass bead were applied as the solid phase; subsequently, solid concentration was specified using Fluent 18.1

Boundary conditions

- Tank wall and baffles were assigned to the no-slip boundary for momentum.
- Liquid level was treated with:

Zero normal velocity at a symmetry plane.

Zero normal gradients of all variables at a symmetry plane.

- Impeller motion was mimicked by MRF approach.

Solution method

- The Eulerian–Eulerian approach was chosen to derive conservation equations for both solid and liquid phases.
- Discretization

All cases were assigned to first-order upwind method with low under-relaxation factor

kinetic and dissipation were kept the same as first order due to hard convergence.

- Pressure–velocity were coupled using a SIMPLE algorithm.
- Time step was picked 0.001 s initially and afterwards switched to 0.01 s and number of time steps = 4000–8000.
- CPU time was 3–5 days with Core i5, 2.4 GHz and 8 GB Memory.

3 Results and Discussion

3.1 Determination of Suitable Impeller Design

The design includes the type of turbine, the number of turbines, the positioning of the blade within the assembly and its diameter. Figure 1 depicts a stirrer with a set of flat blades at a pitch angle of about 45° producing axial flow, Fig. 2 depicts a stirrer with a set of flat blades around a 50 mm shaft hub, and Fig. 3 depicts a set of 6 flat blades straight around the shaft.

3.1.1 Pitched Blade Impeller

Figure 4 shows the stirrer with a set of six flat blades pitched at angle of 45° to the axis of the shaft producing the axial flow whose velocity profile is shown in Fig. 5.

Fig. 4 Six-blade pitched impeller

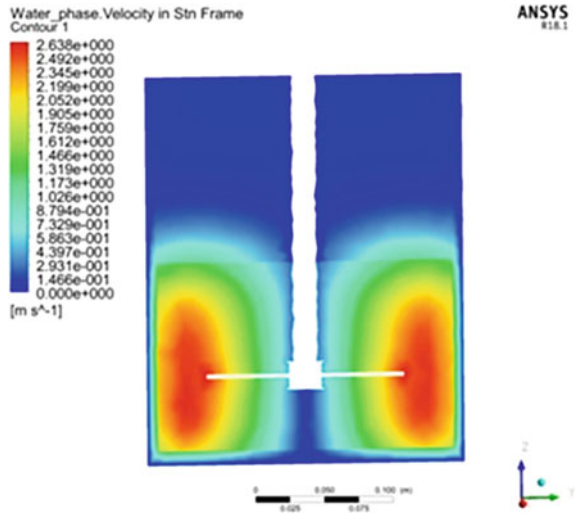
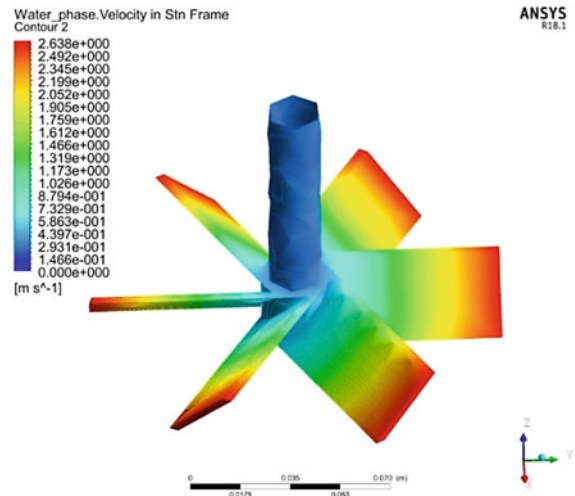


Fig. 5 Velocity profile of the six-blade pitched impeller



The 45° pitched blades contributed to enhanced stirring resulting in good mass and heat transfer. It can be observed from the velocity contours that the mixing was near perfect with minimal dead space directly below the stirrer. There was, however, a high shear at the tips of the blade. The pressure (2.67 kPa) exerted on the stirrer as a result of the mixing was not high as to cause any deformation of the stirrer.

3.1.2 Flat-Blade-Disc Impeller

Figure 6 shows a stirrer with a set of flat blades around a shaft of 50 mm diameter producing the radial flow. Figure 7 shows the velocity profile for the radial impeller. It was observed from the velocity contours that though velocity was well distributed, there were more blue regions, which are the dead zones, directly below the stirrer, around the stirrer shaft and towards the free surface compared to the velocity contours produced by the pitched blade impeller.

Fig. 6 Flat-blade-disc impeller

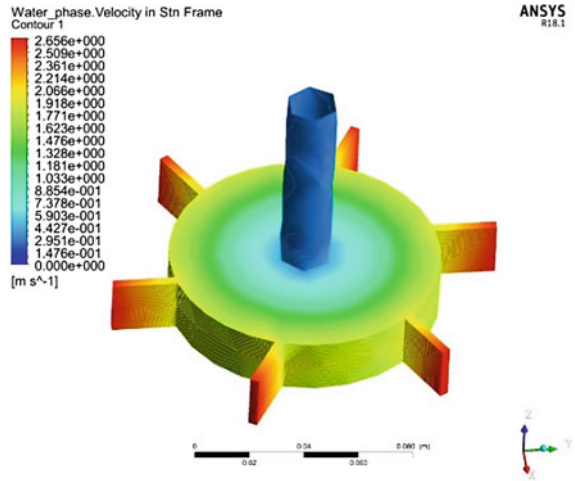
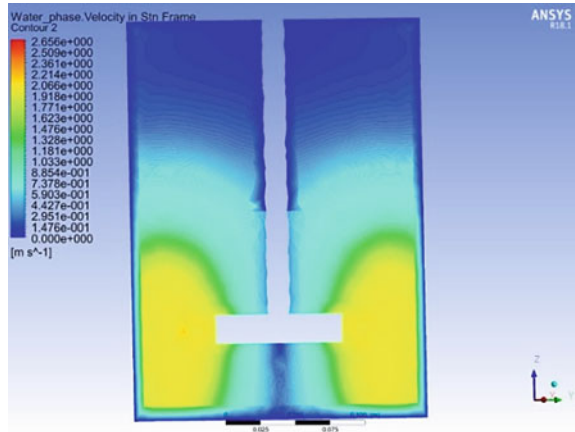


Fig. 7 Velocity profile of radial impeller



3.1.3 Paddle Impeller

Figure 8 shows a stirrer with a paddle blade impeller producing the radial flow. The velocity profile is shown in Fig. 9. Maximum velocity occurs at the tips of the blade, while the minimum velocity occurs near the shaft of the stirrer. There is some dead space directly below the shaft. The velocity contours indicate dead zones below the stirrer, around the stirrer shaft and at the free surface.

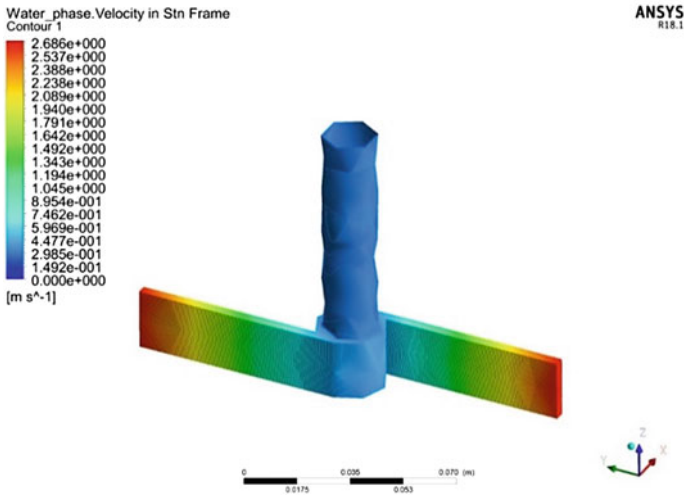
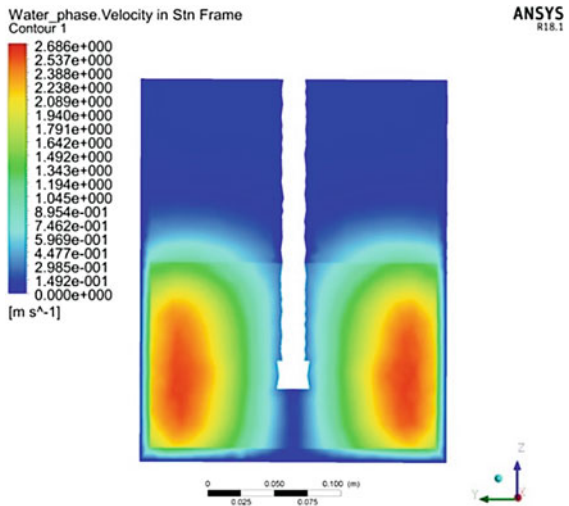


Fig. 8 Flat radial impeller

Fig. 9 Velocity profile of flat radial impeller



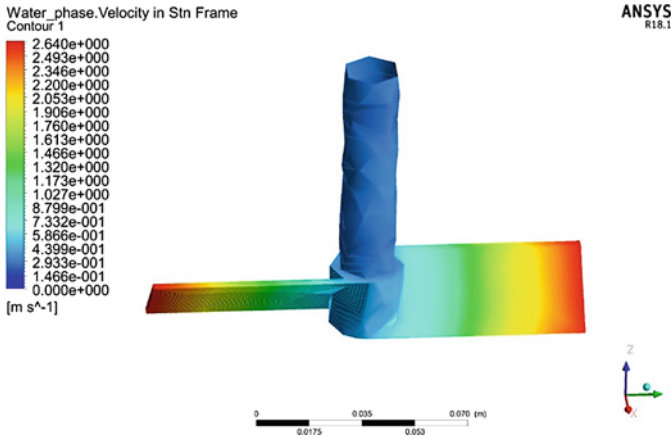


Fig. 10 Two-pitch-blade impeller

From the three different velocity profiles presented, the six-flat-blade turbine impeller was the most appropriate. The velocity profile of the six-flat-blade turbine impeller shows that there are fewer dead spaces below the impeller and towards the walls of the vessel. The axial nature of the flow generated using the 45° pitch blade impeller contributed to the better stirring results.

3.2 Determination of Suitable Number of Blades for the Pitched Impeller

Having selected the pitched blade as the most suitable impeller design, the number of the blades of the pitched impeller was now varied as two, four and six blades. The two-, four- and six-pitched-blade impellers are presented in Figs. 10, 12 and 14, respectively, while Figs. 11, 13 and 15 show the respective velocity profiles. It was observed that the impeller with six blades provided the best mixing quality with the least dead spaces, higher circulation loops and velocity contours suggesting greater fluid movement.

3.3 Determination of Suitable Number of Impellers

The effect of number of sets of impellers on mixing performance was also investigated in this study. The use of one set of impellers was compared with the use of two sets. According to Siddiqui [17], tanks with a ratio of liquid height to tank diameter equal to one ($Z/T = 1$) are ideal for top entry with a single impeller. If the liquid height to

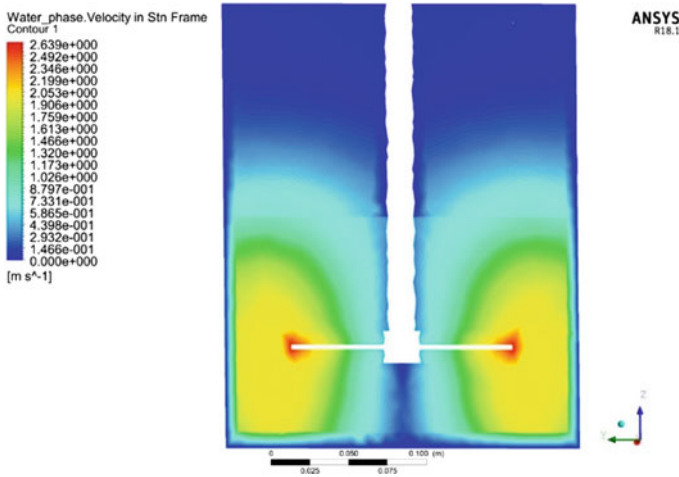


Fig. 11 Velocity profile of two-pitch-blade impeller

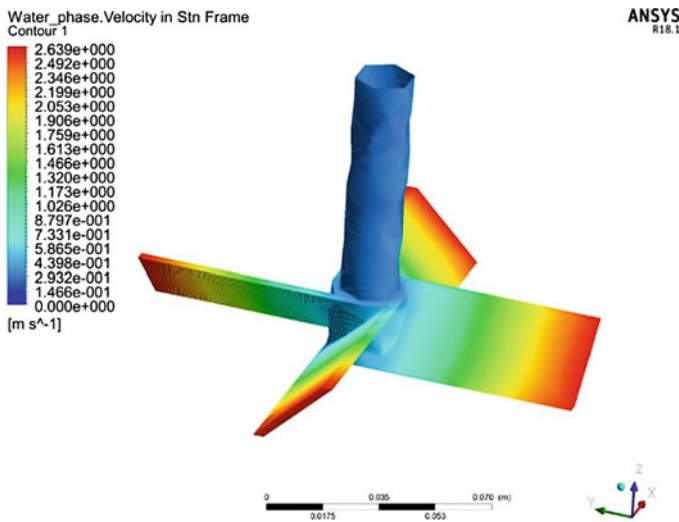


Fig. 12 Four-pitched-blade impeller

tank diameter is more than one ($Z/T > 1$), the number of sets of impellers must be greater than one to achieve perfect mixing.

The model used in this study had a liquid height-to-tank diameter ratio of 1.1 which shows that the number of impellers used could be one, since it slightly exceeds 1. However, the use of two sets of pitched blade impellers was explored. The velocity profile from the model with two sets of impellers (Fig. 16) showed that it produced

Fig. 13 Velocity profile of four-pitched-blade impeller

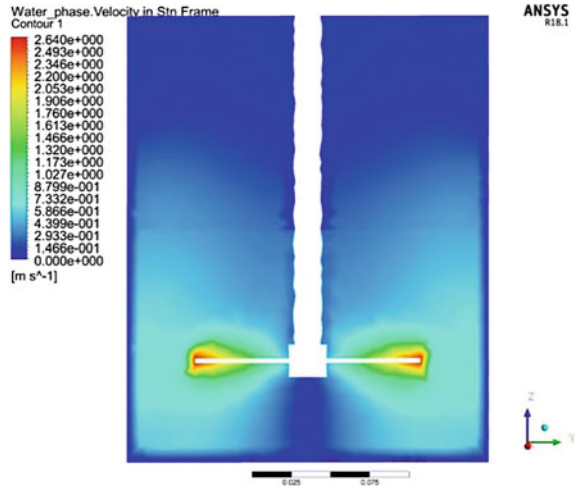
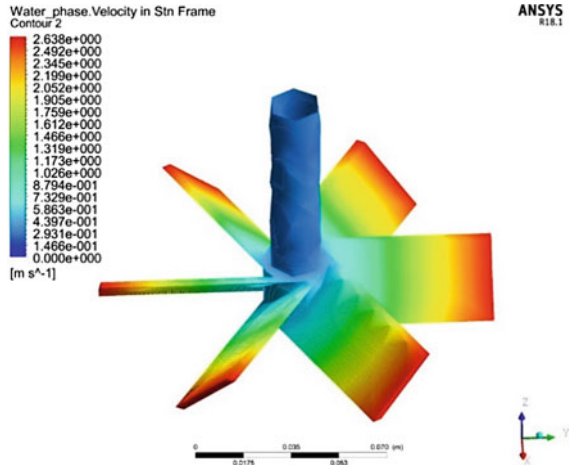


Fig. 14 Six-pitched-blade impeller



better mixing compared to when one set of impellers (Fig. 17) was used. Use of two impellers resulted in fewer dead spaces and wider range of mixing, as seen in Fig. 16.

3.4 Determination of Height of Stirrer from the Base of the Digester

Simulations were run with different the impeller at different vertical height from the bottom of the tank in order to determine the optimum position for the stirrer.

Fig. 15 Velocity profile of six-pitched-blade impeller

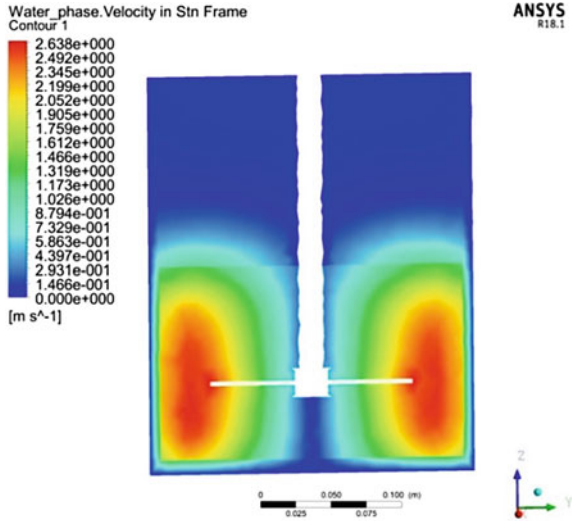
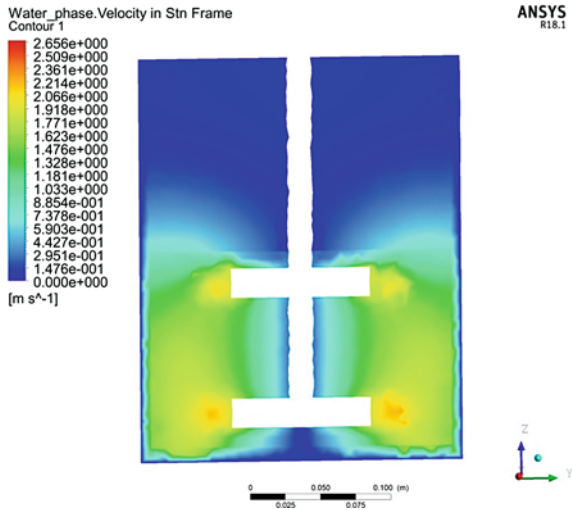


Fig. 16 Velocity and pressure profile with two impellers



The impeller positioned at H/6, H/12 and H/25 from the bottom of the tank was considered as shown in Figs. 18, 19 and 20, respectively. The results from the velocity profiles generated show that the flow had more dead spaces when the impeller was placed at a height of H/6 from the tank bottom when compared to the other two impellers.

Optimum mixing was found in impeller with clearance of H/25 from the tank bottom.

Fig. 17 Velocity and pressure profiles for one impeller

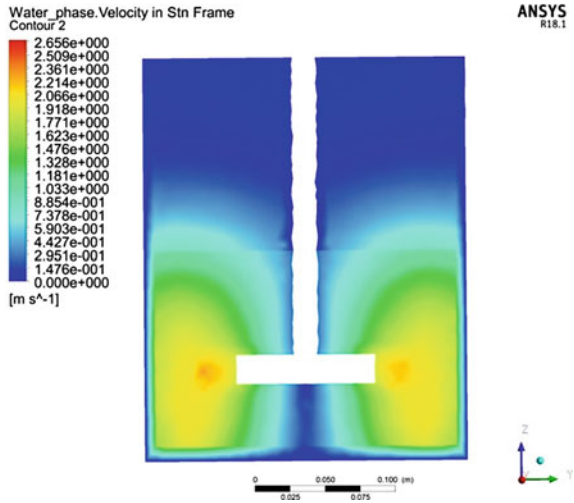
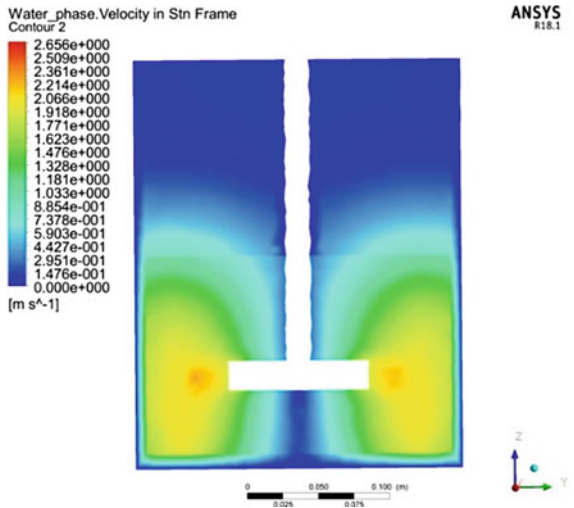


Fig. 18 Velocity profile for H/6 installation height



3.5 Determination of Appropriate Speed

The effect of impeller speed on mixing performance was also investigated in this study. The CFD results showed that stronger flow resulted in better mixing intensity from the velocity profiles. Velocity of 300 rpm was considered initially, and the velocity profile generated is shown in Fig. 21. The velocity profile for the flow at 300 rpm shows that it produces the best mixing quality with very few dead spaces.

Fig. 19 Velocity profile for H/12 installation height

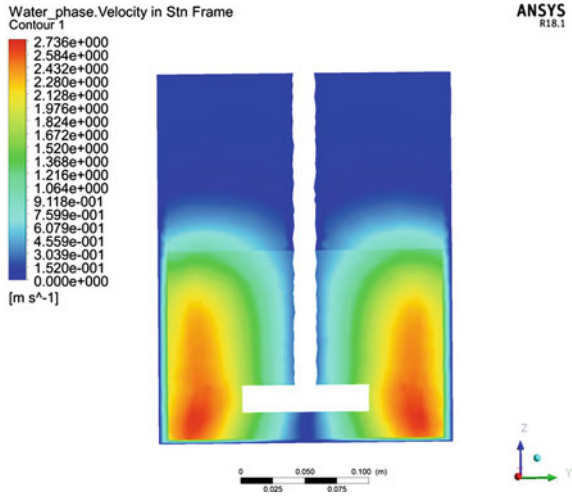
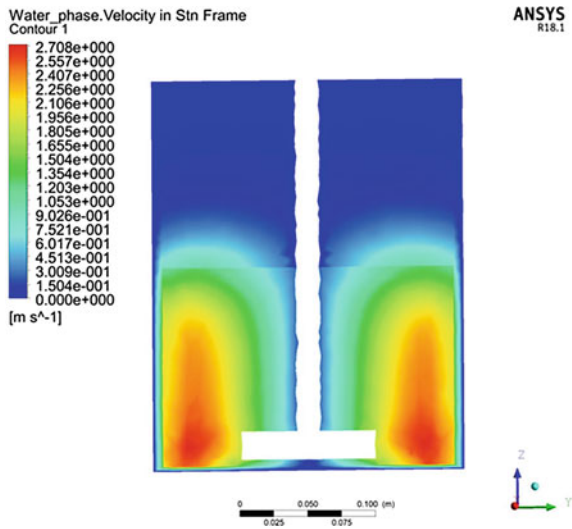


Fig. 20 Velocity profile for H/25 installation height



However, the preservation of the biological system is an important consideration when it comes to stirring in biogas digesters, hence the need for modelling at much lower speeds of 25 rpm as shown in Fig. 22.

Fig. 21 Velocity of 300 rpm

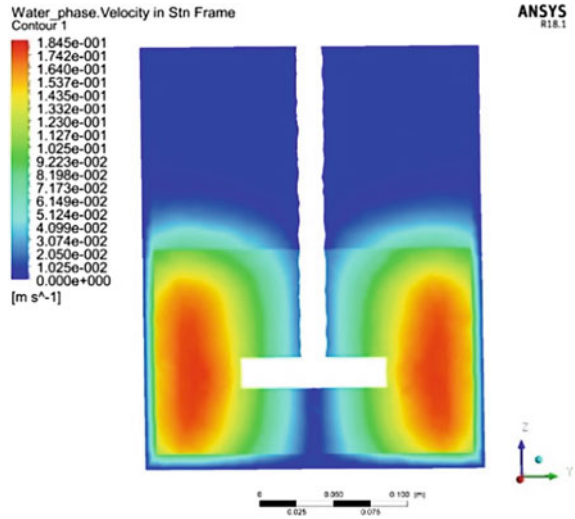
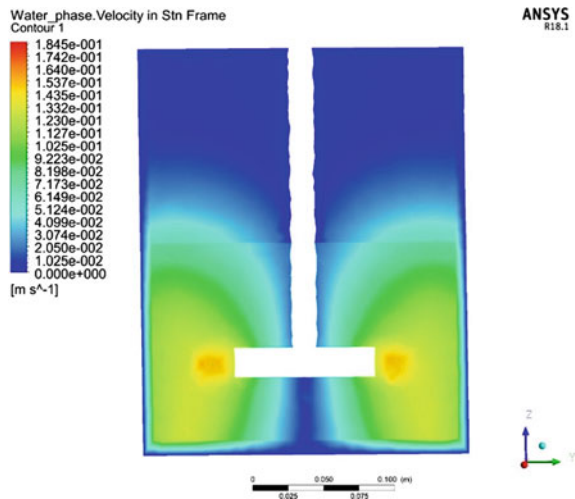


Fig. 22 Velocity profile at 25 rpm



4 Conclusion and Recommendation

The main resolution of mixing is to ensure homogeneity in the biogas reactor's content, avoid the sludge bonds in the lowest area and increase the production of biogas. In this study, the behaviour of three types of impeller privileged the biogas digester was simulated using the rotating frame model and standard $k-\epsilon$ turbulence model utilizing ANSYS Fluent 18.1 Software. The radial six-blade impeller, paddle impeller, and the pitched blade impeller were all investigated. The pitched six-blade impeller was found to provide the best mixing quality when compared to the other

types of impellers. This impeller produces an axial flow characterized by the fluid being pushed up or down along the shaft of the impeller, thereby contributing to the increased homogeneity of fluid.

Other investigations such as optimum installation height, number of blades and number of required versus installation height showed that the best installation height for the six-pitched-blade turbine impeller was $H/25$ from the bottom of the tank and the six blades performed the best in comparison with four and two blade versions of the impeller, the velocity of 25 rpm was the best stirring velocity that ensured preservation of the biological environment in the digester and good mixing of the substrate to ensure optimum production of biogas.

Future work to investigate the effect of more geometrical effects such as shape, angle of pitch of the blades, shape of the tank bottom and baffle height on the stirrer efficiency using CFD should be explored.

References

1. Raven RPJM, Gregersen KH (2007) Biogas plants in Denmark: successes and setbacks. *Renew Sustain Energy Rev* 11(1):116–132. <https://doi.org/10.1016/j.rser.2004.12.002>
2. UNECA (2011) Governing development in Africa—the role of the state in economic transformation. *Econ Report Africa* 201:147p
3. Sreenivas RR, Phil H, Jon W, Andy R (2009) Optimizing biogas fermentation using the taguchi methodology. *Inst Grassland and Environ Res*, North Wyke
4. Chae KJ, Yim SK, Choi KH, Park WK, Lim DK (2002) Anaerobic digestion of swine manure: sung-Hwan farm scale biogas plant in Korea. Division of Agriculture, Environ Ecol, National Inst Agric Sci Technol, Kyungki, Korea
5. Stroot PG, McMahon KD, Mackie RI, Raskin L (2001) Anaerobic co-digestion of municipal solid waste and bio-solids under various mixing conditions-I. Digester perform. *Water Resour* 135(7):1804–1816
6. Karim K, Klasson KT, Hoffmann R, Drescher SR, DePaoli DW, Al-Dahhan MH (2005) Anaerobic digestion of animal waste: effect of mixing. *Biores Technol* 96(14):1607–1612
7. Kayode IA, Ogedengbe EOB, Rosen MA (2016) Design of stirrer impeller with variable operational speed for a food waste homogenizer. *Sustain MDPI* 8:489. <https://doi.org/10.3390/su8050489>
8. Chukwuma EC, Umeghalu ICE, Orakwe LC, Bassey EE, Chukwuma JN (2013) Determination of optimum mixing ratio of cow dung and poultry droppings in biogas production under tropical conditions. *Afr J Agric Res* 8(18):1940–1948
9. Marek J, Mlyncarczykowska, Demurtas L (2020) Effect of impeller design on power characteristics and newtonian fluids mixing efficiency in a mechanically agitated vessel at low reynolds numbers. *Energies MDPI* 13:640. <https://doi.org/10.3390/en13030640>
10. Mohammadrezaei R, Zareei S, Behroozi-Khazaei N (2017) Improving the performance of mechanical stirring in biogas plant by computational fluid dynamics (CFD). *Agric Eng Int CIGR J* 19(4):91–97
11. Zhang Y, Yu G, Yu L, Siddhu MAH, Gao M, Abdeltawaz AA, Chen X (2016) Computational fluid dynamics study on mixing mode and power consumption in anaerobic mono- and co-digestion. *Biores Technol* 203:166–172
12. Jirout T, Reiger F (2011) Impeller design for mixing of suspensions. *Chem Eng Res* 89:1144–1151
13. Ahmad A, Ghobadian B, Najafi G, Motevali A (2014) Analytical and FEM design of mixing system in STR biodiesel production. *Adv Environ Biol* 8(1):325–334

14. Meister M, Rezavand M, Ebner C, Pumpel T, Rauch W (2018) Mixing non-Newtonian flow in anaerobic digesters by impellers and pumped recirculation. *Adv Eng Softw* 115:194–203
15. ANSYS Inc (2018) ANSYS fluent tutorial guide 18. 15317(April):724–746. [https://doi.org/10.1016/0140-3664\(87\)90311-2](https://doi.org/10.1016/0140-3664(87)90311-2)
16. Hosseini S (2008) Solid-liquid mixing in agitated tanks: experimental and CFD analysis
17. Siddiqui H (1993) Mixing technology for buoyant solids in a nonstandard vessel. *AICHE J.* <https://doi.org/10.1002/aic.690390312>

Chapter 52

Studies on Chemical Resistance, Swelling Behaviour and Biodegradability of Natural Fiber-Reinforced Biocomposite



G. Sujaya and V. Anbazhagan

Abstract Biocomposites are promising eco-friendly materials which could replace synthetic plastic in many application fields. However, hydrophilic nature and poor chemical resistance limit their usage. Analysis of their chemical resistance and weathering on exposure to various environmental conditions would be highly beneficial for their suitable modifications, novel developments and thereby commercial acceptability. In the present work, woven palm-cotton fibre-reinforced polystyrene biocomposite samples with different weight % of polystyrene are developed and taken for analysing chemical resistance, swelling behaviour and biodegradability. Chemical resistance test indicated that the composite materials are resistant to concentrated acids (HCl, HNO₃), concentrated alkalis (50% NaOH, 50% KOH, 25% NH₄OH), 2% K₂Cr₂O₇ and 2% KMnO₄. Swelling behaviour is measured by weight gain method using distilled water, sea water, methanol and carbon tetrachloride. The swelling increases with immersion time and maximum swelling occurred in distilled water. Biodegradability test was done by soil burial method and it revealed that woven palm-cotton fibre-reinforced/polystyrene biocomposites are biodegradable and biodegradability increases with increase in burial time and decreases with increase in polystyrene content. This study revealed that properties exhibited by woven palm-cotton fibre-reinforced/polystyrene biocomposites made with environmental threat causing dumped expanded polystyrene foam waste matrix is on par with other natural fibre-reinforced hybrid composite. Hence, the present study is expected to open up new potential applications for this material in various fields as well as scope for further research.

Keywords Woven palm-cotton fibre · Chemical resistance · Biodegradability · Swelling behaviour · Reinforced polymer biocomposite · Water affinity

G. Sujaya

Vinayaka Missions Research Foundation (Deemed To Be University), Salem, Tamil Nadu 636308, India

V. Anbazhagan (✉)

Department of Chemistry, Vinayaka Mission's Kirupananda Variyar Arts and Science College, Vinayaka Missions Research Foundation (Deemed To Be University), Salem, Tamil Nadu 636308, India

1 Introduction

Environmental friendly biocomposite materials are getting global interest due to economic and ecological reasons [1–4]. Natural fibre-reinforced polymer biocomposite materials are booming in recent composite world due to their versatile properties like low density, lightweight, no health hazard, large availability, renewability, good mechanical property, and biodegradability [5, 6]. This made them applied in many fields like automotive, aerospace, packaging, etc. However, the application of natural fibre-reinforced biocomposites is limited due to their hydrophilic nature and comparatively poor resistivity towards chemical reagents and environmental conditions [7–9]. The durability of the material is its resistance towards chemical and environmental degradation. The effect of environmental conditions on the polymer biocomposites has been a subject of research and many studies are going on in this field. It is found that deterioration of biocomposite takes place due to weakening of interfacial bonding within the matrix. It may be resulted by water uptake, acids, alkalis and other solvents [10, 11].

Over the past few years, number of studies has been performed on the durability of biocomposites. But studies carried out or reported on chemical resistivity of natural fibre-reinforced synthetic polymer matrix are less. Varada Rajulu et al. [12] studied chemical resistance of bamboo fibre-reinforced epoxy composites. The results revealed that the prepared composites are resistant to acetic acid, HCl, NaOH, Na_2CO_3 , NH_3 , CCl_4 and toluene. The exposed edges of bamboo fibre of the composite got dissolved in concentrated HNO_3 and weight loss of the sample was observed. Singha and Vijay Kumar Thakur [13] analysed thermal, physical and chemical durability of Hibiscus sabdariffa fibre-reinforced phenol formaldehyde resin composite. They studied chemical resistance against 1 N NaOH, HCl, swelling behaviour in different solvents and moisture absorbency at different humidity levels. The analysis showed that chemical resistance decreases with increase in fibre content. The swelling behaviour of polymer composites increases with increase in fibre content due to greater affinity of water for OH groups present in the fibre-reinforced polymer composites. Raghu et al. [14] studied the chemical resistance of the treated and untreated silk/sisal hybrid composites to various acids, alkalis, and solvents to suggest application in various fields. Aprilia et al. [15] analysed chemical and environmental durability of vinyl ester composites reinforced with jatropha seed shell. They reported better chemical durability and suggestions for application in various fields. Development of new hybrid natural fibre-reinforced thermoplastic polymer matrix is getting research interest as the application of these materials is increasing. There are lot of applications where in composites used could come across occasional or prolonged contact with chemicals, which can be anything like cleaning agents, acids, alkalis or moisture. Their resistivity towards chemicals is very important before suggesting them for various application sectors. In this regard, it is thought to study chemical resistance, swelling behaviour and biodegradability of biocomposite prepared from used polystyrene waste (Fig. 1) which is widely used thermal insulation material reinforced with woven hybrid palm-cotton fibre (WPCF). This study

ANALYSIS OF CHEMICAL RESISTANCE, SWELLING BEHAVIOUR AND BIODEGRADABILITY

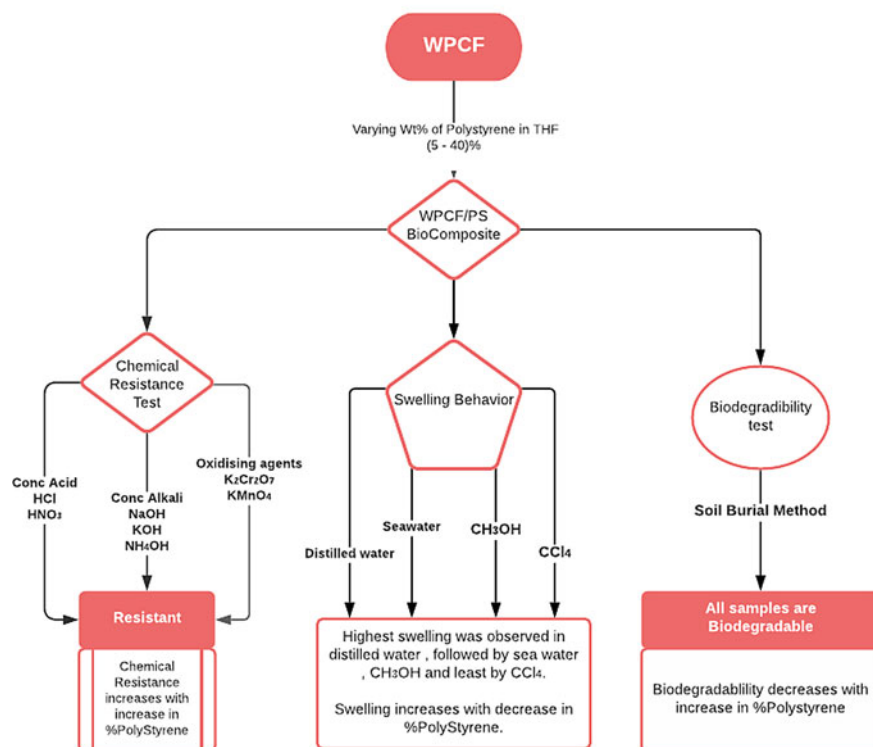


Fig. 1 Schematic diagram of chemical resistance, biodegradability, swelling behaviour of WPCF/PS

sheds light on innovative utility applications for WPCF/PS material since their properties are comparable with other synthetic fibre composites. The palm-cotton fibres are readily available in nature and are cheap. The reuse of expanded polystyrene foam waste reduces the cost of production to 50% and relieves environmental problems occurring due to dumping of polystyrene waste.

2 Experimental

2.1 Materials

HCl, HNO₃, KOH pellets, NaOH pellets, NH₄OH, K₂Cr₂O₇ and KMNO₄ purchased from Nice Chemicals Pvt. Ltd (India) and are used as received. Test samples are prepared using different weight percentages of polystyrene (PS) with fixed WPCF.

The expanded polystyrene (EPS) foam was collected from post-consumed Styrofoam wastes used for protective packaging of electrical appliances. Plain weave palm-cotton material having an average weight of 160 g/m² is obtained from traditional weavers in Sargalaya art and craft village Badagara, Kozhikode, Kerala. Tetrahydrofuran (THF) is used as a precursor which was purchased from Fisher Scientific Company, India Pvt. Ltd. (Molecular formula C₄H₈O and Mol. wt. 72.11).

2.2 Method

2.2.1 Preparation of Samples

The EPS foam waste collected was first processed into small crumbs. EPS in THF solvent is prepared by mechanical stirring of EPS in THF solvent for 15 min with a speed of 435 rpm. A glass mould was used for the preparation of composite. The WPCF material is cut into 8 × 8 cm size, dried in oven to remove moisture and it is placed in the glass mould. The prepared EPS in THF is poured into the fabric material and allowed to spread uniformly. The material is completely dipped in order to ensure better penetration of matrix between the fabric openings and to remove entrapped voids. It is taken out and allowed to dry in air under normal temperature. All the WPCF/PS biocomposite samples are prepared by the same method by varying % of PS (5%, 10%, 20%, 30% and 40%).

2.2.2 Chemical Resistance

Chemical resistance of the samples assessed by weight loss method using concentrated HCl, HNO₃, 50% NaOH, 50% KOH, 25% NH₄OH, 2% KMNO₄ and 2% K₂Cr₂O₇. Biocomposite samples with dimensions 10 × 10 × 0.1 mm³ were dried for 24 h in a vacuum oven (60 °C, 700 mm of Hg) and weighed (W_1). It is immersed in 20 ml solution taken in a container at room temperature. Each sample was removed after 1, 7, 14, 21, and 30 days of time period. Excess liquid is removed after taking out from the solution by pressing between soft tissue papers. It is dried in vacuum oven and weighed (W_2). The percentage chemical resistance was calculated in terms of weight loss in the following manner.

$$\text{Weight Loss (\%)} = \frac{(W_1 - W_2)}{W_1} \times 100$$

2.2.3 Swelling Behaviour

Swelling nature of the WPCF/PS biocomposite samples was analysed by immersing in different solvents such as distilled water, sea water, methanol and carbon tetrachloride. Biocomposite samples with dimensions $10 \times 10 \times 0.1 \text{ mm}^3$ were dried for 24 h in a vacuum oven ($60 \text{ }^\circ\text{C}$, 700 mm of Hg) cooled in a desiccator and then weighed (W_1). It is immersed in 50 ml of different solvents taken in a container at room temperature. Each sample was removed after 1, 7, 14, 21, and 30 days of time period. Excess liquid is removed after taking out from the solution by pressing between soft tissue papers. It is weighed (W_2). The percentage swelling was calculated in the following way by weight gain method.

$$\text{Weight Gain (\%)} = \frac{(W_2 - W_1)}{W_1} \times 100$$

2.2.4 Biodegradability Test

Biodegradability test was conducted by burying the samples in biologically active soil taken in plastic bags. The biocomposite samples were cut $10 \times 10 \times 0.1 \text{ mm}^3$ dimension and dried in oven ($60 \text{ }^\circ\text{C}$, 700 mm of Hg) for 24 h. It is weighed (W_1). The samples were kept in open space to ensure air and natural environment for degradation. Samples were taken out after 1, 7, 14, 21, 30, 45, 60, 75 and 90 days. Then washed thoroughly with distilled water, dried for 24 h in a vacuum oven ($60 \text{ }^\circ\text{C}$, 700 mm of Hg) and weighed (W_2). From the initial and final weight, weight loss percentage can be calculated by the equation given below

$$\text{Weight Loss (\%)} = \frac{(W_1 - W_2)}{W_1} \times 100$$

3 Results and Discussion

3.1 Chemical Resistance

Figure 2 shows degradation of woven palm-cotton material (WPCF) with 5% PS biocomposite sample in acid. Woven palm-cotton biocomposite sample with 5% PS shows higher degradation in acids than other samples with immersion time. It is due to the more exposure of hydrophilic groups in the fibre to acids which can act as the degradation sites and thus, enhance the deterioration. The degradation of other samples is not significant in concentrated HCl and HNO_3 since the fragmentation of

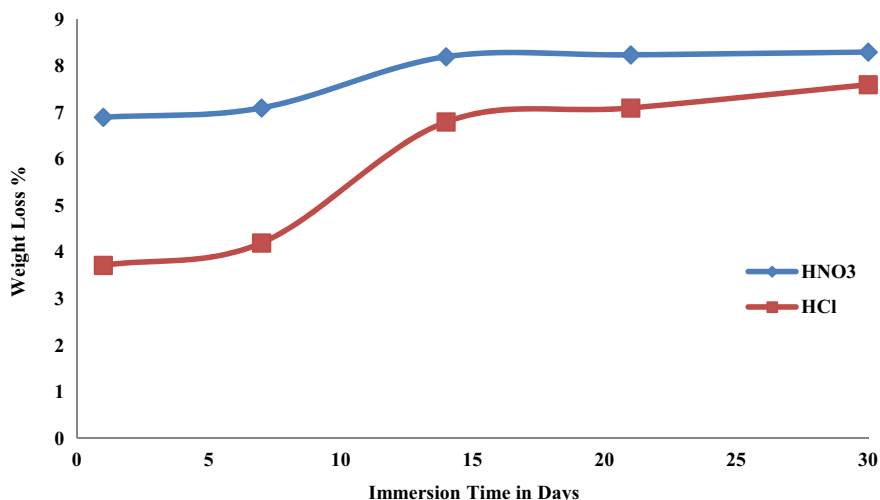


Fig. 2 Weight loss % of WPCF/5% PS biocomposite in strong acid medium

macromolecular chains of the polymer takes place only at the microlevel. Polystyrene matrix in the composite resulted lowest weight loss as its backbone provides inherent resistance to acids, which is not easily susceptible to acids. As the weight % of polystyrene in the biocomposite sample increases, the resistivity also increases.

All samples have same trend of degradation in alkalis and more weight loss is observed in the case of WPCF/5% PS sample. Figure 3 shows the weight loss% of WPCF/5% PS sample in NaOH, KOH and NH_4OH . The degradation takes place more notably in NH_4OH than other alkalis. The %weight loss decreases with increase in PS content and 40% PS-containing sample exhibits a percentage weight loss lower than the other biocomposite samples. All samples show an increase in weight loss with immersion time. These may be attributed to the hydrophilic sites present in the fundamental structure of natural fibre-reinforced composite for hydrolytic reactions mediated by alkalis.

The exposure of samples to 2% aqueous KMnO_4 and $\text{K}_2\text{Cr}_2\text{O}_7$ solutions at room temperature has shown a similar trend of degradation or dissolution effects with a lower extent of degradation. The high inertness of the samples confirms that they have no free sites for simple oxidation except for strong oxidizing agents like concentrated H_2SO_4 . The weight loss of samples is higher in 2% $\text{K}_2\text{Cr}_2\text{O}_7$ solution than 2% KMnO_4 solution at each immersion time. Figure 4 shows the weight loss% of WPCF/5% PS biocomposite in both 2% $\text{K}_2\text{Cr}_2\text{O}_7$ solution and 2% KMnO_4 solution. 40% PS-containing sample shows least degradation in oxidizing agents at each immersion time as the polymer backbone is not easily susceptible to oxidizing agents and thus, provides inherent resistance to these agents. Biocomposites show higher weight loss with decrease in weight% of PS content. The extent of degradation increases with less weight % PS due to the more exposure of hydrophilic sites present in the composite (Fig. 5).

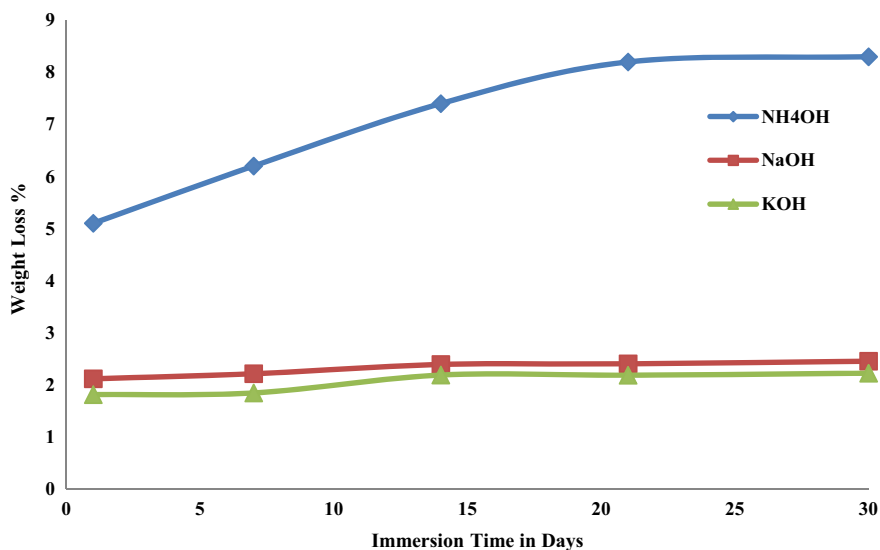


Fig. 3 Weight loss % of WPCF/5% PS biocomposite in strong base medium

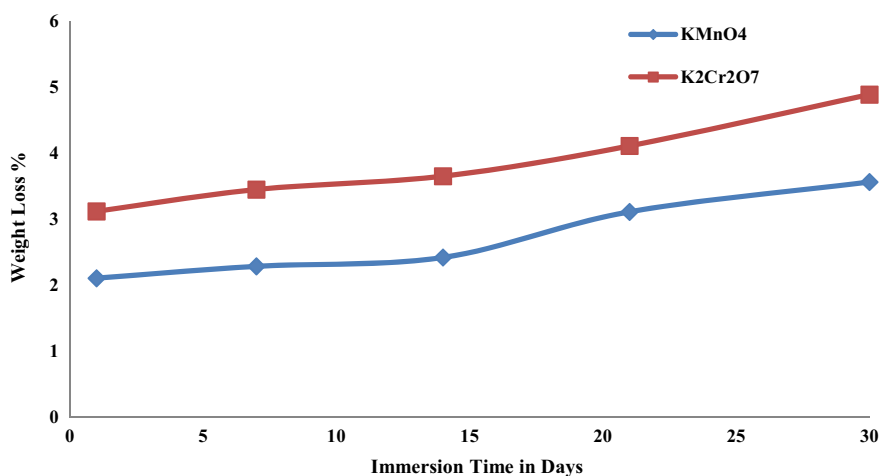


Fig. 4 Weight loss % of WPCF/5% PS in KMnO₄ and K₂Cr₂O₇

3.2 Swelling Behaviour

WPCF-reinforced PS biocomposite samples with different % of PS content show different swelling behaviour in different solvents (Table 1 and 2). The swelling behaviour of composite in different solvents follow the trend distilled water > sea water > CH₃OH > CCl₄. The swelling nature of composite samples increases with

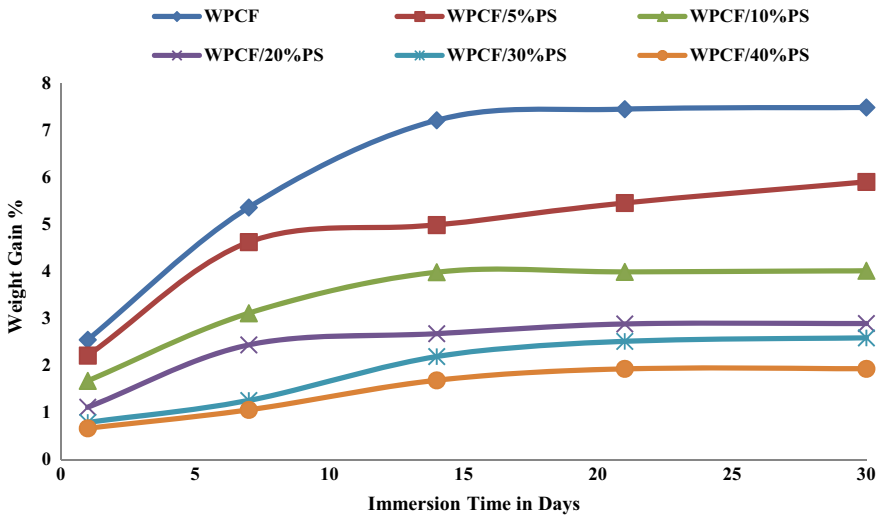


Fig. 5 Weight gain % of all samples in distilled water

Table 1 Swelling behaviour of WPCF/5% PS in different solvents

Immersion time in days	Weight gain% of WPCF/5% PS			
	Distilled water	Sea water	CH ₃ OH	CCl ₄
1	2.211	1.805	1.342	0.9891
7	4.6201	2.989	1.953	1.124
14	4.984	3.221	2.673	1.987
21	5.452	3.891	2.997	2.213
30	5.901	4.12	3.251	2.764

Table 2 Swelling behaviour of WPCF-reinforced PS biocomposite samples with different % of PS content in distilled water

Immersion time in days	Weight gain % in distilled water					
	WPCF	WPCF/5% PS	WPCF/10% PS	WPCF/20% PS	WPCF/30% PS	WPCF/40% PS
1	2.546	2.211	1.673	1.112	0.789	0.6657
7	5.358	4.6201	3.11	2.436	1.256	1.056
14	7.21	4.984	3.982	2.675	2.189	1.685
21	7.445	5.452	3.988	2.881	2.5112	1.928
30	7.481	5.901	4.011	2.89	2.587	1.93

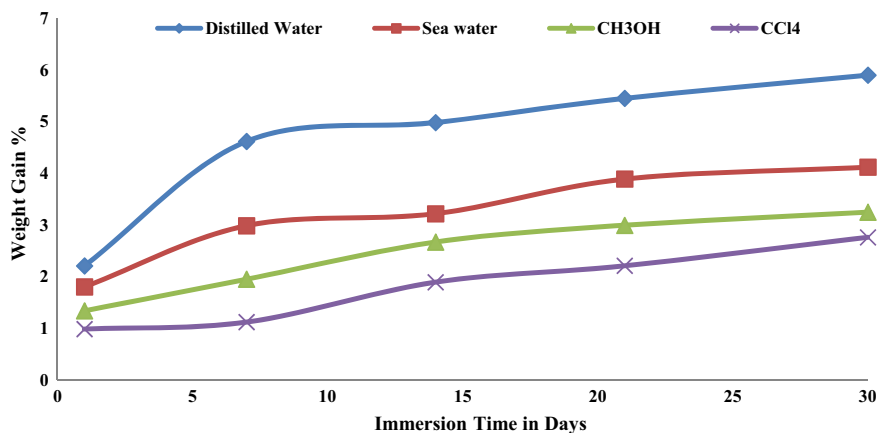


Fig. 6 Weight gain % of WPCF/5% PS in different medium

decrease in PS content due to affinity of solvents for OH groups in the fibre. Among the solvents water has shown maximum swelling due to greater affinity of water molecules to the OH groups present in the fibre. The absorption for all solvents follows the same pattern. All samples have very less swelling in sea water compared to distilled water. The less water uptake in sea water may be due to its density and salinity. Moreover, it resists the trace elements and salt to get adsorbed. The accumulation of salt and trace elements on the surface of the sample and resultant osmotic pressure inhibit water absorption [16–19]. All the samples have very less increase in weight % in sea and distilled water. It is clear from Fig. 6 that with increase in weight % of PS in the sample, water absorption and % weight gain decreases. WPCF and WPCF/5% PS show maximum swelling. Figure 6 indicates swelling behaviour of WPCF/5% PS sample in distilled water, sea water, CH₃OH and CCl₄. It is observed that maximum increase in weight % occurred in distilled water is 5.9% for WPCF/5% PS biocomposite sample. The results revealed that with increase in % PS content, % weight gain decreases and swelling of other samples is very less in distilled water and other solvents. Swelling behaviour of biocomposite samples in methanol and carbon tetrachloride is insignificant and they are almost resistant to these solvents.

3.3 Biodegradability Test

Biodegradability tests revealed that all composite samples are biodegradable and their degradability increases with decrease in polystyrene content. Figure 7 indicates their biodegradability pattern and it is clear that biodegradability increases with increase in burial time. Biodegradation is very prominent for WPCF/5% PS sample after 7 days since it has less polymer content. Natural fibres are water absorbing due to hydrophilic OH groups in the fibre. These biocomposite samples are more prone to the microbial attack, which provides easy access to the matrix interior using water

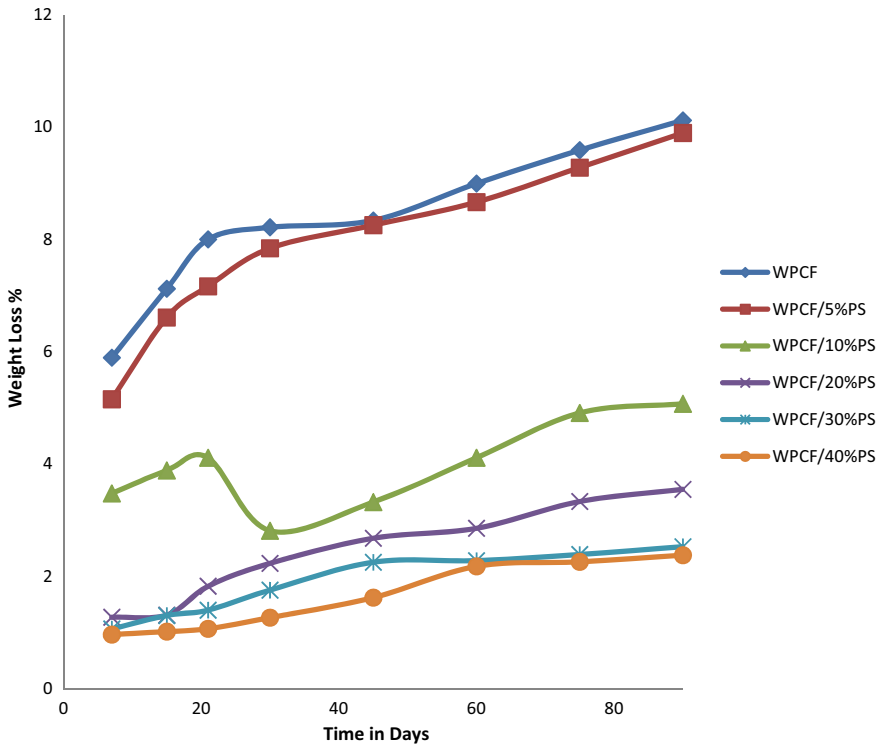


Fig. 7 Biodegradability test for WPCF and WPCF with different % of PS

as a medium [20–22]. Biodegradability decreases with increase in polymer content. Table 3 shows the biodegradability of all samples. WPCF material is also included to show the extent of biodegradability.

Table 3 Biodegradability of WPCF with various percentage of PS

Time in days	Weight loss % of samples					
	WPCF	WPCF/5% PS	WPCF/10% PS	WPCF/20% PS	WPCF/30% PS	WPCF/40% PS
7	5.892	5.151	3.476	1.270	1.062	0.963
15	7.120	6.609	3.885	1.309	1.302	1.015
21	7.998	7.163	4.110	1.822	1.397	1.066
30	8.214	7.840	2.809	2.230	1.753	1.263
45	8.336	8.251	3.322	2.677	2.251	1.621
60	8.992	8.661	4.110	2.854	2.278	2.177
75	9.587	9.277	4.907	3.331	2.388	2.257
90	10.118	9.893	5.071	3.548	2.527	2.376

4 Conclusion

WPCF-reinforced in polystyrene biocomposite samples with varying wt% of PS (5%, 10%, 20%, 30% and 40%) were taken for study. Chemical resistance test revealed that all samples were resistant to acids, alkalis and oxidizing agents. Their % weight loss was very less in conc. HNO_3 , HCl , NaOH , KOH , KMnO_4 and $\text{K}_2\text{Cr}_2\text{O}_7$. Among alkalis, maximum weight loss was observed in NH_4OH . Swelling property of the samples was tested with distilled water, sea water, CH_3OH and CCl_4 . Maximum swelling of the samples was observed in distilled water and they are almost resistant to other solvents. Biodegradability test revealed that all samples are biodegradable and their degradability increases with decrease in % PS content in the biocomposite. WPCF/5% PS biocomposite sample was observed with high biodegradability but its chemical resistance was comparatively less and swelling was more.

Acknowledgements The authors are grateful to Dr. A. Sujith, Associate Professor in Chemistry, National Institute of Technology, Calicut, India, for providing necessary facilities and help for this research work.

References

1. Li H, Sain MM (2003) High stiffness natural fiber-reinforced hybrid polypropylene composites. *Polym Plast Technol Eng* 42(5):853–862
2. Singha AS, Anjali S, Thakur VK (2008) Pressure induced graft co-polymerization of acrylonitrile onto Saccharum Cilliare fiber and evaluation of some properties of grafted fibers. *Bull Mater Sci* 31(1):7–13
3. Naik JB, Mishra S (2007) Esterification effect of maleic anhydride on surface and volume resistivity of natural fiber-polystyrene composites. *Polym Plast Technol Eng* 46(5):537–540
4. Bledzki AK, Faruk O (2004) Wood fiber reinforced polypropylene composites: compression and injection molding process. *Polym Plast Technol Eng* 43(3):871–880
5. Holt GA, Chow P, Wanjura JD et al (2014) Evaluation of thermal treatments to improve physical and mechanical properties of bio-composites made from cotton by products and other agricultural fibers. *Indus Crop Prod* 52:627–632
6. Shamria SL, Shamsun N, Mahbub H (2015) Fabrication and electrical characterization of bamboo fiber-reinforced polypropylene composite. *J Reinf Plast Compos* 34:187–195
7. Qaiss AEK, Bouhfid R, Essabir H (2014) Natural fibers reinforced polymeric matrix: thermal, mechanical and interfacial properties. In: Hakeem KR, Jawaid M, Rashid U (eds) *Biomass and bioenergy: processing and properties*. Springer International Publishing, Switzerland, pp 225–244
8. Clemons C, Sanadi AR (2007) Instrumented impact testing of kenaf fiber reinforced polypropylene composites: effects of temperature and composition. *J Reinf Plast Compos* 26:1587–1602
9. Vasoya PJ, Mehta NM, Parsania PH (2007) Mechanical, electrical and water absorption study of jute-glass, jute-bamboo, glass-bamboo-bisphenol-C-formaldehyde-acrylate a value added composites. *Polym Plast Technol Eng* 46(6):621–628
10. Kumar SMN (2006) Siddaramaiah studies on acrylonitrilebutadiene (NBR) latex-reinforced jute nonwoven fabric composites: chemical resistance, mechanical properties and water absorption. *Polym Plast Technol Eng* 45(3):409–414

11. Ruban YJV, Mon SG, Roy DV (2014) Chemical resistance/thermal and mechanical properties of unsaturated polyester-based nanocomposites. *Appl Nanosci* 4(2):233–240
12. Varada Rajulu A, Allah baksh S, Ramachandra Reddy G, Narasimhachary K (1998) Chemical resistance and tensile properties of short bamboo fiber reinforced epoxy composites. *J Reinf Plast Compos* 17(17):1507–1511
13. Singha AS, Thakur VK (2009) Chemical resistance, mechanical and physical properties of biofibers-based polymer composites. *Polym Plast Technol Eng* 48:736–744
14. Raghu K, Noorunnisa Khanam P, Naidu S (2010) Chemical resistance studies of silk/sisal fiber-reinforced unsaturated polyester-based hybrid composites. *J Reinf Plast Compos* 29(3):343–345
15. Aprilia NS, Hossain MS, Abdullah C, Khalil HA, Rosamah E, Dungani R, Davoudpour Y, Zaidul IM (2015) Environmental durability of vinyl ester composites filled with carbonized jatropha seed shell. *BioResources* 10(2):2350–2359
16. Pandian A, Vairavan M, Thangaiah WJJ, Uthayakumar M (2014) Effect of moisture absorption behavior on mechanical properties of basalt fibre reinforced polymer matrix composites. *J Compos* 2014:8
17. Kahraman R, Sharkh BA (2007) Moisture absorption behavior of palm/polypropylene composites in distilled water and sea water. *Int J Polym Mater Polym Biomater* 56(1):43–53
18. Bradley WL, Grant TS (1995) The effect of the moisture absorption on the interfacial strength of polymeric matrix composites. *J Mater Sci* 30(21):5537–5542
19. Daly HB, Brahim HB, Hfaied N, Harchay M, Boukhili R (2017) Investigation of water absorption in pultruded composites containing fillers and low profile additives. *Polym Compos* 28(3):355–364
20. Lucas N, Bienaime C, Belloy C, Queneudec M, Silvestre F, Saucedo JEN (2008) Polymer biodegradation: mechanisms and estimation techniques—a review. *Chemosphere* 73(4):429–442
21. Sunilkumar M, Francis T, Thachil ET, Sujith A (2012) Low density polyethylene-chitosan composites: a study based on biodegradation. *Chem Eng J* 204–206:114–124
22. Shamsabadi MA, Behzad T, Bagheri R, Nasrabadi BN (2015) Preparation and characterization of low-density polyethylene/thermoplastic starch composites reinforced by cellulose nanofibers. *Polym Compos* 36(12):2309–2316

Chapter 53

Construction and Characterization of Graphene-Polyvinyl Alcohol Nanocomposite as Thermolement With High ZT Factor



K. R. V. Subramanian, B. V. Raghuvamsi Krishna, G. S. Rohith, Raji George, and T. Nageswara Rao

Abstract In this work, we designed and fabricated a thermolement using nano-graphene composite, and its thermoelectric property was enhanced with higher ZT factor. A graphene composite material monolith was synthesized using solid state fabrication techniques and this was characterized for various thermophysical properties. A maximum ZT factor of 4.3 was achieved with 40 wt% graphene-PVA (polyvinyl alcohol) nanocomposite, which is higher than conventional vapor compression thermolements. This would pave the way for more efficient Peltier devices and thermoelectric refrigerators.

Keywords Peltier · Graphene · Nanocomposite · Seebeck · Thermal conductivity · Electrical conductivity

1 Introduction

Refrigeration is a process in which work is done on a system to transfer heat from cold body to hot body to generate cooling effect. It helps to maintain the temperature of certain space at a sub-ambient temperature. Heat is rejected from the system to the surroundings and is driven by a mechanical device. Refrigeration helps in storing food products and preservation of medicine. Another variation is air conditioning employed in hot and humid places. Solar refrigeration system uses electricity directly produced from solar radiation using photovoltaic cells or solar collectors. Use of this will be more widespread with the decrease of fossil fuels and higher pollution levels.

K. R. V. Subramanian (✉) · G. S. Rohith · R. George
Department of Mechanical Engineering, Ramaiah Institute of Technology, MSR Nagar, Bangalore 560054, India
e-mail: krvsubra@msrit.edu

B. V. Raghuvamsi Krishna · T. Nageswara Rao
Department of Mechanical Engineering, GITAM University, Nagadenahalli, Bangalore 562163, India

The conventional vapor compression cycle is widely used due to its fairly good COP (~3–4). These systems use chlorofluorocarbons (CFCs) refrigerants which, however, have a high ozone depletion potential (ODP), and produce greenhouse gases and other pollutants. Thermoelectric devices can be used for cooling purposes and this is called thermoelectric refrigeration. Thermoelectric Refrigeration (TER) or Thermoelectric cooler provides cooling effect by Peltier effect as opposed to ‘vapor compression cycle’ or the ‘gas compression cycle’. In Peltier effect, a current flow produces a temperature gradient across the junctions of two dissimilar metals. The thermal current density q is given by Eq. (1), where π and j are the Peltier coefficient, and electrical current density respectively.

$$q = \pi j \quad (1)$$

The applications for thermoelectric coolers can span different areas and industries. A thermoelectric cooler (TEC) converts electrical energy into a temperature gradient. The TEC is composed of thermoelectric couples.

The coefficient of performance (COP) of vapor compression refrigerators depends upon its capacity. TER gives rise to a low capacity refrigerator with better control over refrigeration space temperature. Researchers over the world are constantly striving for new materials for advanced thermoelectric energy conversion applications and to make existing thermoelements/materials perform better.

The parameter, figure of merit, ZT represents the efficiency of the thermoelements. It is represented by:

$$ZT = \frac{\alpha^2 \sigma}{\kappa T} T \quad (2)$$

where T is the temperature difference, α is the Seebeck coefficient or thermoelectrical power, σ is the electrical conductivity and κT is the total thermal conductivity.

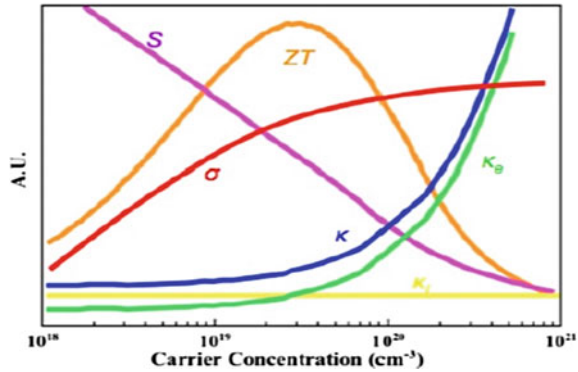
As seen from Eq. (2), a higher ZT results when α and σ is high, and κT is low. High κT (thermal conductivity) reduces the FOM and results in unfavorable thermal exchange between hot and cold sides of a thermoelectric device.

In Fig. 1 this dichotomous behavior is shown; increasing the carrier concentration in order to increase electrical conductivity, also gives rise to high thermal conductivity, and the Seebeck coefficient starts to decrease with higher thermal conductivity.

In this case, thermoelements with a higher ZT is advantageous because it gives a superior cooling capacity and this can be achieved with material optimization.

Riffat [1] has studied thermoelectric refrigeration with use of bismuth telluride. Large temperature differentials (up to 130 °C) can be achieved by multistage (cascade) series with the lowest temperature about –100 °C. Lifetime of this system is about 100,000 h and can withstand harsh environments. Rawat [2], designed and developed 1 L thermoelectric refrigeration system. Cooling is achieved by using four thermoelectric cooling modules ($Q_{\max} = 19 \text{ W}$) and a heat sink fan assembly (R_{th}

Fig. 1 Variation of figure of merit



= 0.50 °C/W) for each thermoelectric module. A no-load temperature reduction of 11 °C and reduction of 9 °C with load has been realized. The COP was 0.1. Abdulwahab [3], developed thermoelectric system using fins for use in arid conditions. The design uses 10 thermoelectric modules. Bass [4] has studied the low COP of 1-D thermoelectric modules using “multilayer quantum wells” which increased the COP by four to five times.

Materials such as Bi_2Te_3 and Bi_2Se_3 have ZT, between 0.8 and 1.0. Nanostructuring these materials to produce a layered doped superlattice structure of alternating Bi_2Te_3 and Sb_2Te_3 layers results in ZT of 2.4 at room temperature [5, 6].

Heremans [7] studied ZT of thallium-doped lead telluride alloy (PbTe) with a value of 1.5 at 773 K. Pei et al. [8] reported ZT ~ 1.4 at 750 K in sodium-doped PbTe and ZT ~ 1.8 at 850 K in sodium-doped $\text{PbTe}_{1-x}\text{Se}_x$ alloy. A heat to electricity conversion ratio of 15–20% was shown in PbTe , with a ZT of 2.2 [9].

Layered $\text{Ca}_3\text{Co}_4\text{O}_9$ demonstrated ZT values of 1.4–2.7 at 900 K. Recently, oxide thermoelectrics such as ZnO , MnO_2 , and NbO_2 showed higher ZT values [10–13].

CNT’s (carbon nanotubes) have proven to be good thermoelectric materials. Hick showed that 1-D conductors or quantum wires have high performance. The ZT value for 1-D Bi_2Te_3 nanomaterials is 2.6, which is much higher than that of the 2-D (ZT = 2.5) and 3-D (ZT = 0.5) materials [14].

Graphene has high electrical conductivity but its thermal conductivity is high, limiting its ZT. Using oxygen plasma treatment, ZT of graphene doubled twice to 2.6 corresponding to an increase in defect density from 0.04 to 2.5 [15, 16].

$\text{Mg}_2\text{B}^{\text{IV}}$ ($\text{B}^{\text{IV}} = \text{Si}, \text{Ge}, \text{Sn}$) compounds and their solid solutions are good thermoelectric materials. Doping, eg. with Sn, Ga, Ag, or Li, gives rise to p-type material which is required for an efficient thermoelectric device. At temperature of 800 K, $\text{Mg}_2\text{Si}_{0.55-x}\text{Sn}_{0.4}\text{Ge}_{0.05}\text{Bi}_x$ has been reported to have ZT of about highest value of 1.4 [17].

Skutterudites having a chemical composition of LM_4X_{12} , exhibit $\text{ZT} > 1.0$ and can be employed in multistage thermoelectric devices.

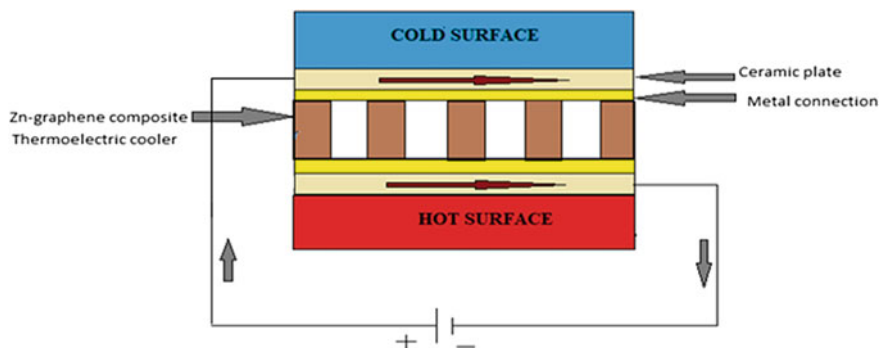


Fig. 2 Peltier cooler setup using graphene composites

Vacancies in these materials can be filled with low-coordination ions (usually rare-earth elements) to reduce thermal conductivity without sacrificing electrical conductivity. The thermal conductivity in skutterudite vacancies can be reduced with an architecture containing nano- and micro-pores [18].

Thermoelectric efficiency can be enhanced if the phonon mean free path is larger than the charge carrier mean free path and can be obtained in amorphous thermoelectrics (Cu–Ge–Te, NbO₂, In–Ga–Zn–O, Zr–Ni–Sn, Si–Au, and Ti–Pb–V–O amorphous systems). Amorphous thermoelectrics however give rise to extensive phonon scattering, which has to be overcome with better material design [19].

In this paper, with the help of Graphene nano composites, it was proposed to increase $ZT > 4$. This will have high electrical conductivity and relatively lower thermal conductivity. A graphene composite material monolith was synthesized using solid state fabrication techniques and this was characterized for thermophysical properties. Using the prepared graphene composites as thermomaterials, the Peltier cooler was developed as in Fig. 2.

A maximum ZT factor of 4.3 was achieved with 40 wt% graphene-PVA (polyvinyl alcohol) nanocomposite.

2 Materials and Methods

2.1 Materials

Graphene nano-powder was procured from Ad-Nano Technologies, Shimoga, India. The graphene powder was subjected to Raman spectra analysis and FESEM at source (Fig. 3a, b). Raman spectra show the G, D, and 2D band at 1600, 1280, and 2690 cm^{-1} respectively.

FESEM shows the flaky nature of graphene.

Polyvinyl alcohol (PVA) powder was purchased from Akshar Chemicals, Gujarat.

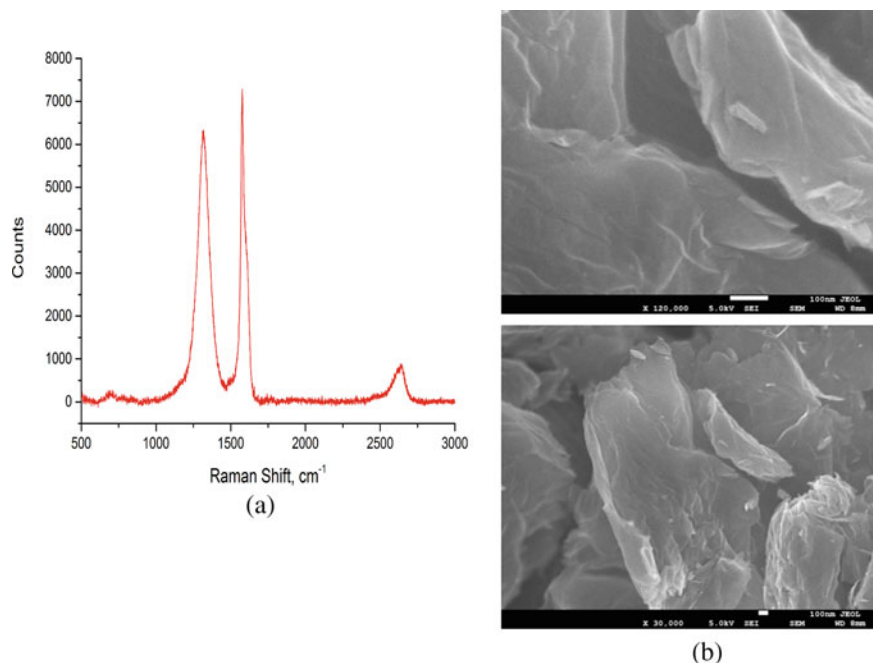


Fig. 3 **a** Raman spectra of graphene, **b** FESEM of graphene flakes

2.2 Preparation of PVA Samples

1.7 g of PVA was weighed using weighing balance and mixed with 2.5 ml of distilled water. The compacting mould was prepared using 20 mm diameter steel rod and subjected to lathe operations such as facing, turning, drilling. PVA is then transferred to a pre-sintering mould and subjected to a temperature of 50–75 °C for 10 min. It is then transferred to a compacting mould and pressure is gently applied using a tensometer to compact the powder (as shown in Fig. 4a, b). After compaction, the green compact is transferred to a sintering mould kept inside a sintering furnace and subjected to varying temperatures and times in order to achieve optimum sintering.

2.3 Preparation of Graphene-PVA Nanocomposite Samples

1.7 g of PVA was weighed using weighing balance and mixed with 2.5 ml of distilled water. The compacting mould was prepared using 20 mm diameter steel rod and subjected to lathe operations such as facing, turning, drilling. Graphene is then added in varying quantities (3%, 4%, 5%, 6%, 30%, 40 wt%) to this mixture. Graphene-PVA mixture is then transferred to a pre-sintering mould and subjected to a temperature

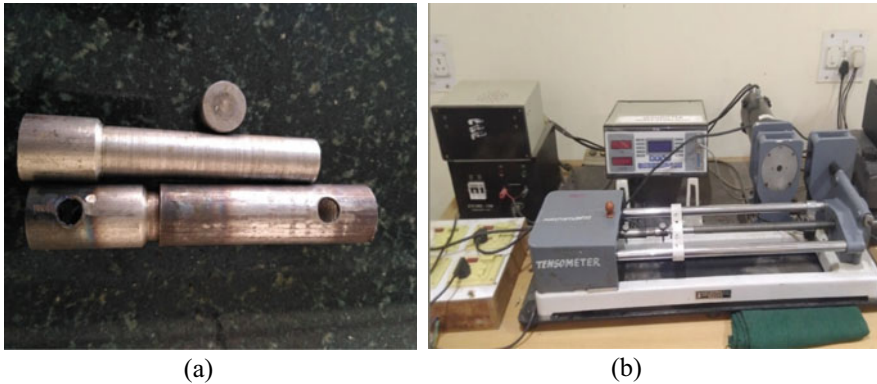


Fig. 4 **a** Compacting mould, **b** Tensometer used for compaction

of 50–75 °C for 10 min. It is then transferred to a compacting mould and pressure is gently applied using a tensometer to compact the powder (as shown in Fig. 4a). After compaction, the green compact is transferred to a sintering mould kept inside a sintering furnace (Fig. 5a, b) and subjected to a temperature of 300 °C for 15 min in order to achieve optimum sintering.

2.4 Measurement of Thermal Conductivity

The thermal conductivity of nanocomposites was measured using thermal conductivity meter (Fig. 6) by varying temperature and power supply. The equipment is used to determine the thermal conductivity of metals, alloys, and metal composite.

ASTM E1225 Test Method is adopted in this tester. ASTM E1225 Test Method is frequently used in axial thermal conductivity tests (Ref. ASTM E125-04 Manual) having thermal conductivity range of 0.2–200 W/mK.

Temperature range: RT—500 °C.

- Power: 10—100 W
- Flow Rate of Cooling Water: 100 mL/min
- Specimen Melting Point: Above 500 °C
- Specimen Dimensions: 8 mm dia. and 50 mm length with a flat surface at both ends of the cylindrical sample

Unique Features of the Model:

- Fabricated to meet the experimental requirements
- In ASTM 1225 test method, only temperatures at the heater side reference specimen 1, junction between specimen 1 and 2 with test specimen, and cooler side reference specimen 2 are sufficient (maximum four temperatures) to find out the thermal conductivity of the materials.

Fig. 5 a Sintering mould,
b Sintering furnace



(a)

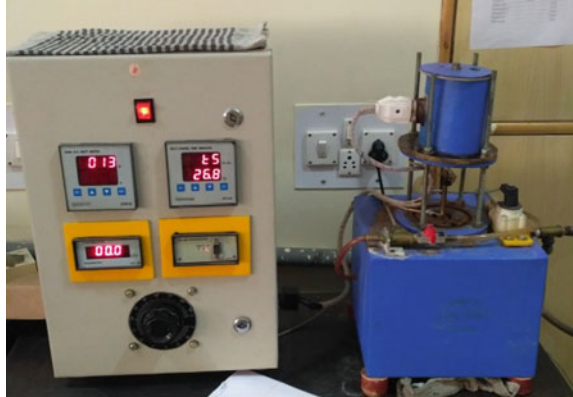


(b)

- Does not require to consider (1) heat flux generation, (2) heat flow rate, (3) heat carried away from the cooling side of the specimen unlike ASTM C177 test method
- In other thermal conductivity test methods, there is a need to consider the heat flux generation (ASTM C177 test method). Measurement of these parameters complicates the equipment design, thus results obtained with ASTM 1225 method will be free from the accuracy dilution.

The thermal conductivity meter consists of four thermocouples which are mounted from top to bottom side of specimen. Once the specimen is set up the power supply is given and corresponding temperature at entry and exit of specimen and water temperature is noted using thermocouples. Let temperature of thermocouples be T_1 ,

Fig. 6 Thermal conductivity meter



T_2, T_3, T_4 . Thermal conductivity is calculated using formula:-

$$K_s = KR \times \frac{L_s}{LR} \times \left(\frac{(T_1 - T_2) + (T_3 - T_4)}{2(T_2 - T_3)} \right) \text{ W/mK} \tag{3}$$

where

T_1, T_2, T_3, T_4 are the thermocouples temperature in kelvin.

L_s = Length of specimen in meter = 0.05 m.

LR = Total length of mounting rod in meter = 0.05 m.

KR = Thermal constant = 135.

2.5 Measurement of Electrical Conductivity

The resistance of the composites is measured using a multimeter. And resistivity is calculated using formula.

$$R = \rho \frac{L}{A} \tag{4}$$

where

R = Resistivity.

ρ = Resistivity constant.

L = Length of specimen in meter.

A = Area of specimen in m^2 .

The reciprocal of conductivity gives resistivity ie.

$$C = \frac{1}{R} \text{ s/m} \tag{5}$$

3 Results and Discussion

The PVA electrodes prepared at varying temperatures and their dimensional stability are shown in Fig. 7a, b, c, d. It is observed sintering at 270 °C (Fig. 7c) gives better dimensional stability for the pure PVA electrodes.

Graphene-PVA nanocomposites were prepared at various wt% of graphene and the sintered electrodes are shown in Fig. 8a–f. It is observed all samples show dimensional stability but 30% and 40 wt% samples are optimized. The temperature of sintering was chosen as 300 °C based on pure PVA studies described earlier.

The thermal conductivity in W/mK of the various wt% graphene-PVA nanocomposites was calculated according to Eq. (3) and tabulated in Table 1. Variation is shown in Fig. 9.

Similarly, electrical conductivity is calculated according to Eq. (4) and results are tabulated in Table 2. The variation is shown in Fig. 10.

The ZT of the various graphene-PVA nanocomposite thermoelements was calculated using Eq. (2) as earlier and tabulated in Table 3.

The Seebeck coefficient was taken as 80 mV/K from literature [20] for pure graphene and proportioned accordingly for $x\%$ graphene-PVA nanocomposite (for eg, a 30% graphene-PVA nanocomposite will have Seebeck coefficient of $0.3 * 0.08 = 0.024$ V/K), max. temperature difference taken as 20° absolute (Fig. 11).

3.1 COP of Peltier Cooler Based on Obtained ZT Factor

The efficiency of obtained Peltier cooler is calculated using Eq. (6).

$$\eta = \frac{\Delta T}{T_h} \frac{\sqrt{1 + ZT} - 1}{\sqrt{1 + ZT} + T_c/T_h} \quad (6)$$

By considering the standard parameters as $\Delta T =$ Temperature difference between hot and cold junction (30 °C). $T_h =$ Temperature at hot junction (50 °C). $T_c =$ Temperature at cold junction (20 °C) (Fig. 12 and Table 4).

Thus, it is seen that 40 wt% graphene-PVA nanocomposites have the highest ZT factor of 4.3. This can be attributed to an optimum combination of not very high thermal conductivity but at the same time possessing high electrical conductivity and dimensional stability. Graphene-PVA nanocomposites can be optimized to achieve high-performance thermoelectric properties. To enhance ZT values in graphene-based thermoelectric materials, two major challenges need to be overcome: (1) the graphene thermal conductivity is very large, and in this study was reduced by blending with PVA, and (2) the Seebeck coefficient is too small due to its zero band gap.

With the help of this optimized thermoelement using nanomaterials, it is proposed to construct a Peltier device and power the same with solar energy. This future work will be undertaken in the next phase.

SL NO	PARAMETER	READINGS	SL NO	PARAMETER	READINGS
1	Temperature deg celsius	200	1	Temperature deg celsius	270
2	Water	Distill	2	Water	Distill
3	Initial dimension	15 mm	3	Initial dimension	16 mm
4	Final dimension	16 mm	4	Final dimension	18 mm



(a)



(b)



(c)



(d)

SL NO	PARAMETER	READINGS
1	Temperature deg celsius	270
2	Water	Normal
3	Initial dimension	14 mm
4	Final dimension	17 mm

SL NO	PARAMETER	READINGS
1	Temperature deg celsius	250
2	Water	Distill
3	Initial dimension	16 mm
4	Final dimension	15 mm

Fig. 7 a PVA sintered at 200 °C, b and c PVA sintered at 270 °C, d PVA sintered at 250 °C

Fig. 8 **a** 3 wt% graphene-PVA nanocomposite, **b** 4 wt% graphene-PVA nanocomposite, **c** 5 wt% graphene-PVA nanocomposite, **d** 6 wt% graphene-PVA nanocomposite, **e** 30 wt% graphene-PVA nanocomposite, **f** 40 wt% graphene-PVA nanocomposite

SL NO	PARAMETER	READING
1	PVA	1.7 g
2	Water	2.5 ml
3	Graphene 3%	0.051g
4	Temperature	300 degeccsius
5	Time	15 min



(a)

SL NO	PARAMETER	READING
1	PVA	1.7 g
2	Water	2.5 ml
3	Graphene 4%	0.06g
4	Temperature	300 degeccsius
5	Time	15 min



(b)

SL NO	PARAMETER	READING
1	PVA	1.7 g
2	Water	2.5 ml
3	Graphene 5%	0.1025g
4	Temperature	300 degeccsius
5	Time	15 min



(c)

SL NO	PARAMETER	READING
1	PVA	1.7 g
2	Water	2.5 ml
3	Graphene 6%	0.1183g
4	Temperature	300 degeccsius
5	Time	15 min



(d)

SL NO	PARAMETER	READING
1	PVA	1.7 g
2	Water	2.5 ml
3	Graphene 30%	0.6372g
4	Temperature	300 degeccsius
5	Time	15 min



(e)

SL NO	PARAMETER	READING
1	PVA	1.7 g
2	Water	2.5 ml
3	Graphene 40%	0.643 g
4	Temperature	300 degeccsius
5	Time	15 min



(f)

Table 1 Thermal conductivity of graphene-PVA nanocomposites of various wt%

Sl No	Graphene composition (wt%)	Thermal conductivity (W/mK)
1	3	19.922×10^{-3}
2	4	20.3175×10^{-3}
3	5	20.7410×10^{-3}
4	6	21.0842×10^{-3}
5	30	26.3677×10^{-3}
6	40	27.6307×10^{-3}

Fig. 9 Variation of thermal conductivity of graphene-PVA nanocomposites of various wt%

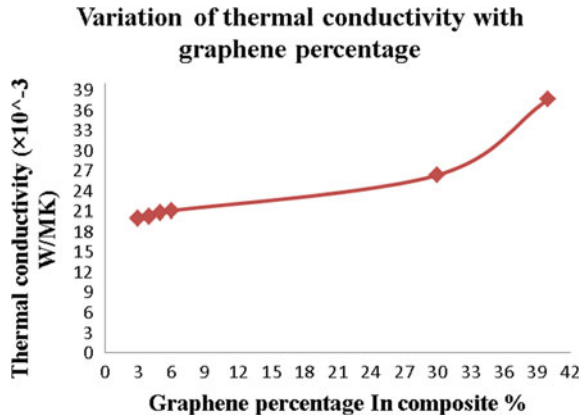


Table 2 Electrical conductivity of graphene-PVA nanocomposites of various wt%

Sl No	Graphene composition (wt%)	Electrical conductivity (S/m)
1	3	4.0987
2	4	4.2568
3	5	4.5649
4	6	4.7865
5	30	5.507
6	40	5.8076

4 Conclusions

Using graphene and PVA nanomaterials, thermoelements were synthesized and optimized. The nanocomposite having 40 wt% graphene and PVA was found to give the highest ZT factor of 4.3 which is higher than conventional vapor compression thermoelements. The thermoelement was also found to possess remarkable dimensional stability thus making it optimum for constructing Peltier electrodes and coupling with solar energy to realize efficient thermoelectric refrigeration.

Fig. 10 Variation of electrical conductivity of graphene-PVA nanocomposites of various wt%

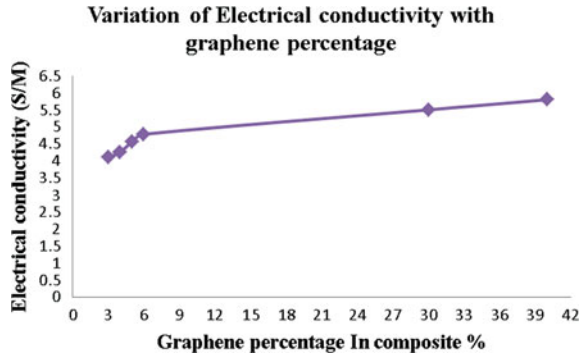


Table 3 Figure of merit (ZT) of different compositions of graphene nanocomposites

Graphene %	Seebeck coefficient	Electrical conductivity	Absolute temp diff	Thermal conductivity	ZT factor
30	0.024	5.507	20	0.0263	2.41
3	0.0024	4.0987	20	0.0199	0.023
4	0.0032	4.2568	20	0.0203	0.043
5	0.004	4.5649	20	0.0207	0.0705
6	0.0048	4.7865	20	0.02108	0.105
40	0.032	5.8076	20	0.0276	4.309

Fig. 11 Variation of ZT with graphene percentage in composite

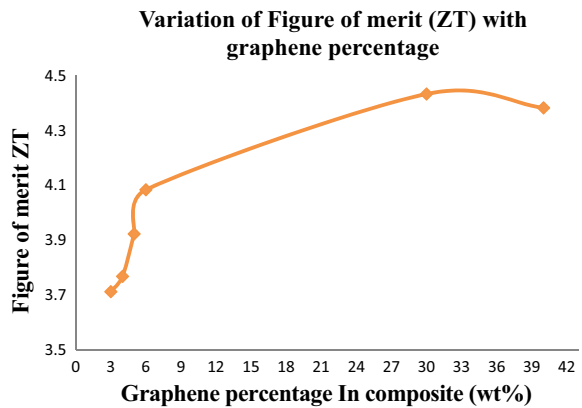


Fig. 12 Variation of Peltier cooler efficiency with graphene % in the composite

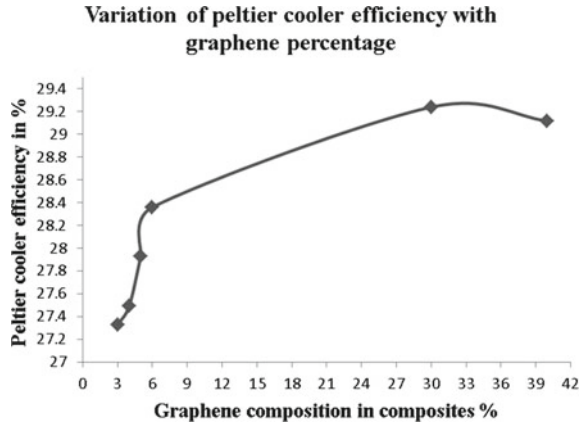


Table 4 Efficiency of peltier cooler for different compositions of graphene composites and their respective ZT

SL NO	Graphene composition (wt%)	Efficiency of peltier cooler (in %)
1	3	27.3271
2	4	27.4889
3	5	27.9245
4	6	28.3588
5	30	29.2406
6	40	29.11789

Acknowledgments The authors would like to acknowledge the management of Ramaiah Institute of Technology and GITAM University for their encouragement and support.

References

1. Riffat SB (2002) Thermoelectrics: a review of present and potential applications, University of Nottingham, NG7 2RD, UK
2. Rawat MK (2013) A review on developments of thermoelectric refrigeration and air conditioning systems: a novel potential green refrigeration and air conditioning technology. Int J 362. ISSN 2250-2459
3. Abdul-Wahab SA, Elkamel A, Al-Damkhi AM, Al-Habsi IA, Al-Rubai'ey HS, Al-Battashi AK, Al-Tamimi AR, Al-Mamari KH, Chutani MU (2009) Design and experimental investigation of portable solar thermoelectric refrigerator. Renew Energy 34:30
4. Bass JC (2004) New technology for thermoelectric cooling, 20th IEEE SEMI-THERM Symposium, San Jose USA
5. Chung DY, Hogan T, Schindler J, Iordarridis L, Brazis P, Kannewurf CR, Chen B, Uher C, Kanatzidis MG (1997) Complex bismuth chalcogenides as thermoelectrics. In: XVI ICT '97.

- Proceedings ICT'97. 16th International Conference on Thermoelectrics (Cat.No.97TH8291), 459
6. Venkatasubramanian R, Siivola E, Colpitts T, O'Quinn B (2001) Thin-film thermoelectric devices with high room-temperature figures of merit. *Nature* 413(6856):602
 7. Heremans JP, Jovovic V, Toberer ES, Saramat A, Kurosaki K, Charoenphakdee A, Yamanaka S, Snyder GJ (2008) Enhancement of thermoelectric efficiency in PbTe by distortion of the electronic density of states. *Science* 321(5888):7
 8. Pei Y, Lalonde A, Iwanaga S, Snyder GJ (2011) High thermoelectric figure of merit in heavy hole dominated PbTe. *Energy Environ Sci* 4(6):2085
 9. Pei Y, Shi X, Lalonde A, Wang H, Chen L, Snyder GJ (2011) Convergence of electronic bands for high performance bulk thermoelectrics. *Nature* 473(7345):9
 10. Ohtaki M (2011) Recent aspects of oxide thermoelectric materials for power generation from mid-to-high temperature heat source. *J Ceram Soc Jpn* 119(1395):770
 11. Matsuno J, Fujioka J, Okuda T, Ueno K, Mizokawa T, Katsufuji T (2018) Strongly correlated oxides for energy harvesting. *Sci Technol Adv Mater* 19(1):908
 12. Music D, Schneider JM (2015) Critical evaluation of the colossal Seebeck coefficient of nanostructured rutile MnO₂. *J Phys Condens Matter* 27(11):115302
 13. Music D, Chen Y-T, Bliem P, Geyer RW (2015) Amorphous-crystalline transition in thermoelectric NbO₂. *J Phys D Appl Phys* 48(27):275301
 14. Harman TC, Taylor PJ, Walsh MP, Laforge BE (2002) Quantum dot superlattice thermoelectric materials and devices. *Science* 297(5590):2229
 15. Anno Y, Imakita Y, Takei K, Akita S, Arie T (2017) Enhancement of graphene thermoelectric performance through defect engineering. *2D Mater* 4(2):025019
 16. Mu X, Wu X, Zhang T, Go DB (2014) Luo: Thermal transport in graphene oxide—from ballistic extreme to amorphous limit. *Sci Rep* 4:3909
 17. Hirayama N, Iida T, Sakamoto M, Nishio K, Hamada N (2019) Substitutional and interstitial impurity p-type doping of thermoelectric Mg₂Si: a theoretical study. *Sci Technol Adv Mater* 20(1):160–172
 18. Khan AU, Kobayashi K, Tang D-M, Yamauchi Y, Hasegawa K, Mitome M, Xue Y, Jiang B, Tsuchiay K, Dmitri G, Mori T (2017) Nano-micro-porous skutterudites with 100% enhancement in ZT for high performance thermoelectricity. *Nano Energy* 31:152–159
 19. Nakamura Y (2018) Nanostructure design for drastic reduction of thermal conductivity while preserving high electrical conductivity. *Sci Technol Adv Mater* 19(1):43
 20. Delong L, Youning G, Yuexing C, Jiamei L, Qasim K, Yupeng Z, Yu L, Han Z, Heping X (2020) Recent progress of 2-D thermoelectric materials. *Nano-Micro Lett* 12:36

Chapter 54

Design of Nanoscale TIEO-Based Arithmetic Circuits Using QCA Implementation Paradigm



M. Jagadeeswari, C. S. Manikandababu, M. Aiswarya, and S. Manju

Abstract Background: By reducing transistor volume, the CMOS design dimension was greatly reduced. Because of actual limitations such as short channel effect, impurity difference increased lithography expense, and an additional significant factor, heat, CMOS technology tend to reach the end of its schedule. According to a record that includes a detailed short-lived approaching technology, QCA is listed as the basic element in the bright future opportunities. **Methodology:** Due to its improved characteristics such as energy efficiency, large density, and fast execution, massive capacity technology (QCA) is being used to render it CMOS. QCA circuits are constructed with QCA cells and circuits with a plurality gate and inverter are implemented. Logic of majority plays an important role in QCA circuit design. Subtractor and adder are essential. Most of the information architecture processing components. The use of independent adder and subtractor hardware improves both the field requirements and the device delay. Generally speaking, a single hardware is used to subtract and add. One of the most basic operations of arithmetic logic is the addition and subtraction unit. The full adder is a fundamental component in the configuration of adder and multiplier circuits. **Results:** This proposed work presents a novel three-input XOR gate-based complete adder with two designs and a full subtractor for a single layer with fewer QCA cells. Concerning single plate, a stronger full adder and full subtractor in QCA technology are proposed.

Keywords QCA designer · QCA designer E tool · TIEO (three-input exclusive OR gate) · Majority gate · Single layer

M. Jagadeeswari · C. S. Manikandababu · M. Aiswarya (✉) · S. Manju
Department of Electronics and Communication Engineering, Sri Ramakrishna Engineering College, Coimbatore 641022, India

M. Jagadeeswari
e-mail: jagadeeswari.m@srec.ac.in

C. S. Manikandababu
e-mail: manikandadababu.selvaraju@srec.ac.in

1 Introduction

Improvements in CMOS industry automation may result in difficulties such as intersect electric wiring, short channel capacitance result, leakage current values, and power dissipation in the circuit, as well as demanding problems found in Si electronic transistor technique such as high energy consumption and difficulty in potential size reduction. Improvements in CMOS industry mechanization might result in disadvantages such as intersect electrical system, short channel capacitance impact, outflow current, and power dissipation. Many factors influence high scaling. These issues include insufficient leakage current, increased power density ratios, and extremely high lithography costs. These issues have been reported as affecting the CMOS revolution's outcome over the next 10–15 years. QCA is one of the many options for nanoscale technology [1–3].

To overcome the shortcomings of CMOS techniques, new nanotechnology called quantum dot cellular automaton (QCA) is being developed [4]. CA is well-known for its benefits, such as its small scope and low power analysis. A self-build method in a QCA cell may produce a small number of nanometers by atomic efficiency. QCA circuits can also achieve 10 devices/cm width and operate at THz frequencies [5–7]. QCA is examined using arrays of quantum dot modules that are self-contained. Tougaw and Lent presented the core principle of QCA in 1993. The unique characteristic is that, unlike traditional electronics, logic conditions are initiated by a cell rather than voltage levels. Nanometer-Scale. The machine will process data using a two-electron configuration. For the standard of circuits, manufacturing inadequacy and inappropriate structure play a critical role [8]. Clocking technology was used in the transfer of information in QCA.

2 Terminology

2.1 QCA Cell

The main component of QCA logic gateways and circuits is the QCA cell. The geometry of a QCA cell resembles a cube, with four quantum dots in each of the cell's four corners. Quantum electrons cannot get away from quantum dots if there is enough electrical potential. Four tunneling junctions connect these four quantum dots. A cell is the fundamental building block of QCA; it is made up of four quantum dots arranged in a square pattern.

Equation 1 can be used to specify the polarization of the QCA cell. The polarization of a QCA cell can be designed by considering the states of four quantum dots: 1, 2, 3, and 4. In most cases, the QCA cell is imposed with two electrons, which are emitted into an underwater corridor near dots. $P = +1$ and $P = -1$ are two potential polarizations for a basic QCA cell. Figure 1 depicts two potential polarization configurations. Binary numerals logic “1” and logic “0” can be encrypted by using

Fig. 1 Advantage of crossover

Layered Approach	Advantages	Drawbacks
	It Provides modularity and clear interfaces.	Data overhead and processing, due to the duplication of functionality.
	Implementation simplicity, maintainability, flexibility, and scalability are maintained.	The more layers you have, the more risks you have for things to breakdown or data to get lost.
	Layered approach supports portability.	Various issues regarding Higher layer Vs. Lower layers.
	It Provides robustness and preserves stability.	Results in complex exploitation of user-intensive applications.
	It is a Time tested approach.	This leads to Sluggish operation modes on various applications.

polarization of $P = +1$ and $P = -1$ (Fig. 2).

$$P = \frac{(\rho_1 + \rho_2) - (\rho_2 + \rho_4)}{(\rho_1 + \rho_3) - (\rho_2 + \rho_4)} \tag{1}$$

The complex form of QCA is based on the important design channel underground within the electrons restrain in the shafts and the coulombic relationship within the electrons. The coulombs law, which states that electrons must occupy a position with a large separation due to coulombic repulsion, is used to track the shift of electrons in QCA cells. This can potentially be accomplished by focusing on the possible electron modification in the cell. The tractable polarization is shown in Fig. 1 since the QCA cell is a quad range configuration. A binary 0 is represented by polarization -1.00 , and a binary 1 is represented by polarization $+1.00$. The only two options are discussed based on the only two practical preparations of the electron are discussed, since all other locations of the electron result in topmost repulsion, as shown in Fig. 3.

Fig. 2 Core QCA cell with two possible options

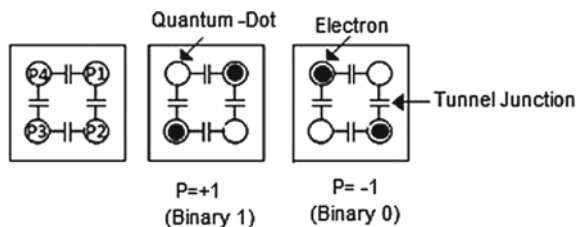


Fig. 3 Maximum and minimum repulsion positions electrons in QCA cell

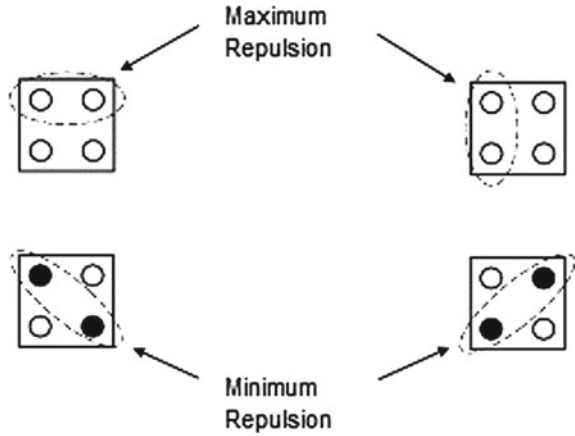


Fig. 4 Types of QCA Wire



2.2 QCA Elements

2.2.1 QCA Wire

An array of QCA cells grows a QCA regular cable. Columbic activity of neighboring cells transmits the input data from input to output. Figure 4 depicts two types of QCA cable, one with a 90-degree type cell and the other with a 45-degree type cell. By columbic association of the chain of QCA cells, the value of logic zero (or) one is passed from input to output.

2.2.2 QCA Logic Gates

Majority Gate (MG) (or) Majority Voter (MV) and QCA inverter is the most important logic primitives in QCA circuits. In QCA technology, such logic primitives are used to designing arithmetic logic circuits. Figure 5a shows two distinct types of QCA inverter designs and their symbol representations, whereas Fig. 5b shows a QCA majority gate design and its symbol representation. The majority gate’s feedback is divided into three categories: three-input MG, five-input MG, and seven input MG. The majorities in the inputs are denoted as the majority gate’s contribution. If the inputs to the majority gate are A, B, and C, the output is $Maj(A, B, C) = AB + BA + AC$.

Then, OR gates are used in QCA circuits with a single majority barrier. Set one input (say C) to 0 for AND process. $Maj(A, B, 0) = AB + 0 + 0 = AB$ is then

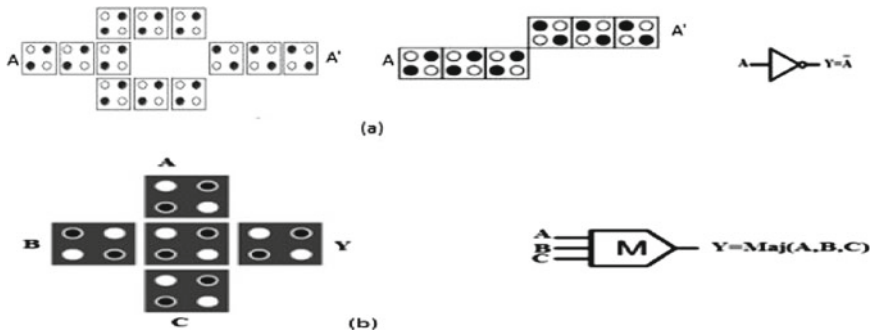


Fig. 5 a QCA inverter, b three-input majority gate (MG) in QCA

used to represent the output. As a result, it executes all operations. Set one input (say C) to 1 in the same way you did with the OR gate. $\text{Maj}(A, B, 1) = AB + B + A = A + B$ denotes the output. As a result, it executes an OR process. With a single majority gate, all AND and OR operations may be performed [9]. We can build complex circuits with fewer cells thanks to its features.

2.2.3 Role of Clocking in QCA

With clocking in QCA, computation with a variety of QCA cells has been presented. Using only input data (without explicit clocking) and one procedure, transmitting the collection to a quantum state of the device with greater force than the ground state. The order is required to solve to a new ground state, which may result in a transistor in a stable halfway position in certain situations [10–12].

It has been proposed that another approach be based on the clock to make it easier to get to a new ground condition. Clocking can be done in one of two ways: zone/sector clocking or uninterrupted clocking. Any QCA cell is moved using a four-phase clocking plan in the zone clock, as shown in Fig. 6. Turn, catch, calm, and release are the four stages. During the switch step, the cell is polarized and has a low potential buffer, but the restrictions are increased. Constraints are maintained at a high level in the control process, but they are reduced at the discharge point. The constraints remain reduced, and the cells remain unpolarized throughout the final stage, precisely relax. Continuous clocking is a variation of the zone clock that uses a series of dipped electrodes to group a possible field [13]. The crucial distinction between QCA and traditional CMOS methods is that a circuit in a QCA has no control over the clocking, unlike in CMOS. Broadcasting data to all cells are simple and unmaintained. Any clock loop, each cell “deletes” its state; additionally, each logic component in the QCA circuit is clocked.

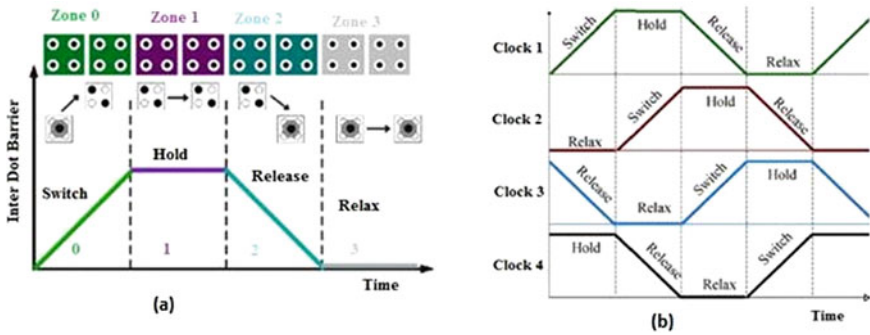


Fig. 6 QCA clocking a different clocking zones, b four phases of clocking zones

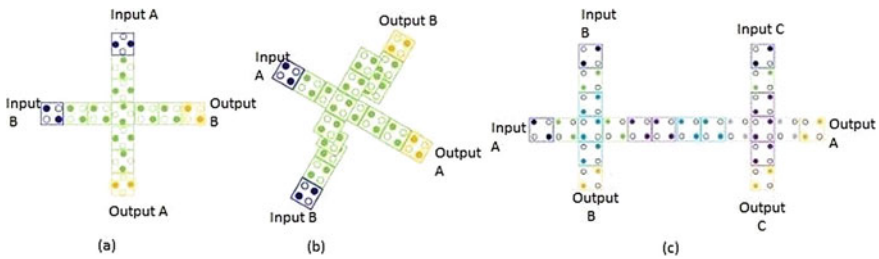


Fig. 7 QCA crossover a coplanar crossover, b multilayer crossover, c logical crossover

2.2.4 Role of Crossover in QCA

Three methods of wire crossing are used in QCA circuits: coplanar crossover, multi-layer crossover and logical crossover. In a coplanar crossover, one QCA wire has a 90-degree type cell and the other has a 45-degree type cell. Excessive engineered sensitivity is a disadvantage of coplanar crossover. The arrangement of coplanar wire crossing is shown in Fig. 7a. Many active QCA layers are used in multilayer crossover. It is much more precise than other crossover methods. As compared to the coplanar crossover, the multilayer crossover achieves more efficient wire crossing. Figure 7b shows a multilayer wire crossing system. The logical crossing is a kind of coplanar crossing. Four clock phases will conduct wire crossing interfering with this structure. The structure of logical wire crossing is shown in Fig. 7c.

3 Previous Full Adder Design in QCA

We tested a range of schematic designs focused on majority gate architecture for a one-bit complete adder with QCA configuration from the literature. Based on this observation, a one-bit complete adder is usually constructed with three inputs (A,

B, and Cin) and two outputs (Sum and Cout). The entire adder operation should be used to extract the output expressions. Equations 2 and 3 can be used to express the simpler output expressions.

$$\text{Sum} = ABC + A'B'C + A'BC' + AB'C' \tag{2}$$

$$\text{Cout} = AB + BC + C \tag{3}$$

QCA circuits can be constructed using primarily voter gate and inverter architecture in QCA technology. These two gates play a crucial role in the architecture of QCA circuits. The multiple minimized configurations of a one-bit complete adder can be reviewed in terms of majority gate in our references. The total equation is expressed as follows, based on the minimized structures.

$$\text{Sum} = \text{Maj}(\text{Maj}(A, B', \text{Cin}), \text{Maj}(A, B, \text{Cin}'), \text{Maj}(A', B, \text{Cin})) \tag{4}$$

$$= \text{Maj}(\text{Maj}(A', B, \text{Cin}), \text{Maj}(A, B', \text{Cin}), \text{Cin}') \tag{5}$$

$$= \text{Maj}(\text{Maj}(A, B, \text{Cin}'), \text{Cout}', \text{Cin}) \tag{6}$$

$$= \text{Maj}(\text{Maj}(A, B, C'), \text{Cout}', \text{Cin}) \tag{7}$$

$$= \text{Maj}(\text{Cout}', \text{Cin}, \text{Maj}(A, B, \text{Cin}')) \tag{8}$$

The schematic representation of Eq. 4 is shown in Fig. 8a, which uses four majority gates and three inverters for the sum process. This scheme employs 192 cells and is implemented using single-layer QCA circuits as described in [14]. Reference [6] shows how to obtain Eq. 5 by modifying Eq. 4 with three majority gates and three inverters for the sum contribution. The representation of Eq. 6 is provided in

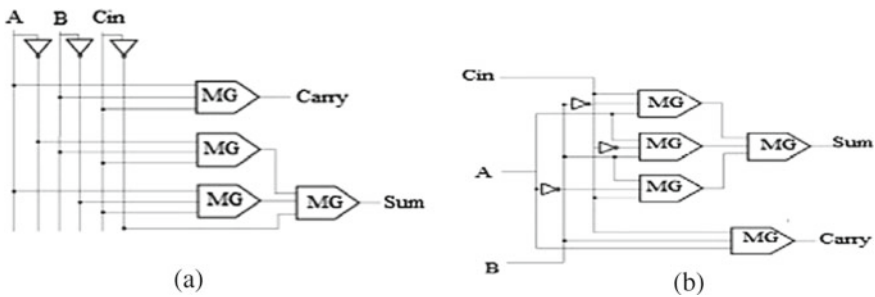


Fig. 8 a Adder circuit presented in [8], b adder circuit presented in [13]

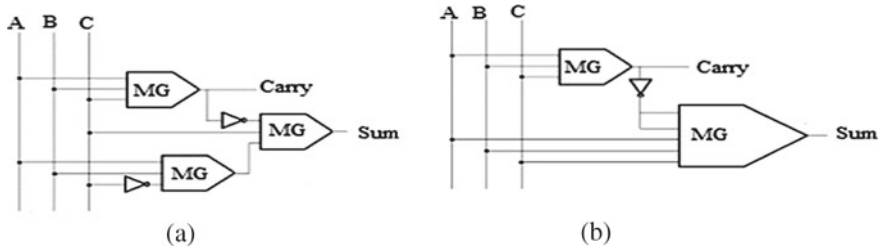


Fig. 9 a Adder circuit presented in [4], b adder circuit presented in [14]

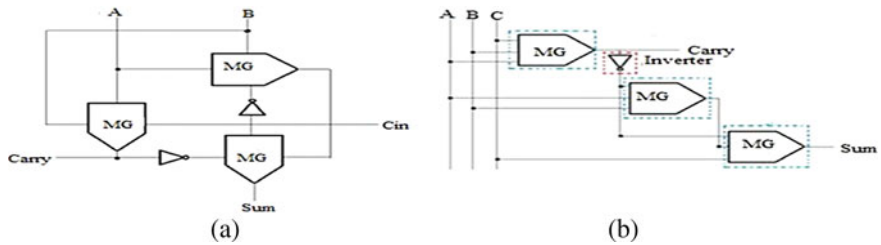


Fig. 10 a Adder circuit presented in [6], b adder circuit presented in [15]

[15] with two majority gates and two inverters, as shown in Fig. 9a. Four clocking stages implement this strategy with 145 cells. The five-input majority gate is a novel QCA circuit architecture. In [16], a novel one-bit adder configuration with five-input plurality was presented, with fewer QCA cells and their size expressed in Eq. 7. In [17] and [18], the QCA architecture of Eq. 8 was implemented in various systems. The QCA configuration in this plan has 82 cells in three clock phases for type-1 and 86 cells for type-2. The proposed configuration of the one-bit complete adder is based on three-input EXOR gates in this work (Fig. 10).

4 Proposed Design of TIEO Based Full Adder and Full Subtractor

4.1 Methodology

The proposed structure of a one-bit complete adder and subtractor can be modeled using three-input XOR (TIEO) operations in our research. In general, the total output of the complete adder can be expressed in terms of the XOR operation in Eq. 9.

$$\text{Sum} = A \text{ XOR } B \text{ XOR } C \tag{9}$$

The gate analysis with the two input and three-input in XOR gates are the most challenging gates in QCA technology's arithmetic architecture. QCA circuits can increase their overall circuit output by reducing latency and increasing cell count. Reference [19] presents a QCA plan of three-input XOR and two majority gates. Figure 11 shows the TIEO gate arrangement and QCA configuration. The proposed strategy in this work is to design a TEIO-based full adder and full subtractor. The proposed structure's power analysis can be investigated using the QCA Designer-E function. The suggested architectures were introduced in a single layer with a smaller number of cells (Fig. 12).

Two fundamental logic blocks have been used to execute TIEO-based full adder and full subtractor operations. Three-input XOR gates in one block execute sum or difference operations. Another stumbling block is the plurality doors. Cout is performed in full adder by a single majority gate, and Bout is performed in full subtractor by a majority gate of one inverter. In this article, the authors present two single-layer plans. Proper placement of these cell types will outline the basic geometry and lane used for QCA implementation of complete adder proposed design1 and design 2 cells, as shown in Fig. 13. Figure 14 depicts the two planned complete subtractor layout designs.

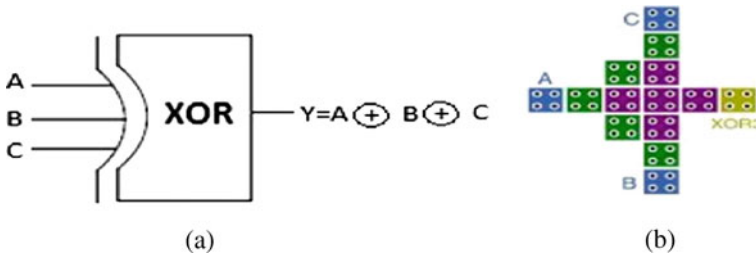


Fig. 11 Three-input XOR gate a symbol, b QCA layout

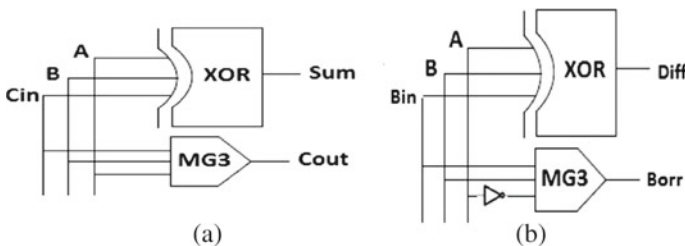


Fig. 12 Logical diagram using TIEO gate a the proposed full adder cell, b the proposed full subtractor cell

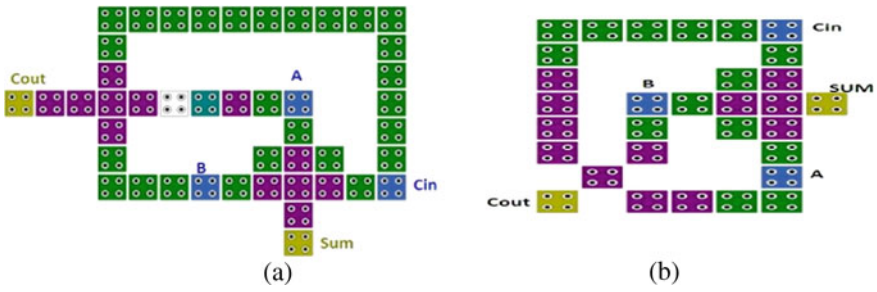


Fig. 13 QCA layout for the proposed full adder **b** design 1, **c** design 2

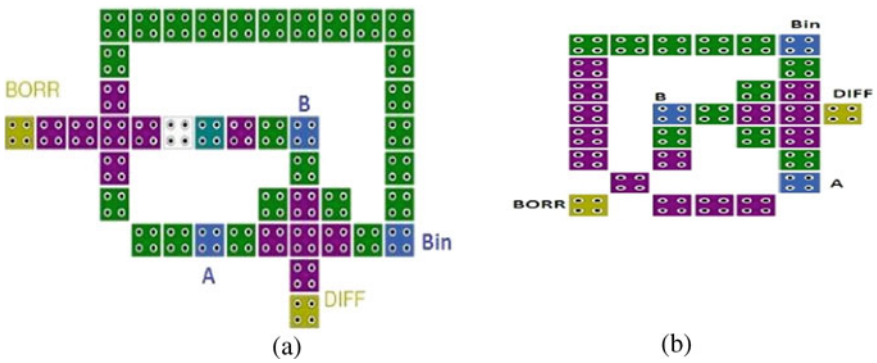


Fig. 14 QCA layout for the proposed full subtractor **a** design 1, **b** design 2

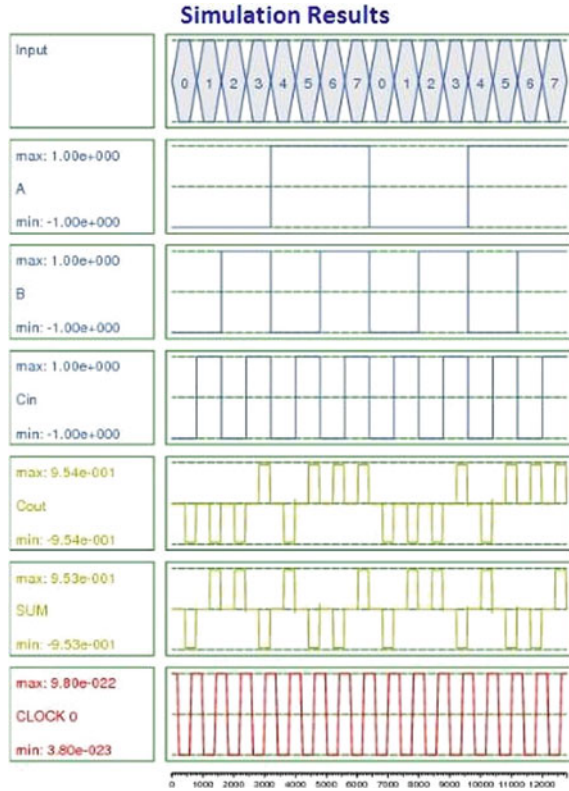
4.2 Result and Discussion

Designer simulations with QCA drive to ensure the circuit’s proper operation. Figures 14 and 15 display the imitation effect of the submitted QCA full adder and full subtractor. As can be shown, the proposed system’s output yields produce precisely severe polarized signals (shown within the rectangle), which are needed to provide the circuit with high drivability.

4.3 Power Analysis of the Proposed Adder

QCA Designer and QCA Designer-E CAD tools can be used to achieve simulation performance. Konrad Walus [20] presents QCA designer E, which is an extension of the QCA designer method. The proposed one-bit complete adder QCA logic circuits, which were simulated using the Bistable approximation simulation engine, have a radius force of 65 nm, a relative permittivity of 12.90, a clock high level of 9.8e-22 J, a clock low level of 3.8e-23 J, a layer separation of 11.50 nm, a total simulation

Fig. 15 Simulation result for the planned full subtractor



time of 7.0×10^{-11} s, and 12,800 samples. QCA designer E was used to do a power analysis of the planned structure. E_{bat} is the form of whole power changes in the graph to the bath of all cells for each register sequence that has been shorted. For each register pattern, E_{ct} is the overall potency proceed between QCA cells and the clock bisected, and E_{Et} is the form of all error of the cell energy scores for each log register. The thesis of inaccuracy is that over the whole log, the number of all power variations of the QCA cell is zero, where error = E_{bath} - (E_{clock} + E_{IO}). S_b is the number of cumulative potency changes to the immersion over the whole posture, and S_{bE} is the fault associated with it. For each register, A_b represents the median degree of energy applied to the bath and illusion. The adder takes 13 iterations and 38 s to whole the imitation procedure, while the subtractor incomes 13 iterations, and the test lasts 31 s [21]. Table 1 show the power overindulgence for the proposed one-bit occupied adder and full subtractor.

Table 1 Power loss in (eV) for the designed full adder

E_bath_total (E _{btx})	E_clk_total (E _{ctx})	E_Error_total (E _{EtX})	Sum_bath (S _b)	Avg_bath (A _b)
2.4010e-003	2.0478e-003	-2.3139e-004	3.11e-002 eV (Er:-3.11e-003 eV)	2.83e-003 eV (Er:-2.83e-004 eV)
2.7444e-003	9.4057e-004	-2.6084e-004		
2.9822e-003	3.3593e-004	-3.1536e-004		
3.3834e-003	8.1947e-004	-3.4484e-004		
2.9861e-003	8.1557e-004	-2.9866e-004		
3.1385e-003	3.2446e-004	-3.1646e-004		
2.5664e-003	9.3612e-004	-2.4068e-004		
2.7753e-003	2.0628e-003	-2.9366e-004		
2.4010e-003	2.0478e-003	-2.3139e-004		
2.7444e-003	9.4057e-004	-2.6084e-004		
2.9822e-003	3.3593e-004	-3.1536e-004		

5 Comparison and Analysis

Table 2 shows the proposed architecture of a TIEO-based full adder and full subtractor, as fit as its efficiency in comparison to an actual adder in terms of gate count, cell count, area, and delay. Our recommended strategy is to use a three-input XOR gate architecture with a single layer to achieve high performance with a low count. The suggested adder consistently performs well. Its clocking process is completed quickly. As shown in Fig. 13, our proposed complete adder design uses 44 and 31 cells with two clock phases and a 0.02 m² region. As shown in Fig. 14, the proposed complete subtractor architecture uses 43 and 30 cells with two clock phases and an approximately 0.02 m² area. The average power dissipation of a full adder is 2.83e-003 eV with a fault voltage of 2.83e-004 eV, and the average power dissipation of a full subtractor is 2.41e-003 eV with a fault voltage of -2.45e-004 eV.

6 Conclusion

The integrated complete adder and full subtractor plan is submitted in this work, along with a novel concept three-input XOR gate for a single layer. This proposed plan produces more precise and reliable data than previous systems. This arrangement would aid in the creation of arithmetic logic functions for high-speed digital circuits. QCADesigner E can also do power analysis and dissipation for proposed structures. The power analysis of the complete adder configuration is summarized in Table 1. Table 2 summarises various core parameters of various complete adder designs previously published in the literature, as well as the proposed design outlined in this

Table 2 Various study of QCA full adders

References	Type of implementation	Gate count	Cell count	Area (μm^2)	Latency (clock cycle)	Crossover type
[3]	Using 3 input MG	9	292	0.62	14	Multilayer crossover
[11]	Using 3 input MG	7	192	0.2	Not applicable	Multilayer crossover
[5]	Using 3 input MG	5	145	0.17	5	Multilayer crossover
[15]	Using 3 input MG	6	73	0.04	3	Multilayer crossover
[17]	Using 3 input MG	5	86	0.1	3	Multilayer crossover
	Using 3 input MG	4	61	0.03	3	Multilayer crossover
[21]	Using 5 input MG	3	51	0.03	3	Multilayer crossover
[18]	Using 3 input MG	4	38	0.02	3	Multilayer crossover
Proposed system	TIEO-based full adder 1	2	44	0.02	2	Not required
	TIEO-based full adder 2	2	31	0.02	2	Not required
	TIEO-based full subtractor 1	2	43	0.02	2	Not required
	TIEO-based full subtractor 2	2	30	0.02	2	Not required

paper. This projected QCA arithmetic has much superior structural and energy dissipation characteristics than previously developed ones, and it has shown significant advantages in all parameters.

References

1. Lent CS, Tougaw PD, Porod W, Bernstein GH (1993) Quantum cellular automata. *Nanotechnology* 4(1):49–57
2. Lent CS, Tougaw PD, Porod W (1994) Quantum cellular automata: the physics of computing with arrays of quantum dot molecules. In: *Proceedings of workshop on physics and computation*, pp 5–13. <https://doi.org/10.1109/PHYCMP.1994.363705>
3. Vetteth A, Walus K, Dimitrov VS, Jullien GA (2002) Quantum-dot cellular automata carry-look-ahead adder and barrel shifter. In: *Proceedings of IEEE emerging telecommunications technologies conference*, pp 2–4
4. Zhang R, Walus K, Wang W, Jullien GA (2004) A method of majority logic reduction for quantum cellular automata. *IEEE Trans Nanotechnol* 3(4):443–450. <https://doi.org/10.1109/>

TNANO.2004.834177

5. Walus K, Jullien GA (2006) Design tools for an emerging SoC technology: quantum-dot cellular automata. *Proc IEEE* 94(6):1225–1244. <https://doi.org/10.1109/JPROC.2006.875791>
6. Cho H, Swartzlander EE (2009) Adder and multiplier design in quantum-dot cellular automata. *IEEE Trans Comput* 58(6):721–727. <https://doi.org/10.1109/TC.2009.21s>
7. Crocker M, Niemier M, Hu XS, Lieberman M (2008) Molecular QCA design with chemically reasonable constraints. *ACM J Emerg Technol Comput Syst* 9:9. <https://doi.org/10.1145/1350763>
8. Tougaw PD, Lent CS (1994) Logical devices implemented using quantum cellular automata. *J Appl Phys* 75:1818. <https://doi.org/10.1063/1.356375>
9. Porod W (1997) Quantum-dot devices and quantum-dot cellular automata. *Int J Bifurc Chaos* 7(2199–2218):8–12. [https://doi.org/10.1016/S0016-0032\(97\)00041-0](https://doi.org/10.1016/S0016-0032(97)00041-0)
10. Tougaw PD, Lent CS, Porod W (1993) Bistable saturation in coupled quantum-dot cells. *J Appl Phys* 74:3558–3566, 9–13. <https://doi.org/10.1063/1.108848>
11. Snider GL, Orlov AO, Amlani I, Bernstein GH, Lent CS, Merz JL, Porod W (1998) Functional cell for quantum-dot cellular automata. *Solid-State Electron* 42:1355–1359, 10–14. [https://doi.org/10.1016/S0038-1101\(98\)00030-6](https://doi.org/10.1016/S0038-1101(98)00030-6)
12. Cho H, Swartzlander EE (2007) Adder designs and analyses for quantum-dot cellular automata. *IEEE Trans Nanotechnol* 6:374–383, 11–15. <https://doi.org/10.1109/TNANO.2007.894839>
13. Navi K, Farazkish R, Sayedsalehi S, Mostafa Rahimi A (2010) A new quantum-dot cellular automata full-adder. *Microelectron J* 41:820–826. <https://doi.org/10.1016/j.mejo.2010.07.003>
14. Azghadi MR, Kavehei O, Navi K (2007) A novel design for quantum—dot cellular automata cells and full adders. *J Appl Sci* 7:3460–3468. <https://doi.org/10.3923/jas.2007.3460.3468>
15. Mohammadi M, Mohammadi M, Gorgin S (2016) An efficient design of full adder in quantum-dot cellular automata (QCA) technology. *Microelectron J* 50:35–43. <https://doi.org/10.1016/j.mejo.2016.02.004>
16. Angizi S, Alkaldy E, Bagherzadeh N, Navi K (2014) Novel robust single layer wire crossing approach for exclusive or sum of products logic design with quantum-dot cellular automata. *J Low Power Electron* 10(2):259–271. <https://doi.org/10.1166/jolpe.2014.1320>
17. Walus K, Dysart TJ, Jullien GA, Budiman RA (2004) QCADesigner: a rapid design and simulation tool for quantum-dot cellular automata. *IEEE Trans Nanotechnol* 3(1):26–31. <https://doi.org/10.1109/TNANO.2003.8208>
18. Hashemi S, Navi K (2012) New robust QCA D flip flop and memory structures. *Microelectron J* 43(12):929–940. <https://doi.org/10.1016/j.mejo.2012.10.007>
19. Kamel K, Kamel E (2019) Process control ladder logic trouble shooting techniques fundamentals. *IRO J Sustain Wireless Syst* 1(4):206–241
20. Sen B, Dutta M, Goswami M, Sikdar BK (2014) Modular design of testable reversible ALU by QCA multiplexer with increase in programmability. *Microelectron J* 45(11):1522–1532. <https://doi.org/10.1016/j.mejo.2014.08.012>
21. Bansal M, Maiya RR (2020) Phototransistor: the story so far. *J Electron* 2(04):202–210

Chapter 55

Experimental and Numerical Determination of Natural Frequency of Woven Basalt Fibre–Vinyl Ester-Reinforced Composite Plates



J. Hemanth Kumar, Mahesh Dutt, and E. R. Babu

Abstract Control parts of an automobile undergo relentless vibration during its motion; to counteract this behaviour of the control parts, it is recommended to select composite materials in the manufacturing process over other available types of materials because of its various advantages. In this scenario, natural fibres, viz. sisal, basalt, etc., could be utilized in manufacturing certain control parts of an automobile as these are biodegradable, economical and light in weight. In this study, woven basalt fibre–vinyl ester-reinforced composite plates are prepared to investigate the free vibration characteristics where basalt fibre is considered as a reinforcement and vinyl ester as a matrix (BFRP). These composite plates are prepared by compression moulding technique with different basalt fibre compositions of 60, 50 and 45%. The natural frequencies and mode shapes for these prepared laminates were determined using impact hammer test maintaining an aspect ratio of 0.83. The measurements were found by fast Fourier transform (FFT)-based spectrum analyser and it was observed that the natural frequency of the laminate increased with the rise in laminate thickness. The frequencies obtained with respect to mode shapes from ANSYS were in par with the experimental values.

Keywords Basalt fibre-reinforced polymer · Compression moulding · Impact hammer test · Natural frequency · Fast Fourier transform

1 Introduction

The composites are found to be used as an alternative to the metal and its alloys in many applications like ship construction, automobile parts, sports equipment, etc.

J. Hemanth Kumar (✉)

Department of Mechanical Engineering, PES University—RR Campus, Bangalore, Karnataka, India

M. Dutt

Department of Mechanical Engineering, DASTM, Bangalore, Karnataka, India

E. R. Babu

Department of Mechanical Engineering, BIT, Bangalore, Karnataka, India

Advantages of fibre composites include better tensile strength, compressive strength, hardness, fatigue strength, etc. Due to low elastic modulus, the strength mass ratio and modulus mass ratio of these composite materials are markedly superior to those of metallic materials in recent years [1–5]. Structural materials with potential efficiency can be manufactured with the natural fibres mixed with suitable matrix material. Natural fibres, viz. sisal, bamboo, basalt, etc., are biodegradable, economical, renewable, easily available, light in weight, have good specific modulus, etc. In recent past, advanced composite materials are developed from materials like carbon, glass, Kevlar, etc. with suitable polymer used for advanced engineering applications. Composites are prepared by reinforcing natural fibre as reinforcement (FRP) using various forms like woven (uni-directional and bi-directional), strands, chopped, etc. and these forms are easily available. These fibres are mixed with commercially available resins to obtain a structure or a laminate. Woven fibres are commonly used for various applications by varying its thickness and structures. These FRPs possess better static as well as dynamic mechanical properties making them more suitable for structural applications. Aeroplane wings, fuselage beams, struts, etc. which are used in airplane structures can be prepared using these FRPs [6–9]. They can also be used in general applications like ship building, automobile body component and even in construction sites. Due to air load, dynamic fluttering occurs on the structures of aircraft during its operation. Damping influences resonant amplitude of vibration which is found on each structural mode. Therefore, it is very efficient to determine the modal damping and natural frequency. Dynamic characteristics of various fibre-reinforced composite materials are carried out by many researchers. Design of composite materials is based on various static and dynamic characteristics like tensile strength, shear modulus, coefficient of damping. Stiffness of composites depends on storage modulus and dissipation of energy of composites is associated with damping coefficient. Damping effect can be improved by strengthening/toughening the polymer matrix. Natural fibres are mixed with nanoparticles to improve certain mechanical, thermal and dynamic properties. Considering the fact that FRP composites (woven fibre) are not completely homogeneous, large areas rich in resins are formed on the boundaries because of different weaving patterns and fills. FRP composite structures performing at higher rate, the difference of stiffness is much lesser than the damping coefficient. Surface areas, where they are rich in large resins, generally act as independent damper elements. More works need to be concentrated on woven fibre orientations and its patterns especially for BFRP composites, to get better vibrational characteristics. Hence, in the present study, a woven fabric of basalt fibre of 350 GSM has been used as reinforcement in vinyl ester matrix. A total of three plates of 250×250 mm each, with varying thickness, were prepared by compression moulding technique to find the mode shapes and its natural frequency. The plate was fixed on to one end and other end was left free accounting an aspect ratio of 0.83. The measurements were analysed and found by fast Fourier transform (FFT)-based spectrum analyser. The natural frequencies of BFRP composite plates are determined experimentally and numerically [10].

2 Preparation of BFRP Composite Plates

BFRP composite plates were prepared by using compression moulding machine (Fig. 1). Fibre fabrics were cut into 250×250 mm size by considering the rule of mixtures; a total 5, 7 and 10 plies of woven basalt fibre were considered for the chosen fibre:resin ratios of 60:40, 50:50 and 45:55, respectively. Fibres were reinforced with vinyl ester resin to prepare the composite plates. The laminate was compressed at a pressure of 100 bar and at temperature of 60°C and cured for 2 h in the press after which the laminates were taken out and air-cooled for 24 h. The fibre and resin were mixed and compressed in the mould to form laminates. In total, three composite plates of above-mentioned fibre resin ratio were prepared as shown in Fig. 2.

Impact hammer/striker is used to study the free vibration analysis and to determine its natural frequencies. The impact hammer test was carried out for fixed-free boundary condition. Then results from these tests were compared with the results of ANSYS.

2.1 Experimentation

Figure 2 shows the laminate plates prepared by compression moulding technique. The laminates consisted of woven untreated basalt fabric of 360 GSM as reinforcement and vinyl ester resin as matrix material which is available commercially. Figure 3 illustrates the experimental set-up in which the composite plate is fixed as a cantilevered structure and the connections are made as shown. The composite plate was fixed on test fixture as shown in Fig. 4 and an impact hammer with a reactive



Fig. 1 Compression moulding equipment (hot press)



Fig. 2 BFRP laminate plates

Fig. 3 Block diagram of impact hammer experimental set-up

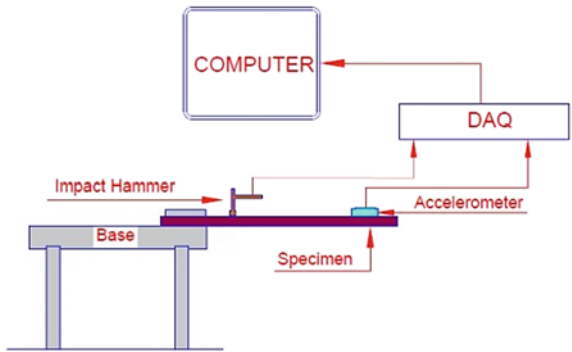


Fig. 4 Actual experimental set-up

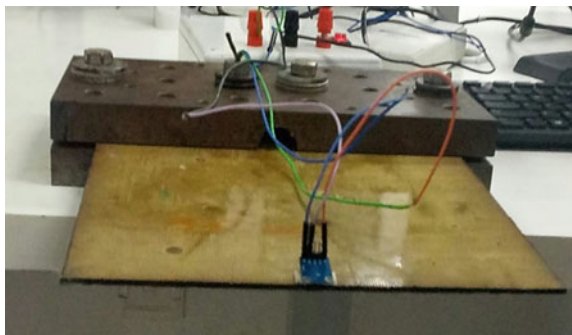


Fig. 5 Impact hammer/striker



technique to register the force input was used to excite the plate structure as shown in Fig. 5. The length of the laminate plate was measured excluding the margin length utilized to clamp the laminate on to the fixture. The remaining length was divided into five parts and the node number was marked in each division. The fixture was made of mild steel. It was made heavy in order to constraint the movement of the plate in both the directions (X and Y). Once the laminate was fixed, impact was provided by the striker on the points marked on the cantilever laminate plate.

An accelerometer was used to capture the displacement which was connected with Data Acquisition System (DAQ). These data were then transferred to the computer to get the frequency versus amplitude plot. Modal analysis was carried out using Ansys software. For this purpose, Shell Element 3D 4 node 181 was selected and orthographic properties of the composite plates were entered in material models. Young's modulus, Poisson's ratio and shear modulus of both fibre and resin material were entered. The number of layers and thickness of each layer which was calculated was also entered. The model was created according to the dimension and meshing was carried out using mesh tool. In order to obtain better results, the mesh was refined using the refine option in the mesh tool. Refining increased the number of elements and nodes which gives better results and then modal analysis was carried out by providing the frequency range. The laminate was considered as a cantilever beam and the results were obtained.

Figures 6, 7 and 8 show the plots obtained for the first node for the ratios 60:40, 50:50 and 45:55, respectively. The relation between the frequency and the time response gives a mathematical relation by combining with the FFT analyser. The resultant functions in the selected frequency range are registered logically. Tables 1, 2 and 3 show the changes in thickness of plate change the natural frequencies of the plates.

3 Results and Discussion

The cantilevered test plates of BFRPs having dimensions of 250×250 mm (thickness is varied from 2.3, 2.4 and 3.2 mm) are tested to obtain the modal properties for the given input frequency. A FFT analyser is used for the measurements and the measured values were carried to the unit for analysis and to fit the curve. Tables 1, 2 and 3 show the modal properties of BFRP 60:40, 50:50 and 45:55 ratios laminate, respectively.

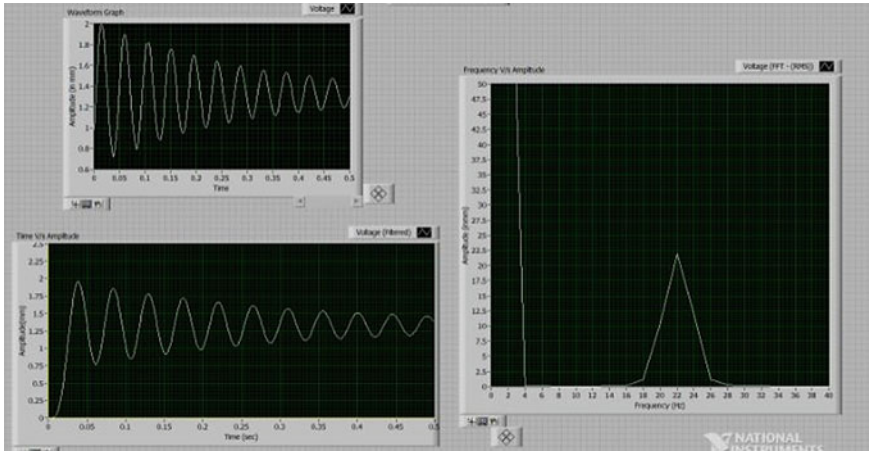


Fig. 6 Frequency versus amplitude plot (60:40 ratio)

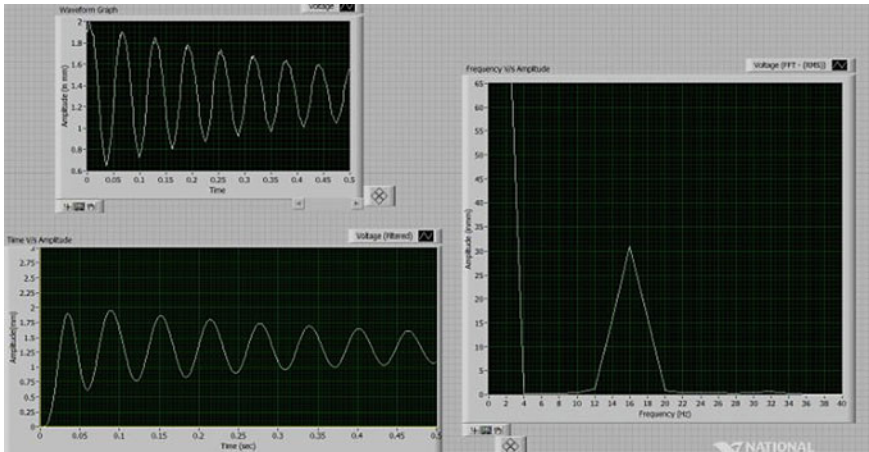


Fig. 7 Frequency versus amplitude plot (50:50 ratio)

A fixed-free boundary condition was used to receive the response from the laminate plate and values are obtained. The mode shape obtained for all three ratios at mode 1 is shown in Figs. 14, 15 and 16, respectively. The dynamic behaviour of the composite plates under various natural frequency ranges is characterized by the different mode shapes obtained during the experimentation. Generally, the mode shapes at different modes for a given test sample are classified as bending, twisting and combination of both [10]. Above data analysis shows that the changes in thickness of the laminate plates changed the natural frequency of the plates. The results of free vibrational characteristics procured experimentally and numerically were in good agreement. Thus, from the data obtained, it indicated that the natural frequency of the laminate

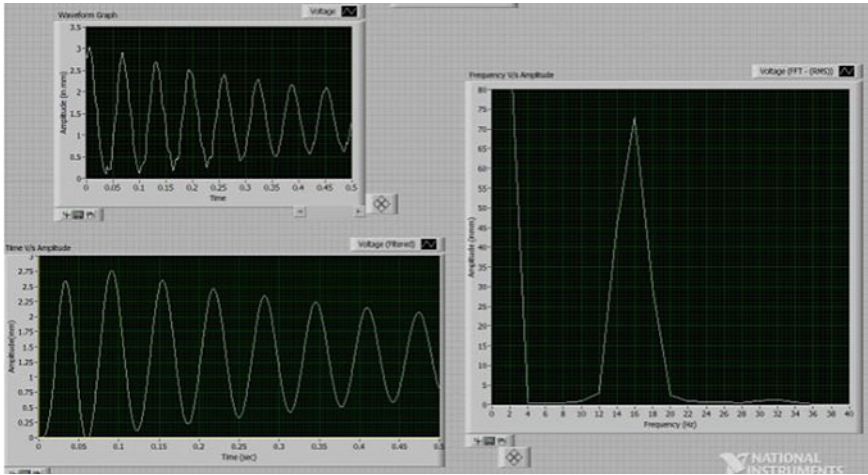


Fig. 8 Frequency versus amplitude plot (45:55)

Table 1 Modal properties of basalt laminate (60:40 ratio)

Mode no.	Frequency (f) (Hz)			
	ANSYS	Experimental	Damping factor (ξ) (%)	Error (%)
1	22.605	22.20	0.853	1.791
2	129.80	128.12	1.569	1.294
3	142.59	141.64	1.391	0.667
4	356.39	355.56	3.827	0.232
5	396.41	395.38	1.443	0.259

Dimension: (250 × 250 × 3.2) mm

Table 2 Modal properties of basalt laminate (50:50 ratio)

Mode no.	Frequency (f) (Hz)			
	ANSYS	Experimental	Damping factor (ξ) (%)	Error (%)
1	16.035	15.80	1.582	1.454
2	101.17	100.34	3.087	0.820
3	109.69	108.70	1.607	0.902
4	281.66	280.76	1.862	0.319
5	288.20	287.04	1.796	0.333

Dimension: (250 × 250 × 2.4) mm

Table 3 Modal properties of basalt laminate (45:55)

Mode no.	Frequency (f) (Hz)			
	ANSYS	Experimental	Damping factor (ξ) (%)	Error (%)
1	15.815	14.96	1.228	5.476
2	106.09	105.8	1.999	0.273
3	125.11	124.8	0.953	0.247
4	300.93	298.94	1.258	0.661
5	312.61	310.54	1.187	0.662

Dimension: (250 × 250 × 2.3) mm

improved with the rise in laminate thickness. Figures 9, 10, 11, 12 and 13 represent the experimental mode shapes obtained. The first mode shape was bending, second was twisting, third was combination of bending and twisting, fourth was double bending and last was a complex mode. The damping factor for each mode is shown in the tables above and can be compared with each mode of all the three laminate plates to conclude the better damping factor amongst the three plates.

Fig. 9 Experimental 1st mode: bending mode

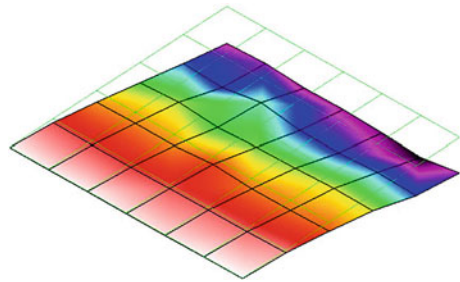


Fig. 10 Experimental 2nd mode: twisting mode

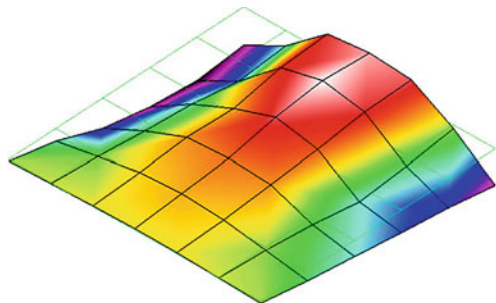


Fig. 11 Experimental 3rd mode: bending and twisting mode

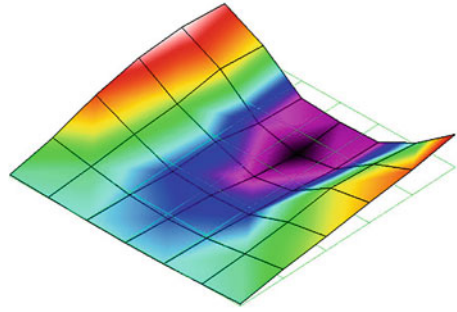


Fig. 12 Experimental 4th mode: double bending mode

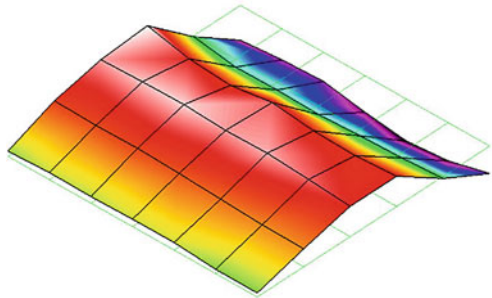


Fig. 13 Experimental 5th mode: complex mode

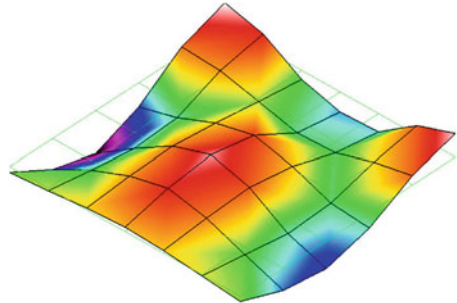


Fig. 14 Ansys mode shape-1, $f = 22.605$ Hz (60:40 ratio)

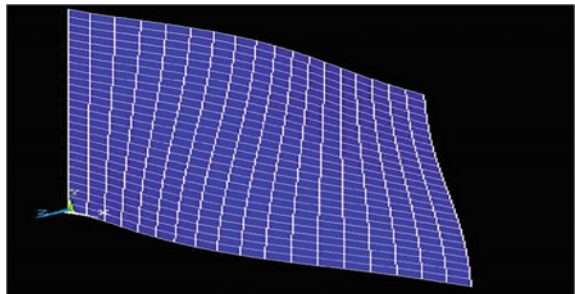


Fig. 15 Ansys mode shape-1, $f = 16.305$ Hz (50:50 ratio)

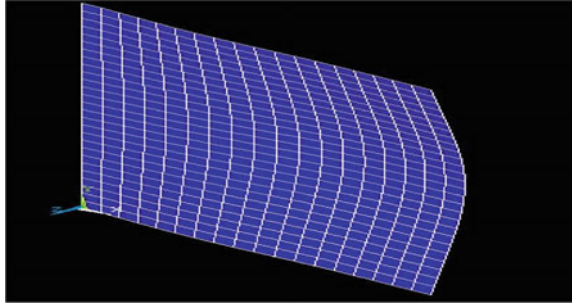
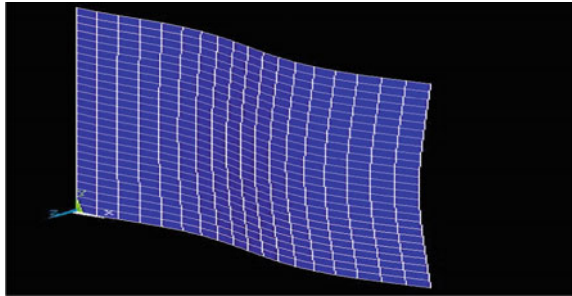


Fig. 16 Ansys mode shape-1, $f = 15.815$ Hz



4 Conclusion

In the present study, both experimental and numerical studies were conducted for woven basalt fibre–vinyl ester composite plate with different fibre-to-resin ratios. Different results were presented to show the effect of thickness in fix-free condition. Increase in density of the laminate plate should decrease the natural frequency [11]. In this study, only the thickness of the plate was varied by increasing the number of plies of woven basalt fibre and constant aspect ratio was maintained. The density of the three laminate plates remained almost the same even in varying thickness and hence the natural frequency increased with the increase in laminate plate thickness. Another parameter to be considered is the aspect ratio, where it can be considered as increase in aspect ratio, increases the natural frequency [12]. ANSYS software was used for the numerical analysis and the results obtained from the ANSYS gave a good agreement with the experimental results. The comparative results show some percentage errors because of manufacturing defects, experimental defects, assumptions considered, etc., but the percentage errors between them are negligible [13, 14]. This method had explored to predict the dynamic behaviour of basalt fibre–vinyl ester-reinforced composite plate, in order to design plates and other similar structures used in different applications such as automobile industry, roofing material used for construction, aerospace and other high-performance structures.

References

1. Munde YS, Ingle RB, Siva I (2018) Investigation to appraise the vibration and damping characteristics of coir fibre reinforced polypropylene composites. *Adv Mater Process Technol* 4(4):639–650. <https://doi.org/10.1080/2374068X.2018.1488798>
2. Pagani GA, Carrera E, Banerjee JR, Cabral PH, Caprio G, Prado A (2014) Free vibration analysis of composite plates by higher-order 1D dynamic stiffness elements and experiments. *Compos Struct* 654–663
3. Boscolo M (2013) Analytical solution for free vibration analysis of composite plates with layer-wise displacement assumptions. *Compos Struct* 493–510
4. Li D, Liu Y, Zhang X (2013) A layerwise/solid-element method of the linear static and free vibration analysis for the composite sandwich plates. *Compos Part B* 187–198
5. Dutta KK (2013) Free vibration analysis of isotropic and composite rectangular plates. *Int J Mech Eng Res* 3(4):301–308
6. Akash DA, Thyaraj Nr, Sudev LJ (2013) Experimental study of dynamic behaviour of hybrid jute/sisal fibre reinforced polyester composite. *Int J Sci Eng Appl* 2(8)
7. Chavan SS, Joshi MM (2015) Study on vibration analysis of composite plate. *Tech Res Organ* 1(4)
8. Gowda TM, Naidu ACB, Chayya R (1999) Some mechanical properties of untreated jute fabric-reinforced polyester composites. *J Compos Part A Appl Sci Manuf* 30:277–284
9. Somireddy M, Rajagopal A (2014) Meshless natural neighbor Galerkin method for the bending and vibration analysis of composite plates. *Compos Struct* 138–146
10. Dey P, Sheikh AH, Sengupta D (2014) A new element for the analysis of composite plates. Elsevier, pp 62–71
11. Deogonda P, Chalwa VN (2013) Mechanical property of glass fiber reinforcement epoxy composites. *Int J Sci Eng Res (IJSER)* 1(4)
12. Papkov SO, Banerjee JR (2014) A new method for free vibration and buckling analysis. *J Sound Vib* 0022–460X
13. Zhang SH, Chen HL (2006) A study on the damping characteristics of laminated composites with integral viscoelastic layers. *Compos Struct* 74:63–69
14. Alexander J, Augustine BSM (2015) Free vibration and damping characteristics of GFRP and BFRP laminated composites at various boundary conditions. *Ind J Sci Technol* 8(12). <https://doi.org/10.17485/ijst/2015/v8i12/54208>

Chapter 56

Mechanical Characteristic of Al 6063 Pipe Joined by Underwater Friction Stir Welding



Ibrahim Sabry, N. Gad Allah, Mohamed A. Nour, and M. Abdel Ghafaar

Abstract Underwater weld repairs on aluminum alloy piping systems and/or installations would be a particular advantage. UWFSW trials were carried out on Al 6063 alloy using a milling machine. Tool rotational speeds range about 480–1800 rpm, with a speed of traverse of rpm. Various mechanistic measurements were utilized to explore the mechanical characteristics of welded joints, comprehensive disruptive tests (tensile test and hardness test). The outcome displays that Al 6063 pipe can be welded using the UWFSW process with an utmost welding competence of 92.7% in terms of (UTS), while the speed of rotation is 1800 rpm, and the travel speed is 4 rpm.

Keywords UWFSW · AA 6063 pipe · Tensile strength · Hardness

1 Introduction

FSW and FSP, a related technique, are solid state processes used in joining and sorting. Joining aluminum structural parts in the Littoral Combat Ship (LCS) [1] and recycling nickel aluminum bronze used in US Navy propellers [2], Automotive (Engine and frame cradles), Railway Industry (Container bodies), Marine Industry (Hulls and superstructures), Construction Industry (Pipe fabrication), and

I. Sabry (✉) · N. Gad Allah · M. Abdel Ghafaar
Department of Mechanical Engineering, Faculty of Engineering, Benha University, Benha 13511,
Egypt
e-mail: ibrahem.sabry@eng.modern-academy.edu.eg

N. Gad Allah
e-mail: nabeel.jad@eng.modern-academy.edu.eg

M. Abdel Ghafaar
e-mail: metwaly.aghafar@eng.modern-academy.edu.eg

M. A. Nour
Department of Production Engineering and Mechanical Design, Faculty of Engineering, Tanta
University, Tanta 31512, Egypt
e-mail: eng.mohammednour@f-eng.tanta.edu.eg

Land Transport Industry (Fuel tankers) [3]. In FSW, a cylindrical, revolving instrument with a shoulder and projection pin is pushed through the surface around the sides of the components to be welded. Frictional and adiabatic heating loosens the material enough for the tool pin to sink into it before the top meets the shoulder. The tool then transverses along the line contact, causing localized extreme plastic deformation in the stir zone to create a weld [4–6].

Fratin et al. [7] used a high-speed tool to press a 6061 aluminum alloy plate underwater, and the outcome showed that the fatigue-resistant of the joint was greater than that of an air joint. Dixit et al. [8] investigated heat treatment with water inflow on the sheet through UWFSW of 6061, and found that heat input was dominated by welding parameters, resulting in refinement of UTS. Benavides et al. [9] also claim that the UTS of the UWFSW process is 75% that of the FSW base metal joint. UWFSW and FSW (in air) are used to weld a pipe made of 6061 aluminum alloy in this study. The UWFSW method is used to minimize heat and strengthen the properties of joints. In comparison to FSW joint properties, UWFSW joint hardness, tensile strength, and plasticity have been increased by reducing residual stress and the thermal period curve. It produces fine grain characteristics that reduce “S line” defects and have a straight boundary line in the center of WNZ and TMAZ, all while lowering HAZ. Zhao et al. [10] investigated UWFSW for AA2219-T6 to better understand the improved tensile strength relative to standard FSW (in air) joints. In another UWFSW study, Liu used aluminum alloy 2219 to investigate the mechanical properties of joints at various welding temperatures. The effect of water as a coolant was discovered in the FSW method, which increased the tensile strength from 324 to 341 Mpa. However, during the tensile inspection, the propensity of UWFSW to crack in the center of the TMAZ and WZ, on the Advancing side (AS), and the weld’s plasticity was weakened [11]. Liu et al. [12] were the first to deal with 6061 aluminum alloy w.p cylindrical and add it to various environments when rotating at high speeds. Joint temperature produces a lower peak than FSW, softens the area decreased by UWFSW, and increases joint efficiency by up to 86%, according to the experimental findings. Hofmann and Vecchio discovered fine grain was developed at a quick cooling rate by experimenting with the submerged method of friction stir (SFSP). boundary migration model and the spotted thermal distribution in the stirred material were utilized to predict grain sizes. Transmission Electron Microscopy was also utilized to examine the microstructures (TEM) [13]. After connecting the experimental sample, Hofmann and Vecchio [14] claimed that the HAZ using UWFSW on Al 2219-T6 is the explanation for improving mechanical properties. The UWFSW approach improves the hardness of the HAZ by narrowing the sedimentation in zone and shortening the hardened sedimentation level, as seen by microstructural study. The essential purpose of various in properties of mechanistic and microstructures in the UWFSW joint HAZ is variations in the heat-treatment effect in welding thermal delivery UWFSW and FSW that are compared. Zhang et al. discovered [15] the aim of this study is to use 1050 aluminum alloy UltraFine-Grained strain resistant to diminish the weakening of mechanical properties of joints. In the stir field, using TEM and X-ray, the grain growth rate and softening in small fine grains and subgrains were reduced (SZ). However, despite the limited HAZ, the tensile and yield power has

been demonstrated [15]. Wang uses metallurgical science to analyse the mechanical properties of UWFSW weld joint 7055-T6 aluminum alloy by enhancing the thermal cycle of welding during in-process heat treatment (water cooling) with effect on reinforcement mechanism and microstructure on joint using equipment such as (OM) and (SEM). In comparison to FSW [16], the UWFSW 1.96% elongation and tensile strength increased to 406.06 Mpa, an increase of 30%. Hofmann and Vecchio found that when UWFSW and FSW were used on 6061-T6 aluminum, the finer grain and plastic deformation resulted in less thermal distribution during the welding process [17]. Hofmann and Vecchio [18] are exploring the impact of in-process heat treatment on AA7075-T6 butt joints at UWFSW. The thermal, tensile, and microstructure distributions are shown as a result. To show and equate the findings with experimental results, Fratini et al. [19] used 3-D thermal modeling and mathematical modeling. In comparison to UWFSW, he discovered that thermal cycles in thermal zones are reduced. Fratini et al. [19] measured a 360 Mpa tensile strength in the 2219-T6 aluminum alloy to reach optimum tensile strength by refining welding parameters. The findings reveal that UWFSW has a 6% higher tensile strength than FSW, which is attributed to improved microstructure and temperature stability. Zhang et al. [20] the microstructure and mechanistic characteristic of the Al 2519-T87 were explored. He destructively tested it and compared it to the same substance joined by FSW. According to a limited element analyses of the width of (TMAZ) and the temperature distribution, UWFSW has a higher peak temperature of 547 °C and a faster cooling rate than FSW. Over time, the TMAZ decreases, and the HAZ increases, while the tensile strength efficiency increases by 60%. The micro-hardness distribution, weld thermal cycles, and toughness of UWFSW of 7050 aluminum alloy were investigated by Zhang and Liu [21]. Generated weld joints in hot and cold water, still as in air for reference, during this analysis. The results showed that the most temperature was reported during the conventional FSW (in the air) welding process. It was discovered that joints on the citizens side accounted for the most temperature in comparison to joints on the AS, and it was bespoke that the weld joint under plight is the highest relative to the other two situations that it increased the mechanical properties of the weld. This outcome in a quantitative relationship of 150th elongations and 92 nd final longevity. The fractures were found in the HAZ space (lowest micro-hardness location). As a result of the near conditions, the width of the minimal hardness region is constantly mutable. In their study, Sree Sabari et al. [22] compare the FSP technicality under three various provisions: traditional FSW (in air), and UW-at-room-temperature. This experiment utilized the AZ31B-O Mg alloy as a victim. It was determined and confirming that UWFSW resulted in increased grain refining, decreased time spent on certain reference and peak temperatures, decreased quality, and increased alloy formability. In a pinch, UWFSW significantly improves the formability of this alloy. The majority of FSW research has been done on plates, and experiments on UWFSW of pipes are rare in the literature. The underwater FSW of Al6063 pipes was conducted in this article, and the mechanical characteristics and microstructure of the pipes were thoroughly examined. The following is the order in which the paper is arranged. The material, experimental setup, welding parameters, and procedure for the experimental research are all defined in the materials

Table 1 Al 6063's chemical composition (%)

Weight%	Al	Si	Fe	Cu	Mn	Mg	Cr	Zn	Ti
6061	Bal	1.9	2.9	0.12	0.38	0.8	0.04	0.11	0.13

Table 2 Al 6061's mechanistic characteristics

Alloy	σ UTS M pa	EL%	VHD
6063	240.690	12	89

and methods section. The outcome and discussion section follow the materials and methods section, in which the impact of rotation speed on weld characteristics, tool exerted TS, and hardness is clarified. Finally, in the conclusion portion, all of the findings are summarized.

2 Experimental Work

2.1 Material

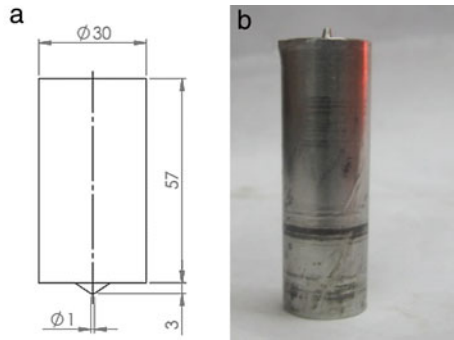
The composition of chemicals and mechanical properties of material with the Miser aluminum company, delivered are specific in Tables 1 and 2, respectively. The AL 6063 alloys pipes were performed with inner thickness-3-mm, and the same outer thickness is 5 cm.

The UTS of AA 6063 and the VH were 240 MPa and 89 HV correspondingly. The findings of the tensile and VH tests carried out to estimasated the mechanical characteristics of the Al 6063 studied were near to the literature values [23–25].

2.2 Material and Design of the Tool

The alloy used for the tool steel (ST316L). It has UTS 485 MPa and VH 95. The geometry of the tool is presented in Fig. 1. The tool pin has a conical shape. In this study, the length of the tool was 50 mm, and pin length (L) (3 mm), the diameter of pin (d) 1 mm and s Diameter of the shoulder (D) (10 mm), the tilt of the tool 2.50 as shown in Fig. 1.

Fig. 1 FSW tool dimensions, **a** working drawing, **b** tool image



2.3 FSW Process

The FSW process we need a milling machine to start the process, the operating principle of FSW is shown in Fig. 2. The tool rotation with a central probe is pressed into the joint and traverse speed the weld line. The frictional heat created essentially under the tool's shoulder, softens the material. The shoulder of the tool else acts to implicate the softened material, which is forced to the back of the tool, in the process attractively incorporated to form a solid-phase weld. As long as the components are adequately restrained, a high-quality solid-phase weld is formed following the considerable hot working of the material at the joint. During the present study, welding FSW for joining of AL 6063 alloy were performed on pipe parts with thickness-3-mm, shown Table 3.

Fig. 2 Milling machine used in UFSW for pipe joint

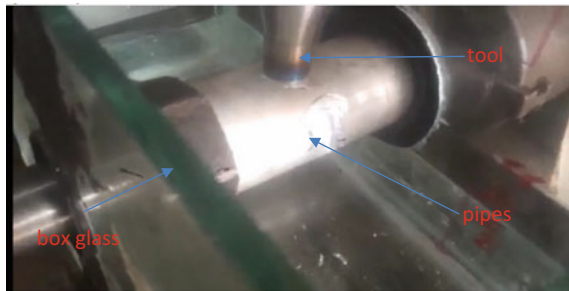


Table 3 Welding parameters utilized in UWFSW

Rotation speed (r·min ⁻¹)	Travel speed (mm·min ⁻¹)	Axial pressure (kN)
1800	4	2

3 Characterization

3.1 Visual Test

An inspector’s eyes are utilized to search for flaws during a visual inspection. To gain access and examine the subject area more closely, the inspector may use special tools such as magnifying glasses, mirrors, or borescopes. Visual tests follow a variety of protocols, ranging from basic to complex. It is one of the most commonly used inspection methods for weld acceptance. VT is also used to identify bad welds before other more expensive or time-consuming forms of inspection are performed. Visual inspection is easy to apply, quick, and relatively inexpensive. Rulers, filet weld gauges, triangles, magnifying glasses, and reference weld samples are among the visual testing tools [26].

3.2 Tensile Testing

After welding, the pipe is splatted into two half using band saw. Then each half is flattened using bending machine. The process produces two plate, from earl pipe. Ultimately the tensile testing specimen machined from then two plates according ASTM standard [7]. The tensile test sample geometry shown in Fig. 3 and Fig. 4 shown as Photos of sample tensile test specimens.

Fig. 3 The tensile test sample geometry

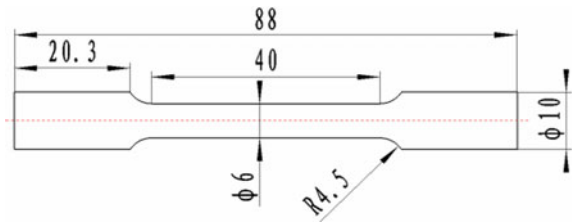
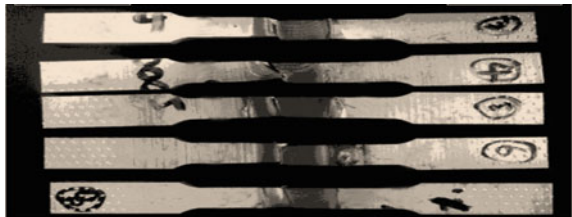


Fig. 4 Photos of sample tensile test specimens



3.3 Vickers Hardness Test

The Vickers hardness has been measurement with the regions NZ, HAZ, and TMAZ. The Vickers hardness Tester (Model: VM-50), these individuals are the testers that are ideal for determining the VH of precision metallic components. They have a broad various types of testing are conducted, ranging from light to heavy, and their precise findings are well-known. IS: 1754 and ISO 6507-2 are strictly followed by these testers.

4 Results and Discussion

4.1 Visual Test

Visual examination of the underwater FSW and traditional FS welded specimens showed uniform curving surface ripples in Fig. 5, in order to with the ultimate sweep of the edge of the rotating shoulder of the tool over weld hunk. The presence of such surface ripples, called union rings, has been antecedent due to FSW [27, 28]. Minor flash an observation for both welding this could be due to the relative high welding and low travel speed [7, 8]. It was hard to observe any surface flaws due to the nature of the surface appearances of FS welded specimens. No important cracks, wormhole, or other discontinuities of the surface were noted in any of the generated samples.

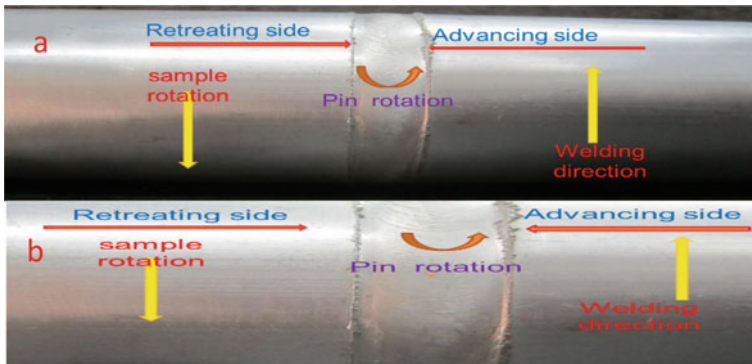


Fig. 5 Finished pipe **a** Slight weld flash on trailing edge that has exhibited better-quality welds at 1800 rpm, **b** excessive weld flash on trailing edge at 485 rpm

4.2 Tensile Strength

Figure 6 introduces the stress–strain relationship acquired for all combinations of parameters by conducting a TS on pipes-joints. From each the shown, the UTS of each pipes-joints was spotted to be less than the base material. For steady travel velocity, the UTS is symmetrical to the rotation speed within the experimented range (485–1800 rpm). For a travel speed 4 mm/min, the TS of sample welded at 485 rpm was 110.7 MPa, which was minimal than 126.7, 147.4, 150.2, 197.7, and 200.3 MPa carried out at 710, 910, 1120, 1400, and 1800 rpm, respectively. The TS of each joint found to be minimal than the TS of the unwelded material. At minimum tool rotation speed, the heat obstetrics is not enough to soften the material and subsequently, the outcome is non-effective. It can be observed in Fig. 6 that the UTS increases with an increase in tool rotation speed. This is essentially due to augmentation heat obstetrics acquired by the rise in tool rotation speed outcome in progressive material flow and blending of the materials. Shown in Fig. 6, relation between UTS and rotation speed (at feed 4 mm/min). Increasing tool rotation speed to 1800 rpm causes increase in UTS whose ability be attributing to decrease in grain size because of heat treatment in the weld zone and colling rate. Moreover, a low tool rotation speed of 480 rpm creates flash and tunnel defects probably because stirring impact of the pin at minimum speed. The aforesaid flash and tunnel defects were seen when the tool rotation speed is decreased 485, 710, and 910 rpm ability be creditable to the rising turmoil in the weld area as it is else seen that the style of several of UTS leftover the same unheeding of travel speed. It observed that the joints made with a tool rotation speed of about 1800 rpm outcome in the largest UTS for a specific weld speed. The impact of travel speed on the UTS and elongation % of the UWFS welded Al6063 pipes joint is presented in Fig. 6. At rotation speed, protracted display of the pipe to friction heating and the stirring of the tool outcome in the formation of flash defects major to weak joints. It is observed from Fig. 7 that the UTS of the joints increases by rising tool rotation speed. Further decrease in rotation speed outcome in

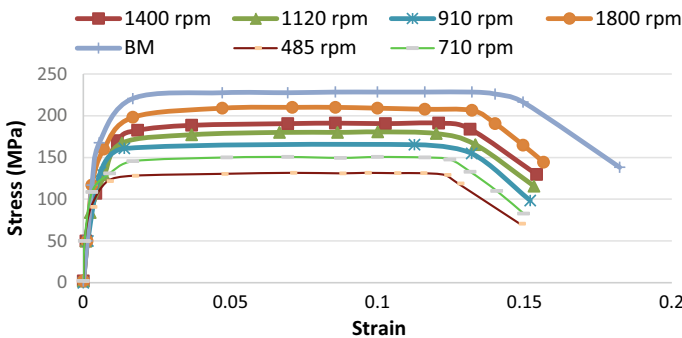


Fig. 6 For different rotation speeds, stress versus strain curve of welded 6063 sample from tensile test

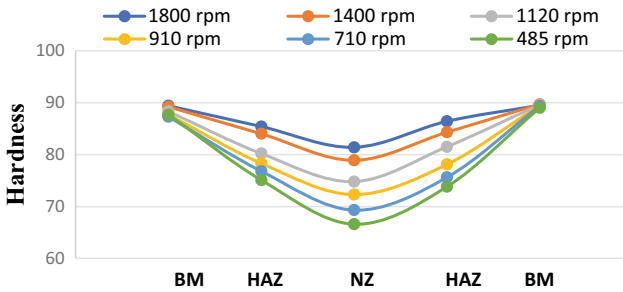


Fig. 7 Vickers hardness at NZ, TMAZ, HAZ, and BM at various rotation speed

a lowering of TS. The identical trend is present at each value of tool rotation speed. At higher rotation speed, the weld area is exposed to friction heating for a higher temperature, outcoming in complete heating and high plastic flow of the metal. This constant stirring of the instrument for a long time at a low rotation speed will lead to the creation of flash defects leading to fragile joints being formed. Generally, these voids acted as stress elevators and influenced the joint's tensile strength.

4.3 Hardness Test

The material flow as well as the heat dissipation rate can trigger metallurgical transformations that change the mechanical properties due to the thermo-mechanical FSW operation. The optical microscopic of the joint cross-section of the pipes as seen in Fig. 7. The pipes joint weld optical microscope clearly distinguished four zones: NZ, HAZ, TMAZ, and BM. Because of the unique material distribution in the weld area, it was essential to inspect the mechanical characteristics of the joint pipes. In the middle section of the transverse cross-section, the Vickers' hardness was measured (see Fig. 7). The hardness of each of the joints was constituted to be less than that of the BM. The micro-hardness of BM was 90 HV. For a mixture of elevated rotation speeds (1800 rpm) in different fields, maximum hardness was obtained for all travel speeds. The metallurgical transformations were clearly illustrated in a UWFSW process. As an outcome, grain dislocated, avoiding moreover deformation, and serving as a slip buffer. As a result of the high dislocation density and fine grain size, the material has a high hardness and strength. Similarly, as opposed to other rotational speed combinations, a low rotational speed resulted in low hardness. In comparison to HAZ and TMAZ, the nugget area had the lowest hardness in both cases [26, 29–31]. In both cases, the nugget area had the lowest hardness as compared to HAZ and TMAZ.

5 Conclusion

The following results are drawn from an experimental discussion of the mechanistic characteristics, of welded Al 6063 pipe prepared using UWFSW processes:

1. The pipe welding of AL(6063)aluminum alloys were successfully achieved, allowing for good-quality welds for UWFSW use.
2. The UWFSW improves the tensile strength of all joints while reducing plasticity.
3. At the interface between NZ and TMZ, the UWFSW joint fractures.
4. The cause for the UTS progressive through UWFSW is that under the integral cooling effect of water, the lower hardness restricted of the poor positions of the standard joint can be comparatively improved.

Acknowledgements We would like to acknowledge the help provided by **Dr. Saly Nabil El-Harras** lecturer in the Faculty of commerce—Tanta University through her guidance, advice, and consistent encouragement in this work. She has been a tremendous source of motivation in realizing this work.

References

1. Halverson B, Hinrichs JF (2007) Friction stir welding (FSW) of littoral combat ship deckhouse structure. *J Ship Prod* 23(3):161–163
2. Kevin J Friction stir welding for ship construction. Technologies Corporation Navy Metalworking Center, operated by Concurrent Technologies Corporation (CTC), under Contract No. N0014-06-D-0048 to the Office of Naval Research as part of the Navy ManTech Program. Approved for public release; distribution is unlimited
3. Patil HS, Soman SN (2010) Experimental study on the effect of welding speed and tool pin profiles on AA6082-O aluminium friction stir welded butt joints. *Int J Eng Sci Technol* 2(5):268–275
4. Khourshid AM, Sabry I (2013) Analysis and design of friction stir welding. *Int J Mech Eng Robot Res* 2(3)
5. Khourshid AM, Sabry I (2013) Friction stir welding study of aluminum pipe. *Int J Mech Eng Robot Res* 2(3)
6. Sarukada D, Katoh K, Tokisue H (2002) Underwater friction welding of 6061 aluminum alloy. *J Jpn Inst Light Metals* 52(1):2–6
7. Fratini L, Buffa G, Shivpuri R (2008) In-process heat treatments to improve FS-welded butt joints. *Int J Mach Tools Manuf* 10(3):42–53
8. Dixit V, Mishra RS, Lederich RJ, Talwar R (2009) Influence of process parameters on microstructural evolution and mechanical properties in friction stirred Al-2024 (T3) alloy. *Sci Technol Weld Join* 14:346–355
9. Benavides S, Li Y, Murr LE, Brown D, McClure JC (1999) Low temperature friction-stir welding of 2024 aluminum. *Scripta Mater* 41:809–815
10. Zhao Y, Wang Q, Chen H, Yan K (2014) Microstructure and mechanical properties of spray formed 7055 aluminum alloy by underwater friction stir welding. *Mater Des* 56:725–730
11. Liu H, Zhang H, Yu L (2011) Homogeneity of mechanical properties of underwater friction stir welded 2219-T6 aluminum alloy. *ASM Int* 4
12. Liu HJ, Zhang HJ, Huang YX, Yu L (2010) Mechanical properties of underwater friction stir welded 2219 aluminum alloy. *Trans Nonferrous Met Soc China* 20:1387–1391

13. Sakurada D, Katoh K, Tokisue H (2002) Underwater friction welding of 6061 aluminum alloy. *J Jpn Inst Light Metals* 52(2):2–6
14. Hofmann DC, Vecchio KS (2007) Thermal history analysis of friction stir processed and submerged friction stir processed aluminum. *Mater Sci Eng, A* 465:165–175
15. Zhang H, Liu H, Yu L (2012) Effect of water cooling on the performances of friction stir welding heat-affected zone. *ASM Int JMEPEG* 21:1182–1187
16. Hosseini M, Danesh Manesh H (2010) Immersed friction stir welding of ultrafine grained accumulative roll-bonded Al alloy. *Mater Des* 31:4786–4791
17. Wang Q, Zhao Z, Zhao Y, Yan K, Liu C, Zhang H (2016) The strengthening mechanism of spray forming Al–Zn–Mg–Cu alloy by underwater friction stir welding. *Mater Des* 102:91–99
18. Hofmann DC, Vecchio KS (2005) Submerged friction stir processing (SFSP): an improved method for creating ultra-fine-grained bulk materials. *Mater Sci Eng, A* 402:234–241
19. Fratini L, Buffa G, Shivpuri R (2010) Mechanical and metallurgical effects of in process cooling during friction stir welding of AA7075-T6 butt joints. *Acta Mater* 58:2056–2067
20. Zhang HJ, Liu HJ, Yu L (2013) Thermal modeling of underwater friction stir welding of high strength aluminum alloy. *Trans Nonferrous Met Soc China* 23:1114–1122
21. Zhang H, Liu H (2013) Mathematical model and optimization for underwater friction stir welding of a heat-treatable aluminum alloy. *Mater Des* 206–211
22. Sree Sabari S, Malarvizhi S, Balasubramanian V, Madusudhan Reddy G (2016) Experimental and numerical investigation on under-water friction stir welding of armour grade AA2519-T87 aluminium alloy. *Defence Technol* 12:324–333
23. Gallais C, Denquin A, Bréchet Y, Lapasset G (2008) Precipitation microstructures in an AA6056 aluminium alloy after friction stir welding: characterisation and modelling. *Mater Sci Eng A* 496(1/2):77–89
24. Sabry I, El-Kassas AM (2019) A new quality monitoring system for friction stir welded joints of aluminum pipes. *Int J Eng Technol (IJET)* 11(1)
25. Yong Z, Jiang S, Yang S, Lu Z, Yan K (2016) Influence of cooling conditions on joint properties and microstructures of aluminium and magnesium dissimilar alloys by friction stir welding. *Int J Adv Manuf Technol* 83:673–679
26. Sabry I, Zaaferani N (2021) Dry and underwater friction stir welding of aa6061 pipes—a comparative study. In: *IOP conference series: materials science and engineering*, vol 1091, p 012032
27. Fu RD, Sun ZQ, Sun RC, Li Y, Liu HJ, Liu L (2011) Improvement of weld temperature distribution and mechanical properties of 7050 aluminum alloy butt joints by submerged friction stir welding. *Mater Des* 4825–4831
28. Darras B, Kishta E (2013) Submerged friction stir processing of AZ31 magnesium alloy. *Mater Des* 47:133–137
29. Shanavas S, Edwin Raja Dhas J, Murugan N (2018) Weldability of marine grade AA 5052 aluminium alloy by underwater friction stir welding. *Int J Adv Manuf Technol* 95:4535–4546
30. Sabry I, Idrisi AH, Mourad AHI (2021) Friction stir welding process parameters optimization through hybrid multi-criteria decision-making approach. *Int Rev Modell Simul (IREMOS)* 14(1):32–43
31. Sabry I, Gadallah N, Abu-Okail M (2020) Optimization of friction stir welding parameters using response surface methodology. In: *IOP conference series: materials science and engineering*, vol 973, p 012017. <https://doi.org/10.1088/1757-899X/973/1/012017>

Chapter 57

Experimental Investigation on Mechanical Properties of Epoxy with Hybrid Filler Composites



J. Balaji, M. M. Nataraja, K. L. Vinod, and K. Sadashiva

Abstract The development and mechanical properties of polymer composites are achieved by using the nanoclay and rice husk powder fillers reinforced in epoxy matrices. The composites were prepared by keeping weight fraction of matrix as 80% and varying the wt% of the reinforcements by using the hand layup technique. The results revealed that 12 wt% of rice husk and 2.5, 5.0 & 7.5 wt% of nanosized nanoclay filler-reinforced composites yield better mechanical properties.

Keywords Polymer composite · Nanoclay · Rice husk · Mechanical properties

1 Introduction

The nanoparticles and natural fibers are utilized in the transportation and packaging industries to overcome two factors, wherein the primary factor is to enhance the characteristics of the composites by incorporating nanofiller. The secondary is to evolve biodegradable filler by utilizing organic fibers as a replacement to strengthen the fibers present in wood plastic composites [1]. Reinforcing synthetic material with natural fibers has got innumerable attractiveness because of the enhanced mechanical characteristics and relatively low cost [2]. The natural wood polymer composites have been spread across world. These are environment friendly, affordable cost, and biodegradable, and they have done enormous job in reducing the environmental concern [3]. The interaction adhesive force between natural fibers and natural polymer matrix is very poor. This poor interaction ends up in poor miscibility and hence reduces the mechanical properties [4]. The addition of nanoparticles can enhance the properties of polymer composites in mechanical, toughness as well

J. Balaji (✉) · M. M. Nataraja · K. L. Vinod · K. Sadashiva
Dr. Ambedkar Institute of Technology, Bengaluru, Karnataka, India

M. M. Nataraja
e-mail: nataraja.mm@dr-ait.org

K. L. Vinod
e-mail: vinodkl@dr-ait.org

as flexural strength and also compares with carbon nanotubes and graphene combination [5]. The hydrophilic property of nanoclay and nanosilica blocks the uniform distribution of nanoparticles in the hydrophobic continuous phase epoxy matrix due to inappropriate interaction between them [6]. The fine-grained nanoclay with thickness less than 0.96 nm was used as filler with polymer matrix to enhance the properties of stiffness & toughness of polymer matrix. These polymer matrices provided better support to the fiber to delay the crack [7]. The addition of nanoclay filler in organic composites varies from between 2 and 6 wt% shows that the flexural strength also increased [8]. Rice husk is naturally available fiber after rice processing. It consists of lignin and cellulose content. It is hydrophilic in nature and insoluble in water and chemically steady [9]. Nanoclay particles have got large surface contact area with polymer composite, so the interaction with polymer matrix is more compared to the microfiller. The thermo-mechanical properties were enhanced. The Rice husk was used as a filler with the matrix Medium-Density polyethylene (MDPE) and varying weight ratio of Rice husk at 2, 4 & 6 % improves the Tensile and flexural strength [10]. The RHA are used as filler for both poly lactic acid and poly amide matrix. The specimen is prepared by injection molding technique suitable for mechanical analysis. The result shows that RHA with polylactic acid have improved mechanical properties than with the poly amide matrix. Adding nanoclay with RHA improves Young's modulus and decreases the tensile strength of poly amide matrix [11].

The reinforced nanoclay with fiber glass in polyester matrix is obtained by using hand layup method. The filler nanoclay content varied from 1, 3, 5 and 7 wt% with 40 wt% of fiber glass, remaining polyester matrix. They found that the optimum load carrier of nanoclay was achieved at 3 wt% and improved in flexural and tensile strength [12]. The fabrication of RH fiber and recycled linear low polyethylene with maleic anhydride by using melt blending method. The nanosilica & nanoclay were added in different ratios like 2,4 & 6% which enhances physical & thermo-mechanical properties. The crystallinity of composites decreases with the addition of RH fibers & increases with incorporation of nanoclay and nanosilica [13]. The development of new nanocomposites by using nanocellulose and nanoclay composites. These hybrid composites can replace for conventional polymer composites because of low density, high strength & low environmental issue [14]. The hybrid fiber of kenaf/glass was reinforced in the epoxy matrix & nanoclay was dispersed using the 3-roller mill machinery. They examined that nanoclay content varied from 1, 3 and 5 wt% and achieved enhanced tensile and flexural properties in both 0° & 90° fiber orientation. 5 wt% of nanoclay incorporation decreases the mechanical strength of composites [15].

The objective of present research work is to explore the mechanical behaviors of rice husk/nanoclay composites and particle laminate oriented rice husk and nanoclay composites for aerospace/automotive applications and to develop a platform for design of given composites with required mechanical properties based on the material property data we know. As a contrast, the mechanical characteristics of rice husk and nanoclay were also estimated under normal test conditions. This research work helps in interpretation of the function of rice husk and nanoclay composites and to understand the role of particulate reinforced in rice husk and nanoclay

under various abrading distances & loads for aerospace/automobile applications. The mechanical characteristics of rice husk and nanoclay composites have been measured and compared with those of unfilled neat rice husk and nanoclay composites. Also this work helps in grasp the function of particle laminate orientation by comparing the results with non-oriented rice husk and nanoclay composites. The mechanical properties of fiber laminate oriented rice husk and nanoclay composites have been measured and compared with those of non-oriented neat rice husk and nanoclay composites.

2 Experimental Analysis

2.1 *Materials and Methodology*

Detail manufacturing of composite structure and the steps used to conduct experiments as per ASTM standard has been discussed in this unit, and also to find out specimen characterization for specific applications is carried out as follows.

Raw materials used for specimen preparation are.

- Epoxy resin.
- Hardener.
- Rice husk powder.
- Nanoclay.

Epoxy Resins LY 556

Generally utilized thermoset resin for manufacturing hard polymer matrix composite is neat epoxies. Epoxy resin comes from family of thermoset polymer which is commonly less reactive to atmospheric condition, and it has some unique properties which favor for structural products, i.e., it has low shrinkage allowance as compared to other resins. Epoxy resin is good in adhesion strength, i.e., with any heterogeneous material, and also good in chemical stability and very low reactive with environmental condition, and it also favors in making good insulating materials. These resins are commonly produced by suitable reaction of epichlorohydrin with bisphenol. More number of resins are manufactured just by varying the combination of these two reacting agents just by varying the molecular weight of any one of the reacting agents. Physical and mechanical properties of composites are mainly depend on the interface resistance between matrix and reinforcement or filler. The interface resistance should be low so that the bonding and the interaction between filler and matrix improves (Fig. 1).

Fig. 1 Epoxy**Hardener 951**

Hardener generally used in the resin is to increase its structural strength and also to cure composite structure earlier, i.e. within stipulated time. Commonly used hardner in room condition is amines at certain mercaptans, and various other special hardners for specific application are also used in resin combination, but they require higher temperature, i.e. near to 150 °C to react with the epoxy resins. This hardner has good characteristics like mechanical, chemical and electrical properties and also have fair curing time (room temperature), does not required any external heat source.

Rice Husk

Rice husk or Rice hulls is the covering/coating on grain of rice, it is formed of hard material like lignin and silica. Rice husk is major by product of grain (rice), it contains 40% of cellulose, 30% of lignin & 20 % of silicon. Rice husk is highly porous in structure, low density and have high surface area. They has been used as additive in many materials manufacturing like refractory bricks, insulation and flame retardants (Figs. 2 and 3).

Reported by environmentalist, the external disposal of rice husk has become a great threat to the environment because of dumping it into the land and the surrounding areas which leads to land pollution and also it breaks the biological chain in nature.

An attempt has been made in this work to effectively utilize biological wastes with some nanofillers used for manufacturing composite structure as to solve this issue to some extent.

Fig. 2 Grinding process**Fig. 3** Rice husk powder

Nanoclay

Nanoclay is naturally available material containing fine-grained mineral. Nanoclays are minerals which have one dimension of material in nanometer measurement. The purity of nanoclay is very prominent role in reaching high level of mechanical characteristics. Impurities in nanoclay perform poor impact in tensile properties. It is used in wastewater treatment in all commercial industries. They have high aspect ratio. It is manufactured by the process called sol-gel, and it is wet chemical process widely used in material science and ceramic industries. The presence of nanoclay in polymer composites which enhances the mechanical properties like tensile as well as flexural strength. The montmorillonite is hydrophilic (water absorb) in nature because of the existence of hydrated inorganic counter ions ($\text{Na}^+/\text{Ca}^{2+}$) in the inner

Fig. 4 Nanoclay

layer space. Natural nanoclays have a great future for industrial and environmental utilization. More research is required to understand the surface properties and reactivity of these nanoclay and the mechanism principles of their reactions with external solvents (Fig. 4).

Fabrication of Composites

Composite structure is fabricated by traditional hand layup technique. The continuous aligned glass fiber, rice husk and nanoclay particulate are used as fillers and epoxy resin as matrix to prepare the specimen Table 1: Various compositions of rice husk + nanoclay.

Preparation of Laminates

Traditional hand-lay-up technique is adopted for manufacturing composite structure, and these structures are cured by compression molding technique. Here standard mixing ratio of neat epoxy resin and hardner, i.e., 100:12, is properly mixed and agitated to control the air bubble formation before pouring in the mold. Firstly, a releasing agent is applied in the mold cavity as for easy removal of the specimen once it is cured, and the required size of available woven glass plain fabric is sliced as the fabric is made of 360 g/m².

Table 1 Various composition of rice husk + nanoclay

Sample	Particle wt in gm	Resin + hardener weight, gm	Total weight of plate in gm
(1) 1% NC	12RH + 2.5NC	260.5 + 25	300
(2) 2% NC	12RH + 5NC	258 + 25	300
(3) 3% NC	12RH + 7.5NC	255.5 + 25	300

3 Experimental Details

3.1 Tension Test

Tensile strength quantifies the ability of specimen that resists the force that allows to pull apart, such as structural beam, rope or a wire to the break point. The tensile strength of a specimen is the maximum amount of tensile stress that it can be exposed to before failure. The failure of material is determined by the type of material and design of material. This is a primary concept in the field of material science engineering, mechanical engineering and structural engineering (Figs. 5, 6 and 7).

It is the test in which a sample is subjected to uniaxial force to pull apart until it reaches break point. These results help to select a material for constructional/structural application for both civil and mechanical engineering, for suitable quality measurement and to predict how a material will behave under different types of forces.



Fig. 5 (a) Experimental setup and (b) loading arrangement of specimen for tensile strength test

Fig. 6 ASTM standard dimension

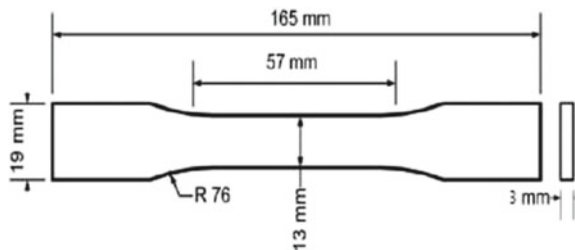




Fig. 7 Tensile test specimen of rice husk and nanoclay-reinforced epoxy composite

3.2 Flexural Strength

Flexural strength is the property of material which defines stresses in the specimen before it yields in flexural strength test, and it is also known as bending strength, modulus of rupture or fracture strength. It is a physio-mechanical characteristic of a brittle material. Flexural strength is defined as the ability of a material to resist deformation under stress (Figs. 8 and 9).

The load applied on the test specimen using a three point bending technique. Flexural strength is also indicated in terms of stress similar to tensile strength. Bending strength determines the maximum stress value experienced by a specimen at the time of rupture.



Fig. 8 Experimental setup for flexural test

Fig. 9 Flexural test specimen



3.3 Hardness

Hardness measures the stress applied on the specimen before it permanently deforms or fractures. The static indentation is the test used in the present research work study to determine the hardness of the specimens in which a ball indenter was forced into the specimens by applying load as shown in the below figure. The hardness of the specimen is measured by resistance to abrasion or wear, cutting, machining and crusting (Figs. 10 and 11).

Fig. 10 Experimental setup for hardness test

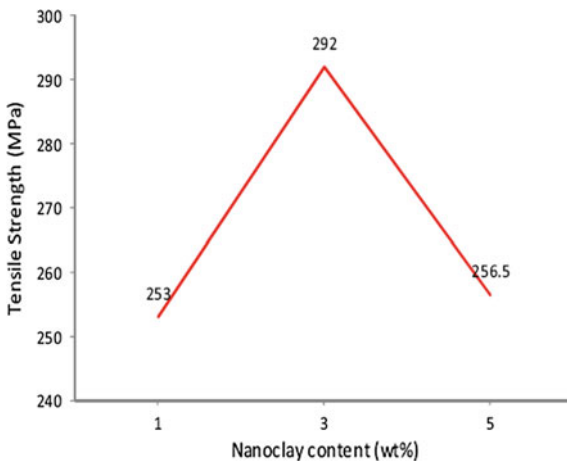


Fig. 11 Hardness test specimen

4 Results and Discussion

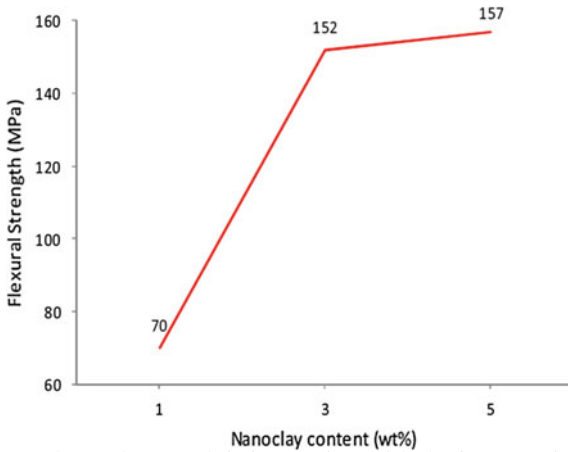
Mechanical properties of polymer composites with hybrid filler Rice husk & nano clay, in which rice husk kept constant of 12 wt% and varying the nano clay 2.5, 5.0 & 7.0 wt% result are revealed. The influence of nanoclay on mechanical properties of composites is determined by conducting the above test, and the results are tabulated. The present research work attempts to understand the influence of reinforcement on the matrix alloy. Figures show the effect of nanoclay on the various mechanical properties like tensile strength, flexural and hardness, respectively.

4.1 Tensile Strength



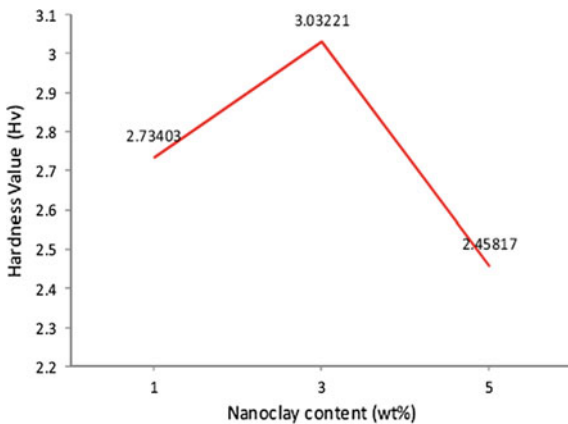
The experimental values are plotted as a graph in which tensile strength is in Mpa in *Y* axis and nanoclay content % in *X* axis. As the nanoclay content increases to 1 and 2 wt%, the tensile strength increases to 253 and 292 Mpa. The tensile strength decreases to 256.5 Mpa with increase in nanoclay to 5 wt%. This shows the brittleness of composites enhances with the increase in nanoclay content, and there might be chance of agglomeration. The increase in tensile strength is due to dispersion of nanoclay uniformly throughout the matrix, and contact surface area is also increased compared to microparticles.

4.2 Flexural Strength



Flexural strength is increasing with the increase in nanoclay content as shown in the above graph. As the clay content increases from 1, 3 and 5 wt% with the increase in flexural strength from 70, 15 and 157 Mpa. The graph shows from 1 to 3 wt% of nanoclay, and the flexural strength increases by 200%. Similarly, from 3 to 5 wt% of nanoclay the flexural strength increases by 5%. From the graph, it is concluded that flexural strength increases with nanoclay content increasing.

4.3 Hardness



Hardness value of the polymer composites with hybrid fillers was plotted in y axis and nanoclay content in x axis. The hardness value of the composites increases with the increase in nanoclay content from 1 and 3 wt%, and the hardness values got in graph are 2.73403 and 3.03221. The hardness value decreases from 3.03221 to

2.45817 when nanoclay content increases from 3 to 5 wt%. This shows the composites decreases in hardness as the nanoclay content increases.

5 Conclusion

A series of rice husk/nanoclay/epoxy hybrid composites were developed and conducted experiment to investigate the effect of nanoclay on the mechanical properties of hybrid composites. A number of examination and conclusions can be drawn from investigation.

Based on the results and discussion of this study, increasing the rice husk and nanoclay particle in the composite would increase the tensile properties, flexural properties and hardness properties of the composite up to 3 wt% of nanoclay.

For further addition of nanoclay, there is a decrease in tensile and hardness strength of the composite and it slightly reduces the flexural strength.

References

1. Khanjanzadeh M, Pirayesh H, Saadatnia MA (2015) Utilization of natural montmorillonite modified with dimethyl, dehydrogenated tallow quaternary ammonium salt as reinforcement in almond shell flour–polypropylene bio-nano composites. *Compos B Eng* 71:143–151
2. Lei Y, Wu Q, Yao F, Xu Y (2007) Preparation and properties of recycled HDPE/natural fiber composites. *Compos A Appl Sci Manuf* 38(7):1664–1674
3. Yang X, Tang X, Ma L, Sun Y (2019) Sound insulation performance of structural wood wall integrated with wood plastic composite. *J Bioresour Bioprod* 4(2):111–118
4. Anbupalani MS, Venkatachalam CD, Rathanasamy R (2020) Influence of coupling agent on altering the reinforcing efficiency of natural fibre-incorporated polymers—a review. *J Reinf Plast Compos* 39:073168442091893. <https://doi.org/10.1177/0731684420918937>
5. Rafiee R, Eskandariyun A (2017) Comparative study on predicting Young's modulus of graphene sheets using nano-scale continuum mechanics approach. *Phys E* 90:42–48
6. Deka BK, Maji TK, Mandal M (2011) Study on properties of nanocomposites based on HDPE, LDPE, PP, PVC, wood and clay. *Polym Bull* 67(9):1875–1892
7. Armimesh Nayak B, Shubham, Prusty RK, Ray BC (2020) Effect of nanosilica and nanoclay reinforcement on flexural and thermal properties of glass fiber/epoxy composites. *Mater Today Proc* 33:5098–5102, Part 8. ISSN 2214-7853. <https://doi.org/10.1016/j.matpr.2020.02.852>
8. Alireza Ashori AN (2009) Effects of nanoclay as a reinforcement filler on the physical and mechanical properties of wood base composite. *J Compos Mater* 43(18)
9. Rosa SML, Santos FE, Ferreira CA, Nachtigall SMB (2009) Studies on the properties of rice-husk-filled-PP composites—effect of maleated PP. *Mater Res* 12:333–338
10. Simão JA, Carmona VB, Marconcinia JM, Mattosoa LHC, Barsberge ST, Sanadic AR (2016) Effect of nanoclay on properties of medium density polyethylene (MDPE)/rice husk flour (RHF) composites. *Mater Res* 19:746–751
11. Battezzozze D, Salvetti O, Frache A, Peduto N, Sio AD, Marino F (2015) Thermomechanical properties enhancement of bio–polyamides (PA10.10 and PA6.10) by using rice husk ash and nanoclay. *Compos: Part A*

12. Somaiah Chowdary M, Niranjan Kumar MSR (2015) Effect of nanoclay on the mechanical properties of polyester and S-glass fiber (A1). *Int J Adv Sci Technol* 74:35–42. <https://doi.org/10.14257/ijast.2015.74.04>
13. Sadik WA, El Demerdash AG, Abbas R, Bedir A Effect of nanosilica and nanoclay on the mechanical, physical, and morphological properties of recycled linear low density polyethylene/rice husk composites. <https://doi.org/10.1007/s10924-020-01983-6>
14. Hussin FNNM, Wahab RA, Attan N (2020) Nanocellulose and nanoclay as reinforcement materials in polymer composites, *Malaysian. J Fund Appl Sci* 16(2):145–153
15. Sapiai N, Jumahat A, Shaari N, Tahir A (2020) Mechanical properties of nanoclay-filled kenaf and hybrid glass/kenaf fiber composites. *Mater Today: Proc.* ISSN 2214–7853

Chapter 58

Morphological and Thermal Behaviour of Monomer Dispersed Liquid Crystal



Santosh Mani, Sameer Hadkar, Krishnakant Mishra, Pushendra Rai, and Pradip Sarawade

Abstract The monomer dispersed liquid crystal is relatively new class of functional materials which has a numerous role in the modern technology. This research work reports the effect of two different concentrations of monomer 2-Ethyl Hexyl Acrylate with on liquid crystals of cholesteryl nonanoate. This monomer is selected due to its low volatile nature and reactivity of double bonds. The thermal behaviour of samples under investigations was studied by differential scanning calorimetry (DSC). The liquid crystal shows a good miscibility with both concentrations of monomer which were confirmed by Fourier transform infrared (FTIR) spectroscopy. The proposed research investigation reveals new phase transitions along with the known phase transitions for this composite system. It was also observed that in the nematic order, the molecules tend to align perpendicular to the surface. This opens a new possibility of this material to be used for variety of new applications like photo-cured network and photopolymer etc.

Keywords Monomer · Liquid crystals · Cholesteryl nonanoate · Differential scanning calorimetry · Dielectric spectroscopy · Fourier transform infrared spectroscopy · Morphological and thermal Properties

1 Introduction

Liquid crystal (LC) materials play an important role in modern technology as their physical properties are strongly linked with their chemical structure. They consist

S. Mani (✉) · P. Rai

K. J. Somaiya College of Engineering, Somaiya Vidyavihar University, Mumbai, India
e-mail: santoshmani@somaiya.edu

S. Mani · S. Hadkar · K. Mishra · P. Sarawade

Department of Physics, University of Mumbai, Mumbai, India

S. Hadkar

Don Bosco Institute of Technology, Mumbai, India

K. Mishra

Thakur College of Engineering and Technology, Kandivali, Mumbai, India

of molecules of anisotropic shape which interact with each other and produce self-organizing effect. In LC, the orientational order is present whereas the positional order is either completely or partially disappears. The information about the amount of orientational order available is measured by a quantity called order parameter. This phase is also called mesophase or mesomorphic phase as they combine properties of crystalline solids and liquids [1–8].

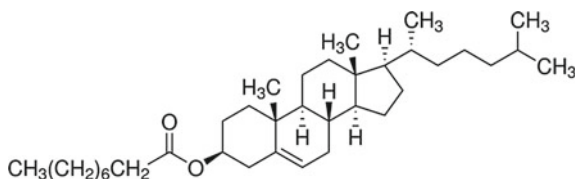
The applications of LC materials range from displays to electronics, sensors, lasers, liquid crystal thermometer and optical computing. However, pure LC-based devices have some drawbacks like achieving useful temperature, ionic impurities, lower contrast ratio, more response time, less angle for view, high threshold voltage etc. These problems can be minimized by synthesizing particular LC materials with specific characteristics or preparing composite materials by dispersing/doping polymers, or nanomaterials into the LC matrix. The dispersion of monomer in LC is preferred as there are no significant structural distortions in LC after dispersion of nanomaterials and such that system is suitable for technological applications [9–18].

The monomer dispersed LC is composites which contain spherical, ellipsoidal or flat LC droplet dispersed in array of solid polymer. Based on the behaviour of the components and the preparation techniques, it exhibits various morphology, i.e. different concentration, size and shape of the LC droplets. The morphology in turn crucially changes the thermal behaviour of those composites and therefore is essential for applications. The main advantage of monomer dispersed liquid crystals is its simple construction and its other advantages like no need of polarizer, aligning layers, hermetizing materials, low cost and mechanical durability [16, 19–26].

Many researchers have observed and reported the various physical properties of these composite materials. Jayoti et al. studied morphological and electro-optical behaviour of silica nanoparticles in polymer dispersed composites [27], Deshmukh and Jain reported morphological, electro-optical and dielectric behaviour of LC dispersed with polymer [28], Ellahi et al. studied Influence of the multi-functional properties [29], Kumar et al. reported Dye-dependent studies on droplet pattern and electro-optic behaviour [30], Zhou et al. reported novel light diffuser based on the combined morphology [31], Kemiklioglu et al. reported the effect of the monomer on the mechanical performance [32], Kizhacidathazhath et al. reported high-performance acrylate monomer [33], Jain et al. reported electro-optical and dielectric behaviour [34], Liang et al. reported Influence of ZnO [35], and Pagidi et al. reported electro-optic characteristics [36]. As per our literature survey, no research group has yet reported the effect of different concentrations of monomer on morphological and thermal behaviour of cholesteric liquid crystals.

2 Materials

2.1 Cholesteryl Nonanoate



Structural Formula: $C_{36} H_{62} O_2$.

Molecular Weight: 526.88.

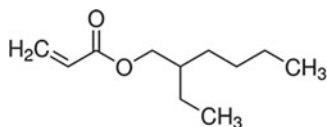
Melting Point: 77–82 °C.

Transition Temperature: Crystalline to smectic 77.5 °C.

:Smectic to N* 79 °C.

:N* to isotropic 90 °C.

2.2 2-Ethyl Hexyl Acrylate



Structural Formula: $CH_2=CHCOOCH_2CH(C_2H_5)(C_2H_5)(CH_2)_3CH_3$.

Melting Point: < -76 °C.

Due to its low volatile nature and reactivity of double bonds, 2-Ethyl Hexyl Acrylate (2-EHA) is perhaps choice for plasticizing many applications. Because of its low viscosity, it is used in dental material, particularly suitable as filling material as dental cement, facing material for crowns and bridges, material for artificial teeth.

The samples under investigation were formed by preparing a composite of cholesteryl nonanoate (NN) and monomer 2-Ethyl Hexyl Acrylate (2-EHA) in two different concentrations are designated as AA = NN (80%) + 2-EHA (20%) and BB = NN (60%) and 2-EHA (40%). The samples were synthesized by chemical method, and to obtain homogeneous mixing, the mixture was heated at temperature slightly above the isotropic temperature, for 30 min. The stabilized samples were obtained by cooling at normal room temperature.

3 Results and Discussion

3.1 Fourier Transform Infrared (FTIR) Study

FTIR spectroscopy is a necessary tool to examine the chemical bonding of the sample under investigation. Examining the wave numbers for the internal vibrations for different mesophases and comparing them with those for the isotropic liquid, we expect that structural difference between phases will show up in terms of wave number shifts, changes in intensity and changes in the shape of a band.

Small shift in the wave number corresponds to some Smectic A compounds. The interpretation of intensity changes lead to some erroneous conclusions about the structural features of the nematic phase. It is possible to observe intensity changes without wave number shifts. The intensity differences are due to the uniform molecular orientation induced by the long-range order in the nematic.

The FTIR spectrum of pure cholesteric nonanoate is shown in Fig. 1. The peaks around 2100 cm^{-1} are due to C=C bond and $3600\text{--}3200\text{ cm}^{-1}$, are due to stretching of O-H, while peaks between $2500\text{ to }3000\text{ cm}^{-1}$ are due to carboxylic acids. Absorption peak between $3200\text{--}3600\text{ cm}^{-1}$ and around 2500 cm^{-1} are due to stretching of O-H bond. The bond in the low frequency range of $900\text{--}670\text{ cm}^{-1}$ arises from out of plane bonding of ring C-H bonds. The bond appeared at 1500 cm^{-1} is due to C-C ring stretch.

The FTIR spectrum of cholesteric nonanoate + 2-EHA monomer (AA) shown in Fig. 2 shows new peak at 1668 cm^{-1} with high intensity. This new peak appear at 1668 is due to C=O stretch.

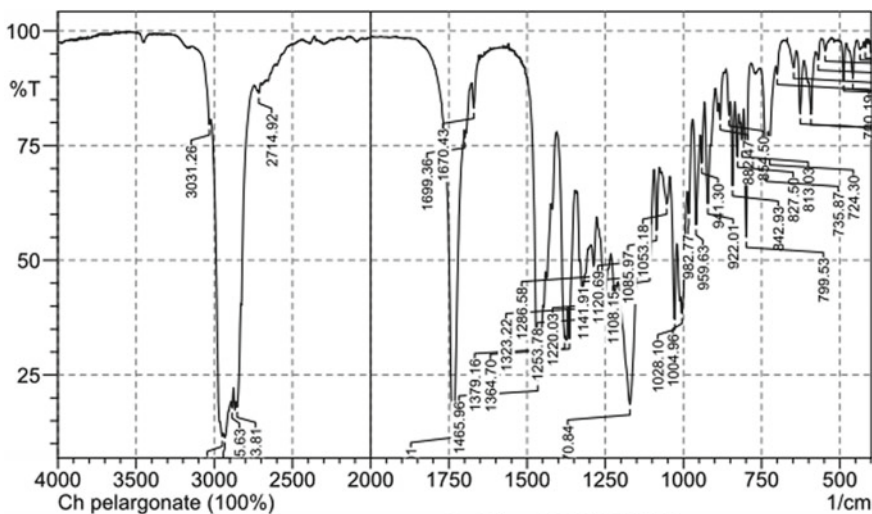


Fig. 1 FTIR spectrum of cholesteric nonanoate

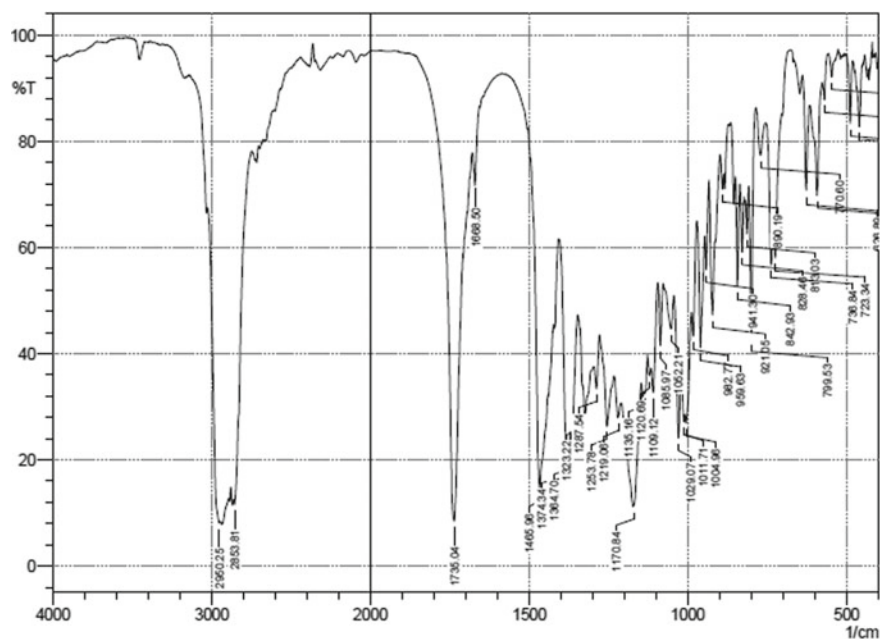


Fig. 2 FTIR spectrum of cholesteric nonanoate + 2-EHA (AA)

The FTIR spectrum of cholesteric nonanoate + 2-EHA (BB) shown in Fig. 3 shows stretching between 1170 and 1465 cm^{-1} stretch is due O–H (H-bonded), 1465–1735 cm^{-1} is due to C=O stretch shows presence of ester, 1735–2853 cm^{-1} shows evidence of alkenes, i.e. C–H stretch and new peak appears at 1670 cm^{-1} of high intensity (Table 1).

It was found that some peaks were suppressed whereas some new peaks were observed in the composite AA and BB. For the peaks having same wave number, there are changes in the intensities of composite. Low values of intensities were found in concentration AA. The peaks at 1506 and 1558 cm^{-1} are suppressed in composite, i.e. nitro group is suppressed in the composite.

3.2 Thermal Characteristics

The thermal properties were investigated by differential scanning calorimeter (DSC). For the DSC measurements, both the cycles of heating and cooling were performed at a scans rate of 10 $^{\circ}\text{C}$ per minute. When material changes a state from solid to a liquid, it requires energy from surrounding. Similarly in the crystallization of energy is released to the surroundings. The transition from solid to liquid phase shows abrupt change in phase transition temperature which is related to structural change and in this

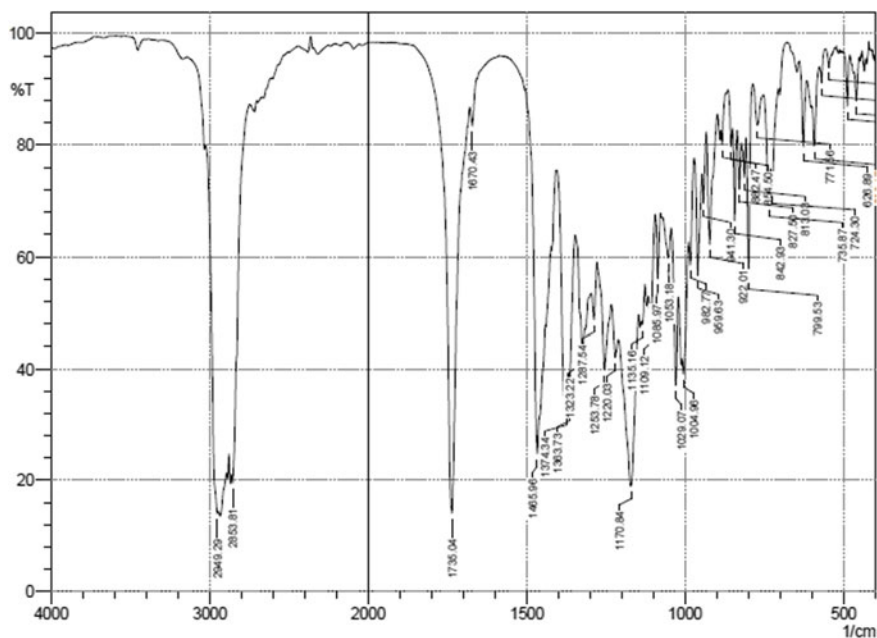


Fig. 3 FTIR spectrum of cholesteric nonanoate + 2EHA (BB)

Table 1 Comparative study of intensities

Ch.NN			NN + 2-EHA (AA)			NN + 2-EHA (BB)		
Wave number	Intensity	Functional group	Wave number	Intensity	Functional group	Wave number	Intensity	Functional group
1457	75	- COO	1465	14	- COO	1465	24	- COO
1506	-	Nitro	1668	72	-	1670	83	C-C
1558	-	-	-	-	-	-	-	-
1734	40	Anhydride	1735	8	Anhydride	1735	14	Anhydride S
2853	40	-	2853	11	-	2853	19	-
-	-	-	2950	8	- CH ₃ A	2949	13	- CH ₃ A
2867	49	- CH ₃ S	-	-	-	-	-	-
2886	-	- CH ₃ S	-	-	-	-	-	-

relatively more transition energy is required. Even if transition peaks are not sharp still, it shows stretches over a certain temperature range. The nematic-isotropic liquid transition tends to be smaller than crystalline-smectic or smectic-isotropic liquid transition.

The DSC thermograms showing the variations of heat flow (mW) with temperature (°C) in the heating and cooling cycles of all the samples are shown below.

The DSC thermogram of pure cholesteric nonanoate shown in Fig. 4 shows two endothermic peaks. The first transition occurs at 76.7 °C indicating the transition from crystalline to smectic A phase. The next peak of transition occur at 91.9 °C corresponds to smectic phase to cholesteric transition. During cooling cycle, a very small exothermic peak is seen. The nonanoate marks the beginning of a new type of order in both the solid and the mesophase. The change in the entropy due to mesophase transition is 3.5% (Figs. 5 and 6; Table 2).

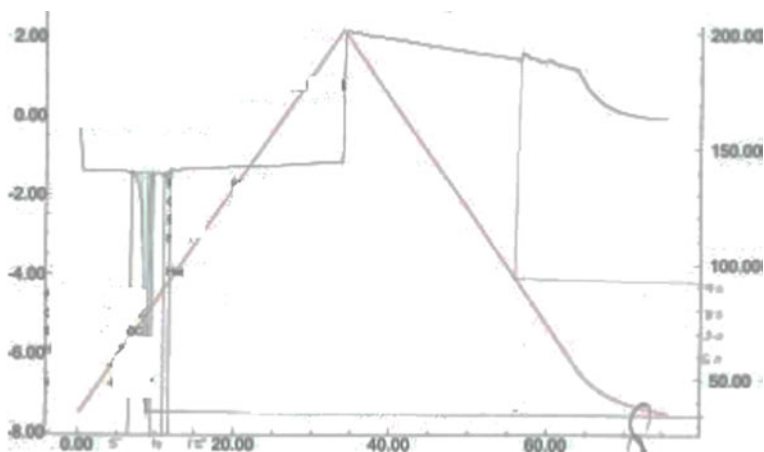


Fig. 4 DSC thermogram of pure cholesteric nonanoate

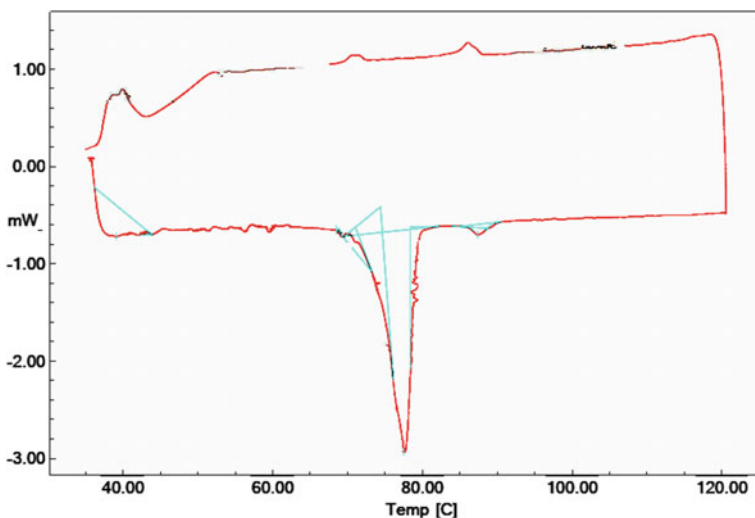


Fig. 5 DSC thermogram of cholesteric nonanoate + 2-EHA (AA)

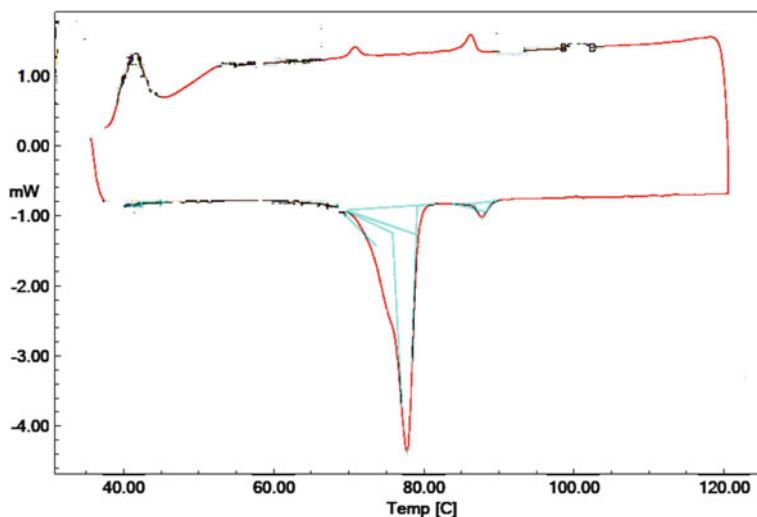


Fig. 6 Thermogram of cholesteryl nonanoate + 2-EHA (BB)

Table 2 Comparison of transition temperatures and enthalpies

	Pure cholesteric nonanoate		Cholesteryl nonanoate + 2-EHA (AA)		Cholesteryl nonanoate + 2-EHA (BB)	
	T_t °C	ΔH_t KJ/mol	T_t °C	ΔH_t KJ/mol	T_t °C	ΔH_t KJ/mol
Heating	77.99	-49.86	77.73	-29.63	77.57	-19.60
	91.41	-1.12	87.73	-0.86	87	-0.58
Cooling	-	-	87.73	-0.01	87.40	-0.25
	-	-	68.58	0.52	68.55	0.88
	-	-	44.88	0.03	39.10	-3.85 S_A

Dispersion of cholesteryl nonanoate in monomer 2-EHA with concentration 20 and 40% is showing minor changes in transition temperature of pure cholesteric nonanoate with decrease in value of enthalpy. Cooling curve of doped liquid shows three peaks, which are not shown in the pure liquid crystal. Heating and cooling cycles show same peaks at 87.73 °C. Cooling peak at 39.10 °C for concentration BB, whose enthalpy value corresponds to Smectic A phase.

4 Conclusion

The morphological and thermal properties of cholesteric nonanoate dispersed with different concentrations of monomer were studied. In FTIR spectrum, the decrease in the intensity of absorption at the transition from isotropic to the nematic is due to

the uniform molecular orientation. This shows the vibrational transition moment is directed along the molecular axes and the molecules tend to align preferentially at an angle which is perpendicular to the surface of LC.

The changes in the transition temperature of pure and two different concentration of monomer were investigated. The variation caused by the clearing point of the composite is result of the bonding, which may be either from the side walls or head part of the crystal molecule. The variation in the transition temperature of the composite depends on the number of carbon atoms. The phase transition temperature of pure LC and its composite depends on the number of carbon atoms in the chain. The cohesive forces are responsible for nematic to isotropic transition temperature decreases with an increase in the chain length. This indicates the wide range of applications of the materials like photo-cured network and photopolymer etc.

References

1. Collings PJ, Hird M (1997) Introduction to liquid crystals. Taylor and Francis Ltd., London
2. Singh S (2001) Fundamentals, liquid crystals. Scientific World
3. Demus D, Goodby J, Gray GW, Spiess HW (1998) Handbook of liquid crystal. Wileyvch, p 145
4. Chandrasekhar S (1994) Liquid crystals. Cambridge University Press
5. Blinov LM, Chigernov VG (1996) Electro-optic effects in liquid crystal materials. Springer, New York
6. Boden N, Bushby RJ, Clements J, Movaghar B (1999) Device applications of charge transport in discotic liquid crystals. *J Mater Chem.* <https://doi.org/10.1039/A903005K>
7. Sellinger A, Tamaki R, Laine RM, Ueno K, Tanabe H, Williams E, Jabbour GE (2005) *Chem Commun* 29:3700
8. Mani SA, Amare JR, Hadkar SU, Mishra KG, Pradhan MS, Al-Johani H, Sarawade PB (2017) Investigations of optical and thermal response of polymer dispersed binary liquid crystals. *Mol Cryst Liq Cryst* 646(1):183–193. <https://doi.org/10.1080/15421406>
9. Kumar S, Naidu JJ (2002) *Mol Cryst Liq Cryst* 378:456
10. Gray GW, Winsor PA (1974) Liquid crystal and plastic crystals, 1 edn. EllisHarwood Ltd., Chichester, England
11. Watson SJ, Gleeson HF, D'Emanuele A, Serak S, Grozhik V (1999) *Mol. Cryst Liq. Crst.* 165(331):2235
12. Gupta VK, Skaife JJ, Dubrovsky TB, Abbott NL (1998) *Science* 279:2077
13. Gharde RA, Pradhan MS, Mani SA, Amare JR (2014) Electro-optical studies on nanopowder doped liquid crystal. *Int J Chem Phys Sci NCRTSM 3(Special Issue)*. ISSN: 2319–6602
14. Barke JM, Daschner MK, Luk YY, Abbott NL (2003) *Science* 302:2094
15. Silva M, Sotomayor J, Figueirinhas J (2015) *J Chem Technol Biotechnol* 90:1565–1569
16. Mishra KG, Dubey SK, Mani SA, Pradhan MS (2016) Comparative study of nanoparticles doped in liquid crystal polymer system. *J Mol Liq* 224:668–671. <https://doi.org/10.1016/j.molliq.2016.10.075>
17. Huang W, Liu Y, Hu L, Mu Q, Peng Z, Yang C, Xuan L (2013) *Org Electron* 14(2299–170):2305
18. Kim M, Park K, Seok S, Ok J, Jung H, Choe J, Kim D (2015) *ACS Appl Mater Interfaces* 7(32):17904–17909
19. Kumar P, Kang S, Lee S, Raina K (2011) *Thin Solid Films* 520(1):457–463
20. Trushkevych O, Eriksson T, Ramadas S, Edwards R (2015) *Appl Phys Lett* 107(5):054102
21. Liu J, Gao W, Kityk IV, Liu X, Zhen Z (2015) *Dyes Pigment* 122:74–84

22. Nicoletta FP, Chidichimo G, Cupelli D, Filpo GD, Benedittis MD, Gabriele BG, Salerno A, Fazio A (2005) *Adv Funct Mater* 15:995–999. <https://doi.org/10.1002/adfm.200400403>
23. Liu J, Ozga K, Liu X, Zhen Z, Plucinski KJ, Szota M, Kityk IV (2016) *Arch Metall Mater* 61(1):457–460, 180
24. Amundson K, van Blaaderen A, Wiltzius P (1997) Morphology and electro-optic properties of polymer-dispersed liquid-crystal films. *Phys Rev E* 55(2):1646–1654
25. Mani S et al (2020) Effect of ferroelectric nanopowder on electrical and acoustical properties of cholesteric liquid crystal. *Non-Met Mater Sci* 02(01). <https://doi.org/10.30564/omms.v2i1.1821>
26. Prakash J, Chandran A, Biradar AM (2017) Scientific developments of liquid crystal-based optical memory: a review. *Rep Prog Phys* 80:16601. <https://doi.org/10.1088/0034-4885/80/1/016601>
27. Jayoti D, Malik P, Singh A (2017) Analysis of morphological behaviour and electro-optical properties of silica nanoparticles doped polymer dispersed liquid crystal composites. *J Mol Liq* 225:456–461. <https://doi.org/10.1016/j.molliq.2016.11.100>
28. Deshmukh RR, Jain AK (2014) The complete morphological, electro-optical and dielectric study of dichroic dye-doped polymer-dispersed liquid crystal. *Liq Cryst* 41(7):960–975. <https://doi.org/10.1080/02678292.2014.896051>
29. Ellahi M, Liu F, Song P et al (2013) Influence of the multi-functional epoxy monomers structure on the electro-optical properties and morphology of polymer-dispersed liquid crystal films. *Polym Bull* 70:2967–2980. <https://doi.org/10.1007/s00289-013-1000-6>
30. Kumar P, Sharma V, Jaggi C, Raina KK (2017) Dye-dependent studies on droplet pattern and electro-optic behaviour of polymer dispersed liquid crystal. *Liq Cryst* 44(4):757–767. <https://doi.org/10.1080/02678292.2016.1240834>
31. Zhou L, Ma H, Han C, Hu W, Zhang S, Zhang L, Yang H (2018) A novel light diffuser based on the combined morphology of polymer networks and polymer balls in a polymer dispersed liquid crystals film. *RSC Adv* (39). <https://doi.org/10.1039/C8RA03426E>
32. Kemiklioglu E, Atik E (2019) The effect of the monomer functionality on the mechanical performance and polymer morphology of polymer stabilized blue phases. *Compos B Eng* 165:96–101. <https://doi.org/10.1016/j.compositesb.2018.11.130>
33. Kizhakidathazhath R, Nishikawa H, Okumura Y, Higuchi H, Kikuchi H (2020) High-performance polymer dispersed liquid crystal enabled by uniquely designed acrylate monomer. *Polymers* 12(8):1625. <https://doi.org/10.3390/polym12081625>
34. Jain AK, Deshmukh RR (2019) Electro-optical and dielectric study of multi-walled carbon nanotube doped polymer dispersed liquid crystal films. *Liq Cryst* 46(8):1191–1202. <https://doi.org/10.1080/02678292.2018.1545264>
35. Liang Z, Zhao Y, Gao H, Wang D, Miao Z, Cao H, Yang Z, He W (2021) Influence of ZnO NPs on morphological and electro-optical properties of polymer-dispersed liquid crystals. *Liq Cryst*. <https://doi.org/10.1080/02678292.2021.1898055>
36. Pagidi S, Manda R, Shin HS, Lee J, Lim YJ, Kim M, Lee SH (2021) Enhanced electro-optic characteristics of polymer-dispersed nano-sized liquid crystal droplets utilizing PEDOT:PSS polymer composite. *J Mol Liq* 322:114959. <https://doi.org/10.1016/j.molliq.2020.114959>

Chapter 59

Design and Analysis of Penta-Magnetic Tunnel Junction Circuit with Transmission Gate Logic



C. S. Manikandababu, M. Jagadeeswari, S. Manju, and M. Aiswarya

Abstract The design of very large-scale integrated circuits passes through many critical stages and challenges the advanced technology of nanometer CMOS technology. The major problem included in the existing process is the leakage current and reliability issues. Penta-magnetic tunnel junction (Penta-MTJ) hybrid with CMOS technology has many advantages in the VLSI strategy such as higher performance and low leakage current. The methodology of the proposed work includes the increase in the storage capacity with optimized power and speed using transmission gate logic and decrease in area and power in combinational and sequential circuits. The structure of Penta-MTJ includes the design of transmission gates to increase the speed with the minimum number of gates to reduce the area and power consumption. By decreasing the number of transistors in transmission gate logic, the power consumption was reduced to 12 and 18%. To overcome the sensing reliability issue, high sensing margin is proposed in the design circuit. With a 43.9 and 10.7% increase in energy delay product (EDP), the proposed approach reduces energy demand while incurring low area overhead.

Keywords Penta-magnetic tunnel junction (MTJ) · Transmission gate logic (TGL) · Spintronics · Energy delay product

1 Introduction

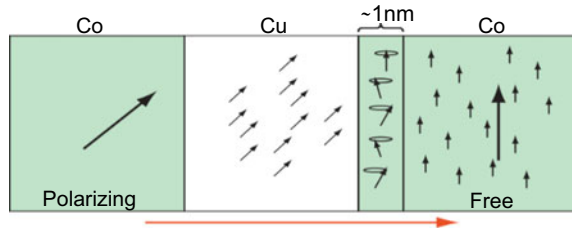
Spintronics, also known as spin electronics, is a growing field of research that combines magnetism and electronics. The spin, which produces new functionalities and machines, is the key benefit of the quantum feature of electrons. The magnetic

C. S. Manikandababu · M. Jagadeeswari · S. Manju (✉) · M. Aiswarya
Department of Electronics and Communication Engineering, Sri Ramakrishna Engineering College, Coimbatore 641022, India

C. S. Manikandababu
e-mail: manikandababu.shelvaraju@srec.ac.in

M. Jagadeeswari
e-mail: jagadeeswari.m@srec.ac.in

Fig. 1 Schematic representation of the spin transfer phenomenon



layers in the spintronic device aid in the transmission of spin-polarized electrons. The invention of spintronics devices began in 1988 with the discovery of the GMR effect, which is based on a significant difference in magnetic layer resistance [1]. Deni et al. invented a spin valve structure that exhibits the resistance value in the GMR effect as well as very sensitive magnetic field sensors. Of 1998, the magnetic tunnel junction in computer disk drives was implemented as the sensing feature of a potential spintronic interface. Based on computer disk drives, they deliver more than 1 billion reading heads per year [2]. Hardware that uses the form factor which is used in electronics items such as camcorders, MP3 players, and movie recorders is some of the most popular implementations of spintronic systems. As seen in Fig. 1, the spintronic layer, which is a magnetic tunnel junction, is made up of two ferromagnetic copper layers separated by two nonmetallic spacers.

As electrons pass from left to right as current moves from right to left transmission gates, polarization occurs between conduction electrons as they migrate between the ferromagnetic layers. Spin polarization parallel to the magnetization characterizes the current that emerges from the copper sheet. The transmitted electron process' spin articulately travels through the electrodes' local exchange field magnetization [3]. At a distance of 1 nm, the spin polarization of incoming electrons reoriented in local magnetization. The tunnel barrier dominates the resistance in the magnetic tunnel junction. The magnetic tunnel junction is much thicker and varies in thickness depending on the application. The resistance area product must be selected correctly to characterize the resistance value in order to obtain the resistance effect. The Penta-MTJ circuit's resistance ranges from 10 to 100 μm or even more. It is possible to reduce the strength of Penta-MTJ circuits by carefully selecting the thickness. This electricity consumption takes place if the inputs are maintained at a valid logic standard and the circuit is not under charging conditions. However, dynamic power usage will significantly add to total energy consumption by switching at a very high frequency. Charging and unloading a power load raise this dynamic power consumption.

When the circuit is working, dynamic power dissipation happens, while static power dissipation becomes a problem when the circuit is out of condition or down power.

1.1 A Novel Design in Penta-MTJ Circuits

(1) Penta-MTJ logic and (2) Penta-MTJ cell. Penta-MTJ for sensing differentiation between the two resistance states: PCSA is a two-stage dynamic logic circuit, respectively, and a pre-load and evaluation process. The discharge of the two PCSA branches depends upon their respective strengths such that the low-resistance branch discharges the capacity of the output node more quickly and discharges the other branch due to its cross-connected PCSA structure. The low-resistance branch descends to the ground, and the high-resistance branch rises to VDD. The Penta-MTJ starts with the conventional logic circuits. The conventional logic circuit includes those three layers with a ferromagnetic layer on the top and a thin oxide barrier layer between the ferromagnetic layers [4]. The ferromagnetic layer has a fixed magnetic direction. The direction has two parallel modes and two resistance values of RL and RH associated with Penta-MTJ. Conventional Penta-MTJ-based circuits are parallel and anti-parallel mode. Various reconfiguration techniques were adapted from Penta-MTJ circuits with reconfigurable torque transfer to reduce energy and delay. The Penta-MTJ best logic includes two CMOS circuits for reading and writing operation [5]. The Penta-MTJ circuits undergo read operation, whereas other undergoes the right operation. Penta-MTJ cell consists of two terminals with three layers as shown in Fig. 2.

The Penta-MTJ cell with CMOS sequential logic and combinational logic acquired more power and delay within the circuit. The proposed magnetic tunnel junction has very low standby power consumption and advantage of non-volatile. The proposed Penta-MTJ with transmission gate preserves the previous gate to reduce power consumption. We also undergo there any disturbance and reconfiguration cause which is added as an advantage. The paper proposes that the Penta-MTJ circuit with pass transistor logic offers low power consumption and lesser delay to increase the speed of the circuit. The paper is composed of the following section. Section 2 includes the literature survey of the proposed work. Section 3 includes the design

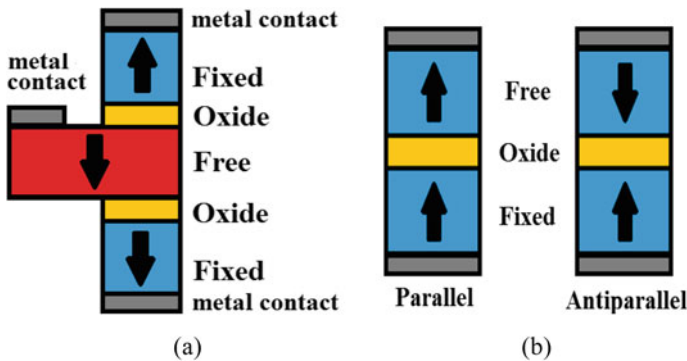


Fig. 2 Structure of the Penta-MTJs: **a** TIO-Penta-MTJ including three ferromagnetic layers and three terminals. **b** Conventional Penta-MTJ including two ferromagnetic layers and two terminals

methodology of the proposed work. Section 4 includes the experimental results, and Sect. 5 includes the discussion of the proposed work.

2 Review of Existing Work

There is much existing work on the digital industry including the logic gate, XOR gates, and 1,4-bit full adder. The survey includes the design of a circuit based on CMOS architectures. It also includes a FinFET-based design and TFET-based designs. Kyu Ming Wang et al. propose the transistor level EXOR and XNOR circuits CMOS configuration. Using a non-complementary signal, this technique includes 4 transistors which decrease the power consumption and power delay. This work cannot be used in the circuit due to a lack of voltage sink when both the inputs are higher [6]. Hanh Lee et al. proposed 7 transistor base XOR and XNOR circuits to decrease the voltage supply. The design was developed with good signal output levels more energy. The disadvantage of the newly developed method is threshold voltage loss [7]. Vesterbacka et al. proposed a pass transistor logic-based CMOS circuit. The circuit has a problem of transistor sharing to acquire the feedback structure. However, the design complexity may increase compared to other structures [8]. KuoHsing Cheng et al. implemented a new concept of high performance of XOR and XNOR using pass transistor logic. The six transistor structure suffers the more power consumption structure. The operating voltage will be limited to the 2v threshold voltage. This work includes 10 transistors that involve the output voltage swing and operation voltage is limited above the threshold voltage. This can be operated at a lower voltage [9]. Summer Goel et al. underwent a design using XOR and XNOR with lower supply voltage. The proposed circuit exhibits lesser delay and more energy efficiency the glitch of more power consumption added as a disadvantage [10]. Azam et al. proposed the XOR circuit with an optimized genetic algorithm and move near the threshold region. The technology file consists of a 22-nm structure to achieve 28–48% energy optimization. The problem persists in the higher area of occupation compared with other standards that have low swing of operation at minimum supply voltage [11]. Nan Zhuang et al. introduced the transmission function with the coupled theory of CMOS full adder to gain the simplicity in the circuit. The drawback is a high impedance state Boolean algebra eliminates the new proposed operation included in the translation process [12]. Reto Zimmermann et al. concluded the full adders that depend on CPL and conventional logic of complementary CMOS. Power consumption is high due to switching activity. It has large circuit currents and high switching capacitance [13]. Ahmed m shams et al. constructed a full adder circuit with 16 transistors and 14 transistors. The design gains advantage of minimum power dissipation speed compared to other standards, but glitches across the output and static power are higher at inverted output [14]. Massimo Alioto et al. include 1-bit full adder topologies and compared various factors such as power consumption, speed, power delay. The result is not attractive under some exceptional cases to acquire minimum power from short chain of blocks [15]. Jieun Lee et al. constructed a different binary full

adder circuit single-electron transistor to improve performance and power reliability. Videos of binary decision diagram technique acquire 1-bit full adder. The problem occurred in the decision diagram for full adders with a lot of threshold logic levels parameter [16]. Sarada et al. proposed a new hybrid one-bit structure. It is designed based on 90 nm technology and compared various transmissions gate. The demerits include the increase in the propagation delay proportional to the chain length of the adder [17]. Tran et al. developed a fundamental circuit of 32-bit adder advantage of high efficiency in the subthreshold region. The energy delay product is high compared to other transistor threshold values [18]. The proposed technique comes up with less area consumption and less power consumption. Developing the Penta-MTJ standards with the transmission logic includes the lesser logic gates which save more area and decrease the power delay.

3 Design Methodology of Penta-MTJ with Transmission Gates

3.1 Structure of Penta-MTJ

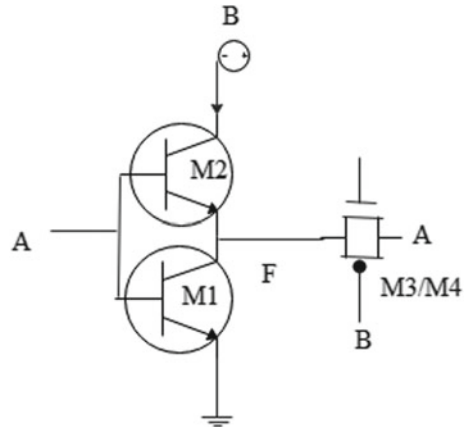
To increase the performance measure in the computing system, a spintronic device named as magnetic tunnel junction is used which has high-speed low power and higher endurance properties. Penta-MTJ circuits are used in various logic circuits. The painter Penta-MTJ-based logic gates have simpler cascading and self-referencing effects. It also has free charge sense amplifier logics, and low area can be covered with disturbance-free reading and writing properties. The model of Penta-MTJ acquires 45 nm technology with the Verilog simulation.

3.2 Proposed Penta-MTJ with Transmission Gates

Transmission gates play a major role in sequential as well as combinational logic circuits. The XOR logic is implemented using the Penta-MTJ having more transistors to consume more power due to static power dissipation [19]. Also, the execution speed is low due to a large delay. To optimize the speed and power in Penta-MTJ-based XOR gate effectively, in this project pass transistor logic and transmission gate logic are implemented.

The transmitting gate logic is used to solve the disadvantages of logic gates, as seen in Fig. 3. The number of transistors is also limited in this case. The nMOS provides good switch output in favorable conditions for itself but not for the pMOS, and the pMOS provides good switch performance in favorable conditions for itself but not for the nMOS.

Fig. 3 XOR using transmission gates



3.3 Design of Combinational Circuits Using Penta-MTJ with Transmission Gate

The combinational logic circuit is one of the digital circuits which is categorized with Boolean circuits and output as present inputs. The combination logic circuit does not have the memory space, the most important type of combinational circuit is ram ROM multiplexers encoders full adder half adder. A combinational circuit has two methods, namely the sum of products and product of sum. The Penta-MTJ technology is used to simulate the output using Tanner software. The proposed technology includes the design of a combinational circuit with Penta-MTJ. The proposed design using the 4-bit adder circuit with transmission gate circuit gives lower power dissipation and speeds up the circuit.

3.3.1 Structural Design of 4 Bit Adder

When a gate’s output logic is based on the majority population of the implemented inputs, it is referred to as majority logic. The use of MTJ, as seen in Fig. 4, will add a variety of common sense. With the top electrode grounded and the bottom electrode attached to a few input terminals, the MTJ is located between the pinnacle and bottom electrodes [20]. Today’s critical switching of the MTJ is less than any pulse amplitude input. If the entire modern is positive and greater than the MTJ mobile’s important switching modern, electrons waft from the loose layer to the constant layer. The polarized electromagnetism is generated when the instrument is used in the parallel domain.

The implementation of majority logic using MTJ and its truth table is shown in Table 1. The simulation in Tanner software is used to apply the built logic and estimate the low power consumption. The key benefit of using a transmission gate configuration is that it easily passes all 0s and 1s as seen below. When PMOS is turned

Fig. 4 Implementation of MTJ logic with adder circuits

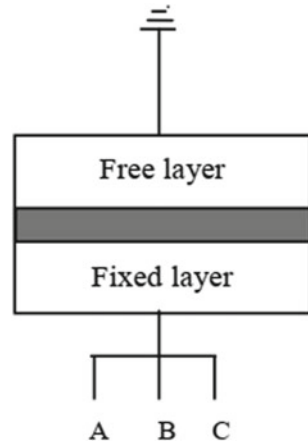


Table 1 Comparison of power

Methodology	Penta-MTJ [15]	Penta-MTJ using PTL (proposed)	Penta-MTJ using transmission gates (proposed)
XOR	10.522 mw	9.422 mw	11.144 mw
4-bit adder	5.55 mw	5.319 mw	7.046 mw
3-bit gray counter	2.75 mw	2.64 mw	4.358 mw

off, NMOS is turned on, and data of logic ‘1’ are effectively passed; conversely, when NMOS is turned off and PMOS is turned on, data of logic ‘0’ are effectively passed.

3.4 Design of Sequential Circuits Using Penta-MTJ with Transmission Gate

The output of a sequential circuit is determined not only by the most recent inputs, but also by the state of earlier inputs. Memory components are used in sequential circuits. There are a variety of sequential circuits that can be built using the suggested transmission logic.

3.4.1 3-Bit Gray Counter

A sequential circuit is the counter. A known counter is a digital circuit that counts the number of pulses. The counter is the most popular place that flip-flops are used. Figure 5 shows a gray clock, which is one of the sequential counters that store data in their respective flip-flops. Gray coding has the advantage of these applications

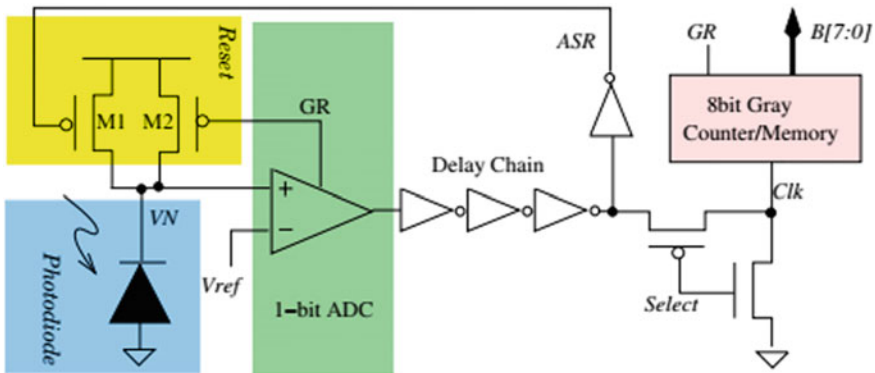


Fig. 5 Memory logic of 3-bit gray counter

because variations in the transmission delays of several wires that represent the bits of the code cannot allow the obtained value to go through states that are not in the gray code series.

The main lead of skip semiconductor tool common sense is reducing the number of transistors compared to the CMOS common sense, but they even have some drawback that the load present in the input is dependent on the load linked to the output. So, the temporal association analysis may become a failure to conquer this; transmission gates are used. The transmission gate logic is hired to resolve the free fall disadvantage of the bypass transistor logic.

4 Experimental Analysis

The proposed logic can be implemented in Tanner software with the dependency of several factors stated below. The designed circuit is simulated using Tanner using the macro-mold for MTJ. This macro-mold represents MTJ as a current-controlled resistor. The proposed Penta-MTJ-based XOR using transmission gates is listed below (Figs. 6 and 7).

Figure 8 shows the power and time delay of XOR Design implementation. The power and delay of the XOR module will be taken from T-Spice.

The device nMOS is OFF and a device pMOS is ON while logic 0. (Case 1). VCC, or logic, is the output voltage 1. In the same way, the related nMOS device is ON and the pMOS device is OFF when input is at logic 1. GND is or logic 0 is the output voltage. Notice that if the gate is in one of these logical states, one of the transistors is still OFF. Since there is no current through the gate terminal, and there is no current path from VCC to GND, the resulting quiescent (state-state) current is zero (Fig. 9).

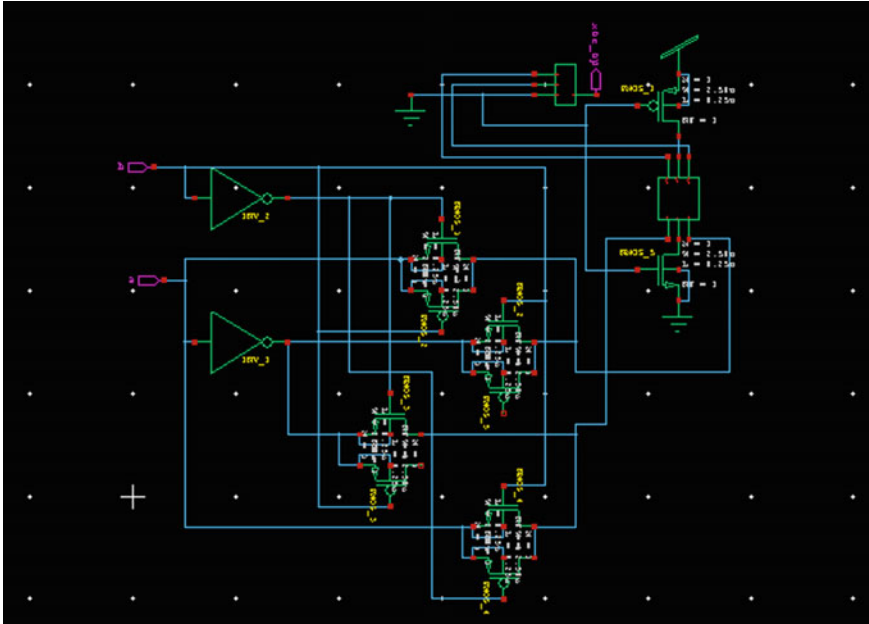


Fig. 6 Schematic diagram of Penta-MTJ-based XOR using transmission gates waveform of Penta-MTJ-based XOR gate using transmission gate

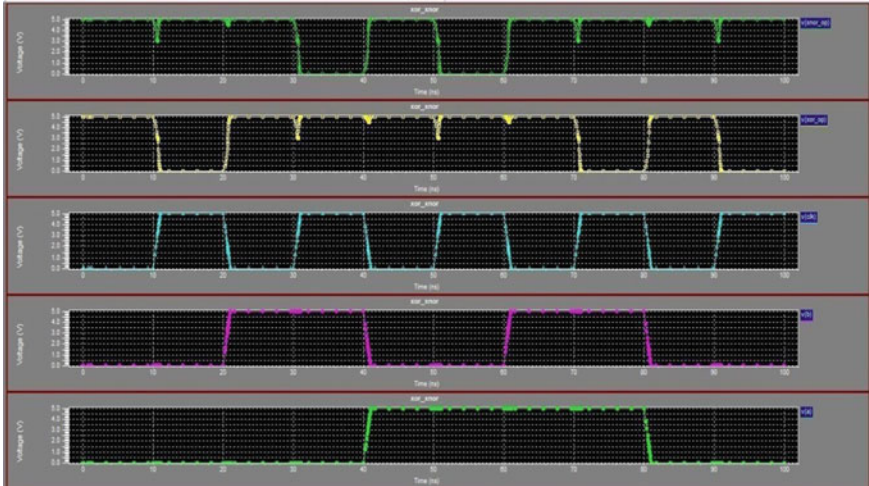


Fig. 7 Waveform of Penta-MTJ-based XOR with transmission gate

```

Average power consumed -> 11.144076e-002 watts
Max power 9.144076e-002 at time 9.86875e-008
Min power 9.144075e-002 at time 9.66875e-008

* END NON-GRAPHICAL DATA
*
* Parsing 0.06 seconds
* Setup 0.06 seconds
* DC operating point 0.35 seconds
* Transient Analysis 0.02 seconds
* Overhead 3.25 seconds
* -----
* Total 3.74 seconds
*
* Simulation completed with 4 Warnings
* End of T-Spice output file
    
```

Status	Input file	Outp...	Start Date/Ti...	Elaps...
Finished	C:\Users\...\Temp\ptl_xo.sp	ptl...	March 11, 2...	00:0...

Fig. 8 Power and time delay of XOR design

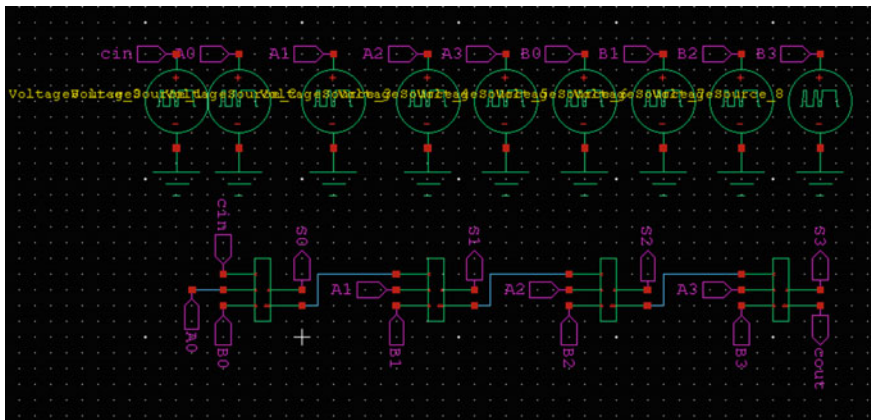


Fig. 9 Schematic diagram of Penta-MTJ-based 4-bit adder using transmission gates

4.1 Comparison

The power and speed of Penta-MTJ-based combinational and sequential circuits can be denoted in terms of transistor counts. The number of transistor counts was reduced by implementing with pass transistor logic (PTL) and transmission gate logic (TGL). Table 1 shows the power comparison of the proposed system and the existing system. In the proposed methodology, it is inferred that the power of XOR using Penta-MTJ based on PTL has a 10% reduction in power compared to the existing methodology, but the TGL logic showed a 6% increase than existing, and then, the power of combinational circuit using Penta-MTJ based on PTL has 4% reduction

Table 2 Comparison of speed

Methodology	Penta-MTJ		Penta-MTJ using PTL		Penta-MTJ using transmission gates (proposed)	
XOR	3.14 s	0.318 bps	2.83 s	0.7067 bps	1.59 s	1.257 bps
4-Bit Adder	2.27 s	3.524 bps	1.67 s	4.790 bps	2.52 s	3.1746 bps
3-Bit Gray Counter	4.94 s	0.607 bps	3.80 s	0.789 bps	3.91 s	0.7672 bps

in power compared to the existing methodology, but the TGL logic showed 28% increase than existing, and then, the power of sequential circuit using Penta-MTJ based on PTL has 4% reduction in power compared to the existing methodology, but the TGL logic showed 58% increase than existing. The improvement in power is achieved compared to the existing methodology shown in Table 1. The existing model is simulated in the same experimental tool analysis.

Table 2 shows the comparison of speed between the existing and proposed systems with various methodologies. Delay of the project is determined in the timing summary present in the synthesized report after completing the systemization and implementation.

5 Conclusion and Future Work

The proposed Penta-MTJ circuit has low power and short delays with non-volatile properties. Penta-MTJ circuit reduces its area-based logic functions. The attractive features of the proposed technique include low static power, short interconnection delay, and lesser power getting effect because of the non-volatile feature. • Biasing magnetism layers of the nanopillars reduce the change time significantly. Despite the very fact that biasing within the case of fastened layer enhances the spin transfer torsion working at the free, in the case of an unfastened layer biasing setup, the quickest magnetization switching is administered at intervals, reducing switching time. • In the case of unfastened layer biasing, an applied magnetism subject generates additional magnetic torque, which reduces the switching time by shortening the spiraling direction of the magnetization mechanical phenomenon. By avoiding the intermediary circuits used to transform voltage to current or current to voltage, the Penta-MTJ circuit reduces the area overhead latency. There is no initial requirement for evaluating the logical operation output, and the self-referencing properties of Penta-MTJ are removed. The proposed Penta-MTJ circuit provides free disturbance from reading and decreases the tolerance rate due to different process variations. From the implementation of the proposed system with pass transistor logic, the power consumption is reduced than the CMOS logic and CMOS Penta-MTJ circuits. The proposed work is non-volatile due to the power gating effect. The future work of

the proposed work includes the switching speed increasing and reduction in current density which is mainly required for the switching process.

References

1. Zabel H (2009) Progress in spintronics. *Superlattices Microstruct* 46(4):541–553
2. Grochowski E, Hoyt RF (1996) Future trends in hard disk drives. *IEEE Trans Magn* 32(3):1850–1854
3. Azzeroni B, Asti G, Pareti L, Ghidini M (eds) (2007) *Magnetic nanostructures in modern technology: spintronics, magnetic MEMS and recording*. Springer, Berlin
4. Sato M, Kobayashi K, Kikuchi H (1999) U.S. patent no. 5,986,858. U.S. Patent and Trademark Office, Washington, DC
5. Ohbayashi S, Yabuuchi M, Nii K, Tsukamoto Y, Imaoka S, Oda Y, Yamaguchi Y (2007) A 65-nm SoC embedded 6T-SRAM designed for manufacturability with read and write operation stabilizing circuits. *IEEE J Solid-State Circuits* 42(4):820–829
6. Chang CH, Gu J, Zhang M (2005) A review of 0.18- μm full adder performances for tree structured arithmetic circuits. *IEEE Trans Very Large Scale Integr (VLSI) Syst* 13(6):686–695
7. Wang JM, Fang SC, Feng WS (1994) New efficient designs for XOR and XNOR functions on the transistor level. *IEEE J Solid-State Circuits* 29(7):780–786
8. Sirunyan AM, Backhaus M, Bäni L, Berger P, Bianchini L, Dissertori G, Hits D (2018) Identification of heavy-flavour jets with the CMS detector in pp collisions at 13 TeV. *J Instrum* 13:P05011
9. Prakash P, Saxena AK (2009) Design of low power high speed ALU using feedback switch logic. In: 2009 International conference on advances in recent technologies in communication and computing, October 2009. IEEE, p 899902
10. Sheu SS, Chang MF, Lin KF, Wu CW, Chen YS, Chiu PF, Lin CH (2011) A 4Mb embedded SLC resistive-RAM macro with 7.2 ns read-write random-access time and 160ns MLC-access capability. In: 2011 IEEE international solid-state circuits conference. IEEE, pp 200–202
11. Linder MC, Hazegh-Azam M (1996) Copper biochemistry and molecular biology. *Am J Clin Nutr* 63(5):797S–811S
12. Zhuang N, Wu H (1992) A new design of the CMOS full adder. *IEEE J Solid-State Circuits* 27(5):840–844
13. Zimmermann R, Fichtner W (1997) Low-power logic styles: CMOS versus pass-transistor logic. *IEEE J Solid-State Circuits* 32(7):1079–1090
14. Shams AM, Darwish TK, Bayoumi MA (2002) Performance analysis of low-power 1-bit CMOS full adder cells. *IEEE Trans Very Large Scale Integr (VLSI) Syst* 10(1):20–29
15. Alioto M (2012) Ultra-low-power VLSI circuit design demystified and explained: a tutorial. *IEEE Trans Circuits Syst I Regul Pap* 59(1):3–29
16. Lee J, Mak KF, Shan J (2016) Electrical control of the valley hall effect in bilayer MoS₂ transistors. *Nat Nanotechnol* 11(5):421–425
17. Dayananda C, Sarada R, Rani MU, Shamala TR, Ravishankar GA (2007) Autotrophic cultivation of *Botryococcus braunii* for the production of hydrocarbons and exopolysaccharides in various media. *Biomass Bioenerg* 31(1):87–93
18. Truong DN, Cheng WH, Mohsenin T, Yu Z, Jacobson AT, Landge G, Work EW (2009) A 167-processor computational platform in 65 nm CMOS. *IEEE J Solid-State Circuits* 44(4):1130–1144
19. Aswini T, Reddy MM 18-nm low-power cascaded design of penta MTJ-based digital circuits using clock gating
20. Chen RKW, Gammel JC, Spires DA (1999) U.S. patent no. 5,881,129. U.S. Patent and Trademark Office, Washington, DC

Chapter 60

Recent Progress in Energy Management System for Fuel Cell Hybrid Electric Vehicle



Md. Rawshan Habib, Koushik Ahmed, Ahmed Yousuf Suhan, Abhishek Vadher, Md. Rashedul Arefin, Md Shahnewaz Tanvir, Sayad Hasan Rizvee, and Md. Ashiqur Rahman Swapno

Abstract Considering the enormous pressure on global demand for fossil fuels and global warming caused by air pollution, fuel cell hybrid electric vehicles (FCHEVs) have a promising future ahead of them because of the advancement of fuel cell technology. Among different fuel cell types, proton exchange membrane fuel cells are the most advantageous due to their high energy and power density. Several studies are carried out, which validate that fuel cells with energy storage systems can produce enough power needed by FCHEVs. However, advanced energy management system (EMS) must be developed to maximize the performance of FCHEVs as well as the lifespan of power sources such as fuel cells and batteries. The goal of this paper is to provide a comprehensive review of various EMSs for FCHEVs. This paper is expected to have a major impact on the development of EMS for FCHEVs as well as researchers involved in this field.

Keywords Electric vehicle · Energy management system · Fuel cell · FCHEV · Clean energy

1 Introduction

Transport sector of today's world is mostly reliant on fossil fuels. Climate change, GHG emissions and ozone layer depletion are all caused by the use of massive amounts of fossil fuels. Furthermore, the heavy use of fossil fuel in automobiles is contributing to the depletion of existing fossil fuels. These problems are leading the

Md. R. Habib · A. Vadher
Murdoch University, Murdoch, Australia

K. Ahmed (✉) · Md. R. Arefin · Md S. Tanvir · Md. A. R. Swapno
Ahsanullah University of Science and Technology, Dhaka, Bangladesh

A. Y. Suhan
Curtin University, Bentley, Australia

S. H. Rizvee
Brac University, Dhaka, Bangladesh

world to think of alternative power sources that are both sustainable and environmentally friendly. However, the growth and popularity of different electric vehicles (EVs) are rising globally. Though EV was first developed in 1834, it got the spotlight in the late twentieth century due to the oil crisis. The concept of a hybrid electric vehicle (HEV) dates back to the early 1900s when EVs almost disappeared from the market because of the steady growth in ICEVs and some major drawbacks of the batteries. Electric drives are a combination of batteries, motors and generators that power an electric vehicle. On the other hand, HEV refers to the hybridization of both IC engine and electric motor (EM). Usually, efficiency of EM is 85–95%, while ICE attains 28–30% [1].

Modern electric vehicle system can be categorized in a variety of sets. Among them, FCHEVs are entirely dependent on a technology where electricity is produced by power sources which include fuel cell, battery, supercapacitor, etc. The fuel cell (FC) usage in automobiles has drawn a lot of interest from academia and industry, since fuel cell technology is more mature now. Fuel cells have gained a lot of attention because they do not emit any greenhouse gases. In a FC, energy is derived by chemical reaction between hydrogen and oxygen, which is a plentiful source. FCs use an electrochemical mechanism to convert chemical energy into electricity. A fuel cell is made up of two electrodes submerged in electrolytes. Different FC types are available nowadays. Efficiency, cost, operating temperature and output powers are some of the most important factors which are considered when it comes to choosing the suitable one.

The best way to lower fuel consumption and cost of the power system is to combine FC with energy storage systems such as batteries and supercapacitors (SCs). When the structure and specifications of the powertrain are developed, an EMS is needed to allocate required power among various sources. EMS is a critical component in lowering total fuel consumption and slowing the deterioration of FC performance. A successful EMS not only guarantees the vehicle's regular operation, but also allows it to completely exploit the capacity of all power sources, satisfy certain design limitations, improve their durability and efficiency, and reduce fuel consumption [2]. Consequently, developing an EMS presents various problems. Thus, EMS for FCHEVs is the subject of several studies, which are reported in [3–6]. In this paper, a detailed review on the main EMS types for FCHEVs which include equivalent consumption minimization strategies, model predictive control, rule-based fuzzy logic control and state machine controller is discussed and analyzed.

2 Fuel Cell Hybrid Electric Vehicle

FCHEV structure can be attained with some modification of FCEV configuration. In a FCHEV, FC works as the primary energy source where additional energy sources are used to help the primary source. Battery or SC is utilized as an energy storage system here since these devices have the ability to charge and discharge themselves according to the demand and supply. Operating principle of a FCHEV is depicted in

Fig. 1. Nowadays, automobile companies are widely developing FCVs. Several FCVs are listed in [7]. Hyundai, the first automobile company to start the development of H₂-based cars, launched several fuel cell vehicles [8]. Table 1 gives an idea about commercially developed fuel cell vehicles.

FC, battery, supercapacitor and flywheel can be the power sources for FCHEV. The power sources are selected in accordance with the prototype design. Here, FCs are regarded as the main power source because it can produce more power than that of other sources. Other sources such as battery or supercapacitor (SC) can be described as energy storage systems (ESS) or secondary power sources. In this hybrid structure, primary and secondary power sources work as steady state and transient power supplier, respectively. ESS can also be utilized as regenerative braking purposes when needed. ESS is critical mostly in situation of a cold start of the fuel cell as well as a

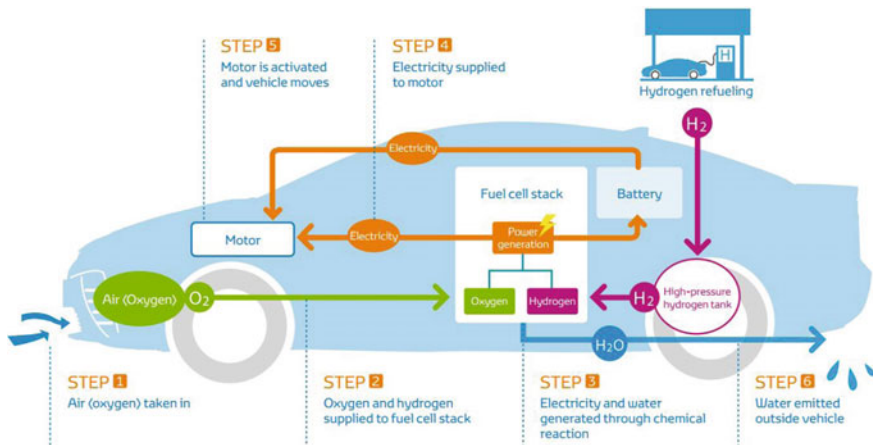


Fig. 1 Operating principle of a FCHEV [9]

Table 1 A summary of the various fuel cell vehicle models [3, 8, 17]

Vehicle	Stack power (kW)	Battery (kWh)	Range (mile)
Hyundai ix35 2013	100	24	369
Toyota FCHV	90	–	400–500
Audi Sportback A7h-tron Quattro 2014	–	8.8	310.7
Mercedes-Benz GLC F-cell	–	13.5	297
Toyota Mirai 2019	114	1.6	312
Honda Clarity Fuel Cell 2017	100	–	434
Hyundai Nexo 2019	95	1.56	380
Hyundai Tucson Fuel Cell 2017	100	0.95	–
Nissan e-Bio Fuel Cell	5	24	373
Gumpert AIWAYS Nathalie	5	Variable	≤530

drastically large power requirement, including when speeding the vehicle. Awareness of energy and power density is needed to accurately determine the primary sources as well as ESS. Power sources for FCHEVs are described in the following subsections.

2.1 Primary Power Source (Fuel Cell)

A fuel cell produces electrical energy via electrochemical reactions where the emission of greenhouse gas is zero. Fuel cells produce electricity directly from chemical energy, whereas conventional power sources use four-step power conversion method (chemical–thermal–kinetic–electrical energy). Thus, the efficiency of those power sources is lower than that of fuel cells. In 1839, an electrolysis demonstration led to the creation of the first FC model by Sir William Robert Grove. Nowadays different types of fuel cells are commercially available depending on their electrolytes and operating temperature. Efficiency, operating temperature and output of different FC types are depicted in Fig. 2. PEMFC is the most frequently used one due to its high efficiency, quick startup and ability to operate at low temperatures. PEMFC is well positioned for electric vehicles, with a lifetime of 5000 h and a power density of 0.3–0.8 W/cm². Even so, PEMFC has drawbacks such as carbon monoxide susceptibility and the need of expensive platinum catalysts [7, 10].

Fuel cell is considered as a green energy source, which generates electrical energy from chemical energy. Fuel and oxidant are supplied into a cell where electrolyte gets involved in the reaction and produces electricity. It produces no carbon dioxide and only releases water and heat as a by-product of the reaction. Therefore, fuel cell

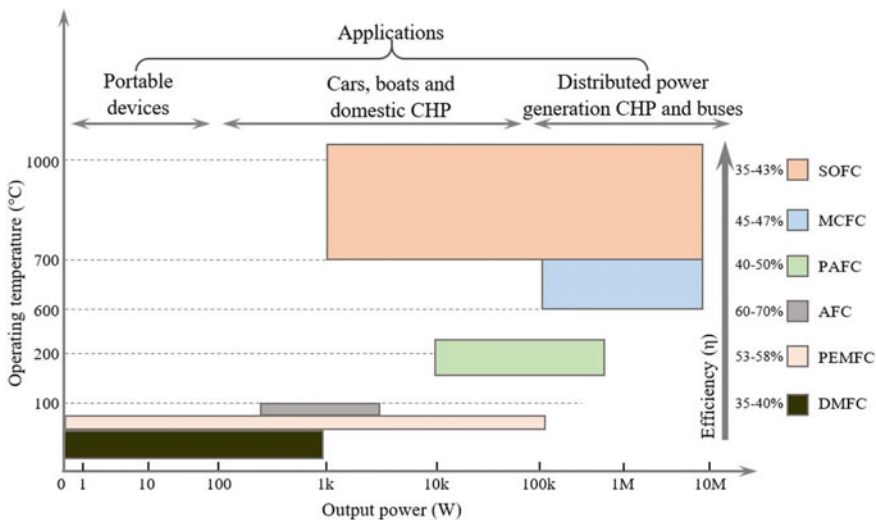


Fig. 2 Different types of fuel cell as per their operating temperature and output power

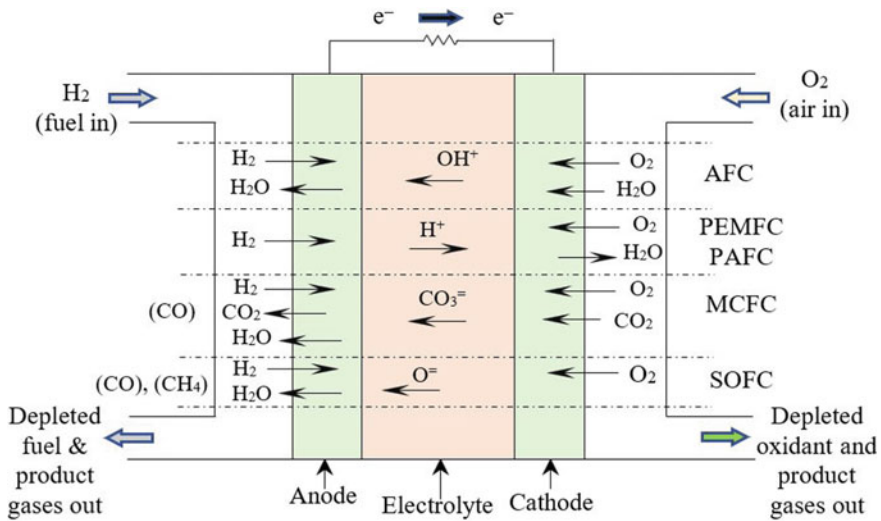


Fig. 3 Chemical reactions of different types of fuel cell

is a clean energy source. Though fuel differs according to the fuel cell types, electrochemical reactions that occur inside the cell are almost identical. The reaction takes place between hydrogen and oxygen, which come from the fuel and air, respectively, and generates water. In Fig. 3, generalized construction is shown schematically with chemical reactions of different fuel cells. FC stack is made of several cells connected in series since individual cell can generate 0–1 V that are inadequate even to power electronic components perfectly [7].

2.2 Energy Storage System

Several researches on FCHEVs are performed, with the aim of developing an effective EMS with the mix of FC and battery or SC, or both. A battery can be utilized to store electrical energy in automotive applications. Battery can be differentiated from a fuel cell by their source of chemical energy. Rechargeable and non-rechargeable, two forms of batteries, are available. Among them, the first one is perfectly suited for automobiles. There are five groups of batteries commercially available in recent times which include lithium, lead acid, ZEBRA, metal air and nickel batteries that are appropriate for use in vehicles. Stored energy and capacity of a battery are calculated in watt-hour and ampere-hour, respectively, while state of charge of a battery is indicated by percentage.

A battery could produce large current for motor start-up and also be able to act as a load-limiting system, allowing the FC to run at lower power at first and then increase to higher power. Pontryagin’s minimal principle-based adaptive EMS

is proposed in [11] for a FC-B hybrid model where co-state adaptation is carried out with a prediction of driving cycle. The proposed method is verified by simulation and found that it reduces fuel consumption by 4%. Simultaneous perturbation stochastic approximation-based EMS is proposed in [12] for an efficient performance of an auxiliary power unit that consists of a SOFC and a battery. This EMS is able to increase the system efficiency by minimizing fuel consumption. Another robust online EMS is developed in [13] to deal with unpredictable driving conditions.

On the other hand, SC shows high power density when compared to battery. As a result, it is an excellent option for supplying peak power or recovering large braking energy. Moreover, lifespan of a SC is quite long, which is almost 10^6 cycles. Fuel cell and SC combination provides great advantages when it comes to designing an efficient hybrid power system. This is because FC works as main source and generates required power for a vehicle, whereas SC works as secondary source, which basically fulfills peak and transient power demand and recovers power at the time of braking [14]. An EMS for fuel cell-SC-powered HEV is developed in [15] where a microcontroller is associated with the system to distribute power among the sources. The proposed EMS improved the system efficiency up to 96.2% at nominal power. A novel control strategy is proposed in [16] for a PEMFC-SC-based hybrid electric city bus. Experimental setup is done using dynamic tests and steady-state tests. This study is focused on power split, controlling current and DC voltage instead of fuel consumption.

Better performance and acceleration of a vehicle need large power and energy density. Therefore, both SC and battery need to be applied since SC shows high power density, while battery provides high energy density. Salp swarm algorithm, a novel EMS, is presented in [18] with an objective to minimize fuel usage of the model, which is made with FC, battery and SC. Then, the proposed strategy is compared with existing EMS to demonstrate its effectiveness. With the proposed EMS, the system provides an efficiency of 81.22%, where the fuel consumption is only 19.95 gm. Three controllers are proposed in [19] to minimize steady-state error. Simulation shows that the proposed controllers fulfill the objective.

3 Energy Management System

Energy management strategy (EMS) should be optimized in such a way that it can maximize battery lifetime and reduce hydrogen consumption. Moreover, EMS needs to make sure of the high overall system efficiency [20]. Experts are showing great interest to increase the system efficiency of FCEVs by reducing hydrogen consumption and extending lifetime of battery. Two novel control methods, which include hydrogen fuel saving (HFS) and life cycle saving (LCS), are proposed in [21]. HFS effectively minimizes fuel consumption by maintaining battery SoC in between 60 and 90%. When compared to the state machine control strategy, the proposed strategies provide great advantages. Results present that 100.6% more fuel is stored by using HFS control method in stop-go road. LCS method provides 1.8 and 23% extra

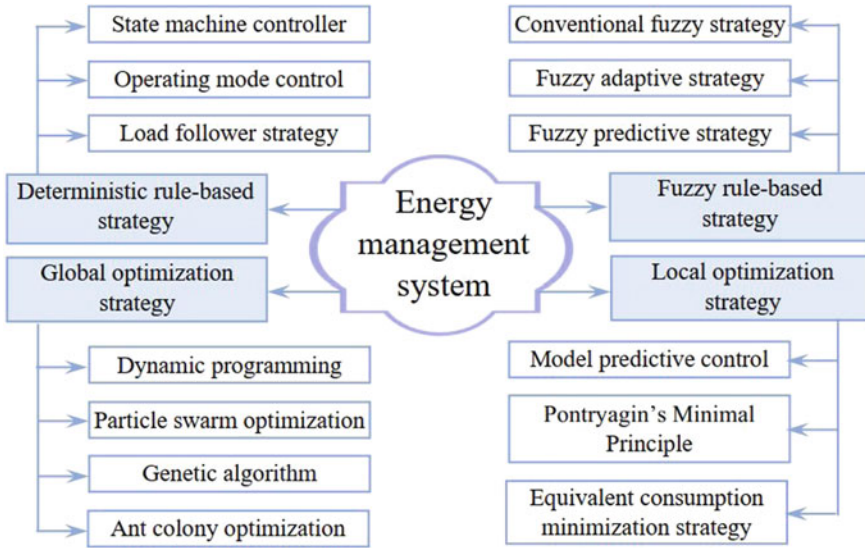


Fig. 4 Classification of EMS

benefits in the stop-go and uphill-downhill road model than that of state machine control method.

Adaptive load strategy (ALS) based on fixed hydrogen consumption because of load shifting is proposed in [22], which can replace the existing EMS. PID controller is widely used in EMS for electric vehicles because of its simplicity and easy tuning system. Moreover, it delivers steady power for fuel cells. A novel control strategy of energy management system (EMS) is presented in [23] where inversion and energetic macroscopic representation (EMR) methods are used to analyze. The benefits of this EMS are that it effectively manages smooth transition to fuel cell current and restrains ultracapacitor (UC) and DC bus voltages to collapse. In addition, EMS remains manageable and load protections do not have effect on overall function. Therefore, the algorithm safely commutes between saturated and nominal modes. In this paper, the focus is only on saturation management and simulation results are not considered. Classification of EMS is shown in Fig. 4. Different EMS are discussed in the following subsections.

3.1 Equivalent Consumption Minimization Strategy (ECMS)

ECMS is a practical one among all EMS because of its near-optimal performance in real-time operation. A new ECMS for a FCHEV is presented in [24] where the vehicle consists of FC, SC and battery. Here, FC works as main source of energy, whereas battery and supercapacitor work as peaking power sources. The new approach aims

to run the FC at maximum efficiency and use the battery as a lengthy ESS, and SC to provide peak power. Urban pattern driving cycle is utilized here to simulate the proposed EMS. PEMFC and battery-based hybrid tramway power system are developed in [25] with an ECMS. RT-LAB platform is utilized to simulate the proposed system with the designed EMS. The proposed EMS, as planned, efficiently splits the necessary power. And the bus voltage is maintained at a constant level, floating around the set point. Heuristic method is developed and compared with ECMS in [26] where simulation results validate that the proposed strategy is advantageous for economic fuel usage. Optimization-oriented adaptive ECMS is presented in [27] to maintain a steady battery charge and consume near-optimal fuel. Results demonstrate that iterative predictor has a high degree of precision, with a correlation of 0.987 among predicted and actual data. The fuel consumption of this EMS is smaller than existing ones. The presented method can easily recover battery SOC within 40 s. Markov chain approach is combined with PMP in [28] to design an ECMS for UDDS driving cycle where hybrid energy sources deliver the desired amount of power. The proposed method has no impact on fuel consumption, which is a major drawback.

3.2 *Model Predictive Control (MPC)*

MPC method applies a model that is based on prior and present inputs to estimate future outputs. An EMS based on both MPC and DP is developed in [29] where results validate that it can increase fuel saving rate by 3.04%. An EMS based on nonlinear MPC and recurrent neural network is designed in [30] for FCHEV. Hardware-in-the-loop test equipped with a 3-kW fuel cell stack is considered for experiment. Results validate that the proposed EMS can fulfill the vehicle's energy requirements while still allowing the FC to work in its most productive area. Furthermore, a comparison of the proposed nonlinear MPC, a linear MPC, and hysteresis band control is carried out. The findings of this comparison show that the nonlinear MPC has a higher fuel economy and can limit FC degradation. MPC-based real-time cost minimization EMS is proposed in [31] and compared with rule-based EMSs. In average, the proposed approach is able to minimize operating costs by 14.17% and increase fuel cell lifespan by 8.48%.

MPC-based EMS is shown in [32] for a fuel cell hybrid construction equipment, where neural network model and Markov chain are utilized for simulation. The proposed EMS reduces fuel consumption and boosts FC durability. In addition, neural network shows better performance than Markov model. A hierarchical MPC is presented in [33] where an upper-level MPC is applied to optimize the power splitting ratio among the FC and battery. On the other hand, lower-level MPC controller is employed to track the highest output power of FC. Proposed EMS is simulated by using US06 driving cycle, and according to the results, around 9.57% equivalent fuel consumption is possible. Two-loop control-based MPC is designed and simulated in [34] for a hybrid structure consisting of FC-UC. Effective power split is shown here without any work on fuel consumption and system price. In the proposed method,

outer loop is operated by MPC, whereas proportional–integral (PI) controller works for inner loop.

3.3 *Fuzzy Logic Control (FLC)*

FLC is dependent on input variables and very effective in uncertain situation; for example, inputs of a technical problem are unpredictable. An adaptive fuzzy EMS is proposed in [35] for power split among power sources. Driving cycle is attained by online neural network classifier. Thus, no driving cycle is needed in advance for simulation. The proposed EMS is able to reduce hydrogen consumption and to maximize the lifespan of FC by minimizing output power. It also reduces the fluctuations of both voltage and current of the fuel cell. PDM-based health-conscious EMS is designed in [36] where five optimized fuzzy logic controllers are developed under various battery and fuel cell degradation conditions. According to the results, the proposed EMS reduces the degradation cost of the power sources as well as extends the lifespan of the system (56%).

A novel online EMS is designed in [37] that controls the power fluxes. Real-time EMS can be obtained by neural networks (NNs). NN associated with HWFET cycle shows around 2% energy savings, and NN with CADC cycle has minimum average error, with almost 18% energy savings. EMS with a combination of novel power sharing method and fuzzy logic control is presented in [38] for a FCHEV. Genetic algorithm and multi-objective optimization function are used to optimize the FLC. The usage of this developed EMS ensures the required power supply and improves vehicle's performance by changing the battery state of charge by less than 2%. Nonetheless, hydrogen consumption is relatively higher for the proposed strategy.

3.4 *State Machine Controller*

Research is going on for improving the EMS of FCHEV by utilizing the state machine method. This strategy performs on particular modes of vehicle and provides a flow chart of stable condition-based output, which is dependent on former states and current inputs. This method is greatly associated with input variables such as speed, load power and battery SoC when applied to the EMS for FCHEV. State machine control strategy of hybrid tramway is proposed in [39] to ensure the steady operation of FC. Efficiency and hydrogen consumption of the proposed tramway are 56.78% and 301.22 g, respectively. In this study, hydrogen consumption is shown without any graph, and battery lifespan depends on minimum deviation of stage of charge. A DC–DC boost converter topology for four operating modes is proposed in [40]. The proposed topology shows great advantages that include less current ripple and harmonic. To design a controller, active current sharing method is introduced in [41], which is based on different modes of operation and effective for real-time application.

In this study, feasibility and lifetime expansion of FC and battery are discussed based on assumption instead of experimental results. An energy management system [42] is incorporated in a hybrid electric vehicle in such a way that power output varies in four operating states. Simulation results validate the energy efficiency of more than 88%.

3.5 Global Optimization Strategies

To determine the optimum operating trajectory of energy sources, a global optimization strategy requires knowledge of road conditions. Experimenting with a global optimization strategy is difficult since exact road information is difficult to obtain in real time. Ant colony optimization, dynamic programming and generic algorithm are some of the globally optimized methods. Ant colony algorithm-based EMS is proposed in [43] to boost the system performance and operation that will make the vehicle economical. This algorithm is a search algorithm which is obtained from the method of ant-searching food. In order to simulate the proposed hybrid model of the vehicle, an object-oriented programming tool is designed. Simulation results show satisfactory outcomes in terms of performance with the proposed EMS. Another ant colony-based EMS is presented in [44] where the hybrid structure is built with fuel cell and ultracapacitor. The proposed EMS minimizes the fuel consumption and maximizes the lifespan of FC. A charge sustaining method is developed for the operation of UC so that it can provide enough power at the beginning of every new cycle. HWEFT driving cycle is utilized here to test the effectiveness of this method.

Several drawbacks of fuzzy EMS are resolved by applying generic algorithm in [45] where HWEFT, UDDS and NEDC driving cycle are utilized for simulation. Results validate that the algorithm reduces current variation by 19% and boosts fuel consumption by 10%. One of the most successful strategies for solving global optimization problems is dynamic programming (DP). Its goal is to use a multistage decision process to determine the best control policies. A dynamic programming-based EMS is proposed in [46] where the proposed EMS causes a 5.36% increase in fuel consumption. A variety of EMSs used for various objectives are listed in Table 2.

Table 2 EMSs for different objectives

	Fuel consumption	Fuel cell lifespan	Battery lifespan
Equivalent consumption minimization strategy	[26, 27]		[27]
Model predictive control	[29, 30, 32, 33]	[30–32]	
Rule-based fuzzy control	[35, 37]	[35, 36]	
State machine controller	[39]	[41]	[39, 41]
Global optimization strategies	[44–49]	[44, 47]	[47, 49]

4 Issues and Challenges

Several difficulties, including such technological, economic, and some others, must be overcome in order for FCHEVs to become a popular and profitable market competitor to traditional vehicles. Further concerns are required while designing a FCHEV, particularly if more than two energy sources are included. PEMFC is the best option for automotive applications. Though the required power for automotive applications is 1 kW/kg, the outcome was just 0.65 kW/kg till 2010 [50]. PEMFC is also very expensive because of its platinum catalyst. Other aspects of PEMFC that must be assured are performance and durability. The efficiency, durability and economic aspects of fuel cells will be the future challenges. The energy storage takes up a significant portion of FCHEV's energy supply. The performance of FCHEV is determined by the storage system's performance, which is defined by the design of the system as well as the storage types. ESS varies according to the vehicle types. FCHEV can perform efficiently only when high energy and high power density are ensured. Therefore, storage system design is a challenge for the experts. The commercialization of hydrogen as a source of vehicle fuel seems ambitious and exciting. The fact of its application, on the other hand, is often more complicated. The availability of hydrogen gas as a source of fuel is a big issue while using an FCHEV because the number of hydrogen refueling stations is not satisfactory. The first hydrogen refueling station of southeast Asia was introduced in 2019, in Malaysia [51]. Japan introduced its first commercial hydrogen filling station in 2014, and the number reached 80 by mid-2016. Following a similar trajectory, the number of such stations in the USA and Germany is growing faster day by day [7].

Once hydrogen is combined with oxygen, they become explosive, creating significant safety issues. The gases do have a large flammability range and a low ignition energy, all of which add to the danger of use. Natural gas accounts for nearly 48% of hydrogen production, while renewable sources account for just 4% of global hydrogen production. Since hydrogen is mostly generated from sulfur-containing hydrocarbon gases, chemical processes used may pollute the environment. EMSs for FCHEV have been the subject of extensive study in recent times. Current EMSs have a number of drawbacks. Most EMSs are only concerned with splitting power among the energy sources, ignoring the fuel cell and battery lifetime. Optimized algorithms also have some limitations. Dynamic programming and ant colony-based strategies are only simulated without any field test. PMP and generic algorithm are applied to a hardware or test configuration, yet battery loss or lifespan is not taken into account [6].

5 Conclusion

When the structure and powertrain components are designed, EMS plays a crucial role in enhancing the efficiency of FCHEVs. First and foremost, objectives should

be defined when developing a novel EMS. To satisfy the load power demand, the type of EMS and subsequent controller design are chosen based on the objectives. In this paper, a detailed review is conducted on different EMSs for FCHEVs such as ECMS, MPC, rule-based FLC, and state machine controller. Some global optimization strategies are also discussed. According to previous research, EMS is a critical component of a FCHEV. Minimizing fuel consumption is the main goal that is focused in most studies. However, the majority of past studies are only simulated without implementing in real-world application.

References

1. Larminie J, Lowry J (2003) *Electric vehicle technology explained*. Wiley, England
2. Herrera V et al (2016) Adaptive energy management strategy and optimal sizing applied on a battery-supercapacitor based tramway. *Appl Energy* 169:831–845
3. Teng T et al (2020) A comprehensive review of energy management optimization strategies for fuel cell passenger vehicle. *Int J Hydrogen Energy* 45:20293–20303
4. Lü X et al (2020) Energy management of hybrid electric vehicles: a review of energy optimization of fuel cell hybrid power system based on genetic algorithm. *Energy Convers Manage* 205:112474
5. Rezk H et al (2021) Comparison among various energy management strategies for reducing hydrogen consumption in a hybrid fuel cell/supercapacitor/battery system. *Int J Hydrogen Energy* 46:6110–6126
6. Sulaiman N et al (2018) Optimization of energy management system for fuel-cell hybrid electric vehicles: issues and recommendations. *Appl Energy* 228:2061–2079
7. Ahmed K, Farrok O, Rahman MM, Ali MS, Haque MM, Azad AK (2020) Proton exchange membrane hydrogen fuel cell as the grid connected power generator. *Energies* 13:6679
8. Hyundai ix35 Fuel Cell. <https://www.hyundai.com/worldwide/en/company/newsroom/hyundai-ix35-fuel-cell-0000001596>
9. Toyota. Outline of the Mirai. https://www.toyota-europe.com/download/cms/euen/ToyotaMiraiFCV_Posters_LR_tcm-11-564265.pdf
10. Ahmed K, Habib MR, Avi SD, Sagor MMI, Farrok O (2019) Behavior of the proton exchange membrane fuel cell around critical fuel and air supply pressure. In: *IEEE International conference on advances in electrical engineering, Dhaka*, pp 591–595
11. Li X, Wang Y, Yang D, Chen Z (2019) Adaptive energy management strategy for fuel cell/battery hybrid vehicles using Pontryagin's Minimal Principle. *J Power Sources* 440:227105
12. Barelli L et al (2020) Stochastic power management approach for a hybrid solid oxide fuel cell/battery auxiliary power unit for heavy duty vehicle applications. *Energy Convers Manage* 221:113197
13. Wu J et al (2020) A robust online energy management strategy for fuel cell/battery hybrid electric vehicles. *Int J Hydrogen Energy* 45:14093–14107
14. Tahri A et al (2018) Management of fuel cell power and supercapacitor state-of-charge for electric vehicles. *Elect Power Syst Res* 160:89–98
15. Wu W, Partridge JS, Bucknall RWG (2018) Stabilised control strategy for PEM fuel cell and supercapacitor propulsion system for a city bus. *Int J Hydrogen Energy* 43:12302–12313
16. Fathabadi H (2018) Fuel cell hybrid electric vehicle (FCHEV): novel fuel cell/SC hybrid power generation system. *Energy Convers Manage* 156:192–201
17. Toyota FCHV hydrogen hybrid vehicle. <https://www.hydrogencarsnow.com/index.php/toyota-fchv/>

18. Fathy A, Rezk H, Nassef AM (2019) Robust hydrogen-consumption-minimization strategy based salp swarm algorithm for energy management of fuel cell/supercapacitor/batteries in highly fluctuated load condition. *Renew Energy* 139:147–160
19. Rahman AU, Ahmad I, Malik AS (2020) Variable structure-based control of fuel cell-supercapacitor-battery based hybrid electric vehicle. *J Energy Storage* 29:101365
20. Motapan SN, Dessaint LA, Haddad KA (2014) A comparative study of energy management schemes for a fuel-cell hybrid emergency power system of more-electric aircraft. *IEEE Trans Ind Electron* 61:1320–1334
21. Kaya K, Hames Y (2019) Two new control strategies: for hydrogen fuel saving and extend the life cycle in the hydrogen fuel cell vehicles. *Int J Hydrogen Energy* 44:18967–18980
22. Sarioglu IL, Klein OP, Schröder H, Küçükay F (2012) Energy management for fuel-cell hybrid vehicles based on specific fuel consumption due to load shifting. *IEEE Trans Intell Transp Syst* 13:1772–1781
23. Azib T, Bethoux O, Remy G, Marchand C (2011) Saturation management of a controlled fuel-cell/ultracapacitor hybrid vehicle. *IEEE Trans Veh Technol* 60:4127–4138
24. Li H, Ravey A, N'Diaye A, Djerdir A (2017) Equivalent consumption minimization strategy for hybrid electric vehicle powered by fuel cell, battery and supercapacitor. In: *IEEE transportation electrification conference and expo, Chicago*, pp 540–544
25. Zhang G, Chen W, Yu J, Li Q (2017) Study on equivalent consumption minimization strategy for fuel cell hybrid tramway. In: *IEEE transportation electrification conference and expo, Asia-Pasific, Harbin*, pp 1–5
26. Carignano M, Roda V, Castello RC, Valino L, Lozano A, Barreras F (2019) Assessment of energy management in a fuel cell/battery hybrid vehicle. *IEEE Access* 7:16110–16122
27. Zeng T et al (2021) Optimization-oriented adaptive equivalent consumption minimization strategy based on short-term demand power prediction for fuel cell hybrid vehicle. *Energy* 227:120305
28. Hemi H, Ghouili J, Cheriti A (2015) Combination of Markov chain and optimal control solved by Pontryagin's Minimum Principle for a fuel cell/supercapacitor vehicle. *Energy Convers Manage* 91:387–393
29. Jinquan G, Hongwen H, Jianwei L, Qingwu L (2021) Real-time energy management of fuel cell hybrid electric buses: fuel cell engines friendly intersection speed planning. *Energy* 226:120440
30. Pereira DF et al (2021) Nonlinear model predictive control for the energy management of fuel cell hybrid electric vehicles in real-time. *IEEE Trans Ind Electron* 68:3213–3223
31. Zhou Y, Ravey A, Pera M (2021) Real-time cost-minimization power-allocating strategy via model predictive control for fuel cell hybrid electric vehicles. *Energy Convers Manage* 229:113721
32. Li T, Liu H, Ding D (2018) Predictive energy management of fuel cell supercapacitor hybrid construction equipment. *Energy* 149:718–729
33. Liu S et al (2018) Hierarchical model predictive control for the fuel cell hybrid electric vehicles. In: *37th Chinese control conference, Wuhan*, pp 3599–3605
34. Mane S, Jagtap P, Kazi F, Singh NM (2016) Model predictive control of complex switched mode FC-UC hybrid structure. In: *Indian control conference, Hyderabad*, pp 66–71
35. Zhang R, Tao J, Zhou H (2019) Fuzzy optimal energy management for fuel cell and supercapacitor systems using neural network based driving pattern recognition. *IEEE Trans Fuzzy Syst* 27:45–57
36. Yue M, Jemei S, Zerhouni N (2019) Health-conscious energy management for fuel cell hybrid electric vehicles based on prognostics-enabled decision-making. *IEEE Trans Veh Technol* 68:11483–11491
37. Munoz PM et al (2017) Energy management control design for fuel cell hybrid electric vehicles using neural networks. *Int J Hydrogen Energy* 42:28932–28944
38. Ahmadi S, Bathaee SMT, Hosseinpour AH (2018) Improving fuel economy and performance of a fuel-cell hybrid electric vehicle (fuel-cell, battery, and ultra-capacitor) using optimized energy management strategy. *Energy Convers Manage* 160:74–84

39. Li Q, Yang H, Han Y, Li M, Chen W (2016) A state machine strategy based on droop control for an energy management system of PEMFC-battery-supercapacitor hybrid tramway. *Int J Hydrogen Energy* 41:16148–16159
40. Benrabeh A et al (2013) FC/battery power management for electric vehicle based interleaved DC–DC boost converter topology. In: 15th European conference on power electronics and applications, Lille, pp 1–9
41. Pany P, Singh RK, Tripathi RK (2016) Active load current sharing in fuel cell and battery fed DC motor drive for electric vehicle application. *Energy Convers Manage* 122:195–206
42. Hwang JJ, Chen YJ, Kuo JK (2012) The study on the power management system in a fuel cell hybrid vehicle. *Int J Hydrogen Energy* 37:4476–4489
43. Pourhashemi AP, Ansarey MSMM (2012) Ant colony optimization applied to optimal energy management of fuel cell hybrid electric vehicle. In: IV International conference on ultra modern telecommunications and control systems, St. Petersburg, pp 497–503
44. Koubaa R, Krichen L (2016) Ant colony optimization based optimal energy management for an FC/UC electric vehicle. In: 17th International conference on sciences and technologies automatic control computer engineering, Sousse, pp 363–367
45. Zhang R, Tao J (2018) GA based fuzzy energy management system for FC/SC powered HEV considering H₂ consumption and load variation. *IEEE Trans Fuzzy Syst* 26:1833–1843
46. Liu J, Chen Y, Li W, Shang F, Zhan J (2018) Hybrid-trip-model-based energy management of a PHEV with computation-optimized dynamic programming. *IEEE Trans Veh Technol* 67:338–353
47. Fares D, Chedid R, Panik F, Karaki S, Jabr R (2015) Dynamic programming technique for optimizing fuel cell hybrid vehicles. *Int J Hydrogen Energy* 40:7777–7790
48. Ahmadi S, Bathaee SMT (2015) Multi-objective genetic optimization of the fuel cell hybrid vehicle supervisory system: fuzzy logic and operating mode control strategies. *Int J Hydrogen Energy* 40:12512–12521
49. Martel F, Kelouwani S, Dub Y, Agbossou K (2015) Optimal economybased battery degradation management dynamics for fuel-cell plug-in hybrid electric vehicles. *J Power Sources* 274:367–381
50. Bing L, Hui L, Jianxin M, Haijiang W (2010) PEM fuel cells: current status and challenges for electrical vehicle applications. *J Autom Saf Energy* 1:260–269
51. Schreiblehner M First hydrogen filling station in South East Asia. <https://www.linkedin.com/pulse/first-hydrogen-filling-station-south-east-asia-martin-schreiblehner/>

Chapter 61

Comparative Study of Application of Artificial Neural Networks for Predicting Engineering Properties of Soil: A Review



Arun W. Dhawale and Shailendra P. Banne

Abstract The primary aim of the synthetic neural network approach was to unravel the issues similarly that a person's brain would. The artificial neural network system was extensively applied in geotechnical engineering. Geotechnical engineering properties of soil hold the solidity of engineering structures. The engineering properties of soils are much worried about the distortion and strength of bodies of soil. Engineering properties of soil which measure the engineering behavior of soils. This review paper presents a quick overview of artificial neural network (ANN) applications of engineering properties of soil, viz. optimum moisture content, maximum dry density, permeability, shear strength parameters, and unconfined compressive strength. The review suggests that ANN with different models can predict the engineering properties of soil accurately. The survey recommends that the ANNs had been exceptionally valuable in effectively interpreting inadequate input information. This study shall help the researchers those working in the area of applications of ANN on soil behavior.

Keywords ANN · Maximum dry density · Optimum moisture content · Shear strength · Permeability · Unconfined compressive strength

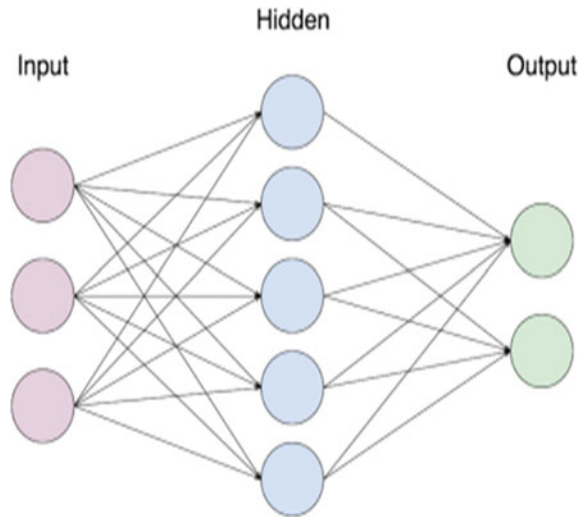
1 Introduction

Artificial neural networks (ANNs) have broad applicability to unravel many problems in the engineering field. ANNs are best at identifying patterns, trends in data; they are well used for prediction purposes in geotechnical engineering. ANN consists of three layers: the input layer represents to provide raw information to the network, the hidden layer establishes between the input and output of the algorithm, and hidden

A. W. Dhawale
Department of Civil Engineering, Imperial College of Engineering and Research, Pune 412207, India

S. P. Banne (✉)
Department of Civil Engineering, JSPM's Rajarshi Shahu College of Engineering, Pune 411033, India

Fig. 1 Working principle of ANN



layer takes action with its input and weights from the preceding layer and applies a nonlinearity to it and sends to the output layer. The output layer in a neural network accumulates and transfers the information in a designed way. Figure 1 shows the simple working principle of the artificial neural network.

The geotechnical index and engineering properties of soils influence each other, and it depends on laboratory testing, time effects, loading effects, inherent soil variability, construction effects, human errors, errors in soil boring, sampling. From the year 1990, ANN has been utilized in various fields in geotechnical engineering like predicting soil behavior, predicting pile capacity, on earth retaining structures, site characterization, liquefaction analysis, slope stability analysis, tunnels, underground openings, and landslides assessment. The present review paper discussed applications of the artificial neural networks on different engineering properties of soil. Engineering properties of soil useful for engineering applications comprise permeability, compressibility, and shear strength parameters of the soil. Engineering properties of soils are those properties that may be used for quantifying the engineering behavior of soils. Engineering properties (Behavior of soil after application of load) of soil depends on Soil Classification, Atterbergs limits, Water content (index properties). So, the determination of those engineering properties of soil in the laboratory is a time-consuming, tedious, costly, and difficult process. The present review paper focuses on the application of various ANN models for predicting engineering properties, viz. maximum dry density (MDD), optimum moisture content (OMC), permeability, unconfined compressive strength (UCS), and shear strength parameters. These engineering properties depend on water content, dry density, bulk density, mineralogy present in the soil, liquid limit, plastic limit, plasticity index, linear shrinkage, grain size distribution, particle shape, and lots of other parameters. In ANN, these parameters were used as input parameters to predict the engineering properties of soils.

2 Literature Review

Many researchers have developed several ANN models to work out the engineering properties of various sorts of soils. The stress is given on the literature supported ANN models, input parameters; output parameters, model checking performance parameters of engineering properties of soils.

2.1 Compaction Parameters

Soil compaction is that the mechanical process whereby soil particles are forced and compress. The compaction parameters (optimum moisture content—OMC and maximum dry density—MDD) of the soil have significant importance for attaining the engineering properties of soil like bearing capacity, strength, permeability, and compressibility. OMC and MDD are determined in a laboratory for various sorts of soil called standard proctor test and modified proctor test in geotechnical engineering. ANN is often to predict the compaction parameters from different index properties of soil. Many researchers used different models, charts, curves to predict compaction parameters. “Gunaydin [1] estimates the compaction parameters using simple multiple analysis and artificial neural network. He developed five ANN models on nine different types of soils, which have several input parameters. The simplest best results were obtained from model II; input parameters were relative density (G), liquid limit (w_L), plastic limit (w_p), and grain size.” “Suman et al. [2] made an exertion to create a prediction model to work out maximum dry density (MDD) and unconfined compressive strength (UCS) of cement stabilized soil. They developed three networks: functional networks (FN), multivariate adaptive regression splines (MARS), and multilinear regression model (MLR). Prediction models for both MDD- and UCS-supported FN and MARS are very inclusionary. Recently, researchers have used ANN for predicting properties of stabilized soil.” Abdel-Rahman [3] developed the empirical equations to forecast compaction parameters of graded cohesionless soils. He compared the forecasted values using ANN and empirical equations with a group of laboratory tests (modified proctor tests). The ANN model grows using the computer program MATLAB 6.5. The input parameters for the ANN model were percentage passing soil from different sieves (20, 5, 2, 0.4, 0.08 mm). He concluded that based on the investigation, the notable factor which affects the MDD was the percentage passing through sieve 0.4 mm (grains of fine sand and smaller), and for OMC, the significant factor was the percentage passing through sieve 0.4 and 0.08 mm (grains of clay and silt). Tipza et al. [4] highlighted prediction models of some geotechnical properties of soil using their index parameters. A total of 580 numbers of knowledge sets have compiled. Maximum dry density (MDD), optimum moisture content (OMC), permeability, and angle of internal friction were predicted using input parameters, viz. specific gravity, grain size distribution, and Atterberg limits. A multilayer perceptron (MLP) artificial neural network sets of

input files on to a group of appropriate outputs. Differential statistical approaches like the coefficient of determination (COD), root mean square error (RMSE), coefficient of residual mass (CRM) were used to estimate the performance of prediction models. They concluded that laboratory tests to work out engineering properties of soil are laborious and time-consuming; it is helpful to develop forecast models to estimate engineering properties using their index properties which are easy to measure. ANN models come up with accurate predictions with experimental results. “Das et al. [5] were developed ANN models using different training algorithms; Levenberg–Marquardt algorithm (LMNN), Bayesian regularization algorithm (BRNN), and differential evaluation algorithm (DENN). LMNN was a widely used algorithm in geotechnical engineering. They concluded that BRNN has limited uses [6, 7], and still there is a wide scope of DENN algorithm in geotechnical engineering. They also used support vector machine (SVM) models for predicting MDD and UCS. SVM models are supported by statistical learning theory. The supported study developed LMNN model was best for predicting MDD and followed by BRNN and DENN. The statistical performance of SVM models is found superior to ANN models.” “Shahiri and Ghasemi [8] were performed laboratory tests to work out MDD and UCS with cement and copper slag stabilized soil. They investigate the impacts of copper slag and cement with different percentages of dosages on MDD and UCS. After experimental testing, the ANN model has been developed using eight input parameters, viz. dry density, water content, liquid limit, plastic limit, P_H , copper slag content, cement content, and Curing age. In the sensitivity analysis, it had been observed that water content was the influential parameter and liquid limit, plastic limit as the least important ones. They concluded that the ANN model was ready to anticipate the elastic modulus of stabilized soil.” “Alavi et al. [9] used modified ANN models to predict MDD and OMC of chemically stabilized soil. Multilayer perceptron (MLP) was used with input parameters like linear shrinkage, liquid limit, plastic limit, percentage of clay, silt, gravel, and three stabilizing additives: cement content, lime content, asphalt content. They evaluate the performance of ANN models using the coefficient of determination (R^2), mean squared error (MSE), and mean absolute error (MAE). They developed two separate ANN-based models, one for MDD and one for OMC, and also developed one combined model to see the effect. Separate models for OMC and MDD give satisfactory results with experimental results. They concluded that modified ANN models were less massive than the other models.” “Salahudeen et al. [10] expand MLP models to predict MDD and OMC of cement kiln dust stabilized black cotton soil. The ten input parameters were used, viz. linear shrinkage, specific gravity, free swell, D_{10} , D_{30} , D_{60} (effective soil particle sizes), coefficient of curvature (C_c), coefficient of uniformity (C_u), liquid limit, and plastic limit. They concluded that simulation results are satisfactory with experimental results. The same statistical parameters (Alavi et al. [9]) were used for checking the performance of models.” Sinha and Wang [11] developed prediction models to predict MDD, OMC, and permeability of the soil. A total of 55 different mixes were prepared with components of limestone, bentonite, dust, sand, and gravel. For training of ANN models, the program NeuralWare (2001) was used. The accuracy of the prediction models was checked using R^2 and RMSE. They concluded that, compared with experimental

test results, predictions within a 95% confidence interval. ANN forecasting models become a systematic tool for the design of compacted soil earthwork. Table 1 shows the detailed summary of artificial neural networks used on compaction parameters of soil.

2.2 Permeability

Permeability is a capacity of soil to permit water passes through it. Permeability is an extremely important engineering property of soil because the designer should know the standards of liquid flow, as groundwater conditions are frequently experienced on construction projects. Permeability is determined in the laboratory for various sorts of soil using a constant head and falling head permeability test. ANN can be used to predict permeability from index parameters of soil. In the present review paper, Tipza et al. [4] and Sinha et al. [11] already discussed prediction of permeability in 2.1.

“Erzin et al. [12] developed ANN and MRA models for determining the hydraulic conductivity of fine-grained soil. They performed a falling head permeability test on silty sand and marine clays in the laboratory. ANN models were developed individually on silty sand and marine clays and one generalized model developed which contains different soils compacted to different states using experimental data. The input parameters were water content, dry density, D_{10} , D_{30} , D_{60} , D_{85} , D_{100} . The performance of both models was checked by the coefficient of correlation, variance (VAF), and RMSE. They concluded that ANN models are better than MRA for determining the hydraulic conductivity of varied soils.” Chapuis [13] assessed methods to predict the saturated hydraulic conductivity, permeability of sand and gravel. Recently, researchers have used neural networks, fuzzy logic, and regression to work out the permeability of coarse and fine-grained soils. El-Sebakhy et al. [14] present functional networks are good to approach to work out the permeability of soils. Permeability prediction has been a provocation for geotechnical engineers. In this study, functional networks were used to predict permeability in a carbonate reservoir. They concluded that developed functional networks give reliable and proper results.

2.3 Shear Strength Parameters

The ability of soil to help a stacking from a structure, or to help its overburden, or to sustain a slope in equilibrium is governed by its shear strength. There are two shear strength parameters called cohesion (c) and the angle of internal friction (ϕ). Shear strength parameters are used for earth and rockfill dam design, earth pressure problems, highway and airfield design, foundation design, and stability of slopes. Cohesion depends upon water content, the grain size of soil particles, minerals,

Table 1 Summary table of application of ANNs on MDD and OMC

S. No.	Author	Year	Model/algorithm	Input parameters	Output parameters	Accuracy/performance parameters	References
1	Gunaydin	2008	MLP	G, w_L , w_p , grain size	MDD, OMC	SRA, MRA	[1]
2	Suman et al.	2016	FN, MARS, MLR	w_L , w_p , PI, % sand, % gravel, moisture content, cement content	MDD, UCS	Statistical analysis	[2]
3	Abdel-Rahman	2008	ANN	Gradation percentage	MDD, OMC	Statistical analysis	[3]
4	Tipza et al.	2014	MLP	Grain size distribution, G, Aterberg limits	permeability, MDD, OMC, effective friction angle	COD, RMSE, CRM	[4]
5	Das et al.	2010	BRNN, LMNN, DENN, SVM	w_L , PI, % clay fraction, % sand, % gravel, cement content, moisture content	MDD, UCS	MAE, AAE, RMSE, statistical analysis	[5]
6	Shahiri and Ghasemi	2017	MLP	Water content, dry density, w_L , w_p , P_H , curing age, copper slag content, cement content	MDD, OMC	Statistical analysis	[8]
7	Alavi et al.	2010	MLP	w_L , w_p , Linear shrinkage, % Gravel, % Clay, % silt, lime content, cement content, asphalt content	MDD, OMC	Coefficient of determination (R^2), MSE, MAE	[9]
8	Salahudeen et al.	2018	MLP	G, linear shrinkage, free swell, D_{10} , D_{30} , D_{60} , C_u , C_c , w_L , w_p	MDD, OMC	Coefficient of determination (R^2), MSE	[10]

(continued)

Table 1 (continued)

S. No.	Author	Year	Model/algorithm	Input parameters	Output parameters	Accuracy/performance parameters	References
9	Simha and Wang	2008	ANN (NeuralWare)	Density of solid phase, fineness modulus, effective grain size, w_L , w_P	Permeability, MDD, OMC	Coefficient of determination (R^2), RMSE	[11]

and promise between the particles, whereas angle on internal friction depends upon water content, particle size distribution, dry density, the shape of particles, and surface texture. These parameters were determined in the laboratory using a direct shear test, triaxial test, vane shear test, and unconfined compression test. ANN can predict the parameters accurately of various sorts of soils. Table 2 shows the detailed summary of artificial neural networks used on shear strength parameters of soil. “Mousavi et al. [15] developed new nonlinear solutions to work out shear strength parameters using linear genetic programming (LGP). An experimental database was established after conducting unconsolidated undrained and unsaturated triaxial tests. They concluded that LGP models were better than regression models. The factors, viz. fine-grained content, D_{30} , C_u , w_L , water content, and dry soil unit weight, represent the behavior of shear strength parameters. Out of that water content and dry soil unit weight effectively affects shear strength parameters.” Iyeke et al. [16] were 83 soil samples collected from Nigeria. They concluded the appliance of those models will help to scale back cost and time. ANN predicts the shear strength parameters for lateritic soils exceed the empirical methods. Kiran and Lal [17] investigated the MLP model to work out cohesion and angle of internal friction. They used soil within the state of Jharkhand (India). Input parameters should be the same as earlier researchers, but they used bulk density (BD) and dry density (DD) separately. The model showed the best performance for the prediction of cohesion and angle in internal friction. Eidgahee et al. [18] evaluated shear strength parameters of granulated waste rubber using the group method of data handling (GMDH) algorithm. GMDH gives well-founded results for shear strength and vertical strain. “Kayadelen et al. [19] conducted consolidated drained triaxial tests (CID) in a laboratory and predict the angle of shearing resistance (ϕ) using gene expression programming (GEP), ANN, and ANFIS models. This study shows that GEP models give exceed results than ANN and ANFIS.”

Khan et al. [20] predicted residual friction angle using SVM, ANN, and FN models. They concluded that FN is best than ANN for predicting the residual strength of clay. “Khanlari et al. [21] utilized MLP and radial basis function (RBF) approach to predict friction angle and cohesion of soils. They used different percentages of soil passing on sieve No. 200, 40, 4, PI, and bulk density as an input layer. This study gives the results of the MLP-ANN model performed better than RBF-ANN.” Lee et al. [22] developed ANN models to estimated unsaturated shear strength (Apparent Cohesion C_{max}). Test investigations of unsaturated soils are exorbitant, tedious, and hard to lead; for that purpose, they formulated the connection between nonlinear unsaturated shear strength and matrix suction in a hyperbolic form. Ly et al. [23] developed a support vector machine (SVM) for prediction of cohesion and angle of internal friction. SVM models performed well prediction and moisture content, w_L , w_P were found most affected factors on soil shear strength. “Sezer [24] utilized three different algorithms scaled conjugate gradient (SCG), gradient descent method with momentum term (GDM), Levenberg–Marquardt (LM) for predicting shear development in clean sand. The input parameters are counting on the particle shape, i.e., roundness, sphericity, area-perimeter fractal dimension, etc. Tests were employed on 33 differing types of sands.” Sezer [25] again performed the estimation of the angle

Table 2 Summary table of application of ANNs on shear strength parameters

S. No.	Author	Year	Model/algorithm	Input parameters	Output parameters	Accuracy/performance analysis	References
1	Mousavi et al.	2011	LGP	% FC, % CC, D_{10} , D_{30} , D_{60} , C_u , C_c , w_L , water content, soil unit weight and dry soil unit weight	Cohesion (c), angle of internal friction (ϕ)	RMSE, MAE	[15]
2	Iyke et al.	2016	MLP	Plasticity index (PI), percentage of particles passing sieve No. 200, G_s , w_L , w_p	Cohesion (c), angle of internal friction (ϕ)	Coefficient of determination (R^2), RMSE, MAE	[16]
3	Kiran and Lal	2015	MLP	Water content, w_L , w_p , dry density, bulk density, % gravel, % sand, % silt, % clay	Cohesion (c), angle of internal friction (ϕ)	RMSE, fractional bias (FB), normalized mean square error (NMSE), model (MB)	[17]
4	Eidgahee et al.	2018	ANN and group method of data handling (GMDH)	Normal stress (σ_n), horizontal strain (ϵ_h), C_u , C_c , D_{50}	Cohesion (c), angle of internal friction (ϕ)	RMSE, MAE, MSE	[18]
5	Kayadelen et al.	2009	Gene expression programming (GEP), ANN, adaptive network-based interference system (ANFIS)	% of coarse-grained soil, % of fine-grained soil, bulk density, w_L	Angle of internal friction (ϕ)	Coefficient of determination (R^2), RMSE, standard deviation (σ)	[19]
6	Khan et al.	2015	ANN, SVM, FN	w_L , w_p , plasticity index, % of clay fraction	Residual friction angle	Coefficient of efficiency (E), absolute average error (AAE), maximum average error (MAE) and root mean square error (RMSE)	[20]

(continued)

Table 2 (continued)

S. No.	Author	Year	Model/algorithm	Input parameters	Output parameters	Accuracy/performance analysis	References
7	Khanlari et al.	2012	MLP-ANN, radial basis function (RBF-ANN)	Percentages of passing the No. 200, 40 and 4 sieves, plasticity index (PI), and density (ρ)	Cohesion (c), angle of internal friction (ϕ)	RMSE, MAE, coefficient of determination (R^2)	[21]
8	Lee et al.	2003	ANN	% sand fraction, and clay and silt fraction, void ratio (e), OMC, c , ϕ	Apparent cohesion (Cmax)	Coefficient of determination (R^2)	[22]
9	Ly et al.	2020	SVM	Moisture content, G , e , w_L , w_p	Cohesion (c), angle of internal friction (ϕ)	RMSE, MAE, coefficient of determination (R^2)	[23]
10	Sezer	2011	Gradient descent method with momentum term (GDM), scaled conjugate gradient (SCG) and Levenberg–Marquardt (LAM)	% gravel, % sand, % silt–clay, C_u , C_c , normal stress (σ), e , relative density, D_{10} , r (roundness), s (sphericity), DR (area–perimeter fractal dimension) and current relative deformation	Angle of internal friction (ϕ)	MSE	[24]
11	Sezer	2013	Multiple regression models (MRM), ANFIS, ANN	Relative density, area–perimeter fractal dimension (D_r), regularity (r), D_{10} , C_c	Angle of internal friction (ϕ)	RMSE, coefficient of determination (R^2)	[25]

of shearing resistance (ϕ) of uniform sands using ANFIS and multiple correlation models (MRM).

2.4 Unconfined Compressive Strength

The unconfined compressive strength is that the load per unit area at which the cylindrical specimen of a cohesive soil falls after applying pressure. The undrained shear strength of the soil is one half of the unconfined compressive strength and it is determined in the laboratory. Suman et al. [2], Das et al. [5], and Shahiri et al. [8] also worked on the application of ANN on Unconfined compressive strength which is already discussed in 2.1. Narendra et al. [26] developed MLP, RBF, and genetic programming (GP) mathematical models to predict the unconfined compressive strength of cement stabilized soft ground soil. The input parameters were curing period, water content, w_L , liquidity index, clay water-cement ratio, cement content. The MLP network gives better results compared to RBF and GP for predicting the unconfined compressive strength of clayey soil.

3 Discussion and Conclusions

The engineering properties of soil depend on soil structure, permeability, swelling, pore water pressure, shrinkage, compressibility, stress–strain relationship, and shear strength parameters. The evolution of accurate engineering properties is a difficult task. The review confirms the application of ANNs completing a spread of classification, prediction, optimization, and modeling-related task in geotechnical engineering. The accuracy for predicting the engineering properties of soil depends on the input parameters. ANN algorithm is favorably used for predicting the engineering properties of soil. The important input parameters which affect the MDD of soils were water content, liquid limit, plastic limit, percentage of fine-grained soil, and relative density, whereas, on OMC, input parameters were the percentage of gravel, percentage of sand, coefficient of uniformity, coefficient of curvature, D_{10} , D_{30} , D_{60} , additive content. For cohesion, the most affected factors were water content, grain size distribution, and liquid limit of soil. Most researchers were to see the model performance using statistical approaches like coefficient of determination (R^2), MSE, RMSE, and MAE. Laboratory tests to work out engineering properties of soil are laborious and time-consuming; it is desirable to develop prediction ANN models to estimate these properties using index parameters.

Acknowledgements “I take this opportunity to thank Dr. Arun W. Dhawale my guide who has been a constant source of inspiration and also took interest in each step of the project development. We are also thankful to our college Director Dr. R. K. Jain and the staff of the Civil Engineering department for providing support throughout this work.”

References

1. Gunaydin O (2009) Estimation of soil compaction parameters by using statistical analyses and artificial neural networks. *Environ Geol* 57:203–215
2. Suman S, Mahamaya M, Das SK (2016) Prediction of maximum dry density and unconfined compressive strength of cement stabilized soil using artificial intelligence techniques. *Int J Geosynth Ground Eng* 2:11
3. Abdel-Rahman AH (2008) Predicting compaction of cohesionless soils using ANN. *Ground Improv* 6:3–8
4. Tizpa P, Chenari RJ, Fard MK, Machado SL (2015) ANN prediction of some geotechnical properties of soil from their index parameters. *Arab J Geosci* 8:2911–2920
5. Das SK, Samui P, Sabat AK (2011) Application of artificial intelligence to maximum dry density and unconfined compressive strength of cement stabilized soil. *Geotech Geol Eng* 29:329–342
6. Goh TC, Kulhawy FH, Chua CG (2005) Bayesian Neural Network Analysis of Undrained Side Resistance of Drilled Shafts. *J Geotech Geoenvironmental Eng* 131:84–93
7. Das SK, Basudhar SK (2008) Prediction of residual friction angle of clays using artificial neural network. *Eng Geol* 100:142–145
8. Shahiri J, Ghasemi M (2017) Utilization of soil stabilization with cement and copper slag as subgrade materials in road embankment construction. *Int J Transp Eng* 5:45–58
9. Alavi AH, Gandomi AH, Mollahassani A, Heshmati AK, Rashed A (2010) Modeling of maximum dry density and optimum moisture content of stabilized soil using artificial neural networks. *J Plant Nutr Soil Sci* 173:368–379
10. Salahudeen AB, Ijimdiya TS, Eberemu AO, Osinubi KJ (2018) Artificial neural networks prediction of compaction characteristics of black cotton soil stabilized with cement kiln dust. *J Soft Comput Civil Eng* 50–71
11. Sinha SK, Wang MC (2008) Artificial neural network prediction models for soil compaction and permeability. *Geotech Geol Eng* 26:47–64
12. Erzin Y, Gumaste SD, Gupta AK, Singh DN (2009) Artificial neural networks (ANN) models for determining hydraulic conductivity of compacted fine-grained soil. *Can Geotech J* 46:955–996
13. Chapuis RP (2004) Predicting the saturated hydraulic conductivity of sand and gravel using effective diameter and void ratio. *Can Geotech J* 41:787–795
14. El-Sebakhy EA, Asparouhov O, Abdulaheem A, Al-Majed A, Wu D, Latinski K, Raharja L (2012) Functional networks as a new data mining predictive paradigm to predict permeability in a carbonate reservoir. *Expert Syst Appl* 39:10359–10375
15. Mousavi SM, Alavi AH, Gandomi AH, Mollahasani A (2011) Nonlinear genetic-based simulation of soil shear strength parameters. *J Earth Syst Sci* 120:1001–1022
16. Iyeke SD, Eze EO, Ehiorobo JO, Osuji SO (2016) Estimation of shear strength parameters of lateritic soils using artificial neural network. *Niger J Technol* 35:260–269
17. Kiran S, Lal B (2015) ANN based prediction of shear strength of soil from their index properties. *Int J Earth Sci Eng* 8:2195–2202
18. Eidgahee DR, Haddad A, Naderpour H (2018) Evaluation of shear strength parameters of granulated waste rubber using artificial neural networks and group method of data handling. *Scientia Iranica*
19. Kayadelen C, Gunaydin O, Fener M, Demir A, Ozvan A (2009) Modeling of the angle of shearing resistance of soils using soft computing systems. *Expert Syst Appl* 36:11814–11826
20. Khan SZ, Suman S, Pavani M, Das SK (2015) Prediction of the residual strength of clay using functional networks. *Geosci Front* 1–8
21. Khanlari GR, Heidari M, Momeni A, Abdilor Y (2012) Prediction of shear strength parameters of soils using artificial neural networks and multivariate regression methods. *Eng Geol* 131–132:11–18
22. Lee SJ, Lee SR, Kim YS (2003) An approach to estimate unsaturated shear strength using artificial neural network and hyperbolic formulation. *Comput Geotech* 30:489–503
23. Ly H-B, Pham B (2020) Prediction of shear strength of soil using direct shear test and support vector machine model. *Open Constr Buil Technol J* 14:41–50

24. Sezer A (2011) Prediction of shear development in clean sands by use of particle shape information and artificial neural networks. *Expert Syst Appl* 38:5603–5613
25. Sezer A (2013) Simple models for the estimation of shearing resistance angle of uniform sands. *Neural Comput Appl* 22:111–123
26. Narendra BS, Sivapullaiah PV, Suresh S, Omkar SN (2006) Prediction of unconfined compressive strength of soft grounds using computational intelligence techniques: a comparative study. *Comput Geotech* 33:196–208

Chapter 62

Structural and Photocatalytic Studies of Ce and Dy Co-doped ZnO Nanoflowers



Syed Irtiqa and Atikur Rahman

Abstract Cerium and dysprosium co-doped ZnO nanoparticles were synthesized through a simple co-precipitation approach at low temperature. X-ray diffraction was used for the structure and purity analysis of the samples prepared. A hexagonal wurtzite structure was observed with no secondary peaks. The average crystallite size was about 35 nm. Morphology was studied using scanning electron microscopy. A change in morphology from elongated nanorods to nanoflowers was observed as the concentration of dopants increased. The photocatalytic activities of the nanoparticles were examined by photodegradation of rhodamine B (RhB) under UV irradiation. The experiment revealed a total degradation of the organic molecules indicated by the elimination of the dye color. The result showed that ZnO photocatalyst, co-doped with cerium and dysprosium ($\text{Zn}_{0.90}\text{Ce}_{0.05}\text{Dy}_{0.05}$), exhibited much improved photocatalytic performance (98% degradation) in comparison with undoped ZnO. The enhanced photocatalytic performance of co-doped samples could be credited to increase in surface oxygen vacancies, improved absorption capacity, and delayed recombination of photogenerated electrons and holes owing to the creation of trap states in the bandgap of ZnO.

Keywords ZnO · Ce · Dy co-doping · Photocatalysis · Rhodamine B dye · Rare earths

1 Introduction

In recent times, semiconductor nanomaterials have been vital in the advancement of electronics and technology. Some semiconductors such as TiO_2 , ZnS, ZnO, ITO, and CdSe exhibit excellent optical properties [1]. Among them, ZnO being the II-VI semiconductor has a high binding energy at room temperature. ZnO also has a wide bandgap (3.37 eV), high chemical stability, and high melting point (1975 °C). It is the most commonly used semiconductor in optoelectronic applications like

S. Irtiqa (✉) · A. Rahman
Department of Metallurgical and Materials Engineering, National Institute of Technology
Srinagar, Hazratbal, Srinagar 190006, India
e-mail: syedirtiqqa62phd17@nitsri.net

© The Author(s), under exclusive license to Springer Nature Singapore Pte Ltd. 2022
V. Bindhu et al. (eds.), *Proceedings of Fourth International Conference on Inventive Material Science Applications*, Advances in Sustainability Science and Technology,
https://doi.org/10.1007/978-981-16-4321-7_62

765

photocatalysis, solar cells, and field emission displays pertaining to its low cost, easy synthesis, low toxicity, electron transport capability, and low crystallization temperature [2–7].

Physical properties of semiconductor nanomaterials are tuned by intentional incorporation of impurity ions into the host lattice—‘doping’ [8–12]. Doping is seen to modulate the optoelectronic and magnetic properties of ZnO. Radiative transitions of $4f$ electrons of rare-earth ions have been under research because of their unique luminescent and recombination sites for electron–hole pairs [13]. Semiconductor-based photocatalysts such as ZnO are of pivotal importance in alleviating the global concerns primarily related to the treatment of wastewater. Water pollution and scarcity of water are the major scientific challenges impacting billions of people world over. Textile industry and dye production units produce enormous amount of effluent water containing intense colored toxic dyes. Rhodamine B (RhB) is the most widely used dye in the textile industry and dye production units owing to its high stability. However, it is extremely harmful to human and aquatic life due to its carcinogenic and mutagenic nature. Hence, degradation and decomposition of rhodamine B dye are absolutely important for conservation of water, aquatic life, and human safety [14]. Photocatalysis has emerged as the most efficient, low cost, and green alternative for wastewater treatment. Many semiconductor nanomaterials like TiO_2 , SnO_2 , and ZnO have been of tremendous interest for researchers due to their excellent photocatalytic performance. Among the semiconductive oxides, ZnO is most suitable for photocatalysis and degradation of organic compounds because of its non-toxicity, inertness to chemicals, stability against corrosion, and low cost [15–19]. However, the major shortcomings of undoped ZnO nanoparticles for practical applications pertain to its narrow range of response that too under UV irradiation ($\lambda < 400$ nm) which constitutes only 6–8% of solar energy while as visible light makes up for 46% of the spectrum. Thus, for attaining better photocatalysis results from ZnO, we need to shift its absorption edge from UV region to visible region of the solar spectrum. Further, less separation gap between electrons and holes, generated after a high energy photon strikes ZnO, leads to recombination and energy dissipation within nanoseconds. As photogenerated electrons and holes can act as powerful oxidizing and reducing agents, respectively, a better charge separation between them can pave the way for redox reactions, and, as a result, improved photocatalysis can be achieved [20, 21]. These improvements in photocatalytic properties can be achieved through monovalent doping using rare-earth ions [22–26]. Monovalent dopings of lanthanides in ZnO have been studied with metals like cerium (Ce), lanthanum (La), and dysprosium (Dy) [27–31]. Among the monovalent rare-earth dopants with $4f$ configuration, cerium is particularly interesting owing to its larger ionic size which causes a localized charge perturbation when substituted into the ZnO lattice, hence increasing its photocatalytic activity [32–35]. But, such monovalent doping of ZnO with rare-earth ions is extensively studied, hardly leaving any scope for further investigations in this area. However, a combination of rare-earth dopings can be investigated for various advantages over the monovalent doping. Very few literature precedents are available on these combination doping studies [36–39]. Our curiosity toward investigating the impact of combination doping on optical properties of semiconductors motivated

us for a detailed analysis of Ce and Dy co-doping into ZnO matrix. We, herein, report an optimized and enhanced photocatalytic performance of ZnO nanoparticles. Rare-earth ion doping of ZnO nanoparticles has been performed by various methods like forced hydrolysis [40], pulsed laser deposition [41], and combustion [29]. These methods are complex and usually require high temperatures, costly machinery, and harmful chemicals.

A simple, cost-effective and environmental friendly method of co-precipitation has been used for the synthesizing Ce and Dy co-doped ZnO nanoparticles in the present work. ZnO nanoparticles with an increasing concentration of co-dopants, i.e., ($\text{Zn}_{0.98}\text{Ce}_{0.01}\text{Dy}_{0.01}\text{O}$, $\text{Zn}_{0.96}\text{Ce}_{0.02}\text{Dy}_{0.02}\text{O}$, $\text{Zn}_{0.94}\text{Ce}_{0.03}\text{Dy}_{0.03}\text{O}$, $\text{Zn}_{0.92}\text{Ce}_{0.04}\text{Dy}_{0.04}\text{O}$, and $\text{Zn}_{0.90}\text{Ce}_{0.05}\text{Dy}_{0.05}\text{O}$), were synthesized for comparative optical studies. Structural and morphological features of the co-doped samples were studied using XRD and SEM in the present work. The photocatalytic performance of the pure and co-doped samples was studied by observing the degradation of rhodamine B dye under UV light irradiation. The degradation of harmful organic waste and consequent removal of color was considerably improved when Ce and Dy co-doped ZnO nanoparticles were used for photocatalysis, in comparison with the undoped ZnO nanoparticles. The mechanism of degradation of rhodamine B dye using nano-photocatalysts is also discussed in the current work.

2 Experimental Procedure

A facile, low cost, and ecofriendly co-precipitation method was used for preparing Ce and Dy co-doped ZnO nanoparticles, i.e., ($\text{Zn}_{0.98}\text{Ce}_{0.01}\text{Dy}_{0.01}\text{O}$, $\text{Zn}_{0.96}\text{Ce}_{0.02}\text{Dy}_{0.02}\text{O}$, $\text{Zn}_{0.94}\text{Ce}_{0.03}\text{Dy}_{0.03}\text{O}$, $\text{Zn}_{0.92}\text{Ce}_{0.04}\text{Dy}_{0.04}\text{O}$, and $\text{Zn}_{0.90}\text{Ce}_{0.05}\text{Dy}_{0.05}\text{O}$). The mole fraction of dopants in the host ZnO nanoparticles was maintained by adjusting the weight ratio of dopants, Ce and Dy, to host Zinc. The starting salt and dopant sources used, i.e., host (zinc(II)acetate dihydrate [$\text{Zn}(\text{COOCH}_3)_2 \cdot 2(\text{H}_2\text{O})$] and dopants cerium(III)acetate-1.5hydrate [$\text{Ce}(\text{CH}_3\text{COO})_3 \cdot 1.5(\text{H}_2\text{O})$], dysprosium(III)acetate-4hydrate [$\text{Dy}(\text{CH}_3\text{COO})_3 \cdot 4\text{H}_2\text{O}$] were of 99% purity (Sigma Aldrich). Distilled water was used as reaction medium, and diethylamine was used as reducing and stabilizing agent. To begin with, pure ZnO nanoparticles were prepared. For this, zinc acetate salt solution of molarity 0.5 M was prepared in a 250 ml beaker at a temperature of 60 °C, and 5 ml of diethylamine was dropwise added to it. The reaction was performed for 30 min followed by heating at 180 °C. The resulting sample was centrifuged and annealed at 500 °C in a muffle furnace for 1 h.

To prepare the Ce and Dy co-doped ZnO nanoparticles, i.e., ($\text{Zn}_{0.98}\text{Ce}_{0.01}\text{Dy}_{0.01}\text{O}$, $\text{Zn}_{0.96}\text{Ce}_{0.02}\text{Dy}_{0.02}\text{O}$, $\text{Zn}_{0.94}\text{Ce}_{0.03}\text{Dy}_{0.03}\text{O}$, $\text{Zn}_{0.92}\text{Ce}_{0.04}\text{Dy}_{0.04}\text{O}$, and $\text{Zn}_{0.90}\text{Ce}_{0.05}\text{Dy}_{0.05}\text{O}$), solutions of dopant ions (cerium (III) Acetate Hydrate-4-Hydrate and dysprosium (III) acetate-4hydrate) of mole fractions from 0.01 to 0.05 and a concentration gradient of 0.01 were prepared in distilled water. These solutions were then added to the solution of 0.5 M zinc acetate. Afterward, 5 ml of diethylamine was slowly dropwise added to the above solution under continuous

Table 1 Standard conditions for synthesizing Ce, Dy co-doped ZnO nanoparticles $x = (0.00-0.05)$

Mole fraction (Ce and Dy)	Zinc acetate (M)	Cerium acetate (M)	Dysprosium acetate (M)	Diethylamine (CC)
0.00	0.5	0.000	0.000	0.5
0.01	0.5	0.005	0.005	0.5
0.02	0.5	0.010	0.010	0.5
0.03	0.5	0.015	0.015	0.5
0.04	0.5	0.020	0.020	0.5
0.05	0.5	0.025	0.025	0.5

stirring at 60 °C. The solution was further heated and stirred for 1 h. The final product obtained was centrifuged, cleaned with ethanol and annealed at 500 °C in a muffle furnace for each molar concentration from 0.01 to 0.05. Table 1 shows the optimized conditions and molarities used in synthesizing Ce and Dy co-doped ZnO nanoparticles.

The structural features of nanoparticles were analyzed using X-ray diffractometer having copper $K\alpha$ target (where $k = 1.54052 \text{ \AA}$). The radiation range over 2Θ varied from 10 to 90° with a step size of 0.01°. The morphology of undoped ZnO and Ce and Dy co-doped ZnO nanoparticles was observed under scanning electron microscope.

2.1 Photocatalytic Activity Measurement

To measure the photocatalytic activity of undoped and Ce and Dy co-doped ZnO nanoparticles, a 10 ppm solution of rhodamine B dye was prepared. 10 ml of this solution was taken in 250 ml beaker, which was then diluted with distilled water to make a total of 40 ml solution. 40 mg of the nanoparticle powder, to be analyzed for photocatalysis, was added to it under constant stirring. The solution was wrapped, kept in dark, and stirred for half 30 min to disperse the nanoparticles (photocatalyst) and to set up the adsorption and desorption equilibrium. Afterward, UV light was used to irradiate the solution in the photocatalytic reactor (M/S Techinstro, Nagpur, Maharashtra) fitted with high-pressure mercury lamp with capacity of 450 W (operating voltage-110–220 V), while the stirring was continued. An aliquot of 3 ml was withdrawn after every 10 min and immediately centrifuged to remove catalyst nanoparticles. The samples were then tested for absorbance with a UV-Vis spectrometer (Perkin Elmer lambda 35) run between 400 and 600 nm wavelength. The gradual decrease in the absorbance of dye, together with the removal of color, confirmed the degeneration of rhodamine B dye when pure and co-doped ZnO nanoparticles are used as photocatalyst.

3 Results and Discussion

3.1 Structural Analysis

XRD peak pattern of undoped and Ce and Dy co-doped ZnO nanoparticles, i.e., ($\text{Zn}_{0.98}\text{Ce}_{0.01}\text{Dy}_{0.01}\text{O}$, $\text{Zn}_{0.96}\text{Ce}_{0.02}\text{Dy}_{0.02}\text{O}$, $\text{Zn}_{0.94}\text{Ce}_{0.03}\text{Dy}_{0.03}\text{O}$, $\text{Zn}_{0.92}\text{Ce}_{0.04}\text{Dy}_{0.04}\text{O}$, and $\text{Zn}_{0.90}\text{Ce}_{0.05}\text{Dy}_{0.05}\text{O}$) is shown in Fig. 1a. All the nanoparticles displayed a hexagonal wurtzite structure according to The International Centre for Diffraction Data (ICDD) database number 01-070-8072. All the peaks were broad indicating the crystalline nature of the samples. The peaks obtained at (100), (002), (101), (102), (110), (103), (112), and (201) planes belonged to varied (hkl) families suggesting that all the samples had polycrystalline nature. No secondary peaks were observed except ZnO suggesting that all samples formed were pure phase. The dopant ions Ce^{3+} and Dy^{3+} have ionic radii of (1.03 Å) and (0.91 Å), respectively, which is considerably large when compared with the ionic radius of parent Zn^{2+} ion (0.72 Å). It causes a little distortion in ZnO lattice. Further, there is a slight shift in the direction of higher angle in the doped nanoparticles as shown in Fig. 1b, which confirms substitutional doping of dopant ions into the ZnO matrix.

The formulae below were used for the calculation of crystallite size and lattice constants, and the values of the same are stated in Table 2.

$$a = \frac{\lambda}{\sqrt[3]{\sin \theta}} \quad (1)$$

$$c = \frac{\lambda}{\sin \theta} \quad (2)$$

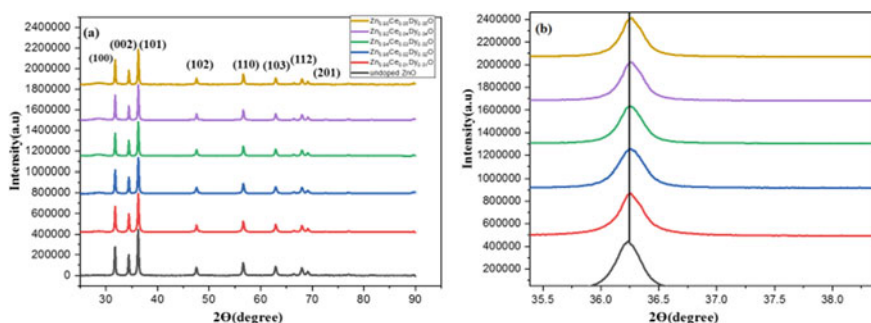


Fig. 1 **a** XRD pattern of undoped ZnO and Ce, Dy co-doped ZnO nanoparticles ($\text{Zn}_{0.98}\text{Ce}_{0.01}\text{Dy}_{0.01}\text{O}$, $\text{Zn}_{0.96}\text{Ce}_{0.02}\text{Dy}_{0.02}\text{O}$, $\text{Zn}_{0.94}\text{Ce}_{0.03}\text{Dy}_{0.03}\text{O}$, $\text{Zn}_{0.92}\text{Ce}_{0.04}\text{Dy}_{0.04}\text{O}$, and $\text{Zn}_{0.90}\text{Ce}_{0.05}\text{Dy}_{0.05}\text{O}$), **b** expanded XRD pattern showing shift toward higher angle with increase in co-dopant concentration

Table 2 Calculated lattice parameters and crystallite size of undoped and Ce, Dy co-doped ZnO nanoparticles

Sample	Lattice parameters		Crystallite size (nm)
	$a(\text{Å})$	$c(\text{Å})$	
Undoped	3.196	5.204	47
0.01 M Ce, Dy co-doped ZnO	3.240	5.210	39
0.02 M Ce, Dy co-doped ZnO	3.243	5.218	36
0.03 M Ce, Dy co-doped ZnO	3.247	5.223	34
0.04 M Ce, Dy co-doped ZnO	3.250	5.230	33
0.05 M Ce, Dy co-doped ZnO	3.253	5.241	30

$$D = \frac{K\lambda}{\beta \cos \theta} \quad (3)$$

where λ denotes the wavelength of the target used, i.e., 1.5406 Å, Θ is the diffraction angle. K is the shape factor, D denotes crystallite size while β represents full width half maximum. It is clearly seen from Table 1, the nanoparticle size decreases with increase in doping concentration. Undoped nanoparticles showed a crystallite size of 47 nm while $\text{Zn}_{0.90}\text{Ce}_{0.05}\text{Dy}_{0.05}$ showed a crystallite size of 30 nm. Mismatch of ionic radii of parent and dopant ions causes an increase in bond length which gets reflected in increased values of lattice constants a and c as shown in Table 2.

3.2 Morphological Studies

The SEM micrographs of undoped and Ce and Dy co-doped ($\text{Zn}_{0.98}\text{Ce}_{0.01}\text{Dy}_{0.01}\text{O}$, $\text{Zn}_{0.96}\text{Ce}_{0.02}\text{Dy}_{0.02}\text{O}$, $\text{Zn}_{0.94}\text{Ce}_{0.03}\text{Dy}_{0.03}\text{O}$, $\text{Zn}_{0.92}\text{Ce}_{0.04}\text{Dy}_{0.04}\text{O}$, and $\text{Zn}_{0.90}\text{Ce}_{0.05}\text{Dy}_{0.05}\text{O}$) ZnO nanoparticles are shown in Fig. 2a–e. SEM images confirm the XRD results. The particle size decreases as the concentration of co-dopants increases. The mismatch of ionic radii between parent Zn^{2+} ion (0.72 Å) and dopant Ce^{3+} (1.03 Å) and Dy^{3+} (0.91 Å) ions leads to lattice strain which eventually leads to smaller grain size of the co-doped nanoparticles. Also, the co-doped ZnO nanoparticles exhibit flower-like morphology, and this can be possibly credited to the doping of Ce^{3+} ions which play a noteworthy role in capping of co-doped nanoparticles formed during nucleation [42]. Ce^{3+} ions in the presence of strongly absorbed stabilizing agent diethylamine cause steric hindrances which lead to the formation of flowers like structure of C co-doped ZnO nanoparticles. This phenomenon is further elaborated on the basis of growth and nucleation of nanoparticles. The formation of seed nuclei is initiated by the precursor, which

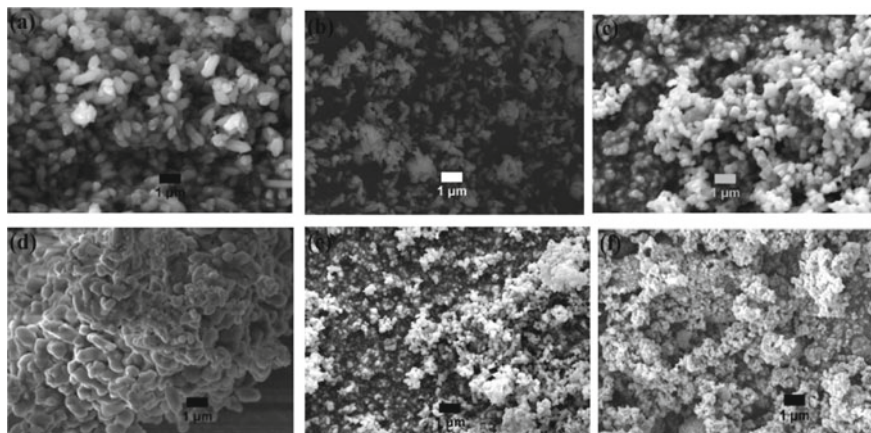


Fig. 2 SEM surface micrographs of undoped ZnO and Ce, Dy co-doped ZnO nanoparticles. **a** Undoped ZnO, **b** $\text{Zn}_{0.98}\text{Ce}_{0.01}\text{Dy}_{0.01}\text{O}$, **c** $\text{Zn}_{0.96}\text{Ce}_{0.02}\text{Dy}_{0.02}\text{O}$, **d** $\text{Zn}_{0.94}\text{Ce}_{0.03}\text{Dy}_{0.03}\text{O}$, **e** $\text{Zn}_{0.92}\text{Ce}_{0.04}\text{Dy}_{0.04}\text{O}$, and **f** $\text{Zn}_{0.90}\text{Ce}_{0.05}\text{Dy}_{0.05}\text{O}$

grows into long rods by Ostwald ripening effect where larger particles enlarge at the expense of smaller particles. This mechanism is facilitated by a solvent, and the various subunits formed by this method are connected by orientation attachment process leading to flower-like structure [43].

3.3 Photocatalytic Studies

Photocatalytic activities of pure and Ce and Dy co-doped ZnO nanoparticles, i.e., ($\text{Zn}_{0.98}\text{Ce}_{0.01}\text{Dy}_{0.01}\text{O}$, $\text{Zn}_{0.96}\text{Ce}_{0.02}\text{Dy}_{0.02}\text{O}$, $\text{Zn}_{0.94}\text{Ce}_{0.03}\text{Dy}_{0.03}\text{O}$, $\text{Zn}_{0.92}\text{Ce}_{0.04}\text{Dy}_{0.04}\text{O}$, and $\text{Zn}_{0.90}\text{Ce}_{0.05}\text{Dy}_{0.05}\text{O}$), were measured through photolytic degradation of rhodamine B dye using UV light irradiation. The photocatalytic degeneration of rhodamine B dye with photocatalysts, ZnO and Ce and Dy co-doped ZnO nanoparticles is shown in Fig. 3a–f at reaction times from 0 to 60 min. As the concentration of dopants increases, the absorbance of dye gets decreased with reaction time. The degradation is fastest and most efficient with Ce and Dy co-doped ($\text{Zn}_{0.90}\text{Ce}_{0.05}\text{Dy}_{0.05}$) ZnO as the photocatalyst. Figure 4a reveals the photocatalytic performance of the undoped and Ce and Dy co-doped ZnO nanoparticles through degradation of dye. The photocatalytic performance is shown as the plot between C_t/C_o and irradiation time (t) where C_o represents the initial concentration of dye and C_t denotes the residual dye concentration after a time gap t . The photocatalytic degradation of rhodamine B dye roughly follows the pseudo-first-order kinetics with lower concentrations of dye [44].

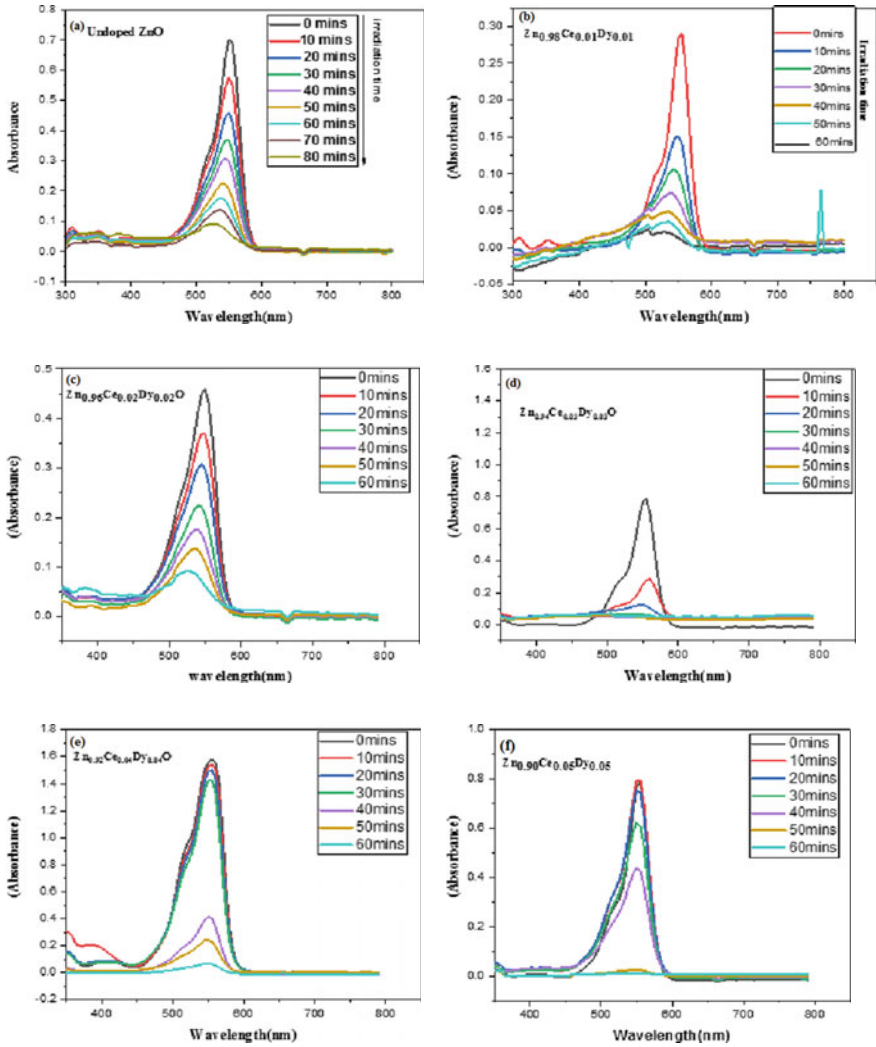


Fig. 3 UV visible absorbance spectra changes of rhodamine B solution during degradation with undoped and Ce, Dy co-doped ZnO nanoparticles under UV irradiation at varied time intervals. **a** Undoped ZnO, **b** Zn_{0.98}Ce_{0.01}Dy_{0.01}O, **c** Zn_{0.96}Ce_{0.02}Dy_{0.02}O, **d** Zn_{0.94}Ce_{0.03}Dy_{0.03}O, **e** Zn_{0.92}Ce_{0.04}Dy_{0.04}O, and **f** Zn_{0.90}Ce_{0.05}Dy_{0.05}O

$$\ln \left[\frac{C_t}{C_o} \right] = K * t \tag{4}$$

In the above equation, value K is the kinetic parameter for different photocatalysts. The value of apparent constant K can be estimated by linear fitting the slope of graph of $\ln(C_t/C_o)$ versus irradiation time t as shown in Fig. 4b.

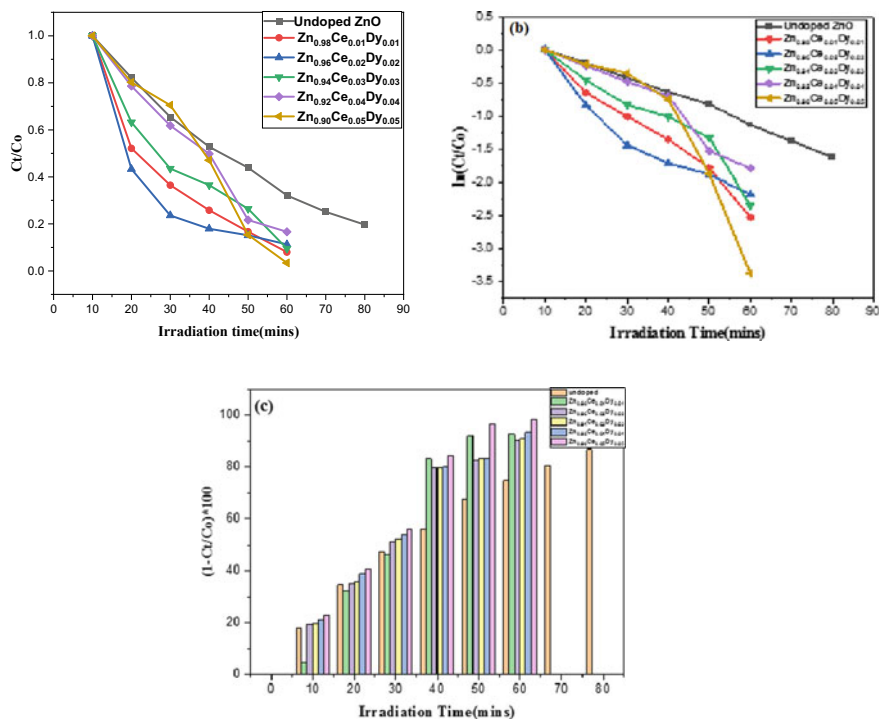


Fig. 4 **a** Photocatalytic degradation of Rhodamine B dye solution with undoped and Ce, Dy co-doped ZnO nanoparticles ($Zn_{0.98}Ce_{0.01}Dy_{0.01}O$, $Zn_{0.96}Ce_{0.02}Dy_{0.02}O$, $Zn_{0.94}Ce_{0.03}Dy_{0.03}O$, $Zn_{0.92}Ce_{0.04}Dy_{0.04}O$, and $Zn_{0.90}Ce_{0.05}Dy_{0.05}O$). **b** Reaction kinetics of photocatalytic degradation with undoped ZnO nanoparticles and co-doped ZnO nanoparticles ($Zn_{0.98}Ce_{0.01}Dy_{0.01}O$, $Zn_{0.96}Ce_{0.02}Dy_{0.02}O$, $Zn_{0.94}Ce_{0.03}Dy_{0.03}O$, $Zn_{0.92}Ce_{0.04}Dy_{0.04}O$, and $Zn_{0.90}Ce_{0.05}Dy_{0.05}O$) under UV irradiation at different time intervals. **c** Photocatalytic degradation percentage of Rhodamine B dye solution with undoped ZnO and Ce, Dy co-doped ZnO nanoparticles ($Zn_{0.98}Ce_{0.01}Dy_{0.01}O$, $Zn_{0.96}Ce_{0.02}Dy_{0.02}O$, $Zn_{0.94}Ce_{0.03}Dy_{0.03}O$, $Zn_{0.92}Ce_{0.04}Dy_{0.04}O$, and $Zn_{0.90}Ce_{0.05}Dy_{0.05}O$) under UV irradiation

The values of K were estimated to be (0.0247S⁻¹), (0.0391S⁻¹), (0.0411S⁻¹), (0.0321), (0.0351), and (0.0428) for undoped ZnO and $Zn_{0.98}Ce_{0.01}Dy_{0.01}O$, $Zn_{0.96}Ce_{0.02}Dy_{0.02}O$, $Zn_{0.94}Ce_{0.03}Dy_{0.03}O$, $Zn_{0.92}Ce_{0.04}Dy_{0.04}O$, $Zn_{0.90}Ce_{0.05}Dy_{0.05}O$, respectively. The value of apparent constant K is highest for $Zn_{0.90}Ce_{0.05}Dy_{0.05}O$. The efficiency of the photocatalysts was further estimated by calculating the degradation percentage using the formula given below.

$$\%D = \left(1 - \frac{C_t}{C_o}\right) \times 100 \quad (5)$$

where $\%D$ is the degradation percentage, C_o and C_t are the initial and residual dye concentrations, respectively. The degradation percentage was highest (98%) with $Zn_{0.90}Ce_{0.05}Dy_{0.05}O$ photocatalyst as revealed in Fig. 4c. The decrease in particle with

increased dopant concentration leads to an increased surface area and eventually enhanced photocatalytic activity.

Improvement of photocatalytic efficiency with Ce and Dy co-doping is understood by looking at the degradation mechanism. Initially, the semiconductor nanoparticles (photocatalyst) under consideration are bombarded with photons having energy ($h\nu$) greater than their bandgap. Excitation by high-energy photons generates the electrons and holes in pairs on the surface of semiconductor nanoparticles. The photogenerated electrons are captured by the oxygen O_2 adsorbed on the nanoparticle surface, and this step decides rate of photocatalysis. Here $4f$ configuration of rare-earth ions Ce and Dy plays the most important role in generation, transfer of charge, and delay in electron–hole recombination. Ce^{4+} and Dy^{4+} act as scavengers for the electrons. Also, Ce^{4+} and Dy^{4+} also act as stronger Lewis acids than O_2 and are better at trapping electrons captured by O_2 . Hence, the co-dopants trap electrons, which the oxidative process get passed on to surface adsorbed oxygen and produce superoxide radicals ($*O^{2-}$). The photo-induced electrons and holes have a tendency to quickly recombine and release energy as heat. Defect states can prevent this from happening. In the current work, electron–hole separation is enhanced by the presence of singly oxygen vacancies (Vo^+) in the bandgap of ZnO. Oxygen vacancies act as electron donors and form charged oxygen vacancies which then act as traps for holes, thus preventing the recombination. When a charged oxygen vacancy reacts with (OH^-), it forms (OH^*), which can also get formed on the reaction of superoxide anion with a hole. This can be written as,

Incident photons + ZnO \rightarrow electrons (e^-) + holes (h^+).

$Ce^{4+} + e^- \rightarrow Ce^{3+}$

$Dy^{4+} + e^- \rightarrow Dy^{3+}$

$e^- + O_2 \rightarrow *O^{2-}$ (superoxide).

$Vo^+ + h^+ \rightarrow Vo^{2+}$

$Vo^{2+} + OH^- \rightarrow Vo^+ + *OH$ (hydroxyl radical)

$*O^{2-} + 2H^+ \rightarrow 2(*OH)$

Organic pollutant + OH^* + $O_2 = CO_2 + H_2O +$ degraded products

The efficiency of photocatalysis hence depends on a number of features like what number of the charge carriers is available on the surface of photocatalyst and the rate at which electrons and holes recombine which eventually is bandgap dependent. In the current work, photocatalytic activities of Ce and Dy co-doped ZnO nanoparticles based photocatalysts are enhanced many folds as compared to undoped ZnO photocatalysts with $Zn_{0.90}Ce_{0.05}Dy_{0.05}$ exhibiting the best results. The reason for much better photocatalytic performance of Ce and Dy co-doped ZnO nanoparticles can be credited to large number of charge carriers on the surface of nanoparticles due to large surface area and availability of oxygen vacancies due to Ce, Dy co-doping as a result of which, the charge carriers (electrons) are transported faster to the oxygen molecules adsorbed on the surface.

4 Conclusion

Facile and cost-effective co-precipitation technique was successfully utilized to obtain pure and Ce and Dy co-doped ZnO nanoparticles. XRD analysis confirmed the successful formation of pure and co-doped ZnO nanoparticles with slight distortion of lattice in co-doped samples due to mismatch of ionic radii of host and dopant ions. The average particle size was calculated to be 35 nm. Morphological studies revealed the formation of flower-shaped nanoparticles with increase in concentration of Ce and Dy co-dopants. Photocatalytic studies showed that Ce and Dy co-doped ZnO nanoparticles had much improved photocatalytic performance as compared to undoped ZnO. The recombination rate of photogenerated charge carriers was suppressed in Ce, Dy co-doped samples due to incorporation of trap levels, increased surface oxygen vacancies, and charge transfer. As a consequence, the photocatalytic activity of co-doped nanoparticles was found to be exceedingly enhanced in comparison with undoped ZnO nanoparticles for the degradation of rhodamine B dye with $\text{Zn}_{0.90}\text{Ce}_{0.05}\text{Dy}_{0.05}$ exhibiting the highest activity.

References

1. Thiagarajan P, Kottaisamy M, Sethupathi K, Rao MSR (2009) A new red colour emitting phosphor—ZnS: Mn co-doped with Ba for electroluminescent (EL) displays. *J Displays* 30:202
2. Zhang C, Lin J (2012) Defect-related luminescent materials: synthesis, emission properties and applications. *Chem Soc Rev* 41:7938
3. Shang M, Li G, Yang D, Kang X, Peng C, Cheng Z, Lin J (2011) $(\text{Zn}, \text{Mg})_2\text{GeO}_4$: Mn^{2+} submicrorods as promising green phosphors for field emission displays: hydrothermal synthesis and luminescence properties. *Dalton Trans* 40:9379
4. Korake PV, Dhabbe RS, Kadam AN, Gaikwad YB, Garadkar KM (2014) Highly active lanthanum doped ZnO nanorods for photodegradation of metasytostox. *J Photochem Photobiol B* 130:11
5. Özgür Ü, Alivov YI, Liu C, Teke A, Reshchikov MA, Doğan S, Avrutin V, Cho SJ, Morkoç H (2005) A comprehensive review of ZnO materials and devices. *J Appl Phys* 98:041301
6. Morkoc UOH (2009) Zinc oxide: fundamentals materials and device technology. Wiley
7. Baskoutas S, Bester G (2010) Conventional optics from unconventional electronics in ZnO quantum dots. *J Phys Chem C* 114:9301
8. Erwin SC, Zu L, Haftel MI, Efros AL, Kennedy TA, Norris DJ (2005) Doping semiconductor nanocrystals. *Nature* 436:91
9. Norris DJ, Efros AL, Erwin SC (2008) Doped nanocrystals. *Science* 319:1776
10. Yim K, Lee J, Lee D, Lee M, Cho E, Lee HS, Nahm H-H, Han S (2017) Property database for single-element doping in ZnO obtained by automated first-principles calculations. *Sci Rep* 7:40907
11. Makino T, Segawa Y, Yoshida S, Tsukazaki A, Ohtomo A, Kawasaki M (2008) Optical properties of ZnO-based quantum structures. *Appl Phys Lett* 85:759
12. Singh S, Rama N, Rao MSR (2006) Influence of d–d transition bands on electrical resistivity in Ni doped polycrystalline ZnO. *Appl Phys Lett* 88:222111
13. Azarov A, Galeckas A, Hallén A, Kuznetsov A, Monakhov E, Svensson BG (2015) Optical activity and defect/dopant evolution in ZnO implanted with Er. *J Appl Phys* 118:125703
14. Kunz A, Peralta-Zamora P, de Moraes SG, Duran N (2002) New tendencies on textile effluent treatment. *Quimica Nova* 25:78

15. Korake PV, Kadam AN, Garadkar KM (2014) Photocatalytic activity of Eu^{3+} -doped ZnO nanorods synthesized via microwave assisted technique. *J Rare Earths* 32:306
16. Shaari N, Tan SH, Mohamed AR (2012) Synthesis and characterization of CNT/Ce-TiO₂ nanocomposite for phenol degradation. *J Rare Earths* 30:651
17. Yu XJ, Xiong LL, Ma GP, Liang Y, Liu KR (2014) Preparation and performance research of Ce-TiO₂/KL ball photocatalysts. *J Rare Earths* 32:849
18. Wang C, Cao L (2011) Preparation, spectral characteristics and photocatalytic activity of Eu^{3+} -doped WO₃ nanoparticles. *J Rare Earths* 29:727
19. Wu J, Zhang GL, Liu J, Gao HB, Song CX, Du HR, Li Z, Gong ZP, Lu YG (2014) Synthesis, characteristics, and antibacterial activity of a rare-earth samarium/silver/titanium dioxide inorganic nanomaterials. *J Rare Earths* 32:727
20. Linsebigler AL, Lu GQ, Yates JT Jr (1995) Photocatalysis on TiO₂ surfaces: principles, mechanisms, and selected results. *Chem Rev* 95:735
21. Romero M, Blanco J, Sanchez B, Vidal A, Malato S, Cardona AI et al (1999) Solar photocatalytic degradation of water and air pollutants: challenges and perspectives. *Sol Energy* 66:169
22. Ahmad M, Ahmed E, Hong ZL, Xu JF, Khalid NR, Elhissi A, Ahmed W (2013) Graphene-Ag/ZnO nanocomposites as high performance photocatalysts under visible light irradiation. *J Alloys Compd* 577:717
23. Ahmad M, Ahmed E, Hong ZL, Iqbal Z, Khalid NR, Abbas T, Ahmad I, Elhissi A, Ahmed W (2013) Structural, optical and photocatalytic properties of hafnium doped zinc oxide nanophotocatalyst. *Ceram Int* 39:8693
24. Ahmad M, Ahmed E, Hong ZL, Jiao XL, Abbas T, Khalid NR (2013) Enhancement in visible light-responsive photocatalytic activity by embedding Cu-doped ZnO nanoparticles on multi-walled carbon nanotubes. *Appl Surf Sci* 285:702
25. Cai HS, Liu GG, Lu WY, Li XX, Yu L, Li DG (2008) Effect of Ho-doping on photocatalytic activity of nanosized TiO₂ catalyst. *J Rare Earths* 26:71
26. Kumar S, Sahare PD (2012) Nd-doped ZnO as a multifunctional nanomaterial. *J Rare Earths* 30:761
27. Sharma DK, Sharma KK, Kumar V, Sharma A (2016) Effect of Ce doping on the structural, optical and magnetic properties of ZnO nanoparticles. *J Mater Sci Mater Electron* 27:10330
28. Shi Q, Wang C, Li S, Wang Q, Zhang B, Wang W, Zhang J, Zhu H (2014) Enhancing blue luminescence from Ce-doped ZnO nanophosphor by Li doping. *Nanoscale Res Lett* 9:480
29. Ahmad M, Ahmed E, Zafar F, Khalid NR, Niaz NA, Hafeez A, Ikram M, Khan MA, Hong Z (2015) Enhanced photocatalytic activity of Ce-doped ZnO nanopowders synthesized by combustion method. *J Rare Earths* 33:255
30. Selvam NCS, Vijaya JJ, Kennedy LJ (2013) Structural, optical and magnetic properties of porous α -Fe₂O₃ nanostructures prepared by rapid combustion method. *J Nanosci Nanotechnol* 13:1
31. Rajendran S, Khan MM, Gracia F, Qin J, Gupta VK, Arumainathan S (2016) Ce³⁺-ion-induced visible-light photocatalytic degradation and electrochemical activity of ZnO/CeO₂ nanocomposite. *Sci Rep* 6:31641
32. Shi HX, Zhang TY, Wang HL (2011) Preparation and photocatalytic activity of La³⁺ and Eu³⁺ co-doped TiO₂ nanoparticles: photo-assisted degradation of methylene blue. *J Rare Earths* 29:746
33. Fan CM, Xue P, Sun YP (2006) Preparation of nano-TiO₂ doped with cerium and its photocatalytic activity. *J Rare Earths* 24:309
34. Bian L, Song MX, Zhou TL, Zhou XY, Dai QQ (2009) Band gap calculation and photocatalytic activity of rare earths doped rutile TiO₂. *J Rare Earths* 27:461
35. Zalaj M (2014) Gadolinium-modified titanium oxide materials for photoenergy applications: a review. *J Rare Earths* 32:487
36. Kalaiezihly RK, Asvini V, Saravanan G, Ravichandran K (2019) Excitation-induced tunable luminescence of luminomagnetic Dy and Ce co-doped ZnO nanoparticles. *Dalton Trans* 48:12228

37. Iqbal J, Liu X, Zhu H, Wua ZB, Zhang Y, Yu D, Yu R (2009) Raman and highly ultraviolet red-shifted near band-edge properties of LaCe-co-doped ZnO nanoparticles. *Acta Mater* 57:4790
38. Pascariu P, Homocianu M, Cojocaru C, Samoila P, Airinei A, Sucheana M (2019) Preparation of La doped ZnO ceramic nanostructures by electrospinning–calcination method: effect of La³⁺ doping on optical and photocatalytic properties. *Appl Surf Sci* 476:16
39. Rahman A, Jayaganthan R (2016) Synthesis, characterization and photocatalytic studies of La, Dy-doped ZnO nanoparticles. *Trans Indian Inst Met* 70:1063
40. Jing LQ, Sun XJ, Cai WM, Xu ZL, Du YG, Fu HG (2003) The preparation and characterization of nanoparticle TiO₂/Ti films and their photocatalytic activity. *J Phys Chem Solid* 64:615
41. Bomila R, Srinivasan S, Venkatesan A, Bharath B, Perinbam K (2017) Structural, optical and antibacterial activity studies of Ce-doped ZnO nanoparticles prepared by wet-chemical method. *Mater Res Innov* 22:379
42. Liu X, Srooppa DG, Heggan M, Ermolenko Y, Offenhausser A, Mourzina Y (2015) Electrochemically induced ostwald ripening in Au/TiO₂ nanocomposite. *J Phys Chem C* 119:10336
43. Wang S, Bai L, Ao X (2018) Preparation and photocatalytic application of a S, Nd double doped nano-TiO₂ photocatalysts. *RSC Adv* 8:36745
44. Chang CJ, Lin CY, Hsu MH (2014) Enhanced photocatalytic activity of Ce-doped ZnO nanorods under UV and visible light. *J Taiwan Inst Chem Eng* 45:1954

Chapter 63

Investigate the Flexural Property of Polylactic Acid (PLA)-Based 3D Printed Part



Nitesh Kumar Dixit and Shweta Mishra

Abstract Present study aims to investigate the influence of process parameter, i.e., slice-height, infill-density and infill-design-pattern on flexural strength of Polylactic-acid-based 3D printed parts. Fused deposition modeling principle-based 3D printer is used to fabricate the parts. From the experimental result it can be clearly stated that all the three different parameters, such as slice-height, infill-density and infill pattern, show significant contribution toward stepup the flexural strength of the component fabricated by 3D printer. The optimal and significant levels of the different process parameters for maximizing the flexural strength of specimens are as follows: the layer thickness 0.2, infill density of 85% and triangular infill pattern. The infill percentage plays a very important role and it is the most influencing 3D printing parameter that most affects the flexural strength of FDM printed PLA specimens.

Keywords Polylactic acid · Additive manufacturing · Layer thickness · Infill density · Infill pattern · Flexural test

1 Introduction

Additive manufacturing or rapid prototyping is a technique in which we add or bond the material in the layered fashion. This definition refers widely to all materials like metals, ceramics, polymers, composites and biological systems. AM technology can be graded according to the source of power or the way the substance is connected, e.g., with a binder, laser, heated pad, etc. A category of materials, including plastics, metals and ceramics, can also be used to categorize. Rapid prototyping is a group of modern manufacturing technologies that are used to produce three-dimensional physical prototypes directly from digital data representations. Rapid prototyping was first developed for prototyping, but presently functional component is directly fabricated which could be used for many industrial applications. Liquid, solid and powder are the three initial form of the material used to categorize the above technologies [1, 2]. This technology is also called as solid freeform fabrication method.

N. K. Dixit (✉) · S. Mishra
Mechanical Engineering, IET, Dr. R.M.L. Avadh University Ayodhya, Faizabad, India

Solid term is used due to the initial form of raw material (liquid, powder, and solid) converted to a final product in the form of solid. The freeform term has an ability to fabricate complex part with this method. The basic principle of this technology is a three-dimensional CAD model, created using three-dimensional software, such as CATIA, ProE, Solid Works, etc., and this model is forwarded into Rapid Prototyping machine for the fabrication of part [2, 3].

2 Literature Review

Liu et al. use Taguchi method to find out the influence of different parameters, such as deposition orientation, width of raster, deposition style, gap between raster, thickness of layer on mechanical properties. Finally, GRA method is used to find out the common optimal solution for the three different mechanical characteristics [4]. Alvarez et al. studied the impact of infill percentage on tensile strength and impact resistance and further author observed that maximum tensile strength and maximum impact strength can be achieved by using 100% of infill. Authors also studied the printing time and found that the printing time is almost the same for 100% and 45% infill part [5]. Shilpesh et al. studied the effect of parameters on the flexural properties of the part fabricated by using 3D printing method. Study showed that flexural strength decreased as slice-height and raster-angle increases [6]. Porter et al., find infill percentage effect on flexural rigidity of FDM printed component and further concluded that above property ranged straightly with respect to percentage of raster infill and optimal infill percentage is determined between 10 and 20% that maximize the flexural rigidity of the FDM printed structural component [7]. Khan et al. concluded that infill patterns influence the mechanical property of 3D-RP object. Authors use different raster designs, such as Rectilinear, Concentric, Honey Comb and Hilbert Curve during fabrication of the component, and they find that rectilinear infill pattern gives best result during evaluation of mechanical property of the part [8, 9]. Aloyaydi et al. found the influence of infill density on flexural and microstructural property of the component fabricated by PLA-based FDM machine. From the result it is concluded that 80% of infill density is the optimum % which gives the considerable amount of toughness and strength to the fabricated component [10]. Camargo et al., found the various strengths associated with characteristics, i.e., flexural strength, impact energy and tensile strength by varying various FDM parameters, such as infill and layer thickness. From the results it is to say that the flexural strength and tensile property of part is improved while increasing the infill percentage [11]. Sanket et al. find the influence of infill pattern and infill % on the mechanical strength of the 3D printed object. From results it is concluded that triangular pattern is extremely influencing parameter [12]. Suteja et al., found the impact of various infill design parameters, i.e., layer thickness, speed of infill deposition, density of infill, pattern of infill and width of infill on the properties of the 3D printed part. High value of slice-height gives high tensile and low value of slice-height gives high flexural strength of the 3D object, respectively. Higher infill density improves stiffness and modulus

elasticity of the component [13]. Shrikant et al. investigated the mechanical strength of RP printed PLA parts by varying machine and obtained higher strength at higher infill and layer height [14]. Dixit et al. studied the object dimensional stability of object by varying the parameters of two different RP systems [15, 16].

3 Experimentation

Extrusion principle-based Prusa mk3, 3D open source printer is used to produce the test specimens for flexural strength measurement. In this research we have used polylactic acid (PLA) material for fabricating the test specimens. PLA is more printable, ecofriendly, and has higher mechanical strength properties than other plastics thus it is chosen for the above research. Polylactic acid is popular for its very successful efficiency and value-for-money quality. Polylactic acid has a wide range of applications where it can be used in the form of holds tremendous packaging material, fibers, packaging films and a host of molded articles. There are two different types of parameters which are associated with any 3D printing system, such as constant and variable parameters. Literature reveals that various machining parameters are associated with the extrusion-based 3D open source printer that influences the various properties of the fabricated object. Thus, the proper selection of suitable machining parameter may enhance the various associated properties, such as strength and stability of the fabricated object. Table 1 expresses constant 3D printer parameters, and Table 2 shows variable parameters with three selected levels. Taguchi parameter design method has been used for the fabrication of experimental object. ASTM D790 standard is used to fabricate the component from 3D open source printer for conducting the flexural strength test. A Presto company-based computerized tensile machine is used to measure flexural property of the 3D printed object. Figure 1a, b. shows the test

Table 1 Constant printing parameters

Parameters	Values
Build volume	12.7 cm * 1.27 cm * 0.32 cm
Printing speed	50 mm/s
Travel speed	50 mm/s

Table 2 Variable machine parameters with three level

Parameter	Level			Unit
	1	2	3	
Layer thickness/Slice-height	0.1	0.15	0.2	mm
Infill percentage/Infill-density	55	70	85	%
Infill pattern/Raster pattern	Rectilinear	Triangular	Full Honey Comb	–

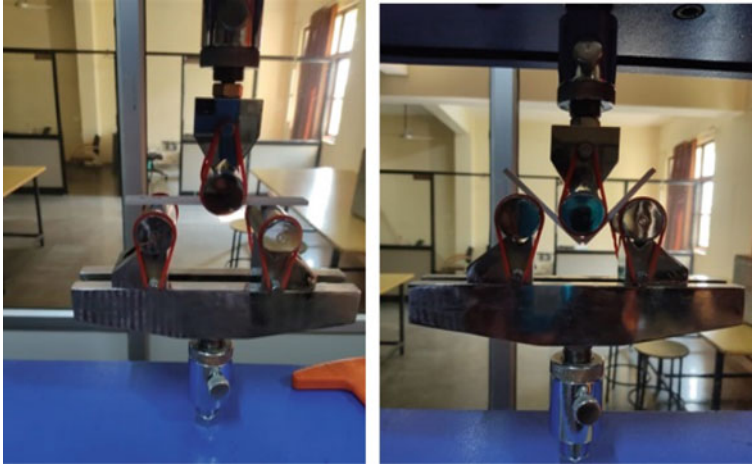


Fig. 1 a Test specimen before test. b Test specimen after test

sample before conducting the flexural strength test and after conducting the flexural strength test.

4 Results and Discussion

From Fig. 2, which is based on the data given in Table 3, it can be noted that flexural strength first increases as the slice-height increases from 0.1 to 0.15 mm and finally 0.2 mm. In this present case, the specimens having 0.2 mm layer thickness with 85% infill percentage and triangular infill pattern exhibited a maximum flexural strength of 50.866 MPa in comparison with the other slice-height ranged from 0.1 to 0.15 mm with similar processing conditions. As infill increased from 55 to 85%, the strength values revealed that the rise deposition of material in the samples showed a growing

Fig. 2 Flexural strength of the fabricated object versus 3D printer machine parameters

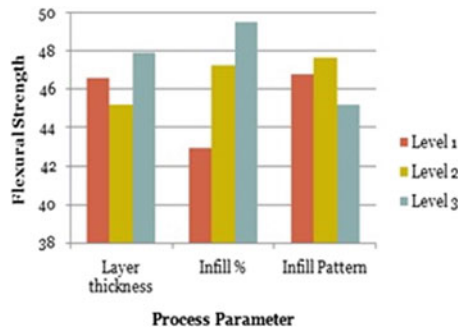


Table 3 Flexural strength of 3D printed part

Ex. No	Layer thickness	Infill percentage	Infill pattern	Flexural strength (MPa)	S/N ratio value for flexural strength
1	0.1	55	Rectilinear	42.077	32.4809
2	0.1	70	Triangular	49.482	33.8889
3	0.1	85	Full Honey Comb	48.167	33.6550
4	0.15	55	Triangular	42.700	32.6086
5	0.15	70	Full Honey Comb	43.392	32.7482
6	0.15	85	Rectilinear	49.482	33.8889
7	0.2	55	Full Honey Comb	44.084	32.8856
8	0.2	70	Rectilinear	48.859	33.7789
9	0.2	85	Triangular	50.866	34.1286

trend. Increased material deposition contributes to an improvement in flexural load resistance. Compared with rectilinear and full honeycomb, Fig. 2 demonstrates that the triangular design pattern has the strongest flexural strength. Out of these three kinds of infill patterns, the honeycomb infill pattern has the lowest flexural properties. Between triangular and honeycomb, the mean flexural intensity difference was 2.26 MPa. This means that before heading to rupture, triangular can tolerate an additional 2.26 MPa of maximum flexural tension relative to honeycomb. The S/N ratio of flexural strength is shown in Table 3 and for this the larger-the-better characteristics feature has been selected. The maximum flexural strength can be obtained at the layer thickness 0.2 mm, infill density of 85% and triangular infill pattern. Most significant process parameters are found out from Table 4. Table 4 shows ANAVO for SN ratios and from this table it is to say that the infill percentage affects the property of the object most for flexural strength. Infill percentage affects the 3D printed part property by more than 70%. The optimized parameters are used to maximize the flexural strength of the specimens and the above optimized parameters were obtained from the response table as it is shown in Table 5 and from the above table the optimum

Table 4 ANOVA table for flexural strength

Parameter	D.O.F	Seq S.S	Adj S.S	Adj M.S	F	P	Parametric effect in %
Layer thickness	2	0.3991	0.3991	0.1995	1.40	0.416	11.93
Infill percentage	2	2.3564	2.3564	1.1782	8.28	0.108	70.41
Infill pattern	2	0.3062	0.3062	0.1531	1.08	0.482	9.15
Error	2	0.2844	0.2844	0.1422			
Total	8	3.3461					

Table 5 Response table for flexural strength

Level	A	B	C
1	46.58	42.95	46.81
2	45.19	47.24	47.68
3	47.94	49.50	45.21
Delta	2.75	6.55	2.47
Rank	2	1	3

levels and significant process parameters for flexural strength is obtained. From Table 5 it is concluded that slice-height of 0.2 mm, infill-density of 85%, and infill pattern of triangular shape, enhance overall flexural strength of object. Figure 3 shows the main effect plot of means for the above strength test. It is also found that, infill pattern is the least influencing parameter which affects the flexural strength of RP objects because the raster pattern gives less variation when the level of parameter changes and the infill percentage is the most influencing parameter that influences the flexural property of the object. Infill percentage of 85% is a major influencing parameter that affects object strength of the specimens.

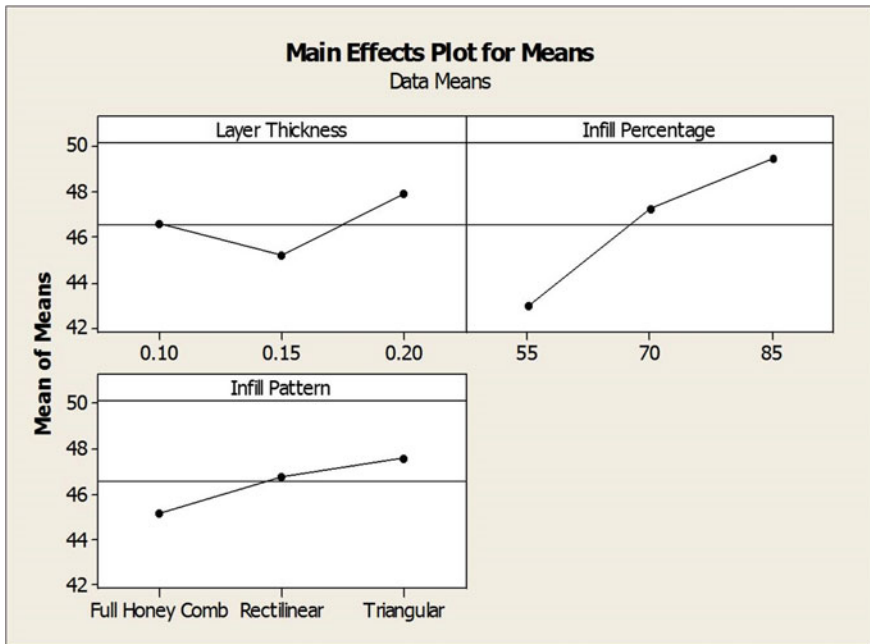


Fig. 3 Main effect plots for means

5 Conclusion

In the present work, the impact of different process parameter of 3D printer, such as layer thickness, infill density and raster infill pattern on flexural strength of the object, has been studied. Therefore, Taguchi design of experiment is a very dominant modeling and analyzing tool that helps to find the effect of machine process parameter on output characteristics of objective function. Two steps are used for completing this research. Part is produced during the first step of experimentation. In the second step flexural strength of the specimens was calculated. Analysis of variance table is generated from Taguchi method and the above table is used to find the consequence of individual 3D printer machine factors on the part strength. After the experimentation the following conclusion can be drawn.

From the result it is observed that all the three different machine parameters, such as layer thickness, infill density and raster infill pattern, influence overall flexural strength of the object and their influencing percentage is 11.93%, 70.41%, and 9.15%, respectively. Strength of the 3D RP Printed object increases as percentage of infill increases while constant layer thickness is maintained during fabrication of the part. Hence, from results it is also accomplished that the various infill percentages have a significant impact on the flexural strength of the RP part. It also concluded that the triangular raster design gives the best mechanical flexural strength in comparison with the three different infill patterns. Thus, from results it is also observed that the various raster patterns have a significant impact toward the flexural strength of the material. The optimal levels of process parameters for maximizing the object strength of the 3D printed specimens are as follows: layer thickness 0.2, infill density of 85% and triangular infill pattern. The infill percentage is one of the key influencing parameters that affect the flexural property of 3D printed PLA specimens.

References

1. Frazier WE (2014) Metal additive manufacturing: a review. *JMEPEG* 23:1917–1928
2. Calignano F, Manfredi D, Ambrosio EP, Biamino S, Lombardi M, Atzeni E, Salmi A, Minetola P, Iuliano L, Fino P (2017) Overview on additive manufacturing technology. *IEEE* 105(4):593–612
3. Singh P, Dixit NK (2020) Impact of process parameter on part properties and material used in FDM: a review. *JES* 11(11):10–11
4. Liu X, Zhang M, Li S, Si L, Peng J, Hu Y (2017) Mechanical property parametric appraisal of fused deposition modeling parts based on the gray Taguchi method. *Int J Adv Manuf Technol* 89:2387–2397
5. Alvarez C KL, Lagos C RF, Aizpun M (2016) Investigating the influence of infill percentage on the mechanical properties of fused deposition modelled ABS parts. *Ing Inv* 36(3):110–116
6. Rajpurohit SR, Dave HK (2018) Flexural strength of fused filament fabricated (FFF) PLA parts on a open-source 3D printer. *Adv Manuf* 6:430–441
7. Porter JH, Cain TM, Fox SL, Harvey PS (2019) Influence of infill properties on flexural rigidity of 3D-printed structural members. *Virtual Phys Prototyping* 14(2):148–159
8. Khan SF, Zakaria H, Chong YL, Saad MAM, Basaruddin K (2018) Effect of infill on tensile and flexural strength of 3D printed PLA parts. *Mater Sci Eng* 429

9. Subramaniam SR, Samykano M, Selvamani SK, Ngui WK, Kadirgama K, Sudhakar K, Idris MS (2019) Preliminary investigations of polylactic acid (PLA) properties. In: AIP conference proceedings, vol 2059
10. Aloyaydi BA, Sivasankaran S, Ammar HR (2019) Influence of infill-density on micro-structure and flexural behavior of 3D-printed polylactic-acid thermoplastic parts processed by fusion deposition modeling. *AIMS Mater Sci* 6(6):1033–1048
11. Camargo JC, Machado AR, Almeida EC, Silva EFMS (2019) Mechanical properties of PLA-graphene filament for FDM 3D printing. *IJAMT* 103:2423–2443
12. Parab S, Zaveri N (2020) Investigating the influence of infill patterns on the compressive strength of fused deposition modelled PLA parts. *ICIMA* 239–247
13. Suteja TJ, Soesanti A (2020) Mechanical properties of 3D printed polylactic acid product for various infill design parameters: a review. *ICST* 1569
14. Bardiya S, Jerald J, Satheesh Kumar V (2020) The impact of process parameters on the tensile strength, flexural strength and the manufacturing time of fused filament fabricated (FFF) parts. *Mater Today Proc*
15. Dixit NK, Srivastava R, Narain R (2016) Comparison of two different rapid prototyping system based on dimensional performance using grey relational grade method. *Procedia Technol* 25:908–915
16. Dixit NK, Srivastava R, Narain R (2016) Dimensional accuracy improvement of part fabricated by low-cost 3D open source printer for industrial application. *IEEE Xplore Digit Libr* 1–6

Chapter 64

Mathematical Modeling Influence Electromagnetic Wave Plane on Functional Materials



Olena Komisarenko , Nataliia Titova , Ievgev O. Zaitsev ,
and Ilona Chernytska 

Abstract The paper presents a mathematical modeling of a plane electromagnetic wave acting on a functional materials' biological object. By considering how electromagnetic fields can act and propagate inside a biological object. The biological object itself is represented as an ellipsoid with a multilayer structure. Here, it is assumed that, each of the layers of the cell is homogeneous; that is, it has a constant dielectric constant. In addition, the electromagnetic field gets penetrated from free space into the cytoplasm, that is, representable in a spherical coordinate system. As a result, a system of four linear algebraic equations is obtained for determining four unknown coefficients.

Keywords Biological object · Functional materials · Electromagnetic field · Scattered wave · Electric component · Magnetic component

1 Introduction

Over the past years, as a result of technical progress, a new, significant environmental factor, radio-frequency electromagnetic radiation, has emerged. The effect of such electromagnetic radiation [1–5] or other radiation on living systems of functional materials (FM) [6] as well as on systems operating under the influence of such fields and their components [1, 7–12] can be significant. An example of such an impact can be an electromagnetic field from a power line [13–15].

O. Komisarenko · N. Titova

Department of Information Systems and Technologies, National Transport University, Kiev, Ukraine

e-mail: olenakomisarenko@ukr.net

I. O. Zaitsev (✉)

Department of Electric and Magnetic Measurements, The Institute of Electrodynamics of the National Academy of Sciences of Ukraine, Kiev, Ukraine

e-mail: zaitsev@i.ua

I. Chernytska

Department of Computer and Information Technologies and Systems, National University “Yuri Kondratyuk Poltava Politechnic” of Ukraine, Poltava, Ukraine

The scientific data available to date convincingly indicate that radio-frequency electromagnetic radiation, including pulse-modulated ones, is characterized by a pronounced effect on both living organisms and devices. To avoid exposure to devices, various methods are used, including the use of fiber optic partially inert to such an effect [16–20], similar developments are also used in medical research [21, 22].

Given this circumstance, as well as an increase in the electromagnetic background induced by low-frequency sources, the World Health Organization (WHO) introduced the concept of “electromagnetic pollution,” reflecting the fact of the establishment of new environmental conditions on Earth. Currently, studies on the effects of electromagnetic pollution on human health and on the biosphere as a whole are being coordinated by WHO.

2 Literature Review

An analysis of the state of the problem [23–25] shows that electromagnetic fields have a specific effect on various biological objects and on systems operating under the influence of such fields and their components [1, 7–12]. There are a significant number of publications [23, 26–28] that highlight various aspects of this influence. Electromagnetic fields of various frequencies and intensities can cause both inhibitory effect and stimulation of vital processes (hormesis). Hormesis manifests itself in favorable biological responses to low exposure to toxins and other stress factors at many publications. For the first time [29–32], the influence of radiation stimulation on plants was observed by M. Maldina and K. Tuvinen in 1898. Physical problems of the influence of weak magnetic fields on biological systems were considered by Bingi V. and Savin A. in 2003. Further consideration of the phenomena occurring in a biological object under the influence of external electromagnetic fields has led to the conclusion that low-energy electromagnetic fields have a significant impact on various processes occurring at the cellular level, which led to close attention to such processes and allowed us to create a new direction in the development of medical therapeutic devices and systems.

3 Material and Method

It follows from the foregoing that the study of this process is possible only if it is known how the acting electromagnetic fields are distributed inside the FM biological object. Therefore, to obtain the necessary results, a mathematical model must be constructed that allows one to find the amplitudes of internal electromagnetic fields in living organisms. Conditionally represent the cell of a living organism in the form of an ellipsoid which has a complex multilayer FM structure.

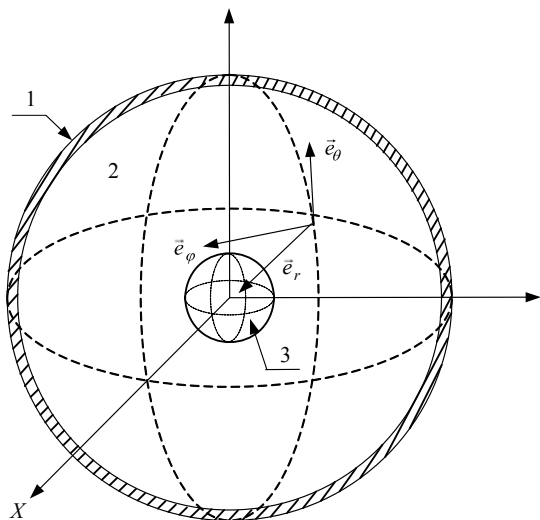
Thus, from the above it follows that it is necessary to solve the problem of scattering an incident plane electromagnetic wave on a multilayer structure having the form of embedded ellipsoids. It is well known that the cell wall is heterogeneous in composition, and therefore in dielectric constant, and has a rather high electric potential.

So, let the center of the cell of the bio-object coincide with the center of the rectangular Cartesian coordinate system. For definiteness, we assume that a plane wave propagates normally to the cell surface, and its electric vector is directed tangentially to the surface (Fig. 1). In addition, for simplicity, we assume that the cell has a spherical shape. The time dependence is determined by the factor $e^{j\omega t}$, which will be omitted in the future. In the arbitrary case of propagation of an electromagnetic wave incident on a cell of a living organism, one can always find the projection of its electric component onto the direction tangential to the surface of the shell.

In the indicated FM consist figure, 1 corresponds to the membrane, 2 to the cytoplasm, 3 to the nucleus.

As is write at [29], in the general case, the electromagnetic field inside the object in question cannot be obtained from a single scalar function, which depends on the coordinate and time. This is possible only in a rectangular coordinate system, wherein a three-dimensional scalar wave equation the variables are easily separated. As for the spherical coordinate system, despite the possibility of separation of variables in the three-dimensional scalar wave equation, it is impossible to obtain the components of the electromagnetic field from the obtained solution. Because of this, it is necessary to find a solution to the vector wave equation. For this, the electromagnetic field must be decomposed into two components, each of which is obtained from one scalar function that satisfies the wave by equation [29, 30].

Fig. 1 Fall of a plane electromagnetic wave on the cell of a bio-object



We assume that each of the layers of the FM cell is homogeneous; that is, it has a constant dielectric constant. We denote the dielectric constant of the medium surrounding the cell ε_0 ; we will also consider the membrane permeability to be the same; the permeability of the cytoplasm is denoted ε_1 , and the nucleus is ε_2 . Since the environment surrounding the cell and the cell itself are non-magnetic, their magnetic permeability is the same and equal $\mu_0 = 4\pi 10^{-7} \text{ H} \cdot \text{M}^{-1}$. As mentioned above, to solve the problem, we expand the incident field in two vector spherical wave functions \vec{M} and \vec{N} [29–31]. The solution is obtained using a spherical coordinate system (r, φ, θ) (Fig. 1).

The electromagnetic field penetrated from free space into the cytoplasm can represent in a spherical coordinate system. In [29], it was shown that in this case, the electric \vec{E}^{pad} and magnetic \vec{E}^{nad} components of the incident field can be written in the form:

$$\begin{aligned} \vec{E}^{\text{pad}} &= E_0 \sum_{n=1}^{\infty} i^n \frac{2n+1}{n(n+1)} \left(\vec{M}_{no}^+ i \vec{N}_{ne}^+ \right); \\ \vec{H}^{\text{nad}} &= -\frac{k_1 E_0}{\mu_0 \omega} \sum_{n=1}^{\infty} i^n \frac{2n+1}{n(n+1)} \left(\vec{M}_{ne}^+ i \vec{N}_{no}^+ \right), \quad i = \sqrt{-1}; \end{aligned} \quad (1)$$

$$\begin{aligned} \vec{M}_{(n^o)}^+ &= \sqrt{\frac{\pi}{2k_1 r}} J_{n+\frac{1}{2}}(k_1 r) \left[\pm \vec{e}_\Theta \frac{1}{\sin \Theta} P_n^{(1)} \right] \\ &\quad \times (\cos \Theta)_{\sin}^{\cos} \varphi - \vec{e}_\varphi \frac{d}{d\Theta} P_n^{(1)} (\cos \Theta)_{\sin}^{\cos} \varphi \Big]; \end{aligned} \quad (2)$$

$$\vec{N}_{n^e}^+ = \sqrt{\frac{\pi}{2}} \frac{1}{k_1 r} \left\{ \begin{aligned} &\vec{e}_r \frac{n(n+1)}{\sqrt{k_1 r}} J_{n+\frac{1}{2}}(k_1 r) P_n^{(1)} (\cos \theta)_{\sin}^{\cos} \varphi \\ &+ \vec{e}_\theta \left[\sqrt{k_1 r} J_{n+\frac{1}{2}}(k_1 r) \right]' \frac{d}{d\theta} P_n^{(1)} (\cos \theta)_{\sin}^{\cos} \varphi \\ &\pm \vec{e}_\theta \frac{1}{\sin \theta} \left[\sqrt{k_1 r} J_{n+\frac{1}{2}}(k_1 r) \right] P_n^{(1)} (\cos \theta)_{\sin}^{\cos} \varphi' \end{aligned} \right\}; \quad (3)$$

where is the n —harmonic number of the incident field; E_0 —the amplitude of the electrical component of the incident field; $P_n^{(1)}(\cos \theta)$ —the associated functions of Legendre; indices o or e mean the choice of the upper or lower variant of the trigonometric function and sign; $J_{n+\frac{1}{2}}(k_1 r)$ —Bessel functions of the first kind of half-integer order; $\vec{e}_r, \vec{e}_\varphi, \vec{e}_\theta$ —coordinate unit vectors; the derivative is taken with respect to the variable $k_1 r$; $k_1 = \omega \sqrt{\varepsilon_1 \mu_0}$ —wave number in the environment surrounding the grain; $\omega = 2\pi f$ —circular frequency of the incident wave.

The components of the scattered wave $\vec{H}^{\text{pacc}}, \vec{E}^{\text{pacc}}$ in this case, have the form:

$$\vec{E}^{\text{pacc}} = E_0 \sum_{n=1}^{\infty} i^n \frac{2n+1}{n(n+1)} \left(a_n^{\text{pacc}} \vec{M}_{no}^- - i b_n^{\text{pacc}} \vec{N}_{ne}^- \right);$$

$$\vec{H}^{\text{pacc}} = -\frac{k_1}{\omega\mu_0} E_0 \sum_{n=1}^{\infty} i^n \frac{2n+1}{n(n+1)} \left(b_n^{\text{pacc}} \vec{M}_{ne}^- - i a_n^{\text{pacc}} \vec{N}_{no}^- \right); \quad (4)$$

where a_n^{pacc} and b_n^{pacc} are the reflection coefficients for the electric and magnetic component of the incident electromagnetic field.

The functions \vec{M}_{ne}^- and \vec{N}_{ne}^- are obtained from \vec{M}_{ne}^+ and \vec{N}_{ne}^+ by replacing $J_{n+\frac{1}{2}}(k_1 r)$ the Hankel function of the second kind of half-integer order $H_{n+\frac{1}{2}}^{(2)}(k_1 r)$, it should be noted that the plus sign refers to the falling fields, and the minus sign refers to the scattered fields.

Finally, the internal field is defined using expressions:

$$\begin{cases} \vec{E} = E_0 \sum_{n=1}^{\infty} i^n \frac{2n+1}{n(n+1)} \left(a_n \vec{M}_{no} - i b_n \vec{N}_{ne} \right) \\ \vec{H} = -\frac{k_1}{\omega\mu_0} E_0 \sum_{n=1}^{\infty} i^n \frac{2n+1}{n(n+1)} \left(b_n \vec{M}_{ne} - i a_n \vec{N}_{no} \right) \end{cases}; \quad (5)$$

where a_n and b_n are the transmission coefficients of the electric and magnetic component of the incident electromagnetic field inside the cell nucleus.

Here \vec{M}_{ne} and \vec{N}_{ne} they have the same form as in (2) and (3), but $k_1 = \omega\sqrt{\varepsilon_1\mu_0}$ are replaced by $k_2 = \omega\sqrt{\varepsilon_2\mu_0}$.

Using the boundary conditions on the surface of the sphere, which sew together the tangential components of the external and internal fields, we obtain the system of equations:

$$\begin{cases} \left[\begin{matrix} \vec{e}_r, \left(\vec{E}^{\text{пад}} + \vec{E}^{\text{pacc}} \right) \end{matrix} \right] = \left[\begin{matrix} \vec{e}_r, \vec{E} \end{matrix} \right] \\ \left[\begin{matrix} \vec{e}_r, \left(\vec{H}^{\text{пад}} + \vec{H}^{\text{pacc}} \right) \end{matrix} \right] = \left[\begin{matrix} \vec{e}_r, \vec{H} \end{matrix} \right] \end{cases}; \quad (6)$$

To solve this system and determine the coefficients a_n , b_n and a_n^{pacc} , b_n^{pacc} substitute expressions (1), (4), (5) into it. As a result, we get:

$$\begin{cases} \left[\begin{matrix} \vec{e}_r, \left(\sum_{n=1}^{\infty} i^n \frac{2n+1}{n(n+1)} \left(\vec{M}_{no}^+ - i \vec{N}_{ne}^+ \right) + \sum_{n=1}^{\infty} i^n \frac{2n+1}{n(n+1)} \left(a_n^{\text{pacc}} \vec{M}_{no}^- - i b_n^{\text{pacc}} \vec{N}_{ne}^- \right) \right) \end{matrix} \right] \\ = \left[\begin{matrix} \vec{e}_r, \sum_{n=1}^{\infty} i^n \frac{2n+1}{n(n+1)} \left(a_n \vec{M}_{no} - i b_n \vec{N}_{ne} \right) \end{matrix} \right] \\ \left[\begin{matrix} \vec{e}_r, k_1 \left(\sum_{n=1}^{\infty} i^n \frac{2n+1}{n(n+1)} \left(\vec{M}_{ne}^+ + i \vec{N}_{no}^+ \right) + \sum_{n=1}^{\infty} i^n \frac{2n+1}{n(n+1)} \left(b_n^{\text{pacc}} \vec{M}_{ne}^- + i a_n^{\text{pacc}} \vec{N}_{no}^- \right) \right) \end{matrix} \right] \\ = \left[\begin{matrix} \vec{e}_r, k_2 \sum_{n=1}^{\infty} i^n \frac{2n+1}{n(n+1)} \left(b_n \vec{M}_{ne} + i a_n \vec{N}_{no} \right) \end{matrix} \right] \end{cases}. \quad (7)$$

We consider that $\vec{M}_{n_e} = M_{\theta n_e} \vec{e}_\theta + M_{\varphi n_e} \vec{e}_\varphi$ and $\vec{N}_{n_e} = N_{r n_e} \vec{e}_r + N_{\theta n_e} \vec{e}_\theta + N_{\varphi n_e} \vec{e}_\varphi$.

Then, based on the rule for computing the vector product [32], we conclude that the equations in the system will contain only θ and φ the components of the vectors. In other words,

$$\begin{aligned}
 & k_1 \left\{ \begin{aligned} & \sum_{n=1}^{\infty} i^n \frac{2n+1}{n(n+1)} [(-M_{\varphi ne}^+ - iN_{\varphi no}^+) \vec{e}_\theta + (M_{\theta ne}^+ + iN_{\theta no}^+) \vec{e}_\varphi] \\ & + \sum_{n=1}^{\infty} i^n \frac{2n+1}{n(n+1)} \left[\begin{aligned} & (-b_n^{\text{pacc}} M_{\varphi ne}^- - ia_n^{\text{pacc}} N_{\varphi no}^-) \vec{e}_\theta \\ & + (b_n^{\text{pacc}} M_{\theta ne}^- + ia_n^{\text{pacc}} N_{\theta no}^-) \vec{e}_\varphi \end{aligned} \right] \end{aligned} \right\} \\
 & = k_2 \sum_{n=1}^{\infty} i^n \frac{2n+1}{n(n+1)} [(-b_n M_{\varphi ne} - ia_n N_{\varphi no}) \vec{e}_\theta + (b_n M_{\theta ne} + ia_n N_{\theta no}) \vec{e}_\varphi]. \quad (8)
 \end{aligned}$$

Since vectors can only be equal if their respective components are equal, we obtain a system of four linear algebraic equations for determining four unknown coefficients. This system is as follows:

$$\begin{aligned}
 & \sum_{n=1}^{\infty} i^n \frac{2n+1}{n(n+1)} (M_{\varphi no}^+ - iN_{\varphi ne}^+) + \sum_{n=1}^{\infty} i^n \frac{2n+1}{n(n+1)} (a_n^{\text{pacc}} M_{\varphi no}^- - ib_n^{\text{pacc}} N_{\varphi ne}^-) \\
 & = \sum_{n=1}^{\infty} i^n \frac{2n+1}{n(n+1)} (a_n M_{\varphi no} - ib_n N_{\varphi ne}); \\
 & \sum_{n=1}^{\infty} i^n \frac{2n+1}{n(n+1)} (M_{\theta no}^+ - iN_{\theta ne}^+) + \sum_{n=1}^{\infty} i^n \frac{2n+1}{n(n+1)} (a_n^{\text{pacc}} M_{\theta no}^- - ib_n^{\text{pacc}} N_{\theta ne}^-) \\
 & = \sum_{n=1}^{\infty} i^n \frac{2n+1}{n(n+1)} (a_n M_{\theta no} - ib_n N_{\theta ne}); \\
 & k_1 \left[\sum_{n=1}^{\infty} i^n \frac{2n+1}{n(n+1)} (M_{\varphi ne}^+ + iN_{\varphi no}^+) + \sum_{n=1}^{\infty} i^n \frac{2n+1}{n(n+1)} (b_n^{\text{pacc}} M_{\varphi ne}^- + ia_n^{\text{pacc}} N_{\varphi no}^-) \right] \\
 & = k_2 \sum_{n=1}^{\infty} i^n \frac{2n+1}{n(n+1)} (b_n M_{\varphi ne} + ia_n N_{\varphi no}); \\
 & k_1 \left[\sum_{n=1}^{\infty} i^n \frac{2n+1}{n(n+1)} (M_{\theta ne}^+ + iN_{\theta no}^+) + \sum_{n=1}^{\infty} i^n \frac{2n+1}{n(n+1)} (b_n^{\text{pacc}} M_{\theta ne}^- + ia_n^{\text{pacc}} N_{\theta no}^-) \right] \\
 & = k_2 \sum_{n=1}^{\infty} i^n \frac{2n+1}{n(n+1)} (b_n M_{\theta ne} + ia_n N_{\theta no}) \quad (9)
 \end{aligned}$$

We bring this system to the standard form of a linear inhomogeneous algebraic equations system [32]:

$$\begin{aligned}
& \sum_{n=1}^{\infty} i^n \frac{2n+1}{n(n+1)} (-a_n M_{\varphi no} + i b_n N_{\varphi ne}) \\
& + \sum_{n=1}^{\infty} i^n \frac{2n+1}{n(n+1)} (a_n^{\text{pacc}} M_{\varphi no}^- - i b_n^{\text{pacc}} N_{\varphi ne}^-) \\
& = \sum_{n=1}^{\infty} i^n \frac{2n+1}{n(n+1)} (-M_{\varphi no}^+ + i N_{\varphi ne}^+); \\
& \sum_{n=1}^{\infty} i^n \frac{2n+1}{n(n+1)} (a_n M_{\theta no} - i b_n N_{\theta ne}) \\
& + \sum_{n=1}^{\infty} i^n \frac{2n+1}{n(n+1)} (-a_n^{\text{pacc}} M_{\theta no}^- + i b_n^{\text{pacc}} N_{\theta ne}^-) \\
& = \sum_{n=1}^{\infty} i^n \frac{2n+1}{n(n+1)} (-M_{\theta no}^+ - i N_{\theta ne}^+); \\
& k_2 \sum_{n=1}^{\infty} i^n \frac{2n+1}{n(n+1)} (-b_n M_{\varphi ne} - i a_n N_{\varphi no}) \\
& + k_1 \sum_{n=1}^{\infty} i^n \frac{2n+1}{n(n+1)} (b_n^{\text{pacc}} M_{\varphi ne}^- + i a_n^{\text{pacc}} N_{\varphi no}^-) \\
& = k_1 \sum_{n=1}^{\infty} i^n \frac{2n+1}{n(n+1)} (-M_{\varphi ne}^+ - i N_{\varphi no}^+); \\
& k_2 \sum_{n=1}^{\infty} i^n \frac{2n+1}{n(n+1)} (b_n M_{\theta ne} + i a_n N_{\theta no}) \\
& + k_1 \sum_{n=1}^{\infty} i^n \frac{2n+1}{n(n+1)} (-b_n^{\text{pacc}} M_{\theta ne}^- - i a_n^{\text{pacc}} N_{\theta no}^-) \\
& = k_1 \sum_{n=1}^{\infty} i^n \frac{2n+1}{n(n+1)} (M_{\theta ne}^+ + i N_{\theta no}^+); \tag{10}
\end{aligned}$$

We will continue further modeling already considering vector functions, which will allow us to calculate the discriminant of system (10). As is known [31], such systems have a unique solution if their discriminant is not equal to zero. This can be verified by substituting in (10) the component of the eigenvector functions \vec{M} and \vec{N} , which are obtained from (2) and (3). This allows us to calculate the discriminant of system (10) and make sure that it is not equal to zero.

4 Experimental Research

Functional materials are used in many developments of the authors [33–51], where it was required to study the effect of a magnetic field on their functioning.

The tests were performed as follows. To assess the effect of the magnetic field of industrial frequency was used special stand. Scheme of which is shown in Fig. 2. The stand consists of a core 1, a coil 2, a power supply 3, and a current meter 4. When supplying AC voltage U from the source 3 to the coil 2 in the air gap λ core 1 creates an alternating magnetic field with induction B_λ . Induction B_λ causes in a special measuring coil 2, also placed in the gap λ , voltage U_{BK} , functionally dependent on induction B_λ .

Using the data of the measuring coil 2, a functional dependence $U_{BK} = f(B_\lambda)$ was determined. As is known [52], the inductive voltage U_{BK} in the coil 5 can be determined as

$$U_{BK} = B_\lambda \cdot S \cdot N \cdot \omega \quad (11)$$

where B_λ —magnetic induction in the gap λ ; S —the area of the coil 5 through which the magnetic flux flow; $N = 10$ —the number of turns of the coil 5; $\omega = 2\pi \cdot 50 \text{ c}^{-1}$ —frequency.

Contrariwise

$$S = \frac{\pi}{4} (D_{BBK} + 2d_\Pi)^2 \quad (12)$$

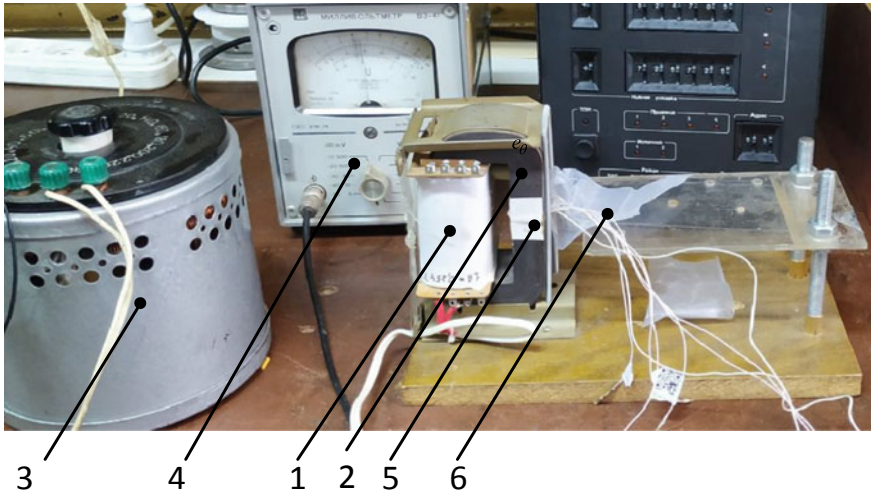


Fig. 2 Experimental research model: 1—special measuring transformer; 2—coil special measuring transformer; 3—power supply AC voltage; 4—test device (current meter); 5—testing sample of functional materials; 6—table

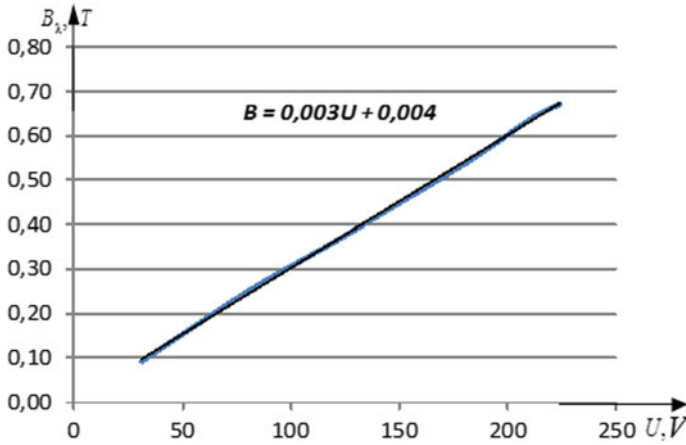


Fig.3 Functional dependence for measuring coil

where $D_{\text{BBK}} = 10,4$ mm—the internal diameter of the measuring coil 5; $d_{\Pi} = 0,1$ mm—the diameter of the wire of the measuring coil 2.

Using (11) and (12) and numerical values, we find that

$$U_{\text{BK}} = 0.267 \cdot B_{\lambda} \tag{13}$$

and

$$B_{\lambda} = \frac{U_{\text{BK}}}{0.267} \tag{14}$$

The results of the experimental determination of the functional dependence $B_{\lambda} = f(U_{\text{BK}})$ for measuring coil 2 (shown in Fig. 1) and its approximation function are shown in Fig. 3.

The results of the experimental study influence industrial frequency magnetic field on sensitive elements as shown in Fig. 4.

In Fig. 4, the determination dependence magnetic induction by influence magnetic field on sensitive elements.

The obtained experimental results allow having information about the electromagnetic situation in the locations of biological objects, sensors, and systems, using the obtained theoretical laws to establish the maximum allowable levels of noise immunity, which provides electromagnetic stability.

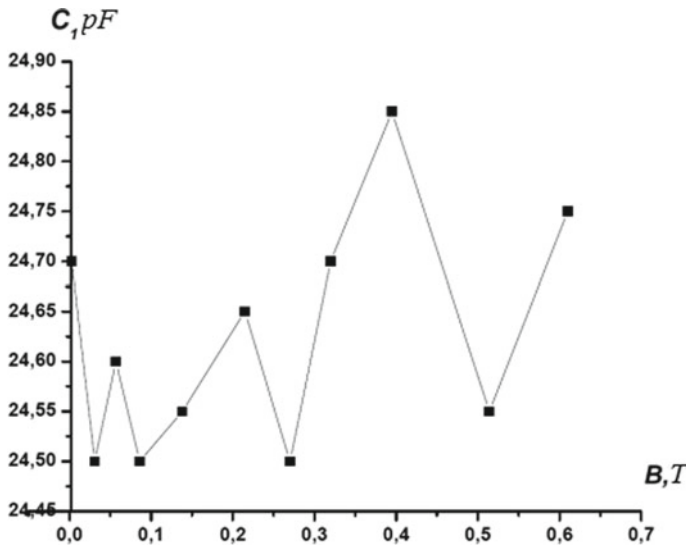


Fig.4 Capacitive C_1 versus magnetic induction B_λ

5 Conclusion

We will continue further modeling already considering vector functions, which will allow us to calculate the discriminant of system (10). Systems have a unique solution if their discriminant is not equal to zero. This can be verified by substituting in (10) the component of the eigenvector functions \vec{M} and \vec{N} , which are obtained from (2) and (3). This allows us to calculate the discriminant of system (10) and make sure that it is not equal to zero. The experimental studies carried out have confirmed the obtained theoretical laws.

References

1. Zaitsev IO, Levytskyi A, Kromplyas B, Panchyk M, Bereznychenko V (2019) Study influence industrial frequency magnetic field on capacitive pressing sensor for large turbogenerator core clamping system. In: Proceedings of the 2019 IEEE Ukraine international conference on electrical and computer engineering (UKRCON-2019), 2–6 July, Lviv(Ukraine):566–569 <https://doi.org/10.1109/UKRCON.2019.8879949>
2. DSTU 2465-94 (1995) Compatibility of technical means of electromagnetic. Resistance to magnetic field frequencies of the network. Technical requirements and test methods (IEC 61000-4-8: 1993), Kiev, 31p
3. DSTU 2793-94 (1994) Compatibility of technical means of an electromagnet. Resistance to strong electromagnetic interference. General provisions. Gosstandart of Ukraine, Kyiv, 15p
4. DSTU 2862-94 (1995) Reliability of technology. Methods of calculation of reliability indicators. General requirements. Gosstandart of Ukraine, Kyiv, 86p

5. STU IES 61000 Electromagnetic compatibility
6. Baranov G, Komisarenko O, Zaitsev IO, Chernytska I (2021) S.M.A.R.T. technologies for transport tests networks, exploitation and repair tools. In: Proceedings of the international conference artificial intelligence and smart systems (ICAIS), 25–27 March 2021, Pichanur(India):621–625 <https://doi.org/10.1109/ICAIS50930.2021.9396055>
7. Zaitsev IO, Levytskyi AS, Kromplyas BA (2019) Capacitive distance sensor with coplanar electrodes for large turbogenerator core clamping system. In: Proceedings of the 2019 IEEE 39th international conference on electronics and nanotechnology (ELNANO), 16–18 April, Kiev(Ukraine):644–647. <https://doi.org/10.1109/ELNANO.2019.8783916>
8. Zaitsev IO, Levytskyi AS, Novik AI, Bereznychenko VO, Smyrnova AM (2019) Research of a capacitive distance sensor to grounded surface. *Telecom Radio Eng* 78(2):173–180. <https://doi.org/10.1615/TelecomRadEng.v78.i2.80>
9. Zaitsev IO, Levytskyi AS (2017) Determination of response characteristic of capacitive coplanar air gap sensor. In: Proceedings of the 2017 IEEE microwaves, radar and remote sensing symposium (MRRS-2017), Aug 29–June 30, Kyiv(Ukraine), pp 85–88. <https://doi.org/10.1109/MRRS.2017.8075034>
10. Jiang X, Chen J, Shu L, Hu J, Zhang Z, Wang S (2013) Studying corona onset characteristics after rime ice accumulation on energized stranded conductors. *IEEE Trans Dielectr Electr Insul* 20(5):1799–1807. <https://doi.org/10.1109/TDEI.2013.6633711>
11. Bian X, Yu D, Meng X, MacAlpine M, Wang L, Guan Z et al (2011) Corona-generated space charge effects on electric field distribution for an indoor corona cage and a monopolar test line. *IEEE Trans Dielectr Electr Insul* 18:1767–1778
12. Komarov EV, Pokrovsky AD, Sergeev VG (1984) Test of magnetic materials and systems: monography. Energoatomizdat, Moscow, 376p
13. Blinov I, Zaitsev IO, Kuchanskyy VV (2020) Problems, methods and means of monitoring power losses in overhead transmission lines. In: Babak V, Isaenko V, Zaporozhets A (eds) *Systems, decision and control in energy I*, Springer, pp 123–136. https://doi.org/10.1007/978-3-030-48583-2_8
14. Zaitsev IO, Kuchanskyy VV (2021) Corona discharge problem in extra high voltage transmission line. In: Zaporozhets A, Artemchuk V (eds) *Systems, decision and control in energy II*. Springer:3–30. https://doi.org/10.1007/978-3-030-69189-9_1
15. Kuchanskyy V, Zaitsev I (2020) Corona discharge power losses measurement systems in extra high voltage transmissions lines. In: Proceedings of 2020 IEEE 7th international conference on energy smart systems (ESS), Kyiv, Ukraine:48–53. <https://doi.org/10.1109/ESS50319.2020.9160088>
16. Zaitsev IO, Levytskyi AS, Kromplyas BA (2017) Hybrid capacitive sensor for hydro- and turbo generator monitoring system. In: Proceedings of the international conference on modern electrical and energy system (MEES-17) Nov 15–17, Kremenchuk(Ukraine):288–291. <https://doi.org/10.1109/MEES.2017.8248913>
17. Zaitsev IO, Levytskyi AS (2020) Hybrid electro-optic capacitive sensors for the fault diagnostic system of power hydrogenerator. In: Ebrahimi A (ed) *Clean generators—advances in modeling of hydro and wind generators*. Intechopen:25–42. <https://doi.org/10.5772/intechopen.77988>
18. Turan J, Ovsenik L, Turan J (2005) Optically powered fiber optic sensors. *Acta Electrotechnica et Informatica* 5–7
19. Rosolem J.B., Florida C, Sanz J (2010) Optical system for hydrogenerator monitoring. In: Proceedings of the international council for power electroenergetical systems CIGRE, France(Paris), pp 1–8
20. Zaitsev I, Shpylka A, Shpylka N (2020) Output signal processing method for fiber bragg grating sensing system. In: Proceedings of the 15th international conference on advanced trends in radioelectronics, telecommunications and computer engineering (TCSET-2020). Lviv-Slavske(Ukraine):152–155. <https://doi.org/10.1109/TCSET49122.2020.23541>
21. Sunmee P, Borton D, Kang M, Nurmikko A, Song Y (2013) An implantable neural sensing microsystem with fiber-optic data transmission and power delivery. *Sensors* 13:6014–6031
22. Bao MH (2000) Electrostatic driving and capacitive sensing. *Handb Sens Actuators* 8:139–198

23. Zade A, Tadayon S (2018) US Patent US20180204111A1. System and method for extremely efficient image and pattern recognition and artificial intelligence platform. published July 19
24. Merzhanov AG (1975) *Combust Sci Technol* 10:195
25. Evans AG, Charles EA (1977) Fracture toughness determination by indentation. *Ceram Soc* 59(7):371–372
26. Baranov GL, Komisarenko OS (2019) Process infological models in problems of heterogeneous interaction of complex dynamic systems and non-stationary environment. *Visnyk Nacionalnogo transportnogo universytetu* 1(40):3–12
27. Baranov GL, Komisarenko OS (2018) Infological modeling of complex processes of formation of new substances. *Modelyuvannya ta informacijni tehnologiyi: zb. nauk. pr. NAS Ukrainy* 85:12–22
28. Leleur S (2012) *Complex strategic choices: applying systemic planning for strategic decision making*. Springer-Verlag, London, p 176
29. Nikolsky VV, Nikolskaya TN (1989) *Electrodynamics and radio wave propagation*. Moscow Izdatel Nauka
30. Pirotti AE, Cherenkov AD (2000) Modeling the distribution of internal electromagnetic fields in deformed biological objects. *Bulletin of the Kharkov State Polytechnic University, Kharkov, Issue 99*:130–133
31. Pirotti OE, Svergun YF (2001) The distribution of electromagnetic fields in deformed biological objects. *Proceedings of the taurida state agrotechnical academy, Melitopol, Issue 1, T 19*, pp 11–15
32. Alberts B, Bray D et al (1994) *Molecular cell biology*. M.: Mir. T 1, 430p
33. Levytskyi AS, Zaitsev IO, Kobzar KO (2018) Measuring the stroke of cone disk springs in power accumulators of the turbogenerator stator core using a capacitive sensor. *Devices Methods Meas* 9(2):121–129. <https://doi.org/10.21122/2220-9506-2018-9-2-121-129>. (IndexinWebOf-Science)
34. Zaitsev IO, Levytskyi AS, Sydorhuk VE (2017) Air gap control system for hydrogenerators 8(2):122–130. <https://doi.org/10.21122/2220-9506-2017-8-2-122-130>
35. Braginet IA, Sydorhuk VE, other (2015) Analysis of phase system of automatic frequency correction in laser rangefinder. *Tekhnichna elektrodynamika* 1:91–94
36. Braginet IA, Nizhensky AD, other (2013) Dynamic properties of frequency-phase laser range finder systems with digital frequency synthesizers. *Tekhnichna elektrodynamika* 3:87–92
37. Braginet IA, Nizhensky AD, other (2013) The phase laser measurer of vibrations parameters with an extended frequency range. *Tekhnichna elektrodynamika* 1:82–86
38. Braginet IA, Masyurenko, YuA, other (2015) Appling of compensatory measuring method of phase shift for laser range finder. *Tekhnichna elektrodynamika* 3:75–80
39. Latenko VI, Ornatsky IA, Fil SO, Zaitsev IO (2021) Digital converters metrological specification for resistant thermal thermosensors compare. *TekhnichnaElektrodynamika* 1:84–89. <https://doi.org/10.15407/techned2021.01.084>
40. Levytskyi AS, Zaitsev IO, Berezhnychenko VO (2019) Features of measurement of radial beating of cylindrical surfaces of a shaft of the hydraulic unit. *Hydropower Ukraine* 1–2:39–44
41. Levytskyi AS, Zaitsev IO, Berezhnychenko VO (2019) Relative and absolute radial vibration of the shaft of the vertical unit. *Hydropower Ukraine* 3–4:36–39
42. Levytskyi AS, Zaitsev IO, Berezhnychenko VO, Sukhorukova OE (2020) Measuring transducer for air gap capacitive sensor in hydrogenerator. *Devices Methods Meas* 11(1):33–41. <https://doi.org/10.21122/2220-9506-2020-11-1-33-41>
43. Zaitsev I, Panchyk MV (2020) Physical processes and their influence on the development of defects in the stator core of powerful generators. *Sci Educ New Dimension. Nat Tech Sci* 224:81–84. <https://doi.org/10.31174/SEND-NT2020-224VIII27-20>
44. Zaitsev IO (2017) Electric machines faults monitoring system with hybrid electro-optic capacitive mechanical sensors. In: *Abstracts of the 2017 IEEE international young scientists forum on applied physics and engineering (YSF-2017)*, 17–20 Oct 2017, Ukraine, Lviv, pp 15–18
45. Levytskyi A, Zaitsev I (2016) Hybrid fiber-optic measuring tools for control and diagnostic parameters of hydrogenerators. *Hydropower of Ukraine* 3–4:32–33

46. Zaitsev IO, Levytskyi AS, Sydorчук VE (2017) Air gap control system for hydrogenerators. *Devices Methods Meas* 8(2):122–130
47. Berezhnychenko VO, Zaitsev IO (2021) Contactless capacitive sensor of the system for monitoring the parameters of the beating of the powerful electrical machines shafts. *Works Inst Electroynamics Nat Acad Sci Ukraine*. 57:81–88. <https://doi.org/10.15407/publishing2020.57.081>
48. Zaitsev I, Levytskyi A, Berezhnychenko V (2021) Development shaft run-out measurement transducers for powerful generators fault control system with capacitive coplanar concentric sensor. In: *Proceedings of the 1st International scientific and practical conference theory and practice of science: key aspects*. Rome(Italy):1014–2021. <https://doi.org/10.51582/interconf.19-20.02.2021.103>
49. Zaitsev I, Levytskyi AS, Kromplyas BA, Panchyk MV, Berezhnychenko VO (2019) Study industrial frequency magnetic field influence on STM32F051K8T6 microcontroller functioning stability. *Works Inst Electroynamics NAS Ukraine* 52:80–86. <https://doi.org/10.15407/publishing2019.52.080>
50. Levytskyi AS, Zaitsev IO, Kromplyas BA (2016) Determination of the response characteristic of the capacitive sensor of the air gap in the hydrogenerator СТК538/160–70М. *Works Inst Electroynamics NAS Ukraine* 43:134–136
51. Levytskyi AS, Zaitsev IO, Kromplyas BA (2016) The errors of the capacitive measurer gap in the hydrogenerator. *Works Inst Electroynamics Nat Acad Sci Ukraine* 44:50–55
52. Komarov EV, Pokrovskii AD, Sergeev VG (1984) *Testing of magnetic materials and systems*. Moscow, 376 p

Chapter 65

Design and Analysis of Combinational Circuits Using Reversible and Irreversible Gates



S. Saiteja, Md. Munwar, Y. MadhukarReddy, and A. PramodKumar

Abstract Traditional CMOS topologies are disseminate power as a piece of data. This dispersal of energy is considered as force scattering and assumes a vital part to the extent of a low force configuration. Now-a-days Reversible logics are used in advanced circuits. Configuration such as empowering better testing of flaws, permitting almost energy free calculation, heat dissemination and empowering better testing on flaws and permitting higher circuit densities depend on reversible logic. A 8-digit Reversible ALU is proposed in this paper. By using 1 bit ALUs, 8 bit ALU is planned. The snake unit and the control unit are the two significant units of a 1 cycle ALU. The Haghparast and Navi Gate (HNG) is utilized in snake unit and the control output gate (COG) is utilized in control unit. The main sector of this paper is that, when it is diverged with a variety of articles, this ALU configuration has decreased entryway tally and semiconductor tally.

Keywords CMOS · ALU · HNG · COG · Reversible logic gate

Objectives of the proposed work

To design the ALU using reversible and irreversible logic gates. To Analysis and calculate the power and size of ALU design.

Motivation

Digital model is an remarkable and a extremely board field. In our daily life we are using digital designs for numerous applications such as mobile phones, computers and video cameras etc... In reality, high performance and low power digital products are the future growing business.

S. Saiteja (✉) · Md. Munwar · Y. MadhukarReddy · A. PramodKumar
Department of ECE, Vardhaman College of Engineering, Shamshabad, Hyderabad, India

A. PramodKumar
e-mail: pramodkumar@vardhaman.org

Methodology

The suggested circuit is designed with the aid of Reversible logic technique. By using this technique, the power and size parameters are measured. As anticipated, the results obtained are efficient, when compared to the existing circuit.

1 Introduction

In the recent days, the major concerns in VLSI chip designing are about size, power dissipation which may hinder the performance of the circuit. Swamynathan [1] makes the application of reversible logic technology mandatory because of its significance over conventional logic gates. The irreversible logic gates do not adhere to the constraints like size, power dissipation etc. Reversible logic acting as a Deepa [2] crucial part in quantum computing and its implementation in nano technology scale. Dhanabal [3] says there are great losses associated with power dissipation and it has been proven that reversible logic has been one of the solutions. In irreversible logic gates the input vector quantity is not equal to the output vector quantity. Mehrabani [4] says these garbage outputs may in turn lead to the power dissipation in the circuits. This drawback of irreversible gates makes the use the logic gates which can be restored is mandatory. Here the output vector quantity has the same value as the input vector quantity. This helps in mapping the inputs and outputs in a one-to-one manner. In this way, it is also helpful in the inputs with the outputs and re-utilizing them for the further stages. Above all quantum cost can be decreased with the reversible logic gates. Srivastava [5] proved Reversible logic has applications in computer security and transaction processing. These advancements in reversible logic and its wide spread applications in designing, paves the way for designing an ALU. The ALU has many applications in performing complex operations and multi-precision arithmetic algorithms. The actual disputes in the model of topologies is by implementing reversible logic. Saligram [6] says that the number of garbage outputs can be mitigated by the reversible logic for the circuit design. Several alternative factors that appear in to the picture are gate tally, number of stable inputs and quantum cost regarding reversible logic is engaged. Landauer [7] In the design Gate tally denotes the number of reversible gates are used. The area and power dissipation is minimized by minimizing the number of transistors. Which is obtaining by minimizing the gate tally. The inputs which are maintained stable at either 0 or 1 are no noise stable inputs, in order to blend the mentioned logic function. The cost of the circuit is determined with the aid of primitive gate cost such as not gate or Feynman Gate. One of the major thing that to be solved now-a-days bansal [8] is power dissipation Nirmal [9] explained that energy dissipation occurs owing to the bits of data loss in the circuits which are constructed using irreversible gates is high. In order to achieve the lower power dissipation and high energy efficiency, reversible kumar [10] stated to increase the performance and speed of the digital designs. By reducing the number of transistors, Anamika [11] said there are several challenges faced by the traditional elements such as energy dissipation and power leakage and so

on. Bennet [12] proved that for each bit of information logic circuits are releases heat wave efficacy confer to the fundamental theory. Moore's law states that the amount of transistors will grows twice for every 18 months.

Arithmetic Logic Unit

Several computing circuits require an ALU as a basic building block. Central processing unit (CPU) is also one of the example of those computing circuits. The operands of n ALU, the inputs are the data on which operations are performed. While discussing the operation of an ALU, generally we use two technical terms called operands and opcode. The operands of an ALU are the inputs applied to the ALU. The opcode is also a input to the ALU which performs the ALU to select which type of operation to be done. An ALU is combinational digital logic circuit whose output does not change accordingly to the change in inputs. For example, a 3 bit opcode can perform 8 different operations.

2 ALU Using Reversible Gates

In Low power VLSI design the power dissipation is the major problem which is minimized by using Reversible logic. Therefore, the reversible logic received great attentions in the present days. There are plenty number of applications of reversible logics in low power CMOS, nanotechnology, quantum computing, DNA computing and Optical information processing. The reversible gates used are the COG and HNG gates. COG stands for Controlled Operation Gate. COG symbol is illustrated in the Fig. 1 and input and output values are mentioned in Table 1.

Fig. 1 Reversible COG gate

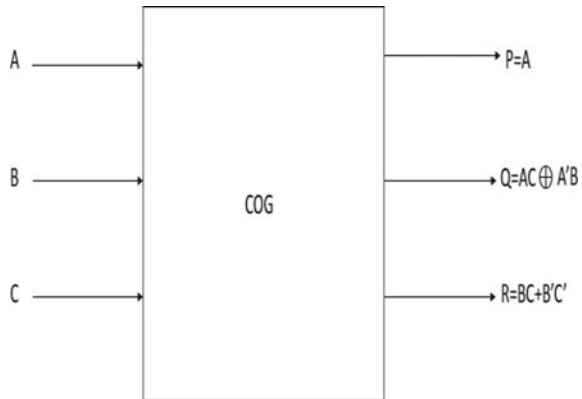


Table 1 Restoring logic COG gate

Input A	Input B	Input C	Input P	Input Q	Input R
1	1	1	1	1	1
1	1	0	1	0	0
1	0	1	1	0	1
1	0	0	1	1	0
0	1	1	0	1	1
0	1	0	0	0	0
0	0	1	0	0	1
0	0	0	0	1	0

2.1 COG Reversible Gate

See Fig. 1

2.2 HNG Reversible Gate

The HNG gate used produces outputs sum and carry. Figure 2 represents the HNG gate symbol.

The Fig. 3 is discuss about the control functions of the COG gates and its electronic circuitry functions are stated clearly. Similarly in the Fig. 4 simple control unit of arithmetic and logical structure of the HNG gate. The schematic diagram of the proposed COG and HNG gates with the aid of reversible logic gates are depicted in the Fig. 5. The Proposed functions are represented in Table 2.

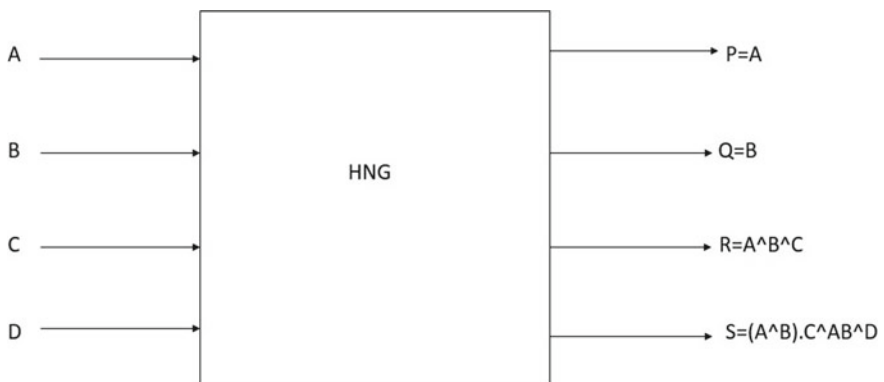


Fig. 2 HNG gate

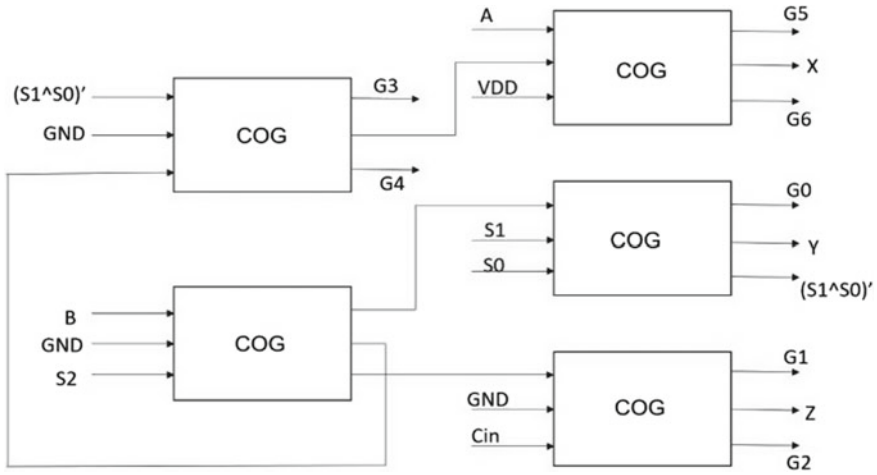


Fig. 3 Block diagram of control electronic circuitry

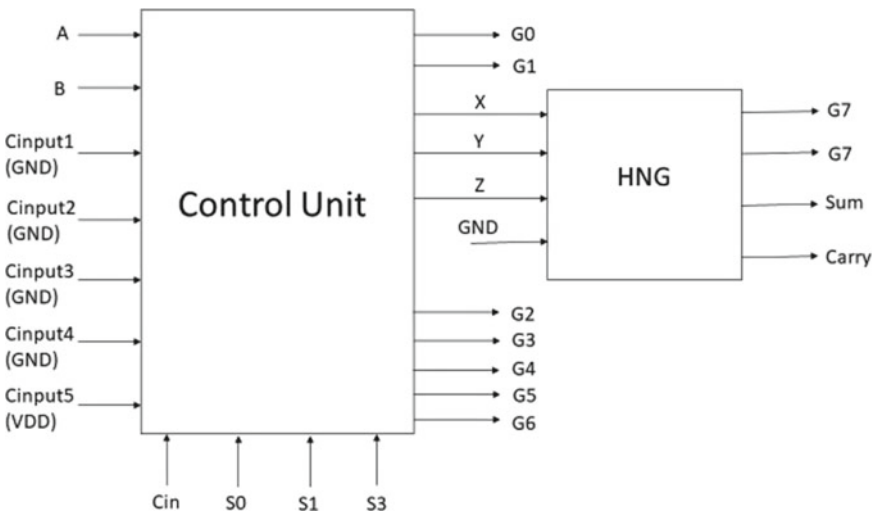


Fig. 4 Block diagram of arithmetic and logical structure

By using cadence virtuoso tool the power analysis of alu using reversible gates is represented in Fig. 6. The schematic of suggested ALU using reversible logic gates is depicted in Fig. 5.

Merits

The digital domain grants the Reversible logic.

1. Power Management

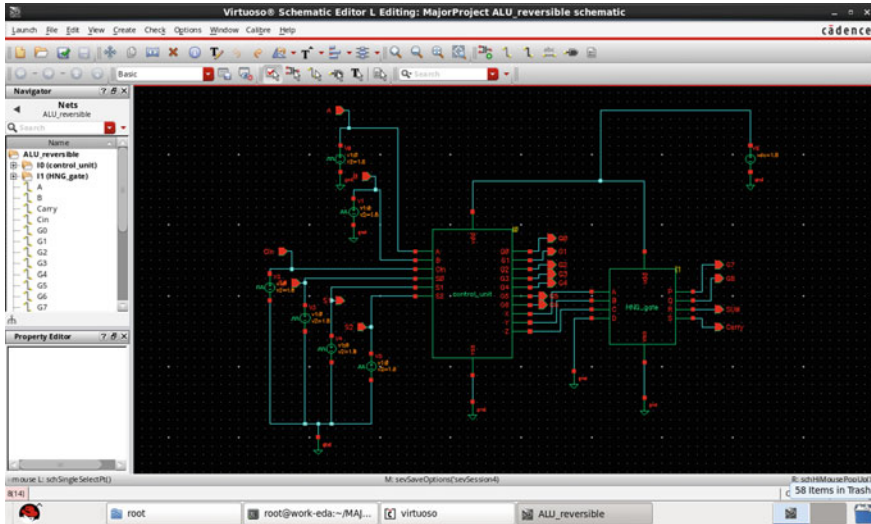


Fig. 5 Schematic diagram of ALU using reversible gates like COG and HNG gates

Table 2 Function table of reversible ALU

S1	S2	S3	C _{in}	Function
0	0	0	1	Increment A
0	0	1	0	Addition
0	1	0	1	Subtraction
0	1	1	0	Decrement
1	0	0	0	Or
1	0	1	0	EXOR
1	1	0	0	EXNOR
1	1	1	0	Nor

2. Heat Management.

Demerits

1. Main disadvantage is high number of constant inputs is used
2. Space consumption is more because of garbage outputs.

3 ALU Using Irreversible Gates

Using these irreversible gates, ALU is constructed. In Fig. 7, ALU carries out 8 operations. Those operations are namely addition, subtraction, Increment A, Decrement A, OR, NOR, XOR, XNOR. These operations are implemented as circuits using basic

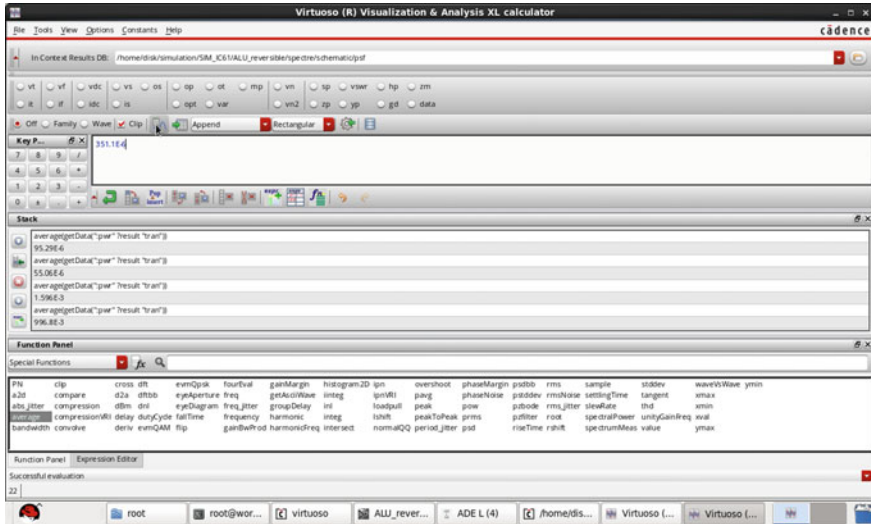


Fig. 6 Power analysis of ALU using reversible gates

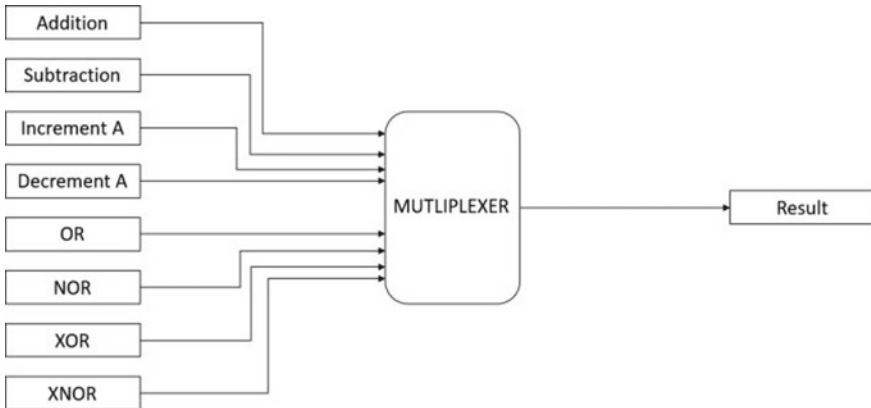


Fig. 7 Block diagram of ALU using irreversible gates

logic gates and then their results are connected to the multiplexer. The multiplexer used here is an 8:1 multiplexer. The multiplexer is used because only one operation is done at a time according to the user requirement. Based on the selection lines and the respective sequence of operations performed the ALU is implemented. The layout of the ALU using irreversible gates is represented in Fig. 7. The schematic diagram of the proposed irreversible gates with the help of multiplexer is represented in Fig. 8.

Figure 9, describe about the power analysis of ALU using irreversible gates. The power consumption is more compare to the reversible gates.

Table 3 Comparison values of proposed reversible and irreversible gates

	Irreversible gate	Reversible gate
Avg. power	1.596E-3 W	351.1E-6 W
No. of transistors	420	332

using reversible gates. The average power required for both the circuits is calculated using the tool and is obtained to be 351.1E-6 W in case of reversible ALU and 1.596E-3 W. The comparison values of the proposed methods are mentioned in Table 3.

5 Conclusion

The advancements in reversible logic and its widespread applications in designing paves the way for designing ALU. The ALU which in turn has many applications in performing complex operations and multiple precision arithmetic algorithms also. Efficiency, quantum cost and power dissipation are certain constraints for reversible logic in producing the outputs and in producing the outputs. When the input and output quantities are same then output vector can determine input vector then it is said to be a reversible circuit. Based on the inputs determined by a programmer a variety of logic outputs must be able to produce any ALU. To enhance the performance of the structure Nanometre size and quantum computing for these reversible gates are used.

It is necessary to reduce the use and defeat of data bits to a minimum by reusing the outputs as inputs to some other stages. All the quantum operations are reversible. The reversible topologies are basic building blocks of quantum computer. It has been proven by many researchers that reversible logic has been one of the solutions in overcoming the drawbacks of irreversible logic like power consumption, production of garbage outputs etc. Reversible logic has utilizations in computer protections, business dealings and the long-term benefits will be in areas like Low power CMOS, quantum computing, nanotechnology, computer visuals, study of low power computations and data path for Digital Signal Processing.

References

1. Swamynathan SM, Banumathi V (2017) Design and analysis of FPGA based 32 bit ALU using reversible gates. In: International conference on electrical, instrumentation and communication engineering (ICEICE2017)
2. Deepa G, Madhuri E, Malashree S, Mamatha K, Supriya KV (2016) Design and implementation of 32-bit ALU with 16 operations using reversible logic gates. *Int Res J Eng Technol* 3(5)
3. Dhanabal R, Bharathi V, Saira S (2013) Design of 16-bit low power ALU-DBGPU. *Int J Eng Technol* 5(3). ISSN: 09754024

4. Mehrabani YS, Eshghi M (2016) Noise and process variation tolerant, low-power, highspeed, and low- energy full adders in CNFET technology. *IEEE Trans VLSI Syst* 24(11):3268–3281
5. Srivastava P, Guduri M, Mehra R, Islam A (2017) Current-mode circuit-level technique to design variation-aware nanoscale summing circuit for ultra-low power applications. *Microsyst Technol* 23(9):4045–4056
6. Saligram R, Rakshith TR (2012) Novel code converter employing reversible logic. *IJCA* 52(18)
7. Landauer R (1961) Irreversibility and heat generation in the computational process. *IBM J Res Develop* 5:183–191
8. Bansal M, Maiya RR (2020) Phototransistor: the story so far. *J Electron* 2(04):202–210
9. Nirmal D (2019) High performance flexible nanoparticles based organic electronics. *J Electron Informatics* 1(1):99–106
10. Kumar U, Sahu L, Sharma U (2016) Performance evaluation of reversible logicgates. In: International conference on ICT in Business Industry and Government (ICTBIG) in 2016
11. Anamika, Bhardwaj R (2018) Reversible logic gates and its performances. In: 2nd International conference on inventive systems and control (ICISC)
12. Bennett CH (1973) Logical reversibility of computations. *IBM J Res Dev* 525–532

Chapter 66

Strengthening a Pavement Layer by Using Fly Ash



Mudigonda Harish kumar and C. Freeda Christy

Abstract Transportation plays an important role in any developing countries. Recently, different modes of transportation are used for traveling, carrying goods, exporting, and importing the goods by comparing with other modes of transportation roads play a key role. In this regard, special care and attention have to be maintained throughout the construction in order to withstand the maximum loads. Stabilization of soil with fly ash will increase the soil properties and by that subgrade and base course strength of the pavement structure will also increase, when compared to normal soil subgrade and base course layers. Test results have shown that the optimum content of fly ash mixed with soil has shown good results.

Keywords Fly ash · Compaction · CBR

1 Introduction

Soil stabilization is the method used to completely modify soil properties and reinforce its engineering functions. Road stabilization will increase the soil strength towards the massive loads of contemporary traffic movements and reduces pavement devastation. The strategies are used to represent the utilization of admixtures in compaction, and coalition of soil. Admixtures are industrial waste, chemical additives and fly ash. The stabilizers determination for a particular region relies essentially upon the sort of soil, assortment of development to create, and accessibility of materials to be pushed off in development. Fly ash base pavement has the benefit of generous strength and sturdiness. Additionally, it is widely available. Subsequently, it turns into the most unequivocal material for the soil stabilization. The moist soil binds with fly ash to make the fly ash settled base. The strength of settled soil can fundamentally depend upon the measure of fly ash utilized in the soil. The extent of fly ash required in soil chooses to help the sort of soil. Portland fly ash is generally

M. Harish kumar (✉) · C. Freeda Christy
School of Civil Engineering, Karunya Institute of Technology and Science, Coimbatore, India

C. Freeda Christy
e-mail: freeda@karunya.edu

utilized as a soil stabilizer attributable to its basic taking care of standard control properties. With the increase in fly ash percentage, the strength of the fly ash in soil will also increase. Many researchers had done research on stabilization of soil with fly ash is also appropriate for granular soil and clay soil with low plasticity index. Unconfined compression strength, subgrade strength are very challenging. Unconfined compression strength worth of stabilized soils will increase with the increment in fly ash to the soil. These soils may be lateritic, black cotton soils, folding soils or the other tropical soils. Soil stabilization mentions to the process within a selected soil. A fly ash material, or alternative chemical or non-chemical materials can be used to boost the properties of soil.

2 Literature Review

Based on the literature review, soil properties can be modified by soil stabilization by using fly ash as a stabilization material, soil stabilization can improve the engineering properties like shear strength of soil, compressive strength and by doing stabilization can control the swell-shrinkage of soil, by that bearing capacity of soil subgrade and base course layers can be increased to support the structures. Different types of stabilizations are available along with different stabilizing materials, which are used all over the world. Some of them are summarized as follows.

In Saksham et al. [1], cement is used for soil stabilization to improve the properties of soil at subgrade and base course layers for the construction of railway track. Cement soil stabilization has improved the desired properties of soil that includes MDD, OMC and CBR of soil. In Ashraf et al. [2], experimental investigation has been carried out to find the optimum cement content for different soil samples obtained from Chittagong and achieved good results.

In Zhang and Tao. [3], they stated that stabilization of soil using cement has been carried out from early twentieth century. Any weak soil is treated with low dosages of cement to achieve required strength.

In Fauzi et al. [4], quality of subgrade will decide the pavement performance and also increases the pavement life. Soils with expansive nature known for unpredictable behavior leads to the pavement failure.

Duraisamy et al. [5] express that peat soil is viewed as unsatisfactory for supporting establishments in its common state. In any case, adjustment of soil is a huge procedure to improve the security of peat soil through blending soil in advantageous materials that have lower penetrability and lower compressibility more than soil.

Zumrawi [6] has contributed significantly to the soil's strength and stability, as well as a decrease in swelling and plasticity. Based on the findings, it is suggested that cement-fly ash admixture be considered as a viable alternative for the stabilization of expansive subgrades.

Cui et al. [7] stated that bearing ability after dynamic consolidation of the testing area is obviously increased in values, indicating that dynamic consolidation is ideal for the testing area's fly ash deposits.

In Horpibulsuk et al. [8], the TCLP results show that these stabilized materials pose no environmental risk. Furthermore, FA geopolymer can minimize heavy metal leach ability in RAP-FA blends. This study's findings support the feasibility of using RAP-FA blend.

In Saride et al. [9], RAP material in road construction has gained its prominence in recent years, using this RAP material with fly ash is suitable as a base course material.

In Tang et al. [10], adding fly ash in asphalt pavement in between subgrade and base course will increase the pavement life and reduce the distresses.

In Qamhia et al. [11], AASHTO T 135 wet-dry and AASHTO T 136 freeze-thaw durability tests were used to develop chemically stabilized QB and QB blended with recycled coarse aggregate applications. The durability study's spectrum involves evaluating both freshly prepared laboratory samples and field samples collected from previously tested test parts with APT.

In Bakare et al. [12], structural evaluation of pavement sections, made by using GSB, has given good results by using CBR test and falling weight deflectometer.

3 Materials

3.1 Materials Used

We conducted this test on clayey soil and added fly ash to this to make this soil stabilize and used materials are:

- Representative clay soil
- Fly ash

3.1.1 Representative Clay Soil

The soil used in this study has been taken from Bogaram village, which is nearby our college. The place where clayey soil is available soil is collected at a certain depth of 1 ft from ground level. The distributed soil sample is then transported to the Geotechnical Laboratory, which is in our college.

3.1.2 Fly Ash

This fly ash is added to the soil in different proportions by weight. In this study, we are adding 1, 2, 3, 4 and 5% of dry weight of soil. These proportions will give different engineering properties values.

4 Tests and Results

The following tests and analysis were carried out in the laboratory before adding fly ash.

4.1 Data Sheet of California Bearing Ratio Test (CBR)

The values are noted in Excel Sheet and drawn a graph which was shown as follows; graph represents the load values at 2.5 and 5 mm penetration (Fig. 1; Table 1).

$$\text{California bearing ratio} = \frac{\text{Test load}}{\text{Standard load}} \times 100$$

1. **2.5 mm Penetration:**

$$\text{CBR Value} = \frac{64.6}{1370} \times 100$$

$$\text{CBR VALUE} = 4.72\%$$

2. **5 mm Penetration:**

$$\text{CBR Value} = \frac{91.2}{2055} \times 100$$

$$\text{CBR VALUE} = 4.44\%$$

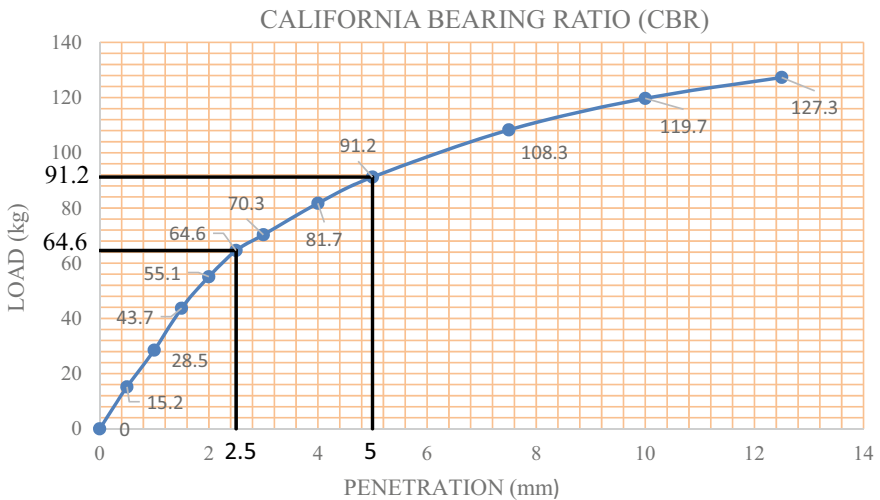


Fig.1 Test results showing CBR value

Table 1 CBR test values

S. No.	Penetration (Mm)	Dial reading	Gauge load (Kg)
1	0	0	0
2	0.5	8	15.2
3	1	15	28.5
4	1.5	23	43.7
5	2	29	55.1
6	2.5	34	64.6
7	3	37	70.3
8	4	43	81.7
9	5	48	91.2
10	7.5	57	108.3
11	10	63	119.7
12	12.5	67	127.3

The values of CBR are 4.72 and 4.44% at 2.5 and 5mm penetration.

4.2 The Following Tests and Analysis Were Carried Out in the Laboratory After Adding Fly Ash

There are two main tests to be conducted after adding fly ash. We are adding different percentages of fly ash to stabilize the soil, percentages are 1%, 2%, 3%, 4%. Concerning these percentages, the test results will change as per the condition of the soil.

4.2.1 Standard Proctor Compaction Test

After adding different proportions of fly ash, optimum moisture content and maximum dry density values will change according to the proportion. The test results after adding fly ash are determined as follows (Figs. 2 and 3; Table 2).

From the above graph, we get that MDD of soil is increased by increasing the fly ash percentage and OMC of soil is decreased by increasing the fly ash percentage.

4.2.2 California Bearing Ratio Test (CBR)

In this test, fly ash is added with different proportions 1, 2, 3, 4 and 5%. The specimens are prepared by mixing different percentages of fly ash, and then, they are kept under a CBR testing machine to determine CBR values. CBR values for soil with varying percentages of Fly ash are given as follows (Tables 3 and 4).

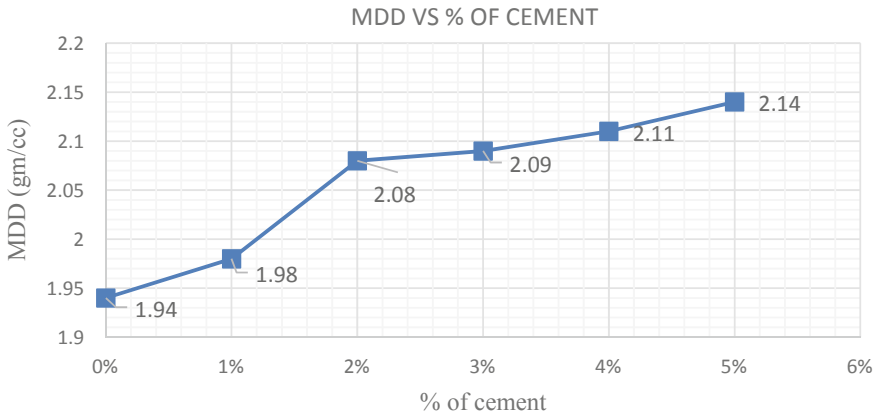


Fig. 2 Test results showing MDD versus % of fly ash

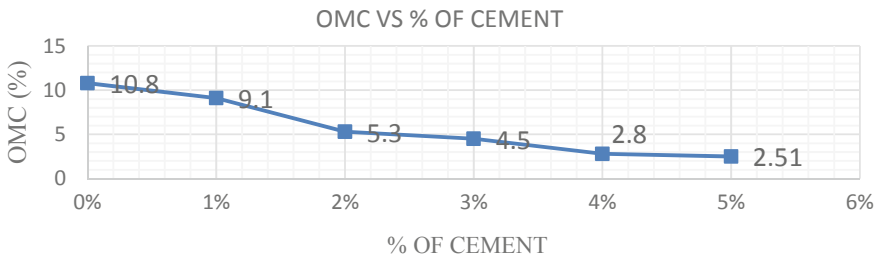


Fig. 3 Test results showing OMC versus % of fly ash

Table 2 Data sheet of MDD, OMC and % of fly ash

S. No	% of fly ash	MDD (gm/cc)	OMC (%)
1	0	1.94	10.8
2	1	1.98	9.1
3	2	2.08	5.3
4	3	2.09	4.5
5	4	2.11	2.8
6	5	2.14	2.51

Table 3 Data sheet of CBR value and % of fly ash

S. No	% of fly ash	CBR value
1	0	4.72
2	1	4.88
3	2	4.96
4	3	5.2
5	4	5.03
6	5	5.05

Table 4 Data sheet of % of fly ash MDD, OMC and CBR

S. No	% of fly ash	MDD (gm/cc)	OMC (%)
1	0	1.94	10.8
2	1	1.98	9.1
3	2	2.08	5.3
4	3	2.09	4.5
5	4	2.11	2.8
6	5	2.14	2.51

5 Conclusion

According to the results obtained, we can conclude that the stabilization of soil with fly ash has given fruitful results when compared to normal soil. Test results showed that adding 3% of fly ash as optimum percentage has showed an increase in bearing capacity of soil and also maximum dry density. This indicates that fly ash stabilized soil can be used in pavement layers to strengthen the pavement layers and it is also a good solution for dumping issues of fly ash.

References

1. Saksham S, Jagdish Y, Rajat P (2018) Analysis of stabilization of soil cement for base of railway track and sub grade. *Int J Eng Res* 6:2321–9939
2. Ali A, Rahman SS, Faruk O, Bashar A (2018) Determination of optimum cement content for stabilization of soft soil and durability analysis of soil stabilized with fly ash. *Am J Civ Eng* 6:39–43
3. Zhang Z, Tao M (2008) Durability of stabilized low plasticity soils. *J Geotech Geoenviron* 134:203–213
4. Fauzi A, Djauhari Z, Fauzi UJ (2016) Soil engineering properties improvement by utilization of cut waste plastic and crushed waste glass as additive. *IACSIT Int J Eng Technol* 8(1)
5. Duraisamy Y, Huat BBK, Aziz AA (2007) Engineering properties and compressibility behavior of tropical peat soil. *Am J Appl Sci* 4(10):768–773
6. Zumrawi MME (2015) Stabilization of pavement subgrade by using fly ash activated by cement. *Am J Civil Eng Archit* 3(6):218–224
7. Cui C, Wang S, Cui W, Zheng X (2019) Bearing behavior of the fly ash deposits on expressway. *Adv Civil Eng* 2019:11. Article ID 8450401
8. Horpibulsuk S, Hoy M, Witchayaphong P, Rachanand R, Arulrajah A (2017) Recycled asphalt pavement—fly ash geopolymer as a sustainable stabilized pavement material. *IOP Conf Ser Mater Sci Eng* 273:012005
9. Saride S, Jallu M (2020) Effect of fly ash geopolymer on layer coefficients of reclaimed asphalt pavement bases. *J Transp Eng Part B: Pavements* 146(3):04020033
10. Tang Q, Zhang Y, Gao Y (2017) Use of cement-chelated, solidified, municipal solid waste incinerator (MSWI) fly ash for pavement material: mechanical and environmental evaluations. *Can Geotech J*. <https://doi.org/10.1139/cgj-2017-0007>

11. Qamhia IIA, Tutumluer E, Ozer H, Boler H, Shoup H, Stolba AJ Durability aspects of chemically stabilized quarry by-product applications in pavement base and subbase. *Transp Res Record* 1–12. <https://doi.org/10.1177/0361198120919113>
12. Bakare MD, Pai RR, Patel S, Shahu JT Environmental sustainability by bulk utilization of fly ash and gbfs as road subbase materials. *J Hazard Toxic, Radioactive Waste*. © ASCE, ISSN 2153–5493

Author Index

A

Abdel Ghafaar, M., 689
Abinaya, K., 417
Ahmed, Koushik, 737
Ahmedov, Kh., 179
Aiswarya, M., 663, 725
Akram, P., 203, 349
Algur, Veerabhadrapa, 217
Amaresh, K., 529
Amruth, C. M., 373
Anbazhagan, V., 635
Arefin, Md. Rashedul, 737
Arunadevi, M., 337
Ayala, Luis, 253, 265, 281, 485

B

Babu, E. R., 677
Bakhodirova, Nigora K., 1
Balaji, J., 701
Banne, Shailendra P., 751
Basavaraj, Yadavalli, 187, 373
Basha, CH Hussaian, 529
Bekpulatov, J. M., 179
Berdiyarov, Bakhriddin T., 121
Bhadri, Karan, 87
Bharathi, 81
Bhattacharjee, Sushmit, 389
Bhavsar, Vaishali, 237
Bhuvanewari, V., 569
Bitla, Shreeja, 23
Bora, Urvi, 87
Bubbly, S. G., 457

C

Castillo, Jonathan, 495, 515
Chakraborty, Divyasree, 457
Chandrasekar, P., 559
Chernytska, Ilona, 787
Chinnaiyan, P., 417
Chinnannavar, Rahul Pandappa, 337

D

Dagar, Rohit, 457
Daivagna, Umesh, 217
Dhatrak, Pankaj, 87
Dhawale, Arun W., 751
Divya, T., 81
Dixit, Nitesh Kumar, 779
Dixit, Ravut, 337
Doddamani, Asifqbal M., 605
Dravid, Sampada, 503
Dutt, Mahesh, 677

F

Fernandez, Noeline B., 67
Freeda Christy, C., 811

G

Gad Allah, N., 689
Gálvez, Edelmira, 253, 265, 485, 495, 515
Geejo, Ajith, 457
George, Raji, 647
González, Javier, 253, 265, 281
González, Yessica, 495
Gottumukkala, Hema T. Raju, 167

© The Editor(s) (if applicable) and The Author(s), under exclusive license
to Springer Nature Singapore Pte Ltd. 2022

V. Bindhu et al. (eds.), *Proceedings of Fourth International Conference on Inventive
Material Science Applications*, Advances in Sustainability Science and Technology,
<https://doi.org/10.1007/978-981-16-4321-7>

Gudennavar, S. B., 457

H

Habib, Md. Rawshan, 737
 Hadkar, Sameer, 715
 Harish kumar, Mudigonda, 811
 Hemanth Kumar, J., 677
 Honnungar, Rajini V., 55
 Hussaian Basha, CH, 203, 349
 Hussain, Syed Sameer, 605

I

Idusuyi, N., 617
 Irtiqah, Syed, 765

J

Jacob, Andrews, 457
 Jagadeeswari, M., 663, 725
 Jain, Padmaja, 55
 Jaipal Reddy, M., 401
 Jammoria, Nitish Singh, 469
 Janamatti, Santosh, 217
 Jayasimha, S. L. N., 373
 Jha, Sushma, 237
 Joshi, Srujana, 87
 Joshi, Venugopal Prasanna, 337

K

Kairamkonda, Dheeraj Dhanvee, 23
 Kale, R. V., 151
 Kamal, Manshi, 9
 Karimova, Tursinoy P., 1
 Karnik, Niharika, 87
 Karthikeyan, R., 417
 Kaur, Jatinder, 141
 Keerthi Kumar, N., 187
 Kiran, Palle, 323, 361
 Kiran, Shaik Rafi, 203, 529
 Komisarenko, Olena, 787
 Kuchulakanti, Harish, 23
 Kulkarni, Atul P., 503
 Kulkarni, Omkar, 503
 Kumar, Harish, 227
 Kumar, J. Siva, 295
 Kumar, Navin, 113
 Kumar, Rajesh, 103
 Kurbet, Ramesh, 373

L

Legrá, Angel Legrá, 515

Lissa, M., 569

M

Madhavarao, S., 167
 MadhukarReddy, Y., 801
 Mahendar Reddy, N., 595
 Mallikarjun, A., 295, 401
 Manikandababu, C. S., 663, 725
 Manirajasekaran, V., 417
 Mani, Santosh, 715
 Manjula, S. H., 361
 Manju, S., 663, 725
 Mariprasath, T., 349
 Matkarimov, Sokhibjon T., 1, 121
 Matkarimov, Zaynobiddin T., 121
 Mekonnen, Seblework, 307
 Meko, Robel Legese, 307
 Melese, Bahiru, 307
 Mettu, Maheshwar Reddy, 295
 Minde, Pravin R., 441
 Mirzajonova, Saodat B., 1
 Mishra, Krishnakant, 715
 Mishra, Shweta, 779
 Money, Benson K., 389
 Monica, J., 429
 Monisha, S., 559
 Mukhametjanova, Sh. A., 179
 Mullassery, Manohar D., 67
 Mundra, Sangeeta S., 195
 Munwar, Md., 801
 Murali, M., 203, 349, 529
 Murkewar, Priya, 503

N

Nagaral, Madeva, 217
 Nageswara Rao, T., 647
 Nancy, S. Patricia, 81
 Naresh, T., 203, 349
 Nataraja, M. M., 701
 Nosirkhujayev, Sardor K., 121
 Nour, Mohamed A., 689

O

Olugasa, Temilola T., 617
 Omokayode, J. O., 617

P

Palada, Rohit Shanakar, 337
 Palma, Hugo Javier Angulo, 515
 Pande, Sachin, 605
 Panicker, Swathy S., 41

Pardeshi, Sujit S., 195
 Paul, Sriya, 457
 Pavan Kumar, B. K., 187
 Penmetsa, Ravi Varma, 167
 Pérez, Kevin, 485
 Prabhu, Srilakshmi, 457
 Prakash, C. P. S., 337
 PramodKumar, A., 801

R

Raghuvamsi Krishna, B. V., 647
 Rahman, Atikur, 765
 Raina, Ankush, 469
 Rai, Pushpendra, 715
 Rajendran, Sasireka, 131
 Rama Bhadri Raju, Ch., 167
 Ramadoss, P., 543
 Ramaiah, Gurumurthy B., 307
 Ramaswamy, Parvati, 389
 Ramdasi, Kedar, 503
 Ramesh, Gubbala V., 585, 595
 Ranjan, Mukesh, 237
 Rathinam, Vinoth, 131
 Reddy Mettu, Maheshwar, 401
 Reddy, M. Jaipal, 295
 Reddy, M. Vikranth, 295
 Reddy, N. Mahender, 585
 Rizvee, Sayad Hasan, 737
 Rodríguez, Marcelo, 485
 Rohith, G. S., 647

S

Sabry, Ibrahim, 689
 Sadashiva, K., 701
 Sadashiva, M., 429
 Saidova, Malika S., 1
 Saiteja, S., 801
 Saldaña, Manuel, 253, 265, 281
 Sandeep, M. J., 187
 Sangeetha, M., 401
 Sankar, B., 543
 Sankhe, Himank Santosh, 151
 Sankhe, Sayli, 151
 Sarawade, Pradip, 715
 Saritha, D., 585, 595
 Satish, S. V., 227
 Saynazarov, Abdukahhar M., 121
 Selvasekarapandian, 559
 Sepúlveda, Rossana, 485
 Shah, Abhijith, 151
 Shanchana, S., 81
 Sharma, Vipin Kumar, 131
 Sharma, Yogesh Koushal, 151

Shelake, Abhaysinha G., 441
 Siddesh Kumar, N. M., 429
 Singh, Namrata, 141
 Siva Kumar, J., 401
 Solomon, Eshetu, 307
 Sooraj, K. P., 237
 Soren, Shatrughan, 113
 Sreekanth, T., 401
 Sreenidhi, P. R., 41
 Srivastava, Shubham, 103
 Srivastava, Yashdeep, 389
 Subramanian, K. R. V., 647
 Suhan, Ahmed Yousuf, 737
 Sujaya, G., 635
 Surya, R., 67
 Swapno, Md. Ashiqur Rahman, 737

T

Tadesse, Kidist, 307
 Tanvir, Md Shahnewaz, 737
 Tegegne, Asmamaw, 307
 Thakur, Pankaj, 141
 Thomas, Diana, 67
 Tikotkar, Ravindra G., 605
 Titova, Nataliia, 787
 Toro, Norman, 495
 Tripathi, Deepti, 237

U

Udhayanila, S., 81
 Ul Haq, Mir Irfan, 469
 Urgellés, Alisa Lamorú, 515

V

Vadher, Abhishek, 737
 Vallinayagam, Sugumari, 131
 Varshini, P., 417
 Vattappara, Kevin, 389
 Vengadesh Krishna, M., 559
 Venkata Jyotsna, R., 559
 Vikranth Reddy, M., 401
 Vinod, K. L., 701

Y

Yadav, Dharmendra Singh, 9
 Yakubov, M. M., 179

Z

Zaitsev, Ievgev O., 787